Transactions of the ASME®

Journal of Applied Mechanics

Published Quarterly by The American Society of Mechanical Engineers

VOLUME 62 • NUMBER 2 • JUNE 1995

Technical Editor, **LEWIS T. WHEELER (1997)**

Department of Mechanical Engineering,
University of Houston,
Houston, TX 77204-4792

APPLIED MECHANICS DIVISION

Chairman, **J. W. HUTCHINSON**
Secretary, **L. ANAND**
Associate Technical Editors,
R. ABEYARATNE (1997)
T. R. AKYLAS (1997)
D. M. BARNETT (1996)
S. A. BERGER (1997)
I. M. DANIEL (1996)
W. J. DRUGAN (1997)
G. J. DVORAK (1995)
E. J. HAUG, JR. (1996)
J. T. JENKINS (1996)
S. KYRIAKIDES (1997)
S. LICHTER (1995)
W. K. LIU (1996)
X. MARKENSCOFF (1997)
D. M. PARKS (1995)
J. N. REDDY (1995)
W. N. SHARPE, JR. (1996)
S. W. SHAW (1997)
C. F. SHIH (1995)
M. SHINOZUKA (1997)
M. TAYA (1996)

BOARD ON COMMUNICATIONS

Chairman and Vice-President
R. D. ROCKE

Members-at-Large
T. BARLOW, N. H. CHAO, A. ERDMAN, G. JOHNSON, L. KEER, W. MORGAN, E. M. PATTON, S. PATULSKI, R. E. REDER, S. ROHDE, R. SHAH, F. WHITE, J. WHITEHEAD

OFFICERS OF THE ASME
President, **P. J. TORPEY**
Exec. Director
D. L. BELDEN
Treasurer
R. A. BENNETT

PUBLISHING STAFF
Mng. Dir., Publ.,
CHARLES W. BEARDSLEY
Managing Editor,
CORNELIA MONAHAN
Production Editor,
JUDITH SIERANT
Production Assistant,
MARISOL ANDINO

Transactions of the ASME, Journal of Applied Mechanics (ISSN 0021-8936) is published quarterly (Mar., June, Sept., Dec.) for $185.00 per year by The American Society of Mechanical Engineers, 345 East 47th Street, New York, NY 10017. Second class postage paid at New York, NY and additional mailing office. POSTMASTER: Send address changes to Transactions of the ASME, Journal of Applied Mechanics, c/o THE AMERICAN SOCIETY OF MECHANICAL ENGINEERS, 22 Law Drive, Box 2300, Fairfield, NJ 07007-2300.

CHANGES OF ADDRESS must be received at Society headquarters seven weeks before they are to be effective. Please send old label and new address.

PRICES: To members, $40.00, annually: to nonmembers, $185.00. Add $30.00 for postage to countries outside the United States and Canada.

STATEMENT from By-Laws. The Society shall not be responsible for statements or opinions advanced in papers or . . . printed in its publications (B7.1, Par. 3).

COPYRIGHT © 1995 by The American Society of Mechanical Engineers. Authorization to photocopy material for internal or personal use under circumstances not falling within the fair use provisions of the Copyright Act is granted by ASME to libraries and other users registered with the Copyright Clearance Center (CCC) Transactional Reporting Service provided that the base fee of $3.00 per article is paid directly to CCC, Inc., 222 Rosewood Drive Danvers, MA 01923. Request for special permission or bulk copying should be addressed to Reprints/Permission Department.

INDEXED by Applied Mechanics Reviews and Engineering Information, Inc. Canadian Goods & Services Tax Registration #126148048

TECHNICAL PAPERS

273 **Three-Dimensional Analysis of Cracking in a Multilayered Composite**
C. H. Kuo and L. M. Keer

282 **Vibration of a Three-Dimensional, FInite Linear, Elastic Solid Containing Cracks**
I. Y. Shen

289 **The Singular Stress Field of a Crack Terminating at a Frictional Interface Between Two Materials**
A. C. Wijeyewickrema, J. Dundurs, and L. M. Keer

294 **An Analytical Crack-Tip Element for Layered Elastic Structures**
B. D. Davidson, Hurang Hu, and R. A. Schapery

306 **Dislocation Inside, Outside, or on the Interface of an Anisotropic Elliptical Inclusion**
Wen J. Yen, Chyanbin Hwu, and Yin Ko Liang

312 **SH-Waves in a Medium Containing a Disordered Periodic Array of Cracks** (95-APM-4)
Y. Mikata

320 **A Statistical Approach for Fracture of Brittle Materials Based on the Chain-of-Bundles Model**
C. Ruggieri, F. Minami, and M. Toyoda

329 **Prediction of Kink Width in Compressed Fiber Composites**
N. A. Fleck, L. Deng, and B. Budiansky

338 **Initial Post-buckling Behavior of Thick Rings Under Uniform External Hydrostatic Pressure**
Lei Fu and A. M. Waas

346 **Three-Dimensional Elasticity Solution of the Buckling of Transversely Isotropic Rods: The Euler Load Revisited** (95-APM-6)
G. A. Kardomateas

356 **Rayleigh-Taylor Instability of a Cylindrical Interface Between Two Inviscid Fluids**
Rui-Qing Li and R. Harris

362 **Smooth Contact Between the Running Rayleigh Wave and a Rigid Strip**
O. Y. Zharii and A. F. Ulitko

368 **Adhesive Contact Between the Surface Wave and a Rigid Strip**
O. Y. Zharii

373 **The Theory of Torsion of Elastic Noncircular Cylinders Under Large Deformations**
L. M. Zubov and L. U. Bogashkova

380 **The Problem of Several Indentors Moving on a Viscoelastic Half-Plane** (95-APM-3)
H. Z. Fan, G. A. C. Graham, and J. M. Golden

390 **Quantitative Characterization of a Flip-Chip Solder Joint**
S. K. Patra, S. S. Sritharan, and Y. C. Lee

398 **Stability of Fiber Networks Under Biaxial Stretching**
Xiaoping Liu and R. D. James

407 **A Time Domain Substructure Synthesis Method for Viscoelastic Structures** (95-APM-2)
Duan Qian and J. S. Hansen

414 **Rotational Representation of a Plate Made of the Grioli-Toupin Material**
G. Jemielita

419 **Optimum Shapes of Elastic Solids With Infinite Branches**
G. P. Cherepanov

423 **Line Force, Charge, and Dislocation in Anisotropic Piezoelectric Composite Wedges and Spaces** (95-APM-1)
M. Y. Chung and T. C. T. Ting

429 **Critical Angles in Bending of Rotationally Inhomogeneous Elastic Wedges**
A. Yu Belov and H. O. K. Kirchner

441 **Elastothermodynamic Damping of Fiber-Reinforced Metal-Matrix Composites**
K. B. Milligan and V. K. Kinra

450 **Damage Deactivation**
N. R. Hansen and H. L. Schreyer

459 **Bending of Superelastic Wires, Part I: Experimental Aspects**
B. T. Berg

466 **Bending of Superelastic Wires, Part II: Application to Three-Point Bending**
B. T. Berg

471 **On the Ordinary, Generalized, and Pseudo-Variational Equations of Motion in Nonlinear Elasticity, Piezoelectricity, and Classical Plate Theories**
Yi-Yuan Yu

479 **Galerkin Projection for Geometrically Exact Sandwich Beams Allowing for Ply Drop-off**
Loc Vu-Quoc and H. Deng

489 **Poincare Linear Interpolated Cell Mapping: Method for Global Analysis of Oscillating Systems**
J. Levitas and T. Weller

496 **Noise-Induced Transitions in Weakly Nonlinear Oscillators Near Resonance** (95-APM-5)
R. V. Roy

(Contents continued on Outside Back Cover)

Downloaded 04 May 2010 to 171.66.16.52. Redistribution subject to ASME license or copyright; see http://www.asme.org/terms/Terms_Use.cfm

505 **Lagrange's Equations, Hamilton's Equations, and Kane's Equations: Interrelations, Energy Integrals, and a Variational Principle**
D. L. Mingori

511 **Stability of a Bicomposite Fiber Spinning Flow**
W.-S. Lee and C.-W. Park

517 ***V(z)* Curve Synthesis Using Two Ultrasonic Transducers**
M. A. Awal and T. Kundu

523 **Fractal Dimensions in Elastic-Plastic Beam Dynamics**
P. S. Symonds and J.-Y. Lee

527 **A New Perspective on the Moment Closure Method**
A. M. Hasofer and M. Grigoriu

BRIEF NOTES

Fourier Series Solution for the Dugdale Crack in a Cylindrical Shell 533
Yee-Chung Fu and C. R. Steele

On the Partly Bonded Thermoelastic Circular Inhomogeneity 535
M. A. Kattis and S. A. Meguid

Dislocation Inside an Isotropic Elliptical Inclusion Surrounded by an Anisotropic Medium 537
M. H. Santare

On the Directional Stability of a Propagating Crack 539
C. Q. Ru and R. C. Batra

540 Instability of Tangential Discontinuities in Elastic Solids
A. A. Koulakov

542 A Treatment of Internally Constrained Materials
J. Casey

544 Divergence Instability of a Spinning Disk With Axial Spindle Displacement in Contact With Evenly Spaced Stationary Springs
Jen-San Chen and Cheng-Chou Wong

547 Radial Stresses in Composite Thick-Walled Shafts
Naki Tutuncu

DISCUSSIONS

550 **Two-Dimensional Grained Composites of Extreme Rigidity, by S. Vigdergauz—Discussion by Y. Grabovsky with Author's Closure**

551 **Buckling of Composite Conical Shells, by Liyong Tong—Discussion by M. Baruch with Author's Closure**

551 **Swerve During Three-Dimensional Impact of Rough Rigid Bodies, by W. J. Stronge—Discussion by G. P. Mac Sithigh with Author's Closure**

552 **On the Geometry of Nonholonomic Dynamics, by H. Essén—Discussion by J. G. Papastavridis**

553 **Analytical Solution of Hill's Equation, by Y. Pala—Discussion by R. T. Shield**

ANNOUNCEMENTS AND SPECIAL NOTES

328 Third International Conference on Vibration Problems—Announcement

355 11th European Conference on Fracture-EFC 11—Announcement and Call for Papers

367 Symposium on Recent Developments in Elasticity—Announcement

389 Change of Address Form

495 19th International Congress of Theoretical and Applied Mechanics—Announcement

554 Worldwide Mechanics Meetings List

Inside back cover Information for Authors

ISSN 0021-8936 JOURNAL CODE JE ISSUE CODE 9502

Downloaded 04 May 2010 to 171.66.16.52. Redistribution subject to ASME license or copyright; see http://www.asme.org/terms/Terms_Use.cfm

Three-Dimensional Analysis of Cracking in a Multilayered Composite

C. H. Kuo
Assoc. Mem. ASME.

L. M. Keer
Fellow ASME.

Department of Civil Engineering,
Northwestern University,
Evanston, IL 60208

The three-dimensional problem of a multilayered composite containing an arbitrarily oriented crack is considered in this paper. The crack problem is analyzed by the equivalent body force method, which reduces the problem to a set of singular integral equations. To compute the kernels of the integral equations, the stiffness matrix for the layered medium is formulated in the Hankel transformed domain. The transformed components of the Green's functions and derivatives are determined by solving the stiffness matrix equations, and the kernels are evaluated by performing the inverse Hankel transform. The crack-opening displacements and the three modes of the stress intensity factor at the crack front are obtained by numerically solving the integral equations. Examples are given for a penny-shaped crack in a bimaterial and a three-material system, and for a semicircular crack in a single layer adhered to an elastic half-space.

Introduction

The study of defects in multilayered composites has been an area of increasing research interest due to the common use of such materials as structural components in modern mechanical systems. The strength of layered composites is enhanced through the combination of layers having various material properties, some of which may include the directional strengthening of the structure by utilization of fiber or filament reinforced layers. In tribological engineering, surface properties of machine elements, such as wear resistance and material strength versus plastic yielding or fatigue failure, can be greatly improved by depositing a protective or strengthening coating layer on the substrate (see, e.g., Chang et al., 1991; Komvopoulous et al., 1987).

Because of the mismatch of mechanical properties between dissimilar layers, the composite material may exhibit much more complicated failure modes than those associated with a homogeneous material. To investigate cracking behavior in layered composites, considerable research effort has been directed towards analyzing the stress intensity factors for cracks in a multilayered medium. Erdogan and Gupta (1971) used the Fourier transform formulation to study the plane strain and antiplane shear problems of a crack in a layered composite. Erdogan and Aksogan (1976) studied the two-dimensional problem of an arbitrarily oriented crack in bonded half-planes. Arin and Erdogan (1971, 1972) investigated the three-dimensional problems of a penny-shaped crack in an elastic layer bonded to dissimilar half-spaces and a crack in the interface between an elastic layer and a half-space. In general, the crack problems are treated by modeling the crack as distributed dislocations with unknown densities, i.e., the gradient of the crack-opening displacements. By applying the appropriate integral transform, the crack problem is reduced to a system of Cauchy singular integral equations. However, for three-dimensional problems the approach is generally limited by crack orientations in the vertical or horizontal directions and by restrictions on the crack geometry, such as penny-shaped or elliptical crack. For the general three-dimensional crack problem, Murakami and Nemat-Nasser (1982, 1983) developed the body force method to study semi-elliptical surface flaws and, subsequently, to analyze the growth of more generally shaped cracks in a half-space. The basis of the equivalent body force method is to model the crack as distributed eigenstrains where the crack problem is reduced to a set of hypersingular integral equations with unknown crack opening displacements. Lee et al. (1986) used the equivalent body force method to analyze a planar crack terminating at an interface of a two-phase material and a crack under general loading and crack orientation conditions (1987). Hanson et al. (1990) studied the three-dimensional problem of cracking through the boundary of a two-phase material. For a crack in a multilayered medium, Lin and Keer (1989) considered the axisymmetric problem of a vertical crack in a multilayered medium and presented a general formulation to determine the mode I stress intensity factors along the crack front.

Contributed by the Applied Mechanics Division of THE AMERICAN SOCIETY OF MECHANICAL ENGINEERS for publication in the ASME JOURNAL OF APPLIED MECHANICS.

Discussion on this paper should be addressed to the Technical Editor, Professor Lewis T. Wheeler, Department of Mechanical Engineering, University of Houston, Houston, TX 77204-4792, and will accepted until four months after final publication of the paper itself in the ASME JOURNAL OF APPLIED MECHANICS.

Manuscript received by the ASME Applied Mechanics Division, Dec. 1, 1992; final revision, Oct. 28, 1993. Associate Technical Editor: D. B. Bogy.

Copyright © 1995 by ASME

Downloaded 04 May 2010 to 171.66.16.28. Redistribution subject to ASME license or copyright; see http://www.asme.org/terms/Terms_Use.cfm

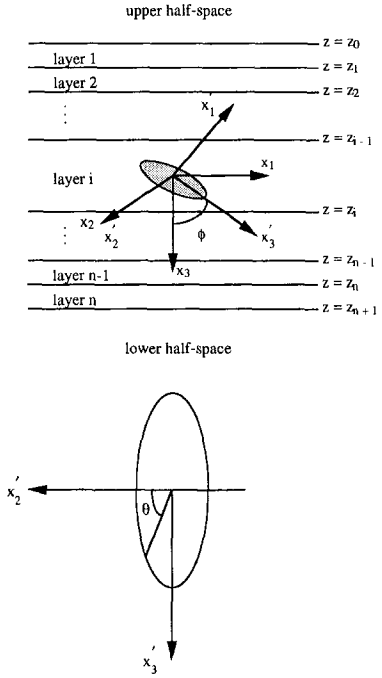

Fig. 1 Geometry and coordinate system for the three-dimensional planar crack in a multilayered medium

In the present paper, a more general three-dimensional problem of a crack in a multilayered medium under general crack geometry, orientation, and loading conditions is considered. The mathematical formulation is based on that developed by Lin and Keer (1989) and the equivalent body force method. Utilizing this approach, the crack is modeled as a distributed eigenstrain with unknown strength, and the problem is reduced to a set of two-dimensional singular integral equations. Since the Green's functions in the integral kernels cannot be expressed explicitly for the layered medium, the stiffness matrix for the layered medium is formulated by the Hankel transform. The crack-opening displacements as well as the three modes of stress intensity factors at the crack front are obtained by solving the integral equations numerically. Numerical examples are given for a penny-shaped crack embedded in bimaterial and three-material systems and for a semicircular surface crack in a single layer attached to an elastic half-space. Stress intensity factors are determined for various parameters, such as the ratio of the elastic constants of the dissimilar layers and the crack location.

Derivation of Integral Equations

Consider the three-dimensional problem of a planar crack embedded in a multilayered composite, as shown in Fig. 1. The layered medium consists of n dissimilar layers which are perfectly bonded to each other and adhere to semi-infinite solids at the upper and lower surfaces. A planar crack of arbitrary shape is embedded in the ith layer at an inclined angle ϕ. Two coordinate systems, $\mathbf{x}$ and $\mathbf{x}'$, are used to represent the global geometric coordinates and crack coordinates, respectively. The relation between the two coordinate systems is defined by the following transformation:

$$\begin{Bmatrix} e'_1 \\ e'_2 \\ e'_3 \end{Bmatrix} = \begin{bmatrix} \cos\phi & 0 & -\sin\phi \\ 0 & 1 & 0 \\ \sin\phi & 0 & \cos\phi \end{bmatrix} \begin{Bmatrix} e_1 \\ e_2 \\ e_3 \end{Bmatrix}. \quad (1)$$

The basis of the equivalent body force method is to model the crack as distributed eigenstrains, within a described domain Ω, having an unknown strength, ϵ'_{mn}. The stress disturbance created by the eigenstrains in an elastic solid may be expressed as

$$\sigma_{ij}(\mathbf{x}) = \int_\Omega C_{ijkl} C_{pqmn} \epsilon^*_{mn} \frac{\partial^2 G_{kp}(\mathbf{x}, \xi)}{\partial x_l \partial \xi_q} d\xi \quad i, j = 1,2,3 \quad (2)$$

where the Green's function $G_{ij}(\mathbf{x}, \xi)$ represents the displacement in the x_i-direction at point $\mathbf{x}$ caused by a unit body force in the x_j-direction at point ξ. Since the layers are assumed to be perfectly bonded, the continuity conditions for the displacement and stress components at the interfaces can be written as

$$u_i^j(x_1, x_2, z_j) = u_i^{j+1}(x_1, x_2, z_j) \quad i = 1,2,3 \quad (3)$$

$$\sigma_{3i}^j(x_1, x_2, z_j) = \sigma_{3i}^{j+1}(x_1, x_2, z_j) \quad i = 1,2,3 \quad (4)$$

with the conditions $u_1 = u_2 = u_3 = 0$ as $\sqrt{x_1^2 + x_2^2 + x_3^2} \to \infty$. In addition, the boundary conditions on the crack surface are described as

$$\sigma'_{1i}(0, x'_2, x'_3) = T'_i(x'_2, x'_3) \quad i = 1,2,3 \quad (x'_2, x'_3) \in D \quad (5)$$

where domain D represents the crack surface, and the applied tractions T'_i correspond to the externally applied forces on the crack surface. To express the stress field in terms of crack opening displacements, we first define the distance to the surface of inclusion Ω (cavity) in the $\pm x'_1$-direction as $\pm g$, and the maximum distance is measured by a_1. Since the crack can be considered as an ellipsoidal void by letting $a_1 \to 0$, the domain of volume integral in Eq. (2) can be reduced to a surface integral, i.e., $\Omega \to D$, and the crack-opening displacements in the limit can be extracted as $g \to 0$ (Mura, 1987)

$$b_1(\xi'_2, \xi'_3) = \int_{-g}^{g} \epsilon^{*\prime}_{11}(\xi'_1, \xi'_2, \xi'_3) d\xi'_1 \quad (6)$$

$$b_2(\xi'_2, \xi'_3) = 2\int_{-g}^{g} \epsilon^{*\prime}_{12}(\xi'_1, \xi'_2, \xi'_3) d\xi'_1 \quad (7)$$

$$b_3(\xi'_2, \xi'_3) = 2\int_{-g}^{g} \epsilon^{*\prime}_{13}(\xi'_1, \xi'_2, \xi'_3) d\xi'_1. \quad (8)$$

By equilibrating the stress components in Eq. (2) with the applied tractions on the crack surface, Eq. (5), a set of integral equations can be derived as follows:

$$T_i(x'_2, x'_3) = \int_D K_{ij}(x'_2, x'_3, \xi'_2, \xi'_3) b_j(\xi'_2, \xi'_3) d\xi'_2 \xi'_3 \quad i = 1,2,3. \quad (9)$$

The integral kernels, K_{ij}, are given as

$$K_{i1} = e_{1p} e_{iq} (A_{pq} + 2B_{pqmn} e_{1m} e_{1n}) \quad i = 1,2,3 \quad (10)$$

$$K_{ij} = e_{1p} e_{iq} B_{pqmn} (e_{jm} e_{1n} + e_{1m} e_{jn}) \quad i = 1,2,3;\ j = 2,3 \quad (11)$$

where

$$A_{ij} = \lambda^2 \delta_{ij} \frac{\partial^2 G_{kp}(\mathbf{x}, \xi)}{\partial x_k \partial \xi_p} + \lambda\mu \left(\frac{\partial^2 G_{ip}(\mathbf{x}, \xi)}{\partial x_j \partial \xi_p} + \frac{\partial^2 G_{jp}(\mathbf{x}, \xi)}{\partial x_i \partial \xi_p} \right) \quad (12)$$

$$B_{ijmn} = \lambda\mu \delta_{ij} \frac{\partial^2 G_{km}(\mathbf{x}, \xi)}{\partial x_k \partial \xi_n} + \mu^2 \left(\frac{\partial^2 G_{im}(\mathbf{x}, \xi)}{\partial x_j \partial \xi_n} + \frac{\partial^2 G_{jm}(\mathbf{x}, \xi)}{\partial x_i \partial \xi_n} \right) \quad (13)$$

and λ and μ are the Lamé constants.

Downloaded 04 May 2010 to 171.66.16.28. Redistribution subject to ASME license or copyright; see http://www.asme.org/terms/Terms_Use.cfm

Equation (9) is a set of two-dimensional integral equations with hypersingular kernels, i.e., the kernels involve the second derivatives of the Green's functions. The evaluation of the integral kernels requires computation of the Green's functions and associated derivatives. However, for the layered medium, the Green's functions, which represent the displacement field due to an applied unit point load, can only be expressed in an integral form rather than in a closed form. In the present analysis, the Green's functions are formulated by the use of Hankel transforms. The transformed components of the elastic fields due to an applied unit loading are determined by constructing the stiffness matrix for the layered medium. The Green's functions and their derivatives are computed by performing the inverse Hankel transforms.

Formulation of Layer Stiffness Matrix

Consider an elastic isotropic layer, e.g., the jth layer, $z_j \le z \le z_{j+1}$. The displacement components for isotropic materials can be expressed in terms of the Papkovich-Neuber potential functions as (Green and Zerna, 1954)

$$u_r = z\frac{\partial \Phi_r}{\partial r} + \frac{\partial \Phi_z}{\partial r} + \frac{2}{r}\frac{\partial \Phi_\theta}{\partial \theta} \tag{14}$$

$$u_\theta = -2\frac{\partial \Phi_\theta}{\partial r} + \frac{z}{r}\frac{\partial \Phi_r}{\partial \theta} + \frac{1}{r}\frac{\partial \Phi_z}{\partial \theta} \tag{15}$$

$$u_z = -\kappa \Phi_r + \frac{\partial \Phi_z}{\partial z} + z\frac{\partial \Phi_r}{\partial z} \tag{16}$$

where $\kappa = 3 - 4\nu$, and ν is the Poisson's ratio. The potential functions Φ_r, Φ_θ, and Φ_z satisfy the Laplace equation. Next, the stiffness matrix is formulated for the cases of a unit force applied in the vertical direction (axisymmetric problem) and a force applied in the horizontal direction (asymmetric problem).

(A) Axisymmetric Problem. For a point force applied in the vertical x_3-direction, the general solutions of the potential functions in the jth layer, $z_j \le z \le z_{j+1}$ can be written as (Sneddon, 1951)

$$\Phi_r = \int_0^\infty \left(A_r e^{-(z-z_j)\eta} + B_r e^{(z-z_{j+1})\eta}\right) J_0(\eta r)\, d\eta \tag{17}$$

$$\Phi_z = \int_0^\infty \left(A_z e^{-(z-z_j)\eta} + B_z e^{(z-z_{j+1})\eta}\right) J_0(\eta r)\, d\eta \tag{18}$$

and

$$\Phi_\theta = 0. \tag{19}$$

The approach used to solve the mixed boundary value problem is to find the unknown functions A_r, A_z, B_r, and B_z that satisfy the prescribed boundary conditions. From Eqs. (14)–(16) and (17)–(19), the displacement and stress components in the Hankel transformed domain can be expressed as

$$\begin{Bmatrix} U_z \\ U_r \\ S_{zz}/2\mu \\ S_{zr}/2\mu \end{Bmatrix} = \begin{bmatrix} -\eta & -\kappa - z\eta & \eta & -\kappa + z\eta \\ -\eta & -z\eta & -\eta & -z\eta \\ \eta & z\eta + 2(1-\nu) & \eta & z\eta - 2(1-\nu) \\ \eta & z\eta + 1 - 2\nu & \eta & -z\eta + 1 - 2\nu \end{bmatrix} \begin{Bmatrix} A_z e^{-(z-z_j)\eta} \\ A_r e^{-(z-z_j)\eta} \\ B_z e^{(z-z_{j+1})\eta} \\ B_r e^{(z-z_{j+1})\eta} \end{Bmatrix}. \tag{20}$$

To formulate the layer stiffness matrix, the displacement and stress vectors in the jth layer are first defined as

$$\{\mathbf{U}^j\} = \begin{Bmatrix} U_z(z_j) \\ U_r(z_j) \\ U_z(z_{j+1}) \\ U_r(z_{j+1}) \end{Bmatrix} \tag{21}$$

and

$$\{\mathbf{S}^j\} = \begin{Bmatrix} S_{zz}(z_j) \\ S_{zr}(z_j) \\ -S_{zz}(z_{j+1}) \\ -S_{zr}(z_{j+1}) \end{Bmatrix}. \tag{22}$$

The components of the displacement and stress vectors can be obtained by introducing $z = z_j$ and $z = z_{j+1}$ into Eq. (20), which are expressed as

$$\{\mathbf{U}^j\} = [\mathbf{f}^j]\{\mathbf{T}^j\} \tag{23}$$

and

$$\{\mathbf{S}^j\} = [\mathbf{g}^j]\{\mathbf{T}^j\}. \tag{24}$$

The vector $\{\mathbf{T}^j\}$ is the vector consisting of the unknown functions: A_z, A_r, B_z, B_r. By eliminating the unknown vector, $\{\mathbf{T}^j\}$, in Eqs. (23) and (24), the layer stiffness matrix can be obtained as

$$[\mathbf{k}^j] = [\mathbf{g}^j][\mathbf{f}^j]^{-1} \tag{25}$$

such that

$$\{\mathbf{S}^j\} = [\mathbf{k}^j]\{\mathbf{U}^j\}. \tag{26}$$

If a body force is applied in the layer, the displacement and stress fields in the transformed domain can be written as

$$\{\mathbf{U}^j\}_T = \{\mathbf{f}^j\}_F + \{\mathbf{U}^j\} \tag{27}$$

$$\{\mathbf{S}^j\}_T = \{\mathbf{S}^j\}_F + \{\mathbf{S}^j\}. \tag{28}$$

Here, the subscript "F" represents the elastic fields due to the body force applied in the full-space and "T" represents the total elastic fields. From Eqs. (26)–(28), the relations between the displacement and stress components are

$$[\mathbf{k}^j]\{\mathbf{U}^j\}_T = [\mathbf{k}^j]\{\mathbf{U}^j\}_F + \{\mathbf{S}^j\}_T - \{\mathbf{S}^j\}_F. \tag{29}$$

Furthermore, the transformed components of the elastic fields in a full-space due to a unit vertical point force applied in the x_3-direction are as follows:

$$U_z = C(\kappa + |x_3 - \xi_3|\eta)e^{-|x_3-\xi_3|\eta} \tag{30}$$

$$U_r = C(x_3 - \xi_3)\eta e^{-|x_3-\xi_3|\eta} \tag{31}$$

$$S_{zz} = -2\mu C\left[2(1-\nu)\mathrm{sgn}(x_3 - \xi_3) + (x_3 - \xi_3)\eta\right]e^{-|x_3-\xi_3|\eta} \tag{32}$$

$$S_{zr} = -2\mu C(1 - 2\nu + |x_3 - \xi_3|\eta)e^{-|x_3-\xi_3|\eta} \tag{33}$$

where $C = \dfrac{1}{16\pi\mu(1-\nu)}$.

Downloaded 04 May 2010 to 171.66.16.28. Redistribution subject to ASME license or copyright; see http://www.asme.org/terms/Terms_Use.cfm

(B) Asymmetric Problem. For a point load applied in the x_1-direction, the solution of the potential functions in the jth layer, $z_j \le z \le z_{j+1}$, can be expressed as

$$\Phi_r = \cos\theta \int_0^\infty \left(A_r e^{-(z-z_j)\eta} + B_r e^{(z-z_{j+1})\eta} \right) J_1(\eta r) d\eta \quad (34)$$

$$\Phi_\theta = \sin\theta \int_0^\infty \left(A_\theta e^{-(z-z_j)\eta} + B_\theta e^{(z-z_{j+1})\eta} \right) J_1(\eta r) d\eta \quad (35)$$

and

$$\Phi_z = \cos\theta \int_0^\infty \left(A_z e^{-(z-z_j)\eta} + B_z e^{(z-z_{j+1})\eta} \right) J_1(\eta r) d\eta. \quad (36)$$

Thus, the displacement and stress fields can be written as

$$\begin{Bmatrix} u_z/\cos\theta \\ u_r/\cos\theta + u_\theta/\sin\theta \\ u_r/\cos\theta - u_\theta/\sin\theta \\ \sigma_{zz}/\cos\theta \\ \sigma_{zr}/\cos\theta + \sigma_{z\theta}/\sin\theta \\ \sigma_{zr}/\cos\theta - \sigma_{z\theta}/\sin\theta \end{Bmatrix} = \int_0^\infty \begin{Bmatrix} U_z(z,\eta) J_1(z,\eta) \\ (U_r(z,\eta) + U_\theta(z,\eta)) J_2(z,\eta) \\ (U_r(z,\eta) - U_\theta(z,\eta)) J_0(z,\eta) \\ S_{zz}(z,\eta) J_1(z,\eta) \\ (S_{zr}(z,\eta) + S_{z\theta}(z,\eta)) J_2(z,\eta) \\ (S_{zr}(z,\eta) - S_{z\theta}(z,\eta)) J_0(z,\eta) \end{Bmatrix} d\eta \quad (37)$$

where the transformed components are

$$\begin{Bmatrix} U_z \\ U_r + U_\theta \\ U_r - U_\theta \\ S_{zz} \\ S_{zr} + S_{z\theta} \\ S_{zr} - S_{z\theta} \end{Bmatrix} = \begin{bmatrix} -\eta & -\kappa - z\eta & 0 & \eta & -\kappa + z\eta & 0 \\ -\eta & -z\eta & 2\eta & -\eta & -z\eta & 2\eta \\ \eta & z\eta & 2\eta & \eta & z\eta & 2\eta \\ \eta & \kappa - \beta + z\eta & 0 & \eta & \beta - \kappa + z\eta & 0 \\ \eta & \beta + z\eta & -\eta & -\eta & \beta - z\eta & \eta \\ -\eta & -\beta - z\eta & -\eta & \eta & -\beta + z\eta & \eta \end{bmatrix} \begin{Bmatrix} A_z e^{-(z-z_j)\eta} \\ A_r e^{-(z-z_j)\eta} \\ A_\theta e^{-(z-z_j)\eta} \\ B_z e^{(z-z_{j+1})\eta} \\ B_r e^{(z-z_{j+1})\eta} \\ B_\theta e^{(z-z_{j+1})\eta} \end{Bmatrix} \quad (38)$$

where $\beta = 1 - 2\nu$. Similarly, the displacement and stress vectors for the jth layer can be defined as

$$\{\mathbf{U}^j\} = \begin{Bmatrix} U_z(z_j) \\ U_r(z_j) + U_\theta(z_j) \\ U_r(z_j) - U_\theta(z_j) \\ U_z(z_{j+1}) \\ U_r(z_{j+1}) + U_\theta(z_{j+1}) \\ U_r(z_{j+1}) - U_\theta(z_{j+1}) \end{Bmatrix} \quad (39)$$

and

$$\{\mathbf{S}^j\} = \begin{Bmatrix} S_{zz}(z_j) \\ S_{zr}(z_j) \\ S_{z\theta}(z_j) \\ -S_{zz}(z_{j+1}) \\ -S_{zr}(z_{j+1}) \\ -S_{z\theta}(z_{j+1}) \end{Bmatrix}. \quad (40)$$

The stiffness matrix for the layer can be obtained by using Eqs. (25) and (26), where the matrix $[\mathbf{g}^j]$ and $[\mathbf{f}^j]$ are obtained from Eqs. (23)–(24) and (38)–(40). For a body force applied in the x_1-direction, the relations between the displacement and stress components in the transformed domain are

$$[\mathbf{k}^j]\{\mathbf{U}^j\}_T = [\mathbf{k}^j]\{\mathbf{U}^j\}_F + \{\mathbf{S}^j\}_T - \{\mathbf{S}^j\}_F \quad (41)$$

where the transformed components of the elastic fields in a full-space due to a unit point load applied in the x_1-direction are

$$\frac{U_z}{\cos\theta} = C(x_3 - \xi_3)\eta e^{-|x_3-\xi_3|\eta} \quad (42)$$

$$\frac{U_r}{\cos\theta} + \frac{U_\theta}{\sin\theta} = C(1 + |x_3 - \xi_3|\eta) e^{-|x_3-\xi_3|\eta} \quad (43)$$

$$\frac{U_r}{\cos\theta} - \frac{U_\theta}{\sin\theta} = C(7 - 8\nu - |x_3 - \xi_3|\eta) e^{-|x_3-\xi_3|\eta} \quad (44)$$

$$\frac{S_{zz}}{\cos\theta} = 2\mu C(1 - 2\nu - |x_3 - \xi_3|\eta) e^{-|x_3-\xi_3|\eta} \quad (45)$$

$$\frac{S_{zr}}{\cos\theta} + \frac{S_{z\theta}}{\sin\theta} = -2\mu C(x_3 - \xi_3)\eta e^{-|x_3-\xi_3|\eta} \quad (46)$$

$$\frac{S_{zr}}{\cos\theta} - \frac{S_{z\theta}}{\sin\theta} = 2\mu C[(x_3 - \xi_3)\eta - 4(1-\nu)\mathrm{sgn}(x_3 - \xi_3)] e^{-|x_3-\xi_3|\eta}. \quad (47)$$

Formulation of Global Stiffness Matrix

In the previous section the layer stiffness matrix, which expresses the relation of displacement and stress components in the single isotropic layer, is derived in the Hankel transformed domain. For the multilayered structure, the global stiffness matrix can be formulated by assembling each layer

Downloaded 04 May 2010 to 171.66.16.28. Redistribution subject to ASME license or copyright; see http://www.asme.org/terms/Terms_Use.cfm

matrix. For simplicity of presentation, the procedure used to derive the global stiffness matrix is described in detail only for the axisymmetric problem.

Consider two consecutive layers, layer j and layer $j+1$. From the interfacial conditions at $x_3 = z_{j+1}$, Eqs. (3) and (4), the continuity and equilibrium conditions can be expressed as

$$\begin{Bmatrix} U_z^j(z_{j+1}) \\ U_r^j(z_{j+1}) \end{Bmatrix} = \begin{Bmatrix} U_z^{j+1}(z_{j+1}) \\ U_r^j(z_{j+1}) \end{Bmatrix} \tag{48}$$

$$\begin{Bmatrix} S_{zz}^j(z_{j+1}) \\ U_{zr}^j(z_{j+1}) \end{Bmatrix} = \begin{Bmatrix} S_{zz}^{j+1}(z_{j+1}) \\ S_{zr}^j(z_{j+1}) \end{Bmatrix}. \tag{49}$$

Therefore, the displacement vector for the two consecutive layers can be assembled as

$$\{U_z(z_j),\ U_r(z_j),\ U_z(z_{j+1}),\ U_r(z_{j+1}),\ U_z(z_{j+2}),\ U_r(z_{j+2})\}_T \tag{50}$$

and the stress vector is

$$\{S_{zz}(z_j),\ S_{zr}(z_j),\ 0,\ 0,\ S_{zz}(z_{j+2}),\ S_{zr}(z_{j+2})\}_T \tag{51}$$

where subscript "T" represents the transposed vector. The stiffness matrix after assembly is

$$[\mathbf{K}] = [\mathbf{k}^j] + [\mathbf{k}^{j+1}]. \tag{52}$$

By following the procedure indicated by equations (48)–(52) for every two consecutive layers, the global matrix for the multilayered medium can be constructed. This matrix relates the displacement and stress vectors through the following equation:

$$[\mathbf{K}]\{\mathbf{U}\} = \{\mathbf{S}\} \tag{53}$$

where the vector {S} represents the transformed components of equivalent external force at the interface due to a unit point load applied in the layer. Therefore, the transformed displacement components at the interface, {U}, are determined by solving the algebraic Eq. (53) and the interior displacement field in each layer can be obtained from Eq. (23).

Numerical Analysis

The numerical approach to solve the integral Eqs. (9) is analogous to that developed by Lee et al. (1987). Since the crack-opening displacements vanish in a square root sense as the point at the crack surface approaches the crack front, more accurate results near the crack front can be obtained when the crack openings are approximated as

$$b_j(\xi_2', \xi_3') = \sqrt{2a\epsilon - \epsilon^2}\, f_j(\zeta_2', \zeta_3') \tag{54}$$

where "ϵ" is the shortest distance from the integration point to the crack boundary and "a" represents the characteristic crack length.

In order to solve the integral equations numerically, the crack surface, i.e., the domain D, is first discretized by dividing it into N triangular elements and over each element, the unknown functions $f_j(\xi_2', \xi_3')$ are assumed to be constant. The function $f_j(\xi_2', \xi_3')$ is evaluated at the center of each triangular, i.e., the collocation point of the triangular element. The integral equations are reduced to the following algebraic equations:

$$\sum_{j=1}^{3} \sum_{n=1}^{N} K_{ij}^{mn} f_j^n = T_i(\mathbf{x}'^m) \quad i = 1,2,3 \quad m = 1,2,\ldots N \tag{55}$$

where the kernel K_{ij}^{mn} is obtained by evaluating separately the kernels that represent the full-space and the layer effect. Since Eq. (9) involves a hypersingular kernel, the singular term in the integral can be extracted from the integral equation as

$$\int_D K_{ij} b_j dS = \int_D K_{ij}^F b_j dS + \int_D K_{ij}^L b_j dS \tag{56}$$

where K_{ij}^F is the full-space kernel, which contains the singular effect. The kernel $K_{ij}^L = K_{ij} - K_{ij}^F$ is a regular kernel, which represents the effect of dissimilar layers. The full-space kernels, K_{ij}^F, can be directly derived from the full-space Green's functions as

$$K_{11}^F = \frac{\mu}{\pi(\kappa+1)r^3} \tag{57}$$

$$K_{22}^F = \frac{\mu}{4\pi(\kappa+1)}\left[\frac{2(\kappa-1)}{r^3} + \frac{3(3-\kappa)(x_2'-\xi_2')^2}{r^5}\right] \tag{58}$$

$$K_{33}^F = \frac{\mu}{4\pi(\kappa+1)}\left[\frac{2(\kappa-1)}{r^3} + \frac{3(3-\kappa)(x_3'-\xi_3')^2}{r^5}\right] \tag{59}$$

$$K_{23}^F = \frac{3\mu(3-\kappa)(x_2'-\xi_2')(x_3'-\xi_3')}{4\pi(\kappa+1)r^5} \tag{60}$$

where $r^2 = (x_2' - \xi_2')^2 + (x_3' - \xi_3')^2$. The kernels involve the singularity of $O(1/r^3)$ and are defined in the sense of finite part integrals. A detailed discussion of the hypersingular integral equations that arise in general three-dimensional crack problems is given by Krishnasamy et al. (1990), and the details of numerical integrations are given by Lee et al. (1987).

For the kernel that represents the layer effect, the transformed components of derivatives associated with the Green's functions are first determined from the stiffness matrix, as described in the previous section. Then the kernels are themselves evaluated from the inverse Hankel transform, and a regular integration scheme, such as Gauss integration, is applied to perform the numerical integration of the kernels over the crack surface domain.

Results and Discussions

In the present section, three examples are considered: a penny-shaped crack in a bimaterial, a penny-shaped crack in a three-material system, and a semicircular surface crack in a layered half-space. The results are represented as the variation of the stress intensity factors, i.e., the singular stress field along the crack front. Points along the crack front are located by the angle θ between the x_2'-axis and the point of observation, as shown in Fig. 1.

Before the results are presented, we first compare the special case of a semicircular surface crack in an elastic half-space to the numerical results given by Murakami (1985) and Lee et al. (1987). Table 1 shows that the average discrepancies between the compared results are less than three percent. The results have better agreement at the deepest point (point B) than at the surface point (point A). This is due to the change of the order of the singularity at the surface, where the order of singularity is less than $O(1/2)$ of singularity elsewhere on the crack front (Benthem, 1977, 1980).

Bimaterial System. Consider a penny-shaped crack of radius c, in a two-material system which is constructed of two elastic half-spaces bonded together. The elastic constants for the two materials are denoted by μ_1 (shear modulus) and ν_1

Downloaded 04 May 2010 to 171.66.16.28. Redistribution subject to ASME license or copyright; see http://www.asme.org/terms/Terms_Use.cfm

Table 1 Stress intensity factors for semicircular surface cracks in the half-space with different crack angles

ϕ	0			15			30			45		
	present	[1]	[2]	present	[1]	[2]	present	[1]	[2]	present	[1]	[2]
$\frac{K_I^A}{\sigma_0\sqrt{\pi c}}$	0.734	0.744	0.748	0.698	0.692	0.703	0.594	0.588	0.569	0.443	0.402	0.360
$\frac{K_I^B}{\sigma_0\sqrt{\pi c}}$	0.663	0.666	0.666	0.629	0.626	0.632	0.535	0.533	0.538	0.405	0.406	0.401
$\frac{K_{II}^A}{\sigma_0\sqrt{\pi c}}$	0	0	0	−0.046	−0.035	−0.035	−0.082	−0.061	−0.058	−0.099	−0.061	−0.058
$\frac{K_{II}^B}{\sigma_0\sqrt{\pi c}}$	0	0	0	0.148	0.147	0.132	0.260	0.259	0.247	0.309	0.311	0.319
$\frac{K_{III}^A}{\sigma_0\sqrt{\pi c}}$	0	0	0	0.110	0.109	0.100	0.199	0.201	0.206	0.248	0.268	0.296

[1] Lee et al. (1987)
[2] Murakami (1985)

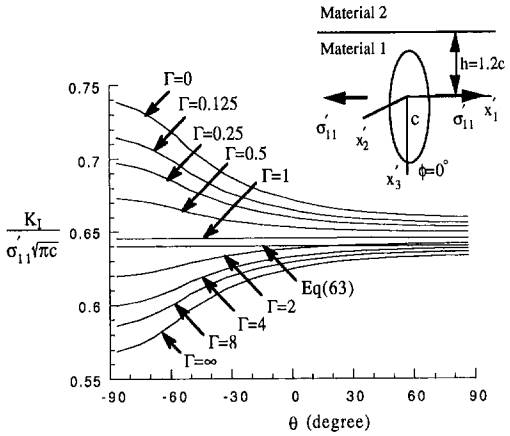

Fig. 2(a)

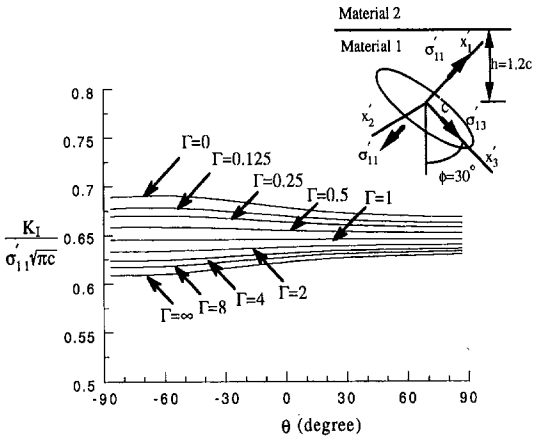

Fig. 2(b)

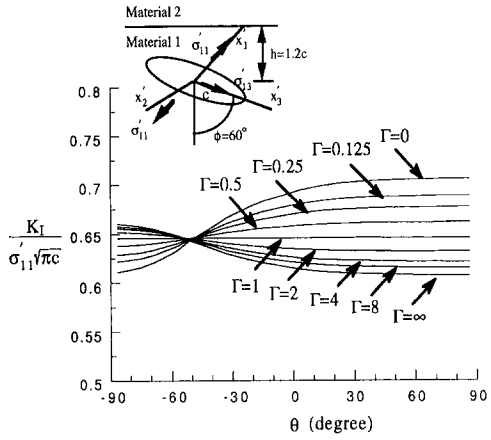

Fig. 2(c)

Fig. 2 Mode I stress intensity factors for a penny-shaped crack in the bimaterial medium with different values of Γ, $h = 1.2c$: (a) $\phi = 0$, (b) $\phi = 30$, and (c) $\phi = 60$

(Poisson's ratio) for the lower half-space and μ_2, ν_2 for the upper half-space, where the ratio of shear moduli is $\Gamma = \mu_2/\mu_1$. The center of the crack is located in the lower half-space at a distance h from the interface of the two materials. The crack is subjected to uniform tractions $\sigma'_{11} = -\cos^2\phi\sigma_0$ and $\sigma'_{13} = -\sin\phi\cos\phi\sigma_0$ applied on the crack surface. The mode I stress intensity factors are normalized with the square root of the crack radius and the normal traction across the crack face whereas the mode II and III stress intensity factors are normalized by the shear traction acting on the crack surface.

Figures 2(*a–c*) show the mode I stress intensity factors along the crack front for the crack at a depth of $h = 1.2c$ with different values of Γ and crack orientation, ϕ. The Poisson's ratio $\nu = 0.3$ is chosen for both materials. It is noted that the lines of $\Gamma = 1$ and $\Gamma = 0$ correspond, respectively, to the solutions of a penny-shaped crack in a full-space and half-space. The line, $\Gamma = \infty$, represents the crack in the lower half-space that is perfectly bonded to a rigid upper half-space. For the cases of $\phi = 0$ deg and $\phi = 30$ deg, as shown in Figs. 2(*a*) and (*b*), the mode I stress intensity factors increase for $\Gamma < 1$ and decrease for $\Gamma > 1$ as a point along the crack front approaches the interface, i.e., $\theta \to -90$ deg. For the crack in a more compliant body, $\Gamma > 1$, the crack opening is constrained by the stiffer upper half-space, and the constraint becomes more pronounced along the crack front closer to the interface. On the other hand, for $\Gamma < 1$, the crack is in a stiffer solid, and the compliant upper body tends to increase the stress intensity factors along the crack front in the stiffer solid closer to the interface. As the crack front moves away from the interface, the influence of the upper solid becomes negligible, and the stress intensity factors are virtually constants. For a large crack angle, e.g. $\phi = 60$ deg, the influence of interfacial boundary on the stress intensity factors is more uniformly distributed over the crack surface. In addition, the magnitude of applied normal tractions decreases, and the shear tractions act to partially close one half of the crack and further open the remaining half of the crack. The mode I stress intensity factor is more uniformly distributed along the crack front, as shown in Fig.

Downloaded 04 May 2010 to 171.66.16.28. Redistribution subject to ASME license or copyright; see http://www.asme.org/terms/Terms_Use.cfm

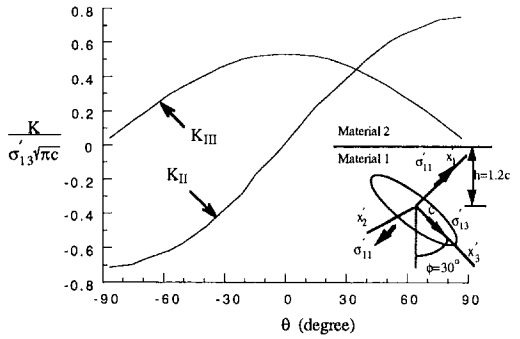

Fig. 3 Mode II and mode III stress intensity factors for a penny-shaped crack in the bimaterial medium with different values of Γ, ϕ = 30 deg, and h = 1.2c

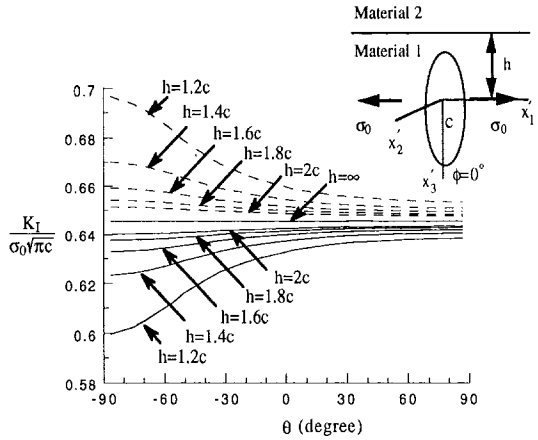

Fig. 4 Mode I stress intensity factors for a penny-shaped crack at different depths form the interface of the bimaterial medium, Γ = 4 (solid line), Γ = 0.25 (dash line), and ϕ = 0 deg

2(c), and the stress intensity factors increase for Γ < 1 as a point along the crack front moves away from the interface. For comparison, the results for identical materials (Γ = 1) are also compared with analytical solutions derived by Kassir and Sih (1966)

$$\frac{K_I}{\sigma_0\sqrt{\pi c}} = \frac{1}{E(k)}\left(\frac{x_2'^2}{a^2} + \frac{x_3'^2 a^2}{b^4}\right)^{1/4} \tag{61}$$

where E is the complete elliptic integral of the second kinds, $k = 1 - (a/b)^2$, a and b are major and minor semi-axes of the elliptical cracks. Figure 3 represents the corresponding mode II and mode III stress intensity factors for a crack with an angle ϕ = 30 deg and Γ = 4. Since the effect of the boundary on K_{II} and K_{III} is less than its effect on K_I, the stress intensity factors shown are less sensitive to the inhomogeneous effect. The effect only takes place in the local region of the crack front near the interface, in which the average discrepancies are about ten percents between two extreme cases, Γ = 0 and Γ = ∞.

To investigate the influence of upper half-space on the crack, the variation of stress intensity factors for a penny-shaped crack at different depths from the interface are shown in Fig. 4, where the solid lines represent the solutions for Γ = 4 and the dash lines for Γ = 0.25. As the crack moves away from the interface, the boundary effect becomes negligible, and the results converge to the solution of the penny-shaped crack in an infinite solid, Eq. (61).

Three Material System. Consider the case of a penny-shaped crack in the three material system, which is composed of an elastic layer of thickness 2h bounded by two semi-infinite solids at the upper and lower surfaces. The shear modulus and the Poisson's ratio are denoted as μ_1 and ν_1 for the layer and μ_2 and ν_2 for the half-spaces and the ratio of shear moduli is defined as Γ = μ_1/μ_2. The crack of radius c, subjected to uniform internal pressure, is parallel to the interface and located at the midplane of the layer. Figure 5 represents the mode I stress intensity factors as a function of layer thickness for Γ = 4, 1, and 0.25. The Poisson's ratios are $\nu_1 = \nu_2 = 0.3$, and the crack is subjected to a uniform internal pressure σ_0. The layer thickness is normalized by the radius of the crack and applied traction. It is shown that if the stiffness of the layer is less than the adjacent media, Γ < 1, the stress intensity factor is less than that corresponding to an infinite space with a penny-shaped crack, and the fracture resistance of the layer increases with decreasing layer thickness for the compliant layer bounded by stiffer media. The opposite is the case if the layer is stiffer. As the thickness increases, the solutions converge to the horizontal line, Γ = 1, which corresponds to the solution of the penny-shaped crack in a full-space.

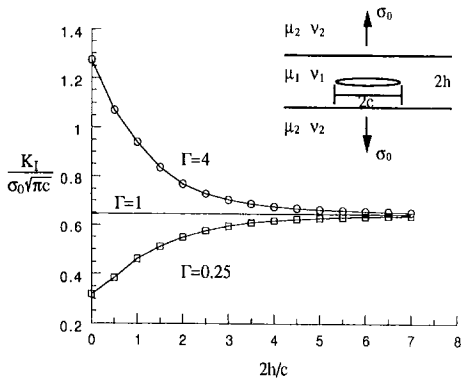

Fig. 5 Mode I stress intensity factors for a penny-shaped crack in the three-material medium as a function of layer thickness, Γ = 4 (solid line), Γ = 0.25 (dash line)

For the limiting case of $h \to 0^+$, the problem is reduced to the penny-shaped crack in a homogeneous medium, and the limit of the stress intensity factors can be derived from the continuity of strain energy release rate (Erdogan and Ozturk, 1992). The strain energy release rate for the horizontal crack in the layer is given by

$$G(h) = \frac{1-\nu_1}{2\mu_1} K_1^2(h) \tag{62}$$

with $K_{II} = K_{III} = 0$. For the crack in an infinite medium, we have

$$G_0 = \frac{1-\nu_2}{2\mu_2}\left(\frac{2}{\pi}\sigma_0\sqrt{\pi c}\right)^2. \tag{63}$$

Thus, from

$$\lim_{h\to 0^+} G(h) = G_0 \tag{64}$$

the limit of stress intensity factors can be obtained as

$$\lim_{h\to 0^+} K_I(h) = \sqrt{\frac{\mu_1(1-\nu_2)}{\mu_2(1+\nu_1)}}\,\frac{2}{\pi}\sigma_0\sqrt{\pi c}\,. \tag{65}$$

The solutions converge to $K_I/\sigma_0\sqrt{\pi c}$ = 1.2732 for Γ = 4 and $K_I/\sigma_0\sqrt{\pi c}$ = 0.3183 for Γ = 0.25.

Semicircular Surface Crack. Consider a semicircular surface crack in a layer adhered to an elastic half-space. The problem can be treated as the special case of a three-material system with the shear modulus of the upper half-space,

Downloaded 04 May 2010 to 171.66.16.28. Redistribution subject to ASME license or copyright; see http://www.asme.org/terms/Terms_Use.cfm

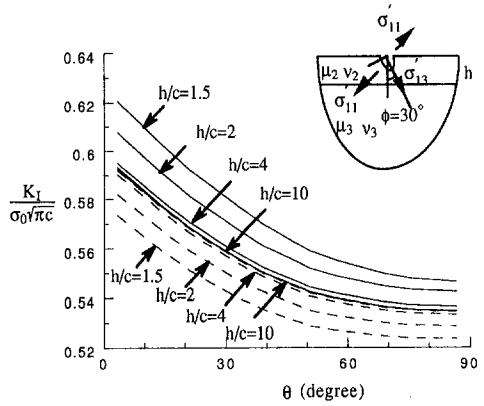

Fig. 6 Mode I stress intensity factors for a semicircular surface crack in the single layered half-space with different layer thicknesses, ϕ = 30 deg, Γ = 4 (solid line), and Γ = 0.25 (dash line)

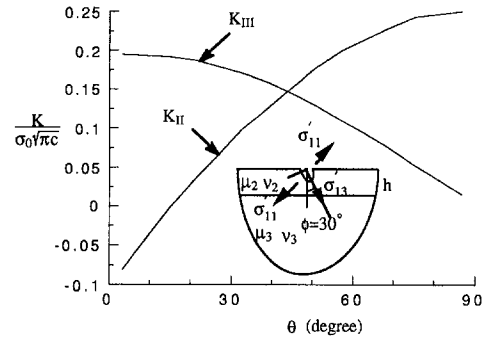

Fig. 7 Mode II and mode III stress intensity factors for a semicircular surface crack in the single layered half-space, ϕ = 30 deg, Γ = 4 and h = 1.5c

$\mu_1 = 0$. The ratio of elastic constants of the layer to the lower half-space is denoted as $\Gamma = \mu_2/\mu_3$, and the Poisson's ratio $\nu = 0.3$ are chosen for both layer and half-space.

Figure 6 shows the mode I stress intensity factors for a semicircular crack in a layer with various thicknesses for $\Gamma = 4$ and $\Gamma = 0.25$. The crack with an angle $\phi = 30$ deg is subjected to a uniform internal pressure $\sigma'_{11} = -\cos^2 \phi\sigma_0$ and shear traction $\sigma'_{13} = -\sin \phi \cos \phi\sigma_0$ on the crack surface. It is noted that the maximum mode I stress intensity factors appear to occur at the surface point, and the stress intensity factors are much smaller and uniform at the bottom part of the crack. Therefore, the cracks may expand rapidly near the surface such that the crack is more likely to growth into a shallow elliptical crack. For the case of layer stiffer than the half-space, e.g., $\Gamma = 4$, the stress intensity factors decrease with increasing layer thickness. The opposite is the case when the layer is more compliant than the substrate, e.g., $\Gamma = 0.25$. As the layer is thick enough compared to the crack size, $h/c > 4$, the boundary effect from the substrate half-space vanishes, and the stress intensity factors converge to the solution of a surface crack in the half-space composed of the layer material. Figure 7 shows the mode II and mode III stress intensity factors for $\Gamma = 4$. The effect of the substrate material on the K_{II} and K_{III} are relatively small and localized within the region of the crack front near the interface. The variations of mode I stress intensity factors for the crack in a layered half-space with different values of Γ are shown in Fig. 8. It is seen that the thin compliant layer exhibits better fracture resistance than that in the stiffer layer.

Concluding Remarks

In this paper, a general approach is developed for the three-dimensional analysis of cracks in multilayered media. A greatly reduced effort in solving the multilayered problem is achieved by formulating the stiffness matrix in the Hankel transform domain. By using appropriate weighting function representing the asymptotic behavior near the crack front, the body force method can give an accurate analysis for the crack with arbitrary shape and orientation. The variation of stress intensity factors are presented for the cracks in various layered media.

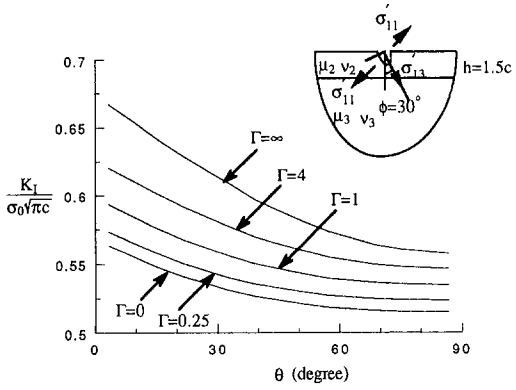

Fig. 8 Mode I stress intensity factors for a semicircular surface crack in the single layered half-space with different Γ, ϕ = 30 deg and h = 1.5c

For the crack in a bimaterial medium, it is shown that fracture resistance for the crack in a more compliant material can be enhanced by the adjacent stiffer solid, and the constraints become more pronounced as the crack is close to the interface. However, the mode II and III stress intensity factors are less sensitive to the interfacial boundary effect. For a surface crack in a layered half-space, the fracture resistance of thin compliant layer is better than that of a thin and stiff layer.

The present analysis develops a useful approach for quantifying the fracture behavior of an arbitrarily shaped crack in layered media such as ceramic coated components and articular cartilage in human joints.

Acknowledgment

The authors are grateful for support from the National Science Foundation under Grants No. BCS-9022052 and 9024671. They also acknowledge helpful advice and suggestions from Prof. J. L. Lewis of the University of Minnesota, and valuable comments from the referees.

References

Arin, K., and Erdogan, F., 1971, "Penny-Shaped Crack in an Elastic Layer Bonded to Dissimilar Half Spaces," *Int. J. of Eng. Sci.*, Vol. 9, pp. 213–232.

Arin, K., and Erdogan, F., 1972, "Penny-Shaped Interface Crack Between an Elastic Layer and A Half Space," *Int. J. of Eng. Sci.*, Vol. 10, pp. 115–125.

Benthem, J. P., 1977, "State of Stress at the Vertex of a Quarter-Infinite Crack in a Half-Space," *Int. J. Solids Structures*, Vol. 13, pp. 479–492.

Benthem, J. P., 1980, "The Quarter-Infinite Crack in a Half-Space; Alternative and Additional Solutions," *Int. J. Solids Structures*, Vol. 16, pp. 119–130.

Chang, T. P., Cheng, H. S., Chiou, W. A., and Sproul, W. D., 1991, "A Comparison of Fatigue Failure Morphology Between TiN Coated and Uncoated Lubricated Rollers," ASME *Journal of Tribology*, Vol. 34, pp. 408–410.

Erdogan, F., and Aksogan, O., 1976, "Bonded Half-Planes Containing an Arbitrarily Oriented Crack," *Int. J. of Solids and Structures*, Vol. 10, pp. 569–585.

Erdogan, F., and Gupta, G. D., 1971, "The Stress Analysis of Multi-Layered Composites with a Flaw," *Int. J. of Solids and Structures*, Vol. 7, pp. 39–61.

Erdogan, F., and Gupta, G. D., 1971, "Layered Composites with an Interface Flaw," *Int. J. of Solids and Structures*, Vol. 7, pp. 1089–1107.

Downloaded 04 May 2010 to 171.66.16.28. Redistribution subject to ASME license or copyright; see http://www.asme.org/terms/Terms_Use.cfm

Erdogan, F., and Ozturk, M., 1992, "Diffusion Problems in Bonded Nonhomogeneous Materials with an Interface Cut," *Int. J. of Eng. Sci.*, Vol. 30, pp. 1507–1523.

Green, A. E., and Zerna, W., 1954, *Theoretical Elasticity*, Oxford Univ. Press, Oxford, U.K., pp. 169–171.

Hanson, M. T., Lin, W., and Keer, L. M., 1989, "Three-Dimensional Analysis of Cracking Through the Boundary of a Two-Phase Material," ASME JOURNAL OF APPLIED MECHANICS, Vol. 56, pp. 850–857.

Kassir, M. K., and Sih, G. C., 1966, "Three-Dimensional Stress Distribution Around and Elliptical Crack Under Arbitrary Loadings," ASME JOURNAL OF APPLIED MECHANICS, Vol. 33, pp. 601–611.

Komvopoulous, K., Saka, N., and Suh, N. P., 1987, "The Role of Hard Layers in Lubricated and Dry Sliding," ASME *Journal of Tribology*, Vol. 109, pp. 223–231.

Krishnasamy, G., Schnerr, L. W., Rudolphi, T. J., and Rizzo, F. J., 1990, "Hypersingular Boundary Integral Equations: Some Applications in Acoustic and Elastic Wave Scattering," ASME JOURNAL OF APPLIED MECHANICS, Vol. 57, pp. 404–414.

Lee, J. C., Farris, T. N., and Keer, L. M., 1987, "Stress Intensity Factors for Cracks of Arbitrary Shape Near an Interfacial Boundary," *Eng. Fracture Mech.*, Vol. 27, pp. 27–41.

Lin, W., and Keer, L. M., 1989, "Analysis of a Vertical Crack in a Multilayered Medium," ASME JOURNAL OF APPLIED MECHANICS, Vol. 56, pp. 63–69.

Mura, T., 1987, *Micromechanics of Defects in Solids*, Martinus Nijhoff, The Netherlands, pp. 240–248.

Murakami, Y., and Nemat-Nasser, S., 1982, "Interacting Dissimilar Semi-Elliptical Surface Flaws under Tension and Bending," *Eng. Fracture Mech.*, Vol. 16, pp. 373–386.

Murakami, Y., and Nemat-Nasser, S., 1983, "Growth and Stability of Interacting Surface Flaws of Arbitrary Shape," *Eng. Fracture Mech.*, Vol. 17, pp. 193–210.

Murakami, Y., 1985, "Analysis of Stress Intensity Factors of Modes I, II and III for Inclined Surface Cracks of Arbitrary Shape," *Eng. Fracture Mech.*, Vol. 22, pp. 101–114.

Sneddon, I. N., 1951, *Fourier Transforms*, McGraw-Hill, New York.

Downloaded 04 May 2010 to 171.66.16.28. Redistribution subject to ASME license or copyright; see http://www.asme.org/terms/Terms_Use.cfm

Vibration of a Three-Dimensional, Finite Linear, Elastic Solid Containing Cracks[1]

I. Y. Shen
Assistant Professor,
Department of Mechanical Engineering,
University of Washington,
Seattle, WA 98195
Mem. ASME

This paper is to determine vibrational eigensolutions $[\lambda_m^2, v_m(r)]_{m=1}^{\infty}$ *of a three-dimensional, finite, linear, elastic solid* C *containing cracks in terms of crack configuration* σ_c *and eigensolutions* $[\omega_n^2, u_n(r)]_{n=1}^{\infty}$ *of a perfect elastic solid* P *without the cracks. Use of Betti reciprocal theorem and the Green's function of* P *expands* $v_m(r)$ *in terms of an infinite series of* $u_n(r)$. *Substitution of the* $v_m(r)$ *series representation into the Kamke quotient of* C *and stationarity of the quotient result in a Fredholm integral equation whose nontrivial solutions predict* λ_m^2 *and* $v_m(r)$ *of* C. *Finally, natural frequencies and mode shapes of a circular shaft of finite length containing a circumferential crack under torsional vibration are predicted through a two-term Ritz approximation of the Fredholm integral equation. The results differ significantly from those predicted by the method of flexibility matrices, when the ratio of the shaft length to the shaft radius is small.*

Introduction

Cracks usually emerge in machine structures as a result of cyclic fatigue loading. Emerging cracks will not only lower the performance of machines but subsequently will also cause sudden fracture of the machines. For example, cracks in spinning rotors will change rotor stiffness resulting in parametric resonances of the rotors (Grabowski, 1980; Mayes and Davies, 1984; Wauer, 1990). Cracks in pipes and pressure vessels can cause unexpected pressure loss resulting in shutdown of nuclear power plants (Petroski, 1983). Other examples include cracks in rolling-element bearings causing excessive rotor vibration and noise (Collacott, 1979), cracks in welding joints resulting in amplified vibration of the structure components welded to the joints (Chondros and Dimarogonas, 1980), and cracks in civil structures causing devastating damage in earthquakes.

Because occurrence of cracks will accompany changes in natural frequencies and mode shapes of a machine structure, engineers have been trying to monitor, for example, the vibration response of spinning rotors and bearings in order to detect the cracks as early as possible (Collacott, 1979; Wauer, 1990). Researchers are also developing smart structures that possess embedded sensors to detect possible internal damages (cracks) in the structures (Hickman et al., 1991; Glass and Macalow, 1991). Field engineers usually tap pipes or pressure vessels to sense existence of cracks from the echo of the tap. Even baseball players check the integrity of their bats by tapping the bats on home plate (Chang and Petroski, 1986). Successful implementation of these innovative ideas such as vibration monitoring and smart structures, however, requires a thorough understanding of how cracks will affect vibration response of a dynamical system.

Analytical, numerical, and experimental methods have been developed to predict vibration response of elastic systems containing cracks. Existing analytical methods primarily focus on vibration of simple engineering structural components with simple crack geometry. For example, Stahl and Keer (1972) study the vibration of rectangular plates with internal cracks parallel to the edges of the plates. Christides and Barr (1984, 1986) study bending and torsional vibration of an Euler-Bernoulli beam with a crack perpendicular to the beam's longitudinal axis. Shen (1993) studies antiplane strain vibration of a finite linear elastic solid containing cracks of arbitrary geometry. Another example is vibration of cracked rotors. According to a review paper by Wauer (1990), existing theories of cracked rotor vibration are one-dimensional theories assuming that planes remain planes, and can only predict vibration response of cracked rotors whose crack is perpendicular to the rotor axis. If the crack is inclined, plane cross-sections will not remain plane near the crack, and the displacement field near the crack is three-dimensional. How the orientation of an inclined crack affects vibration response

[1]Work on this paper was performed while author was an Assistant Professor at the Department of Engineering Mechanics, University of Nebraska, Lincoln, NE 68588-0347.

Contributed by the Applied Mechanics Division of THE AMERICAN SOCIETY OF MECHANICAL ENGINEERS for publication in the ASME JOURNAL OF APPLIED MECHANICS.

Discussion of this paper should be addressed to the Technical Editor, Professor Lewis T. Wheeler, Department of Mechanical Engineering, University of Houston, Houston, TX 77204-4792, and will be accepted until four months after final publication of the paper itself in the ASME JOURNAL OF APPLIED MECHANICS.

Manuscript received by the ASME Applied Mechanics Division, Feb. 2, 1993; final revision, Oct. 11, 1993. Associate Technical Editor: X. Markenscoff.

Copyright © 1995 by ASME

Downloaded 04 May 2010 to 171.66.16.28. Redistribution subject to ASME license or copyright; see http://www.asme.org/terms/Terms_Use.cfm

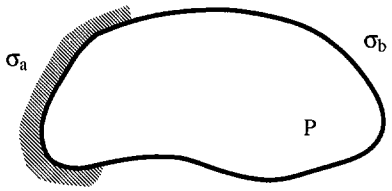

(a) A Perfect Structure P

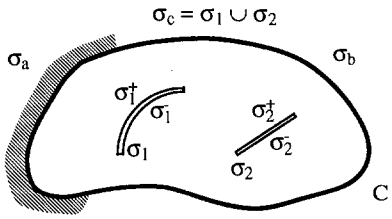

(b) A Structure C with Cracks

Fig. 1 (*a*) A perfect finite, elastic solid without cracks, and (*b*) an elastic solid containing n_c cracks

of a plate, a beam, a rotor, or a dynamical system in general remains open thus far in the literature.

Existing numerical methods primarily focus on finite element analyses (Mote, 1972; Tang and Huang, 1983; Yuen, 1985; Gounaris and Dimarogonas, 1988; Shen and Pierre, 1990). Existing experimental methods primarily focus on experimental modal analysis (Tang and Huang, 1983; Yu and Mote, 1987; Ju and Mimovitch, 1988). Both numerical and experimental methods, however, cannot describe qualitatively and quantitatively how crack location and geometry affect vibration characteristics of an elastic system.

The purpose of this paper is to develop an analytical approach to predict how cracks affect vibration response of a distributed elastic system when the cracks are introduced. To explain this objective more precisely, consider a perfect structure P with eigenvalues ω_n^2 and eigenfunctions $\mathbf{u}_n(\mathbf{r})$; see Fig. 1(*a*). When cracks σ_c emerge in P, the eigensolutions $[\omega_n^2, \mathbf{u}_n(\mathbf{r})]_{n=1}^{\infty}$ shift to $[\lambda_m^2, \mathbf{v}_m(\mathbf{r})]_{m=1}^{\infty}$. See the structure C in Fig. 1(*b*). The objective of this paper is to determine representations $f_m(\cdot)$ and $\mathbf{g}_m(\cdot)$ such that

$$\begin{cases} \lambda_m^2 = f_m(\omega_n^2, \mathbf{u}_n(\mathbf{r}); \sigma_c), \\ \mathbf{v}_m(\mathbf{r}) = \mathbf{g}_m(\omega_n^2, \mathbf{u}_n(\mathbf{r}); \sigma_c), \end{cases} \quad m, n = 1, 2, 3, \ldots \quad (1)$$

In this paper, σ_c is assumed to be traction-free as a first approximation. More sophisticated models such as opening and closing of crack faces during a load cycle (Collins et al., 1992) or friction produced during contact of crack faces will be left as future research.

This paper generalizes the approach of Shen (1993) to predict how crack location and geometry affect eigensolutions of a three-dimensional, finite linear, elastic solid. Use of Betti reciprocal theorem and the Green's function of P expands $\mathbf{v}_m(\mathbf{r})$ of C in terms of an infinite series of $\mathbf{u}_n(\mathbf{r})$ of P. Substitution of the $\mathbf{v}_m(\mathbf{r})$ series representation into the Kamke quotient of C and stationarity of the quotient result in a Fredholm integral equation whose nontrivial solutions predict λ_m^2 and $\mathbf{v}_m(\mathbf{r})$ of C. Finally, natural frequencies and mode shapes of a circular shaft of finite length containing a circumferential crack under torsional vibration are predicted through a two-term Ritz approximation of the Fredholm integral equation.

2 Formulation

Consider a three-dimensional, linear elastic solid P occupying a finite domain τ with fixed boundary σ_a and zero traction boundary σ_b. See Fig. 1(*a*). The density of P is $\rho(\mathbf{r})$ and the elastic constants are $c_{ijkl}(\mathbf{r})$ with

$$c_{ijkl}(\mathbf{r}) = c_{jikl}(\mathbf{r}) = c_{ijlk}(\mathbf{r}) = c_{klij}(\mathbf{r}). \quad (2)$$

Complex eigenfunctions $\mathbf{u}_n(\mathbf{r})$ and real eigenvalues ω_n^2 of P then satisfy

$$\boldsymbol{L}\mathbf{u}_n(\mathbf{r}) = -\omega_n^2 \rho(\mathbf{r})\mathbf{u}_n(\mathbf{r}), \quad \mathbf{r} \in \tau \quad (3)$$

with boundary conditions

$$\mathbf{u}_n(\mathbf{r}) = 0, \quad \mathbf{r} \in \sigma_a \quad (4)$$

$$\boldsymbol{T}\mathbf{u}_n(\mathbf{r}) = 0, \quad \mathbf{r} \in \sigma_b \quad (5)$$

Here $\boldsymbol{L}$ is an elasticity operator and $\boldsymbol{T}$ is a traction operator defined as

$$\boldsymbol{L} \equiv \frac{\partial}{\partial x_j}\left[c_{ijkl}(\mathbf{r})\frac{\partial}{\partial x_k}\right] \quad (6)$$

and

$$\boldsymbol{T} = n_j c_{ijkl}(\mathbf{r})\frac{\partial}{\partial x_k} \quad (7)$$

where the summation convention is used. In addition, the eigenfunctions $\mathbf{u}_n(\mathbf{r})$ also satisfy orthonormality conditions[2]

$$\int_\tau \rho(\mathbf{r})\bar{\mathbf{u}}_m(\mathbf{r}) \cdot \mathbf{u}_n(\mathbf{r})d\tau = \delta_{mn} \quad (8)$$

and

$$-\int_\tau \bar{\mathbf{u}}_m \cdot \boldsymbol{L}\mathbf{u}_n d\tau = \int_\tau W(\mathbf{u}_m, \mathbf{u}_n)d\tau = \omega_n^2 \delta_{mn} \quad (9)$$

Here the overbar denotes complex conjugation, δ_{mn} is the Kronecker delta, and $W(\cdot, \cdot)$ is a quadratic operator defined as

$$W(\mathbf{u}, \mathbf{v}) \equiv c_{ijkl}(\mathbf{r})\epsilon_{ij}(\bar{\mathbf{u}})\epsilon_{kl}(\mathbf{v}) \quad (10)$$

where $\epsilon_{ij}(\mathbf{u})$ is the infinitesimal strain field associated with $\mathbf{u}$.

Consider an elastic structure C occupying the same domain τ with n_c cracks possessing zero traction. In addition, the crack thickness is infinitesimal. See Fig. 1(*b*). Complex eigenfunctions $\mathbf{v}(\mathbf{r})$ and real eigenvalues λ^2 of C satisfy

$$\boldsymbol{L}\mathbf{v}(\mathbf{r}) = -\lambda^2 \rho(\mathbf{r})\mathbf{v}(\mathbf{r}), \quad \mathbf{r} \in \tau' \quad (11)$$

with boundary conditions

$$\mathbf{v}(\mathbf{r}) = 0, \quad \mathbf{r} \in \sigma_a \quad (12)$$

$$\boldsymbol{T}\mathbf{v}(\mathbf{r}) = 0, \quad \mathbf{r} \in \sigma_b \cup \sigma_c. \quad (13)$$

Here $\sigma_c \equiv \cup_{i=1}^{n_c}\sigma_i$, where σ_i is the boundary of the ith crack, and $\tau' \equiv \tau - \sigma_c$.

3 Eigenfunctions of C

Consider the Betti reciprocal theorem over the cracked domain τ'

$$\int_{\tau'}(\bar{\mathbf{v}} \cdot \boldsymbol{L}\mathbf{u} - \mathbf{u} \cdot \boldsymbol{L}\bar{\mathbf{v}})d\tau = \oint_{\sigma_b \cup \sigma_c}(\bar{\mathbf{v}} \cdot \boldsymbol{T}\mathbf{u} - \mathbf{u} \cdot \boldsymbol{T}\bar{\mathbf{v}})d\sigma \quad (14)$$

and

$$\int_{\tau'}(\bar{\mathbf{v}} \cdot \boldsymbol{L}\mathbf{u})d\tau = \oint_{\sigma_b \cup \sigma_c}(\bar{\mathbf{v}} \cdot \boldsymbol{T}\mathbf{u})d\sigma - \int_{\tau'} W(\mathbf{v}, \mathbf{u})d\tau \quad (15)$$

[2]The purpose of the normalizations is to normalize the *magnitude* of $\mathbf{u}_n(\mathbf{r})$ not the *dimension* of $\mathbf{u}_n(\mathbf{r})$. To obtain consistent dimensions of natural frequencies, mode shapes, and stresses throughout this paper, one should include dimensions in the normalizations and read (8) as $\int_\tau \rho(\mathbf{r})\bar{\mathbf{u}}_m(\mathbf{r}) \cdot \mathbf{u}_n(\mathbf{r})d\tau = \delta_{mn}(ML^2)$.

Downloaded 04 May 2010 to 171.66.16.28. Redistribution subject to ASME license or copyright; see http://www.asme.org/terms/Terms_Use.cfm

where $\mathbf{u}(\mathbf{r})$ and $\mathbf{v}(\mathbf{r})$ are two admissible functions satisfying $\mathbf{u}(\mathbf{r}) = 0$ and $\mathbf{v}(\mathbf{r}) = 0$ on σ_a. Let $\mathbf{v}(\mathbf{r})$ be an eigenfunction of C satisfying (11), (12), and (13). Let $\mathbf{u}(\mathbf{r})$ be the Green's function $\mathbf{G}^k(\mathbf{r}|\mathbf{r}_0)$ of P under a concentrated harmonic load $\delta(\mathbf{r} - \mathbf{r}_0)e^{i\lambda t}$ acting at $\mathbf{r}_0$ in the x_k-direction, $k = 1, 2, 3$. Therefore, $\mathbf{G}^k(\mathbf{r}|\mathbf{r}_0)$ satisfies

$$L\mathbf{G}^k(\mathbf{r}|\mathbf{r}_0) = -\rho\lambda^2\mathbf{G}^k(\mathbf{r}|\mathbf{r}_0) - \delta(\mathbf{r} - \mathbf{r}_0)\mathbf{I}_k, \quad \mathbf{r}, \mathbf{r}_0 \in \tau \tag{16}$$

with boundary conditions

$$\mathbf{G}^k(\mathbf{r}|\mathbf{r}_0) = 0, \quad \mathbf{r} \in \sigma_a, \quad \mathbf{r}_0 \in \tau \tag{17}$$

$$T\mathbf{G}^k(\mathbf{r}|\mathbf{r}_0) = 0, \quad \mathbf{r} \in \sigma_b, \quad \mathbf{r}_0 \in \tau \tag{18}$$

In Eq. (16), $\mathbf{I}_k \equiv [\delta_{1k}, \delta_{2k}, \delta_{3k}]^T$ is a column vector. In addition, $\mathbf{G}^k(\mathbf{r}|\mathbf{r}_0)$ allows an eigenfunction expansion

$$\mathbf{G}^k(\mathbf{r}|\mathbf{r}_0) = -\sum_{n=1}^{\infty} \frac{\bar{u}_n^{(k)}(\mathbf{r}_0)}{\lambda^2 - \omega_n^2}\mathbf{u}_n(\mathbf{r}) \tag{19}$$

where $\mathbf{u}_n \equiv [u_n^{(1)}, u_n^{(2)}, u_n^{(3)}]^T$. Substitute (11)–(13) and (16)–(19) into (14) to obtain

$$\mathbf{v}(\mathbf{r}) = \sum_{n=1}^{\infty} \frac{A_n}{\lambda^2 - \omega_n^2}\mathbf{u}_n(\mathbf{r}), \quad \mathbf{r} \in \tau' \tag{20}$$

where

$$A_n = \oint_{\sigma_c} T\bar{\mathbf{u}}_n(\mathbf{r}) \cdot \mathbf{v}(\mathbf{r})d\sigma \tag{21}$$

Define the following column vectors

$$T\mathbf{U}_n \equiv \left(T\mathbf{u}_n(\sigma_1^+), T\mathbf{u}_n(\sigma_2^+), \ldots, T\mathbf{u}_n(\sigma_{n_c}^+)\right)^T \tag{22}$$

and

$$\Delta\mathbf{V} \equiv \left(\Delta\mathbf{v}(\sigma_1), \Delta\mathbf{v}(\sigma_2), \ldots, \Delta\mathbf{v}(\sigma_{n_c})\right)^T \tag{23}$$

where $\Delta\mathbf{v}(\sigma_i) \equiv \mathbf{v}(\sigma_i^+) - \mathbf{v}(\sigma_i^-)$ is the opening shape of the ith crack in Fig. 1(b). In addition, define an inner product

$$\langle T\mathbf{U}_n|\Delta\mathbf{V}\rangle \equiv \sum_{i=1}^{n_c} \int_{\sigma_i^+} T\bar{\mathbf{u}}_n(\mathbf{r}) \cdot \Delta\mathbf{v}(\mathbf{r})d\sigma \tag{24}$$

Then

$$A_n = \langle T\mathbf{U}_n|\Delta\mathbf{V}\rangle. \tag{25}$$

Moreover, in case that σ_c coincides with antinodes of $\mathbf{u}_N(\mathbf{r})$, the $T\mathbf{U}_N = 0$ and $A_N = 0$. Therefore, the Nth term in (20) vanishes, and the Nth eigenvalue of P remains unchanged when the cracks σ_c are introduced.

4 Kamke Quotient of C

Consider the Kamke quotient of C

$$\lambda^2[\mathbf{v}] = \frac{I_s[\mathbf{v}]}{I_k[\mathbf{v}]} \tag{26}$$

where

$$I_k[\mathbf{v}] = \int_{\tau'} \rho(\mathbf{r})\bar{\mathbf{v}}(\mathbf{r}) \cdot \mathbf{v}(\mathbf{r})d\tau \tag{27}$$

and

$$I_s[\mathbf{v}] = \int_{\tau'} W(\mathbf{v}, \mathbf{v})d\tau \tag{28}$$

For $I_k[\mathbf{v}]$, (20) implies that

$$I_k[\mathbf{v}] = \sum_{n=1}^{\infty} \frac{|A_n|^2}{\left(\lambda^2 - \omega_n^2\right)^2} \tag{29}$$

where the orthonormality (8) has been used. For $I_s[\mathbf{v}]$, however, direct substitution of (20) into (28) does not result in an L_2 convergent series because of the discontinuity $\Delta\mathbf{v}$ across σ_c. Let $\epsilon_{ij}(\mathbf{v})$ be the infinitesimal strain field associated with $\mathbf{v}$. Decompose $\epsilon_{ij}(\mathbf{v})$ into

$$\epsilon_{ij}(\mathbf{v}) = \sum_{n=1}^{\infty} C_n\epsilon_{ij}(\mathbf{u}_n) + \phi_{ij}(\mathbf{r}), \quad \mathbf{r} \in \tau' \tag{30}$$

where $\phi_{ij}(\mathbf{r})$ is orthogonal to $\epsilon_{ij}(\mathbf{u}_n)$ through

$$\int_{\tau'} c_{ijkl}(\mathbf{r})\epsilon_{ij}(\bar{\mathbf{u}}_n)\phi_{kl}(\mathbf{r})d\tau = 0, \quad n = 1, 2, \ldots. \tag{31}$$

In addition, C_n is determined by

$$C_n = \frac{1}{\omega_n^2}\int_{\tau'} W(\mathbf{u}_n, \mathbf{v})d\tau. \tag{32}$$

Notice that both $\epsilon_{ij}(\mathbf{v})$ and $\sum_{n=1}^{\infty} C_n\epsilon_{ij}(\mathbf{u}_n)$ satisfy the compatibility equations of linear elasticity in τ'. Therefore, $\phi_{ij}(\mathbf{r})$ from (30) must satisfy the compatibility equations in τ' implying that there exists a single-valued displacement field $\mathbf{w}(\mathbf{r})$ such that

$$\phi_{ij}(\mathbf{r}) = \epsilon_{ij}(\mathbf{w}), \quad \mathbf{r} \in \tau'.$$

Hence

$$\mathbf{v}(\mathbf{r}) = \sum_{n=1}^{\infty} C_n\mathbf{u}_n(\mathbf{r}) + \mathbf{w}(\mathbf{r}), \quad \mathbf{r} \in \tau'. \tag{33}$$

To determine C_n and $\mathbf{w}(\mathbf{r})$ explicitly, $\mathbf{v}(\mathbf{r})$ is expanded as an eigenfunction series

$$\begin{aligned}\mathbf{v}(\mathbf{r}) &= \sum_{n=1}^{\infty}\left[\int_{\tau'}\rho(\mathbf{r})\bar{\mathbf{u}}_n(\mathbf{r}) \cdot \mathbf{v}(\mathbf{r})d\tau\right]\mathbf{u}_n(\mathbf{r}) \\ &= -\sum_{n=1}^{\infty}\left[\frac{1}{\omega_n^2}\int_{\tau'} L\bar{\mathbf{u}}_n(\mathbf{r}) \cdot \mathbf{v}(\mathbf{r})d\tau\right]\mathbf{u}_n(\mathbf{r}) \\ &= \sum_{n=1}^{\infty}\left[\frac{1}{\omega_n^2}\int_{\tau'} W(\mathbf{u}_n, \mathbf{v})d\tau - \frac{1}{\omega_n^2}\oint_{\sigma_c} T\bar{\mathbf{u}}_n \cdot \mathbf{v}d\sigma\right]\mathbf{u}_n(r) \\ &= \sum_{n=1}^{\infty}\left[C_n - \frac{A_n}{\omega_n^2}\right]\mathbf{u}_n(\mathbf{r}).\end{aligned} \tag{34}$$

Compare (20) and (34) to obtain

$$C_n = \frac{A_n}{\lambda^2 - \omega_n^2} + \frac{A_n}{\omega_n^2} = \frac{\lambda^2 A_n}{\omega_n^2\left(\lambda^2 - \omega_n^2\right)}. \tag{35}$$

Compare (34) with (33) to obtain

$$\mathbf{w}(\mathbf{r}) = -\sum_{n=1}^{\infty} \frac{A_n}{\omega_n^2}\mathbf{u}_n(\mathbf{r}), \quad \mathbf{r} \in \tau'. \tag{36}$$

In addition, $\sum_{n=1}^{\infty} C_n\mathbf{u}_n(\mathbf{r})$ is continuous across σ_c, because $\sum_{n=1}^{\infty} C_n\epsilon_{ij}(\mathbf{u}_n)$ converges in the L_2 sense for all $\mathbf{r} \in \tau$. Therefore, (33) implies that $\mathbf{w}(\mathbf{r})$ undergoes a discontinuity

$$\Delta\mathbf{w}(\mathbf{r}) \equiv \mathbf{w}(\sigma_c^+) - \mathbf{w}(\sigma_c^-) = \Delta\mathbf{v}(\mathbf{r}), \quad \mathbf{r} \in \sigma_c. \tag{37}$$

Substitute (33) into (28) and recall the orthonormality condition (9) and (31) to obtain

$$I_s[\mathbf{v}] = \sum_{n=1}^{\infty} \frac{\lambda^4|A_n|^2}{\omega_n^2\left(\lambda^2 - \omega_n^2\right)^2} + \|\mathbf{w}\|_W^2 \tag{38}$$

where

$$\|\mathbf{w}\|_W^2 = \int_{\tau'} W(\mathbf{w}, \mathbf{w})d\tau. \tag{39}$$

Notice that $\|\mathbf{w}\|_W^2$ is independent of λ^2. In addition, $W(\mathbf{w}, \mathbf{w})$ cannot be determined by direct differentiation of (36), be-

Downloaded 04 May 2010 to 171.66.16.28. Redistribution subject to ASME license or copyright; see http://www.asme.org/terms/Terms_Use.cfm

cause $\mathbf{w}(\mathbf{r})$ possesses the discontinuity (37) across σ_c. An analytic representation of $\|\mathbf{w}\|_W^2$ in terms of $\Delta\mathbf{v}(\mathbf{r})$ is derived in the Appendix.

5 Eigenvalues of C

Eigenvalues λ^2 of C must satisfy stationarity of the Kamke quotient (26), i.e.,

$$\delta I_s[\mathbf{v}] - \lambda^2 \delta I_k[\mathbf{v}] = \sum_{n=1}^{\infty} \frac{\lambda^2 \delta |A_n|^2}{\omega_n^2(\lambda^2 - \omega_n^2)} + \delta \|\mathbf{w}\|_W^2 = 0 \quad (40)$$

Substitute (21) into (40) and recall that $\delta\Delta\mathbf{v}$ is arbitrary on σ_c to obtain the following Fredholm integral equation:

$$\mathbf{A}(\lambda^2)\Delta\mathbf{V} \equiv \sum_{n=1}^{\infty} \frac{\lambda^2 \boldsymbol{T}\mathbf{U}_n \langle \boldsymbol{T}\mathbf{U}_n | \Delta\mathbf{V}\rangle}{\omega_n^2(\lambda^2 - \omega_n^2)} + \mathbf{R}\Delta\mathbf{V} = \mathbf{0} \quad (41)$$

Here $\mathbf{R}$ is a symmetric, positive definite operator satisfying

$$\langle \Delta\mathbf{V} | \mathbf{R}\Delta\mathbf{V}\rangle = \|\mathbf{w}\|_W^2 \quad (42)$$

Also notice that $\mathbf{A}(\lambda^2)$ is self-adjoint under the inner product defined in (24), i.e.,

$$\langle \mathbf{u} | \mathbf{A}\mathbf{v}\rangle = \langle \mathbf{A}\mathbf{u} | \mathbf{v}\rangle \quad (43)$$

for arbitrary $\mathbf{u}$ and $\mathbf{v}$ satisfying $\mathbf{u} = \mathbf{0}$ and $\mathbf{v} = \mathbf{0}$ at σ_a.

Obtaining nontrivial λ^2 and $\Delta\mathbf{V}$ from (41) is generally unwieldy, because (41) is nonlinear in λ^2. For example, (41) may or may not have nontrivial λ^2 in a given interval $[a, b]$. If it does, (41) may have multiple nontrivial λ^2 sparsely spaced in $[a, b]$ or clustered in a small subinterval of $[a, b]$. Therefore, searching nontrivial λ^2 of (41) in $[a, b]$ can be unwieldy, because an optimal step size is difficult to determine.

To overcome such problems, an algorithm that will predict nontrivial λ^2 and $\Delta\mathbf{V}$ systematically is proposed as follows. Let $\alpha(\lambda^2)$ and $\mathbf{f}(\lambda^2)$ be eigenvalues and eigenfunctions of the Fredholm operator $\mathbf{A}(\lambda^2)$ in (41), i.e.,

$$\mathbf{A}(\lambda^2)\mathbf{f}(\lambda^2) = \alpha(\lambda^2)\mathbf{f}(\lambda^2). \quad (44)$$

Comparison of (41) with (44) shows that the mth eigenvalue λ_m^2 of C is the mth zero of $\alpha(\lambda^2)$, i.e.,

$$\alpha(\lambda_m^2) = 0 \quad (45)$$

and vice versa. In addition, the mth opening shape is $\Delta\mathbf{V}_m = \mathbf{f}(\lambda_m^2)$.

6 Circular Shafts With a Circumferential Crack

This example illustrates natural frequencies and mode shapes of a circular shaft with a circumferential crack under torsional vibration as shown in Fig. 2. The circular shaft has length L, radius a, density ρ, shear modulus μ, and shear wave speed $c_2 \equiv \sqrt{\mu/\rho}$. The lateral surface $r = a$ and the two end surfaces at $x = 0$ and L are traction-free. In addition, a circumferential crack is located at $z = b$ extending from $r = c$ to $r = a$.

The corresponding circular shaft without the crack has the following normalized eigenfunctions for torsional vibration (Eringen and Suhubi, 1975)

$$\mathbf{u}_{in}(\mathbf{r}) = \left(u_{in}^{(r)}, u_{in}^{(\theta)}, u_{in}^{(z)}\right)^T \quad (46)$$

where $u_{in}^{(r)} = u_{in}^{(z)} = 0$ are the radial and the axial components of the displacement field, and $u_{in}^{(\theta)}$ is the circumferential component given by

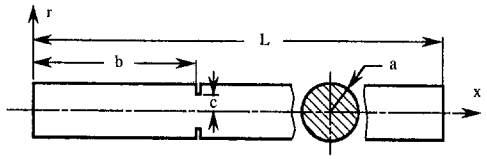

Fig. 2 A circular shaft containing a circumferential crack under torsional vibration

$$u_{in}^{(\theta)} = \begin{cases} \dfrac{2z_n r}{a\sqrt{m}} \cos\dfrac{n\pi z}{L}, & i = 0, \\ \dfrac{z_n}{K_i} J_1(\beta_i r) \cos\dfrac{n\pi z}{L}, & i = 1, 2, \ldots, \end{cases}$$

$$n = 0, 1, 2, \ldots. \quad (47)$$

Here $m \equiv \rho\pi a^2 L$ is the mass of the shaft, $K_i \equiv \sqrt{\rho\pi L \int_0^a J_1^2(\beta_i r) r dr}$, $\beta_i a \equiv \rho_i$ is the ith nontrivial root of $J_2(\rho) = 0$, and z_n is a normalization constant defined as

$$z_n = \begin{cases} \dfrac{1}{\sqrt{2}}, & n = 0 \\ 1, & n \neq 0. \end{cases} \quad (48)$$

In addition, the eigenvalues ω_{in}^2 of the circular shaft without the crack are

$$\omega_{in}^2 = c_2^2\left[\beta_i^2 + \left(\frac{n\pi}{L}\right)^2\right] = \left(\frac{c_2}{a}\right)^2\left[\rho_i^2 + n^2\pi^2\left(\frac{a}{L}\right)^2\right],$$

$$i, n = 0, 1, 2, \ldots \quad (49)$$

where $\beta_0 \equiv 0$ and $\rho_0 \equiv 0$. Moreover, the only nontrivial stress components corresponding to the eigenfunction (47) are

$$\tau_{in}^{(r\theta)} = \begin{cases} 0, & i = 0 \\ -\dfrac{\mu z_n}{K_i}\beta_i J_2(\beta_i r)\cos\dfrac{n\pi z}{L}, & i = 1, 2, \ldots \end{cases} \quad (50)$$

$$\tau_{in}^{(\theta z)} = \begin{cases} -\mu\left(\dfrac{n\pi}{L}\right)\left(\dfrac{2z_n}{a\sqrt{m}}\right) r \sin\dfrac{n\pi z}{L}, & i = 0 \\ -\mu\left(\dfrac{n\pi}{L}\right)\dfrac{z_n}{K_i} J_1(\beta_i r)\sin\dfrac{n\pi z}{L}, & i = 1, 2, \ldots \end{cases} \quad (51)$$

Also notice that $u_{0n}^{(\theta)}$ in (47) are eigenfunctions of torsional vibration derived under the mechanics of material approach assuming that $u^{(\theta)}$ is linear in r.

When the circumferential crack is introduced,

$$\sigma_c = \{(r, \theta, z) | c \le r \le a, \quad 0 \le \theta \le 2\pi, \quad z = b\}. \quad (52)$$

Hence (7) implies that

$$\boldsymbol{T}\mathbf{u}_{in} = \left(0, \tau_{in}^{(\theta z)}(r, \theta, z = b), 0\right)^T. \quad (53)$$

In addition, the crack opening shape is assumed by $\Delta\mathbf{V} \approx (0, \Delta v^{(\theta)}(r), 0)^T$. Therefore, (21) implies

Downloaded 04 May 2010 to 171.66.16.28. Redistribution subject to ASME license or copyright; see http://www.asme.org/terms/Terms_Use.cfm

$$A_{in}[\Delta v^{(\theta)}] = \begin{cases} -2\mu\pi\left(\frac{2z_n}{a\sqrt{m}}\right)\left(\frac{n\pi}{L}\right)\sin\frac{n\pi b}{L}\int_c^a r^2\Delta v^{(\theta)}(r)dr, & i=0 \\ -2\mu\pi\left(\frac{z_n}{K_i}\right)\left(\frac{n\pi}{L}\right)\sin\frac{n\pi b}{L}\int_c^a J_1(\beta_i r)\Delta v^{(\theta)}(r)rdr, & i\neq 0 \end{cases} \quad (54)$$

To determine $\|\mathbf{w}\|_W^2$, follow the procedure in the Appendix and select

$$\mathbf{p}(\mathbf{r}) = (0, p^{(\theta)}, 0)^T \quad (55)$$

where

$$p^{(\theta)} \equiv \begin{cases} \left(\frac{2z-b}{b}\right)\Delta v^{(\theta)}(r), & \frac{b}{2} \le z \le b, \quad c \le r \le a \\ 0, & \text{Otherwise} \end{cases} \quad (56)$$

Substitute (55) and (56) into (69) of the Appendix to obtain

$$\|\mathbf{w}\|_W^2 = F[\Delta v^{(\theta)}, \Delta v^{(\theta)}] \quad (57)$$

where

$$F[u, v] \equiv \frac{\mu\pi b}{3}\int_c^a r\left[\left(\frac{du}{dr} - \frac{u}{r}\right)\left(\frac{dv}{dr} - \frac{v}{r}\right) + 12\left(\frac{u}{b}\right)\left(\frac{v}{b}\right)\right]dr - \sum_{\substack{i,n=0 \\ (i,n)\neq(0,0)}}^{\infty} \frac{|B_{in}[u]B_{in}[v]|}{\omega_{in}^2} \quad (58)$$

Here

$$B_{in}[v] = -\frac{8\mu\pi z_n}{ab\sqrt{m}}\left(\cos\frac{n\pi b}{2L} - \cos\frac{n\pi b}{L}\right)\int_c^a r^2 v(r)dr \quad (59)$$

for $i = 0$,

$$B_{in}[v] = -\frac{2\mu\pi z_n}{K_i}\left\{\beta_i\left(\frac{L}{n\pi}\right)\left[\sin\frac{n\pi b}{L} + \frac{2}{b}\left(\frac{L}{n\pi}\right)\times\left(\cos\frac{n\pi b}{L} - \cos\frac{n\pi b}{2L}\right)\right]\int_c^a\left[\frac{dv}{dr} - \frac{v}{r}\right]J_2(\beta_i r)rdr - \frac{2}{b}\left(\cos\frac{n\pi b}{L} - \cos\frac{n\pi b}{2L}\right)\int_c^a v(r)J_1(\beta_i r)rdr\right\} \quad (60)$$

for $i \neq 0$ and $n \neq 0$, and

$$B_{in}[v] = -\frac{2\mu\pi z_n}{K_i}\left(\frac{b\beta_i}{4}\right)\int_c^a\left(\frac{dv}{dr} - \frac{v}{r}\right)J_2(\beta_i r)rdr \quad (61)$$

for $i \neq 0$ and $n = 0$.

A Ritz method is used to obtain approximate solutions of the Fredholm integral equation (41). Assume that

$$\Delta v^{(\theta)}(r) = \sum_{p=1}^{\infty} c_p e_p(r). \quad (62)$$

Substitute (62) into (40) and the stationarity results in

$$\mathbf{A}(\lambda^2)\mathbf{c} \equiv \left[\sum_{\substack{i,n=0 \\ (i,n)\neq(0,0)}}^{\infty} \frac{\lambda^2 \mathbf{a}_{in}\mathbf{a}_{in}^T}{\omega_{in}^2(\lambda^2 - \omega_{in}^2)} + \mathbf{Q}\right]\mathbf{c} = \mathbf{0} \quad (63)$$

where $\mathbf{a}_{in} = (A_{in}[e_1(r)], A_{in}[e_2(r)], \ldots)^T$, $\mathbf{c} = (c_1, c_2, \ldots)^T$, and $\mathbf{Q} = [Q_{ij}]$ with $Q_{ij} = F[e_i(r), e_j(r)]$.

As a numerical example, consider the cracked shaft in Fig. 2 with $L = \pi$ m, $b = 2$ m, $L/a = 5$, and $c/a = 0.5$. In addition, a two-term approximation is used with

$$e_p(r) = (r - c)^p, \quad p = 1, 2. \quad (64)$$

Moreover, the infinite series in (63) is approximated by retaining finite terms with $0 \le i \le 5$ and $0 \le n \le 115$.

Figure 3 shows eigenvalue loci $\alpha(\lambda^2)$ of $\mathbf{A}(\lambda^2)$. The vertical lines represent natural frequencies ω_{in} (divided by c_2) of the uncracked shaft given in (49). The circular points, denoting zeros of $\alpha(\lambda^2)$, will predict natural frequencies λ of the cracked shaft. The first five eigenvalues are shown in Table 1. Notice that the presence of the crack may reduce eigenvalues substantially; see the first and the fourth eigenvalues.

Figure 4 shows the first two eigenfunctions of the cracked shaft. Let r be the radial position of a longitudinal fiber of the cracked shafts. For those fibers with $r < c$, the fibers do not intersect with the crack surface; therefore, the angular displacement $v^{(\theta)}$ remains continuous. For fibers with $r > c$, the fibers penetrate through the crack surface; therefore, $v^{(\theta)}$ undergoes abrupt jumps across the crack. The jumps are characterized by continuous but steep gradients. In addition, the overshoots of $v^{(\theta)}$ near the jumps are known as the Gibb's phenomena.

Figure 5 shows variation of the first two eigenvalues of the cracked shaft with respect to the aspect ratio L/a. The thick lines and the thin lines are eigenvalues obtained through a two-term ($p = 1, 2$) and a one-term ($p = 1$) Ritz method,

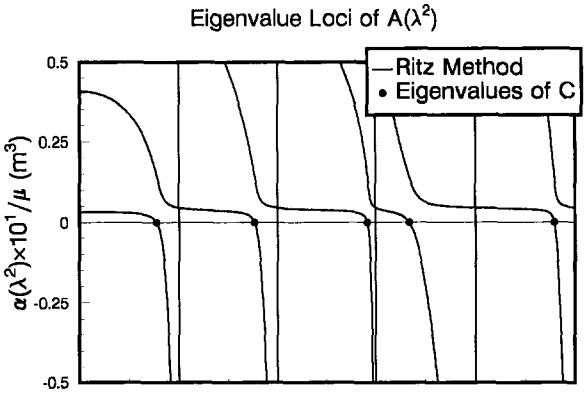

Fig. 3 Eigenvalue loci $\alpha(\lambda^2)$ of $\mathbf{A}(\lambda^2)$ for the cracked shaft with $L = \pi$ m, $b = 2$ m, $L/a = 5$, and $c/a = 0.5$

Table 1 The first five eigenvalues of a cracked shaft with $L = \pi$ m, $b = 2$ m, $L/a = 5$, and $c/a = 0.5$

Mode	ω_{in}/c_2	λ/c_2	$(\omega_{in} - \lambda)/\omega_{in}$
1	1.0000	0.7731	22.69%
2	2.0000	1.7668	11.66%
3	3.0000	2.9158	2.81%
4	4.0000	3.3368	16.58%
5	5.0000	4.7904	4.19%

Downloaded 04 May 2010 to 171.66.16.28. Redistribution subject to ASME license or copyright; see http://www.asme.org/terms/Terms_Use.cfm

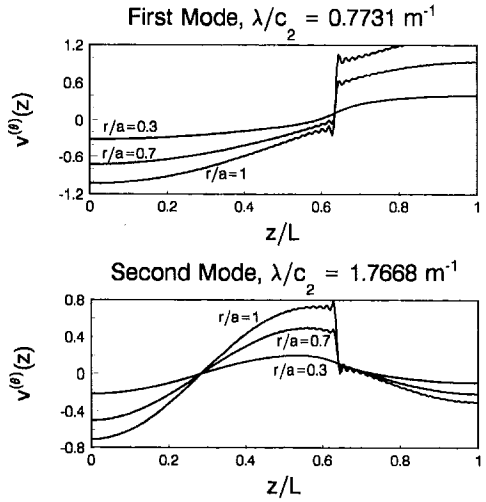

Fig. 4 First two eigenfunctions of the cracked shaft with $L = \pi$ m, $b = 2$ m, $L/a = 5$, and $c/a = 0.5$

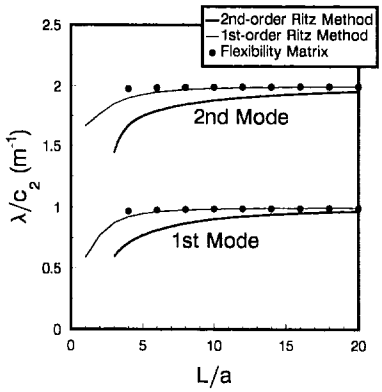

Fig. 5 Variation of the first two eigenvalues of the cracked shaft with respect to L/a

respectively. The one-term Ritz solution assumes that the crack opening shape $\Delta v^{(\theta)}(r)$ is linear in r. In addition, the infinite series in (63) is approximated by retaining finite terms with $j = 0$ and $0 \le n \le 1000$. In contrast, the two-term Ritz solution assumes that the crack opening shape $\Delta v^{(\theta)}(r)$ is quadratic in r. In addition, the infinite series in (63) is approximated by retaining finite terms with $0 \le i \le 5$ and $0 \le n \le 115$. Moreover, the circular points are eigenvalues obtained through the method of flexibility matrices by Dimarogonas and Massouros (1980). The basic idea of the method of flexibility matrices is to consider the cracked shaft as two separate shafts connected through a torsional spring at the crack. The vibration of the two separate shafts is analyzed through a "mechanics-of-materials" approach and the stiffness of the torsional spring is determined by the stress intensity factor of the crack.

According to Fig. 5, the results from the method of flexibility matrices agree very well with the one-term Ritz solutions. Nevertheless, both the one-term Ritz solution and the results from the method of flexibility matrices deviate away from the two-term Ritz solutions for small L/a. This is because the exact angular displacement $v^{(\theta)}$ of a cracked shaft under torsional vibration is not linear in r. In addition, the nonlinear radial distribution of $v^{(\theta)}$ is localized near the crack. For shafts with large L/a ratios, $v^{(\theta)}$ remains linear in r for most portions of the shafts except near the crack. As a consequence, the method of flexibility matrices and the one-term Ritz approximation, both assuming linear distribution of $v^{(\theta)}$ in r, can give satisfactory results. For shafts with small L/a ratios, the crack will result in nonlinear radial distribution of $v^{(\theta)}$ for most portions of the shafts. In this case, a two-term Ritz method should be used to obtain better approximations.

7 Conclusions

(1) This paper presents an algorithm to determine eigensolutions $[\lambda_m^2, \mathbf{v}_m(\mathbf{r})]_{m=1}^{\infty}$ of a three-dimensional, finite linear, elastic solid with cracks in terms of crack configuration σ_c and eigensolutions $[\omega_n^2, \mathbf{u}_n(\mathbf{r})]_{n=1}^{\infty}$ of a perfect elastic solid without the cracks. Eigenfunctions $\mathbf{v}(\mathbf{r})$ of the cracked solid are determined through (20). In addition, eigenvalues λ^2 and the crack-opening shape $\Delta\mathbf{v}$ are predicted through nontrivial solutions of the Fredholm integral Eq. (41).

(2) Application of this algorithm to circular shafts containing a circumferential crack under torsional vibration shows that eigenvalues of the cracked shafts are significantly lower than those predicted by the method of flexibility matrices when the shaft aspect ratio L/a is small.

References

Chang, H.-Y., and Petroski, H. J., 1986, "On Detecting a Crack by Tapping a Beam," *International Journal of Pressure Vessels and Piping*, Vol. 22, pp. 41–55.

Chondros, T. G., and Dimarogonas, A. D., 1980, "Identification of Cracks in Welded Joints of Complex Structures," *Journal of Sound and Vibration*, Vol. 69, pp. 531–538.

Christides, S., and Barr, A. D. S., 1984, "One-Dimensional Theory of Cracked Bernoulli-Euler Beams," *International Journal of Mechanical Science*, Vol. 26, pp. 639–648.

Christides, S., and Barr, A. D. S., 1986, "Torsional Vibration of Cracked Beams of Noncircular Cross-Section," *International Journal of Mechanical Science*, Vol. 28, pp. 473–490.

Collacott, R. A., 1979, *Vibration Monitoring and Diagnosis*, John Wiley and Sons, New York.

Collins, K. R., Plaut, R. H., and Wauer, J., 1992, "Free and Forced Longitudinal Vibration of a Cantilevered Bar with a Crack," ASME *Journal of Vibration and Acoustics*, Vol. 114, pp. 171–177.

Dimarogonas, A., and Massouros, G., 1980, "Torsional Vibration of a Shaft with a Circumferential Crack," *Engineering Fracture Mechanics*, Vol. 15, pp. 439–444.

Eringen, A. C., and Suhubi, E. S., 1975, *Elastodynamics, Vol. II: Linear Theory*, Academic Press, New York.

Glass, B. J., and Macalow, A., 1991, "Search-Based Model Identification of Smart-Structure Damage," *Smart Structures and Materials*, AD-Vol. 24/AMD-Vol. 123, ASME, New York, pp. 33–40.

Gounaris, G., and Dimarogonas, A., 1988, "A Finite Element of a Cracked Prismatic Beam for Structural Analysis," *Computers & Structures*, Vol. 28, pp. 309–313.

Grabowski, B., 1980, "The Vibrational Behavior of a Turbine Rotor Containing a Transverse Crack," ASME *Journal of Mechanical Design*, Vol. 102, pp. 140–146.

Hickman, G. A., Gerardi, J. J., and Feng, Y., 1991, "Application of Smart Structures to Aircraft Health Monitoring," *Journal of Intelligent Materials, Systems, and Structures*, Vol. 2, pp. 411–430.

Ju, F. D., and Mimovich, M. E., 1988, "Experimental Diagnosis of Fracture Damage in Structures by the Modal Frequency Method," ASME *Journal of Vibration, Acoustics, Stress, and Reliability in Design*, Vol. 110, pp. 456–463.

Mayes, I. W., and Davies, W. G. R., 1984, "Analysis of the Response of a Multi-Rotor-Bearing System Containing a Transverse Crack in a Rotor," ASME *Journal of Vibration, Acoustics, Stress, and Reliability in Design*, Vol. 106, pp. 139–145.

Mote, C. D., Jr., 1972, "Stability Control Analysis of Rotating Plates by Finite Element: Emphasis on Slots and Holes," ASME *Journal of Dynamic Systems, Measurement, and Control*, Vol. 22, pp. 64–70.

Petroski, H. J., 1983, "Structural Dynamics of Piping with Stable Cracks: Some Simple Models," *International Journal of Pressure Vessels and Piping*, Vol. 13, pp. 1–18.

Shen, I. Y., 1993, "Vibration of Elastic Structures With Cracks," ASME JOURNAL OF APPLIED MECHANICS, Vol. 60, pp. 414–421.

Shen, M.-H. H., and Pierre, C., 1990, "Natural Modes of Bernoulli-Euler Beams with Symmetric Cracks," *Journal of Sound and Vibration*, Vol. 138, pp. 115–134.

Stahl, B., and Keer, L. M., 1972, "Vibration and Stability of Cracked Rectangular Plates," *International Journal of Solids and Structures*, Vol. 8, pp. 69–91.

Tang, Z. Q., and Huang, T. C., 1983, "Modal Analysis of a Cylindrical Shell with a Longitudinal Crack," *Modal Testing and Model Refinement*, ASME, AMD-Vol. 59, pp. 77–84.

Wauer, Jörg, 1990, "On the Dynamics of Cracked Rotors: A Literature Survey," ASME *Applied Mechanics Review*, Vol. 43, pp. 13–17.

Downloaded 04 May 2010 to 171.66.16.28. Redistribution subject to ASME license or copyright; see http://www.asme.org/terms/Terms_Use.cfm

Yu, R. C., and Mote, C. D., Jr., 1987, "Vibration and Parametric Excitation in Asymmetric Circular Plates Under Moving Loads," *Journal of Sound and Vibration*, Vol. 119, pp. 409–427.

Yuen, M. M. F., 1985, "A Numerical Study of the Eigenparameters of a Damaged Cantilever," *Journal of Sound and Vibration*, Vol. 103, pp. 301–310.

APPENDIX

Evaluation of $\|\mathbf{W}\|_W^2$

The purpose of this Appendix is to derive an explicit formula to represent $\|\mathbf{w}\|_W^2$ in terms of $\Delta\mathbf{v}(\mathbf{r})$. Consider any piecewise continuous function $\mathbf{p}(\mathbf{r})$, $\mathbf{r} \in \tau'$, satisfying

$$\Delta\mathbf{p}(\mathbf{r}) = \Delta\mathbf{v}(\mathbf{r}), \quad \mathbf{r} \in \sigma_c \tag{65}$$

and the boundary condition

$$\mathbf{p}(\mathbf{r}) = \mathbf{0}, \quad \mathbf{r} \in \sigma_a. \tag{66}$$

Expand $\mathbf{p}(\mathbf{r})$, through a derivation similar to (34), to obtain

$$\mathbf{p}(\mathbf{r}) = \sum_{n=1}^{\infty} \left[\int_{\tau'} \rho(\mathbf{r})\mathbf{p}(\mathbf{r}) \cdot \bar{\mathbf{u}}_n(\mathbf{r}) d\tau\right] \mathbf{u}_n(\mathbf{r}) = \mathbf{w}(\mathbf{r}) + \sum_{n=1}^{\infty} \frac{B_n}{\omega_n^2} \mathbf{u}_n(\mathbf{r}) \tag{67}$$

where $\mathbf{w}(\mathbf{r})$ is given in (36) and

$$B_n = \int_{\tau'} W(\mathbf{u}_n, \mathbf{p}) d\tau \tag{68}$$

Substitute (67) into (39) and recall (9) and (68) to obtain

$$\|\mathbf{w}\|_W^2 = \int_{\tau'} W(\mathbf{p}, \mathbf{p}) d\tau - \sum_{n=1}^{\infty} \frac{|B_n|^2}{\omega_n^2} \tag{69}$$

$\|\mathbf{w}\|_W^2$ can be determined explicitly, if the geometry of σ_c is given explicitly. Let ξ_i, η_i, and ζ_i be a convenient set of coordinates associated with the ith crack σ_i. In addition, let the crack σ_i be on the ξ_i-η_i plane. Let $\mathbf{p}(\mathbf{r})$ be chosen as

$$\mathbf{p}(\mathbf{r}) = \sum_{i=1}^{n_c} \mathbf{p}_i[\Delta\mathbf{v}(\sigma_i)]. \tag{70}$$

Here

$$\mathbf{p}_i[\Delta\mathbf{v}(\sigma_i)] \equiv \begin{cases} \Delta\mathbf{v}(\xi_i, \eta_i)\left[1 - \dfrac{\zeta_i}{\zeta_i^+(\xi_i, \eta_i)}\right]; & (\xi_i, \eta_i, \zeta_i) \in \tau_i \\ 0; & \text{Otherwise} \end{cases} \tag{71}$$

where $\tau_i \equiv \{(\xi_i, \eta_i, \zeta_i) | 0 < \zeta_i < \zeta_i^+(\xi_i, \eta_i)\} \subset \tau'$. In addition, $\tau_1, \tau_2, \ldots, \tau_{n_c}$ are disconnected. Therefore, $\mathbf{p}(\mathbf{r})$ satisfies (65) and (66). Substitution of (71) into (69) yields an explicit representation of $\|\mathbf{w}\|_W^2$ in terms of $\Delta\mathbf{V}(\xi, \eta)$.

Downloaded 04 May 2010 to 171.66.16.28. Redistribution subject to ASME license or copyright; see http://www.asme.org/terms/Terms_Use.cfm

A. C. Wijeyewickrema

J. Dundurs
Fellow ASME.

L. M. Keer
Fellow ASME.

Department of Civil Engineering,
Northwestern University,
Evanston, IL 60208

The Singular Stress Field of a Crack Terminating at a Frictional Interface Between Two Materials

The problem of a crack terminating at an interface between two materials which is governed by Coulomb's law of friction is studied using Mellin integral transforms. Depending on the relative slip directions of the two wedges that are created by the crack, both the case of the two wedges moving in opposite directions and that of the two wedges moving in the same direction are treated. The characteristic equations which yield the order of the crack-tip singularity are obtained in terms of the Dundurs constants, the inclination of the crack and the coefficient of friction. For the special case when the crack is perpendicular to the interface and the two wedges slip in opposite directions, it is shown that the problem decouples into mode I (symmetric) and mode II (antisymmetric) cracks, and numerical results are presented for this case.

Introduction

The multiple matrix fracture of brittle matrix fiber-reinforced composites under longitudinal tensile loading has been observed in many experimental investigations (Evans and Marshall 1989; Lee and Daniel 1992). In most theoretical investigations of fiber-reinforced composites the well-known concentric circular cylinders model first proposed by Hill (1964) is used. When orthogonal annular cracks surrounding fibers are considered an integral equation formulation makes use of Love's stress functions (Wijeyewickrema et al., 1991). The general form of the integral equation obtained is

$$\frac{1}{\pi}\int_c^d \left\{\frac{1}{t-r} + k(r,t)\right\}\phi(t)dt = -p(r), \quad c < r < d \quad (1)$$

where the unknown $\phi(t)$ is related to the crack-opening displacement, $p(r)$ is the crack face applied pressure, and the limits of integration c and d are the inner and outer radii of the annular crack. The kernel $k(r, t)$ consists of an infinite integral $k_2(r, t)$ of the form $\int_0^\infty \bar{k}_2\,(r, t, s)\,ds$ among other terms. The crack tip has the well-known square-root singularity and $k(r, t)$ is bounded when the inner crack front is away from the interface, but the singularity depends on the material properties of the matrix and fiber and the interfacial bonding conditions, and $k(r, t)$ is no longer bounded when the inner crack front is at the interface. The characteristic equation to determine the crack-tip singularity is obtained by first carrying out an asymptotic analysis of $\bar{k}_2(r, t, s)$ for large values of s followed by using the function theoretic methods of Muskhelishvili (1953) on the dominant part of the singular integral equation.

A check on the characteristic equation obtained in the axisymmetric case is that it should be identical to that of the analogous plane-strain case. When a fully bonded interface was considered by Wijeyewickrema et al. (1991), the characteristic equation was shown to agree with the plane-strain case studied by Zak and Williams (1963), Bogy (1971), and Erdogan, Gupta, and Cook (1973). For the case of a crack terminating at a slipping interface, it was shown by Wijeyewickrema and Keer (1993) that the characteristic equation agreed with that of Gharpuray et al. (1991). In the present investigation a singularity analysis of a crack terminating at an interface governed by Coulomb's friction law is considered, the motivation being that this solution will be of importance when the related fiber-reinforced composite problem is considered.

In general, the methods used in singularity analyses of this kind are the separation of variables associated with Airy stress functions, complex potentials, or Mellin integral transforms. The related problems of a crack tip terminating at a well bonded interface was studied by Bogy (1971) and that of a slipping interface by Gharpuray et al. (1991).

Formulation of the Problem

The two half-planes with different elastic constants are shown in Fig. 1 where the crack terminating at the frictional interface is located in the upper half-plane and makes an angle γ with the positive x-axis. The upper half-plane can also be visualized as two planar wedges pressed against the lower half-plane. The following two configurations are investigated in the present analysis.

Contributed by the Applied Mechanics Division of THE AMERICAN SOCIETY OF MECHANICAL ENGINEERS for publication in the ASME JOURNAL OF APPLIED MECHANICS.

Discussion on this paper should be addressed to the Technical Editor, Professor Lewis T. Wheeler, Department of Mechanical Engineering, University of Houston, Houston, TX 77204-4792, and will be accepted until four months after final publication of the paper itself in the ASME JOURNAL OF APPLIED MECHANICS.

Manuscript received by the ASME Applied Mechanics Division, Jan. 19, 1993; final revision, July 15, 1993. Associate Technical Editor: X. Markenscoff.

Copyright © 1995 by ASME

Downloaded 04 May 2010 to 171.66.16.28. Redistribution subject to ASME license or copyright; see http://www.asme.org/terms/Terms_Use.cfm

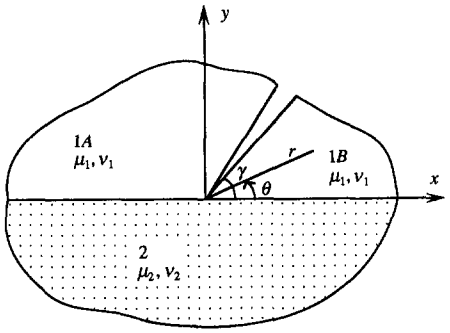

Fig. 1 A crack terminating at a frictional material interface

Case I: The two wedges slip in opposite directions.

Case II: The two wedges slip in the same direction.

The Mellin transform method used by Bogy (1968, 1971) is adopted in the present study. The singular nature of the crack-tip stresses depends on the system of simultaneous equations associated with the interfacial and boundary conditions. Let Δ be the characteristic determinant and B the coefficient matrix of this system of equations.

The order of the singularities in the stresses for $r \to 0$ are (Dempsey and Sinclair 1979, 1981)

$$\sigma_{ij} = \begin{cases} O(r^{p-1}) \text{ when } p \text{ is a zero of } \Delta,\ p \text{ is real, and } 0 < p < 1; \\ O\left[r^{\xi-1}\cos(\eta \log r)\right] \text{ or } O\left[r^{\xi-1}\sin(\eta \log r)\right] \text{ when } p \text{ is a zero of } \Delta,\ p = \xi + i\eta \text{ is complex, and } 0 < \xi < 1; \\ O(r^{p-1}\log r) \text{ when } p \text{ is such that rank } B = m < 12,\ \partial^{12-m}\Delta/\partial p^{12-m} = 0,\ p \text{ is real, and } 0 < p < 1; \\ O\left[r^{\xi-1}\log r\cos(\eta \log r)\right] \text{ or } O\left[r^{\xi-1}\log r\sin(\eta \log r)\right] \text{ when } p \text{ is such that rank } B = m < 12, \\ \partial^{12-m}\Delta/\partial p^{12-m} = 0,\ p = \xi + i\eta \text{ is complex, and } 0 < \xi < 1; \\ O(\log r) \text{ when there are no zeros of } \Delta \text{ in } 0 < \mathrm{Re}(p) < 1,\ p = 1 \text{ is a zero of } \Delta, \text{ and } \partial\Delta/\partial p = 0 \text{ at } p = +1; \\ O(1) \text{ when there are no zeros of } \Delta \text{ in } 0 < \mathrm{Re}(p) < 1, \text{ and } \partial\Delta/\partial p \neq 0 \text{ at } p = 1. \end{cases} \quad (2)$$

Here $p = -(s + 1)$, where s is the Mellin transform variable. It is noted that the zero of Δ with the smallest real part dominates the asymptotic expansion of the stress σ_{ij}.

Case I: The Two Wedges Slip in Opposite Directions. When the two top wedges slip in opposite directions (Figs. 2(a) and 2(b)) the conditions at the interface are

$$u_\theta^{1A}(r,-\pi) = u_\theta^2(r,-\pi) \quad (3)$$

$$\sigma_{r\theta}^{1A}(r,-\pi) = \sigma_{r\theta}^2(r,-\pi) \quad (4)$$

$$\sigma_{\theta\theta}^{1A}(r,-\pi) = \sigma_{\theta\theta}^2(r,-\pi) \le 0 \quad (5)$$

$$\sigma_{r\theta}^{1A}(r,-\pi) = +f\sigma_{\theta\theta}^{1A}(r,-\pi) \quad (6)$$

$$u_\theta^{1B}(r,0) = u_\theta^2(r,0) \quad (7)$$

$$\sigma_{r\theta}^{1B}(r,0) = \sigma_{r\theta}^2(r,0) \quad (8)$$

$$\sigma_{\theta\theta}^{1B}(r,0) = \sigma_{\theta\theta}^2(r,0) \le 0 \quad (9)$$

$$\sigma_{r\theta}^{1B}(r,0) = -f\sigma_{\theta\theta}^{1B}(r,0) \quad (10)$$

and the crack face boundary conditions are

$$\sigma_{r\theta}^{1B}(r,\gamma) = S_1(r), \quad \sigma_{\theta\theta}^{1B}(r,\gamma) = N_1(r) \quad (11)$$

$$\sigma_{r\theta}^{1A}(r,\gamma-2\pi) = S_2(r), \quad \sigma_{\theta\theta}^{1A}(r,\gamma-2\pi) = N_2(r) \quad (12)$$

where N_i and S_i $(i = 1, 2)$ are the normal and shear tractions applied on the crack faces which are assumed to be continuously differentiable and absolutely integrable on $0 \le r < \infty$.

Both the case of wedges slipping in directions away from each other (Fig. 2(a)) and the case of wedges slipping in directions toward each other (Fig. 2(b)) can be treated at the same time by allowing the coefficient of friction f to be either positive or negative. The positive values of f correspond to wedges moving away while negative values of f correspond to wedges moving toward each other. The expressions for the displacements and stresses in the Mellin transform domain are given by Bogy (1968). The interface conditions (3-10) and crack-face boundary conditions (11) and (12) yield a system of twelve equations for the twelve unknown coefficients associated with the displacement and stress fields. The determinant of the coefficients of the system of equations which characterizes the singularity of the crack tip is obtained as

$$\begin{aligned} \Delta_I(p;\alpha,\beta,\gamma,f)/(4\sin p\pi) &= \sin p\pi\langle\cos p\pi\left[-2(1-\alpha)p^2\sin^2\gamma\cos p(\pi-2\gamma)\right. \\ &+(1+\alpha)p\sin 2\gamma\sin p(\pi-2\gamma)+2\sin p\gamma\sin p(\pi-\gamma)] \\ &-(1-\alpha)^2p^4\sin^4\gamma+p^2\sin^2\gamma\left[(1+\alpha)^2\sin^2\gamma-4\alpha\right] \\ &+2\alpha\cos p(\pi-2\gamma)\sin p\gamma\sin p(\pi-\gamma)\rangle \\ &+f\langle p\sin^2\gamma\{(1+\alpha)[(1+\alpha)(1+p) \\ &-2\beta p]\sin^2 p\pi\cos p(\pi-2\gamma) \\ &+(1-\alpha)[(1+\alpha)(1+p) \\ &-4\beta_p]\cos p\pi[1-\cos p\pi\cos p(\pi-2\gamma)]\} \\ &-2(1-\alpha)p^3[(1+\alpha)(1+p)-2\beta p]\cos p\pi\sin^4\gamma \\ &+\beta\{(1+\alpha)\sin^2 p\pi[p\sin 2\gamma\sin p(\pi-2\gamma) \\ &+2\sin p(\pi-\gamma)\sin p\gamma] \\ &+4(1-\alpha)\cos p\pi\sin^2 p\gamma\sin^2 p(\pi-\gamma)\}\rangle \\ &+f^2\sin p\pi\langle p[(1+\alpha)(1+p) \\ &-2\beta p]\sin^2\gamma\{p[(1+\alpha)(1+p)-2\beta p]\sin^2\gamma \\ &+2\beta[1-\cos p\pi\cos p(\pi-2\gamma)]\} \\ &+4\beta^2\sin^2 p\gamma\sin^2 p(\pi-\gamma)\rangle. \end{aligned} \quad (13)$$

Here

$$\alpha = \frac{\Gamma(\kappa_1+1)-(\kappa_2+1)}{\Gamma(\kappa_1+1)+(\kappa_2+1)}, \quad \beta = \frac{\Gamma(\kappa_1-1)-(\kappa_2-1)}{\Gamma(\kappa_1+1)+(\kappa_2+1)} \quad (14)$$

are the constants introduced by Dundurs (1969), where $\kappa = 3 - 4\nu$ for plane strain, ν denotes Poisson's ratio, and $\Gamma = \mu_2/\mu_1$. Note that Δ_I has a complicated structure in the

Downloaded 04 May 2010 to 171.66.16.28. Redistribution subject to ASME license or copyright; see http://www.asme.org/terms/Terms_Use.cfm

transform variable p, but is simply quadratic in the material constants α and β and the friction coefficient f.

The determinant Δ_I satisfies the conditions

$$\Delta_I(p;\alpha,\beta,\gamma,f) = \Delta_I(p;\alpha,\beta,\pi-\gamma,f) \quad (15)$$

$$\Delta_I(p;\alpha,\beta,\gamma,-f) = \Delta_I(p;\alpha,\beta,\pi-\gamma,-f) \quad (16)$$

which are required by the physics of the problem (see Figs. 2(*a*) and 2(*b*)).

When the crack is perpendicular to the interface, i.e., when $\gamma = \pi/2$,

$$\Delta_I(p;\alpha,\beta,\pi/2,f) = -4\Delta_1(p;\alpha,\beta,f)\,\Delta_2(p;\alpha,\beta,f) \quad (17)$$

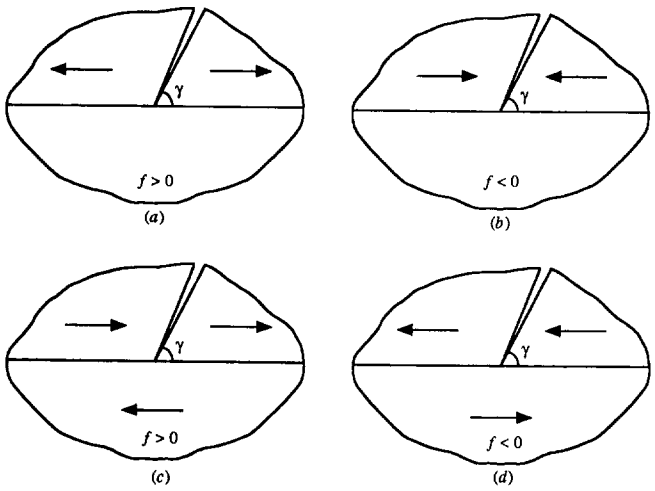

Fig. 2 Wedge configurations: The two wedges slip in opposite directions (*a*) away from each other, (*b*) toward each other. The two wedges slip in the same direction (c) to the right relative to the bottom half-plane, (*d*) to the left relative to the bottom half-plane.

where

$$\Delta_1(p;\alpha,\beta,f) = (1+\cos p\pi)\{\cos p\pi + [(1-\alpha)p^2 - 1]\} - f\sin p\pi\{p[(1+\alpha)(1+p) - 2\beta p] + \beta(1-\cos p\pi)\} \quad (18)$$

$$\Delta_2(p;\alpha,\beta,f) = (1-\cos p\pi)\{\cos p\pi + [(1-\alpha)p^2 + \alpha]\} + f\sin p\pi\{p[(1+\alpha)(1+p) - 2\beta p] + \beta(1-\cos p\pi)\}. \quad (19)$$

Here Δ_1 and Δ_2 correspond to the characteristic equations for a mode I (symmetric) crack and a mode II (antisymmetric) crack, respectively. The factors Δ_1 and Δ_2 agree with the formulae that can be obtained by specializing the equations given by Dempsey and Sinclair (1981).

A change of variable $\lambda = p - 1$ is used in the plots, so that for $\to 0$,

$$\sigma_{ij} = O(r^\lambda), \quad -1 < \lambda < 0. \quad (20)$$

In the following, the question of complex roots is left open and only real roots are considered. If the curves for different values of λ intersect only the curves with the lowest value of λ are shown. The roots of $\Delta_1(\lambda;\alpha,\beta,f) = 0$ are plotted in Fig. 33for $f = -0.1$, -0.25, -0.5, and -1.0 in the α, β parallelogram which covers the physical range of all material combinations (Dundurs, 1969). It is observed that, when $f < 0$ and $|f|$ gets smaller, the order of the power singularity λ becomes smaller. It is noted that Δ_1 does not have roots in the range $-1 < \lambda < 0$ when $f = 0$. When $f > 0$ (i.e., the case that corresponds to a perpendicular pressurized mode I crack) the roots of $\Delta_1(\lambda;\alpha,\beta,f) = 0$ for $f = +1.0$, $+5.0$, and $+10.0$ are shown in Fig. 4. The roots of the characteristic equation $\Delta_2(\lambda;\alpha,\beta,f) = 0$ (i.e., for the mode II crack) when $f < 0$ and $f \geq 0$ are shown in Figs. 5 and 6, respectively. Here it can be observed that as the friction coefficient

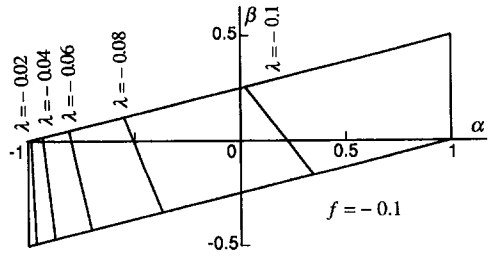

Fig. 3 (*a*)

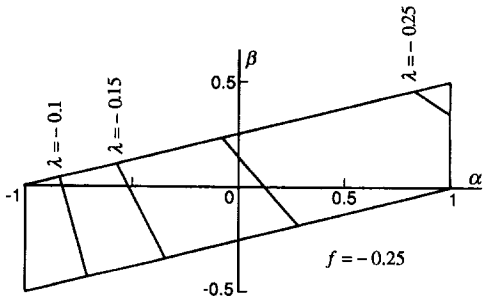

Fig. 3 (*b*)

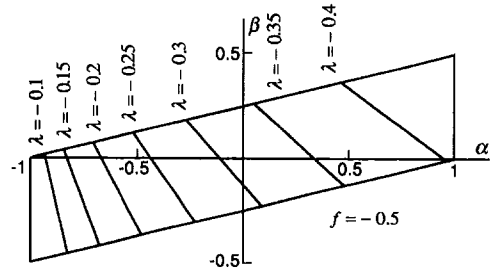

Fig. 3 (*c*)

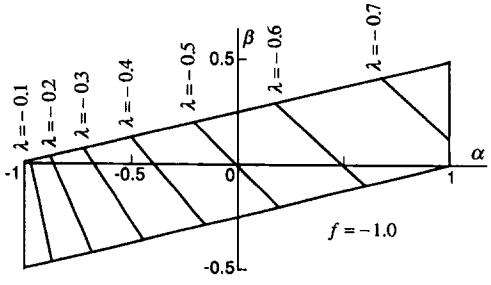

Fig. 3 (*d*)

Fig. 3 Roots of $\Delta_1(\lambda;\alpha,\beta,f) = 0$, for (*a*) f = -0.1, (*b*) f = -0.25, (c) f = -0.5, and (*d*) f = -1.0.

Downloaded 04 May 2010 to 171.66.16.28. Redistribution subject to ASME license or copyright; see http://www.asme.org/terms/Terms_Use.cfm

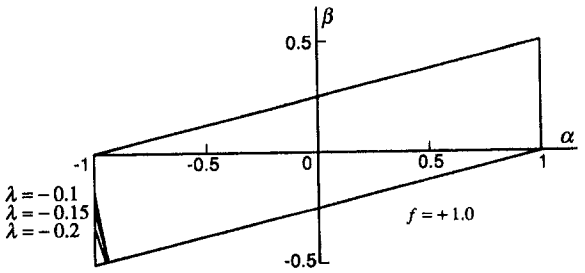

Fig. 4 (a)

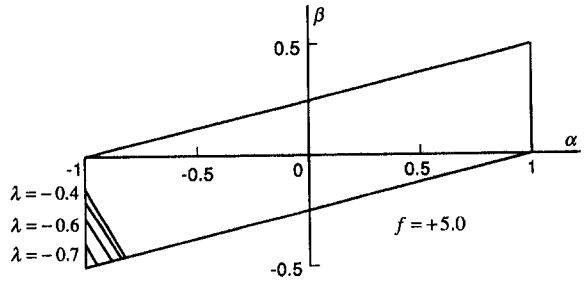

Fig. 4 (b)

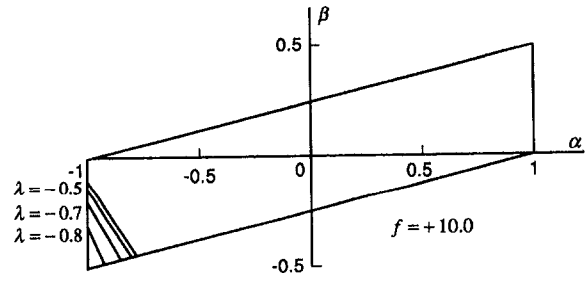

Fig. 4 (c)

Fig. 4 Roots of $\Delta_1(\lambda; \alpha, \beta, f) = 0$, for (a) $f = +1.0$, (b) $f = +5.0$, and (c) $f = +10.0$.

increases, the λ curves come closer to each other, and finally there is a region in the α, β parallelogram where there are no power singularities. A similar behavior was noted by Gdoutos and Theocaris (1975) for a single wedge pressing against a half-plane.

For the special case of $\mu_2/\mu_1 \to \infty$, i.e, when $\Gamma \to \infty$ corresponding to the lower half-plane becoming rigid, the composite parameter $\alpha \to 1$ and

$$\Delta_1(p; 1, \beta, \gamma, f) = 4F(p; \beta, \gamma, f)F(p; \beta, \pi - \gamma, f) \quad (21)$$

where

$$F(p; \beta, \gamma, f) = \sin p\pi(\sin 2p\gamma + p \sin 2\gamma)$$

$$+f \sin p\pi\{2p[1 + (1 - \beta)p] \sin^2 \gamma + 2\beta \sin^2 p\gamma\}. \quad (22)$$

Here the factor $F(p; \beta, \gamma, f)$ is the characteristic determinant obtained when a single wedge with the angle γ is pressed against a rigid half-plane, and it agrees with that given by Comninou (1976) after making suitable changes to accommodate the different notation.

Case II: The Two Wedges Slip in the Same Direction. When the two top wedges slip in the same direction (Figs. 2(*c*) and 2(*d*)), the conditions at the interface are given by (3)–(10), but (6) must be replaced with

$$\sigma_{r\theta}^{1A}(r, -\pi) = -f\sigma_{\theta\theta}^{1A}(r, -\pi) \quad (23)$$

The crack face conditions are the same as in Case I. Here positive values of f correspond to the two top wedges moving to the right (Fig. 2(*c*)) and negative values of f correspond to the two top wedges moving to the left, relative to the bottom half-plane (Fig. 2(*d*)).

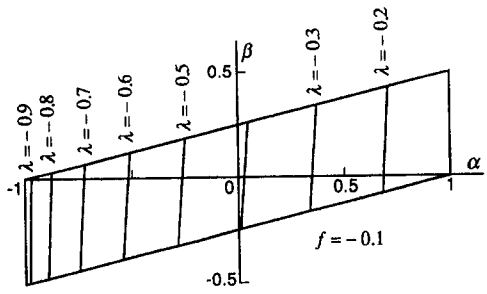

Fig. 5 (a)

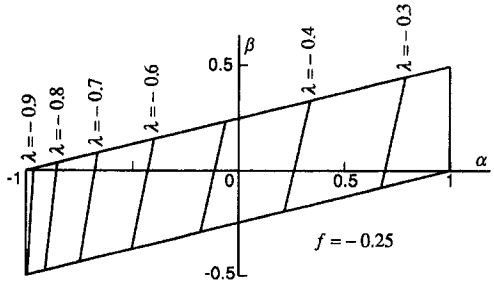

Fig. 5 (b)

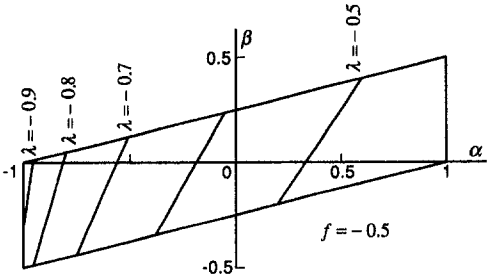

Fig. 5 (c)

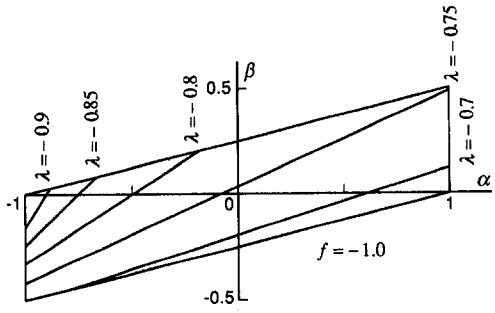

Fig. 5 (d)

Fig. 5 Roots of $\Delta_2(\lambda; \alpha, \beta, f) = 0$, for (a) $f = -1.0$, (b) $f = -0.25$, (c) $f = -0.5$, and (d) $f = -1.0$.

Downloaded 04 May 2010 to 171.66.16.28. Redistribution subject to ASME license or copyright; see http://www.asme.org/terms/Terms_Use.cfm

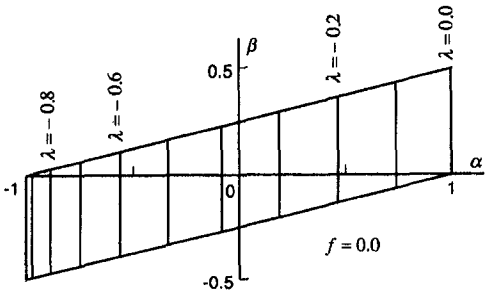

Fig. 6 (a)

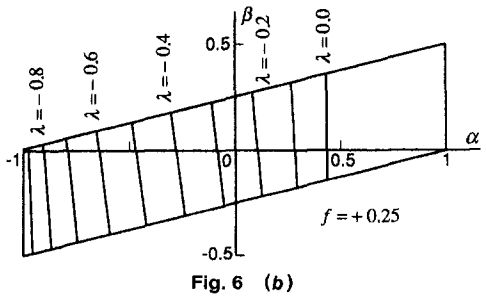

Fig. 6 (b)

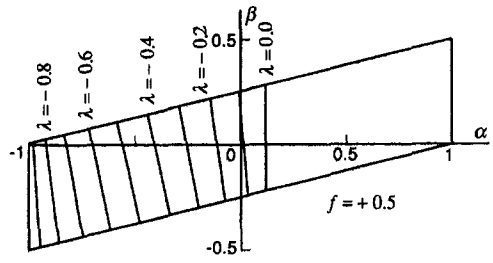

Fig. 6 (c)

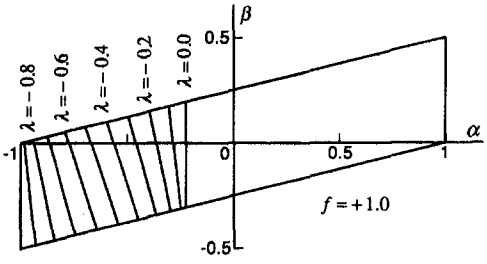

Fig. 6 (d)

Fig. 6 Roots of $\Delta_2(\lambda; \alpha, \beta, f) = 0$ for (a) $f = 0.0$, (b) $f = +0.25$, (c) $f = +0.5$, and (d) $f = +1.0$.

Here the determinant of the coefficients of the system of equations is obtained as

$$\begin{aligned}\Delta_{II}(p;\alpha,\beta,\gamma,f)/(\sin^2 p\pi)\\ = \cos p\pi\big[-8(1-\alpha)p^2\sin^2\gamma\cos p(\pi-2\gamma)\\ +4(1+\alpha)p\sin 2\gamma\sin p(\pi-2\gamma)\\ +8\sin p\gamma\sin p(\pi-\gamma)\big]-4(1-\alpha)^2p^4\sin^4\gamma\\ +4p^2\sin^2\gamma\big[(1+\alpha)^2\sin^2\gamma-4\alpha\big]\\ +8\alpha\cos p(\pi-2\gamma)\sin p\gamma\sin p(\pi-\gamma)\\ +4(1+\alpha)f\langle p\sin^2\gamma\{2[1+(1-\beta)p]\\ \cos p\pi\sin p(\pi-2\gamma)-p[(1+\alpha)(1+p)\\ -2\beta p]\sin 2\gamma\}-\beta\{p\sin 2\gamma[1-\cos p\pi\cos p(\pi-2\gamma)]\\ +2\sin p(\pi-\gamma)\sin p\gamma\sin p(\pi-2\gamma)\}\rangle\\ -4f^2\langle p[(1+\alpha)(1+p)\\ -2\beta p]\sin^2\gamma\{p[(1+\alpha)(1+p)-2\beta p]\sin^2\gamma\\ +2\beta[1-\cos p\pi\cos p(\pi-2\gamma)]\}\\ +4\beta^2\sin^2 p\gamma\sin^2 p(\pi-\gamma)\rangle. \quad (24)\end{aligned}$$

It can be shown from (24) that the following conditions which must be required on physical grounds are satisfied:

$$\Delta_{II}(p;\alpha,\beta,\gamma,f)=\Delta_{II}(p;\alpha,\beta,\pi-\gamma,-f) \quad (25)$$

$$\Delta_{II}(p;\alpha,\beta,\gamma,-f)=\Delta_{II}(p;\alpha,\beta,\pi-\gamma,f). \quad (26)$$

For the special case of $\mu_2/\mu_1 \to \infty$, i.e., when $\alpha \to 1$

$$\Delta_{II}(p;1,\beta,\gamma,f)=4F(p;\beta,\gamma,f)F(p;\beta,\pi-\gamma,-f) \quad (27)$$

where $F(p;\beta,\gamma,f)$ is defined by (22).

Acknowledgment

The authors are pleased to acknowledge support from the Air Force Office of Scientific Research under Award No. F49620-92-J-0173 DEF/AFOSR.

References

Bogy, D. B., 1968, "Edge-Bonded Dissimilar Orthogonal Elastic Wedges Under Normal and Shear Loading," ASME JOURNAL OF APPLIED MECHANICS, Vol. 35, pp. 460–466.

Bogy, D. B., 1971, "On the Plane Elastostatic Problem of a Loaded Crack Terminating at a Material Interface," ASME JOURNAL OF APPLIED MECHANICS, Vol. 38, pp. 911–918.

Comninou, M., 1976, "Stress Singularity at a Sharp Edge in Contact Problems with Friction," *Journal of Applied Mathematics and Physics (ZAMP)*, Vol. 27, pp. 493–499.

Dempsey, J. P., and Sinclair, G. B., 1979, "On the Stress Singularities in the Plane Elasticity of the Composite Wedge," *Journal of Elasticity*, Vol. 9, pp. 373–391.

Dempsey, J. P., and Sinclair, G. B., 1981, "On the Singular Behavior at the Vertex of a Bi-Material Wedge," *Journal of Elasticity*, Vol. 11, pp. 317–327.

Dundurs, J., 1969, discussion, ASME JOURNAL OF APPLIED MECHANICS, Vol. 36, pp. 650–652.

Erdogan, F., Gupta, G. D., and Cook, T. S., 1973, "Numerical Solution of Singular Integral Equations," *Mechanics of Fracture I: Methods of Analysis and Solutions of Crack Problems*, G. C. Sih, ed., Noordhoff, Leyden, pp. 368–425.

Evans, A. G., and Marshall, D. B., 1989, "The Mechanical Behavior of Ceramic Matrix Composites," *Acta Metallurgica*, Vol. 37, pp. 2567–2583.

Gdoutos, E. E. and Theocaris, P. S., 1975, "Stress Concentrations at the Apex of a Plane Indenter Acting on an Elastic Half Plane," ASME JOURNAL OF APPLIED MECHANICS, Vol. 42, pp. 688–692.

Gharpuray, V. M., Dundurs, J., and Keer, L. M., 1991, "A Crack Terminating at a Slipping Interface Between Two Materials," ASME JOURNAL OF APPLIED MECHANICS, Vol. 58, pp. 960–963.

Hill, R., 1964, "Theory of Mechanical Properties of Fiber-Strengthened Materials: I. Elastic Behaviour," *Journal of the Mechanics and Physics of Solids*, Vol. 12, pp. 213–218.

Lee, J.-W., and Daniel, I. M., 1992, "Deformation and Failure of Longitudinally Loaded Brittle-Matrix Composites," *Composite Materials: Testing and Design*, C. M. Glenn, ed., ASTM-STP 1120, pp. 204–221.

Muskhelishvili, N. I., 1953, *Singular Integral Equations*, Noordhoff, Groningen, Holland.

Wijeyewickrema, A. C., Keer, L. M., Hirashima, K., and Mura, T., 1991, "The Annular Crack Surrounding an Elastic Fiber in a Tension Field," *International Journal of Solids and Structures*, Vol. 27, pp. 315–328.

Wijeyewickrema, A. C., and Keer, L. M., 1993, "Matrix Cracking in a Fiber-Reinforced Composite with Slip at the Fiber-Matrix Interface," *International Journal of Solids and Structures*, Vol. 30, pp. 91–113.

Zak, A. R., and Williams, M. L., 1963, "Crack Point Stress Singularities at a Bimaterial Interface," ASME JOURNAL OF APPLIED MECHANICS, Vol. 30, pp. 142–143.

Downloaded 04 May 2010 to 171.66.16.28. Redistribution subject to ASME license or copyright; see http://www.asme.org/terms/Terms_Use.cfm

An Analytical Crack-Tip Element for Layered Elastic Structures

B. D. Davidson

Hurang Hu

Department of Mechanical, Aerospace, and Manufacturing Engineering, Syracuse University, Syracuse, NY 13244

R. A. Schapery

Department of Aerospace Engineering and Engineering Mechanics, University of Texas, Austin, TX 78712

A previously developed linear elastic crack-tip element analysis is reviewed briefly, and then extended and refined for practical applications. The element provides analytical expressions for total energy release rate and mode mix in terms of plate theory force and moment resultants near the crack tip. The element may be used for cracks within or between homogeneous isotropic or orthotropic layers, as well as for delamination of laminated composites. Classical plate theory is used to derive the equations for total energy release rate and mode mix; a "mode mix parameter," Ω, as obtained from a separate continuum analysis is necessary to complete the mode mix decomposition. This parameter depends upon the elastic and geometrical properties of the materials above and below the crack plane, but not on the loading. A relatively simple finite element technique for determining the mode-mix parameter is presented and convergence in terms of mesh refinement is studied. Specific values of Ω are also presented for a large number of cases. For those interfaces where a linear elastic solution predicts an oscillatory singularity, an approach is described which allows a unique, physically meaningful value of fracture mode ratio to be defined. This approach is shown to provide predictions of crack growth between dissimilar homogeneous materials that are equivalent to those obtained from the oscillatory field solution. Application of the approach to delamination in fiber-reinforced laminated composites is also discussed.

Introduction

The analysis of interfacial fracture is becoming increasingly important. Practical problems where interfacial fracture is of concern include the decohesion of a coating from a dissimilar substrate (Hu, et al., 1988) or delamination of laminated composite materials (e.g., Pagano, 1989). For these and many other problems, the local crack-tip geometry may be idealized as shown in Fig. 1. Provided that the length-to-thickness ratios of the uncracked region and of the cracked regions are large, the stress intensity factor and energy release rate in these types of problems can be obtained using primarily classical beam or plate theory (Schapery and Davidson, 1990; Suo and Hutchinson, 1990; Suo, 1990a). This approach results in a relatively simple computational technique for making crack growth predictions.

In recent works, Schapery and Davidson (1990) and Suo and Hutchinson (1990) independently showed that for two-dimensional crack problems in which a beam or a plate theory is utilized to determine the deflections and strain energies of the cracked and uncracked regions, the stress intensity factor and energy release rate may be expressed in terms of only two independent load parameters. Schapery and Davidson chose these parameters as a concentrated crack-tip force and moment; using a superposition argument, Suo and Hutchinson chose these parameters as an external load and moment. In both of these works, it was found that a beam or plate theory analysis does not give sufficient information to completely decompose the total energy release rate to obtain mode mixity. Rather, one additional parameter is required; this parameter is independent of the loading and depends only upon geometric and material properties. This parameter, designated herein as Ω, may be obtained by finite element analysis (Schapery and Davidson, 1990). Suo and Hutchinson (1990) used a different but related parameter which they evaluated by numerical solution of integral equations.

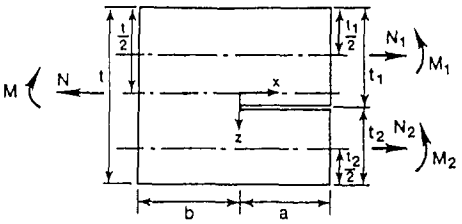

Fig. 1 Crack-tip element and local loading

In the present work, the crack-tip element previously developed by Schapery and Davidson (1990) is extended to

Contributed by the Applied Mechanics Division of THE AMERICAN SOCIETY OF MECHANICAL ENGINEERS for publication in the JOURNAL OF APPLIED MECHANICS.

Discussion on this paper should be addressed to the Technical Editor, Professor Lewis T. Wheeler, Department of Mechanical Engineering, University of Houston, Houston, TX 77204-4792, and will be accepted until four months after final publication of the paper itself in the ASME JOURNAL OF APPLIED MECHANICS.

Manuscript received by the ASME Applied Mechanics Division, May 6, 1993; final revision, Apr. 5, 1994. Associate Technical Editor: G. J. Dvorak.

Copyright © 1995 by ASME

Downloaded 04 May 2010 to 171.66.16.28. Redistribution subject to ASME license or copyright; see http://www.asme.org/terms/Terms_Use.cfm

cover the case of the nonzero bimaterial constant (which produces the oscillating singularity). A formulation is utilized which allows analysis of cracks which display either oscillatory or nonoscillatory fields using the same set of equations. A general methodology for determining Ω is presented and specific values of Ω are given for cracks between homogeneous isotropic and orthotropic layers. By comparison with finite element results, it is confirmed that the crack-tip element allows energy release rate and mode mixity to accurately be determined from a set of closed-form equations. Also, a means of characterizing fracture in bimaterial problems is discussed which circumvents much of the difficulty associated with the nonzero bimaterial constant and resulting oscillatory singularity. For certain cases of fracture between dissimilar isotropic or orthotropic materials, the method gives results that are equivalent to those obtained from the oscillatory field solution. The method is particularly well suited to predicting delamination growth in composite structures.

Theory

Total Energy Release Rate. Consider the "crack-tip element" of Fig. 1. This element represents a three-dimensional portion of the crack-tip region in a general interfacial fracture problem. It is assumed that the crack lies locally in the x-y plane at constant z. The complete crack front may be straight or curved; however, the length of the element in the y-direction is assumed to be short enough that there is no significant variation in the loading and in the orientation of the edges of the element with respect to y. It is further assumed that the lengths of the cracked and uncracked regions comprising the element are large with respect to their thicknesses, but are sufficiently small for geometric nonlinearities to be negligible. Thus, classical plate theory may be used to predict the overall deformations and strain energies of the element. In what follows, the element is assumed to be in a state of plane stress or plane strain with respect to the y-coordinate direction. An extension of the crack-tip element to three-dimensional deformations is given by Schapery and Davidson (1990).

In classical plate theory, deformations are defined entirely by midsurface strains and curvatures. For the uncracked portion of the element, the equations relating these midsurface strains and curvatures to the load and moment resultants are given by

$$\begin{aligned} N &= A\epsilon^0 + B\kappa \\ M &= B\epsilon^0 + D\kappa. \end{aligned} \tag{1}$$

Or, in their inverted form,

$$\begin{aligned} \epsilon^0 &= A'N + B'M \\ \kappa &= B'N + D'M, \end{aligned} \tag{2}$$

where ϵ^0 is the strain in the x-direction and κ is the plate theory curvature ($= -\partial^2 w/\partial x^2$) of the uncracked region. N and M are the load and moment resultants per unit width, respectively, and are defined positive as shown in Fig. 1. The coupling stiffness, B, and compliance, B', are zero for problems in which the uncracked region possesses midplane symmetry. A homogeneous material is one special case.

For the region above the crack plane (plate 1) or below the crack plane (plate 2), the midsurface strains and curvatures are related to the load and moment resultants by

$$\begin{aligned} N_i &= A_i\epsilon_i^0 + B_i\kappa_i, \quad i = 1,2 \\ M_i &= B_i\epsilon_i^0 + D_i\kappa_i, \quad i = 1,2. \end{aligned} \tag{3}$$

Or, in their inverted form

$$\begin{aligned} \epsilon_i^0 &= A_i'N_i + B_i'M_i, \quad i = 1,2 \\ \kappa_i &= B_i'N_i + D_i'M_i, \quad i = 1,2, \end{aligned} \tag{4}$$

where ϵ_i^0 is the midplane strain in the x-direction in plate "i"; κ_i is the curvature in the x-direction in plate "i"; and N_1, N_2, M_1, and M_2 are positive as shown in Fig. 1. The index "i" in (3) and (4) is not summed.

Schapery and Davidson (1990) showed that the loading on the crack-tip element which produces the stress singularity can be fully characterized in terms of a concentrated crack-tip force, N_c, and moment, M_c; this follows from linearity and the observation that when $N_c = M_c = 0$, there are no loads transmitted across the crack plane and the exact stress distribution is that of classical plate theory. The concentrated crack-tip force and moment occur, within the context of classical plate theory, to enforce displacement compatibility along the crack plane over $-b < x < 0$. The element equations are valid only when the combination of the loading and the moduli of the regions above and below the crack plane are such that crack face interpenetration does not occur in the remote portions of the element (i.e., away from the crack tip). This covers many cases of practical interest (Davidson, 1994a; 1994b). To analyze other configurations, crack face contact constraints must be incorporated into the element formulation.

The energy release rate, G, of the crack-tip element may be obtained through a modified virtual crack closure method. This allows the energy release rate to be expressed in terms of N_c and M_c, rather than the four independent quantities N_1, N_2, M_1, and M_2, and results in the following relation (Schapery and Davidson, 1990):

$$G = \frac{1}{2}\left(c_1N_c^2 + c_2M_c^2 + 2\sqrt{c_1c_2}\,N_cM_c\sin\Gamma\right) \tag{5}$$

where

$$\sin\Gamma = \frac{c_{12}}{\sqrt{c_1c_2}} \tag{6}$$

and Γ has been introduced for later use. Also,

$$\begin{aligned} c_1 &= A_1' + A_2' + B_1't_1 - B_2't_2 + D_1't_1^2/4 + D_2't_2^2/4 \\ c_2 &= D_1' + D_2' \\ c_{12} &= D_2't_2/2 - D_1't_1/2 - B_1' - B_2'. \end{aligned} \tag{7}$$

The concentrated crack-tip force and moment are given by

$$N_c = -N_1 + a_{11}N + a_{12}M \tag{8}$$

and

$$M_c = M_1 - N_1t_1/2 + (a_{11}t_1/2 - a_{21})N + (a_{12}t_1/2 - a_{22})M \tag{9}$$

where

$$\begin{aligned} a_{11} &= A_1A' + (B_1 - A_1t_2/2)B' \\ a_{12} &= A_1B' + (B_1 - A_1t_2/2)D' \\ a_{21} &= B_1A' + (D_1 - B_1t_2/2)B' \\ a_{22} &= B_1B' + (D_1 - B_1t_2/2)D' \end{aligned} \tag{10}$$

and t_1 and t_2 are the thicknesses of plates 1 and 2 as shown in Fig. 1. Geometric and material scaling of these equations are given in Schapery and Davidson (1990).

Mode Decomposition. In this section, the stress intensity factor for the crack-tip element is obtained and used to decompose the energy release rate, Eq. (5), into suitably defined opening and shearing mode components. It is assumed that the regions immediately above and below the crack plane are homogeneous and orthotropic with their

Downloaded 04 May 2010 to 171.66.16.28. Redistribution subject to ASME license or copyright; see http://www.asme.org/terms/Terms_Use.cfm

principal material axes aligned with the reference coordinate axes. For fiber composites, this situation arises when the delamination is bounded by 0 deg, 90 deg, and/or $\pm\theta$ deg plies. In this latter case, the approximation must be made that the properties of the $\pm\theta$ layers may be "smeared" together to create an equivalent orthotropic layer with principal axes at 0 and 90 deg (e.g., Davidson, 1994a; Davidson and Hu, 1995). For other cases, the starting point for the derivation below, Eq. (11), is replaced by the more general expression given by Suo (1990b) for a crack between two anisotropic solids.

The relationship between the energy release rate and the modulus of the stress intensity factor is given by (Suo, 1990b)

$$G = H_{11}|K|^2/(4\cosh^2\pi\epsilon) \tag{11}$$

where

$$\epsilon = (1/2\pi)\ln[(1-\beta)/(1+\beta)] \tag{12}$$

$$\beta = \left(\left[(s_{11}s_{33})^{1/2} + s_{13}\right]_2 - \left[(s_{11}s_{33})^{1/2} + s_{13}\right]_1\right)(H_{11}H_{33})^{-1/2} \tag{13}$$

$$H_{11} = \left[2n\lambda^{1/4}(s_{11}s_{33})^{1/2}\right]_1 + \left[2n\lambda^{1/4}(s_{11}s_{33})^{1/2}\right]_2 \tag{14}$$

and

$$H_{33} = \left[2n\lambda^{-1/4}(s_{11}s_{33})^{1/2}\right]_1 + \left[2n\lambda^{-1/4}(s_{11}s_{33})^{1/2}\right]_2. \tag{15}$$

Here, β is a generalization of one of Dundurs' (1969) parameters for isotropic materials and ϵ is the bimaterial constant. The subscripts "1" and "2" used outside the square brackets in the expressions for β, H_{11}, and H_{33} refer to the materials immediately above and below the crack plane, respectively. The nondimensional parameters λ and n are given by

$$\lambda = s_{11}/s_{33} \tag{16}$$

and

$$n = \left[\tfrac{1}{2}(1+\rho)\right]^{1/2} \tag{17}$$

where

$$\rho = \tfrac{1}{2}(2s_{13} + s_{55})(s_{11}s_{33})^{-1/2}. \tag{18}$$

Material compliances, s_{ij}, are defined in the conventional sense; that is, the stress-strain relations for either material (immediately above or below the crack plane) have the form

$$\epsilon_i = s_{ij}\sigma_j. \tag{19}$$

Standard contracted notation is used (Whitney, 1987). Using s_{ij} as defined in (19) gives plane stress results; plane strain values are obtained by replacing s_{ij} by s'_{ij}, where

$$s'_{ij} = s_{ij} - s_{i2}s_{j2}/s_{22}. \tag{20}$$

The complex stress intensity factor introduced in (11) is related to the stresses a distance r ahead of the crack tip by (Suo, 1990b).

$$\sigma_{zz}\sqrt{H_{33}/H_{11}} + i\tau_{xz} = Kr^{i\epsilon}/\sqrt{2\pi r}. \tag{21}$$

Guided by dimensional considerations and linearity, the complex stress intensity factor is written as

$$K = \left[(2\cosh^2\pi\epsilon)/H_{11}\right]^{1/2}(pN_c + qM_c)L^{-i\epsilon} \tag{22}$$

where L is a characteristic dimension that is introduced to simplify the dimensions of p and q when $\epsilon \neq 0$. The complex constants p and q can be found, apart from an angle Ω, by substituting (22) into (11) and comparing the result to (5). This gives

$$p = i\sqrt{c_1}e^{i\Omega} \quad q = \sqrt{c_2}e^{i(\Omega+\Gamma)}. \tag{23}$$

Note that Ω is needed to determine the mode mix (i.e., the ratio Im[K]/Re[K]), but cannot be obtained from classical plate theory. Combining (22) and (23), the stress intensity factor becomes

$$K = (2/H_{11})^{1/2}\cosh\pi\epsilon\left(iN_c\sqrt{c_1} + M_c\sqrt{c_2}e^{i\Gamma}\right)L^{-i\epsilon}e^{i\Omega}. \tag{24}$$

The choice of the characteristic dimension, L, which appears in (22) and (24) is arbitrary. However, *it is preferable to use a value of L which scales with layer thickness*. It may be demonstrated by dimensional analysis that choosing L in this manner makes Ω independent of plate thickness for geometrically and physically similar crack-tip elements.

The preceding representation of the complex stress intensity factor is similar to that first proposed by Suo and Hutchinson (1990), who expressed their results in terms of an external load and moment and a mode-mix parameter designated as ω. However, by working with N_c, M_c and the $[A\text{-}B\text{-}D]$ matrices (and their inverses), the present approach may be more readily applied to laminated composite materials. Also, as will be discussed in subsequent sections, the parameter Ω leads to other advantages and provides for certain simplifications. The relationship between Ω and Suo and Hutchinson's ω is presented in Appendix A.

Following Rice's (1988) suggestion, we define K_I and K_{II} through the equation

$$K\hat{L}^{i\epsilon} = K_I + iK_{II}. \tag{25}$$

As will be discussed below, $\hat{L}$ may be specified to scale with the body, such as when Ω is determined from theory, or it may be specified as a fixed quantity, as in the use of (25) with fracture characterization data. Using (24) and (25) and noting that $(\hat{L}/L)^{i\epsilon} = e^{i\epsilon\ln(\hat{L}/L)}$, the individual stress intensity factors are given by

$$K_I = (2/H_{11})^{1/2}\cosh(\pi\epsilon)\left[-N_c\sqrt{c_1}\sin\hat{\Omega} + M_c\sqrt{c_2}\cos(\hat{\Omega}+\Gamma)\right] \tag{26}$$

$$K_{II} = (2/H_{11})^{1/2}\cosh(\pi\epsilon)\left[N_c\sqrt{c_1}\cos\hat{\Omega} + M_c\sqrt{c_2}\sin(\hat{\Omega}+\Gamma)\right] \tag{27}$$

where

$$\hat{\Omega} = \Omega + \epsilon\ln(\hat{L}/L). \tag{28}$$

When $\epsilon = 0$, this definition of K_I reduces to the classical definition, in terms of σ_{zz} (cf. Eq. (21)), for those cases where $(H_{11}/H_{33}) = 1$; when $\epsilon = 0$ and $(H_{11}/H_{33}) \neq 1$, the quantity $(H_{11}/H_{33})^{1/2}K_I$ relates to σ_{zz} in the classical sense. That is, the present formulation and definitions are utilized for both $\epsilon = 0$ and $\epsilon \neq 0$, and for both isotropic and orthotropic materials. With these definitions, $|K|^2 = K_I^2 + K_{II}^2$, regardless of the value of ϵ, H_{11}, and H_{33}. Guided by (11), the associated mode I and mode II energy release rates are defined as

$$G_I = \frac{1}{2}\left[-N_c\sqrt{c_1}\sin\hat{\Omega} + M_c\sqrt{c_2}\cos(\hat{\Omega}+\Gamma)\right]^2 \tag{29}$$

and

$$G_{II} = \frac{1}{2}\left[N_c\sqrt{c_1}\cos\hat{\Omega} + M_c\sqrt{c_2}\sin(\hat{\Omega}+\Gamma)\right]^2. \tag{30}$$

The total energy release rate, $G = G_I + G_{II}$, is independent of the value of $\hat{\Omega}$ and will always equal that given by (5). When $\epsilon = 0$, the energy release rate components retain their classical definitions (in terms of σ_{zz} and τ_{xz}) and, except for the redefinition of variables, are identical to those derived in the earlier work by Schapery and Davidson (1990). Also, if

Downloaded 04 May 2010 to 171.66.16.28. Redistribution subject to ASME license or copyright; see http://www.asme.org/terms/Terms_Use.cfm

$\epsilon = 0$, then $\hat{\Omega} = \Omega$ and it is convenient, in terms of notation, to make this substitution in (26), (27), (29), and (30). When $\epsilon \neq 0$, G_I and G_{II} are dimensionally convenient generalizations of the classical definitions, and their use in fracture problems is similar to the use of K_I and K_{II}.

Determination of Ω. In order to obtain the mode-mix parameter, Ω, it is necessary to have results from a continuum analysis of one special loading case. We prefer to perform a finite element analysis of the crack-tip element; as noted above, integral equation methods have also been used (Suo and Hutchinson, 1990). One special case where no analysis is required is when the crack plane is a plane of mirror symmetry. For this case, $\epsilon = 0$ and loading defined by $M_2 = -M_1$ and $N_1 = N_2 = M = N = 0$ must produce $K_{II} = G_{II} = 0$. From (6), (8), and (9), $\Gamma = 0$, $N_c = 0$, $M_c = M_1$ and, by (27) or (30), $\Omega = 0$. The determination of Ω for other geometries is discussed below.

For the case where $\epsilon = 0$, Ω is most accurately obtained from the results of a finite element analysis of the crack-tip element geometry with the loading chosen such that $M_c = 0$. This will be demonstrated in a subsequent section. In order to avoid calculation of H_{11} and H_{33}, we prefer to extract Ω using the expression given by (29),

$$\sin \Omega = -\sqrt{2G_I}/N_c\sqrt{c_1}, \tag{31}$$

where the mode I energy release rate is obtained using the virtual crack closure technique as originally proposed by Rybicki and Kanninen (1977). In this technique, G is obtained from a single finite element analysis using the nodal forces in the uncracked region and the nodal displacements just behind the crack tip. In order to ensure that the proper sign for Ω is obtained, the loading on the finite element model should produce a positive opening mode stress intensity factor (cf. Eq. (26)). A positive K_I is guaranteed by a positive crack-opening displacement; this may be checked by examining the finite element results to ensure that crack face overlap does not occur near the crack tip. Based on the physical condition that the signs of K_{II} and N_c should be the same, Ω will lie in the first or fourth quadrant.

When $\epsilon \neq 0$, Ω is also readily determined from finite element results. Note that there is no need to specify $\hat{L}$ for this procedure; fundamentally, Ω is obtained by a comparison of (24) with the results of a continuum analysis of a single loading case. However, we find it convenient to utilize the definition of K as given by (25) for both the determination of Ω and the characterization of fracture. Thus, *when determining Ω, $\hat{L}$ can be taken equal to L without loss in generality.*

The phase angle of the stress intensity factor, ψ, is given by

$$\tan \psi = K_{II}/K_I = \frac{N_c\sqrt{c_1}\cos\hat{\Omega} + M_c\sqrt{c_2}\sin(\hat{\Omega}+\Gamma)}{-N_c\sqrt{c_1}\sin\hat{\Omega} + M_c\sqrt{c_2}\cos(\hat{\Omega}+\Gamma)}. \tag{32}$$

The value of Ω may be obtained from (32), using the phase angle as found by a finite element analysis of the crack-tip element under one specific loading. Following the procedure for the $\epsilon = 0$ case, we prefer to use a loading defined by $M_c = 0$. Choosing this loading and $L = T$, where T is a convenient characteristic dimension, for example t_1, we may replace $\hat{\Omega}$ by Ω (cf. Eq. (28)), and (32) reduces to

$$\tan \Omega = -1/\tan \psi. \tag{33}$$

We evaluate the phase angle, ψ, using a modified crack surface displacement (CSD) method, originally developed by Matos et al. (1989) for isotropic, bimaterial problems. The only differences between our modified CSD and the original method are that we use the near-tip displacement field given by Suo (1990b), which allows the method to be used for isotropic or orthotropic interfaces, and we obtain the total energy release rate by the virtual crack closure technique (VCCT); Matos et al. (1989) utilized a virtual crack extension method. Although the mode I and mode II energy release rates as obtained by the VCCT do not have their classical interpretations if $\epsilon \neq 0$, for self-similar crack advance the total energy release rate is correct. We will designate the value of Ω that is computed from (33) as $\Omega(T)$, i.e., Ω based on the length scale $L = T$. This scale enters explicitly into the calculation of ψ from the finite element results. The relationship between $\Omega(T)$ and Ω based on another characteristic length, $\hat{T}$, is given by

$$\Omega(\hat{T}) = \Omega(T) + \epsilon \ln(\hat{T}/T). \tag{34}$$

Thus, if the length scale used in the determination of Ω is sufficiently large, Ω will lie outside of the first or fourth quadrant. This issue was investigated numerically. It was found that, for all bimaterial problems comprised of homogeneous isotropic layers, $\Omega(t_1)$ lies in the first or fourth quadrant. This same conclusion has been reached for all other problems studied to date. As in the case where $\epsilon = 0$, the loading on the element used to determine Ω should be chosen such that crack face overlap, outside of the singular zone, does not occur in the finite element model.

Finally, we point out that as a result of our choice of coordinate system, substitution of Eq. (24) into the classical expressions for the near-tip displacement field (e.g., Matos et al., 1989; Suo, 1990b) will yield the correct magnitudes, but incorrect signs, for the vertical and horizontal near-tip displacement components. That is, the classical expressions may still be used if the sign conventions corresponding to the different coordinate systems are correctly accounted for. For example, when determining Ω by the modified CSD method, the shear and normal displacement jumps across the crack plane are first found by finite element analysis and are defined positive according to our coordinate system (Fig. 1). Then, change their signs for direct substitution into the expressions of Matos et al. (1989) or Suo (1990b) to obtain the stress intensity factor and phase angle.

Fracture Characterization

For the case of small-scale contact and process zones, the mechanical conditions for crack growth at an interface may be fully characterized in terms of K_I and K_{II}. Equivalently, we may use the energy release rate and phase angle, ψ, Eq. (32). Using this latter representation, suppose that a failure locus, defined as the critical strain energy release rate as a function of a phase angle, is determined experimentally, i.e.,

$$G_c = G_c(\psi) \tag{35}$$

where ψ is commonly referred to as the *mode mixity*. This failure locus may be used with the crack-tip element analysis to predict fracture in structures of any absolute dimension, *providing that $\hat{L}$ is taken as a fixed quantity*. The distinction between L, which always scales with plate thickness, and $\hat{L}$, which cannot scale if a specimen-size-independent failure locus is desired, also enters if specimens of different absolute size and/or geometry are used to develop the failure locus (i.e., to provide convenient tests to produce various mode mixities). To assure that this classical approach is valid, the contact zone size may be estimated by substituting (24) into the near-tip displacement field (Suo, 1990b), and evaluating the last "crossover" point in crack face displacements (Rice, 1988).

As an alternative to the above fracture prediction methodology, one could simplify matters by ignoring ϵ-based effects, both in the experimental determination of toughness data

Downloaded 04 May 2010 to 171.66.16.28. Redistribution subject to ASME license or copyright; see http://www.asme.org/terms/Terms_Use.cfm

and in the application of this data when making fracture predictions (He and Hutchinson, 1989; Suo and Hutchinson, 1989). If ϵ-based effects are to be ignored, the condition that $\epsilon = 0$, is, by (12), equivalent to setting $\beta = 0$. By (13), this will occur if

$$\left[(s_{11}s_{33})^{1/2} + s_{13}\right]_2 = \left[(s_{11}s_{33})^{1/2} + s_{13}\right]_1. \qquad (36)$$

This is a local condition, i.e., $\epsilon = 0$ for delamination in a laminated composite if the two layers bounding the crack plane satisfy this equation. Eliminating the oscillating singularity in this fashion was proposed by He and Hutchinson (1989) for isotropic, bimaterial problems, and was adopted by Davidson (1994a) for predicting edge delamination in a multidirectional graphite/epoxy composite laminate. Davidson refers to this as the "$\beta = 0$ approach." In this approach, the parameter β is taken equal to zero *only* in the finite element model that is utilized to evaluate Ω. This is done by altering a Poisson's ratio of one of the layers bounding the crack; a specific methodology for accomplishing this is presented in Appendix B. With $\epsilon = 0$, the determination of Ω is relatively straightforward using the virtual crack closure technique and Eq. (31). When experimentally determining a failure locus or analyzing typical structural geometries, the mode mixity is determined from (32), with $\hat{\Omega}$ given by (28), along with the actual value of ϵ and the value of Ω that was obtained from the finite element model with the altered material properties. To predict crack growth under arbitrary loadings, if there is *only* a difference in scale between the body to be analyzed and that used for fracture characterization, then one can use this same value of Ω; the accuracy of this $\beta \approx 0$ approach for predicting fracture is the same as when the actual value of β is employed. That is, all effects of scaling are rigorously accounted for through $\hat{\Omega}$ in Eq. (28).

The $\beta \approx 0$ approach is particularly attractive for laminated, fiber composite materials. Engineering studies of delamination in these materials generally require analysis of many different layups and crack locations; thus, it would be impractical to characterize crack growth using an ϵ-based approach for every interface of interest. In fact, it is likely that the additional accuracy in the solution structure gained by a consideration of ϵ-based effects would not improve the accuracy of fracture predictions in these materials. We make this statement based on the following two observations: first, toughness values for laminated composites often do not come from experiments involving the interface of interest, but rather from tests of unidirectional laminates, and second, the oscillatory singularity in these problems is based on the modelling assumption that individual layers in the composite are homogeneous and orthotropic. Even in the case of small-scale damage, delaminations will propagate through resin-rich regions with varying amounts of local fiber constraint or along fiber/matrix interfaces; the near-tip field in the physical problem is therefore rather different from that predicted by a microscopically homogeneous model. To become overly concerned with ϵ-based effects in these problems would therefore appear to be unwarranted.

In addition to the above considerations, many laminated composite materials exhibit large damage or process zones at the delamination tip (e.g., Chai, 1984; Nicholls and Gallagher, 1983). These damage zones may be comparable to or larger than the single-ply thickness, which generally scales the near-tip stress field. When this is the case, the concept of a "singular zone," as postulated by classical linear elastic fracture mechanics, no longer applies. It follows that the true stress field at the delamination tip is quite different from that predicted by analytical models which assume the damage zone is small, and it is not apparent that characterizing fracture in terms of classical parameters which define the singular field will provide the best predictive methodology. Rather, a better measure of the crack-tip stress field may be in terms of parameters which measure a "mode mix," but are insensitive to the details of the crack tip damage state. The concentrated crack-tip moment, M_c, and shear force, N_c, which are computed as part of the crack-tip element analysis appear to be well suited for this purpose, since they do *not* depend on the existence of a singular zone. These quantities provide energy release rate and may be used to define a "mode mix," for example, as N_c/M_c. However, because the ratio N_c/M_c is not dimensionless, a failure locus based on $G_c(N_c/M_c)$ would be sensitive to any changes in geometry and therefore would not be suited to characterizing crack growth in materials or interfaces in which G_c is dependent on ψ. If a dimension (such as a single-ply thickness) is introduced to nondimensionalize N_c/M_c, there is no guarantee that this ratio will provide a failure locus that is invariant with respect to changes in laminate structure.

A better approach, and in the same spirit, is based on (32) and (35) and an effective value of $\hat{\Omega}$. An effective $\hat{\Omega}$ used in determining ψ provides the necessary scaling normalization for the influence of N_c/M_c, and contains the solution with a singular zone as a special case. As the energy release rate (5) is independent of Ω, ϵ, and the existence of a singular zone, the primary issues concern an appropriate $\hat{\Omega}$ that may be used in the reduction of data from tests on specific specimens in order to produce a failure locus $G_c(\psi)$, as well as in subsequent predictions of fracture in common structural geometries, i.e., when the size and/or the laminate structure are changed. This issue has also been investigated by Kinloch, et al. (1993). With respect to our notation, Kinloch et al. reduced the data from delamination tests of unidirectional laminates to develop failure loci, in the form of G_I versus G_{II}, using both the singular field mode mix decomposition and using a mode mix obtained by choosing $\hat{\Omega} = 0$. They referred to this latter decomposition as the "global mix," and referred to that obtained using the singular field-based value of $\hat{\Omega}$ (in our notation) as the "local mix." Setting $\hat{\Omega} = 0$ reduces to the approximation originally proposed by Schapery and Davidson (1990); considering the change in notation from our previous work, $\hat{\Omega} = 0$ corresponds to $k_1 = 0$ in the (1990) notation. Setting $\hat{\Omega} = 0$ also reduces to the mode separation procedure utilized by Williams (1988). Note that, for unidirectional laminates containing a midplane delamination, the singular field solution also results in $\hat{\Omega} = 0$. Thus, Kinloch et al. (1993) first experimentally determined the failure loci of unidirectional specimens containing midplane delaminations. They next used this locus to predict interfacial failure for unidirectional specimens containing offset delaminations, and compared the predictions using a singular field-based mode-mix decomposition to that based on $\hat{\Omega} = 0$. Better predictions for failure were achieved by using the $\hat{\Omega} = 0$ decomposition than by using the true value of $\hat{\Omega}$. However, their study was restricted to only unidirectional specimens, and it is not clear that these results are applicable to multidirectional layups.

We are currently performing a more extensive experimental investigation of the above issue, to ascertain whether $\hat{\Omega} = 0$, or some other choice of $\hat{\Omega}$, may be used as part of an engineering methodology to predict fracture at bimaterial interfaces, as well as delamination at interfaces of arbitrary relative ply orientations in laminated composites. Specifically, we are conducting experiments where various definitions of $\hat{\Omega}$ are used to reduce data from fracture tests to describe a failure locus. For fiber composites, tests are being conducted over a range of mode mixities and with a variety of relative fiber angles bounding the delamination. In a concurrent fashion, approaches are being evaluated that (1) explicitly account for both the effect of fiber angle and ψ on G_c, and (2) at a given mode mixity, utilize the minimum G_c, with respect to fiber orientation, to define a "minimum toughness"

Downloaded 04 May 2010 to 171.66.16.28. Redistribution subject to ASME license or copyright; see http://www.asme.org/terms/Terms_Use.cfm

locus. In both of the above approaches, the experimentally determined failure locus and the associated value of $\hat{\Omega}$ are used to predict delamination growth for other geometries, loadings, and interfaces, and these predictions are compared to additional experimental results. For interfaces between homogeneous materials, tests are being performed for various interfacial pairs over a range of thickness ratios and mode mixities. Expressions for the effective $\hat{\Omega}$ that we are considering include those based on the $[A]$, $[B]$, and $[D]$ matrices (Whitney, 1987) defining the cracked portions of the plate and/or on values for homogeneous materials. For example, one could choose $\hat{\Omega}$ based on (28) and (42), with α and β defined to be for the layers adjacent to the crack plane and $\hat{L}$ defined to be the ply thickness. If such an approach is successful, then the need for additional continuum analyses as part of a fracture or delamination growth prediction methodology will be eliminated.

Until further experimental evidence is available, it is probably best to limit simplifications to the $\beta = 0$ approach for predicting delamination in laminated composites. If this approach is adopted, the error incurred by setting $\beta = 0$ to define a mode ratio is likely small compared to other inherent approximations in the methodology. However, the $\beta = 0$ approach to mode-mix decomposition is still fundamentally based on the singular field. To ensure that this is valid, an interim methodology has recently been described (Davidson, 1994b). This methodology may be used to verify the $\beta = 0$ approach, or to experimentally determine effective values of $\hat{\Omega}$ for those cases where the singular field-based mode-mix decomposition does not satisfactorily predict failure. Since Ω will change with laminated structure, the effects of scaling, which enter only through the usually small quantity $\epsilon \ln(\hat{L}/L)$, are likely not of practical concern. Rather, Ω is obtained for each layup of interest; the energy release rate and mode ratio for a variety of loadings are then computed by the crack-tip element analysis. For practical reasons, it is likely best to base delamination growth predictions on a comparison of G, at a particular mode mixity, to the "minimum" value of G_c at this same mode mixity, as discussed above. This results in a conservative design philosophy, analogous to using plane strain fracture toughness values to predict crack growth in metals (Broek, 1982).

Finally, one other means of eliminating the difficulties associated with the oscillatory singularity in delamination of fiber-reinforced laminated composites is to assume that the crack is within a thin adhesive interlayer (Raju et al., 1988). Davidson and Hu (1995) compared mode ratio as predicted by the $\beta = 0$ approach to this "adhesive interlayer" approach. As would be expected, it was found that the fracture mode mixity is strongly dependent upon the modulus of the (isotropic) adhesive interlayer. The introduction of the resin interlayer produces a singular zone which exists on a scale much smaller than the interlayer thickness. However, the "outer" stress singularity, which defines the stress field on a scale which is large compared to the interlayer thickness, is unaffected. Basing fracture predictions on the inner singularity would only seem to be appropriate when an adhesive interlayer actually exists, and the fracture process zone is small compared to the thickness of the interlayer. Interestingly, Davidson and Hu (1995) found that for any given remote loading, the $\beta = 0$ approach, applied to interfaces without an interlayer, predicted a fracture mode mixity which was within the range of mode mixities which could be obtained by placing an interlayer at the interface and varying its elastic modulus within physically realistic bounds.

Results for $\epsilon = 0$

In this section, results are presented for problems where the crack-tip singularity is nonoscillatory. Specific mesh refinement requirements for the finite element model utilized to obtain Ω are described, and comparisons between predictions of mixed-mode energy release rates between the crack-tip element and finite element methods are presented. Also, analytical expressions for Ω as a function of thickness ratio and material properties are given for homogeneous isotropic and orthotropic plates, and the results are compared to those obtained by Suo and Hutchinson (1990) and Suo (1990a).

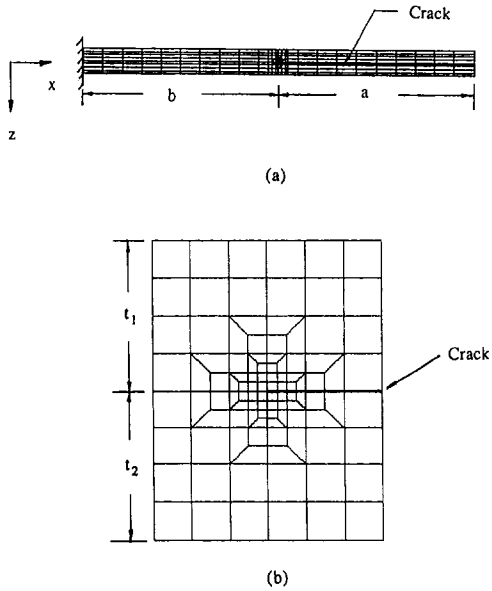

Fig. 2 (a) Typical finite element mesh for $t_1 = t_2$; (b) expanded view of crack-tip neighborhood

Finite Element Model. Finite element models of the crack-tip element developed using the finite element code ABAQUS, licensed from Hibbitt, Karlsson and Sorensen, Inc. A typical finite element model for a problem where $t_1 = t_2$ is shown in Fig. 2. The model has square elements at the crack tip; for the model shown, the size of the elements at the crack tip, Δ/t_1, is equal to 0.0625, where Δ is the length of the element at the crack tip. Eight-node, biquadratic, plane strain continuum elements were utilized. As will be discussed below, extensive mesh refinement studies on this model were performed. In addition to the mesh shown, other mesh refinement techniques were tried, such as that used by Schapery and Davidson (1990) and Raju et al. (1988). These more "conventional" meshes also used square elements at the crack tip; however, the number of elements through the thickness of the model was kept constant along its entire length. This resulted in a large number of elements in order to keep the aspect (length-to-width) ratio of any individual element within reasonable limits. We found that the mesh shown required significantly less global degrees of freedom and gave the same results for energy release rate and mode mixity as these more conventional meshes. Further, for the mesh shown, refining the crack-tip region is extremely simple, as none of the far-field nodes need to be changed.

Mesh Refinement Studies. Mesh refinement studies were conducted for both laminated and homogeneous plates comprising a wide range of material properties. For the laminated plates, individual layers were considered which were both orthotropic and isotropic. The orthotropic layers which were considered had longitudinal moduli approximately 10 to 20 times larger than their transverse and through-thickness moduli, and had a longitudinal to shear modulus ratio on the order of 20/1. The specific layer properties used were typical of graphite or glass-fiber-reinforced polymeric matrix materials (Hoskin and Baker, 1986; Tsai, 1988). Various layer angles bounding the crack were considered; however, the

Downloaded 04 May 2010 to 171.66.16.28. Redistribution subject to ASME license or copyright; see http://www.asme.org/terms/Terms_Use.cfm

material properties immediately above and below the crack plane were always chosen such that $\epsilon = 0$.

For our mesh refinement studies, one finite element run was first performed to obtain Ω. The loading on the model was chosen such that $M_c = 0$. The loads and moments, N_1, N_2, M_1, and M_2, were applied to the model as distributed in-plane forces acting on the end nodes of the cracked regions. The uncracked end of the model was fully fixed. G_I and G_{II} were obtained by the virtual crack closure technique, and Ω was calculated from (31). Using this value of Ω and the crack-tip element analysis, loadings were then determined analytically which would correspond to mode ratios, G_I/G, of approximately 0.01, 0.2, 0.5, 0.8, and 0.99. The energy release rate and mode ratio under these five same loadings were then calculated using the finite element model. The finite element mesh was then refined by halving the previous near-tip element sizes, and the value of Ω and the value of the energy release rate and mode ratio under the five same loadings were calculated using the refined model. This process was repeated until essentially no change was observed in the total energy release rate or mode ratio from successively refined element models.

As discussed previously, a remote loading corresponding to $M_c = 0$ was always used to obtain Ω. It was found that, once the value of Ω converged within one percent, the values of the energy release rate and mode ratio under the various loadings also converged within one percent. Here and in succeeding discussions, "convergence" is defined to mean that the finite element results at this level of mesh refinement were within one percent of the results from the previous refined mesh for all mode ratios and all materials studied. Once Ω converged, energy release rates and mode ratios as predicted by the crack-tip element approach under arbitrary loadings agreed with those predicted by the finite element analysis within approximately 0.5 percent. In general, the accuracy of Ω is wholly dependent upon having a well-converged finite element model. Interestingly, it was found that, for arbitrarily chosen loading, the amount of mesh refinement necessary to give convergence did not guarantee convergence under all loadings. That is, if the finite element model converged for a specific mode ratio, it did not necessarily follow that it converged for all mode ratios. The exception to this was the mode ratio used to obtain Ω, which was always predominantly mode II.

For problems where the materials above and below the crack plane are homogeneous, it was found that a mesh with elements at the crack tip of size Δ/t_i equal to 1/16 was sufficient to guarantee convergence, where t_i is taken to be the lesser of t_1 and t_2. For laminated materials where each of the regions above and below the crack plane are four or more layers thick, it was found that the size of the elements at the crack tip, Δ/h, equal to 1/8 was sufficient to guarantee convergence, where h is the single layer thickness. Converged results, as defined above, were found to be within 1.5 percent of the most refined mesh considered. Specifically, for those cases where the materials above and below the crack plane were homogeneous, the most refined mesh examined was $\Delta/t_i = 1/128$. For those cases where the materials above and below the crack plane were laminated, the most refined mesh examined was $\Delta/h = 1/128$.

Length Effects. The crack-tip element analysis assumes that classical plate theory is applicable for predicting overall deformations and strain energies. In general, the loads and moments which act on this element are found from a global analysis. However, it is important to ascertain the minimum length to thickness ratio for which the element equations apply, as well as the minimum ratio required in the finite element model that is used to obtain Ω. To do this, a finite element model with a refined (converged) mesh was chosen with $a = b$ and $b \gg t$, where these lengths are as defined in Fig. 1. For the loadings corresponding to the five mode ratios (G_I/G equal to approximately 0.01, 0.2, 0.5, 0.8, and 0.99), a and b were incrementally decreased until the finite element results and crack-tip element analysis results began to disagree (i.e., until the finite element results began to measurably change). A wide range of material properties were considered, with E_{11}/G_{13} ratios ranging from 2.0 to 32.0, where E_{11} is the Young's modulus in the x direction, and G_{13} is the shear modulus in the x–z plane. For all loadings, E_{11}/G_{13} ratios and laminated plates studied to date, we have found that for a/t, $b/t \geq 8$, the finite element results show length effects which influence the energy release rate and mode ratio by less than 0.1 percent. Thus, these are excellent ratios to use when generating models to determine Ω for arbitrary problems. For problems where the cracked regions are isotropic and homogeneous, or are laminated and comprised of isotropic layers, for a/t, $b/t \geq 2.5$, the finite element results show length effects which influence the mode ratio by a maximum of approximately one percent, and the total energy release rate by a maximum of approximately 0.1 percent. Since a/t and b/t do not have to be large, relative rotations in the crack-tip element will normally be small. Thus, the element is also useful for geometrically nonlinear problems, where all effects of the geometric nonlinearity are accounted for through the loading on the element (Davidson and Krafchak, 1993).

Preferred Loadings to Obtain Ω. Four convenient loading cases for obtaining Ω from finite element results were examined. That is, if a finite element analysis of the crack-tip element is performed with the loading chosen such that $M_c = 0$, one may obtain Ω from G_I, Eq. (31), or one may obtain Ω from an analogous equation involving G_{II}, derived from (30). Because the finite element results are not exact, slightly different values of Ω will be obtained. Alternatively, one could choose a global loading on the finite element model such that $N_c = 0$ and use (29) and (30) to develop two additional expressions for Ω involving G_I and G_{II}. Thus, there are four relatively simple alternatives for evaluating Ω from finite element results. We evaluated Ω by each of these methods and compared the predictions for mode ratio from the crack-tip element and finite element analyses for loadings which produced mode ratios, G_I/G, of approximately 0.01, 0.2, 0.5, 0.8, and 0.99 for a number of different problems. In all cases, it was found that using (31) to obtain Ω, where G_I is found from a loading defined by $M_c = 0$, gave the best overall correlation between crack-tip element and finite element results. Although not explicitly stated in their previous work, this is the same conclusion reached by Schapery and Davidson (1990) in a more limited numerical study.

Example Problem. As an example illustrating the correspondence between the crack-tip element and finite element analyses, consider a laminated plate with two different homogeneous isotropic layers, designated by 1 and 2, and arranged as follows (starting at $z = -t_1$): [1/2/2/1/crack/2/1/1/2]. Thus, the regions above and below the crack plane individually possess midplane symmetry, however, the global laminate does not. The material properties are given by $E_1 = 1$, $\nu_1 = 0.3$, $E_2 = 1.923$ and $\nu_2 = 0$. This combination satisfies (36), i.e., $\beta = \epsilon = 0$. Each layer has a thickness of 0.01. We chose a loading defined by $N_1 = 1$, $N_2 = -1$, $M_1 = t_1/2 = 0.02$ and $M_2 = t_2/2 = 0.02$ to evaluate Ω by comparison with finite element results. Note that this loading gives $N = M = 0$ (by global equilibrium considerations); by (8) and (9), $N_c = -1$ and $M_c = 0$. These loads were applied to a finite element model similar to that shown in Fig. 2, but with $\Delta/h = 0.125$. That is, referring to Fig. 2, the model used contained an additional refinement of the 4×4 region of square elements surrounding the crack tip, performed in an identical manner to the two refinements shown in the figure. The VCCT was used to obtain $G_I = 0.78$ and $G_{II} = 67.56$. Using

Downloaded 04 May 2010 to 171.66.16.28. Redistribution subject to ASME license or copyright; see http://www.asme.org/terms/Terms_Use.cfm

Table 1 Comparison of crack-tip element and finite element results for an eight-layered plate (cte = crack-tip element analysis, fea = finite element analysis)

N_c	M_c	G(cte)	G(fea)	$(G_I/G)_{cte}$	$(G_I/G)_{fea}$
-1.2250	0.0003	102.97	102.93	0.014	0.014
-2.6250	0.0236	608.76	608.24	0.191	0.191
-1.2500	0.0249	220.08	219.73	0.458	0.458
-0.8125	0.0629	611.69	610.83	0.887	0.888
-0.0500	0.0398	207.43	206.89	0.990	0.991

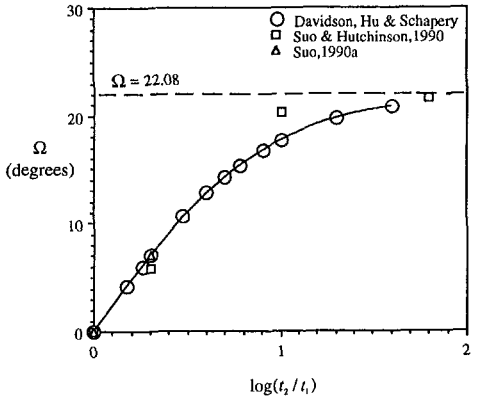

Fig. 3 Mode-mix parameter for a homogeneous, isotropic material

the conventional laminated plate theory definitions (Whitney, 1987), A, B, and D were evaluated for the uncracked and for each of the cracked regions, substituted into (7), and using (31), $\Omega = 6.13$ deg. Using this value of Ω, (29) and (30) were used to predict G_I and G_{II} for arbitrary loadings. These results were compared to finite element predictions for the same loadings and the results are presented in Table 1. Note that essentially the same results are obtained by both methods. Similar correlation between crack-tip element and finite element results have been obtained by Schapery and Davidson (1990), Davidson (1994a), and Davidson and Krafchak (1993).

Mode-Mix Parameter for Homogeneous Isotropic and Orthotropic Materials. For problems where the same material is above and below the crack plane and the material is isotropic, Ω is a function of only the thickness ratio, i.e., $\Omega = \Omega(t_2/t_1)$. Using our finite element model, Ω was evaluated over a range of thickness ratios for this case and the results are presented in Fig. 3. Also shown in the figure are values of Ω as found by Suo and Hutchinson (1990) and Suo (1990a) using integral equation methods. As previously discussed, Suo and Hutchinson defined their mode-mix parameter, ω, in a different fashion, and the correspondence between Ω and ω is presented in Appendix A. We favor the use of Ω, as it is an odd function of $\log(t_2/t_1)$. This is also shown in Appendix A. The limiting value of $\Omega = 22.08$ deg as $t_2/t_1 \to \infty$ is also shown in Fig. 3 and is taken from the corresponding value of ω as given by Suo and Hutchinson (1990).

The finite element results for $0.025 \le t_2/t_1 \le 40$ are fit nicely by the equation

$$\Omega = 23.529\eta - 6.8406\eta^3 + 1.0706\eta^5 \qquad (37)$$

where

$$\eta = \log(t_2/t_1) \qquad (38)$$

and $\log \equiv \log_{10}$. Equation (37) provides the continuous line shown in Fig. 3.

For problems where the same material is above and below the crack plane and the material is orthotropic, $\Omega = \Omega(t_2/t_1, \rho)$, where the dimensionless parameter ρ is given by (18) and is equal to 1 for isotropic materials (Suo, 1990a). We used our finite element model to obtain Ω for various orthotropic materials. The values of ρ considered spanned those values for virtually all structural composite materials for which we could obtain properties which are currently in use or proposed in the near future (Tsai, 1988; Hoskin and Baker, 1986). The results are presented in Table 2, and are very similar to each other and to those of Fig. 3. For example, using the results for $\rho = 2$ as a general expression for Ω for $1 \le \rho \le 8$ gives a maximum error of 1.26 percent (at $t_2/t_1 = 4.0$). Excellent curve fits of the data of Table 2 are obtained using the following equations:

Table 2 $\Omega(t_2/t_1, \rho)$ for homogeneous, orthotropic materials (Ω in degrees)

t_2/t_1 \ ρ	1.0	2.0	4.0	8.0
1	0.00	0.00	0.00	0.00
2	7.02	7.10	7.16	7.16
4	12.74	12.90	12.99	12.98
8	16.76	16.88	16.96	16.93
10	17.68	17.81	17.88	17.84
20	19.71	19.83	19.88	19.83

$$\Omega(\rho = 2) = 24.158\eta - 7.9834\eta^3 + 1.6055\eta^5 \qquad (39)$$

$$\Omega(\rho = 4) = 24.375\eta - 8.1897\eta^3 + 1.6650\eta^5 \qquad (40)$$

$$\Omega(\rho = 8) = 24.382\eta - 8.2627\eta^3 + 1.6924\eta^5. \qquad (41)$$

To obtain results for values of ρ which are not included in (37) or (39)–(41), linear interpolation (at fixed η) works very well. For example, for $(t_2/t_1, \rho) = (6, 6)$, linearly interpolating between equations (40) and (41) yields $\Omega = 15.57$ deg. A finite element analysis of this case yielded $\Omega = 15.53$ deg; -0.3% different from the value obtained by linear interpolation. This difference is fairly unimportant; for arbitrary loadings, the difference in predicted mode ratio between these values of Ω is less than one percent. We also checked the correlation of Suo's (1990a) results to those presented in (39)–(41). In general, it was very good and similar to the comparison shown in Fig. 3 between his (1990a) values and our results.

Finally, as a test of the numerical solution method, several material property "sets" were chosen which corresponded to vastly different materials. According to the theory, the value of Ω should not change if t_2/t_1 and ρ are fixed. Thus, each material property set was chosen to give the same value of ρ. For example, for the different material property sets, E_{11}/G_{13} varied from 2 to 32, E_{11}/E_{22} varied from 0.3 to 20 and λ (Eq. (16)) varied from 0.2 to 20. We evaluated Ω for the different property sets and found that the maximum change of any value in Table 2 was 0.7 percent.

Downloaded 04 May 2010 to 171.66.16.28. Redistribution subject to ASME license or copyright; see http://www.asme.org/terms/Terms_Use.cfm

Results for $\epsilon \neq 0$

Comparisons between the crack-tip element analysis and finite element analyses were also conducted for a number of bimaterial problems in which $\epsilon \neq 0$. Typical results are presented in Table 3. These results are for a cracked bimaterial plate in which the regions above and below the crack plane are homogeneous and isotropic and for which $t_1 = 0.04$, $E_1 = 1$, $\nu_1 = 0.2$, $t_2 = 0.08$, $E_2 = 2.333$ and $\nu_2 = 0.467$. Plane stress conditions are assumed, which gives $\beta = -0.2$ and $\epsilon = 0.0645$.

In order to determine Ω, a plane stress finite element analysis of the crack-tip element geometry was performed with $N_1 = N_2 = 0$, $M_1 = 2.0075$ and $M_2 = 7.9925$; this corresponds to $N_c = -88.4422$ and $M_c = 0$. The VCCT was used to obtain $G = 474{,}936$; by (11), $|K| = 832.2$. Next, $|K|$ was evaluated by the CSD method using various pairs of nodes behind the crack tip until the nodal location was found which gave this same value. The displacements at that nodal pair were used to evaluate ψ; selecting $L = t_1$, we obtained $\psi = -69.9$ deg and, by (33), $\Omega = 20.1$ deg. This value of Ω was then used to predict K for loadings corresponding to various mode mixities and compared to the values obtained by the CSD/finite element method. As can be seen from Table 3, excellent correlation is obtained for all mode mixities. Notice that, due to numerical error, the percent difference between K_{II} as obtained by the two methods is large when ψ is small, and the percent difference between K_I by the two methods is large when ψ is large. However, in both cases the absolute difference, with respect to $|K|$, is small.

In an effort to find a general expression for Ω for cracks between homogeneous isotropic layers, which, as discussed previously, may be a candidate for an effective Ω for laminated materials, we examined Suo and Hutchinson's (1990) results. Tabulated values of their mode-mix parameter were first transformed to equivalent values of $\Omega(t_1)$ using the procedure in Appendix A. Next, these tabulated values were "smoothed" numerically, using symmetry and antisymmetry arguments similar to those of Appendix A. We found all of these data can be represented by the following expression:

$$\Omega(t_1) = \Omega_0 - (135 + 16e^{-|10\eta|})\beta/\pi \qquad (42)$$

Table 3 Comparison of crack-tip element and finite element results for an isotropic, bimaterial interface (cte = crack-tip element analysis, fea = finite element analysis)

N_c	M_c	ψ (deg)	K_I (fea)	K_{II} (fea)	K_I (cte, Ω=20.1°)	K_{II} (cte, Ω=20.1°)	K_I (cte, Ω=18.4°)	K_{II} (cte, Ω=18.4°)
46.9338	2.7955	-0.3	824.0	-4.2	824.6	-0.3	824.2	-24.8
96.1868	3.6303	17.6	958.4	303.8	956.9	310.9	965.7	282.4
31.9329	0.9311	32.5	223.1	141.8	221.9	143.9	226.1	137.3
22.6258	0.3998	64.2	67.7	139.9	66.5	140.6	70.6	138.5
48.5323	0.4497	89.8	1.3	362.0	0.1	362.1	10.9	361.9

$K_I = \mathrm{Re}[Kt_1^{i\epsilon}]$ $\quad K_{II} = \mathrm{Im}[Kt_1^{i\epsilon}]$ $\quad \tan\psi = (K_{II}/K_I)_{fea}$

where $\Omega(t_1)$ and Ω_0 are in degrees, Ω_0 denotes the value of Ω for a bimaterial problem with the same value of α as the problem of interest, yet with $\beta = 0$, and η is as given in (38). For isotropic layers, α is the other of Dundurs' (1969) parameters and measures the relative stiffness of the two materials. In addition to β, it is the only other bimaterial parameter required for traction prescribed boundary value problems (Suo, 1990b). A generalized value of α for homogeneous orthotropic layers has been derived by Suo (1990b), and is given by

$$\alpha = -(1 - \Sigma)/(1 + \Sigma) \qquad (43)$$

where

$$\Sigma = \left[(s_{11}s_{33})^{1/2}\right]_2 / \left[(s_{11}s_{33})^{1/2}\right]_1. \qquad (44)$$

Values for Ω_0 as a function of α and thickness ratio, t_2/t_1, are presented in Table 4. The values of Ω_0 in Table 4 come from the smoothing process on Suo and Hutchinson's (1990) tabulated values. As a verification step, these values were used with Eq. (42) and were compared to finite element results for a number of specific cases. For all cases evaluated to date, the two methods gave values of $\Omega(t_1)$ that coincided within less than 2 deg.

The accuracy of (42) was also examined for various values of η and α for which Ω_0 values are *not* presented in the table. Specifically, the results of Table 4 were used, along with the discussion of Appendix A and the observation that interchanging the materials above and below the crack plane produces a sign change in α, to determine values of Ω_0 for $t_2/t_1 = 0.1$ and $t_2/t_1 = 0.5$ for each value of α. Next, cubic interpolation was performed, at each α and as a function of η, to generate values of Ω_0 for $-1 \leq \eta \leq 1$. Finally, cubic interpolation as a function of α at fixed η was used to obtain Ω_0 for $-0.8 \leq \alpha \leq 0.8$, and Eq. (42) was used to obtain $\Omega(t_1)$. For all cases examined to date, the resulting values of $\Omega(t_1)$ have been within 2 deg of those obtained by the finite element/CSD procedure. We also examined extrapolating the results in the table with respect to α over the range $|0.8| \leq \alpha \leq |0.94|$. The best comparison between Eq. (42) and the finite element results was obtained by performing cubic interpolation with respect to η and linear extrapolation with respect to α; that is, only the results for $\alpha = |0.6|$ and $|0.8|$ were used in the extrapolation process. Use of this technique also gave values of $\Omega(t_1)$ that were within 2 deg of the finite element results.

To illustrate the use and accuracy of (42), consider the example problem of Table 3, for which $\alpha = -0.4$. Using (42), along with the results of Table 4, gives $\Omega(t_1) = 18.4$ deg. Comparison of the crack-tip element to finite element results for this value of Ω are also presented in Table 3. Except for extreme values of phase angle, the sensitivity of mode mix to Ω is fairly small. Thus, for practical applications, it is likely acceptable to use values of Ω computed by (42) and Table 4, along with interpolation or extrapolation as necessary.

Finally, when obtaining Ω from finite element results, it was observed that a more refined finite element mesh is generally required to accurately obtain Ω for the case where

Table 4 $\Omega_0 = \Omega(t_2/t_1, \alpha, \beta = 0)$ for cracks between homogeneous isotropic layers (in degrees)

t_2/t_1 \ α	-0.8	-0.6	-0.4	-0.2	0.0	0.2	0.4	0.6	0.8
1	11.2	8.4	5.6	2.8	0.0	-2.8	-5.6	-8.4	-11.2
2	13.7	11.8	9.8	7.9	6.1	4.2	1.8	-1.6	-7.0
10	16.8	17.8	18.7	19.6	20.3	20.6	20.1	17.8	13.1
∞	16.5	17.8	19.1	20.5	22.1	24.1	26.8	30.5	35.7

Downloaded 04 May 2010 to 171.66.16.28. Redistribution subject to ASME license or copyright; see http://www.asme.org/terms/Terms_Use.cfm

Table 5 Results of mesh refinement study for the isotropic, bimaterial example problem

Δ/t_1	ψ (degrees)	Ω (degrees)
1/16	-68.94	21.06
1/32	-69.16	20.84
1/64	-69.48	20.52
1/128	-69.66	20.34
1/256	-69.81	20.19
1/512	-69.88	20.12

$\epsilon \neq 0$ than for $\epsilon = 0$. For example, in the above example problem, Ω converged to within approximately one percent for a finite element mesh with an element size at the crack tip, $\Delta/t_1 = 1/128$; for the same geometry but $\epsilon = 0$, Ω converged to within one percent at $\Delta/t_1 = 1/16$. With our mesh refinement technique (cf. Fig. 2), refining the crack-tip region is relatively straightforward and does not appreciably increase the model's run-time. Results of a typical mesh refinement study, conducted for the above example problem for the load case where $M_c = 0$, are presented in Table 5.

Conclusions

An analysis has been presented for predicting energy release rates and mode mixities for interfacial fracture problems using an analytical crack-tip element. Equations for determining the energy release rate and mode mixity as a function of the loading on the element were derived using classical plate theory. A formulation was adopted which allows the same set of equations to be utilized for cracks within or between isotropic or orthotropic layers. As found previously (Schapery and Davidson, 1990; Suo and Hutchinson, 1990), the equations for mode mixity contain one unknown parameter which must be obtained from a single continuum analysis. This parameter, designated herein as Ω, was calculated by finite element analysis. Given Ω, for those problems where classical plate theory is applicable for determining the overall strain energy of the region surrounding the crack tip, the crack-tip element approach provides total energy release rate and mode mixity as analytical functions of the applied loads and moments.

Values of Ω have been presented for isotropic and orthotropic materials. These values are useful for developing closed-form solutions to a number of problems using the crack-tip element analysis. For those problems where Ω must be calculated, a simple technique has been presented wherein Ω may be obtained from a single finite element analysis, and specific mesh refinement requirements have been described. It has been demonstrated that once Ω is known, the crack-tip element analysis predicts essentially the same energy release rate and mode mix for arbitrary loadings as is obtained by finite element analysis.

As mentioned above, the crack-tip element analysis does not completely eliminate the need for finite element analysis; one analysis is still required to obtain Ω. However, this analysis need be of the crack-tip element geometry only. Thus, the finite element model necessary to augment the crack-tip element analysis is relatively simple and essentially independent of the global geometry. Consequently, despite the need for a single finite element analysis, the crack-tip element approach provides an extremely computationally efficient methodology. The advantages of this approach are particularly significant for problems where there are a large number of loading cases to be considered (Davidson, 1994a; Davidson 1994c), for geometrically nonlinear problems (Davidson and Krafchak, 1993), or where linear viscoelastic effects are of interest, including the effects of temperature and moisture on the laminate's properties.

Finally, for those problems where a linear elastic analysis predicts an oscillatory crack-tip stress singularity, it has been discussed how a previously suggested approximation may be used to define a unique value of mode ratio. This approach was originally suggested by He and Hutchinson (1989) for isotropic problems and was adopted by Davidson (1994a) for laminated orthotropic problems. The approach consists of modifying the elastic constants so that one of Dundurs' generalized parameters, β, vanishes in order to remove the oscillatory nature of the singularity. It was observed that for problems where there is only a difference of scale between the body to be analyzed and that used for fracture characterization, if β is set equal to zero according to the approach proposed herein, then predictions of fracture by this $\beta = 0$ approach have the same accuracy as those made using the actual value of β. Use of the $\beta = 0$ approach significantly simplifies interpretation and reporting of interfacial fracture data and allows for a consistent engineering methodology for predicting delamination growth in fiber-reinforced laminated composite materials.

Acknowledgments

The work of BDD and HH was supported by the National Science Foundation under Grant MSS-9210844. That of RAS was sponsored by the National Science Foundation through the Offshore Technology Research Center.

References

Biot, M. A., 1972, "Nonlinear Effect of Initial Stress on Crack Propagation Between Similar and Dissimilar Orthotropic Media," *Quarterly of Applied Mathematics*, Vol. 30.

Broek, D., 1982, *Elementary Engineering Fracture Mechanics*, Martinus Nijhoff.

Chai, H., 1984, "The Characterization of Mode I Delamination Failure in Non-Woven, Multidirectional Laminates," *Composites*, Vol. 15, No. 4, pp. 277–290.

Davidson, B. D., 1994a, "Prediction of Energy Release Rate for Edge Delamination Using a Crack Tip Element Approach," *Fifth ASTM Symposium on Composite Materials: Fatigue and Fracture*, R. H. Martin, ed., American Society for Testing and Materials, ASTM STP 1230.

Davidson, B. D., 1994b, "Prediction of Delamination Growth in Laminated Structures," *Failure Mechanics in Advanced Polymeric Composites, AMD-Vol. 196*, G. A. Kardomateas and Y. D. S. Rajapakse, eds., ASME, New York, pp. 43–65.

Davidson, B. D., 1994c, "Energy Release Rate Determination for Edge Delamination Under Combined In-Plane, Bending and Hygrothermal Loading—Part I: Delamination at a Single Interface," *Journal of Composite Materials*, Volume 28, No. 11, pp. 1009–1031.

Davidson, B. D., and Hu, H., 1995, "Effect of Interlayer Modulus on Fracture Mode Ratio for Interleaved Composite Laminates," *Engineering Fracture Mechanics*, Vol. 52, No. 2.

Davidson, B. D., and Krafchak, T. M., 1993, "Analysis of Instability-Related Delamination Growth Using a Crack Tip Element," *AIAA Journal*, Vol. 31, No. 11, pp. 2130–2136.

Dundurs, J., 1969, "Mathematical Theory of Dislocations," ASME JOURNAL OF APPLIED MECHANICS, Vol. 36, pp. 650–652.

He, M-Y., and Hutchinson, J. W., 1989, "Kinking of a Crack out of an Interface," ASME JOURNAL OF APPLIED MECHANICS, Vol. 56, pp. 270–278.

Hoskins, B. C., and Baker, A. A., eds., 1986, *Composite Materials for Aircraft Structures*, AIAA Education Series, American Institute of Aeronautics and Astronautics.

Hu, M. S., Thouless, M. D., and Evans, A. G., 1988, "The Decohesion of Thin Films from Brittle Substrates," *Acta Metallurgica*, Vol. 36, No. 5, pp. 917–925.

Kinloch, A. J., Wang, Y., Williams, J. G., and Yayla, P., 1993, "The Mixed-Mode Delamination of Fibre Composite Materials," *Composites Science and Technology*, Vol. 47, pp. 225–237.

Matos, P. P. L., McMeeking, R. M., Charalambides, P. G., and Drory, M. D., 1989, "A Method for Calculating Stress Intensities in Bimaterial Fracture," *International Journal of Fracture*, Vol. 40, pp. 235–254.

Nicholls, D. J., and Gallagher, J. P., 1983, "Determination of G_{Ic} in Angle Ply Composites Using a Cantilever Beam Test Method," *Journal of Reinforced Plastics and Composites*, Vol. 2, pp. 2–17.

Pagano, N. J., ed., 1989, "Interlaminar Response of Composite Materials," *Composite Material Series*, Vol. 5, Elsevier, New York.

Raju, I. S., Crews, J. H., Jr., and Aminpour, M. A., 1988, "Convergence

Downloaded 04 May 2010 to 171.66.16.28. Redistribution subject to ASME license or copyright; see http://www.asme.org/terms/Terms_Use.cfm

of Strain Energy Release Rate Components for Edge-Delaminated Composite Laminates," *Engineering Fracture Mechanics*, Vol. 30, No. 3, pp. 383–396.

Rice, J. R., 1988, "Elastic Fracture Mechanics Concepts for Interfacial Cracks," ASME JOURNAL OF APPLIED MECHANICS, Vol. 55, pp. 98–103.

Rybicki, E. F., and Kanninen, M. F., 1977, "A Finite Element Calculation of Stress Intensity Factors by a Modified Crack Closure Integral," *Engineering Fracture Mechanics*, Vol. 9, pp. 931–938.

Schapery, R. A., and Davidson, B. D., 1990, "Prediction of Energy Release Rate for Mixed-Mode Delamination Using Classical Plate Theory," *Applied Mechanics Reviews*, Vol. 43, No. 5, pp. S281–S287.

Suo, Z., 1990a, "Delamination Specimens for Orthotropic Materials," ASME JOURNAL OF APPLIED MECHANICS, Vol. 57, pp. 627–634.

Suo, Z., 1990b, "Singularities, Interfaces and Cracks in Dissimilar Anisotropic Media," *Proceedings of the Royal Society of London*, Vol. A427, pp. 331–358.

Suo, Z., and Hutchinson, J. W., 1990, "Interface Crack Between Two Elastic Layers," *International Journal of Fracture*, Vol. 43, pp. 1–18.

Suo, Z., and Hutchinson, J. W., 1989, "Sandwich Test Specimens for Measuring Interface Crack Toughness," *Materials Science and Engineering*, A107, pp. 135–143.

Tsai, S. W., 1988, *Composites Design*, 4th ed., Think Composites, Dayton, OH.

Whitney, J. M., 1987, *Structural Analysis of Laminated Anisotropic* Plates, Technomic.

Williams, J. G., 1988, "On the Calculation of Energy Release Rates for Cracked Laminates," *International Journal of Fracture*, Vol. 36, pp. 101–119.

APPENDIX A

The relation between Suo and Hutchinson's (1990) mode-mix parameter, ω, and that used in the present work, Ω, is developed here. The antisymmetric nature of Ω is also demonstrated. Considering an interface crack between two isotropic elastic layers, Suo and Hutchinson showed that the singularity depends on only two suitably defined loading parameters, an in-plane load P and moment M (designated here by M_s in order to distinguish it from M in Fig. 1). For their two-layer problem, we find that the concentrated crack-tip force and moment are

$$N_c = P \qquad M_c = M_s + \frac{Pt_1}{2}. \tag{A1}$$

The energy release rate is a positive-definite, quadratic function of P and M_s and thus may be written in the same form as (5),

$$G = \frac{1}{2}\left(\hat{c}_1 P^2 + \hat{c}_2 M_s^2 + 2\sqrt{\hat{c}_1\hat{c}_2}\, PM_s \sin\hat{\Gamma}\right) \tag{A2}$$

where

$$\sin\hat{\Gamma} = \frac{\hat{c}_{12}}{\sqrt{\hat{c}_1\hat{c}_2}}. \tag{A3}$$

Substituting (A1) into (5) and comparing the result with (A2) gives

$$\begin{aligned} \hat{c}_1 &= c_1 + c_2 t_1^2/4 + c_{12} t_1 \\ \hat{c}_2 &= c_2 \\ \hat{c}_{12} &= c_2 t_1/2 + c_{12}. \end{aligned} \tag{A4}$$

The stress intensity factor, (24), may be written as

$$K = k_c\left[N_c\sqrt{c_1}\, e^{i\pi/2} + M_c\sqrt{c_2}\, e^{i\Gamma}\right] L^{-i\epsilon} e^{i\Omega} \tag{A5}$$

where k_c is a real constant. Suo and Hutchinson's (1990) stress intensity factor is, in the present notation,

$$K = k_c\left[P\sqrt{\hat{c}_1} + M_s\sqrt{\hat{c}_2}\, e^{i(\hat{\Gamma}-\pi/2)}\right] t_1^{-i\epsilon} e^{i\omega} \tag{A6}$$

where ω is their mode-mix parameter. Both Ω and ω are independent of the loading. Thus, for simplicity, take $P = N_c = 0$ and $M_c = M_s$ (cf. Eq. (A1)) and compare (A5) and (A6) to obtain

$$\omega = \Omega + \Gamma - \hat{\Gamma} + \pi/2 + \epsilon \ln(t_1/L) \tag{A7}$$

For subsequent discussions, we choose $L = t_1$.

Before applying (A7) to two special cases, it is of interest to show that Ω changes sign when the materials above and below the crack plane are interchanged (i.e., a 180-deg rotation of the plate about the x-axis). This behavior occurs whether or not ϵ vanishes, and may be seen by substituting K from (A5) into the expression for the singular stresses along the crack plane just ahead of the crack tip,

$$\sigma_{zz} + i\tau_{xz} = Kr^{i\epsilon}/\sqrt{2\pi r} \tag{A8}$$

where $r = |x|$. After equating real and imaginary parts, we obtain

$$\begin{aligned} \sigma_{zz} = k_c(2\pi r)^{-1/2}\Big\{&-N_c\sqrt{c_1}\sin[\Omega + \epsilon\ln(r/L)] \\ &+ M_c\sqrt{c_2}\cos[\Omega + \Gamma + \epsilon\ln(r/L)]\Big\} \end{aligned} \tag{A9}$$

$$\begin{aligned} \tau_{xz} = k_c(2\pi r)^{-1/2}\Big\{&N_c\sqrt{c_1}\cos[\Omega + \epsilon\ln(r/L)] \\ &+ M_c\sqrt{c_2}\sin[\Omega + \Gamma + \epsilon\ln(r/L)]\Big\}. \end{aligned} \tag{A10}$$

Now, suppose that the external loading is maintained such that the state of stress does not change when the geometry is rotated 180 deg about the x-axis. Then, τ_{xz} and N_c change sign while σ_{zz} and M_c do not. Also, ϵ, (12) and c_{12} change sign, while c_1 and c_2, (7), do not; thus, Γ, (6), changes sign. By (A9) and (A10), we see that Ω must also change sign to maintain the proper signs and magnitudes of the near-tip stresses.

For the special case of a homogeneous plate with a crack located as in Fig. 1, it is useful to introduce the parameter η, (38). With a 180-deg rotation, t_1 and t_2 are interchanged, which means η changes sign. That is, Ω is an odd function of η. Thus, for a central crack, $\eta = \Omega = 0$.

Considering the special case of an isotropic homogeneous plate with a central crack; (A3) and (A4), together with the expressions for c_1, c_2, and c_{12} (Schapery and Davidson, 1990), yield $\Gamma = 0$ and $\hat{\Gamma} = \sin^{-1}(\sqrt{3/7}) \approx 40.893$ deg. From (A7), $\omega \approx 49.107$ deg, which essentially agrees with Suo and Hutchinson (1990). Another interesting case is that for a vanishingly thin top layer, $\eta \to \infty$. Suo and Hutchinson calculate a value of $\omega = 52.08$ deg. In this case, $\Gamma = -60$ deg and $\hat{\Gamma} = 0$, which gives $\Omega = 22.08$ from (A7).

APPENDIX B

In this Appendix, we consider the specific technique to alter the elastic moduli in a manner such that $\beta = 0$ while the total energy release rate and other significant parameters are unaffected. Considering a crack-tip element in which each of the materials above and below the crack plane are homogeneous, orthotropic, and have their material axes aligned with the coordinate axes, (7) reduces to

$$\begin{aligned} c_1 &= (4/t_1)[s_{11}]_1(1 + X\Upsilon) \\ c_2 &= (12/t_1^3)[s_{11}]_1(1 + X\Upsilon^3) \\ c_{12} &= -(6/t_1^2)[s_{11}]_1(1 - X\Upsilon^2) \end{aligned} \tag{B1}$$

where

$$X = [s_{11}]_2/[s_{11}]_1, \qquad \Upsilon = t_1/t_2 \tag{B2}$$

and the subscripts outside of the square brackets denote materials 1 and 2 (above and below the crack plane, respectively). Results in (B1) and (B2) are for plane stress; for plane strain, replace s_{11} by s'_{11} (cf. Eq. (20)).

From (36), the condition $\beta = 0$ may be satisfied by chang-

Downloaded 04 May 2010 to 171.66.16.28. Redistribution subject to ASME license or copyright; see http://www.asme.org/terms/Terms_Use.cfm

Table B1 Considerations for choosing $\beta = 0$

Condition	Result
G unchanged	$[E'_{11}]_1$, $[E'_{11}]_2$ not altered
α unchanged	$[E'_{33}]_1/[E'_{33}]_2$ not altered
$\beta=0$	$[\{(E'_{11}/E'_{33})^{1/4} - \nu'_{13}\}/E'_{11}]_1 = [\{(E'_{11}/E'_{33})^{1/4} - \nu'_{13}\}/E'_{11}]_2$

where:

For plane stress, $E'_{ii} = E_{ii}$; For plane strain, $E'_{ii} = E_{ii}/(1-\nu_{i2}\nu_{2i})$; i = 1,3

For plane stress, $\nu'_{13} = \nu_{13}$; For plane strain, $\nu'_{13} = (\nu_{13} + \nu_{12}\nu_{23})/(1-\nu_{12}\nu_{21})$

ing s_{11}, s_{33} and/or s_{13} of either or both materials. However, from (5), (8), (9), (B1), and (B2), it is difficult to change s_{11} of either or both materials in such a manner that G is unaffected. Thus, we choose not to alter $[s_{11}]_1$ and $[s_{11}]_2$ (and hence X).

Next, it is useful to examine the other generalized Dundurs' (1969) parameter, α, Eq. (43). Because of the significance of α, as discussed in the body of this work, as well as its importance in determining kink angle in isotropic bimaterial problems (He and Hutchinson, 1989), we choose to also require α to be unchanged when altering properties to obtain $\beta = 0$. In view of the previous requirements on s_{11}, this implies that the ratio $[s_{33}]_1/[s_{33}]_2$ remain invariant.

Table B1 gives the preceding results in terms of engineering constants for plane stress and plane strain. From this table, our proposed method of choosing $\beta = 0$ is to alter ν'_{13} of the material with the smaller E'_{11}/E'_{33} ratio; for the material pairs considered to date, less of a percentage change in this value is necessary than if the other ν'_{13} is altered. For plane stress, this means ν_{13} must be altered. For plane strain, in the past we have chosen to alter ν_{23} (Davidson, 1994a; 1994c).

If the condition $\beta = 0$ is obtained by the above procedure, the change in ν'_{13} may be quite large (e.g., Davidson, 1994c). However, this does not alter the accuracy of the $\beta = 0$ approach for use in making fracture predictions; as discussed in this work, for problems where there is only a difference in scale between the body to be analyzed and that used for fracture characterization, the $\beta = 0$ approach predicts the same remote loads for fracture as are obtained using the actual value of β. Thus, even if the change in Poisson's ratio is large, one may still use this procedure in a finite element model in order to determine Ω. However, in those cases where this same model is used for other structural considerations, such as to determine global deflections, then ν should be left as its true value for these latter assessments. For laminated composite materials, there is generally more than a difference in scale between the body being analyzed and that used for fracture characterization. However, as discussed in this work, it is doubtful that the $\beta = 0$ approach introduces significant error with respect to other inherent approximations in typical methodologies used for predicting fracture of these materials.

Finally, for *plane stress* bimaterial problems involving isotropic layers, note that as a result of material incompressibility requirements, it will be possible to enforce the conditions of Table B1 only if $0.5 \leq [E]_1/[E]_2 \leq 2$. Also, note that for crack growth between incompressible isotropic or orthotropic materials in *plane strain*, $\beta = \epsilon = 0$, as shown by Biot (1972).

Downloaded 04 May 2010 to 171.66.16.28. Redistribution subject to ASME license or copyright; see http://www.asme.org/terms/Terms_Use.cfm

Wen J. Yen
Associate Researcher,
Aeronautical Industry Development Center,
Taichung, Taiwan, R.O.C.

Chyanbin Hwu
Professor.

Yin Ko Liang
Graduate Student.

Institute of Aeronautics and Astronautics,
National Cheng Kung University,
Tainan, Taiwan 70101, R.O.C.

Dislocation Inside, Outside, or on the Interface of an Anisotropic Elliptical Inclusion

The plane elasticity problem of dislocation inside, outside, or on the interface of an anisotropic elliptical inclusion in an unbounded anisotropic matrix is considered. A general solution for the stresses and deformations in the entire domain is obtained by applying the Stroh's formalism and the method of analytical continuation. Since the general solutions have not been found in the literature, in order to verify the present solution, comparison is made with some special cases of which the analytical solutions exist, which shows that our results are exact and universal.

1 Introduction

In our recent study about inclusion problems (Hwu and Yen, 1993), a general analytical solution has been obtained by combining the Stroh's formalism for anisotropic elasticity, and the method of analytical continuation for the manipulation of complex variable formulation. Using that result, further study has been explored for the interaction between dislocations and elliptical inclusions (Yen and Hwu, 1994). Although the solutions presented in (Yen and Hwu, 1994) are general enough to include all the general anisotropic elastic materials, the dislocations considered are restricted to be located outside the inclusion. For the problems that the dislocation located inside the inclusion or along the interface between the matrix and the inclusion, no general analytical solutions can be found in the literature except the special cases for isotropic materials such as Dundurs and Sendeckyj (1965) and Warren (1983). It is known that solutions of dislocations are frequently used as kernel functions of integral equations to consider the interactions between inclusions and cracks. If one is interested in the problems like a crack penetrating an inclusion or a crack lying around the interface between inclusion and matrix, the solution for the dislocation inside, or on the interface of the inclusion may become useful.

At the beginning it looks easy to extend the technique using in the problems with dislocation located outside the inclusion. After further study, it is found that "inside," "outside," and "on the interface" are three different categories and cannot be included in one unified solution. The main reason is the transformation function used in our solution technique is single valued outside the elliptic inclusion but nonsingle valued inside the inclusion. With this understanding, the introduction of the singular function accounting for the dislocation is made carefully by considering the inclusion problems to be a combination of the hole problems and the elliptic plate problems. After obtaining the analytical solutions for the general anisotropic elastic materials, comparison is made with some special cases of which the analytical solutions exist because the general solutions cannot be found in the literature, which shows that our results are exact and universal.

2 Elasticity Formulation

The basic equations for two-dimensional anisotropic elasticity are the strain-displacement equations, the stress-strain laws, and the equations of equilibrium. By applying the Stroh's formalism (Stroh, 1958; Ting, 1988), a general solution satisfying these equations may be expressed as (Hwu and Yen, 1993)

$$\mathbf{u} = \mathbf{A}\mathbf{f}(z) + \overline{\mathbf{A}}\,\overline{\mathbf{f}(z)}, \quad \boldsymbol{\phi} = \mathbf{B}\mathbf{f}(z) + \overline{\mathbf{B}}\,\overline{\mathbf{f}(z)}, \qquad (1a)$$

where

$$\mathbf{A} = [\mathbf{a}_1 \quad \mathbf{a}_2 \quad \mathbf{a}_3], \quad \mathbf{B} = [\mathbf{b}_1 \quad \mathbf{b}_2 \quad \mathbf{b}_3],$$

$$\mathbf{f}(z) = [f_1(z_1) \quad f_2(z_2) \quad f_3(z_3)]^T,$$

$$z_\alpha = x_1 + p_\alpha x_2, \quad \alpha = 1, 2, 3. \qquad (1b)$$

In the above equation, (x_1, x_2) is a fixed rectangular coordinate system; $\mathbf{u}$ and $\boldsymbol{\phi}$ represent, respectively, the displacements and stress functions; p_α, $(\mathbf{a}_\alpha, \mathbf{b}_\alpha)$, $\alpha = 1, 2, 3$, are the eigenvalues and eigenvectors of the materials; $\mathbf{f}(z)$ is a holomorphic complex function vector to be determined by satisfying the boundary condition of the problems considered. The superscript T denotes the transpose and the overbar represents the conjugate of a complex number. Note that in the

Contributed by the Applied Mechanics Division of THE AMERICAN SOCIETY OF MECHANICAL ENGINEERS for publication in the ASME JOURNAL OF APPLIED MECHANICS.

Discussion on this paper should be addressed to the Technical Editor, Professor Lewis T. Wheeler, Department of Mechanical Engineering, University of Houston, Houston, TX 77204-4792, and will be accepted until four months after final publication of the paper itself in the ASME JOURNAL OF APPLIED MECHANICS.

Manuscript received by the ASME Applied Mechanics Division, Sept. 13, 1993; final revision, Mar. 1, 1994. Associate Technical Editor: D. M. Barnett.

Copyright © 1995 by ASME

Downloaded 04 May 2010 to 171.66.16.28. Redistribution subject to ASME license or copyright; see http://www.asme.org/terms/Terms_Use.cfm

derivation throughout this paper, the argument of each component function of $\mathbf{f}(z)$ is written as $z = x_1 + px_2$ without referring to the associated eigenvalues p_α. Once the solution of $\mathbf{f}(z)$ is obtained for a given boundary value problem, a replacement of z_1, z_2, or z_3 should be made for each component function to calculate field quantities from (1). It should also be noted that the solutions given in (1) are derived under the assumption that the eigenvalues p_α, $\alpha = 1, 2, 3$, are distinct. For the materials with repeated eigenvalues p_α such as the isotropic materials, a small perturbation in the values of p_α may be used in order to perform the numerical calculation on the solutions derived from Eq. (1).

To consider the problem with elliptical inclusion, it is convenient to express all the functions in terms of the transformed variables ζ_α instead of z_α, whose relation is

$$z_\alpha = \frac{1}{2}\left\{(a - ibp_\alpha)\zeta_\alpha + (a + ibp_\alpha)\frac{1}{\zeta_\alpha}\right\}, \tag{2}$$

where $2a$ and $2b$ are the major and minor axes of the ellipse. The general solution for the inclusion problems may now be written as

$$\left.\begin{aligned}\mathbf{u}_1 &= \mathbf{A}_1[\mathbf{f}_o(\zeta) + \mathbf{f}_1(\zeta)] + \bar{\mathbf{A}}_1[\overline{\mathbf{f}_o(\zeta)} + \overline{\mathbf{f}_1(\zeta)}]\\ \boldsymbol{\phi}_1 &= \mathbf{B}_1[\mathbf{f}_o(\zeta) + \mathbf{f}_1(\zeta)] + \bar{\mathbf{B}}_1[\overline{\mathbf{f}_o(\zeta)} + \overline{\mathbf{f}_1(\zeta)}]\end{aligned}\right\}, \quad \zeta \in S_1 \tag{3a}$$

and

$$\left.\begin{aligned}\mathbf{u}_2 &= \mathbf{A}_2[\mathbf{f}_o^*(\zeta) + \mathbf{f}_2(\zeta)] + \bar{\mathbf{A}}_2[\overline{\mathbf{f}_o^*(\zeta)} + \overline{\mathbf{f}_2(\zeta)}]\\ \boldsymbol{\phi}_2 &= \mathbf{B}_2[\mathbf{f}_o^*(\zeta) + \mathbf{f}_2(\zeta)] + \bar{\mathbf{B}}_2[\overline{\mathbf{f}_o^*(\zeta)} + \overline{\mathbf{f}_2(\zeta)}]\end{aligned}\right\}, \quad \zeta \in S_2 \tag{3b}$$

where the subscripts 1 and 2 denote, respectively, the matrix and inclusion. $\mathbf{f}_o$ and $\mathbf{f}_o^*$ represent the function associated with the singularity behavior caused by the dislocation. $\mathbf{f}_1$ (or $\mathbf{f}_2$) is the function corresponding to the field of matrix (or inclusion) and is holomorphic in region S_1 (or S_2). S_1 and S_2 denote, respectively, the regions occupied by the matrix and inclusion.

In general, the transformation function used in Eq. (2) is multivalued. However, by choosing only the mapped points outside the unit circle, the transformation function will map the region outside the elliptic inclusion onto the exterior of a unit circle and is single valued outside the inclusion. The z_α along the interface ($x_1 = a\cos\psi$, $x_2 = b\sin\psi$) will then be mapped onto a unit circle $\zeta_\alpha = e^{i\psi} = \sigma$. However, by choosing only the mapped points inside the unit circle, the transformation is still double-valued inside the inclusion. To have a one-to-one transformation inside the inclusion, a special choice has been made and a certain restriction should be satisfied for the function $\mathbf{f}_2(z)$ and the series form expression may be written as (Lekhnitskii, 1968; Hwu and Yen, 1993)

$$\mathbf{f}_2(\zeta) = \sum_{k=0}^{\infty}\mathbf{c}_k\zeta^k + \sum_{k=1}^{\infty}\langle\!\langle\gamma_\alpha^k\rangle\!\rangle\mathbf{c}_k\zeta^{-k} \tag{4a}$$

where

$$\gamma_\alpha = \frac{a + ibp_\alpha^*}{a - ibp_\alpha^*}. \tag{4b}$$

and p_α^* is the material eigenvalue of the inclusion. The angular bracket stands for the diagonal matrix, i.e., $\langle\!\langle f_\alpha\rangle\!\rangle = \text{diag}\,\{f_1 f_2 f_3\}$.

3 Dislocation Outside an Elliptical Inclusion

Consider an anisotropic elastic elliptical inclusion imbedded in an infinite matrix and the dislocation with Burgers vector $\hat{\mathbf{b}}$ located at the point $(\hat{x}_1, \hat{x}_2)$ which is outside the inclusion. If the inclusion and the matrix are assumed to be perfectly bonded along the interface, the displacements and surface tractions across the interface should be continuous. That is,

$$\left.\begin{aligned}\mathbf{u}_1 &= \mathbf{u}_2\\ \boldsymbol{\phi}_1 &= \boldsymbol{\phi}_2\end{aligned}\right\}, \quad \text{along the interface} \tag{5}$$

where the second equation of (5) comes from the relation $\mathbf{t} = \partial\boldsymbol{\phi}/\partial s$ in which $\mathbf{t}$ is the surface traction and s is the arc length measured along the curved boundary. An elasticity solution satisfying the dislocation singularity and the interface continuity condition has been found in (Yen and Hwu, 1993). For the ease of reference, the solution is listed as follows:

$$\mathbf{f}_o(\zeta) = \frac{1}{2\pi i}\langle\!\langle\log(\zeta_\alpha - \hat{\zeta}_\alpha)\rangle\!\rangle\mathbf{B}_1^T\hat{\mathbf{b}},$$

$$\mathbf{f}_o^*(\zeta) = \mathbf{0},$$

$$\mathbf{f}_1(\zeta) = \mathbf{B}_1^{-1}\sum_{k=1}^{\infty}\left\{\left(\bar{\mathbf{B}}_2\bar{\mathbf{c}}_k + \mathbf{B}_2\langle\!\langle\gamma_\alpha^k\rangle\!\rangle\mathbf{c}_k\right)\zeta^{-k} - \bar{\mathbf{B}}_1\bar{\mathbf{f}}_o(1/\zeta)\right\},$$

$$\mathbf{f}_2(\zeta) = \sum_{k=1}^{\infty}\left\{\mathbf{c}_k\zeta^k + \langle\!\langle\gamma_\alpha^k\rangle\!\rangle\mathbf{c}_k\zeta^{-k}\right\}, \tag{6a}$$

where

$$\mathbf{c}_k = \left\{\mathbf{G}_o - \bar{\mathbf{G}}_k\bar{\mathbf{G}}_o^{-1}\mathbf{G}_k\right\}^{-1}\left\{\mathbf{t}_k - \bar{\mathbf{G}}_k\bar{\mathbf{G}}_o^{-1}\bar{\mathbf{t}}_k\right\}, \quad k = 1, 2, \ldots, \infty \tag{6b}$$

and

$$\mathbf{G}_o = (\bar{\mathbf{M}}_1 + \mathbf{M}_2)\mathbf{A}_2,$$

$$\mathbf{G}_k = (\mathbf{M}_1 - \mathbf{M}_2)\mathbf{A}_2\langle\!\langle\gamma_\alpha^k\rangle\!\rangle,$$

$$\mathbf{t}_k = \frac{-1}{2\pi}\mathbf{A}_1^{-T}\left\langle\!\left\langle -\frac{1}{k}\hat{\zeta}_\alpha^{-k}\right\rangle\!\right\rangle\mathbf{B}_1^T\hat{\mathbf{b}}. \tag{6c}$$

$\mathbf{M}_k$, $\mathbf{k} = 1, 2$, are the impedance matrices defined as $\mathbf{M}_k = -i\mathbf{B}_k\mathbf{A}_k^{-1}$. Note that the solutions associated with $\mathbf{c}_o$ are ignored because the constant stress function does not produce stress, which represents the rigid-body motion.

4 Dislocation Inside an Elliptical Inclusion

When the dislocation is located at the point $(\hat{x}_1, \hat{x}_2)$ which is inside the inclusion, the choice of $\mathbf{f}_o$ and $\mathbf{f}_o^*$ should be very careful in order to find an elasticity solution satisfying the dislocation singularity and the interface continuity condition. A proper choice has been made as follows:

$$\mathbf{f}_o(\zeta) = \langle\!\langle\log\zeta_\alpha\rangle\!\rangle\mathbf{d},$$

$$\mathbf{f}_o^*(\zeta) = \frac{1}{2\pi i}\langle\!\langle\log(z_\alpha - \hat{z}_\alpha)\rangle\!\rangle\mathbf{B}_2^T\hat{\mathbf{b}}, \tag{7a}$$

where $\mathbf{d}$ is the unknown coefficient to be determined by the satisfaction of the continuity condition along the interface. The main consideration for the above choice is the singularity characteristics. Since $\mathbf{f}_o$ corresponds to the field of matrix (S_1) and has the responsibility to reveal the singularity behavior at infinity caused by the dislocation, it becomes clear why we have the choice shown in Eq. $(7a)_1$. As to the choice of $\mathbf{f}_o^*$, the only singularity point is the location of the dislocation $\hat{z}_\alpha$. Therefore, the most appropriate choice is the exact solution for the dislocation in a homogeneous medium, which is shown in Eq. $(7a)_2$. Besides, one should note that the argument z_α is used instead of ζ_α, which is different from that

Downloaded 04 May 2010 to 171.66.16.28. Redistribution subject to ASME license or copyright; see http://www.asme.org/terms/Terms_Use.cfm

shown in $(6a)_1$ for dislocation outside the inclusion. The reason for this difference is that the mapping from z_α-plane to ζ_α-plane is single valued outside the inclusion and nonsingle valued inside the inclusion. Hence, one may use the argument ζ_α or z_α for $(6a)_1$ without affecting the holomorphic property of $\mathbf{f}_1(\zeta)$. Due to the convenience of derivation, we choose argument ζ_α in $(6a)_1$. However, for the present problem, if the argument ζ_α is used, $\mathbf{f}_o^*$ will not be single valued inside the inclusion since the mapping is nonconformal. To avoid this harassment, the argument z_α is used in $(7a)_2$. By the relation shown in Eq. (2), $\mathbf{f}_o^*(\zeta)$ may also be written as

$$\mathbf{f}_o^*(\zeta) = \frac{1}{2\pi i}\left\langle\left\langle \log\left(\zeta_\alpha - \hat{\zeta}_\alpha\right) + \log\left(1 - \frac{\gamma_\alpha}{\zeta_\alpha \hat{\zeta}_\alpha}\right) + \log\frac{a - ibp_\alpha^*}{2}\right\rangle\right\rangle \mathbf{B}_2^T\hat{\mathbf{b}}. \quad (7b)$$

Moreover, if we consider the points where $|\zeta_\alpha| > |\hat{\zeta}_\alpha|$, by series expansion it can be proved that

$$\mathbf{f}_o^*(\zeta) = \frac{1}{2\pi i}\left\langle\left\langle \log\zeta_\alpha - \sum_{k=1}^{\infty} e_{k\alpha}\zeta_\alpha^{-k}\right\rangle\right\rangle \mathbf{B}_2^T\hat{\mathbf{b}}, \quad \text{for} \quad |\zeta_\alpha| > |\hat{\zeta}_\alpha| \quad (7c)$$

where

$$e_{k\alpha} = \frac{1}{k}\left(\hat{\zeta}_\alpha^k + \frac{\gamma_\alpha^k}{\hat{\zeta}_\alpha^k}\right).$$

Note that in (7c), the constant term $\log(a - ibp_\alpha^*)/2$ has been neglected since it corresponds to rigid body motion and has no contribution to the deformation.

With a proper choice shown in (7a) for $\mathbf{f}_o$ and $\mathbf{f}_o^*$, and that shown in (4) for $\mathbf{f}_2$, the function remained to be determined is $\mathbf{f}_1$ which should be holomorphic in S_1. Besides $\mathbf{f}_1$, the unknown coefficients to be determined are $\mathbf{d}$ in $(7a)_1$ and $\mathbf{c}_k$ in $(4a)$. All these unknowns may now be found by the satisfaction of the continuity conditions given in (5) through the use of analytical continuation method.

Substituting $(7a)_1$, (7c) and $(4a)$ into $(3a, b)$, the stress continuity condition $\boldsymbol{\phi}_1 = \boldsymbol{\phi}_2$ along the interface $\zeta_\alpha = e^{i\psi} = \sigma$ leads to

$$\begin{aligned}\mathbf{B}_1\left[(\log\sigma)\mathbf{d} + \mathbf{f}_1(\sigma)\right] + \overline{\mathbf{B}}_1\left[\overline{(\log\sigma)}\bar{\mathbf{d}} + \overline{\mathbf{f}_1(\sigma)}\right] &= \mathbf{B}_2\left[\frac{1}{2\pi i}\left(\log\sigma - \sum_{k=1}^{\infty}\langle\langle e_{k\alpha}\rangle\rangle\sigma^{-k}\right)\mathbf{B}_2^T\hat{\mathbf{b}} + \sum_{k=1}^{\infty}\langle\langle\gamma_\alpha^k\rangle\rangle\mathbf{c}_k\sigma^{-k} + \sum_{k=1}^{\infty}\mathbf{c}_k\sigma^k\right] \\ &+ \overline{\mathbf{B}}_2\left[-\frac{1}{2\pi i}\left(\overline{\log\sigma} - \sum_{k=1}^{\infty}\langle\langle\bar{e}_{k\alpha}\rangle\rangle\sigma^k\right)\overline{\mathbf{B}}_2^T\hat{\mathbf{b}} + \sum_{k=1}^{\infty}\langle\langle\overline{\gamma_\alpha^k}\rangle\rangle\bar{\mathbf{c}}_k\sigma^k + \sum_{k=1}^{\infty}\bar{\mathbf{c}}_k\sigma^{-k}\right], \quad (8)\end{aligned}$$

Comparison of the coefficients of the log terms on both sides of the equation provides that

$$\mathbf{B}_1\mathbf{d} - \overline{\mathbf{B}}_1\bar{\mathbf{d}} = \mathbf{0}. \quad (9)$$

According to the holomorphic property in S_1 and S_2, and deleting the log terms through (9) we now rearrange Eq. (8) as

$$\mathbf{B}_1\mathbf{f}_1(\sigma) + \boldsymbol{\theta}_1(\sigma) = -\overline{\mathbf{B}}_1\overline{\mathbf{f}_1(\sigma)} + \boldsymbol{\theta}_2(\sigma), \quad (10a)$$

where

$$\begin{aligned}\boldsymbol{\theta}_1(\sigma) &= \frac{1}{2\pi i}\sum_{k=1}^{\infty}\left\{\mathbf{B}_2\langle\langle e_{k\alpha}\rangle\rangle\mathbf{B}_2^T\hat{\mathbf{b}}\right\}\sigma^{-k} - \sum_{k=1}^{\infty}\left\{\overline{\mathbf{B}}_2\bar{\mathbf{c}}_k + \mathbf{B}_2\langle\langle\gamma_\alpha^k\rangle\rangle\mathbf{c}_k\right\}\sigma^{-k}, \\ \boldsymbol{\theta}_2(\sigma) &= \frac{1}{2\pi i}\sum_{k=1}^{\infty}\left\{\overline{\mathbf{B}}_2\langle\langle\bar{e}_{k\alpha}\rangle\rangle\overline{\mathbf{B}}_2^T\hat{\mathbf{b}}\right\}\sigma^k + \sum_{k=1}^{\infty}\left\{\mathbf{B}_2\mathbf{c}_k + \overline{\mathbf{B}}_2\langle\langle\overline{\gamma_\alpha^k}\rangle\rangle\bar{\mathbf{c}}_k\right\}\sigma^k. \quad (10b)\end{aligned}$$

One of the important properties of holomorphic functions used in the method of analytic continuation is that if $\mathbf{f}(\zeta)$ is holomorphic in S^+ then $\overline{\mathbf{f}(1/\bar{\zeta})}$ is holomorphic in S^-, where S^+ and S^- denote, respectively, the regions outside and inside the unit circle. From this property and Eq. (10), we may introduce a function which is holomorphic in the entire domain including the interface boundary, i.e.,

$$\boldsymbol{\theta}(\zeta) = \begin{cases}\mathbf{B}_1\mathbf{f}_1(\zeta) + \boldsymbol{\theta}_1(\zeta), & \zeta \in S^+, \\ -\overline{\mathbf{B}}_1\overline{\mathbf{f}_1(1/\bar{\zeta})} + \boldsymbol{\theta}_2(\zeta), & \zeta \in S^-.\end{cases} \quad (11)$$

Since $\boldsymbol{\theta}(\zeta)$ is now holomorphic and single valued in the whole plane including the point at infinity, by Liouville's theorem we have $\boldsymbol{\theta}(\zeta) \equiv$ constant. However, constant function $\mathbf{f}$ corresponds to rigid-body motion which may be neglected. Therefore, $\boldsymbol{\theta}(\zeta) \equiv \mathbf{0}$. With this result Eq. (11) leads to

$$\begin{aligned}\mathbf{B}_1\mathbf{f}_1(\zeta) &= -\frac{1}{2\pi i}\sum_{k=1}^{\infty}\left\{\mathbf{B}_2\langle\langle e_{k\alpha}\rangle\rangle\mathbf{B}_2^T\hat{\mathbf{b}}\right\}\zeta^{-k} + \sum_{k=1}^{\infty}\left\{\overline{\mathbf{B}}_2\bar{\mathbf{c}}_k + \mathbf{B}_2\langle\langle\gamma_\alpha^k\rangle\rangle\mathbf{c}_k\right\}\zeta^{-k}, \quad \zeta \in S^+, \\ \overline{\mathbf{B}}_1\bar{\mathbf{f}}_1(1/\zeta) &= \frac{1}{2\pi i}\sum_{k=1}^{\infty}\left\{\overline{\mathbf{B}}_2\langle\langle\bar{e}_{k\alpha}\rangle\rangle\overline{\mathbf{B}}_2^T\hat{\mathbf{b}}\right\}\zeta^k + \sum_{k=1}^{\infty}\left\{\mathbf{B}_2\mathbf{c}_k + \overline{\mathbf{B}}_2\langle\langle\overline{\gamma_\alpha^k}\rangle\rangle\bar{\mathbf{c}}_k\right\}\zeta^k, \quad \zeta \in S^-. \quad (12)\end{aligned}$$

Similarly, the boundary condition $\mathbf{u}_1 = \mathbf{u}_2$ provides

$$\mathbf{A}_1\mathbf{d} - \overline{\mathbf{A}}_1\bar{\mathbf{d}} = \frac{1}{2\pi i}\hat{\mathbf{b}}, \quad (13)$$

and

$$\begin{aligned}\mathbf{A}_1\mathbf{f}_1(\zeta) &= -\frac{1}{2\pi i}\sum_{k=1}^{\infty}\left\{\mathbf{A}_2\langle\langle e_{k\alpha}\rangle\rangle\mathbf{B}_2^T\hat{\mathbf{b}}\right\}\zeta^{-k} + \sum_{k=1}^{\infty}\left\{\overline{\mathbf{A}}_2\bar{\mathbf{c}}_k + \mathbf{A}_2\langle\langle\gamma_\alpha^k\rangle\rangle\mathbf{c}_k\right\}\zeta^{-k}, \quad \zeta \in S^+, \\ \overline{\mathbf{A}}_1\bar{\mathbf{f}}_1(1/\zeta) &= \frac{1}{2\pi i}\sum_{k=1}^{\infty}\left\{\overline{\mathbf{A}}_2\langle\langle\bar{e}_{k\alpha}\rangle\rangle\overline{\mathbf{B}}_2^T\hat{\mathbf{b}}\right\}\zeta^k + \sum_{k=1}^{\infty}\left\{\mathbf{A}_2\mathbf{c}_k + \overline{\mathbf{A}}_2\langle\langle\overline{\gamma_\alpha^k}\rangle\rangle\bar{\mathbf{c}}_k\right\}\zeta^k, \quad \zeta \in S^-. \quad (14)\end{aligned}$$

From Eqs. (9) and (13), we obtain

$$\mathbf{d} = \frac{1}{2\pi i}\mathbf{B}_1^T\hat{\mathbf{b}}. \quad (15)$$

By canceling $\mathbf{f}_1(\zeta)$ between (12) and (14), and comparing the coefficients of corresponding terms, the unknown constants

Downloaded 04 May 2010 to 171.66.16.28. Redistribution subject to ASME license or copyright; see http://www.asme.org/terms/Terms_Use.cfm

$\mathbf{c}_k$ can be determined to have the same expression as (6*b*) except

$$\mathbf{t}_k = \frac{-1}{2\pi i}\left(\overline{\mathbf{M}}_1 - \overline{\mathbf{M}}_2\right)\overline{\mathbf{A}}_2 \langle\!\langle \bar{e}_{k\alpha} \rangle\!\rangle \overline{\mathbf{B}}_2^T \hat{\mathbf{b}}. \tag{16}$$

Having the solution of $\mathbf{c}_k$, function $\mathbf{f}_1(\zeta)$ can now be obtained from $(12)_1$ or $(14)_1$ with the understanding that the subscripts of ζ in (12) or (14) are dropped. Once the solution of $\mathbf{f}_1(\zeta)$ is obtained from $(12)_1$ or $(14)_1$, a replacement of ζ_1, ζ_2, or ζ_3 should be made for each component function. This calculation procedure will be applied throughout this paper. The whole field solution can then be found by using Eq. (3).

Since the analytical solution is not available in the literature for the general anisotropic elastic inclusion, to verify the present results some simplified cases are considered. First, we check the condition when the matrix and inclusion are composed of the same material. If $\mathbf{A}_1 = \mathbf{A}_2 = \mathbf{A}$, $\mathbf{B}_1 = \mathbf{B}_2 = \mathbf{B}$, $\mathbf{M}_1 = \mathbf{M}_2 = \mathbf{M}$, by Eqs. (6*b*), $(6c)_{1,2}$ and (16) we have

$$\mathbf{G}_o = -i\mathbf{A}^{-T}, \quad \mathbf{G}_k = \mathbf{0}, \quad \mathbf{t}_k = \mathbf{0}, \quad \mathbf{c}_k = \mathbf{0}. \qquad k = 1, 2, \ldots \infty. \tag{17}$$

With the use of (7*a*), (15), (12), and (17), we obtain

$$\mathbf{f}_0(\zeta) = \frac{1}{2\pi i}\langle\!\langle \log \zeta_\alpha \rangle\!\rangle \mathbf{B}^T \hat{\mathbf{b}},$$

$$\mathbf{f}_o^*(\zeta) = \frac{1}{2\pi i}\langle\!\langle \log (z_\alpha - \hat{z}_\alpha) \rangle\!\rangle \mathbf{B}^T \hat{\mathbf{b}},$$

$$\mathbf{f}_1(\zeta) = \frac{1}{2\pi i}\sum_{k=1}^{\infty} \langle\!\langle -e_{k\alpha}\zeta_\alpha^{-k} \rangle\!\rangle \mathbf{B}^T \hat{\mathbf{b}},$$

$$\mathbf{f}_2(\zeta) = \mathbf{0}. \tag{18}$$

Combining the results of (7*a*), (7*b*), (7*c*), and (18), one may prove that

$$\mathbf{f}_o(\zeta) + \mathbf{f}_1(\zeta) = \mathbf{f}_o^*(\zeta) + \mathbf{f}_2(\zeta) = \frac{1}{2\pi i}\langle\!\langle \log (z_\alpha - \hat{z}_\alpha) \rangle\!\rangle \mathbf{B}^T \hat{\mathbf{b}}, \tag{19}$$

which is the exact solution for the dislocation in a homogeneous medium. The next simplified case we like to check is the condition for isotropic materials. Before presenting the results, we should mention again that the calculation is based upon the introduction of a small perturbation in the values of p_α such as $p_1 = 0.9952i$, $p_2 = i$, $p_3 = 1.0048i$ since the eigenvalues p_α of isotropic materials are repeated which violates the assumption used in Eq. (1). By implementing the numerical calculation it is proved that our solutions are identical to those presented by Dundurs and Sendeckyj (1965) for this special case. The difference is that our solutions are suitable for general anisotropic media and the shape of the inclusion is ellipse which includes circle and line, however, those presented by Dundurs and Sendeckyj (1965) are valid only for isotropic media and circular inclusion.

5 Dislocation on the Interface Between Inclusion and Matrix

Before getting involved in the derivation for the present problem, it might be thought that the problem is trivial since it may be solved by using the results of "inside" or "outside" by just limiting the point to the interface. When actually employing the limiting procedure, we found that the convergent rate of the series form solutions shown in Sections 3 and 4 is very bad when we put the dislocation point on the interface, since during derivation, we have used the series expansions to represent the log terms, which may not be good for the dislocation located on the interface. Therefore, it becomes necessary to find the solution independently. Moreover, the continuity across the interface from the three different solution forms "inside," "outside," and "interface" should also be ensured. Following is the presentation for the solution of "interface."

When the dislocation is located at the point $(\hat{x}_1, \hat{x}_2)$ which is on the interface, the choice of $\mathbf{f}_0$ and $\mathbf{f}_0^*$ is not so clear as that shown in Sections 3 and 4 since the singular point is covered by both of the inclusion and matrix. To find an appropriate function form for $\mathbf{f}_o$ and $\mathbf{f}_o^*$, we consider the problem as a combination of the hole problems and the elliptic plate problems. For a plate containing a hole with a singular point located on the hole boundary, a good reference is the solution for the elliptic hole subjected to a concentrated force on the hole boundary (Hwu and Yen, 1992). In that solution, the singularity is revealed by the function forms as $\langle\!\langle \log (\zeta_\alpha - \hat{\zeta}_\alpha) \rangle\!\rangle$ and $\langle\!\langle \log (\zeta_\alpha^{-1} - \overline{\hat{\zeta}_\alpha}) \rangle\!\rangle$. The former also covers the singular behavior at infinity. In the case of the elliptic plate with a singular point on the elliptic boundary, a suitable reference may also be provided by the solution for the elliptic plate subjected to a concentrated force on the elliptic boundary. The singularity for this problem is revealed by $\langle\!\langle \log (z_\alpha - \hat{z}_\alpha) \rangle\!\rangle$. The reason that the argument z_α is used instead of ζ_α is the same as that described in Section 4. From the above description, we may choose

$$\mathbf{f}_o(\zeta) = \langle\!\langle \log \left(\zeta_\alpha - \hat{\zeta}_\alpha\right) \rangle\!\rangle \mathbf{q}_1 + \langle\!\langle \log \left(\zeta_\alpha^{-1} - \overline{\hat{\zeta}_\alpha}\right) \rangle\!\rangle \mathbf{q}_1',$$

$$\mathbf{f}_o^*(\zeta) = \langle\!\langle \log (z_\alpha - \hat{z}_\alpha) \rangle\!\rangle \mathbf{q}_2, \tag{20}$$

where $\mathbf{q}_1$, $\mathbf{q}_1'$, and $\mathbf{q}_2$ are the unknown coefficients to be determined. It should be noted that unlike those shown in Eqs. $(6a)_1$ and $(7a)_2$ whose singular point is in a homogeneous medium (matrix or inclusion), the coefficients $\mathbf{q}_1$, $\mathbf{q}_1'$ and $\mathbf{q}_2$ are still unknown in the present stage because they will be influenced by the interface condition. That two separate problems, holes and elliptic plates, are only used to help us to choose the appropriate function forms like those shown in Eq. (20). Until now, the entire problem is reduced to finding the unknown coefficients $\mathbf{q}_1$, $\mathbf{q}_1'$, and $\mathbf{q}_2$ in (20), c_k in (4*a*), and the unknown function $\mathbf{f}_1$ in (3*a*) through the use of continuity condition along the interface, the equilibrium, and the dislocation singularity, i.e.,

$$\left.\begin{aligned} \mathbf{u}_1 &= \mathbf{u}_2 \\ \boldsymbol{\phi}_1 &= \boldsymbol{\phi}_2 \end{aligned}\right\}, \quad \text{along the interface except the point } \hat{\mathbf{x}} \tag{21a}$$

$$\left.\begin{aligned} \oint d\boldsymbol{\phi} &= \mathbf{0} \\ \oint d\mathbf{u} &= \hat{\mathbf{b}} \end{aligned}\right\}, \quad \text{around the point } \hat{\mathbf{x}}. \tag{21b}$$

Consider Eq. (21*b*), the mapped points around $\hat{\mathbf{x}}$ may be expressed as $\zeta_\alpha = \hat{\zeta}_\alpha + \rho e^{i\theta}$, $\rho \to 0$, where θ starts from the line tangent to the interface. Hence, the closed integrals may be expressed by $\oint d\boldsymbol{\phi} = \boldsymbol{\phi}_1(\pi) - \boldsymbol{\phi}_1(0) + \boldsymbol{\phi}_2(2\pi) - \boldsymbol{\phi}_2(\pi)$ and $\oint d\mathbf{u} = \mathbf{u}_1(\pi) - \mathbf{u}_1(0) + \mathbf{u}_2(2\pi) - \mathbf{u}_2(\pi)$. Substituting (20) and (4*a*) into (3*a*, *b*), the equilibrium and the dislocation singularity conditions shown in (21*b*) now provide

$$\mathbf{B}_1\mathbf{q}_1 + \mathbf{B}_1\mathbf{q}_1' + \mathbf{B}_2\mathbf{q}_2 - \overline{\mathbf{B}}_1\bar{\mathbf{q}}_1 - \overline{\mathbf{B}}_1\bar{\mathbf{q}}_1' - \overline{\mathbf{B}}_2\bar{\mathbf{q}}_2 = \mathbf{0},$$

$$\mathbf{A}_1\mathbf{q}_1 + \mathbf{A}_1\mathbf{q}_1' + \mathbf{A}_2\mathbf{q}_2 - \overline{\mathbf{A}}_1\bar{\mathbf{q}}_1 - \overline{\mathbf{A}}_1\bar{\mathbf{q}}_1' - \overline{\mathbf{A}}_2\bar{\mathbf{q}}_2 = \frac{1}{\pi i}\hat{\mathbf{b}}. \tag{22}$$

As to the continuity conditions shown in (21*a*), the method of analytical continuation as that presented in Section 4 will be employed. Like Eq. (9) and (13), comparison of the coefficients of the log terms provides that

Downloaded 04 May 2010 to 171.66.16.28. Redistribution subject to ASME license or copyright; see http://www.asme.org/terms/Terms_Use.cfm

$$\mathbf{B}_1\mathbf{q}_1 + \mathbf{B}_1\mathbf{q}_1' - \mathbf{B}_2\mathbf{q}_2 + \bar{\mathbf{B}}_1\bar{\mathbf{q}}_1 + \bar{\mathbf{B}}_1\bar{\mathbf{q}}_1' - \bar{\mathbf{B}}_2\bar{\mathbf{q}}_2 = \mathbf{0},$$

$$\mathbf{B}_1\mathbf{q}_1 - \mathbf{B}_1\mathbf{q}_1' - \mathbf{B}_2\mathbf{q}_2 - \bar{\mathbf{B}}_1\bar{\mathbf{q}}_1 + \bar{\mathbf{B}}_1\bar{\mathbf{q}}_1' + \bar{\mathbf{B}}_2\bar{\mathbf{q}}_2 = \mathbf{0}. \quad (23a)$$

$$\mathbf{A}_1\mathbf{q}_1 + \mathbf{A}_1\mathbf{q}_1' - \mathbf{A}_2\mathbf{q}_2 + \bar{\mathbf{A}}_1\bar{\mathbf{q}}_1 + \bar{\mathbf{A}}_1\bar{\mathbf{q}}_1' - \bar{\mathbf{A}}_2\bar{\mathbf{q}}_2 = \mathbf{0},$$

$$\mathbf{A}_1\mathbf{q}_1 - \mathbf{A}_1\mathbf{q}_1' - \mathbf{A}_2\mathbf{q}_2 - \bar{\mathbf{A}}_1\bar{\mathbf{q}}_1 + \bar{\mathbf{A}}_1\bar{\mathbf{q}}_1' + \bar{\mathbf{A}}_2\bar{\mathbf{q}}_2 = \mathbf{0}. \quad (23b)$$

Like those described in (10), (11), (12), (14), and (16), the holomorphic properties will help us to obtain

$$\mathbf{B}_1\mathbf{f}_1(\zeta) = -\sum_{k=1}^{\infty}\left\{\mathbf{B}_2\left\langle\left\langle\frac{1}{k}\left(\frac{\gamma_\alpha}{\hat{\zeta}_\alpha}\right)^k\right\rangle\right\rangle\mathbf{q}_2\right\}\zeta^{-k} + \sum_{k=1}^{\infty}\left\{\bar{\mathbf{B}}_2\bar{\mathbf{c}}_k + \mathbf{B}_2\langle\langle\gamma_\alpha^k\rangle\rangle\mathbf{c}_k\right\}\zeta^{-k}, \quad \zeta \in S^+,$$

$$\bar{\mathbf{B}}_1\bar{\mathbf{f}}_1(1/\zeta) = -\sum_{k=1}^{\infty}\left\{\bar{\mathbf{B}}_2\left\langle\left\langle\overline{\frac{1}{k}\left(\frac{\gamma_\alpha}{\hat{\zeta}_\alpha}\right)^k}\right\rangle\right\rangle\bar{\mathbf{q}}_2\right\}\zeta^{k} + \sum_{k=1}^{\infty}\left\{\mathbf{B}_2\mathbf{c}_k + \bar{\mathbf{B}}_2\langle\langle\overline{\gamma_\alpha^k}\rangle\rangle\bar{\mathbf{c}}_k\right\}\zeta^{k}, \quad \zeta \in S^-, \quad (24a)$$

$$\mathbf{A}_1\mathbf{f}_1(\zeta) = -\sum_{k=1}^{\infty}\left\{\mathbf{A}_2\left\langle\left\langle\frac{1}{k}\left(\frac{\gamma_\alpha}{\hat{\zeta}_\alpha}\right)^k\right\rangle\right\rangle\mathbf{q}_2\right\}\zeta^{-k} + \sum_{k=1}^{\infty}\left\{\bar{\mathbf{A}}_2\bar{\mathbf{c}}_k + \mathbf{A}_2\langle\langle\gamma_\alpha^k\rangle\rangle\mathbf{c}_k\right\}\zeta^{-k}, \quad \zeta \in S^+,$$

$$\bar{\mathbf{A}}_1\bar{\mathbf{f}}_1(1/\zeta) = -\sum_{k=1}^{\infty}\left\{\bar{\mathbf{A}}_2\left\langle\left\langle\overline{\frac{1}{k}\left(\frac{\gamma_\alpha}{\hat{\zeta}_\alpha}\right)^k}\right\rangle\right\rangle\bar{\mathbf{q}}_2\right\}\zeta^{k} + \sum_{k=1}^{\infty}\left\{\mathbf{A}_2\mathbf{c}_k + \bar{\mathbf{A}}_2\langle\langle\overline{\gamma_\alpha^k}\rangle\rangle\bar{\mathbf{c}}_k\right\}\zeta^{k}, \quad \zeta \in S^-. \quad (24b)$$

From (22) and (23a, b) we obtain

$$\mathbf{q}_1 = \frac{1}{2\pi i}\mathbf{B}_1^T\hat{\mathbf{b}},$$

$$\mathbf{q}_1' = \frac{1}{2\pi i}\left(\bar{\mathbf{A}}_2^{-1}\mathbf{A}_1 - \bar{\mathbf{B}}_2^{-1}\mathbf{B}_1\right)^{-1}\left(\bar{\mathbf{A}}_2^{-1}\bar{\mathbf{A}}_1 - \bar{\mathbf{B}}_2^{-1}\bar{\mathbf{B}}_1\right)\bar{\mathbf{B}}_1^T\hat{\mathbf{b}},$$

$$\mathbf{q}_2 = \frac{1}{2\pi i}\left(\bar{\mathbf{A}}_1^{-1}\mathbf{A}_2 - \bar{\mathbf{B}}_1^{-1}\mathbf{B}_2\right)^{-1}\left(\bar{\mathbf{A}}_1^{-1}\mathbf{A}_1 - \bar{\mathbf{B}}_1^{-1}\mathbf{B}_1\right)\mathbf{B}_1^T\hat{\mathbf{b}}. \quad (25)$$

By canceling $\mathbf{f}_1(\zeta)$ between (24a) and (24b), and comparing the coefficients of corresponding terms, the unknown constants $\mathbf{c}_k$ can be determined to have the same expression as (6b) except

$$\mathbf{t}_k = \left(\bar{\mathbf{M}}_1 - \bar{\mathbf{M}}_2\right)\bar{\mathbf{A}}_2\left\langle\left\langle\overline{\frac{1}{k}\left(\frac{\gamma_\alpha}{\hat{\zeta}_\alpha}\right)^k}\right\rangle\right\rangle\bar{\mathbf{q}}_2. \quad (26)$$

Having the solution of $\mathbf{c}_k$, function $\mathbf{f}_1(\zeta)$ can now be obtained from $(24a)_1$ or $(24b)_1$ with the understanding that the subscripts of ζ in (24a) or (24b) are dropped. Once the solution of $\mathbf{f}_1(\zeta)$ is obtained from $(24a)_1$ or $(24b)_1$, a replacement of ζ_1, ζ_2, or ζ_3 should be made for each component function. The whole field solution can then be found by using Eq. (3).

The verification of this problem is also done by checking (1) the simplest condition that the matrix and the inclusion are composed of the same material, and (2) the cases that both of the inclusion and matrix are isotropic. The first one is similar to that shown in Section 4 and will not be repeated here. The second one is also compared numerically with those presented by Dundurs and Sendeckyj (1965), and the results shows that our solutions are exact and universal.

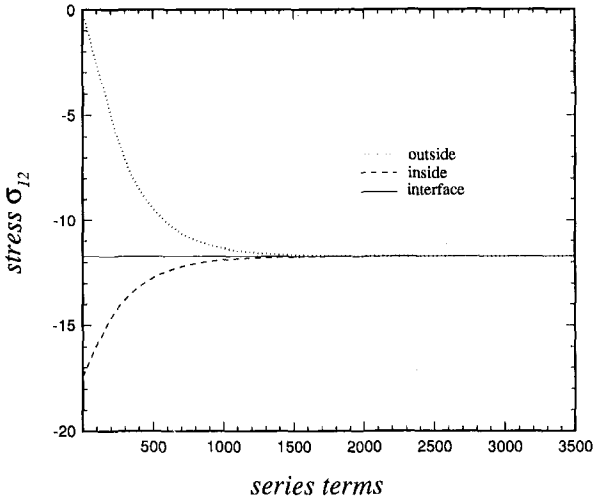

Fig. 1 Convergency of the series form solution when the dislocation is located on the interface ($b/a = 1/2$, $\hat{b}/a = (0.25, 0, 0)$, $(\hat{x}_1/a, \hat{x}_2/a) = (1.0, 0)$, $(x_1/a, x_2/a) = (0.99, 0)$)

6 Discussion

In order to show the continuity across the interface from the three different solution forms shown in Sections 2–5, we now compare numerically the solutions from "interface," "inside," and "outside" by putting the dislocation on the interface. In the following examples, the material properties of the matrix are

$$E_1 = 144.8 \text{ Gpa}, \quad E_2 = E_3 = 10.7 \text{ Gpa}$$

$$\nu_{12} = \nu_{13} = \nu_{23} = 0.31$$

$$G_{12} = G_{13} = G_{23} = 4.5 \text{ Gpa}$$

while the properties of the inclusions are assumed to be proportional to the matrix as

$$2 = \frac{(E_i)_2}{(E_i)_1} = \frac{(G_{ij})_2}{(G_{ij})_1}, \quad i, j = 1, 2, 3.$$

The Poisson's ratios ν_{ij} of the inclusions are assumed to be identical to those of the matrix. The stresses are nondimensionalized by dividing the Young's modulus E_2 of the matrix. Figure 1 shows the convergency of the series form solutions obtained in this paper, from which we see that the solutions from "outside," "inside," and "interface" will converge to the same value by different speed, and hence the continuity across the interface is ensured. It is also interesting to see that the terms needed for the "interface" solution (below 10) is far less than the terms needed for "inside" or "outside" solution (over 1000), which further explains why we need to derive the "interface" solution independently.

To see the overall convergent rate for the "inside," "outside," and "interface" solutions, we pick some representative positions for the dislocation and the calculated stresses. From Table 1, we see that when the dislocations are located inside or outside the inclusion and are not close to the interface, the series terms needed for a converged value of stress are usually below 20. When the dislocation is near the interface, more series terms are needed if the distance from the calculated stresses is closer. For the dislocation on the

Downloaded 04 May 2010 to 171.66.16.28. Redistribution subject to ASME license or copyright; see http://www.asme.org/terms/Terms_Use.cfm

Table 1 The stresses induced by a dislocation inside, outside, or on the interface of an anisotropic elliptical inclusion ($b/a = 1/2$, $\hat{b}/a = (0.25, 0, 0)$)

				stress			series terms		
$\hat{x}_1/a$	$\hat{x}_2/a$	x_1/a	x_2/a	σ_{11}	σ_{12}	σ_{22}	inside	interface	outside
0.5	0.0	0.2	0.0	0.0	−0.5441	0.0	17		
0.0	0.25	0.2	0.0	0.5459	−0.0598	0.0665	19		
0.1	0.1	0.2	0.0	1.7314	−0.0966	0.1025	19		
0.5	0.0	0.49	0.0	0.0	−17.4163	0.0	18		
0.99	0.0	0.2	0.0	0.0	−0.1560	0.0	28		
0.99	0.0	0.98	0.0	0.0	−15.4324	0.0	1045		
0.0	0.49	0.0	0.48	15.3866	0.0	5.4527	495		
1.0	0.0	0.2	0.0	0.0	−0.1535	0.0	24	5	27
0.0	0.5	0.2	0.0	0.1901	−0.0242	0.0455	23	7	27
0.5	0.433	0.2	0.0	0.2385	0.0281	0.0298	25	7	28
1.0	0.0	1.01	0.0	0.0	11.6962	0.0	3960	9	3960
1.0	0.0	0.99	0.0	0.0	−11.7260	0.0	3611	11	3343
0.0	0.5	0.0	0.49	11.5853	0.0	4.3136	1539	11	1831
2.0	0.0	0.2	0.0	0.0	−0.0665	0.0			11
0.0	1.0	0.2	0.0	0.0944	−0.0066	0.0267			13
1.0	1.0	0.2	0.0	0.1061	0.0084	0.0093			7
2.0	0.0	2.01	0.0	0.0	8.7350	0.0			10
1.01	0.0	0.2	0.0	0.0	−0.1512	0.0			29
1.01	0.0	1.02	0.0	0.0	9.7368	0.0			1093
0.0	0.51	0.0	0.52	−9.5265	0.0	−2.2351			637

interface, the series terms needed for the "interface" solution are usually far less than those for the "inside" or "outside" solution.

7 Conclusions

The problems of dislocation inside, outside or on the interface of an anisotropic elliptical inclusion are divided into three different categories in this paper since the transformation function used in our solution technique is single valued outside the inclusion but nonsingle valued inside the inclusion. These three categories are solved separately by applying Stroh's formalism and the method of analytical continuation. The results are proved to be exact and universal. The continuity across the interface from the three different solution forms is ensured numerically by putting the dislocation on the interface. The convergent rate is also studied to enhance the necessity of the "interface" solution.

By combining the technique of numerical solution on the singular integral equation, the present analytical solutions can be applied to treat the problems like a crack penetrating an inclusion or a crack lying around the interface or the other crack and inclusion interaction problem. Moreover, the Green's function for the inclusion problems can be obtained in a straightforward manner from the present solutions by using a certain analogy between dislocations and point forces.

Acknowledgments

The authors would like to thank the support by National Science Council, Republic of China, through Grant No. NSC 81-0401-E006-12 and NSC84-2212-E006-026.

References

Dundurs, J., and Sendeckyj, G. P., 1965, "Edge Dislocation Inside a Circular Inclusion," *Journal of the Mechanics and Physics of Solids*, Vol. 13, pp. 141–147.

Hwu, C., and Yen, W. J., 1992, "Plane Problems for Anisotropic Bodies With an Elliptic Hole Subjected to Arbitrary Loading," *The Chinese Journal of Mechanics*, Vol. 8, No. 2, pp. 123–129.

Hwu, C., and Yen, W. J., 1993, "On the Anisotropic Elastic Inclusion in Plane Elastostatics," ASME JOURNAL OF APPLIED MECHANICS, Vol. 60, pp. 626–632.

Lekhnitskii, S. G., 1968, *Anisotropic Plates*, Gordon and Breach.

Stroh, A. N., 1958, "Dislocations and Cracks in Anisotropic Elasticity," *Philosophical Magazine*, Vol. 7, pp. 625–646.

Ting, T. C. T., 1988, "Some Identities and the Structure of N_i in the Stroh Formalism of Anisotropic Elasticity," *Quarterly Journal of Applied Mathematics*, Vol. 46, pp. 109–120.

Warren, W. E., 1983, "The Edge Dislocation Inside an Elliptical Inclusion," *Mechanics of Materials*, Vol. 2, pp. 319–330.

Yen, W. J., and Hwu, C., 1993, "Interaction between Dislocations and Anisotropic Elliptical Inclusions," ASME JOURNAL OF APPLIED MECHANICS, Vol. 61, pp. 548–554.

Downloaded 04 May 2010 to 171.66.16.28. Redistribution subject to ASME license or copyright; see http://www.asme.org/terms/Terms_Use.cfm

SH-Waves in a Medium Containing a Disordered Periodic Array of Cracks

Y. Mikata
Department of Mechanical Engineering,
Old Dominion University,
238 Kaufman / Duckworth Hall,
Norfolk, VA 23529
Assoc. Mem. ASME.

Reflection and transmission of an SH-wave by a disordered periodic array of coplanar cracks is investigated, and subsequently its application to the dispersion and attenuation of an SH-wave in a disorderedly cracked medium is also treated. This is a stochastic boundary value problem. The formulation largely follows Mikata and Achenbach (1988b). The problem is formulated for an averaged scattered field, and the governing singular integral equation is derived for a conditionally averaged crack-opening displacement using a quasi-crystalline-like approximation. Unlike our previous study (Mikata and Achenbach, 1988b) where a point scatterer approximation was used for the regular part of the integral kernel, however, no further approximation is introduced. The singular integral equation is solved by an eigenfunction expansion involving Chebyschev polynomials. Numerical results are presented for the averaged reflection and transmission coefficients of zeroth order as a function of the wave number for normal incidence, a completely disordered crack spacing, and various values of the ratio of crack length and average crack spacing. Numerical results are also presented for the dispersion and attenuation of an SH-wave in a disorderedly cracked medium.

1 Introduction

This paper deals with the problem of scattering of an antiplane shear wave (SH-wave) by a disordered periodic array of coplanar cracks and its application to the dispersion and attenuation of an SH-wave in a disorderedly cracked medium. This study was motivated by the desire to better understand the detection and characterization of a flaw plane, i.e., a plane of microcracks, in a more realistic situation. Most of the previous studies related to this problem model a flaw plane as a periodic array of cracks (Achenbach and Li, 1986a; Angel and Achenbach, 1985a,b; Mikata, 1993; Mikata and Achenbach, 1988a). In reality, however, an array of cracks is never periodic but rather disordered. Thus in our previous paper (Mikata and Achenbach, 1988b), we have treated scattering of an SH-wave by an infinite array of randomly oriented cracks. That problem as well as the present problem belong to multiple scattering problems. There exists an extensive literature on this topic (e.g., Foldy, 1945; Gubernatis and Domany, 1984; Kinra, Petraitis and Datta, 1980; Lax, 1952; McCarthy and Carroll, 1984; Sobczyk, 1985; Twersky, 1983; Varadan and Varadan, 1979; Waterman and Truell, 1961; Weaver, 1985; Willis, 1980). To our knowledge, however, there is not much literature on the type of problems treated in this paper, where reflection and transmission of waves are investigated for random scatterers located in a line. Most of the literature in multiple scattering problems focus on the effective wave number of waves in random media where the scatterers are distributed randomly in the entire space. Whereas in the present problem the focus is on the reflection and transmission of waves, and the scatterers are distributed disorderedly but localized in space. This type of problem is more difficult to solve than the traditional problems in multiple scattering.

Once the solution to the scattering of an SH-wave by a disordered periodic array of coplanar cracks is achieved, it will be used to obtain also the dispersion and attenuation of an SH-wave in a disorderedly cracked medium in an approximate manner. The same procedure was employed before for periodic systems (Achenbach and Kitahara, 1987; Achenbach and Li, 1986; Angel and Achenbach, 1987). This second part of the present paper corresponds to obtaining the effective wave number as in the case for the traditional problems in multiple scattering. This indicates that the solution to our original problem posed in the first part of this paper provides more information than just obtaining the effective wave number of an SH-wave in a disorderedly cracked medium.

Contributed by the Applied Mechanics Division of THE AMERICAN SOCIETY OF MECHANICAL ENGINEERS for presentation at the Joint Applied Mechanics and Materials Summer Meeting of the ASME, Los Angeles, CA, June 28–30, 1995.

Discussion on this paper should be addressed to the Technical Editor, Professor Lewis T. Wheeler, Department of Mechanical Engineering, University of Houston, Houston, TX 77204-4792, and will be accepted until four months after final publication of the paper itself in the ASME JOURNAL OF APPLIED MECHANICS.

Manuscript received by the ASME Applied Mechanics Division, Mar. 21, 1994; final revision, Oct. 4, 1994. Associate Technical Editor: D. M. Barnett.

Paper No. 95-APM-4.

Copyright © 1995 by ASME

Downloaded 04 May 2010 to 171.66.16.28. Redistribution subject to ASME license or copyright; see http://www.asme.org/terms/Terms_Use.cfm

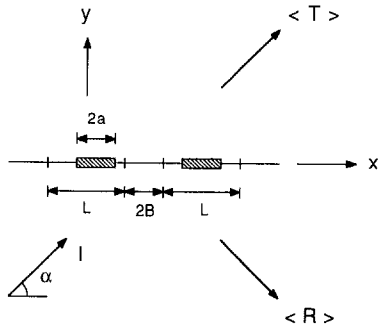

Fig. 1 Antiplane shear wave incident on a disordered periodic array of coplanar cracks

2 Statement of the Problem

A time-harmonic antiplane shear wave incident on a disordered periodic array of coplanar cracks is shown in Fig. 1. The crack length is $2a$, and the average crack spacing is $L + 2B$. The propagation vector of the incident wave makes an angle α with the x-axis. The most important feature of this problem is that the crack location is a random variable. This means, in Fig. 1, that the center point of a crack is located within the region of length L with a certain probability.

Let us consider a time-harmonic displacement wave of the form $w(x, y)e^{-i\omega t}$, where $w(x, y)$ and ω are the amplitude and the angular frequency of the wave. The governing equation for $w(x, y)$ is

$$\nabla^2 w + k^2 w = 0, \quad k = \frac{\omega}{c}, \quad c = \sqrt{\frac{\mu}{\rho}} \tag{1}$$

where μ and ρ are the shear modulus and the mass density, respectively. The displacement field w is decomposed into two parts, the incident field w^{in} and the scattered field w^{sc}:

$$w(x, y) = w^{in}(x, y) + w^{sc}(x, y) \tag{2}$$

where the incident field is given by

$$w^{in}(x, y) = e^{i\mathbf{k}\cdot\mathbf{x}}, \quad \mathbf{k} = (k\cos\alpha, k\sin\alpha), \quad \mathbf{x} = (x, y). \tag{3}$$

The incident field w^{in} satisfies Eq. (1). Therefore the scattered field w^{sc} must also satisfy the same equation. Since the traction vanishes on the faces of the cracks, the boundary conditions for the problem are given by

$$\left.\frac{\partial w^{sc}}{\partial \eta_i}\right|_{\eta_i = 0} = -\left.\frac{\partial w^{in}}{\partial \eta_i}\right|_{\eta_i = 0}, \quad -a \le \xi_i \le a, \quad i \in \mathbf{Z} \equiv \{0, \pm 1, \pm 2, \ldots\} \tag{4}$$

where (ξ_i, η_i) are local coordinates defined on each crack. The global coordinates (x, y) and the local coordinates (ξ_i, η_i) are related by

$$\begin{pmatrix} x \\ y \end{pmatrix} = \begin{pmatrix} \xi_i \\ \eta_i \end{pmatrix} + \begin{pmatrix} a_i \\ 0 \end{pmatrix} + \begin{pmatrix} b_i \\ 0 \end{pmatrix}, \quad i \in \mathbf{Z} \tag{5}$$

where a_i is given by

$$a_i = i(L + 2B), \quad B \ge a, \quad i \in \mathbf{Z} \tag{6}$$

and b_i is a random variable, which will be precisely defined in the next section. In addition to Eq. (4), the scattered field must also satisfy the Sommerfeld radiation condition. Our problem is to solve Eq. (1) under the boundary conditions (4). Because the crack location is a random variable, this is a stochastic boundary value problem.

3 Mathematical Formulation

By using the reciprocity relation in elastodynamics (Achenbach, Gautesen, and McMaken, 1982), along with the Sommerfeld radiation condition, we obtain the following integral representation for the scattered field w^{sc}:

$$w^{sc}(\mathbf{x}, \mathbf{b}) = \mu \sum_{j=-\infty}^{\infty} \int_{-a}^{a} \Delta w_j(\xi_j', \mathbf{b}) \frac{\partial w^0}{\partial \eta_j'}(\mathbf{x}; \mathbf{x}')|_{\eta_j' = 0} d\xi_j' \tag{7}$$

where $\mathbf{b}$ denotes $\{b_i | i \in \mathbf{Z}\}$, and Δw_j is an unknown crack-opening displacement for jth crack:

$$\Delta w_j(\xi_j', \mathbf{b}) = w^{sc}(\xi_j', 0^+, \mathbf{b}) - w^{sc}(\xi_j', 0^-, \mathbf{b}), \quad -a \le \xi_j' \le a. \tag{8}$$

w^0 is the Green's function for the Helmholtz operator in a free space, which may be written as

$$w^0(\mathbf{x}; \mathbf{x}') = \frac{i}{4\mu} H_0^{(1)}(kR) \tag{9}$$

where $H_0^{(1)}$ is the Hankel function of the first kind of order zero, and

$$R^2 = (x - x')^2 + (y - y')^2$$
$$\begin{pmatrix} x' \\ y' \end{pmatrix} = \begin{pmatrix} \xi_i' \\ \eta_i' \end{pmatrix} + \begin{pmatrix} a_i \\ 0 \end{pmatrix} + \begin{pmatrix} b_i \\ 0 \end{pmatrix}, \quad i \in \mathbf{Z}. \tag{10}$$

Substituting (7) into (4), we have

$$f(\xi_i) e^{ik(a_i + b_i)\cos\alpha} = \mu \sum_{j=-\infty}^{\infty} \int_{-a}^{a} \Delta w_j(\xi_j', \mathbf{b}) \times L(\xi_i, \xi_j'; a_i - a_j; b_i - b_j) d\xi_j', \quad -a \le \xi_i \le a, \ i \in \mathbf{Z} \tag{11}$$

where

$$f(\xi_i) = -ik \sin\alpha e^{ik\xi_i \cos\alpha}$$
$$L(\xi_i, \xi_j'; a_i - a_j; b_i - b_j) = \frac{\partial}{\partial \eta_i}\left[\frac{\partial w^0}{\partial \eta_j'}(\mathbf{x}; \mathbf{x}')|_{\eta_j' = 0}\right]_{\eta_i = 0}. \tag{12}$$

Equation (11) is an infinite system of integral equations for unknown crack-opening displacements Δw_j. By using Eqs. (5), (9), (10), and (12b), it can be easily shown that $L(\xi_i, \xi_i'; 0; 0)$ does not depend on either a_i or b_i. Thus let us set

$$L(\xi_i, \xi_i') \equiv L(\xi_i, \xi_i'; 0; 0). \tag{13}$$

Changing the dummy variables ξ_i, ξ_i' into ξ, ξ' in (11), and using (13), we arrive at

$$f(\xi) e^{ik(a_i + b_i)\cos\alpha} = \mu \int_{-a}^{a} \Delta w_i(\xi', \mathbf{b}) L(\xi, \xi') d\xi' + \mu \sum_{\substack{j=-\infty \\ j \ne i}}^{\infty} \int_{-a}^{a} \Delta w_j(\xi', \mathbf{b}) L(\xi, \xi'; a_i - a_j; b_i - b_j) d\xi', \quad -a \le \xi \le a, \quad i \in \mathbf{Z}. \tag{14}$$

Let us now remind ourselves that the crack location constant b_i of ith crack is a random variable. Each random variable b_i has a probability density $P_i(b_i)$, which satisfies the normalization condition.

$$\int_{-\frac{L}{2}}^{\frac{L}{2}} P_i(b_i) db_i = 1, \quad i \in \mathbf{Z} \tag{15}$$

Downloaded 04 May 2010 to 171.66.16.28. Redistribution subject to ASME license or copyright; see http://www.asme.org/terms/Terms_Use.cfm

Similarly, the entire set of random variables $\mathbf{b}$ has a probability density $P_{\mathbf{z}}(\mathbf{b})$. In the following analysis, the variations of the location constants b_i are assumed to be independent. Thus we have

$$P_{\mathbf{z}}(\mathbf{b}) = \prod_{i \in \mathbf{Z}} P_i(b_i) \tag{16}$$

By using (15) and (16), the normalization condition for $P_{\mathbf{z}}(\mathbf{b})$ readily follows. Now let us define an averaged scattered field $\langle w^{sc} \rangle (\mathbf{x})$ as

$$\langle w^{sc} \rangle (\mathbf{x}) = \prod_{k \in \mathbf{Z}} M_k w^{sc}(\mathbf{x}, \mathbf{b}) \tag{17}$$

where M_k is an integral operator defined by

$$M_k \chi(b_k) = \int_{-\frac{L}{2}}^{\frac{L}{2}} P_k(b_k) \chi(b_k) db_k. \tag{18}$$

Similarly, conditionally averaged crack-opening displacements $\psi_i^i(\xi', b_i)$ and $\psi_{ij}^j(\xi', b_i, b_j)$ are defined as

$$\psi_i^i(\xi', b_i) = \prod_{\substack{k \in \mathbf{Z} \\ k \neq i}} M_k \Delta w_i(\xi', \mathbf{b})$$

$$\psi_{ij}^j(\xi', b_i, b_j) = \prod_{\substack{k \in \mathbf{Z} \\ k \neq i, j}} M_k \Delta w_j(\xi', \mathbf{b}). \tag{19}$$

It will be assume in the following analysis that all the probability densities $P_i(x)$ are the same, thereby define a common probability density $P(x)$.

$$P_i(x) = P_j(x) (\equiv P(x)), \quad i, j \in \mathbf{Z} \tag{20}$$

Now let us take a conditional average of the Eq. (14):

$$f(\xi) e^{ik(a_i + b_i)\cos\alpha} = \mu \int_{-a}^{a} \psi_i^i(\xi', b_i) L(\xi, \xi') d\xi'$$

$$+ \mu \sum_{\substack{j \in \mathbf{Z} \\ j \neq i}} \int_{-\frac{L}{2}}^{\frac{L}{2}} db_j \int_{-a}^{a} \psi_{ij}^j(\xi', b_i, b_j) L(\xi, \xi'; a_i - a_j; b_i - b_j)$$

$$\times P(b_j) d\xi',$$

$$-a \le \xi \le a, \quad \frac{L}{2} \le b_i \le \frac{L}{2}, \quad i \in \mathbf{Z} \tag{21a}$$

$$\psi_i^i(\xi, b_i) = \int_{-\frac{L}{2}}^{\frac{L}{2}} \psi_{ki}^i(\xi, b_k, b_i) P(b_k) db_k,$$

$$-a \le \xi \le a, \quad -\frac{L}{2} \le b_i \le \frac{L}{2}, \quad i, k \in \mathbf{Z}. \tag{21b}$$

Equations (21a, b) form an infinite ($\infty \times \infty$) set of integral equations for $\psi_{ij}^j(\xi', b_i)$ and $\psi_{ki}^i(\xi', b_k, b_i)$, $i, k \in \mathbf{Z}$, $i \neq k$. However, it is easily seen from (21) that the pair of Eqs. (21) is an underdetermined system. This is due to the averaging. When the Eq. (14) was averaged, a certain amount of information in the original equation was lost. To remedy this situation, we introduce the following approximation:

$$\psi_{ij}^j(\xi', b_i, b_j) = \psi_j^j(\xi', b_j), \quad i, j \in \mathbf{Z}. \tag{22}$$

Although this relation is physically different from the Lax's quasi-crystalline approximation, both of these approximations have the same mathematical structure (see also Eq. (5.18) of Willis, 1981). It should be also mentioned here that Eq. (23) of our previous paper (Mikata and Achenbach, 1988b) was erroneously called the Lax's quasi-crystalline approximation. Substituting (22) into (21a), we find

$$f(\xi) e^{ik(a_i + b_i)\cos\alpha} = \mu \int_{-a}^{a} \psi_i^i(\xi', b_i) L(\xi, \xi') d\xi'$$

$$+ \mu \sum_{\substack{j \in \mathbf{Z} \\ j \neq i}} \int_{-\frac{L}{2}}^{\frac{L}{2}} db_j \int_{-a}^{a} \psi_j^j(\xi', b_j) L(\xi, \xi'; a_i - a_j; b_i - b_j)$$

$$\times P(b_j) d\xi',$$

$$-a \le \xi \le a, \quad -\frac{L}{2} \le b_i \le \frac{L}{2}, \quad i \in \mathbf{Z}. \tag{23}$$

Substitution of (22) into (21b) yields an identity. Equation (23) represents an infinite (∞) set of simultaneous integral equations for the unknown conditionally averaged crack-opening displacements $\psi_i^i(\xi', b_i)$, $i \in \mathbf{Z}$. Changing the dummy variables b_i and b_j into u and v, we have

$$f(\xi) e^{ik(a_i + u)\cos\alpha} = \mu \int_{-a}^{a} \psi_i^i(\xi', u) L(\xi, \xi') d\xi'$$

$$+ \mu \sum_{\substack{j \in \mathbf{Z} \\ j \neq i}} \int_{-\frac{L}{2}}^{\frac{L}{2}} dv \int_{-a}^{a} \psi_j^j(\xi', v) L(\xi, \xi'; a_i - a_j; u - v)$$

$$\times P(v) d\xi',$$

$$-a \le \xi \le a, \quad -\frac{L}{2} \le u \le \frac{L}{2}, \quad i \in \mathbf{Z}. \tag{24}$$

We will show that the infinite set of integral Eqs. (24) permits a set of solutions which satisfy the following relations among themselves,

$$\psi_j^j(\xi', v) = e^{ik(a_j - a_i)\cos\alpha} \psi_i^i(\xi', v), \quad i, j \in \mathbf{Z}, \tag{25}$$

and therefore reduces to a single integral equation. Equation (25) is a periodicity condition. Let us prove that (24) is consistent with (25). Using (25), (24) is rewritten as

$$f(\xi) e^{iku\cos\alpha} = \mu e^{ika_0\cos\alpha} \left[\int_{-a}^{a} \psi_0^0(\xi', u) L(\xi, \xi') d\xi' \right.$$

$$\left. + \int_{-\frac{L}{2}}^{\frac{L}{2}} dv \int_{-a}^{a} \psi_0^0(\xi', v) P(v) \sum_{\substack{j \in \mathbf{Z} \\ j \neq i}} L(\xi, \xi'; a_i - a_j; u - v) \right.$$

$$\left. \times e^{ik(a_i - a_j)\cos\alpha} d\xi' \right],$$

$$-a \le \xi \le a, \quad -\frac{L}{2} \le u \le \frac{L}{2}, \quad i \in \mathbf{Z}. \tag{26}$$

We now want to show that all the equations involved in the infinite set of integral equations (26) are equivalent. To this end, let us set

$$a_{ij} = a_i - a_j$$

$$N(a_{ij}) = L(\xi, \xi'; a_{ij}; u - v) e^{ika_{ij}\cos\alpha}$$

$$I(i) = \sum_{\substack{j \in \mathbf{Z} \\ j \neq i}} N(a_{ij}). \tag{27}$$

Using Eq. (6), it is readily shown that

$$\{a_{ij} | j \in \mathbf{Z}, j \neq i\} = \{m(L + 2B) | m \in \mathbf{Z}, m \neq 0\},$$

for fixed $i \in \mathbf{Z}$.

Therefore, we have

$$I(i_1) = I(i_2), \quad i_1, i_2 \in \mathbf{Z}. \tag{28}$$

Downloaded 04 May 2010 to 171.66.16.28. Redistribution subject to ASME license or copyright; see http://www.asme.org/terms/Terms_Use.cfm

This completes the proof that (24) is consistent with (25).

By using (12) in (26), the resulting single integral equation is obtained as

$$f(\xi,u)=\frac{i}{4}\int_{-\frac{L}{2}}^{\frac{L}{2}}d\upsilon\int_{-a}^{a}\psi(\xi',\upsilon)F(\xi,\xi';u,\upsilon)d\xi' \qquad -a\le\xi\le a,\quad -\frac{L}{2}\le u\le\frac{L}{2} \tag{29}$$

where $\psi(\xi',\upsilon)$ is the unknown conditionally averaged crack-opening displacement for the zeroth crack, and

$$f(\xi,u)=-ik\sin\alpha e^{ik(\xi+u)\cos\alpha}$$

$$F(\xi,\xi';u,\upsilon)=\delta(u-\upsilon)F_1(\xi,\xi')+P(\upsilon)F_2(\xi,\xi';u-\upsilon)$$

$$F_1(\xi,\xi')=\frac{\partial}{\partial\eta}\left[\frac{\partial}{\partial\eta'}H_0^{(1)}(kR)|_{\eta'=0}\right]_{\eta=0}$$

$$F_2(\xi,\xi';u-\upsilon)=\frac{\partial}{\partial\eta}\left[\frac{\partial}{\partial\eta'}\sum_{\substack{m=-\infty\\ m\neq 0}}^{\infty}H_0^{(1)}(kR_m)e^{-ikm(L+2B)\cos\alpha}|_{\eta'=0}\right]_{\eta=0}$$

$$R^2=(x-x')^2+(y-y')^2=(\xi-\xi')^2+(\eta-\eta')^2$$

$$R_m^2=(x-x')^2+(y-y')^2=[\xi-\xi'+u-\upsilon+m(L+2B)]^2+(\eta-\eta')^2. \tag{30}$$

Once Eq. (29) is solved for $\psi(\xi',\upsilon)$, the averaged scattered field is obtained as

$$\langle w^{sc}\rangle(\mathbf{x})=\frac{i}{4}\int_{-\frac{L}{2}}^{\frac{L}{2}}d\upsilon\int_{-a}^{a}\psi(\xi',\upsilon)P(\upsilon)G(\mathbf{x};\xi',\upsilon)d\xi' \tag{31}$$

where

$$G(\mathbf{x};\xi',\upsilon)=\frac{\partial}{\partial\eta'}\sum_{m=-\infty}^{\infty}H_0^{(1)}\left(k\hat{R}_m\right)e^{ikm(L+2B)\cos\alpha}|_{\eta'=0}$$

$$\hat{R}_m^2=(x-x')^2+(y-y')^2=[x-\xi'-\upsilon-m(L+2B)]^2+(y-\eta')^2. \tag{32}$$

4 Reduction to a Periodic System

Let us consider a special case:

$$P(\upsilon)=\delta(\upsilon-\upsilon^*),\quad -\frac{L}{2}\le\upsilon\le\frac{L}{2}. \tag{33}$$

Equation (33) corresponds to a deterministic periodic system. Substituting (33) into (29), we obtain

$$\frac{4}{i}f(\xi,u)=\int_{-a}^{a}\psi(\xi',u)F_1(\xi,\xi')d\xi'+\int_{-a}^{a}\psi(\xi',\upsilon^*)F_2(\xi,\xi';u-\upsilon^*)d\xi' \qquad -a\le\xi\le a,\quad -\frac{L}{2}\le u\le\frac{L}{2}. \tag{34}$$

Similarly, by substituting (33) into (31), we have

$$\langle w^{sc}\rangle(\mathbf{x})=\frac{1}{4}\int_{-a}^{a}\psi(\xi',\upsilon^*)G(\mathbf{x};\xi',\upsilon^*)d\xi'. \tag{35}$$

Since only $\psi(\xi',\upsilon^*)$ is needed for the averaged scattered field $\langle w^{sc}\rangle(\mathbf{x})$, we may further simplify (34) to

$$\frac{4}{i}f(\xi,\upsilon^*)=\int_{-a}^{a}\psi(\xi',\upsilon^*)F_1(\xi,\xi')d\xi'+\int_{-a}^{a}\psi(\xi',\upsilon^*)F_2(\xi,\xi')d\xi' \tag{36}$$

where

$$F_2(\xi,\xi')=F_2(\xi,\xi';0). \tag{37}$$

Noting that our system is no longer random, we may write (36) as

$$\frac{4}{i}f(\xi)=\int_{-a}^{a}\psi(\xi')F_1(\xi,\xi')d\xi'+\int_{-a}^{a}\psi(\xi')F_2(\xi,\xi')d\xi' \tag{38}$$

where we have suppressed the υ^* dependence of $f(\xi,\upsilon^*)$ and $\psi(\xi',\upsilon^*)$. Accordingly, (35) is rewritten as

$$\langle w^{sc}\rangle(\mathbf{x})=\frac{i}{4}\int_{-a}^{a}\psi(\xi')G(\mathbf{x};\xi')d\xi' \tag{39}$$

where we have also suppressed the υ^* dependence of $G(\mathbf{x};\xi',\upsilon^*)$. Equations (38) and (39) correspond to the scattering problem of an SH-wave by a periodic array of coplanar cracks (Achenbach and Li, 1986) with crack centers located at $x=x_i$ where

$$x_i=\upsilon^*+iD,\quad i\in\mathbf{Z}. \tag{40}$$

5 Completely Disordered System

As a very important special case, let us consider a completely disordered system. The probability density $P(\upsilon)$ for the completely disordered system is given by

$$P(\upsilon)=\frac{1}{L},\quad -\frac{L}{2}\le\upsilon\le\frac{L}{2}. \tag{41}$$

Now, in order to solve the integral Eq. (29), let us expand $\psi(\xi',\upsilon)$ as

$$\psi(\xi',\upsilon)=\sum_{n=1}^{\infty}\sum_{j=-\infty}^{\infty}C_{nj}\phi_n^1(\xi')\phi_j^2(\upsilon) \tag{42}$$

where

$$\phi_n^1(\xi')=\begin{cases}\cos\left(n\sin^{-1}\dfrac{\xi'}{a}\right), & n=\text{odd}\\ i\sin\left(n\sin^{-1}\dfrac{\xi'}{a}\right), & n=\text{even}\end{cases}$$

$$\phi_j^2(\upsilon)=e^{i(2\pi j/L)\upsilon}. \tag{43}$$

Let us also define a set of conjugate functions as

$$\phi_p^{1*}(\xi)=\begin{cases}\cos\left(p\sin^{-1}\dfrac{\xi}{a}\right), & p=\text{odd}\\ -i\sin\left(p\sin^{-1}\dfrac{\xi}{a}\right), & p=\text{even}\end{cases}$$

$$\phi_q^{2*}(u)=\frac{1}{L}e^{-i(2\pi q/L)u}. \tag{44}$$

The key to the success of our method is the following representation of Hankel function:

Downloaded 04 May 2010 to 171.66.16.28. Redistribution subject to ASME license or copyright; see http://www.asme.org/terms/Terms_Use.cfm

$$H_0^{(1)}(kR) = \frac{1}{\pi}\int_{-\infty}^{\infty} \frac{1}{\sqrt{k^2-\zeta^2}} \times \exp\left[i\zeta(x-x') + i\sqrt{k^2-\zeta^2}|y-y'|\right]d\zeta$$

$$= \frac{1}{\pi}\int_{-\infty}^{\infty} \frac{1}{\sqrt{k^2-\zeta^2}} \times \exp\left[i\zeta(\xi-\xi') + i\sqrt{k^2-\zeta^2}|\eta-\eta'|\right]d\zeta$$

$$H_0^{(1)}(kR_m) = \frac{1}{\pi}\int_{-\infty}^{\infty} \frac{1}{\sqrt{k^2-\xi^2}} \times \exp\left[i\zeta\{\xi-\xi'+u-\upsilon+m(L+2B)\} + i\sqrt{k^2-\zeta^2}|\eta-\eta'|\right]d\zeta. \quad (45)$$

Substitution of (45) into (30c, d) yields

$$F_1(\xi,\xi') = \frac{1}{\pi}\int_{-\infty}^{\infty}\sqrt{k^2-\zeta^2}\,e^{i\zeta(\xi-\xi')}d\zeta$$

$$F_2(\xi,\xi';u-\upsilon) = \frac{1}{\pi}\sum_{\substack{m=-\infty\\ m\neq 0}}^{\infty} e^{-ikm(L+2B)\cos\alpha} \times \int_{-\infty}^{\infty}\sqrt{k^2-\zeta^2}\,e^{i\zeta[\xi-\xi'+u-\upsilon+m(L+2B)]}d\zeta. \quad (46)$$

We will obtain an infinite system of linear algebraic equations for C_{nj} by multiplying the both sides of (29) by the conjugate functions $\phi_p^{1*}(\xi)$ and $\phi_p^{2*}(u)$, and integrating them over $\xi \in [-a, a]$, $u \in \left[-\frac{L}{2}, \frac{L}{2}\right]$. By using Eqs. (30$a$,$b$) and (46), the resulting system reduces, after some manipulations, to

$$d_{pq} = \sum_{n=1}^{\infty} K_{pn}^1 C_{nq} + \sum_{n=1}^{\infty}\sum_{j=-\infty}^{\infty} K_{pqnj}^2 C_{nj}, \quad p \in \mathbf{Z}^+, \quad q \in \mathbf{Z} \quad (47)$$

where $\mathbf{Z}^+ \equiv \{1, 2, 3, \ldots\}$, and

$$d_{pq} = -8J_p(ka\cos\alpha)\tan\alpha\frac{\sin\frac{1}{2}(kL\cos\alpha - 2\pi q)}{kL\cos\alpha - 2\pi q}$$

$$K_{pn}^1 = n\int_{-\infty}^{\infty}\frac{\sqrt{k^2-\zeta^2}}{\zeta^2}J_p(a\zeta)J_n(a\zeta)d\zeta$$

$$K_{pqnj}^2 = 4n\left[\frac{2\pi}{L+2B}\sum_{m=-\infty}^{\infty}F_{pqnj}(\zeta_m) - \int_{-\infty}^{\infty}F_{pqnj}(\zeta)d\zeta\right]$$

$$F_{pqnj}(\zeta) = \frac{1}{2}\frac{\sqrt{k^2-\zeta^2}}{\zeta^2}J_p(a\zeta)J_n(a\zeta) \times \frac{\sin\frac{1}{2}(L\zeta-2\pi q)}{L\zeta-2\pi q}\int_{-\frac{L}{2}}^{\frac{L}{2}}P(\upsilon)e^{-i\upsilon\left(\zeta-\frac{2\pi j}{L}\right)}d\upsilon$$

$$\zeta_m = k\cos\alpha + \frac{2\pi m}{L+2B}. \quad (48)$$

It should be noted here that Eqs. (47) and (48) are for an arbitrarily disordered system. For the completely disordered system, by substituting (41) into (48d), we obtain

$$F_{pqnj}(\zeta) = \frac{\sqrt{k^2-\zeta^2}}{\zeta^2}J_p(a\zeta)J_n(a\zeta) \times \frac{\sin\frac{1}{2}(L\zeta-2\pi q)}{L\zeta-2\pi q}\frac{\sin\frac{1}{2}(L\zeta-2\pi j)}{L\zeta-z\pi j}. \quad (49)$$

In deriving Eqs. (47) and (48), we have used the following formulas:

$$\int_{-a}^{a}\phi_n^1(\xi')e^{-i\zeta\xi'}d\xi' = \frac{\pi n}{\zeta}J_n(a\zeta)$$

$$\int_{-a}^{a}\phi_p^{1*}(\xi)e^{i\zeta\xi}d\xi = \frac{\pi p}{\zeta}J_p(a\zeta) \quad (50)$$

$$\sum_{m=-\infty}^{\infty}e^{2\pi imz} = \sum_{m=-\infty}^{\infty}\delta(z-m) \quad (51)$$

where J_n is the Bessel function of order n and $\delta(z)$ is the Dirac delta function. It should be also noted here that the Poisson's summation formula (51) has to be understood in the sense of distribution (Stakgold, 1979). Once the solution to Eq. (47) is obtained, the averaged scattered field is given by substituting (42) into (31) as

$$\langle w^{sc}\rangle(\mathbf{x}) = \frac{i}{4}\sum_{n=1}^{\infty}\sum_{j=-\infty}^{\infty}C_{nj}\int_{-\frac{L}{2}}^{\frac{L}{2}}d\upsilon\int_{-a}^{a}\phi_n^1(\xi') \times \phi_j^2(\upsilon)P(\upsilon)G(\mathbf{x};\xi',\upsilon)d\xi'. \quad (52)$$

Substitution of (45b) into (32a) yields

$$G(\mathbf{x};\xi',\upsilon) = \begin{cases} -\dfrac{2i}{L+2B}\displaystyle\sum_{m=-\infty}^{\infty}e^{i\zeta_m(x-\xi'-\upsilon)+iy\sqrt{k^2-\zeta_m^2}}, & y \geq 0 \\ \dfrac{2i}{L+2B}\displaystyle\sum_{m=-\infty}^{\infty}e^{i\zeta_m(x-\xi'-\upsilon)-iy\sqrt{k^2-\zeta_m^2}}, & y \leq 0. \end{cases} \quad (53)$$

Substituting (43) and (53) into (52), we obtain

$$\langle w^{sc}\rangle(x) = \begin{cases} \displaystyle\sum_{m=-\infty}^{\infty}\langle w\rangle_m^+ e^{i\zeta_m x+iy\sqrt{k^2-\zeta_m^2}}, & y \geq 0 \\ \displaystyle\sum_{m=-\infty}^{\infty}\langle w\rangle_m^- e^{i\zeta_m x-iy\sqrt{k^2-\zeta_m^2}}, & y \leq 0 \end{cases} \quad (54)$$

where

$$\langle w\rangle_m^{\pm} = \pm\frac{\pi}{2(L+2B)}\sum_{n=1}^{\infty}\sum_{j=-\infty}^{\infty}nC_{nj} \times \frac{J_n(a\zeta_m)}{\zeta_m}\int_{-\frac{L}{2}}^{\frac{L}{2}}P(\upsilon)\phi_j^2(\upsilon)e^{-i\zeta_m\upsilon}d\upsilon. \quad (55)$$

It should be mentioned here that Eq. (55) is for an arbitrarily disordered system. For the completely disordered system, by substituting (41) and (43b) into (55), we obtain

$$\langle w\rangle_m^{\pm} = \pm\frac{\pi}{L+2B}\sum_{n=1}^{\infty}\sum_{j=-\infty}^{\infty}nC_{nj} \times \frac{J_n(a\zeta_m)}{\zeta_m}\frac{\sin\frac{1}{2}(L\zeta_m-2\pi j)}{L\zeta_m-2\pi j}. \quad (56)$$

Downloaded 04 May 2010 to 171.66.16.28. Redistribution subject to ASME license or copyright; see http://www.asme.org/terms/Terms_Use.cfm

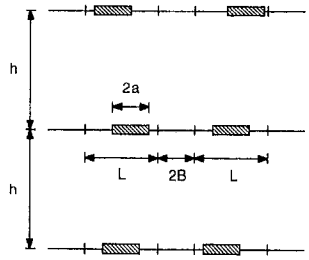

Fig. 2 Theoretical model for a disorderedly cracked medium

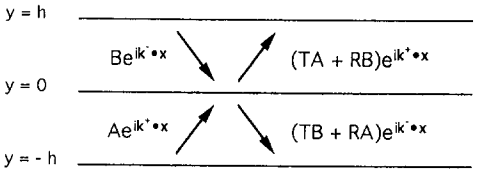

Fig. 3 Periodic system of reflecting and transmitting planes

The averaged zeroth-order reflection and transmission coefficients may be defined from (54) as (see also Sobczyk, 1985, pp. 226–229)

$$\langle R\rangle_0 = \langle w\rangle_0^-$$
$$\langle T\rangle_0 = 1 + \langle w\rangle_0^+. \tag{57}$$

When the incidence angle $\alpha = \dfrac{\pi}{2}$ (normal incidence), from (48*a*,*e*) and (56), we obtain

$$d_{pq} = -2ka\delta_{1p}\delta_{0q}$$
$$\langle w\rangle_0^{\pm} = \pm\frac{\pi a}{4(L+2B)}C_{10}. \tag{58}$$

6 Dispersion Relation

By using the results on reflection and transmission of an SH-wave by a disordered periodic array of coplanar cracks, the wave propagation of an SH-wave in a disorderedly cracked medium can be treated in an approximate manner. The disorderedly cracked medium is defined to be a body containing vertically periodic layers of horizontally-disordered-periodic coplanar cracks (Fig. 2). The average horizontal crack spacing is $L + 2B$, and the vertical crack spacing is h.

Our problem can be modeled as a periodic system of reflecting and transmitting planes in the y-direction, each plane being extended in the x-direction, and located at $y = nh$ ($n \in \mathbf{Z}$). For the reflection and transmission coefficients, the results obtained in the previous sections may be used. Let us now assume that the frequency ω of the wave is sufficiently low, and the crack spacing h in the y-direction is sufficiently large so that only the zeroth-order wave needs to be considered. Then the averaged displacement field is given by (see Fig. 3)

$$\langle w\rangle(\mathbf{x}) = Be^{i\mathbf{k}^-\cdot\mathbf{x}} + TAe^{i\mathbf{k}^+\cdot\mathbf{x}} + RBe^{i\mathbf{k}^+\cdot\mathbf{x}}, \quad 0 < y < h$$
$$\langle w\rangle(\mathbf{x}) = Ae^{i\mathbf{k}^+\cdot\mathbf{x}} + TBe^{i\mathbf{k}^-\cdot\mathbf{x}} + RAe^{i\mathbf{k}^-\cdot\mathbf{x}}, \quad -h < y < 0 \tag{59}$$

where

$$\mathbf{k}^+ = k(\cos\alpha, \sin\alpha), \quad \mathbf{k}^- = k(\cos\alpha, -\sin\alpha). \tag{60}$$

Here $Ae^{i\mathbf{k}^+\cdot\mathbf{x}}$ and $Be^{i\mathbf{k}^-\cdot\mathbf{x}}$ are "incident waves" on the reflecting and transmitting plane at $y = 0$, and R and T are the averaged zeroth-order reflection and transmission coefficients defined by (57) (i.e., $R \equiv \langle R\rangle_0$, $T \equiv \langle T\rangle_0$). Since the reflecting and transmitting planes are periodically located in the y-direction, the displacement field and the stress field become quasi-periodic. Specifically, we have

$$\langle w\rangle\left(0, \frac{h}{2}\right) = \langle w\rangle\left(0, -\frac{h}{2}\right)e^{iqh\sin\alpha}$$
$$\frac{d}{dy}\langle w\rangle\left(0, \frac{h}{2}\right) = \frac{d}{dy}\langle w\rangle\left(0, -\frac{h}{2}\right)e^{iqh\sin\alpha} \tag{61}$$

where q is an effective wave number of an SH-wave in the disorderedly cracked medium. Substitution of (59) into (61) yields

$$Ae^{iqh\sin\alpha}\left[Te^{-iqh\sin\alpha} - (R + e^{-ikh\sin\alpha})\right] - B\left[Te^{iqh\sin\alpha} - (R + e^{-ikh\sin\alpha})\right] = 0$$
$$Ae^{iqh\sin\alpha}\left[Te^{-iqh\sin\alpha} + R - e^{-ikh\sin\alpha}\right] + B\left[Te^{iqh\sin\alpha} + R - e^{-ikh\sin\alpha}\right] = 0. \tag{62}$$

The condition for a nontrivial solution (A, B) for Eq. (62) to exist leads, after some manipulations, to

$$\cos(qh\sin\alpha) = \frac{1}{2T}\left[(T^2 - R^2 - 1)e^{ikh\sin\alpha} + 2\cos(kh\sin\alpha)\right]. \tag{63}$$

Equation (63) is the dispersion relation for an SH-wave with an arbitrary angle of incidence α, and it reduces to the one given in the Achenbach and Kitahara (1987) when $\alpha = \pi/2$. It should be noted that as long as the wave in question has a scalar character, the dispersion relation is always of the form given by (63). As a matter of fact, in the aforementioned work, Achenbach and Kitahara (1987) treated a longitudinal wave propagating in a three-dimensional elastic solid with a periodic distribution of spherical cavities. The real part of q defines the phase velocity of the propagating wave, while the imaginary part determines the geometrical attenuation of an SH-wave in the disorderedly cracked medium. It is seen from (54) that the scattered field is a sum of an infinite number of different wave modes, each corresponding to a different m. When the frequency ω is low, the only propagating wave is the zeroth-order ($m = 0$) wave. It can be easily seen from Eqs. (48*e*) and (54) that the next higher order wave ($m \neq 0$) which becomes propagating as $\omega(= kc$ from (1)) increases is the wave of order -1 when $\alpha \in [0, \pi/2]$ (see also Mikata, 1993). Let us call the wave number corresponding to the onset of the propagation of the wave of order -1 as the critical wave number (Mikata, 1993). From Eqs. (48*e*) and (54), the critical wave number k_{cr} can be calculated as

$$k_{cr} = \frac{2\pi}{(L+2B)(1+\cos\alpha)}. \tag{64}$$

The range of wave number which guarantees the status of the zeroth-order wave as the only propagating wave is given by $k < k_{cr}$. Therefore, the dispersion relation (63) is expected to be very accurate when $k < k_{cr}$ provided that the vertical crack spacing h is not too small.

7 Numerical Results and Discussion

In all of the following results, computations are performed for the completely disordered system (41) and normal incidence ($\alpha = \pi/2$). As a reference, however, the results for a periodic array of coplanar cracks are also shown in all of the following figures. Also, in the following, whenever the reflection coefficients are referred to for a disordered system, they should be regarded as the averaged zeroth-order reflection

Downloaded 04 May 2010 to 171.66.16.28. Redistribution subject to ASME license or copyright; see http://www.asme.org/terms/Terms_Use.cfm

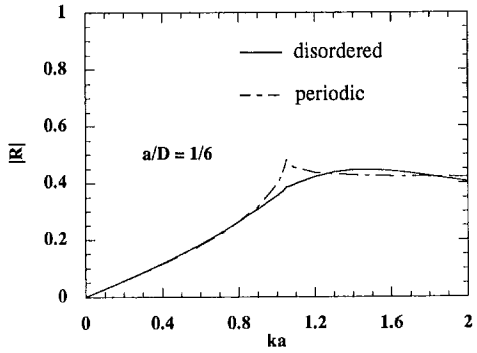

Fig. 4(*a*)

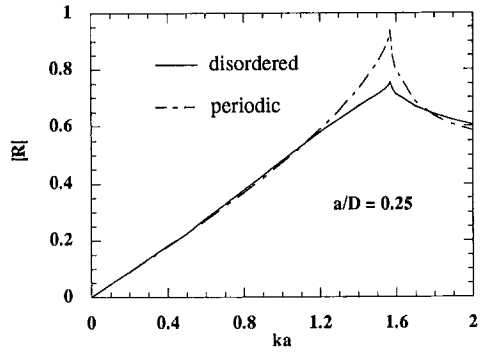

Fig. 4(*b*)

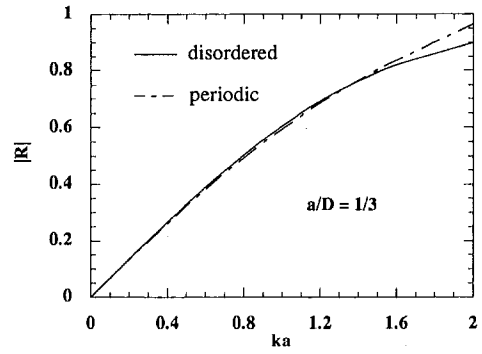

Fig. 4(*c*)

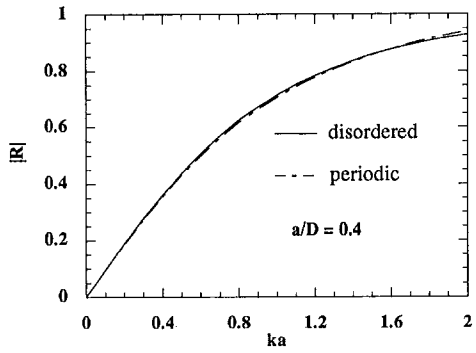

Fig. 4(*d*)

Fig. 4 Absolute values of the averaged zeroth order reflection coefficients of a normally incident SH wave

coefficients given by (57*a*). In Figs. 4(*a*)–4(*d*), the absolute values of the reflection coefficients are shown for various ratios of crack length to average crack spacing, a/D, where $D = L + 2B$. In these calculations as well as in the subsequent calculations, we have set $B = a$. In Figs. 4(*a*) and 4(*b*), we see cusps in the graphs. It is observed from Figs. 4(*a*) and

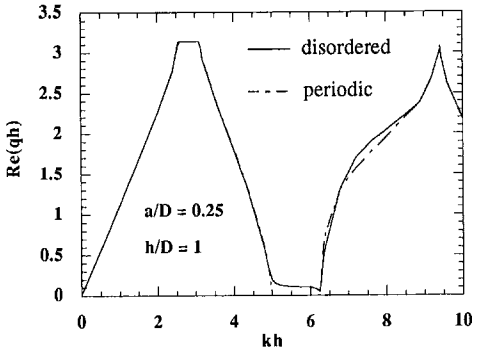

Fig. 5 Dispersion curve for an SH wave in a disorderedly cracked medium

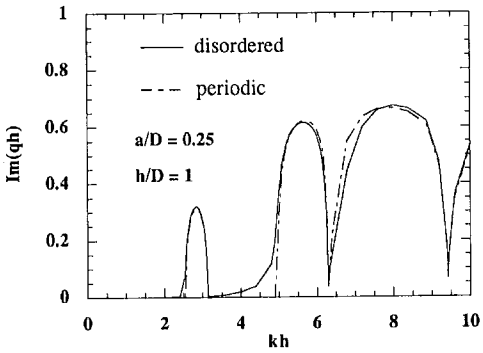

Fig. 6 Attenuation coefficients of a propagating SH wave in a disorderedly cracked medium

4(*b*) that the wave numbers corresponding to these cusps are very close to the critical wave numbers defined by (64). It is also seen from Figs. 4(*a*)–4(*d*) that, in the low wave number range up to near the critical wave number, the absolute values of the reflection coefficients for disorderedly spaced cracks are close to the one for periodically spaced cracks. In Fig. 5 and Fig. 6, the dispersion curve and the attenuation curve are shown, respectively, for the disorderedly cracked medium with $a/D = 0.25$ and $h/D = 1$. It is seen from Fig. 5 that the dispersion curve for the disorderedly cracked medium is almost the same for the one for the periodically cracked medium up to near the wave number corresponding to the end of the first optical branch. It is seen, on the other hand, from Fig. 6 that although the overall shape of the attenuation curve for the disorderedly cracked medium is similar to the one for the periodically cracked medium, there is a significant difference between the two curves approximately in the range $kh \epsilon (\pi, 4.95)$. While the attenuation coefficients for the periodically cracked medium are zero in that range, the attenuation coefficients for the disorderedly cracked medium have finite values. The implication is that while the periodically cracked medium has a passing band, the disorderedly cracked medium has none. It is also seen from Fig. 6 that the attenuation coefficients for the disorderedly cracked medium start having nonzero values earlier than the one for the periodically cracked medium after the respective acoustical branch.

References

Achenbach, A. D., Gautesen, A. K., and McMaken, H., 1982, *Ray Methods for Waves in Elastic Solids*, Pitman, London.

Achenbach, J. D., and Kitahara, M., 1987, "Harmonic Waves in a Solid with a Periodic Distribution of Spherical Cavities," *Journal of Acoustical Society of American*, Vol. 81, pp. 595–598.

Achenbach, A. D., and Li, Z. L., 1986, "Reflection and Transmission of Scalar Waves by a Periodic Array of Screens," *Wave Motion*, Vol. 8, pp. 225–234.

Achenbach, A. D., and Li, Z. L., 1986, "Propagation of Horizontally

Downloaded 04 May 2010 to 171.66.16.28. Redistribution subject to ASME license or copyright; see http://www.asme.org/terms/Terms_Use.cfm

Polarized Transverse Waves in a Solid with a Periodic Distribution of Cracks," *Wave Motion*, Vol. 8, pp. 371–379.

Angel, Y. C., and Achenbach, J. D., 1985a, "Reflection and Transmission of Elastic Waves by a Periodic Array of Cracks," ASME JOURNAL OF APPLIED MECHANICS, Vol. 52, pp. 33–41.

Angel, Y. C., and Achenbach, J. D., 1985b, "Reflection and Transmission of Elastic Waves by a Periodic Array of Cracks: Oblique Incidence," *Wave Motion*, Vol. 7, pp. 375–397.

Angel, Y. C., and Achenbach, J. D., 1987, "Harmonic Waves in an Elastic Solid Containing a Doubly Periodic Array of Cracks," *Wave Motion*, Vol. 9, pp. 377–386.

Foldy, L. L., 1945, "The Multiple Scattering of Waves," *Physical Review*, Vol. 67, pp. 107–119.

Gubernatis, J. E., and Domany, E., 1984, "Effects of Microstructure on the Speed and Attenuation of Elastic Waves in Porous Materials," *Wave Motion*, Vol. 6, pp. 579–589.

Kinra, V. K., Petraitis, M. S., and Datta, S. K., 1980, "Ultrasonic Propagation in a Random Particulate Composite," *International Journal of Solids and Structures*, Vol. 16, pp. 301–312.

Lax, M., 1952, "Multiple Scattering of Waves II. The Effective Field in Dense Systems," *Physical Review*, Vol. 85, pp. 621–629.

McCarthy, M. F., and Carroll, M. M., 1984, "Multiple Scattering of SH Waves by Randomly Distributed Dissimilar Scatterers," *Wave Phenomena: Modern Theory and Applications*, edited by C. Rogers and T. B. Moodie, eds., North-Holland, pp. 433–451.

Mikata, Y., 1993, "Reflection and Transmission by a Periodic Array of Coplanar Cracks: Normal and Oblique Incidence," ASME *Journal of Applied Mechanics*, Vol. 60, pp. 911–919.

Mikata, Y., and Achenbach, J. D., 1988a, "Interaction of Harmonic Waves with a Periodic Array of Inclined Cracks," *Wave Motion*, Vol. 10, pp. 59–72.

Mikata, Y., and Achenbach, J. D., 1988b, "Reflection and Transmission by an Infinite Array of Randomly Oriented Cracks," *Journal of Acoustical Society of America*, Vol. 83, pp. 38–45.

Sobczyk, K., 1985, *Stochastic Wave Propagation*, Elsevier, New York.

Stakgold, I., 1979, *Green's Functions and Boundary Value Problems*, John Wiley and Sons, New York.

Twersky, V., 1983, "Reflection and Scattering of Sound by Correlated Rough Surfaces," *Journal of Acoustical Society of America*, Vol. 73, pp. 85–95.

Varadan, V. K., and Varadan, V. V., 1979, "Frequency Dependence of Elastic (SH) Wave Velocity and Attenuation in Anisotropic Two Phase Media," *Wave Motion*, Vol. 1, pp. 53–63.

Waterman, P. C., and Truell, R., 1961, Multiple Scattering of Waves," *Journal of Mathematical Physics*, Vol. 2, pp. 512–537.

Weaver, R. L., 1985, "A Variational Principle for Waves in Discrete Random Media," *Wave Motion*, Vol. 7, pp. 105–121.

Willis, J. R., 1980, "A Polarization Approach to the Scattering of Elastic Waves—II. Multiple Scattering From Inclusions," *Journal of the Mechanics and Physics of Solids*, Vol. 28, pp. 307–327.

Willis, J. R., 1981, "Variational Principles for Dynamic Problems for Inhomogeneous Elastic Media," *Wave Motion*, Vol. 3, pp. 1–11.

Downloaded 04 May 2010 to 171.66.16.28. Redistribution subject to ASME license or copyright; see http://www.asme.org/terms/Terms_Use.cfm

A Statistical Approach for Fracture of Brittle Materials Based on the Chain-of-Bundles Model

C. Ruggieri
Department of Civil Engineering,
University of Illinois at Urbana-Champaign,
2105 Newmark Laboratory, MC-250
Urbana, IL 61801-2397

F. Minami

M. Toyoda

Faculty of Engineering,
Osaka University,
2-1 Yamada-Oka, Suita,
Osaka 565, Japan

An analytical method for the assessment of failure probability of brittle materials exhibiting progressive cracking prior to cleavage fracture is presented. The underlying fracture mechanism is based on the assumption that instability of a critical flaw no longer leads to failure and causes redistribution of the local stresses. The fracture process progresses by consecutive unstable propagation of the surviving flaws up to total failure. A limiting distribution for the fracture stress, which is identical with the first asymptotic distribution of smallest values, is derived on the basis of a chain-of-bundles probability model. Numerical procedures for calculating the parameters of the limiting distribution are also described. Due to the nature of the resulting distribution, the method employs the maximum likelihood estimation of parameters combined with a finite element solution to the crack-tip fields. An application of the present model to analyze the effect of notch depth on fracture toughness values obtained from single-edge notch bend (SENB) specimens is also included.

1 Introduction

Brittle fracture has long been recognized as a highly localized phenomenon where fracture initiation is mainly controlled by the incidence of microcracks that inherently occur in the material. In the fundamental cleavage failure mechanism, it is postulated that these microcracks will produce stress concentration of sufficient magnitude so that unstable crack propagation takes place where a local fracture stress exceeds a critical value (Griffith, 1924; Orowan, 1948). Such a model provides a connection between the material fracture behavior and the remote stress field by introducing a local crack-tip parameter controlling fracture. While generalization of this theory by a continuum mechanical approach may resolve the local stresses leading to failure in a large class of crack problems, it does not take into consideration the statistical behavior of fracture. Due to inhomogeneity in the local characteristics of the material, such as strength and inherent size of flaw, fracture is of a random nature which should also be analyzed by statistical methods.

Earlier studies on the randomness of fracture have been based on the weakest link model (Weibull, 1939). Extension of this theory to the mechanical assessment of cracked bodies under general loading has provided further methods to analyze the brittle fracture problem (see, e.g., Batdorf and Crose, 1974; Evans, 1978; Matsuo, 1981; Lin, Evans, and Ritchie, 1986). All these models combine the weakest link hypothesis with the stress field ahead of the crack, which leads to a third asymptotic distribution of extreme values for the fracture stress. Significance of such probabilistic approaches, however, strongly relies on the catastrophic failure being controlled by the instability of the weakest flaw, which may not necessarily describe the local fracture mechanism.

For materials having local inhomogeneity in strength, the unstable propagation of a flaw may be arrested by the surrounding region having higher fracture resistance. Failure of a critical flaw in any small element of the material causes redistribution of the local stresses, so that increasing in the applied load is necessary to promote further cracking. Only after a number of elements have cracked does the failure occur in a macroscopic scale, ultimately via a weakest link mechanism. Such a problem has been addressed earlier by Gücer and Gurland (1962) using composite specimens subjected primarily to tension. Brittle fracture preceded by extensive near-tip plastic deformation, as observed in most steels in the transition region, also bears strong similarity to this mechanism. Large plastic strains arising directly ahead of the crack promote intense blunting of the tip with consequent crack growth. The local stresses are therefore redistributed to the uncracked near-tip elements until a local critical stress is reached. Fracture is thus locally progressive to the extent that instability of a critical flaw may no longer lead to total failure. Another study along this line has also been made by Curtin and Scher (1990), where microstructural mechanisms, such as interaction of microcracks and

Contributed by the Applied Mechanics Division of THE AMERICAN SOCIETY OF MECHANICAL ENGINEERS for publication in the ASME JOURNAL OF APPLIED MECHANICS.

Discussion on this paper should be addressed to the Technical Editor, Professor Lewis T. Wheeler, Department of Mechanical Engineering, University of Houston, Houston, TX 77204-4792, and will be accepted until four months after final publication of the paper itself in the ASME JOURNAL OF APPLIED MECHANICS.

Manuscript received by the ASME Applied Mechanics Division, Nov. 13, 1992; final revision, Sept. 14, 1993. Associate Technical Editor: C. F. Shih.

Copyright © 1995 by ASME

Downloaded 04 May 2010 to 171.66.16.28. Redistribution subject to ASME license or copyright; see http://www.asme.org/terms/Terms_Use.cfm

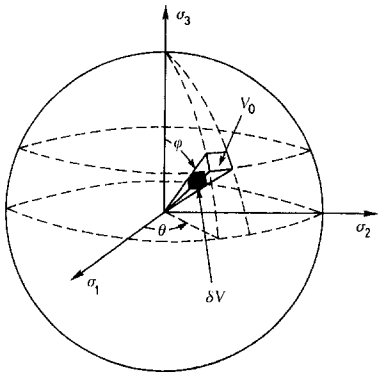

Fig. 1(*a*)

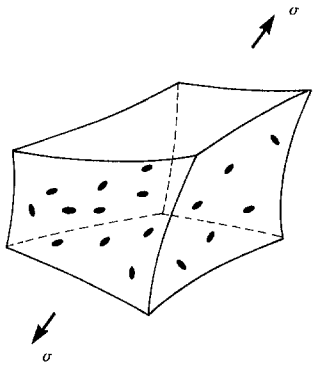

Fig. 1(*b*)

Fig. 1 Model for brittle fracture with progressive cracking, (*b*) uniform distribution of flaws in a volume element δ V

growth of flaws, are viewed as disorders in length scales comparable with the size of the region where fracture takes place. A network of small elements is then used, so as to include the local constitutive laws and random characteristics of the material, which serves to calculate the local stresses leading to failure.

In the present work, the problem of brittle fracture with progressive cracking is addressed by a statistical approach based on the so-called chain-of-bundles probability model (Gücer and Gurland, 1962; Harlow and Phoenix, 1978). A limiting distribution for the fracture stress is derived which is identical with the first asymptotic distribution of smallest values. The approach leads to an alternative parameter controlling fracture which relates the random incidence of microcracks with the crack-tip fields. Numerical methods based on a finite element solution to the crack-tip fields are described for calculating the parameters of the probability distribution. An application follows on the prediction of the effect of notch depth on fracture toughness values obtained from single-edge notch bend (SENB) specimens.

2 The Chain-of-Bundles Model to Brittle Fracture

Consider a volume V of a stressed region of a solid subjected to the principal stresses (σ_1, σ_2, σ_3) and let V_{0_i} ($i = 1, \ldots, p$) be a small volume uniformly stressed, as shown in Fig. 1(*a*). Also let δV_j ($j = 1, \ldots, n$) be a volume element contained in V_0 and large enough to contain a substantial number r of statistically independent flaws uniformly distributed, as illustrated in Fig. 1(*b*) We postulate that the instability of the weakest flaw contained in a volume element no longer leads to catastrophic failure, but promotes redistribution of the local stresses over the surrounding region. The fracture process progresses by consecutive instability of the surviving flaws until a critical load is reached. The

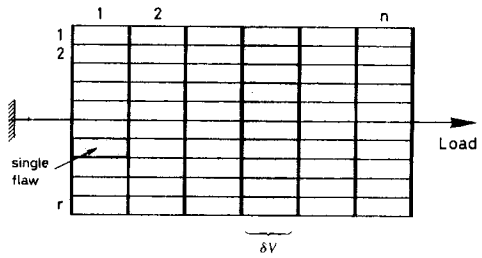

Fig. 2 Equivalent statistical model for brittle fracture with progressive cracking

critical event in the fracture process is therefore associated to the independent unstable propagation of a number of such flaws via a bundle mechanism. Furthermore, we also assume that fracture of a small volume V_0, and consequently of the entire volume V, is controlled by the first failure of a volume element δV via a weakest link mechanism. Hence, the equivalent statistical formulation of this problem reduces to a chain of n statistically independent bundles, each bundle having r independent elements in parallel, as shown in Fig. 2.

Define the failure of the jth volume element δV_j as the random variable X_j and assume $X_1, \ldots, X_n$ are independent and identically distributed. If ζ is the probability of fracture taking place in each δV_j under the stress σ, then the probability that q failures occur is given by the binomial distribution

$$P(S_n = q) = \binom{n}{q} \zeta^q (1 - \zeta)^{n-q}, \quad 0 \le q \le n \tag{1}$$

where S_n denotes the total number of failures occurred in n volume elements. When n is large and ζ is small, by the Poisson limit theorem, the distribution of the number of failures converges to a Poisson distribution with parameter λ in the form

$$P(S_n = q) = \frac{e^{-\lambda}\lambda^q}{q!} \tag{2}$$

where $\lambda = n\zeta$ is the expectation of the binomial distribution. In particular, we seek the probability that there is at least one failure. Thus, the failure probability of V_0 has the distribution

$$P(S_n \ge 1) = 1 - P(S_n = 0) = 1 - e^{-n\zeta}. \tag{3}$$

For each volume element δV_j we assume that the local fracture mechanism is described by a fiber bundle model with equal load sharing (Daniels, 1945). According to this model, δV is considered as a single bundle with independent elements in parallel, each one having the same cross section, so that the load is equally redistributed among the unfailed elements when an element fractures. Let the fracture strength of each element be denoted by $T_1, T_2, \ldots, T_r$ and let these strengths be the order statistics $T_1 \le T_2 \le \ldots \le T_r$, then the failure of the bundle under stress σ can be given by the following condition:

$$\sigma \ge \max\left\{T_1, \left(\frac{r-1}{r}\right)T_2, \ldots, \left(\frac{1}{r}\right)T_r\right\}. \tag{4}$$

For large number of elements, it has been shown by Daniels (1945) that the bundle strength is asymptotically normally distributed with expectation μ and standard deviation γ. Thus, the fracture strength σ of a volume element δV has distribution

$$\zeta = \Phi(z) = \frac{1}{\sqrt{2\pi}} \int_{-\infty}^{z} e^{-t^2/2}\, dt \tag{5}$$

Downloaded 04 May 2010 to 171.66.16.28. Redistribution subject to ASME license or copyright; see http://www.asme.org/terms/Terms_Use.cfm

where $\Phi(z)$ is the standard normal distribution function with expectation zero and standard deviation one and $z = (\sigma - \mu)/\gamma$. Here the parameters μ and γ are related to the material properties through the fracture strength distribution of a bundle element (Gücer and Gurland, 1962). Hence, substituting (5) into (3), the failure probability of a small volume V_0 under stress σ is given by

$$F(z) = 1 - \exp\left(-\frac{n}{\sqrt{2\pi}}\int_{-\infty}^{z} e^{-t^2/2}\,dt\right). \tag{6}$$

Define now the random variable ξ as

$$\xi = \frac{n}{\sqrt{2\pi}}\int_{-\infty}^{z} e^{-t^2/2}\,dt \tag{7}$$

which, for large n, is shown to have an asymptotic solution in the form (Cramér, 1946; Epstein, 1960)

$$z = a_n + b_n \ln \xi \tag{8}$$

where a_n and b_n are constants. Thus, replacing z by $(\sigma - \mu)/\gamma$ and working out the resulting expression, the random variable ξ is expressed by

$$\xi = \exp\left(\frac{\sigma - \alpha}{\beta}\right) \tag{9}$$

where the parameters α and β are related to the material properties μ and γ and to the constants a_n and b_n. Hence, it follows that the fracture strength of V_0 is distributed asymptotically as

$$F(\sigma) = 1 - \exp\left[-\exp\left(\frac{\sigma - \alpha}{\beta}\right)\right] \tag{10}$$

which is identical with the first asymptotic distribution of the smallest value with location parameter α and scale parameter β (Gumbel, 1958).

Now consider the entire volume V in Fig. 1(*a*) and let Y_i, $i = 1, \ldots, p$, be the failure of the ith volume V_0. Assume Y_i to be an independent and identically distributed random variable with distribution $F(\sigma)$, as given by (10). We postulate that the failure of the volume V is controlled by the weakest small volume V_0. Thus, the strength of V is $S_p = \min\{Y_1, \ldots, Y_p\}$ which has distribution

$$G(y) = 1 - [1 - F(y)]^p. \tag{11}$$

Substituting (10), the distribution of the fracture strength for the entire volume V yields.

$$G_f = 1 - \exp\left[-\sum_p \exp\left(\frac{\sigma - \alpha}{\beta}\right)\right]. \tag{12}$$

The sum approaches an integral for a continuous distribution of the stress and (12) can be expressed by

$$G_f = 1 - \exp\left[-\frac{1}{V_0}\int_V \exp\left(\frac{\sigma - \alpha}{\beta}\right)dV\right] \tag{13}$$

which is again a type I asymptotic distribution of smallest values. Now, employing the usual transformation of Cartesian coordinates (x_1, x_2, x_3) into spherical coordinates (R, θ, φ) by the mapping

$$\begin{aligned} x_1 &= R\sin\varphi\cos\theta \\ x_2 &= R\sin\varphi\sin\theta \\ x_3 &= R\cos\varphi \end{aligned} \tag{14}$$

and letting V be a unit volume, (13) yields

$$G_f = 1 - \exp\left[-\frac{1}{4\pi V_0}\int_0^{2\pi}\int_0^{\pi}\exp\left(\frac{\sigma - \alpha}{\beta}\right)\sin\varphi\,d\varphi\,d\theta\right]. \tag{15}$$

This equation applies to any multiaxially stressed region of the material and, therefore, can take into account the large stress gradients that arise from a sharp crack or a notch. Conventional models to unstable crack propagation in structural steels have postulated that cleavage fracture is associated with formation and growth of microcracks in regions near the crack tip which undergo inhomogeneous plastic flow (Smith, 1968). This would suggest that the critical event in the fracture process occurs in the plastic zone ahead of crack. However, experimental evidences have also shown that the onset of stress-controlled cleavage fracture generally takes place over a region near the crack tip comparable in size to few crack-tip opening displacements, hereafter denoted as CTOD or δ (see, e.g., Brückner-Foit et al., 1990). Thus, we define a fracture process zone, which is appropriate for this analysis, as the region confined to distances less than 10δ from the crack tip. Hence, generalization of (15) yields the limiting distribution for the fracture strength of a notched body subjected to a multiaxial stress state in the form

$$H_f = 1 - \exp \times\left[-\frac{1}{4\pi V_0}\int_\Omega\int_0^{2\pi}\int_0^{\pi}\exp\left(\frac{\sigma - \alpha}{\beta}\right)\sin\varphi\,d\varphi\,d\theta d\Omega\right] \tag{16}$$

where Ω is the volume of the fracture process zone ahead of the notch. Here we note that the stress tensor acting on any region inside the volume can be reduced to an equivalent tensile stress to the microcrack plane, σ_Q, once an appropriate shape is adopted for the microcrack and a fracture criterion is postulated. The probability distribution of the fracture strength can thus be determined by simply replacing σ by σ_Q in (16).

It is worth examining here the development of the present model in the case of well-contained plasticity. At load levels sufficiently low, so that small-scale yielding conditions prevail, the crack-tip fields are governed by the asymptotic singular field derived by Hutchinson (1968) and Rice and Rosengren (1968), which is referred to as the HRR singularity. A power-hardening idealization of the uniaxial stress-strain curve of the material is employed in the form

$$\frac{\epsilon_p}{\epsilon_Y} = \kappa\left(\frac{\sigma_e}{\sigma_Y}\right)^h \tag{17}$$

where ϵ_p is the plastic strain, σ_Y is the yield stress, $\epsilon_Y = \sigma_Y/E$ is the associated yield strain, κ is a dimensionless material constant, and h is the strain-hardening exponent. Here σ_e is the equivalent Mises stress given by $\sigma_e = (3/2\, S_{ij}\, S_{ij})^{1/2}$, where S_{ij} is the stress deviator. Employing polar coordinates (R, θ) with origin at the crack tip, the form of the plane strain HRR stress fields is given by

$$\sigma_{ij} = \sigma_Y\left(\frac{EJ}{\kappa\sigma_Y^2 I_h R}\right)^{1/(h+1)} g_{ij}(\theta, h) \tag{18}$$

where σ_{ij} is the stress tensor, the J-integral (Rice, 1968) is the amplitude of crack-tip fields, I_h is an integration constant which is a function of h only, and g_{ij} is a dimensionless function which depends on h and θ.

Now, assuming that the fracture process zone ahead of crack tip, which is shown in Fig. 3, is uniform along the crack front, a volume element $d\Omega$ is given by $B\,dA$, where B is the thickness of the notched body and A is the area of the fracture process zone in the plane $x_1 - x_2$. Then $dA = R\,dR\,d\theta$ and the probability distribution of fracture strength, as given by (13), can be directly generalized over the region Ω in the form

Downloaded 04 May 2010 to 171.66.16.28. Redistribution subject to ASME license or copyright; see http://www.asme.org/terms/Terms_Use.cfm

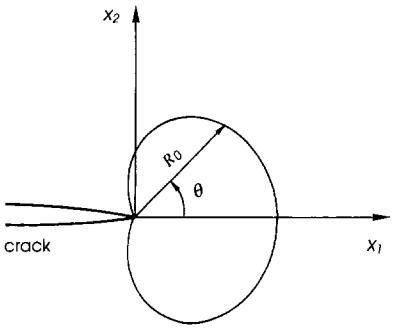

Fig. 3 Two-dimensional representation of fracture process zone ahead of crack

$$H_f = 1 - \exp\left[-\frac{B}{V_0}\int_0^{2\pi}\int_0^{R_0}\exp\left(\frac{\sigma-\alpha}{\beta}\right) R\, dR\, d\theta\right] \quad (19)$$

where R_0 is the radius of the fracture process zone.

In view of the dominance of local tensile stresses on cleavage fracture, the connection between the limiting distribution (19) and the HRR stress fields can be obtained by rewriting (18) in terms of the maximum principal stress σ_1. Then, employing the nondimensional radius $\rho = R\sigma_Y/J$, (18) can be rewritten as

$$\sigma_1 = \sigma_Y\left(\frac{E}{\kappa\sigma_Y I_h \rho}\right)^{1/(h+1)} g_1(\theta, h) = \sigma_Y f(\rho, h) g_1(\theta, h). \quad (20)$$

Here g_1 denotes the dimensionless function g_{ij} relative to the maximum principal stress and f describes a dimensionless function of ρ and h. While this expression does not adequately describe the stresses within the blunted region near the crack tip ($R < 2\delta$) where finite strain effects prevail (McMeeking, 1977), one may neglect such differences for the present analysis. Hence, the limiting distribution for the fracture strength under J-controlled conditions can be obtained by inserting (20) into (19). Working out the resulting expression in terms of the nondimensional radius ρ, one can show that under small-scale yielding conditions H_f is given by

$$H_f = 1 - \exp\left[-\left(\frac{J}{b}\right)^2\right] \quad (21)$$

which is a Weibull distribution with shape parameter equal to 2. Here, b is the scale parameter which is given by

$$b = \left\{\frac{B}{V_0\sigma_Y^2}\int_0^{2\pi}\int_0^{\rho_0} M(\rho, \theta, h)\rho\, d\rho\, d\theta\right\}^{-1/2} \quad (22)$$

where ρ_0 is the nondimensional radius of the fracture process zone and

$$M(\rho, \theta, h) = \exp\left[\frac{\sigma_Y f(\rho, h)\, g_1(\theta, h) - \alpha}{\beta}\right]. \quad (23)$$

3 Numerical Solution and Related Formulations

3.1 Estimation Procedure for the Parameters of the Limiting Distribution. The parameters α and β which define the limiting distribution of the fracture strength can be evaluated from a statistical analysis of the experimental results once the near-tip stress fields are known. Define the random variable and the parameters of the fracture strength distribution as

$$\sigma = \ln\chi$$
$$\alpha = \ln u$$
$$\beta = w^{-1} \quad (24)$$

so that (16) takes the form

$$H_f = 1 - \exp\left[-\frac{1}{4\pi V_0}\int_\Omega\int_0^{2\pi}\int_0^{\pi}\left(\frac{\chi}{u}\right)^w \sin\varphi\, d\varphi\, d\theta\, d\Omega\right]. \quad (25)$$

Define now the integral

$$\psi^w = \frac{1}{4\pi V_0}\int_\Omega\int_0^{2\pi}\int_0^{\pi}\chi^w \sin\varphi\, d\varphi\, d\theta\, d\Omega \quad (26)$$

and (25) becomes

$$H_f(\psi) = 1 - \exp\left[-\left(\frac{\psi}{u}\right)^w\right] \quad (27)$$

which is a Weibull distribution with shape parameter w and scale parameter u.

Let now $H_{\text{fem}}(\psi)$ and $H_{\text{exp}}(\psi)$ be the distribution of ψ corresponding to the stress state obtained by finite element analysis and the one arising from the notched body, respectively. We postulate that $H_{\text{fem}}(\psi)$ and $H_{\text{exp}}(\psi)$ are identically distributed and the problem is to determine a set of parameters $\{u, w\}$ that satisfies this condition. An estimation procedure for such parameters has been given by Minami et al. (1992) and a similar approach will be used here. The procedure also requires that the near-tip stress fields be described by a single parameter in order to correlate the crack-tip fields of the notched body with that obtained by finite element analysis. Here, the crack-tip opening displacement, δ, is used, which leads to the following notation: δ_T denotes the value of the crack-tip opening displacement computed from the finite element model and δ_{cl} denotes the experimental value of the crack-tip opening displacement measured at the onset of cleavage fracture.

The algorithm starts by determining $\psi_{\text{fem}} = f(\delta_T)$ for a given parameter w_0. By interpolation we then find $\psi_{\text{exp}} = g(\delta_{cl})$ for the known experimental data. Using the values of ψ_{exp} we determine, through the maximum likelihood method, the parameters $\{w_1, u_1\}$ of the distribution $H_{\text{exp}}(\psi)$. If $w_1 \neq w_0$ then we compute a new distribution $\psi_{\text{fem}} = f(\delta_T)$ for the parameter w_1 and the iteration proceeds as shown in Fig. 4. For a sample of size s, the likelihood function L_W of the Weibull distribution can be expressed as

$$L_W = \left(\frac{w}{u}\right)^s \prod_{i=1}^{s}\left(\frac{\psi_i}{u}\right)^{w-1}\exp\left[-\prod_{i=1}^{s}\left(\frac{\psi_i}{u}\right)^w\right]. \quad (28)$$

Thus, the maximum likelihood estimators of the distribution are obtained by simply finding the values of u and w that maximize (28). A detailed discussion of the maximum likelihood estimation of the Weibull distribution has been given by Mann, Schafer, and Singpurwalla (1974).

3.2 Evaluation of the Integral ψ. In (26), the integration of the exponential of the stress tensor over the volume of the fracture process zone defines the fracture controlling parameter for the present model. Once an accurate finite element solution to the continuum near-tip stress distribution is obtained, the integral can be splitted up into a sum of integrals over the yielded elements as follows:

$$\psi^w = \frac{1}{4\pi V_0}\sum_{n_e}\int_{\Omega_e}\int_0^{2\pi}\int_0^{\pi}\chi^w \sin\varphi\, d\varphi\, d\theta\, d\Omega_e \quad (29)$$

where n_e is the number of elements included in the process

Downloaded 04 May 2010 to 171.66.16.28. Redistribution subject to ASME license or copyright; see http://www.asme.org/terms/Terms_Use.cfm

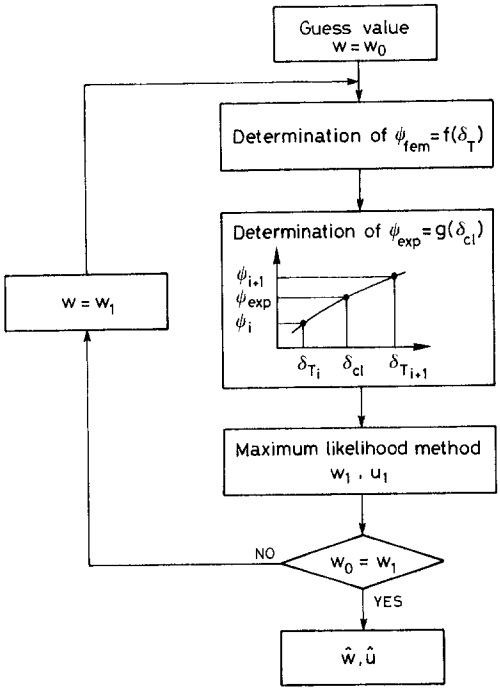

Fig. 4 Estimation procedure for the parameters of the distribution of the integral ψ

zone and Ω_e is the volume of the yielded element. Evaluation of this equation can be accomplished by taking the transformation of Cartesian coordinates (x_1, x_2, x_3) of the deformed elements into natural coordinates (η_1, η_2, η_3), $(-1 \le \eta_i \le 1,\ i = 1, 2, 3)$. Since $d\Omega_e = \det \mathbf{D}\, d\eta_1 d\eta_2 d\eta_3$, where $\det \mathbf{D}$ is the determinant of the Jacobian matrix of the transformation, (29) yields

$$\psi^w = \frac{1}{4\pi V_0} \sum_{ne} \int_{-1}^{1}\int_{-1}^{1}\int_{-1}^{1}\int_{0}^{2\pi}\int_{0}^{\pi} \times \det \mathbf{D}\, \chi^w \sin\varphi\, d\varphi\, d\theta\, d\eta_1\, d\eta_2\, d\eta_3. \quad (30)$$

In this work, an isoparametric hexahedron element with eight nodes is employed for the finite element solution of the crack-tip fields. The Cartesian coordinates x of any point inside the element are related to the natural coordinates η_i through the relationship (Zienkiewicz, 1989)

$$x_i = \sum_{k=1}^{8} N_k x_{ik}, \quad i = 1, 2, 3 \quad (31)$$

where N_k are the shape functions corresponding to the node k and x_{ik} are its nodal coordinates. These shape functions can be expressed as

$$N_k = \frac{1}{8} \prod_{i=1}^{3} (1 + \eta_i \eta_{ik}), \quad k = 1, \ldots, 8 \quad (32)$$

where η_{ik} are the natural coordinates of node k. Yet in (30), $\mathbf{D}$ is a square matrix of order 3×3 given by

$$D_{ij} = \sum_{k=1}^{8} \frac{\partial N_k}{\partial \eta_i} x_{jk}, \quad i, j = 1, 2, 3 \quad (33)$$

where D_{ij} is the ith element of the jth row. Upon combining these expressions, we then arrive at a set of equations that can be directly evaluated by numerical quadrature and from which the unknown integral ψ can be determined.

3.3 Fracture Criterion. We define the microcrack as a penny-shaped crack with size a subjected to a normal stress σ_n and an in-plane shear stress τ. The simplest fracture

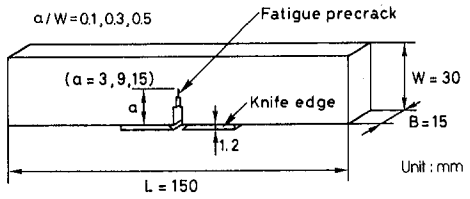

Fig. 5 Schematic of three-point SENB specimens with different *a*/*W*-ratio used in the analysis

criterion is based on the assumption that fracture propagates in the crack plane so that the direction of the three modes of deformation will be identical (Paris and Sih, 1965). Thus, by equating the total coplanar energy release rate in plane strain to an equivalent energy release rate for pure mode I loading, the equivalent stress σ_Q for a crack extending in its own plane is given by

$$\sigma_Q^2 = \sigma_n^2 + \frac{4\tau^2}{(2-\nu)^2} \quad (34)$$

where ν is the Poisson's ratio. Here the normal stress σ_n to the microcrack plane and the in-plane shear stress τ follow from the usual tensor transformation by using the mapping given by (14) and are expressed by

$$\sigma_n = \sigma_1 \sin^2\varphi \cos^2\theta + \sigma_2 \sin^2\varphi \sin^2\theta + \sigma_3 \cos^2\varphi$$
$$\tau^2 = \sigma_1^2 \sin^2\varphi \cos^2\theta + \sigma_2^2 \sin^2\varphi \sin^2\theta + \sigma_3^2 \cos^2\varphi - \sigma_n^2 \quad (35)$$

where σ_1, σ_2, and σ_3 are the principal stresses corresponding to the axes x_1, x_2, and x_3.

4 Application to Failure Prediction of Notched Bodies

Assessment of flawed structural components against brittle fracture from laboratory deep crack specimens poses a difficult problem in reliability analysis due to the geometry dependence of fracture mechanics parameters governing the near-tip fields. Furthermore, it is well known that fracture toughness values for brittle failure of materials exhibit large scatter, which implies that fracture assessment has also to be made on the basis of statistical methods. As an application, we address the problem of predicting crack extension behavior of shallow notched specimens from elastic-plastic fracture toughness values obtained from deeply notched specimens on the basis of the present model. For completeness, an analysis based on weakest link statistics for multiaxial stress states, which is presented in the Appendix, is also carried out in order to compare the results obtained. This weakest link formulation has been derived earlier by Batdorf and Crose (1974) and Matsuo (1981), so it is referred to here as the BCM model.

4.1 Experimental Data. Fracture toughness data, here characterized by critical values of CTOD, were obtained from single-edge notch bend (SENB) specimens with different a/W-ratio (crack depth to specimen width ratio), as shown in Fig. 5, namely $a/W = 0.1$, 0.3 and 0.5. All specimens were extracted from a 15-mm thick high-strength steel with 663 MPa yield stress (0.2 percent proof stress) and 716 MPa tensile strength at room temperature. Testing of specimens was conducted at -120°C, which corresponds to the lower shelf of ductile-brittle transition temperature for this steel, in accordance primarily with BS7448. For the deep notch bend specimens ($a/W = 0.5$), the fracture toughness values were obtained as based on the elastic and plastic components of CTOD in the form

Downloaded 04 May 2010 to 171.66.16.28. Redistribution subject to ASME license or copyright; see http://www.asme.org/terms/Terms_Use.cfm

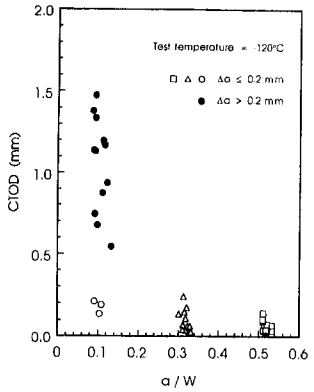

Fig. 6 Effect of *a* /*W*-ratio on critical CTOD values

$$\delta = \frac{K^2(1-\nu^2)}{2\sigma_Y E} + \frac{r_p(W-a)}{r_p(W-a)+a+Z} V_p. \quad (36)$$

Here, σ_Y is the yield stress at the test temperature, E is the Young's modulus, K is the stress intensity factor, V_p is the plastic component of crack mouth opening displacement, CMOD, Z is the height of the knife edge, and r_p is the plastic rotational factor. The plastic rotational factor was computed from the deformation of the specimen (as obtained in the finite element analysis) on the basis of a plastic hinge model. Although not shown here in the interest of space, the r_p-values obtained by this method closely matches the value of $r_p = 0.4$ given by existing standards (i.e., BS7448).

For the shallow notched specimens ($a/W = 0.1$ and 0.3), we employ a recent CTOD estimation procedure proposed by Wang and Gordon (1992). This procedure is based on the plastic component of the area under the load versus CMOD record, A_{pl}, and takes into account the work-hardening behavior of the material as well. Employing the notation used in this paper, their formula then gives the CTOD as

$$\delta = \frac{K^2(1-\nu^2)}{2\sigma_Y E} + \eta_c^{\delta}\frac{A_{pl}}{\sigma_Y B(W-a)} \quad (37)$$

where

$$\eta_c^{\delta} = 4.292 - 1.667\,(a/W) + 0.304\,A^2 - 2A \quad (38)$$

and

$$A = \left(\frac{1}{0.002h}\right)^{1/h} \exp\left(-\frac{1}{h}\right). \quad (39)$$

The effect of a/W-ratio on the critical CTOD value at cleavage fracture initiation is shown in Fig. 6. It is noted that most of SENB specimens with $a/W = 0.1$ failed with significant ductile crack extension, Δa, prior to cleavage fracture so as to provide much larger values of CTOD. Examination of fracture surfaces for measuring crack extension revealed stable crack growth as large as 1 mm in some specimens. By contrast, specimens with $a/W = 0.5$ exhibited completely brittle behavior with negligible crack extension.

4.2 Numerical Simulation of SENB Specimens. Three-dimensional finite element analyses were conducted to obtain the crack-tip stress fields of the SENB specimens. The plastic response of the material is described by the power-hardening law described in (17), where a fit to the uniaxial stress-strain curve of the material gave $\kappa = 4.0$ and $h = 10.5$. The Young's modulus and Poisson's ratio were taken as 206 GPa and 0.3, respectively. The NIKE3D (Halquist, 1984) finite element code was used in all numerical computations. An elastic-plastic material model with associated Von Mises flow rule was used in the analyses. All meshes employed 8-node isoparametric elements with selective/reduced quadrature ($2 \times 2 \times 2$). A stiffness matrix based on the B-bar method (Hughes, 1980) is used to preclude mesh lockups and associated anomalous stress states that arise in plasticity problems due to nearly incompressible behavior. The nonlinear finite element equations are solved incrementally using a BFGS method with line search (Mathies and Strang, 1979).

Due to symmetry, only one quarter of the specimens was modeled. The core near the crack-tip region was common to all configurations and was constructed by 624 elements and 837 nodes. Specimens with $a/W = 0.3$ and $a/W = 0.5$ were modeled using 1449 elements and 1112 nodes while specimens with $a/W = 0.1$ were modeled by 1431 elements and 1088 nodes. The meshes for all configurations consisted of eight layers through half the thickness of the plate. The layers interfaces are located at $2x_3/B = 0.16$, 0.32, 0.48, 0.64, 0.80, 0.90, 0.97, where B is the specimen thickness. The crack-tip element size in the in-plane mesh ($x_1 - x_2$ plane) was 0.2×0.2 mm. Crack-tip opening displacements in the finite element model were calculated according to the extrapolated crack flank procedure (Leggatt and Gordon, 1992).

4.3 Prediction of Crack Size Effect. A computer program was developed to determine the parameters of the probability distribution of the fracture stress. The distribution of ψ, given by (27), was computed for the deeply notched specimen ($a/W = 0.5$) according to the numerical procedure presented in the previous section. In (30), integration of the exponential of the stress was solved numerically by Gaussian quadrature. Hereafter, the equivalent stress at each integration point is determined by (34) in GPa. Since the shape parameter of the Weibull distribution of the integral ψ does not depend on the volume V_0 this volume was assumed to be unity. Once numerical convergence is attained, the maximum likelihood estimators w and u for the limiting distribution of the integral ψ are 9.45 and 6.91, respectively. It is important to point out that the particular size of the fracture process zone, Ω, has only little effect on the results for the present analysis, provided that Ω fully encompasses the highly stressed region ahead of crack for all load steps.

For the BCM model, we employ a similar numerical procedure for estimation of parameters of the corresponding failure distributions, which are given by (A4) and (A5) (see Appendix). The likelihood estimators m and σ_u in (A5) are found to be 19.26 and 1.92. In (A4), the threshold stress, S_0, can be assessed from further experimental observations. Metalographic and fracture analysis conducted by Fujita (1992) have revealed a microstructure predominantly martensic for this material. On the basis of micro-Vickers hardness measurements reported in his work, we estimate S_0 as the average value of the tensile strength of martensite at -120°C, which yields 1.08 GPa. Using this value, the likelihood estimators m and S_u in (A4) are given as 10.41 and 0.97.

The procedure for estimation of the distribution of fracture toughness values for different specimen geometries is based on the identity $H_{\text{fem}}(\psi) = H_{\text{exp}}(\psi)$ for the computed parameters $\{u, w\}$. As noted earlier, these parameters can be assumed as material properties and, therefore, independent of geometry. Thus, they can be used to evaluate the distribution of fracture toughness for shallow notched specimens. A graphical method for predicting the distribution of fracture toughness values is presented by Minami et al. (1992) and here we generalize such procedure in the form

$$H_f(\delta^1) = 1 - \exp\left\{-\left[\frac{f^1(\delta^1)}{u^0}\right]^{w^0}\right\} \quad (40)$$

where $\{u^0, w^0\}$ are the parameters of the distribution of the

Downloaded 04 May 2010 to 171.66.16.28. Redistribution subject to ASME license or copyright; see http://www.asme.org/terms/Terms_Use.cfm

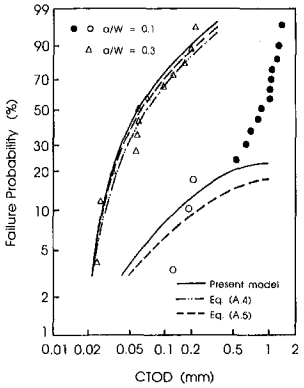

Fig. 7 Prediction of the probability distribution for critical CTOD values of specimens with $a/W = 0.1$ and $a/W = 0.3$

integral ψ for the specimen designated by 0, δ^1 is the CTOD value and $f(\ )$ is the relationship between the CTOD and the integral ψ, both for the specimens with geometry designated by 1. It should be noted that a similar relationship also holds for the prediction of the probability distribution of fracture toughness values according to the BCM model.

Figure 7 presents a Weibull plot of critical CTOD values for SENB specimens with $a/W = 0.1$ and $a/W = 0.3$ as well as the prediction of the corrresponding probability distribution by using the parameters obtained for SENB specimens with $a/W = 0.5$. It is seen that the predicted distribution for SENB specimens with $a/W = 0.3$ agrees well with experimental data. Further, both models provide essentially the same distribution, so that differences between the BCM model using (A4) and (A5) and our results are very small. By contrast, the predicted distribution for SENB specimens with $a/W = 0.1$ deviate from the experimental distribution as the critical CTOD value increases. Note that we could not obtain any reasonable prediction for this specimen on the basis of the BCM model using (A4). In this case, we carried out additional computations using different values of S_0 ranging from 0.7 GPa (which corresponds to the tensile strength of the ferritic matrix for the material employed) up to 1 GPa, but the resulting distribution continued to be in very poor agreement with experimental data. We see, however, that the present model indeed provides satisfactory agreement with experimental data, but only in the range where stable crack growth is limited. As noted before, some specimens exhibited ductile crack extension as large as 1 mm, which may not be described by the microstructural failure mechanism assumed in the analysis.

4.4 Discussion. Having seen the essential features of the present model and its application to prediction of the geometry dependence of elastic-plastic fracture toughness data, we discuss further aspects of our procedure. As noted before, the central feature emerging from our statistical analysis is the characterization of brittle fracture by a first asymptotic distribution of extreme values, which leads to a two-parameter Weibull distribution once an appropriate parametrization is used. Conventional statistical approaches based on this distribution have been successful in describing the scatter of experimental data associated with rupture phenomena. However, a major theoretical objection to the two-parameter Weibull distribution as broadly applicable to fracture of materials is that it predicts zero as the absolute lower bound for fracture toughness. Indeed, a more rigorous treatment to the crack problem would lead to a bounded distribution as there must be sufficient build-up of the near-tip driving forces for unstable crack propagation. Such a drawback could be circumvented by replacing the parameter ψ in (27) by $(\psi^* - \psi_0)$, so that equation leads to a three-parameter Weibull distribution. Here, ψ_0 is the threshold parameter and ψ^* is the *new* fracture-controlling parameter. We note that ψ^* will assume a form which is different from (26), so as to satisfy the condition $\psi = (\psi^* - \psi_0)$. Similar procedures along this line have been used by Satoh, Toyoda, and Minami (1985) and Bakker and Koers (1989), where a threshold fracture parameter is employed in connection with the weakest link model. Their analyses, however, suggest strong similarities for both distributions. In particular, Bakker and Koers have noted that predictions obtained by using a two-parameter and three-parameter Weibull model are essentially equivalent, albeit differing significantly for very low probability values. We also recall that the statistical estimation of the threshold parameter is strongly dependent upon the number of experimental data and on the nature of the statistical population being analyzed, which can make such parameter of no particular relevance for fracture analysis.

Our results show good prediction of the geometry dependence of cracked specimens for cleavage fracture initiation in a structural steel. To the extent that brittle fracture is preceded by a small amount of ductile crack growth, as in the case of SENB specimens with $a/W = 0.3$, the prediction through the present model essentially converge onto the corresponding one for the BCM model. This is suggestive of very similar behavior of both extreme-value distributions in this range. For SENB specimens with $a/W = 0.1$, we find a slightly better agreement with experimental data through our formulation when stable crack growth is limited. At larger CTOD values, however, the predicted distribution results in lower values of failure probability than the corresponding experimental values. This effect is suggestive of insufficient buildup of the parameter ψ as the load increases, which may be associated with severe loss of constraint at larger CTOD values. Further examination of this aspect reveals that ψ begins to increase only moderately as the plastic deformation progresses. Then, there comes a point where it starts to decrease due to large reduction in the equivalent stress, σ_Q, within the fracture process zone. Such a feature becomes clear upon examining (26). In a recent review, Pineau (1992) has pointed out the strong effect of tensile plastic strains on cleavage fracture under large scale yielding, which promote increase in the fracture stress. Thus, large plastic flow developing ahead of crack tip imposes limitations on the stress-based criterion adopted as describing the microstructural operative mechanism at larger CTOD values.

5 Conclusions

The present model for brittle fracture incorporates a redistribution of local stresses during the fracture process into a statistical approach to brittle fracture. The assumption that instability of the weakest microcrack no longer causes catastrophic failure leads to a first asymptotic distribution of the smallest value for the fracture stress. The two parameters of this probability distribution are related to the material properties and can thus be determined from experimental fracture strength data. The approach presented here is based on the chain-of-bundles probability model and introduces an alternative crack-tip parameter controlling fracture, which is given by integration of the exponential of the stress tensor ahead of the crack. Evaluation of this parameter is made on the basis of a finite element solution to the crack-tip fields, which implies that large stress gradients and complex loading can be taken into account. Furthermore, the approach also employs a spatial random distribution of penny-shaped microcracks which serves to include a criterion for crack extension as well as an equivalent tensile stress for multiaxial stress fields. The present model is applied to the problem of predicting crack extension behavior in SENB specimens con-

Downloaded 04 May 2010 to 171.66.16.28. Redistribution subject to ASME license or copyright; see http://www.asme.org/terms/Terms_Use.cfm

taining shallow cracks from fracture toughness values obtained from deep notched specimens in bending. While large plastic flow ahead of crack tip may invalidate the microstructural failure model adopted, fracture strength predictions based on the present analysis are found to agree rather well with experimental data when stress-dominated mechanisms control cleavage fracture.

Acknowledgments

CTOD tests were made possible by funding from Nippon Steel Corporation. The authors gratefully acknowledge Dr. Giuseppe Pezzoti, Dr. Yukito Hagiwara, and Mr. Takehiro Inoue for many useful discussions.

References

Bakker, A., and Koers, R. W. J., 1989, "Prediction of Cleavage Fracture Events in the Brittle-Ductile Transition Region of a Ferritic Steel," *European Symposium on Elastic-Plastic Fracture Mechanics*, Freiburg.

Batdorf, S. B., and Crose, J. G., 1974, "A Statistical Theory for the Fracture of Brittle Structures Subjected to Nonuniform Polyaxial Stresses," ASME JOURNAL OF APPLIED MECHANICS, Vol. 41, pp. 459–464.

Brückner-Foit, A., Ehl, W., Munz, D., and Trolldenier, B., 1990, "The Size Effect and Microstructural Implications of the Weakest Link Model," *Fatigue and Fracture of Engineering Materials and Structures*, Vol. 13, pp. 185–200.

Cramér, H., 1946, *Mathematical Methods of Statistics*, Princeton University Press, New Jersey.

Curtin, W. A., and Scher, H., 1990, "Brittle Fracture in Disordered Materials: A Spring Network Model," *Journal of Materials Research*, Vol. 5, pp. 535–553.

Daniels, H. E., 1945, "The Statistical Theory of the Strength of Bundles of Threads," *Proceeding of the Royal Society of London*, Vol. A183, pp. 405–435.

Epstein, B., 1960, "Elements of the Theory of Extreme Values," *Technometrics*, Vol. 2, pp. 27–41.

Evans, A. G., and Langdon, T. G., 1976, "Structural Ceramics," *Progress in Materials Science*, Vol. 21, B. Chalmers, ed., Pergamon Press, New York.

Evans, A. G., 1978, "A General Approach for the Statistical Analysis of Multiaxial Fracture," *Journal of the American Ceramic Society*, Vol. 61, pp. 302–308.

Fujita, A., 1993, "Effect of Work Hardening on Fracture Behavior of Structural Steels," M. Sc. Thesis, Dep. Welding and Production Engineering, Osaka University (in Japanese).

Griffith, A. A., 1924, "The Theory of Rupture," *Proceedings of the First International Congress for Applied Mechanics*, Delft, pp. 55–63.

Gumbel, E. J., 1958, *Statistics of Extremes*, Columbia University Press, New York.

Gücer, D. E., and Gurland, J., 1962, "Comparison of the Statistics of Two Fracture Modes," *Journal of the Mechanics and Physics of Solids*, Vol. 10, pp. 365–373.

Halquist, J. O., 1984, "NIKE3D—An Implicit, Finite Deformation, Finite Element Code for Analysing the Static and Dynamic Response of Three-Dimensional Solids," *University of California Report*, UCID-18822, Rev. 1.

Harlow, D. G., and Phoenix, S. L., 1978, "The Chain-of-Bundles Probability Model for the Strength of Fibrous Materials I: Analysis and Conjectures," *Journal of Composite Materials*, Vol. 12, pp. 195–214.

Hughes, T. J. R., 1980, "Generalization of Selective Integration Procedures to Anisotropic and Nonlinear Media," *International Journal for Numerical Methods in Engineering*, Vol. 14, pp. 1613–1626.

Hutchinson, J. W., 1968, "Singular Behavior at the End of a Tensile Crack in a Hardening Material," *Journal of Mechanics and Physics of Solids*, Vol. 13, pp. 13–31.

Leggatt, R. H., and Gordon, J. R., 1992, "3D Elastic-Plastic Finite Element Analysis for CTOD and J in SENB, SENAB and SENT Specimen Geometries," *Proc. of Shallow Crack Fracture Mechanics, Toughness Tests and Applications*, Cambridge Univ. Press, Cambridge, UK.

Lin, T., Evans, A. G., and Ritchie, R. O., 1986, "A Statistical Model of Brittle Fracture by Transgranular Cleavage," *Journal of Mechanics and Physics of Solids*, Vol. 34, pp. 477–497.

Mann, N. R., Schafer, R. E., and Singpurwalla, N. D., 1974, *Methods for Statistical Analysis of Reliability and Life Data*, John Wiley and Sons, New York.

Mathies, H., and Strang, G., 1979, "The Solution of Nonlinear Finite Element Equations," *International Journal for Numerical Methods in Engineering*, Vol. 14, pp. 1613–1626.

Matsuo, Y., 1981, "Statistical Fracture Theory for Multiaxial Stress States Using Weibull's Three-Parameter Function," *Engineering Fracture Mechanics*, Vol. 14, pp. 527–538.

McMeeking, R. M., 1977, "Finite Deformation Analysis of Crack Tip Opening in Elastic-Plastic Materials and Implications for Fracture," *Journal of Mechanics and Physics of Solids*, Vol. 125, pp. 357–381.

Minami, F., Brückner-Foit, A., Munz, D., and Trolldenier, B., 1992, "Estimation Procedure for the Weibull Parameters Used in the Local Approach," *International Journal of Fracture*, Vol. 54, pp. 197–210.

Orowan, E., 1948, "Fracture and Strength of Solids," *Reports on Progress in Physics*, Vol. 12, pp. 185–232.

Paris, P. C., and Sih, G. C., 1965, "Stress Analysis of Cracks," *Fracture Toughness and its Application*, ASTM-STP-381, pp. 30–83.

Pineau, A., 1992, "Global and Local Approaches of Fracture—Transferability of Laboratory Test Results to Components," *Topics in Fracture and Fatigue*, A. S. Argon, ed., Springer-Verlag, New York, pp. 197–234.

Rice, J. R., and Rosengren, G. F., 1968, "Plane Strain Deformation Near a Crack Tip in a Power-Law Hardening Material," *Journal of Mechanics and Physics of Solids*, Vol. 16, pp. 1–12.

Rice, J. R., 1968, "A Path Independent Integral and the Approximate Analysis of Strain Concentration by Notches and Cracks," ASME JOURNAL OF APPLIED MECHANICS, Vol. 35, pp. 379–386.

Satoh, K., Toyoda, M., and Minami, F., 1985, "A Probabilistic Approach to Evaluation of Fracture Toughness of Welds with Heterogeneity," *Trans. Japan Welding Society*, Vol. 16, pp. 70–81.

Smith, E., 1968, "Cleavage Fracture in Mild Steel," *International Journal of Fracture Mechanics*, Vol. 4, pp. 131–145.

Wang, Y.-Y., and Gordon, J. R., 1992, "The Limits of Applicability of J and CTOD Estimation Procedures for Shallow-Cracked SENB Specimens," *Proc. of Shallow Crack Fracture Mechanics, Toughness Tests and Applications*, Cambridge Univ. Press, Cambridge, U.K.

Weibull, W., 1939, "The Phenomenon of Rupture in Solids," *Ingeniors Vetenskaps Akademien, Handlingar*, Vol. 153.

Zienkiewicz, O. C., 1989, *The Finite Element Method*, 3rd ed., McGraw-Hill, London.

APPENDIX

The Batdorf-Crose-Matsuo (BCM) Model

The statistical approach to modeling brittle fracture, as given by Batdorf and Crose (1974) and Matsuo (1981), is based on a random incidence of microcracks (uniformly distributed in position and direction) within a material subjected to a multiaxial stress state. Further, cleavage fracture is described by unstable propagation of microcracks according to the weakest link theory. Let Φ be the solid angle containing the normal to all orientations for which the applied equivalent tensile stress to the microcrack plane is $\sigma_Q > \sigma_c > S_0$, where σ_c is a critical stress and S_0 is a threshold fracture stress. For a microcrack under a stress σ, the probability of failure is therefore given by

$$P_f = \frac{\Phi(\sigma, \sigma_c, S_0)}{4\pi}. \tag{A1}$$

Now assume that a distribution function $g(S)$ characterizes the distribution of crack size and shape, so that $g(S)dS$ is the number of microcracks per unit volume having strength between S and $S + dS$. Then, employing the mapping given by (14), one may show that the failure probability of a volume V of the material takes the form

$$P_V = 1 - \exp\left[-\frac{1}{2\pi}\int_V \int_0^{\pi}\int_0^{\pi}\int_0^{\sigma} g(S)dS \sin\varphi\, d\varphi\, d\theta\, dV\right]. \tag{A2}$$

A widely used expression for the inner integral is given by Weibull (1939) as

$$\int_0^{\sigma} g(S)dS = \left(\frac{\sigma - S_0}{S_u}\right)^m, \tag{A3}$$

where m and S_u are the shape and scale parameters, respectively, and S_0 is the threshold stress.

For a notched body, we employ the definition of the fracture process zone given in the text. Then the failure probability takes the form

Downloaded 04 May 2010 to 171.66.16.28. Redistribution subject to ASME license or copyright; see http://www.asme.org/terms/Terms_Use.cfm

$$P_\Omega = 1 - \exp \times \left[-\frac{1}{2\pi} \int_\Omega \int_0^\pi \int_0^\pi \left(\frac{\sigma_Q - S_0}{S_u} \right)^m \sin \varphi \, d\varphi \, d\theta \, d\Omega \right] \quad \text{(A4)}$$

where Ω is the volume of the fracture process zone ahead of crack tip. Here, we note that this expression is similar to the third asymptotic extreme value distribution for a bounded population. For $S_0 = 0$, (A4) can be rewritten as

$$P_\Omega = 1 - \exp \left[-\frac{1}{2\pi} \int_\Omega \int_0^\pi \int_0^\pi \left(\frac{\sigma_Q}{\sigma_u} \right)^m \sin \varphi \, d\varphi \, d\theta \, d\Omega \right] \quad \text{(A5)}$$

which is identical with the failure probability of a body containing a large number of spatially random flaws with a Cauchy extreme flaw size distribution, and subjected to a multiaxial stress state (Evans and Langdon, 1976).

Downloaded 04 May 2010 to 171.66.16.28. Redistribution subject to ASME license or copyright; see http://www.asme.org/terms/Terms_Use.cfm

Prediction of Kink Width in Compressed Fiber Composites

N. A. Fleck
Engineering Department,
Trumpington Street,
Cambridge University,
Cambridge CB2 1PZ, U.K.

L. Deng

B. Budiansky
Fellow ASME.

Division of Applied Sciences,
Harvard University,
Cambridge, MA 02138

Couple stress theory is used in the prediction of the size of the kink band width that occurs in the compressive failure of a fiber composite by microbuckling. The composite is assumed to be inextensible in the fiber direction, and to deform as a Ramberg-Osgood solid in shear and in transverse tension. Predictions are given for the kink width as a function of the fiber diameter, modulus and strength; the material nonlinearity of the composite; and the amplitude and wavelength of fiber waviness. The kink width scales with fiber diameter but is fairly insensitive to variations in other material properties and in the amplitude and wavelength of initial fiber waviness. For typical polymer matrix composites, the predicted kink width is of the order of 10–15 fiber diameters, in agreement with observed values. The couple stress theory is also used to assess the role of fiber bending resistance in the compressive strength of fiber composites that fail by microbuckling. It is found that although the compressive strength is sensitive to the amplitude of the initial waviness, it is not very sensitive to its wavelength.

Introduction

Microbuckling is recognized as the dominant compressive failure mechanism in aligned-fiber polymeric matrix composites. Microbuckling occurs in a localized band, which is inclined typically at an angle $\beta = 10$ deg $-$ 30 deg to the transverse direction, as shown in Fig. 1. The width of the kink band at failure is of the order of 10–15 fiber diameters, as reviewed by Jelf and Fleck (1992).

Several authors have attempted to predict the compressive strength due to microbuckling. The pioneering analysis of kinking by Rosen (1965) was based on the assumption of elastic microbuckling. The evidence is now compelling that nonlinear deformation of the matrix, together with the presence of small initial fiber misalignments, are essential features of the kinking process. On the basis of a one-dimensional theory that assumes inextensible fibers and neglects fiber bending resistance, Budiansky and Fleck (1993) found that small fiber misalignments of the order of two degrees can account for the observed compressive strengths. They further showed that the assumption of fiber inextensibility is justified for the large fiber to matrix stiffness ratios typical of polymer matrices reinforced with ceramic fibers. We shall refer to the Budiansky-Fleck theory as *kinking theory* in this paper.

Little attention has been paid to the prediction of kink width. Hahn (1987) has predicted kink widths for a kink band inclination $\beta = 0$ by treating the fibrous composite as a layered solid, with the fibers undergoing bending and the matrix deforming predominantly in shear. Budiansky (1983) used a couple-stress analysis to calculate kink width in a composite comprising perfectly aligned fibers of zero tensile strength in a rigid, ideally plastic matrix. For $\beta = 0$, he derived the formula

$$\frac{w}{d} = \frac{\pi}{4}\left(\frac{E}{2\tau_Y}\right)^{1/3} \tag{1}$$

for the ratio of the kink width w to fiber diameter d, in terms of the shear yield stress τ_Y and the axial modulus E of the composite.

In the present paper, a couple stress theory is used to take fiber bending resistance into account; we shall refer to this theory as *bending theory*. The bending theory is used to calculate the dependence of kink width and failure stress upon fiber diameter, modulus and strength, matrix nonlinearity, and the amplitude and wavelength of fiber waviness. A comparison is also made between the collapse response predicted by the bending theory and by the previous kinking theory of Budiansky and Fleck (1993).

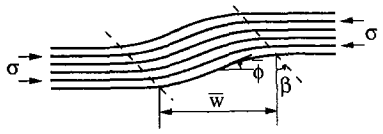

Fig. 1 The basic problem. A unidirectional composite with an initial fiber misalignment is subjected to a remote compressive stress σ. The fiber misalignment is correlated along the β direction.

Contributed by the Applied Mechanics Division of THE AMERICAN SOCIETY OF MECHANICAL ENGINEERS for publication in the ASME JOURNAL OF APPLIED MECHANICS.

Discussion on this paper should be addressed to the Technical Editor, Professor Lewis T. Wheeler, Department of Mechanical Engineering, University of Houston, Houston, TX 77204-4792, and will be accepted until four months after final publication of the paper itself in the ASME JOURNAL OF APPLIED MECHANICS.

Manuscript received by the ASME Applied Mechanics Division, Jan. 21, 1993; final revision, Jan. 26, 1994. Associate Technical Editor: R. M. McMeeking.

Copyright © 1995 by ASME

Downloaded 04 May 2010 to 171.66.16.28. Redistribution subject to ASME license or copyright; see http://www.asme.org/terms/Terms_Use.cfm

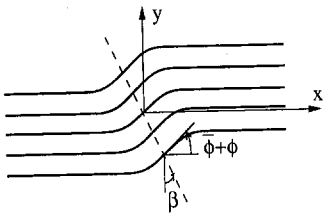

Fig. 2 Deformed geometry. Under load, the fibers rotate from an initial inclination $\bar{\phi}(x)$ to a deformed inclination $\bar{\phi}(x) + \phi(x)$.

The basic problem analyzed is shown in Fig. 1. The fibers are assumed to have an initial, isolated half-sinusoid of waviness perfectly correlated in a direction inclined at an angle β to the transverse direction. Upon loading, additional deformation occurs mainly within a finite band, not necessarily coincident with the band of initial imperfection. With continued rotation of the fibers, the load attains a maximum and then drops continuously until the fibers break in bending. Fiber breakage sets the width of the resulting kink band.

Kink Band Analysis

We smear out the fibers and matrix, and consider the composite to behave as a homogeneous anisotropic solid. A couple stress formulation is used to take fiber bending resistance into account.

Kinematics. In the initial stress-free configuration, the fibers are assumed to possess a small initial angular misalignment $\bar{\phi}$ which is perfectly correlated along a direction inclined at an angle β to the transverse direction. Thus $\bar{\phi}$ depends upon the single variable $x + y \tan \beta$, where the Cartesian coordinates (x, y) are parallel and transverse to the ideal fiber direction, respectively, as shown in Fig. 2. For $y = 0$, we will assume that $\bar{\phi}$ is an even function of x.

When the unidirectional composite is loaded by a compressive stress σ, the fibers suffer an additional rotation ϕ; by symmetry ϕ is also a function of the combined coordinate $(x + y \tan \beta)$. Upon invoking fiber inextensibility and the assumption that ϕ is small, we find that the displacement field (u, v) associated with ϕ satisfies

$$u = 0, \quad \frac{\partial v}{\partial x} = \phi. \tag{2}$$

Now define a shear strain γ_S along the fiber direction, and a transverse strain ϵ_T which is transverse to the fiber direction. The usual strain-displacement relations for small strains and rotations give the shear strain γ_S and transverse strain ϵ_T in terms of ϕ as

$$\gamma_S = \frac{\partial v}{\partial x} = \phi \tag{3}$$

$$\epsilon_T = \frac{\partial v}{\partial y} = \frac{\partial v}{\partial x} \tan \beta = \phi \tan \beta \tag{4}$$

Equilibrium. We consider equilibrium of a representative material element in the deformed configuration (see Fig. 3). The element is subjected to a longitudinal compressive stress σ_L aligned with the fiber direction, a sliding shear stress τ_S, a transverse shear stress τ_T, and a transverse tensile stress σ_T. The fibers embedded in the material offer bending resistance; thus the representative material element carries a bending moment per unit area, or couple stress, m.

Equilibrium of forces in the fiber direction gives to first order

$$\frac{\partial \sigma_L}{\partial x} = 0 \tag{5}$$

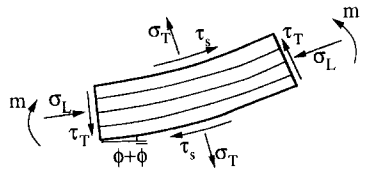

Fig. 3 Stresses on a representative element of the solid. The fibers and matrix have been smeared out to a continuum.

and so σ_L is related to the remote compressive stress σ by

$$\sigma_L = \sigma. \tag{6}$$

Force equilibrium in the transverse direction gives

$$\frac{\partial \sigma_T}{\partial y} + \frac{\partial \tau_T}{\partial x} - \sigma_L \left(\frac{\partial \phi}{\partial x} + \frac{\partial \bar{\phi}}{\partial x} \right) = 0 \tag{7}$$

and moment equilibrium gives

$$\frac{\partial m}{\partial x} = \tau_S - \tau_T. \tag{8}$$

We note that the presence of couple stresses makes the stress tensor unsymmetric, with $\tau_S \neq \tau_T$.

Elimination of σ_L and τ_T from the equilibrium Eq. (7) gives via (6) and (8)

$$\frac{\partial^2 m}{\partial x^2} + \sigma \left(\frac{\partial \phi}{\partial x} + \frac{\partial \bar{\phi}}{\partial x} \right) = \frac{\partial \tau_S}{\partial x} + \frac{\partial \sigma_T}{\partial y}. \tag{9}$$

Since all dependent variables are functions only of the combined coordinate $(x + y \tan \beta)$, (9) can be rewritten as

$$\frac{\partial^2 m}{\partial x^2} + \sigma \left(\frac{\partial \phi}{\partial x} + \frac{\partial \bar{\phi}}{\partial x} \right) = \frac{\partial \tau_S}{\partial x} + \frac{\partial \sigma_T}{\partial x} \tan \beta \tag{10}$$

and from now on we regard m as an odd function, and ϕ, τ_S, and σ_T as even functions, of the single independent variable x. Finally, Eq. (10) may be integrated with respect to x to provide the governing differential equation of equilibrium

$$\frac{dm}{dx} + \sigma \left(\phi + \bar{\phi} \right) = \tau_S + \sigma_T \tan \beta. \tag{11}$$

In order to proceed, we need a constitutive law in order to relate the generalized stress components (m, τ_S, σ_T) to the fiber rotation ϕ.

Constitutive Law. We assume that the fibers behave as linear elastic beams undergoing inextensible bending, and we neglect matrix contributions to couple stresses. Simple beam theory for circular fibers of diameter d, Young's modulus E_f, and volume fraction c_f gives the relation between the couple stress m on the composite and the associated curvature $d\phi/dx$ as

$$m = \frac{c_f E_f d^2}{16} \frac{d\phi}{dx}. \tag{12}$$

The shear and transverse responses of the composite are taken to be those of a nonlinear deformation-theory solid, as suggested by Budiansky and Fleck (1993). They proposed an effective shear stress τ_e defined by

$$\tau_e^2 = \tau_S^2 + \frac{\sigma_T^2}{R^2} \tag{13}$$

where the constant R is interpreted as the ratio of yield stresses in transverse tension and in shear. The constitutive relations for the combined stress state were given as[1]

[1]An additional simplifying assumption made in the development of the constitutive relations was that R is also equal to $\sqrt{E_T/G}$, where E_T is the transverse elastic modulus and G is the elastic shear modulus of the composite.

Downloaded 04 May 2010 to 171.66.16.28. Redistribution subject to ASME license or copyright; see http://www.asme.org/terms/Terms_Use.cfm

$$\gamma_S = \frac{\gamma_e}{\tau_e}\tau_S \tag{14a}$$

$$\epsilon_T = \frac{\gamma_e}{\tau_e}\frac{\sigma_T}{R^2} \tag{14b}$$

where the effective shear strain γ_e, defined via the virtual work relation $\tau_e\gamma_e \equiv \tau_S\gamma_S + \sigma_T\epsilon_T$, is

$$\gamma_e^2 = \gamma_S^2 + R^2\epsilon_T^2. \tag{15}$$

The three-parameter (γ_Y, τ_Y, n) Ramberg-Osgood representation for the in-plane shear stress-strain curve of the composite is taken as the connection

$$\frac{\gamma_e}{\gamma_Y} = \frac{\tau_e}{\tau_Y} + \frac{3}{7}\left(\frac{\tau_e}{\tau_Y}\right)^n \tag{16}$$

between the effective stress and effective strain. Here τ_Y is defined as the composite shear yield stress and γ_Y is the shear yield strain. We note from (16) that τ_Y is the shear stress and 10/7 γ_Y is the shear strain at the point on the stress-strain curve where the secant modulus is 70 percent of its initial elastic value $G \equiv \tau_Y/\gamma_Y$. The strain-hardening parameter n ranges from 1 to ∞, but for the limit of $n = 1$ we replace (16) by the law $\gamma_e = \tau_e/G$; we refer to this as the *elastic case*.

Fiber Fracture Criterion. It is found experimentally (see, for example, Soutis and Fleck, 1990) that the width of the kink band is set by fiber fracture in tension due to local fiber bending. The strain in the fibers is the sum of the bending strain and the compressive strain associated with the axial stress σ. We equate the maximum tensile strain in each fiber to the tensile fracture strain of the fiber ϵ_F to get the fracture criterion

$$\epsilon_F = \left(\frac{d}{2}\right)\left|\frac{d\phi}{dx}\right|_{\max} - \frac{\sigma}{E} \tag{17}$$

where $|d\phi/dx|_{\max}$ is the maximum absolute value of curvature along each fiber and E is the longitudinal Young's modulus of the composite. This fracture condition will be satisfied at two locations $x = \pm x_F$, and the width of the kink band is defined as the distance $2|x_F|$ along the fibers between the points of fiber fracture.

It is noted that the assumption of inextensible fibers was made in the kinematics and equilibrium relations, but axial straining of the fibers is implicit here in the fiber fracture condition. Budiansky and Fleck (1993) have included fiber extensibility in the kinematic and equilibrium relations of a particular version of their kinking analysis, and found that for typical polymer-matrix composites, fiber extensibility has little effect upon the collapse response.

Solution Method. In this section, we combine the equations of kinematics, equilibrium, and constitutive response in order to obtain a single nonlinear differential equation. The equations are nondimensionalized and the solution method is outlined. Details of the analytic and numerical procedures are given in the Appendix.

It is clear from Eqs. (3) and (4) that straining is proportional at each material point and so the constitutive relations (14)–(16) imply that loading is also proportional, with

$$\sigma_T = \tau_s R^2 \tan\beta. \tag{18}$$

Thus deformation and flow theories of plasticity give identical predictions.

The equilibrium Eq. (11) may be reduced to a differential equation in ϕ by eliminating m, τ_s and σ_T via (12), (13), and (18); then

$$\frac{Ed^2}{16}\frac{d^2\phi}{dx^2} + \sigma\left(\phi + \bar{\phi}\right) = \tau_e\sqrt{1 + R^2\tan^2\beta} \tag{19}$$

where the composite modulus E has been used as an approximation for $c_f E_f$. The effective stress τ_e is related to the effective strain γ_e by the nonlinear Ramberg-Osgood relation (16), and in turn, γ_e may be written in terms of ϕ on the basis of (3), (4), and (15) as

$$\gamma_e = \phi\sqrt{1 + R^2\tan^2\beta}. \tag{20}$$

We treat (19) as the governing nonlinear differential equation to be solved, together with (20) and the Ramberg-Osgood relation (16), for the rotation $\phi(x)$.

The imperfection in fiber alignment $\bar{\phi}(x)$ is assumed to take the form

$$\left.\begin{aligned} \bar{\phi}(x) &= \bar{\phi}_0\cos\left(\frac{\pi x}{\bar{w}}\right) \quad |x| < \frac{\bar{w}}{2} \\ \bar{\phi}(x) &= 0 \qquad\qquad\qquad |x| > \frac{\bar{w}}{2} \end{aligned}\right\} \tag{21}$$

where the magnitude of the fiber waviness $\bar{\phi}_0$ and the wavelength $\bar{w}$ characterize the imperfection.

To proceed, we nondimensionalize the problem by introducing the nondimensional quantities

$$\Lambda \equiv \frac{\sigma}{G^*}, \quad \omega \equiv \frac{\phi}{\gamma_Y^*}, \quad \bar{\omega} = \frac{\bar{\phi}_0}{\gamma_Y^*}, \quad g \equiv \frac{\tau_e}{\tau_Y},$$

$$\xi \equiv \frac{4x}{d}\sqrt{\frac{G^*}{E}}, \quad \xi_I \equiv \frac{2\bar{w}}{d}\sqrt{\frac{G^*}{E}} \tag{22}$$

where

$$G^* \equiv \alpha^2 G, \quad \gamma_Y^* \equiv \gamma_Y/\alpha, \text{ and } \alpha \equiv \sqrt{1 + R^2\tan^2\beta}. \tag{23}$$

Then

$$\bar{\omega} = \begin{cases} \dfrac{\bar{\phi}_0}{\gamma_Y^*}\cos\left(\dfrac{\pi\xi}{2\xi_I}\right) & \xi < \xi_I \\ 0 & \xi > \xi_I \end{cases} \tag{24}$$

and the governing differential Eq. (19) gives

$$\frac{d^2\omega}{d\xi^2} + \Lambda(\omega + \bar{\omega}) = g, \tag{25}$$

where g is defined implicitly in terms of ω by the nondimensional form

$$\omega = g + \frac{3}{7}g^n \tag{26}$$

of the constitutive relation (16). Equation (25) applies, of course, only for plastic "loading", for which ω is increasing. For the elastic case, Eq. (26) is replaced by the relation $\omega = g$. In the elastic-ideally plastic limit of $n = \infty$, the Ramberg-Osgood solid possesses a shear yield stress τ_Y and a shear modulus $G \equiv \tau_Y/\gamma_Y$, and then Eq. (25) is replaced by

$$\frac{d^2\omega}{d\xi^2} + (\Lambda - 1)\omega = -\Lambda\bar{\omega} \tag{27a}$$

in the elastic region ($\omega = g < 1$) and

$$\frac{d^2\omega}{d\xi^2} + \Lambda\omega = 1 - \Lambda\bar{\omega} \tag{27b}$$

in the plastic region ($g = 1$; $\omega > 1$, ω increasing).

Downloaded 04 May 2010 to 171.66.16.28. Redistribution subject to ASME license or copyright; see http://www.asme.org/terms/Terms_Use.cfm

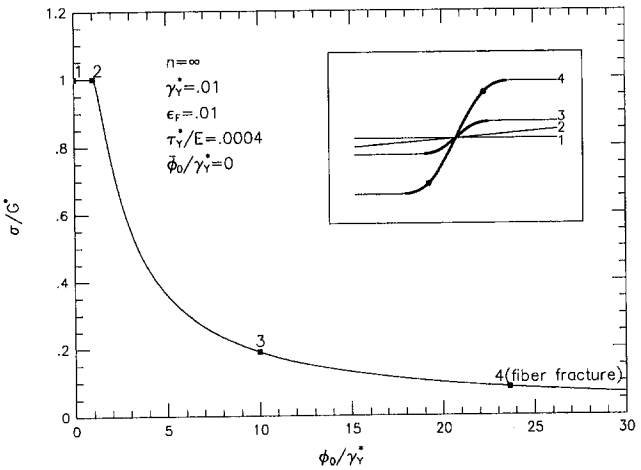

Fig. 4 Collapse response of an elastic-ideally plastic composite with zero initial misalignment. The insert gives the fiber shape at four stages of deformation, with the vertical deflection magnified by a factor of 100. The symbol ● depicts the location of the fiber fracture.

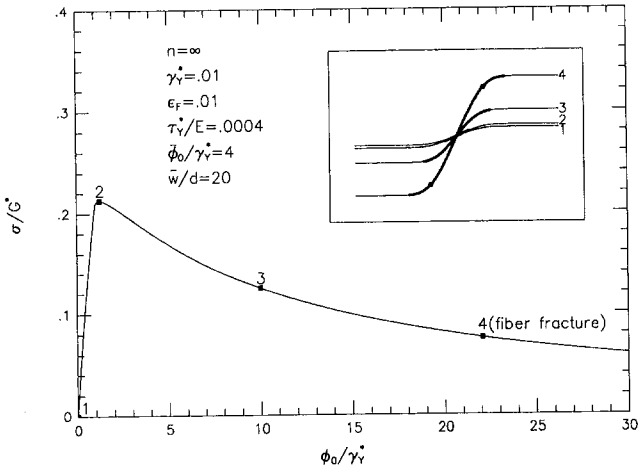

Fig. 5 Collapse response of an elastic-ideally plastic composite with an initial misalignment characterized by $\bar{\phi}_0 / \gamma_Y^* = 4$ and $\bar{w} / d = 20$. The insert gives the fiber shape at four stages of deformation, with the vertical deflection magnified by a factor of 100. The symbol ● depicts the sites of fiber fracture.

Recall that the width w of the kink band is defined as the length of broken fibers. Fiber breakage occurs at the locations $\xi = \pm\xi_F$ where (17) is first satisfied; in nondimensional form this condition is

$$\epsilon_F = 2\sqrt{\frac{\tau_Y^*}{E}}\sqrt{\gamma_Y^*}\left|\frac{d\omega}{d\xi}\right|_{\max} - \frac{\Lambda}{\gamma_Y^*}\left(\frac{\tau_Y^*}{E}\right) \tag{28}$$

where

$$\tau_Y^* \equiv \alpha\tau_Y. \tag{29}$$

The kink band width w is related to ξ_F via (22) by

$$\frac{w}{d} = \frac{\xi_F}{2}\sqrt{\frac{E}{G^*}}. \tag{30}$$

We note in passing that the inclination β of the kink band has been absorbed into the material properties τ_Y^*, γ_Y^*, and G^*.

Results and Discussion

We begin by describing the collapse response σ versus $\phi_0 \equiv \phi(0)$ for the composite over a range of values of imperfection magnitude $\bar{\phi}_0$ and imperfection wavelength $\bar{w}$. Before proceeding to kink-width prediction, we will digress to discuss the dependence of the maximum compressive stress σ_c on the imperfection parameters $\bar{\phi}_0$ and $\bar{w}$ and the material nonlinearity index n, and the accuracy of the bending theory vis-a-vis kinking theory will be assessed. Finally, calculated results for the width of kind band will be presented. Rather remarkably, we will find that the predicted width of kink band is in the range 10–15 fiber diameters for a wide range of material properties and imperfection magnitudes and wavelengths.

Collapse Response. The collapse response was calculated by solving the nonlinear second-order differential Eqs. (25) or (27), as described in Appendix. In all cases, it was found that plastic unloading never occurred.

Consider first the elastic-ideally plastic solid. A typical collapse response is given in Fig. 4 for the perfectly aligned composite ($\bar{\phi}_0 = 0$) and in Fig. 5 for a misaligned composite ($\bar{\phi}_0/\gamma_Y^* = 4$, $\bar{w}/d = 20$). The values $\gamma_Y^* = .01$, $\epsilon_F = .01$, and $\tau_Y^*/E = .0004$ in these figures are typical for polymer-matrix composites. The insert of each figure displays the deformed shape of a representative fiber at four stages of loading; an enhanced line thickness is used to depict the extent of the plastic zone at each stage.

For the perfectly aligned composite (see Fig. 4), and any assumed value of β, the fibers start to rotate at the bifurcation stress G^*, in agreement with the Rosen (1965) result for $\beta = 0$. The bifurcation mode consists of uniform rotation, with the composite deforming elastically and the fibers suffering no bending. Between points 1 and 2 of Fig. 4, elastic deformation continues as the fibers rotate uniformly, until the matrix yields at $\phi_0 = \gamma_Y^*$. Active plastic loading then occurs immediately in the finite interval

$$|x| \le \frac{\pi d}{8}\sqrt{\frac{E}{G^*}} \tag{31}$$

and elsewhere the composite unloads elastically. With further increase of the maximum rotation ϕ_0, the collapse response shown in Fig. 4 obeys the relation

$$\frac{\phi_0}{\gamma_Y^*} = \frac{1 + \sqrt{1 - \sigma/G^*}}{\sigma/G^*} \tag{32}$$

as the load drops smoothly, and the plastic zone extends in width. Fiber bending now occurs everywhere, but is concentrated within the plastic zone. When the maximum surface strain in the fibers equals the tensile fracture strain of the fibers, the fiber break in accordance with the fracture criterion (28). Point 4 on the main plot of Fig. 4 shows the remote stress σ and fiber rotation ϕ_0 at the point of fiber fracture; the solid circles on the curve labeled 4 in the figure insert depict the sites of fiber fracture. The length of fiber between the two fracture locations is taken as the definition of the width of the resulting kink band, to be discussed in the next section. After fiber fracture, the fibers are unable to carry a bending moment at the locations of fiber fracture, and the load on the composite drops discontinuously to a lower value (not shown). Thereafter the fibers in the kink band suffer no further bending and the collapse response is given by the kinking theory. This regime is of little practical relevance and is not explored further.

Now consider the typical collapse response of the misaligned composite, as shown in Fig. 5. Since the composite possesses an initial waviness, deformation begins at zero load. The initial response of the composite is elastic and involves elastic bending of the fibers. At $\phi_0 = \gamma_Y^*$ the matrix yields at the single location $x = 0$; we term the correspond-

Downloaded 04 May 2010 to 171.66.16.28. Redistribution subject to ASME license or copyright; see http://www.asme.org/terms/Terms_Use.cfm

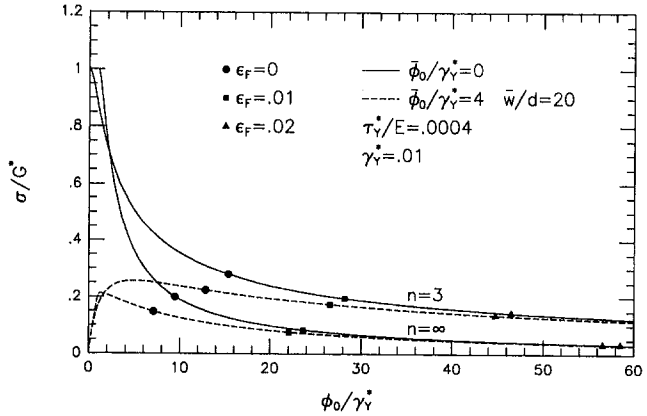

Fig. 6 Collapse response of perfectly aligned ($\bar{\phi}_0 / \gamma_Y^* = 0$) and misaligned composite ($\bar{\phi}_0 / \gamma_Y^* = 4$, $\bar{w} / d = 20$), for $n = 3$ and ∞. The fiber rotation ϕ_0 / γ_Y^* at fiber fracture is sensitive to the value of the fiber fracture strain ϵ_F, as shown.

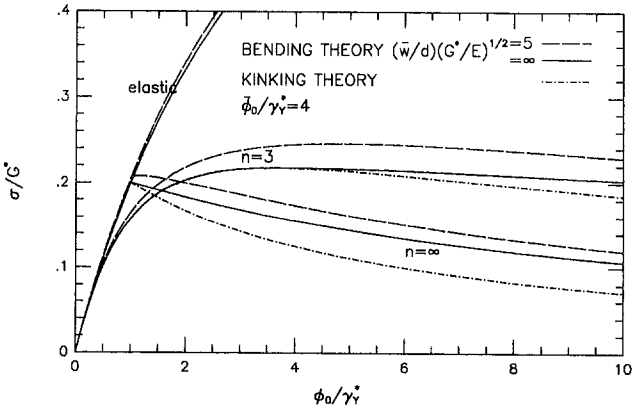

Fig. 7 Collapse response for a typical misalignment angle $\bar{\phi}_0 / \gamma_Y^* = 4$. Predictions are given for two imperfection widths $\bar{w} / d\sqrt{G^* / E} = 5$, ∞, and for the full range of matrix nonlinearity (elastic case, $n = 3$ and $n = \infty$). The predictions of kinking theory are included.

ing load the yield load. The plastic zone spreads quickly and a maximum in the load (point 2) is attained at a load only slightly above the yield load. In fact, for the elastic-ideally plastic body, the maximum load occurs at the yield load for imperfections of sufficiently large wavelengths. Post maximum load, the load drops smoothly with increasing fiber rotation ϕ_0, and the plastic zone continues to spread. Finally, at point 4 the fiber fracture criterion (28) is met, and a kind band is formed. The solid circles on curve 4 of the insert of Fig. 5 show the locations of fiber fracture. The response of the misaligned composite in Fig. 5 asymptotes towards the response of the perfect composite in Fig. 4 at sufficiently large ϕ_0. Since fiber fracture occurs at large ϕ_0, the width of the kink band determined by fiber fracture can be expected to be little influenced by the existence of initial fiber waviness.

This last point is amplified in Fig. 6, wherein the curves for $n = \infty$ of Figs. (4) and (5) are reproduced, together with response curves for $n = 3$. In addition, the fiber fracture points on each curve are shown for $\epsilon_F = 0$, .01, and .02. These results show that for each n the values of rotation ϕ_0 and load σ at fiber fracture are insensitive to the initial misalignment. Thus, even for small values of ϵ_F, for which ϕ_0 at fracture is not large, we expect kink widths to be insensitive to the size of the imperfection $\bar{\phi}_0$.

Comparisons of Collapse Response via Bending and Kinking Theories. The collapse response predicted by kinking theory is compared with that given by bending theory in Fig. 7, for the elastic solid, elastic-ideally plastic solid and the intermediate case of a Ramberg-Osgood solid with $n = 3$. Results are shown for a typical imperfection magnitude of $\bar{\phi}_0/\gamma_Y^* = 4$, and for the bending theory with imperfection widths of $\bar{w}/d\sqrt{G^*/E} = 5$ and ∞. (For typical values of G^*/E, the finite width corresponds to $\bar{w}/d \approx 25$.) In the case of the elastic solid, the normalized load σ/G^* increases monotonically with normalized fiber rotation ϕ_0/γ_Y^* and tends to unity at large fiber rotations. For $\bar{w}/d\sqrt{G^*/E} = \infty$ (and $\bar{w}/d\sqrt{G^*/E} = 0$) uniform fiber rotation occurs with no fiber bending, and the response predicted by the bending theory is identical to that predicted by the kinking theory. Otherwise fiber bending occurs and the bending theory gives a stiffer response than kinking theory.

Now examine the case $n = 3$. The bending theory suggests a small influence of wavelength of initial waviness upon the collapse response. Plastic deformation of the matrix with elastic bending of the fibers begins at zero load, and the composite is everywhere in a plastic state at finite loads. A mild maximum in the load is attained, which is a consequence of the competition between geometric softening associated with fiber rotation and strain hardening. The kinking theory prediction lies very slightly below the bending theory prediction for $\bar{w}/d\sqrt{G^*/E} = \infty$. Note that this limiting value of normalized width of initial waviness should be interpreted as the limit $\bar{w} \to \infty$ rather than the limit $d \to 0$. In the limit $d \to 0$ the bending theory formally reduces to the kinking theory.

For the elastic-ideally plastic solid, both theories give an initial elastic response. The bending theory with $\bar{w}/d\sqrt{G^*/E} = 5$ gives a maximum load which is slightly greater than the yield load. In contrast, the bending theory with $\bar{w}/d\sqrt{G^*/E} = \infty$ and the kinking theory predict that maximum load occurs at the onset of yield; thereafter the load drops in a smooth manner until fiber fracture intervenes. In the plastic range the kinking response is given by

$$\frac{\sigma}{G^*} = \left(\frac{\phi_0}{\gamma_Y^*} + \frac{\bar{\phi}_0}{\gamma_Y^*} \right)^{-1} \tag{33}$$

while in the limit of large ϕ_0/γ_Y^* and $\bar{w}/d\sqrt{G^*/E} = \infty$ an asymptotic formula may be derived for the collapse response by bending theory as

$$\frac{\sigma}{G^*} \approx \left(\frac{\phi_0}{2\gamma_Y^*} + \frac{\bar{\phi}_0}{\gamma_Y^*} \right)^{-1}. \tag{34}$$

The above two formulas show that at large values of ϕ_0/γ_Y^* the load carrying capacity is nearly doubled by the presence of fiber bending resistance.

Regardless of the degree of material nonlinearity the strongest response is consistently shown in Fig. 7 by the bending theory for a short wavelength of initial misalignment, and the weakest response is given by the kinking theory. However, the effect of fiber bending resistance upon the response up to the critical load is small. Furthermore, the maximum stress σ_c/G^* is little influenced by the value of $n \geq 3$ for the nonlinear solid.

The normalized critical stress σ_c/G^* is a function of the nondimensional groups $\bar{\phi}_0/\gamma_Y^*$ and n in the kinking analysis, and of the groups $\bar{\phi}_0/\gamma_Y^*$, $\bar{w}/d\sqrt{G^*/E}$ and n in the bending analysis. The dominant independent group for both theories is the imperfection magnitude $\bar{\phi}_0/\gamma_Y^*$. Budiansky and Fleck (1993) have given an analytic formula for the effect of imperfection magnitude upon the critical compression strength σ_c^k/G^* by the kinking theory. They find

Downloaded 04 May 2010 to 171.66.16.28. Redistribution subject to ASME license or copyright; see http://www.asme.org/terms/Terms_Use.cfm

$$\frac{\sigma_c^k}{G^*} = \frac{1}{1 + n\left(\frac{3}{7}\right)^{1/n}\left(\frac{\bar{\phi}_0/\gamma_Y^*}{n-1}\right)^{n-1/n}} \tag{35}$$

The ratio of the critical load σ_c^b predicted by bending theory to the value σ_c^k by kinking theory is given in Fig. 8 as a function of $\bar{\phi}_0/\gamma_Y^*$, for $n = 3$ and ∞ and two finite imperfection wavelengths. For the limiting case of $\bar{w}/d\sqrt{G^*/E} = \infty$ (omitted from Fig. 8 for the sake of clarity), the ratio σ_c^b/σ_c^k equals unity to within 0.1 percent for $\bar{\phi}_0/\gamma_Y^* = 2$ and 4, and for all n in the range $1 \le n \le \infty$. The effect of the imperfection-wavelength parameter $\bar{w}/d\sqrt{G^*/E}$ on the value of σ_c/G^* given by bending theory is shown explicitly in Fig. 9, for the two imperfection sizes $\bar{\sigma}_0/\gamma_Y^* = 2$ and 4. The results in Figs. 8 and 9 imply that, in general, the strength predictions of the bending and kinking theories differ little for realistic composites; only if the *dominant* imperfection wavelength $\bar{w}/d\sqrt{G^*/E}$ in the composite has an unrealistically small value less than 5 will the ratio σ_c^b/σ_c^k be substantially larger than unity.

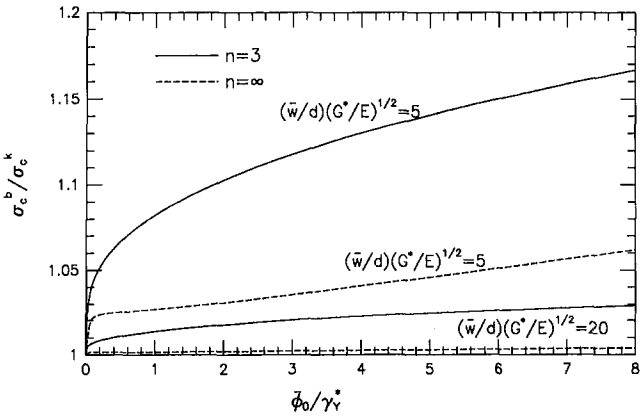

Fig. 8 Ratio of critical stress from bending theory σ_c^b to the critical stress from kinking theory σ_c^k as a function of fiber misalignment $\bar{\phi}_0/\gamma_Y^*$, for a wide range of matrix nonlinearity n and misalignment wavelength $\bar{w}/d\sqrt{G^*/E}$.

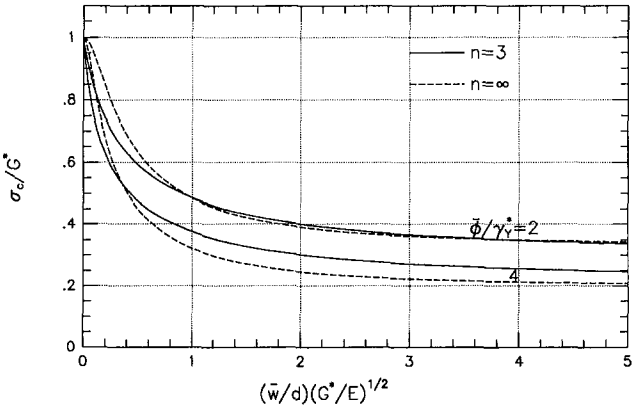

Fig. 9 The effect of wavelength of misalignment $\bar{w}/d\sqrt{G^*/E}$ upon the critical stress σ_c/G^* for some typical values of matrix nonlinearity n and misalignment angle $\bar{\phi}_0/\gamma_Y^*$; bending theory.

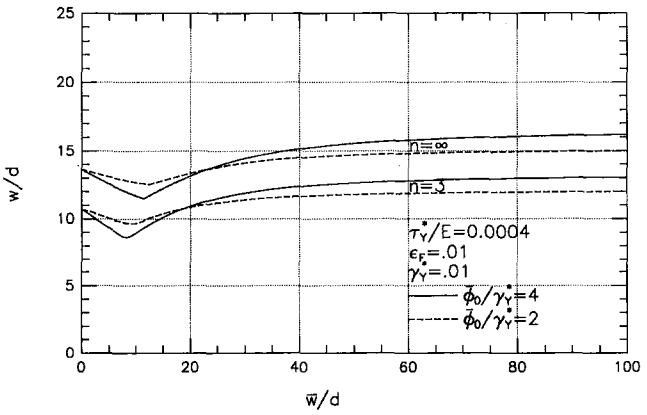

Fig. 10 Effect of misalignment wavelength $\bar{w}/d$ upon width of kink band w/d, for $n = 3$ and ∞, and $\bar{\phi}_0/\gamma_Y^* = 2$ and 4.

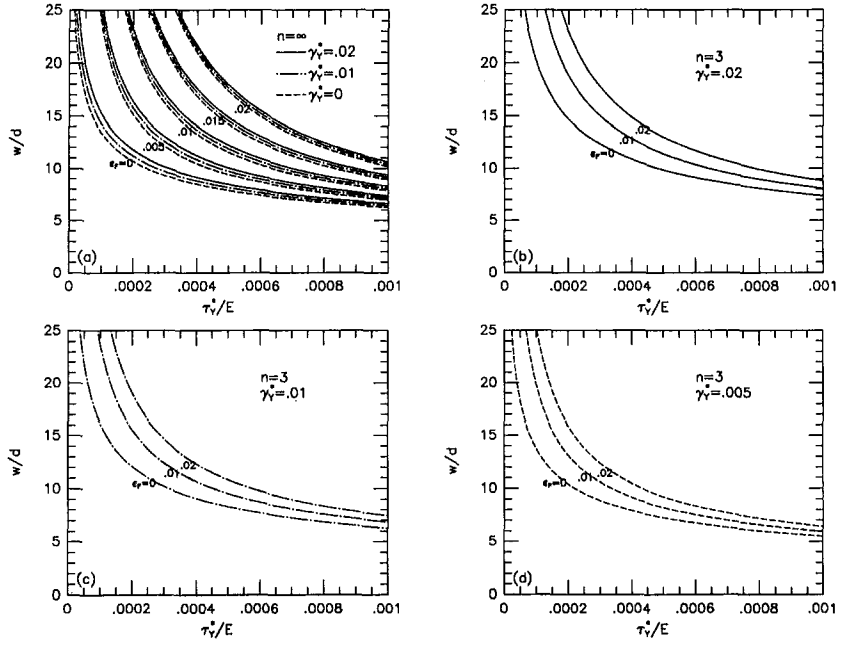

Fig. 11 Width of kink band for perfectly aligned composite ($\bar{\phi}_0/\gamma_Y^* = 0$) as a function of τ_Y^*/E, and ϵ_F in the range 0 - .02. (a) Elastic-ideally plastic response, for $\gamma_Y^* = 0$, .01 and .02. The remaining plots are for $n = 3$: (b) $\gamma_Y^* = .02$; (c) $\gamma_Y^* = .01$; and (d) $\gamma_Y^* = .005$.

Downloaded 04 May 2010 to 171.66.16.28. Redistribution subject to ASME license or copyright; see http://www.asme.org/terms/Terms_Use.cfm

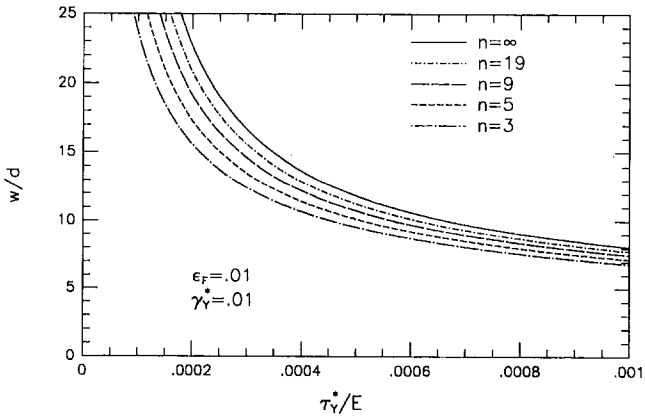

Fig. 12 Effect of τ_Y^*/E upon width of kink band, for $3 \le n \le \infty$ and $\epsilon_F = 0.01$, $\gamma_Y^* = .01$; perfectly aligned composite ($\bar{\phi}_0/\gamma_Y^* = 0$).

Note that in the limit $\bar{w}/d\sqrt{G^*/E} = 0$, the imperfection vanishes and the bending theory gives a critical load $\sigma_c/G^* = 1$ for all n and all $\bar{\phi}_0/\gamma_Y^*$.

Prediction of Kink Band Width. The normalized kink band width w/d is a function of the six nondimensional parameters and groups

$$\epsilon_F, \quad \gamma_Y^*, \quad n, \quad \tau_Y^*/E, \quad \bar{w}/d, \quad \bar{\phi}_0/\gamma_Y^*. \tag{36}$$

The effect of the wavelength $\bar{w}/d$ of the initial misalignment upon kink width w/d is shown in Fig. 10 for $n = 3$ and ∞ and typical values of $\bar{\phi}_0/\gamma_Y^*$, ϵ_F, γ_Y^*, and τ_Y^*/E. The kink width w/d is little influenced by the wavelength $\bar{w}/d$ or magnitude $\bar{\phi}_0/\gamma_Y^*$ of the initial imperfection (and by the degree of material nonlinearity n). Note that the kink width arising from an initial misalignment is never far from the kink width for the perfectly aligned composite, given by the limit $\bar{w}/d = 0$ in Fig. 10. A definite minimum in kink width w/d occurs very near an imperfection width given by $\bar{w}/d = w/d$. This suggests a "lock-in" type of behavior, whereby the minimum kink width corresponds to the condition where it is nearly matched by the wavelength of the initial imperfection.

The effect of the nondimensional groups τ_Y^*/E, ϵ_F, γ_Y^*, and n upon the kink band width w/d is explored in Figs. 11 and 12. Since the imperfection wavelength and magnitude play a minor role in setting the kink width, we consider only results for the perfectly aligned composite. The kink width is shown as a function of τ_Y^*/E in Fig. 11, for a range of values of ϵ_F and γ_Y^*, and $n = 3$ and ∞. Consider first the results given in Fig. 11(a) for the elastic-ideally plastic solid ($n = \infty$). As shown in the Appendix, the curves in Fig. 11(a) satisfy

$$4\left(\tau_y^*/E\right)^2\left[\left(\frac{4w}{\pi d}\right)^2 - \gamma_Y^*\left(\tau_Y^*/E\right)^{-1}\right] = \left[\epsilon_F + \left(\frac{4w}{\pi d}\right)^{-2}\right]^2. \tag{37}$$

For $\epsilon_F = \gamma_Y^* = 0$, this reduces to the Budiansky (1983) result given by Eq. (1). For unusually low values of τ_Y^*/E (say, less than .0004), the kink width is seen to be sensitive to fiber failure strain ϵ_F, but it is always very insensitive to the value of yield strain γ_Y^*. Further, if τ_Y^*/E exceeds about .0004, changes in τ_Y^*/E have only a minor effect upon kink width. This may also be seen from the analytic formula (1) for the rigid-ideally plastic solid ($\gamma_Y^* = 0$), where w/d varies with τ_Y^*/E to the $-1/3$ power. We note that w/d increases with both increasing ϵ_F and increasing γ_Y^*.

Results for the nonlinear solid ($n = 3$) are given for $\gamma_Y^* = 0.02$, 0.01, and 0.005 in Figs. 11(b, c, and d), respectively. As n is decreased from ∞ to 3, the kink width w/d becomes considerably less sensitive to the failure strain ϵ_F and somewhat more sensitive to γ_Y^*; otherwise, the trends are the same for $n = 3$ and for $n = \infty$. For finite n, the composite adopts an infinite initial stiffness in the limit $\gamma_Y^* = 0$, and the constitutive description becomes unacceptable. We have found for $n = 3$ that as γ_Y^* is decreased from a value of 0.001 to zero, w/d drops steeply to zero; no curves are given to show this, as the effect is of no practical relevance.

The effect of strain hardening index n upon kink width is given in Fig. 12 for $\epsilon_F = 0.01$ and $\gamma_Y^* = 0.01$. We observe that w/d increases only slightly with increasing n. In conclusion, the predicted kink width w/d is of the order 10–15 for a wide range of values for the six independent parameters (36) characterizing the imperfection and the material properties.

Concluding Remarks

In this paper, a nonlinear couple stress theory was used to incorporate the effect of fiber bending resistance into the analysis of compressive failure and kink-band formation of fiber composites. We have assumed an initial imperfection that was perfectly correlated in a direction inclined at an angle β to the transverse direction. It was found that while fiber bending resistance plays an essential role in the prediction of kink band width, it can be neglected in predicting failure strength. The imperfection wavelength has little effect on both compressive strength and kink width, and although the magnitude of the waviness strongly influenced compressive strength, it has only a minor influence on kink width. Except for very low values of the composite shear yield stress or high values of the Ramberg-Osgood hardening parameter n, kink width is fairly insensitive to material properties. The predicted values of w/d in the neighborhood of 10–15 are roughly the same as the experimental data for polymer-matrix fiber composites collected and reviewed by Jelf and Fleck (1992).

Acknowledgments

The authors are grateful for financial support from the National Science Foundation (contract MSS-9216135), the Office of Naval Research (contract 0014-91-J-1916), the Procurement Executive of the Ministry of Defense (contract 2029/267), the Department of Engineering, Cambridge University, and the Division of Applied Sciences, Harvard University.

References

Argon, A. S., 1972, "Fracture of Composites," *Treatise of Materials Science and Technology*, Vol. 1, Academic Press, New York.

Budiansky, B., 1983, "Micromechanics," *Computeres and Structures*, Vol. 16, No. 1, pp. 3–12.

Budiansky, B., and Fleck, N. A., 1993, "Compressive Failure of Fiber Composites," *J. Mech. Phys. Solids*, Vol. 41, pp. 183–211.

Hahn, H. T., 1987, "Compressive Failure of Unidirectional Composites," *13th Annual Int. Symp. for Testing and Failure Analysis*, Los Angeles, CA.

Jelf, P. M., and Fleck, N. A., 1992, "Compressive Failure Mechanisms in Unidirectional Composites," to appear in *J. Composite Materials*.

Rosen, B. W., 1965, "Mechanics of Composite Strengthening," *Fiber Composite Materials*, Am. Soc. Metals Seminar, Chapter 3, pp. 37–75.

Soutis, C., and Fleck, N. A., 1990, "Static Compression Failure of Carbon Fiber T800/924C Composite Plate with a Single Hole," *J. Composite Materials*, Vol. 24, pp. 536–558.

APPENDIX

Analytic and Numerical Solutions

Here we describe the procedures used to calculate response and the kink band width. By symmetry, we need only consider the domain $\xi \ge 0$ in all cases.

Downloaded 04 May 2010 to 171.66.16.28. Redistribution subject to ASME license or copyright; see http://www.asme.org/terms/Terms_Use.cfm

Elastic-Ideally Plastic Body ($n = \infty$). For the perfect ($\bar{\omega} \equiv 0$) elastic-ideally plastic solid the governing Eqs. (27) admit the following solution. Under increasing load Λ, ω stays equal to zero until the bifurcation load $\Lambda = 1$ is reached, and then, in accordance with Eq. (27*a*), ω increases everywhere, uniformly and elastically, up to the value $\omega = 1$, with Λ remaining equal to 1. We assume that plastic yield will start at $\xi = 0$ and spread into a finite vicinity of the origin. At the elastic-plastic boundary ξ_P, we have $\gamma_e = \gamma_Y$, which, by (20), (22), (23) requires

$$\omega(\xi_P) = 1. \tag{A1}$$

Solutions of Eqs. (27*a*, *b*) satisfying this requirement are given by

$$\omega(\xi) = \begin{cases} \dfrac{1}{\Lambda} + \left(1 - \dfrac{1}{\Lambda}\right)\dfrac{\cos\sqrt{\Lambda}\,\xi}{\cos\sqrt{\Lambda}\,\xi_P} & 0 \le \xi \le \xi_P \\ \exp\left[-\sqrt{1-\Lambda}\,(\xi - \xi_P)\right] & \xi \ge \xi_P \end{cases} \tag{A2}$$

wherein the conditions $\omega'(0) = 0$ and $\omega'(\infty) = 0$ have been imposed. The additional bending continuity condition $\omega'(\xi_P^+) = \omega'(\xi_P^-)$ implies

$$\cos\left(\sqrt{\Lambda}\,\xi_P\right) = -\sqrt{1-\Lambda}\,. \tag{A3}$$

Equation (32) of the text can be obtained by setting $\xi = 0$ in (A2). Also, (A3) implies that ξ_P jumps discontinuously to the value $\pi/2$ at $\Lambda = 1$ when $\omega(0)$ just begins to increase beyond 1, and then continues to grow smoothly as Λ decreases.

Fiber fracture occurs in the plastic region at

$$\xi_F = \frac{\pi}{2\sqrt{\Lambda}} \tag{A4}$$

where

$$\omega''(\xi_F) = 0. \tag{A5}$$

Then

$$|\omega'(\xi_F)| = \left|\frac{d\omega}{d\xi}\right|_{\max} = \sqrt{\frac{1-\Lambda}{\Lambda}} \tag{A6}$$

and using (A4) together with (A6) in (28) and (30) gives the analytic result (37) for the kink width.

For the imperfect composite ($\bar{\omega} \neq 0$), the solutions of (27) satisfying $\omega'(0) = \omega'(\infty) = 0$ are as follows. For $\xi_P \le \xi_I$,

$$\omega(\xi) = \begin{cases} \dfrac{1}{\Lambda} + C_1\cos\left(\sqrt{\Lambda}\,\xi\right) + \dfrac{\Lambda\bar{\omega}_0}{\left(\dfrac{\pi}{2\xi_I}\right)^2 - \Lambda}\cos\left(\dfrac{\pi\xi}{2\xi_I}\right) & 0 \le \xi \le \xi_P \\ C_2 e^{\sqrt{1-\Lambda}\,\xi} + C_3 e^{-\sqrt{1-\Lambda}\,\xi} + \dfrac{\Lambda\bar{\omega}_0}{1 - \Lambda + \left(\dfrac{\pi}{2\xi_I}\right)^2}\cos\left(\dfrac{\pi\xi}{2\xi_I}\right) & \xi_P \le \xi \le \xi_I \\ C_4 e^{-\sqrt{1-\Lambda}\,\xi} & \xi \ge \xi_I \end{cases} \tag{A7a}$$

and for $\xi_P \ge \xi_I$

$$\omega(\xi) = \begin{cases} \dfrac{1}{\Lambda} + C_1\cos\left(\sqrt{\Lambda}\,\xi\right) + \dfrac{\Lambda\bar{\omega}_0}{\left(\dfrac{\pi}{2\xi_I}\right)^2 - \Lambda}\cos\left(\dfrac{\pi\xi}{2\xi_I}\right) & 0 \le \xi \le \xi_P \\ \dfrac{1}{\Lambda} + C_2\cos\left(\sqrt{\Lambda}\,\xi\right) + C_3\sin\left(\sqrt{\lambda}\,\xi\right) & \xi_I \le \xi \le \xi_P \\ C_4 e^{-\sqrt{1-\Lambda}\,\xi} & \xi \ge \xi_I. \end{cases} \tag{A7b}$$

The desired relation between the load and rotation variables Λ and $\omega(0)$ is found from

$$\omega(0) = \frac{1}{\Lambda} + C_1 + \frac{\Lambda\bar{\omega}_0}{\left(\dfrac{\pi}{2\xi_I}\right)^2 - \Lambda}, \tag{A8}$$

imposition the five consistency and continuity relations

$$\omega(\xi_P^+) = \omega(\xi_P^-) = 1, \quad \omega'(\xi_P^+) = \omega'(\xi_P^-),$$
$$\omega(\xi_I^+) = \omega(\xi_I^-), \quad \omega'(\xi_I^+) = \omega'(\xi_I^-), \tag{A9}$$

and solving the system (A8)–(A9) of six nonlinear equations for the six unknowns Λ, ξ_P, C_1, C_2, C_3, C_4 in terms of prescribed values of $\omega(0)$. The solutions (obtained via a Newton-Raphson iterative scheme) provided the results for $n = \infty$ in Figs. 5–9.

As in the case of the perfect composite fiber fracture occurs at $\xi = \xi_F$, satisfying Eq. (A5). For prescribed values of ϵ_F, τ_Y^*/E, and γ_Y^*, Eqs. (28), (A9), and (A5) now provide seven simultaneous equations for ξ_F and the values of Λ, ξ_P, and C_1–C_4 at fracture. The solution (by the Newton-Raphson method) gives the width of kink band via (30).

Ramberg-Osgood Solid ($1 < n < \infty$). For the perfect composite ($\bar{\partial} \equiv 0$), we can use (26), together with the assumed boundary conditions $\omega(\infty) = \omega'(\infty) = 0$, to get a first integral of the differential Eq. (25) in the form

$$\omega'^2 = G^2 + \frac{6}{7}\frac{n}{n+1}g^{n+1} - \Lambda\left(g + \frac{3}{7}g^n\right)^2. \tag{A10}$$

At the origin, $\omega'(0) = 0$ and (A10) implies

$$g(0) = \left[\frac{7}{3}\frac{\sqrt{\left(\Lambda - \dfrac{n}{n+1}\right)^2 + \Lambda(1-\Lambda)} - \left(\Lambda - \dfrac{n}{n+1}\right)}{\Lambda}\right]^{\frac{1}{n-1}}. \tag{A11}$$

Downloaded 04 May 2010 to 171.66.16.28. Redistribution subject to ASME license or copyright; see http://www.asme.org/terms/Terms_Use.cfm

Equations (A11) and (26) provide the relation between Λ and $\omega(0)$.

Inserting into Eq. (25) the condition (A5) on the fracture location ξ_F gives

$$g(\xi_F) = \left[\frac{7}{3}\left(\frac{1-\Lambda}{\Lambda}\right)\right]^{\frac{1}{n-1}} \tag{A12}$$

and the corresponding value of $|\omega'(\xi_F)|$ in terms of Λ follows from (A10). Substitution into the the fiber failure criterion (28) then provides a nonlinear equation that can be solved numerically for the value of Λ at fracture. Finally, by use of (26) in the integration of (A10), the fiber fracture location ξ_F is given by

$$\xi_F = \int_{g(\xi_F)}^{g(0)} \frac{\left[1 + \frac{3}{7}ng^{n-1}\right]dg}{\sqrt{g^2 + \frac{6}{7}\frac{n}{n+1}g^{n+1} - \Lambda\left[g + \frac{3}{7}g^n\right]^2}} \tag{A13}$$

where the limits of integration are given by (A11) and (A12). The kink band width w is related to ξ_F via (30).

Now consider the Eq. (24) for the imperfect composite. Equation (A10) remains valid for $\xi > \xi_I$; and integration from ξ_I to an arbitrary point $\xi > \xi_I$ gives

$$\xi = \xi_I + \int_{g}^{g(\xi_I)} \frac{\left[1 + \frac{3}{7}ng^{n-1}\right]dg}{\sqrt{g^2 + \frac{6}{7}\frac{n}{n+1}g^{n+1} - \Lambda\left[g + \frac{3}{7}g^n\right]^2}}. \tag{A14}$$

Inside the imperfection band ($\xi < \xi_I$), Eq. (25) may be reduced to a system of three first-order nonlinear equations for the dependent variables $y_1 \equiv g$, $y_2 \equiv g'$ and $y_3 \equiv \Lambda$. The resulting system is

$$\begin{cases} y_1' = y_2 \\ y_2' = \dfrac{1}{1 + \frac{3}{7}ny_1^{n-1}}\left[y_1 - y_3\bar{\omega} - y_3\left(y_1 + \frac{3}{7}y_1^n\right) - \frac{3}{7}n(n-1)y_1^{n-2}y_2^2\right] \\ y_3' = 0 \end{cases} \tag{A15}$$

To solve (A15), we prescribe the boundary condition $y_1(0) \equiv g(0)$, and the symmetry condition $y_2(0) = 0$. The required third boundary condition is the following relation among $y_1(\xi_I)$, $y_2(\xi_I)$, and $y_3(\xi_I)$, that asserts Eq. (A10) at $\xi = \xi_I$:

$$y_2^2(\xi_I)\left[1 + \frac{3}{7}ny_1^{n-1}(\xi_I)\right]^2 - y_1^2(\xi_I)\left[1 + \frac{6}{7}\frac{n}{n+1}y_1^{n-1}(\xi_I) - y_3(\xi_I)\left[1 + \frac{3}{7}y_1^{n-1}(\xi_I)\right]^2\right] = 0. \tag{A16}$$

The numerical solution of the system of Eqs. (A15) by a finite difference scheme and direct Gaussian elimination was found to be numerically stable, even when the load Λ exhibited a limit point. With use of the connection (26) between ω and g, the solutions provide the connection between Λ and $\omega(\xi)$, and the desired response curves of Λ versus $\omega(0)$.

The fiber fracture location ξ_F to be used in Eq. (30) for the kink width was found by iteration. The boundary value $y_1(0)$ was varied until the values of Λ and $|\omega'|_{\max}$ produced by the solution of Eqs. (A15) satisfied Eq. (28).

Elastic Solid. The response of the elastic solid, governed by Eq. (27*a*), is given by the last two members of Eqs. (A7*a*), with $\xi_P = 0$. Applying the conditions of continuity of ω and ω' at $\xi = \xi_I$ leads directly to the relation

$$\omega(0) = \frac{\bar{\omega}_0}{1 - \Lambda + \left(\frac{\pi}{2\xi_I}\right)^2}\left[1 + \frac{\pi}{2\xi_I}\frac{1}{\sqrt{1-\Lambda}}e^{-\sqrt{1-\Lambda}\,\xi_I}\right] \tag{A17}$$

used to plot the elastic response curves in Fig. 7.

Downloaded 04 May 2010 to 171.66.16.28. Redistribution subject to ASME license or copyright; see http://www.asme.org/terms/Terms_Use.cfm

Initial Post-buckling Behavior of Thick Rings Under Uniform External Hydrostatic Pressure

Lei Fu[1]

A. M. Waas
Mem. ASME.

Composite Structures Laboratory,
Department of Aerospace Engineering,
College of Engineering,
University of Michigan,
Ann Arbor, MI 48109-2118

The initial post-buckling behavior of thick rings under external uniform hydrostatic pressure is investigated. In the analysis, no assumptions are placed upon the relative magnitudes of the elongations and rotations, and the ring is assumed to be elastic and extensional. The importance of including certain nonlinear terms in the initial post-buckling stability analysis and the effects of nonzero shearing strains on the buckling load and the initial post-buckling stability are examined. It is shown that the classical Kirchhoff assumptions, when employed for a ring lead to nonvanishing through thickness strains, ϵ_{zz} and $\epsilon_{z\theta}$, with the latter being proportional to the through thickness coordinate z. An approximate first order shear deformation analysis and a two-dimensional elasticity analysis (without beam-type kinematical assumptions) of the initial post-buckling behavior of thick rings are presented and the thickness effects on the buckling load and the initial post-buckling behavior are examined. The formulation for the composite ring was reduced to that of an isotropic ring and the results thus obtained were compared with published one-dimensional results in the literature. It is found from both the shear deformation and the two-dimensional analysis that the initial post-buckling behavior of the isotropic ring and the composite rings studied are stable. The influence of thickness on the degree of stability in the immediate post-buckling response is characterized.

Introduction

There is a vast amount of work in the open literature on the buckling and post-buckling behavior of homogeneous isotropic rings since the beginning of the 20th century. Much of the theoretical work done on the buckling and initial post-buckling behavior of isotropic rings were based on the general theory for the equilibrium and stability of elastic and discrete structures proposed in Koiter (1963), Thompson (1969), Carrier (1947), and Budiansky (1974). It has been shown in Bodner (1958) that in the three cases of a ring under external hydrostatic, constant directional, and centrally directed pressure, that the applied loading system is conservative if the magnitude of the pressure is constant during buckling. Thus, even though the direction of external pressure is continuously dependent on the ring motion during buckling in the case of hydrostatic pressure loading, a static stability criterion is still valid.

Publications by Budiansky (1974), Bodner (1958), Anderson and Boresi (1962), Lo et al. (1962), Hubka (1973), Brush and Almroth (1975), Singer and Babcock (1970), Kyriakides and Babcock (1981), and Ju and Kyriakides (1991) reported on investigations pertaining to the buckling of thin rings or tubes under external hydrostatic pressure. There are many engineering examples in everyday life where the results of such a study would be indispensable. Two such situations are under sea cables and submersible vessels. In these situations, it was found that the critical buckling pressure of an isotropic vessel is given by the relation ($P_{cr} = (Et^3)/(4R^3)$ where E is the ring material's Young's modulus, R its mean radius, and t its thickness. Depending on the nondimensional ratio R/t, it is possible that effects of plasticity need be included to properly account for the ring's response. Kyriakides and co-workers have examined different aspects of this problem and their findings are reported in numerous publications, two of which are cited here (Kyriakides et al., 1981, 1991).

Boresi (1955) was the first to examine the effect of transverse shear and load behavior on ring stability. However, a complete treatment in the context of thin ring theory was presented by Smith and Simitses (1969). Marshall and Moshaiov (1990) have examined the case of the buckling of a delaminated ring and numerous publications (Duffey et al.,

[1]Currently, Staff Scientist, McDonnell Douglas Aerospace, Long Beach, CA 90810.

Contributed by the Applied Mechanics Division of THE AMERICAN SOCIETY OF MECHANICAL ENGINEERS for publication in the JOURNAL OF APPLIED MECHANICS.

Discussion on this paper should be addressed to the Technical Editor, Professor Lewis T. Wheeler, Department of Mechanical Engineering, University of Houston, Houston, TX 77204-4792, and will be accepted until four months after final publication of the paper itself in the ASME JOURNAL OF APPLIED MECHANICS.

Manuscript received by the ASME Applied Mechanics Division, July 5, 1993; final revision, Mar. 21, 1994. Associate Technical Editor: J. N. Reddy.

Copyright © 1995 by ASME

Downloaded 04 May 2010 to 171.66.16.28. Redistribution subject to ASME license or copyright; see http://www.asme.org/terms/Terms_Use.cfm

1991; Sills and Budiansky, 1978; El Naschie, 1975a, b; El Naschie and El Nashai, 1976) exist in the literature on the initial post-buckling behavior of thin isotropic rings. These have shown that a thin isotropic ring displays a stable initial post-buckling response.

Kardomateas (1992, 1993) concluded that the buckling loads of rings are highly influenced by the thickness of the rings under investigation. He performed a two-dimensional buckling analysis for a thick ring employing the linearized stability equations for a two-dimensional elastic continuum as given in Novozhilov (1953). In Kardomateas (1993), the classical buckling pressure is compared with the two-dimensional result and it is evident that for rings with D/t less than 20, the one-dimensional prediction overestimates the buckling pressure by an amount as large as 20 percent.

In the analysis to be presented here, it is demonstrated that a "zero shear deformation" analysis does not exist for rings if the deformations $u = \hat{u} + z\Phi$ and $w = \hat{w} + z\kappa$ are assumed on the displacement field, where $\hat{u}$ and $\hat{w}$ are the center-line tangential and radial deformations, respectively, and Φ and κ are the associated rotations. Results are reported for the buckling and initial post-buckling behavior of linearly elastic orthotropic and isotropic rings of arbitrary thickness based on two-dimensional elasticity theory, in conjunction with a variational analysis. These results are compared to those obtained from a one-dimensional shear deformation analysis. This is performed so as to examine the validity of utilizing a first-order shear deformation theory to predict the initial post-buckling stability of thick rings.

In the analysis of the initial post-buckling behavior of laminated rings, the solution procedure adopted is similar to that performed in Novozhilov (1953). The analysis performed is for thick composite rings with the elastic constants specialized appropriately to produce the results for thick isotropic rings. The validity of the formulation is checked by reducing the derived ring stability equations to those for a beam in the limit when the radius of curvature tends to infinity. It is found, via the two-dimensional variational analysis, that the initial post-buckling behavior of isotropic rings is stable. A similar conclusion is reached for the example orthotropic ring analyzed. However, in this case the initial post-buckling behavior is strongly dependent on the orthotropic mechanical properties of the ring. The results obtained utilizing the shear deformation theory was found to be inadequate in analyzing the initial post-buckling behavior of thick rings with a diameter-to-thickness ratio that is less than 20. Finally, we conclude that most kinematically based theories yield satisfactory predictions for the buckling pressure. In contrast, the initial post-buckling response is highly influenced by the types of assumptions and constraints placed upon the assumed displacement field. The results presented herein for the two-dimensional case may be used as a benchmark for evaluating other approximate theories, particularly beyond the buckling load.

Problem Formulation

We consider a symmetrically laminated circular ring of mean radius R, outer radius R_{outer}, and inner radius R_{inner}. The ring thickness is denoted t and by definition, $t = R_{\text{outer}} - R_{\text{inner}}$. The ring cross-section is rectangular with a unit height into the plane of the paper. We assume that strains are small compared to unity, and that planes normal to the centroidal line in the undeformed state remain plane but are not restricted to be normal to the deformed centroidal line. No restrictions are placed on the extensibility of the centroidal line. We choose a Lagrangian description with a fixed right-handed cylindrical frame of reference to be used, with the θ-axis ($s = R\theta$), coinciding with the centroidal line of the ring in the initial undeformed state and the x-axis normal to it. The z-axis is placed radially and is positive pointing outwards from the ring center.

Let the components of the displacement of a particle positioned initially at (r, θ) be denoted by (w, u). In the Lagrangian description, the Green's strain tensor referred to the initial configuration is used. The Green's strain components in a cartesian frame of reference are (Novozhilov, 1953),

$$\epsilon_{11} = e_{11} + \frac{1}{2}\left[e_{11}^2 + \left(\frac{1}{2}e_{12} + \omega_3\right)^2 + \left(\frac{1}{2}e_{13} - \omega_2\right)^2\right]$$

$$\epsilon_{22} = e_{22} + \frac{1}{2}\left[e_{22}^2 + \left(\frac{1}{2}e_{12} - \omega_3\right)^2 + \left(\frac{1}{2}e_{23} + \omega_1\right)^2\right]$$

$$\epsilon_{33} = e_{33} + \frac{1}{2}\left[e_{33}^2 + \left(\frac{1}{2}e_{13} + \omega_2\right)^2 + \left(\frac{1}{2}e_{23} - \omega_1\right)^2\right]$$

$$\epsilon_{12} = e_{12} + e_{11}\left(\frac{1}{2}e_{12} - \omega_3\right) + e_{22}\left(\frac{1}{2}e_{12} + \omega_3\right) + \left(\frac{1}{2}e_{13} - \omega_2\right)\left(\frac{1}{2}e_{23} + \omega_1\right)$$

$$\epsilon_{13} = e_{13} + e_{11}\left(\frac{1}{2}e_{13} + \omega_2\right) + e_{33}\left(\frac{1}{2}e_{13} - \omega_2\right) + \left(\frac{1}{2}e_{12} + \omega_3\right)\left(\frac{1}{2}e_{23} - \omega_1\right)$$

$$\epsilon_{23} = e_{23} + e_{22}\left(\frac{1}{2}e_{23} - \omega_1\right) + e_{33}\left(\frac{1}{2}e_{23} + \omega_1\right) + \left(\frac{1}{2}e_{12} - \omega_3\right)\left(\frac{1}{2}e_{13} + \omega_2\right) \quad (1)$$

where e_{11}, e_{22}, and e_{33} are the small strain elongations, e_{12}, e_{12}, and e_{23} are the small strain shears and ω_1, ω_2, and ω_3 are the small rotations. Consistent with the assumptions stated before, and guided by the general first-order shear deformation theories of Timoshenko (1921), we assume the following displacement field:

$$u = \hat{u} + z\Phi$$
$$w = \hat{w} + z\kappa. \quad (2)$$

Here Φ and κ are functions of θ, which are as yet to be determined, and $\hat{u}$, $\hat{w}$ are the center-line deformations. Upon substituting (2) into (1) and simplifying, we obtain the following nonlinear strains:

$$\epsilon_{zz} = \kappa^2 + \frac{1}{2}(\kappa^2 + \Phi^2)$$

$$\epsilon_{z\theta} = (1 + \kappa)\left(\frac{1}{2}\frac{\partial\hat{w}}{\partial\theta} - \frac{\hat{u}}{R}\right) + \Phi\left(1 + \frac{1}{R}\frac{\partial\hat{u}}{\partial\theta} + \frac{\hat{w}}{R}\right) + z\left[(1 + \kappa)\left(\frac{1}{R}\frac{\partial\kappa}{\partial\theta} - \frac{\Phi}{R}\right) + \Phi\left(\frac{1}{R}\frac{\partial\Phi}{\partial\theta} + \frac{\kappa}{R}\right)\right]$$

$$\epsilon_{\theta\theta} = \left(\frac{1}{R}\frac{\partial\hat{u}}{\partial\theta} + \frac{\hat{w}}{R}\right) + \frac{1}{2}\left[\left(\frac{1}{R}\frac{\partial\hat{u}}{\partial\theta} + \frac{\hat{w}}{R}\right)^2 + \left(\frac{1}{R}\frac{\partial\hat{w}}{\partial\theta} - \frac{\hat{u}}{R}\right)^2\right] + z\left[\left(\frac{1}{R}\frac{\partial\Phi}{\partial\theta} + \frac{\kappa}{R}\right) + \left(\frac{1}{R}\frac{\partial\Phi}{\partial\theta} + \frac{\kappa}{R}\right)\left(\frac{1}{R}\frac{\partial\hat{u}}{\partial\theta} + \frac{\hat{w}}{R}\right)\right.$$

Downloaded 04 May 2010 to 171.66.16.28. Redistribution subject to ASME license or copyright; see http://www.asme.org/terms/Terms_Use.cfm

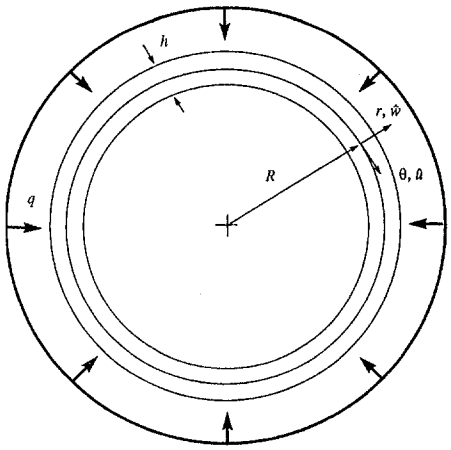

Fig. 1 Coordinate convention adopted (shear deformation analysis)

$$+\left(\frac{1}{R}\frac{\partial\kappa}{\partial\theta}-\frac{\Phi}{R}\right)\left(\frac{1}{R}\frac{\partial\hat{w}}{\partial\theta}-\frac{\hat{u}}{R}\right)\Bigg]$$

$$+z^2\,(\text{higher - order terms}). \quad (3)$$

Kirchhoff's assumption that straight fibers which are normal to the centroidal line of the ring before deformation remain straight and normal to the centroidal line after deformation are not utilized here (i.e., if we set $\kappa = \partial w/(R\partial\theta)$ and $\Phi = \partial u/(\partial r)$, then we recover the classical result; see Stoker, 1968). If Kirchhoff's assumptions were used here, we would not be able to satisfy the three independent equations generated by setting ϵ_{zz} and $\epsilon_{z\theta}$ in (3) to zero. Indeed, if Kirchhoff's assumptions are employed, then such a displacement field when substituted to the fully nonlinear strains (3), produces a nonvanishing shear strain component $\epsilon_{z\theta}$, that is proportional to the through thickness coordinate z and inversely proportional to the radius of curvature R. Instead of using a displacement field deduced on the basis of examining the structure of the nonlinear strains given by (3), we have adopted a first-order shear deformation theory to investigate the stability response of a thick ring, in which we allow Φ and κ to remain as independent variables. Note that in the limit $R \to \infty$ (such as in the beam problem), the equations in (3) in conjunction with the displacement field (2) produces the correct expressions for the beam curvatures (Dym, 1974).

Shear Deformation Analysis. In the shear deformation analysis, no assumptions are placed on the direction of the normal to the deformed plane sections. These sections are allowed to rotate with respect to the line of centroids of the ring. The following coordinate convention is adopted for the shear deformation analysis (refer to Fig. 1). We assume the first-order shear deformation field as in (2). We do not place any assumptions on Φ and κ, and treat them as independent variables. The internal strain energy, U_{int}, is given by

$$U_{\text{int}} = \frac{1}{2}\int_V \sigma_i\epsilon_i dV \quad i = 1,3$$

$$= \frac{1}{2}\int_0^{2\pi} u_{\text{int}} d\theta, \quad (4)$$

where we have used a contracted notation $\sigma_2 = \sigma_{zz}$, $\sigma_1 = \sigma_{\theta\theta}$, $\sigma_3 = \sigma_{z\theta}$, and similarly for the corresponding strains. The constitutive description of the ring then follows as

$$\begin{bmatrix}\sigma_{\theta\theta}\\ \sigma_{zz}\\ \sigma_{z\theta}\end{bmatrix} = [Q_{ij}]\begin{bmatrix}\epsilon_{\theta\theta}\\ \epsilon_{zz}\\ \epsilon_{z\theta}\end{bmatrix}. \quad (5)$$

Since we are modeling the ring under conditions of generalized plane stress, Q_{ij} is given by

$$[Q_{ij}] = \begin{bmatrix}\dfrac{E_1}{1-\nu_{12}\nu_{21}} & \dfrac{\nu_{12}E_2}{1-\nu_{12}\nu_{21}} & 0\\ \dfrac{\nu_{12}E_2}{1-\nu_{12}\nu_{21}} & \dfrac{E_2}{1-\nu_{12}\nu_{21}} & 0\\ 0 & 0 & G_{12}\end{bmatrix}. \quad (6)$$

Here, E_1, E_2, ν_{12}, and G_{12} are the four independent material properties for the composite. For an isotropic analysis $E_1 = E_2 = E$, $\nu_{12} = \nu$ and $G_{12} = E/(2(1+\nu))$ where E is Young's Modulus and ν, Poisson's Ratio. The work done by the uniform external hydrostatic pressure, U_{ext}, is given by

$$U_{\text{ext}} = \frac{qR}{2}\int_0^{2\pi}\left(\hat{w} + \frac{1}{2R}\left(\hat{u}^2 - \hat{u}\frac{\partial\hat{w}}{\partial\theta} + \frac{\partial\hat{u}}{\partial\theta}\hat{w} + \hat{w}^2\right)\right)d\theta \quad (7)$$

where q has units of force per unit length and is the uniform external edge pressure applied to the ring under analysis. Thus the total energy is given by the addition of (4) and (7),

$$U_{\text{total}} = U_{\text{int}} + U_{\text{ext}} = \frac{1}{2}\int_0^{2\pi}\Omega d\theta, \quad (8)$$

where Ω is the total energy per unit θ and is a function of $\hat{u}$, $\hat{w}$, Φ, and κ.

From the Calculus of Variations we have the following four Euler's equations which enforce stationarity of U_{total}. These four equations are the variationally consistent equilibrium equations for the problem.

$$\frac{\partial\Omega}{\partial\hat{u}} + \frac{\partial}{\partial\theta}\left(\frac{\partial\Omega}{\partial\hat{u}}\right) = 0$$

$$\frac{\partial\Omega}{\partial\hat{w}} + \frac{\partial}{\partial\theta}\left(\frac{\partial\Omega}{\partial\hat{w}'}\right) = 0$$

$$\frac{\partial\Omega}{\partial\Phi} + \frac{\partial}{\partial\theta}\left(\frac{\partial\Omega}{\partial\Phi'}\right) = 0$$

$$\frac{\partial\Omega}{\partial\kappa} + \frac{\partial}{\partial\theta}\left(\frac{\partial\Omega}{\partial\kappa'}\right) = 0 \quad (9)$$

To find the buckling load and the initial post-buckling response, we use the adjacent equilibrium method. The following perturbations for $\hat{u}$, $\hat{w}$, Φ, κ and q are substituted into (9) and the coefficients of different powers in e, an infinitesimal perturbation magnitude, are collected and grouped together:

$$\hat{u} = eu_1 + e^2u_2 + e^3u_3$$

$$\hat{w} = w_0 + ew_1 + e^2w_2 + e^3w_3$$

$$\Phi = e\Phi_1 + e^2\Phi_2 + e^3\Phi_3$$

$$\kappa = e\kappa_1 + e^2\kappa_2 + e^3\kappa_3$$

$$q = q_0 + eq_1 + e^2q_2 + e^3q_3. \quad (10)$$

The pertubations are carried out up to terms that are $O(e^3)$. We have set u_0, Φ_0, and κ_0 to zero and w_0 to be independent of θ in the perturbation analysis, since we are interested in investigating adjacent equilibrium states that are characterized by the prebuckling solution, u_0, Φ_0, $\kappa_0 = 0$ and w_0 = constant. Substituting (10) into (9) we have the following governing equations:

$$e(\text{Buckling}_1) + e^2(\text{Post - buckling1}_1) + e^3(\text{Post - buckling2}_1) + \ldots \approx 0$$

$$\text{Prebuckling} + e(\text{Buckling}_2) + e^2(\text{Post - buckling1}_2)$$

Downloaded 04 May 2010 to 171.66.16.28. Redistribution subject to ASME license or copyright; see http://www.asme.org/terms/Terms_Use.cfm

$$+ e^3(\text{Post - buckling2}_2) + \ldots \approx 0$$

$$e(\text{Buckling}_3) + e^2(\text{Post - buckling1}_3) + e^3(\text{Post - buckling2}_3) + \ldots \approx 0$$

$$e(\text{Buckling}_4) + e^2(\text{Post - buckling1}_4) + e^3(\text{Post - buckling2}_4) + \ldots \approx 0, \quad (11)$$

where the meaning of the terms in the bracketed quantities will become apparent.

To obtain the prebuckling response of the ring we collect constant terms $O(e^0)$ in the second of Eq. (11) and solve for w_0, the prebuckling radial displacement. In this manner, we obtain the prebuckling radial displacement, in the case of an isotropic ring to be

$$w_0 = -a + \frac{a\sqrt{AE - 2aq_0(1 - \nu^2)}}{\sqrt{AE}}. \quad (12)$$

Where A is the cross-sectional area and a, the mean radius of the ring. Substituting (12) into the equations obtained by collecting terms that are coefficients of e and solving for the nontrivial solution to the homogeneous equations thus obtained, we compute the buckling load of the ring. Since a symbolic solution to the problem is not easily obtainable due to the complexity of the nonlinear strain-displacement relationships used, a numerical solution is presented. The results of the buckling load obtained with the one-dimensional shear deformation analysis for different (D/t) ratios are compared to those obtained by El Naschie and El Nashai (1976) and a two-dimensional ring analysis which will be presented later in the paper. The buckling mode is obtained by normalizing the amplitude with respect to w_1.

Collecting terms associated with $O(e^2)$ in each of the equations of (11) and substituting in the values for w_0 and the buckling load and mode, we have the governing equations for the solution of q_1, the asymmetric initial post-buckling coefficient of the problem. To obtain the initial post-buckling response, we have to proceed to a higher order, that is equations associated with e^3. Solving for the particular solution associated with the equations generated by terms associated with e^2 in (11), we obtain the solution to u_2, w_2, Φ_2 and κ_2.

In a similar manner, collecting terms associated with $O(e^3)$ in each of the equation in (11) and substituting in the various values of w_0, q_0, q_1, u_1, w_1, Φ_1, κ_1, u_2, w_2, Φ_2 and κ_2, we obtain equations for the solution of q_2, the symmetric initial post-buckling response of the ring. Through the elimination of "secular terms" in the resulting equation, we obtain the solution to q_2 and this is presented alongside values for q_2 obtained from El Naschie and El Nashai (1976) and the two-dimensional ring analysis (to be presented next) in Table 1.

In order to convey the meaning of q_2, all of the theories are employed to predict the response of imperfect rings and the results for the radial displacement predicted by each theory, are graphically presented, as a function of external pressure in Figs. 5, 6, 8, and 9.

Two-Dimensional Buckling and Initial Post-buckling Ring Analysis. Kardomates (1992, 1993), showed that the buckling loads of thick rings are highly dependent on the ring thickness. He also showed that one-dimensional models are poor in predicting the buckling load of thick rings. In the analysis to be presented, a variational method based on an energy approach is used to investigate thickness effects on the initial post-buckling behavior of thick rings, adopting the two-dimensional elastic stability equations.

Figure 2 will help illustrate the problem that is being studied. No assumptions are placed on the displacement fields, u_r(radial) or u_θ (circumferential) and they are functions of both r and θ, the radial and circumferential coordinates, respectively. The uniform external pressure is applied on the outer radius of the ring rather than the centroidal line, unlike in the one-dimensional shear deformation model.

In polar coordinates

$$x = r\cos\theta$$
$$y = r\sin\theta$$
$$z = z. \quad (13)$$

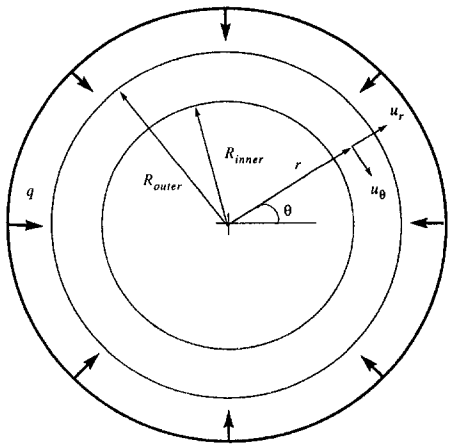

Fig. 2 Coordinate convention adopted (two-dimensional analysis)

Table 1 Buckling and initial post-buckling (q2) values for aluminum ring

Diameter./ Thickness	2-D Buckling Load (psi)	1-D Shear Deformation Buckling Load (psi)	El Naschie's Buckling Load (psi)	2-D Initial postbuckling	1-D Shear Initial Post-bucking	El Naschie's Initial postbuckling
80	39.035	38.086	39.063	2.0253	2.4718	2.0599
60	92.476	90.239	92.593	8.6268	10.401	8.6806
40	311.61	304.18	312.50	65.177	78.666	65.918
20	2471.3	2417.2	2500.0	2014.4	2462.7	2109.4
18	3380.7	3308.9	3429.4	3374.0	4142.1	3572.3
16	4795.1	4697.7	4882.8	5986.6	7392.9	6437.3
14	7117.5	6982.8	7288.6	11408.	14213.	12551.
12	11204.	11017.	11574.	23792.	30063.	27127.
10	19083.	18836.	20000.	55704.	72167.	67500.
8	36290.	36084.	39063.	151100.	206068.	206000.
6	81232.	82125.	92593.	477760.	750593.	868060.

Downloaded 04 May 2010 to 171.66.16.28. Redistribution subject to ASME license or copyright; see http://www.asme.org/terms/Terms_Use.cfm

Simplifying equation (1) for a two-dimensional ring, we have the following expressions for the nonlinear strains:

$$\epsilon_{22} = \epsilon_{rr} = \frac{\partial u_r}{\partial r} + \frac{1}{2}\left[\left(\frac{\partial u_r}{\partial r}\right)^2 + \left(\frac{\partial u_\theta}{\partial r}\right)^2\right]$$

$$\epsilon_{11} = \epsilon_{\theta\theta} = \left(\frac{1}{r}\frac{\partial u_\theta}{\partial \theta} + \frac{u_r}{r}\right) + \frac{1}{2}\left[\left(\frac{1}{r}\frac{\partial u_\theta}{\partial \theta} + \frac{u_r}{r}\right)^2 + \left(\frac{1}{r}\frac{\partial u_r}{\partial \theta} - \frac{u_\theta}{r}\right)^2\right]$$

$$\epsilon_{12} = \epsilon_{r\theta} = \left(\frac{\partial u_\theta}{\partial r} - \frac{u_\theta}{r} + \frac{1}{r}\frac{\partial u_r}{\partial \theta}\right) + \frac{\partial u_r}{\partial r}\left(\frac{1}{r}\frac{\partial u_r}{\partial \theta} - \frac{u_\theta}{r}\right) + \frac{\partial u_\theta}{\partial r}\left(\frac{1}{r}\frac{\partial u_\theta}{\partial \theta} + \frac{u_r}{r}\right). \quad (14)$$

The two-dimensional isotropic generalized plane stress relationships are as given by (6). If a composite ring is being analyzed, the Q_{ij} matrix used will be that for the composite material in question (15).

$$[Q_{ij}] = \begin{bmatrix} \frac{E_\theta}{1-\nu_{r\theta}\nu_{\theta r}} & \frac{\nu_{r\theta}E_r}{1-\nu_{r\theta}\nu_{\theta r}} & 0 \\ \frac{\nu_{r\theta}E_r}{1-\nu_{r\theta}\nu_{\theta r}} & \frac{E_r}{1-\nu_{r\theta}\nu_{\theta r}} & 0 \\ 0 & 0 & G_{r\theta} \end{bmatrix}, \quad (15)$$

where standard notation is used (see Lekhnitskii (1981) or Jones (1975), for example).

The internal strain energy is given by

$$U_{\text{int}} = \frac{1}{2}\int_V \sigma_{ij}\epsilon_{ij}dV = \frac{t}{2}\int_0^{2\pi}\int_{R_{\text{inner}}}^{R_{\text{outer}}} \sigma_{ij}\epsilon_{ij}rdrd\theta = \frac{t}{2}\int_0^{2\pi}\int_{R_{\text{inner}}}^{R_{\text{outer}}} [Q_{rrrr}\epsilon_{rr}^2 + Q_{r\theta r\theta}\epsilon_{r\theta}^2 + Q_{\theta\theta\theta\theta}\epsilon_{\theta\theta}^2 + 2Q_{rr\theta\theta}\epsilon_{\theta\theta}\epsilon_{rr}]rdrd\theta \quad (16)$$

and the work done by the external pressure loading acting on the edge $r = R_{\text{outer}}$ is given by

$$\Omega = qR_{\text{outer}}\int_0^{2\pi}\left[u_r + \frac{1}{2}\left(\frac{u_\theta^2}{R_{\text{outer}}} - \frac{u_\theta}{R_{\text{outer}}}\frac{\partial u_r}{\partial \theta} + \frac{u_r}{R_{\text{outer}}}\frac{\partial u_\theta}{\partial \theta} + \frac{u_r^2}{R_{\text{outer}}}\right)\right]_{r=R_{\text{outer}}} d\theta. \quad (17)$$

Thus the total work done is given by

$$U_{\text{total}} = U_{\text{int}} + \Omega. \quad (18)$$

Utilizing the Principle of Virtual Work and the Calculus of Variations, we have the following two governing equations for the problem:

$$\delta U_{\text{total},u_r} = t\int_0^{2\pi}\int_{R_{\text{inner}}}^{R_{\text{outer}}}\left[A_1\frac{\partial}{\partial r}(\delta u_r) + \frac{A_2}{r}\frac{\partial}{\partial \theta}(\delta u_r) + \frac{A_3}{r}(\delta u_r)\right]drd\theta$$

$$\delta U_{\text{total},u_\theta} = t\int_0^{2\pi}\int_{R_{\text{inner}}}^{R_{\text{outer}}}\left[A_4\frac{\partial}{\partial r}(\delta u_\theta) + \frac{A_5}{r}\frac{\partial}{\partial \theta}(\delta u_\theta) + \frac{A_6}{r}(\delta u_\theta)\right]drd\theta \quad (19)$$

where A_i, $i = 1,2,3,4,5,6$ are functions of r and θ. Here

$$A_1 = r\left[\sigma_{rr}\left(1 + \frac{\partial u_r}{\partial r}\right) + \sigma_{r\theta}\left(\frac{1}{r}\frac{\partial u_r}{\partial \theta} - \frac{u_\theta}{r}\right)\right]$$

$$A_2 = r\left[\sigma_{\theta\theta}\left(\frac{1}{r}\frac{\partial u_r}{\partial \theta} - \frac{u_\theta}{r}\right) + \sigma_{r\theta}\left(1 + \frac{\partial u_r}{\partial r}\right)\right]$$

$$A_3 = r\left[\sigma_{\theta\theta}\left(1 + \frac{u_r}{r} + \frac{1}{r}\frac{\partial u_\theta}{\partial \theta}\right) + \sigma_{r\theta}\left(\frac{\partial u_\theta}{\partial r}\right)\right] \quad (20)$$

and

$$A_4 = r\left[\sigma_{rr}\left(\frac{\partial u_\theta}{\partial r}\right) + \sigma_{r\theta}\left(1 + \frac{u_r}{r} + \frac{1}{r}\frac{\partial u_\theta}{\partial \theta}\right)\right]$$

$$A_5 = r\left[\sigma_{\theta\theta}\left(1 + \frac{u_r}{r} + \frac{1}{r}\frac{\partial u_\theta}{\partial \theta}\right) + \sigma_{r\theta}\left(\frac{\partial u_\theta}{\partial r}\right)\right]$$

$$A_6 = (-r)\left[\sigma_{\theta\theta}\left(\frac{1}{r}\frac{\partial u_r}{\partial \theta} - \frac{u_\theta}{r}\right) + \sigma_{r\theta}\left(1 + \frac{\partial u_r}{\partial r}\right)\right]. \quad (21)$$

Integrating (19) by parts, we have the following set of two governing equations and four boundary conditions:

$$\frac{A_6}{r} - \frac{\partial A_4}{\partial r} - \frac{1}{r}\frac{\partial A_5}{\partial \theta} = 0$$

$$\frac{A_3}{r} - \frac{\partial A_1}{\partial r} - \frac{1}{r}\frac{\partial A^2}{\partial \theta} = 0 \quad (22)$$

and

$$\left[A_1 + qR_{\text{outer}}\left(1 + \frac{u_r}{R_{\text{outer}}} + \frac{1}{R_{\text{outer}}}\frac{\partial u_\theta}{\partial \theta}\right)\right]_{r=R_{\text{outer}}} = 0$$

$$\left[A_4 + qR_{\text{outer}}\left(\frac{u_\theta}{R_{\text{outer}}} - \frac{1}{R_{\text{outer}}}\frac{\partial u_r}{\partial \theta}\right)\right]_{r=R_{\text{outer}}} = 0$$

$$A_1|_{r=R_{\text{inner}}} = 0$$

$$A_4|_{r=R_{\text{inner}}} = 0. \quad (23)$$

Again, by substituting the following perturbations (24) into (22) and (23) and collecting terms in e^0, e^1, e^2, and e^3, we have a set of two governing second-order differential equations and four associated boundary conditions for each of the prebuckling, buckling, and post-buckling states. Thus,

$$u_r = u_{r0} + eu_{r1} + e^2u_{r2} + e^3u_{r3} + \ldots$$

$$u_\theta = eu_{\theta 1} + e^2u_{\theta 2} + e^2u_{\theta 3} + \ldots$$

$$q = q_0 + eq_1 + e^2q_2 + e^3q_3 + \ldots. \quad (24)$$

The prebuckling equations are solved symbolically but the buckling and initial post-buckling solutions are obtained numerically utilizing Galerkin's method. The numerical approach is adopted as the symbolic solutions are too complicated and time consuming. From the eliminations of secular terms in the resulting differential equations, we found that q_1 is again identically zero and that the ring exhibits symmetric post-buckling response. Numerical results were obtained for aluminum rings for various diameters with a fixed thickness of 0.1 inches. These results are presented in the next section along with the results obtained for the buckling load by Brush and Almroth (1975) and the initial post-buckling response by El Naschie (1975).

Downloaded 04 May 2010 to 171.66.16.28. Redistribution subject to ASME license or copyright; see http://www.asme.org/terms/Terms_Use.cfm

Galerkin Solution Technique. Since a symbolic solution to the buckling and initial post-buckling analysis is not readily obtainable, Galerkin's Method was utilized to obtain a numerical solution to the problem. The buckling load requires the solution of an eigenvalue problem, and the displacement field chosen is

$$u_{r1} = \sum_{i=1}^{N} A_i L_i(r) \cos(\lambda\theta)$$

$$u_{\theta 1} = \sum_{i=1}^{N} B_i L_i(r) \sin(\lambda\theta). \tag{25}$$

Here A_i and B_i are the unknown coefficients of the problem and $L_i(r)$ is the ith Legendre polynomial. Equations (25) are substituted into the $O(\epsilon)$ governing and boundary equations from which the buckling load, q_0, and the value of λ in (25) are computed.

The initial post-buckling solution was obtained by seeking the approximation to the displacement fields as given by

$$u_{r2} = \sum_{i=1}^{N} C_i L_i(r) \cos(n\theta) \quad \text{and} \quad u_{\theta 2} = \sum_{i=1}^{N} D_i L_i(r) \sin(n\theta)$$

with C_i and D_i as yet undetermined constants. The solutions obtained from the buckling analysis (i.e., u_r, u_θ, λ, and q_0) were substituted into the $O(\epsilon^2)$ governing and boundary equations, and through the elimination of secular terms in the resulting equations, q_1 was obtained. In addition, the displacement fields u_{r2} and $u_{\theta 2}$ were obtained. q_1 was determined to be identically zero.

Next, displacement fields similar to (26) were utilized for u_{r3}, $u_{\theta 3}$ and these were substituted, along with the previously determined solution of u_{r2}, $u_{\theta 2}$ and q_1(q_1 turned out to be zero), into the $O(\epsilon^3)$ governing and boundary equations. Through the elimination of secular terms in the resulting equations, we obtained the nontrivial solution to the symmetric initial post-buckling coefficient, q_2, the numerical results of which are presented in Table 1. Since the governing equations are highly nonlinear it was not possible to effect a closed-form solution, even with the aid of a powerful symbolic solver such as Mathematica. However, with the assumed displacement fields (25)–(27) in conjunction with the Galerkin Method, we were able to obtain converged results, while adopting only a few terms in the series for the displacements u_{ri} and $u_{\theta i}$ $[i = 1, 2, 3]$. It is to be noted that the symbolic manipulator affords internal precision in its computation to many significant digits, which can be defined by the user. For more details about the precision involved in computation using Mathematica, the reader is referred to Wolfram (1992).

Results and Discussion

Example results are presented for aluminum and S-2 Glass/Epoxy rings of different diameter to thickness ratios. The Young's Modulus used here for the isotropic aluminum ring is 10E6 psi and the Poisson's ratio is 0.33 while the S-2 Glass/Epoxy properties are $E_{\theta\theta} = 7.83 \times 10^6$ psi, $E_{rr} = 1.87 \times 10^6$ psi, $G_{r\theta} = 0.98 \times 10^6$ psi and $\nu_{r\theta} = 0.31$. Figure 3 indicates the material coordinate directions. The thickness of the aluminum rings are kept constant at 0.1 in. while the diameter of the rings are varied to produce different diameter/thickness ratios. First, we shall examine the results for the isotropic ring.

It is observed from the table of results above and Fig. 4 that the two-dimensional and the one-dimensional shear deformation buckling loads are lower than the classical Levy result presented in Brush and Almroth (1975) and Sills and Budiansky (1978). It is also observed that as the diameter-to-thickness ratio decreases, the difference in the results between those obtained via the formulation in El Naschie and El Nashai (1976) and the two-dimensional and one-dimensional shear deformation formulation presented here increases. This finding indicates that the formulation in El Naschie and El Nashai (1976), Brush and Almroth (1975) and Sills and Budiansky (1978) is good for predicting the buckling load of isotropic rings with a diameter-to-thickness ratio of greater than about 20. The shear deformation results were found to approach the two-dimensional results from below, thus indicating that the one-dimensional shear deformation model is "softer" and underpredicts the buckling load of the ring. The results for the buckling load obtained from the two-dimensional analysis and the one-dimensional shear deformation analysis are compared to that presented in Brush and Almroth (1975). From Table 1, it is seen that for a ring of diameter-to-thickness ratio of 20, the one-dimensional shear deformation theory underpredicts the buckling load (as compared to the two-dimensional theory which is more exact) by 2.2 percent while the classical theory overpredicts this number 1.2 percent.

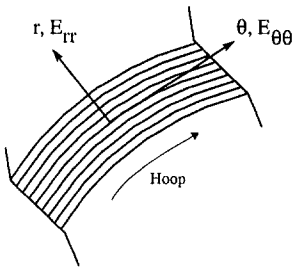

Fig. 3 Coordinate and material axes for orthotropic ring

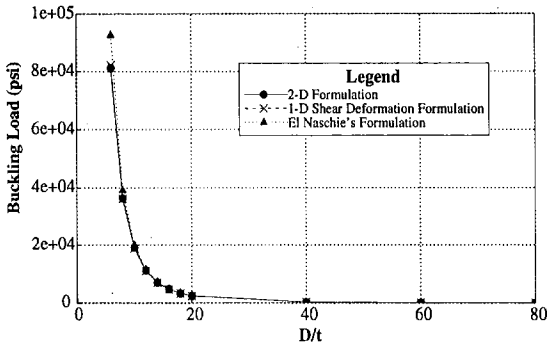

Fig. 4 Plot of buckling load versus diameter / thickness ratio (Al Rings)

Similarly, it is evident from Table 1 that both the one-dimensional shear and El Naschie's results for the initial post-buckling coefficient over predicts the initial post-buckling stability of the ring. From the results obtained above in Table 1 it can be concluded that if the diameter-to-thickness ratio is less than about 20, then a two-dimensional analysis would have to be used to predict the initial post-buckling behavior of the ring in question. The initial post-buckling response of imperfect rings, based on the various theories presented so far and computed on the basis of q_2 and the Koiter (asymptotic) approach to initial post-buckling behavior (see Koiter, 1970; Hutchinson and Koiter, 1970; Dym, 1974) is shown in Figs. 5 and 6. The results in Fig. 5 are for a ring whose $D/t = 80$ (thin) while those in Fig. 6 are for a ring whose $D/t = 8$ (thick). The results in these figures are for an aluminium ring. Notice that now, both the one-dimensional shear deformation and El Naschie (1975) results predict a post-buckling response that shows less stiffness in the initial post-buckling regime compared to the two-dimensional result.

For the hoop wound S-2 Glass/Epoxy rings, we would

Downloaded 04 May 2010 to 171.66.16.28. Redistribution subject to ASME license or copyright; see http://www.asme.org/terms/Terms_Use.cfm

expect the differences in the buckling load and the initial post-buckling coefficient obtained via different theories to be even larger as the shear modulus now is much less than $E_{\theta\theta}/(2(1+\nu_{r\theta}))$ and $E_{rr} < E_{\theta\theta}$. The results computed for the S-2 Glass/Epoxy rings of different diameter/thickness ratios are presented in Table 2 below.

From Table 2 and Fig. 7 we can see that though the different theories converge to the same results for the buckling load at high diameter/thickness ratios, the results obtained for low diameter/thickness ratio rings via the different theories are markedly different from each other. Comparing the results from Fig. 4 and Fig. 7 it is noted that the percentage error in the buckling loads computed is even higher (as compared with the aluminum rings) for the hoop wound S-2 Glass/Epoxy rings as the diameter/thickness ratio increases. This is as expected as the hoop wound S-2 Glass/Epoxy rings are very weak in shear when compared to their isotropic counterparts. As indicated in Fig. 7, the buckling load prediction for the S-2 Glass/Epoxy rings utilizing the formulation in El Naschie and El Nashai (1976), is only accurate for a diameter/thickness ratio larger than about 50. For diameter/thickness ratios smaller than 50, a two-dimensional or a one-dimensional shear deformation formulation predicts accurate buckling results. Also included in Fig. 7 is the experimental data obtained by Fu and Waas (1994). As can be seen, the experimental results are modeled well by the two-dimensional and one-dimensional shear deformation theories. From Table 2 it is also clear that the one-dimensional shear deformation formulation is quite accurate in predicting the buckling load of thick rings for a diameter/thickness ratio over about 16 and that in general is a good formulation for predicting the buckling load of relatively thick composite rings.

Plots corresponding to Fig. 5 and Fig. 6, but for a S-2

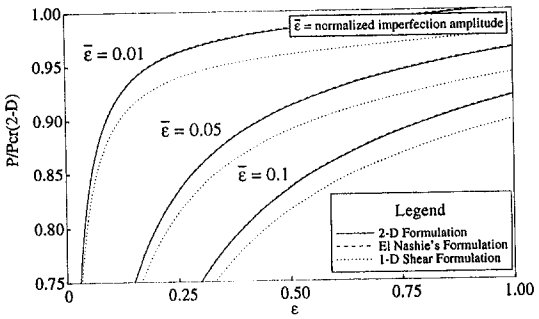

Fig. 5 Plot of radial deflection versus pressure for aluminium ring with diameter / thickness ratio of 80

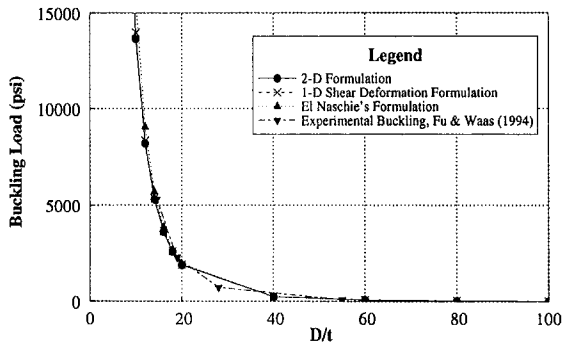

Fig. 7 Plot of buckling load versus diameter / thickness ratio (S-2 glass / epoxy rings)

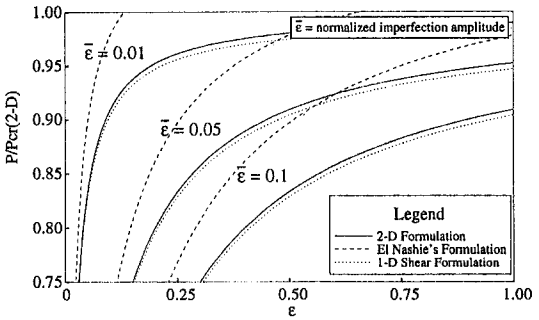

Fig. 6 Plot of radial deflection versus pressure for aluminium ring with diameter / thickness ratio of 8

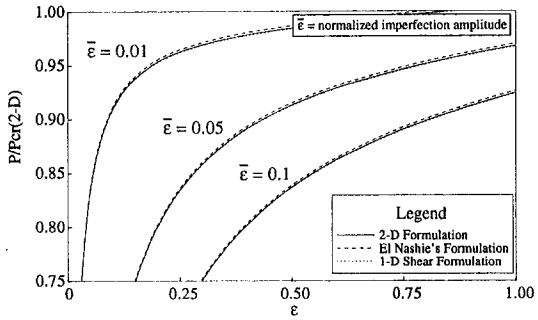

Fig. 8 Plot of radial deflection versus pressure for S-2 glass / epoxy ring with diameter/ thickness ratio of 80

Table 2 Buckling and initial post-buckling (q2) values for S-2 glass / epoxy ring

Diameter./ Thickness	2-D Buckling Load (psi)	1-D Shear Deformation Buckling Load (psi)	El Naschie's Buckling Load (psi)	2-D Initial postbuckling	1-D Shear Initial Post-bucking	El Naschie's Initial postbuckling
100	15.6446	15.6346	15.6660	0.56991	0.64990	0.52873
80	30.5305	30.5157	30.5977	1.65019	1.97907	1.61355
60	72.2472	72.2285	72.5278	6.69049	8.30098	6.79948
40	242.321	242.764	244.781	49.8582	62.1995	51.6335
20	1889.86	1899.72	1958.25	1428.41	1850.63	1652.27
18	2570.95	2588.24	2686.21	2334.34	3062.71	2798.14
16	3618.49	3650.58	3824.71	3998.08	5343.00	5042.34
14	5311.59	5375.55	5709.18	7221.41	9930.14	9830.86
12	8221.93	8361.82	9065.97	13791.5	19913.7	21248.4
10	13626.8	13975.4	15666.0	27495.5	43578.5	52872.8
8	24725.9	25740.0	30597.7	49762.8	103173.	161355.

Downloaded 04 May 2010 to 171.66.16.28. Redistribution subject to ASME license or copyright; see http://www.asme.org/terms/Terms_Use.cfm

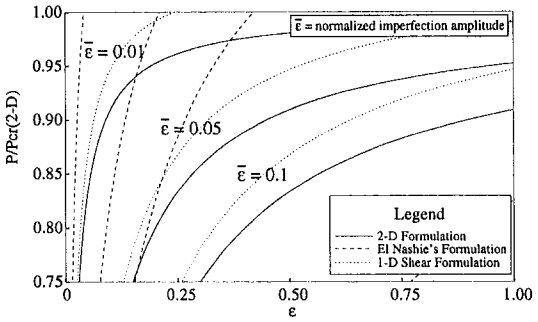

Fig. 9 Plot of radial deflection versus pressure for S-2 glass / epoxy ring with diameter / thickness ratio of 8

Glass/Epoxy ring, are presented in Fig. 8 and Fig. 9. The difference in the predictions from the different theories are more pronounced here than for the isotropic case, as is evident in these figures. This is due to the fact that the shear modulus and the through thickness Young's modulus is much smaller compared to the hoop modulus. Such a disparity did not exist for the isotropic case. The one-dimensional shear deformation formulations (presented here and in El Naschie, 1975) are found to be less accurate in predicting the initial post-buckling stability of a thick composite ring than it did in the buckling load calculations. Thus, the use of one-dimensional theories for post-buckling calculations involving thick rings, similar to that studied here, is not recommended. The one-dimensional model fails to account for the weak through the thickness properties. In spite of this the buckling loads were predicted with a reasonable level of accuracy for a wide range of (diameter/thickness) ratios. However, unless the rings are very "thin" (diameter/thickness > 50, say), the one-dimensional theories are inadequate in describing the initial post-buckling behavior. Thus, it appears that the orthotropicity of the ring structure has a considerable influence upon the post-buckling deformations of the rings and this feature necessitates a two-dimensional treatment in considering the post-buckling response of composite rings.

Concluding Remarks

In this paper, a two-dimensional elasticity solution for the buckling and initial post-buckling behavior of thick isotropic and composite rings have been presented. Example results for aluminum and hoop wound S-2 Glass/Epoxy rings have been presented. The two-dimensional elasticity result serves as a benchmark to evaluate other approximate theories for the modeling of thick composite rings. It is seen that, in the case of composite rings, the (diameter/thickness) ratios beyond which a"thin" ring assumption can be utilized is dependent on the orthotropic material constants of the ring material and cannot be guided by standards based upon theories established for isotropic materials. Furthermore, for $(D/t) \leq 15$, the initial post-buckling behavior of any ring, isotropic or otherwise, is not adequately described by one-dimensional beam-type theories. Therefore, in examining the post-buckling behavior of thick composite shells, one needs to adopt higher-order shell theories that are capable of accounting for the through thickness (transverse) properties of the shell material in a systematic way, in light of the presented findings.

Acknowledgments

The authors are appreciative of the financial sponsorship of the ONR, Mechanics Division, through grant N00014-91-J-1705, with Dr. Y. D. S. Rajapakse as the Scientific Officer.

References

Anderson, R. H., and Boresi, A. P., 1962, "Equilibrium and Stability of Rings Under Nonuniformly Distributed Loads," *Proceedings of the 4th U.S. National Congress of Applied Mechanics*, Vol. 1, pp. 459–468.

Bodner, S. R., 1958, "On the Conservativeness of Various Distributed Force Systems," *Journal of Aeronautical Sciences*, Vol. 25, No. 2, pp. 132.

Boresi, A. P., 1955, "A Refinement of the Theory of Buckling of Rings under Uniform Pressure," ASME JOURNAL OF APPLIED MECHANICS, Vol. 22, pp. 95–102.

Brush, D. O., and Almroth, B. O., 1975, *Buckling of Bars, Plates and Shells*, McGraw-Hill, New York, pp. 186–198.

Budiansky, B., 1974, "Theory of Buckling and Postbuckling Behavior of Elastic Structures," *Advances in Applied Mechanics*, Vol. 14, pp. 1–65.

Carrier, G. F., 1947, "On the Buckling of Elastic Rings," *Journal Mathematics and Physics*, Vol. 17, pp. 94–103.

Duffey, T. A., Warnes, R. H., and Greene, J. M., 1991, "Growth of Buckling Instabilities during Radial Collapse of a Ring," *Journal of Pressure Vessel Technology*, Vol. 112, pp. 145–151.

Dym, C. L., 1974, *Stability Theory and Its Applications to Structural Mechanics*, Noordhoff, Leyden, Netherlands.

El Naschie, M. S., 1975a, "Asymptotic Postbuckling Solution of the Ring in an Elastic Foundation," *AIAA Journal*, Vol. 13, No. 1, pp. 113–114.

El Naschie, M. S., 1975b, "The Initial Postbuckling of an Extensional Ring under External Pressure," *International Journal of Mechanical Sciences*, Vol. 17, pp. 387–388.

El Naschie, M. S., and El Nashai, A., 1976, "Influence of Loading Behavior on the Postbuckling of Circular Rings," *AIAA Journal*, Vol. 14, No. 2, pp. 266–267.

Fu, L., and Waas, A. M., 1994, "Experimental Testing of Composite Rings under Uniform Hydrostatic Pressure," *AIAA-94-1343-CP*, presented at the 35th AIAA SDM Meeting, Apr. 18–20, 1994; full paper to appear in *J. Composite Structures* (1995).

Hubka, W. F., 1973, "Post-buckling Analysis of a Circular Ring Subjected to Hydrostatic Pressure," ASME JOURNAL OF APPLIED MECHANICS, Vol. 40, pp. 819–898.

Hutchinson, J. W., and Koiter, W. T., 1970, "Postbuckling Theory," *Applied Mechanics Reviews*, Vol. 23, No. 12, p. 1353.

Jones, R. M., 1975, *Mechanics of Composite Materials*, Hemisphere, New York.

Ju, G. T., and Kyriakides, S., 1991, "Bifurcation Buckling versus Limit Load Instabilities of Elastic-Plastic Tubes under Bending and External Pressure," *Journal of Offshore Mechanics and Arctic Engineering*, Vol. 113, pp. 43–52.

Kardomateas, G. A., 1992, "Stability Loss in Thick Orthotropic Cylindrical Shells under External Pressure," AIAA-92-2231-CP, pp. 79–85.

Kardomateas, G. A., "Buckling of Thick Orthotropic Cylindrical Shells under External Pressure," ASME JOURNAL OF APPLIED MECHANICS, to be published.

Koiter, W. T., 1963, "Elastic Stability and Postbuckling Behavior," *Proceedings of the Symposium on Nonlinear Problems*, R. E. Langer, ed., University of Wisconsin Press, Madison, pp. 257–275.

Koiter, W. T., 1970, "The Stability of Elastic Equilibrium," Technical Report AFFDL TR-70-25, Wright-Patterson Air Force Base.

Kyriakides, S., and Babcock, C. D., 1981, "Large Deflection Collapse Analysis of an Inelastic Inextensional Ring under External Pressure," *International Journal of Solids Structures*, Vol. 17, No. 10, pp. 981–993.

Lekhnitskii, S. G., 1981, *Theory of Elasticity of an Anisotropic Body*, Mir Publishers, Moscow.

Lo, H., Bogdanoff, J. L., and Goldberg, J. E., 1962, "A Buckling Problem of a Circular Ring," *ASME Proceedings of the Fourth U. S. National Congress of Applied Mechanics*, pp. 691–695.

Marshall, J. G., and Moshaiov, A., 1990, "The Buckling of Delaminated Rings Subjected to Hydrostatic Pressure," *Composite Structures*, Vol. 14, pp. 193–211.

Novozhilov, V. V., 1953, *Foundations of the Nonlinear Theory of Elasticity*, Graylock Press, Rochester, New York.

Reddy, J. N., 1984, "A Simple Higher Order Theory for Laminated Composite Plates," ASME JOURNAL OF APPLIED MECHANICS, Vol. 51, pp. 745–755.

Sills, L. B., and Budiansky, B., 1978, "Postbuckling Ring Analysis," ASME JOURNAL OF APPLIED MECHANICS, Vol. 45, pp. 208–210.

Smith, C. V., and Simitses, G. J., 1969, "Effect of Shear and Load Behavior on Ring Stability," *ASCE Journal of the Engineering Mechanics Division*, Vol. 95, No. EM3, pp. 559–569.

Singer, J., and Babcock, C. D., 1970, "On the Buckling of Rings Under Constant Directional and Centrally Directed Pressure," ASME JOURNAL OF APPLIED MECHANICS, Vol. 37, pp. 215–218.

Stoker, J. J., 1968, *Nonlinear Elasticity*, Gordon and Breach, New York.

Thompson, J. M. T., 1969, "A General Theory for the Equilibrium and Stability of Discrete Conservative Systems," *Zeitschrift fuer Angewandt Mathematik und Physik*, Vol. 20, pp. 797–846.

Timoshenko, S. P., 1921, "On the Correction for Shear of the Differential Equation of Transverse Vibrations of Prismatic Bars," *Philos. Mag.*, Ser. 6, Vol. 21.

Wolfram, S., 1988, *Mathematica, A System for Doing Mathematics by Computer*, Addison-Wesley, New York.

Downloaded 04 May 2010 to 171.66.16.28. Redistribution subject to ASME license or copyright; see http://www.asme.org/terms/Terms_Use.cfm

Three-Dimensional Elasticity Solution for the Buckling of Transversely Isotropic Rods: The Euler Load Revisited

G. A. Kardomateas
School of Aerospace Engineering,
Georgia Institute of Technology,
Atlanta, GA 30332-0150
Mem. ASME

The bifurcation of equilibrium of a compressed transversely isotropic bar is investigated by using a three-dimensional elasticity formulation. In this manner, an assessment of the thickness effects can be accurately performed. For isotropic rods of circular cross-section, the bifurcation value of the compressive force turns out to coincide with the Euler critical load for values of the length-over-radius ratio approximately greater than 15. The elasticity approach predicts always a lower (than the Euler value) critical load for isotropic bodies; the two examples of transversely isotropic bodies considered show also a lower critical load in comparison with the Euler value based on the axial modulus, and the reduction is larger than the one corresponding to isotropic rods with the same length over radius ratio. However, for the isotropic material, both Timoshenko's formulas for transverse shear correction are conservative; i.e., they predict a lower critical load than the elasticity solution. For a generally transversely isotropic material only the first Timoshenko shear correction formula proved to be a conservative estimate in all cases considered. However, in all cases considered, the second estimate is always closer to the elasticity solution than the first one and therefore, a more precise estimate of the transverse shear effects. Furthermore, by performing a series expansion of the terms of the resulting characteristic equation from the elasticity formulation for the isotropic case, the Euler load is proven to be the solution in the first approximation; consideration of the second approximation gives a direct expression for the correction to the Euler load, therefore defining a new, revised, yet simple formula for column buckling. Finally, the examination of a rod with different end conditions, namely a pinned-pinned rod, shows that the thickness effects depend also on the end fixity.

Introduction

The elastic buckling of slender rods and beams was the first stability problem to be investigated because of its historical importance in construction engineering. Recently, demands in the analysis and the design of light and highly stiff structures of many types, made of advanced composite materials and capable of carrying relatively high loads have been directly responsible for increased interest in extending the theoretical knowledge in this area.

When a bar is initially straight and of perfect geometry, and subjected to the action of a compressive force without eccentricity, it has been called an "ideal column."The case of a slender, ideal column, which is built in vertically at the base, free at the upper end, and subjected to an axial force P, constitutes the first problem of bifurcation buckling, the one that was originally solved by Euler (1744, 1933). The Euler solution is based on the well known Euler-Bernoulli assumptions (i.e., plane sections remain plane after bending, no effect of transverse shear) and for an isotropic elastic material. Nontrivial solutions (nonzero transverse deflections) are then sought for the equations governing bending of the column under an axial compressive load, and subject to the particular set of boundary conditions; thus, the problem is reduced to an eigen boundary value problem (e.g., Simitses, 1986).

As the cross-sectional dimensions of a rod increase relative to the length, it is naturally expected that the classical Euler

Contributed by the Applied Mechanics Division of THE AMERICAN SOCIETY OF MECHANICAL ENGINEERS for presentation at the Joint Applied Mechanics and Materials Summer Meeting of the ASME, Los Angeles, CA, June 28–30, 1995.

Discussion on this paper should be addressed to the Technical Editor, Professor Lewis T. Wheeler, Department of Mechanical Engineering, University of Houston, Houston, TX 77204-4792, and will be accepted until four months after final publication of the paper itself in the ASME JOURNAL OF APPLIED MECHANICS.

Manuscript received by the ASME Applied Mechanics Division, June 20, 1994; final revision, Oct. 27, 1994. Associate Technical Editor: R. Abeyaratne.

Paper No. 95-APM-6.

Copyright © 1995 by ASME

Downloaded 04 May 2010 to 171.66.16.28. Redistribution subject to ASME license or copyright; see http://www.asme.org/terms/Terms_Use.cfm

load would deviate from the exact critical load. A similar deviation is expected if the materials laws are not isotropic. The objective of the present paper is to investigate the extent to which the classical Euler load represents the critical load, as derived by three-dimensional elasticity analyses for a generally transversely isotropic rod with no restrictive assumptions regarding the cross-sectional dimensions.

Regarding elasticity solutions to buckling, Kumar and Niyogi (1982) studied the bifurcations in axially compressed thick elastic tubes by using the strain-energy function of Ogden (1972) to represent the material behavior in isotropic solids. A three-dimensional elasticity formulation and solution for buckling of orthotropic composite materials was presented by Kardomateas (1993a) in connection with the problem of buckling of thick cylindrical orthotropic shells subjected to external pressure. It was shown that the critical load predicted by shell theory can be quite non-conservative for thick construction. This work was based on the simplifying assumption that the pre-buckling stress and displacement field was axisymmetric, and the buckling modes were assumed two-dimensional (ring assumption); i.e., no z (axial) component of the displacement field, and no z-dependence of the r and θ displacement components. In a subsequent article, Kardomateas and Chung (1994) presented a solution that relaxes this ring approximation, i.e., based on a nonzero axial displacement and a full dependence of the buckling modes on the three coordinates.

In order to further assess the thickness effects on the stability of shells, Kardomateas (1993b) presented a solution for the case of a transversely isotropic thick cylindrical shell under axial compression. In that work, a full dependence on r, θ, and z of the buckling modes was assumed. The reason for restricting the material to transversely isotropic was the desire to produce closed form analytical solutions. The same problem of an axially loaded moderately thick cylindrical shell was treated in a subsequent study for the case of a generally orthotropic shell (Kardomateas, 1995). A comparison with various shell theories showed that for the isotropic material cases considered, both the Flügge (1960) and Danielson and Simmonds (1969) shell theories predicted critical loads much closer to the elasticity value than the Donnell (Brush and Almroth, 1975) theory; the elasticity approach predicted a lower critical load than all these classical shell theories, the percentage reduction being larger with increasing thickness. However, in this study, an additional shell theory, namely that of Timoshenko and Gere (1961), was examined. It was found that for both the orthotropic and the isotropic material cases, the Timoshenko bifurcation points are lower than the elasticity ones. This means that the Timoshenko formulation is conservative, unlike all the other shell theories examined.

Regarding the stability loss of elastic bars, the only alternative direct expressions to the Euler load that exist in the literature are two formulas suggested by Timoshenko and Gere (1961). These were intended to account for the influence of transverse shearing forces. These load expressions, denoted by P_{T1} and P_{T2}, are given in the Results section. Despite the simplicity of the derivation of these formulas, it will be seen that they perform remarkably well in accounting for the thickness effects as well as for the effects of a low ratio of shear versus extensional modulus. It should be noted that although a study of the buckling of a generally anisotropic rod would be desirable, this work is restricted to the case of transverse isotropy, because more general anisotropy would not allow a direct closed-form solution of the corresponding three-dimensional elasticity problem.

The study conducted in this paper includes specific results for the critical load and the buckling modes of a cylindrical rod under axial compression for various ratios of length over radius l/R. The effect of transverse isotropy is examined by considering two material cases: one that approximates glass/epoxy and the other that approximates graphite/epoxy, both with reinforcing direction along the z-axis. The results from the elasticity formulation will be compared with the classical Euler load predictions and with Timoshenko and Gere's (1961) column buckling with transverse shear correction formulas. Moreover, in addition to the historically important Euler rod of one end fixed and the other free, results for the bifurcation load of a rod with both ends pinned are produced.

Another important contribution of this work is the derivation of a new, simple formula for column buckling. This is achieved by performing a series expansion of the terms of the resulting characteristic equation from the elasticity formulation for the isotropic case. It is also proved that the Euler load is the solution of this elasticity formulation in the first approximation. The direct formula thus produced is shown to provide an excellent agreement to the elasticity results for isotropic columns.

Formulation

The equilibrium of a rod, considered as a three-dimensional elastic body, can be described in terms of the second Piola-Kirchhoff stress tensor $\mathbf{\Sigma}$ as follows (e.g., Ciarlet, 1988):

$$\mathrm{div}(\mathbf{\Sigma} \cdot \mathbf{F}^{\mathrm{T}}) = 0. \tag{1a}$$

Here $\mathbf{F}$ is the deformation gradient defined by

$$\mathbf{F} = \mathbf{I} + \mathrm{grad}V, \tag{1b}$$

where V is the displacement vector and $\mathbf{I}$ is the identity tensor.

It should be noticed that the strain tensor is defined by

$$\mathbf{E} = \frac{1}{2}(\mathbf{F}^{\mathrm{T}} \cdot \mathbf{F} - \mathbf{I}). \tag{1c}$$

Since we consider a circular section, we employ cylindrical coordinates, and we can specifically write the components of the deformation gradient $\mathbf{F}$ in terms of the linear strains:

$$\epsilon_{rr} = \frac{\partial u}{\partial r}, \quad \epsilon_{\theta\theta} = \frac{1}{r}\frac{\partial v}{\partial \theta} + \frac{u}{r}, \quad \epsilon_{zz} = \frac{\partial w}{\partial z}, \tag{2a}$$

$$\gamma_{r\theta} = \frac{1}{r}\frac{\partial u}{\partial \theta} + \frac{\partial v}{\partial r} - \frac{v}{r}, \quad \gamma_{rz} = \frac{\partial u}{\partial z} + \frac{\partial w}{\partial r},$$

$$\gamma_{\theta z} = \frac{\partial v}{\partial z} + \frac{1}{r}\frac{\partial w}{\partial \theta}, \tag{2b}$$

and the linear rotations:

$$2\omega_r = \frac{1}{r}\frac{\partial w}{\partial \theta} - \frac{\partial v}{\partial z}, \quad 2\omega_\theta = \frac{\partial u}{\partial z} - \frac{\partial w}{\partial r},$$

$$2\omega_z = \frac{\partial v}{\partial r} + \frac{v}{r} - \frac{1}{r}\frac{\partial u}{\partial \theta}, \tag{2c}$$

as follows:

$$\mathbf{F} = \begin{bmatrix} 1 + \epsilon_{rr} & \frac{1}{2}\gamma_{r\theta} - \omega_z & \frac{1}{2}\gamma_{rz} + \omega_\theta \\ \frac{1}{2}\gamma_{r\theta} + \omega_z & 1 + \epsilon_{\theta\theta} & \frac{1}{2}\gamma_{\theta z} - \omega_r \\ \frac{1}{2}\gamma_{rz} - \omega_\theta & \frac{1}{2}\gamma_{\theta z} + \omega_r & 1 + \epsilon_{zz} \end{bmatrix}. \tag{3}$$

At the critical load there are two possible infinitely close positions of equilibrium. Denote by u_0, v_0, w_0 the r, θ and z components of the displacement corresponding to the primary position. A perturbed position is denoted by

Downloaded 04 May 2010 to 171.66.16.28. Redistribution subject to ASME license or copyright; see http://www.asme.org/terms/Terms_Use.cfm

$$u = u_0 + \alpha u_1; \quad v = v_0 + \alpha v_1; \quad w = w_0 + \alpha w_1, \quad (4)$$

where α is an infinitesimally small quantity. Here, $\alpha u_1(r, \theta, z)$, $\alpha v_1(r, \theta, z)$, $\alpha w_1(r, \theta, z)$ are the displacements to which the points of the body must be subjected to shift them from the initial position of equilibrium to the new equilibrium position. The functions $u_1(r, \theta, z)$, $v_1(r, \theta, z)$, $w_1(r, \theta, z)$ are assumed finite and α is an infinitesimally small quantity independent of r, θ, z.

Following Kardomateas (1993a), we obtain the following buckling equations:

$$\frac{\partial}{\partial r}\left(\sigma'_{rr} - \tau^0_{r\theta}\omega'_z + \tau^0_{rz}\omega'_\theta\right) + \frac{1}{r}\frac{\partial}{\partial \theta}\left(\tau'_{r\theta} - \sigma^0_{\theta\theta}\omega'_z + \tau^0_{\theta z}\omega'_\theta\right) + \frac{\partial}{\partial z}\left(\tau'_{rz} - \tau^0_{\theta z}\omega'_z + \sigma^0_{zz}\omega'_\theta\right) + \frac{1}{r}\left(\sigma'_{rr} - \sigma'_{\theta\theta} + \tau^0_{rz}\omega'_\theta + \tau^0_{\theta z}\omega'_r - 2\tau^0_{r\theta}\omega'_z\right) = 0, \quad (5a)$$

$$\frac{\partial}{\partial r}\left(\tau'_{r\theta} + \sigma^0_{rr}\omega'_z - \tau^0_{rz}\omega'_r\right) + \frac{1}{r}\frac{\partial}{\partial \theta}\left(\sigma'_{\theta\theta} + \tau^0_{r\theta}\omega'_z - \tau^0_{\theta z}\omega'_r\right) + \frac{\partial}{\partial z}\left(\tau'_{\theta z} + \tau^0_{rz}\omega'_z - \sigma^0_{zz}\omega'_r\right) + \frac{1}{r}\left(2\tau'_{r\theta} + \sigma^0_{rr}\omega'_z - \sigma^0_{\theta\theta}\omega'_z + \tau^0_{\theta z}\omega'_\theta - \tau^0_{rz}\omega'_r\right) = 0, \quad (5b)$$

$$\frac{\partial}{\partial r}\left(\tau'_{rz} - \sigma^0_{rr}\omega'_\theta + \tau^0_{r\theta}\omega'_r\right) + \frac{1}{r}\frac{\partial}{\partial \theta}\left(\tau'_{\theta z} - \tau^0_{r\theta}\omega'_\theta + \sigma^0_{\theta\theta}\omega'_r\right) + \frac{\partial}{\partial z}\left(\sigma'_{zz} - \tau^0_{rz}\omega'_\theta + \tau^0_{\theta z}\omega'_r\right) + \frac{1}{r}\left(\tau'_{rz} - \sigma^0_{rr}\omega'_\theta + \tau^0_{r\theta}\omega'_r\right) = 0. \quad (5c)$$

In these equations, σ^0_{ij} and ω^0_j are the values of σ_{ij} and ω_j at the initial equilibrium position; i.e., for $u = u_0$, $v = v_0$ and $w = w_0$, and σ'_{ij} and ω'_j are the values at the perturbed position; i.e., for $u = u_1$, $v = v_1$ and $w = w_1$.

The boundary conditions associated with (1*a*) can be expressed as (e.g., Ciarlet, 1988):

$$(\mathbf{F} \cdot \mathbf{\Sigma}^{\mathrm{T}}) \cdot \hat{n} = t(V), \quad (6)$$

where t is the traction vector on the surface which has outward unit normal $\hat{n} = (l, m, n)$ before any deformation. The traction vector t depends on the displacement field $V = (u, v, w)$. Again, following Kardomateas (1993a), we obtain for the lateral and end surfaces:

$$\left(\sigma'_{rr} - \tau^0_{r\theta}\omega'_z + \tau^0_{rz}\omega'_\theta\right)l + \left(\tau'_{r\theta} - \sigma^0_{\theta\theta}\omega'_z + \tau^0_{\theta z}\omega'_\theta\right)m + \left(\tau'_{rz} - \tau^0_{\theta z}\omega'_z + \sigma^0_{zz}\omega'_\theta\right)n = 0, \quad (7a)$$

$$\left(\tau'_{r\theta} + \sigma^0_{rr}\omega'_z - \tau^0_{rz}\omega'_r\right)l + \left(\sigma'_{\theta\theta} + \tau^0_{r\theta}\omega'_z - \tau^0_{\theta z}\omega'_r\right)m + \left(\tau'_{\theta z} + \tau^0_{rz}\omega'_z - \sigma^0_{zz}\omega'_r\right)n = 0, \quad (7b)$$

$$\left(\tau'_{rz} + \tau^0_{r\theta}\omega'_r - \sigma^0_{rr}\omega'_\theta\right)l + \left(\tau'_{\theta z} + \sigma^0_{\theta\theta}\omega'_r - \tau^0_{r\theta}\omega'_\theta\right)m + \left(\sigma'_{zz} + \tau^0_{\theta z}\omega'_r - \tau^0_{rz}\omega'_\theta\right)n = 0. \quad (7c)$$

Prebuckling State. We consider the case of a cylindrical rod compressed by an axial force, P, applied at the one end, which is free. The other end of the rod is fixed. Denote the length of the rod by l and the area of the transverse section by A. The material is transversely isotropic, obeying the stress-strain relations:

$$\begin{bmatrix} \sigma_{rr} \\ \sigma_{\theta\theta} \\ \sigma_{zz} \\ \tau_{\theta z} \\ \tau_{rz} \\ \tau_{r\theta} \end{bmatrix} = \begin{bmatrix} c_{11} & c_{12} & c_{12} & 0 & 0 & 0 \\ c_{12} & c_{11} & c_{13} & 0 & 0 & 0 \\ c_{13} & c_{13} & c_{33} & 0 & 0 & 0 \\ 0 & 0 & 0 & c_{55} & 0 & 0 \\ 0 & 0 & 0 & 0 & c_{55} & 0 \\ 0 & 0 & 0 & 0 & 0 & (c_{11} - c_{12})/2 \end{bmatrix} \begin{bmatrix} \epsilon_{rr} \\ \epsilon_{\theta\theta} \\ \epsilon_{zz} \\ \gamma_{\theta z} \\ \gamma_{rz} \\ \gamma_{r\theta} \end{bmatrix}, \quad (8)$$

where c_{ij} are the elastic constants (we have used the notation $1 \equiv r$, $2 \equiv \theta$, $3 \equiv z$).

If we assume that the stresses along the loaded upper end ($z = l$) and the reaction along the lower ($z = 0$) end of the rod are distributed uniformly and are normal to the bounding planes, then the components of stress tensor that satisfy the equations of equilibrium and the traction conditions on the surfaces are simply

$$\sigma^0_{zz} = -\frac{P}{A} = -\sigma_0; \quad \sigma^0_{rr} = \sigma^0_{\theta\theta} = \tau^0_{r\theta} = \tau^0_{rz} = \tau^0_{\theta z} = 0. \quad (9)$$

Perturbed State. Using (5) and (9), the three-dimensional elasticity equilibrium equations for the perturbed position can be written as follows (primes denote values at the perturbed position):

$$\frac{\partial \sigma'_{rr}}{\partial r} + \frac{1}{r}\frac{\partial \tau'_{r\theta}}{\partial \theta} + \frac{\partial}{\partial z}\left(\tau'_{rz} - \sigma_0\omega'_\theta\right) + \frac{1}{r}\left(\sigma'_{rr} - \sigma'_{\theta\theta}\right) = 0, \quad (10a)$$

$$\frac{\partial \tau'_{r\theta}}{\partial r} + \frac{1}{r}\frac{\partial \sigma'_{\theta\theta}}{\partial \theta} + \frac{\partial}{\partial z}\left(\tau'_{\theta z} + \sigma_0\omega'_r\right) + \frac{2\tau'_{r\theta}}{r} = 0, \quad (10b)$$

$$\frac{\partial \tau'_{rz}}{\partial r} + \frac{1}{r}\frac{\partial \tau'_{\theta z}}{\partial \theta} + \frac{\partial \sigma'_{zz}}{\partial z} + \frac{\tau'_{rz}}{r} = 0. \quad (10c)$$

In the above equations, σ^0_{ij}, σ'_{ij} are expressed in terms of ϵ^0_{ij}, ϵ'_{ij}, respectively, in the same manner as the stress-strain law; i.e., Eqs. (8), for σ_{ij} in terms of ϵ_{ij}. The strains ϵ'_{ij}, are in turn expressed in terms of the displacements, u_1, v_1, w_1, in the same manner as the linear strain displacement relations (2). Substituting, we obtain the equations of equilibrium in terms of the displacements at the perturbed state, u_1, v_1, w_1 as follows:

$$c_{11}\left(\frac{\partial^2 u_1}{\partial r^2} + \frac{1}{r}\frac{\partial u_1}{\partial r} - \frac{u_1}{r^2}\right) + \frac{1}{2}(c_{11} - c_{12})\frac{1}{r^2}\frac{\partial^2 u_1}{\partial \theta^2} + \left(c_{55} - \frac{\sigma_0}{2}\right)\frac{\partial^2 u_1}{\partial z^2} + \frac{1}{2}(c_{11} + c_{12})\frac{\partial}{\partial r}\left(\frac{1}{r}\frac{\partial v_1}{\partial \theta}\right) - (c_{11} - c_{12})\frac{1}{r^2}\frac{\partial v_1}{\partial \theta} + \left[(c_{13} + c_{55}) + \frac{\sigma_0}{2}\right]\frac{\partial^2 w_1}{\partial r \partial z} = 0, \quad (11a)$$

$$\frac{1}{2}(c_{11} - c_{12})\left(\frac{\partial^2 v_1}{\partial r^2} + \frac{1}{r}\frac{\partial v_1}{\partial r} - \frac{v_1}{r^2}\right) + c_{11}\frac{1}{r^2}\frac{\partial^2 v_1}{\partial \theta^2} + \left(c_{55} - \frac{\sigma_0}{2}\right)\frac{\partial^2 v_1}{\partial z^2} + \frac{1}{r}\frac{\partial}{\partial \theta}\left\{\frac{1}{2}(c_{11} + c_{12})\left(\frac{\partial u_1}{\partial r} + \frac{u_1}{r}\right) + (c_{11} - c_{12})\frac{u_1}{r} + \left[(c_{13} + c_{55}) + \frac{\sigma_0}{2}\right]\frac{\partial w_1}{\partial z}\right\} = 0, \quad (11b)$$

Downloaded 04 May 2010 to 171.66.16.28. Redistribution subject to ASME license or copyright; see http://www.asme.org/terms/Terms_Use.cfm

$$c_{55}\left(\frac{\partial^2 w_1}{\partial r^2}+\frac{1}{r}\frac{\partial w_1}{\partial r}+\frac{1}{r^2}\frac{\partial^2 w_1}{\partial \theta^2}\right)+c_{33}\frac{\partial^2 w_1}{\partial z^2}$$
$$+(c_{13}+c_{55})\frac{\partial}{\partial z}\left(\frac{\partial u_1}{\partial r}+\frac{u_1}{r}+\frac{1}{r}\frac{\partial v_1}{\partial \theta}\right)=0. \quad (11c)$$

We seek a *first group of solutions* in terms of a function ϕ in the form

$$u_1=\frac{\partial \phi}{\partial r};\quad v_1=\frac{1}{r}\frac{\partial \phi}{\partial \theta};\quad w_1=k\frac{\partial \phi}{\partial z}. \quad (12)$$

A similar form had been used by Elliott (1948) for Cartesian coordinates. Then equations (11a) and (11b) are satisfied if

$$c_{11}\left(\frac{\partial^2 \phi}{\partial r^2}+\frac{1}{r}\frac{\partial \phi}{\partial r}+\frac{1}{r^2}\frac{\partial^2 \phi}{\partial \theta^2}\right)$$
$$+\left[c_{55}+k(c_{13}+c_{55})+\frac{\sigma_0}{2}(k-1)\right]\frac{\partial^2 \phi}{\partial z^2}=0, \quad (13a)$$

and (11c) is satisfied if

$$[(c_{13}+c_{55})+kc_{55}]\left(\frac{\partial^2 \phi}{\partial r^2}+\frac{1}{r}\frac{\partial \phi}{\partial r}+\frac{1}{r^2}\frac{\partial^2 \phi}{\partial \theta^2}\right)$$
$$+kc_{33}\frac{\partial^2 \phi}{\partial z^2}=0. \quad (13b)$$

A nonzero solution of these Eqs. (13a) and (13b) can be found only if they are identical; this occurs if

$$\frac{c_{55}+k(c_{13}+c_{55})+(k-1)(\sigma_0/2)}{c_{11}}$$
$$=\frac{kc_{33}}{(c_{13}+c_{55}+kc_{55})}\equiv s^2. \quad (14a)$$

This gives a quadratic equation for s^2 or k. The equation for $x=s^2$, with roots s_1^2 and s_2^2, depending on the compressive stress σ_0, is

$$c_{11}c_{55}x^2+\left[(c_{13}+c_{55})\left(c_{13}+c_{55}+\frac{\sigma_0}{2}\right)\right.$$
$$\left.-c_{55}\left(c_{55}-\frac{\sigma_0}{2}\right)-c_{11}c_{33}\right]x+c_{33}\left(c_{55}-\frac{\sigma_0}{2}\right)=0, \quad (14b)$$

and the corresponding k_i:

$$k_i=\frac{s_i^2c_{11}-c_{55}+(\sigma_0/2)}{c_{13}+c_{55}+(\sigma_0/2)}\,i=1,2. \quad (14c)$$

A *second group of solutions* is sought in terms of the function ψ in the form

$$u_1=\frac{1}{r}\frac{\partial \psi}{\partial \theta};\quad v_1=-\frac{\partial \psi}{\partial r};\quad w_1=0. \quad (15)$$

Then Eqs. (11a) and (11b) are satisfied if

$$\frac{1}{2}(c_{11}-c_{12})\left(\frac{\partial^2 \psi}{\partial r^2}+\frac{1}{r}\frac{\partial \psi}{\partial r}+\frac{1}{r^2}\frac{\partial^2 \psi}{\partial \theta^2}\right)$$
$$+\left(c_{55}-\frac{\sigma_0}{2}\right)\frac{\partial^2 \psi}{\partial z^2}=0, \quad (16)$$

and Eq. (11c) is identically satisfied.

Finally, an obvious *third group of solutions* is the rigid-body displacement field with components V_x, V_y, and V_z along the Cartesian x, y, z coordinate system:

$$u_1=V_x\cos\theta+V_y\sin\theta;\quad v_1=-V_x\sin\theta+V_y\cos\theta;$$
$$w_1=V_z. \quad (17)$$

The displacement is a superposition of these three fields.

Now, the functions ϕ and ψ are sought in a separable form:

$$\phi_i(r,\theta,z)=Z(z)A_i(\lambda r)\cos\theta;$$
$$i=1,2 \text{ corresponding to } s_1, s_2, \quad (18a)$$
$$\psi(r,\theta,z)=Z(z)B(\lambda r)\sin\theta. \quad (18b)$$

Set

$$\rho=\lambda r. \quad (18c)$$

Substituting in (13a), we obtain the ordinary differential equations:

$$A_i''(\rho)+\frac{1}{\rho}A_i'(\rho)-\left(s_i^2+\frac{1}{\rho^2}\right)A_i(\rho)=0 \quad (19a)$$

where s_i^2 are given in (14a). In a similar fashion, substituting in (16), we obtain the ordinary differential equation

$$B''(\rho)+\frac{1}{\rho}B'(\rho)-\left(q^2+\frac{1}{\rho^2}\right)B(\rho)=0$$
$$\text{where } q^2=\frac{2c_{55}-\sigma_0}{c_{11}-c_{12}}. \quad (19b)$$

Moreover, $Z(z)$ is found to satisfy

$$Z''(z)+\lambda^2 Z(z)=0. \quad (19c)$$

The assumption

$$Z(z)=\cos\lambda z \quad (19d)$$

satisfies the third differential equation, (19c).

The solution to the two Eqs. (19a) and (19b) involves only the modified Bessel functions of first order of the first kind:

$$A_i(\rho)=C_iI_1(s_i\rho);\quad B(\rho)=C_0I_1(q\rho), \quad (20)$$

where the constants C_i are in general complex conjugates and C_0 is real.

Before satisfying the boundary conditions at the lateral surface, which will ultimately provide the system of equations for the eigenvalue problem, we shall discuss the boundary conditions at the ends. From (7) the boundary conditions on the ends are

$$\tau_{rz}'+\sigma_{zz}^0\omega_\theta'=0;\quad \tau_{\theta z}'-\sigma_{zz}^0\omega_r'=0;\quad \sigma_{zz}'=0,\quad \text{at } z=0,l. \quad (21)$$

Since σ_{zz}' varies as $\cos\lambda z$, the condition $\sigma_{zz}=0$ on the upper end $z=l$ is satisfied if

$$\lambda=\frac{\pi}{2l}. \quad (22)$$

In a cartesian coordinate system (x, y, z), the first two of the conditions in (21) can be written as follows:

$$\tau_{xz}'+\sigma_{zz}^0\omega_y'=0;\quad \tau_{yz}'-\sigma_{zz}^0\omega_x'=0. \quad (23)$$

It will be proved that these remaining two conditions are satisfied on the average. At this point, it should be noted that for some of the boundary conditions, a form of resultant instead of pointwise conditions has been frequently used in elasticity treatments, and can be considered as based on some form of the Saint-Venant's principle. For this reason, they are sometimes referred to as relaxed end conditions of the Saint-Venant's type (Horgan, 1989). Now the lateral surface boundary conditions in the cartesian coordinate system, with $\hat{n}$ the normal to the circular contour are from (7):

Downloaded 04 May 2010 to 171.66.16.28. Redistribution subject to ASME license or copyright; see http://www.asme.org/terms/Terms_Use.cfm

$$\sigma'_{xx}\cos(\hat{n},x)+\tau'_{xy}\cos(\hat{n},y)=0, \quad (24a)$$

$$\tau'_{xy}\cos(\hat{n},x)+\sigma'_{yy}\cos(\hat{n},y)=0, \quad (24b)$$

with $\hat{n}$ the normal to the circular contour. Using the equilibrium equation in cartesian coordinates, Green's theorem for transformation of an area integral into a contour integral, and the above conditions on the contour, we obtain

$$\frac{\partial}{\partial z}\iint_A\left(\tau'_{xz}+\sigma^0_{zz}\omega'_y\right)dA=-\iint_A\left(\frac{\partial\sigma'_{xx}}{\partial x}+\frac{\partial\tau'_{xy}}{\partial y}\right)dA. \quad (25a)$$

The previous integral then becomes

$$-\int_\gamma\left[\sigma'_{xx}\cos(\hat{n},x)+\tau'_{xy}\cos(\hat{n},y)\right]ds=0,$$

where A denotes the area of the annular cross-section and γ the corresponding contour. Therefore

$$\iint_A\left(\tau'_{xz}+\sigma^0_{zz}\omega'_y\right)dA=\text{const.} \quad (25b)$$

Since at $z=0$, $\tau'_{xz}=\omega'_y=0$ because τ'_{xz}, τ'_{yz} and ω'_y, ω'_x all have a $\sin[\pi z/(2l)]$ variation (and so do τ'_{rz}, $\tau'_{\theta z}$ and ω'_θ, ω'_r), it is concluded that this constant is zero. Similar arguments hold for τ'_{yz}.

Moreover, it can also be proved that this system of stresses would produce no torsional moment. Indeed,

$$\frac{\partial}{\partial z}\iint_A\left[x\left(\tau'_{yz}-\sigma^0_{zz}\omega'_x\right)-y\left(\tau'_{xz}+\sigma^0_{zz}\omega'_y\right)\right]dA$$
$$=-\iint_A\left\{x\left(\frac{\partial\tau'_{xy}}{\partial x}+\frac{\partial\sigma'_{yy}}{\partial y}\right)-y\left(\frac{\partial\sigma'_{xx}}{\partial x}+\frac{\partial\tau'_{xy}}{\partial y}\right)\right\}dA.$$

Again, using the divergence theorem, the previous integral becomes

$$-\int_\gamma\left\{x\left[\tau'_{xy}\cos(\hat{n},x)+\sigma'_{yy}\cos(\hat{n},y)\right]\right.$$
$$\left.-y\left[\sigma'_{xx}\cos(\hat{n},x)+\tau'_{xy}\cos(\hat{n},y)\right]\right\}ds=0, \quad (25c)$$

hence

$$\iint_A\left[x\left(\tau'_{yz}-\sigma^0_{zz}\omega'_x\right)-y\left(\tau'_{xz}+\sigma^0_{zz}\omega'_y\right)\right]dA=\text{const}, \quad (25d)$$

and this constant is again zero since $\tau'_{xz}=\tau'_{yz}=\omega'_x=\omega'_y=0$ at $z=0$.

Finally, it should be noted that concerning the variation along z,

$$w_1,\quad \frac{\partial u_1}{\partial z},\quad \frac{\partial v_1}{\partial z}\sim Z'(z)\sim\sin\lambda z, \quad (25e)$$

therefore at $z=0$, $w_1=\partial u_1/\partial z=\partial v_1/\partial z=0$ and u_1 and v_1 and can be made equal to zero at some point of the end $z=0$ by the choice of the constants V_i in (17). In this sense, the end $z=0$ is "clamped."

Notice that based on the previous analysis, we have found that

$$\phi_i(r,\theta,z)=C_iI_1(s_i\lambda r)\cos\theta\cos\lambda z;\quad i=1,2 \quad (26a)$$

and

$$\psi(r,\theta,z)=C_0I_1(q\lambda r)\sin\theta\cos\lambda z. \quad (26b)$$

Now we proceed to the boundary conditions on the lateral surface $r=R$. From (7), we obtain

$$\sigma'_{rr}=0;\quad \tau'_{r\theta}=0;\quad \tau'_{rz}=0,\quad \text{at}\quad r=R. \quad (27)$$

Substituting in (27), (15), (12), (2), and (8), and using the identities for the derivatives of Bessel functions, we obtain a system of three linear homogeneous equations in C_i, $i=1,2$ and C_0:

$$C_0(c_{11}-c_{12})q\frac{I_2(\lambda qR)}{R}$$
$$+\sum_{i=1,2}C_i\left\{c_{11}\left[\lambda s_i^2I_1(\lambda s_iR)-s_i\frac{I_2(\lambda s_iR)}{R}\right]\right.$$
$$\left.+c_{12}s_i\frac{I_2(\lambda s_iR)}{R}-c_{13}k_i\lambda I_1(\lambda s_iR)\right\}=0, \quad (28a)$$

$$C_0\left[2q\frac{I_2(\lambda qR)}{R}-\lambda q^2I_1(\lambda qR)\right]-\sum_{i=1,2}C_i2s_i\frac{I_2(\lambda s_iR)}{R}=0, \quad (28b)$$

$$C_0\frac{I_1(\lambda qR)}{R}$$
$$+\sum_{i=1,2}C_i(k_i+1)\left[\frac{I_1(\lambda s_iR)}{R}+\lambda s_iI_2(\lambda s_iR)\right]=0. \quad (28c)$$

By equating the determinant of the above system (28) to zero, we obtain an equation for σ_0 (characteristic equation) which can be solved to obtain the critical load. In general, the roots s_1 and s_2 are either both real or complex conjugates, whereas q, defined in (19b), is normally a real variable. In the case of real s_1, s_2 the determinant of the linear system (28) is real.

In the case of a complex conjugate pair $\{s_1, s_2\}$, the Bessel functions have complex arguments and the constants C_1, C_2 are complex conjugates, whereas C_0 is a real number. Furthermore, $\{I_1(\lambda s_1R),\ I_1(\lambda s_2R)\}$ and $\{I_2(\lambda s_1R),\ I_2(\lambda s_2R)\}$ are also complex conjugate pairs. The 3×3 matrix of coefficients of the linear system (28) has one real column (corresponding to C_0) and the remaining two are two pairs of complex conjugates. Therefore, it turns out that in this case the determinant of (28) is pure imaginary. In either case, equating the determinant to zero results in a nonlinear real equation for σ_0.

In performing the numerical calculations, the modified Bessel function of zero and first order can be evaluated from polynomial coefficients given by Abramowitz and Stegun (1964) and that of the second order from the associated recurrence relations.

A New, Improved, Direct Formula for Isotropic Column Buckling: The Euler Load Revisited

In the case of isotropy, in which $s_1=1$ and $s_2=q$, expansion of the determinant for the system of linear homogeneous Eqs. (28) and use of the series expansion of the Bessel functions can lead to direct formulas for the critical load. Notice that for isotropy, $c_{12}=c_{13}=c_{11}-2c_{55}$.

Set

$$\tilde{\lambda}=\lambda2\sqrt{I/A}=\lambda R=\frac{\pi R}{2l}, \quad (29a)$$

where $A=\pi R^2$ is the cross-sectional area and $I=\pi R^4/4$ is the moment of inertia of the cross-section. Furthermore, we can define the quantity ϵ by using (19b):

$$\epsilon=1-q^2=\frac{\sigma_0}{2c_{55}}. \quad (29b)$$

From (14c), since for isotropy $s_1=1$ and $s_2=q$, we find that $k_1=1$, and $k_2=k$ is expanded by substituting $q^2=1-\epsilon$:

Downloaded 04 May 2010 to 171.66.16.28. Redistribution subject to ASME license or copyright; see http://www.asme.org/terms/Terms_Use.cfm

$$k = \frac{q^2(c_{11} - c_{55})}{c_{11} - c_{55}q^2} = 1 - \frac{c_{11}}{c_{11} - c_{55}}\epsilon + \frac{c_{11}c_{55}}{(c_{11} - c_{55})^2}\epsilon^2 - \frac{c_{11}c_{55}^2}{(c_{11} - c_{55})^3}\epsilon^3 + \ldots. \quad (29c)$$

The Bessel functions in (28) are then expanded in powers of $\tilde{\lambda}$ or $\tilde{\lambda}q$ by using the series expansions: $I_1(x) = x/2 + x^3/16 + x^5/16.24 + x^7/16.24.48 + \ldots$, and $I_2(x) = x^2/8 + x^4/6.16 + x^6/8.16.24 + x^8/10.16.24.48 + \ldots$.

Now since $\epsilon = O(\tilde{\lambda}^2)$, in the first approximation the characteristic equation would include the terms: ϵ, $\tilde{\lambda}^2$, ϵ^2, $\tilde{\lambda}^2\epsilon$, and $\tilde{\lambda}^4$; in the second approximation it would also include ϵ^3, $\tilde{\lambda}^2\epsilon^2$, $\tilde{\lambda}^4\epsilon$, and $\tilde{\lambda}^6$. Therefore, in performing the calculations, only terms up to $\tilde{\lambda}^6$ need be retained. The detailed expressions for the resulting coefficients of the system (28) are given in the Appendix. Equating the 3×3 determinant to zero results in the following equation:

$$c_{55}\frac{q^2\tilde{\lambda}^5}{32}\left\{4\epsilon^2 + \left[\frac{c_{55}}{2(c_{11} - c_{55})} - \frac{3}{2}\right]\tilde{\lambda}^2\epsilon - 4\frac{c_{11}}{c_{11} - c_{55}}\epsilon^3 + \left[\frac{19}{6} + \frac{4c_{11}}{3(c_{11} - c_{55})} - \frac{c_{11}c_{55}}{2(c_{11} - c_{55})^2}\right]\tilde{\lambda}^2\epsilon^2 + \left[\frac{7c_{55}}{48(c_{11} - c_{55})} - \frac{25}{48}\right]\tilde{\lambda}^4\epsilon\right\} = 0. \quad (30)$$

Notice that the coefficients of ϵ, $\tilde{\lambda}^2$, $\tilde{\lambda}^4$, and $\tilde{\lambda}^6$ turn out to be zero.

In terms of the Poisson's ratio, ν, and the Young's modulus, E,

$$c_{11} = E\frac{1 - \nu}{(1 + \nu)(1 - 2\nu)}; \quad c_{55} = \frac{E}{2(1 + \nu)}. \quad (31)$$

Substituting into (30) gives in the first approximation, i.e., terms $O(\epsilon^2)$:

$$\epsilon = \frac{1 + \nu}{4}\tilde{\lambda}^2. \quad (32a)$$

Notice that the parameter $\epsilon = \sigma_0/(2c_{55})$ comes naturally from the formulation of the problem. It can also be written as $\epsilon = \sigma_0(1 + \nu)/E$, hence it is a suitable small parameter since the axial stress, σ_0, is much smaller than the modulus, E.

Now, using the definitions (29a,b) gives

$$\sigma_0 = E\frac{\lambda^2R^2}{4}. \quad (32b)$$

Hence, the critical load is

$$P_{cr} = \sigma_0 A = E\lambda^2\frac{\pi R^4}{4} = \lambda^2 EI; \quad (32c)$$

i.e., from the first approximation we recover the classic Euler load.

In the second approximation, we keep all the terms in (30) and, substituting (31), we obtain the following quadratic equation in ϵ:

$$8(1 - \nu)\epsilon^2 - \left[4 + \frac{\tilde{\lambda}^2}{6}(29 + 2\nu - 12\nu^2)\right]\epsilon + \tilde{\lambda}^2(1 + \nu) + \frac{\tilde{\lambda}^4}{24}(9 + 7\nu) = 0. \quad (33)$$

The solution to this equation can be written in the form

$$\epsilon = \frac{1 + \nu}{4}\tilde{\lambda}^2 - \frac{\epsilon_2}{16(1 - \nu)}, \quad (34a)$$

where

$$\epsilon_2 = \sqrt{\Delta} - 4 - \frac{\tilde{\lambda}^2}{6}(5 + 2\nu + 12\nu^2), \quad (34b)$$

and

$$\Delta = 16 + \frac{\tilde{\lambda}^2}{3}(20 + 8\nu + 48\nu^2) + \frac{\tilde{\lambda}^4}{36}(409 + 212\nu - 356\nu^2 - 48\nu^3 + 144\nu^4). \quad (34c)$$

Using (29a, b) gives now the critical load as follows:

$$P_{cr} = \lambda^2 EI - \frac{\epsilon_2}{16(1 - \nu^2)}EA. \quad (35)$$

Therefore, *in the second approximation, the Euler load, $\lambda^2 EI$, is reduced by the quantity $\epsilon_2 EA/[16(1 - \nu^2)]$*. Equation (35) provides a new, improved, direct formula for isotropic column buckling. As with the Euler load, the end fixity is accounted for in λ, which for the fixed-free case is: $\lambda = \pi/2l$. Results that will be presented in the next section will show that formula (35) provides estimates that almost coincide with the elasticity results, therefore providing an excellent account of the thickness effects for isotropic columns.

Discussion of Results

The Euler critical load for a compressed fixed-free column is

$$P_{\text{Euler}} = \frac{\pi^2 E_3 I}{4l^2} = E_3 I\lambda^2 = E_3 A\frac{R^2\lambda^2}{4} \quad (36)$$

where I is the moment of inertia of the cross section.

Concerning the present elasticity formulation, the critical load is obtained by finding the solution σ_0 of the determinant of (28). The ratio $P_{\text{Euler}}/P_{\text{elast}} = E_3\pi^3R^4/(\sigma_0 4l^2)$ of Table 1 compares the critical load, as predicted by the present three-dimensional elasticity formulation, with the Euler load. The other numbers in brackets and in parentheses represent the predictions of the two Timoshenko transverse shear correction formulas that will be discussed later.

Three material cases have been considered with the following properties (we have used the notation $1 \equiv r$, $2 \equiv \theta$, $3 \equiv z$): (a) Isotropic material with modulus $E = E_3$ and Poisson's ratio $\nu = 0.3$. (b) Material No. 1 (which approximates glass/epoxy with reinforcement along the z-axis) with moduli in GPa: $E_3 = 57$, $E_2 = E_1 = 14$, $G_{31} = G_{23} = 5.7$ and Poisson's ratios: $\nu_{12} = 0.400$, $\nu_{23} = \nu_{13} = 0.068$. (c) Material No. 2 (which approximates graphite/epoxy with reinforcement along the z-axis) with moduli in GPa: $E_3 = 140$, $E_2 = E_1 = 10$, $G_{31} = G_{23} = 5.0$ and Poisson's ratios: $\nu_{12} = 0.53$, $\nu_{23} = \nu_{13} = 0.02$.

It can be proved that for an isotropic material, which is characterized by the two stiffness constants $c_{11} = c_{33}$ and c_{55}, ($c_{12} = c_{13} = c_{11} - 2c_{55}$), the roots of (14$b$) are

$$s_1 = 1 \quad \text{and} \quad s_2 = q = \left(1 - \frac{\sigma_0}{2c_{55}}\right)^{1/2}. \quad (37)$$

For a transversely isotropic material, like the two cases (b) and (c), the roots are in general complex conjugates.

The critical load from the elasticity solution, is presented graphically in Fig. 1. From both Fig. 1 and Table 1, it can be concluded that the critical load for isotropic bodies is in general lower than the Euler value. The difference is, how-

Downloaded 04 May 2010 to 171.66.16.28. Redistribution subject to ASME license or copyright; see http://www.asme.org/terms/Terms_Use.cfm

Table 1 One end fixed, the other free

Critical Loads, $P^{\dagger}_{\text{Euler}}/P_{\text{elast}}$ $[P^{\ddagger}_{T1}/P_{\text{elast}}]$ $(P^{\ddagger}_{T2}/P_{\text{elast}})$			
l/R	Isotropic	Material 1	Material 2
15.0	1.000 [0.992] (0.992)	1.017 [0.988] (0.988)	1.050 [0.968] (0.973)
13.0	1.001 [0.991] (0.991)	1.022 [0.982] (0.984)	1.065 [0.956] (0.966)
11.0	1.006 [0.991] (0.991)	1.031 [0.975] (0.978)	1.093 [0.943] (0.960)
9.0	1.012 [0.990] (0.990)	1.047 [0.965] (0.971)	1.138 [0.921] (0.950)
7.0	1.017 [0.981] (0.982)	1.080 [0.947] (0.961)	1.228 [0.883] (0.944)
5.0	1.036 [0.968] (0.971)	1.159 [0.910] (0.947)	1.449 [0.820] (0.961)
3.0	1.101 [0.919] (0.941)	1.439 [0.817] (0.955)	2.227 [0.713] (1.091)

$^{\dagger}P_{\text{Euler}}/P_{\text{elast}} = E_3\pi^3R^4/(\sigma_0 4l^2)$, where σ_0 is from the elasticity solution (the determinant of (28)).

‡Timoshenko's first and second transverse shear correction formulas, Eqs. (40*a*, *b*).

Table 2 Both ends pinned

Critical Loads, $P^{\dagger}_{\text{Euler}}/P_{\text{elast}}$ $[P^{\ddagger}_{T1}/P_{\text{elast}}]$ $(P^{\ddagger}_{T2}/P_{\text{elast}})$			
l/R	Isotropic	Material 1	Material 2
17.0	1.012 [0.988] (0.989)	1.054 [0.962] (0.970)	1.155 [0.912] (0.948)
15.0	1.014 [0.983] (0.984)	1.068 [0.953] (0.962)	1.198 [0.894] (0.944)
13.0	1.019 [0.978] (0.979)	1.093 [0.941] (0.957)	1.266 [0.871] (0.946)
11.0	1.028 [0.970] (0.973)	1.131 [0.922] (0.950)	1.370 [0.838] (0.951)
9.0	1.045 [0.960] (0.967)	1.195 [0.893] (0.943)	1.555 [0.799] (0.975)
7.0	1.074 [0.938] (0.952)	1.321 [0.848] (0.944)	1.908 [0.744] (1.032)
5.0	1.148 [0.893] (0.932)	1.629 [0.777] (0.981)	2.755 [0.678] (1.187)
3.0	1.414 [0.789] (0.930)	2.717 [0.671] (1.174)	5.682 [0.597] (1.642)

$^{\dagger}P_{\text{Euler}}/P_{\text{elast}} = E_3\pi^3R^4/(\sigma_0 4l^2)$, where σ_0 is from the elasticity solution (the determinant of (28)).

‡Timoshenko's first and second transverse shear correction formulas, Eqs. (40*a*, *b*).

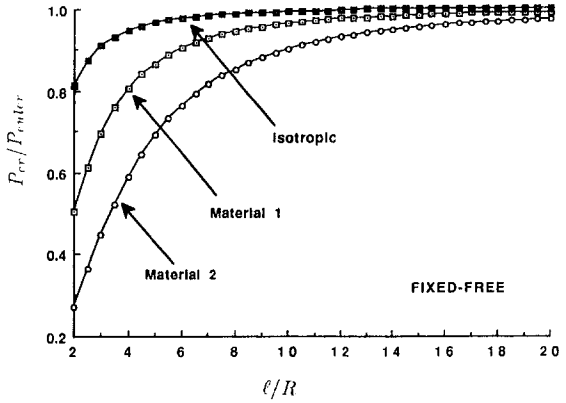

Fig. 1 Eigenvalues P_{cr}/P_{Euler} from the elasticity solution as a function of the length over radius ratio, l/R, for three cases of material data (isotropic plus two transversely isotropic: material 1 approximating glass / epoxy and material 2 approximating graphite / epoxy, both with axial reinforcement). One end is fixed, the other free.

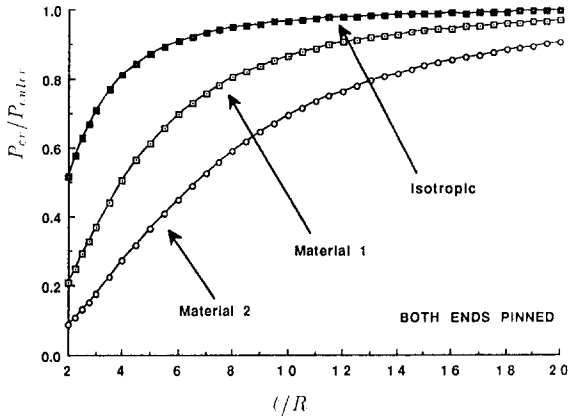

Fig. 2 Eigenvalues P_{cr}/P_{Euler} from the elasticity solution for the three cases of material data (isotropic plus two transversely isotropic) in the case where both ends are pinned

ever, very small for relatively long rods and indeed, it converges to the Euler load for values of length-over-radius ratio greater than about 15. The two examples of transversely isotropic bodies had lower critical loads in comparison with the Euler value based on the axial modulus, and the reduction was larger than that corresponding to isotropic rods with the same length over radius ratio. Especially for material no. 2, which has a markedly reduced shear and radial modulus compared to the (axial) extensional one, reductions of more than ten percent occurred for a length-over-radius ratio less than 10.

The case of a bar with hinged ends is probably an equally important and fundamental case of buckling of a prismatic bar. In this case

$$Z(z) = \sin \lambda z; \quad \lambda = \frac{\pi}{l}, \tag{38a}$$

and the Euler load is

$$P_{\text{Euler}} = \frac{\pi^2 E_3 I}{l^2} = E_3 I \lambda^2. \tag{38b}$$

Table 2 provides a comparison of the critical load for a simply supported bar, as predicted by the present three-dimensional elasticity formulation, with the Euler load. Again, the same three material cases have been considered. The critical load from the elasticity solution, normalized with the Euler load for a simply supported beam, is also given graphically in Fig. 2. It can be concluded that the thickness effect is stronger in this case of end fixity. Again, the critical load is always lower than the Euler value. The two examples of transversely isotropic bodies also had lower critical loads in comparison with the Euler values based on the axial modulus, and the reduction was larger than that for isotropic rods with the same length over radius ratio. Furthermore, the reduction was larger than that for the fixed-free case. For this case, material no. 2 has reductions of more than 30 percent for a length over radius ratio less than 10.

If the displacements of the elasticity solution in the fixed-free case are set in a form

$$u_1 = U(r)\cos\theta\cos\frac{\pi z}{2l}, \quad v_1 = V(r)\sin\theta\cos\frac{\pi z}{2l}. \tag{39a}$$

$$w_1 = W(r)\cos\theta\sin\frac{\pi z}{2l}, \tag{39b}$$

we can write these r-dependences as follows:

$$U(r) = C_0\frac{I_1(\lambda q r)}{r} + \sum_{i=1,2} C_i\left[\frac{I_1(\lambda s_i r)}{r} + \lambda s_i I_2(\lambda s_i r)\right], \tag{39c}$$

$$V(r) = -\left\{C_0\left[\frac{I_1(\lambda q r)}{r} + \lambda q I_2(\lambda q r)\right] + \sum_{i=1,2} C_i\frac{I_1(\lambda s_i r)}{r}\right\}, \tag{39d}$$

$$W(r) = -\lambda\sum_{i=1,2} C_i k_i I_1(\lambda s_i r). \tag{39e}$$

As an illustration, for the critical load of the previous example of a transversely isotropic rod made out of Material No. 2 and of length $l/R = 5$ and 8, Figs. 3(*a*, *b*, *c*) show the eigenfunctions $U(r)$, $V(r)$, and $W(r)$. It has been assumed that $U = 1.0$ at the boundary $r = R$. In all cases the shorter

Downloaded 04 May 2010 to 171.66.16.28. Redistribution subject to ASME license or copyright; see http://www.asme.org/terms/Terms_Use.cfm

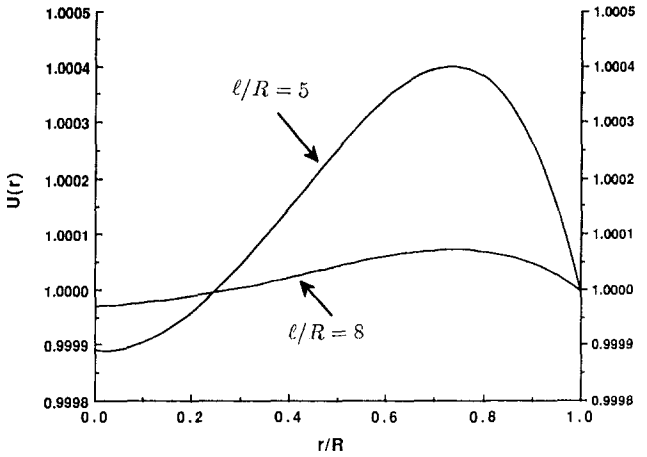

Fig. 3(*a*) "Eigenfunction" $U(r)$ versus normalized radial distance r/R for a transversely isotropic rod made out of Material No. 2 and of length $l/R = 5$ and 8. A unit value for U at the lateral surface $r = R$ has arbitrarily been set (column theory would have a constant value, $U = 1.0$).

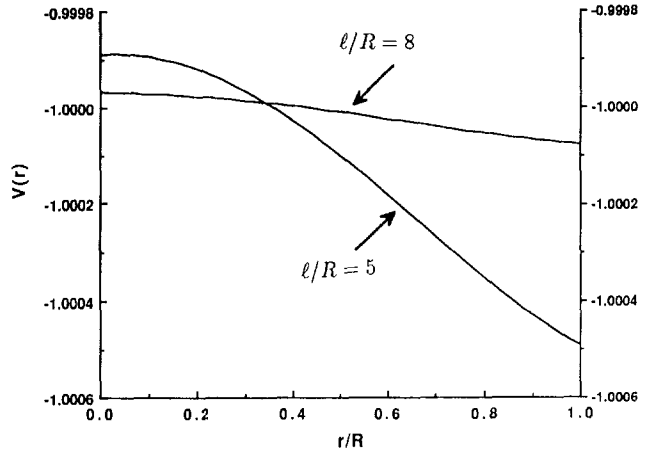

Fig. 3(*b*) "Eigenfunction" $V(r)$ versus normalized radial distance r/R for a transversely isotropic rod made out of Material No. 2 and of length $l/R = 5$ and 8 (column theory would have a linear variation for V)

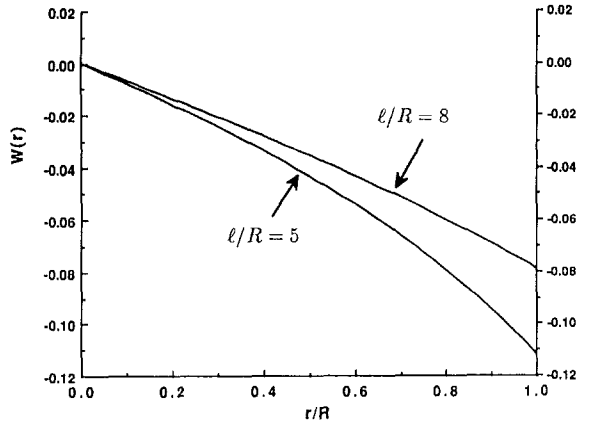

Fig. 3(*c*) "Eigenfunction" $W(r)$ versus normalized radial distance r/R for a transversely isotropic rod made out of Material No. 2 and of length $l/R = 5$ and 8 (column theory would have a linear variation for W)

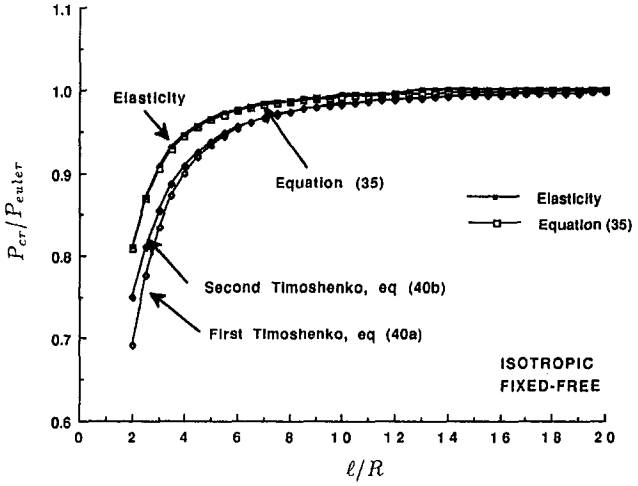

Fig. 4 Comparison of the different direct formulas for isotropic column buckling. Eigenvalues P_{cr}/P_{Euler} from the elasticity solution, Eq. (35), and the two Timoshenko formulas, P_{T1} and P_{T2}, Eqs. (40*a*, *b*) as a function of the length over radius ratio, l/R.

beam, $l/R = 5$, in which transverse normal strains are expected to be of greater importance, shows a higher variation in the displacement fields and a highly nonlinear radial displacement $U(r)$. For the longer beam, $l/R = 8$, the variation is smaller. Notice that classical column theory would have a constant value of $U = 1.0$ and a linear variation for V and W.

A comparison with an improved beam theory will be considered next. Timoshenko suggested two formulas that provide a correction to the Euler load, P_e, due to the influence of transverse shearing forces. The Timoshenko formulas for the critical load, P_{T1} and P_{T2} are (Timoshenko and Gere, 1961):

$$P_{T1} = \frac{P_e}{1 + \alpha P_e/AG}, \tag{40a}$$

$$P_{T2} = \frac{\sqrt{1 + 4\alpha P_e/AG} - 1}{2\alpha/AG}, \tag{40b}$$

where α is a numerical factor depending on the shape of the transverse section, A is the cross-sectional area ($= \pi R^2$), and G is the shear modulus. For a circular cross-section, $\alpha = 1.11$.

Tables 1 and 2 compare results for the Timoshenko formulas with the Euler load and the elasticity solution for the two cases of fixed-free and pinned-pinned rod, respectively, isotropic case and the case of material no. 2 (in the transversely isotropic case we have used $G_{23} = G_{31}$ in place of G in (40); the Euler load P_e is always based on the axial modulus, E_3).

Finally, Fig. 4 compares results from formula (35) with the exact elasticity solution and the two Timoshenko formulas, Eqs. (40*a*, *b*), for a range of l/R values. It is seen that formula (35) almost coincides with the elasticity results.

Conclusions from the comparison of the results in Tables 1 and 2 and from Fig. 4, are summarized next.

Summary and Conclusions

(1) The first Timoshenko estimate, P_{T1}, always underestimates the elasticity solution, for both cases of end fixity considered (i.e., fixed-free and pinned-pinned). It is, therefore, a conservative estimate.

(2) The second Timoshenko estimate, P_{T2}, (which is larger than P_{T1}) is always closer to the elasticity solution

Downloaded 04 May 2010 to 171.66.16.28. Redistribution subject to ASME license or copyright; see http://www.asme.org/terms/Terms_Use.cfm

than P_{T1} and it is, therefore, a more precise estimate of the transverse shear effects for both cases of end fixity considered.

(3) For the isotropic material and for both end fixity cases examined, P_{T2} also underestimates the elasticity solution, hence both P_{T1} and P_{T2} are conservative estimates.

(4) For the transversely isotropic materials considered, the second estimate, P_{T2} (which is always closer to the elasticity solution than P_{T1}) may be larger than the elasticity solution for rods of sizable thickness (e.g., this occurs for material no. 2 in the pinned-pinned case for l/R less than 9) and therefore it may provide a nonconservative estimate for rods of sizable thickness.

(5) The new, direct formula (35) that was derived in the present work for isotropic column buckling, gives results that almost coincide with the elasticity solution. Hence, this formula provides the best agreement to the elasticity solution and the best account of the thickness effects in the isotropic case.

In short, the previous results show that the thickness, the end fixity, and the material data have to be jointly considered in assessing the performance of the classical column buckling formulas for cases beyond the traditional long, isotropic rods. If a conservative estimate is desired, then P_{T1} can be used. P_{T2} is more accurate but it may be nonconservative for nonisotropic rods of sizable thickness. If the column is isotropic, the simple direct formula (35) provides an excellent account of the thickness effects.

Acknowledgment

The financial support of the Office of Naval Research, Ship Structures and Systems, S & T Division, Grant N00014-91-J-1892, and the interest and encouragement of the Grant Monitor, Dr. Y. D. S. Rajapakse, are both gratefully acknowledged.

References

Abramowitz, M., and Stegun, I. A., 1964, *Handbook of Mathematical Functions*, Applied Mathematics Series Vol. 55, Washington National Bureau of Standards (reprinted 1968 by Dover Publications, New York, Sect. 9.8).

Brush, D. O., and Almroth, B. O., 1975, *Buckling of Bars, Plates, and Shells*, McGraw-Hill, New York.

Ciarlet, P. G., 1988, *Mathematical Elasticity, Vol. I: Three-Dimensional Elasticity*, North Holland, Amsterdam.

Danielson, D. A., and Simmonds, J. G., 1969, "Accurate Buckling Equations for Arbitrary and Cylindrical Elastic Shells," *International Journal of Engineering Science*, Vol. 7, pp. 459–468.

Elliott, H. A., 1948, "Three-Dimensional Stress Distribution in Hexagonal Aeolotropic Crystals," *Proceedings of the Cambridge Philosophical Society*, Vol. 44, pp. 522–533.

Euler, L., 1744, 1933, *De Curvis Elasticis*, Vol. 20, No. 58, P. 1, Nov. 1933, Bruges, Belgium (English translation of the book "Methodus Inveniendi Lineas Curvas Maximi Minimive Proprietate Gaudentes," 1744, Lausanne).

Flügge, W., 1960, *Stresses in Shells*, Springer, pp. 426–432.

Horgan, C. O., 1989, "Recent Developments Concerning Saint-Venant's Principle: An Update," ASME *Applied Mechanics Reviews*, Vol. 42, No. 11, pp. 295–303.

Kardomateas, G. A., 1993a, "Buckling of Thick Orthotropic Cylindrical Shells Under External Pressure," ASME JOURNAL OF APPLIED MECHANICS, Vol. 60, pp. 195–202.

Kardomateas, G. A., 1993b, "Stability Loss in Thick Transversely Isotropic Cylindrical Shells Under Axial Compression," ASME JOURNAL OF APPLIED MECHANICS, Vol. 60, pp. 506–513.

Kardomateas, G. A., 1995, "Bifurcation of Equilibrium in Thick Orthotropic Cylindrical Shells Under Axial Compression," ASME JOURNAL OF APPLIED MECHANICS, Vol. 62, pp. 43–52.

Kardomateas, G. A., and Chung, C. B., 1994, "Buckling of Thick Orthotropic Cylindrical Shells Under External Pressure Based on Non-Planar Equilibrium Modes," *International Journal of Solids and Structures*, Vol. 31, No. 16, pp. 2195–2210.

Kumar, A., and Niyogi, B. B., 1982, "Bifurcations in Axially Compressed Thick Elastic Tubes," *International Journal of Engineering Science*, Vol. 20, No. 12, pp. 1311–1324.

Ogden, R. W., 1972, "Large Deformation Isotropic Elasticity: on the Correlation of Theory and Experiment for Compressible Rubberlike Solids," *Proceedings of the Royal Society London*, Vol. A328, pp. 567–583.

Simitses, G. J., 1986, *An Introduction to the Elastic Stability of Structures*, Krieger.

Timoshenko, S. P., and Gere, J. M., 1961, *Theory of Elastic Stability*, McGraw-Hill, New York.

APPENDIX

Using the series expansion of the Bessel functions results in a determinant of order three with elements a_{ij}, $i, j = 1, 3$ as follows. From the first equation, (28*a*),

$$a_{11} = (c_{11} - c_{12})qI_2(\tilde{\lambda}q) = c_{55}\frac{\tilde{\lambda}^2 q}{4}\left(1 + \frac{\tilde{\lambda}^2}{12} - \epsilon - \frac{\tilde{\lambda}^2\epsilon}{6} + \frac{\tilde{\lambda}^4}{16.24} + \frac{\tilde{\lambda}^2\epsilon^2}{12} - \frac{\tilde{\lambda}^4\epsilon}{8.16} + \frac{\tilde{\lambda}^6}{6.15.16.16}\right), \quad \text{(A1)}$$

$$a_{12} = c_{11}q\left[\tilde{\lambda}qI_1(\tilde{\lambda}q) - I_2(\tilde{\lambda}q)\right] + c_{12}\left[qI_2(\tilde{\lambda}q) - k\tilde{\lambda}I_1(\tilde{\lambda}q)\right] = c_{55}\frac{\tilde{\lambda}^2 q}{4}\left\{3 + \frac{5}{12}\tilde{\lambda}^2 - \left(\frac{c_{11} + c_{55}}{c_{11} - c_{55}}\right)\epsilon - \frac{2c_{11}c_{12}}{(c_{11} - c_{55})^2}\epsilon^2 - \left(\frac{7c_{11} - 4c_{55}}{c_{11} - c_{55}}\right)\frac{\tilde{\lambda}^2\epsilon}{12} + \frac{7}{16.24}\tilde{\lambda}^4 + \frac{2c_{11}c_{12}c_{55}}{(c_{11} - c_{55})^3}\epsilon^3 + \left[\frac{3c_{11}c_{55}}{(c_{11} - c_{55})^2} - 1\right]\frac{\tilde{\lambda}^2\epsilon^2}{12} - \left(\frac{17c_{11} - 13c_{55}}{c_{11} - c_{55}}\right)\frac{\tilde{\lambda}^4\epsilon}{16.24} + \frac{\tilde{\lambda}^6}{10.16.16}\right\}, \quad \text{(A2)}$$

$$a_{13} = (c_{11} - c_{12})\left[\tilde{\lambda}I_1(\tilde{\lambda}) - I_2(\tilde{\lambda})\right] = c_{55}\frac{\tilde{\lambda}^2}{4}\left(3 + \frac{5}{12}\tilde{\lambda}^2 + \frac{7}{16.24}\tilde{\lambda}^4 + \frac{1}{10.16.16}\tilde{\lambda}^6\right). \quad \text{(A3)}$$

From the second equation, (28*b*), we obtain

$$a_{21} = q\left[2I_2(\tilde{\lambda}q) - \tilde{\lambda}qI_1(\tilde{\lambda}q)\right] = -\frac{\tilde{\lambda}^2 q}{4}\left(1 + \frac{\tilde{\lambda}^2}{6} - \epsilon - \frac{\tilde{\lambda}^2\epsilon}{3} + \frac{\tilde{\lambda}^4}{8.16} + \frac{\tilde{\lambda}^2\epsilon^2}{6} - \frac{3}{8.16}\tilde{\lambda}^4\epsilon + \frac{\tilde{\lambda}^6}{5.6.12.16}\right), \quad \text{(B1)}$$

$$a_{22} = -2qI_2(\tilde{\lambda}q) = -\frac{\tilde{\lambda}^2 q}{4}\left(1 + \frac{\tilde{\lambda}^2}{12} - \epsilon - \frac{\tilde{\lambda}^2\epsilon}{6} + \frac{\tilde{\lambda}^4}{16.24} + \frac{\tilde{\lambda}^2\epsilon^2}{12} - \frac{\tilde{\lambda}^4\epsilon}{8.16} + \frac{\tilde{\lambda}^6}{6.15.16.16}\right), \quad \text{(B2)}$$

$$a_{23} = -2I_2(\tilde{\lambda}) = -\frac{\tilde{\lambda}^2}{4}\left(1 + \frac{\tilde{\lambda}^2}{12} + \frac{\tilde{\lambda}^4}{16.24} + \frac{\tilde{\lambda}^6}{6.15.16.16}\right). \quad \text{(B3)}$$

Finally, the third equation, (28*c*), gives

$$a_{31} = I_1(\tilde{\lambda}q) = \frac{\tilde{\lambda}q}{2}\left(1 + \frac{\tilde{\lambda}^2}{8} - \frac{\tilde{\lambda}^2\epsilon}{8} + \frac{\tilde{\lambda}^4}{8.24} - \frac{\tilde{\lambda}^4\epsilon}{8.12} + \frac{\tilde{\lambda}^6}{8.24.48}\right), \quad \text{(C1)}$$

Downloaded 04 May 2010 to 171.66.16.28. Redistribution subject to ASME license or copyright; see http://www.asme.org/terms/Terms_Use.cfm

$$a_{32} = (k+1)\left[I_1(\tilde{\lambda}q) + \tilde{\lambda}qI_2(\tilde{\lambda}q)\right]$$

$$= \tilde{\lambda}q\left[1 + \frac{3}{8}\tilde{\lambda}^2 - \frac{c_{11}}{2(c_{11}-c_{55})}\epsilon + \frac{c_{11}c_{55}}{2(c_{11}-c_{55})^2}\epsilon^2 - \frac{3}{16}\left(\frac{3c_{11}-2c_{55}}{c_{11}-c_{55}}\right)\tilde{\lambda}^2\epsilon + \frac{5}{12.16}\tilde{\lambda}^4 - \frac{c_{11}c_{55}^2}{2(c_{11}-c_{55})^3}\epsilon^3 + \frac{3}{16}\left(\frac{c_{11}}{c_{11}-c_{55}}\right)^2\tilde{\lambda}^2\epsilon^2 - \frac{5}{16.24}\left(\frac{5c_{11}-4c_{55}}{c_{11}-c_{55}}\right)\tilde{\lambda}^4\epsilon + \frac{7}{16.24.24}\tilde{\lambda}^6\right], \quad \text{(C2)}$$

$$a_{33} = 2\left[I_1(\tilde{\lambda}) + \tilde{\lambda}I_2(\tilde{\lambda})\right]$$

$$= \tilde{\lambda}\left(1 + \frac{3}{8}\tilde{\lambda}^2 + \frac{5}{12.16}\tilde{\lambda}^4 + \frac{7}{16.24.24}\tilde{\lambda}^6\right). \quad \text{(C3)}$$

Downloaded 04 May 2010 to 171.66.16.28. Redistribution subject to ASME license or copyright; see http://www.asme.org/terms/Terms_Use.cfm

Rayleigh-Taylor Instability of a Cylindrical Interface Between Two Inviscid Fluids

Rui-Qing Li[1]

R. Harris

Department of Mining and Metallurgical Engineering, McGill University, 3450 University Street, Montreal, PQ H3A 2A7, Canada

A theoretical analysis for the instability of a fluid film around a cylinder in an immiscible fluid is presented. A general dispersion equation, relating wave number to growth rate, is derived with consideration of the effects of the cylindrical interface and a finite film thickness. Application of the dispersion equation to the breakup of a liquid film around a cylindrical body in still air leads to a prediction of the dominant wavelength by $\lambda = 2\pi\sqrt{2}/\sqrt{(1/R^2 + \rho_l g/q)}$, *where* R *is the radius of the cylinder,* ρ_l *is the density of the liquid,* **g** *is the acceleration due to gravity,* σ *is the surface tension. Experiments showed good agreement with the present analysis. The dominant wavelength decreases with a decrease in the radius of the cylindrical body. A previous report on the breakup of a liquid film around a horizontal cylindrical body is shown to be in error.*

1 Introduction

The stability of the interface between two superposed fluids under the action of gravity was first investigated by Stokes (Lamb, 1932). Rayleigh (1900) analyzed the stability of a fluid with variable density. The stability of two immiscible fluids accelerated in the direction perpendicular to the plane of stratification can also be treated by the Rayleigh's formalism. Harrison (1908) obtained the relevant dispersion equation, relating the wave number and growth rate taking into account surface tension and viscosity. Harrison's discussion was complete from an analytical standpoint. The problem was analyzed by Taylor (1950) who also published excellent experimental confirmation of the theory, Lewis (1951). The instability of liquid surfaces accelerated in a direction perpendicular to their planes is now commonly referred to as the Rayleigh-Taylor instability, which occurs through nature in an astonishing diversity of physical, chemical and engineering systems. The Rayleigh-Taylor instability plays an important role in film boiling and film condensation heat transfer. Bellman and Pennington (1954) also analyzed this instability problem taking into account the surface tension and the viscosity. They obtained a dispersion equation which, though very different in form, is nevertheless the same as Harrison's result when certain of Harrison's misprints are corrected.

Lee (1963) was the first to consider the Rayleigh-Taylor instability of a cylindrical interface between two inviscid, immiscible fluids. When an infinite, uniform, horizontal cylindrical body is coated with a thin film of liquid and placed in still air, the liquid film will break away from the cylindrical body under the action of gravity due to the Rayleigh-Taylor instability. Lee's analysis approximated the behavior of the three-dimensional cylindrical interface using two-dimensional Cartesian coordinates on a right, longitudinal section through the coating to express the velocity potentials of the two fluids, the coating and the air. Unfortunately, Lee's analysis included mathematical errors which resulted in prediction of counterintuitive behavior.

In an attempt to explain the film boiling phenomena on a horizontal cylindrical heater, Lienhard et al. (Lienhard and Wong, 1964; Dhir and Lienhard, 1973), following the same mathematical procedure as used by Bellman and Pennington but including a transverse pressure term due to the cylindrical curvature, obtained dispersion equations for both inviscid and viscous fluid. Lienhard et al. also employed two-dimensional expressions for the Stokes's stream functions to analyze the instability problem for three dimensional cylindrical interface.

It is safe to say that Lee and Lienhard et al. oversimplified the instability problem for the cylindrical interface due to the use of two-dimensional Cartesian coordinates. The purposes of the present paper are: (1) to outline Lee's analysis so that the mathematical errors are clarified, (2) to analyze the Rayleigh-Taylor instability of a cylindrical interface between two fluids using the velocity potentials of fluids expressed in three-dimensional cylindrical coordinates, and (3) to experimentally verify the present theoretical predictions.

[1]Currently with Noranda Technology Center, Pointe Claire, PQ H9R 1G5, Canada.

Contributed by the Applied Mechanics Division of THE AMERICAN SOCIETY OF MECHANICAL ENGINEERS for publication in the ASME JOURNAL OF APPLIED MECHANICS.

Discussion on this paper should be addressed to the Technical Editor, Professor Lewis T. Wheeler, Department of Mechanical Engineering, University of Houston, Houston, TX 77204-4792, and will be accepted until four months after final publication of the paper itself in the ASME JOURNAL OF APPLIED MECHANICS.

Manuscript received by the ASME Applied Mechanics Division, Aug. 3, 1992; final revision, July 1, 1993. Associate Technical Editor: S. Lichter.

Copyright © 1995 by ASME

Downloaded 04 May 2010 to 171.66.16.28. Redistribution subject to ASME license or copyright; see http://www.asme.org/terms/Terms_Use.cfm

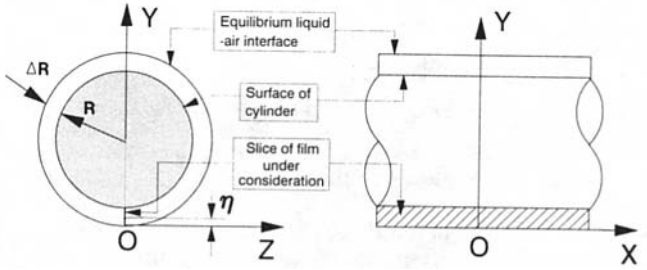

Fig. 1 Lee's definitions for the coordinates and interface geometry

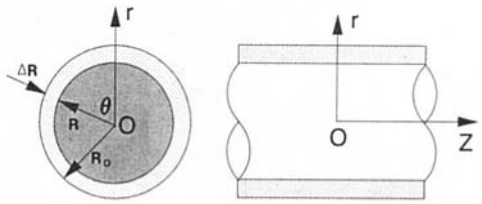

Fig. 2 The assumed geometry of gas-liquid interface during liquid film breakup on a cylindrical body

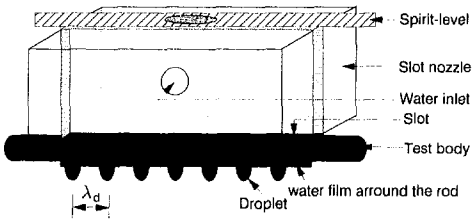

Fig. 3 Schematic representation of the experimental system

2 Lee's Analysis

Figure 1 shows the assumed geometry of an infinitely long circular cylindrical gas-liquid interface and the coordinates used by Lee (1963). Lee employed the continuity and motion equations for a two-dimensional flow in the labelled x-y plane. After considering the continuity of velocity components of the two fluids at the interface, Lee expressed the velocity potentials of fluid 1 and fluid 2 as

$$\phi_1 = K_1 \exp(\pm i\beta_1 x - \beta_1 y + c_1 t) \quad \text{for } y > \eta$$
$$\phi_2 = -K_1 \exp(\pm i\beta_1 x + \beta_1 y + c_1 t) \quad \text{for } y < \eta \quad (1)$$

and the pressure condition at the interface as

$$p_1|_{y=\eta} = p_2|_{y=\eta} + \sigma\left(1/R_{(x)} + 1/R_{(z)}\right) \quad (2)$$

where

K_1 = constant
c_1 = exponential growth rate
β_1 = wave number
$p_1|_{y=\eta}$ = static pressure at the upper side of the interface
$p_2|_{y=\eta}$ = static pressure at the lower side of the interface
σ = surface tension
$R_{(x)}$ = radius of curvature of the interface in the x-y plane
$R_{(z)}$ = radius of curvature in the y-z plane.

From the Bernoulli equation, the static pressures on the two sides of the interface were expressed as

$$p_1|_{y=\eta} = (p_0)_1 - c_1 K_1 \rho_1 \exp(\pm i\beta_1 x + c_1 t) - \rho_1 g\eta$$
$$p_2|_{y=\eta} = (p_0)_2 + c_1 K_1 \rho_2 \exp(\pm i\beta_1 x + c_1 t) - \rho_2 g\eta \quad (3)$$

where g is the acceleration due to gravity; ρ_1 and ρ_2 are the densities of fluid 1, liquid and fluid 2, air; $(p_0)_1$ and $(p_0)_2$ are, respectively, the stagnant values of $p_1|_{y=\eta}$ and $p_2|_{y=\eta}$ and are related by equation

$$(p_0)_1 = (p_0)_2 + \sigma/(R + \Delta R). \quad (4)$$

The gravity terms shown in Eq. (3) were missing in Lee's paper. Nevertheless, Lee considered them in his analysis. Lee expressed the curvature of the interface in the x-y plane as

$$\frac{1}{R_{(x)}} = \frac{\partial^2 \eta}{\partial x^2} \quad (5)$$

and the curvature of the interface in the y-z plane as

$$\frac{1}{R_{(z)}} = \frac{\partial^2 y}{\partial z^2} = \frac{1}{R + \Delta R} - \frac{\eta}{(R + \Delta R)^2} \quad (6)$$

Lee then considered a so-called "kinetic free-surface" condition at the interface $y = \eta$, i.e.:

$$-u\frac{\partial \eta}{\partial x} - \frac{\partial \eta}{\partial t} = 0. \quad (7)$$

From this, Lee obtained an expression for the disturbance interface,

$$\frac{\partial \eta}{\partial t} = \beta_1 K_1 \exp(\pm i\beta_1 x + c_1 t). \quad (8)$$

Combining Eqs. (1)–(6) and (8), Lee obtained the following dispersion equation:

$$c_1^2 = \left[g(\rho_2 - \rho_1) + \sigma\left(\beta_1^2 + 1/R^2\right)\right]\beta_1/(\rho_1 + \rho_2). \quad (9)$$

Since the wave amplitude grows according to $\exp(c_1 t)$, the interface is unstable when c_1^2 is greater than zero, i.e., when

$$\beta_1^2 > \left[\frac{(\rho_1 - \rho_2)g}{\sigma} - \frac{1}{R^2}\right]. \quad (10)$$

Consequently according to Lee, a shorter wavelength (larger wave number) would produce an unstable interface.

By maximizing the growth rate, C_1^2, for each fixed value of R, Lee obtained expressions for the most dangerous wave number which Lee designated the critical frequency:

$$\beta_c = \frac{\left(\frac{(\rho_1 - \rho_2)g}{\sigma} - \frac{1}{R^2}\right)^{1/2}}{\sqrt{3}}, \quad (11)$$

and the most dangerous wavelength which Lee designated the critical wavelength:

$$\lambda_c = \frac{2\pi\sqrt{3}}{\left(\frac{(\rho_1 - \rho_2)g}{\sigma} - \frac{1}{R^2}\right)^{1/2}}. \quad (12)$$

Thus according to Lee, the most dangerous wavelength increases with a decrease of the radius of the cylinder, which means that extremely thin wires would give the most stable interface. From Fig. 3 of Lee, the interface is stable for all wavelengths when the dimensionless radius is less than 1, i.e., $(g(\rho_1 - \rho_2)/\sigma)^{1/2}R < 1$. Again, this conclusion is questionable despite Lee's experimental verification.

In fact, Lee's analysis includes some mathematical errors which lead to the above conclusions. According to the definition of Lee's coordinates, the radius of curvature of the interface in the y-z plane is expressed as

$$R_{(z)} = R + \Delta R - \eta. \quad (13)$$

Using a Taylor expansion, Eq. (13) leads to

$$\frac{1}{R_{(z)}} = \frac{1}{R + \Delta R} + \frac{\eta}{(R + \Delta R)^2}. \quad (14)$$

Downloaded 04 May 2010 to 171.66.16.28. Redistribution subject to ASME license or copyright; see http://www.asme.org/terms/Terms_Use.cfm

By comparing Eq. (14) with Eq. (6), we find that the second term of Lee's expression for $1/R_{(z)}$ has the wrong sign. Furthermore, the correct kinetic condition at the interface, $y = \eta$, is that the radial velocity component must be continuous, i.e.,

$$\left(\frac{\partial \phi_1}{\partial y}\right)_{y=\eta} = \frac{\partial \eta}{\partial t} \tag{15}$$

rather than Lee's condition, Eq. (7). Combining Eqs. (1) and (15) yields

$$\frac{\partial \eta}{\partial t} = -\beta_1 K_1 \exp(\pm i\beta_1 x + c_1 t). \tag{16}$$

Comparison with Eq. (8) shows that Lee's expression for the disturbance interface, $y = \eta$, has missed a minus sign. Using Eqs. (14) and (16), Lee's dispersion equation, Eq. (9), becomes

$$c_1^2 = -\left[g(\rho_2 - \rho_1) + \sigma(\beta_1^2 - 1/R^2)\right]\beta_1/(\rho_1 + \rho_2) \tag{17}$$

Equation (17) shows that the interface is unstable when

$$\beta_1^2 < \left[\frac{(\rho_1 - \rho_2)g}{\sigma} + \frac{1}{R^2}\right] \tag{18}$$

i.e., longer wavelength (shorter wave number) will give an unstable interface, which is reasonable because the longer the wavelength, the higher the energy. The most dangerous wavelength is

$$\lambda_c = \frac{2\pi\sqrt{3}}{\left(\frac{(\rho_1 - \rho_2)g}{\sigma} + \frac{1}{R^2}\right)^{1/2}}, \tag{19}$$

i.e., the most dangerous wavelength decreases with a decrease in the radius of the cylinder. Notwithstanding the mathematical correctness of Eq. (19), it can only be considered as an approximation to the real solution because of the use of inappropriate velocity potentials and the negligence of the boundary condition on the cylindrical body.

3 A New Analysis

The present instability analysis for a cylindrical interface is carried out in the three-dimensional cylindrical coordinates. The steps involved are almost the same as the previous analysis. Figure 2 shows the assumed geometry in the cylindrical coordinates. Using Lee's denotation, Fig. 1, the interface between two fluids is assumed to be at $r = R + \Delta R \equiv R_0$, where R is the radius of the horizontal cylindrical body.

If the fluids are inviscid, the perturbed flow can be assumed to be irrotational. We then have

$$\nabla^2 \Phi = 0. \tag{20}$$

In the Laplace equation, Φ is the velocity potential. Thus,

$$U_r = \frac{\partial \Phi}{\partial r}, \quad U_\theta = \frac{1}{r}\frac{\partial \Phi}{\partial \theta}, \quad U_z = \frac{\partial \Phi}{\partial z} \tag{21}$$

where U_r, U_θ, and U_z are the velocity components in the cylindrical coordinates. The Laplace equation in cylindrical polar coordinates can be expressed as

$$\nabla^2 \Phi = \frac{\partial^2 \Phi}{\partial r^2} + \frac{1}{r}\frac{\partial \Phi}{\partial r} + \frac{1}{r^2}\frac{\partial^2 \Phi}{\partial \theta^2} + \frac{\partial^2 \Phi}{\partial z^2}. \tag{22}$$

The solution of the Laplace equation can be obtained by using the method of separation of variables (Bland, 1965), i.e.:

$$\Phi = R(r) \cdot \Theta(\theta) \cdot Z(z). \tag{23}$$

Furthermore, the velocity potential can be expressed as

$$\Phi = AI_n(\beta_1 r)\exp[c_1 t + i\beta_1 z]\cos(n\theta) + BK_n(\beta_1 r)\exp[c_1 t + i\beta_1 z]\cos(n\theta) \tag{24}$$

in which, A and B are constants and n, the order of Bessel functions, is an integer so that the velocity potential has the same value at $\theta = 0$ and at $\theta = 2\pi$. $I_n(\beta_1 r)$ and $K_n(\beta_1 r)$ are known as modified Bessel functions of the first kind and the second kind, respectively. Considering the geometry of the fluid system, Fig. 2, the velocity potentials for fluid 1 and fluid 2 (Φ_1 and Φ_2) can be expressed as

$$\Phi_1 = A(K_n'(\beta_1 R)I_n(\beta_1 r) - I_n'(\beta_1 R)K_n(\beta_1 r))\exp[c_1 t + i\beta_1 z)] \cdot \cos(n\theta) R \le r \le R_0$$

$$\Phi_2 = BK_n(\beta_1 r)\exp[c_1 t + i\beta_1 z)]\cos(n\theta) \quad r \ge R_0. \tag{25}$$

Let the disturbance of interface ($r = R_0$) be

$$r = R_0 + \eta(\theta, z, t) \tag{26}$$

The kinetic condition at the interface is that the radial velocity component must be continuous, and this demands

$$\frac{\partial \Phi_1}{\partial r} = \frac{\partial \Phi_2}{\partial r} = \frac{\partial \eta}{\partial t} \quad \text{at } r = R_0. \tag{27}$$

From Eq. (25) we have

$$A[K_n'(\beta_1 R)I_n'(\beta_1 R_0) - I_n'(\beta_1 R)K_n'(\beta_1 R_0)] = BK_n'(\beta_1 R_0), \tag{28}$$

while

$$\eta(\theta, z, t) = \int U_r dt = \int \left(\frac{\partial \Phi}{\partial r}\right)_{r=R_0} dt = \frac{1}{c_1}\left(\frac{\partial \Phi}{\partial r}\right)_{r=R_0}. \tag{29}$$

The dynamic boundary condition at the interface is

$$P_1' = P_2' + \sigma\left(\frac{1}{R_1} + \frac{1}{R_2}\right) \tag{30}$$

where P_1' and P_2' are the total pressures of fluid 1 and 2; R_1 and R_2 are the principal radii, counted positive if the centers of curvature are toward the symmetrical axis of cylindrical interface. In the case of absence of a disturbance, Eq. (30) becomes

$$P_{10}' = P_{20}' + \frac{\sigma}{R_0} \tag{31}$$

where P_{10}' and P_{20}' are the equilibrium pressures of fluids 1 and 2.

For the disturbance, the curvature in the direction of z is

$$\frac{1}{R_1} = -\frac{\partial^2 \eta}{\partial z^2}. \tag{32}$$

While the curvature of the surface which differs infinitely little from a circle having its center at the origin is

$$\frac{1}{R_2} = \frac{1}{r} - \frac{1}{r^2}\frac{\partial^2 r}{\partial \theta^2}. \tag{33}$$

From Eq. (26) and if the disturbance (η) is small, we have

$$\frac{1}{r} = \frac{1}{R_0} - \frac{\eta(\theta, z, t)}{R_0^2} \tag{34}$$

Moreover,

$$\frac{1}{R_2} = \frac{1}{R_0} - \frac{1}{R_0^2}\left(\eta(\theta, z, t) + \frac{\partial^2 \eta}{\partial \theta^2}\right) \tag{35}$$

Downloaded 04 May 2010 to 171.66.16.28. Redistribution subject to ASME license or copyright; see http://www.asme.org/terms/Terms_Use.cfm

Thus, the perturbation pressures, P_1^d and P_2^d, must then satisfy the following condition:

$$P_1^d = P_2^d + \sigma\left(-\frac{\partial^2\eta}{\partial z^2} - \frac{\eta}{R_0^2} - \frac{1}{R_0^2}\frac{\partial^2\eta}{\partial\theta^2}\right). \quad (36)$$

From Eqs. (25) and (29), we have

$$\frac{\partial^2\eta}{\partial z^2} = \frac{1}{c_1}\left(\frac{\partial\Phi}{\partial r}\right)(-\beta_1^2) = -\beta_1^2\eta \quad (37)$$

$$\frac{\partial^2\eta}{\partial\theta^2} = \frac{1}{c_1}\left(\frac{\partial\phi}{\partial r}\right)(-n^2) = -n^2\eta. \quad (38)$$

Thus

$$P_1^d = P_2^d + \left(\beta_1^2 - \frac{1}{R_0^2} - \frac{n^2}{R_0^2}\right)\eta\sigma. \quad (39)$$

From the Bernoulli equation, neglecting the second-order velocity term, we have

$$P_1^d = -\rho_1\left(\frac{\partial\Phi_1}{\partial t} + g\eta\cos(\theta)\right),$$

$$P_2^d = -\rho_2\left(\frac{\partial\Phi_2}{\partial t} + g\eta\cos(\theta)\right). \quad (40)$$

Substituting Eqs. (29) and (40) into Eq. (39) and rearranging give

$$c_1^2 = -\frac{\sigma\left(-\beta_1^2 + \frac{1}{R_0^2} - \frac{n^2}{R_0^2} + \frac{(\rho_2-\rho_1)g\cos(\theta)}{\sigma}\right)\left(\frac{\partial\Phi}{\partial r}\right)_{r=R_0}}{\rho_2\Phi_2|_{r=R_0} - \rho_1\Phi_1|_{r=R_0}}. \quad (41)$$

Substituting Eqs. (25) and (27) into above equation, we get the required formula:

$$c_1^2 = \frac{\sigma\beta_1\left(\beta_1^2 - \frac{1-n^2}{R_0^2} - \frac{(\rho_2-\rho_1)g\cos(\theta)}{\sigma}\right)}{\rho_2\frac{K_n(\beta_1R_0)}{K_n'(\beta_1R_0)} - \rho_1\frac{K_n'(\beta_1R)I_n(\beta_1R_0) - I_n'(\beta_1R)K_n(\beta_1R_0)}{K_n'(\beta_1R)I_n'(\beta_1R_0) - I_n'(\beta_1R)K_n'(\beta_1R_0)}}. \quad (42)$$

Equation (42) gives the relationship between the exponential growth rate (c_1) and the wave number (β_1) for a cylindrical interface. The nature of c_1 governs the stability of the disturbance. If c_1 is imaginary, the stabilizing effect of surface tension in the axial direction will smooth out the disturbance. If c_1 is real, the force of gravity will dominate and the disturbance will increase exponentially. c_1 passes from real to imaginary as the right-hand side of Eq. (42) passes through zero. The critical wave number and critical wavelength are then obtained by equating the right-hand side to zero:

$$\lambda = \frac{2\pi}{\beta_1} = \frac{2\pi}{\left(\frac{(\rho_2-\rho_1)g\cos(\theta)}{\sigma} + \frac{(1-n^2)}{R_0^2}\right)^{1/2}}. \quad (43)$$

The most dangerous wave number and wavelength were obtained by maximizing c_1 using a numerical optimization technique such as the commercial available software *TK-Solver* (1989).

Since the order of Bessel function, n, equals 0 for a cylindrical interface, the dispersion Eq. (42) becomes

$$c_1^2 = \frac{\sigma\beta_1\left(\beta_1^2 - \frac{1}{R_0^2} - \frac{(\rho_2-\rho_1)g\cos(\theta)}{\sigma}\right)}{-\rho_2\frac{K_0(\beta_1R_0)}{K_1(\beta_1R_0)} - \rho_1\frac{K_1(\beta_1R)I_0(\beta_1R_0) + I_1(\beta_1R)K_0(\beta_1R_0)}{K_1(\beta_1R)I_1(\beta_1R_0) - I_1(\beta_1R)K_1(\beta_1R_0)}}. \quad (44)$$

Equation (44) can be greatly simplified for the following two extremes:

(1) $R = 0$

In the absence of the cylindrical body, $R = 0$, Eq. (44) is simplified as

$$c_1^2 = -\frac{\sigma\beta_1\left(\beta_1^2 - \frac{1}{R_0^2} - \frac{(\rho_2-\rho_1)g\cos(\omega)}{\sigma}\right)}{\rho_2\frac{K_0(\beta_1R_0)}{K_1(\beta_1R_0)} + \rho_1\frac{I_0(\beta_1R_0)}{I_1(\beta_1R_0)}}. \quad (45)$$

(2) $\Delta R \ll R$

When the cylindrical body is coated with a very thin film, $\Delta R \ll R$ and $R \approx R_0$, Eq. (44) is simplified as

$$c_1^2 = -\frac{\sigma\beta_1^2\Delta R\left(\beta_1^2 - \frac{1}{R^2} - \frac{(\rho_2-\rho_1)g\cos(\theta)}{\sigma}\right)}{\rho_2\beta_1\Delta R\frac{K_0(\beta_1R)}{K_1(\beta_1R)} + \rho_1}. \quad (46)$$

Equation (46) has potential applications in film boiling and film condensation on a horizontal cylinder. During film boiling on a horizontal cylinder, the cylindrical body is coated by a gas layer and unstable gas-liquid interface is formed on top of the horizontal cylinder (Lienhard and Wong, 1963). After

Downloaded 04 May 2010 to 171.66.16.28. Redistribution subject to ASME license or copyright; see http://www.asme.org/terms/Terms_Use.cfm

substitution of $\rho_1 = \rho_g$, $\rho_2 = \rho_l$ and $\theta = 0$, Eq. (46) becomes

$$c_1^2 = -\frac{\sigma\beta_1^2\Delta R\left(\beta_1^2 - \frac{1}{R^2} - \frac{(\rho_l - \rho_g)g}{\sigma}\right)}{\rho_l\beta_1\Delta R\frac{K_0(\beta_1 R)}{K_1(\beta_1 R)} + \rho_g}. \quad (47)$$

Equation (47) can be further simplified by considering the following order of magnitude: $\beta_1 R = 2\pi R/\lambda$ has a value of almost 6 since λ is in the order of R. Therefore, $K_0(\beta_1 R)/K_1(\beta_1 R)$ is almost 1. If the thickness of the film surrounding the cylinder is about ten percent of the radius of the cylinder, $\beta_1\Delta R = 2\pi\Delta R/\lambda$ is then about 0.6. ρ_l is a few hundreds times greater than ρ_g. Consequently, the gas density term of Eq. (47) can be neglected, i.e.,

$$c_1^2 = -\frac{\sigma\beta_1\left(\beta_1^2 - \frac{1}{R^2} - \frac{\rho_l g}{\sigma}\right)}{\rho_l\frac{K_0(\beta_1 R)}{K_1(\beta_1 R)}}. \quad (48)$$

After modification by taking into consideration of asymmetrical effect of the gas-liquid interface. Equation (48) has been successfully used to predict the dominant wavelength during film boiling on a cylinder heater (Li and Harris, 1993).

For liquid film breakup from the bottom of a cylindrical body in still air, substituting $\theta = 180$ deg, $\rho_1 = \rho_l$ and $\rho_2 = \rho_g$ into Eq. (46) yields

$$c_1^2 = -\frac{\sigma\beta_1^2\Delta R\left(\beta_1^2 - \frac{1}{R^2} - \frac{(\rho_l - \rho_g)g}{\sigma}\right)}{\rho_g\beta_1\Delta R\frac{K_0(\beta_1 R)}{K_1(\beta_1 R)} + \rho_l}. \quad (49)$$

Equation (49) can be further simplified by neglecting the gas density term, i.e.,

$$c_1^2 = -\frac{\sigma\beta_1^2\Delta R}{\rho_l}\left(\beta_1^2 - \frac{1}{R^2} - \frac{\rho_l g}{\sigma}\right). \quad (50)$$

In order to express above equation in a convenient dimensionless form, we define following dimensionless variables:

(1) *Dimensionless radius:*

$$R^* = R\left(\frac{\rho_l g}{\sigma}\right)^{1/2}. \quad (51)$$

(2) *Dimensionless wave number:*

$$\beta^* = \beta_1\left(\frac{\sigma}{\rho_l g}\right)^{1/2}. \quad (52)$$

(3) *Dimensionless growth rate:*

$$C^* = c_1\left[\frac{\sigma}{\rho_l g^3}\right]^{1/4} \quad (53)$$

(4) *Dimensionless liquid film thickness:*

$$\Delta R^* = \Delta R\left(\frac{\rho_l g}{\sigma}\right)^{1/2} \quad (54)$$

From Eq. (52), we have dimensionless wavelength:

$$\lambda^* = \frac{2\pi}{\beta^*} = \frac{2\pi}{\beta_1}\left(\frac{\rho_l g}{\sigma}\right)^{1/2} = \lambda\left(\frac{\rho_l g}{\sigma}\right)^{1/2}. \quad (55)$$

Table 1 Experimental results for the breakup of liquid film

Material of rod	Steel	Steel	Steel	Steel	Glass	Glass
Rod diameter, $D = 2R$ (mm)	15.88	9.53	5.16	3.76	7.12	3.94
Average, λ_d (cm)	2.54	2.48	1.84	1.69	2.10	1.90
Standard deviation, $\sigma_{sd}(\lambda_d)$	0.48	0.24	0.25	0.25	0.16	0.16

Finally, Eq. (50) can be expressed in dimensionless form:

$$C^{*2} = -\Delta R^*\left[\beta^{*2} - \frac{1}{R^{*2}} - 1\right]\beta^{*2}. \quad (56)$$

Equation (56) is independent of the properties of fluids. Maximizing the dimensionless growth rate, C^*, for each fixed value of R^* gives the most dangerous dimensionless wavelength, λ_d^*,

$$\lambda_d^* = \frac{2\pi\sqrt{2}}{\sqrt{1 + \frac{1}{R^{*2}}}} \quad (57)$$

or in dimensional form

$$\lambda_d = \frac{2\pi\sqrt{2}}{\sqrt{\frac{1}{R^2} + \frac{\rho_l g}{\sigma}}}. \quad (58)$$

4 Experiments

Experiments were carried out to measure the most dangerous wavelength during liquid film breakup from a cylindrical body. The apparatus is shown in Fig. 3. It consisted of a horizontal water supply slot, a cylindrical rod attached beneath the slot and a spirit level. The spacing and length of the slot were $W = 120$ μm and $L = 20$ cm. A ruler was placed below the rod, providing a scale to measure the droplet spacing. Tap water was fed through the slot onto the cylindrical rod to form a liquid film around the rod. The flow rate of water was maintained at the minimum required to form a continuous film around the rod. The horizontal attitude of the rod was guaranteed by the spirit level. For each of the given rods, five to ten pictures were taken at different liquid flow rates. The distance between the nodes from which the liquid film breaks up into droplets were measured from each of the pictures. Results are presented in Table 1 and Fig. 4.

Figure 5 presents the breakup of liquid film around a cylindrical rod due to the Rayleigh-Taylor instability. The distance between the nodes decreases with a decrease in the diameter of the rod.

The diameters of the glass and the stainless steel rods used are in the range of 0.6–8 mm. Photographs were taken at 1/500s with a macrolens 35 mm camera. For each trial, the rod diameter and material were indicated on a panel included on the photographs. The predicted dimensionless most dangerous wavelength based on Eq. (57) is also shown in Fig. 4 by a solid line. Equation (57) predicts the dimensionless wavelength with a great success.

5 Conclusions

1 A general dispersion equation, relating wave number, β_1, to growth rate, c_1, was derived for the Rayleigh-Taylor instability of an axisymmetric cylindrical interface between two inviscid fluids with the consideration of the effects of the cylindrical interface and finite film thickness.

Downloaded 04 May 2010 to 171.66.16.28. Redistribution subject to ASME license or copyright; see http://www.asme.org/terms/Terms_Use.cfm

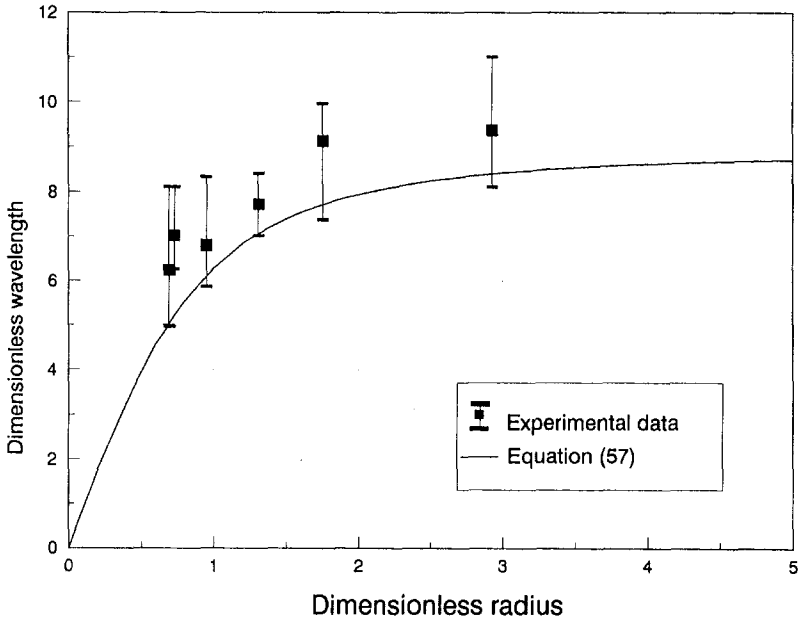

Fig. 4 The relationship between the dimensionless most dangerous wavelength and dimensionless radius of the tube

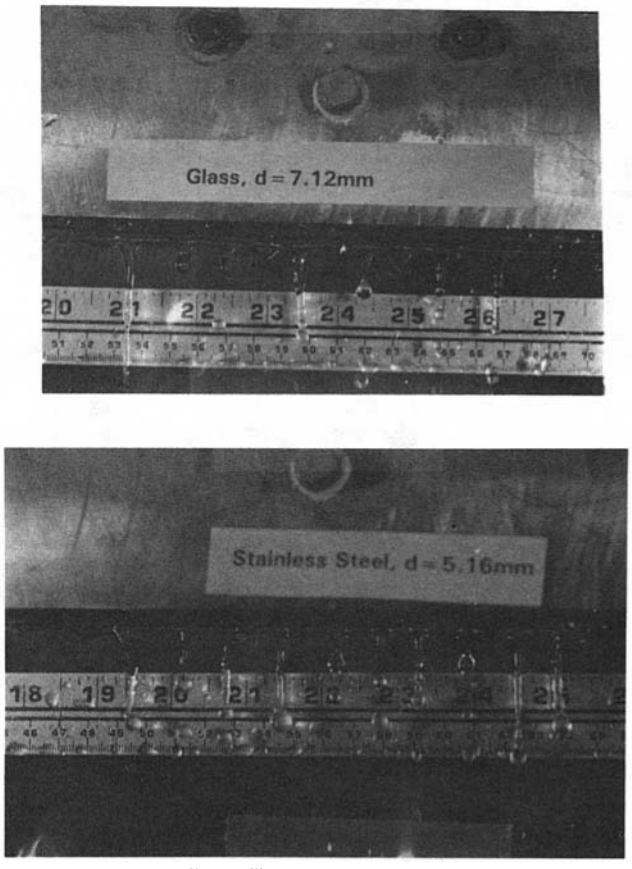

Fig. 5 Breakup a liquid film around a horizontal cylindrical tube

2 Experiments and a theoretical analysis were carried out to measure and to predict the dominant wavelength during cylindrical liquid film breakup. It was found that the distance between the nodes decreases with a decrease in the radius of the cylindrical body. The most dangerous wavelength is predicted successfully by Eq. (57).

References

Bellman, R., and Pennington, R. H., 1954, "Effects of Surface Tension and Viscosity on Taylor Instability," *Quart. Appl. Math.*, Vol. 12, pp. 151–162.

Bland, D. R. 1965, *Solutions of Laplace's Equation*, Routledge and Kegan Paul, London.

Dhir, V. K., and Lienhard, J. H., 1973, "Taylor Stability of Viscous Fluids with Application to Film Boiling," *Int. J. Heat Mass Transfer*, Vol. 16, pp. 2097–2109.

Harrison, W. J., 1908, "The Influence of Viscosity on the Oscillations of Superposed Fluids," *Proc. London Math. Soc.*, Vol. 6, pp. 396–405.

Lamb, H., 1932, *Hydrodynamics*, Cambridge, U.K., pp. 370–372.

Lee, S. L., 1963, "Taylor Instability of a Liquid Film Around a Long, Horizontal, Circular Cylindrical Body in Still Air," ASME JOURNAL OF APPLIED MECHANICS, Vol. 30, Vol. 85, pp. 443–447.

Lewis, D. J., 1951, "The Instability of Liquid Surfaces when Accelerated in a Direction Perpendicular to their Planes. II," *Proc. Roy. Soc., London*, Vol. A202, pp. 81–96.

Li, R., and Harris, R., 1993, "On the Dominant Unstable Wavelength During Film Boiling on a Horizontal Cylinder," ASME *J. Heat Transfer*, Vol. 115, No. 2, pp. 498–501.

Lienhard, J. H., and Wong, P. T. Y., 1964, "The Dominant Unstable Wavelength and Minimum Heat Flux During Film Boiling on a Horizontal Cylinder," ASME *J. Heat Transfer*, Vol. 88, pp. 220–226.

Rayleigh, L., 1990, "Investigation of the Character of the Equilibrium of an Incompressible Heavy Fluid of Variable Density," *Scientific Papers*, Vol. II, Cambridge University Press, Cambridge, U.K., pp. 200–207.

Taylor, G., 1950, "The Stability of Fluid Surfaces when Accelerated in a Direction Perpendicular to their Planes. I," *Proc. Roy. Soc.*, London, Vol. A201, pp. 192–196.

Tk-Solver, 1989, Universal Technical Systems, Rockford, IL.

Downloaded 04 May 2010 to 171.66.16.28. Redistribution subject to ASME license or copyright; see http://www.asme.org/terms/Terms_Use.cfm

O. Y. Zharii

A. F. Ulitko

Department of Theoretical and Applied Mechanics, Kiev University, 64 Vladimirskaya Street, Kiev 252017, Ukraine

Smooth Contact Between the Running Rayleigh Wave and a Rigid Strip

A problem of frictionless contact between the running Rayleigh wave and a rigid strip is investigated. The corresponding mixed boundary value problem of elastodynamics is reduced to a system of dual series equations involving trigonometric functions. On the base of the closed-form solution obtained, explicit analytic expressions for distributions of normal displacements and stresses and of tangential velocities on the surface have been derived.

1 Introduction

Problems of dynamic contact interaction between vibrating surfaces of solids and rigid bodies are of interest at least for two reasons. First, because they are "inverse" as compared to classic "direct" contact problems of elastodynamics, in which wave fields in solids generated by moving and/or vibrating stamps are investigated. The two kinds of problems are quite different both in the very approach to their formulation and solution, and in the viewpoint from which solutions obtained are analyzed.

Second, these problems are of practical value in modeling of ultrasonic motors. Ultrasonic motors is the name of devices that transform vibrational and wave motions of solids into progressive or rotational motions of rigid bodies by means of frictional forces in contact. Both for establishing design procedure and improving characteristics, precise theoretical treatment is necessary although the fundamental principle is known (Ueha, 1989; Zharii, 1993).

The subject of this paper is connected with the particular kind of ultrasonic motors, namely that of traveling wave type. Existing theoretical models of this kind of motors (Kurosawa and Ueha, 1988; Suzuki et al., 1990) reproduce its characteristics only partially.

It is well known (Johnson, 1987; Mindlin and Deresiewicz, 1953), that in a general case the area of contact between two solids is subdivided into portions of adhesion and slip. Boundaries of these portions cannot be indicated in advance. Solution of an elastodynamic contact problem is complicated by its inherent nonlinearity (distributions of surface stresses depend on unknown in advance velocities). The size of contact area and the location of adhesive and slip zones are undefined too. They are determined in the course of solution. These circumstances make the rigorous solution of the dynamic contact problem to be very difficult.

On the base of the knowledge achieved in the static contact mechanics (Johnson, 1987), we try to develop an approximate approach to a dynamic problem by subdivision of it into two steps. At the first stage the influence of tangential stresses on the size of the contact area and on the normal stresses distribution is ignored and a problem of smooth contact is considered. It means that tangential stresses are taken to be equal to zero on the whole boundary $y = 0$.

At the second stage using already found solutions for normal stresses and tangential velocities, under several additional assumptions, one can try to restore the tangential stresses approximately. As a result, the progressive motion of the rotor under the action of tangential stresses can be investigated.

In this paper, we consider a smooth dynamic problem. The analogous periodic static problem was solved by Westergaard (1939).

2 Formulation of the Problem

The stator of an ultrasonic motor is represented as a piezoceramic plate of thickness h: $-h/2 < z < h/2$, polarized in the z-direction. The plate is a half-plane in shape: $-\infty < x < \infty$, $y > 0$ (Fig. 1). Vibrations are excited by the running electric field,

$$E_z = E_0 \cos(kx - \omega t), \tag{1}$$

where k is the wave number, ω is the angular frequency of excitation, $\lambda = 2\pi/k$ is the wavelength. By this is meant that electrodes are thin strips parallel to the y-axis. They are separated by narrow dielectric gaps.

The rotor is modeled by a rigid strip. Notice that the assumption of absolute rigidity of the rotor as compared to the stator is realistic when elastic moduli of the stator mate-

Contributed by the Applied Mechanics Division of THE AMERICAN SOCIETY OF MECHANICAL ENGINEERS for publication in the ASME JOURNAL OF APPLIED MECHANICS.

Discussion on this paper should be addressed to the Technical Editor, Professor Lewis T. Wheeler, Department of Mechanical Engineering, University of Houston, Houston, TX 77204-4792, and will be accepted until four months after final publication of the paper itself in the ASME JOURNAL OF APPLIED MECHANICS.

Manuscript received and accepted by the ASME Applied Mechanics Division, July 15, 1993. Associate Technical Editor: T. R. Akylas.

Copyright © 1995 by ASME

Downloaded 04 May 2010 to 171.66.16.28. Redistribution subject to ASME license or copyright; see http://www.asme.org/terms/Terms_Use.cfm

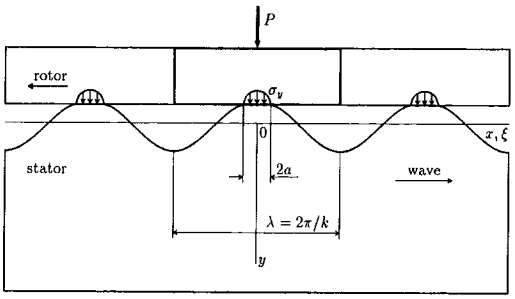

Fig. 1 Geometry of the problem

rial are less than those of the rotor by a factor of 2–3. For a steel rotor this relation does occur.

The equation of motion of the plate in the plane stress approximation is (Grinchenko et al., 1976, 1989)

$$c_1^2 \,\text{grad div}\,\mathbf{u} - c_2^2 \,\text{rot rot}\,\mathbf{u} - (1+\nu)d_{31}c_1^2 \,\text{grad}\, E_z = \frac{\partial^2 \mathbf{u}}{\partial t^2}, \tag{2}$$

where $\mathbf{u} = \mathbf{i}u_x(x, y, t) + \mathbf{j}u_y(x, y, t)$ is the displacement vector and

$$c_1 = \left[\rho s_{11}^E(1-\nu^2)\right]^{-1/2}, \quad c_2 = \left[2\rho s_{11}^E(1+\nu)\right]^{-1/2} \tag{3}$$

are the longitudinal and transverse wave velocities. These and forthcoming notations have been universally accepted (American National Standard, 1984; Berlincourt et al., 1964).

Taking into account the specific form of excitation, we pass on to the movable coordinate system, $\xi = x - \omega t/k$, y. In this system, equations of motion (2) become

$$c_1^2 \,\text{grad div}\,\mathbf{u} - c_2^2 \,\text{rot rot}\,\mathbf{u} + \mathbf{i}(1+\nu)d_{31}c_1^2 E_0 k \sin k\xi - \frac{\omega^2}{k^2}\frac{\partial^2 \mathbf{u}}{\partial \xi^2} = 0. \tag{4}$$

In the absence of the rotor, excited in the stator are the running waves of wavelength λ. If now a rigid rotor is pressed to the surface $y = 0$ by means of the force P per unit wavelength, after decaying of the transient process, contact areas of length $2a$ arise.

We presume that inside the contact area $-a < \xi < a$, an unknown symmetrical on the coordinate ξ distribution of normal stresses is prescribed and tangential stresses vanish:

$$\sigma_y = f(\xi), \quad \tau_{\xi y} = 0, \quad -a < \xi < a, \quad y = 0. \tag{5}$$

Outside the contact area both components of stresses vanish:

$$\sigma_y = \tau_{\xi y} = 0, \quad a < |\xi| < \pi/k, \quad y = 0. \tag{6}$$

The unknown function $f(\xi)$ is to be determined from the kinematic contact condition,

$$u_y|_{y=0} = u_{y0} = \text{const}, \quad -a < \xi < a. \tag{7}$$

In addition, the resultant of normal stresses is to be equal in magnitude and opposite in sign to the pressing force P:

$$\int_{-a}^{a} f(\xi)d\xi = -P. \tag{8}$$

Equations (4), complemented with boundary conditions (5)–(7) and the static condition (8), completely determine the problem of smooth contact.

3 Derivation of the System of Dual Equations

We write the solution of the problem formulated in the form

$$u_x(s, y) = \sum_{n=1}^{\infty} U_n(y) \sin ns,$$

$$u_y(s, y) = \frac{1}{2}V_0(y) + \sum_{n=1}^{\infty} V_n(y) \cos ns, \tag{9}$$

where $s = k\xi$ is the nondimensional coordinate, U_n, V_n are functions to be determined.

Substituting (9) into (4), multiplying the equations obtained by sin ms, cos ms (m is natural) and integrating with respect to s from 0 to π, we obtain the system of equations

$$-c_1^2 nk\left(nkU_n + \frac{dV_n}{dy}\right) + c_2^2\frac{d}{dy}\left(nkV_n + \frac{dU_n}{dy}\right) + \omega^2 n^2 U_n + \delta_{n1}(1+\nu)d_{31}c_1^2 kE_0 = 0,$$

$$c_1^2\frac{d}{dy}\left(nkU_n + \frac{dV_n}{dy}\right) - c_2^2 nk\left(nkV_n + \frac{dU_n}{dy}\right) + \omega^2 n^2 V_n = 0,$$

$$\frac{d^2 V_0}{dy^2} = 0, \tag{10}$$

where δ_{n1} is the Kronecker delta.

The general solution of (10) is

$$U_n = nkA_n e^{-n\gamma_1 y} + n\gamma_2 B_n e^{-n\gamma_2 y} + \delta_{n1}k\frac{(1+\nu)d_{31}E_0}{\gamma_1^2},$$

$$V_n = n\gamma_1 A_n e^{-n\gamma_1 y} + nkB_n e^{-n\gamma_2 y},$$

$$V_0 = v_0 + v_1 y. \tag{11}$$

In these formulae, A_n, $B_n (n \geq 1)$, v_0, v_1 are arbitrary constants, $\gamma_{1,2} = (k^2 - \omega^2/c_{1,2}^2)^{1/2}$.

To satisfy boundary conditions, we use the expressions for contact stresses (Grinchenko et al., 1989):

$$\sigma_y = \frac{1}{s_{11}^E(1-\nu^2)}\left[\nu\frac{\partial u_x}{\partial \xi} + \frac{\partial u_y}{\partial y} - d_{31}(1+\nu)E_z\right],$$

$$\tau_{\xi y} = \frac{1}{2s_{11}^E(1+\nu)}\left(\frac{\partial u_x}{\partial y} + \frac{\partial u_y}{\partial \xi}\right). \tag{12}$$

Substitution of (9) and (11) into (12) gives

$$\sigma_y = \frac{\rho c_1^2}{2}v_1 - \rho c_2^2\sum_{n=1}^{\infty} n^2\left[\left(k^2+\gamma_2^2\right)A_n e^{-n\gamma_1 y} + 2k\gamma_2 B_n e^{-n\gamma_2 y} + \delta_{n1}(1+\nu)d_{31}E_0\frac{k^2+\gamma_2^2}{\gamma_1^2}\right]\cos ns,$$

$$\tau_{\xi y} = -\rho c_2^2\sum_{n=1}^{\infty} n^2\left[2k\gamma_1 A_n e^{-n\gamma_1 y} + \left(k^2+\gamma_2^2\right)B_n e^{-n\gamma_2 y}\right]\sin ns. \tag{13}$$

Let us represent the unknown contact stresses in the form of Fourier series on the interval $-\pi < s < \pi$:

$$f(s) = \frac{f_0}{2} + \sum_{n=1}^{\infty} f_n \cos ns. \tag{14}$$

Building on this expansion, we combine boundary conditions (5), (6),

Downloaded 04 May 2010 to 171.66.16.28. Redistribution subject to ASME license or copyright; see http://www.asme.org/terms/Terms_Use.cfm

$$\sigma_y|_{y=0} = \frac{f_0}{2} + \sum_{n=1}^{\infty} f_n \cos ns, \quad \tau_{\xi y}|_{y=0} = 0, \quad |s| < \pi. \quad (15)$$

Now, comparing series (15) and (13) at $y = 0$, one obtains a system of algebraic equations for determination of A_n, B_n

$$(k^2 + \gamma_2^2)A_n + 2k\gamma_2 B_n = -\frac{1}{n^2}\left[\delta_{n1}(1+\nu)d_{31}E_0\frac{k^2+\gamma_2^2}{\gamma_1^2} + \frac{f_n}{\rho c_2^2}\right],$$

$$2k\gamma_1 A_n + (k^2 + \gamma_2^2)B_n = 0,$$

$$v_1 = \frac{f_0}{\rho c_1^2}. \quad (16)$$

After solution of the system and substitution of A_n, B_n, v_1 into (11), (9), we find the expressions for displacements

$$u_x = (1+\nu)d_{31}E_0\frac{k}{\gamma_1^2} \times \left[(k^2+\gamma_2^2)\frac{-(k^2+\gamma_2^2)e^{-\gamma_1 y} + 2\gamma_1\gamma_2 e^{-\gamma_2 y}}{\Delta_R} + 1\right]\sin s + \frac{k}{\rho c_2^2}\frac{1}{\Delta_R}\sum_{n=1}^{\infty}\frac{f_n}{n}\left[-(k^2+\gamma_2^2)e^{-n\gamma_1 y} + 2\gamma_1\gamma_2 e^{-n\gamma_2 y}\right]\sin ns,$$

$$u_y = \frac{v_0}{2} + \frac{f_0}{2\rho c_1^2}y + (1+\nu)d_{31}E_0\frac{k^2+\gamma_2^2}{\gamma_1} \times \frac{-(k^2+\gamma_2^2)e^{-\gamma_1 y} + 2k^2 e^{-\gamma_2 y}}{\Delta_R}\cos s + \frac{\gamma_1}{\rho c_2^2}\frac{1}{\Delta_R}\sum_{n=1}^{\infty}\frac{f_n}{n}\left[-(k^2+\gamma_2^2)e^{-n\gamma_1 y} + 2k^2 e^{-n\gamma_2 y}\right]\cos ns, \quad (17)$$

where $\Delta_R = (k^2 + \gamma_2^2)^2 - 4k^2\gamma_1\gamma_2$ is the Rayleigh determinant.

Inserting the second of expressions (17) into (7), after obvious transformations we obtain

$$\sum_{n=1}^{\infty}\frac{f_n}{n}\cos ns = A\cos s + B, \quad 0 < s < \alpha. \quad (18)$$

From this point onward,

$$A = -(1+\nu)d_{31}E_0 \cdot \rho c_2^2\frac{k^2+\gamma_2^2}{\gamma_1^2},$$

$$B = \frac{\rho c_2^2\Delta_R}{\gamma_1(k^2-\gamma_2^2)}\left(u_{y0} - \frac{v_0}{2}\right), \quad (19)$$

and $\alpha = ka$ is the nondimensional half-length of the contact area.

In order to exclude the unknown quantity B, we differentiate (18) with respect to s. Appending the equation obtained by the condition of the absence of normal stresses outside the contact area ($\alpha < |s| < \pi$), we come to a dual system of series equations for Fourier coefficients f_n of the function $f(s)$:

$$\sum_{n=1}^{\infty} f_n \sin ns = A\sin s, \quad 0 < s < \alpha,$$

$$\frac{f_0}{2} + \sum_{n=1}^{\infty} f_n \cos ns = 0, \quad \alpha < s < \pi. \quad (20)$$

4 Solution of Dual Equations

We solve the system of dual equations using the technique developed by Srivastav (1964). Introducing an integral representation of $f(s)$ using an auxiliary function $F(s)$.

$$f(s) = \frac{f_0}{2} + \sum_{n=1}^{\infty} f_n \cos ns = \cos\frac{s}{2}\int_s^{\alpha}\frac{F(s_1)ds_1}{\sqrt{\cos s - \cos s_1}}, \quad 0 < s < \alpha, \quad (21)$$

one can see that thanks to the following from (6), condition

$$f(s) \equiv 0, \quad s > \alpha, \quad (22)$$

representation (21) identically satisfies the second part of (20). Substitution of (21) into the inversion formulas

$$f_0 = \frac{2}{\pi}\int_0^{\alpha} f(s)ds, \quad f_n = \frac{2}{\pi}\int_0^{\alpha} f(s)\cos nsds \quad (23)$$

and use of the integral representation of Legendre polynomials (Srivastav, 1964)

$$P_n(\cos s) = \frac{\sqrt{2}}{\pi}\int_s^{\pi}\frac{\sin(n+1/2)s_1 ds_1}{\sqrt{\cos s - \cos s_1}} \quad (24)$$

gives rise the expressions

$$f_0 = \sqrt{2}\int_0^{\alpha} F(s)ds,$$

$$f_n = \frac{1}{\sqrt{2}}\int_0^{\alpha} F(s)\left[P_n(\cos s) + P_{n-1}(\cos s)\right]ds \quad (n \geq 1). \quad (25)$$

Finally, after substitution of (25) into the first part of (20) and using the formula

$$\sum_{n=1}^{\infty}\left[P_n(\cos\varphi) + P_{n-1}(\cos\varphi)\right]\sin n\beta = \begin{cases}\dfrac{\sqrt{2}\cos\beta/2}{\sqrt{\cos\varphi - \cos\beta}}, & \varphi < \beta,\\ 0, & \varphi > \beta,\end{cases} \quad (26)$$

one obtains the Abel equation

$$\cos\frac{s}{2}\int_0^{s}\frac{F(s_1)ds_1}{\sqrt{\cos s_1 - \cos s}} = A\sin s \quad (27)$$

which has the unique solution

$$F(s) = \frac{A}{\sqrt{2}}\sin s. \quad (28)$$

After that, the contact stresses distribution can be found by means of integration in (21):

$$f(s) = 2A\cos\frac{s}{2}\sqrt{\cos^2\frac{s}{2} - \cos^2\frac{\alpha}{2}}, \quad s < \alpha. \quad (29)$$

Now, having determined the term f_0 from (28) and from the first of Eqs. (25),

$$f_0 = 2A\sin^2\frac{\alpha}{2}, \quad (30)$$

Downloaded 04 May 2010 to 171.66.16.28. Redistribution subject to ASME license or copyright; see http://www.asme.org/terms/Terms_Use.cfm

we use the static condition (8), which is equivalent to

$$f_0 = -\frac{kP}{\pi}. \tag{31}$$

From the two latter equalities one obtains an equation that determines the length of the contact area,

$$\sin^2\frac{\alpha}{2} = -\frac{1}{A}\frac{kP}{2\pi}. \tag{32}$$

Analysis of this equation is performed below.

5 Analysis of Solution

Let us consider kinematic characteristics of the running wave in smooth contact with the rotor.

According to (17), (25), (28), vertical displacements of the boundary $y = 0$ are defined by the formula

$$u_y|_{y=0} = \frac{v_0}{2} - U\left\{\cos s - \frac{1}{2}\sum_{n=1}^{\infty}\frac{1}{n}\int_0^{\alpha}\sin s_1\left[P_n(\cos s_1) + P_{n-1}(\cos s_1)\right]ds_1 \cdot \cos ns\right\}, \tag{33}$$

where

$$U = -(1+\nu)d_{31}E_0\frac{(k^2-\gamma_2^2)(k^2+\gamma_2^2)}{\gamma_1\Delta_R} \tag{34}$$

is the amplitude of vertical displacement of the boundary $y = 0$ in the absence of a rotor. Taking into account that $d_{31} < 0$, and $\Delta_R < 0$ in the interval $0 < \omega < kc_R$ (c_R is the Rayleigh wave velocity), we find $U \geq 0$ at $E_0 < 0$. The profile of an undisturbed wave is represented by the formula $u_y|_{y=0} = v_0/2 - U\cos s$ and contact surfaces are truly located as shown in Fig. 1.

Changing orders of summation and integration in (33), using (26) and the formula (Brychkov et al., 1981),

$$\sum_{n=1}^{\infty}\frac{1}{n}\left[P_n(\cos s) + P_{n-1}(\cos s)\right] = -2\ln\sin\frac{s}{2}, \tag{35}$$

and calculating the integrals obtained, displacements of the boundary outside the contact region ($\alpha < |s| < \pi$) can be represented as follows:

$$u_y|_{y=0} = U\left[2\sin^2\frac{\alpha}{2}\ln\frac{1+\cos\frac{\alpha}{2}}{\sin\frac{s}{2} + \sqrt{\sin^2\frac{s}{2} - \sin^2\frac{\alpha}{2}}} + 2\left(\sin\frac{s}{2}\sqrt{\sin^2\frac{s}{2} - \sin^2\frac{\alpha}{2}} - \cos\frac{\alpha}{2}\right) + 1\right]. \tag{36}$$

In the final form of (36), the constant v_0 was determined from an additional equality,

$$u_y|_{y=0,s=\pi} = U. \tag{37}$$

The meaning of the latter is as follows. In plane problems of elasticity (in particular, it follows from the second of (17)), displacements are determined with an accuracy of a constant addend. The condition (37) establishes a specific connection between this addend and the contact force P. When the latter changes, the points of maximal deflections $y = 0$, $s = m\pi$ (m is integer) preserve their location irrespective of the value of P.

Through such a definition of v_0, we simultaneously found the constant u_{y0} which enters the condition (7)

$$u_{y0} = U\left[2\sin^2\frac{\alpha}{2}\ln\frac{1+\cos\frac{\alpha}{2}}{\sin\frac{\alpha}{2}} + 1 - 2\cos\frac{\alpha}{2}\right]. \tag{38}$$

It was determined from the continuity of $u_y|_{y=0}$ at points $s = \pm\alpha$.

Presence of the linear term in (17) for u_y and of corresponding nonvanishing at $y \to +\infty$ component $\rho c_1^2 v_1/2$ of σ_y in (13) have the following meaning. In order to prevent the half-plane from "coming down" under the action of the contact pressure, it is necessary to support it at $y = +\infty$ by constant forces with the resultant P per unit wavelength.

It follows from (32) that in a limiting case, when the pressing force equals

$$P = P_{\max} = -\frac{2\pi A}{k} = -\lambda A, \tag{39}$$

contact sections merge all together (the quantity A is negative in accordance with (19) and the already accepted condition $E_0 < 0$). The distribution of contact stresses at $P = P_{\max}$ and $\alpha = \pi$ on the base of (29) takes the form

$$f(s) = -\frac{kP_{\max}}{\pi}\cos^2\frac{s}{2}. \tag{40}$$

In view of expressions (19), (34), (39), quantities $P_{\max}$ and U are the functions of the excitation frequency ω. But with respect to $f(s)$ and $u_y|_{y=0}$ determined by formulae (29) and (36), (38), respectively, this dependence is displayed only in changes of amplitude. Therefore, for graphic representation in Fig. 2(a–f), we took nondimensional quantities

$$\sigma_y = f(s)\Big/\left(-\frac{kP_{\max}}{2\pi}\right) = 2\cos\frac{s}{2}\sqrt{\cos^2\frac{s}{2} - \cos^2\frac{\alpha}{2}} \tag{41}$$

and $\bar{u}_y = U^{-1}u$ calculated on the base of (36), (38). The dimension of contact area, according to (32) and (39), is determined by the formula

$$\sin^2\frac{\alpha}{2} = \frac{P}{P_{\max}}. \tag{42}$$

Now we obtain expressions for the tangential velocity of the half-plane surface. Within the contact area, $|s| < \alpha$, on the base of (17), its value (in the fixed coordinate system) is equal to

$$v_x(s) = \left.\frac{\partial u_x}{\partial t}\right|_{y=0} = -\omega\left.\frac{\partial u_x}{\partial s}\right|_{y=0} = -\omega(1+\nu)d_{31}E_0\frac{k}{\gamma_1^2} \times\left[\left(k^2+\gamma_2^2\right)\left(2\gamma_1\gamma_2 - \left(k^2+\gamma_2^2\right)\right)\frac{1}{\Delta_R} \times\left(\cos s - \frac{1}{A}\sum_{n=1}^{\infty}f_n\cos ns\right) + \cos s\right]. \tag{43}$$

Combining (43) with (14), (19), (29), (31), and (34), one obtains

$$v_x(s) = \frac{\omega k}{\gamma_1}U\left[\frac{2\gamma_1\gamma_2 - \left(k^2+\gamma_2^2\right)}{k^2-\gamma_2^2} \times\left(\cos\frac{s}{2} - \sqrt{\cos^2\frac{s}{2} - \cos^2\frac{\alpha}{2}}\right)^2 + \frac{\Delta_R\cos s}{\left(k^2+\gamma_2^2\right)\left(k^2-\gamma_2^2\right)}\right], \quad |s| < \alpha. \tag{44}$$

Downloaded 04 May 2010 to 171.66.16.28. Redistribution subject to ASME license or copyright; see http://www.asme.org/terms/Terms_Use.cfm

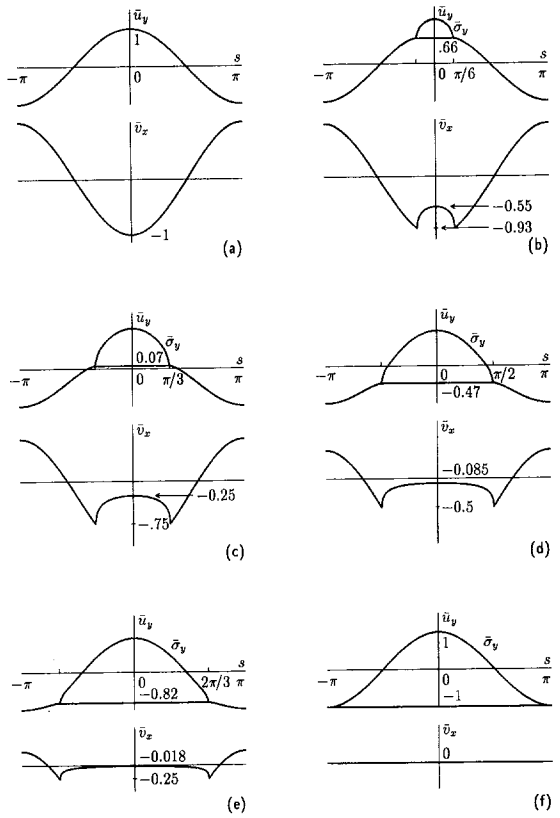

Fig. 2 Vertical displacements of the boundary of the half-plane and normal stress distributions (41) (upper graphs) and tangential velocity of the surface (45), (48) (lower graphs) for values of $P/P_{max} = 0$ ((a), $\alpha = 0$); 0.067 ((b), $\alpha = \pi/6$); 0.25 ((c), $\alpha = \pi/3$); 0.5 ((d), $\alpha = \pi/2$); 0.75 ((e), $\alpha = 2\pi/3$); 1.0 ((f), $\alpha = \pi$)

It is seen from the last formula that unlike contact stresses and surface displacements, the frequency dependence of the velocity is more complicated. Because of this, we consider only the practically important case of resonant excitation when the phase velocity of the running wave $c_f = \omega/k$ becomes equal to c_R: $\omega = kc_R$. In this case we have $\Delta_R = 0$ and $U = \infty$. For practical materials, which do not allow infinite growth of displacements, one can restrict field variables by introducing of small energy dissipation. In harmonic problems, it is equivalent to the assumption that elastic moduli have small imaginary parts. But in the two-dimensional problem considered a question arises: How do we specify imaginary parts of two elastic constants which appear in (2) and (12)?

As for our case, finite values of characteristics of a stress strain state can be obtained if we prescribe a finite amplitude of displacements U in (34). In a result, Δ_R acquires a small positive value. Naturally, at $\omega = kc_R$, a phase shift for $\pi/2$ between the exciting electric field (1) and mechanical quantities occurs. But this will not affect the distribution of the latter in the movable coordinate system related to the middle of the contact area.

From this point onward we consider both the amplitude of excitation E_0 and the free surface displacement $U_R = U|_{\omega = kc_R}$ to be prescribed. Neglecting the second term in square brackets in (44) as compared to the first one, we find the velocity distribution within the contact area:

$$v_x(s) = -V_R\left(\cos\frac{s}{2} - \sqrt{\cos^2\frac{s}{2} - \cos^2\frac{\alpha}{2}}\right)^2, \quad |s| < \alpha \tag{45}$$

where

$$V_R = \frac{2l_2}{1 + l_2^2} kc_R U_R \tag{46}$$

is the maximal value of particle velocity in an undamped Rayleigh wave.

In the transition from (44) to (45) we used an equation that determines the Rayleigh wave velocity,

$$\left(1 + l_2^2\right)^2 - 4l_1 l_2 = 0, \quad l_{1,2} = \left(1 - (c_R/c_{1,2})^2\right)^{1/2}. \tag{47}$$

Velocities of the free portion of the surface can be deduced from (43) using the condition $f(s) \equiv 0$ at $s > \alpha$:

$$v_x(s) = -V_R\left(\cos s + \sin^2\frac{\alpha}{2}\right), \quad \alpha < |s| < \pi. \tag{48}$$

Plots of nondimensional tangential velocity $\bar{v}_x(s) = v_x(s)/V_R$, determined by expressions (45) and (48) are presented in Fig. 2 under the corresponding plots of vertical displacements and normal stresses.

One can see that inside the contact area $v_x < 0$. So, the rotor is to move with an intermediate value of $v_x(s)$ in the direction shown in Fig. 1.

The velocity distribution is nonuniform and the degree of nonuniformity

$$\frac{v_x(\alpha)}{v_x(0)} = \frac{\cos^2\dfrac{\alpha}{2}}{\left(1 - \sin\dfrac{\alpha}{2}\right)^2} \tag{49}$$

increases with α.

When the pressing force P increases to its critical value P_{max} the velocity decreases, and at $P = P_{max}$ we have $v_x(s) \equiv 0$ for all s; i.e., under the complete damping of the wave, the motion of the rotor is absent.

6 Conclusions

We obtained a closed-form solution of the problem of frictionless contact between the running Rayleigh wave and a rigid strip. The analysis performed above have displayed complex nature of the dynamic field inside the half-plane. The most important feature of tangential velocity plots is that they "fall down" inside the contact area (lower graphs in Fig. 2(b–e)) as compared to their distribution in an undamped Rayleigh wave (Fig. 2(a)).

The tangential velocity within the contact area is strongly nonuniform. Distributions of $\bar{v}_x(s)$ have vertical tangents at $s = \pm\alpha$, i.e., the tangential component of acceleration of the surface becomes infinite at these points.

In the case of finite friction between the wave and a strip, the contact area is subdivided into zones of adhesion (in the middle of the area) and those of slip, adjacent to its ends. Modeling of dynamic interaction of a running wave of deformation and a strip is a very complicated problem which is now under investigation.

Acknowledgment

This work was performed with the support of the Ukrainian Ministry of Education. This support is gratefully acknowledged.

References

American National Standard: IEEE Standard on Piezoelectricity, 1984, *IEEE Transactions on Sonics and Ultrasonics*, Vol. SU-31, No. 2, Pt. 2, pp. 1–55.

Berlincourt, D. A., Curran, D. R., and Jaffe, H. J., 1964, "Piezoelectric and Piezomagnetic Materials and Their Function in Transducers," *Physi-*

Downloaded 04 May 2010 to 171.66.16.28. Redistribution subject to ASME license or copyright; see http://www.asme.org/terms/Terms_Use.cfm

cal Acoustics, W. P. Mason, ed., Vol. I, Pt. A, Academic Press, New York, pp. 169–270.

Brychkov, Yu, A., Prudnikov, A. P., and Marichev, O. A., 1981, *Integrals and Series*, Nauka, Moscow, in Russian.

Grinchenko, V. T., Karlash, V. L., Meleshko, V. V., and Ulitko, A. F., 1976, "Investigation of Planar Vibrations of Rectangular Piezoceramic Plates," *Soviet Applied Mechanics*, Vol. 12, pp. 483–488.

Grinchenko, V. T., Ulitko, A. F., and Shul'ga, N. A., 1989, "Electroelasticity," *Mechanics of Coupled Fields in Elements of Structures*, Vol. 5, Kiev, Naukova Dumka, in Russian.

Johnson, K., 1987, *Contact Mechanics*, Cambridge University Press, Cambridge, MA.

Kurosawa, M., and Ueha, S., 1988, "Efficiency of Ultrasonic Motor Using Travelling Wave," *Journal of the Acoustical Society of Japan*, Vol. 44, pp. 40–46, in Japanese.

Mindlin, R. D., and Deresiewicz, H., 1953, "Elastic Spheres in Contact Under Varying Oblique Forces," ASME JOURNAL OF APPLIED MECHANICS, Vol. 75, pp. 327–344.

Srivastav, R., 1964, "Duel Relations Involving Trigonometric Series," *Proceedings Royal Society Edinburg*, Vol. 46, Pt. 3, pp. 173–184.

Suzuki, T., Kamano, T., and Kazuhara, T., 1990, "Modelling of Progressive Wave Type Ultrasonic Motor," *Japanese Journal of Applied Physics*, Vol. 29, Suppl. 29-1, pp. 194–196.

Ueha, S., 1989, "Present Status of Ultrasonic Motors," *Proceedings of IEEE 1989 Ultrasonic Symposium*, Vol. 2, pp. 749–753.

Westergaard, H. M., 1939, "Bearing Pressures and Cracks," ASME JOURNAL OF APPLIED MECHANICS, Vol. 6, pp. 49–53.

Zharii, O. Yu., 1993, "Modeling of a Mode Conversion Ultrasonic Motor in the Regime of Slip," *IEEE Transactions on Ultrasonics, Ferroelectrics and Frequency Control*, Vol. 40, pp. 411–417.

Downloaded 04 May 2010 to 171.66.16.28. Redistribution subject to ASME license or copyright; see http://www.asme.org/terms/Terms_Use.cfm

Adhesive Contact Between the Surface Wave and a Rigid Strip

O. Y. Zharii
Department of Theoretical and Applied Mechanics,
Kiev University,
64 Vladimirskaya Street,
Kiev 252017, Ukraine

A problem of adhesive contact between the running surface wave and a rigid strip is investigated. The mixed boundary-value problem of elastodynamics is reduced to a singular integral equation for a complex combination of stresses and an exact closed-form solution of it has been derived. Analysis of variation of contact area dimensions, stress distribution and rotor velocity on the frequency of excitation displayed significant differences between the results corresponding to conditions of adhesion and slipping in contact area. The origin of these differences is discussed.

1 Introduction

Studies of dynamic interaction between vibrating surfaces of solids and rigid bodies are interesting from the viewpoint of creating motions in ultrasonic motors (Ueha, 1989; Zharii, 1993). One of the types of these devices is a traveling wave motor (Ueha, 1989). In the article by Zharii and Ulitko (1995), referred to as (I) in this paper, a problem of smooth contact between the running Rayleigh wave and a rigid strip has been considered. That work was performed as a natural first step in the way of developing a grounded model of the wave motion transformation into the progressive rotor motion.

Under a vanishing coefficient of dry friction ($\mu = 0$), the motion is, of course, impossible. To approach the real situation with finite μ, in this paper we consider the other limiting case of infinitely large friction ($\mu = \infty$), representing the case of the perfect adhesion between the stator (elastic half-plane) and the rotor (rigid strip). Doing so, we follow the conventional methodology of the static contact mechanics (Johnson, 1987). Having solved these two problems, one will have the necessary information for treating a very complex problem with finite friction.

2 Formulation and Solution of a Problem

2.1 Statement of the Problem. The geometry of the problem is the same as in (I) and it is shown in Fig. 1. Crosses at the interface between the surface wave and the rotor indicate complete adhesion (velocities of points within the contact area coincide).

The way of excitation is the same as in (I):

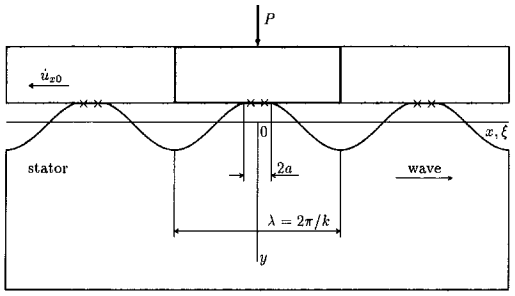

Fig. 1 Geometry of the problem

$$E_z = E_0 \cos(kx - \omega t), \tag{1}$$

as well as the equation of a piezoceramic half-plane motion (Grinchenko et al., 1989):

$$c_1^2 \text{grad div } \mathbf{u} - c_2^2 \text{rot rot } \mathbf{u} - (1 + \nu) d_{31} c_1^2 \text{ grad } E_z = \frac{\partial^2 \mathbf{u}}{\partial t^2}. \tag{2}$$

In the movable coordinate system, $\xi = x - \omega t/k$, y, Eq. (2) becomes

$$c_1^2 \text{grad div } \mathbf{u} - c_2^2 \text{rot rot } \mathbf{u} + \mathbf{i}(1 + \nu) d_{31} c_1^2 E_0 k \sin k\xi - \frac{\omega^2}{k^2} \frac{\partial^2 \mathbf{u}}{\partial \xi^2} = 0. \tag{3}$$

Considering the problem of adhesive contact, we demand that on the adhered portion of the surface, the tangential velocity is the same for all points. It is equal to an unknown in advance velocity of the rotor $\dot{u}_{x0}$. As in the smooth contact problem, the vertical displacement is constant:

$$\dot{u}_x|_{y=0} = \dot{u}_{x0}, \; u_y|_{y=0} = u_{y0}, \; 0 < s < \alpha. \tag{4}$$

On the free surface, both normal and tangential stresses vanish,

Contributed by the Applied Mechanics Division of THE AMERICAN SOCIETY OF MECHANICAL ENGINEERS for publication in the ASME JOURNAL OF APPLIED MECHANICS.
Discussion on this paper should be addressed to the Technical Editor, Professor Lewis T. Wheeler, Department of Mechanical Engineering, University of Houston, Houston, TX 77204-4792, and will be accepted until four months after final publication of the paper itself in the ASME JOURNAL OF APPLIED MECHANICS.
Manuscript received and accepted by the ASME Applied Mechanics Division, July 15, 1993. Associate Technical Editor: T. R. Akylas.

Copyright © 1995 by ASME
Downloaded 04 May 2010 to 171.66.16.28. Redistribution subject to ASME license or copyright; see http://www.asme.org/terms/Terms_Use.cfm

$$\sigma_y|_{y=0} = 0,\ \tau_{\xi y}|_{y=0} = 0,\ \alpha < s < \pi, \tag{5}$$

where, as earlier, $s = k\xi$.

2.2 Derivation of a Singular Integral Equation. Representing unknown stresses by the Fourier series,

$$\sigma_y \equiv f(s) = \frac{f_0}{2} + \sum_{n=1}^{\infty} f_n \cos ns,$$

$$\tau_{\xi y} \equiv g(s) = \sum_{n=1}^{\infty} g_n \sin ns, \quad -\alpha < s < \alpha, \tag{6}$$

we obtain the general solution of (3) in the way similar to that in (I). This solution is

$$u_x = (1+\nu)d_{31}E_0\frac{k}{\gamma_1^2}$$
$$\times\left[\left(k^2+\gamma_2^2\right)\frac{-\left(k^2+\gamma_2^2\right)e^{-\gamma_1 y}+2\gamma_1\gamma_2 e^{-\gamma_2 y}}{\Delta_R}+1\right]\sin s$$
$$+\frac{k}{\rho c_2^2}\frac{1}{\Delta_R}\sum_{n=1}^{\infty}\frac{f_n}{n}\left[-\left(k^2+\gamma_2^2\right)e^{-n\gamma_1 y}+2\gamma_1\gamma_2 e^{-n\gamma_2 y}\right]\sin ns$$
$$+\frac{\gamma_2}{\rho c_2^2}\frac{1}{\Delta_R}\sum_{n=1}^{\infty}\frac{g_n}{n}\left[2k^2e^{-n\gamma_1 y}-\left(k^2+\gamma_2^2\right)e^{-n\gamma_2 y}\right]\sin ns,$$
$$u_y = (1+\nu)d_{31}E_0$$
$$\times\frac{k^2+\gamma_2^2}{\gamma_1}\frac{-\left(k^2+\gamma_2^2\right)e^{-\gamma_1 y}+2k^2e^{-\gamma_2 y}}{\Delta_R}\cos s+\frac{V_0(y)}{2}$$
$$+\frac{\gamma_1}{\rho c_2^2}\frac{1}{\Delta_R}\sum_{n=1}^{\infty}\frac{f_n}{n}\left[-\left(k^2+\gamma_2^2\right)e^{-n\gamma_1 y}+2k^2e^{-n\gamma_2 y}\right]\cos ns$$
$$+\frac{k}{\rho c_2^2}\frac{1}{\Delta_R}\sum_{n=1}^{\infty}\frac{g_n}{n}\left[2\gamma_1\gamma_2 e^{-n\gamma_1 y}-\left(k^2+\gamma_2^2\right)e^{-n\gamma_2 y}\right]\cos ns. \tag{7}$$

Satisfying the boundary conditions (4), (5), we come to the system of series equations

$$\sum_{n=1}^{\infty} f_n \sin ns + \frac{k}{\gamma_1}w\sum_{n=1}^{\infty} g_n \sin ns = A\sin s, \quad 0 < s < \alpha,$$
$$\frac{k}{\gamma_2}w\sum_{n=1}^{\infty} f_n \cos ns + \sum_{n=1}^{\infty} g_n \cos ns = -\frac{2k\gamma_1}{k^2+\gamma_2^2}A\cos s + D, \quad 0 < s < \alpha,$$
$$\frac{f_0}{2} + \sum_{n=1}^{\infty} f_n \cos ns = 0, \quad \alpha < s < \pi,$$
$$\sum_{n=1}^{\infty} g_n \sin ns = 0, \quad \alpha < s < \pi, \tag{8}$$

where we introduced the notations

$$w = \frac{2\gamma_1\gamma_2 - \left(k^2+\gamma_2^2\right)}{k^2-\gamma_2^2}, \quad D = -\frac{\dot{u}_{x0}}{\omega}\frac{\rho c_2^2\Delta_R}{\gamma_2\left(k^2-\gamma_2^2\right)}, \tag{9}$$

and A, B are identical with those in (I),

$$A = -(1+\nu)d_{31}E_0\cdot\rho c_2^2\frac{k^2+\gamma_2^2}{\gamma_1^2},$$
$$B = \frac{\rho c_2^2\Delta_R}{\gamma_1\left(k^2-\gamma_2^2\right)}\left(u_{y0}-\frac{v_0}{2}\right). \tag{10}$$

To solve (8), unlike (I), it is convenient to reduce this system to a single integral equation. For this purpose, using integral representations of Fourier coefficients that follow from (5), (6) (the two last equations in (8) are satisfied identically)

$$f_n = \frac{2}{\pi}\int_0^{\alpha} f(s_1)\cos ns_1 ds_1, \quad g_n = \frac{2}{\pi}\int_0^{\alpha} g(s_1)\sin ns_1 ds_1, \tag{11}$$

and the value of sum

$$\sum_{n=1}^{\infty}\sin ns = \frac{1}{2}\cot\frac{s}{2}, \tag{12}$$

we transform series that enter (8) to the form

$$\sum_{n=1}^{\infty} f_n \sin ns = -\frac{1}{2\pi}\int_{-\alpha}^{\alpha} f(s_1)\cot\frac{s_1-s}{2}ds_1,$$
$$\sum_{n=1}^{\infty} g_n \cos ns = \frac{1}{2\pi}\int_{-\alpha}^{\alpha} g(s_1)\cot\frac{s_1-s}{2}ds_1. \tag{13}$$

After the introduction of a new function

$$g(s) = \sqrt{\frac{\gamma_1}{\gamma_2}}\,g_1(s), \tag{14}$$

Eqs. (8) change to

$$f(s) + \frac{\kappa}{2\pi}\int_{-\alpha}^{\alpha} g_1(s_1)\cot\frac{s_1-s}{2}ds_1 = -\frac{2k\gamma_1}{k^2+\gamma_2^2}\frac{\gamma_2}{kw}A\cos s + \frac{\gamma_2}{kw}D + \frac{f_0}{2},$$
$$g_1(s) - \frac{\kappa}{2\pi}\int_{-\alpha}^{\alpha} f(s_1)\cot\frac{s_1-s}{2}ds_1 = \frac{\sqrt{\gamma_1\gamma_2}}{kw}A\sin s. \tag{15}$$

Adding the second of these equations multiplied by i to the first, we obtain a single singular integral equation

$$\chi(s) + \frac{\kappa}{2\pi i}\int_{-\alpha}^{\alpha}\chi(s_1)\cot\frac{s_1-s}{2}ds_1$$
$$= -\frac{A}{kw}\left(\frac{2k\gamma_1\gamma_2}{k^2+\gamma_2^2}\cos s - i\sqrt{\gamma_1\gamma_2}\sin s\right) + \frac{\gamma_2}{kw}D + \frac{f_0}{2}, \quad -\alpha < s < \alpha, \tag{16}$$

where $\chi(s)$ is a complex combination of normal and tangential stresses

$$\chi(s) = f(s) + ig_1(s) = f(s) + i\sqrt{\frac{\gamma_2}{\gamma_1}}\,g(s). \tag{17}$$

2.3 Solution of the Integral Equation. Equation (16) is reduced to the standard form by replacement of both independent and dependent variables

$$\eta = \tan\frac{s}{2}, \quad \eta_1 = \tan\frac{s_1}{2}, \quad \varphi(\eta) = \chi(s)\cos^2\frac{s}{2}, \tag{18}$$

after which it is transformed to

$$\varphi(\eta) + \frac{\kappa}{\pi i}\int_{-c}^{c}\frac{\varphi(\eta_1)d\eta_1}{\eta_1-\eta} = G(\eta), \quad -c < \eta < c, \tag{19}$$

where we used the notations

$$\kappa = \frac{\sqrt{\gamma_1\gamma_2}}{kw} = \frac{\sqrt{\gamma_1\gamma_2}}{k}\frac{k^2-\gamma_2^2}{2\gamma_1\gamma_2-\left(k^2+\gamma_2^2\right)}, \quad c = \tan\frac{\alpha}{2}. \tag{20}$$

Downloaded 04 May 2010 to 171.66.16.28. Redistribution subject to ASME license or copyright; see http://www.asme.org/terms/Terms_Use.cfm

The function on the right-hand side of (19) is

$$G(\eta) = -\frac{2\eta}{1+\eta^2}\frac{\kappa}{2\pi i}\int_{-c}^{c}\varphi(\eta_1)d\eta_1 - \kappa A\frac{1}{1+\eta^2}\left(\frac{2k\sqrt{\gamma_1\gamma_2}}{k^2+\gamma_2^2}\frac{1-\eta^2}{1+\eta^2} - i\frac{2\eta}{1+\eta^2}\right) + \frac{1}{1+\eta^2}\left(\frac{\gamma_2 D}{kw} + \frac{f_0}{2}\right). \quad (21)$$

The solution of Eq. (19) is given by the formula (Mikhlin, 1949)

$$\varphi(\eta) = -\frac{1}{\kappa^2-1}G(\eta) + \frac{\kappa}{(\kappa^2-1)\pi i(c+\eta)^{1-m}(c-\eta)^m}\int_{-c}^{c}\times\frac{(c+\zeta)^{1-m}(c-\zeta)^m}{\zeta-\eta}G(\zeta)d\zeta + \frac{C}{(c+\eta)^{1-m}(c-\eta)^m} \quad (22)$$

where C is an arbitrary constant. New constants have values

$$m = \frac{1}{2\pi i}\ln\frac{1+\kappa}{1-\kappa} = \frac{1}{2} + i\beta, \quad \beta = \frac{1}{2\pi}\ln\frac{\kappa-1}{\kappa+1}. \quad (23)$$

Taking into account relations

$$\int_{-c}^{c}\varphi(\eta_1)d\eta_1 = -\frac{kP}{2}, \quad f_0 = -\frac{kP}{\pi}, \quad (24)$$

which follow for the static condition

$$\int_{-a}^{a}\sigma_{\xi y}d\xi = \frac{1}{k}\int_{-\alpha}^{\alpha}\chi(s)ds = -P, \quad (25)$$

and introducing new notations

$$R = \frac{2k\sqrt{\gamma_1\gamma_2}}{k^2+\gamma_2^2}, \quad \sigma_0 = \frac{kP}{2\pi}, \quad (26)$$

one can write (21) in the form

$$G(\eta) = \left(R\kappa A + \frac{\gamma_2}{kw}D - \sigma_0\right)q_1(\eta) - i\kappa\sigma_0 q_2(\eta) - 2R\kappa A q_3(\eta) + 2i\kappa A q_4(\eta), \quad (27)$$

where

$$q_1(\eta) = \frac{1}{1+\eta^2}, \quad q_2(\eta) = \frac{\eta}{1+\eta^2}, \quad q_3(\eta) = \frac{1}{(1+\eta^2)^2}, \quad q_4(\eta) = \frac{\eta}{(1+\eta^2)^2}. \quad (28)$$

2.4 Kinematic and Dynamic Characteristics of a Solution. After calculation of integrals in (22) in the way described in the Appendix, one obtains a rather complicated expression for $\varphi(\eta)$ containing four unknown constants. They are the half-length of contact area α, the rotor velocity $\dot{u}_{x0}$, and the complex constant C. These are determined from the condition of boundedness of contact stresses at the ends of the contact area (Gladwell, 1980)

$$\varphi(-c) = \varphi(c) = 0 \quad (29)$$

and from the static condition (24). Realization of the latter requires calculation of integrals similar to, but simpler than, those listed in the Appendix. After calculations one obtains

$$C = -\sigma_0\cosh\beta\pi. \quad (30)$$

The value of α is determined from the transcendental equation

$$\sin^2\frac{\alpha}{2}\sinh^2\beta\alpha + R(\beta\sin\alpha - \sinh\beta\alpha\cosh\beta\alpha) = -\frac{\sigma_0}{A} \quad (31)$$

and the rotor velocity can be found from (9) and the following equality

$$\frac{1}{A}\frac{\gamma_2 D}{kw} = \frac{\cos^2\frac{\alpha}{2}(\sinh\beta\pi - R\cosh\beta\pi) - \sinh\beta(\pi-\alpha)(\cosh\beta\alpha - R\sinh\beta\alpha)}{\sinh\beta\pi} - \beta(R - \coth\beta\pi)\sin\alpha. \quad (32)$$

After cumbersome transformations, the solution of (16) takes the form

$$\chi(s) = 2A\left[\cos\frac{s}{2}(\cosh\beta\alpha - R\sinh\beta\alpha) + i\sin\frac{s}{2}(\sinh\beta\alpha - R\cosh\beta\alpha)\right]\sqrt{\cos^2\frac{s}{2} - \cos^2\frac{\alpha}{2}} \times\cosh\beta\pi\left(\sin\frac{\alpha+s}{2}\Big/\sin\frac{\alpha-s}{2}\right)^{i\beta}. \quad (33)$$

3 Analysis of a Solution

Let us consider the dependence of adhesive contact length α_{adh} on the frequency of excitation ω, which is determined by Eq. (31). In Fig. 2 we present plots of α for adhesive and smooth contact. The latter quantity α_{sm} have been calculated on the base of (32) of (I) and in doing so we took into account the ω-dependence of P_{max} following from (19), (39) of (I) and substituted to the equation

$$\alpha_{sm} = 2\arcsin\sqrt{P/P_{max}}. \quad (34)$$

where P_{max} has the same meaning as in (I).

It is seen that lengths of contact area for either conditions of contact both slightly increase and are approximately equal

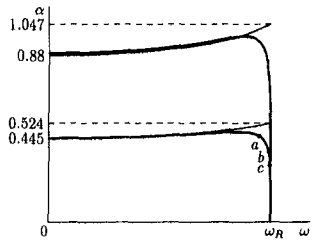

Fig. 2 Variation of smooth contact length α_{sm} (thin lines) and adhesive one α_{adh} (thick lines) on the frequency of excitation. Marks *a*, *b*, *c* correspond to subfigures in Fig. 4.

Downloaded 04 May 2010 to 171.66.16.28. Redistribution subject to ASME license or copyright; see http://www.asme.org/terms/Terms_Use.cfm

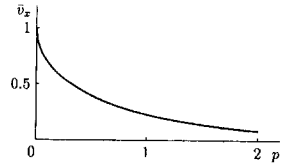

Fig. 3 Nondimensional rotor velocity as a function of the pressing force

to each other for low frequencies, but they differ considerably when ω approaches the resonance frequency $\omega_R = \alpha c_R$ (c_R is the Rayleigh wave velocity). The smooth contact length remains finite while the adhesive one tends to zero in the vicinity of ω_R. As in (I) we presume that due to small dissipation, the vertical displacement in an undamped Rayleigh wave becomes large but finite. To find the value of rotor velocity, we note that the value of β determined by (23) approaches infinity at $\omega \to \omega_R$, but the limit $\lim_{\omega \to \omega_R} \alpha\beta = K$ exists. It can be determined from the equation

$$K - \frac{1}{2}(1 - e^{-2K}) = -\frac{\sigma_0}{A}, \tag{35}$$

which has a unique solution.

After solution of (35) we pass to the same limit in (32) and find

$$\dot{u}_{x0} = -e^{-2K} V_R, \tag{36}$$

where V_R is the maximal velocity in an undamped Rayleigh wave determined by (46) of (I). Introducing the nondimensional pressing force $p = P/P_{\max}$, we plot an implicit dependence of nondimensional rotor velocity $\bar{v}_x = |\dot{u}_{x0}/V_R|$ on p in Fig. 3. It follows from the analysis of (32) that $\alpha_{\text{adh}} < \pi$ for all positive P, therefore, contact areas never merge together in the model of adhesive contact. Though the size of the contact area is very small at any P when $\omega \to \omega_R$, the rotor velocity decreases rapidly when P increases.

Stress distributions determined by (17), (33) vary at $\omega \to \omega_R$ primarily due to changes in the size of the contact area. Plots of the nondimensional quantities

$$\sigma = \left[A|_{\omega=\omega_R}\right]^{-1} \text{Re}\, \chi(s),$$
$$\tau = \left[A|_{\omega=\omega_R}\right]^{-1} \sqrt{\frac{\gamma_1}{\gamma_2}}\, \text{Im}\, \chi(s) \tag{37}$$

are presented in Fig. 4 for the values of (ω, α_{adh}) indicated by points a, b, and c in Fig. 2.

Like in the static contact problems, expressions (17) represent oscillating functions at $s \to \pm\alpha$. These oscillations are more pronounced with normal stresses than with tangential ones. Unlike static problems (Johnson, 1987), regions of oscillation cover significant portions of the contact area and the relative sizes of these portions increase when the contact length α_{adh} decreases. One more feature of graphs in Fig. 4 is that the maximal value of the tangential stress increases at $\omega \to \omega_R$ more rapidly than that of the normal ones.

Conclusions

We have found a closed-form solution of a new mixed boundary value problem of elastodynamics. Note that the very existence of this relatively simple solution could not be anticipated in advance.

The solution obtained displayed the feature familiar from static contact problems with adhesion, namely stress oscillations in the vicinity of the contact area boundary (Johnson, 1987). In the problem just considered, however, this phenomenon is much more pronounced (in statics, the oscillation zone covers about 0.0003 fraction of the contact area). Rapid

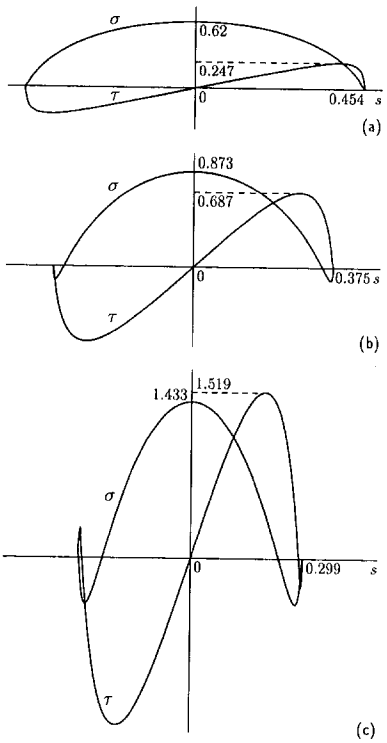

Fig. 4 Distributions of nondimensional normal (σ) and tangential (τ) stresses at (a), $\omega = 0.95\ \omega_R$; (b) $\omega = 0.99\ \omega_R$ and (c) $\omega = 0.998\ \omega_R$

growth of this zone and of tangential stresses in the vicinity of the resonance indicates that conditions of work for elastic material in dynamics are much worse than those in statics.

Significant differences between α_{sm} and α_{adh} at $\omega \to \omega_R$ make the transition from the two limiting cases $\mu = 0$ and $\mu = \infty$ to a finite value of μ to be very difficult. Unlike statics (Johnson, 1987), one cannot use distributions of normal stresses found in the smooth contact problem for approximate restoring tangential stresses (see the Introduction of (I)). Therefore, another way of reducing a very complicated problem with finite friction to two consequent problems should be found. Several ideas in this respect are under investigation now.

Acknowledgment

The author takes pleasure in acknowledging his indebtedness to Dr. D. N. Parfenenko for many helpful discussions.

References

Gladwell, G. M. L., 1980, *Contact Problems in the Classical Theory of Elasticity*, Sijthoff & Noordorf, Alphen aan den Rijn.

Grinchenko, V. T., Ulitko, A. F., and Shul'ga, N. A., 1989, "Electroelasticity," *Mechanics of Coupled Fields in Elements of Structures*, Vol. 5, Kiev, Naukova Dumka, in Russian.

Johnson, K., 1987, *Contact Mechanics*, Cambridge University Press, Cambridge, MA.

Markushevich, A. I., 1950, *Theory of Analytical Functions*, Moscow, GITTL, in Russian.

Mikhlin, S. G., 1949, *Integral Equations*, Moscow, OGIZ, in Russian.

Ueha, S., 1989, "Present Status of Ultrasonic Motors," *Proceedings of IEEE 1989 Ultrasonic Symposium*, Vol. 2, pp. 749–753.

Zharii, O. Yu., 1993, "Modeling of a Mode Conversion Ultrasonic Motor in the Regime of Slip," *IEEE Transactions on Ultrasonics, Ferroelectrics and Frequency Control*, Vol. 40, pp. 411–417.

Zharii, O. Yu., and Ulitko, A. F., 1995, "Smooth Contact Between the Running Rayleigh Wave and a Rigid Strip," ASME JOURNAL OF APPLIED MECHANICS, Vol. 62, pp. 362–367.

Downloaded 04 May 2010 to 171.66.16.28. Redistribution subject to ASME license or copyright; see http://www.asme.org/terms/Terms_Use.cfm

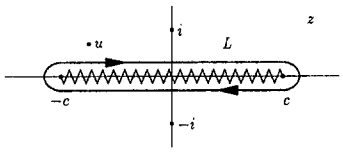

Fig. A1 Contour of integration in (A3)

APPENDIX

For calculation of Cauchy principal value integrals,

$$\Phi_r(\eta) = \frac{1}{2\pi i}\int_{-c}^{c} \frac{(c+\zeta)^{1-m}(c-\zeta)^m}{\zeta-\eta} q_r(\zeta)d\zeta, \quad r = 1,2,3,4. \tag{A1}$$

where q_r are rational functions listed in (28) and m has the value defined by (23), we introduce an auxiliary function of a complex variable z and a complex parameter u,

$$\phi(z) = \frac{(z+c)^{1-m}(z-c)^m}{z-u} q(z) \tag{A2}$$

(for brevity the index r is omitted).

This function is single valued in a complex z-plane cut along the section $(-c, c)$ connecting branch points $z = \pm c$ (Fig. A1). Calculating the integral of $\phi(z)$ along the closed contour L which bypasses the segment clockwise we find

$$\frac{1}{2\pi i}\oint_L \phi(z)dz = \frac{1}{2\pi i}\int_{-c}^{c} \phi^+(\zeta)d\zeta - \frac{1}{2\pi i}\int_{-c}^{c} \phi^-(\zeta)d\zeta = 2i \sin m\pi \Phi(u) \tag{A3}$$

where ϕ^+ and ϕ^- are the limiting values of ϕ on the upper and lower sides of the cut, respectively.

On the other hand, the contour integral in (A3) is equal to the sum of residues of the integrand at points $z = \pm i$, $z = u$, and $z = \infty$ (the latter in nonzero only for $r = 2$).

So we can write

$$\Phi(u) = \frac{1}{2i \sin m\pi} \Sigma \operatorname{res} \phi(z) \tag{A4}$$

and the Cauchy integrals (A1) can finally be calculated on the base of the Plemelj formula (Markushevich, 1950),

$$\Phi(\eta) = \frac{1}{2}(\Phi^+(\eta) + \Phi^-(\eta)). \tag{A5}$$

In this way we find

$$\Phi_1(\eta) = \frac{\sqrt{c^2+1}}{2}\left(\frac{\sinh \beta\alpha}{\cosh \beta\pi} q_1(\eta) + i\frac{\cosh \beta\alpha}{\cosh \beta\pi} q_2(\eta)\right) - \frac{1}{2}(c+\eta)^{1-m}(c-\eta)^m \tanh \beta\pi \cdot q_1(\eta),$$

$$\Phi_2(\eta) = \frac{\sqrt{c^2+1}}{2}\left(-i\frac{\cosh \beta\alpha}{\cosh \beta\pi} q_1(\eta) + \frac{\sinh \beta\alpha}{\cosh \beta\pi} q_2(\eta)\right) - \frac{1}{2}(c+\eta)^{1-m}(c-\eta)^m \tanh \beta\pi \cdot q_2(\eta) + \frac{i}{2\cosh \beta\pi},$$

$$\Phi_3(\eta) = -\frac{1}{4}\left(\frac{\sinh \beta\alpha}{\cosh \beta\pi}\cos\frac{\alpha}{2} - 2\beta\frac{\cosh \beta\alpha}{\cosh \beta\pi}\sin\frac{\alpha}{2}\right) q_1(\eta) - \frac{i}{4}\left(\frac{\cosh \beta\alpha}{\cosh \beta\pi}\cos\frac{\alpha}{2} - 2\beta\frac{\sinh \beta\alpha}{\cosh \beta\pi}\sin\frac{\alpha}{2}\right) q_2(\eta) + \frac{\sqrt{c^2+1}}{4} \times \left(i\frac{\cosh \beta\alpha}{\cosh \beta\pi} q_2(\eta) + 2\frac{\sinh \beta\alpha}{\cosh \beta\pi} q_3(\eta) + 2i\frac{\cosh \beta\alpha}{\cosh \beta\pi} q_4(\eta)\right) - \frac{1}{2}(c+\eta)^{1-m}(c-\eta)^m \tanh \beta\pi \cdot q_3(\eta),$$

$$\Phi_4(\eta) = \frac{i}{4}\left(\frac{\cosh \beta\alpha}{\cosh \beta\pi}\cos\frac{\alpha}{2} - 2\beta\frac{\sinh \beta\alpha}{\cosh \beta\pi}\sin\frac{\alpha}{2}\right) q_1(\eta) - \frac{1}{4}\left(\frac{\sinh \beta\alpha}{\cosh \beta\pi}\cos\frac{\alpha}{2} - 2\beta\frac{\cosh \beta\alpha}{\cosh \beta\pi}\sin\frac{\alpha}{2}\right) q_2(\eta) + \frac{\sqrt{c^2+1}}{4} \times \left(i\frac{\cosh \beta\alpha}{\cosh \beta\pi} q_1(\eta) - 2i\frac{\cosh \beta\alpha}{\cosh \beta\pi} q_3(\eta) + 2\frac{\sinh \beta\alpha}{\cosh \beta\pi} q_4(\eta)\right) - \frac{1}{2}(c+\eta)^{1-m}(c-\eta)^m \tanh \beta\pi \cdot q_4(\eta),$$

$$\alpha = 2 \arctan c. \tag{A6}$$

Downloaded 04 May 2010 to 171.66.16.28. Redistribution subject to ASME license or copyright; see http://www.asme.org/terms/Terms_Use.cfm

L. M. Zubov
Professor,
Department of Mechanics and Mathematics,
Rostov State University,
344104 Rostov-on-Don,
Zorge 5, Russia

L. U. Bogachkova
Assistant Professor,
Department of Mathematics,
Volgograd State University,
400062 Volgograd,
2-Prodolnaya 30,
Russia

The Theory of Torsion of Elastic Noncircular Cylinders Under Large Deformations

The Saint-Venant semi-inverse method generalization for the problem of torsion under large deformations is presented. The case where a prism cross-section possesses central symmetry is regarded. The torsion problem is reduced to a two-dimensional nonlinear boundary value problem. Differential balance equations and lateral conditions are satisfied by solving the boundary value problem. End conditions are implemented so that the stress system is equivalent to the torsion moment, and to the axial force passing through the cross-section center of inertia. The energy method, used to solve the torsion problem under small twist angles, is extended to the case of finite deformations. Approximate solutions of the torsion problem for elliptical, rectangular, and quadrantal cylinders made of Treloar and Blatz-Ko materials are obtained.

1 Introduction

In the linear theory of elasticity, the torsion problem was solved more than 100 years ago by Saint-Venant. In the nonlinear theory of elasticity, the problem of torsion of a prism under arbitrary twist angles is investigated for the cylinder of circular section only. In this case, the problem is reduced to a boundary value problem for ordinary differential equations (Green and Adkins, 1960). The boundary value problem is solvable by quadrature for incompressible material (Green and Adkins, 1960; Lurje, 1980), and it is integrated numerically for a compressible one (Zubov and Ovseenko, 1980). In the case of small twist angles, the torsion of cylinders of noncircular cross-sections is investigated by means of the perturbation method considering the nonlinear effects of the second order (Green and Adkins, 1960; Lurje, 1980). In the above works the perturbation method (the method of small parameter) is used to solve the three-dimensional problem of nonlinear elastostatics for a cylinder, so that the solution of classical linear torsion problem is taken as the first approximation.

The work of Zubov (1983) generalized the Saint-Venant semi-inverse method in torsion for the case when an elastic bar of an arbitrary cross-section undergoes large deformations. The present work develops the methods of the solution of a nonlinear torsion problem. On the basis of the Saint-Venant method generalization, a variational (energy) method is worked out. By the latter method the approximate solutions are obtained for elliptical, rectangular, and quadrantal bars made of Treloar and Blatz-Ko materials.

2 General Formulation

Consider the generalization (Zubov, 1983) of the Saint-Venant semi-inverse method in torsion for the case when an elastic bar of an arbitrary cross-section undergoes large deformations.

Consider an elastic body, having the form of a prismatic bar in the reference configuration (in the undeformed state). We shall count off the Cartesian coordinates x_1, x_2 from the cross-section center of inertia on the plane of the cross-section. The coordinate x_3 is read off along the bar axis. Let $\mathbf{e}_k$ ($k = 1, 2, 3$) denote the coordinate unit vectors. The vectors will be designated by bold-faced lower case letters. We shall use X_n ($n = 1, 2, 3$) to denote the deformed body particle Cartesian coordinates, which are counted off along the same directions as $\mathbf{e}_k$ and from the same reference point.

The equation system of elastostatics for a nonlinear isotropic body consists (Lurje, 1980) of the balance equation

$$\partial D^*_{nk}/\partial x_n = 0, \quad \text{where } D^*_{nk} = \mathbf{e}_n \cdot \mathbf{D} \cdot \mathbf{e}_k, \quad n, k = 1, 2, 3, \tag{1}$$

and the constitutive equation

$$\mathbf{D} = a_1(I_q)\mathbf{C} + a_2(I_q)\mathbf{G} \cdot \mathbf{C} + a_3(I_q)(\mathbf{C}^T)^{-1}, \tag{2}$$

in which

$$\mathbf{C} = \partial X_n/\partial x_k \mathbf{e}_k \mathbf{e}_n, \quad \mathbf{G} = \mathbf{C} \cdot \mathbf{C}^T,$$

$$I_1 = tr\mathbf{G}, \quad I_2 = (tr^2\mathbf{G} - tr\mathbf{G}^2)/2, \quad I_3 = \det\mathbf{G} = (\det\mathbf{C})^2. \tag{3}$$

Contributed by the Applied Mechanics Division of THE AMERICAN SOCIETY OF MECHANICAL ENGINEERS for publication in the ASME JOURNAL OF APPLIED MECHANICS.

Discussion on this paper should be addressed to the Technical Editor, Professor Lewis T. Wheeler, Department of Mechanical Engineering, University of Houston, Houston, TX 77204-4792, and will be accepted until four months after final publication of the paper itself in the ASME JOURNAL OF APPLIED MECHANICS.

Manuscript received by the ASME Applied Mechanics Division, June 21, 1993; final revision, Dec. 30, 1993. Associate Technical Editor: R. L. Huston.

Copyright © 1995 by ASME

Downloaded 04 May 2010 to 171.66.16.28. Redistribution subject to ASME license or copyright; see http://www.asme.org/terms/Terms_Use.cfm

Bold-faced capital letters are used to designate tensors. Here **D** is a nonsymmetric Piola-Kirchhoff stress tensor, **C** denotes a deformation gradient, **G** is a Cauchy-Green deformation measure, I_q ($q = 1, 2, 3$) are invariants of the tensor **G**, and a_j ($j = 1, 2, 3$) denote certain scalar functions of the invariants. A dot between vectors or tensors signifies a contracted product. An absence of a symbol between vectors or tensors stands for a tensor product, so that **ab** is the tensor, whose ij-component is $(\mathbf{ab})_{ij} = a_i b_j$. Symbol tr denotes a trace of tensor, in particular,

$$tr\mathbf{G} = \mathbf{e}_k \cdot \mathbf{G} \cdot \mathbf{e}_k = \mathbf{e}_1 \cdot \mathbf{G} \cdot \mathbf{e}_1 + \mathbf{e}_2 \cdot \mathbf{G} \cdot \mathbf{e}_2 + \mathbf{e}_3 \cdot \mathbf{G} \cdot \mathbf{e}_3.$$

Here and below a twice-repeated index signifies summation. In (1) we assume the absence of mass forces.

We shall use complex coordinates $(\zeta, \bar{\zeta})$ and $(z, \bar{z})$:

$$\zeta = x_1 + ix_2, \quad \bar{\zeta} = x_1 - ix_2,$$
$$z = X_1 + iX_2, \quad \bar{z} = X_1 - iX_2, \tag{4}$$

where i denotes an imaginary unit, and a line above a letter signifies a cojugate complex value. We shall also apply the designations

$$\zeta^1 = \zeta, \quad \zeta^2 = \bar{\zeta}, \quad \zeta^3 = x_3, \quad z^1 = z, \quad z^2 = \bar{z}, \quad z^3 = X_3.$$

A complex description in the problems of plane and generalized plane deformations of a nonlinear elastic body was used by Green and Adkins (1960) and Lurje (1980).

The main $\mathbf{f}_k$ ($k = 1, 2, 3$) and the reciprocal $\mathbf{f}^n$ ($n = 1, 2, 3$) vector bases, associated with coordinates (4), are defined by equations

$$\mathbf{f}_k = \frac{\partial}{\partial \zeta^k}(x_m \mathbf{e}_m) = \frac{\partial}{\partial z^k}(X_m \mathbf{e}_m), \quad \mathbf{f}_k \cdot \mathbf{f}^n = \delta_k^n,$$

where δ_k^n is a Kronecker delta. Using the above formulae, we have

$$\mathbf{f}_1 = \frac{1}{2}(\mathbf{e}_1 - i\mathbf{e}_2), \quad \mathbf{f}_2 = \bar{\mathbf{f}}_1, \quad \mathbf{f}^1 = \mathbf{e}_1 + i\mathbf{e}_2, \quad \mathbf{f}^2 = \bar{\mathbf{f}}^1,$$

$$\mathbf{f}_3 = \mathbf{f}^3 = \mathbf{e}_3.$$

Let D_n^k ($n, k = 1, 2, 3$) denote co-contra-variant components of the tensor **D**, so that

$$D_n^k = \mathbf{f}_n \cdot \mathbf{D} \cdot \mathbf{f}^k, \quad \mathbf{D} = D_n^k \mathbf{f}^n \mathbf{f}_k.$$

In terms of the complex components D_n^k balance Eq. (1) has the form

$$\frac{\partial D_1^1}{\partial \bar{\zeta}} + \frac{\partial D_2^1}{\partial \zeta} + \frac{1}{2} \cdot \frac{\partial D_3^1}{\partial x_3} = 0,$$
$$\frac{\partial D_1^3}{\partial \bar{\zeta}} + \frac{\partial D_2^3}{\partial \zeta} + \frac{1}{2} \cdot \frac{\partial D_3^3}{\partial x_3} = 0. \tag{5}$$

The Piola tensor complex components D_n^k are expressed by D_{nk}^* in the following way:

$$D_1^1 = \frac{1}{2}(D_{11}^* + iD_{12}^* - iD_{21}^* + D_{22}^*), \quad D_2^2 = \overline{D_1^1},$$
$$D_1^2 = \frac{1}{2}(D_{11}^* - iD_{12}^* - iD_{21}^* - D_{22}^*), \quad D_2^1 = \overline{D_1^2},$$
$$D_1^3 = \frac{1}{2}(D_{13}^* - iD_{23}^*), \quad D_2^3 = \overline{D_1^3},$$
$$D_3^1 = (D_{31}^* + iD_{32}^*), \quad D_3^2 = \overline{D_3^1},$$
$$D_3^3 = D_{33}^*.$$

Describe a prismatic bar torsion by formulae

$$z = z_o(\zeta, \bar{\zeta}) \exp(i\psi x_3), \quad X_3 = \lambda x_3 + w(\zeta, \bar{\zeta}), \tag{6}$$

where ψ, λ are positive constants, w is a real-valued function, and z_o denotes a complex-valued function. The geometrical meaning of representations (6) is the following: the bar cross-section, x_3 distant from the original of coordinates, undergoes some plane deformation, defined by the function z_o, the rotation about the bar axis through the angle ψx_3, translation along the axis, expressed by $(\lambda - 1)x_3$, and warping, described by the function w. The deformation gradient, corresponding to transformation (6), is defined by equations

$$\mathbf{C} = C_n^k \mathbf{f}^n \mathbf{f}_k, \quad C_n^k = \frac{\partial z^k}{\partial \zeta^n},$$

$$C_1^1 = \frac{\partial z_o}{\partial \zeta} \exp(i\psi x_3), \quad C_2^1 = \frac{\partial z_o}{\partial \bar{\zeta}} \exp(i\psi x_3),$$

$$C_2^2 = \overline{C_1^1}, \quad C_1^2 = \overline{C_2^1},$$

$$C_3^1 = i\psi z_o \exp(i\psi x_3), \quad C_1^3 = \frac{\partial w}{\partial \zeta}, \quad C_3^2 = \overline{C_3^1}, \quad C_2^3 = \overline{C_1^3},$$

$$C_3^3 = \lambda. \tag{7}$$

Using (7), for the complex components of the Cauchy-Green deformation measure $G_{nk} = \mathbf{f}_n \cdot \mathbf{G} \cdot \mathbf{f}_k$, we have

$$G_{11} = \frac{\partial z_o}{\partial \zeta}\frac{\partial \bar{z}_o}{\partial \zeta} + \left(\frac{\partial w}{\partial \zeta}\right)^2; \quad G_{22} = \overline{G}_{11};$$

$$G_{12} = G_{21} = \frac{1}{2}\left(\frac{\partial z_o}{\partial \zeta}\frac{\partial \bar{z}_o}{\partial \bar{\zeta}} + \frac{\partial \bar{z}_o}{\partial \zeta}\frac{\partial z_o}{\partial \bar{\zeta}}\right) + \frac{\partial w}{\partial \zeta}\frac{\partial w}{\partial \bar{\zeta}};$$

$$G_{13} = G_{31} = \frac{1}{2}i\psi\left(z_o\frac{\partial \bar{z}_o}{\partial \zeta} - \bar{z}_o\frac{\partial z_o}{\partial \zeta}\right) + \lambda\frac{\partial w}{\partial \zeta};$$

$$G_{23} = G_{32} = \overline{G}_{13}; \quad G_{33} = \psi^2 z_o \bar{z}_o + \lambda^2. \tag{8}$$

The invariants I_q are expressed as

$$I_1 = 4G_{12} + G_{33};$$

$$I_2 = 4\left[(G_{12})^2 + G_{12}G_{33} - G_{11}G_{22} - G_{13}G_{23}\right];$$

$$\sqrt{I_3} = \lambda\left(\frac{\partial z_o}{\partial \zeta}\frac{\partial \bar{z}_o}{\partial \bar{\zeta}} - \frac{\partial \bar{z}_o}{\partial \zeta}\frac{\partial z_o}{\partial \bar{\zeta}}\right)$$
$$+ 2\psi \operatorname{Im}\left(\bar{z}_o\frac{\partial w}{\partial \zeta}\frac{\partial z_o}{\partial \bar{\zeta}} - \bar{z}_o\frac{\partial w}{\partial \bar{\zeta}}\frac{\partial z_o}{\partial \zeta}\right). \tag{9}$$

As follows from (8), (9), the tensor **G** and its invariants, corresponding to deformation (6), do not depend on the coordinate x_3. The tensors $\mathbf{G} \cdot \mathbf{C}$ and $(\mathbf{C}^T)^{-1}$, used in constitutive Eqs. (2), are expressed as

$$\mathbf{G} \cdot \mathbf{C} = K_m^s \mathbf{f}^m \mathbf{f}_s, \quad \sqrt{I_3}\mathbf{C}^{-T} = L_m^s \mathbf{f}^m \mathbf{f}_s, \tag{10}$$

where

$$K_1^1 = \left[\frac{\partial z_o}{\partial \zeta}\left(3\frac{\partial \bar{z}_o}{\partial \zeta}\frac{\partial z_o}{\partial \bar{\zeta}} + \frac{\partial \bar{z}_o}{\partial \bar{\zeta}}\frac{\partial z_o}{\partial \zeta} + 2\frac{\partial w}{\partial \zeta}\frac{\partial w}{\partial \bar{\zeta}} + \frac{1}{2}\psi^2 z_o \bar{z}_o\right)\right.$$
$$\left. + \frac{\partial w}{\partial \zeta}\left(2\frac{\partial w}{\partial \zeta}\frac{\partial z_o}{\partial \bar{\zeta}} + i\lambda\psi z_o\right) - \frac{1}{2}\psi^2 z_o^2 \frac{\partial \bar{z}_o}{\partial \zeta}\right] \exp(i\psi x_3),$$

$$K_2^2 = \overline{K_1^1},$$

$$K_2^1 = \left[\frac{\partial z_o}{\partial \bar{\zeta}}\left(3\frac{\partial z_o}{\partial \zeta}\frac{\partial \bar{z}_o}{\partial \bar{\zeta}} + \frac{\partial \bar{z}_o}{\partial \zeta}\frac{\partial z_o}{\partial \bar{\zeta}}\right.\right.$$

Downloaded 04 May 2010 to 171.66.16.28. Redistribution subject to ASME license or copyright; see http://www.asme.org/terms/Terms_Use.cfm

$$+2\frac{\partial w}{\partial\zeta}\frac{\partial w}{\partial\bar\zeta}+\frac{1}{2}\psi^2 z_o\bar z_o\Big)+\frac{\partial w}{\partial\bar\zeta}\Big(2\frac{\partial w}{\partial\bar\zeta}\frac{\partial z_o}{\partial\zeta}+i\lambda\psi z_o\Big)-\frac{1}{2}\psi^2 z_o^2\frac{\partial\bar z_o}{\partial\bar\zeta}\Big]\exp(i\psi x_3),$$

$$K_1^2=\overline{K_2^1},$$

$$K_3^1=\Big\{i\psi\Big[z_o\Big(\frac{\partial\bar z_o}{\partial\bar\zeta}\frac{\partial z_o}{\partial\zeta}+\frac{\partial\bar z_o}{\partial\zeta}\frac{\partial z_o}{\partial\bar\zeta}\Big)-2\bar z_o\frac{\partial z_o}{\partial\zeta}\frac{\partial z_o}{\partial\bar\zeta}\Big]+2\lambda\Big(\frac{\partial w}{\partial\zeta}\frac{\partial z_o}{\partial\bar\zeta}+\frac{\partial w}{\partial\bar\zeta}\frac{\partial z_o}{\partial\zeta}\Big)+i\psi z_o\big(\psi^2 z_o\bar z_o+\lambda^2\big)\Big\}\exp(i\psi x_3),$$

$$K_3^2=\overline{K_3^1},$$

$$K_1^3=\frac{\partial w}{\partial\bar\zeta}\Big[2\frac{\partial z_o}{\partial\zeta}\frac{\partial z_o}{\partial\bar\zeta}+4\Big(\frac{\partial w}{\partial\zeta}\Big)^2\Big]+\frac{1}{2}i\psi\lambda\Big(z_o\frac{\partial\bar z_o}{\partial\zeta}-\bar z_o\frac{\partial z_o}{\partial\zeta}\Big)+\frac{\partial w}{\partial\zeta}\Big(\frac{\partial z_o}{\partial\zeta}\frac{\partial\bar z_o}{\partial\bar\zeta}+\frac{\partial\bar z_o}{\partial\zeta}\frac{\partial z_o}{\partial\bar\zeta}+\lambda^2\Big),$$

$$K_2^3=\overline{K_1^3},$$

$$K_3^3=4\lambda\frac{\partial w}{\partial\zeta}\frac{\partial w}{\partial\bar\zeta}+i\psi z_o\Big(\frac{\partial\bar z_o}{\partial\zeta}\frac{\partial w}{\partial\bar\zeta}+\frac{\partial\bar z_o}{\partial\bar\zeta}\frac{\partial w}{\partial\zeta}\Big)-i\psi\bar z_o\Big(\frac{\partial z_o}{\partial\bar\zeta}\frac{\partial w}{\partial\zeta}+\frac{\partial z_o}{\partial\zeta}\frac{\partial w}{\partial\bar\zeta}\Big)+\lambda\big(\psi^2 z_o\bar z_o+\lambda^2\big),$$

$$L_1^1=\Big(\lambda\frac{\partial z_o}{\partial\zeta}-i\psi z_o\frac{\partial w}{\partial\zeta}\Big)\exp(i\psi x_3),\quad L_2^2=\overline{L_1^1},$$

$$L_2^1=\Big(i\psi z_o\frac{\partial w}{\partial\bar\zeta}-\lambda\frac{\partial z_o}{\partial\bar\zeta}\Big)\exp(i\psi x_3),\quad L_1^2=\overline{L_2^1},$$

$$L_3^1=2\Big(\frac{\partial w}{\partial\zeta}\frac{\partial z_o}{\partial\bar\zeta}-\frac{\partial w}{\partial\bar\zeta}\frac{\partial z_o}{\partial\zeta}\Big)\exp(i\psi x_3),\quad L_3^2=\overline{L_3^1},$$

$$L_1^3=\frac{1}{2}i\psi\Big(\bar z_o\frac{\partial z_o}{\partial\zeta}+z_o\frac{\partial\bar z_o}{\partial\zeta}\Big),\quad L_2^3=\overline{L_1^3},$$

$$L_3^3=\frac{\partial z_o}{\partial\zeta}\frac{\partial\bar z_o}{\partial\bar\zeta}-\frac{\partial\bar z_o}{\partial\zeta}\frac{\partial z_o}{\partial\bar\zeta}.$$

In cylindrical coordinates, deformation (6) is described by the following equations:

$$R=R(r,\varphi),\quad \Phi=\psi z+g(r,\varphi),\quad Z=\lambda z+w(r,\varphi).$$

The torsion of a circular cylinder is a particular case of these equations, when the function R does not depend on the variable φ, $g(r,\varphi)\equiv\varphi$, and $w(r,\varphi)\equiv 0$.

Using (2), (7), and (10), we have the representations

$$D_n^1=d_n^1(\zeta,\bar\zeta)\exp(i\psi x_3),\quad D_n^2=d_n^2(\zeta,\bar\zeta)\exp(-i\psi x_3),\tag{11}$$

and $D_n^3=d_n^3(\zeta,\bar\zeta)$, where $n=1,2,3$, and d_n^k $(k=1,2,3)$ denote the following:

$$d_1^1=a_1\frac{\partial z_o}{\partial\zeta}+a_2\Big[\frac{\partial z_o}{\partial\zeta}\Big(3\frac{\partial\bar z_o}{\partial\zeta}\frac{\partial z_o}{\partial\bar\zeta}+\frac{\partial\bar z_o}{\partial\bar\zeta}\frac{\partial z_o}{\partial\zeta}+2\frac{\partial w}{\partial\zeta}\frac{\partial w}{\partial\bar\zeta}+\frac{1}{2}\psi^2 z_o\bar z_o\Big)+\frac{\partial w}{\partial\zeta}\Big(2\frac{\partial w}{\partial\zeta}\frac{\partial z_o}{\partial\bar\zeta}+i\lambda\psi z_o\Big)-\frac{1}{2}\psi^2 z_0^2\frac{\partial\bar z_o}{\partial\zeta}\Big]+\frac{a_3}{\sqrt{I_3}}\Big(\lambda\frac{\partial z_o}{\partial\zeta}-i\psi z_o\frac{\partial w}{\partial\zeta}\Big),\tag{12}$$

$$d_2^1=a_1\frac{\partial z_o}{\partial\bar\zeta}+a_2\Big[\frac{\partial z_o}{\partial\bar\zeta}\Big(3\frac{\partial z_o}{\partial\zeta}\frac{\partial\bar z_o}{\partial\bar\zeta}+\frac{\partial\bar z_o}{\partial\zeta}\frac{\partial z_o}{\partial\bar\zeta}+2\frac{\partial w}{\partial\zeta}\frac{\partial w}{\partial\bar\zeta}+\frac{1}{2}\psi^2 z_o\bar z_o\Big)+\frac{\partial w}{\partial\bar\zeta}\Big(2\frac{\partial w}{\partial\bar\zeta}\frac{\partial z_o}{\partial z}+i\lambda\psi z_o\Big)-\frac{1}{2}\psi^2 z_o^2\frac{\partial\bar z_o}{\partial\bar\zeta}\Big]+\frac{a_3}{\sqrt{I_3}}\Big(i\psi z_o\frac{\partial w}{\partial\bar\zeta}-\lambda\frac{\partial z_o}{\partial\bar\zeta}\Big),$$

$$d_3^1=a_1 i\psi z_o+a_2\Big\{i\psi\Big[z_o\Big(\frac{\partial\bar z_o}{\partial\bar\zeta}\frac{\partial z_o}{\partial\zeta}+\frac{\partial\bar z_o}{\partial\zeta}\frac{\partial z_o}{\partial\bar\zeta}\Big)-2\bar z_o\frac{\partial z_o}{\partial\zeta}\frac{\partial z_o}{\partial\bar\zeta}\Big]+2\lambda\Big(\frac{\partial w}{\partial\zeta}\frac{\partial z_o}{\partial\bar\zeta}+\frac{\partial w}{\partial\bar\zeta}\frac{\partial z_o}{\partial\zeta}\Big)+i\psi z_o\big(\psi^2 z_o\bar z_o+\lambda^2\big)\Big\}+\frac{2a_3}{\sqrt{I_3}}\Big(\frac{\partial w}{\partial\zeta}\frac{\partial z_o}{\partial\bar\zeta}-\frac{\partial w}{\partial\bar\zeta}\frac{\partial z_o}{\partial\zeta}\Big),$$

$$d_1^3=a_1\frac{\partial w}{\partial\zeta}+a_2\Big\{\frac{\partial w}{\partial\bar\zeta}\Big[2\frac{\partial z_o}{\partial\zeta}\frac{\partial z_o}{\partial\bar\zeta}+4\Big(\frac{\partial w}{\partial\zeta}\Big)^2\Big]+\frac{1}{2}i\psi\lambda\Big(z_o\frac{\partial\bar z_o}{\partial\zeta}-\bar z_o\frac{\partial z_o}{\partial\zeta}\Big)+\frac{\partial w}{\partial\zeta}\Big(\frac{\partial z_o}{\partial\zeta}\frac{\partial\bar z_o}{\partial\bar\zeta}+\frac{\partial\bar z_o}{\partial\zeta}\frac{\partial z_o}{\partial\bar\zeta}+\lambda^2\Big)\Big\}+\frac{a_3 i\psi}{2\sqrt{I_3}}\Big(\bar z_o\frac{\partial z_o}{\partial\zeta}+z_o\frac{\partial\bar z_o}{\partial\zeta}\Big),$$

$$d_3^3=a_1\lambda+a_2\Big\{4\lambda\frac{\partial w}{\partial\zeta}\frac{\partial w}{\partial\bar\zeta}+i\psi z_o\Big(\frac{\partial\bar z_o}{\partial\zeta}\frac{\partial w}{\partial\bar\zeta}+\frac{\partial\bar z_o}{\partial\bar\zeta}\frac{\partial w}{\partial\zeta}\Big)-i\psi\bar z_o\Big(\frac{\partial z_o}{\partial\bar\zeta}\frac{\partial w}{\partial\zeta}+\frac{\partial z_o}{\partial\zeta}\frac{\partial w}{\partial\bar\zeta}\Big)+\lambda\big(\psi^2 z_o\bar z_o+\lambda^2\big)\Big\}+\frac{a_3}{\sqrt{I_3}}\Big(\frac{\partial z_o}{\partial\zeta}\frac{\partial\bar z_o}{\partial\bar\zeta}-\frac{\partial\bar z_o}{\partial\zeta}\frac{\partial z_o}{\partial\bar\zeta}\Big),$$

$$d_2^2=\bar d_1^1,\quad d_1^2=\bar d_2^1,\quad d_3^2=\bar d_3^1,\quad d_2^3=\bar d_1^3.$$

Note that the quantities d_n^k do not depend on the axial coordinate x_3. With regard to (11), balance Eq. (5) has the form

$$\frac{\partial d_1^1}{\partial\bar\zeta}+\frac{\partial d_2^1}{\partial\zeta}+\frac{i}{2}\psi d_3^1=0,\quad\text{and}\quad\frac{\partial d_1^3}{\partial\bar\zeta}+\frac{\partial d_2^3}{\partial\zeta}=0.\tag{13}$$

If the constants λ and ψ are given, then relations (13) form the system of equation of two functions: z_o, being the complex function of two arguments, and w, being the real function of two arguments.

To solve the problem, the boundary conditions must be applied to (13). In the case when the surface is free of load, the boundary conditions can be written down in the following form:

$$\frac{\partial\bar\zeta}{\partial s}d_2^1-\frac{\partial\zeta}{\partial s}d_1^1=0,\quad\text{and}\quad\frac{\partial\bar\zeta}{\partial s}d_2^3-\frac{\partial\zeta}{\partial s}d_1^3=0.\tag{14}$$

Downloaded 04 May 2010 to 171.66.16.28. Redistribution subject to ASME license or copyright; see http://www.asme.org/terms/Terms_Use.cfm

Here $\zeta(s)$ is the equation of the contour of the bar cross-section, and s denotes the contour arc.

Linearization of the boundary value problem (13), (14) relative to the ψ, $\lambda - 1$, $z_0 - \zeta$, w results in the classic linear Saint-Venant problem (Lurje, 1970) of torsion of a bar.

Note, that in the case of finite twist angles, in contrast to the linear theory of elasticity of an homogeneous isotropic body, the torsion of the prismatic bar is accompanied by not only warping, but nonuniform plane deformation of the cross-section as well.

It is easy to see that if z_0, w are certain solutions for boundary value problems (13), (14), then the functions $z_o \exp(i\omega)$, $w + a$, where ω, a denote real constants, also satisfy conditions (13), (14). This ambiguity of the solution can be resolved if we impose the following constraints on the functions z_o, w:

$$\iint_\sigma \left(\mathrm{Re}\left(\left| \frac{\partial z_o}{\partial \zeta} \right|^{-1} \frac{\partial z_o}{\partial \zeta} \right) - 1 \right) d\sigma = 0, \quad \iint_\sigma w d\sigma = 0. \quad (15)$$

Here σ denotes the cross-section of an undeformed prism. The first restriction shown in (15) states that, at $x_3 = 0$, rotation about the axis x_3, being average over the cross-section, is absent. The second restriction shown in (15) means that the axial displacement, being average over the cross-section, is equal to zero. If conditions (15) are implemented, we have a unique solution to (13) subjected to the boundary conditions (14), at least, for not too large twist angles ψ.

Suppose that the bar cross-section possesses central symmetry, i.e., it superposes with itself by rotating through 180 deg about the bar axis. A cross-section, having the form of the letter Z, may be taken as an example. Obviously, cross-sections, having two symmetry axes, belong to the same class as the cross-sections possessing central symmetry. In equation system (13) and boundary conditions (14) substitute independent variables and unknown functions from the following:

$$\zeta' = -\zeta, \quad \bar{\zeta}' = -\bar{\zeta}, \quad z_o' = -z_o, \quad w' = w; \quad (16)$$

$$\zeta'' = \bar{\zeta}, \quad \overline{\zeta''} = \zeta, \quad z_o'' = \bar{z}_o, \quad w'' = -w. \quad (17)$$

If a cross-section possesses central symmetry, then the transformation of the independent variables ζ and $\bar{\zeta}$ shown in (16) represents the region σ into itself. The section having two symmetry axes can be represented into itself by the transformations of independent variables contained in (16) and (17). The following theorem defining symmetry of boundary value problem (13)–(15) is true.

Theorem I. For a homogeneous isotropic elastic body, in the region s, having central symmetry, boundary value problem (13)–(15) *is invariant relative to transformations* (16) *and* (17).

The theorem can be proven by substitution from (16) and (17) into the boundary value problem.

Let $z_o = h(\zeta, \bar{\zeta})$, $w = m(\zeta, \bar{\zeta})$ be the solution of problems (13)–(15). By Theorem I the functions $z_o = -h(-\zeta, -\bar{\zeta})$ and $w = m(-\zeta, -\bar{\zeta})$ satisfy the same Eqs. (13)–(15). Since the solution is unique, we obtain $h(\zeta, \bar{\zeta}) = -h(-\zeta, -\bar{\zeta})$, $m(\zeta, \bar{\zeta}) = m(-\zeta, -\bar{\zeta})$. Thus, if the cross-section has central symmetry, the solution possesses property

$$z_o(-\zeta, -\bar{\zeta}) = -z_o(\zeta, \bar{\zeta}), \quad w(-\zeta, -\bar{\zeta}) = w(\zeta, \bar{\zeta}). \quad (18)$$

For a cross-section, having two symmetry axes, in addition to (18), the following equation is satisfied:

$$z_o(\bar{\zeta}, \zeta) = \overline{z_o(\zeta, \bar{\zeta})}, \quad w(\bar{\zeta}, \zeta) = -w(\zeta, \bar{\zeta}). \quad (19)$$

From (12) and (18), the results are as follows:

$$d_\alpha^\beta(-\zeta, -\bar{\zeta}) = d_\alpha^\beta(\zeta, \bar{\zeta}), \quad d_3^\alpha(-\zeta, -\bar{\zeta}) = -d_3^\alpha(\zeta, \bar{\zeta}),$$

$$d_\alpha^3(-\zeta, -\bar{\zeta}) = -d_\alpha^3(\zeta, \bar{\zeta}), \quad \text{where } \alpha, \beta = 1, 2, \quad (20)$$

and

$$d_3^3(-\zeta, -\bar{\zeta}) = d_3^3(\zeta, \bar{\zeta}).$$

For a cross-section with two symmetry axes, the following relations are also correct:

$$d_3^\alpha(\bar{\zeta}, \zeta) = -d_3^\alpha(\zeta, \bar{\zeta}), \quad d_3^3(\bar{\zeta}, \zeta) = d_3^3(\zeta, \bar{\zeta}). \quad (21)$$

The resultant vector $\mathbf{F}$ and the resultant moment $\mathbf{M}$ of forces, acting in an arbitrary cross-section of the bar ($x_3 = \text{const}$), are expressed by formulae

$$\mathbf{F} = \iint_\sigma \mathbf{f}_3 \cdot \mathbf{D} d\sigma, \quad \mathbf{M} = -\iint_\sigma \mathbf{f}_3 \cdot \mathbf{D} x (\mathbf{R} - \mathbf{R}_o) d\sigma$$

$$\mathbf{R} = X_m \mathbf{e}_m = z^k \mathbf{f}_k, \quad \mathbf{R}_o = X_3(0, 0, x_3)\mathbf{f}_3. \quad (22)$$

The designation $X_3(0, 0, x_3)$ states that the function X_3 of three variables x_1, x_2, x_3 is considered in $x_1 = x_2 = 0$. The letter $\mathbf{R}$ denotes the radius vector of the deformed body particle, and $\mathbf{R}_o$ is the radius vector of a reference point. The inertia center of the deformed bar is chosen as the reference point. The symbol x denotes a vector product. Basing on (6), (11), and (22), we have

$$\mathbf{F} = \iint_\sigma \left(d_3^1 \exp(i\psi x_3)\mathbf{f}_1 + d_3^2 \exp(-i\psi x_3)\mathbf{f}_2 + d_3^3 \mathbf{f}_3 \right) d\sigma,$$

$$\mathbf{M} = i \iint_\sigma \left[\frac{1}{2}\left(z_o d_3^2 - \bar{z}_o d_3^1 \right)\mathbf{f}_3 + \left(w^* d_3^1 - z_o d_3^3 \right) \exp(i\psi x_3)\mathbf{f}_1 \right.$$

$$\left. + \left(w^* d_3^2 - \bar{z}_o d_3^3 \right) \exp(-i\psi x_3)\mathbf{f}_2 \right] d\sigma, \quad (23)$$

where $w^* = w(\zeta, \bar{\zeta}) - w(0, 0)$. Using (18) and (20), we obtain

$$\mathbf{F} \cdot \mathbf{f}^\beta = \mathbf{M} \cdot \mathbf{f}^\beta = 0, \quad \text{where } \beta = 1, 2. \quad (24)$$

Relations (24) state that stresses acting on any cross-section of a cylinder under deformation (6) are reduced to the axial force F_3 and to the torsional moment M_3. These quantities are the same in all prism cross-sections. After solving the boundary value problem (13)–(15), the F_3 and the M_3 will be known functions of the parameters ψ and λ. One can define the functions by formulae

$$F = F_3 = \mathbf{F} \cdot \mathbf{f}_3 = \iint_\sigma d_3^3 d\sigma,$$

$$M = M_3 = \mathbf{M} \cdot \mathbf{f}_3 = -\iint_\sigma \mathrm{Im}(z_o d_3^2) d\sigma. \quad (25)$$

Thus, we assume that the torsion of a noncircular cylinder under large deformations may be described by formulae (6). Then the balance equation and lateral boundary conditions can be accomplished exactly by solving the two-dimensional boundary value problem (13)–(15). In the case when a cylinder has a cross-section possessing central symmetry, end conditions turn into (25). They can be satisfied in integral meaning by the choice of the parameters ψ and λ.

In general, if a cross-section of a cylinder does not possess central symmetry, then relations (24) do not take place. This indicates that, in contrast to the linear isotropic theory of elasticity, the action of a merely twisting moment on the ends of a bar produces not only torsion, but also bending of the bar.

3 Variational Formulation

According to the Lagrange variational principle of the nonlinear theory of elasticity (Lurje, 1980), we have

Downloaded 04 May 2010 to 171.66.16.28. Redistribution subject to ASME license or copyright; see http://www.asme.org/terms/Terms_Use.cfm

$$\delta \iiint_{\upsilon} W d\upsilon - \iint_{o} \mathbf{F} \cdot \delta \mathbf{R} do = 0. \tag{26}$$

Here υ is the volume of a body in the reference configuration, o denotes the surface limiting the body, $\mathbf{F}$ is the vector of external forces intensity, δ denotes variation symbol, and W is the strain energy density.

In accordance with (6), (11), the elementary work of forces, acting in the prism section $x_3 = \text{const}$, is written in the form

$$\iint_{\sigma} \mathbf{f}_3 \cdot \mathbf{D} \cdot \delta \mathbf{R} d\sigma = i\frac{1}{2}\iint_{\sigma}\left(z_o d_3^2 - \bar{z}_o d_3^1\right) d\sigma \delta(x_3\psi)$$
$$+ \iint_{\sigma} d_3^3 d\sigma \delta(x_3\lambda) + \iint_{\sigma}\left[d_3^3 \delta w + \frac{1}{2}\left(d_3^1 \delta \bar{z}_o + d_3^2 \delta z_o\right)\right] d\sigma. \tag{27}$$

By (19)–(21), for the section having two symmetry axes, the last integral in (27) is equal to zero, and, according to (25), we obtain

$$\iint_{\sigma} \mathbf{f}_3 \cdot \mathbf{D} \cdot \delta \mathbf{R} d\sigma = M\delta(x_3\psi) + F\delta(x_3\lambda). \tag{28}$$

Let Π denote the functional of strain energy, measured per unit of the bar length. At displacements (6), where z_o and w present the solution of boundary value problem (13)–(15), the functional Π is a certain function of the parameters ψ and λ. From (26) and (28), the energy relations of the nonlinear theory of elastic prismatic body torsion and tension result in

$$M = \frac{\partial \Pi}{\partial \psi}, \quad F = \frac{\partial \Pi}{\partial \lambda}, \quad \Pi = \iint_{\sigma} W d\sigma. \tag{29}$$

Since the constants ψ, λ are given, the boundary value problem (13), (14) is equal to the variational principle

$$\delta \Pi(z_o, w) = 0. \tag{30}$$

This allows us to employ approximate methods of calculus of variations for the solution of the nonlinear torsion problem. Note that functions subjected to variation in the Lagrange variational principle are not required to satisfy force boundary conditions.

4 The Energy Method to Solve the Torsion Problem for Elliptical and Rectangular Elastic Bars Under Large Deformations

We shall obtain the solution of the variational problem (30) by means of the Ritz method. Consider prisms of elliptical and rectangular cross-sections. Choose such approximations of unknown functions which satisfy the following requirements: first, they must possess properties (18), (19) and, second, under small twist angles they must reduce to known solutions of corresponding linear torsion problems.

For both of the aforementioned of the bar cross-section, we shall accept the simplest polynomial representation z_o, satisfying conditions (18), (19) and describing affine deformation in the plane of the cross-section

$$z_o = A\bar{\zeta} + B\zeta. \tag{31}$$

Here A and B denote real constants. By (4), (6) at $x_3 = 0$ in Cartesian coordinates, we have

$$X_1 = (A + B)x_1, \quad X_2 = (B - A)x_2.$$

Under such deformation the shape of the section does not change qualitatively, i.e., ellipse remains ellipse and rectangle remains rectangle. But semi-axes of symmetry of the figures become longer or shorter, and the ratio of the semi-axes also changes.

For the bar of an elliptical section, the warping function may be approximated by the expression

$$w = i\frac{C}{2}\left(\zeta^2 - \bar{\zeta}^2\right), \tag{32}$$

where C is a real constant. The difference between relation (32) and the corresponding w expression of the linear torsion theory is only a constant multiplier.

For a rectangular bar, in the linear theory of elasticity, the warping function w is defined (Lurje, 1970) with accuracy to an arbitrary constant by equation

$$dw = \psi\left(\frac{\partial \Phi}{\partial x_2} + x_2\right) dx_1 - \psi\left(\frac{\partial \Phi}{\partial x_1} + x_1\right) dx_2,$$

where

$$\Phi = b^2 - x_2^2 + \frac{32b^2}{\pi^3}\sum_{k=0}^{\infty}\frac{(-1)^{k+1}}{(2k+1)^3} \cdot \frac{ch\dfrac{(2k+1)\pi x_1}{2b}}{ch\dfrac{(2k+1)\pi a}{2b}} \cdot \cos\frac{(2k+1)\pi x_2}{2b}.$$

Note that Φ is the stress function satisfying equation $\Delta\Phi = -2$ and boundary condition $\Phi = 0$; and a, b denote the semi-axes of the rectangular (i.e., $-a \le x_1 \le a$, $-b \le x_2 \le b$). Suppose that $w(0, 0) = 0$, and consider the explicit w expression for the case of small twist angles

$w = -\psi\gamma$, where

$$\gamma = x_1 x_2 + \frac{32b^2}{\pi^3}\sum_{k=0}^{\infty}\frac{(-1)^{k+1} sh\dfrac{(2k+1)\pi x_1}{2b}}{(2k+1)^3 ch\dfrac{(2k+1)\pi a}{2b}} \cdot \sin\frac{(2k+1)\pi x_2}{2b}. \tag{33}$$

For a rectangular bar under finite deformations we shall use the following w approximation

$$w = C\gamma, \tag{34}$$

where C denotes a real constant. The coefficients A, B, C are defined from the condition that in a state of balance, the potential energy Π remains stationary. Relations

$$\frac{\partial \Pi}{\partial A} = \frac{\partial \Pi}{\partial B} = \frac{\partial \Pi}{\partial C} = 0 \tag{35}$$

form a system of nonlinear equations of A, B, C.

For incompressible material, according to the accuracy of the plane deformation accounting, accepted in (31), the satisfaction of an incompressibility condition will be demanded on the average over the cross-section

$$\iint_{\sigma}\left(\sqrt{I_3} - 1\right) d\sigma = 0. \tag{36}$$

In this case, the coefficients of the Ritz decomposition are defined from the condition that the functional

$$\Pi = \iint_{\sigma}\left[W + L\left(\sqrt{I_3} - 1\right)\right] d\sigma$$

remains stationary. Here L denotes the Lagrange multiplier for restriction (36), the multiplier being an unknown constant.

If one sets the longitudinal force F, the axial elongation λ is also unknown. In this case the first relation (25) is to be added to the above system of nonlinear equations. The

Downloaded 04 May 2010 to 171.66.16.28. Redistribution subject to ASME license or copyright; see http://www.asme.org/terms/Terms_Use.cfm

Table 1 The results for an elliptical cross-section with a semi-axes ratio of $t = b/a = 0.5$. The data corresponding to the Treloar and Blatz-Ko potentials are presented in columns I and II, respectively.

	$\psi^* = 0.1$		$\psi^* = 0.5$		$\psi^* = 1.0$	
	I	II	I	II	I	II
A	0.0005	0.0009	0.0127	0.0139	0.0660	0.0258
B	0.9996	0.9995	0.9886	0.9883	0.9494	0.9604
C^*	0.0300	0.0298	0.1554	0.1318	0.3541	0.1934
λ	0.9998	1.0000	0.9930	1.0082	0.9488	1.0498

Table 2 The results for a rectangular cross-section with a semi-axes ratio of $t = b/a = 0.5$. The data corresponding to the Treloar and Blatz-Ko potentials are presented in columns I and II, respectively.

	$\psi^* = 0.1$		$\psi^* = 0.5$		$\psi^* = 1.0$	
	I	II	I	II	I	II
A	0.0006	0.0009	0.0168	0.0162	0.0863	0.0311
B	0.9993	0.9993	0.9832	0.9826	0.9263	0.9375
C^*	−0.1004	−0.0994	−0.5148	−0.4295	−1.1506	−0.6287
λ	0.9994	1.0000	0.9342	1.0051	0.9043	1.0515

torsional moment M is defined by the second formula in (25).

Consider two widely used models of hyperelastic materials: the compressible material with the strain energy density of the Blatz-Ko form

$$W = \frac{1}{2}\mu\left(\frac{I_2}{I_3} + 2\sqrt{I_3} - 5\right) \tag{37}$$

and the incompressible Neo-Hookean material (the Treloar material) with the strain energy of the following form:

$$W = \frac{1}{2}\mu(I_1 - 3). \tag{38}$$

In the above formulae, μ denotes a shear modulus. The invariants I_1, I_2, I_3 are defined by relations (8), (9), (31), and (32)–(34).

5 Numerical Results for Bars of Treloar and Blatz-Ko Materials

The results are obtained for the cylinders of elliptical and rectangular cross-sections with the ratio of semi-axes $t = b/a = 1/2$ and for the bar of the quadrantal cross-section with the side length $2a$. The regarded case is the torsion without longitudinal force, i.e., $F = 0$.

In order to solve numerically the systems of equations of A, B, C, λ, and L, for potentials (37) and (38), the continuation by means of the parameter ψ and the Newton method were used. In the undeformed state at $\psi = 0$ and $\lambda = 1$, the coefficients of decompositions (31), (32), (34) assume the values $A = 0$, $B = 1$, $C = 0$, and for the Neo-Hookean material the relation $L/\mu = -1$ is completed.

Obtained values of A, B, $C^* = Ca$ and λ at a number of $\psi^* = \psi a$ are shown in Tables 1–3. Data corresponding to Treloar and Blatz-Ko potentials are given in columns I and II, respectively. For the quadrantal prism we have $A = 0$ at any value ψ.

The values λ for elliptical and rectangular prisms made of incompressible material are less than 1.0. Consequently, these bodies shorten while twisting. But the circular cylinder made of the Neo-Hookean material is known to elongate while twisting. Considering ellipses of semi-axes ratios $0.5 \le t \le 1.0$, we see that the character of changing of the prism length depends on t continuously. The graphs of λ dependence on ψ^* are shown on Fig. 1. According to the data, given in Table 3, the quadrantal prism made of the Treloar material elongates. Tables 1–3 show that all the regarded bodies made of the Blatz-Ko material also become longer.

Table 3 The results for a quadrantal cross-section with a side length $2a$. The data corresponding to the Treloar and Blatz-Ko potentials are presented in columns I and II, respectively.

	$\psi^* = 0.1$		$\psi^* = 0.5$		$\psi^* = 1.0$	
	I	II	I	II	I	II
B	0.9993	0.9992	0.9825	0.9825	0.9376	0.9476
C^*	−0.1000	−0.0976	−0.5048	−0.3042	−0.0302	−0.3279
λ	1.0000	1.0017	1.0100	1.0492	1.0300	1.1921

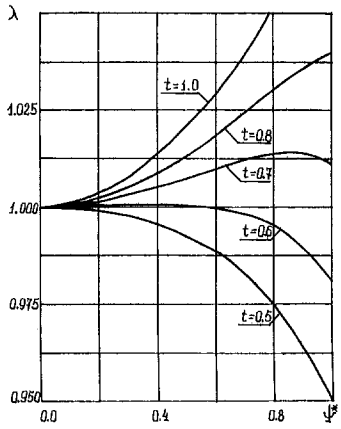

Fig. 1 Dependence of the elongation coefficient λ on the twist angle $\psi^* = \psi a$ for a number of elliptical bars of the Treloar material. The letter t denotes the ratio of the bar cross-section semi-axes, i.e., $t = b/a$.

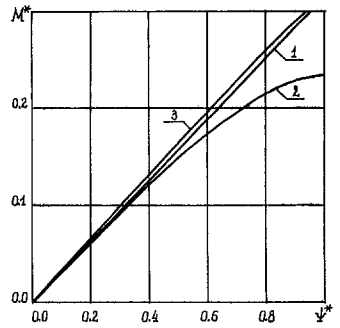

Fig. 2 Dependence of the torque $M^* = M/(\mu a^3)$ on the twist angle $\psi^* = \psi a$ for an elliptical cross-section with a semi-axes ratio of $t = b/a = 0.5$. Numerical notations: 1—solution of linear theory, 2—the Treloar material, 3—the Blatz-Ko material.

At $\psi^* = 0.1$ the values A, B, C^*, and λ, given in the tables, correspond with the known (Lurje, 1970) solutions of linear torsion problems for the same bodies. Thus, B and λ are approximately equal to one, and A is close to zero. In the linear torsion theory, the warping of the elliptical prism is described by equation $w = (\psi(b^2 - a^2)/(a^2 + b^2))x_1x_2$, and the warping of the rectangular and quadrantal bar is defined by (33). Calculated by these formulae values, $C^* = 0.03$ (for the ellipse) and $C^* = -0.1$ (for the rectangle and the quadrant) are about those given in the first columns of Tables 1–3.

Dependences of the torque $M^* = M/(\mu a^3)$ on twist angle $\psi^* = \psi a$ for elliptical, rectangular, and quadrantal prisms are shown in Figs. 2–4, respectively. On the graphs the straight lines, presenting the solutions of linear theory, are marked by 1. The curves, obtained for Treloar and Blats-Ko materials, are designated by 2 and 3.

Downloaded 04 May 2010 to 171.66.16.28. Redistribution subject to ASME license or copyright; see http://www.asme.org/terms/Terms_Use.cfm

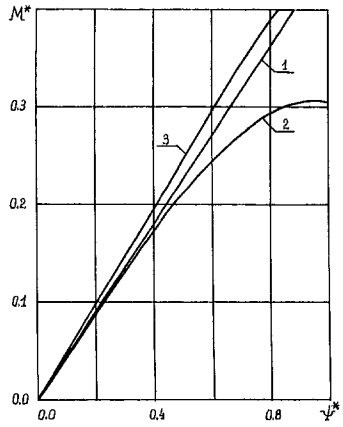

Fig. 3 Dependence of the torque $M^* = M / (\mu a^2)$ on the twist angle $\psi^* = \psi a$ for a rectangular cross-section with a semi-axes ratio of $t = b / a = 0.5$. Numerical notations are the same as on Fig. 2.

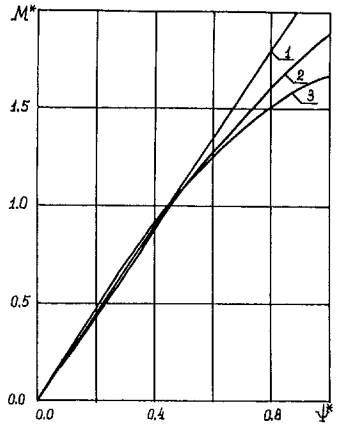

Fig. 4 Dependence of the torque $M^* = M / (\mu a^3)$ on the twist angle $\psi^* = \psi a$ for a quadrantal cross-section with the side length $2a$. Numerical notations are the same as on Fig. 2.

On Figs. 2–4, at $\psi^* \to 0$, curves of dependence of M^* on ψ^* are seen to transform into straight lines corresponding to linear solutions.

For a circular bar of the Treloar material, the solution, received by the described method, practically does not differ from the exact one (Lurje, 1970). For example, at $\psi^* = 1.0$, the approximate solution for a circular bar predicts $M^* = 1.4581$ while the exact solution is $M^* = 1.4585$.

The approximate solution presented in Sections 4 and 5 is founded on the simple choice of trial functions in the Ritz method and it does not pretend to be a good description of the stress field in the elastic cylinder. At the same time we hope that this simple solution gives a satisfactory accuracy of definition of such integral torsion features as the dependence of the torque on the twist angle and the value of the elongation coefficient, not only in the case of the circular cross-section but in the case of other sections as well.

To more exactly define the stress field in the twisted cylinder, one should solve the boundary value problem (13)–(15) numerically by, for example, the method of finite element.

6 Concluding Remark

In this work the nonlinear theory of torsion of prismatic elastic bars has been developed. By means of the semi-inverse method, the torsion problem has been reduced to the two-dimensional nonlinear boundary value problem for the plane region, which is the bar cross-section. The solution of the two-dimensional problem makes it possible to satisfy the balance equations and the lateral conditions. If the bar cross-section possesses two symmetry axes, then the stresses acting on the cross-section are proved to be equal to the torque and axial force. The proposed theory describes the bars in torsion under large deformations, and it holds true for any nonlinear elastic isotropic body.

Variational formulation of the aforementioned boundary value problem has been received. It has been used to solve approximately, by the Ritz method, the problem of torsion under large deformations for the bars of elliptical, rectangular, and quadrantal cross-sections. The models of the incompressible Treloar material and the compressible Blatz-Ko material have been employed. The nonlinear dependences of the torque on the twist angle have been constructed for the above cases and the quantity of axial elongation of the bar twisted without application of the longitudinal force has been defined.

References

Green, A. E., and Adkins, J. E., 1960, *Large Elastic Deformations and Non-Linear Continuum Mechanics*, Oxford Univ. Press, Oxford, U.K.

Lurje, A. I., 1980, *Nelinejnaja Teorija Uprugosti*, Nauka, Moscow.

Lurje, A. I., 1970, *Teorija Uprugosti*, Nauka, Moscow.

Poynting, J. H., 1909, "On Pressure Perpendicular to the Shear Planes in Finite Pure Shears and on the Lengthening of Loaded Wires when Twisted," *Proceedings of the Royal Society of London*, Vol. A82, pp. 546–559.

Zubov, L. M., and Ovseenko, S. U., 1980, "Metodika Raschota Bolshih Deformatsij Kruchenija i Radialnogo Sdviga Tsilindrov iz Szhimaemyh Rezinopodobnyh Materialov," *Tezisy Dokladov Vsesojuznoj Nauchno-Technicheskoj Konferentsii po Metodam Raschota Izdelij z Vysokoelastichnyh Materialov*, Riga, pp. 42–43.

Zubov, L. M., 1983, "Teorija Kruchenija Prizmaticheskih Sterzhnej pri Konechnyh Deformatsijah," *Doklady Akademii Nauk SSSR*, Vol. 270, N4, pp. 827–831.

Downloaded 04 May 2010 to 171.66.16.28. Redistribution subject to ASME license or copyright; see http://www.asme.org/terms/Terms_Use.cfm

H. Z. Fan

G. A. C. Graham

Applied and Computational Mathematics Program, Simon Fraser University, Burnaby BC V5A 1S6, Canada

J. M. Golden

Department of Mathematics, Statistics, and Computer Science, Dublin Institute of Technology, Dublin 8, Ireland

The Problem of Several Indentors Moving on a Viscoelastic Half-Plane

The problem of several indentors moving on a viscoelastic half-plane is considered in the noninertial approximation. The solution of this mixed boundary value problem is formulated in terms of a coupled system of integral equations in space and time. These are solved numerically in the steady-state limit for the case of two indentors. The phenomena of hysteretic friction and interaction between the two indentors are explored.

1 Introduction

The problem of indentors moving across a viscoelastic half-space is of considerable interest, largely because it offers a theoretical framework in which to investigate the phenomenon of hysteretic friction (Golden and Graham, 1988). If surface friction is neglected, the problem can be regarded as that of indentors sliding across a lubricated half-plane, or cylinders rolling over the plane. In the latter case, hysteretic friction is manifested as resistance to rolling, often termed rolling friction. The problem of a single smooth indentor moving across a viscoelastic half-plane has a history stretching back over 30 years, which is outlined in (Golden and Graham, 1988). In this paper the problem of two or more indentors moving on a viscoelastic half-plane is analyzed, for the first time, and detailed numerical results are presented for the case of a standard linear solid.

This is a mixed boundary value problem with moving boundary regions, which cannot be solved in terms of the corresponding elastic solution. The crux of the problem is the determination of a certain function on the boundary. In Section 3 we use the method of decomposition of hereditary integrals to reduce this problem to a coupled system of integral equations valid for general linear viscoelastic materials. Together with this set of integral equations, subsidiary conditions are given to determine the extent of the contact regions. Numerical results are obtained in Section 6 and, based on these, the phenomenon of hysteretic friction and the interaction between the indentors are discussed.

Contributed by the Applied Mechanics Division of THE AMERICAN SOCIETY OF MECHANICAL ENGINEERS for presentation at the Joint Applied Mechanics and Materials Summer Meeting of the ASME, Los Angeles, CA, June 28–30, 1995.

Discussion on this paper should be addressed to the Technical Editor, Professor Lewis T. Wheeler, Department of Mechanical Engineering, University of Houston, Houston, TX 77204-4792, and will be accepted until four months after final publication of the paper itself in the ASME JOURNAL OF APPLIED MECHANICS.

Manuscript received and accepted by the ASME Applied Mechanics Division, Mar. 14, 1994. Associate Technical Editor: J. T. Jenkins.

Paper No. 95-APM-3.

2 Fundamental Equations

We are considering the problem of n rigid indentors pressed into a viscoelastic half-plane ($y > 0$) and moving across it in the negative x-direction. On the boundary of the x-axis, we denote the contact regions by $c(t)$,

$$c(t) = \bigcup_{j=1}^{n} c_j(t),\ c_j(t) = \left[a_j(t), b_j(t)\right],\ j = 1, n \quad (2.1)$$

and its complement on the boundary by $c'(t)$. The speed of the indentors is assumed to be sufficiently small for inertial effects to be neglected. The quantities $a_j(t)$, $b_j(t)$ $j = 1, n$ are not known until the problem is solved.

The boundary conditions on the x-axis are formulated as follows. The displacement in the y-direction is given by

$$u_2(x,t) = \begin{cases} d_j(t) + F_j\left(x - x_{0j}(t)\right), & x \in c_j(t), \\ \text{unknown}, & x \in c'(t), \end{cases} \quad (2.2)$$

and the complex stress, if Coulomb's law applies, by

$$\Sigma(x,t) \equiv \sigma_{22} - i\sigma_{12} = \begin{cases} -(1 + if)p(x), \text{ unknown}, & x \in c_j(t), \\ 0, & x \in c'(t), \end{cases} \quad (2.3)$$

where F_j is the shape function of jth indentor, d_j is the displacement under the deepest point $x_{0j}(t)$ of the indentor, and f is the coefficient of friction. The quantities $d_j(t)$ are indeterminate, due to the well-known logarithmic divergence in plane-strain problems with nonzero resulting loads acting on the material. However, only the derivative of $u_2(x, t)$ will occur in the equations. The displacement in the x-direction is unprescribed. This is a mixed boundary value problem with

Copyright © 1995 by ASME

Downloaded 04 May 2010 to 171.66.16.28. Redistribution subject to ASME license or copyright; see http://www.asme.org/terms/Terms_Use.cfm

moving boundary regions, to which the classical correspondence principle is not applicable (Golden and Graham, 1988).

Using the formal developments of (Golden and Graham, 1988; Muskhelishvili, 1963) to adapt the viscoelastic Kolosov-Muskhelishvili equations (Muskhelishvili, 1963; Sokolnikoff, 1956) to the upper half-plane and assuming that the material possesses the proportionality property (Golden and Graham, 1988), giving a unique Poisson's ratio ν_0, we find that this moving multiindentor problem is determined by the quantity $v(x, t)$ defined by

$$v(x,t) = \int_{-\infty}^{t} dt' l(t-t') u_2'(x,t'), \text{ for } x \in c(t); \quad (2.4)$$

$$v(x,t) = \frac{-\sin(\pi\theta) e^{i\pi\theta} X(x,t)}{\pi} \times \int_{c(t)} dx' \frac{v(x',t)}{(x'-x)X^+(x',t)'}, \text{ for } x \in c'(t), \quad (2.5)$$

where

$$u_2'(x,t) = \frac{d}{dx} u_2(x,t), \quad (2.6)$$

with n conditions for solvability

$$\int_{c(t)} dx \frac{x^r v(x,t)}{X^+(x,t)} = 0, \quad r = 0, n-1, \quad (2.7)$$

where $l(t)$ is a singular viscoelastic function related to the relaxation behavior of the viscoelastic material (Golden and Graham, 1988). The quantities $X(x, t)$ and $X^+(x, t)$ are the boundary values of the function,

$$X(z,t) = \prod_{j=1}^{n} \left(z - a_j(t)\right)^{1-\theta} \left(z - b_j(t)\right)^{\theta}; \; z = x + iy \quad (2.8)$$

on $x \in c'(t)$ and $x \in c(t)$, respectively. For $x \in c(t)$, the limit is taken from above. For $x \in c'(t)$, it has the same limit from above and below. The quantity θ is defined as

$$\theta = \frac{1}{\pi} \tan^{-1}\left(\frac{h}{f}\right),$$

$$h = \frac{\kappa_0 + 1}{\kappa_0 - 1} = \frac{2(1-\nu_0)}{1-2\nu_0}, \theta \in \left[0, \frac{1}{2}\right], \quad (2.9)$$

$$\kappa_0 = 3 - 4\nu_0. \quad (2.10)$$

The pressure $p(x, t)$ on the contact regions is given in terms of $v(x, t)$ by

$$p(x,t) = -\frac{ie^{i\pi\theta}}{1+if}\left[\frac{\sin(\pi\theta)X^+(x,t)}{\pi} \times \int_{c(t)} \frac{dx' v(x',t)}{(x'-x)X^+(x',t)} + \cos(\pi\theta) v(x,t)\right]. \quad (2.11)$$

The loads W_j per unit length under each punch are specified. This gives n additional conditions

$$W_j = \int_{a_j(t)}^{b_j(t)} dx p(x,t) = \int_{c(t)} dx J_j(x,t) v(x,t) + q\cos(\pi\theta) \int_{a_j(t)}^{b_j(t)} dx v(x,t), \quad (2.12)$$

where

$$J_j(x,t) = \frac{q\sin(\pi\theta)}{\pi X^+(x,t)} \int_{a_j(t)}^{b_j(t)} dx' \frac{X^+(x',t)}{x-x'}, \quad (2.13)$$

$$q = -\frac{ie^{-i\pi\theta}}{1+if}. \quad (2.14)$$

Once the quantity $v(x, t)$ and the contact intervals $c(t)$ are known, all other quantities of interest can be determined easily (Golden and Graham, 1988). We will now show that $v(x, t)$ obeys an integral equation, which together with (2.7) and (2.12), determines both this quantity and the parameters $a_j(t)$, $b_j(t)$ of the contact region. The derivation of this equation relies upon a fundamental decomposition of the hereditary integrals of linear viscoelasticity (Golden and Graham, 1988).

3 Decomposition of Hereditary Integrals

From the Eq. (2.4), we can solve for the function $u_2'(x, t)$ in terms of $v(x, t)$:

$$u_2'(x,t) \equiv u'(x,t) = \int_{-\infty}^{t} dt' k(t-t') v(x,t'), \quad (3.1)$$

where $k(t)$ is a another causal function related to $l(t)$ by the convolution relation

$$\int_0^t dt' k(t-t') l(t') = \int_0^t dt' l(t-t') k(t') = \delta(t). \quad (3.2)$$

The singular function $k(t)$ is related to the creep behavior of the viscoelastic material (Golden and Graham, 1988). For standard linear solid (Golden and Graham, 1988)

$$l(t) = l_0\delta(t) + l_1 e^{-\alpha t} H(t), \; k(t) = k_0\delta(t) + k_1 e^{-\beta t} H(t), \quad (3.3)$$

where α and β are the inverse decay times given by

$$\alpha = 1/\tau, \quad \beta = 1/\tau', \quad (3.4)$$

$$\tau' = \tau \frac{G_0 + G_1}{G_0} > \tau, \quad (3.5)$$

and l_0, l_1, k_0, k_1, and β are given by

$$l_0 = \bar{h}(G_0 + G_1), \quad l_1 = -\bar{h}\alpha G_1 < 0, \quad (3.6)$$

$$k_1 = -l_1/l_0^2, \; k_0 l_1 = -\alpha \frac{G_1}{G_0 + G_1}, \; \beta = \alpha G_0/(G_0 + G_1) \quad (3.7)$$

$$\bar{h} = \frac{4}{(3-4\nu_0) - a}, \; a = -\frac{1-if}{1+if}, \quad (3.8)$$

in term of G_0 and G_1 which are the positive coefficients in the shear relaxation function

$$G(t) = G_0 + G_1 e^{-t/\tau} \quad (3.9)$$

and can be determined from a mechanical experiment. In the absence of friction,

$$\bar{h} = \frac{1}{1-\nu_0}. \quad (3.10)$$

Let $\Theta(x, t)$ be the set of the present and all past times, $(-\infty, t]$, which we decompose into two disjoint sets $W_u(x, t)$ and $W_\sigma(x, t)$, i.e.,

$$\Theta(x,t) = W_u(x,t) \cup W_\sigma(x,t), \quad (3.11)$$

Downloaded 04 May 2010 to 171.66.16.28. Redistribution subject to ASME license or copyright; see http://www.asme.org/terms/Terms_Use.cfm

where $W_u(x, t)$ is the set of all those times $t' \le t$ such that $x \in c(t')$ which consists of the contact regions in which the displacement in the y-direction is known, and $W_\sigma(x, t)$ is the set of all those times $t' \le t$ such that $x \in c'(t')$; i.e., outside the contact interval in which stress distributions are known to be zero. When the jth indentor is passing point x at time t, we take the quantity $t_{2j-1}(x)$ to be the time when the front end point of first contact interval coincided with point x and $t_{2j-2}(x)$ to be the time when the rear end point of the first contact interval passed x. The point x is in $c_j(t)$, the jth contact interval at time t. Also $t_1(x)$ is the time when the front end of the jth indentor coincided with the point x. Thus, if x lies in jth contact interval,

$$W_u(x,t) = \left[t_{2j-1}(x), t_{2j-2}(x)\right] \cup \cdots \cup \left[t_3(x), t_2(x)\right] \cup \left[t_1(x), t\right], \quad (3.12)$$

$$W_\sigma(x,t) = \left(-\infty, t_{2j-1}(x)\right) \cup \cdots \cup \left(t_4(x), t_3(x)\right) \cup \left(t_2(x), t_1(x)\right). \quad (3.13)$$

Now we decompose Eq. (2.4) for $v(x, t)$ when x in the contact regions by using Eq. (3.1). First we have

$$v(x,t) = \int_{t_1(x)}^{t} dt' l(t-t') u'(x,t') + \int_{-\infty}^{t_1(x)} dt' l(t-t') u'(x,t'), \; x \in c(t), \quad (3.14)$$

where in the second term $u'(x, t')$ is given by Eq. (3.1). Then carrying out an interchange of integrations, we have

$$v(x,t) = \int_{t_1(x)}^{t} dt' l(t-t') u'(x,t') + \int_{-\infty}^{t_1(x)} dt' T_1(t,t';x) v(x,t'), \quad (3.15)$$

where

$$T_1(t,t';x) = \int_{t'}^{t_1(x)} dt'' k(t-t'') l(t''-t'). \quad (3.16)$$

The procedure can be repeated. We obtain

$$v(x,t) = \int_{t_1(x)}^{t} dt' l(t-t') u'(x,t') + \int_{t_2(x)}^{t_1(x)} dt' T_1(t,t';x) v(x,t') + \int_{-\infty}^{t_2(x)} dt' T_2(t,t';x) u'(x,t'), \quad (3.17)$$

where

$$T_2(t,t';x) = \int_{t'}^{t_2(x)} dt'' T_1(t,t'';x) k(t''-t').$$

Continuing this process gives the decomposition for $x \in c(t)$ or $t \in W_u(x, t)$ (Golden and Graham, 1988),

$$v(x,t) = \int_{W_u} dt' \, \Pi_u(t,t';x) u'(x,t') + \int_{W_\sigma} dt' \Pi_\sigma(t,t';x) v(x,t'), \; x \in c(t), \quad (3.18)$$

where

$$\Pi_u(t,t';x) = T_0(t,t') R(t';t_1(x),t) + T_2(t,t';x) R(t';t_3(x),t_2(x)) + T_4(t,t';x) R(t';t_5(x),t_4(x)) + \cdots, \quad (3.19)$$

$$\Pi_\sigma(t,t';x) = T_1(t,t';x) R(t';t_2(x),t_1(x)) + T_3(t,t';x) R(t';t_4(x),t_3(x)) + T_5(t,t';x) R(t';t_6(x),t_5(x)) + \cdots, \quad (3.20)$$

$$T_0(t,t') = l(t-t'), \quad (3.21)$$

$$T_j(t,t';x) = \begin{cases} \int_{t'}^{t_j(x)} dt'' T_{j-1}(t,t'';x) l(t''-t'), & \text{if } j \text{ even}, \\ \int_{t'}^{t_j(x)} dt'' T_{j-1}(t,t'';x) k(t''-t'), & \text{if } j \text{ odd}, \end{cases} \quad (3.22)$$

and

$$R(t;t_{k+1},t_k) = \begin{cases} 1, & t \in [t_{k+1}, t_k], \\ 0, & \text{otherwise}, \end{cases} \quad k = 1, 2, \cdots. \quad (3.23)$$

The quantity $v(x, t')$, occurring in the second integral on the right of Eq. (3.18), is always evaluated outside of $c(t')$, by definition of $W_\sigma(x, t)$. We substitute the expression (2.5) for it to obtain the integral equation:

$$v(x,t) = \int_{W_\sigma(x,t)} dt' \int_{c(t')} dx' K(x,x';t,t') v(x',t') + I(x,t), \; x \in c(t), \quad (3.24)$$

where

$$K(x,x';t,t') = -\frac{\sin(\pi\theta) e^{i\pi\theta} \Pi_\sigma(t,t';x) X(x,t')}{\pi X^+(x',t')(x'-x)}, \quad (3.25)$$

$$I(x,t) = \int_{W_u(x,t)} dt' \Pi_u(t,t';x) u'(x,t'). \quad (3.26)$$

By definition of $W_\sigma(x, t)$, $x \in c'(t')$, so that the equation is in fact nonsingular. This may be more clearly seen for special cases discussed later. There are integrable singularities, due to the function $X^+(x', t')$, but these cause no problem.

The detailed form of the integral Eq. (3.24) depends on which contact region x belongs to. For the general case, if x lies in the jth interval $c_j(t)$, we have that $W_u(x, t)$ and $W_\sigma(x, t)$ are the same as in (3.12) and (3.13), where

t_1 satisfies $a_j(t_1(x)) = x$,

t_2 satisfies $b_{j-1}(t_2(x)) = x$,

t_3 satisfies $a_{j-1}(t_3(x)) = x$,

$\vdots$

t_{2k} satisfies $b_{j-k}(t_{2k}(x)) = x$,

t_{2k-1} satisfies $a_{j-k}(t_{2k-1}(x)) = x$, $1 \le k < j$

$\vdots$

t_{2j-1} satisfies $a_1(t_{2j-1}(x)) = x$,

and

$t_{2j} = -\infty$.

Downloaded 04 May 2010 to 171.66.16.28. Redistribution subject to ASME license or copyright; see http://www.asme.org/terms/Terms_Use.cfm

The function $K(x, x'; t, t')$ is formed by functions

$$K_k(x,x';t,t') = -T_k(t,t';x)Y(x,x';t')R(t';t_{k+1},t_k),$$

$$Y(x,x';t') = \frac{\sin(\pi\theta)e^{i\pi\theta}X(x,t')}{\pi X^+(x',t')(x'-x)},$$

$$t' \in (t_{k+1},t_k),\ k = 1,3,\cdots,2j-1. \quad (3.27)$$

The function I has the form, for $x \in c_j(t)$

$$I_j(x,t) = \sum_{k+1}^{j} \int_{t_{2j-2k+1}(x)}^{t_{2j-2k}(x)} dt' \times T_{2j-2k}(t,t';x) f_k(x - \bar{x}_{0k}(t')),$$

$$f_k(x-\bar{x}_{0k}(t')) = \frac{d}{dx}F_k(x-\bar{x}_{0k}(t')),$$

$$x \in c_j(t), \quad (3.28)$$

where $t_0 = t$. The integral equation for $v(x, t)$ reads

$$v(x,t) = \sum_{k=1}^{j} \int_{t_{2k}(x)}^{t_{2k-1}(x)} dt' \times \int_{c(t')} dx' K_{2k-1}(x,x';t,t')v(x',t') + I_j(x,t),$$

$$x \in c_j(t). \quad (3.29)$$

Equation (3.24) involves both space and time variables occurring in an interdependent manner, which renders it unlikely that exact solutions will be available, even for simple problems. The only methods of solution, with any wide degree of applicability, would be numerical or iterative. This is for the general transient case. However, if the assumption is made that steady-state conditions prevail, the integral equation simplifies apporecably. This case will be considered in Section 4 and subsequently.

4 The Steady-State Limit for Two Loads

We now consider the two indentor case. Let the indentors have been moving at the same speed V for a long time, so that transient effects have died away. Then we have

$$a_j(t) = a_{0j} - Vt,\ b_j(t) = b_{0j} - Vt,\ j = 1,2. \quad (4.1)$$

Introducting the variable $y = x + Vt$, all quantities such as $u'(x, t)$, $v(x, t)$, $p(x, t)$ and so on will be functions of y rather than x, t separately. The contact regions are the stationary regions

$$s = s_1 \cup s_2,\quad s_1 = [a_{01}, b_{01}],\quad s_2 = [a_{02}, b_{02}]. \quad (4.2)$$

Also, the limit of the function $X(z, t)$, given by (2.8), on the x-axis, becomes $X^+(y)$, where

$$X^+(y) = \begin{cases} m(y), & -\infty < y < a_{01}, \\ -m(y)e^{i\pi\theta}, & y \in s_1, \\ -m(y), & b_{01} < y < a_{02}, \\ m(y)e^{i\pi\theta}, & y \in s_2, \\ m(y), & ,b_{02} < y < \infty, \end{cases} \quad (4.3)$$

$$m(y) = |y-a_{01}|^{1-\theta}|y-b_{01}|^{\theta}|y-a_{02}|^{1-\theta}|y-b_{02}|^{\theta}. \quad (4.4)$$

As noted for the transient case, outside of contact intervals, namely for the first, third and last case above, $X^-(y) = X^+(y)$ and they can be taken to be one function $X(y)$.

The integral Eq. (3.24), in the steady-state limit, depends on which stationary contact interval y belongs to, namely either s_1 or s_2. First, we consider the case where y belongs to $s_1 = [a_{01}, b_{01}]$.

Using stationary variables

$$u = x + Vt'',\quad z = x + Vt',\quad y = x + Vt, \quad (4.5)$$

we obtain from Eqs. (3.24) and (4.3) the following integral equation for $v(y)$ by changing the order of integration:

$$v(y) = \int_s dy' K_1(y,y')v(y') + I_1(y),\quad y \in s_1, \quad (4.6)$$

where $K_1(y, y')$ is given by

$$K_1(y,y') = \begin{cases} K_{11}(y,y') = K_{10}(y,y'), & y' \in s_1, \\ K_{12}(y,y') = -K_{10}(y,y'), & y' \in s_2, \end{cases} \quad (4.7)$$

$$K_{10}(y,y') = \frac{\sin(\pi\theta)}{\pi}\int_{-\infty}^{\alpha_{01}} \frac{dz}{V}\frac{T_{11}(y,z)m(z)}{m(y')(y'-z)}. \quad (4.8)$$

Also,

$$T_{10}(y,z) = l\left(\frac{y-z}{V}\right),$$

$$T_{11}(y,z) = \int_z^{a_{01}} \frac{du}{V} l\left(\frac{y-u}{V}\right)k\left(\frac{u-z}{V}\right), \quad (4.9)$$

and $I_1(y)$ has the form

$$I_1(y) = \int_{a_{01}}^{y} \frac{dz}{V} T_{10}(y,z)f_1(z),\ y \in s_1 \quad (4.10)$$

where $f_1(z)$ is the displacement derivative $f_1(x - x_{01}(t'))$. It is zero at $\bar{x}_{01}$, the deepest point of the first punch at $t = 0$.

Secondly, we consider the case where y lies on $s_2 = [a_{02}, b_{02}]$. In terms of stationary variables, the equation for $v(y)$ now takes the form

$$v(y) = \int_{s(y')} dy' K_2(y,y')v(y') + I_2(y),\ y \in s_2, \quad (4.11)$$

where $K_2(y, y')$ is given by

$$K_2(y,y') = \begin{cases} K_{21}(y,y') = K_{20}(y,y'),\ y' \in s_1, \\ K_{22}(y,y') = -K_{20}(y,y'),\ y' \in s_2, \end{cases} \quad (4.12)$$

$$K_{20}(y,y') = \frac{\sin(\pi\theta)}{\pi}\left[\int_{-\infty}^{a_{01}} \frac{dz}{V}\frac{T_{23}(y,z)m(z)}{m(y')(y'-z)} - \int_{b_{01}}^{a_{02}} \frac{dz}{V}\frac{T_{21}(y,z)m(z)}{m(y')(y'-z)}\right], \quad (4.13)$$

where

$$T_{20}(y,z) = l\left(\frac{y-z}{V}\right),$$

$$T_{21}(y,z) = \int_z^{a_{02}} \frac{du}{V} l\left(\frac{y-u}{V}\right)k\left(\frac{u-z}{V}\right),$$

$$T_{22}(y,z) = \int_z^{b_{01}} \frac{du}{V} T_{21}(y,u)l\left(\frac{y-z}{V}\right),$$

$$T_{23}(y,z) = \int_z^{a_{01}} \frac{du}{V} T_{22}(y,u)k\left(\frac{y-z}{V}\right). \quad (4.14)$$

Also we have

$$I_2(y) = \int_{a_{01}}^{b_{01}} \frac{dz}{V} T_{22}(y,z)f_1(z) + \int_{a_{02}}^{y} \frac{dz}{V} T_{20}(y,z)f_2(z),\ y \in s_2, \quad (4.15)$$

Downloaded 04 May 2010 to 171.66.16.28. Redistribution subject to ASME license or copyright; see http://www.asme.org/terms/Terms_Use.cfm

where $f_2(z)$ is $f_2(x - x_{02}(t'))$ expressed in stationary coordinate system. It is zero at $\bar{x}_{02}$, the deepest point of the second punch at $t = 0$.

The solvability conditions become

$$\sum_{j=1}^{2} \int_{s_j} dy \frac{\upsilon(y)}{m_j(y)} = 0, \sum_{j=1}^{2} \int_{s_j} dy \frac{y\upsilon(y)}{m_j(y)} = 0, \quad (4.16)$$

where

$$m_j(y) = (-1)^j m(y), \quad y \in s_j, j = 1,2.$$

The pressure in the stationary contact region is

$$p(y) = q\left[\frac{\sin(\pi\theta)X^+(y)}{\pi} \int_s dy' \frac{\upsilon(y')}{(y' - y)X^+(y')} + \cos(\pi\theta)\upsilon(y)\right], \quad (4.17)$$

where q is given by (2.14). The two subsidiary conditions for loading are given by

$$W_j = \int_{s_j} dyp(y) = \int_S dy' J_j(y')\upsilon(y') + q\cos(\pi\theta)\int_{a_{0j}}^{b_{0j}} dy\upsilon(y), j = 1,2, \quad (4.18)$$

where

$$J_j(y') = \frac{q\sin(\pi\theta)}{\pi X^+(y')} \int_{a_{0j}}^{b_{0j}} dy \frac{X^+(y)}{(y' - y)}.$$

5 Dimensionless System

It is convenient to consider the moving indentor problem in a dimensionless system. Take the deepest points of indentation of the two punches to be $\bar{x}_{01}$ and $\bar{x}_{02}$, respectively. We put it this way:

$$\bar{x}_{02} - \bar{x}_{01} = 2C, \quad (5.1)$$

$$\bar{x}_{01} + \bar{x}_{02} = x_p, \quad (5.2)$$

so that the two punches are a distance $2C$ apart and x_p indicates the overall position of the system. The quantity x_p can be chosen arbitrarily. We take it to be zero.

Let us choose length units and origin so that

$$\bar{x}_{01} \Rightarrow -1.0, \bar{x}_{02} \Rightarrow 1.0,$$

and time unit such that the new speed of the punches will be 1. We get that any quantity of dimension length, which has value of coordinate $x = L$ in the initial system, becomes l, where

$$l = \frac{L}{C}, \quad (5.3)$$

and any time t in the initial system becomes $\bar{t}$, where

$$\bar{t} = \frac{t}{\lambda}, \lambda = \frac{C}{V}, \quad (5.4)$$

in the dimensionless system.

In the new system, the stationary contact region will be

$$S = S_1 \cup S_2, S_1 = [A_1, B_1], S_2 = [A_2, B_2], \quad (5.5)$$

$$A_i = \frac{a_{0i} + Vt}{C}, B_i = \frac{b_{0i} + Vt}{C}, i = 1,2.$$

and one can set

$$D_1 = \frac{b_{01} - a_{01}}{C} = B_1 - A_1, D_2 = \frac{b_{02} - a_{02}}{C} = B_2 - A_2, \quad (5.6)$$

where D_1 and D_2 are the contact interval lengths in the dimensionless system.

It should be noted that the lengths of contact intervals $(b_{01} - a_{01})$ or $(b_{02} - a_{02})$ are small compared with the radii R_j of the punches. Thus, D_1, D_2 must be small quantities compared with R_j/C.

The integral equation for $\upsilon(y)$ in dimensionless coordinates is

$$\upsilon(y) = \int_S dy' K(y, y')\upsilon(y') + I(y) \quad y', y \in S = S_1 \cup S_2, \quad (5.7)$$

where $K(y, y')$ is defined in the dimensionless region S and takes values K_{ij}, $i, j = 1, 2$, which are given by in (4.7) and (4.12), respectively, in dimensionless coordinates. The quantity $m(y)$ now has the form

$$m(y) = |y - A_1|^{1-\theta}|y - B_1|^{\theta}|y - A_2|^{1-\theta}|y - B_2|^{\theta}. \quad (5.8)$$

For the standard linear solid (3.3), the inverse decay times in dimensionless coordinates are

$$\alpha = \frac{\lambda}{\tau}, \beta = \frac{\lambda}{\tau'}, \lambda = \frac{C}{V}. \quad (5.9)$$

The quantities T_{ij} in the dimensionless system are obtained from (4.9) and (4.14) as follows:

For $y \in S_1$,

$$T_{10}(y, z) = l_0\delta(y - z) + l_1 e^{-\alpha(y-z)}, \quad z \in S_1, \quad (5.10)$$

$$T_{11}(y, z) = k_0 l_1 e^{-\alpha(y-A_1)} e^{\beta(z-A_1)}, z < A_1. \quad (5.11)$$

For $y \in S_2$,

$$T_{20}(y, z) = l_0\delta(y - z) + l_1 e^{-\alpha(y-z)}, z \in S_2, \quad (5.12)$$

$$T_{21}(y, z) = k_0 l_1 e^{-\alpha(y-A_2)} e^{\beta(z-A_2)}, B_1 < z < A_2, \quad (5.13)$$

$$T_{22}(y, z) = l_1 e^{(\alpha-\beta)(A_2-B_1)} e^{-\alpha(y-z)}, z \in S_1, \quad (5.14)$$

$$T_{23}(y, z) = k_0 l_1 e^{-\alpha(y-A_2)} e^{\beta(z-A_1)} e^{-\alpha D_1} e^{-\beta(A_2-B_1)}, z < A_1, \quad (5.15)$$

where l_0, l_1, k_0 are given by (3.6)–(3.8).

Using these relations, the equations for $K_{ij}(y, y')$ given by (4.7) and (4.12) in dimensionless coordinates can be simplified to

$$K_{11}(y, y') = C_{11} e^{-\alpha(y-A_1)} \frac{J_{11}(y')}{m(y')}, \quad y \in S_1, y' \in S_1, \quad (5.16)$$

$$K_{12}(y, y') = C_{12} e^{-\alpha(y-A_1)} \frac{J_{12}(y')}{m(y')}, \quad y \in S_1, y' \in S_2, \quad (5.17)$$

$$K_{21}(y, y') = C_{21} e^{-\alpha(y-A_2)} \frac{C_0 J_{11}(y') - J_{21}(y')}{m(y')}, \quad y \in S_2, y' \in S_1, \quad (5.18)$$

$$K_{22}(y, y') = C_{22} e^{-\alpha(y-A_2)} \frac{C_0 J_{12}(y') - J_{22}(y')}{m(y')}, \quad y \in S_2, y' \in S_2, \quad (5.19)$$

Downloaded 04 May 2010 to 171.66.16.28. Redistribution subject to ASME license or copyright; see http://www.asme.org/terms/Terms_Use.cfm

where

$$C_{11} = C_{21} = \frac{\sin(\pi\theta)}{\pi} k_0 l_1,$$

$$C_{12} = C_{22} = -C_{11}, C_0 = e^{-\alpha D_1 - \beta(A_2 - B_1)}, \quad (5.20)$$

$$J_{11}(y') = \int_{-\infty}^{A_1} dz \frac{e^{\beta(z-A_1)} m(z)}{y' - z}, \; y' \in S_1, \quad (5.21)$$

$$J_{12}(y') = J_{11}(y'), \; y' \in S_2, \quad (5.22)$$

$$J_{21}(y') = \int_{B_1}^{A_2} dz \frac{e^{\beta(z-A_2)} m(z)}{y' - z}, \; y' \in S_1, \quad (5.23)$$

$$J_{22}(y') = J_{21}(y'), \; y' \in S_2. \quad (5.24)$$

Using (5.10)–(5.15), Eqs. (4.10) and (4.15) give that $I(y)$ has the form

$$I_1(y) = l_1 \int_{A_1}^{y} dz e^{\alpha(z-y)} f_1(z) + l_0 f_1(y), \; y \in S_1, \quad (5.25)$$

$$I_2(y) = l_1 \int_{A_2}^{y} dz e^{\alpha(z-y)} f_2(z) + I_{12}(y) + l_0 f_2(y), \; y \in S_2, \quad (5.26)$$

$$I_{12}(y) = l_1 e^{(\alpha-\beta)(A_2 - B_1)} \int_{A_1}^{B_1} dz e^{\alpha(z-y)} f_1(z). \quad (5.27)$$

We consider a simple example case where the slopes of the indentor profiles are given as

$$f_1(t) = -\frac{C}{R}(t+1), \; t \in S_1, \; f_2(t) = -\frac{C}{R}(t-1), \; t \in S_2, \quad (5.28)$$

which is an approximate model of cylinders where the lengths of dimensionless contact intervals D_1 and D_2 are small compared with the dimensionless radius R/C of the cylinders. Alternately, they can be regarded as two parabolas.

For this case, the elastic solutions are given as follows (Gladwell, 1980); for the single parabolic indentor

$$f(t) = -\frac{C}{R} t,$$

the contact pressure distribution $p(t)$ has the form

$$\frac{p(t)}{GR} = \frac{C}{R^2(1-\mu)} \sqrt{a_0^2 - t^2},$$

where the semicontact length a_0 is related to the total load W by

$$\frac{W}{GR} = \frac{\pi a_0^2}{2(1-\mu)} \left(\frac{C}{R}\right)^2. \quad (5.29)$$

The elastic solutions are important as baseline data for the viscoelastic solutions.

In the dimensionless system, the solvability conditions take the same form as (4.16) but evaluated in dimensionless region S. The pressure in the contact region is given by (4.17) but now evaluated over the dimensionless region S also. The loading conditions are given as follows:

$$L_j = \int_{S_j} dy' p(y') = \frac{W_j}{C}, \; j = 1, 2, \quad (5.30)$$

which replace the conditions (4.18).

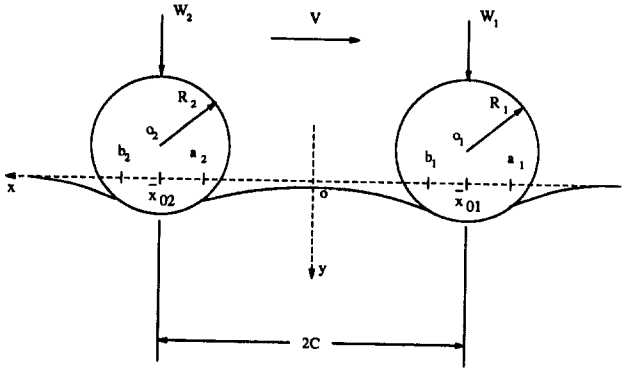

Fig. 1 Two indentors moving along the negative direction of x-axis. Contact regions are $[a_1, b_1]$ and $[a_2, b_2]$. The distance between the deepest points, x_{01} and x_{02}, of indentation of the two indentors is 2C.

6 The Numerical Results

In the preceding sections, the solution for the several indentor case is given formally. Detailed numerical work for two indentors on a standard linear solid, in the steady-state limit, has been undertaken for three values of the viscoelastic parameter

$$C_v = G_1/G_0. \quad (6.1)$$

Only the frictionless problem was considered.

For the two-load case, whose cross-section is shown in Fig. 1, the integral Eq. (5.7) for $v(y)$, could not be simplified in terms of the modified Bessel functions with imaginary argument as in the single load case (Golden and Graham, 1988; Hunter, 1961). The kernels $K_{ij}(y, y')$ given by Eqs. (5.16–5.19) must be evaluated numerically. There are integrable singularities in the kernels $K_{ij}(y, y')$ and in the integrals of both solvability conditions (4.16) and load conditions (4.18) as well. The appropriate quadrature formula, either the midpoint rule or the left-end-point rule or the right-end-point rule, was chosen depending on where the singularities were. The goal of such a choice was to ensure that integrable singularities occurring at such points were avoided. For example, we used the right-end point rule or midpoint rule to evaluate J_{11}, J_{12} or J_{21} and the left-end point rule or mid-point rule for J_{22}, which occur in the expression for $K_{ij}(y, y')$.

A complication, arising in the moving indentation problem, is that the extent of the contact regions is unknown a priori. Integral Eq. (5.7) and the subsidiary conditions (4.16) and (4.18), determine implicitly the function $v(y)$ and the end points A_j and B_j of the contact regions. This system must be solved iteratively by numerical methods.

The iteration scheme proposed here may be described as follows. Make some initial guess at the values of A_j and B_j, $j = 1, 2$. The quantities K_{ij} and I_j are then determined by equations (5.16–5.19) and (5.25, 5.26). The results are substituted in (5.7), to obtain $v(y)$. We refer to these as $\{A_j^{(0)}, B_j^{(0)}, v^{(0)}(y)\}$. Applying the two-load conditions, (5.30), we adjust the lengths of each interval D_i, respectively. The shifts of the front end points, δA_j, are determined by using solvability conditions (4.16), and the new lengths, D_j. From the values of δA_j and D_j, we get a new set values of A_j and B_j, which we take as the next approximation. The iteration procedure may be repeated to the desired level of accuracy. We need to make a good guess at the initial values of A_j and B_j, so that the iteration converges sufficiently rapidly. In particular, a natural starting point is to use the contact region for the single-indentor problem in the viscoelastic case.

In the two indentor case, the contact geometry is described by two sets of data $\{A, B, R, W\}$ for each indentor and the

Downloaded 04 May 2010 to 171.66.16.28. Redistribution subject to ASME license or copyright; see http://www.asme.org/terms/Terms_Use.cfm

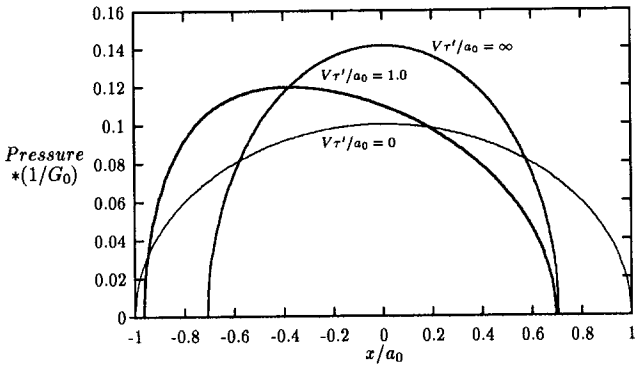

Fig. 2 One indentor: pressure distribution over the contact region, $C_v = 1$

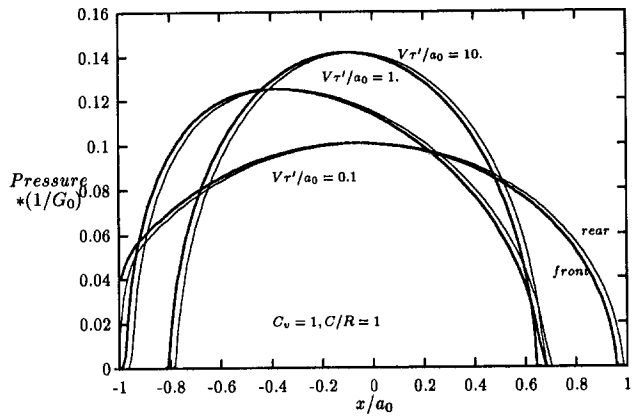

Fig. 3 The two-indentor case: pressure distributions over the contact regions. For comparison, the two contact regions are plotted together with the deepest points, $\bar{x}_{01}$ and $\bar{x}_{02}$, coinciding at $x = 0$. In this figure $C/R = 1$, $C_v = 1$.

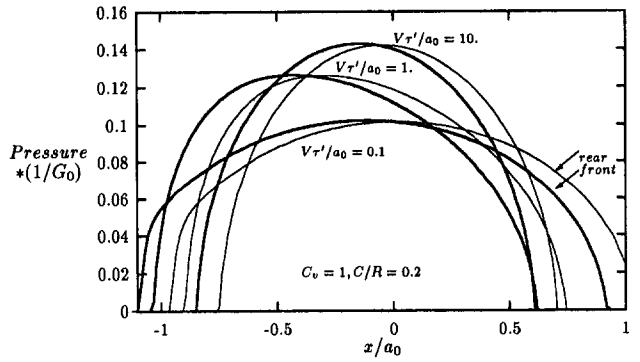

Fig. 4 The two-indentor case: pressure distributions, $C/R = 0.2$, $C_v = 1$

distance $2C$ between the two indentor axes, (Fig. 1). In the numerical results presented here the ratios of static semicontact width to radius (a_0/R) of both indentors are fixed as 0.05. Then each supporting load W_i depends on radius in the manner indicated by (5.29).

Taking both radii to be equal, $R_1 = R_2$, we show the pressure distributions under both indentors in Figs. 3, 4 for the case of $C_v = 1$. For comparison, the two contact regions are plotted together with the deepest points $\bar{x}_{01}$ and $\bar{x}_{02}$ coinciding at $x = 0$ in the figures.

In each figure, three pairs of the pressure distributions are represented for $V\tau'/a_0 = 0.1$, 1, and 10. When compared with Fig. 2, the pressure of the one-load case, the numerical results in Figs. 3 and 4 show that the solution obtained degenerates into the appropriate elastic solution, the Hertzian pressure distribution in two ways as follows. First, for sufficiently large velocities, the pressure distributions are symmetric about $x = \bar{x}_{0j}$, the deepest points of the indentors. This is a reflection of the fact that the viscoelastic medium behaves in this limit as an elastic solid with shear modulus

$$G_d = G_0 + G_1, \tag{6.2}$$

which is the dynamic shear modulus. In this case, the contact interval length reduces to about $100/\sqrt{G_d/G_0}$ percent of $2a_0$. The maximum pressure increases to about $100\sqrt{G_d/G_0}$ percent of the maximum static pressure P_0 which is related to the mean elastic pressure P_m (Johnson, 1985) by

$$P_0 = \frac{2W}{\pi a_0} = \frac{4}{\pi} P_m, P_m = \frac{W}{2a_0},$$

$$P_0 = \sqrt{\frac{WG_0}{\pi R(1-\mu)}}.$$

Secondly, for sufficiently small velocities, the results again reduce to the elastic case but with G_d replaced by the "static" modulus G_0, which is the shear modulus at the large time limit. We refer to G_0 as the elastic shear modulus. A similar argument applies in the one-load case (Hunter, 1961).

Also, the results in Figs. 3 and 4 illustrate a phenomenon that the pressure distributions under the front indentor are always to the left of those under the rear indentor. In other words, the contact area of the front one is shifted a little more than that of the rear one, along the direction of motion. As C/R reduces, which means that the two indentors are close to each other, there is a more pronounced difference between the shapes of the pressure distribution under each indentor.

We now give the results for the coefficient of hysteretic friction (Golden, 1977, 1986; Golden and Graham, 1988, Greenwood, 1961; Morland, 1962). Adapted to the dimensionless system for two cylindrical indentors, the coefficient of hysteretic friction in the stationary coordinate system has a general form:

$$f_H = \frac{C}{W} \int_S dx p(x) f(x) \tag{6.3}$$

where $p(x)$ is the pressure distribution in the contact regions while the function $f(x)$ is the derivative of the indentor profiles given by (5.28), and S represents the stationary contact regions given by Eq. (5.5). Also

$$W = W_1 + W_2 \tag{6.4}$$

is the total load.

For each indentor, the tangential force coefficient has the form

$$f_{H_j} = \frac{C}{W_j} \int_{S_j} dx p(x) f_j(x). \tag{6.5}$$

The general form (6.3) shows that f_H is an average obtained by summing the individual f_{H_i}, weighted with respect to loads:

$$f_H = \sum_{j=1}^{2} \frac{W_j}{W} f_{H_j}. \tag{6.6}$$

Each of the moving indentors considered here has an axis of symmetry, and the distance, $2C$, between these two indentors does not change. Equation (6.3) shows that the fundamental reason for hysteretic friction on a well-lubricated surface is caused by deformation and recovery under the indentor or indentors. The deformation and recovery are not symmetrical with respect to each axis of symmetry in the viscoelastic case.

Downloaded 04 May 2010 to 171.66.16.28. Redistribution subject to ASME license or copyright; see http://www.asme.org/terms/Terms_Use.cfm

Table 1 Comparison of the elastic tangential force under each indentor with the hysteretic friction force for different distances between the two indentors. The quantity f_{e1} is the coefficient of the elastic tangential force under the front indentor. The quantity f_H is the maximum coefficient of hysteretic friction for the two-indentor system. Also $C_v = G_1/G_0$, $a_0/R = 0.05$.

	$C/R = 5.0$	$C/R = 1.0$	$C/R = 0.2$	$C/R = 0.1$
f_{e1}, $C_v = 0$	0.00252	0.0129	0.0660	0.148
f_H, $C_v = 0.2$	0.0574	0.0579	0.0579	0.0567
f_H, $C_v = 1$	0.198	0.206	0.201	0.196
f_H, $C_v = 9$	0.481	0.498	0.482	0.470

Table 2 The relative percentage difference, δ, of f_{H_j} for two indentors when they take their maximum values, where $\delta = 100|f_{H1} - f_{H2}|/f_H$.

	$C/R = 5.0$	$C/R = 1.0$	$C/R = 0.2$
$C_v = 0.2$	10.7	44.6	230.
$C_v = 1$	3.47	13.2	67.4
$C_v = 9$	3.61	6.14	28.0

In fact the asymmetry occurs in the elastic case too, since the deformation on the surface between two indentors is much larger than that on the outer parts of the surface. In general, a nonzero tangential force acts on each indentor. However, on the whole system, the total tangential force must be zero as the total loss of energy is zero.

In the elastic case, when the indentors are in motion, the force under the front one resists the motion, and the rear contact exerts a force of the same magnitude but in the opposite direction. We may refer to the force under the front indentor as F_{e1}, the force under the rear indentor as F_{e2}, and

$$F_{e1} = f_{e1}W_1, \quad F_{e2} = f_{e2}W_2, \tag{6.7}$$

where f_{ej}, $j = 1, 2$ are the coefficients of the elastic tangential forces under each indentor. The forces obey $F_{e1} + F_{e2} = 0$. The magnitude of f_{ej} can be computed by a formula similar to Eq. (6.5). The solution for the elastic case can be obtained by setting $C_v = 0$ or by solving multiindentor equations (Gladwell, 1980) in elasticity.

Using formula (6.5) for the tangential force coefficient of an individual indentor, we see that it is affected by both the viscous and elastic asymmetry forces.

Table 1 gives the values of f_{e1} and maximum f_H for a range of spacings and C_v values. In each case, the two indentors have the same size and loading. The results show that the closer the indentors, the larger f_{e1} becomes. The quantity f_H is not proportional to the coefficient C_v and f_H does not change significantly when the distance apart C/R changes, while f_{ej} does. The data on Table 1 allows interesting comparisons between the magnitude of f_H and f_{e1} for various values of C_v and C/R.

The differences between the tangential force coefficients as a percentage of f_H are presented on Table 2 for the same values of C_v and C/R. The results show that the difference between the tangential forces decrease as the difference between the indentors increase and as viscous losses increase. For $C/R > 5$, the maximum resisting force on each indentor differs by only about four percent for both medium and large viscous losses.

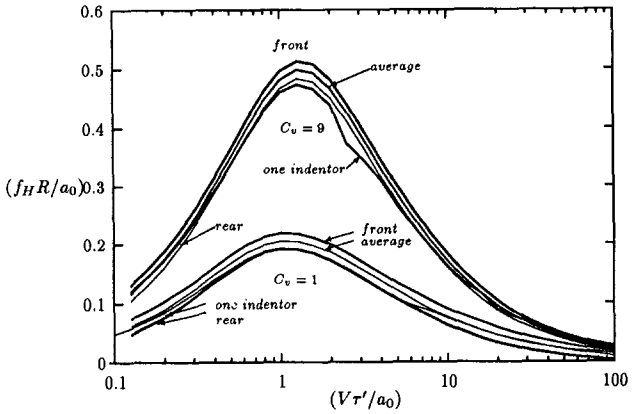

Fig. 5 The two-indentor case: variation of the coefficient of hysteretic friction with velocity, $C/R = 1$, $C_v = 1$ and 9

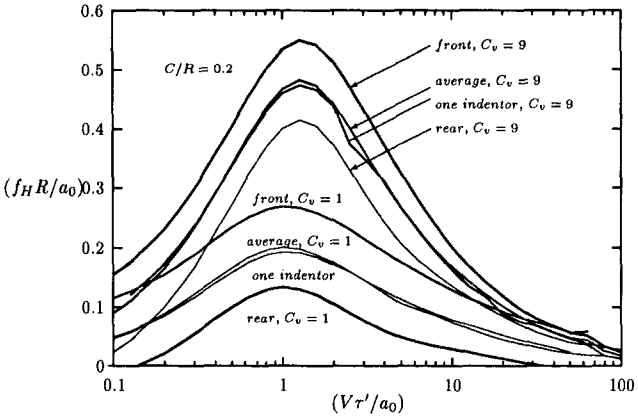

Fig. 6 The two-indentor case: variation of the coefficient of hysteretic friction with velocity, $C/R = 0.2$, $C_v = 1$ and 9

It may be expected that if $C \gg V\tau'$ the two indentors will be independent as far as viscoelastic effects are concerned. Dividing this inequality by R, we obtain

$$C/R \gg \frac{V\tau'}{a_0}\frac{a_0}{R}. \tag{6.8}$$

If $C/R > 5$ for example, this is certainly true for speeds at which maximum friction prevails; i.e., when $V\tau'/a_0 \approx 1$, since a_0/R is in general much less than unity.

Figures 5 and 6 give the coefficient of hysteretic friction as a function of $(V\tau'/a_0)$ for $C/R = 1$ and 0.2, respectively. Each one presents f_{H_j}, the average value f_H, and the result for a single indentor. These are for two materials $C_v = 1$ and $C_v = 9$. Figures 7 and 8 present similar data for $C_v = 0.2$ and 1. Figure 9 compares the hysteretic friction force with the elastic tangential force under the front indentor. The tangential force, f_{e2}, under the rear indentor is constant and always negative in the elastic limit. For material $C_v = 0.2$, it varies with velocity but takes only negative valeus when $C/R = 0.2$ (see Fig. 8). When $C/R = 1$, $C_v = 0.2$ (Fig. 7) or $C/R = 0.2$, $C_v = 1$ (Fig. 9), it takes a negative value only when the velocity is small or large.

These results for the coefficient of hysteretic friction also indicate that the hysteretic friction for the two-indentor case as a function of speed has, roughly speaking, the hump shape observed experimentally. It reaches its maximum value when the velocity is of order a_0/τ'. For the cases considered, in each of which the sizes of the two indentors are the same, the function is virtually independent of separation and very close to the f_H curve of the one-indentor case. Also, it approaches zero for sufficiently small and large values of velocity. The

Downloaded 04 May 2010 to 171.66.16.28. Redistribution subject to ASME license or copyright; see http://www.asme.org/terms/Terms_Use.cfm

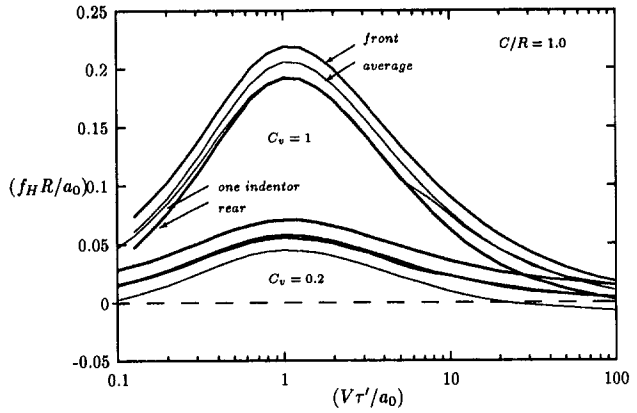

Fig. 7 The two-indentor case: variation of the coefficient of hysteretic friction with velocity, $C/R = 1$, $C_v = 0.2$ and 1

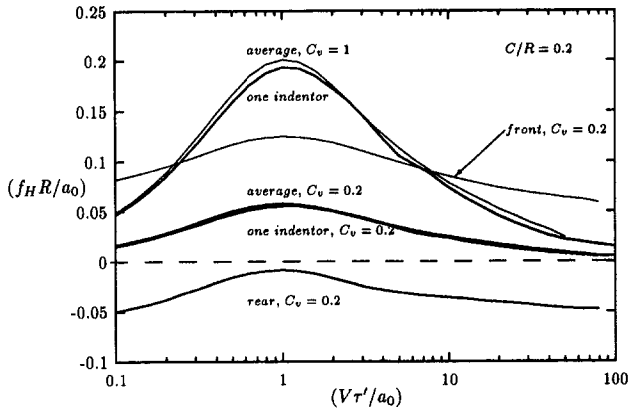

Fig. 8 The two-indentor case: variation of the coefficient of hysteretic friction with velocity, $C/R = 0.2$, $C_v = 0.2$ and 1

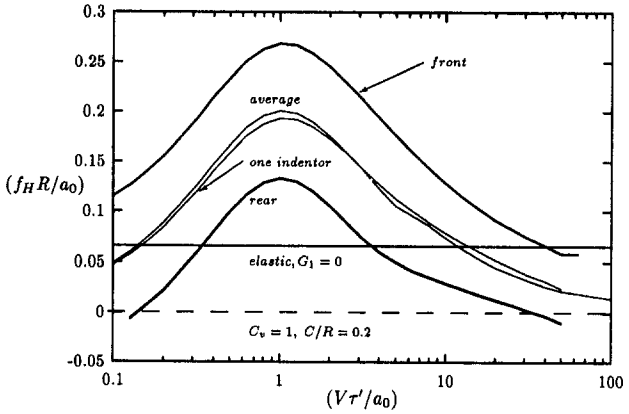

Fig. 9 The two-indentor case: hysteretic friction force compared with the elastic tangential force under front indentor, $C/R = 0.2$, $C_v = 1$

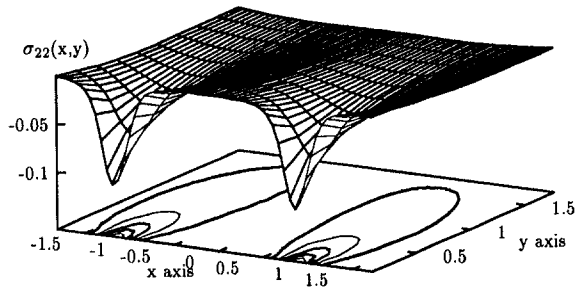

Fig. 10 The stress σ_{22} distribution in the material, $y > 0$. When $y = 0$, this distribution illustrates the pressure on the contact regions. $C_v = 9$, $C/R = 0.2$.

latter observation corresponds to the fact that the pressure distribution tends to be symmetric for $V \to 0$ or $V \to \infty$, which are the two elastic limits mentioned above.

Intuitively, we can see that on a slightly viscoelastic material with moving indentors, the resistance to the motion of the front indentor will increase compared with an elastic material, and the forward force on the rear indentor will diminish. The latter passes through zero for a certain level of viscoelastic loss which will depend on speed and the separation of the indentors. As viscous effects increase further, both indentors experience resisting forces, although that on the rear indentor is less than that on the front indentor. For any level of viscoelasticity, the sum of the forces is nonzero and in a direction opposing the motion.

This intuitive prediction is supported by the numerical results shown in Figs. 5–9 and Tables 1 and 2.

Figure 10 shows the results of the stress σ_{22} distribution in the material, $y > 0$. This is an example which shows that quantities of interest can easily be obtained after the quantity $v(x)$ and the contact intervals are known. When $y = 0$, Fig. 10 illustrates the pressure distribution along the boundary.

7 Conclusions

A general method is given for solving the two-dimensional, noninertial problem of several rigid loaded indentors moving across a viscoelastic half-plane, where steady-state conditions prevail. Using a decomposition of hereditary integrals, the problem is reduced to solving a set of nonsingular (apart from integrable singularities) coupled integral equations subject to certain constraints. These equations are considered in detail for the case of two indentors. A reduction to algebraic form is achieved and the resultant equations are solved numerically.

In the elastic case, the front indentor experiences a resisting force and the rear indentor an equal and opposite force in the direction of motion. These are due to the asymmetry in the contact regions and are more pronounced, the closer the indentors are together.

On a slightly viscoelastic material, i.e., one in which the internal rate of energy loss is small, the resistance to the motion of the front indentor increases and the forward force on the rear indentor diminishes. The latter passes through zero for a certain level of viscoelastic loss which depends on the speed and the separation of the indentors. As viscous effects increase further, both indentors experience resisting forces although that on the rear indentor is less than that on the front indentor. For any finite level of viscoelasticity, the sum of the forces is nonzero and in a direction opposing the motion. This effect shows up when comparing the pressure distributions and contact regions under both indentors. The pressure distribution and contact region under the rear indentor is always shifted with respect to those underneath the front indentor in a direction opposite to the motion.

For identical indentors, the analysis indicates that the overall hysteretic friction coefficient is virtually independent of the separation of the indentors and is close to that for a single indentor of the same size. Also, the difference between the tangential forces on each indentor decreases as the distance between the indentors increases and as viscous effects increase. When the separation of two identical indentors is greater than ten times their radii, the maximum resisting forces on each indentor (which occur at very similar speeds) differs by only about four percent of their average value for both medium and large viscous losses.

Downloaded 04 May 2010 to 171.66.16.28. Redistribution subject to ASME license or copyright; see http://www.asme.org/terms/Terms_Use.cfm

Acknowledgment

This work was supported by funds provided by the Natural Sciences and Engineering Research Council of Canada.

References

Gladwell, G. M. L., 1980, *Contact Problems in the Classical Theory of Elasticity*, Sijthoff and Nordhoff, The Netherlands.

Golden, J. M., 1986, "Frictional Viscoelastic Contact Problem," *Quarterly Journal of Mechanics and Applied Mathematics*, Vol. 39, No. 1, pp. 125–137.

Golden, J. M., 1977, "Hysteretic Friction of a Plane Punch on a Half-plane with Arbitrary Viscoelastic Behaviour," *Quarterly Journal of Mechanics and Applied Mathematics*, Vol. 30, No. 1, pp. 23–49.

Golden, J. M., and Graham, G. A. C., 1988, *Boundary Value Problems in Linear Viscoelasticity*, Spring-Verlag, Berlin.

Greenwood, J. A., and Tabor, D., 1961, "Hysteresis Losses in Rolling and Sliding Friction," *Proceedings of the Royal Society*, London, Vol. A259, pp. 180–507.

Hunter, S. C., 1961, "The Rolling Contact of a Rigid Cylinder with a Viscoelastic Half-Space," ASME JOURNAL OF APPLIED MECHANICS, Vol. 28, pp. 611–617.

Johnson, K. L., 1985, *Contact Mechanics*, Cambridge University Press, Cambridge, U.K.

Morland, L. W., 1962, "A Plane Problem of Rolling Contact in Linear Viscoelasticity Theory," ASME JOURNAL OF APPLIED MECHANICS, Vol. 29, pp. 345–352.

Muskhelishvili, N. I., 1963, *Some Basic Problems of the Mathematical Theory of Elasticity* (translated from the Russian by J. R. M. Radok), P. Noordhoff, Groninen, The Netherlands.

Sokolnikoff, I. S., 1956, *Mathematical Theory of Elasticity*, McGraw-Hill, New York.

Tabor, D., 1952, "Mechanism of Rolling Friction," *Journal of Theoretical, Experimental and Applied Physics*, Vol. 43, No. 7, pp. 1055–1059.

Downloaded 04 May 2010 to 171.66.16.28. Redistribution subject to ASME license or copyright; see http://www.asme.org/terms/Terms_Use.cfm

S. K. Patra[1]
Department of Mechanical Engineering,
University of Colorado,
Boulder, CO 80309

S. S. Sritharan
Department of Mathematics,
University of California,
Los Angeles, CA 90024-1555

Y. C. Lee
Department of Mechanical Engineering,
University of Colorado,
Boulder, CO 80309
Assoc. Mem. ASME.

Quantitative Characterization of a Flip-Chip Solder Joint

Based on an energy minimization principle, a mathematical/numerical model has been developed to study the impact of design and process variations associated with flip-chip solder joint on its ability to align in lateral and axial direction. The minimum-energy shape needed for joint evaluation is computed by a novel numerical method based on motion by mean curvature. The analysis shows that (1) the magnitude of the reaction force in lateral and axial direction reduces with increase in solder volume, (2) the normal reaction is an order of magnitude higher compared to the lateral reaction (restoring force) thus making the joint more susceptible to lateral misalignment compared to the axial misalignment, and (3) the axial misalignment is primarily dictated by the accuracy of the solder deposition height.

1 Introduction

Due to its self-aligning capability, the flip-chip solder joint is finding increasing application in optoelectronic packaging where the alignment between the mating components is a critical assembly issue. It provides a cost-effective precision alignment between the mating components such as (i) modulators and detectors in an optoelectronic chip, (ii) optical elements to an optoelectronic chip, and (iii) optical elements among each other. In addition, it also provides electrical connection, structural support, and a path for heat transfer. This approach is being widely developed in R & D laboratories (Tsunetsugu et al., 1992). Figure 1 shows a GTE low-cost laser array package where the alignments in lateral and axial direction between the laser array and the fibers are achieved automatically by flip-chip soldering (Armiento et al., 1991).

The principle of self-aligning motion of a flip-chip solder joint is explained by Fig. 2. Figure 2(*a*) shows a component tacked to the substrate with solder bump at the corresponding solder wetting pads or bump sites. During reflow, the molten solder spreads over the pads and creates momentarily a shape with higher energy (see Fig. 2(*b*)), which causes the component to move relative to the substrate till the solder joint attains the minimum total energy (see Fig. 2(*c*)). In reality, the aligning motion is affected by several design and processing factors associated with solder joint formation. Therefore quantitative characterization of a flip-chip solder joint is necessary for evaluating the impact of such parameters. The present paper proposes a mathematical model to analyze the impact of design and process variations on the self-aligning behavior of a flip-chip solder joint.

Most of the published works on the minimum-energy joint shape are limited to the axisymmetric case with circular pads (solid/liquid interface). Gillette et al. (1971) developed the stability criteria for the joint on the basis of the geometry of the liquid surface. Patra et al. (1991) and Goldmann (1972) developed models for asymmetric solder joints. Both studies were limited to a circular pad. A general purpose model for minimal surface area has been developed by Brakke (1992). This model, however, does not consider the impact of the vertical loading. A general reference for the mathematical aspects of this problem is Finn (1986).

The numerical method to calculate a joint shape under quasi-static condition is presented in Section 2. Numerical results characterizing a solder joint are presented in Section 3.

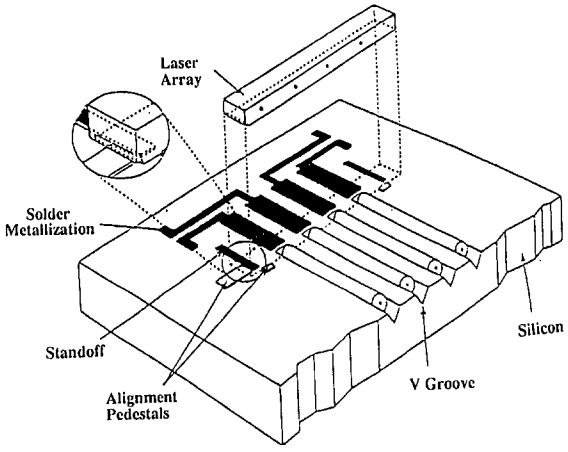

Fig. 1 GTE low-cost laser array package

[1]Current address: Department of Electrical and Computer Engineering, University of California, La Jolla, CA 92093.

Contributed by the Applied Mechanics Division of THE AMERICAN SOCIETY OF MECHANICAL ENGINEERS for publication in the ASME JOURNAL OF APPLIED MECHANICS.

Discussion on this paper should be addressed to the Technical Editor, Professor Lewis T. Wheeler, Department of Mechanical Engineering, University of Houston, Houston, TX 77204-4792, and will be accepted until four months after final publication of the paper itself in the ASME JOURNAL OF APPLIED MECHANICS.

Manuscript received by the ASME Applied Mechanics Division, June 15, 1993; final revision, Nov. 17, 1993. Associate Technical Editor: J. W. Rudnicki.

Copyright © 1995 by ASME

Downloaded 04 May 2010 to 171.66.16.28. Redistribution subject to ASME license or copyright; see http://www.asme.org/terms/Terms_Use.cfm

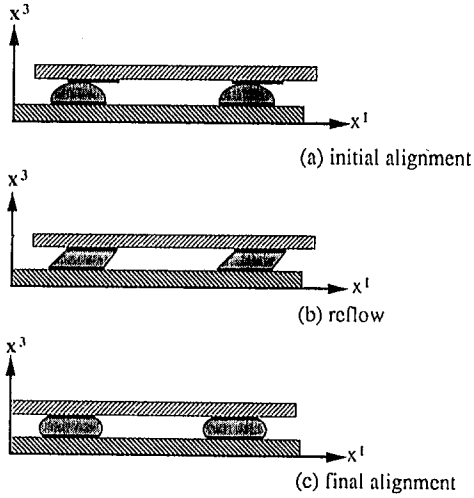

Fig. 2 The self-alignment mechanism of a solder joint

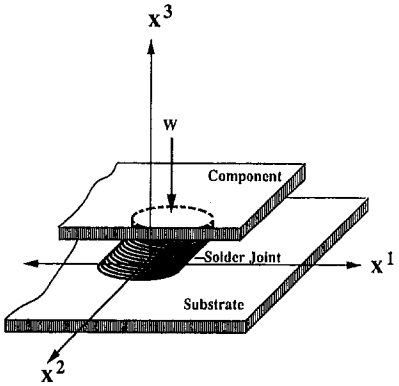

Fig. 3 System configuration of a flip-chip joint

2 Numerical Model

The system to be modeled consists of a component and a substrate, and a liquid column of solder supporting the component (see Fig. 3). The solder pad geometry is predefined. The substrate is assumed to be fixed, while the component is free to move. The model consists of two major parts: (1) calculation of total energy of the solder joint for any given height by determining the minimum-energy joint shape at that height, and (2) calculation of the quasi-static height and associated joint shape that satisfies the force balance between the vertical loading and the normal reaction due to the deformed solder joint.

The variational problem associated with the above described system is formulated with the following assumptions:

1 The solder volume is constant.

2 The boundary of the solder pad represents the separation between wetting and nonwetting surface and coincides with the three-phase contact line (solder/vapor/pad).

3 The equilibrium contact angle defined by the liquid solder and the wettable surface will not be used as a boundary condition because of the effect of the contact angle hysteresis. The contact angle hysteresis refers to the deviation of the angle from its equilibrium value due to abrupt changes in the magnitude of the equilibrium contact angle (representing that of wetting and nonwetting surface) across the three-phase contact line (Neumann et al., 1972; Johnson Jr et al., 1964). For a given pad size, the magnitude of the hysteresis contact angle will depend upon (i) equilibrium contact angle of the wetting and non-wetting surface, (ii) solder volume and the joint height (determined by the vertical loading). Therefore an unique value can not be assigned to the contact angle as a part of the boundary condition. It may also be noted that such contact angle hysteresis is exhibited when the wettable and nonwettable surfaces are not co-planner (Oliver et al., 1977; Wilkinson et al., 1979).

4 The potential energy of the solder itself is neglected because it is much less than the surface and the potential energy of the system.

The total energy of the system shown in Fig. 3 is

$$\mathbf{\Pi} = \int_{\Omega} \gamma\sqrt{\mathbf{G}}\, du^1 du^2 + \sigma \mathbf{A}_p + \mathbf{BV} + \mathbf{W}h \tag{1}$$

where γ is the surface tension coefficient, $\mathbf{G}$ is the determinant of the surface metric of the solder joint (a metric space defined by the surface coordinates), $\mathbf{A}_p$ is the solder/pad interface area, σ is the adhesive coefficient representing the wettability of the liquid solder on solder pad, $\mathbf{B}$ is the unit body force of the joint, $\mathbf{V}$ is the solder volume, $\mathbf{W}$ is the vertical loading, and h is the joint height. The first three terms in (1) represent the surface energy, wetting energy, and potential energy of the solder joint, respectively. The last term represents that potential energy of the component. *For a system with a small physical dimension, the potential energy of a joint is negligible* compared to its surface energy and vertical loading $\mathbf{W}$ (see assumption No. 3), and can be neglected. Therefore the total energy of the system (1) reduces to

$$\mathbf{\Pi} = \int_{\Omega} \gamma\sqrt{\mathbf{G}}\, du^1 du^2 + \sigma \mathbf{A}_p + \mathbf{W}h \tag{2}$$

The static equilibrium of the system represents the balance between the weight of the component and the normal reaction due to the solder joint:

$$\mathbf{\Lambda} = \mathbf{Y} - \mathbf{W}$$

$$= 2\mathbf{H}_q \gamma A_p - \gamma \int_{\partial\Omega} \cos\theta_t ds - \mathbf{W} = 0 \tag{3}$$

where $\mathbf{H}$ is the prescribed mean curvature of the fluid/solder interface. $\mathbf{Y}$ is the force due to the solder joint on the component. The angle θ_t represents the hysteresis contact angle at the top solder/pad interface. The subscript q in prescribed mean curvature $\mathbf{H}_q$ indicates that the joint shape is evaluated under a quasi-static equilibrium condition. In general, the prescribed mean curvature $\mathbf{H}$ of a joint with height h is obtained from the solution to the variational problem that involves *minimizing*

$$\int_{\Omega} \gamma\sqrt{\mathbf{G}}\, du^1 du^2 + \sigma \mathbf{A}_p \tag{4}$$

subject to the constant-volume constraint

$$\int_{\Omega} \sqrt{\mathbf{g}}\, d\zeta^1 d\zeta^2 d\zeta^3 - \mathbf{V} = 0 \tag{5}$$

and is defined by the Laplace-Young equation (see Appendix A)

$$\frac{\lambda}{\gamma} = K_{11} \frac{\partial^2 \zeta^1}{\partial {u^1}^2} + 2K_{12} \frac{\partial^2 \zeta^1}{\partial u^1 \partial u^2} + K_{22} \frac{\partial^2 \zeta^1}{\partial {u^2}^2} + K_{00} = 2\mathbf{H} \tag{6}$$

where λ is the Lagrange multiplier.

Next we developed a numerical method capable of performing the following tasks:

1 The monotonic convergence behavior is needed, i.e., the correction to the initial and the intermediate profiles is made in such a way that the new profile has smaller surface area than the previous one.

2 The intermediate profiles should satisfy the volume constraint.

Downloaded 04 May 2010 to 171.66.16.28. Redistribution subject to ASME license or copyright; see http://www.asme.org/terms/Terms_Use.cfm

3 The optimum profile should satisfy the Laplace-Young Eq. (6) and the volume constraint (5) simultaneously.

4 Select and update the Lagrange multiplier λ, its value monotonically converges to the optimum one.

In conventional methods, such as the nonlinear optimization method, the quality of the initial guess is critical to the successful convergence. Unfortunately except for simple geometry such as axisymmetrical joints with circular pads, it is very difficult to generate an initial guess that will be guaranteed to converge to a global minimum. The technique based on motion by mean curvature overcomes these limitations as the correction provided to the initial and the intermediate profiles are proportional to the difference between the λ and the curvature $\mathbf{H}_{u^1u^2}$ at that point so that each iteration, the solution converges towards (6). This method, unlike previous methods for surface modeling (Katyl, et al., 1992), is not restricted to the axisymmetric case.

The numerical method used to solve Eq. (3) is divided into two parts:

- Calculate the prescribed mean curvature (6) of a joint from an initial surface of local mean curvature H_{u^1,u^2} and height h that satisfies the volume constraint (5). The correction to the initial surface is based on motion by mean curvature.

$$\frac{\partial \mathbf{x}}{\partial t} = \mathbf{n}F; \quad F = \frac{\lambda^*}{\gamma} - 2\mathbf{H}_{u^1,u^2} \tag{7}$$

where F is the curvature-dependent speed, $\mathbf{n}$ is normal to the moving surface, and λ^* is an approximation of the Lagrange multiplier.

- Calculate the quasi-static height from an initial height h. The correction to the initial height is based on Eq. (3). *It is proportional to the difference between the vertical loading and the normal reaction due to the joint*, i.e.,

$$\frac{\partial h}{\partial t} = G; \quad G = \mathbf{Y} - \mathbf{W}. \tag{8}$$

where G is the load-dependent speed.

The approximate Lagrange multiplier λ^* that enforces the constant-volume constraint is described below. The equation of motion (7) in curvilinear coordinate system $\zeta^l(u^\alpha, t)$ is given by

$$\frac{\partial \zeta^l}{\partial t} = Fg^{li}n_i \tag{9}$$

where g^{li} is the inverse of g_{li}—a point in the global metric (a metric space defined by the global coordinates). It represents the angles between coordinate curves and rates of change along coordinate curves measured with a dot product of the natural tangent vector fields (see Appendix A for details). Considering the radial motion of the curvature, the equation of the motion of the surface (9) becomes

$$\frac{\partial \zeta^1}{\partial t} = \frac{\mathbf{g}^{1/2}}{\mathbf{G}^{1/2}}F\left[g^{11} - g^{12}\frac{\partial \zeta^1}{\partial u^1} - g^{13}\frac{\partial \zeta^1}{\partial u^2}\right]. \tag{10}$$

Using a forward difference method in a time domain, Eq. (10) can be written as

$$\zeta_{n+1} = \zeta_n + kF\Psi_n \tag{11}$$

where

$$\Psi = \frac{\mathbf{g}^{1/2}}{\mathbf{G}^{1/2}}\left[g^{11} - g^{12}\mathbf{B}_1^1 - g^{13}\mathbf{B}_2^1\right]. \tag{12}$$

The subscript N denotes that the surface is evaluated at time n with k as the time increment. Squaring both sides of Eq. (11) and integrating it yields

$$\int_\Omega \frac{1}{2}\zeta_{n+1}^{1^2}du^1du^2 = \int_\Omega \frac{1}{2}\zeta_n^{1^2}du^1du^2 + \int_\Omega \frac{k}{2}F\Psi\left[kF\Psi + 2\zeta_n^1\right]du^1du^2. \tag{13}$$

For the chosen coordinate system the left-hand side of the equation and the first term of the right-hand side of Eq. (13) represent the solder volume at time step $n+1$ and n, respectively. Enforcing the constant-volume constraint condition at every time step, we get

$$\int_\Omega \frac{k}{2}\left(\frac{\lambda^*}{\gamma} - \mathbf{H}_{u^1u^2}\right)\Psi\left[k\left(\frac{\lambda^*}{\gamma} - \mathbf{H}_{u^1u^2}\right)\Psi + 2\zeta_n^1\right]du^1du^2 = 0. \tag{14}$$

At any given time step, λ^* is the only unknown in Eq. (14), which can be calculated by an iterative method.

The equation of motion of the perturbed surface (10) is a quasi-linear parabolic equation. A suitable mathematical notion for the generalized solution of Eq. (10) is the *Viscosity Solution* as defined by Crandall et al. (1992). At this point we do not know whether our numerical scheme rigorously con-

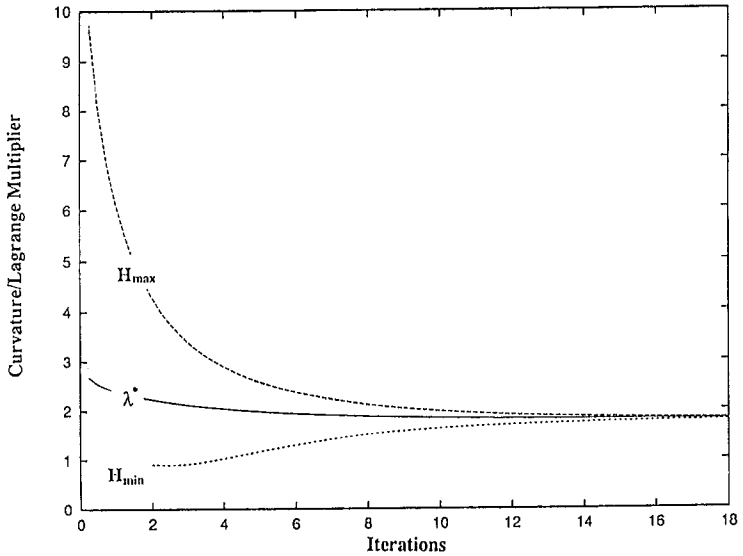

Fig. 4 Numerical representation of the convergence criterion

Downloaded 04 May 2010 to 171.66.16.28. Redistribution subject to ASME license or copyright; see http://www.asme.org/terms/Terms_Use.cfm

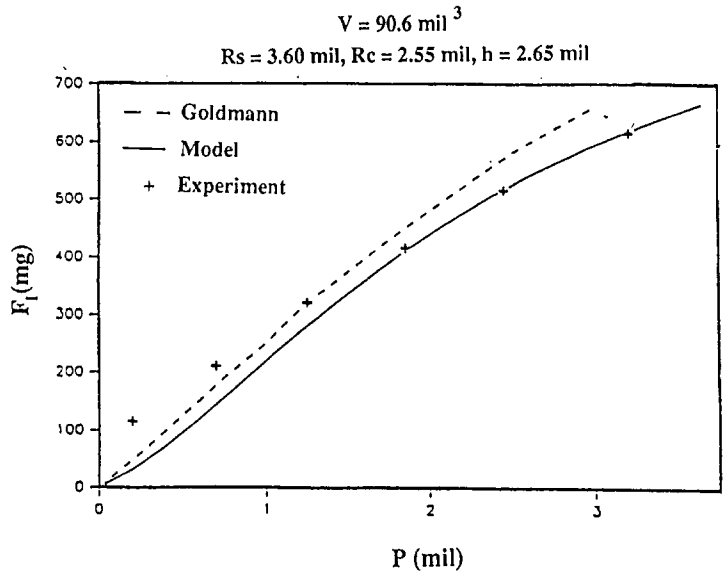

Fig. 5 Comparison between calculated restoring force and Goldmann (1972)s result

verges to the viscosity solution and we will address this issue in a future paper. We remark here that such convergence theorem for nonlinear elliptic problems has been established by Trudinger et al. (1992). Figure 4 shows an empirical indicator of convergence of our numerical scheme. It satisfies the following condition:

$$\frac{\|H_{\max}\| - \|H_{\min}\|}{\lambda^*} = \epsilon, \tag{15}$$

where $H_{\max}$ the maximum value of $\mathbf{H}_{u^1u^2}$ and $H_{\min}$ the minimum value of $\mathbf{H}_{u^1u^2}$ are evaluated at every iteration and are compared to the approximation of the Lagrange multiplier (λ^*) used in Eq. (14). As the solution converges, both $H_{\max}$ and $H_{\min}$ converge to λ^*. Figure 5 shows the accuracy of the model compared to the data obtained from Goldman (1972). The solid line represents the prediction by the current model.

3 Quantitative Characterization of the Solder Joint

Quantitative characterization of the solder joint is necessary for evaluating the impact of design and process variation on its self-aligning ability. The following characteristics of a solder joint are studied: (1) solder joint shape as a function of applied vertical loading, lateral misalignment, and pad geometry, (2) restoring force generated by the solder joint as the function of solder volume, (3) normal reaction generated by the solder joint as the function of solder volume, (4) variation of joint height as a function of vertical loading and solder volume.

The numerical results to be presented next are for a flip-chip joint assembly with the following process-related parameters; 40 μm pad size (i.e., 40μm diameter circular pad and 40μm $\times$ 40μm square pad), mean solder deposition height of 20 μm, 325 dyne/cm for the surface tension coefficient, and 0.37 dyne for mean vertical loading per joint.

Figure 6 shows the minimum-energy shape of a joint with different design and process conditions. Figure 6(a) shows the joint shape for circular pad geometry under a compressive vertical loading and with 5μm lateral misalignment. Figure 6(b) shows the minimum-energy shape of a joint with square pads under similar conditions. The minimum-energy shapes obtained for these joints, in addition to being key to the quasi-static analysis, are important for evaluating the reliability of the joint. The joint shape and the corresponding surface area are important input parameters needed for the thermal stress analysis of the solder joint.

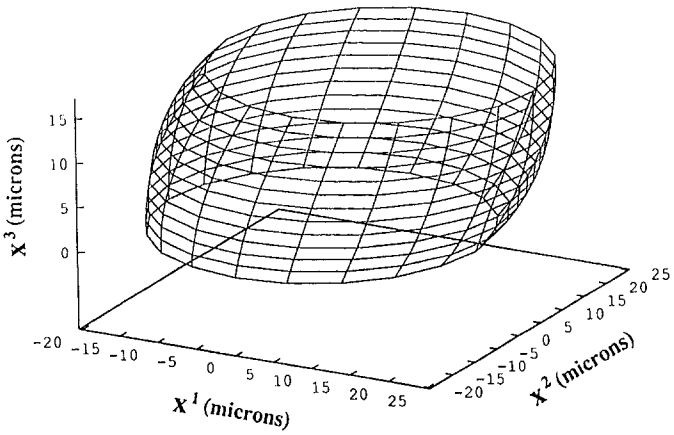

Fig. 6(a)

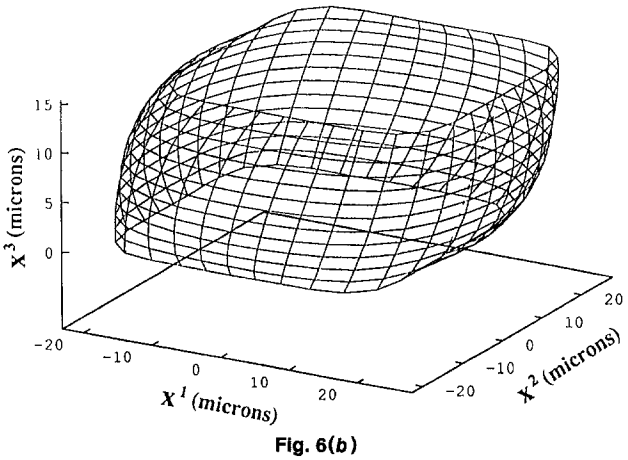

Fig. 6(b)

Fig. 6 Solder joint profile as a function of design and process parameters (a) circular pad, compressive load, and 5μm lateral misalignment level (b) square pad, compressive load, and 5μm lateral misalignment level

Downloaded 04 May 2010 to 171.66.16.28. Redistribution subject to ASME license or copyright; see http://www.asme.org/terms/Terms_Use.cfm

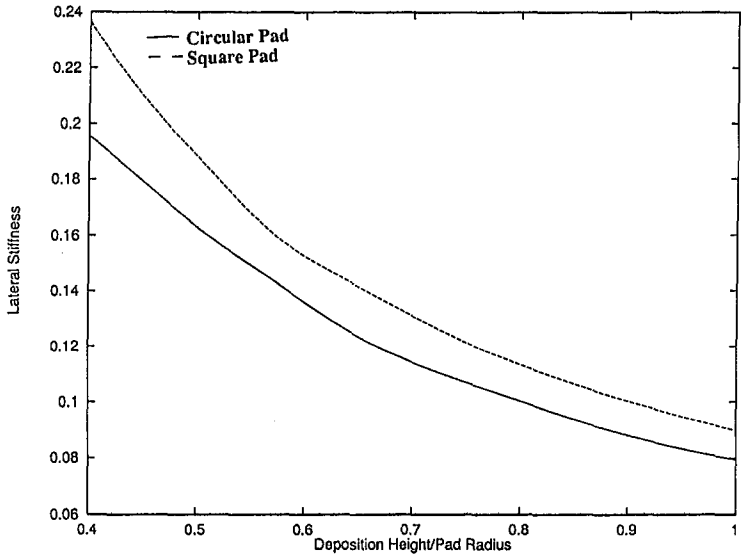

Fig. 7 Lateral stiffness as a function of solder volume

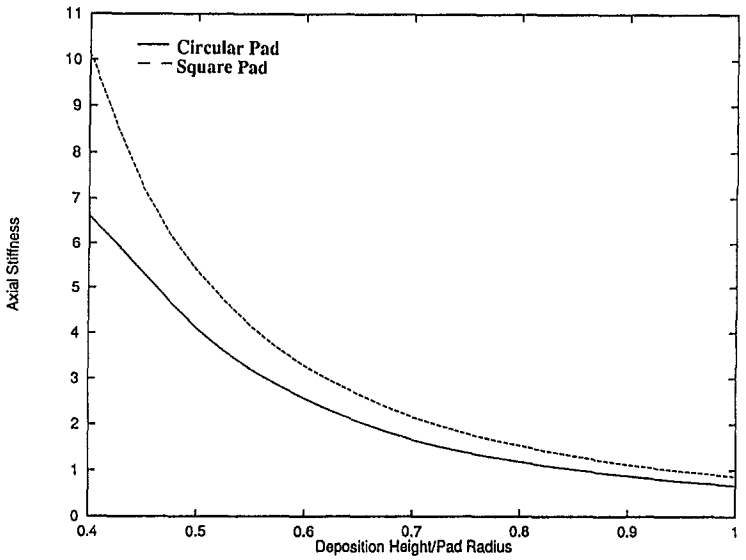

Fig. 8 Axial stiffness as a function of solder volume

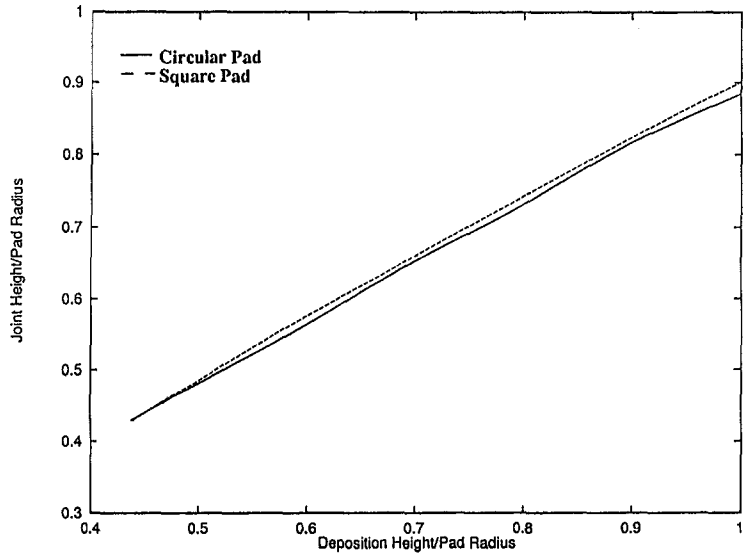

Fig. 9 Equilibrium position of the solder joint as a function of solder volume

Downloaded 04 May 2010 to 171.66.16.28. Redistribution subject to ASME license or copyright; see http://www.asme.org/terms/Terms_Use.cfm

The reaction force generated by a solder joint either due to misalignment or due to the action of vertical loading or the combination of both can be characterized as the reaction force from an equivalent spring. Like a spring, the generated force is proportional to the deviation of the solder joint from its equilibrium position. The equilibrium position is defined as the position occupied by the solder joint under zero misalignment and zero vertical loading. Following the same logic, the resultant force generated by the solder joint under a nonequilibrium condition can be resolved into lateral and axial components. If these two components of force are assumed to be proportional to the "lateral stiffness" and "axial stiffness" of the equivalent spring, then these "stiffnesses" are defined as

$$K_l = \left.\frac{\partial F_l}{\partial p}\right|_{h=c1} = \gamma \left.\frac{\partial^2 \mathbf{A}}{\partial p^2}\right|_{h=c1} \tag{16}$$

$$K_a = \left.\frac{\partial F_n}{\partial h}\right|_{p=c2} = \gamma \left.\frac{\partial^2 \mathbf{A}}{\partial h^2}\right|_{p=c2} \tag{17}$$

where K_l and K_a represent the lateral and axial stiffness, respectively. The lateral stiffness is evaluated at a constant height $h = c1$ and the axial misalignment is evaluated at misalignment $p = c2$.

Figure 7 shows the nondimensional representation of lateral stiffness as a function of solder volume. It is evaluated for a solder joint with unit pad size, unit deposition height, and unit surface tension coefficient. Similarly, Fig. 8 shows the nondimensional representation of the axial stiffness as a function of solder volume. The *x-axis* presents the solder volume; represented as the ratio of solder deposition height to the substrate pad radius. It can be observed from Figs. 7 and 8 that the stiffness reduces with increase in volume and for the same volume, the solder joints with square pads generate more reaction force in a lateral/normal direction, compared to those with a circular pad. Both the results were obtained at misalignment level of ten percent of substrate pad radius. Note that the axial stiffness differs from the lateral stiffness by an order of magnitude. Thus the solder joint is more susceptible to lateral misalignment compared to the axial misalignment. Figure 9 shows the equilibrium position (joint height under zero vertical loading) as a function of the solder volume. This is the primary cause of the axial misalignment, i.e., the achievable tolerance on axial misalignment is dictated by the achievable accuracy in solder deposition height.

4 Conclusion

Based on an energy minimization principle, a mathematical model has been developed to study the impact of design and process parameters such as vertical loading, solder deposition height, and initial misalignment level on the joint's alignment capability in a lateral and axial direction under a quasi-static condition. The minimum-energy shape needed for joint evaluation is computed by a novel numerical method based on the motion by mean curvature. It calculates the solder joint shape as a function of vertical loading, misalignment, pad geometry, surface tension coefficient, and solder volume. It provides a tool to evaluate and optimize design and process parameters associated with flip-chip solder joint. The results provide a better insight to the design and process aspect of flip-chip soldering to achieve the desired alignment.

Acknowledgment

The first and the third author gratefully acknowledge the support of National Science Foundation through a Presidential Young Investigator Award (Grant # MIP-9054809), and an AT & T Bell Laboratory Fellowship. Discussions with Dr. Deni M. Ors and Dr. Nagesh R. Basavanhally of AT & T Bell Laboratory, Princeton have also been critical to this research.

References

Armiento, C. A., Jagannath, C., and Tabasky, M., 1991, "Silicon Wafer Board: Extension of MCM Technology to the Optical Domain," *IEPS*, Vol. 1, p. 4.

Brakke, K. A., 1992, "Surface Evolver Manual," version 1.87, The National Science & Technology Research Center for Computation and Visualization of Geometric Structures, University of Minnesota.

Crandall, M. G., Ishii, H., and Lions, P. L., 1992, "User's Guide to Viscosity Solutions of Second Order Partial Differential Equations," *Bulletin of the American Mathematical Society*, Vol. 27, No. 1, p. 1–67.

Finn, R., 1986, *Equilibrium Capillary Surfaces*, Springer-Verlag, New York.

Gillette, R. D., and Dyson, D. C., 1971, "Stability of Fluid Interface between Equal Solid Circular Plates," *Chemical Engineering*, No. 2, pp. 44–54.

Goldmann, L. S., 1972, "Self-Alignment Capability of Controlled-Collapse Chip Joining," *Proc. 22nd Electronic Component Conference*, pp. 332–339.

Katyl, H., and Pimbley, W. T., 1992, "Shape and Force Relationships for Molten Axisymmetric Solder Connections," ASME *Journal of Electronic Packaging*, Vol. 114, pp. 336–341.

Johnson, Jr., R. E., and Dettre, R. H., 1964, "Contact Angle Hysteresis III: Study of an Idealized Heterogeneous Surface," *The Journal of Physical Chemistry*, Vol. 68, No. 7, pp. 1744–1750.

Neumann, A. W., and Good, R. J., 1972, "Thermodynamics of Contact Angles, I. Heterogeneous Solid Surfaces," *Journal of Colloid and Interface Science*, Vol. 38, No. 2, pp. 341–358.

Oliver, J. F., Huh, C., and Mason, S. G., 1977, "Resistance of Spreading Liquid by Sharp Edge," *Journal of Colloid and Interface Science*, Vol. 59, No. 3, pp. 568–581.

Patra, S. K., and Lee, Y. C., 1991, "Quasi-Static Modeling of Self-Alignment Mechanism in Flip-Chip Soldering Process, Part I: Single Joint," ASME *Journal of Electronic Packaging*.

Trudinger, N. S., and Kuo, H. J., 1992, "Discrete Methods for Fully Nonlinear Elliptic Equations," *SIAM Journal on Numerical Analysis*, Vol. 29, No. 1, p. 123.

Tsunetsugu, H., Katasura, K., Hayashi, T., Ishitsuka, F., Hata, S., and Takachio, N., 1991, "A New Packaging Technology for High-Speed Photoreceivers Using Micro-Solder Bumps," 41 ECTC p. 479–482.

Wilkinson, M. C., Zettlemoyer, A. C., Aronson, M, P., and Vanderhoff, J. W., 1979, "Spreading and Wetting Phenomena in Four-Phase (Liquid/Liquid/Substrate/Vapor) Configuration, I. Experimental Studies of Static Profiles," *Journal of Colloid and Interface Science*, Vol. 68, No. 3, p. 508–544.

APPENDIX A

The Laplace-Young Equation

The Laplace-Young equation for the solder joint is derived from a variational principle similar to that in Finn (1986). From (4) and (5), the functional to be minimized is

$$I = \gamma\left[\mathbf{A}_s - \frac{\lambda}{\gamma}\mathbf{V} + \frac{\sigma}{\gamma}\mathbf{A}_p\right] \tag{A1}$$

where λ is the Lagrange multiplier, $\mathbf{A}_s$ the liquid/fluid interface area (surface area), A_p the solid/liquid interface area, and $\mathbf{V}$ the constant-volume constraint.

Applying the principle of virtual work, the varied surface is denoted by

$$\mathbf{x}^0(u^1,u^2) + \epsilon(\xi\mathbf{n} + \eta\mathbf{t}) + \mathbf{O}(\epsilon^2) \tag{A2}$$

whose area is $\mathbf{A}_s^\epsilon$. $\epsilon(\xi\mathbf{n} + \eta\mathbf{t})$ represents a virtual variation over the surface Ω with $\mathbf{n}$ the unit normal to surface Ω and $\mathbf{t}$ the unit tangent, defined in a close strip $\partial\Omega_\delta$ of width δ. $\partial\Omega$ represents the three-phase contact line (liquid/solid/fluid). The tangential component $\mathbf{t}$ is defined such that it is orthogonal to $\partial\Omega$ and directed out of Ω. The functions ξ and η are arbitrary but subjected to the following condition:

Downloaded 04 May 2010 to 171.66.16.28. Redistribution subject to ASME license or copyright; see http://www.asme.org/terms/Terms_Use.cfm

$$\xi^2 + \eta^2 \le 1$$

$$supp\ \eta \subset \partial\Omega_\delta$$

$$\xi\mathbf{n} + \eta\mathbf{t}\ tangent\ to\ the\ solid\ on\ \partial\Omega.$$

After variation, let the surface area be given by

$$\mathbf{A}_s^\epsilon = \int_\Omega \sqrt{\mathbf{G}^\epsilon}\, du^1 du^2 \tag{A3}$$

$\mathbf{G}^\epsilon$ is the determinant of surface metric $G_{\alpha\beta}^\epsilon$

$$\mathbf{G}^\epsilon = \mathbf{G}^o + 2\epsilon Q + \mathbf{O}(\epsilon^2) \tag{A4}$$

where

$$Q = -2\xi\mathbf{G}^{1/2}\mathbf{H} + G_{11}^o(\eta\mathbf{t})_{u_2}\cdot\mathbf{x}_u^o{}_2 + G_{22}^o(\eta\mathbf{t})_{u^1}\cdot\mathbf{x}_u^o{}_1 - G_{12}^o\left[(\eta\mathbf{t})_{u^1}\cdot\mathbf{x}_u^o{}_2 + (\eta\mathbf{t})_{u^2}\cdot\mathbf{x}_u^o{}_1\right] \tag{A5}$$

where $\mathbf{H}$ is the prescribed mean curvature and is given in tensor form (Gauss-Weingerten equation) as

$$2\mathbf{H} = \frac{1}{\mathbf{G}}\left[G_{11}n_k\mathbf{B}_{2\|2}^k - 2G_{12}n_k\mathbf{B}_{1\|2}^k + G_{22}n_k\mathbf{B}_{1\|1}^k\right]. \tag{A6}$$

$\mathbf{B}_{\alpha\|\beta}^i$ denotes the covariant differentiation,

$$\mathbf{B}_{\alpha\|\beta}^i = \frac{\partial^2\zeta^i}{\partial u^1\partial u^2} + \mathbf{\Gamma}_{rs}^i\mathbf{B}_\alpha^r\mathbf{B}_\beta^s - \mathbf{\Gamma}_{\alpha\beta}^\tau\mathbf{B}_\tau^i \text{ and} \tag{A7}$$

n_k is the normal to the surface

$$n_k = \frac{1}{2}\sqrt{\frac{\mathbf{g}}{\mathbf{G}}}\,\epsilon_{ijk}\epsilon^{\alpha\beta}\mathbf{B}_\alpha^i\mathbf{B}_\beta^j. \tag{A8}$$

$\mathbf{\Gamma}_{rs}^i$ and $\mathbf{\Gamma}_{\alpha\beta}^\tau$ are Christoffel symbols and are defined by

$$\mathbf{\Gamma}_{rs}^i = \frac{g^{im}}{2}\left[\frac{\partial g_{ms}}{\partial\zeta^r} + \frac{\partial g_{mr}}{\partial\zeta^r} - \frac{\partial g_{rs}}{\partial\zeta^m}\right] \tag{A9}$$

$$\mathbf{\Gamma}_{\alpha\beta}^\tau = \frac{G^{\tau\theta}}{2}\left[\frac{\partial G_{\theta\beta}}{\partial u^\alpha} + \frac{\partial G_{\theta\alpha}}{\partial u^\beta} - \frac{\partial G_{\alpha\beta}}{\partial u^\theta}\right] \tag{A10}$$

and

$$\mathbf{B}_\alpha^i = \frac{\partial\zeta^i}{\partial u^\alpha}. \tag{A11}$$

The metric g_{ij} is given by

$$g_{ij} = \frac{\partial x^k}{\partial\zeta^i}\frac{\partial x^k}{\partial\zeta^j} \tag{A12}$$

The surface metric $G_{\alpha\beta}$ is obtained from the global metric as

$$G_{\alpha\beta} = \frac{\partial x^k}{\partial u^\alpha}\frac{\partial x^k}{\partial u^\beta} = \frac{\partial x^k}{\partial\zeta^i}\frac{\partial x^k}{\partial\zeta^j}\frac{\partial\zeta^i}{\partial u^\alpha}\frac{\partial\zeta^j}{\partial u^\beta} = g_{ij}\mathbf{B}_\alpha^i\mathbf{B}_\beta^j \tag{A13}$$

where u^α represents a surface coordinate system, i.e., $\zeta^i = \zeta^i(u^1, u^2)$.

From (A3) and (A4), the area of the varied surface is

$$\mathbf{A}_s^\epsilon = \int_\Omega \mathbf{G}^{o1/2}\left[1 + 2\epsilon\frac{Q}{\mathbf{G}^o}\right]^{1/2} du^1 du^2 = \int_\Omega \mathbf{G}^{o1/2}\left[1 + \epsilon\frac{Q}{\mathbf{G}^o} + \mathbf{O}(\epsilon^2)\right] du^1 du^2 \tag{A14}$$

and from (A14),

$$\left.\frac{\partial\mathbf{A}^\epsilon}{\partial\epsilon}\right|_{e\to 0} = \dot{A}_s^\epsilon = -\int_\Omega 2\xi\mathbf{H}\,du^1 du^2 + \int_{\partial\Omega}\eta ds. \tag{A15}$$

Similarly, under varied conditions, the volume constraint is given by

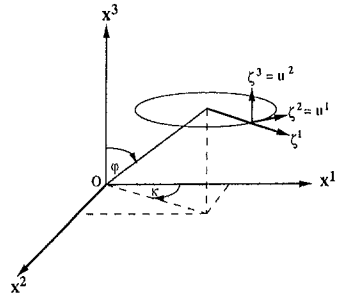

Fig. 10 Generalized coordinate system to define a solder joint

$$\dot{\mathbf{V}}^\epsilon = \int_\Omega \xi\, du^1 du^2, \tag{A16}$$

and the variation of the pad surface area $\mathbf{A}_p$ is

$$\dot{\mathbf{A}}_p^\epsilon = \int_{\partial\Omega}(\xi\sin\theta + \eta\cos\theta)ds, \tag{A17}$$

as $\xi\mathbf{n} + \eta\mathbf{t}$ is orthogonal to $\partial\Omega$ in the tangent plane of $\mathbf{A}_p$. From (A15), (A16), and (A17), the variation of the total energy of the solder joint with constant-volume constraint is

$$\dot{I} = \int_\Omega \gamma\xi\left[2\mathbf{H} - \frac{\lambda}{\gamma}\right] du^1 du^2 + \int_{\partial\Omega}\left\{\frac{\sigma}{\gamma}\xi\sin\theta + \left(1 + \frac{\sigma}{\gamma}\cos\theta\right)\eta\right\} ds = 0. \tag{A18}$$

For the fixed boundary problem both ξ and η vanish on the boundary, reducing the second integral of (A18) to zero. Also noting that ξ is an arbitrary function, Eq. (A18) will remain valid only if

$$\frac{\lambda}{\gamma} = 2\mathbf{H}. \tag{A19}$$

Equation (A19) is called the Laplace-Young equation.

For our specific problem, we will write for $\mathbf{x} \in \mathbf{R}^3$,

$$\mathbf{x} = x^i(\zeta^1, \zeta^2, \zeta^3)\hat{\mathbf{u}}_i \tag{A20}$$

where $\mathbf{u}_i$ denotes a unit vector along the Cartesian coordinate system x^i in $\mathbf{R}^3$. For the specific system shown in Fig. 10

$$x^1 = \zeta^1\cos\zeta^2 + \zeta^3\tan\phi\cos\kappa$$

$$x^2 = \zeta^1\sin\zeta^2 + \zeta^3\tan\phi\sin\kappa$$

$$x^3 = \zeta^3. \tag{A21}$$

If u^α are chosen as

$$u^1 = \zeta^2$$

$$u^2 = \zeta^3, \tag{A22}$$

then the Laplace-Young Eq. (A19) describing the relationship between the pressure difference at the liquid/fluid interface and the prescribed mean curvature is

$$\frac{\lambda}{\gamma} = K_{11}\frac{\partial^2\zeta^1}{\partial u^{1^2}} + 2K_{12}\frac{\partial^2\zeta^1}{\partial u^1\partial u^2} + K_{22}\frac{\partial^2\zeta^1}{\partial u^{2^2}} + K_{00} = 2\mathbf{H} \tag{A23}$$

Downloaded 04 May 2010 to 171.66.16.28. Redistribution subject to ASME license or copyright; see http://www.asme.org/terms/Terms_Use.cfm

where

$$K_{11} = \mathbf{g}^{1/2}\mathbf{G}^{-3/2}G_{22}$$

$$K_{12} = -\mathbf{g}^{1/2}\mathbf{G}^{-3/2}G_{12}$$

$$K_{22} = \mathbf{g}^{1/2}\mathbf{G}^{-3/2}G_{11}$$

$$K_{00} = \eta^{1/2}\mathbf{G}^{-3/2}\left[2K_{01}\left\{G_{22}\mathbf{B}_1^1 - G_{12}\mathbf{B}_2^1\right\} + K_{02}G_{22}\right]$$

and

$$K_{01} = \mathbf{\Gamma}_{12}^1 - \mathbf{\Gamma}_{12}^2\mathbf{B}_1^1 - \mathbf{\Gamma}_{12}^3\mathbf{B}_2^1$$

$$K_{02} = \mathbf{\Gamma}_{22}^1 - \mathbf{\Gamma}_{22}^2\mathbf{B}_1^1 - \mathbf{\Gamma}_{22}^3\mathbf{B}_2^1. \qquad \text{(A24)}$$

Downloaded 04 May 2010 to 171.66.16.28. Redistribution subject to ASME license or copyright; see http://www.asme.org/terms/Terms_Use.cfm

Xiaoping Liu
Graduate Programs in Manufacturing Systems Engineering,
University of St. Thomas,
St. Paul, MN 55105

R. D. James[1]
Department of Aerospace Engineering and Mechanics,
University of Minnesota,
110 Union Street, S.E.,
Minneapolis, MN 55455

Stability of Fiber Networks Under Biaxial Stretching

This paper is concerned with the constitutive behavior of a particular orthogonal fiber network under biaxial dead loading. We also describe a new kind of biaxial, dead-loading machine which is applicable to anisotropic materials. The machine does not require that the loads are exerted along symmetry axes of the material. A specimen of the cloth was loaded by different loading paths to the same equibiaxial dead-load, and two different final deformations were observed. A related observation was reported by Treloar for rubber in 1948. In order to understand this instability, we experimentally determined the energy function for the cloth. The energy function is then used in a variational calculation to explain this instability.

1 Introduction

In this paper we introduce a new biaxial testing machine that imposes approximately uniform dead-load tractions to the edges of a plate, and we study the deformation of cloth. The machine is applicable to anisotropic materials, which may undergo large deformations, and the tractions need not be imposed along symmetry axes of the material.

To test the ability of the machine to accurately impose these tractions, we placed in the machine an extremely anisotropic material which also easily undergoes large deformations, this being a sample of Kevlar® parachute cloth with a relatively open orthogonal weave. Usually we found that an assignment of the two resultant forces yielded a unique homogeneous deformation, regardless of the loading path. The homogeneity of this deformation and the independence of the loading path are quantified in Section 4. However, when we loaded to an equibiaxial load, we observed that the final deformation was not unique. More specially, we found that associated to each equibiaxial load there are precisely two homogeneous deformations, and the observed deformation is always near one of these, although there is some scatter (see Section 4). This nonuniqueness admits a simple interpretation based on symmetry and nonlinearity (Section 5).

To explain these observations, we settled on a simple model for the cloth. We noted that, while the cloth behaves in a highly inelastic manner under small forces, it becomes highly elastic, except for the aforementioned instability, under a large range of biaxial tensions of sufficient magnitude. It is also approximately inextensible in fiber directions. We therefore model the cloth as an inextensible nonlinear elastic material, in the spirit of Pipkin and Rivlin (Pipkin, 1974 and 1987; Pipkin and Rivlin, 1963; Rivlin, 1955) (Section 6). We use the experimental measurements of Piola-Kirchhoff stress versus deformation gradient to evaluate the energy function for the cloth. The resulting energy function exhibits potential wells. Because the experimental data leave gaps in the domain of the energy function, due to the equibiaxial instability, we are not able to uniquely assign a potential well structure to the energy function in all of its domain, but we suggest several reasonable alternatives (Section 7).

A related observation for rubber was reported by Treloar (1948). He carried out an experiment in which a rectangular sheet of rubber was subjected to equal dead-load tensions at its edges. In some cases the resulting deformations were asymmetric, with unequal principal stretches even though the loading was symmetric. At about the same time, Rivlin (1948) studied equilibrium deformations of a cube of neo-Hookean material subjected to three pairs of equal and opposite dead-load surface tractions. He showed that at least seven equilibrium configurations are possible when the tensile forces exceed a certain critical value, and of the seven, only one has all the symmetries of the given loading. Furthermore, he found that the symmetric configuration is unstable for large values of the tensile forces (Rivlin, 1974). Ball and Schaeffer (1983) considered the same problem for general isotropic incompressible materials. Kearsley (1986), MacSithigh (1986), and Chen (1987) also studied the similar problem for isotropic incompressible elastic materials, and some stability approaches have been employed to explain Treloar's observations. A difference between the results of these analyses and the behavior of the cloth studied in this paper is that they predict an infinite number of stable deformations while in the cloth we observe only two.

[1]To whom all correspondence should be addressed.

Contributed by the Applied Mechanics Division of THE AMERICAN SOCIETY OF MECHANICAL ENGINEERS for publication in the ASME JOURNAL OF APPLIED MECHANICS.

Discussion on this paper should be addressed to the Technical Editor, Professor Lewis T. Wheeler, Department of Mechanical Engineering, University of Houston, Houston, TX 77204-4792, and will be accepted until four months after final publication of the paper itself in the ASME JOURNAL OF APPLIED MECHANICS.

Manuscript received by the ASME Applied Mechanics Division, July 1, 1993; final revision, Nov. 4, 1993. Associate Technical Editor: R. Abeyaratne.

Copyright © 1995 by ASME

Downloaded 04 May 2010 to 171.66.16.28. Redistribution subject to ASME license or copyright; see http://www.asme.org/terms/Terms_Use.cfm

2 Preliminaries and Notation

In this section we describe the terminology used for describing the deformation and energy function of the cloth. We consider a body which can be represented in a fixed reference configuration by a bounded regular domain $R \in \mathbb{R}^2$. A particle of the body is represented by $\mathbf{x} \in R$. To formulate constitutive relations for the material, we first define the deformation. A deformation $\mathbf{y}$ is an invertible function

$$\mathbf{y}: R \to \mathbf{y}(R) \tag{1}$$

which maps the reference shape R onto the present shape $\mathbf{y}(R) \in \mathbb{R}^2$. We assume $\mathbf{y}$ is differentiable at $\mathbf{x} \in R$, we call

$$\mathbf{F} = \nabla \mathbf{y}(\mathbf{x}), \tag{2}$$

the deformation gradient at $\mathbf{x}$. We shall assume throughout this paper, in addition to the invertibility of $\mathbf{y}$, that the deformation gradient satisfies

$$\det \mathbf{F} > 0. \tag{3}$$

In view of our assumption (3), the tensor $\mathbf{F}$ has the unique decomposition:

$$\mathbf{F} = \mathbf{RU} \tag{4}$$

where $\mathbf{U}$ is a positive-definite symmetric tensor called the *stretch* and $\mathbf{R}$ is a proper orthogonal tensor called the *rotation*.

Later we shall assume that the cloth specimen is a homogeneous elastic material which possesses a strain-energy function φ depending on the local change of shape:

$$\varphi(\mathbf{F}). \tag{5}$$

The value of the strain-energy function $\varphi(\mathbf{F})$ corresponds to the strain energy, per unit area in the reference configuration, stored in the body when it undergoes a deformation with the deformation gradient $\mathbf{F}$. The strain-energy function is assumed to satisfy the condition of material frame indifference,

$$\varphi(\mathbf{RF}) = \varphi(\mathbf{F}), \tag{6}$$

$\mathbf{R}$ being any proper orthogonal tensor in two-dimensional space. According to standard continuum mechanics (Chadwick, 1976), if $\mathbf{H}$ is a rotation which belongs to the material symmetry group, φ satisfies

$$\varphi(\mathbf{FH}) = \varphi(\mathbf{F}) \tag{7}$$

for all admissible $\mathbf{F}$. We shall use the notation $\mathbf{H}(\theta)$ to denote a clockwise rotation through the angle θ.

The assumption (6) implies that φ can be expressed as a function of $\mathbf{F}^T\mathbf{F}$ only:

$$\varphi(\mathbf{F}) = \bar{\varphi}(\mathbf{C}), \quad \mathbf{C} = \mathbf{F}^T\mathbf{F}. \tag{8}$$

Let $\mathbf{t}$ represent the force per unit reference length applied to the boundary ∂R of the specimen, which we call the traction, and s the length measure of the boundary. The physical interpretation of a *dead-loading* device is that the imposed force $\mathbf{t}(\mathbf{x})ds$ applied at $\mathbf{y}(\mathbf{x})$ maintains its magnitude and direction regardless of how the body deforms. The design of the machine is such as to impose a dead-load traction $\mathbf{t}(\mathbf{x})$ of the form

$$\mathbf{t}(\mathbf{x}) = \mathbf{Tn}(\mathbf{x}),$$

where $\mathbf{n}(\mathbf{x})$ is the unit normal to ∂R at $\mathbf{x}$ and $\mathbf{T} = \sum_{i=1}^{2} T_i \mathbf{e}_i \otimes \mathbf{e}_i$, where T_1, T_2 are constants and $\mathbf{e}_1$, $\mathbf{e}_2 \in \mathbb{R}^2$ are orthogonal. In the equibiaxial case $T_1 = T_2$.

The total potential energy $E[\mathbf{y}]$ of a dead-loaded body is defined by

$$E[\mathbf{y}] = \int_R \varphi(\nabla \mathbf{y}(\mathbf{x}))d\mathbf{x} - \int_{\partial R} \mathbf{t}(\mathbf{x}) \cdot \mathbf{y}(\mathbf{x})ds. \tag{9}$$

Given a traction field $\mathbf{t}(\mathbf{x})$, a deformation $\mathbf{y}^*(\mathbf{x})$ is stable in a dead loading device, if it minimizes the total potential energy; the inequality

$$E[\mathbf{y}^*] \le E[\mathbf{y}] \tag{10}$$

holds for all admissible deformations $\mathbf{y}$. For our purposes, the set of admissible deformations will be all smooth deformations whose gradient lies in the domain of the function φ.

3 The Testing Machine and Specimen

By looking at the reports available in literature on biaxial loading experiments, we found that two test devices were reported in early days. Treloar (1949) designed a series of experiments using vulcanized natural rubber to test the applicability of the neo-Hooken form of the strain-energy function. Among his experiments, there was a biaxial test machine, which stretched a thin square sheet of rubber. In Treloar's experiment the square test-piece had five projecting lugs on each side as indicated schematically in Fig. 1, and strings were tied to these for the application of loads. The surface of the sheet was marked out with lines forming a square lattice. With the sheet placed horizontally, the three middle lugs on a side were loaded by means of three equal weights attached to each string, while the strings attached to the two outermost lugs were secured to a rectangular frame.

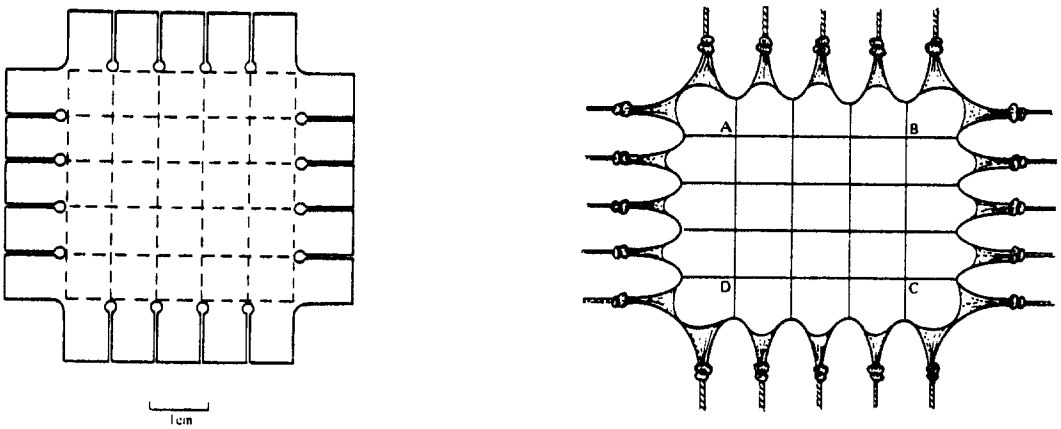

Fig. 1 From Treloar, 1958 (With permission from R. J. Atkin and N. Fox, *An Introduction to the Theory of Elasticity*, Fig. 3.6 and 3.7, Longman, London and New York, 1980)

Downloaded 04 May 2010 to 171.66.16.28. Redistribution subject to ASME license or copyright; see http://www.asme.org/terms/Terms_Use.cfm

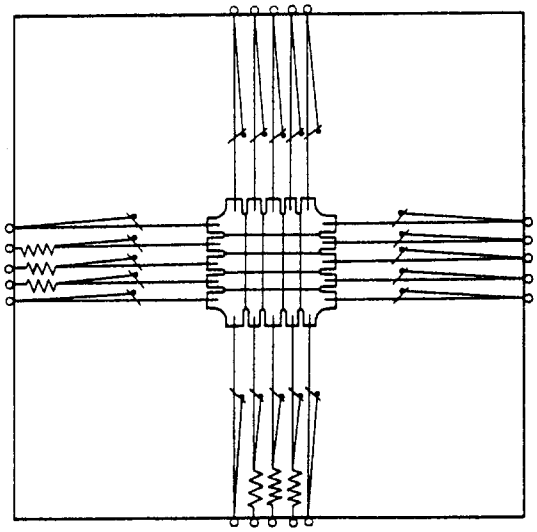

Fig. 2 Experimental set-up of Rivlin and Saunders, 1951 (With permission from R. J. Atkin and N. Fox, *An Introduction to the Theory of Elasticity*, Fig. 3.9, Longman, London and New York, 1980)

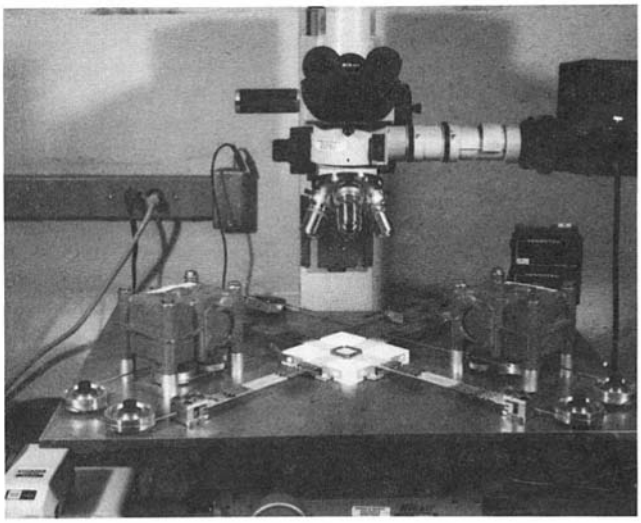

Fig. 3 A view of the loading arrangement of the biaxial machine

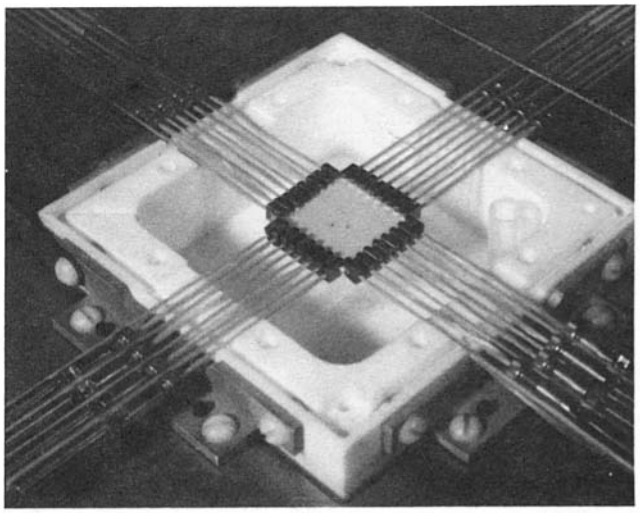

Fig. 4 A view of the environment chamber and specimen

Similar arrangements were used on the other three sides, and by applying different weights, different extensions were obtained. The appearance of the stretched sheet is shown in Fig. 1. By measuring the lengths of the sides of rectangles drawn on the sheet in their deformed and undeformed states, he determined the principal stretches. In the experiment it was assumed that the traction operative in producing the pure homogeneous deformation of the rectangle ABCD was computed from the loads applied to the three central lugs on each side of the test piece.

Rivlin and Saunders (1951) used the arrangement shown in Fig. 2. One difference between their arrangement and that of Treloar's is that springs were used instead of weights, so that rapid, continuous variation of the applied traction was possible. Again it was assumed that the traction operative in producing the pure homogeneous deformation of the central nine squares was computed from the central three strings on each side of the test piece.

When the material shears, the line connecting the loading points rotates relative to the direction of the applied force. In this case Treloar and Rivlin and Saunders' machines will give a nonuniform load distribution. This fact makes their machines inapplicable to the testing of anisotropic materials. Secondly, the five loading points on each side of the specimen seem insufficient to approximate a uniform load distribution. Additionally, with modern instrumentation and a high precision X-Y table it is possible to get more accurate measurements.

Our biaxial dead loading machine is pictured in Figs. 3 and 4 and is described in detail as follows. The standard specimens are thin square sheets of approximate dimensions 3.175 cm with eight epoxy dots on each edge. Eight C-clamps or grips are fastened to each edge. Each grip is fastened to the specimen by two #0 − 80 screws, one from above and one from below. This construction allows each grip to pivot on the epoxy dot. Each of the 32 grips is in turn attached via Kevlar® fibers to a soft spring. The function of the spring is to keep the force in Kevlar® fibers relatively uniform. Hence, there are four sets of eight fibers attached to the edges of the specimen, one set or "group" per side. The ends of each group of fibers are linearly fastened to a steel arm which is encased in a housing which allows the entire set of fibers to pivot. This arrangement has the property that the steel arm will turn so as to equalize, on average, the forces in the fibers.

The arm is attached to a steel tensioning cable. After a 180 deg change of direction through the utilization of a companion pair of pulleys, the cable is attached to a 60:1 worm reducer. There is one worm reducer for each axis of the specimen. This arrangement forms a closed loop (i.e., specimen-fiber-reducer-fiber-specimen) so that the force produced along each edge is equal to the force produced on its opposing edge. This also allows the resultant force on each axis to be measured by a load cell which is attached to one of the cables for each axis. To change the force along either axis, one must only adjust the knob on the appropriate reducer, which in turn drives a disk around which the cable is wound. This process lengthens or shortens the springs attached to the fibers, thus increasing or decreasing the applied force.

This construction of fibers, springs, arms, cables, pulleys, load cells, and reducers constitutes our biaxial dead loading testing machine. Its components are mounted on a precisely machined, high-strength aluminum plate ensuring that accurate and appropriate geometrical positioning of these parts is achieved. The plate is in turn mounted on the X-Y table of an optical microscope. The microscope is equipped with a movable stage which can be positioned through the use of two independent controls: one for the X-axis and one for the

Downloaded 04 May 2010 to 171.66.16.28. Redistribution subject to ASME license or copyright; see http://www.asme.org/terms/Terms_Use.cfm

Y-axis. These axial controls are wired to a Metronics Quadra-Chek II which allows the operator to monitor the stage's X and Y coordinates (± 0.00013 cm resolution, 0.0005 cm accuracy) relative to an arbitrarily set origin. We obtained the deformation gradient by measuring the coordinates of three noncollinear markers on the specimen both before and after deformation.

In addition, the load cells are wired to two independent Sensotec load monitors (± 0.0445 N resolution), one for each of the specimen's axes. The arrangement allows the operator of the microscope access to his position of observation and the loads applied to the specimen.

The material studied was supplied by the Fibers Development Center, DuPont Company, Wilmington, DE. The fabric was woven from 55 denier Kevlar® and is 3.3 mils thick. The fabric is formed by two perpendicular families of filaments. Thus, we are led to assume that $\mathbf{H}(n\pi/2)$ where n is the integer belongs to the material symmetry group of undistorted cloth.

To make the specimens, we cut the material at an angle θ to the fibers (see Fig. 5). After cutting square specimens, we glued eight dots of epoxy per edge on both the top and bottom of the specimen for a total 32 equidistant points of contact per side. These epoxy dots did not touch each other. Next, a grip was fastened to each pair of epoxy contact points by two tiny screws, as described above. This allowed the force applied to the edge to be approximately uniform without damaging the specimen. The square defined by the center lines of the screws had dimensions 2.54 cm × 2.54 cm in all cases.

After some preliminary experiments, it was found that another apparatus was needed to aid in attaching the grips with proper alignment. For this purpose we built a device to successively hold the eight grips in their precise location while we systematically attached each side of the cloth to them. This device helped to ensure that the traction force applied to each edge would be uniform.

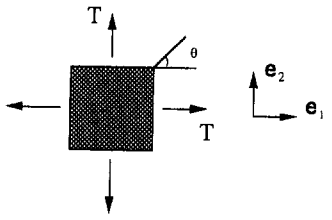

Fig. 5 Notation

4 Experimental Observations

We first conducted a series of experiments to check the homogeneity of the deformations. We randomly chose six points on the specimen, and grouped them in threes. We applied a suitable force in each direction, and measured the coordinates of those six points on the specimen before and after the loading process. According to $\mathbf{dy} = \mathbf{F}\mathbf{dx}$, for each three-point group we can determine a deformation gradient $\mathbf{F}$. In order to quantify the difference between these two deformation gradients, we define $\epsilon = \|\mathbf{F}(2) - \mathbf{F}(1)\|/\|\mathbf{F}(2)\|$, where 1 and 2 represent the group 1 and the group 2 and $\|\mathbf{F}\| = \sqrt{\mathbf{F} \cdot \mathbf{F}}$. Because of the limited accuracy of the x-y table, we kept only the third decimal place in our results. Typically in our tests $\epsilon < 0.004$, so the deformations can be considered nearly homogeneous.

Now we report the observations of instability under equibiaxial tension. First we tested the piece which was cut at $\theta = 22.5$ deg. After we affixed this specimen to the machine, several equibiaxial dead loads were applied, in this case 22.25 N, 26.7 N, 31.5 N, and 35.6 N consecutively. We loaded the force in the $\mathbf{e}_1$ direction first, then loaded to the same force in the $\mathbf{e}_2$ direction. We got a deformation gradient $\mathbf{F}_1$. Next we loaded the force in the $\mathbf{e}_2$ direction first, then loaded the same force in the $\mathbf{e}_1$ direction. We got another deformation gradient $\mathbf{F}_2$. These deformation gradients and corresponding stretch tensors $\mathbf{U}$ and rotation tensors $\mathbf{R}$, are listed in Table 1.

We next tested the fabric by cutting it at an angle $\theta = 35$ deg to the fibers. In exactly the same way, we loaded the forces to 26.7 N and 35.6 N, respectively. We got two sets of $\mathbf{F}$, $\mathbf{U}$ and $\mathbf{R}$. They are listed in Table 2.

When we loaded the specimen, always trying as closely as possible to keep the loads equal during loading, we found that the deformation gradient always adopted a value near those in Table 1 and Table 2 at the corresponding load.

5 Analysis of the Nonuniqueness

The nonuniqueness that is evident from the observation in the equibiaxial case admits the following simple interpretation.

Suppose the observed deformations of the cloth are stable

Table 1

Force	F	U	R
T=22.5 N	$\mathbf{F}_1=\begin{pmatrix} 1.0116 & .0068 \\ .0032 & .9935 \end{pmatrix}$	$\mathbf{U}_1=\begin{pmatrix} 1.0116 & .0050 \\ .0050 & .9935 \end{pmatrix}$	$\mathbf{R}_1=\begin{pmatrix} 1.0000 & .0018 \\ -.0018 & 1.0000 \end{pmatrix}$
	$\mathbf{F}_2=\begin{pmatrix} .9958 & -.0066 \\ -.0031 & 1.0065 \end{pmatrix}$	$\mathbf{U}_2=\begin{pmatrix} .9958 & -.0049 \\ -.0049 & 1.0065 \end{pmatrix}$	$\mathbf{R}_2=\begin{pmatrix} 1.0000 & -.0017 \\ .0017 & 1.0000 \end{pmatrix}$
T = 26.7 N:	$\mathbf{F}_1=\begin{pmatrix} 1.0162 & .0189 \\ .0102 & .9793 \end{pmatrix}$	$\mathbf{U}_1=\begin{pmatrix} 1.0161 & .0146 \\ .0146 & .9794 \end{pmatrix}$	$\mathbf{R}_1=\begin{pmatrix} 1.0000 & .0043 \\ -.0043 & 1.0000 \end{pmatrix}$
	$\mathbf{F}_2=\begin{pmatrix} .9935 & -.0032 \\ -.0068 & 1.0114 \end{pmatrix}$	$\mathbf{U}_2=\begin{pmatrix} .9935 & -.0050 \\ -.0050 & 1.0114 \end{pmatrix}$	$\mathbf{R}_2=\begin{pmatrix} 1.0000 & .0018 \\ -.0018 & 1.0000 \end{pmatrix}$
T=31.5 N	$\mathbf{F}_1=\begin{pmatrix} 1.0062 & .0100 \\ .0032 & .9934 \end{pmatrix}$	$\mathbf{U}_1=\begin{pmatrix} 1.0062 & .0066 \\ .0066 & .9935 \end{pmatrix}$	$\mathbf{R}_1=\begin{pmatrix} 1.0000 & .0034 \\ -.0034 & 1.0000 \end{pmatrix}$
	$\mathbf{F}_2=\begin{pmatrix} .9917 & -.0133 \\ -.0085 & 1.0098 \end{pmatrix}$	$\mathbf{U}_2=\begin{pmatrix} .9916 & -.0108 \\ -.0108 & 1.0098 \end{pmatrix}$	$\mathbf{R}_2=\begin{pmatrix} 1.0000 & -.0015 \\ .0015 & 1.0000 \end{pmatrix}$
T=35.6 N:	$\mathbf{F}_1=\begin{pmatrix} 1.0097 & .0067 \\ .0104 & .9929 \end{pmatrix}$	$\mathbf{U}_1=\begin{pmatrix} 1.0097 & .0085 \\ .0085 & .9928 \end{pmatrix}$	$\mathbf{R}_1=\begin{pmatrix} 1.0000 & -.0019 \\ .0019 & 1.0000 \end{pmatrix}$
	$\mathbf{F}_2=\begin{pmatrix} .9861 & -.0121 \\ -.0092 & 1.0130 \end{pmatrix}$	$\mathbf{U}_2=\begin{pmatrix} .9860 & -.0106 \\ -.0106 & 1.0130 \end{pmatrix}$	$\mathbf{R}_2=\begin{pmatrix} 1.0000 & -.0015 \\ .0015 & 1.0000 \end{pmatrix}$

Downloaded 04 May 2010 to 171.66.16.28. Redistribution subject to ASME license or copyright; see http://www.asme.org/terms/Terms_Use.cfm

Table 2

Force	F	U	R
T=26.7 N:	$\mathbf{F}_1=\begin{pmatrix} 1.0252 & .0108 \\ .0076 & .9768 \end{pmatrix}$	$\mathbf{U}_1=\begin{pmatrix} 1.0252 & .0092 \\ .0092 & .9768 \end{pmatrix}$	$\mathbf{R}_1=\begin{pmatrix} 1.0000 & .0016 \\ -.0016 & 1.0000 \end{pmatrix}$
	$\mathbf{F}_2=\begin{pmatrix} .9704 & -.0085 \\ -.0092 & 1.0320 \end{pmatrix}$	$\mathbf{U}_2=\begin{pmatrix} .9704 & -.0089 \\ -.0089 & 1.0320 \end{pmatrix}$	$\mathbf{R}_2=\begin{pmatrix} 1.0000 & .0003 \\ -.0003 & 1.0000 \end{pmatrix}$
T=35.6 N:	$\mathbf{F}_1=\begin{pmatrix} 1.0216 & .0099 \\ .0070 & .9811 \end{pmatrix}$	$\mathbf{U}_1=\begin{pmatrix} 1.0215 & .0085 \\ .0085 & .9812 \end{pmatrix}$	$\mathbf{R}_1=\begin{pmatrix} 1.0000 & .0014 \\ -.0014 & 1.0000 \end{pmatrix}$
	$\mathbf{F}_2=\begin{pmatrix} .9906 & -.0009 \\ -.0026 & 1.0106 \end{pmatrix}$	$\mathbf{U}_2=\begin{pmatrix} .9906 & -.0018 \\ -.0018 & 1.0106 \end{pmatrix}$	$\mathbf{R}_2=\begin{pmatrix} 1.0000 & .0009 \\ -.0009 & 1.0000 \end{pmatrix}$

deformations in the appropriate dead-loading device. Suppose also that these deformations are each homogeneous, as indicated in the experiments, although this is not really essential to the argument. If $\mathbf{y}^* = \mathbf{F}^*\mathbf{x}$ is one of these deformations corresponding to the applied tractions $T\mathbf{e}_1$ and $T\mathbf{e}_2$, then $\mathbf{y}^*$ satisfies

$$E[\mathbf{y}^*] \leq E[\mathbf{y}] \tag{11}$$

where $E[\mathbf{y}]$ is defined in (9).

Using the divergence theorem on the second term in (9) we get

$$E[\mathbf{y}] = \int_R (\varphi(\nabla\mathbf{y}(\mathbf{x}))d\mathbf{x} - \mathbf{T}\cdot\nabla(\mathbf{x}))d\mathbf{x}. \tag{12}$$

In particular,

$$E[\mathbf{y}^*] = \int_R (\varphi(\mathbf{F}^*) - \mathbf{T}\cdot\mathbf{F}^*)d\mathbf{x}. \tag{13}$$

As mentioned above, the symmetry group of the cloth used in the experiments contains the group $\mathcal{G} = \{\mathbf{H}(\pi/2), \mathbf{H}(\pi), \mathbf{H}(3\pi/2), \mathbf{1}\}$. Hence, combining this symmetry with the condition of frame indifference, we have

$$\varphi(\mathbf{HFH}^T) = \varphi(\mathbf{F}) \quad \text{for all } \mathbf{H} \in \mathcal{G} \tag{14}$$

and for all admissible $\mathbf{F}$. Generally, the term $-\mathbf{T}\cdot\mathbf{F}$ has no particular symmetry under $\mathbf{F} \to \mathbf{HFH}^T$, except in the special case $T_1 = T_2$, in which case

$$\mathbf{T}\cdot\mathbf{HFH}^T = T_1\mathbf{1}\cdot\mathbf{HFH}^T = \mathbf{T}\cdot\mathbf{F}. \tag{15}$$

Hence, in the equibiaxial case,

$$E[\mathbf{y}^*] = E[\hat{\mathbf{y}}],\ \hat{\mathbf{y}}(x) = \mathbf{HF}^*\mathbf{H}^T\mathbf{x}. \tag{16}$$

Now the deformation $\hat{\mathbf{y}}$ may or may not coincide with $\mathbf{y}^*$. Of course, $\mathbf{H}(\pi)\mathbf{FH}(\pi)^T = \mathbf{F}$ for all 2×2 tensors $\mathbf{F}$. Generally, $\mathbf{H}(\pi/2)\mathbf{F}^*\mathbf{H}(\pi/2)^T \neq \mathbf{F}^*$ and we certainly expect these to be different in a highly nonlinear material like cloth. The other symmetries give nothing new, and a deeper analysis shows that the symmetry-induced instability just analyzed is the only one expected.

If $\mathbf{F}^*$ has the form

$$\begin{pmatrix} F_{11} & F_{12} \\ F_{21} & F_{22} \end{pmatrix} \tag{17}$$

in an orthonormal basis, then $\mathbf{H}(\pi/2)\mathbf{F}^*\mathbf{H}(\pi/2)^T$ has the form

$$\begin{pmatrix} F_{22} & -F_{21} \\ -F_{12} & F_{11} \end{pmatrix} \tag{18}$$

in the same basis. Referring to the results in Section 4, we can see that the pairs of deformation gradients in the equibiaxial case are related approximately by (17) and (18).

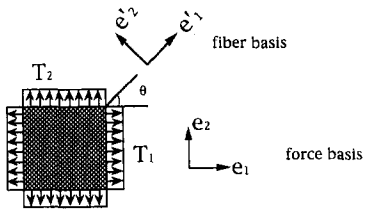

Fig. 6 Definitions of the force and fiber bases

It is often expected that a symmetry-induced nonuniqueness, such as the one analyzed here, has as its origins a bifurcation from a more symmetric deformation, which might occur at some different equibiaxial stress. No such bifurcation was detected in any of the tests in the range of loading suitable for the machine.

6 Strain-Energy Function in Inextensible Fiber Case

We have assumed that the strain energy of the cloth is a function of deformation gradient $\mathbf{F}$. In the general orthotropic case, this function depends on several invariants. We want to simplify this strain-energy function by using some available information. In previous work on similar materials by Pipkin and Rivlin (Pipkin, 1974 and 1987; Pipkin and Rivlin, 1963; Rivlin, 1955), the fibers have been treated as inextensible. In order to check this assumption in our material, let $\mathbf{e}'_1$, $\mathbf{e}'_2$ be an orthonormal basis along the fibers of the cloth in the undistorted configuration R (see Fig. 6). We assume that the tensor $\mathbf{C}$ has the following form:

$$\mathbf{C} = \mathbf{F}^T\mathbf{F} = \begin{pmatrix} C_{11} & C_{12} \\ C_{12} & C_{22} \end{pmatrix} \tag{19}$$

in the $\mathbf{e}'_1$, $\mathbf{e}'_2$ basis. It is convenient to use the basis $\mathbf{e}'_1$, $\mathbf{e}'_2$ for the derivation of the strain energy, since the argument of this function assumes a simple form in this basis.

We measured C_{11} and C_{22} when different biaxial loads were applied. The results indicate that the assumption of inextensibility is fairly reasonable (see the data in the last two columns of Tables 3 and 4), although the extension in the fiber directions was larger than the typical scatter of $\|\mathbf{F}\|$. Our observations suggested that the origin of this slight extensibility was due mainly to the bending of the fibers of the cloth. Since these fibers were forced to pass over and under each other due to the weave of the cloth, there was noticeable bending of the fibers when the tension was applied.

Under the inextensible assumption for the fibers, we have

$$C_{11} = F_{11}^2 + F_{21}^2 = 1, \tag{20}$$

and

$$C_{22} = F_{12}^2 + F_{22}^2 = 1. \tag{21}$$

Downloaded 04 May 2010 to 171.66.16.28. Redistribution subject to ASME license or copyright; see http://www.asme.org/terms/Terms_Use.cfm

Thus the strain-energy function depends only upon C_{12}. According to (20) and (21) we have, in the basis $(\mathbf{e}'_1, \mathbf{e}'_2)$,

$$\mathbf{F} = \begin{pmatrix} \cos\alpha & \sin\beta \\ \sin\alpha & \cos\beta \end{pmatrix}. \tag{22}$$

Then

$$\mathbf{C} = \mathbf{F}^T\mathbf{F} = \begin{pmatrix} 1 & \sin(\alpha+\beta) \\ \sin(\alpha+\beta) & 1 \end{pmatrix}. \tag{23}$$

Note that $\alpha + \beta$ is the angle change experienced by the originally orthogonal fibers during deformation. Let us assume that the strain-energy function has the following form:

$$\varphi = \phi(C_{12}), \quad -1 < \mathbf{C}_{12} < 1. \tag{24}$$

We define the total potential energy as in (9), which has the alternative form (12). Using $(24)_2$ we assume $|\alpha + \beta| < 90$ deg, which has the geometric interpretation of forbidding the fibers to become parallel.

A necessary and sufficient condition that a homogeneous deformation $\mathbf{y}(\mathbf{x}) = \mathbf{F}\mathbf{x}$ minimize the total potential energy is that it minimizes the integrand

$$\phi - \mathbf{F}\cdot\mathbf{T}. \tag{25}$$

Under the test machine (force) basis $\mathbf{e}_1$ and $\mathbf{e}_2$ (see Fig. 6), the expression for $\mathbf{T}$ in (25) is

$$\mathbf{T} = \sum_{i=1}^{2} T_i \mathbf{e}_i \otimes \mathbf{e}_i, \tag{26}$$

where $T_i > 0$. Let θ represent the angle between the fiber direction and the force direction (as shown in Fig. 6). In order to bring out the dependence on θ we write the expression (26) in the $\mathbf{e}'_1$ and $\mathbf{e}'_2$ basis, which gives

$$\mathbf{T} = \begin{pmatrix} T_1\cos^2\theta + T_2\sin^2\theta & (T_2 - T_1)\sin\theta\cos\theta \\ (T_2 - T_1)\sin\theta\cos\theta & T_2\cos^2\theta + T_1\sin^2\theta \end{pmatrix}. \tag{27}$$

Then we have

$$\begin{aligned} E := \phi - \mathbf{F}\cdot\mathbf{T} = \phi(\sin(\alpha+\beta)) \\ -(T_1\cos^2\theta + T_2\sin^2\theta)\cos\alpha \\ -(T_1\sin^2\theta + T_2\cos^2\theta)\cos\beta \\ -(T_2 - T_1)\sin\theta\cos\theta(\sin\alpha + \sin\beta). \end{aligned} \tag{28}$$

In order to discuss the stability of the deformation, we study the formula (28). If (α^*, β^*) is a local minimizer, then

$$\left.\frac{\partial E}{\partial\alpha}\right|_{\alpha^*,\beta^*} = \left.\frac{\partial E}{\partial\beta}\right|_{\alpha^*,\beta^*} = 0. \tag{29}$$

These give two equations for the determination of α^* and β^* which can be put in the forms

$$\begin{aligned} (T_1\cos^2\theta + T_2\sin^2\theta)\sin\alpha^* \\ +(T_1 - T_2)\sin\theta\cos\theta\cos\alpha^* \\ = (T_2\cos^2\theta + T_1\sin^2\theta)\sin\beta^* \\ +(T_1 - T_2)\sin\theta\cos\theta\cos\beta^* \end{aligned} \tag{30}$$

$$\phi'(\sin(\alpha^* + \beta^*)) = \frac{-(T_1\cos^2\theta + T_2\sin^2\theta)\sin\alpha^* + (T_2 - T_1)\sin\theta\cos\theta\cos\alpha^*}{\cos(\alpha^* + \beta^*)}. \tag{31}$$

The first of these conditions is a universal relation, expressing the fact that $\mathbf{T}\mathbf{F}^{*\mathrm{T}}$ is symmetric. This condition effectively determines the rigid rotation of the specimen.

If we let

$$A = \frac{\partial^2 E}{\partial\alpha^2}, \quad B = \frac{\partial^2 E}{\partial\alpha\partial\beta}, \quad C = \frac{\partial^2 E}{\partial\beta^2},$$

sufficient conditions for the potential energy E to have a local minimum at (α^*, β^*) are (29) and

$$B^2 - AC|_{\alpha^*,\beta^*} < 0, \tag{32}$$

$$A|_{\alpha^*,\beta^*} > 0. \tag{33}$$

Substituting A, B, and C into (32) we get the following condition for local stability:

$$\phi'' J_2 > \frac{J_1 J_2 - J_3 - J_4}{\cos^2(\alpha^* + \beta^*)} \tag{34}$$

where

$$\begin{aligned} J_1 = \phi'\sin(\alpha^* + \beta^*) \\ = \tan(\alpha^* + \beta^*)\big(-(T_1\cos^2\theta + T_2\sin^2\theta)\sin\alpha^* \\ +(T_2 - T_1)\sin\theta\cos\theta\cos\alpha^*\big), \end{aligned}$$

$$\begin{aligned} J_2 = (T_1\sin^2\theta + T_2\cos^2\theta)\cos\beta^* \\ +(T_2 - T_1)\sin\theta\cos\theta\sin\beta^* \\ +(T_1\cos^2\theta + T_2\sin^2\theta)\cos\alpha^* \\ +(T_2 - T_1)\sin\theta\cos\theta\sin\alpha^*, \end{aligned}$$

$$\begin{aligned} J_3 = (T_2 - T_1)\sin\theta\cos\theta \\ \times\big[(T_1\cos^2\theta + T_2\sin^2\theta)\cos\alpha^*\sin\beta^* \end{aligned}$$

Table 3 θ = 22.5 deg

Force (N)		C_{11}	C_{22}
T_1	T_2		
26.7	17.8	0.9999	0.9955
26.7	26.7	0.9984	1.0009
35.6	26.7	1.0017	1.0003
35.6	35.6	0.9991	1.0048
26.7	35.6	0.9996	1.0088
26.7	26.7	0.9998	1.0040
17.8	26.7	1.0004	1.0086
17.8	26.7	1.0006	1.0089
26.7	26.7	0.9994	1.0040
26.7	35.6	1.0012	1.0087
35.6	35.6	1.0003	1.0060
35.6	26.7	0.9997	1.0011
26.7	26.7	1.0009	1.0027
26.7	17.8	1.0005	0.9984

Table 4 θ = 35 deg

Force (N)		C_{11}	C_{22}
T_1	T_2		
17.8	26.7	0.9960	0.9997
26.7	26.7	0.9988	1.0022
26.7	35.6	0.9944	1.0018
35.6	35.6	0.9977	1.0048
35.6	26.7	1.0040	1.0027
26.7	26.7	1.0019	1.0034
26.7	17.8	1.0060	1.0016
26.7	17.8	1.0049	0.9992
26.7	26.7	1.0041	1.0026
35.6	26.7	1.0042	1.0031
35.6	35.6	1.0010	1.0053
26.7	35.6	0.9964	1.1132
26.7	26.7	0.9983	1.0047
17.8	26.7	0.9926	1.0027

Downloaded 04 May 2010 to 171.66.16.28. Redistribution subject to ASME license or copyright; see http://www.asme.org/terms/Terms_Use.cfm

$$+\left(T_1 \sin^2\theta + T_2 \cos^2\theta\right)\sin\alpha^* \cos\beta^*$$
$$+(T_2 - T_1)\sin\theta\cos\theta\sin\alpha^*\sin\beta^*\Big],$$
$$J_4 = \left(T_1\cos^2\theta + T_2\sin^2\theta\right)$$
$$\times\left(T_1\sin^2\theta + T_2\cos^2\theta\right)\cos\alpha^*\cos\beta^*.$$

Similarly, substituting A into (33) and using (31), we have

$$\phi'' > \frac{-\left(T_1\cos^2\theta + T_2\sin^2\theta\right)(\tan(\alpha^*+\beta^*)\sin\alpha^* + \cos\alpha^*)}{\cos^2(\alpha^*+\beta^*)} + \frac{(T_2 - T_1)\sin\theta\cos\theta(\tan(\alpha^*+\beta^*)\cos\alpha^* - \sin\alpha^*)}{\cos^2(\alpha^*+\beta^*)}. \tag{35}$$

Hence, in the case $J_2 > 0$ (which is the case in all of our experiments) sufficient conditions for stability represent a simple lower bound on ϕ'', either (34) or (35), which depends only on the load and the deformation. These conditions are necessary if equality is allowed.

Now let us specialize to the situation of $T_1 = T_2 = :T > 0$. In this case (30) becomes

$$\sin\alpha^* = \sin\beta^*. \tag{36}$$

Using $|\alpha + \beta| < 90$ deg we get from (36)

$$\alpha^* = \beta^* = :\gamma. \tag{37}$$

The conditions (34) and (35) in the equibiaxial case reduce to the following forms:

$$\phi'' > -\frac{T(2\tan 2\gamma \sin\gamma + \cos\gamma)}{2\cos^2 2\gamma}, \tag{38}$$

and

$$\phi'' > -\frac{T(\cos\gamma + \tan 2\gamma \sin\gamma)}{\cos^2 2\gamma}. \tag{39}$$

According to (22) and (37), the locally stable deformation gradient has the following form:

$$\mathbf{F} = \begin{pmatrix} \cos\gamma & \sin\gamma \\ \sin\gamma & \cos\gamma \end{pmatrix}. \tag{40}$$

At the same time, the total potential energy function becomes

$$E = \phi - \mathbf{F}\cdot\mathbf{T} = \phi(\sin 2\gamma) - 2T\cos\gamma. \tag{41}$$

If we change γ to $-\gamma$, the total potential energy will stay the same. This change in the sign of γ is equivalent to the symmetry transformation $\mathbf{H}(n\pi/2)$, where n is odd integer. The resulting deformation gradient (40) will change to the form

$$\mathbf{F} = \begin{pmatrix} \cos\gamma & -\sin\gamma \\ -\sin\gamma & \cos\gamma \end{pmatrix}. \tag{42}$$

Now let us transform (40) and (42) into the force basis. We get in the basis $(\mathbf{e}_1, \mathbf{e}_2)$

$$\mathbf{F} = \begin{pmatrix} \cos\gamma - 2\sin\gamma\sin\theta\cos\theta & -\cos 2\theta\sin\gamma \\ -\sin 2\theta\sin\gamma & \cos\gamma + 2\sin\gamma\sin\theta\cos\theta \end{pmatrix} \tag{43}$$

and

$$\mathbf{F} = \begin{pmatrix} \cos\gamma + 2\sin\gamma\sin\theta\cos\theta & \cos 2\theta\sin\gamma \\ \sin 2\theta\sin\gamma & \cos\gamma - 2\sin\gamma\sin\theta\cos\theta \end{pmatrix}. \tag{44}$$

If we compare (43) and (44) with Table 1 and Table 2, we find that the deformation gradients in these tables have the forms of (43) and (44).

Further, using the assumption of inextensible cords and the stability conditions given above, in Section 7 we can restrict the possible forms of the energy function by measuring the angles α and β of the deformed fibers.

7 Evaluation of the Strain-Energy Function

In order to find the strain-energy function, several experiments were carried out in our biaxial machine. In these experiments, pieces of cloth which were cut at $\theta = 22.5$ deg and $\theta = 35$ deg were tested under different loads and the deformations were recorded, respectively. To reveal the nature of $d\phi/dC_{12}$ versus C_{12} we decided to take the average values of data, bearing in mind the scatter discussed at the beginning of Section 4. Besides C_{12} and $d\phi/dC_{12}$, the right-hand sides of inequalities (34) and (35) were also calculated for the purpose of checking the stability. From the direct measurements of the deformation gradient $\mathbf{F}$, we can compute C_{12} and, from Eq. (31), ϕ' (see Table 5 for these measured data).

$d\phi/dC_{12}$ versus C_{12} was plotted as shown in Fig. 5, and it was found that all the points in the central part belonged to the equibiaxial load, i.e., $T_1 = T_2$. Among those points, the positive $d\phi/dC_{12}$ points correspond to the negative C_{12} and the negative $d\phi/dC_{12}$ points corresponds to the positive C_{12}.

According to the experimental results, there are several possible strain-energy functions which are consistent with the experimental data. Since the strain-energy function is an even function of C_{12} by (7), we only need to discuss it for $C_{12} \geq 0$.

Hypothesis 1 is shown in Fig. 8. From this assumption, the strain-energy function ϕ has the shape as shown in Fig. 9.

Let us discuss the stability for an equibiaxial load case. Equation (29) is satisfied at $\alpha = \beta = 0$. The second derivative tests (conditions (38) and (39)) have the forms

$$\phi'' > -\frac{T}{2} \tag{45}$$

and

Table 5

Force (N)		C_{12}	$\frac{d\phi}{dC_{12}}$
T_1	T_2		
24.5	15.5	0.1204	1.9656
24.5	24.5	0.0219	-0.1731
33.4	24.5	0.0881	1.8623
33.4	33.4	0.0247	-0.2700
24.5	33.4	-0.0734	-1.8548
24.5	24.5	-0.0227	0.3560
15.5	24.5	-0.1231	-1.8783
33.4	33.4	-0.0156	0.3653
15.5	28.9	-0.1888	-2.6175
28.9	15.5	0.1851	2.6896
33.4	20.0	0.1808	2.3652
20.0	33.4	-0.1435	-2.7514
26.7	31.2	-0.0436	-0.7779
15.5	20.0	-0.0503	-1.0756
24.5	20.0	0.0530	0.9990
28.9	24.5	0.0456	1.0075
20.0	15.5	0.0553	1.0920

Downloaded 04 May 2010 to 171.66.16.28. Redistribution subject to ASME license or copyright; see http://www.asme.org/terms/Terms_Use.cfm

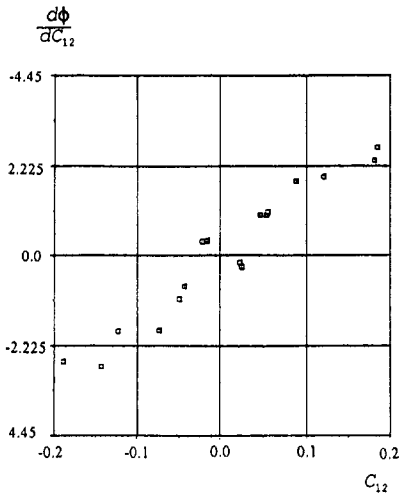

Fig. 7 $d\phi / dC_{12}$ versus C_{12} from Experimental data, Table 5

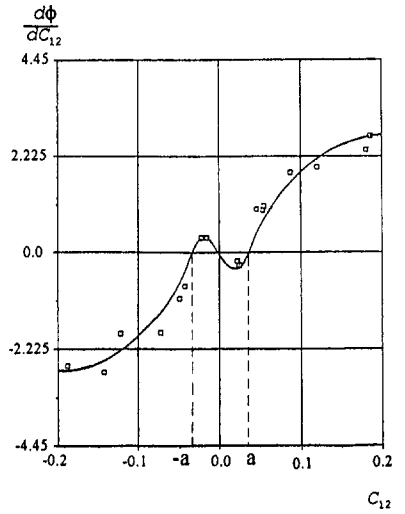

Fig. 8 $d\phi / dC_{12}$ versus C_{12} corresponding to Hypothesis 1

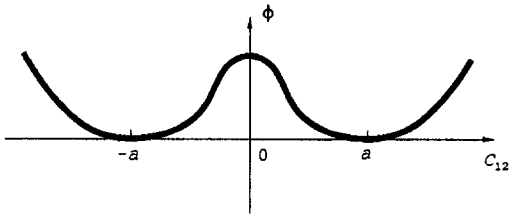

Fig. 9 Strain-energy function corresponding to Hypothesis 1

$$\phi'' > -T \tag{46}$$

These conditions are inconclusive because the precise value of $\phi''(0)$ is not known. However, Hypothesis 1 with ϕ'' sufficiently negative near $C_{12} = 0$ would rule out a locally stable equilibrium near $C_{12} = 0$, consistent with experiments. Of course, it must be appreciated that this hypothesis cannot be applied to the situation of zero load, because the natural state $\alpha = \beta = 0$ appears to be stable under zero load.

In order to discuss the possible global minima, let us rewrite (41) in the following form:

$$E = \phi(C_{12}) - 2T\cos\left(\frac{1}{2}\sin^{-1} C_{12}\right). \tag{47}$$

Subtracting $2T\cos(1/2\sin^{-1} C_{12})$ from Fig. 9 yields Fig. 10.

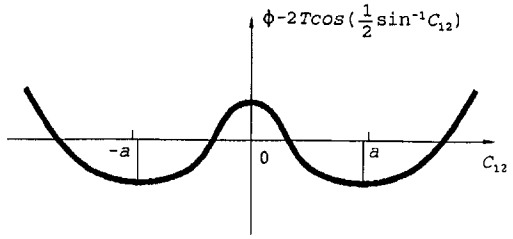

Fig. 10 The function $\phi(C_{12}) - 2T\cos\left(1/2\sin^{-1} C_{12}\right)$ under Hypothesis 1

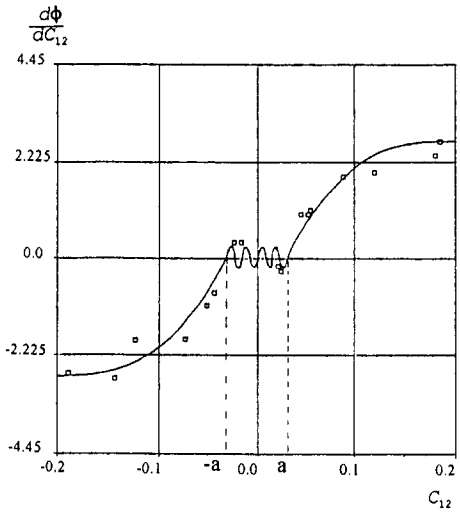

Fig. 11 $d\phi / dC_{12}$ versus C_{12} corresponding to Hypothesis 2

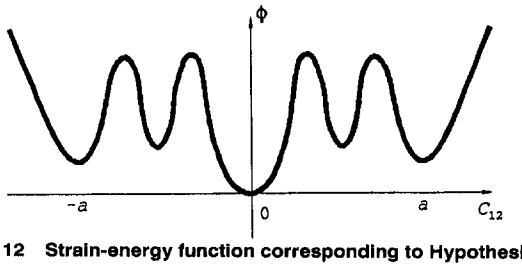

Fig. 12 Strain-energy function corresponding to Hypothesis 2

Since $2T\cos(1/2\sin^{-1} C_{12})$ is concave and almost flat between $C_{12} = 0$ and $C_{12} = a$, a global minimum is expected just to the left of $C_{12} = a$, as shown in Fig. 10. Therefore, Hypothesis 1 is at least consistent with all the measured data.

Hypothesis 2 is based upon the curve of $d\phi/dC_{12}$ versus C_{12} as shown in the Fig. 11. The strain energy function has some wells as shown in Fig. 12. In this case we assume that the well at $C_{12} = 0$ has the lowest value. Checking the function (41) at $C_{12} = 0$ gives

$$E = \phi(0) - 2T = -2T. \tag{48}$$

This is the global minimum. Hence, if Hypothesis 2 was the case, we expect to have observed deformation $\alpha = \beta = 0$, particularly during loading with $T_1 = T_2$ beginning at the natural state. Since we did not observe $\alpha = \beta = 0$ in any experiment, we conclude that Hypothesis 2 is not the case.

Hypothesis 3 is also based upon a similar curve of $d\phi/dC_{12}$ versus C_{12} as that shown in the Fig. 11 for Hypothesis 2, but the shape of the strain energy function is as shown in Fig. 13. The difference from Hypothesis 2 is that the two outside wells have lower values than those inside.

Similarly, subtracting $2T\cos(1/2\sin^{-1} C_{12})$ from Fig. 13 yields Fig. 14. Depending on the relative heights of the inside wells relative to the two outside wells, we can retain the

Downloaded 04 May 2010 to 171.66.16.28. Redistribution subject to ASME license or copyright; see http://www.asme.org/terms/Terms_Use.cfm

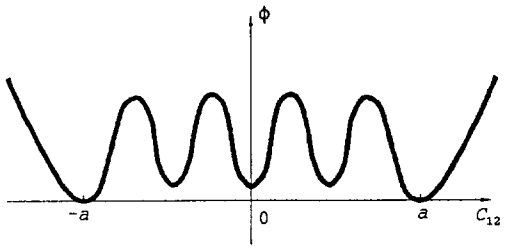

Fig. 13 Strain-energy function corresponding to Hypothesis 3

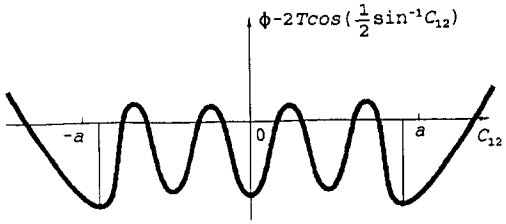

Fig. 14 The function $\phi(C_{12}) - 2T\cos\left(1/2\sin^{-1}C_{12}\right)$ under Hypothesis 3

feature that there are global minima near $\pm a$. In addition, there remain several local minimizers in the interval $(-a, a)$.

From the above discussion, we see that Hypothesis 1 and Hypothesis 3 are consistent with our experiments and obviously there are many other possibilities.

Since it may not be possible to observe any local minimizers, it is not known how many potential wells lie between $C_{12} = -a$ and $C_{12} = a$. From experience with cloth-type materials under no loads, we know that cloth has many stable (or metastable) deformed configurations. In fact, when the cloth was unloaded along an equibiaxial loading path from an unsymmetrical state, it remained unsymmetrical even under zero load. It is thus conceivable that the cloth is modeled by a ϕ with many potential wells between $-a$ and $+a$. It is interesting to note that the point $C_{12} = 0$ would become stable for sufficiently large loads under any of the hypotheses 1–3. This was not observed in our limited loading range.

Acknowledgment

The authors thank ONR (N00014-91-J-4034), AFOSR (AFOSR-91-0301), NSF (NSF/DMS-8718881) and ARO (28987 MA/27063 MA-SM) for supporting this work.

References

Ball, J. M., and Schaeffer, D. G., 1983, "Bifurcation and Stability of Homogeneous Equilibrium Configurations of an Elastic Body under Dead-Load Tractions," *Mathematical Proceeding Cambridge Philosophical Society*, Vol. 94, pp. 315–339.

Chadwick, P., 1976, *Continuum Mechanics: Concise theory and problems*, George Allen & Unwin, London, pp. 22, 138.

Chen, Y. C., 1987, "Stability of Homogeneous Deformations of an Incompressible Elastic Body under Dead-Load Surface Tractions," *Journal of Elasticity*, Vol. 17, pp. 223–248.

Kearsley, E. A., 1986, "Asymmetric Stretching of a Symmetrically Loaded Elastic Sheet," *International Journal of Solids and Structures*, Vol. 22, pp. 111–119.

MacSithigh, G. P., 1986, "Energy-Minimal Finite Deformations of a Symmetrically Loaded Elastic Sheet," *Quarterly Journal of Mechanics and Applied Mathematics*, Vol. 39, pp. 111–123.

Pipkin, A. C., 1974, "Generalized Plane Deformations of Ideal Fiber-Reinforced Materials," *Quarterly Applied Mathematics*, Vol. 32, pp. 253–263.

Pipkin, A. C., 1974, "Infinitesimal Plane Wrinkling of Inextensible Networks," *Journal of Elasticity*, Vol. 17, pp. 35–52.

Pipkin, A. C., and Rivlin, R. S., 1963, "Minimum-Weight Design for Pressure Vessels Reinforced with Inextensible Fibers," ASME JOURNAL OF APPLIED MECHANICS, Vol. 30, pp. 103–108.

Rivlin, R. S., 1955, "Plane Strain of a Net Formed by Inextensible Cords," *Journal of Rational Mechanics and Analysis*, Vol. 4, pp. 951–974.

Rivlin, R. S., 1948, "Large Elastic Deformations of Isotropic Materials II: Some Uniqueness Theorems for Pure Homogeneous Deformation," *Philosophical Transactions, Royal Society of Lond.*, Vol. A240, pp. 491–508.

Rivlin, R. S., 1974, "Stability of Pure Homogeneous Deformation of an Elastic Cube under Dead Loading," *Quarterly Applied Mechanics*, Vol. 32, pp. 265–271.

Rivlin, R. S., and Saunders, D. W., 1951, "Large Elastic Deformations of Isotropic Materials VII: Experiments on the Deformation of Rubber," *Philosophical Transactions, Royal Society of Lond.*, Vol. A243, pp. 251–288.

Treloar, L. R. G., 1948, "Stress and Birefringence in Rubber Subjected to General Homogeneous Strain," *Proceedings, Physics Society*, Vol. 60, pp. 135–144.

Treloar, L. R. G., 1949, *Physics of Rubber Elasticity*, Oxford University Press, London, pp. 116.

Downloaded 04 May 2010 to 171.66.16.28. Redistribution subject to ASME license or copyright; see http://www.asme.org/terms/Terms_Use.cfm

A Time Domain Substructure Synthesis Method for Viscoelastic Structures

Duan Qian
Ph.D., Senior Engineer,
de Havilland, Inc.
Downsview, ON M3K 1Y5, Canada

J. S. Hansen
Professor,
Institute for Aerospace Studies,
University of Toronto,
Toronto, ON M3H 5T6, Canada

The method of substructure synthesis, originally conceived for undamped and viscously damped systems, has been extended to systems with viscoelastic damping in the hereditary integral form. Based on a new variational principle, the substructure synthesis method is formulated in the time domain. The displacement in each substructure is represented by a set of real admissible trial vectors. The traditional state space formulation is avoided by the proposed method so that the approach is independent of the form of viscoelastic models. Effectiveness of the method is illustrated through numerical examples.

Introduction

Dynamic analysis of large complex structures is usually performed using the finite element method or other discretization techniques. The result is a large system of ordinary differential equations in time. Then, substructure synthesis techniques are used to reduce the problem size while still retaining desired accuracy. The approach consists of the following steps: (1) divide the system into substructures, (2) approximate the displacement in each substructure with trial vectors, (3) couple the substructures by enforcing compatibility at interfaces, (4) solve the reduced problem, and (5) transform results back to the original system.

Since the first paper by Hurty (1965) on this subject, numerous substructure synthesis methods have been documented. Most of the work has been related to the analysis of undamped structures using substructure modes as trial vectors (Dowell, 1971; Kubomura, 1982; Suarez and Singh, 1991). The treatment for proportional viscous damping is straightforward since the eigenvectors are those of the undamped structure. Nonproportional viscous damping is traditionally accommodated by a state space formulation leading to complex substructure modes (Hasselman and Kaplan, 1974; Béliveau and Soucy, 1985; Craig and Ni, 1989). The complex modes are more expensive to compute; also they cannot be used in the time domain because of the resulting complex matrices. As pointed out by Meirovitch and Hale (1981), a suitable set of admissible vectors is all that is necessary to represent a substructure since the synthesis may be regarded as the Rayleigh-Ritz method. Hale and Bergman (1985) applied this concept to structures with viscous damping. In their state space formulation, the Ritz expansion and interface compatibility were applied to the displacement as well as the velocity. The research done on transient response is much less complete than that dealing with eigensolution substructure synthesis; current methods are available only for systems with proportional viscous damping based on modal superposition (Yee and Tsuei, 1990).

Composite materials are classified as viscoelastic. It is both desirable and possible to formulate viscoelastic damping matrices in a manner and with the accuracy of stiffness matrix calculation in the finite element method (Qian, 1993). The introduction of general viscoelastic damping significantly complicates the motion equations, hence order reduction is even more useful for numerical solutions. This paper extends previous work by including structures with nonproportional viscoelastic damping in the hereditary integral form. Based on a new variational principle containing initial conditions and initial strain memory effects, a substructure synthesis method is formulated in the time domain for the solution of transient problems. The solution of eigenvalue problems or frequency response can be readily made through a Laplace or Fourier transformation of the reduced motion equations if the transform of the viscoelastic constitutive relation exists. The traditional state space formulation for systems with viscous damping is avoided in the proposed approach. Traditional state space techniques are undesirable for systems with general viscoelastic damping for the following reasons. First, state space formulations depend on the form of the viscoelastic damping, which makes a unified method very difficult. Secondly, the size of the state space substructure equations

Contributed by the Applied Mechanics Division of THE AMERICAN SOCIETY OF MECHANICAL ENGINEERS for presentation at the Joint Applied Mechanics and Material Division Summer Annual Meeting of the ASME, Los Angeles, CA, June 28–30, 1995.

Discussion on this paper should be addressed to the Technical Editor, Professor Lewis T. Wheeler, Department of Mechanical Engineering, University of Houston, Houston, TX 77204-4792, and will be accepted until four months after final publication of the paper itself in the ASME JOURNAL OF APPLIED MECHANICS.

Manuscript received by the ASME Applied Mechanics Division, July 23, 1993; final revision, Aug. 16, 1994. Associate Technical Editor: R. Abeyaratne.

Paper No. 95-APM-2.

Copyright © 1995 by ASME

Downloaded 04 May 2010 to 171.66.16.28. Redistribution subject to ASME license or copyright; see http://www.asme.org/terms/Terms_Use.cfm

increases with the number of viscoelastic constants used in the model. In addition, Ritz expansions for the newly introduced state variables are required and the geometric compatibility between substructures has also to be treated in the new variables. With the proposed method, each substructure is represented by a set of real admissible trial vectors on the basis of a Rayleigh-Ritz approach. Eigenvectors of the corresponding undamped substructure and Ritz vectors obtained by spatial discretization using simple functions are recommended as trial vectors. The method is independent of the viscoelastic damping models and the effort spent on the reduction process is similar to that of classic component mode synthesis for undamped systems. In the absence of damping, it reduces to the classic method.

Viscoelastic Constitutive Relations

Based on the hypothesis that the stress history is completely determined by the strain history as well as linearity, continuity, causality, and translation invariance in time, an integral representation can be deduced for the most general linear hereditary stress-strain law. If the strain derivative $\dot{\epsilon}_{ij}(t)$ is assumed continuous on the interval $[0, \infty)$ and $\dot{\epsilon}_{ij}(t) = 0$ in $(-\infty, 0)$, then the dependence of the stress on the complete history of strain can be expressed as (Christensen, 1982)

$$\sigma_{ij}(t) = \hat{G}_{ijkl}(t)\epsilon_{kl}(0) + \int_0^t \hat{G}_{ijkl}(t-\tau)\dot{\epsilon}_{kl}(\tau)d\tau, \quad t \in [0, \infty) \quad (1)$$

where $\hat{G}_{ijkl}(t)$ are termed relaxation functions and comprise a fourth-order tensor that is continuous on $[0, \infty)$ and $\hat{G}_{ijkl}(t) = 0$ in $(-\infty, 0)$. The following symmetric properties exist for relaxation functions:

$$\hat{G}_{ijkl}(t) = \hat{G}_{jikl}(t) = \hat{G}_{ijlk}(t) = \hat{G}_{klij}(t). \quad (2)$$

It is convenient and sometime necessary to decompose $\hat{G}_{ijkl}(t)$ into two parts,

$$\hat{G}_{ijkl}(t) = E_{ijkl} + G_{ijkl}(t) \quad (3)$$

where

$$E_{ijkl} = \lim_{t\to\infty} \hat{G}_{ijkl}(t); \quad \lim_{t\to\infty} G_{ijkl}(t) = 0. \quad (4)$$

The symmetric properties in Eq. (2) exist for E_{ijkl} and $G_{ijkl}(t)$. With Eq. (3), Eq. (1) becomes

$$\sigma_{ij}(t) = E_{ijkl}\epsilon_{kl}(t) + G_{ijkl}(t)\epsilon_{kl}(0) + \int_0^t G_{ijkl}(t+\tau)\dot{\epsilon}_{kl}(\tau)d\tau, \quad t \in [0, \infty). \quad (5)$$

The time dependence of $G_{ijkl}(t)$ can be expressed as a series of exponentials, such as by Staverman and Schwarzl (1952)

$$G_{ijkl}(t) = \sum_{s=1}^{n} G^{(s)}_{ijkl} e^{-\theta_s t}. \quad (6)$$

The problem of requiring a large number of $G^{(s)}_{ijkl}$ and relaxation constants θ_s to describe a viscoelastic material prompts a representation with a continuous distribution of relaxation constants. This was done by Biot (1954)

$$G_{ijkl}(t) = \int_0^\infty G^{(0)}_{ijkl}(\theta)\gamma(\theta)e^{-\theta t}d\theta. \quad (7)$$

The classic Kelvin-Voigt model, comprised of a spring in parallel with a dashpot,

$$\sigma(t) = E\epsilon(t) + C\dot{\epsilon}(t) \quad (8)$$

represents a special case of (5) when

$$G(t) = C\delta(t), \quad \epsilon(0) = 0 \quad (9)$$

where $\delta(t)$ is the Dirac delta function. The constitutive relation (8) represents the commonly used viscous damping model.

Motion Equations

Discretized motion equations of a viscoelastic system have the following general form:

$$\mathbf{M}\ddot{\mathbf{U}} + \mathbf{D}*\dot{\mathbf{U}} + \mathbf{K}\mathbf{U} = \mathbf{F} - \mathbf{D}\mathbf{U}(0), \quad t \in [0, \infty) \quad (10)$$

$$\mathbf{U}(0) = \mathbf{W}, \quad \dot{\mathbf{U}}(0) = \mathbf{V} \quad (11)$$

where "$*$" denotes the Riemann convolution

$$\mathbf{D}*\dot{\mathbf{U}} = \int_0^t \mathbf{D}(t-\tau)\dot{\mathbf{U}}(\tau)d\tau. \quad (12)$$

Matrices $\mathbf{M}$, $\mathbf{D}(t)$, and $\mathbf{K}$ denote the mass, damping, and stiffness, respectively. They are symmetric and further $\mathbf{M}$ is positive definite. Matrix $\mathbf{K}$ can be used in deriving the damping matrix $\mathbf{D}(t)$ when appropriate time dependence is accounted for; the former depends on the elastic moduli E_{ijkl} while the latter depends on the relaxation moduli $G_{ijkl}(t)$ (Qian, 1993). The term $\mathbf{D}\mathbf{U}(0)$ represents the memory effect of initial strain in accordance with the initial displacement vector $\mathbf{U}(0)$. Displacement and force vectors $\mathbf{U}$ and $\mathbf{F}$ represent generalized displacements and forces. Vectors $\mathbf{W}$ and $\mathbf{V}$ denote the prescribed initial displacements and velocities.

For a structure with viscous damping, Eq. (9) yields

$$\mathbf{D}(t) = \mathbf{C}\delta(t), \quad \mathbf{C}\mathbf{U}(0) = 0 \quad (13)$$

and the system of integro-differential Eqs. (10) degenerates into a set of second-order differential equations with constant coefficients

$$\mathbf{M}\ddot{\mathbf{U}} + \mathbf{C}\dot{\mathbf{U}} + \mathbf{K}\mathbf{U} = \mathbf{F}. \quad (14)$$

Variational Principle

Adopting the approach of Oden and Reddy (1976), the bilinear form of two vector functions $\mathbf{x}$ and $\mathbf{y}$ is defined as

$$\langle \mathbf{x}, \mathbf{y} \rangle = \int_0^t \mathbf{x}^T(t-\tau)\mathbf{y}(\tau)d\tau = \mathbf{x}^T * \mathbf{y}. \quad (15)$$

Also, the notation

$$\langle \mathbf{x}, \mathbf{y} \rangle_0 = \mathbf{x}^T(0)\mathbf{y}(t) = \mathbf{x}^T(0)\mathbf{y} \quad (16)$$

is adopted. In the above, it is clear that $\langle \cdot, \cdot \rangle$ commutes while $\langle \cdot, \cdot \rangle_0$ does not. That is

$$\langle \mathbf{x}, \mathbf{y} \rangle = \langle \mathbf{y}, \mathbf{x} \rangle, \quad \langle \mathbf{x}, \mathbf{y} \rangle_0 \neq \langle \mathbf{y}, \mathbf{x} \rangle_0. \quad (17)$$

A bilinear functional is defined in the following form:

$$\Pi = \frac{1}{2}\langle \mathbf{M}\dot{\mathbf{U}}, \dot{\mathbf{U}} \rangle + \frac{1}{2}\langle \mathbf{K}\mathbf{U}, \mathbf{U} \rangle + \frac{1}{2}\langle \mathbf{D}*\dot{\mathbf{U}}, \mathbf{U} \rangle + \frac{1}{2}\langle \mathbf{D}\mathbf{U}(0), \mathbf{U} \rangle - \langle \mathbf{F}, \mathbf{U} \rangle + \langle \mathbf{M}(\mathbf{U} - \mathbf{W}), \dot{\mathbf{U}} \rangle_0 - \langle \mathbf{M}\mathbf{V}, \mathbf{U} \rangle_0. \quad (18)$$

The first variation of this functional Π is

$$\delta\Pi = \frac{1}{2}\langle \mathbf{M}\delta\dot{\mathbf{U}}, \dot{\mathbf{U}} \rangle + \frac{1}{2}\langle \mathbf{M}\dot{\mathbf{U}}, \delta\dot{\mathbf{U}} \rangle + \frac{1}{2}\langle \mathbf{K}\delta\mathbf{U}, \mathbf{U} \rangle + \frac{1}{2}\langle \mathbf{K}\mathbf{U}, \delta\mathbf{U} \rangle + \frac{1}{2}\langle \mathbf{D}*\delta\dot{\mathbf{U}}, \mathbf{U} \rangle + \frac{1}{2}\langle \mathbf{D}*\dot{\mathbf{U}}, \delta\mathbf{U} \rangle + \frac{1}{2}\langle \mathbf{D}\delta\mathbf{U}(0), \mathbf{U} \rangle + \frac{1}{2}\langle \mathbf{D}\mathbf{U}(0), \delta\mathbf{U} \rangle - \langle \mathbf{F}, \delta\mathbf{U} \rangle + \langle \mathbf{M}\delta\mathbf{U}, \dot{\mathbf{U}} \rangle_0 + \langle \mathbf{M}(\mathbf{U} - \mathbf{W}), \delta\dot{\mathbf{U}} \rangle_0 - \langle \mathbf{M}\mathbf{V}, \delta\mathbf{U} \rangle_0. \quad (19)$$

Downloaded 04 May 2010 to 171.66.16.28. Redistribution subject to ASME license or copyright; see http://www.asme.org/terms/Terms_Use.cfm

The symmetry of $\mathbf{M}$ and $\mathbf{K}$ yields

$$\langle \mathbf{M}\delta\dot{\mathbf{U}}, \dot{\mathbf{U}}\rangle = \langle \mathbf{M}\dot{\mathbf{U}}, \delta\dot{\mathbf{U}}\rangle \tag{20}$$

$$\langle \mathbf{K}\delta\mathbf{U}, \mathbf{U}\rangle = \langle \mathbf{K}\mathbf{U}, \delta\mathbf{U}\rangle. \tag{21}$$

Also, the commutativity, associativity, and distributivity of the Riemann convolutions and the symmetry of the $\mathbf{D}$ matrix result in

$$\langle \mathbf{D}*\delta\dot{\mathbf{U}} + \mathbf{D}\delta\mathbf{U}(0), \mathbf{U}\rangle = \langle \mathbf{D}*\dot{\mathbf{U}} + \mathbf{D}\mathbf{U}(0), \delta\mathbf{U}\rangle. \tag{22}$$

Integrating Eq. (20) by parts

$$\langle \mathbf{M}\dot{\mathbf{U}}, \delta\dot{\mathbf{U}}\rangle = \langle \mathbf{M}\ddot{\mathbf{U}}, \delta\mathbf{U}\rangle + \langle \mathbf{M}\dot{\mathbf{U}}, \delta\mathbf{U}\rangle_0 - \langle \mathbf{M}\delta\mathbf{U}, \dot{\mathbf{U}}\rangle_0 \tag{23}$$

and substituting Eqs. (21), (22), and (23) into Eq. (19) yields the desired form

$$\delta\Pi = \langle \mathbf{M}\ddot{\mathbf{U}} + \mathbf{K}\mathbf{U} + \mathbf{D}*\dot{\mathbf{U}} + \mathbf{D}\mathbf{U}(0) - \mathbf{F}, \delta\mathbf{U}\rangle + \langle \mathbf{M}(\mathbf{U} - \mathbf{W}), \delta\dot{\mathbf{U}}\rangle_0 + \langle \mathbf{M}(\dot{\mathbf{U}} - \mathbf{V}), \delta\mathbf{U}\rangle_0. \tag{24}$$

Since $\delta\mathbf{U}$ is arbitrary in $(0, t)$ and $\delta\mathbf{U}$ and $\delta\dot{\mathbf{U}}$ are arbitrary at time t, stationarity $\delta\Pi = 0$ implies

$$\mathbf{M}\ddot{\mathbf{U}} + \mathbf{K}\mathbf{U} + \mathbf{D}*\dot{\mathbf{U}} + \mathbf{D}\mathbf{U}(0) - \mathbf{F} = \mathbf{0}, \quad \tau \in (0, t) \tag{25}$$

$$\mathbf{M}[\mathbf{U}(0) + \mathbf{W}] = \mathbf{0}, \quad \mathbf{M}[\dot{\mathbf{U}}(0) - \mathbf{V}] = \mathbf{0}. \tag{26}$$

Since t is arbitrary over the range $(0, \infty)$ and $\mathbf{M}$ is positive definite, the above are equivalent to Eqs. (10) and (11).

Substructure Synthesis

Assume that the whole structure is divided into N substructures. The motion of each substructure s satisfies N_s simultaneous integro-differential equations

$$\mathbf{M}_s\ddot{\mathbf{U}}_s + \mathbf{D}_s*\dot{\mathbf{U}}_s + \mathbf{K}_s\mathbf{U}_s = \mathbf{F}_{E_s} + \mathbf{F}_{I_s} - \mathbf{D}_s\mathbf{U}_s(0), \quad t \in [0, \infty) \tag{27}$$

with initial conditions

$$\mathbf{U}_s(0) = \mathbf{W}_s, \quad \dot{\mathbf{U}}_s(0) = \mathbf{V}_s. \tag{28}$$

The substructure matrices $\mathbf{M}_s$, $\mathbf{D}_s(t)$ and $\mathbf{K}_s$ are symmetric and further $\mathbf{M}_s$ is positive definite. $\mathbf{U}_s$ is the generalized substructure displacement vector. The generalized force vector consists of the sum of two parts, namely, a vector $\mathbf{F}_{E_s}$ of external forces acting on substructure s and a vector $\mathbf{F}_{I_s}$ of forces exerted on the boundaries B_{rs} of substructure s by all other substructures r ($r = 1, \ldots, N$, $r \neq s$). Based on the variational principle given by Eq. (18), Eqs. (27) and (28) can be obtained as conditions for stationarity of the bilinear functional

$$\Pi_s = \frac{1}{2}\langle \mathbf{M}_s\dot{\mathbf{U}}_s, \dot{\mathbf{U}}_s\rangle + \frac{1}{2}\langle \mathbf{K}_s\mathbf{U}_s, \mathbf{U}_s\rangle + \frac{1}{2}\langle \mathbf{D}_s*\dot{\mathbf{U}}_s, \mathbf{U}_s\rangle + \frac{1}{2}\langle \mathbf{D}_s\mathbf{U}_s(0), \mathbf{U}_s\rangle - \langle \mathbf{F}_{E_s} + \mathbf{F}_{I_s}, \mathbf{U}_s\rangle + \langle \mathbf{M}_s(\mathbf{U}_s - \mathbf{W}_s), \dot{\mathbf{U}}_s\rangle_0 - \langle \mathbf{M}_s\mathbf{V}_s, \mathbf{U}_s\rangle_0. \tag{29}$$

The motion equations of the assembled system result from the conditions of stationarity of the bilinear functional

$$\Pi = \sum_{s=1}^{N} \Pi_s \tag{30}$$

while the stationary conditions are subject to internal boundary compatibility constraints between adjacent substructures. According to the force equilibrium conditions on internal boundary B_{rs} shared by substructure s and r, the force $\mathbf{F}_{I_r}|_{B_{rs}}$ exerted by substructure s on substructure r must be equal in magnitude and opposite in sign to $\mathbf{F}_{I_s}|_{B_{rs}}$ exerted by substructure r on substructure s. It is convenient to write

$$\mathbf{F}_{I_s}|_{B_{rs}} = -\mathbf{F}_{I_r}|_{B_{rs}} = \mathbf{F}_{rs}, \quad r \neq s \tag{31}$$

where intersubstructure force vector $\mathbf{F}_{rs}$ is assumed to be L_{rs}-dimensional. We have $L_{rs} = 0$ if substructure r and s do not share a common boundary. Now Π can be written as

$$\Pi = \sum_{s=1}^{N}\left\{\frac{1}{2}\langle \mathbf{M}_s\dot{\mathbf{U}}_s, \dot{\mathbf{U}}_s\rangle + \frac{1}{2}\langle \mathbf{K}_s\mathbf{U}_s, \mathbf{U}_s\rangle + \frac{1}{2}\langle \mathbf{D}_s*\dot{\mathbf{U}}_s, \mathbf{U}_s\rangle + \frac{1}{2}\langle \mathbf{D}_s\mathbf{U}_s(0), \mathbf{U}_s\rangle - \langle \mathbf{F}_{E_s}, \mathbf{U}_s\rangle\right\} - \sum_{s=1}^{N}\sum_{r=s+1}^{N}\langle \mathbf{U}_s|_{B_{rs}} - \mathbf{U}_r|_{B_{rs}}, \mathbf{F}_{rs}\rangle + \sum_{s=1}^{N}\left\{\langle \mathbf{M}_s(\mathbf{U}_s - \mathbf{W}_s), \dot{\mathbf{U}}_s\rangle_0 - \langle \mathbf{M}_s\mathbf{V}_s, \mathbf{U}_s\rangle_0\right\} \tag{32}$$

where $\mathbf{U}_r|_{B_{rs}}$ and $\mathbf{U}_s|_{B_{rs}}$ denote the parts of $\mathbf{U}_r$ and $\mathbf{U}_s$ on the internal boundary B_{rs}, respectively.

It is assumed that the number of degrees-of-freedom N_s for each substructure s is large enough that a reduction is required. The method of Rayleigh-Ritz is applied to this discrete system. The generalized displacement vector $\mathbf{U}_s$ of each substructure s is approximately represented by the sum of n_s trial vectors ϕ_{si} multiplying unknown time-dependent coefficients u_{si}

$$\mathbf{U}_s(t) = \sum_{i=1}^{n_s}\phi_{si}u_{si}(t) = \mathbf{\Phi}_s\mathbf{u}_s(t) \tag{33}$$

where $\mathbf{u}_s$ is n_s-dimensional unknown vector with $n_s \leq N_s$. The column trial vectors ϕ_{si} in $\mathbf{\Phi}_s$ are called admissible vectors by analogy to the admissible functions used in the finite element method. It is assumed that the admissible vectors $\phi_{si}(i = 1, \ldots, n_s)$ are linearly independent and satisfy the external geometric boundary conditions. Substituting Eq. (33) in Eq. (32) yields

$$\Pi = \sum_{s=1}^{N}\left\{\frac{1}{2}\langle \mathbf{m}_s\dot{\mathbf{u}}_s, \dot{\mathbf{u}}_s\rangle + \frac{1}{2}\langle \mathbf{k}_s\mathbf{u}_s, \mathbf{u}_s\rangle + \frac{1}{2}\langle \mathbf{d}_s*\dot{\mathbf{u}}_s, \mathbf{u}_s\rangle + \frac{1}{2}\langle \mathbf{d}_s\mathbf{u}_s(0), \mathbf{u}_s\rangle - \langle \mathbf{f}_{E_s}, \mathbf{u}_s\rangle\right\} - \sum_{s=1}^{N}\sum_{r=s+1}^{N}\langle (\mathbf{\Phi}_s\mathbf{u}_s)|_{B_{rs}} - (\mathbf{\Phi}_r\mathbf{u}_r)|_{B_{rs}}, \mathbf{F}_{rs}\rangle + \sum_{s=1}^{N}\left\{\langle \mathbf{m}_s(\mathbf{u}_s - \mathbf{w}_s), \dot{\mathbf{u}}_s\rangle_0 + \langle \mathbf{m}_s\mathbf{v}_s, \mathbf{u}_s\rangle_0\right\} \tag{34}$$

where the $n_s \times n_s$ reduced substructure matrices are

$$\mathbf{m}_s = \mathbf{\Phi}_s^T\mathbf{M}_s\mathbf{\Phi}_s, \quad \mathbf{d}_s(t) = \mathbf{\Phi}_s^T\mathbf{D}_s(t)\mathbf{\Phi}_s, \quad \mathbf{k}_s = \mathbf{\Phi}_s^T\mathbf{K}_s\mathbf{\Phi}_s \tag{35}$$

and the n_s-dimensional reduced substructure vectors are

$$\mathbf{f}_{E_s} = \mathbf{\Phi}_s^T\mathbf{F}_{E_s}, \quad \mathbf{w}_s = \mathbf{m}_s^{-1}\mathbf{\Phi}_s^T\mathbf{M}_s\mathbf{W}_s, \quad \mathbf{v}_s = \mathbf{m}_s^{-1}\mathbf{\Phi}_s^T\mathbf{M}_s\mathbf{V}_s. \tag{36}$$

The inverse of matrix $\mathbf{m}_s$ exists since $\mathbf{M}_s$ is positive definite and $\mathbf{\Phi}_s$ consists of linearly independent vectors. If the normalized substructure eigenvectors are used as admissible vectors, we have $\mathbf{\Phi}_s^T\mathbf{M}_s\mathbf{\Phi}_s = \mathbf{I}$ and $\mathbf{m}_s^{-1} = \mathbf{I}$. There is no order reduction if $n_s = N_s$. Consequently,

$$\mathbf{w}_s = \mathbf{\Phi}_s^{-1}\mathbf{W}_s, \quad \mathbf{v}_s = \mathbf{\Phi}_s^{-1}\mathbf{V}_s \tag{37}$$

Downloaded 04 May 2010 to 171.66.16.28. Redistribution subject to ASME license or copyright; see http://www.asme.org/terms/Terms_Use.cfm

Rewriting Eq. (34) in block-diagonal form yields

$$\Pi = \frac{1}{2}\langle \mathbf{m}_a\dot{\mathbf{u}}_a, \dot{\mathbf{u}}_a\rangle + \frac{1}{2}\langle \mathbf{k}_a\mathbf{u}_a, \mathbf{u}_a\rangle + \frac{1}{2}\langle \mathbf{d}_a * \dot{\mathbf{u}}_a, \mathbf{u}_a\rangle + \frac{1}{2}\langle \mathbf{d}_a\mathbf{u}_a(0), \mathbf{u}_a\rangle - \langle \mathbf{f}_{E_a}, \mathbf{u}_a\rangle - \langle \mathbf{C}_a\mathbf{u}_a, \mathbf{F}_{I_a}\rangle + \langle \mathbf{m}_a(\mathbf{u}_a - \mathbf{w}_a), \dot{\mathbf{u}}_a\rangle_0 - \langle \mathbf{m}_a\mathbf{v}_a, \mathbf{u}_a\rangle_0 \quad (38)$$

where with $n_a = \Sigma_{s=1}^{N} n_s$, the $n_a \times n_a$ block-diagonal matrices are

$$\mathbf{m}_a = \text{blk-diag } \mathbf{m}_s, \quad \mathbf{d}_a(t) = \text{blk-diag } \mathbf{d}_s(t), \quad \mathbf{k}_a = \text{blk-diag } \mathbf{k}_s \quad (39)$$

and the n_a-dimensional disjoint vectors are

$$\mathbf{u}_a = \left\{\mathbf{u}_1^T, \ldots, \mathbf{u}_m^T\right\}^T, \quad \mathbf{f}_{E_a} = \left\{\mathbf{f}_{E_1}^T, \ldots, \mathbf{f}_{E_m}^T\right\}^T$$
$$\mathbf{w}_a = \left\{\mathbf{w}_1^T, \ldots, \mathbf{w}_m^T\right\}^T, \quad \mathbf{v}_a = \left\{\mathbf{v}_1^T, \ldots, \mathbf{v}_m^T\right\}^T \quad (40)$$

In the above, the notation $\langle \mathbf{C}_a\mathbf{u}_a, \mathbf{F}_{I_a}\rangle$ represents the summation given by

$$\langle \mathbf{C}_a\mathbf{u}_a, \mathbf{F}_{I_a}\rangle = \sum_{s=1}^{N}\sum_{r=s+1}^{N} \langle (\mathbf{\Phi}_s\mathbf{u}_s)|_{B_{rs}} - (\mathbf{\Phi}_r\mathbf{u}_r)|_{B_{rs}}, \mathbf{F}_{rs}\rangle \quad (41)$$

where $\mathbf{F}_{I_a}$ is the L_a-dimensional vector formed by concatenating all the vectors $\mathbf{F}_{rs}$; also, $L_a = \Sigma_{s=1}^{N}\Sigma_{r=s+1}^{N} L_{rs}$. It will soon be clear that the $L_a \times n_a$ matrix $\mathbf{C}_a$ couples the substructures.

To ensure the structural integrity of the assembled system, geometric compatibility conditions are required as follows:

$$\mathbf{U}_s|_{B_{rs}} - \mathbf{U}_r|_{B_{rs}} = \mathbf{0}, \quad r, s = 1, \ldots, N, r \neq s. \quad (42)$$

Substituting Eq. (33) in Eq. (42) yields

$$(\mathbf{\Phi}_s\mathbf{u}_s)|_{B_{rs}} - (\mathbf{\Phi}_r\mathbf{u}_r)|_{B_{rs}} = \mathbf{0}, \quad r, s = 1, \ldots, N, r \neq s \quad (43)$$

and using the notation of Eq. (41), the geometric compatibility conditions become

$$\mathbf{C}_a\mathbf{u}_a = \mathbf{0}. \quad (44)$$

When adjacent substructures are connected at a single point as in the case of one-dimensional substructures, the geometric compatibility conditions can be satisfied exactly. When adjacent substructures are two or three-dimensional, however, the internal boundaries consist of lines and surfaces. During substructure order reduction the geometric boundary conditions imposed by Eq. (44) may not be satisfied exactly and therefore approximations must be made. An approach based on a weighted residual method is employed here. The L_{rs}-dimensional arbitrary vectors $\mathbf{F}_{rs}$ can be approximated by the truncated sum of l_{rs} linearly independent weighting vectors ψ_{rsj} multiplying time-dependent coefficients f_{rsj}. That is

$$\mathbf{F}_{rs}(t) = \sum_{j=1}^{l_{rs}} \psi_{rsj} f_{rsj}(t) = \mathbf{\Psi}_{rs}\mathbf{f}_{rs}(t), \quad r \neq s \quad (45)$$

where $l_{rs} \leq L_{rs}$. Equation (42) is equivalent to

$$\langle \mathbf{U}_s|_{B_{rs}} - \mathbf{U}_r|_{B_{rs}}, \mathbf{F}_{rs}\rangle = 0, \quad r, s = 1, \ldots, N, r \neq s \quad (46)$$

being satisfied for all possible vectors $\mathbf{F}_{rs}$. Substituting Eqs. (33) and (45) in Eq. (46) shows that the compatibility conditions are satisfied approximately if each of the following l_{rs} conditions are satisfied:

$$\mathbf{\Psi}_{rs}^T\left[(\mathbf{\Phi}_s\mathbf{u}_s)|_{B_{rs}} - (\mathbf{\Phi}_r\mathbf{u}_r)|_{B_{rs}}\right] = \mathbf{0}, \quad r, s = 1, \ldots, N, r \neq s. \quad (47)$$

Note that the compatibility conditions on B_{rs} are satisfied exactly if we let $l_{sr} = L_{rs}$ when $L_{rs} \leq \min(n_r, n_s)$ in Eq. (45). Equation (47) can be written in assembled form

$$\mathbf{\Psi}_a^T\mathbf{C}_a\mathbf{u}_a = \mathbf{0} \quad (48)$$

where the $n_a \times l_a$ matrix $\mathbf{\Psi}_a = \text{blk-diag}\,\mathbf{\Psi}_{rs}$ contains $l_a = \Sigma_{s=1}^{N}\Sigma_{r=s+1}^{N} l_{rs}$ weighting vectors.

When the approximate geometric compatibility conditions (48) are applied, the coupled reduced order system has only $n = n_a - l_a$ independent degrees-of-freedom. With $\mathbf{u}$ denoting the independent unknown vector, the disjoint generalized displacement vector $\mathbf{u}_a$ can be related to $\mathbf{u}$ by the equation

$$\mathbf{u}_a = \mathbf{C}\mathbf{u} \quad (49)$$

where $\mathbf{C}$ is the $n_a \times n$ transformation matrix. Note that $n = n_a - L_a$ when the exact geometric compatibility conditions (44) are applied. Finally, introducing Eq. (49) into Eq. (38) yields

$$\Pi = \frac{1}{2}\langle \mathbf{m}\dot{\mathbf{u}}, \dot{\mathbf{u}}\rangle + \frac{1}{2}\langle \mathbf{k}\mathbf{u}, \mathbf{u}\rangle + \frac{1}{2}\langle \mathbf{d} * \dot{\mathbf{u}}, \mathbf{u}\rangle + \frac{1}{2}\langle \mathbf{d}\mathbf{u}(0), \mathbf{u}\rangle - \langle \mathbf{f}, \mathbf{u}\rangle + \langle \mathbf{m}(\mathbf{u} - \mathbf{w}), \dot{\mathbf{u}}\rangle_0 - \langle \mathbf{m}\mathbf{v}, \mathbf{u}\rangle_0 \quad (50)$$

where the $n \times n$ coupled matrices are given by

$$\mathbf{m} = \mathbf{C}^T\mathbf{m}_a\mathbf{C}, \quad \mathbf{d}(t) = \mathbf{C}^T\mathbf{d}_a(t)\mathbf{C}, \quad \mathbf{k} = \mathbf{C}^T\mathbf{k}_a\mathbf{C} \quad (51)$$

and the n-dimensional coupled vectors are given by

$$\mathbf{f} = \mathbf{C}^T\mathbf{f}_{E_a}, \quad \mathbf{w} = \mathbf{m}^{-1}\mathbf{C}^T\mathbf{m}_a\mathbf{w}_a, \quad \mathbf{v} = \mathbf{m}^{-1}\mathbf{C}^T\mathbf{m}_a\mathbf{v}_a. \quad (52)$$

Also, $\mathbf{m}^{-1}$ exists for reasons as above for $\mathbf{m}_s^{-1}$. Since matrices $\mathbf{m}$, $\mathbf{d}(t)$, and $\mathbf{k}$ are all symmetric and $\mathbf{m}$ is positive definite, the condition of stationarity $\delta\Pi = 0$ gives both the motion equations

$$\mathbf{m}\ddot{\mathbf{u}} + \mathbf{d} * \dot{\mathbf{u}} + \mathbf{k}\mathbf{u} = \mathbf{f} - \mathbf{d}\mathbf{u}(0), \quad t \in [0, \infty) \quad (53)$$

and the initial conditions

$$\mathbf{u}(0) = \mathbf{w}, \quad \dot{\mathbf{u}}(0) = \mathbf{v}. \quad (54)$$

Selection of Trial Vectors

Substructure trial vectors must satisfy two necessary conditions: (a) They are linearly independent. (b) They satisfy the external geometric boundary conditions. These conditions guarantee the exact representation of the substructure when $n_s = N_s$. In addition, the trial vectors should be reasonably smooth so that the dynamic response of the structure in the low frequency range is accurately represented.

The motion of each substructure is traditionally represented by a linear combination of its eigenvectors. With the presence of viscous damping, the matrix size of the eigenproblem doubles compared to the undamped case due to the state space formulation; also the eigenvectors are generally complex. The complex substructure eigenvectors not only become more difficult to compute, but also lead to complex reduced substructure matrices and finally complex reduced system matrices. The inclusion of general viscoelastic damping adds further complications. To obtain the substructure eigenvectors, the eigenvalue problems have to be defined in terms of the particular form of viscoelastic damping involved such that the coefficient matrices can be diagonalized. The task of finding the substructure eigensolutions can be more challenging than our original task of calculating the transient or steady-state system response.

The eigenvectors of a viscoelastic substructure are admissible vectors, but admissible vectors of a viscoelastic substructure do not have to be its eigenvectors. By definition, the admissible vectors of a viscoelastic substructure are also those of the corresponding fully elastic substructure and vice

Downloaded 04 May 2010 to 171.66.16.28. Redistribution subject to ASME license or copyright; see http://www.asme.org/terms/Terms_Use.cfm

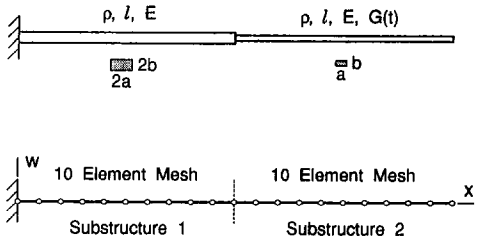

Fig. 1 Cantilevered beam model

versa. Therefore, all types of admissible vectors for undamped systems can be used for damped systems. The eigenvectors of undamped substructures, such as fixed and free interface normal modes, qualify as admissible vectors for damped substructures; so are the static constraint and attachment modes. With the use of the undamped substructure modes as trial vectors, the definition of substructure eigenproblems involving viscoelastic damping and the subsequent solution for complex eigenvectors is avoided. The solution of the substructure eigenproblems can be circumvented completely by the use of load-dependent Lanczos vectors (Wilson and Bayo, 1986). The generation of Lanczos vectors involves factorization of substructural stiffness matrix and orthogonalization of vectors, which were claimed less expensive than the solution of eigenproblems. Admissible Ritz vectors represent a much larger class of vectors than the substructure eigenvectors. However, the generation of these vectors still remains a question. A convenient method is presented by Meirovitch and Hale (1981) for constructing a set of admissible vectors by discretizing, or call sampling in space, a set of admissible functions.

Numerical Examples

Consider a cantilevered beam which consists of two uniform sections with the same density 1kg/m, Young's modulus 10^{11}N/m^2 and length 50m but different sectional geometries 1m × 0.5m and 0.5m × 0.25m as shown in Fig. 1. Since the natural frequencies of a uniform beam with length l, linear density ρ and bending stiffness EI are proportional to $\sqrt{EI/\rho l^4}$, only the sectional geometry has to be varied in a parametric study. The beam is naturally divided into two substructures. The one-dimensional viscoelastic constitutive relation is

$$\sigma(t) = E\epsilon(t) + G(t)\epsilon(0) + \int_0^t G(t-\tau)\dot{\epsilon}(\tau)d\tau. \quad (55)$$

Substructure 1 is assumed to be elastic, while substructure 2 governed by the hereditary integral law with the exponential series presentation

$$G(t) = c\sum_{k=1}^{7} e^{-10^{k-2}t} \quad (56)$$

where parameter c dictates the level of damping. Damping is proportional to stiffness in substructure 2. However, the combination of substructures 1 and 2 results in non-proportional damping.

The finite element method is used to discretized the substructures. Two degrees-of-freedom are defined at each node: deflection w and slope dw/dx. Viscoelastic damping is incorporated into the elastic element by the correspondence principle at the element level. The full-sized discrete model uses a mesh of ten uniform length elements in each substructure. Therefore, accounting for two constraints, there are a total of 40 degrees-of-freedom in the coupled system. The substructure synthesis method (SSM) is then used to approximate the full-sized model through an order reduction. Since the resulting reduced order model can only be as good as the full-sized model, the solution based on the latter is considered exact. Convergence of the substructure synthesis method (SEM) can be demonstrated by increasing the number of trial vectors in each substructures. Three types of trial vectors are considered here. (1) Discretized Simple Polynomials (SSM1). The values of polynomial x^i and its slope ix^{i-1} at the coordinates of the nodal points are taken as the nodal values of displacement w and rotation dw/dx, respectively. Since substructure 1 is clamped at $x = 0$, external boundary conditions $w = 0$ and $dw/dx = 0$ must be satisfied by the choice of trial vectors. Hence, an incomplete sequence x^i, $i = 2, 3, \ldots, n$ is used for substructure 1 and a complete sequence x^i, $i = 0, 1, \ldots, n$ for substructure 2. (2) Fixed Modes plus Constraint Modes (SSM2). The normal modes are calculated from each undamped substructure with the deflection and slope fixed at the interface between the two substructures. Two constraint modes are obtained by statically imposing a unit deflection and a unit slope, respectively, with the other boundary freedom constrained. (3) Free Modes plus Attachment Modes (SSM3). The undamped normal modes are calculated from cantilevered substructure 1 and unconstrained substructure 2. Two attachment modes are obtained by statically imposing a unit force and a unit moment, respectively, at the unconstrained internal boundary. Statically determined constraints are applied at the other end of substructure 2 inhibiting rigid-body motion. Comparisons of convergence are made with the finite element method with which the solutions are obtained by increasing the number of elements from one in each substructure to approximate the full sized model.

Eigenvalues. The eigenequations of a viscoelastic system can be obtained by a Laplace transformation

$$\left[p^2\mathbf{M} + p\mathbf{D}(p) + \mathbf{K}\right]\tilde{\mathbf{U}} = \mathbf{0}. \quad (57)$$

Eigenvalues and eigenvectors of the undamped M-K system are determined first. Then, under the assumption of small damping, the root perturbation technique is applied to the damped system. Its eigenvalues are expressed as the sum of the natural frequencies of the undamped system and the corresponding perturbations due to damping. Relative errors of the ith natural frequency ω_i and the real part of the eigenvalue perturbation δp_i are defined as

$$\frac{|\omega_i^a - \omega_i^e|}{\omega_i^e}, \quad \frac{|\text{Re}(\delta p_i^a) - \text{Re}(\delta p_i^e)|}{|\text{Re}(\delta p_i^e)|} \quad (58)$$

where the superscripts "a" and "e" denote approximate and exact solutions, respectively. The first eigenvalue of a system is usually of the most interest but easiest to approximate. In order to show the ability of the SSM to approximate the higher order eigenvalues, the fifth one is also illustrated. Convergence of the natural frequencies of the undamped beam is shown in Fig. 2. A monotonic decrease of the frequencies is guaranteed in the absence of damping with an increase of substructural trial vectors or a refinement of finite element meshes. It is obvious that all the SSM converge faster than the finite element method. The SSM1 and SSM2 provide a much better convergence rate than the finite element method. A few fixed substructure modes is capable of giving an accurate estimate of the frequencies. Trial vectors discretized from simple polynomials offer a greater rate of convergence than fixed modes with a moderate number of degrees-of-freedom. The SSM3 still performs significantly better than the finite element method. The real part of an eigenvalue is indicative of model damping. Its convergence is illustrated in Fig. 3 for the first and fifth eigenvalues. It is clear that all the SSM converge faster than the finite element method. Since both the finite element method and the SSM

Downloaded 04 May 2010 to 171.66.16.28. Redistribution subject to ASME license or copyright; see http://www.asme.org/terms/Terms_Use.cfm

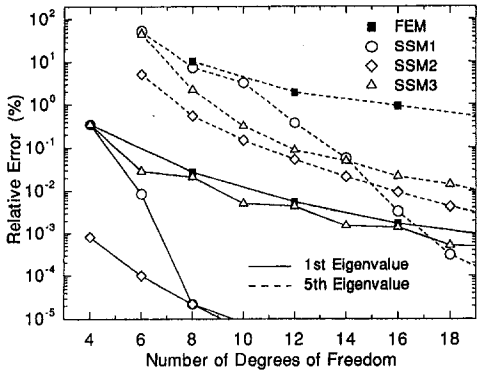

Fig. 2 Convergence of natural frequencies

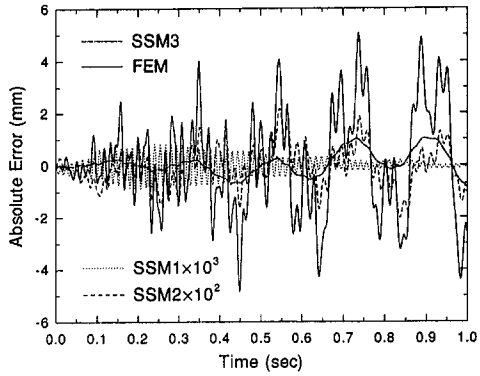

Fig. 3 Convergence of the real perturbation of eigenvalues

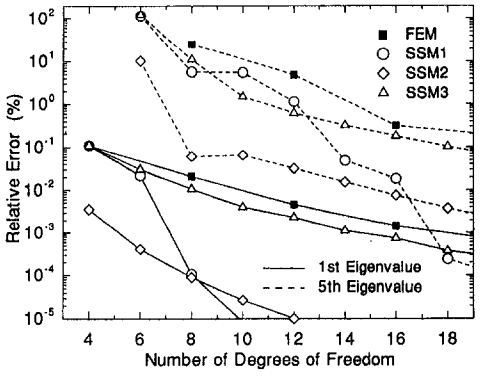

Fig. 4 Comparison of the transient responses between the finite element method and SSM

for damped systems are derived under stationary rather than extrema principles, monotonic convergence is not expected for the perturbation. The relative positions of convergence curves of the perturbation by the finite element method and the various SSM are similar to those of the natural frequencies.

Transient Response. Consider a uniformly distributed load of 1kN/m imposed over the entire length of the beam for a duration of 0.1 seconds. This time, let $c = 5 \times 10^9$ and damping in substructure 1 to be ten percent of that in substructure 2. The displacement at the beam tip $\Delta(t)$ is used to monitor the absolute error between approximate and exact solutions

$$\Delta^a(t) - \Delta^e(t). \tag{59}$$

Since high-frequency modes have very little participation in the transient response, only the first six modes of the undamped coupled system are retained in the final solution. A central finite difference scheme is used for time domain solution of the coupled integro-differential equations,

$$\mathbf{M}\ddot{\mathbf{U}}(t) + \int_0^t \mathbf{D}(t-\tau)\dot{\mathbf{U}}(\tau)d\tau + \mathbf{K}\mathbf{U}(t) = \mathbf{F}(t). \tag{60}$$

The time-step size, initially based on the highest natural frequency involved in the solution, is refined until convergence of absolute error is reached. The peak positive and negative responses occur within the first second. The absolute error of the SSM with three types of trial vectors is compared to that of the finite element method for the 20-degree-of-freedom system in Fig. 4. The error of the SSM1 and SSM2 has been magnified by 1000 and 100, respectively, in order to make them reasonably visible. The error of the SSM1 is at least three orders of magnitude lower than that of the finite element method. Only one dominant frequency is visible in the total error due to all the modes. This frequency coincides with the sixth eigenvalue (68Hz). We therefore conclude that the error is mostly due to the sixth mode. Confirmed by the corresponding frequency response, all lower modes are more accurately represented by polynomials. In the case of the finite element method, the error contains multiple frequency components. The contributions of the second (5Hz) and higher modes can be clearly observed. The error of the SSM2 is at least two orders of magnitude lower than the finite element method; the similar profile of the two error curves is in accordance with the uniform improvement over a wide frequency range. The error of the SSM3 is approximately 20 percent of that of the finite element method and mostly at low frequency, since most of the improvement is made in the higher frequency range.

Conclusion

A substructure synthesis method is developed in the time domain for structures with viscoelastic damping in the hereditary integral form. It is an extension of existing methods for structures with viscous damping. The formulation is based on a new variational principle for symmetric viscoelastic systems, which permits nonzero initial strains corresponding to nonhomogeneous initial conditions of displacements. The traditional state space formulation for systems with viscous damping is avoided since it is undesirable for systems with general viscoelastic damping. As a result, the approach is independent of the form of viscoelastic damping models and the effort spent on the reduction process is similar to the classic component mode synthesis for undamped systems. On the basis of the Rayleigh-Ritz method, each substructure is represented by a set of real admissible trial vectors. Eigenvectors of the corresponding undamped substructure and Ritz vectors obtained by spatial discretization of admissible functions are recommended. In the absence of damping, the proposed method reduces to the classic synthesis method. The effectiveness of the proposed method in terms of reducing the size of final equations is illustrated through viscoelastic beam examples with three different types of substructure trial vectors.

The substructure synthesis method presented in this paper for symmetric viscoelastic systems can be readily extended to nonsymmetric viscoelastic systems by introducing the adjoint systems in the formulation. This later development is presented in a separate paper by Qian and Hansen (1995).

References

Bêliveau, J.-G., and Soucy, Y., 1985, "Damping Synthesis Using Complex Substructure Modes and a Hermitian System Representation," *AIAA Journal*, Vol. 23, pp. 1952–1956.

Biot, M. A., 1954, "The Theory of Stress-Strain Relations in Anisotropic Viscoelasticity and Relaxation Phenomena," *Journal of Applied Physics*, Vol. 25, pp. 1385–1391.

Downloaded 04 May 2010 to 171.66.16.28. Redistribution subject to ASME license or copyright; see http://www.asme.org/terms/Terms_Use.cfm

Christensen, R. M., 1982, *Theory of Viscoelasticity*, Academic Press, New York.

Craig, R. R., Jr., and Ni, Z., 1989, "Component Mode Synthesis for Model Order Reduction of Nonclassically Damped Systems," *Journal of Guidance, Control and Dynamics*, Vol. 12, pp. 577–584.

Dowell, E. H., 1972, "Free Vibration of an Arbitrary Structure in Term of Component Modes," ASME JOURNAL OF APPLIED MECHANICS, Vol. 39, pp. 727–732.

Hale, A. L., and Bergman, L. A., 1985, "The Dynamic Synthesis of General Nonconservative Structures from Separately Identified Substructure Models," *Journal of Sound and Vibration*, Vol. 98, pp. 431–446.

Hasselman, T. K., and Kaplan, A., 1974, "Dynamic Analysis of Large Systems by Complex Mode Synthesis," ASME *Journal of Dynamic Systems, Measurement and Control*, Vol. 96, pp. 327–333.

Hurty, W. C., 1965, "Dynamic Analysis of Structural Systems Using Component Modes," *AIAA Journal*, Vol. 3, pp. 678–685.

Kubomura, K., 1982, "A Theory of Substructure Modal Synthesis," ASME JOURNAL OF APPLIED MECHANICS, Vol. 49, pp. 903–909.

Meirovitch, L., and Hale, A. L., 1981, "On the Substructure Synthesis Method," *AIAA Journal*, Vol. 19, pp. 940–947.

Oden, J. T., and Reddy, J. N., 1976, *Variational Methods in Theoretical Mechanics*, Springer-Verlag, New York.

Qian, D., 1993, "Substructure Synthesis Methods for Viscoelastic Structures," Ph.D. thesis, University of Toronto.

Qian, D., and Hansen, J. S., 1995, "A Substructure Synthesis Method for Non-Symmetric Viscoelastic Systems," *Journal of Sound and Vibration*, accepted for publication.

Staverman, A. J., and Schwarzl, F., 1952, "Non-Equilibrium Thermodynamics of Viscoelastic Behavior," *Koninklijke Nederlandse Akademic Van Wetenschappen, Proceeding of the Section of Sciences, Series B*, Vol. 55, pp. 486–492.

Suarez, L. E., and Singh, M. P., 1991, "Successive Synthesis of Substructure Modes," ASME JOURNAL OF APPLIED MECHANICS, Vol. 58, pp. 759–765.

Wilson, E. L., and Bayo, E. P., 1986, "Use of Special Ritz Vectors in Dynamic Substructure Analysis," *Journal of Structural Engineering*, Vol. 112, pp. 1944–1956.

Yee, E. K. L., and Tsuei, Y. G., 1990, "Transient Responses by Component Mode Synthesis Method," ASME *Journal of Vibration and Acoustics*, Vol. 112, pp. 21–25.

Downloaded 04 May 2010 to 171.66.16.28. Redistribution subject to ASME license or copyright; see http://www.asme.org/terms/Terms_Use.cfm

Rotational Representation of a Plate Made of Grioli-Toupin Material

G. Jemielita
Warsaw University of Technology,
Faculty of Civil Engineering,
Institute of Structural Mechanics,
Warsaw 00-637, Poland

A solenoidal part of displacement field appearing in a plate made of material with constraints has been determined. The semi-inverse method has been applied to description. The results being obtained together with the already known biharmonic representation (Jemielita, 1992) might be useful in a new micropolar plate theory formulation.

1 Introduction

The biharmonic representation in an elastic layer made of the Grioli-Toupin (1960, 1962) material (G-T material) was set forth by Jemielita (1992). The displacements and stresses determined there define the so-called generalized plane-stress state (GPSS), in which the components of stress and couple stress tensors, respectively, have the form

$$\boldsymbol{\sigma} = \begin{bmatrix} \sigma_{11} & \sigma_{12} & \sigma_{13} \\ \sigma_{21} & \sigma_{22} & \sigma_{23} \\ \sigma_{31} & \sigma_{32} & 0 \end{bmatrix}, \quad \boldsymbol{\mu} = \begin{bmatrix} \mu_{11} & \mu_{12} & \mu_{13} \\ \mu_{21} & \mu_{22} & \mu_{23} \\ \mu_{31} & \mu_{32} & 0 \end{bmatrix}, \quad (1)$$

while on the faces of layer of thickness h, the following conditions are fulfilled:

$$\sigma_{3i}(x^\beta, \pm h/2) = 0, \quad \mu_{3i}\sigma(x^\beta, \pm h/2) = 0, \quad i = 1,2,3. \quad (2)$$

Let us set forth the right-handed normal coordinate system $\{x^\alpha,\ x^3 = z\}$. The summation convention holds. Latin indices run over 1,2,3, while Greek indices take values of 1 and 2 only. The comma denotes partial differentiation.

In the present contribution a homogeneous micropolar elastic layer of constant thickness h will be presented. We will seek a solenoidal displacement field satisfying

$$\operatorname{div} \mathbf{u} = 0. \quad (3)$$

The following stress state corresponds to the aforementioned representation

$$\boldsymbol{\sigma} = \begin{bmatrix} \sigma_{11} & \sigma_{12} & \sigma_{13} \\ \sigma_{21} & \sigma_{22} & \sigma_{23} \\ \sigma_{31} & \sigma_{32} & 0 \end{bmatrix}, \quad \boldsymbol{\mu} = \begin{bmatrix} \mu_{11} & \mu_{12} & \mu_{13} \\ \mu_{21} & \mu_{22} & \mu_{23} \\ \mu_{31} & \mu_{32} & \mu_{33} \end{bmatrix}, \quad (4)$$

while on the layer faces, the following homogeneous boundary conditions are met:

$$\sigma_{33}(x^\beta, \pm h/2) = 0, \quad \mu_{3\alpha}(x^\beta, \pm h/2) = 0. \quad (5)$$

$$\sigma_{3\alpha}(x^\gamma, \pm h/2) + \frac{1}{2}\epsilon_\alpha^\beta \mu_{33,\beta}(x^\gamma, \pm h/2) = 0. \quad (6)$$

2 Governing Equations of the Grioli-Toupin Material

Let us apply the governing equations of an isotropic, homogeneous, and centrosymmetric medium in the form proposed by Koiter (1964), Nowacki (1970, 1971, 1981), and Sokołowski (1972)

$$\sigma_{ji} = \mu\left[u_{j,i} + u_{i,j} + \frac{2\nu}{1-2\nu}\left(u^\gamma_{,\gamma} + u^3_{,3}\right)\delta_{ji}\right] - \frac{1}{2}\epsilon_{kji}\,\mu^{lk}_{,l}, \quad (7)$$

$$\mu_{ji} = \gamma(\varphi_{i,j} + \varphi_{j,i}) + \epsilon(\varphi_{i,j} - \varphi_{j,i}) = 4\mu l^2(\varphi_{i,j} + \eta\varphi_{j,i}), \quad (8)$$

where

$$\varphi_i = \frac{1}{2}\epsilon_i^{jk}u_{k,j}, \quad (9)$$

$$l^2 = \frac{\gamma + \epsilon}{4\eta}, \quad \eta = \frac{\gamma - \epsilon}{\gamma + \epsilon}, \quad (10)$$

and

σ_{ji} = stress tensor,
μ_{ji} = couple stress tensor,
ϵ_{ijk} = Levi-Civita symbol,
δ_{ij} = Kronecker delta,
u_i = components of the displacement vector,

Contributed by the Applied Mechanics Division of THE AMERICAN SOCIETY OF MECHANICAL ENGINEERS for publication in the ASME JOURNAL OF APPLIED MECHANICS.

Discussion on this paper should be addressed to the Technical Editor, Professor Lewis T. Wheeler, Department of Mechanical Engineering, University of Houston, Houston, TX 77204-4792, and will be accepted until four months after final publication of the paper itself in the ASME JOURNAL OF APPLIED MECHANICS.

Manuscript received by the ASME Applied Mechanics Division, July 15, 1993; final revision, Jan. 20, 1994. Associate Technical Editor: J. N. Reddy.

Copyright © 1995 by ASME

Downloaded 04 May 2010 to 171.66.16.28. Redistribution subject to ASME license or copyright; see http://www.asme.org/terms/Terms_Use.cfm

φ_i = components of the vector of infinitesimal rotations,
μ = Lamé constant,
ν = Poisson ratio, and
$\gamma, \epsilon, l, \eta$ = moduli describing micropolar properties.

Neglecting the body forces we arrive at the following equations of force and moment equilibrium:

$$\sigma^{ji}_{,j} = 0, \quad \epsilon^{ijk}\sigma_{jk} + \mu^{ji}_{,j} = 0. \tag{11}$$

The form of equilibrium equations can be expressed in terms of displacements as

$$\tilde{\nabla}^2 u_i + \frac{1}{1-2\nu} u^k_{,ki} + l^2\tilde{\nabla}^2\left(u^k_{,ki} - \tilde{\nabla}^2 u_i\right) = 0 \tag{12}$$

where $\tilde{\nabla}^2$ represents the Laplace operator in R^3 written as

$$\tilde{\nabla}^2 = \nabla^2 + \frac{\partial^2}{\partial z^2}. \tag{13}$$

Koiter (1964) proved [1] that on the G-T body surface only the five conditions of a dynamic nature can be fulfilled: three of them imposed on the reduced surface forces

$$\hat{p}^i = \sigma^{ji} n_j - \frac{1}{2}\epsilon^{ijk}\dot{m}_{,k} n_j \tag{14}$$

and the remaining two imposed on reduced surface moments

$$\hat{q}^i = \mu^{ji} n_j - \dot{m} n^i, \tag{15}$$

where

$$\dot{m} = \mu^{ij} n_i n_j, \tag{16}$$

and n_i represent the components of the vector normal to a body surface.

The reduced surface forces $\hat{p}_i$ and moments $\hat{q}_i$, respectively, are given by the following formulae:

$$\hat{p}_i = p_i - \frac{1}{2}\epsilon_{ijk}\dot{q}_{,k} n_j, \tag{17}$$

$$\hat{q}_i = q_i - \dot{q} n_i, \tag{18}$$

where p_i are given surface forces and q_i represent given surface moments, while $\dot{q}$ reads

$$\dot{q} = q^i n_i. \tag{19}$$

3 Rotational Representation

Consider an elastic layer of thickness h freed from loads on the faces $x^3 = z = \pm h/2$. The solutions to the differential equations (12), satisfying the condition (3), will be constructed by the semi-inverse method. Let us write down the displacement vector u_i as

$$u_\alpha(x^\gamma, z) = hf(z)\epsilon^\beta_\alpha \psi(x^\gamma)_{,\beta}, \quad u_3(x^\alpha, z) = 0, \tag{20}$$

where $f(z)$ and ψ are unknown functions.

The vector of infinitesimal rotations is given as

$$\varphi_\alpha(x^\beta, \zeta) = f'(\zeta)\psi(x^\beta)_{,\alpha}, \tag{21}$$

$$\varphi_3 = -\frac{h}{2} f(\zeta)\nabla^2\psi, \tag{22}$$

where the dimensionless variable $\zeta = \frac{2}{h} z$, $\zeta \subset \langle -1, 1\rangle$, has been introduced and

$$(..)' = \frac{d}{d\zeta}(..). \tag{23}$$

Substituting Eq. (20) into Eq. (11) it turns out that a nonzero solution to the set (11) exists if the function $\psi(x^\alpha)$ satisfies the Helmholtz equation

$$\nabla^2\psi - \frac{4k^2}{h^2}\psi = 0, \tag{24}$$

and $f(\zeta)$ satisfies the differential equation

$$\left(\frac{d^2}{d\zeta^2} + k^2\right)\left(\frac{d^2}{d\zeta^2} - \frac{1}{4\delta^2} + k^2\right) f(\zeta) = 0, \tag{25}$$

where

$$\delta = \frac{1}{h}, \tag{26}$$

while k stands for the so far unknown coefficient.

Substituting Eq. (20) into the governing Eqs. (7) and (8) and having in mind Eq. (24) we obtain the following formulae for stress and couple stress, respectively:

$$\mu_{33}(x^\alpha, \zeta) = -16\mu\delta^2(1+\eta)k^2 f'(\zeta)\psi(x^\alpha), \tag{27}$$

$$\sigma_{33}(x^\alpha, \zeta) = 0, \tag{28}$$

$$\mu_{3\alpha}(x^\beta, \zeta) = 8\mu h\delta^2(f'' - \eta k^2 f)\psi_{,\alpha}, \tag{29}$$

$$\sigma_{3\alpha}(x^\beta, \zeta) = 2\mu\epsilon^\beta_\alpha\left[f' - 4\delta^2(f''' + k^2 f')\right]\psi_{,\beta}, \tag{30}$$

$$\mu_{\alpha 3}(x^\beta, \zeta) = 8\mu h\delta^2(\eta f'' - k^2 f)\psi_{,\alpha}, \tag{31}$$

$$\sigma_{\alpha 3}(x^\beta, \zeta) = 2\mu\epsilon^\beta_\alpha\left[f' + 4\delta^2(f''' + k^2 f')\right]\psi_{,\beta}, \tag{32}$$

$$\mu_{\alpha\beta}(x^\gamma, \zeta) = 4\mu l^2(1+\eta)f'\psi_{,\alpha\beta}, \tag{33}$$

$$\sigma_{\alpha\beta}(x^\gamma, \zeta) = \mu h\left[f\left(\epsilon^\gamma_\alpha\psi_{,\gamma\beta} + \epsilon^\gamma_\beta\psi_{,\gamma\alpha}\right) + \frac{16}{h^2}\delta^2 k^2\epsilon_{\alpha\beta}(f'' + k^2 f)\psi\right]. \tag{34}$$

On the faces $\zeta = \pm 1$, in which $\mathbf{n} = (0, 0, \pm 1)$, we rewrite the homogeneous boundary conditions (14) and (15) imposed in the following form:

$$\sigma_{33}(x^\alpha, \pm 1) = 0, \quad \mu_{3\alpha}(x^\alpha, \pm 1) = 0, \tag{35}$$

$$\sigma_{3\alpha}(x^\alpha, \pm 1) + \frac{1}{2}\epsilon^\beta_\alpha\mu_{33,\beta}(x^\alpha, \pm 1) = 0. \tag{36}$$

Substituting (27)–(30) into (35) and (36) we arrive at the following conditions upon $f(\zeta)$:

$$f''(\pm 1) - \eta k^2 f(\pm 1) = 0, \tag{37}$$

$$4\delta^2 f'''(\pm 1) - \left[1 - 4\delta^2 k^2(2+\eta)\right] f'(\pm 1) = 0. \tag{38}$$

When applying the above conditions, one can calculate the constant parameter k.

In the present contribution we will confine ourselves to the formulation of the rotational representation of a plate under bending.

4 Bending State

The following functions meet Eq. (25) in the bending state:

(1) for $\frac{1}{4\delta^2} > k^2$

$$f(\zeta) = C_1 \sin(k\zeta) + C_2 \sinh(\kappa\zeta), \tag{39}$$

where

$$\kappa = \sqrt{\frac{1}{4\delta^2} - k^2}, \tag{40}$$

[1] Sokołowski (1972) in terms of the direct method derived in a plain way from the permissible boundary conditions.

Downloaded 04 May 2010 to 171.66.16.28. Redistribution subject to ASME license or copyright; see http://www.asme.org/terms/Terms_Use.cfm

(2) at $\frac{1}{4\delta^2} = k^2$

$$f(\zeta) = C_1 \sin(k\zeta) + C_2 \zeta, \tag{41}$$

(3) for $\frac{1}{4\delta^2} < k^2$

$$f(\zeta) = C_1 \sin(k\zeta) + C_2 \sin(\dot{\kappa}\zeta). \tag{42}$$

Here

$$\dot{\kappa} = \sqrt{k^2 - \frac{1}{4\delta^2}} \tag{43}$$

and C_1 and C_2 are unknown constants.

Applying the boundary condition $(35)_2$ we obtain the following relationships between C_2 and C_1:

(1) for $\frac{1}{4\delta^2} > k^2$

$$C_2 = \frac{(1+\eta)k^2 \sin(k)}{\kappa^2 - \eta k^2 \sinh(\kappa)} C_1, \tag{44}$$

(2) at $\frac{1}{4\delta^2} = k^2$

$$C_2 = -\frac{(1+\eta)}{\eta} C_1 \sin(k), \tag{45}$$

(3) for $\frac{1}{4\delta^2} < k^2$

$$C_2 = -\frac{(1+\eta)k^2}{\dot{\kappa}^2 + \eta k^2} \frac{\sin(k)}{\sinh(\dot{\kappa})} C_1. \tag{46}$$

The boundary conditions (36) will be met if the constant k is chosen as follows:

(1) for $k^2 < \frac{1}{4\delta^2}$

$$\left(\frac{1}{4\delta^2} - k^2(1+\eta)\right)^2 \cos(k) - \kappa(1+\eta)^2 k^3 ctgh(\kappa)\sin(k) = 0, \tag{47}$$

(2) at $k^2 = \frac{1}{4\delta^2}$

$$tg(k) = \frac{\eta^2}{(1+\eta)^2} k, \tag{48}$$

(3) for $k^2 > \frac{1}{4\delta^2}$

$$\left(\frac{1}{4\delta^2} - k^2(1+\eta)\right)^2 \cos(k) - \dot{\kappa}(1+\eta)^2 k^3 ctgh(\dot{\kappa})\sin(k) = 0. \tag{49}$$

Since roots k_i of the aforementioned equation depend on two dimensionless parameters η and δ, the notation $k_i(\eta, \delta)$, $i = 1,2,3,\ldots$ is obvious.

It can be easily shown that there exist values of δ for which (48) has roots of the form $x_p = \frac{1}{2\delta_p}$, which at $\eta = 0$ are equal to

$$x_p = \frac{1}{2\delta_p} = p\pi, \quad p = 1,2,3,\ldots. \tag{50}$$

If $\eta \neq 0$, then for sufficiently large values of p one can calculate the roots x_p using the following approximate formula:

Table 1

	$\frac{1}{2\delta} = 5$		$\frac{1}{2\delta} = 10$	
No.	$\eta = 0$	$\eta = 1$	$\eta = 0$	$\eta = 1$
1	1.537 086 57	1.440 007 86	1.566 803 93	1.554 411 94
2	3.745 454 66	3.185 855 18	4.576 824 48	4.161 877 52
3	5.245 860 22	5.482 917 74	7.069 322 94	6.332 943 23
4	—	—	9.464 344 47	11.086 550 45
5	—	—	10.121 932 54	17.403 239 75
6	—	—	11.056 737 82	—
7	—	—	17.346 805 29	—

Table 2

	$\frac{1}{2\delta} = 50$		$\delta = 0$
No.	$\eta = 0$	$\eta = 1$	0
1	1.570 765 28	1.570 671 90	1.570 796 33
2	4.711 540 99	4.708 941 28	4.712 388 98
3	7.849 964 20	7.837 156 95	7.853 981 63
4	10.984 156 18	10.945 530 86	10.995 574 29
5	14.111 709 78	14.018 587 15	14.137 166 94
6	17.229 341 47	17.031 841 93	17.278 759 59
7	20.332 392 00	19.955 034 57	20.420 352 25
8	23.414 165 76	22.783 906 85	23.561 944 90
9	26.465 333 82	25.590 023 82	26.703 537 56
10	29.474 450 35	28.474 868 17	29.845 130 21
11	32.432 416 61	31.471 491 84	32.986 722 86
12	35.343 888 78	34.559 594 44	36.128 315 52
13	38.238 072 26	37.716 005 98	39.269 908 17
14	41.157 849 36	40.932 366 46	42.411 500 82
15	44.132 191 38	44.224 337 82	45.553 093 48
16	47.167 377 33	47.697 104 70	48.694 686 13
17	50.024 671 88	50.095 982 05	51.836 278 78
18	50.223 444 96	50.401 608 72	54.977 871 44
19	50.263 117 54	50.989 442 00	58.119 464 09
20	50.611 490 35	52.010 123 36	61.261 056 75
21	51.193 161 11	53.453 302 75	64.402 649 40
22	51.960 858 77	55.438 416 23	67.544 242 05
23	52.923 265 12	58.303 941 97	70.685 834 71
24	53.403 133 04	62.111 115 35	73.827 427 36
25	53.977 801 74	67.747 406 58	76.969 020 01
26	55.284 015 26	76.043 564 24	80.110 612 67
27	58.238 236 42	87.081 397 78	83.252 205 32
28	61.749 451 53	105.537 533 60	86.393 797 97
29	62.986 613 96	137.039 463 15	89.535 390 63
30	63.330 541 47	202.342 786 20	92.676 983 28
31	67.664 191 64	399.926 431 20	95.818 575 93
32	74.589 461 85	—	98.960 168 59
33	75.285 561 12	—	102.101 761 24
34	76.505 683 56	—	105.243 353 90
35	86.741 930 28	—	108.384 946 55
36	88.190 802 96	—	111.526 539 20
37	88.717 985 83	—	114.668 131 86
38	105.397 204 28	—	117.809 724 51
39	136.850 490 75	—	120.951 317 16
40	202.487 820 08	—	124.092 909 82
41	398.038 605 63	—	127.234 502 47
42	398.731 810 29	—	130.376 095 12
43	400.264 269 02	—	133.517 687 78

$$x_p \cong \frac{2p+1}{2}\pi, \quad p = 1,2,3,\ldots. \tag{51}$$

For any $\delta \neq 0$ we obtain a finite number of roots of Eqs. (47)–(49). For example, if $\delta = 0.5$, for any η we obtain only the unique root; for $\eta = 0$, $k = 0.67716672$, while for $\eta = 1$, $k = 0.48092886$. If $\delta \to 0$ (the Hookean material), then, for any value of η, we obtain an infinite number of roots k_i, which can be written down as

$$k_i = \frac{2i-1}{2}\pi, \quad i = 1,2,3,\ldots. \tag{52}$$

The roots $k_i(\eta, \delta)$ for different values of η and δ are shown in Tables 1 and 2, while Table 3 shows a number of roots x_p at $\eta = 0$, 0.5, and 1, respectively.

Downloaded 04 May 2010 to 171.66.16.28. Redistribution subject to ASME license or copyright; see http://www.asme.org/terms/Terms_Use.cfm

Table 3

	$x_p = \frac{1}{2\delta_p}$		
p	$\eta = 0$	$\eta = 0.5$	$\eta = 1$
1	3.141 592 65	3.513 816 77	3.916 435 37
2	6.283 185 31	6.940 065 77	7.355 927 02
3	9.424 777 96	10.276 289 98	10.635 851 42
4	12.566 370 61	13.550 899 98	13.856 126 66
5	15.707 963 27	16.786 618 66	17.048 300 68
6	18.849 555 92	19.997 450 62	20.225 097 92
7	21.991 148 58	23.191 766 20	23.392 588 50
8	25.132 741 23	26.734 691 34	26.554 025 37
9	28.274 333 88	29.549 482 51	29.711 305 97
10	31.415 926 54	32.718 286 43	32.865 610 76
50	157.079 632 68	158.592 741 04	158.625 217 68
500	1570.796 3226 79	1572.361 399 31	1572.364 579 19

Finally, taking Eqs. (20), (21), and (27)–(34) into consideration we can write the following formulae for displacements, infinitesimal rotations, and components of stress and couple stress tensors, respectively:

$$u_\alpha(x^\gamma, z) = h\epsilon_\alpha^\beta \sum_{i=1} f_i(\zeta)\psi_i(x^\gamma)_{,\beta}, \quad u_3(x^\alpha, z) = 0, \tag{53}$$

$$\varphi_\alpha(x^\beta, \zeta) = \sum_{i=1} f_i'(\zeta)\psi_i(x^\beta)_{,\alpha}, \tag{54}$$

$$\varphi_3(x^\beta, \zeta) = -\frac{h}{2}\sum_{i=1} f_i(\zeta)\nabla^2\psi_i, \tag{55}$$

$$\mu_{33}(x^\alpha, \zeta) = -16\mu\delta^2(1+\eta)\sum_{i=1} k_i^2 f_i'(\zeta)\psi_i(x^\alpha), \tag{56}$$

$$\delta_{33}(x^\alpha, \zeta) = 0, \tag{57}$$

$$\mu_{3\alpha}(x^\beta, \zeta) = 8\mu h\delta^2 \sum_{i=1}\left(f_i'' - \eta k_i^2 f_i\right)\psi_{i,\alpha}, \tag{58}$$

$$\sigma_{3\alpha}(x^\beta, \zeta) = 2\mu\epsilon_\alpha^\beta \sum_{i=1}\left[f_i' - 4\delta^2\left(f_i''' + k_i^2 f_i'\right)\right]\psi_{i,\beta}, \tag{59}$$

$$\mu_{\alpha 3}(x^\beta, \zeta) = 8\mu h\delta^2 \sum_{i=1}\left(\eta f_i'' - k_i^2 f_i\right)\psi_{i,\alpha}, \tag{60}$$

$$\sigma_{\alpha 3}(x^\beta, \zeta) = 2\mu\epsilon_\alpha^\beta \sum_{i=1}\left[f_i' + 4\delta^2\left(f_i''' + k_i^2 f_i'\right)\right]\psi_{i,\beta}, \tag{61}$$

$$\mu_{\alpha\beta}(x^\gamma, \zeta) = 4\mu l^2(1+\eta)\sum_{i=l} f_i'\psi_{i,\alpha\beta}, \tag{62}$$

$$\sigma_{\alpha\beta}(x^\gamma, \zeta) = \mu h \sum_{i=1}\left[f_i\left(\epsilon_\alpha^\gamma\psi_{i,\gamma\beta} + \epsilon_\beta^\gamma\psi_{i,\gamma\alpha}\right) + \frac{16}{h^2}\delta^2 k_i^2\epsilon_{\alpha\beta}\left(f_i' + k_i^2 f_i\right)\psi_i\right], \tag{63}$$

where the functions $\psi_i(x^\alpha)$ satisfy the Helmholtz equation

$$\nabla^2\psi_i - \frac{4k_i^2}{h^2}\psi_i = 0, \quad i = 1,2,3,\ldots \tag{64}$$

while the functions f_i, depending on the value of δ, read

(1) for $\frac{1}{4\delta^2} > k_i^2$

$$f_i(\zeta) = C_{1i}\left(\sin(k_i\zeta) + \frac{(1+\eta)k_i^2\sin(k_i)}{\left(\kappa_i^2 - \eta k_i^2\right)\sinh(\kappa_i)}\sinh(\kappa_i\zeta)\right), \tag{65}$$

$$\kappa_i = \sqrt{\frac{1}{4\delta^2} - k_i^2}, \tag{66}$$

(2) at $\frac{1}{4\delta^2} = k_i^2$

$$f_i(\zeta) = C_{1i}\left(\sin(k_i\zeta) - \zeta\frac{(1+\eta)}{\eta}\sin(\kappa_i)\right), \tag{67}$$

(3) for $\frac{1}{4\delta^2} < k_i^2$

$$f_i(\zeta) = C_{1i}\left(\sin(k_i\zeta) - \frac{(1+\eta)k_i^2\sin(k_i)}{\left(\dot{\kappa}_i^2 + \eta k_i^2\right)\sin\left(\dot{\kappa}_i\right)}\sin\left(\dot{\kappa}_i\zeta\right)\right), \tag{68}$$

$$\dot{\kappa}_i = \sqrt{k_i^2 - \frac{1}{4\delta^2}}. \tag{69}$$

Arbitrary constants C_{1i} define the physical meaning of ψ_i. It can be easily shown that if the functions ψ_i meet Eqs. (23), the differential Eqs. (11) and (12) together with the boundary conditions will also be satisfied. Proper choice of the parameters C_{1i} ensures that the function

$$\Psi(x^\alpha) = \sum_{i=1}\psi_i(x^\alpha) \tag{70}$$

has a clear physical meaning.

The rotational part of the nondilatational transverse shear strain in the midplane can be written as

$$\gamma_{\alpha 3}(x^\beta) = (u_{\alpha,3} + u_{3,\alpha})_{z=0} = 2\epsilon_\alpha^\beta\sum_{i=1} f_i'(0)\psi_i(x^\gamma)_{,\beta}. \tag{71}$$

Assuming for every value of i,

$$f_i'(0) = \frac{1}{2}, \tag{72}$$

we determine the constants C_{1i} values, such that

$$\gamma_{\alpha 3}(x^\beta) = \epsilon_\alpha^\beta\Psi_{,\beta}. \tag{73}$$

It is obvious that for the values of C_{1i} determined from the condition (72), the corresponding derivatives of Ψ represent the nondilatational strain angles in the midplane of a plate.

After employing the Boggio (1903) theorem, the set of equations (64) can be rewritten in the following form of a product

$$\prod_{i=1}\left(1 - \frac{h^2\nabla^2}{4k_i^2}\right)\Psi = 0. \tag{74}$$

To the best of author's knowledge, Eqs. (53)–(69) are given in the form presented for the first time.

5 Rotational Representation in the Plate Made of the Hookean Material

To obtain the displacements and stresses in the plate made of the classical Hookean material one should let $l \to 0$. On computing limits of the expressions (53)–(74) we arrive at

$$f_i(\zeta) = C_{1i}\sin(k_i\zeta), \tag{75}$$

$$k_i = \frac{2i-1}{2}\pi, \quad i = 1,2,3,\ldots, \tag{76}$$

$$u_\alpha(x^\gamma, z) = h\epsilon_\alpha^\beta\sum_{i=1}^{\infty} C_{1i}\psi_i(x^\gamma)_{,\beta}\sin\frac{2i-1}{2}\pi\zeta, \quad u_3 = 0, \tag{77}$$

Downloaded 04 May 2010 to 171.66.16.28. Redistribution subject to ASME license or copyright; see http://www.asme.org/terms/Terms_Use.cfm

$$\sigma_{\alpha\beta}(x^\gamma, \zeta) = \mu h \sum_{i=1}^{\infty} \left[C_{1i}(\epsilon_\alpha^\gamma \psi_{i,\gamma\beta} + \epsilon_\beta^\gamma \psi_{i,\gamma\alpha}) \sin \frac{2i-1}{2} \pi\zeta \right], \tag{78}$$

$$\sigma_{\alpha 3}(x^\beta, \zeta) = \sigma_{3\alpha}(x^\beta, \zeta) = 2\mu\epsilon_\alpha^\beta \sum_{i=1}^{\infty} C_{1i} k_i \psi_{i,\beta} \cos \frac{2i-1}{2} \pi\zeta, \tag{79}$$

$$\sigma_{33}(x^\alpha, \zeta) = 0, \quad \mu_{ij}(x^\alpha, \zeta) = 0, \tag{80}$$

$$\nabla^2 \psi_i - \frac{(2i-1)^2}{h^2} \pi^2 \psi_i = 0, \quad i = 1,2,3,\ldots. \tag{81}$$

At $C_{1i} = \dfrac{1}{2k_i} = \dfrac{1}{(2i-1)\pi}$ the function Ψ meets the equation of infinite order as follows:

$$\prod_{i=1}^{\infty} \left(1 - \frac{h^2 \nabla^{2i}}{(2i-1)^2 \pi} \right) \Psi = \sum_{i=0}^{\infty} \frac{(-1)^i h_i^2 \nabla^{2i}}{(2i)! 2^{2i}} \Psi = 0. \tag{82}$$

Lévy (1877) first found the particular form ($i = 1$) of the solution (77), (81). His solution referred to the case $C_{1i} = 1$. Dougall (1904), using different method, derived the complete form of Eqs. (77) and (81) (at $C_{1i} = 1$). Assuming $C_i = \dfrac{h}{(1-2\nu)(2i+1)}$ one can arrive at the Lur'e (1942) solution (cf. Jemielita, 1993).

References

Boggio, T., 1903, "Sull integrazione di alcuna equationi linerari alle derivate parziale," *Annali di Matematica Pura ed Applicata*, Ser. III, Vol. 8, p. 181.

Dougall, J., 1904, "An Analytical Theory of the Equilibrium of an Isotropic Elastic Plate," *Transaction of the Royal Society of Edinburgh*, Vol. 41, Part 1, No. 8, pp. 129–228.

Grioli, G., 1960, "Elasticità asimmetrica," *Annali di Matematica Pura de Applicata*, Ser. IV, Vol. 50, pp. 389–417.

Jemielita, G., 1992, "Biharmonic Representation in the Analysis of Plates Made of the Grioli-Toupin Material," *Journal of Theoretical and Applied Mechanics*, Vol. 30, No. 1, pp. 101–107.

Jemielita, G., 1993, "Exact Equations Theory of Plates (in Polish)," *Prace Naukowe Politechniki Warszawskiej. Budownictwo*, No. 124, pp. 1–153.

Koiter, W. T., 1964, "Couple Stresses in the Theory of Elasticity I–II," *Proceedings Koninklijke Nederlandse Akademie van Wetenschappen*, Ser. B, Vol. 67, No. 1, pp. 17–44.

Lévy, M., 1877, "Mémoire sur la théorie des plaques élastiques planes," *Journal de Mathématiques Pures et Appliquées*, Ser. 3, Vol. 3, pp. 219–306.

Lur'e, A. I., 1942, "On the Theory of Thick Plates," *Prikladnaya Matematika i Mekhanika*, Vol. 6, Nos. 2–3, pp. 151–168.

Nowacki, W., 1970, *Theory of Elasticity (in Polish)*, PWN, Warszawa, pp. 757–759.

Nowacki, W., 1970, *Theory of Micropolar Elasticity*, CISM, (Courses and Lectures), Springer-Verlag, Vienna.

Nowacki, W., 1971, *Theory of Asymmetric Elasticity*, PWN, Warsaw (in Polish).

Nowacki, W., 1981, *Theory of Asymmetric Elasticity*, 2nd ed., PWN, Warsaw (in Polish).

Sokołowski, M., 1972, *On the Theory of Couple Stresses in Media with Constrained Rotations*, PWN, Warsaw (in Polish).

Toupin, R. A., 1962, "Elastic Materials with Couple-Stresses," *Archive for Rational Mechanics and Analysis*, Vol. 11, No. 5, pp. 385–414.

Downloaded 04 May 2010 to 171.66.16.28. Redistribution subject to ASME license or copyright; see http://www.asme.org/terms/Terms_Use.cfm

Optimum Shapes of Elastic Solids With Infinite Branches

G. P. Cherepanov
Florida International University,
Department of Mechanical Engineering,
Miami, FL 33199
Mem. ASME

The classical inverse problem of the plane theory of elasticity, in which the stress along the boundary contour is rendered uniform, is considered. The exact solution to the problem delivering symmetrical optimum shapes with four infinite branches along the axes of symmetry is constructed. The method enables one to find many other optimum shapes with two, three, four, five, etc., infinite branches.

Introduction

The optimization technique currently used for design of engineering structures is not absolute because it is not based on a sound physical principle. It factually optimizes one property of a structure for the cost of the rest. The principle of equistrength suggested in Cherepanov and Tagizade (1975a) for in-plane loaded plates of variable thickness may serve such a physical principle. The main difficulty in finding equistrong designs is the existence problem connected with the strong nonlinearity of problems with an unknown boundary; however, if an equistrong design exists, it can become an ideal design pattern.

The history of this approach starts with Galileo Galilei, who was the first to advance the equistrong design of the beam bent by an edge transverse force. It is remarkable that this discovery was done simultaneously with the introduction of the notion of the strength and stress itself, which appeared to be too difficult a problem, even for Leonardo da Vinci. The equistrong design—that of equistrong heavy chain—was next advanced in the middle of the last century. A solid spinning disk of uniform strength devised by engineers at the Laval Company in Sweden in about 1900, provides another equistrong design. The latter is a particular case of the equistrong design suggested in Cherepanov, ed. (1995). The concept of uniform strength was utilized also in the theory of membrane shells of uniform strength. For a more detailed reference, see the book by Bienzeno and Grammel (1956). For example, Bienzeno in 1922 designed a head of uniform strength on a cylindrical pressure vessel. With constant thickness throughout the cylinder and head, the shape of the head was found that makes the maximum shear stress constant everywhere.

In stress concentration problems, the optimal design formulation and solution to some two and three-dimensional problems has been provided in Cherepanov (1963, 1966a,b, 1974), Cherepanov and Liberman (1971), Cherepanov and Tagizade (1975b), Wheeler (1976, 1978) and Wheeler and Kunin (1982). A list of some other relevant references can be found in the recent review paper on the topic by Wheeler (1992). The general formulation of the principle of equistrength in arbitrary two and three-dimensional domains was given in the book by Cherepanov and Yershov (1977).

In the present paper, the classic inverse problem of the plane theory of elasticity, when the boundary is free of tractions and the tangent stress is uniform along the boundary, is considered. A solution to this problem provides an equistrong design or optimum shape with minimum stress concentration in this case. If the unknown boundary contour is single and limited, the optimum shape is an ellipse (Cherepanov, 1963; Wheeler, 1992). Multiple optimum shapes of limited length were studied in Cherepanov (1974). The goal of the present paper is to find some optimum shapes for an infinite, single boundary contour.

Formulation of the Problem

Let us consider an elastic body subject to the conditions of plane strain or plane stress. In the complex plane, $z = x + iy$, the Cartesian axes, x and y, are assumed to be the axes of symmetry of the body. At infinity, the body has four branches extended along the axes of symmetry and approaching asymptotically the strips of constant thickness, $2h_1$ and $2h_2$ (Fig. 1).

The surface of the body is assumed to be free of tractions. At infinity, there is a state of uniform extension or compression along the axes of symmetry.

Along the unknown boundary of the body, tangent stress, σ_t, is supposed to be uniform. This condition provides optimum shapes of minimum stress concentration and minimum weight plates. Use the general representation equations by Kolosov-Muskhelishvili:

$$\sigma_x + \sigma_y = \sigma_t + \sigma_n = 4\mathrm{Re}\Phi(z)$$

$$\sigma_y - \sigma_x + 2i\tau_{xy} = e^{-2i\alpha}(\sigma_n - \sigma_t + 2i\tau_{tn}) = 2[\bar{z}\Phi'(z) + \Psi(z)]. \quad (1)$$

Contributed by the Applied Mechanics Division of THE AMERICAN SOCIETY OF MECHANICAL ENGINEERS for publication in the ASME JOURNAL OF APPLIED MECHANICS.
Discussion on this paper should be addressed to the Technical Editor, Professor Lewis T. Wheeler, Department of Mechanical Engineering, University of Houston, Houston, TX 77204-4792, and will be accepted until four months after final publication of the paper itself in the ASME JOURNAL OF APPLIED MECHANICS.
Manuscript received and accepted by the ASME Applied Mechanics Division, Sept. 17, 1993. Associate Technical Editor: X. Markenscoff.

Copyright © 1995 by ASME
Downloaded 04 May 2010 to 171.66.16.28. Redistribution subject to ASME license or copyright; see http://www.asme.org/terms/Terms_Use.cfm

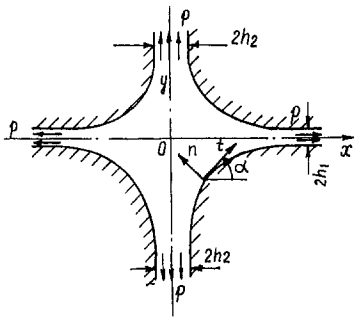

Fig. 1 Physical plane of the complex variable z

Here, σ_x, σ_y, σ_n, σ_t, τ_{xy}, and τ_{tn} are stresses; $\Phi(z)$ and $\Psi(z)$ are analytic functions; t and n are the Cartesian rectangular coordinates associated with the boundary contour, L. Namely, t is the direction of a tangent to L, and n is an outer normal; α is the angle between the x and t axes (in the direction of rotation from x to t, Fig. 1).

According to Eqs. (1), the boundary value problem in the z-plane may be formulated as follows:

$$\mathrm{Re}\Phi(z) = \frac{1}{4}p \quad (z \in L) \tag{2}$$

$$2e^{2i\alpha}[\bar{z}\Phi'(z) + \Psi(z)] = -p \quad (z \in L). \tag{3}$$

Here, p is the tensile stress at infinity. From Eqs. (1) and (2), it follows that $\sigma_t = p$ along L because $\sigma_n = 0$ along L.

According to Eqs. (1), the following conditions hold:

$$\Phi(z) = \frac{1}{4}p \quad \text{for} \quad z \to \infty; \tag{4}$$

$$\Psi(z) = \begin{cases} \dfrac{1}{2}p \text{ for } z \to \infty \text{ along } V \\ -\dfrac{1}{2}p \text{ for } z \to \infty \text{ along } H. \end{cases} \tag{5}$$

Here, V and H are respective vertical and horizontal branches (Fig. 1).

The limited solution to the Dirichlet problem, Eqs. (2) and (4), is

$$\phi(z) = \frac{1}{4}p. \tag{6}$$

From here and Eq. (3), taking into account that $\Phi'(z) = 0$, we find

$$2e^{2i\alpha}\Psi(z) = -p \quad (z \in L), \tag{7}$$

where $\Psi(z)$ should satisfy the condition at infinity, Eq. (5).

This nonlinear boundary value problem will be solved in the next section.

Solution

Let us introduce the parametric plane of the auxiliary complex variable, ζ, by means of the analytic function, $z = \omega(\zeta)$, conformally mapping the interior of the unit circle of the ζ plane of Fig. 2 onto the elastic domain with the boundary contour, L, of the z plane (Fig. 1). The following correspondence of points of the conformal mapping is accepted:

$$\omega(1) \to +\infty, \quad \omega(i) \to i\infty$$
$$\omega(-1) \to -\infty, \quad \omega(-i) \to -i\infty. \tag{8}$$

For an increment of z along t, we have (Fig. 1):

$$dz = |dz|e^{i\alpha}. \tag{9}$$

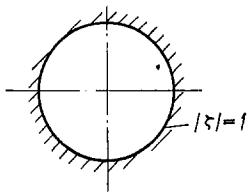

Fig. 2 Parametric plane of the complex variable ζ

For the respective increment of ζ along unit circle, $\zeta = e^{i\theta}$, we find

$$d\zeta = i\zeta|d\zeta|, \tag{10}$$

and hence,

$$\frac{dz}{d\zeta} = \frac{|dz|e^{i\alpha}}{i|d\zeta|\zeta}, \text{ i.e., } e^{i\alpha} = \frac{i\zeta\omega'(\zeta)}{|\omega'(\zeta)|}. \tag{11}$$

Substituting $e^{i\alpha}$ in Eq. (7) by Eq. (11) provides

$$2\zeta^2\frac{\omega'(\zeta)}{\overline{\omega'(\zeta)}}\psi(\zeta) = p \quad (|\zeta| = 1); \tag{12}$$

$$\begin{aligned} &\text{for } \zeta \to \pm 1 \quad \psi(\zeta) \to -\tfrac{1}{2}p, \quad \omega(\zeta) \to \pm\infty \\ &\text{for } \zeta \to \pm i \quad \psi(\zeta) \to \tfrac{1}{2}p, \quad \omega(\zeta) \to \pm\infty i, \end{aligned} \tag{12'}$$

where $\psi(\zeta) = \Psi[\omega(\zeta)]$.

The nonlinear boundary value problem (Eq. (12)) serves to determine two unknown functions, $\psi(\zeta)$ and $\omega(\zeta)$, analytic inside the unit circle.

Let us introduce new functions, $F'(\zeta)$ and $G'(\zeta)$:

$$\begin{aligned} F'(\zeta) &= 2\zeta^2\omega'(\zeta)\psi(\zeta) - p\omega'(\zeta) \\ G'(\zeta) &= 2\zeta^2\omega'(\zeta)\psi(\zeta) + p\omega'(\zeta). \end{aligned} \tag{13}$$

Using these functions, we reduce the boundary value problem (Eq. (12)) to the following Dirichlet problems:

$$\mathrm{Re}F'(\zeta) = 0 \quad (|\zeta| = 1) \tag{14}$$

$$\mathrm{Im}G'(\zeta) = 0 \quad (|\zeta| = 1). \tag{15}$$

On the basis of Eqs. (12') and (13), $F'(\zeta)$ and $G'(\zeta)$ are infinite at four points of the unit circle:

$$\text{when } \zeta \to \pm 1 \text{ and } \zeta \to \pm i, \ F'(\zeta) \text{ and } G'(\zeta) \to \infty. \tag{16}$$

We continue $F'(\zeta)$ and $G'(\zeta)$ analytically onto the entire ζ plane by means of the following functional equations:

$$F'(\zeta) = -\overline{F}'\left(\frac{1}{\zeta}\right), \quad G'(\zeta) = \overline{G}'\left(\frac{1}{\zeta}\right). \tag{17}$$

According to Eqs. (17), the boundary value conditions (Eqs. (14) and (15)) are satisfied.

On the basis of Eqs. (16) and (17), $F'(\zeta)$ and $G'(\zeta)$ will be analytical and limited everywhere throughout the ζ plane except for the points, $\zeta \to \pm 1$ and $\zeta \to \pm i$, where these functions may have single-valued singularities.

We seek the solution having first-order poles at the exceptional points as follows:

$$F'(\zeta) = \frac{A_1}{\zeta - 1} - \frac{\overline{A}_1}{\dfrac{1}{\zeta} - 1} + \frac{A_2}{\zeta + 1} - \frac{\overline{A}_2}{\dfrac{1}{\zeta} + 1} + \frac{A_3}{\zeta - i} - \frac{\overline{A}_3}{\dfrac{1}{\zeta} + i} + \frac{A_4}{\zeta + 1} - \frac{\overline{A}_4}{\dfrac{1}{\zeta} - i} \tag{18}$$

Downloaded 04 May 2010 to 171.66.16.28. Redistribution subject to ASME license or copyright; see http://www.asme.org/terms/Terms_Use.cfm

$$G'(\zeta) = \frac{B_1}{\zeta - 1} + \frac{\bar{B}_1}{\frac{1}{\zeta} - 1} + \frac{B_2}{\zeta + 1} + \frac{\bar{B}_2}{\frac{1}{\zeta} + 1}$$

$$+ \frac{B_3}{\zeta - i} + \frac{\bar{B}_3}{\frac{1}{\zeta} + i} + \frac{B_4}{\zeta + 1} + \frac{\bar{B}_4}{\frac{1}{\zeta} - i}. \quad (19)$$

Here, A_1, A_2, A_3, A_4, B_1, B_2, B_3, and B_4 are complex constants.

Equations (14), (15), and (17) and the condition Eqs. (16) are satisfied by any values of A_i and B_i.

From Eq. (13), we have

$$\omega'(\zeta) = \frac{G'(\zeta) - F'(\zeta)}{2p} \quad (20)$$

$$\psi(\zeta) = \frac{F'(\zeta) + G'(\zeta)}{4\zeta^2 \omega'(\zeta)}. \quad (21)$$

Hence, substituting Eqs. (18) and (19) for $F'(\zeta)$ and $G'(\zeta)$ in Eq. (20) and integrating provides

$$\omega(\zeta) = \frac{1}{2p}\{(B_1 - A_2)\ln(\zeta - 1)$$

$$-(\bar{B}_1 + \bar{A}_1)[\zeta + \ln(\zeta - 1)] + (B_2 - A_2)\ln(\zeta + 1)$$

$$+(\bar{B}_2 + \bar{A}_2)[\zeta - \ln(\zeta + 1)] + (B_3 - A_3)\ln(\zeta - i)$$

$$-(\bar{B}_3 + \bar{A}_3)[i\zeta - \ln(\zeta - i)] + (B_4 - A_4)\ln(\zeta + i)$$

$$+(\bar{B}_4 + \bar{A}_4)[i\zeta + \ln(\zeta + i)]\} + C_0. \quad (22)$$

From the condition of symmetry, it follows that $\omega'(\zeta)$ is real for real and imaginary values of ζ. Hence, A_1, B_1, and A_2, B_2 will be real, but A_3, A_4, and B_3, B_4 will be imaginary. Moreover, the following relations must be met:

$$B_2 = -B_1,\ A_2 = -A_1,\ A_3 = -A_4,\ B_3 = -B_4,\ B_1 = -A_1. \quad (23)$$

Using Eqs. (18) to (23) we can obtain

for $\zeta \to \pm 1$ $G'(\zeta) = 0(1)$,

$$F'(\zeta) = \frac{\pm 2A_1}{\zeta \mp 1},\ \psi(\zeta) = -\frac{p}{2}$$

for $\zeta \to \pm i$ $G'(\zeta) = 0(1)$, $F'(\zeta) = \frac{\pm 2A_3}{\zeta \mp i}$, $\psi(\zeta) = \frac{p}{2}$, (24)

which accords with the conditions (Eq. 12′) at infinity.

From the condition $\omega(0) = 0$, we find $pC_0 = -\pi i(A_1 + A_3)$. By denoting

$$A_1 = a,\ B_3 = -(b + c)i,\ A_3 + B_3 = -ci, \quad (25)$$

and using Eq. (23), one can reduce the function, $\omega(\zeta)$, in Eq. (22) to the following Form:

$$\omega(\zeta) = \frac{1}{p}\left(a\ln\frac{1 + \zeta}{1 - \zeta} + bi\ln\frac{i + \zeta}{i - \zeta} + c\zeta\right). \quad (26)$$

From Eq. (24), it follows that $G'(\zeta)$ is limited at all singular points. On the basis of the Liouville theorem, the function, $G'(\zeta)$, equals the constant everywhere in the whole plane, and we can find

$$G'(\zeta) = 2a + 2(b + c). \quad (27)$$

The function, $\psi(\zeta)$, should be analytical everywhere inside the unit circle. According to Eq. (21), we must require

$$F'(\zeta) + G'(\zeta) \to 0 \text{ when } \zeta \to 0 \quad (28)$$

in order to eliminate a singularity at $\zeta = 0$.

From Eqs. (18), (19), (23), (25), and (28), we can derive that

$$c = 0, \quad (29)$$

and Eq. (26) becomes

$$\omega(\zeta) = \frac{1}{p}\left(a\ln\frac{1 + \zeta}{1 - \zeta} + bi\ln\frac{i + \zeta}{i - \zeta}\right). \quad (30)$$

The functions, $F'(\zeta)$ and $G'(\zeta)$ in Eqs. (18) and (19) can be transformed to the form:

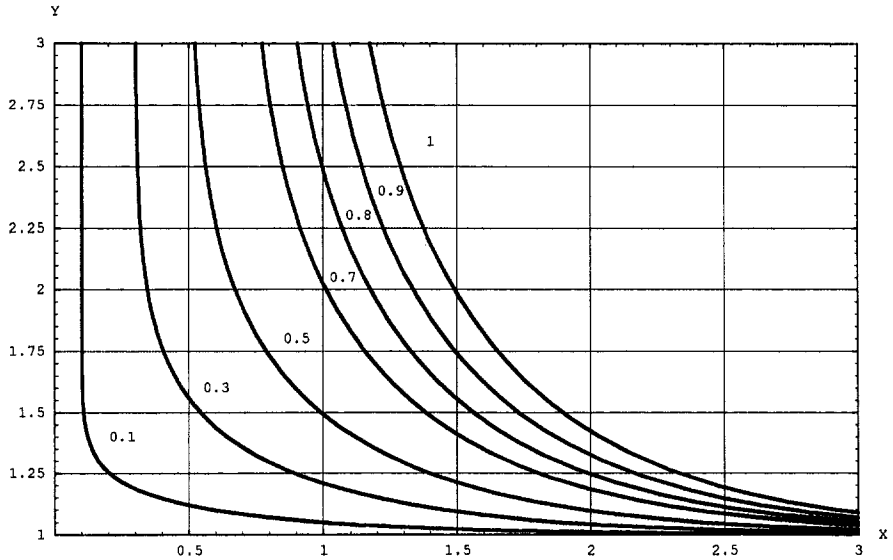

Fig. 3 The album of optimum shapes for different values of $\lambda = h_2/h_1$ (λ = 0.1, 0.3, 0.5, 0.7, 0.8, 0.9, 1.0)

Downloaded 04 May 2010 to 171.66.16.28. Redistribution subject to ASME license or copyright; see http://www.asme.org/terms/Terms_Use.cfm

$$F'(\zeta) = -2a\frac{1+\zeta^2}{1-\zeta^2} - 2b\frac{1-\zeta^2}{1+\zeta^2},$$

$$G'(\zeta) = 2(a+b). \tag{31}$$

Conformal mapping is realized if $\omega'(\zeta) \neq 0$ inside the unit circle. From Eq. (30), $\omega'(\zeta)$ is equal to

$$\omega'(\zeta) = \frac{2}{p}\frac{(a-b)\zeta^2 + (a+b)}{1-\zeta^4}. \tag{32}$$

Hence, $\omega'(\zeta)$ has the following roots:

$$\zeta = \pm\sqrt{\frac{b+a}{b-a}}. \tag{33}$$

These roots must be outside the unit circle, and we obtain

$$\left|\frac{a+b}{b-a}\right| > 1. \tag{34}$$

Equations (30) and (34) provide the solution to the inverse problem of optimum shape.

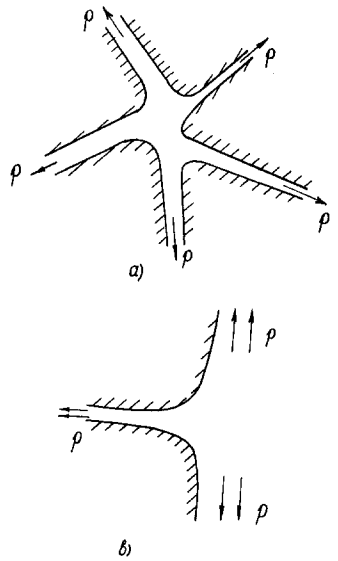

Fig. 4 Other inverse problems solvable by the method suggested

Discussion

The optimum shape depends on two parameters, a and b, the values of which control the thickness of strips V and H. Substituting $e^{i\theta}$ for ζ in Eq. (30), we can write the equations of optimum shape:

$$x = \frac{1}{p}\left(\frac{\pi}{2}b + a\ln\operatorname{cotan}\frac{\theta}{2}\right)$$

$$y = \frac{1}{p}\left[\frac{\pi}{2}a + b\ln\operatorname{cotan}\left(\frac{\pi}{4} - \frac{\theta}{2}\right)\right]\left(0 < \theta < \frac{\pi}{2}\right). \tag{35}$$

For $\pi/2 < \theta < 2\pi$, the optimum shape can be easily found using the problem symmetry.

The parameters, a and b, can be expressed in terms of the thicknesses of the respective asymptotic strips at infinity (Fig. 1). With the help of Eq. (35), we obtain

$$a = \frac{2}{\pi}ph_1, \quad b = \frac{2}{\pi}ph_2, \tag{36}$$

and the final result takes the form

$$x = h_2 + \frac{2}{\pi}h_1\ln\operatorname{cotan}\frac{\theta}{2}$$

$$y = h_1 + \frac{2}{\pi}h_2\ln\operatorname{cotan}\left(\frac{\pi}{4} - \frac{\theta}{2}\right)\left(0 < \theta < \frac{\pi}{2}\right). \tag{37}$$

Figure 3 provides an album of optimum shapes at different values of the dimensionless parameter, $\lambda = h_2/h_1$; namely, at $\lambda = 0.1, 0.3, 0.5, 0.7, 0.8, 0.9$, and 1.0. In Fig. 3, the following designations are used:

$$X = \frac{x}{h_1}, \quad Y = \frac{y}{h_1}.$$

Here, X and Y are dimensionless coordinates.

It is easy to verify that the solvability condition, Eq. (34), is met for arbitrary choice of h_1 and h_2. It is noteworthy that the optimum shapes in the case under consideration do not depend on the applied stress at infinity, p.

Conclusion

The method of the present paper may be effectively utilized also in many other inverse problems, two of which are pictured in Fig. 4. These are problems of a contour with five infinite branches, and the plane-strain problem of conjunction of a plate of variable thickness with a half-space. The solution of the first problem can be found in the class of $F'(\zeta)$ and $G'(\zeta)$ having five simple poles, and of the second in the class of $F'(\zeta)$ and $G'(\zeta)$ with two simple poles. The latter can be considered also as a limiting case of the problem under study, when $h_1 \to \infty$ and h_2 is finite. Similarly, optimum shapes of elastic solids with any number of infinite branches can be found and studied.

Acknowledgment

The typescript was prepared by Larisa Cherepanov and Vlad Sutyrin.

References

Bienzeno, C. B., and Grammel, R., 1956, *Engineering Dynamics*, Vol. II (*Elastic Problems of Single Machine Elements*), Blackie & Son Ltd., Glasgow, pp. 267–290 (English translation of 1939 edition in German).

Cherepanov, G. P., 1963, "An Inverse Elastic-Plastic Problem Under Plane Strain," *Notices of the USSR Academy of Sciences, Mekhanika i Mashinostroenie*, No. 1, pp. 63–71, in Russian.

Cherepanov, G. P., 1966a, "Equistrong Mine in a Rock," *Problems of Rock Mechanics*, A. Erzhanov, ed., Nauka, Alma-Ata, pp. 166–178, in Russian.

Cherepanov, G. P., 1966b, "One Inverse Problem of the Theory of Elasticity," *Engineering Journal* (*Solid Mechanics*), No. 3, pp. 518–525, in Russian.

Cherepanov, G. P., and Liberman, L. K., 1971, "Mathematical Method of Optimal Design in Mining," *Mining Journal*, No. 9, pp. 987–992, in Russian.

Cherepanov, G. P., 1974, "Inverse Problems of the Plane Theory of Elasticity," *Applied Mathematics and Mechanics* (*PMM*), Vol. 38, pp. 963–979.

Cherepanov, G. P., and Tagizade, A. G., 1975a, "Extension of Plates and Shells of Uniform Strength," *Letters to Applied and Engineering Science*, No. 3, pp. 64–69.

Cherepanov, G. P., and Tagizade, A. G., 1975b, "Bending of Plates and Shells of Uniform Strength," *Letters to Applied and Engineering Science*, No. 2, pp. 38–43.

Cherepanov, G. P., and Yershov, L. V., 1977, *Fracture Mechanics*, Moscow, Mashinostroenie Press, pp. 1–240, in Russian.

Cherepanov, G. P., ed., 1995, *Fracture: A Topical Encyclopedia Dedicated to A. A. Griffith*, Krieger Publ., Melbourne, FL.

Wheeler, L. T., 1976, "On the Role of Constant-Stress Surfaces in the Problem of Minimizing Elastic Stress Concentration," *J. Solids and Structures*, Vol. 12, pp. 779–789.

Wheeler, L. T., 1978, "On Optimum Profiles for the Minimization of Elastic Stress Concentration," *ZAMM*, pp. 235–236.

Wheeler, L. T., and Kunin, I. A., 1982, "On Voids of Minimum Stress Concentration," *J. Solids and Structures*, Vol. 18, pp. 85–89.

Wheeler, L. T., 1992, "Stress Minimum Forms for Elastic Solids," ASME *Applied Mechanics Reviews*, Vol. 45, pp. 110–125.

Downloaded 04 May 2010 to 171.66.16.28. Redistribution subject to ASME license or copyright; see http://www.asme.org/terms/Terms_Use.cfm

Line Force, Charge, and Dislocation in Anisotropic Piezoelectric Composite Wedges and Spaces

M. Y. Chung
Graduate Student.

T. C. T. Ting
Professor,
Fellow ASME.

Department of Civil and Materials Engineering, University of Illinois at Chicago, 842 W. Taylor Street (M / C 246), Chicago, IL 60607-7023

Two-dimensional problems of anisotropic piezoelectric composite wedges and spaces are studied. The Stroh formalism is employed to obtain the basic real-form solution in terms of two arbitrary constant vectors for a particular wedge. Explicit real-form solutions are then obtained for (i) a composite wedge subjected to a line force and a line charge at the apex of the wedge and (ii) a composite space subjected to a line force, line charge, line dislocation, and an electric dipole at the center of the composite space. For the composite wedge the surface traction on any radial plane θ = constant and the electric displacement D_θ normal to the radial plane θ = constant vanish everywhere. For the composite space these quantities may not vanish but they are invariant with the choice of the radial plane.

1 Introduction

The Stroh formalism is known to be a powerful method for solving anisotropic elasticity problems in two-dimensional deformations. In this paper the Stroh formalism is extended to piezoelectricity problems. Due to the mathematical similarity between elasticity and piezoelectricity, the results in elasticity can be employed readily except that certain matrices are not positive definite.

Consider a composite wedge or space which consists of n different anisotropic piezoelectric wedges. In the cylindrical coordinate system (r, θ, x_3), each wedge occupies the region (Fig. 1)

$$\theta_{k-1} \le \theta \le \theta_k \qquad (k = 1, 2, 3, \ldots, n) \qquad (1.1)$$

in which $0 \le \theta_0 < \theta_1 < \ldots < \theta_n$. For the composite wedge $\theta_n < 2\pi + \theta_0$ and for the composite space $\theta_n = 2\pi + \theta_0$. Along an interface between two individual wedges the displacement, the tangential component of electric field, the surface traction and the normal component of electric displacement are continuous. The continuity of tangential component of electric field implies that the electrostatic potential is also continuous.

For the case of a composite wedge, the sides $\theta = \theta_0$, θ_n are traction-free and electrically open, i.e., the normal component of electric displacement vanishes (Kuo and Barnett, 1991). A concentrated line force and a line charge are applied at the wedge apex.

For the case of a composite space, the surfaces $\theta = \theta_0$, θ_n are physically the same surface and the surface traction and the normal component of electric displacement are continuous. However, the displacement and the electrostatic potential are discontinuous by the amount equal to the generalized Burgers vector $\hat{\mathbf{b}}^T = [b_1, b_2, b_3, b_4]$. $b_4 \neq 0$ corresponds to an electric dipole layer along the cut plane and $b_4 = 0$ implies that the electrostatic potential is continuous along the cut plane (Barnett and Lothe, 1975). In addition a line force and a line charge are applied at the center of the composite space.

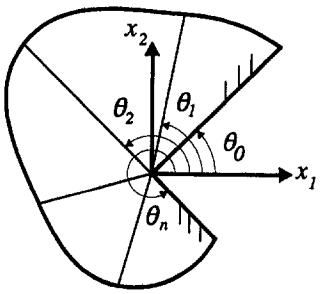

Fig. 1 Geometry of a composite wedge in which $\theta_n < 2\pi + \theta_0$. For a composite space, $\theta_n = 2\pi + \theta_0$.

Contributed by the Applied Mechanics Division of THE AMERICAN SOCIETY OF MECHANICAL ENGINEERS for presentation at the Applied Mechanics and Materials Division Summer Annual Meeting of the ASME, Los Angeles, CA, June 28–30, 1995.

Discussion on this paper should be addressed to the Technical Editor, Professor Lewis T. Wheeler, Department of Mechanical Engineering, University of Houston, Houston, TX 77204-4792, and will be accepted until four months after final publication of the paper itself in the ASME JOURNAL OF APPLIED MECHANICS.

Manuscript received and accepted by the ASME Applied Mechanics Division, June 8, 1994. Associate Technical Editor: D. M. Barnett.

Paper No. 95-APM-1.

Copyright © 1995 by ASME

Downloaded 04 May 2010 to 171.66.16.28. Redistribution subject to ASME license or copyright; see http://www.asme.org/terms/Terms_Use.cfm

2 Basic Equations and Solutions

In a fixed rectangular coordinate system (x_1, x_2, x_3), the constitutive equations relating mechanical stresses σ_{ij} and electric displacements D_i to the elastic displacement gradients $u_{i,j}$ and electrostatic potential φ are

$$\begin{cases} \sigma_{ij} = C_{ijkm}u_{k,m} + e_{mij}\varphi_{,m}, \\ D_i = e_{ikm}u_{k,m} - \omega_{im}\varphi_{,m}, \end{cases} \quad (i,j,k,m = 1,2,3) \quad (2.1)$$

where repeated indices means summation and a comma stands for partial differentiation. C_{ijkm} are the elastic stiffnesses under constant electric field, e_{mij} are the piezoelectric stress constants, and ω_{im} are the permittivities under constant strain field. They satisfy the symmetry relations

$$C_{ijkm} = C_{jikm} = C_{ijmk} = C_{kmij}, \quad e_{mij} = e_{mji}, \quad \omega_{im} = \omega_{mi}, \quad (2.2)$$

and the positive definite property

$$C_{ijkm}u_{i,j}u_{k,m} > 0, \quad \omega_{im}E_iE_m > 0. \quad (2.3)$$

The electric field $\mathbf{E}$ is given by

$$E_m = -\varphi_{,m}. \quad (2.4)$$

In the absence of body forces and free charges the equilibrium equations are

$$\sigma_{ij,i} = 0, \quad D_{i,i} = 0. \quad (2.5)$$

By letting

$$u_4 = \varphi, \quad (2.6)$$

a general solution of (2.1) and (2.5) is

$$\mathbf{u} = \mathbf{a}f(z), \quad z = x_1 + px_2, \quad (2.7)$$

where $\mathbf{u}^T = [u_1, u_2, u_3, u_4]$ is the generalized displacement, $f(z)$ is an arbitrary function of z, and p and $\mathbf{a}$ satisfy the relation

$$[\mathbf{Q} + p(\mathbf{R} + \mathbf{R}^T) + p^2\mathbf{T}]\mathbf{a} = \mathbf{0}. \quad (2.8)$$

In (2.8),

$$\mathbf{Q} = \begin{bmatrix} \mathbf{Q}^E & \mathbf{e}_{11} \\ \mathbf{e}_{11}^T & -\omega_{11} \end{bmatrix}, \quad \mathbf{R} = \begin{bmatrix} \mathbf{R}^E & \mathbf{e}_{21} \\ \mathbf{e}_{12}^T & -\omega_{12} \end{bmatrix},$$

$$\mathbf{T} = \begin{bmatrix} \mathbf{T}^E & \mathbf{e}_{22} \\ \mathbf{e}_{22}^T & -\omega_{22} \end{bmatrix}, \quad (2.9)$$

$$(\mathbf{Q}^E)_{ik} = C_{i1k1}, \quad (\mathbf{R}^E)_{ik} = C_{i1k2},$$
$$(\mathbf{T}^E)_{ik} = C_{i2k2}, \quad (\mathbf{e}_{ij})_m = \mathbf{e}_{ijm}, \quad (2.10)$$

and

$$\mathbf{a}^T = [a_1, a_2, a_3, a_4]. \quad (2.11)$$

Notice that $\mathbf{e}_{ij} \neq \mathbf{e}_{ji}$ and $\mathbf{Q}^E$, $\mathbf{T}^E$ are symmetric and positive definite. The matrices $\mathbf{Q}$ and $\mathbf{T}$ are symmetric, and can be shown to be nonsingular.

Introducing the generalized stress function

$$\boldsymbol{\phi} = \mathbf{b}f(z), \quad (2.12)$$

$$\mathbf{b} = (\mathbf{R}^T + p\mathbf{T})\mathbf{a} = \frac{-1}{p}(\mathbf{Q} + p\mathbf{R})\mathbf{a}, \quad (2.13)$$

in which the second equality of (2.13) follows from (2.8), the elastic stress obtained from $(2.1)_1$ can be written as

$$\sigma_{2j} = \phi_{j,1}, \quad \sigma_{1j} = -\phi_{j,2}, \quad (j = 1,2,3) \quad (2.14)$$

and the electric displacement obtained from $(2.1)_2$ is

$$D_1 = -\phi_{4,2}, \quad D_2 = \phi_{4,1}. \quad (2.15)$$

The two equations in (2.13) can be cast in a standard eigenrelation

$$\mathbf{N}\xi = p\xi, \quad (2.16)$$

$$\mathbf{N} = \begin{bmatrix} \mathbf{N}_1 & \mathbf{N}_2 \\ \mathbf{N}_3 & \mathbf{N}_1^T \end{bmatrix}, \quad \xi = \begin{bmatrix} \mathbf{a} \\ \mathbf{b} \end{bmatrix}, \quad (2.17)$$

in which

$$\mathbf{N}_1 = -\mathbf{T}^{-1}\mathbf{R}^T, \quad \mathbf{N}_2 = \mathbf{T}^{-1}, \quad \mathbf{N}_3 = \mathbf{R}\mathbf{T}^{-1}\mathbf{R}^T - \mathbf{Q}. \quad (2.18)$$

The 4×4 matrices $\mathbf{N}_2$ and $\mathbf{N}_3$ are symmetric. The eigenvalues of Eq. (2.16) are the roots of

$$|\mathbf{N} - p\mathbf{I}| = 0 \quad (2.19)$$

which is a polynomial of degree 8 in p. The general solutions obtained by superposing eight solutions of the form (2.7) and (2.12) are

$$\mathbf{u} = \sum_{\alpha=1}^{8} \mathbf{a}_\alpha f_\alpha(z_\alpha), \quad (2.20)$$

$$\boldsymbol{\phi} = \sum_{\alpha=1}^{8} \mathbf{b}_\alpha f_\alpha(z_\alpha), \quad (2.21)$$

where

$$z_\alpha = x_1 + p_\alpha x_2. \quad (2.22)$$

For stable materials defined by (2.3) it can be shown that p_α cannot be real. By letting

$$p_{\alpha+4} = \overline{p_\alpha}, \quad Im\{p_\alpha\} > 0, \quad (\alpha = 1,2,3,4) \quad (2.23)$$

in which an overbar denotes the complex conjugate and Im stands for imaginary part, the associated eigenvectors are

$$\mathbf{a}_{\alpha+4} = \overline{\mathbf{a}_\alpha}, \quad \mathbf{b}_{\alpha+4} = \overline{\mathbf{b}_\alpha}. \quad (\alpha = 1,2,3,4) \quad (2.24)$$

For $\mathbf{u}$ and $\boldsymbol{\phi}$ to be real, we choose $f_{\alpha+4}(z_{\alpha+4}) = \overline{f_\alpha(z_\alpha)}$ $(\alpha = 1,2,3,4)$ so that

$$\mathbf{u} = \sum_{\alpha=1}^{4} \mathbf{a}_\alpha f_\alpha(z_\alpha) + \overline{\mathbf{a}_\alpha}\,\overline{f_\alpha(z_\alpha)}, \quad (2.25)$$

$$\boldsymbol{\phi} = \sum_{\alpha=1}^{4} \mathbf{b}_\alpha f_\alpha(z_\alpha) + \overline{\mathbf{b}_\alpha}\,\overline{f_\alpha(z_\alpha)}. \quad (2.26)$$

In most applications we may set

$$f_\alpha(z_\alpha) = q_\alpha f(z_\alpha), \quad (\alpha \text{ not summed}) \quad (2.27)$$

where q_α are arbitrary complex constants. Thus, the general solutions reduce to

$$\mathbf{u} = \sum_{\alpha=1}^{4} \mathbf{a}_\alpha q_\alpha f(z_\alpha) + \overline{\mathbf{a}_\alpha}\,\overline{q_\alpha}\,\overline{f(z_\alpha)}, \quad (2.28)$$

$$\boldsymbol{\phi} = \sum_{\alpha=1}^{4} \mathbf{b}_\alpha q_\alpha f(z_\alpha) + \overline{\mathbf{b}_\alpha}\,\overline{q_\alpha}\,\overline{f(_\alpha)}. \quad (2.29)$$

For the problem of a line dislocation, a line force, and a line charge, we choose $f(z_\alpha) = \ln z_\alpha$ (Barnett and Lothe, 1975; Ting, 1988a). Hence (2.28) and (2.29) become

$$\mathbf{u} = \sum_{\alpha=1}^{4} q_\alpha \mathbf{a}_\alpha \ln z_\alpha + \overline{q_\alpha}\,\overline{\mathbf{a}_\alpha} \ln \overline{z_\alpha}, \quad (2.30)$$

$$\boldsymbol{\phi} = \sum_{\alpha=1}^{4} q_\alpha \mathbf{b}_\alpha \ln z_\alpha + \overline{q_\alpha}\,\overline{\mathbf{b}_\alpha} \ln \overline{z_\alpha}. \quad (2.31)$$

Introducing the two 4×4 matrices $\mathbf{A}$ and $\mathbf{B}$ defined by

$$\mathbf{A} = [\mathbf{a}_1, \mathbf{a}_2, \mathbf{a}_3, \mathbf{a}_4], \quad \mathbf{B} = [\mathbf{b}_1, \mathbf{b}_2, \mathbf{b}_3, \mathbf{b}_4] \quad (2.32)$$

and the diagonal matrix

Downloaded 04 May 2010 to 171.66.16.28. Redistribution subject to ASME license or copyright; see http://www.asme.org/terms/Terms_Use.cfm

$$\langle \ln z_* \rangle = \text{diag}\langle \ln z_1, \ln z_2, \ln z_3, \ln z_4 \rangle, \quad (2.33)$$

(2.30) and (2.31) can be rewritten as

$$\mathbf{u} = 2\,\text{Re}\{\mathbf{A}\langle \ln z_* \rangle \mathbf{q}\}, \quad (2.34)$$

$$\boldsymbol{\phi} = 2\,\text{Re}\{\mathbf{B}\langle \ln z_* \rangle \mathbf{q}\}. \quad (2.35)$$

The 4×1 matrix $\mathbf{q}$ is $\mathbf{q}^T = [q_1, q_2, q_3, q_4]$ and Re stands for the real part. To insure the single-valuedness of the generalized displacement vector $\mathbf{u}$ and the generalized stress function vector $\boldsymbol{\phi}$, a cut along the radial line $\theta = \theta_0$ is introduced.

In the cylindrical coordinate system (r, θ, x_3) where $x_1 = r\cos\theta$, $x_2 = r\sin\theta$ the surface traction $\mathbf{t}_\theta$ and the normal component of electric displacement D_θ on a radial plane $\theta =$ constant are

$$(\mathbf{t}_\theta)_j = \frac{\partial \phi_j}{\partial r}, \quad (j = 1, 2, 3), \quad D_\theta = \frac{\partial \phi_4}{\partial r}. \quad (2.36)$$

The surface traction $\mathbf{t}_r$ and the normal component of electric displacement D_r on a cylindrical surface $r =$ constant are

$$(\mathbf{t}_r)_j = -\frac{1}{r}\frac{\partial \phi_j}{\partial \theta}, \quad (j = 1, 2, 3), \quad D_r = -\frac{1}{r}\frac{\partial \phi_4}{\partial \theta}. \quad (2.37)$$

3 Useful Identities

The 4×4 complex matrices $\mathbf{A}$ and $\mathbf{B}$ in (2.32) have the similar property as the 3×3 complex matrices $\mathbf{A}$ and $\mathbf{B}$ for purely elastic materials have. Following Barnett and Lothe (1975), Chadwick and Smith (1977), and Ting (1988c) it can be shown that the 4×4 matrices $\mathbf{S}$, $\mathbf{H}$, $\mathbf{L}$ defined by

$$\mathbf{S} = i(2\mathbf{A}\mathbf{B}^T - \mathbf{I}), \quad \mathbf{H} = 2i\mathbf{A}\mathbf{A}^T, \quad \mathbf{L} = -2i\mathbf{B}\mathbf{B}^T \quad (3.1)$$

are real. $\mathbf{H}$ and $\mathbf{L}$ are symmetric, and can be shown to be nonsingular (Lothe and Barnett, 1976). They satisfy the following identity

$$\mathbf{H}\mathbf{L} - \mathbf{S}\mathbf{S} = \mathbf{I}. \quad (3.2)$$

Moreover, $\mathbf{S}\mathbf{H}$, $\mathbf{L}\mathbf{S}$, $\mathbf{H}^{-1}\mathbf{S}$, and $\mathbf{S}\mathbf{L}^{-1}$ are skew symmetric.

An alternate to (3.1) is the integral formalism of Barnett and Lothe (1973, 1975). Instead of (2.7) we consider a more general form of solution

$$\mathbf{u} = \mathbf{a} f(\hat{z}), \quad \hat{z} = \mathbf{x}\cdot\mathbf{n}(\omega) + p(\omega)\mathbf{x}\cdot\mathbf{m}(\omega) \quad (3.3)$$

where $p(\omega)$ depends on a real parameter ω and

$$\mathbf{n}^T(\omega) = [\cos\omega, \sin\omega, 0], \quad \mathbf{m}^T(\omega) = [-\sin\omega, \cos\omega, 0]. \quad (3.4)$$

Equations (2.13) are replaced by

$$\mathbf{b} = \left[\mathbf{R}^T(\omega) + p(\omega)\mathbf{T}(\omega)\right]\mathbf{a} = \frac{-1}{p(\omega)}[\mathbf{Q}(\omega) + p(\omega)\mathbf{R}(\omega)]\mathbf{a} \quad (3.5)$$

in which

$$\begin{aligned} Q_{JK}(\omega) &= n_i(\omega)E_{iJKm}n_m(\omega), \\ R_{JK}(\omega) &= n_i(\omega)E_{iJKm}m_m(\omega), \\ T_{JK}(\omega) &= m_i(\omega)E_{iJKm}m_m(\omega), \end{aligned} \quad (3.6)$$

and (Kuo and Barnett, 1991; Barnett and Lothe, 1975)

$$\begin{aligned} E_{iJKm} &= C_{ijkm} \quad (J, K = 1, 2, 3), \\ &= e_{mij} \quad (J = 1, 2, 3; \quad K = 4), \\ &= e_{ikm} \quad (J = 4; \quad K = 1, 2, 3), \\ &= -\omega_{im} \quad (J = K = 4). \end{aligned} \quad (3.7)$$

The two equations in (3.5) can be cast in the following standard eigenrelation:

$$\mathbf{N}(\omega)\xi = p(\omega)\xi \quad (3.8)$$

$$\mathbf{N}(\omega) = \begin{bmatrix} \mathbf{N}_1(\omega) & \mathbf{N}_2(\omega) \\ \mathbf{N}_3(\omega) & \mathbf{N}_1^T(\omega) \end{bmatrix}, \quad \xi = \begin{bmatrix} \mathbf{a} \\ \mathbf{b} \end{bmatrix} \quad (3.9)$$

$$\mathbf{N}_1(\omega) = -\mathbf{T}^{-1}(\omega)\mathbf{R}^T(\omega), \quad \mathbf{N}_2(\omega) = \mathbf{T}^{-1}(\omega),$$
$$\mathbf{N}_3(\omega) = \mathbf{R}(\omega)\mathbf{T}^{-1}(\omega)\mathbf{R}^T(\omega) - \mathbf{Q}(\omega). \quad (3.10)$$

They reduce to (2.16), (2.17), (2.18) when $\omega = 0$. If we define

$$\left.\begin{aligned} \mathbf{S}(\theta) &= \frac{1}{\pi}\int_0^\theta \mathbf{N}_1(\omega)d\omega, \\ \mathbf{H}(\theta) &= \frac{1}{\pi}\int_0^\theta \mathbf{N}_2(\omega)d\omega, \\ \mathbf{L}(\theta) &= \frac{-1}{\pi}\int_0^\theta \mathbf{N}_3(\omega)d\omega, \end{aligned}\right\} \quad (3.11)$$

Lothe and Barnett (1976) have shown that (3.1) can be replaced by

$$\mathbf{S} = \mathbf{S}(\pi), \quad \mathbf{H} = \mathbf{H}(\pi), \quad \mathbf{L} = \mathbf{L}(\pi). \quad (3.12)$$

It should be noted that $\mathbf{N}_i(\omega)$ $(i = 1, 2, 3)$ are periodic in ω with periodicity π, so is $p(\omega)$ which is related to p of (2.8) by (Suo et al., 1992)

$$p(\omega) = \frac{p\cos\omega - \sin\omega}{p\sin\omega + \cos\omega}. \quad (3.13)$$

Introducing the function

$$\psi_\alpha(\omega) = \ln\zeta_\alpha(\omega), \quad \zeta_\alpha(\omega) = \cos\omega + p_\alpha\sin\omega, \quad (3.14)$$

we have

$$\frac{d}{d\omega}\psi_\alpha(\omega) = p_\alpha(\omega). \quad (3.15)$$

Since

$$z_\alpha = x_1 + p_\alpha x_2 = r(\cos\theta + p_\alpha\sin\theta), \quad (3.16)$$

one obtains

$$\ln z_\alpha = \ln r + \psi_\alpha(\theta). \quad (3.17)$$

Equation (3.8) for $p_\alpha(\omega)$, $\alpha = 1, 2, 3, 4$, can be combined into one equation as

$$\begin{bmatrix} \mathbf{N}_1(\omega) & \mathbf{N}_2(\omega) \\ \mathbf{N}_3(\omega) & \mathbf{N}_1^T(\omega) \end{bmatrix}\begin{bmatrix} \mathbf{A} \\ \mathbf{B} \end{bmatrix} = \begin{bmatrix} \mathbf{A}\mathbf{P}(\omega) \\ \mathbf{B}\mathbf{P}(\omega) \end{bmatrix} = \begin{bmatrix} \mathbf{A}\dfrac{d}{d\omega}\boldsymbol{\psi}(\omega) \\ \mathbf{B}\dfrac{d}{d\omega}\boldsymbol{\psi}(\omega) \end{bmatrix} \quad (3.18)$$

where

$$\mathbf{P}(\omega) = \text{diag}\langle p_1(\omega), p_2(\omega), p_3(\omega), p_4(\omega)\rangle,$$
$$\boldsymbol{\psi}(\omega) = \text{diag}\langle \ln\zeta_1(\omega), \ln\zeta_2(\omega), \ln\zeta_3(\omega), \ln\zeta_4(\omega)\rangle.$$

Post-multiply by $[\mathbf{A}^T, \mathbf{B}^T]$ and write explicitly,

$$\begin{aligned} \mathbf{N}_1(\omega)\mathbf{A}\mathbf{A}^T + \mathbf{N}_2(\omega)\mathbf{B}\mathbf{A}^T &= \mathbf{A}\left[\frac{d}{d\omega}\boldsymbol{\psi}(\omega)\right]\mathbf{A}^T, \\ \mathbf{N}_1(\omega)\mathbf{A}\mathbf{B}^T + \mathbf{N}_2(\omega)\mathbf{B}\mathbf{B}^T &= \mathbf{A}\left[\frac{d}{d\omega}\boldsymbol{\psi}(\omega)\right]\mathbf{B}^T, \\ \mathbf{N}_3(\omega)\mathbf{A}\mathbf{A}^T + \mathbf{N}_1^T(\omega)\mathbf{B}\mathbf{A}^T &= \mathbf{B}\left[\frac{d}{d\omega}\boldsymbol{\psi}(\omega)\right]\mathbf{A}^T, \\ \mathbf{N}_3(\omega)\mathbf{A}\mathbf{B}^T + \mathbf{N}_1^T(\omega)\mathbf{B}\mathbf{B}^T &= \mathbf{B}\left[\frac{d}{d\omega}\boldsymbol{\psi}(\omega)\right]\mathbf{B}^T. \end{aligned} \quad (3.19)$$

Downloaded 04 May 2010 to 171.66.16.28. Redistribution subject to ASME license or copyright; see http://www.asme.org/terms/Terms_Use.cfm

Making use of the identities (3.1) and integrating (3.19) with ω yields

$$\frac{\pi}{2}\left[-i\mathbf{S}(\theta)\mathbf{H} + \mathbf{H}(\theta)(\mathbf{I} - i\mathbf{S}^T)\right] = \mathbf{A}\boldsymbol{\psi}(\theta)\mathbf{A}^T,$$

$$\frac{\pi}{2}\left[\mathbf{S}(\theta)(\mathbf{I} - i\mathbf{S}) + i\mathbf{H}(\theta)\mathbf{L}\right] = \mathbf{A}\boldsymbol{\psi}(\theta)\mathbf{B}^T,$$

$$\frac{\pi}{2}\left[i\mathbf{L}(\theta)\mathbf{H} + \mathbf{S}^T(\theta)(\mathbf{I} - i\mathbf{S}^T)\right] = \mathbf{B}\boldsymbol{\psi}(\theta)\mathbf{A}^T,$$

$$\frac{\pi}{2}\left[-\mathbf{L}(\theta)(\mathbf{I} - i\mathbf{S}) + i\mathbf{S}^T(\theta)\mathbf{L}\right] = \mathbf{B}\boldsymbol{\psi}(\theta)\mathbf{B}^T. \quad (3.20)$$

Equations (2.33), (3.17), and (3.20) leads to the following identities:

$$2\mathbf{A}\langle \ln z_* \rangle \mathbf{A}^T = 2(\ln r)\mathbf{A}\mathbf{A}^T + 2\mathbf{A}\boldsymbol{\psi}(\theta)\mathbf{A}^T$$
$$= -i(\ln r)\mathbf{H} + \pi\left\{\mathbf{H}(\theta) - i\left[\mathbf{S}(\theta)\mathbf{H} + \mathbf{H}(\theta)\mathbf{S}^T\right]\right\},$$
$$2\mathbf{A}\langle \ln z_* \rangle \mathbf{B}^T = 2(\ln r)\mathbf{A}\mathbf{B}^T + 2\mathbf{A}\boldsymbol{\psi}(\theta)\mathbf{B}^T$$
$$= \ln r(\mathbf{I} - i\mathbf{S}) + \pi\left\{\mathbf{S}(\theta) + i\left[\mathbf{H}(\theta)\mathbf{L} - \mathbf{S}(\theta)\mathbf{S}\right]\right\},$$
$$2\mathbf{B}\langle \ln z_* \rangle \mathbf{A}^T = 2(\ln r)\mathbf{B}\mathbf{A}^T + 2\mathbf{B}\boldsymbol{\psi}(\theta)\mathbf{A}^T$$
$$= \ln r(\mathbf{I} - i\mathbf{S}^T) + \pi\left\{\mathbf{S}^T(\theta) + i\left[\mathbf{L}(\theta)\mathbf{H} - \mathbf{S}^T(\theta)\mathbf{S}^T\right]\right\},$$
$$2\mathbf{B}\langle \ln z_* \rangle \mathbf{B}^T = 2(\ln r)\mathbf{B}\mathbf{B}^T + 2\mathbf{B}\boldsymbol{\psi}(\theta)\mathbf{B}^T$$
$$= i(\ln r)\mathbf{L} + \pi\left\{-\mathbf{L}(\theta) + i\left[\mathbf{L}(\theta)\mathbf{S} + \mathbf{S}^T(\theta)\mathbf{L}\right]\right\}. \quad (3.21)$$

Following the work of Kirchner and Lothe (1986) in pure elasticity, it can be shown that the products

$$\mathbf{N}(\omega)\mathbf{N}(\omega') = \mathbf{N}(\omega')\mathbf{N}(\omega) \quad (3.22)$$

commute. Integration of ω from 0 to θ and ω' from 0 to π yields

$$\begin{bmatrix} \mathbf{S}(\theta) & \mathbf{H}(\theta) \\ -\mathbf{L}(\theta) & \mathbf{S}^T(\theta) \end{bmatrix}\begin{bmatrix} \mathbf{S} & \mathbf{H} \\ -\mathbf{L} & \mathbf{S}^T \end{bmatrix}$$
$$= \begin{bmatrix} \mathbf{S} & \mathbf{H} \\ -\mathbf{L} & \mathbf{S}^T \end{bmatrix}\begin{bmatrix} \mathbf{S}(\theta) & \mathbf{H}(\theta) \\ -\mathbf{L}(\theta) & \mathbf{S}^T(\theta) \end{bmatrix}. \quad (3.23)$$

With (3.23), it can be verified that $(3.21)_2$ is the transpose of $(3.21)_3$, and that the right sides of $(3.21)_1$ and $(3.21)_4$ are indeed symmetric.

Finally, one can establish from (3.6) that

$$Q_{Jk}(\omega)m_k(\omega) = R_{Jk}(\omega)n_k(\omega),$$
$$R_{jK}(\omega)m_j(\omega) = T_{jK}(\omega)n_j(\omega). \quad (3.24)$$

Therefore

$$(\mathbf{N}_1(\omega))_{kj}m_j(\omega) = -n_k(\omega), \quad (\mathbf{N}_1(\omega))_{4j}m_j(\omega) = 0,$$
$$(\mathbf{N}_3(\omega))_{Jj}m_j(\omega) = 0, \quad (3.25)$$

where $J, K = 1, 2, 3, 4$ and $j, k = 1, 2, 3$.

4 Basic Real-Form Solution for a Wedge

In order to express the right sides of (2.34) and (2.35) in terms of real quantities, the arbitrary complex constant vector $\mathbf{q}$ is replaced by

$$\mathbf{q} = \frac{1}{\pi}(\mathbf{A}^T\mathbf{g} - \mathbf{B}^T\mathbf{h}) \quad (4.1)$$

in which $\mathbf{g}$ and $\mathbf{h}$ are real constant vectors. Employing the identities (3.21), the generalized displacement $\mathbf{u}$ for an individual wedge of the composite reduces to

$$\mathbf{u} = -\frac{\ln r}{\pi}\mathbf{h} - \mathbf{S}(\theta)\mathbf{h} + \mathbf{H}(\theta)\mathbf{g} + \mathbf{u}_0, \quad (4.2)$$

where $\mathbf{u}_0$ is a constant vector which produces no stresses and no electric displacements. Similarly, the generalized stress function is

$$\boldsymbol{\phi} = \frac{\ln r}{\pi}\mathbf{g} + \mathbf{S}^T(\theta)\mathbf{g} + \mathbf{L}(\theta)\mathbf{h}. \quad (4.3)$$

The constant vectors $\mathbf{u}_0$, $\mathbf{g}$, and $\mathbf{h}$ must be determined for each wedge. The continuity of displacement and electrostatic potential across an interface between two wedges implies that the $\ln r$ term in (4.2) must be continuous. Hence, $\mathbf{h}$ is the same for all wedges in the composite. The surface traction $\mathbf{t}_\theta$ on a radial plane θ = constant and the electric displacement D_θ normal to the radial plane θ = constant are, by (2.36),

$$(\mathbf{t}_\theta)_j = \frac{\partial \phi_j}{\partial r} = \frac{1}{\pi r}g_j, \quad (j = 1, 2, 3),$$
$$D_\theta = \frac{\partial \phi_4}{\partial r} = \frac{1}{\pi r}g_4. \quad (4.4)$$

Since they are continuous across an interface, $\mathbf{g}$ must be the same for all wedges. Thus, the constants $\mathbf{g}$ and $\mathbf{h}$ in (4.2) and (4.3) are invariant with respect to the choice of the individual wedge in the composite. In particular, (4.4) indicates that the surface traction and the normal component of the electric displacement on any radial plane of the composite is invariant with the choice of the radial plane.

From

$$u_{J,k} = \frac{\partial u_J}{\partial r}\frac{\partial r}{\partial x_k} + \frac{\partial u_J}{\partial \theta}\frac{\partial \theta}{\partial x_k} = \frac{\partial u_J}{\partial r}n_k(\theta) + \frac{\partial u_J}{\partial \theta}\frac{1}{r}m_k(\theta), \quad (4.5)$$

we obtain by (4.2)

$$u_{J,k} = \frac{1}{\pi r}\left\{-h_J n_k(\theta) + (\mathbf{N}_2(\theta)\mathbf{g} - \mathbf{N}_1(\theta)\mathbf{h})_J m_k(\theta)\right\}. \quad (4.6)$$

The dilatation of the elastic part is given by

$$u_{k,k} = \frac{1}{\pi r}\left\{-h_k n_k(\theta) + (\mathbf{N}_2(\theta)\mathbf{g} - \mathbf{N}_1(\theta)\mathbf{h})_k m_k(\theta)\right\}. \quad (4.7)$$

Since $\mathbf{m}(\theta)$, $\mathbf{n}(\theta)$, and $\mathbf{e}_3^T = [0, 0, 1]$ are, respectively, the unit normal and the two tangential vectors to the radial plane θ = constant, by $(4.4)_1$,

$$\begin{cases} \sigma_{\theta\theta} = \mathbf{t}_\theta \cdot \mathbf{m}(\theta) = \dfrac{1}{\pi r}g_j m_j(\theta), \\ \sigma_{\theta r} = \mathbf{t}_\theta \cdot \mathbf{n}(\theta) = \dfrac{1}{\pi r}g_j n_j(\theta), \quad (j = 1, 2, 3) \\ \sigma_{\theta 3} = \mathbf{t}_\theta \cdot \mathbf{e}_3 = \dfrac{1}{\pi r}g_3. \end{cases} \quad (4.8)$$

The unit normal and the two tangential vectors on the cylindrical surface r = constant are $\mathbf{n}(\theta)$, $\mathbf{m}(\theta)$, and $\mathbf{e}_3$, respectively. The surface traction vector $\mathbf{t}_r$ on the cylindrical surface r = constant and the normal electric displacement D_r are given in (2.37). Insertion of (4.3) into (2.37) gives

$$(\mathbf{t}_r)_j = \frac{1}{\pi r}\left\{\mathbf{N}_3(\theta)\mathbf{h} - \mathbf{N}_1^T(\theta)\mathbf{g}\right\}_j, \quad (j = 1, 2, 3) \quad (4.9)$$

$$D_r = \frac{1}{\pi r}\left\{\mathbf{N}_3(\theta)\mathbf{h} - \mathbf{N}_1^T(\theta)\mathbf{g}\right\}_4. \quad (4.10)$$

The elastic stress components on the cylindrical surface are

Downloaded 04 May 2010 to 171.66.16.28. Redistribution subject to ASME license or copyright; see http://www.asme.org/terms/Terms_Use.cfm

$$\sigma_{rr} = \mathbf{t}_r \cdot \mathbf{n}(\theta) = \frac{1}{\pi r}\left[\mathbf{N}_3(\theta)\mathbf{h} - \mathbf{N}_1^T(\theta)\mathbf{g}\right]_j n_j(\theta),$$

$$\sigma_{r\theta} = \mathbf{t}_r \cdot \mathbf{m}(\theta) = \frac{1}{\pi r}\left[\mathbf{N}_3(\theta)\mathbf{h} - \mathbf{N}_1^T(\theta)\mathbf{g}\right]_j m_j(\theta),$$

$$\sigma_{r3} = \mathbf{t}_r \cdot \mathbf{e}_3 = \frac{1}{\pi r}\left[\mathbf{N}_3(\theta)\mathbf{h} - \mathbf{N}_1^T(\theta)\mathbf{g}\right]_3. \tag{4.11}$$

Employing the identities in (3.25), the stress component $\sigma_{r\theta}$ in $(4.11)_2$ can be shown to be identical to $\sigma_{\theta r}$ in $(4.8)_2$.

In summary, when $\mathbf{g}$ and $\mathbf{h}$ are determined, $(4.4)_2$ and (4.8) give the normal component of electric displacement and the stress components on a radial surface θ = constant while (4.10) and (4.11) give the corresponding components on a cylindrical surface r = constant.

5 Composite Wedge Subject to Line Force and Line Charge

For a composite wedge that consists of n anisotropic piezoelectric wedges, (4.2) and (4.3) give

$$\mathbf{u}^{(k)} = -\frac{\ln r}{\pi}\mathbf{h} - \mathbf{S}^{(k)}(\theta)\mathbf{h} + \mathbf{H}^{(k)}(\theta)\mathbf{g} + \mathbf{u}_0^{(k)}, \tag{5.1}$$

$$\boldsymbol{\phi}^{(k)} = \frac{\ln r}{\pi}\mathbf{g} + \mathbf{S}^{(k)T}(\theta)\mathbf{g} + \mathbf{L}^{(k)}(\theta)\mathbf{h}, \tag{5.2}$$

for the kth wedge. It had been shown that $\mathbf{g}$ and $\mathbf{h}$ remain the same for $k = 1, 2, \ldots, n$. The sides $\theta = \theta_0$ and $\theta = \theta_n$ are traction-free and electrically open, i.e., the normal component of electric displacement is zero. By (4.4),

$$\mathbf{g} = \mathbf{0} \tag{5.3}$$

and (5.1) and (5.2) reduce to

$$\mathbf{u}^{(k)} = -\frac{\ln r}{\pi}\mathbf{h} - \mathbf{S}^{(k)}(\theta)\mathbf{h} + \mathbf{u}_0^{(k)}, \tag{5.4}$$

$$\boldsymbol{\phi}^{(k)} = \mathbf{L}^{(k)}(\theta)\mathbf{h}. \tag{5.5}$$

The continuity requirement for elastic displacement and electrostatic potential across the interfaces $\theta = \theta_1, \theta_2, \ldots, \theta_{n-1}$ implies that $\mathbf{u}^{(k)}(\theta_k) = \mathbf{u}^{(k+1)}(\theta_k)$. From (5.4),

$$\mathbf{u}_0^{(k)} - \mathbf{S}^{(k)}(\theta_k)\mathbf{h} = \mathbf{u}_0^{(k+1)} - \mathbf{S}^{(k+1)}(\theta_k)\mathbf{h}. \qquad (k = 1, 2, \ldots, n-1). \tag{5.6}$$

This gives $\mathbf{u}_0^{(2)}, \mathbf{u}_0^{(3)}, \ldots, \mathbf{u}_0^{(n)}$ in terms of $\mathbf{u}_0^{(1)}$ which can be arbitrary.

For a line force $\mathbf{f}$ and a line charge λ applied at the wedge apex,

$$\oint_{S'} \mathbf{t}_r dA = -\mathbf{f}, \quad \oint_{S'} \mathbf{D} \cdot d\mathbf{A} = \lambda \tag{5.7}$$

in which S' is the closed surface of the composite wedge within a right circular cylinder of unit height and radius r. Note that for two-dimensional deformation the integrals at the top and bottom surfaces of S' cancel each other. The equilibrium of the cylinder reduce to

$$\sum_{k=1}^{n} \int_{\theta_{k-1}}^{\theta_k} \mathbf{t}_r^{(k)} r d\theta = -\mathbf{f}, \quad \sum_{k=1}^{n} \int_{\theta_{k-1}}^{\theta_k} D_r^{(k)} r d\theta = \lambda, \tag{5.8}$$

or, by (2.37),

$$\begin{cases} \sum_{k=1}^{n} \left[\phi_j^{(k)}(\theta_k) - \phi_j^{(k)}(\theta_{k-1})\right] = f_j, & (j = 1, 2, 3) \\ \sum_{k=1}^{n} \left[\phi_4^{(k)}(\theta_k) - \phi_4^{(k)}(\theta_{k-1})\right] = -\lambda. \end{cases} \tag{5.9}$$

In matrix form we have

$$\sum_{k=1}^{n} \left[\boldsymbol{\phi}^{(k)}(\theta_k) - \boldsymbol{\phi}^{(k)}(\theta_{k-1})\right] = \begin{bmatrix} \mathbf{f} \\ -\lambda \end{bmatrix} = \hat{\mathbf{f}}, \tag{5.10}$$

and, by (5.5),

$$\sum_{k=1}^{n} \left[\mathbf{L}^{(k)}(\theta_k) - \mathbf{L}^{(k)}(\theta_{k-1})\right]\mathbf{h} = \hat{\mathbf{f}}. \tag{5.11}$$

Hence,

$$\mathbf{h} = \tilde{\mathbf{L}}^{-1}\hat{\mathbf{f}} \tag{5.12}$$

where

$$\begin{aligned} \tilde{\mathbf{L}} &= \sum_{k=1}^{n} \left[\mathbf{L}^{(k)}(\theta_k) - \mathbf{L}^{(k)}(\theta_{k-1})\right] \\ &= \sum_{k=1}^{n} \frac{1}{\pi} \int_{\theta_{k-1}}^{\theta_k} - \mathbf{N}_3^{(k)}(\omega) d\omega \\ &= \frac{1}{\pi} \int_{\theta_0}^{\theta_n} - \mathbf{N}_3(\omega) d\omega. \end{aligned} \tag{5.13}$$

6 Composite Space Subject to a Line Dislocation, A Line Force, and a Line Charge

For a composite space with a line dislocation, a line force, and a line charge applied at the origin $r = 0$, (5.1) and (5.2) still give the general solutions for the kth wedge. This time, both $\mathbf{g}$ and $\mathbf{h}$ are nonzero.

With $\mathbf{f}$ and λ being the applied line force and the applied line charge, respectively, substitution of (5.2) into the balance Eq. (5.10) yields

$$\sum_{k=1}^{n} \left[\mathbf{S}^{(k)T}(\theta_k) - \mathbf{S}^{(k)T}(\theta_{k-1})\right]\mathbf{g} + \sum_{k=1}^{n} \left[\mathbf{L}^{(k)}(\theta_k) - \mathbf{L}^{(k)}(\theta_{k-1})\right]\mathbf{h} = \hat{\mathbf{f}}. \tag{6.1}$$

If we define

$$\begin{aligned} \tilde{\mathbf{S}} &= \sum_{k=1}^{n} \left[\mathbf{S}^{(k)}(\theta_k) - \mathbf{S}^{(k)}(\theta_{k-1})\right] = \sum_{k=1}^{n} \frac{1}{\pi} \int_{\theta_{k-1}}^{\theta_k} \mathbf{N}_1^{(k)}(\omega) d\omega \\ &= \frac{1}{\pi} \int_{\theta_0}^{\theta_n} \mathbf{N}_1(\omega) d\omega, \end{aligned} \tag{6.2}$$

(6.1) is written as

$$\tilde{\mathbf{S}}^T\mathbf{g} + \tilde{\mathbf{L}}\mathbf{h} = \hat{\mathbf{f}}. \tag{6.3}$$

Let $\mathbf{b}$ be the Burgers vector for the line dislocation at $r = 0$, so that

$$\mathbf{u}^{(n)}(\theta_n) = \mathbf{u}^{(1)}(\theta_0) + \hat{\mathbf{b}}, \quad \hat{\mathbf{b}} = \begin{bmatrix} \mathbf{b} \\ b_4 \end{bmatrix}. \tag{6.4}$$

$b_4 \neq 0$ implies that there is an electric dipole layer along the cut plane $\theta = \theta_0 = \theta_n$. Employing (5.1) in (6.4) we have

$$\mathbf{u}_0^{(n)} + \mathbf{H}^{(n)}(\theta_n)\mathbf{g} - \mathbf{S}^{(n)}(\theta_n)\mathbf{h} = \mathbf{u}_0^{(1)} + \mathbf{H}^{(1)}(\theta_0)\mathbf{g} - \mathbf{S}^{(1)}(\theta_0)\mathbf{h} + \hat{\mathbf{b}}. \tag{6.5}$$

The continuity condition at the interfaces $\theta = \theta_1, \theta_2, \ldots, \theta_{n-1}$ requires that $\mathbf{u}^{(k)}(\theta_k) = \mathbf{u}^{(k+1)}(\theta_k)$, or

$$\mathbf{u}_0^{(k)} + \mathbf{H}^{(k)}(\theta_k)\mathbf{g} - \mathbf{S}^{(k)}(\theta_k)\mathbf{h} = \mathbf{u}_0^{(k+1)} + \mathbf{H}^{(k+1)}(\theta_k)\mathbf{g} - \mathbf{S}^{(k+1)}(\theta_k)\mathbf{h}, \tag{6.6}$$

with $k = 1, 2, \ldots, n-1$. Adding the n equations given by (6.5) and (6.6) yields

Downloaded 04 May 2010 to 171.66.16.28. Redistribution subject to ASME license or copyright; see http://www.asme.org/terms/Terms_Use.cfm

$$\tilde{\mathbf{H}}\mathbf{g} - \tilde{\mathbf{S}}\mathbf{h} = \hat{\mathbf{b}} \tag{6.7}$$

where

$$\begin{aligned}\tilde{\mathbf{H}} &= \sum_{k=1}^{n}\left[\mathbf{H}^{(k)}(\theta_k) - \mathbf{H}^{(k)}(\theta_{k-1})\right] \\ &= \sum_{k=1}^{n}\frac{1}{\pi}\int_{\theta_{k-1}}^{\theta_k}\mathbf{N}_2^{(k)}(\omega)d\omega \\ &= \frac{1}{\pi}\int_{\theta_0}^{\theta_n}\mathbf{N}_2(\omega)d\omega. \end{aligned}\tag{6.8}$$

It should be noted that $\theta_n = \theta_0 + 2\pi$ for the composite space.

The constant vectors $\mathbf{g}$ and $\mathbf{h}$ can be solved from (6.3) and (6.7) as follows. Premultiply (6.3) by $\tilde{\mathbf{S}}\tilde{\mathbf{L}}^{-1}$ and eliminate $\tilde{\mathbf{S}}\mathbf{h}$ from (6.7) gives

$$\left[\tilde{\mathbf{H}} + \tilde{\mathbf{S}}\tilde{\mathbf{L}}^{-1}\tilde{\mathbf{S}}^T\right]\mathbf{g} = \tilde{\mathbf{S}}\tilde{\mathbf{L}}^{-1}\hat{\mathbf{f}} + \hat{\mathbf{b}}.$$

Hence

$$\mathbf{g} = \mathbf{U}^{-1}\left(\tilde{\mathbf{S}}\tilde{\mathbf{L}}^{-1}\hat{\mathbf{f}} + \hat{\mathbf{b}}\right), \tag{6.9}$$

$$\mathbf{U} = \tilde{\mathbf{H}} + \tilde{\mathbf{S}}\tilde{\mathbf{L}}^{-1}\tilde{\mathbf{S}}^T. \tag{6.10}$$

Similarly, premultiply (6.7) by $\tilde{\mathbf{S}}^T\tilde{\mathbf{H}}^{-1}$ and eliminate $\tilde{\mathbf{S}}^T\mathbf{g}$ from (6.3) leads to

$$\left(\tilde{\mathbf{S}}^T\tilde{\mathbf{H}}^{-1}\tilde{\mathbf{S}} + \tilde{\mathbf{L}}\right)\mathbf{h} = \hat{\mathbf{f}} - \tilde{\mathbf{S}}^T\tilde{\mathbf{H}}^{-1}\hat{\mathbf{b}}.$$

Thus

$$\mathbf{h} = \mathbf{V}^{-1}\left(\hat{\mathbf{f}} - \tilde{\mathbf{S}}^T\tilde{\mathbf{H}}^{-1}\hat{\mathbf{b}}\right), \tag{6.11}$$

$$\mathbf{V} = \tilde{\mathbf{L}} + \tilde{\mathbf{S}}^T\tilde{\mathbf{H}}^{-1}\tilde{\mathbf{S}}. \tag{6.12}$$

With $\mathbf{g}$ and $\mathbf{h}$ so determined, (6.6) provides expressions for $\mathbf{u}_0^{(2)}, \mathbf{u}_0^{(3)}, \ldots, \mathbf{u}_0^{(n)}$ in terms of $\mathbf{u}_0^{(1)}$ which can be arbitrary.

7 Discussion

In the special case of a homogeneous space the superscript (k) can be ignored. $\tilde{\mathbf{S}}$, $\tilde{\mathbf{H}}$, and $\tilde{\mathbf{L}}$ reduce to $2\mathbf{S}$, $2\mathbf{H}$, and $2\mathbf{L}$, respectively. Equation (6.10) becomes

$$\mathbf{U} = 2\mathbf{H} + 2\mathbf{S}(2\mathbf{L})^{-1}(2\mathbf{S})^T = 2(\mathbf{H} + \mathbf{S}\mathbf{L}^{-1}\mathbf{S}^T).$$

Since $\mathbf{L}^{-1}\mathbf{S}^T$ is antisymmetric,

$$\mathbf{U} = 2(\mathbf{H} - \mathbf{S}\mathbf{S}\mathbf{L}^{-1}) = 2(\mathbf{H}\mathbf{L} - \mathbf{S}\mathbf{S})\mathbf{L}^{-1} = 2\mathbf{L}^{-1} \tag{7.1}$$

by virtue of (3.2). Similarly it can be shown that

$$\mathbf{V} = 2\mathbf{H}^{-1}. \tag{7.2}$$

Equations (6.9) and (6.11) reduce to

$$\mathbf{g} = \frac{1}{2}(\mathbf{L}\hat{\mathbf{b}} - \mathbf{S}^T\hat{\mathbf{f}}), \tag{7.3}$$

$$\mathbf{h} = \frac{1}{2}(\mathbf{H}\hat{\mathbf{f}} + \mathbf{S}\hat{\mathbf{b}}). \tag{7.4}$$

Equation (4.6) can be written as

$$\begin{aligned}u_{J,k} = &-\frac{1}{2\pi r}(\mathbf{H}\hat{\mathbf{f}} + \mathbf{S}\hat{\mathbf{b}})_J n_k(\theta) \\ &-\frac{1}{2\pi r}\left[(\mathbf{N}_1(\theta)\mathbf{S} - \mathbf{N}_2(\theta)\mathbf{L})\hat{\mathbf{b}}\right. \\ &\left.+(\mathbf{N}_1(\theta)\mathbf{H} + \mathbf{N}_2(\theta)\mathbf{S}^T)\hat{\mathbf{f}}\right]_J m_k(\theta). \end{aligned}\tag{7.5}$$

which is essentially Eq. (32) in Barnett and Lothe (1975).

Equation (3.22), after integrating with ω' from 0 to π and replacing ω by θ, can be written explicitly as

$$\begin{cases} \mathbf{N}_1(\theta)\mathbf{S} - \mathbf{N}_2(\theta)\mathbf{L} = \mathbf{S}\mathbf{N}_1(\theta) - \mathbf{H}\mathbf{N}_3(\theta), \\ \mathbf{N}_1(\theta)\mathbf{H} + \mathbf{N}_2(\theta)\mathbf{S}^T = \mathbf{S}\mathbf{N}_2(\theta) + \mathbf{H}\mathbf{N}_1^T(\theta), \\ -\mathbf{N}_3(\theta)\mathbf{S} - \mathbf{N}_1^T(\theta)\mathbf{L} = -\mathbf{L}\mathbf{N}_1(\theta) - \mathbf{S}^T\mathbf{N}_3(\theta), \\ -\mathbf{N}_3(\theta)\mathbf{H} + \mathbf{N}_1^T(\theta)\mathbf{S}^T = -\mathbf{L}\mathbf{N}_2(\theta) + \mathbf{S}^T\mathbf{N}_1^T(\theta). \end{cases}\tag{7.6}$$

With the use of $(7.6)_1$ and $(7.6)_2$, (7.5) has the alternate form

$$\begin{aligned}u_{J,k} = &-\frac{1}{2\pi r}(\mathbf{H}\hat{\mathbf{f}} + \mathbf{S}\hat{\mathbf{b}})_J n_k(\theta) \\ &-\frac{1}{2\pi r}\left[\mathbf{S}\left(\mathbf{N}_1(\theta)\hat{\mathbf{b}} + \mathbf{N}_2(\theta)\hat{\mathbf{f}}\right)\right. \\ &\left.+\mathbf{H}\left(\mathbf{N}_3(\theta)\hat{\mathbf{b}} + \mathbf{N}_1^T(\theta)\hat{\mathbf{f}}\right)\right]_J m_k(\theta). \end{aligned}\tag{7.7}$$

Acknowledgments

The work presented here is supported by the U.S. Air Force Office of Scientific Research through grant F49620-92-J-0087.

References

Barnett, D. M., and Lothe, J., 1973, "Synthesis of the Sextic and the Integral Formalism for Dislocations, Greens Functions and Surface Waves in Anisotropic Elastic Solids," *Physica Norvegica*, Vol. 7, pp. 13–19.

Barnett, D. M., and Lothe, J., 1975, "Dislocations and Line Charges in Anisotropic Piezoelectric Insulators," *Physica Status Solidi B*, Vol. 67, pp. 105–111.

Cady, W. G., 1946, *Piezoelectricity*, McGraw-Hill, New York.

Chadwick, P., and Smith, G. D., 1977, "Foundations of the Theory of Surface Waves in Anisotropic Elastic Materials," *Advances in Applied Mechanics*, Vol. 17, pp. 303–376.

Eshelby, J. D., Read, W. T., and Shockley, W., 1953, "Anisotropic Elasticity with Applications to Dislocation Theory," *Acta Metallurgica*, Vol. 1, pp. 251–259.

Horn, R. A., and Johnson, C. R., 1990, *Matrix Analysis*, Cambridge University Press, New York, pp. 21–22.

Hwu, Chyanbin, and Ting, T. C. T., 1990, "Solutions for the Anisotropic Elastic Wedges at Critical Wedge Angles," *Journal of Elasticity*, Vol. 24, pp. 1–20.

Kirchner, H. O. K., and Lothe, J., 1986, "On the Redundancy of the $\overline{\mathbf{N}}$ Matrix of Anisotropic Elasticity," *Philosophical Magazine A*, Vol. 53, pp. L7–L10.

Kuo, C. M., and Barnett, D. M., 1991, "Stress Singularities of Interface Cracks in Bonded Piezoelectric Half-Spaces," *Modern Theory of Anisotropic Elasticity and Applications*, J. J. Wu, T. C. T. Ting, and D. M. Barnett, eds., SIAM Proceedings Series, SIAM, Philadelphia, PA, pp. 33–51.

Lothe, J., and Barnett, D. M., 1976, "Integral Formalism for Surface Waves in Piezoelectric Crystals. Existence Considerations," *Journal of Applied Physics*, Vol. 47, pp. 1799–1807.

Pak, Y. Eugene, 1992, "Circular Inclusion Problem in Antiplane Piezoelectricity," *International Journal of Solids and Structures*, Vol. 29, pp. 2403–2419.

Reitz, J. R., Milford, F. J., and Christy, R. W., 1980, *Foundations of Electromagnetic Theory*, Addison-Wesley, MA.

Sosa, Horacio, 1991, "Plane Problems in Piezoelectric Media with Defects," *International Journal of Solids and Structures*, Vol. 28, pp. 491–505.

Stroh, A. N., 1958, "Dislocations and Cracks in Anisotropic Elasticity," *Philosophical Magazine*, Vol. 3, pp. 625–646.

Stroh, A. N., 1962, "Steady State Problems in Anisotropic Elasticity," *Journal of Mathematics and Physics*, Vol. 41, pp. 77–103.

Suo, Z., Kuo, C. M., Barnett, D. M., and Willis, J. R., 1992, "Fracture Mechanics for Piezoelectric Ceramics," *Journal of Mechanics and Physics of Solids*, Vol. 40, pp. 739–765.

Tiersten, H. F., 1969, *Linear Piezoelectric Plate Vibrations*, Plenum Press, New York.

Ting, T. C. T., 1986, "Explicit Solution and Invariance of the Singularities at an Interface Crack in Anisotropic Composites," *International Journal of Solids and Structures*, Vol. 22, pp. 965–983.

Ting, T. C. T., 1988a, "Line Forces and Dislocations in Anisotropic Elastic Composite Wedges and Spaces," *Physica Status Solidi B*, Vol. 145, pp. 81–90.

Ting, T. C. T., 1988b, "The Anisotropic Elastic Wedge Under a Concentrated Couple," *Quarterly Journal of Mechanics and Applied Mathematics*, Vol. 41, pp. 563–578.

Ting, T. C. T., 1988c, "Some Identities and the Structure of N_i in the Stroh Formalism of Anisotropic Elasticity," *Quarterly of Applied Mathematics*, Vol. 46, pp. 109–120.

Ting, T. C. T., and Yan, Gongpu, 1991, "The Anisotropic Elastic Solid with an Elliptic Hole or Rigid Inclusion," *International Journal of Solids and Structures*, Vol. 27, pp. 1879–1894.

Downloaded 04 May 2010 to 171.66.16.28. Redistribution subject to ASME license or copyright; see http://www.asme.org/terms/Terms_Use.cfm

Critical Angles in Bending of Rotationally Inhomogeneous Elastic Wedges

A. Yu Belov
Institute of Crystallography,
Russian Academy of Sciences,
Leninsky Prospect 59,
Moscow 117333, Russia

H. O. K. Kirchner
Institute de Sciences des Materiaux,
Université Paris-Sud,
Batiment 413,
F-91405, Orsay, France

An anisotropic rotationally inhomogeneous wedge bent by either a concentrated couple applied at the tip (Carothers problem) or uniform surface loadings (Levy problem) is considered. The existence criteria for homogeneous solutions describing stresses and strains in both problems are established. In the Levy problem there are two types of critical wedge angles, at which homogeneous solutions break down and become infinite. The first type critical wedge angles of Levy's problem are shown to be critical also for Carothers' problem whatever the rotational inhomogeneity. Particular solutions to both problems are obtained at the critical wedge angle. The form of these solutions is established to depend on two factors: the multiplicity degree of roots of some eigenvalue equation and the number of independent eigenvectors of some real matrix. It is shown also that the eigenvalue equation does not provide an alternative way to calculate the critical angles and in the first-order perturbation theory results in just the same equations for the critical angles.

1 Introduction

As is well known (Levy, 1898; Carothers, 1912; Timoshenko and Goodier, 1970), the elementary homogeneous solutions for the stresses in an elastic wedge of the wedge angle $\alpha = 2\gamma$ occupying in polar coordinates (r, ϕ) the region

$$0 \le r < \infty, \quad -\gamma \le \phi \le \gamma, \tag{1}$$

and deformed by either a concentrated couple (Carothers' problem) or a uniform surface loading (Levy's problem) exhibit anomalous behavior at some critical wedge angles. For elastically isotropic materials the critical angles of the two problems coincide. This follows from the explicit expressions for a biharmonic stress function $\Phi(r, \phi)$. In view of the absence of a characteristic length in Eq. (1), the stress function exhibits scaling and can be established directly from simple dimensional considerations. In particular, in the Carothers case (Fig. 1) it is r-independent,

$$\Phi(r, \phi) = -Mf(\phi), \tag{2}$$

while in the Levy case (Fig. 2) it increases as r^2,

$$\Phi(r, \phi) = kr^2 f(\phi). \tag{3}$$

The function $f(\phi)$ is given by the expression

$$f(\phi) = (\sin 2\phi - 2\phi \cos 2\gamma)/2(\sin 2\gamma - 2\gamma \cos 2\gamma) \tag{4}$$

for both bending schemes shown in Fig. 1 and 2 in spite of the very different boundary conditions in the problems of Carothers and Levy. Here M and k denote the moment of the couple and the density of normal loading, respectively. The critical wedge angle α_* results from the vanishing of the denominator in Eq. (4),

$$\sin \alpha_* - \alpha_* \cos \alpha_* = 0, \tag{5}$$

so that stresses derivable from the stress function (2) or (3) at $\alpha = \alpha_*$ become infinite for all (r, ϕ). A specific feature of isotropic materials is that the function $f(\phi)$ does not depend on elastic constants and hence is equally applicable to both plane-strain and plane-stress situations. In turn, by Eq. (5), in isotropic wedges the critical angle $\alpha_* = 1.43\pi$ is independent of elastic constants.

Recently it was shown by Ting (1988a, 1988b) that the critical wedge angles in the problems of Carothers and Levy coincide not only for isotropic but also for elastically anisotropic materials. However, unlike Eq. (5), Ting's equation for the critical angle of an anisotropic wedge depends on elastic constants and describes only the generalized plane-strain situation. Nevertheless, modification of this equation to the plane-stress case does not cause difficulties and reduces to a renormalization of elastic constants. Although Ting (1988a, 1988b) confined himself only to elastically homogeneous wedges, the conclusion on the critical angles

Contributed by the Applied Mechanics Division of THE AMERICAN SOCIETY OF MECHANICAL ENGINEERS for publication in the ASME JOURNAL OF APPLIED MECHANICS.

Discussion on this paper should be addressed to the Technical Editor, Professor Lewis T. Wheeler, Department of Mechanical Engineering, University of Houston, Houston, TX 77204-4792, and will be accepted until four months after final publication of the paper itself in the ASME JOURNAL OF APPLIED MECHANICS.

Manuscript received by the ASME Applied Mechanics Division, Mar. 12, 1993; final revision, Dec. 3, 1993. Associate Technical Editor: X. Markenscoff.

Copyright © 1995 by ASME

Downloaded 04 May 2010 to 171.66.16.28. Redistribution subject to ASME license or copyright; see http://www.asme.org/terms/Terms_Use.cfm

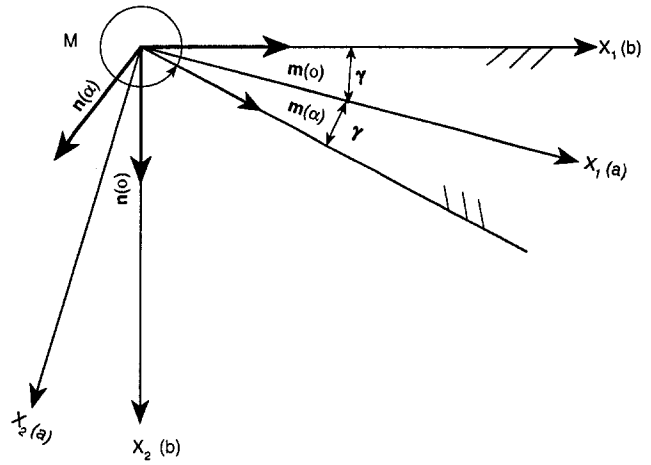

Fig. 1 An elastic wedge of the wedge angle $\alpha = 2\gamma$ subjected to a concentrated couple. Two choices of the coordinate system x_i are shown: (a) for an isotropic homogeneous wedge, (b) for a rotationally inhomogeneous wedge.

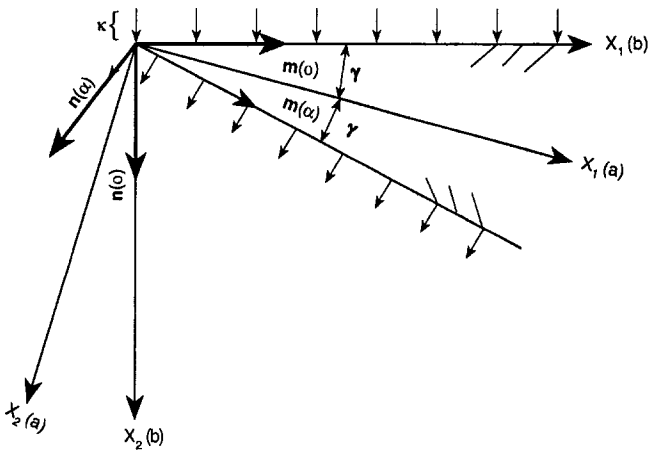

Fig. 2 An elastic wedge of the wedge angle $\alpha = 2\gamma$ subjected to uniform and normal surface loadings. Two choices of the coordinate system x_i are shown: (a) for an isotropic homogeneous wedge, (b) for a rotationally inhomogeneous wedge.

equality does not depend on the assumption of material homogeneity and follows from fundamental principles of linear elasticity theory. The main purpose of this paper is to show that the critical angles of the two problems coincide for a rotationally inhomogeneous wedge where elastic constants depend on the azimuth ϕ. It will be proved that the critical angle α_*^C of the Carothers problem is necessarily a critical angle α_*^L for the Levy problem, where additional critical angles can occur as well. It will be also shown that the wedge angles α_*^C and α_*^L coincide solely due to the symmetry of the elastic constants tensor or, which is the same, due to the existence of the elastic potential which makes the elastic constants tensor fully symmetric.

2 Dimensional Considerations

Because of Eq. (4), the dimensional arguments which led to the homogeneous solutions (2) and (3) break down at the critical angle α_*, which is a violation of St. Venant's principle. This physical paradox was first discussed by Sternberg and Koiter (1958) who examined the asymptotic behavior of a modified problem in which the couple was replaced by a statically equivalent pressure distribution on the sides of the wedge over a finite interval $0 \le r \le a$. The main conclusion of Sternberg and Koiter is that the stress asymptote in the modified problem as $r/a \to \infty$ behaves as r^{-2} and coincides with the homogeneous Carothers stress, which is independent on the choice of pressure distribution, provided that the wedge angle α is less that α_*. When α exceeds α_* the principal term of the stress asymptote follows the scaling law again, however somewhat more slowly than in the previous case, namely as $r^{-1}(r/a)^{s(\alpha)}$, where the exponent $s(\alpha)$ is the root of the equation

$$s \sin \alpha - \sin s\alpha = 0 \tag{6}$$

that lies in the interval $-1 < s(\alpha) < 0$. Finally, if the wedge angle is exactly equal to the critical value, the stress asymptote does not exhibit scaling at all, but follows the logarithmic law, $r^{-2}\ln(r/a)$, which cannot be established from dimensional analysis as $a \to 0$. The remarkable result of Sternberg and Koiter is that the stress asymptote in the two last cases essentially depends on the choice of the pressure distribution and thus the conventional statement of St. Venants' principle is not valid when $\alpha \ge \alpha_*$.

Besides the Carothers-Sternberg-Koiter paradox, there are many static and dynamic problems, both linear and nonlinear, in which dimensional arguments fail at some critical parameters, and solutions exhibit a drastic change in the type of asymptotic similarity. The term *similarity* is used here in its broad sense meaning self-similarity in dynamics, and scaling (homogeneity) in statics. Barenblatt (1979) proposes a general analysis of such phenomena and derives an intimate connection between the failure of dimensional arguments and irregularity of the limiting passage.

Self-similar solutions always represent solutions of degenerate problems where all constant parameters governing the spatial and time scales (characteristic lengths and times) vanish or become infinite. However, the limiting process in passing from the original nondegenerate problem to a degenerate problem (which are, for example, the Sternberg-Koiter and Carothers problems) is not necessarily regular which can result in two different types of self-similar solutions. Their origin is revealed most clearly in dimensional analysis of the limiting passage.

Let us consider the simplest situation, when there are only two independent variables r and t (which may be interpreted as a spatial coordinate and time or somehow else), and one scale governing parameter, characteristic length R, in the problem. By Barenblatt's Π-theorem, any solution $U(r, t)$ of the nondegenerate problem can be expressed as a relation among dimensionless quantities: $U(r, t)/m(r)$, ξ, η, and $\Pi = (\Pi_1, \Pi_2, \Pi_3, \ldots)$,

$$U(r,t)/m(r) = F(\xi, \eta, \Pi), \tag{7}$$

where $m(r) \simeq r^p$ is the scale of the unknown quantity $U(r, t)$, $\xi \simeq r^n/t$ is the self-similar variable, $\eta = r/R$, and the parameters Π_i depend neither on r, t, or R. Thus the scale R enters the problem only through the parameter η and the problem becomes degenerate when R tends to infinity and $\eta \to 0$, or, alternatively, when R goes to zero and $\eta \to \infty$. Then, if the limit of the function F exists and is finite, the statement of the degenerate problem is legitimate and its solution,

$$U(r, t)/m(r) = F_0(\xi, \Pi), \tag{8}$$

where

$$F_0(\xi, \Pi) = \begin{cases} F(\xi, 0, \Pi) \\ F(\xi, \infty, \Pi) \end{cases} \quad \text{for} \quad \begin{cases} \eta \to 0 \\ \eta \to \infty \end{cases}, \tag{9}$$

is a self-similar solution of the *first type*. In this case exponents p and n are determined from dimensional considerations.

Downloaded 04 May 2010 to 171.66.16.28. Redistribution subject to ASME license or copyright; see http://www.asme.org/terms/Terms_Use.cfm

Self-similar solution of the *second type* correspond to the special situation when, as $\eta \to 0$ or $\eta \to \infty$, the limit of the function $F(\xi, \eta, \Pi)$ is infinity, but there is a number λ (which here is assumed real) such that the function F behaves in accordance with a scaling law

$$F(\xi, \eta, \Pi) = \eta^{\lambda(\Pi)} F_1(\xi, \Pi), \tag{10}$$

the critical exponent $\lambda = \lambda(\Pi)$ being negative in the case $\eta \to 0$ and positive in the case $\eta \to \infty$. The exponent λ is a solution of a certain eigenvalue problem and can not be established by dimensional considerations. The statement of a degenerate problem corresponding to $R \to 0$ or $R \to \infty$ is obviously illegitimate in this case.

Equations (9) and (10) describe only the asymptotic dependence of solutions to nondegenerate problems on the parameter η, but do not reveal the mechanism underlying the irregularity of the limiting passage. In linear problems this mechanism can be traced explicitly. In particular, instead of looking for the critical point $\Pi = \Pi_*$ as a point of failure of the solution $F_0(\xi, \Pi)$, one can solve the equation $\lambda(\Pi_*) = 0$ resulting in just the same Π_*. In linear problems this equation is derived explicitly.

Let us now turn back to the elastic wedge and introduce instead of the self-similar variable $\xi = x_2/x_1$ a related quantity, the azimuth $\phi = \tan^{-1}\xi$. Let also Π_i denote the wedge angle and a set (discrete or continuous) of dimensionless elastic parameters describing rotational inhomogeneity. We further suppose the wedge region to be $0 \le \phi \le \alpha$, since the symmetry under reflection $\phi \to -\phi$ fails in the case of anisotropy and rotational inhomogeneity.

Owing to linearity, away from the critical angles any solution of a nondegenerate problem for the wedge can be written as

$$U(r, \phi)/m(r) = F_0(\phi, \Pi) + \sum_{n=1}^{\infty} k_n \eta^{\lambda_n(\Pi)} F_n(\phi, \Pi). \tag{11}$$

Here the dimensionless solution $F_0(\phi, \Pi)$, resulting in the prescribed uniform tractions at the wedge sides $\phi = 0$ and $\phi = \alpha$ or in the couple at the wedge tip, is completed by an infinite number of the dimensionless homogeneous eigensolutions $\eta^{\lambda_n(\Pi)} F_n(\phi, \Pi)$, which satisfy at the wedge sides the traction-free boundary condition. The sense of the characteristic length R entering the parameter η in Eq. (11) largely depends on the statement of the corresponding nondegenerate problem. For this purpose Carothers' problem is modified by an outer problem for the region

$$r_0 \le r < \infty, \quad 0 \le \phi \le \alpha, \tag{12}$$

subjected at the arc $r = r_0$ to a distribution of self-equilibrated tractions resulting in the couple M, while Levy's one is modified by an inner problem for the region

$$0 \le r \le R_0, \quad 0 \le \phi \le \alpha, \tag{13}$$

uniformly and normally loaded at $\phi = 0$ and $\phi = \alpha$. Thus the parameter R is equal to either r_0 or R_0. In turn, the coefficients k_n can be determined from the boundary condition at $r = r_0$ or $r = R_0$, depending on whether the problem is outer or inner. They are nonzero only for eigensolutions satisfying the condition of bounded elastic energy, which is $s_n > 0$ for inner and $s_n < 0$ for outer problems. Here $s_n = p + \lambda_n(\Pi)$, and p is the exponent of r in the *displacement* scale $m(r) \simeq r^p$ which can be derived by dimensional arguments (in the Carothers problem $p = -1$, and in the Levy problem $p = 1$). If we are interested only in antisymmetric eigensolutions of the isotropic wedge, s_n are roots of Eq. (6). Hence, the coincidence of the critical angles in these problems in the case of isotropic materials simply follows from the symmetry of Eq. (6), in which the opposite roots s and $-s$ appear simultaneously.

In elasticity theory we meet a specific feature of dimensional analysis. The point is that the displacement field $\mathbf{u}(\mathbf{r})$ is not defined unambiguously but only up to a rigid-body displacement

$$\mathbf{u}(\mathbf{r}) \to \mathbf{u}(\mathbf{r}) + \mathbf{b}_0 + [\boldsymbol{\omega}_0 \times \mathbf{r}], \tag{14}$$

where $\mathbf{b}_0$ is a rigid-body translation and $\boldsymbol{\omega}_0$ is a rigid-body rotation. By this reason Eq. (11) is applicable to stresses and strains, but not to displacements and rotations, which are not "good" physical quantities. As result, the η-independent part of displacements giving rise to the first type self-similar strains may contain the term

$$\mathbf{u}(\mathbf{r}) = [\boldsymbol{\omega}_0 \times \mathbf{r}] \ln(r/L) + \ldots, \tag{15}$$

which is illegitimate from the point of view of dimensional analysis, since the parameter L in Eq. (15) is arbitrary, and unlike R, has not the sense of a characteristic length. Any variation of L results only in adding of a rigid-body rotation.

3 Self-Similarities. Rotational Inhomogeneity

We need to find self-similarities entering Eq. (11) in the case of rotationally inhomogeneous elastic wedges.

3.1 Some Matrix Identities. First, we discuss some peculiarities of the elasticity theory of rotationally inhomogeneous media. Let the elastic constants have an angular dependence $C_{ijkl}(\phi)$ on the azimuth ϕ around the axis $\mathbf{t}(x_3$-axis). We consider the generalized plane-strain situation, when the displacement vector $\mathbf{u}$ remains invariant along x_3, and has both plane (u_1 and u_2) and antiplane (u_3) components. In this case the elastic constants enter the problem only through the elements of the 6×6 real matrix

$$\hat{\mathbf{N}}(\phi) = \begin{bmatrix} \hat{\mathbf{N}}_1 & \hat{\mathbf{N}}_2 \\ \hat{\mathbf{N}}_3 & \hat{\mathbf{N}}_4 \end{bmatrix} \tag{16}$$

consisting of the blocks

$$\hat{\mathbf{N}}_1 = -(nn)^{-1}(nm), \qquad \hat{\mathbf{N}}_2 = -(nn)^{-1},$$

$$\hat{\mathbf{N}}_3 = (mm) - (mn)(nn)^{-1}(nm), \quad \hat{\mathbf{N}}_4 = -(mn)(nn)^{-1},$$

where the parentheses

$$(ab)_{jk} = a_i C_{ijkl}(\phi) b_l \tag{17}$$

denote real 3×3 matrices, and the unit basis $(\mathbf{m}, \mathbf{n}, \mathbf{t})$ results from rotation of the Cartesian right-hand basis $(\mathbf{m}_0, \mathbf{n}_0, \mathbf{t})$ by an angle ϕ around $\mathbf{t}$. This result does not depend on whether a material is homogeneous (Stroh 1958, 1962) or rotationally inhomogeneous and forms the basis of the six-dimensional consistency equation method (Kirchner, 1989).

There is a considerable distinction in behavior of the $\hat{\mathbf{N}}(\phi)$ matrices in the case of homogeneous and rotationally inhomogeneous media. It is due to the fact that in the first case the matrices $\hat{\mathbf{N}}(\phi)$ commute for different values of the argument (Kirchner and Lothe, 1986), whereas in the second case the commutator

$$\left[\hat{\mathbf{N}}(\phi), \hat{\mathbf{N}}(\theta)\right] = \hat{\mathbf{N}}(\phi)\hat{\mathbf{N}}(\theta) - \hat{\mathbf{N}}(\theta)\hat{\mathbf{N}}(\phi) \tag{18}$$

is nonvanishing.

The incommutability of the matrices $\hat{\mathbf{N}}(\phi)$ determines properties of two real 6×6 matrices: the ordered exponential,

$$\hat{\mathbf{V}}^{(s)}(\phi) = \begin{bmatrix} \hat{\mathbf{V}}_1^{(s)} & \hat{\mathbf{V}}_2^{(s)} \\ \hat{\mathbf{V}}_3^{(s)} & \hat{\mathbf{V}}_4^{(s)} \end{bmatrix} \tag{19}$$

Downloaded 04 May 2010 to 171.66.16.28. Redistribution subject to ASME license or copyright; see http://www.asme.org/terms/Terms_Use.cfm

defined as

$$\hat{\mathbf{V}}^{(s)}(\phi) = \mathrm{Ordexp}\left(s\int_0^{\phi}\hat{\mathbf{N}}(\theta)d\theta\right) = \prod_{\substack{i=1\\k\to\infty}}^{k}\exp\left(s\hat{\mathbf{N}}(\theta_{i-1})\delta\theta_i\right) \quad (20)$$

where $\delta\theta_i = \phi/k$, and the pseudo-logarithm

$$\ln\hat{\mathbf{V}}^{(s)}(\phi) = \begin{bmatrix}\left[\ln\hat{\mathbf{V}}^{(s)}(\phi)\right]_1 & \left[\ln\hat{\mathbf{V}}^{(s)}(\phi)\right]_2\\ \left[\ln\hat{\mathbf{V}}^{(s)}(\phi)\right]_3 & \left[\ln\hat{\mathbf{V}}^{(s)}(\phi)\right]_4\end{bmatrix} \quad (21)$$

defined as

$$\ln\hat{\mathbf{V}}^{(s)}(\phi) = \hat{\mathbf{V}}^{(s)}(\phi)\left(\int_0^{\phi}\left[\hat{\mathbf{V}}^{(s)}(\theta)\right]^{-1}\hat{\mathbf{N}}(\theta)\hat{\mathbf{V}}^{(s)}(\theta)d\theta\right)\times\left[\hat{\mathbf{V}}^{(s)}(\phi)\right]^{-1}. \quad (22)$$

By definition

$$\hat{\mathbf{V}}^{(s)}(0) = \hat{\mathbf{I}}, \quad \ln\hat{\mathbf{V}}^{(s)}(0) = \hat{\mathbf{0}}, \quad (23)$$

where $\hat{\mathbf{I}}$ and $\hat{\mathbf{0}}$ denote the 6×6 unit and zero matrices. The ordered exponential obeys the Schrodinger equation

$$\frac{d\hat{\mathbf{V}}^{(s)}(\phi)}{d\phi} = s\hat{\mathbf{N}}(\phi)\hat{\mathbf{V}}^{(s)}(\phi), \quad (24)$$

in which $\hat{\mathbf{V}}^{(s)}(\phi)$ and $s\hat{\mathbf{N}}(\phi)$ behave like the scattering matrix and the Hamiltonian. The pseudo-logarithm satisfies the equation

$$\frac{d\ln\hat{\mathbf{V}}^{(s)}(\phi)}{d\phi} = \hat{\mathbf{N}}(\phi) + s\left[\hat{\mathbf{N}}(\phi), \ln\hat{\mathbf{V}}^{(s)}(\phi)\right]. \quad (25)$$

In the case of homogeneity, owing to the commutability of the ordered exponentials, the pseudo-logarithm does not depend on the index s at all and reduces to

$$\ln\hat{\mathbf{V}}^{(s)}(\phi) = \int_0^{\phi}\hat{\mathbf{N}}(\theta)d\theta \quad (26)$$

for any s. In turn, the ordered exponentials in the case of homogeneity become the usual exponentials. For integer s

$$\hat{\mathbf{V}}^{(s)}(\phi) = \left(\hat{\mathbf{I}}\cos\phi + \hat{\mathbf{N}}(0)\sin\phi\right)^s, \quad (27)$$

$$\left[\hat{\mathbf{V}}^{(s)}(\phi)\right]^{-1} = \left(\hat{\mathbf{I}}\cos\phi - \hat{\mathbf{N}}(\phi)\sin\phi\right)^s. \quad (28)$$

Otherwise, the powers of matrices are defined using their spectral decompositions.

In what follows we need two properties of the ordered exponentials. One of them concerns the case $s = 1$ and states that the action of the matrix $\hat{\mathbf{V}}^{(1)}(\phi)$ from the left on the six-dimensional vector $(\mathbf{n}(0), \mathbf{0})$ rotates it by an angle ϕ,

$$\hat{\mathbf{V}}^{(1)}(\phi)\begin{pmatrix}\mathbf{n}(0)\\ \mathbf{0}\end{pmatrix} = \begin{pmatrix}\mathbf{n}(\phi)\\ \mathbf{0}\end{pmatrix}. \quad (29)$$

Equation (29) follows from the equality for infinitesimal rotations

$$\exp\left(\hat{\mathbf{N}}(\phi)\delta\phi\right)\begin{pmatrix}\mathbf{n}(\phi)\\ \mathbf{0}\end{pmatrix} = \begin{pmatrix}\mathbf{n}(\phi+\delta\phi)\\ \mathbf{0}\end{pmatrix}, \quad (30)$$

which in turn can be proved by the expansion of the exponential into a power series up to the first power of the infinitesimal rotation $\delta\phi$ and taking into account that

$$\hat{\mathbf{N}}(\phi)\begin{pmatrix}\mathbf{n}(\phi)\\ \mathbf{0}\end{pmatrix} = \begin{pmatrix}-\mathbf{m}(\phi)\\ \mathbf{0}\end{pmatrix}. \quad (31)$$

Another property concerns the case $s = -1$ and states that

$$(\mathbf{0}, \mathbf{n}(\phi))\hat{\mathbf{V}}^{(-1)}(\phi) = (\mathbf{0}, \mathbf{n}(0)). \quad (32)$$

The corresponding identity for an infinitesimal rotation reads as

$$(\mathbf{0}, \mathbf{n}(\phi))\exp\left\{-\hat{\mathbf{N}}(\phi)\delta\phi\right\} = (\mathbf{0}, \mathbf{n}(\phi-\delta\phi)). \quad (33)$$

The physical sense of Eqs. (29) and (32) will be clarified later.

3.2 Consistent Forms. Self-similar solutions of the problems under consideration can be derived from the consistency equation. The symmetric stress tensor is related to the displacement $\mathbf{u}$ via

$$\sigma_{ik} = C_{iklj}(\phi)u_{j,l}, \quad (34)$$

and to the Airy stress function $\boldsymbol{\phi}$ via

$$\sigma_{ik} = \epsilon_{kl}\phi_{i,l}, \quad (35)$$

only provided that the six-dimensional vector $(\mathbf{u}, \boldsymbol{\phi})$ is a consistent form satisfying the equation (Kirchner, 1989)

$$\frac{\partial}{\partial x_i}\begin{pmatrix}\mathbf{u}(r,\phi)\\ \boldsymbol{\phi}(r,\phi)\end{pmatrix} = -\left(m_i\hat{\mathbf{I}} + n_i\hat{\mathbf{N}}(\phi)\right)\begin{pmatrix}\mathbf{a}(r,\phi)\\ \mathbf{b}(r,\phi)\end{pmatrix}, \quad (36)$$

where the source vector $(\mathbf{a}, \mathbf{b})$ may depend on both r and ϕ, and the nonzero elements of the two-dimensional tensor ϵ_{kl} are $\epsilon_{12} = -\epsilon_{21} = 1$. The consistency Eq. (36) ensures that the equations of both compatibility and equilibrium are fulfilled, and replaces the second-order differential equation for the displacement vector by the system of two first-order differential equations for the displacement and Airy stress function vectors.

A consistent form varying like r^s can be written as (Kirchner, 1989)

$$\begin{pmatrix}\mathbf{u}(r,\phi)\\ \boldsymbol{\phi}(r,\phi)\end{pmatrix} = r^s\hat{\mathbf{V}}^{(s)}(\phi)\begin{pmatrix}\mathbf{a}\\ \mathbf{b}\end{pmatrix}, \quad (37)$$

where $(\mathbf{a}, \mathbf{b})$ is a constant six-dimensional source vector. The consistency equation in this case reduces to Eq. (24).

Another example of a consistent form behaves like $r^s\ln r$,

$$\begin{pmatrix}\mathbf{u}(r,\phi)\\ \boldsymbol{\phi}(r,\phi)\end{pmatrix} = r^s\left(\ln(r/eL)\hat{\mathbf{I}} + \ln\hat{\mathbf{V}}^{(s)}(\phi)\right)\hat{\mathbf{V}}^{(s)}(\phi)\begin{pmatrix}\mathbf{a}\\ \mathbf{b}\end{pmatrix}, \quad (38)$$

where the source vector $(\mathbf{a}, \mathbf{b})$ is again constant. The consistency condition is given here by the system of Eqs. (24) and (25).

By Eq. (29), the consistent form

$$\begin{pmatrix}\mathbf{u}(r,\phi)\\ \boldsymbol{\phi}(r,\phi)\end{pmatrix} = \omega r\hat{\mathbf{V}}^{(1)}(\phi)\begin{pmatrix}\mathbf{n}(0)\\ 0\end{pmatrix} = \omega r\begin{pmatrix}\mathbf{n}(\phi)\\ 0\end{pmatrix} \quad (39)$$

does not induce strains and stresses at all. The physical reason for this is that Eq. (39) represents a rigid-body rotation by an angle ω around $\mathbf{t}$.

4 Wedge Under a Uniform Surface Loading

In the Levy problem we seek a solution which has the required dimension and is independent of the geometrical parameter R. If such a solution exists, it must have the form

$$\begin{pmatrix}\mathbf{u}(r,\phi)\\ \boldsymbol{\phi}(r,\phi)\end{pmatrix} = r\hat{\mathbf{V}}^{(1)}(\phi)\begin{pmatrix}\mathbf{a}\\ \mathbf{b}\end{pmatrix} + r\left(\ln(r/eL)\hat{\mathbf{I}} + \ln\hat{\mathbf{V}}^{(1)}(\phi)\right)\hat{\mathbf{V}}^{(1)}(\phi)\begin{pmatrix}\mathbf{c}\\ \mathbf{d}\end{pmatrix}, \quad (40)$$

Downloaded 04 May 2010 to 171.66.16.28. Redistribution subject to ASME license or copyright; see http://www.asme.org/terms/Terms_Use.cfm

where the unknown constant vectors (**a**, **b**) and (**c**, **d**) are to be found from the boundary conditions

$$\partial \boldsymbol{\phi}(r, 0)/\partial r = k\mathbf{n}(0), \quad \partial \boldsymbol{\phi}(r, \alpha)/\partial r = -k\mathbf{n}(\alpha) \quad (41)$$

at the wedge sides $\phi = 0$ and $\phi = \alpha$ subjected to the uniform bending tractions. The condition at the side $\phi = 0$ demands

$$\mathbf{b} = k\mathbf{n}(0), \quad \mathbf{d} = \mathbf{0}. \quad (42)$$

Likewise, the condition at the side $\phi = \alpha$ yields

$$\begin{cases} \hat{\mathbf{V}}_3^{(1)}(\alpha)\mathbf{c} = \mathbf{0}, & (43) \\ \hat{\mathbf{V}}_3^{(1)}(\alpha)\mathbf{a} + \hat{\mathbf{V}}_4^{(1)}(\alpha)\mathbf{b} \\ \quad + \left\{\left[\ln \hat{\mathbf{V}}^{(1)}(\alpha)\right]\hat{\mathbf{V}}^{(1)}(\alpha)\right\}_3 \mathbf{c} = -k\mathbf{n}(\alpha). & (44) \end{cases}$$

Equation (29) implies

$$\hat{\mathbf{V}}_1^{(1)}(\alpha)\mathbf{n}(0) = \mathbf{n}(\alpha), \quad \hat{\mathbf{V}}_3^{(1)}(\alpha)\mathbf{n}(0) = \mathbf{0}, \quad (45)$$

so that the second column of the matrix $\hat{\mathbf{V}}_3^{(1)}(\alpha)$ is vanishing,

$$\hat{\mathbf{V}}_3^{(1)}(\alpha) = [\mathbf{v}, \mathbf{0}, \mathbf{w}] = \begin{bmatrix} v_1 & 0 & w_1 \\ v_2 & 0 & w_2 \\ v_3 & 0 & w_3 \end{bmatrix}, \quad (46)$$

and thereby for any wedge angle α and angular inhomogeneity $C_{ijkl}(\phi)$ there always exists at least one independent eigenvector $\boldsymbol{\eta}^{(1)} = \mathbf{n}(0)$ which fulfills

$$\hat{\mathbf{V}}_3^{(1)}(\alpha)\boldsymbol{\eta}^{(1)} = \mathbf{0}. \quad (47)$$

Suppose that $\boldsymbol{\eta}^{(1)}$ is the only normalized eigenvector satisfying Eq. (47) or, in other words, that the vectors **v** and **w**, which form the first and third columns of the matrix (46), are linearly independent. Then it can be only,

$$\begin{pmatrix} \mathbf{c} \\ \mathbf{d} \end{pmatrix} = \omega_0 \begin{pmatrix} \mathbf{n}(0) \\ \mathbf{0} \end{pmatrix}, \quad (48)$$

where ω_0 is a scalar factor, and any variation of the parameter L in Eq. (40) can only result in adding a rigid-body rotation. Thus Eq. (48) can be established directly from the invariance of the problem under the rigid-body rotations. Equation (48) is also in accordance with the previous calculations for homogeneous anisotropic wedges (Ting, 1988a, b; Hwu and Ting, 1990).

In view of Eq. (48) one obtains an algebraic system,

$$\hat{\mathbf{V}}_3^{(1)}(\alpha)\mathbf{a} + \omega_0\left[\ln \hat{\mathbf{V}}^{(1)}(\alpha)\right]_3 \mathbf{n}(\alpha) = -k\left\{\mathbf{n}(\alpha) + \hat{\mathbf{V}}_4^{(1)}(\alpha)\mathbf{n}(0)\right\}, \quad (49)$$

which contains three equations for three unknown quantities ω_0, a_1, and a_3. As concerns the component a_2, it drops out the problem and remains arbitrary. Hence, the first term in the particular solution (40) is ambiguous and any change in a_2 results in the solution which differs from the previous one in a rigid-body rotation.

The solution to the system (49) exists provided that

$$\det \hat{\mathbf{L}}(\alpha) \neq 0, \quad (50)$$

where the matrix $\hat{\mathbf{L}}(\alpha)$ has the elements

$$\hat{\mathbf{L}}(\alpha) = \left[\mathbf{v}, \left[\ln \hat{\mathbf{V}}^{(1)}(\alpha)\right]_3 \mathbf{n}(\alpha), \mathbf{w}\right]. \quad (51)$$

The condition (50) is sufficient for Levy's problem to have a solution independent on R. However, as is known from the theory of linear algebraic systems, Eq. (50) does not coincide with the necessity condition. At the critical wedge angle α_*^L satisfying the equation

$$\det \hat{\mathbf{L}}(\alpha_*^L) = [\mathbf{v} \times \mathbf{w}]\left[\ln \hat{\mathbf{V}}^{(1)}(\alpha_*^L)\right]_3 \mathbf{n}(\alpha_*^L) = 0 \quad (52)$$

the R-independent solution (40) becomes infinite for all (r, ϕ). The determinant is represented in Eq. (52) as the mixed product of the vectors which form columns of the matrix (51).

Equation (52) is satisfied in two cases: (a) if the matrix (46) has only one eigenvector $\boldsymbol{\eta}^{(1)}$, and the vector $[\ln \hat{\mathbf{V}}^{(1)}(\alpha)]_3 \mathbf{n}(\alpha)$ is orthogonal to the vector $[\mathbf{v} \times \mathbf{w}]$, which in this case is nonvanishing, and (b) if the matrix (46) has another eigenvector $\boldsymbol{\eta}^{(2)}$. In this case $\det \hat{\mathbf{L}}(\alpha)$ vanishes because of the vanishing of the vector $[\mathbf{v} \times \mathbf{w}]$.

In Section 11 it will be shown that there is an essential distinction between solutions of Levy's problem in the two cases.

5 Wedge Under a Concentrated Couple

For a concentrated couple a solution of the required dimension is given by

$$\begin{pmatrix} \mathbf{u}(r, \phi) \\ \boldsymbol{\phi}(r, \phi) \end{pmatrix} = r^{-1}\hat{\mathbf{V}}^{(-1)}(\phi)\begin{pmatrix} \mathbf{a} \\ \mathbf{b} \end{pmatrix}, \quad (53)$$

where the constant vector (**a**, **b**) is to be determined from the conditions at the wedge sides $\phi = 0$ and $\phi = \alpha$, supplemented by the condition of the moment balance

$$\int_0^\alpha r^2 \sigma_{r\theta}\, d\theta = -M. \quad (54)$$

In this paper we focus our attention mainly on the Carothers problem of a free surface wedge. Besides it, some related problems will be discussed as well. In particular, we will consider an anisotropic version of the Dundurs and Markenscoff (1989) problem (a wedge embedded into another material and loaded at the tip by a couple) and its generalization to the case of a couple applied to the axis of an arbitrary rotationally inhomogeneous medium. Instead of the free-surface boundary conditions, in these problems we have the continuity condition of both the displacement **u** and the Airy stress function $\boldsymbol{\phi}$ across any radial plane. This condition should be supplemented by the equation of the moment balance

$$\int_0^{2\pi} r^2 \sigma_{r\theta}\, d\theta = -M. \quad (55)$$

5.1 Free Surface Wedge. The condition of the traction-free side $\phi = 0$ demands

$$r\boldsymbol{\phi}(r, 0) = \mathbf{b} = \mathbf{0}, \quad (56)$$

whereas the condition at the side $\phi = \alpha$ yields

$$r\boldsymbol{\phi}(r, \alpha) = \hat{\mathbf{V}}_3^{(-1)}(\alpha)\mathbf{a} = \mathbf{0}. \quad (57)$$

Together with Eq. (54), the system (57) forms a system of four equations for only three unknowns a_1, a_2, and a_3. Nevertheless, the system obtained is not redefined, since, according to Eq. (32), the matrix $\hat{\mathbf{V}}_3^{(-1)}(\alpha)$ has relatively to the rotated basis $(\mathbf{m}(\alpha), \mathbf{n}(\alpha), \mathbf{t})$ the vanishing second row

$$\hat{\mathbf{V}}_3^{(-1)}(\alpha) = \begin{bmatrix} x & x & x \\ 0 & 0 & 0 \\ x & x & x \end{bmatrix}. \quad (58)$$

Thus, we conclude the system (57) to contain in fact only two linearly independent equations for three unknown variables. In other words, the matrix $\hat{\mathbf{V}}_3^{(-1)}(\alpha)$ always has at least one eigenvector $\boldsymbol{\xi} = \boldsymbol{\xi}^{(1)}$ satisfying the equation

Downloaded 04 May 2010 to 171.66.16.28. Redistribution subject to ASME license or copyright; see http://www.asme.org/terms/Terms_Use.cfm

$$\hat{\mathbf{V}}_3^{(-1)}(\alpha)\boldsymbol{\xi}^{(1)} = \mathbf{0}. \tag{59}$$

Suppose that $\boldsymbol{\xi}^{(1)}$ is the only independent eigenvector, and the linearly independent columns of the matrix (58) are the first and the third. Then $\boldsymbol{\xi}^{(1)}$ can be chosen as

$$\boldsymbol{\xi}^{(1)} = \beta_1\mathbf{m}(\alpha) + \mathbf{n}(\alpha) + \beta_3\mathbf{t} \tag{60}$$

where β_1 and β_3 are uniquely determined from Eq. (59). The vector $\mathbf{a}$ is along $\boldsymbol{\xi}^{(1)}$,

$$\mathbf{a} = \tau\boldsymbol{\xi}^{(1)}, \tag{61}$$

and the scalar factor τ is to be found from the moment balance.

Taking into account that

$$(\mathbf{0}, \mathbf{n}(\phi)) = (\mathbf{0}, \mathbf{n}(0))\left[\hat{\mathbf{V}}^{(-1)}(\phi)\right]^{-1}, \tag{62}$$

the stress $\sigma_{r\phi}$ can be written as a contraction of some 6×6 matrix with two constant six-dimensional vectors,

$$\sigma_{r\phi} = -r^{-2}(\mathbf{0}, \mathbf{n}(0))\left[\hat{\mathbf{V}}^{(-1)}(\phi)\right]^{-1}\hat{\mathbf{N}}(\phi)\hat{\mathbf{V}}^{(-1)}(\phi)\begin{pmatrix}\mathbf{a}\\ \mathbf{0}\end{pmatrix}. \tag{63}$$

Being substituted into Eq. (54), Eq. (63) yields

$$\tau\mathbf{n}(\alpha)\left[\ln\hat{\mathbf{V}}^{(-1)}(\alpha)\right]_3\hat{\mathbf{V}}_1^{(-1)}(\alpha)\boldsymbol{\xi}^{(1)} = M, \tag{64}$$

wherefrom one finds that

$$\tau = \frac{M}{\mathbf{n}(\alpha)\left[\ln\hat{\mathbf{V}}^{(-1)}(\alpha)\right]_3\hat{\mathbf{V}}_1^{(-1)}(\alpha)\boldsymbol{\xi}^{(1)}}. \tag{65}$$

Consequently, the homogeneous solution (53) fails at the wedge angle α_*^C satisfying

$$\mathbf{n}(\alpha_*^C)\left[\ln\hat{\mathbf{V}}^{(-1)}(\alpha_*^C)\right]_3\hat{\mathbf{V}}_1^{(-1)}(\alpha_*^C)\boldsymbol{\xi}^{(1)} = 0. \tag{66}$$

5.2 Wedge Embedded into Another Material. Let a wedge of the opening angle α and of the elastic constants $C_{ijkl}^{(1)}$ be embedded into a material with the elastic constants $C_{ijkl}^{(2)}$. In the case of homogeneity, $[\hat{\mathbf{V}}^{(s)}(\phi)]^{-1} = \hat{\mathbf{V}}^{(-s)}(\phi)$. Consequently, for each homogeneous region the solution sought can be written as

(a) for $0 \le \phi \le \alpha$

$$\begin{bmatrix}\mathbf{u}(r,\phi)\\ \boldsymbol{\phi}(r,\phi)\end{bmatrix} = r^{-1}\left(\hat{\mathbf{I}}\cos\phi - \hat{\mathbf{N}}^{(1)}(\phi)\sin\phi\right)\begin{pmatrix}\mathbf{a}_1\\ \mathbf{b}_1\end{pmatrix}, \tag{67}$$

(b) for $\alpha \le \phi \le 2\pi$

$$\begin{bmatrix}\mathbf{u}(r,\phi)\\ \boldsymbol{\phi}(r,\phi)\end{bmatrix} = r^{-1}\left(\hat{\mathbf{I}}\cos\phi - \hat{\mathbf{N}}^{(2)}(\phi)\sin\phi\right)\begin{pmatrix}\mathbf{a}_2\\ \mathbf{b}_2\end{pmatrix}, \tag{68}$$

The matrices $\hat{\mathbf{N}}^{(i)}(\phi)$ are given by Eq. (16) where $C_{ijkl}(\phi) = C_{ijkl}^{(i)}$, $(i = 1, 2)$.

From the continuity of $(\mathbf{u}, \boldsymbol{\phi})$ across the radial plane $\phi = 0$ we find that the constant source vectors for both regions are equal

$$\begin{pmatrix}\mathbf{a}_1\\ \mathbf{b}_1\end{pmatrix} = \begin{pmatrix}\mathbf{a}_2\\ \mathbf{b}_2\end{pmatrix} = \begin{pmatrix}\mathbf{a}\\ \mathbf{b}\end{pmatrix}, \tag{69}$$

whereas the continuity across $\phi = \alpha$ yields the algebraic system

$$\sin\alpha\left(\hat{\mathbf{N}}^{(1)}(\alpha) - \hat{\mathbf{N}}^{(2)}(\alpha)\right)\begin{pmatrix}\mathbf{a}\\ \mathbf{b}\end{pmatrix} = \begin{pmatrix}\mathbf{0}\\ \mathbf{0}\end{pmatrix}. \tag{70}$$

Although this system is homogeneous, it nevertheless has a nonzero solution for $(\mathbf{a}, \mathbf{b})$. In fact, relative to the rotated basis $(\mathbf{m}(\alpha), \mathbf{n}(\alpha), \mathbf{t})$ the matrix $\hat{\mathbf{N}}^{(1)}(\alpha) - \hat{\mathbf{N}}^{(2)}(\alpha)$ has the elements

$$\hat{\mathbf{N}}^{(1)}(\alpha) - \hat{\mathbf{N}}^{(2)}(\alpha) = \begin{bmatrix} x & 0 & x & x & x & x\\ x & 0 & x & x & x & x\\ x & 0 & x & x & x & x\\ x & 0 & x & x & x & x\\ 0 & 0 & 0 & 0 & 0 & 0\\ x & 0 & x & x & x & x\end{bmatrix}. \tag{71}$$

So for any wedge angle α the system (70) has at least one solution

$$\begin{pmatrix}\mathbf{a}\\ \mathbf{b}\end{pmatrix} = \tau\boldsymbol{\xi} = \tau\begin{pmatrix}\mathbf{n}(\alpha)\\ 0\end{pmatrix}. \tag{72}$$

where τ is a scalar factor, which can be found from Eq. (55). Let us assume that $\sin\alpha \ne 0$ and the nonzero columns of the matrix (71) are linearly independent (i.e., $\boldsymbol{\xi}$ is the only eigenvector satisfying $\{\hat{\mathbf{N}}^{(1)}(\alpha) - \hat{\mathbf{N}}^{(2)}(\alpha)\}\boldsymbol{\xi} = 0$). Then Eq. (72) yields the only solution of the system (70).

In view of Eq. (69), Eqs. (67) and (68) can be combined as

$$\begin{pmatrix}\mathbf{u}(r,\phi)\\ \phi(r,\phi)\end{pmatrix} = \tau r^{-1}\left(\hat{\mathbf{I}}\cos\phi - \hat{\mathbf{N}}(\phi)\sin\phi\right)\begin{pmatrix}\mathbf{n}(\alpha)\\ \mathbf{0}\end{pmatrix} \tag{73}$$

where $\hat{\mathbf{N}}(\phi) = \hat{\mathbf{N}}^{(1)}(\phi)$ for $0 \le \phi \le \alpha$, and $\hat{\mathbf{N}}^{(2)}(\phi)$ for $\alpha \le \phi \le 2\pi$. Then the stress $\sigma_{r\phi}$ can be written as

$$\sigma_{r\phi} = \tau r^{-2}\sin\phi\mathbf{m}(\phi)\hat{\mathbf{N}}_3(\phi)\mathbf{n}(\alpha), \tag{74}$$

wherefrom the equation for τ is

$$\tau\mathbf{n}(0)\int_0^{2\pi}d\theta\hat{\mathbf{N}}_3(\theta)\mathbf{n}(\alpha) = -M. \tag{75}$$

Finally, the scalar factor τ is given by

$$\tau = -\frac{M}{\mathbf{n}(0)\int_0^{2\pi}d\theta\hat{\mathbf{N}}_3(\theta)\mathbf{n}(\alpha)} \tag{76}$$

and hence the generalization of the Dundurs and Markenscoff equation for the critical angle α_* to the case of anisotropy reads as

$$\mathbf{n}(0)\int_0^{2\pi}d\theta\hat{\mathbf{N}}_3(\theta)\mathbf{n}(\alpha_*) = 0. \tag{77}$$

5.3 A Couple at the Axis of an Arbitrary Rotationally Inhomogeneous Material. Now a couple is applied to the axis of an elastic medium of general rotational inhomogeneity $C_{ijkl}(\phi)$. Suppose that the solution sought is given again by Eq. (53). Then the unknown constant vector $(\mathbf{a}, \mathbf{b})$ is obtainable from

$$\left(\hat{\mathbf{V}}^{(-1)}(2\pi) - \hat{\mathbf{I}}\right)\begin{pmatrix}\mathbf{a}\\ \mathbf{b}\end{pmatrix} = \begin{pmatrix}\mathbf{0}\\ \mathbf{0}\end{pmatrix} \tag{78}$$

and from the moment balance Eq. (55).

According to the following equality (see Eq. (32) and taking into account that $\mathbf{n}(2\pi) = \mathbf{n}(0)$),

$$(\mathbf{0}, \mathbf{n}(0))\hat{\mathbf{V}}^{(-1)}(2\pi) = (\mathbf{0}, \mathbf{n}(0)), \tag{79}$$

the matrix $\hat{\mathbf{V}}^{(-1)}(2\pi) - \hat{\mathbf{I}}$ must have the vanishing fifth row

$$\hat{\mathbf{V}}^{(-1)}(2\pi) - \hat{\mathbf{I}} = \begin{bmatrix} x & x & x & x & x & x\\ x & x & x & x & x & x\\ x & x & x & x & x & x\\ x & x & x & x & x & x\\ 0 & 0 & 0 & 0 & 0 & 0\\ x & x & x & x & x & x\end{bmatrix}. \tag{80}$$

Downloaded 04 May 2010 to 171.66.16.28. Redistribution subject to ASME license or copyright; see http://www.asme.org/terms/Terms_Use.cfm

By this reason, the system (78) contains only five equations, which, being supplemented by the moment balance equation, can generally have a solution. Being chosen as

$$\begin{pmatrix} \mathbf{a} \\ \mathbf{b} \end{pmatrix} = \tau\boldsymbol{\xi} = \tau \begin{pmatrix} \beta_1\mathbf{m}(0) + \mathbf{n}(0) + \beta_3\mathbf{t} \\ \gamma_1\mathbf{m}(0) + \gamma_2\mathbf{n}(0) + \gamma_3\mathbf{t} \end{pmatrix} \tag{81}$$

the source vector (**a**, **b**) can be found from the system (78) again up to an arbitrary scalar factor τ.

The stress $\sigma_{r\phi}$ is derived to be

$$\sigma_{r\phi} = \tau r^{-2}(\mathbf{0}, \mathbf{m}(\phi))\hat{\mathbf{V}}^{(-1)}(\phi)\boldsymbol{\xi}, \tag{82}$$

so that the moment balance gives for τ

$$\tau = \frac{M}{\int_0^{2\pi} d\theta(\mathbf{0}, \mathbf{m}(\theta))\hat{\mathbf{V}}^{(-1)}(\theta)\boldsymbol{\xi}}. \tag{83}$$

The vanishing of the denominator in Eq. (83) gives the condition of the failure of the homogeneous solution, Eq. (53), in the problem under consideration and defines the critical dependencies $C_{ijkl}(\phi)$.

6 Discussion for Homogeneous Wedges

Althought Eqs. (52) and (66) for the critical wedge angles $\alpha_*^{L,C}$ do not coincide, they have nevertheless common roots. The general proof which covers the case of rotationally inhomogeneous wedges is presented in Section 10. Here we confine ourselves only to elastically homogeneous anisotropic materials and discuss properties of Eqs. (52) and (66) in this case. Since for homogeneity the matrix (46) has the structure

$$\hat{\mathbf{V}}_3^{(1)}(\alpha) = \sin\alpha\hat{\mathbf{N}}_3(0) = \sin\alpha \begin{bmatrix} x & 0 & x \\ 0 & 0 & 0 \\ x & 0 & x \end{bmatrix}, \tag{84}$$

Eq. (52) splits into two equations,

$$\mathbf{n}(0)\left[\ln\hat{\mathbf{V}}^{(1)}(\alpha_*^L)\right]_3\mathbf{n}(\alpha_*^L) = 0, \tag{85}$$

and

$$\sin\alpha_*^L = 0, \tag{86}$$

the first of which corresponds to the case (a), and the second to the case (b) of the Section 4. Therefore, there are two sorts of the critical angles in Levy's problem for homogeneous anisotropic wedges. Let us now examine the behavior of the solutions to the algebraic system (49) close to the critical angles $\alpha_*^L = \pi, 2\pi$. The solution for ω_0 has the form

$$\omega_0 = -2k\cos\alpha/\mathbf{n}(0)\left[\ln\hat{\mathbf{V}}^{(1)}(\alpha)\right]_3\mathbf{n}(\alpha) \tag{87}$$

and is regular, whereas the solution for **a** tends to infinity as

$$\mathbf{a}_\mathbf{n} = (1/\sin\alpha)[(mm)_\mathbf{n}^*]^{-1}\mathbf{g}, \tag{88}$$

where the vectors $\mathbf{a}_\mathbf{n} = \mathbf{a} - \alpha_2\mathbf{n}$ and

$$\mathbf{g} = -\omega_0\left[\ln\hat{\mathbf{V}}^{(1)}(\alpha)\right]_3\mathbf{n}(\alpha) - k\left(\mathbf{n}(\alpha) + \hat{\mathbf{V}}_4^{(1)}(\alpha)\mathbf{n}(0)\right) \tag{89}$$

are orthogonal to the vector **n**, and $(mm)_\mathbf{n}^*$ denotes the 2×2 matrix, which results from deleting the second column and the second row in the matrix $\hat{\mathbf{N}}_3(0)$. Because in the general anisotropic case the vector **g** is nonvanishing, the Levy problem indeed has no self-similar solutions at $\alpha_*^L = \pi, 2\pi$. One should also notice that at $\alpha = \pi, 2\pi$ the matrix (46) vanishes and has three eigenvectors $\boldsymbol{\eta}^{(1)}$, $\boldsymbol{\eta}^{(2)}$, $\boldsymbol{\eta}^{(3)}$, which can be shown arbitrarily.

As regards Eq. (66), for homogeneous anisotropic materials it reduces to

$$\mathbf{n}(\alpha_*^C)\left[\ln\hat{\mathbf{V}}^{(-1)}(\alpha_*^C)\right]_3\mathbf{n}(0) = 0 \tag{87}$$

and is identical to Eq. (85) because homogeneity makes the pseudo-logarithm independent of the index s, and the block $\hat{\mathbf{N}}_3(\phi)$ in Eq. (26) is symmetric. Consequently, in accordance with (Ting, 1988a, 1988b), the critical angle α_*^C of the Carothers problem is a critical angle of the Levy problem. The wedge angles π and 2π are, however, not critical for the Carothers problem whatever the type of elastic anisotropy. In fact, for homogeneous materials the eigenvector $\boldsymbol{\xi}^{(1)}$ in Eq. (60) reduces to $\mathbf{n}(\alpha)$ so that the solution given in Eqs. (53), (61), and (65) remains finite when $\alpha = \pi, 2\pi$. However, at the wedge angle π and 2π this solution is not unique. Since the matrix (58) in this case vanishes and has three eigenvectors $\boldsymbol{\xi}^{(1)}$, $\boldsymbol{\xi}^{(2)}$, $\boldsymbol{\xi}^{(3)}$, there exist three independent homogeneous solutions of the Carothers problem. These solutions give rise to the same moment M about the x_3-axis, but to the different moments about the axes x_1 and x_2 (see also Ting, 1988a).

7 Discussion for Inhomogeneous Wedges

So far it has been shown that the problems of Levy and Carothers for a rotationally inhomogeneous elastic wedge have particular solutions, which are self-similar (of the first type) and do not depend on geometrical parameters with a dimension of length. As in the case of elastically homogeneous wedges, the self-similarities become infinite at some critical wedge angles. However, the main question remains open—whether the critical angles α_*^L and α_*^C of Levy's and Carothers' problems coincide for rotationally inhomogeneous wedges.

Now we will prove that the wedge angle α_*^C, which is critical for the Carothers problem, is also critical for the Levy problem. The critical angles in both problems arise from the analysis of roots $s_n(\alpha)$ of some eigenvalue equation. These roots serve as exponents governing the radial dependence $r^{s_n(\alpha)}$ of the homogeneous displacements, which are eigensolutions of a free surface wedge and, following Barenblatt (1979), are called the second type self-similarities. Peculiarities in the behavior of some branches $s_n(\alpha)$ close to $\alpha = \alpha_*^{L,C}$ are intimately connected with the mechanism of elimination the divergencies in the non self-similar solution (11) of the corresponding nondegenerate boundary problem, where the boundary conditions are imposed not only at the wedge sides but also at the arc $r = R$. Since there are no physical reasons for anomalies in the non-self-similar solution, the series over eigensolutions in Eq. (11) must contain a term which close to $\alpha = \alpha_*^{L,C}$ has the same radial dependence as the particular divergent self-similar solution. With an appropriate choice of the coefficient k_1 this term cancels at $\alpha = \alpha_*^{L,C}$ the divergent part of the particular self-similar solution: in the nondegenerate boundary problem this happens automatically. Ting (1985b) was first to show that by adding an eigensolution to the particular self-similar solution one can obtain a new particular solution which is valid both close to and at the critical angle of a homogeneous isotropic elastic wedge loaded by a couple. Ting (1985b) chose the coefficient k_1 in such a way as to make the new solution regular at the critical angle. Now we will prove that in the Levy problem at the critical angle it should be $s_1(\alpha_*^L) = 1$, while in the Carothers problem it should be $s_1(\alpha_*^C) = -1$, in both cases at $\alpha = \alpha_*^{L,C}$ the roots $s_1(\alpha_*^{L,C})$ are multiple. We further derive and examine particular solutions for the critical wedge angles. It will be shown that the behavior of these solutions depends not only on the multiplicity degree of the roots $s_1(\alpha_*^{L,C})$, but also on some other factors. Our attention is mainly focused on the Levy problem, which is of special interest because two different types of critical angles and solutions occur there.

Downloaded 04 May 2010 to 171.66.16.28. Redistribution subject to ASME license or copyright; see http://www.asme.org/terms/Terms_Use.cfm

8 New Solutions

Disregarding the boundary conditions at the wedge sides, a new class of particular solutions for a wedge can be derived differentiating homogeneous solutions, Eq. (37), with respect to the index s. The homogeneous solution can be conveniently represented as

$$\begin{pmatrix} \mathbf{u}(r,\phi) \\ \boldsymbol{\phi}(r,\phi) \end{pmatrix} = R\eta^s \hat{\mathbf{V}}^{(s)}(\phi) \begin{pmatrix} \mathbf{a} \\ \mathbf{b} \end{pmatrix}, \tag{88}$$

making the constant vectors $\mathbf{a}$ and $\mathbf{b}$ dimensionless. Here $\eta = r/R$ and R is some constant, which has the dimension of length but does not necessarily coincide with the characteristic length in Eq. (11).

When $\mathbf{a}$ and $\mathbf{b}$ are independent of s, the first and the second derivatives of the solution (88) with respect to the parameter s give a solution varying like $\eta^s \ln \eta$,

$$\begin{pmatrix} \mathbf{u}(r,\phi) \\ \boldsymbol{\phi}(r,\phi) \end{pmatrix} = R\eta^s \left(\ln \eta \hat{\mathbf{V}}^{(s)}(\phi) + \frac{d\hat{\mathbf{V}}^{(s)}(\phi)}{ds} \right) \begin{pmatrix} \mathbf{a} \\ \mathbf{b} \end{pmatrix}, \tag{89}$$

and a solution varying like $\eta^s \ln^2 \eta$,

$$\begin{pmatrix} \mathbf{u}(r,\phi) \\ \boldsymbol{\phi}(r,\phi) \end{pmatrix} = R\eta^s \left(\ln^2 \eta \hat{\mathbf{V}}^{(s)}(\phi) + 2\ln\eta \frac{d\hat{\mathbf{V}}^{(s)}(\phi)}{ds} + \frac{d^2\hat{\mathbf{V}}^{(s)}(\phi)}{ds^2} \right) \begin{pmatrix} \mathbf{a} \\ \mathbf{b} \end{pmatrix}. \tag{90}$$

Explicit expressions for the matrix $\hat{\mathbf{V}}^{(s)}(\phi)$ derivatives with respect to the index s have the form

$$\frac{d\hat{\mathbf{V}}^{(s)}(\phi)}{ds} = \hat{\mathbf{V}}^{(s)}(\phi)\hat{\mathbf{P}}^{(s)}(\phi), \tag{91}$$

(compare Eq. (89) and Eq. (38)) and

$$\frac{d^2\hat{\mathbf{V}}^{(s)}(\phi)}{ds^2} = \hat{\mathbf{V}}^{(s)}(\phi) \left(\left\{ \hat{\mathbf{P}}^{(s)}(\phi) \right\}^2 + \int_0^\phi \left[\left\{ \hat{\mathbf{V}}^{(s)}(\theta) \right\}^{-1} \hat{\mathbf{N}}(\theta) \hat{\mathbf{V}}^{(s)}(\theta), \hat{\mathbf{P}}^{(s)}(\theta) \right] d\theta \right), \tag{92}$$

where

$$\hat{\mathbf{P}}^{(s)}(\phi) = \int_0^\phi \left\{ \hat{\mathbf{V}}^{(s)}(\theta) \right\}^{-1} \hat{\mathbf{N}}(\theta) \hat{\mathbf{V}}^{(s)}(\theta) d\theta \tag{93}$$

and the brackets denote the commutator of two matrices: $[\hat{\mathbf{A}}, \hat{\mathbf{B}}] = \hat{\mathbf{A}}\hat{\mathbf{B}} - \hat{\mathbf{B}}\hat{\mathbf{A}}$. If now $s = 1$, the solution (89) behaves like $r \ln \eta$

$$\begin{pmatrix} \mathbf{u}(r,\phi) \\ \boldsymbol{\phi}(r,\phi) \end{pmatrix} = r\hat{\mathbf{V}}^{(1)}(\phi) \left(\ln \eta \hat{\mathbf{I}} + \hat{\mathbf{P}}^{(1)}(\phi) \right) \begin{pmatrix} \mathbf{a} \\ \mathbf{b} \end{pmatrix}, \tag{94}$$

whereas the solution (90) like $r \ln^2 \eta$,

$$\begin{pmatrix} \mathbf{u}(r,\phi) \\ \boldsymbol{\phi}(r,\phi) \end{pmatrix} = r\hat{\mathbf{V}}^{(1)}(\phi) \left(\ln^2 \eta \hat{\mathbf{I}} + 2\ln\eta \hat{\mathbf{P}}^{(1)}(\phi) + \left\{ \hat{\mathbf{P}}^{(1)}(\phi) \right\}^2 + \int_0^\phi \left[\left\{ \hat{\mathbf{V}}^{(1)}(\theta) \right\}^{-1} \hat{\mathbf{N}}(\theta) \hat{\mathbf{V}}^{(1)}(\theta), \hat{\mathbf{P}}^{(1)}(\theta) \right] d\theta \right) \begin{pmatrix} \mathbf{a} \\ \mathbf{b} \end{pmatrix}. \tag{95}$$

In the case of homogeneous anisotropic media,

$$\hat{\mathbf{P}}^{(s)}(\phi) = \int_0^\phi \hat{\mathbf{N}}(\theta) d\theta. \tag{96}$$

So, because of the commutator linearity, the integrand in Eq. (95) vanishes

$$\left[\left\{ \hat{\mathbf{V}}^{(1)}(\theta) \right\}^{-1} \hat{\mathbf{N}}(\theta) \hat{\mathbf{V}}^{(1)}(\theta), \hat{\mathbf{P}}^{(1)}(\theta) \right] = \left[\hat{\mathbf{N}}(\theta), \hat{\mathbf{P}}^{(1)}(\theta) \right] = \left[\hat{\mathbf{N}}(\theta), \sum_i \hat{\mathbf{N}}(\theta_i) \delta\theta_i \right] = 0 \tag{97}$$

and the solution (95) reduces to the result by Hwu and Ting (1990).

9 Free Surface Wedge Eigensolutions

Equation (88) gives eigensolutions of a free-surface wedge,

$$\begin{pmatrix} \mathbf{u}(r,\phi) \\ \boldsymbol{\phi}(r,\phi) \end{pmatrix} = R\eta^s \hat{\mathbf{V}}^{(s)}(\phi) \begin{pmatrix} \mathbf{a}^{(s)} \\ \mathbf{b}^{(s)} \end{pmatrix}, \tag{98}$$

when the constant vectors $\mathbf{a}^{(s)}$ and $\mathbf{b}^{(s)}$ are chosen so that to make the wedge sides $\phi = 0$ and $\phi = \alpha$ free of tractions. In view of Eq. (23), the boundary condition at the side $\phi = 0$ demands that

$$\mathbf{b}^{(s)} = \mathbf{0}. \tag{99}$$

In turn, free-surface condition at the side $\phi = \alpha$ implies $\mathbf{a}^{(s)}$ to be an eigenvector of the matrix $\hat{\mathbf{V}}_3^{(s)}(\alpha)$,

$$\hat{\mathbf{V}}_3^{(s)}(\alpha)\mathbf{a}^{(s)} = \mathbf{0}. \tag{100}$$

Equation (100) has a nonzero solution for $\mathbf{a}^{(s)}$ only provided that s is a root of the eigenvalue equation

$$\det\left\{ \hat{\mathbf{V}}_3^{(s)}(\alpha) \right\} = 0, \tag{101}$$

which has infinitely many roots $s_n(\alpha)$ satisfying the bounded elastic energy condition for both inner ($s_n(\alpha) > 0$) and outer ($s_n(\alpha) < 0$) boundary problems.

Because of vanishing of the second column (Eq. (46)), the determinant of the matrix $\hat{\mathbf{V}}_3^{(1)}(\alpha)$ also vanishes. Hence, $s(\alpha) = 1$ is a root of Eq. (101) whatever the wedge angle α and angular behavior of $C_{ijkl}(\phi)$. The corresponding eigenvector

$$\mathbf{a}^{(1)} = \boldsymbol{\eta}^{(1)} = \mathbf{n}(0) \tag{102}$$

describes a rigid-body rotation.

Let us now derive the condition for $s = 1$ to be a multiple root of Eq. (101). Using Eq. (91), one can expand the matrix $\hat{\mathbf{V}}_3^{(s)}(\phi)$ into a power series over the index deviation $\delta s = s - 1$. Up to the first power

$$\hat{\mathbf{V}}_3^{(1+\delta s)}(\alpha) = \hat{\mathbf{V}}_3^{(1)}(\alpha) + \delta s \left\{ \left[\ln \hat{\mathbf{V}}^{(1)}(\alpha) \right] \hat{\mathbf{V}}^{(1)}(\alpha) \right\}_3 + \ldots \tag{103}$$

and, in view of Eq. (46), the perturbation expansion of Eq. (101) becomes

$$\det\left\{ \hat{\mathbf{V}}_3^{(1+\delta s)}(\alpha) \right\} = \left\| \mathbf{v} + \delta s \left\{ \left[\ln \hat{\mathbf{V}}^{(1)}(\alpha) \right] \hat{\mathbf{V}}^{(1)}(\alpha) \right\}_3 \mathbf{m}(0), \delta s \left[\ln \hat{\mathbf{V}}^{(1)}(\alpha) \right]_3 \mathbf{n}(\alpha), \mathbf{w} + \delta s \left\{ \left[\ln \hat{\mathbf{V}}^{(1)}(\alpha) \right] \hat{\mathbf{V}}^{(1)}(\alpha) \right\}_3 \mathbf{t} \right\| = 0, \tag{104}$$

where $\| \quad \|$ is a brief notation for the determinant. Now two cases are possible (compare with Section 4).

(a) $\boldsymbol{\eta}^{(1)}$ is the only eigenvector of the matrix $\hat{\mathbf{V}}_3^{(1)}(\alpha)$ so that the vectors $\mathbf{v}$ and $\mathbf{w}$ are linearly independent. Then

$$\det\left\{ \hat{\mathbf{V}}_3^{(1+\delta s)}(\alpha) \right\} = \delta s \left\{ \det\left\{ \hat{\mathbf{L}}(\alpha) \right\} + \ldots \right\} = 0, \tag{105}$$

where the matrix $\hat{\mathbf{L}}(\alpha)$ is defined in Eq. (51). Therefore, $s = 1$ is generally a single root of Eq. (101) and becomes a double root only at critical angle α_*^L of the Levy problem which satisfies Eq. (52).

(b) There exists another eigenvector $\boldsymbol{\eta}^{(2)} = (q, 0, 1)$ distinct from $\boldsymbol{\eta}^{(1)}$. In this case Eq. (52) is also satisfied, and the

Downloaded 04 May 2010 to 171.66.16.28. Redistribution subject to ASME license or copyright; see http://www.asme.org/terms/Terms_Use.cfm

expansion of the eigenvalue Eq. (101) into the power series begins from the second power of δs,

$$\det\left\{\hat{\mathbf{V}}_3^{(1+\delta s)}(\alpha)\right\} = (\delta s)^2\left\{\left\|\mathbf{v},\left[\ln\hat{\mathbf{V}}^{(1)}(\alpha)\right]_3\mathbf{n}(\alpha),\right.\right.$$

$$\left.\left.\times\left\{\left[\ln\hat{\mathbf{V}}^{(1)}(\alpha)\right]\hat{\mathbf{V}}^{(1)}(\alpha)\right\}_3\boldsymbol{\eta}^{(2)}\right\| + \ldots\right\} = 0. \quad (106)$$

In this case $s = 1$ is at least a double root.

Degree of multiplicity gives the number of branches which exist near the critical angle. But the multiplicity degree can differ from the number of independent eigenvectors of the $\hat{\mathbf{V}}_3^{(1)}(\alpha)$ matrix. The number of eigenvectors is exactly the minimum multiplicity degree, that is, every eigenvector at $s = 1$ necessarily results at least in one branch near $s = 1$. However, some eigenvectors may generate two or more branches. Let us consider as an illustration the case (a) and prove that close to the critical angle the eigenvector $\boldsymbol{\eta}^{(1)}$ generates two entirely different branches $s_1(\alpha)$ and $s_2(\alpha)$.

Close to the critical angle the perturbation expansion of the eigenvector problem has the form

$$\mathbf{a}^{(1+\delta s)} = \omega_0\mathbf{n}_0 + \delta s(\alpha)\left(\frac{d\mathbf{a}^{(s)}}{ds}\right)_{s=1} + \ldots, \quad (107)$$

$$\hat{\mathbf{V}}_3^{(s)}(\alpha)\mathbf{a}^{(s)} = \delta s(\alpha)\left(\omega_0\left[\ln\hat{\mathbf{V}}^{(1)}(\alpha)\right]_3\mathbf{n}(\alpha)\right.$$

$$\left.+\hat{\mathbf{V}}_3^{(1)}(\alpha)\left(\frac{d\mathbf{a}^{(s)}}{ds}\right)_{s=1}\right) + \ldots + = \mathbf{0} \quad (108)$$

where $\omega_0 = a_2^{(1)}$. Consequently, we have either

(i) $\delta s(\alpha) = 0$ – the branch $s(\alpha) = 1$, which always exists and corresponds to rigid-body rotations, or

(ii) $\delta s(\alpha) \neq 0$, but $\omega_0[\ln\hat{\mathbf{V}}^{(1)}(\alpha)]_3\mathbf{n}(\alpha) + \hat{\mathbf{V}}_3^{(1)}(\alpha)\left(\frac{d\mathbf{a}^{(s)}}{ds}\right)_{s=1} = \mathbf{0}$.

This branch exists only close to the critical wedge angle α_*^L of Levy's problem.

10 The Proof

Let us now prove that although equations for the critical wedge angles α_*^C and α_*^L do not coincide, they have common roots. The idea of the proof is to use the relationship between the ordered exponentials of the opposite indices. As follows from Eq. (A8) of the Appendix, the matrices $\hat{\mathbf{V}}^{(s)}(\alpha)$ and $\hat{\mathbf{V}}^{(-s)}(\alpha)$ are related via

$$\hat{\mathbf{T}}\left[\hat{\mathbf{V}}^{(-s)}(\alpha)\right]^t\hat{\mathbf{T}}\hat{\mathbf{V}}^{(s)}(\alpha) = \hat{\mathbf{I}}, \quad (109)$$

where

$$\hat{\mathbf{T}} = \begin{pmatrix}\mathbf{0} & \mathbf{I}\\ \mathbf{I} & \mathbf{0}\end{pmatrix}. \quad (110)$$

Using the 3×3 SW-block of Eq. (109), one obtains

$$\left[\hat{\mathbf{V}}_3^{(-s)}(\alpha)\right]^t\hat{\mathbf{V}}_1^{(s)}(\alpha) = -\left[\hat{\mathbf{V}}_1^{(-s)}(\alpha)\right]^t\hat{\mathbf{V}}_3^{(s)}(\alpha), \quad (111)$$

whereas for $s = 1$

$$\left[\hat{\mathbf{V}}_3^{(-1)}(\alpha)\right]^t\hat{\mathbf{V}}_1^{(1)}(\alpha) = -\left[\hat{\mathbf{V}}_1^{(-1)}(\alpha)\right]^t\hat{\mathbf{V}}_3^{(1)}(\alpha). \quad (112)$$

Equation (112) allows to establish a relationship between the eigenvectors of the matrices $\hat{\mathbf{V}}_3^{(1)}(\alpha)$ and $\hat{\mathbf{V}}_3^{(-1)}(\alpha)$. Let $\boldsymbol{\xi}$ be an eigenvector of the matrix $\hat{\mathbf{V}}_3^{(-1)}(\alpha)$, that is

$$\hat{\mathbf{V}}_3^{(-1)}(\alpha)\boldsymbol{\xi} = \mathbf{0}. \quad (113)$$

Then Eq. (112) implies that the vector

$$\boldsymbol{\zeta} = \hat{\mathbf{V}}_1^{(-1)}(\alpha)\boldsymbol{\xi} \quad (114)$$

is an eigenvector of the transpose of $\hat{\mathbf{V}}_3^{(1)}(\alpha)$,

$$\left[\hat{\mathbf{V}}_3^{(1)}(\alpha)\right]^t\boldsymbol{\zeta} = \mathbf{0}. \quad (115)$$

Likewise, if $\boldsymbol{\eta}$ is an eigenvector of $\hat{\mathbf{V}}_3^{(1)}(\alpha)$,

$$\hat{\mathbf{V}}_3^{(1)}(\alpha)\boldsymbol{\eta} = \mathbf{0}, \quad (116)$$

the vector

$$\boldsymbol{\varkappa} = \hat{\mathbf{V}}_1^{(1)}(\alpha)\boldsymbol{\eta} \quad (117)$$

is an eigenvector of the transpose of $\hat{\mathbf{V}}_3^{(-1)}(\alpha)$

$$\left[\hat{\mathbf{V}}_3^{(-1)}(\alpha)\right]^t\boldsymbol{\varkappa} = \mathbf{0}. \quad (118)$$

Let us now expand Eq. (111) into a power series close the point $s = 1$ into a power series over the index deviation $\delta s = s - 1$. Using the perturbation expansion of the ordered exponentials

$$\mathbf{V}^{(1+\delta s)}(\alpha) = \hat{\mathbf{V}}^{(1)}(\alpha) + \delta s\left\{\left[\ln\hat{\mathbf{V}}^{(1)}(\alpha)\right]\hat{\mathbf{V}}^{(1)}(\alpha)\right\} + \ldots, \quad (119)$$

$$\mathbf{V}^{(-1-\delta s)}(\alpha) = \hat{\mathbf{V}}^{(-1)}(\alpha) - \delta s\left\{\left[\ln\hat{\mathbf{V}}^{(-1)}(\alpha)\right]\hat{\mathbf{V}}^{(-1)}(\alpha)\right\} + \ldots, \quad (120)$$

one obtains in the first-order of perturbations the relation between the pseudo-logarithms of the indices $s = \pm 1$,

$$\left[\hat{\mathbf{V}}_3^{(1)}(\alpha)\right]^t\left\{\left[\ln\hat{\mathbf{V}}^{(1)}(\alpha)\right]\hat{\mathbf{V}}^{(1)}(\alpha)\right\}_1 + \left[\hat{\mathbf{V}}_1^{(-1)}(\alpha)\right]^t\left\{\left[\ln\hat{\mathbf{V}}^{(1)}(\alpha)\right]\hat{\mathbf{V}}^{(1)}(\alpha)\right\}_3$$

$$= \left\{\left[\ln\hat{\mathbf{V}}^{(-1)}(\alpha)\right]\hat{\mathbf{V}}^{(-1)}(\alpha)\right\}_1^t\hat{\mathbf{V}}_3^{(1)}(\alpha) + \left\{\left[\ln\hat{\mathbf{V}}^{(-1)}(\alpha)\right]\hat{\mathbf{V}}^{(-1)}(\alpha)\right\}_3^t\hat{\mathbf{V}}_1^{(1)}(\alpha). \quad (121)$$

When multiplied from the right by the vector $\mathbf{n}(0)$ and from the left by the vector $\boldsymbol{\xi}$, Eq. (121) gives rise to the relation between the matrix elements of the pseudo-logarithms with opposite indices

$$\boldsymbol{\zeta}\left[\ln\hat{\mathbf{V}}^{(1)}(\alpha)\right]_3\mathbf{n}(\alpha) = \mathbf{n}(\alpha)\left[\ln\hat{\mathbf{V}}^{(-1)}(\alpha)\right]_3\boldsymbol{\zeta}. \quad (122)$$

Equation (122) is valid whatever the number of the eigenvectors of the matrices $\hat{\mathbf{V}}_3^{(-1)}(\alpha)$ and $\hat{\mathbf{V}}_3^{(1)}(\alpha)$. However, it is important that according to Eqs. (114) and (117) the two matrices, and hence the matrix $[\hat{\mathbf{V}}_3^{(1)}(\alpha)]^t$ too, have equal number of eigenvectors.

Let us first consider the case when there is only one eigenvector. By Eq. (46) the matrix $[\hat{\mathbf{V}}_3^{(1)}(\alpha)]^t$ has the structure

$$\left[\hat{\mathbf{V}}_3^{(1)}(\alpha)\right]^t = \begin{bmatrix}\mathbf{v}\\ \mathbf{0}\\ \mathbf{w}\end{bmatrix} = \begin{bmatrix}v_1 & v_2 & v_3\\ 0 & 0 & 0\\ w_1 & w_2 & w_3\end{bmatrix}. \quad (123)$$

As one can establish by direct inspection, if the matrix (123) has only one eigenvector $\boldsymbol{\zeta} = \boldsymbol{\zeta}^{(1)}$, it can be chosen as

$$\boldsymbol{\zeta}^{(1)} = [\mathbf{v} \times \mathbf{w}]. \quad (124)$$

Now, taking into account Eq. (114), one can rewrite Eq. (66) for the critical angle of the Carothers problem as

$$\mathbf{n}(\alpha_*^C)\left[\ln\hat{\mathbf{V}}^{(-1)}(\alpha_*^C)\right]_3[\mathbf{v} \times \mathbf{w}] = 0. \quad (125)$$

Downloaded 04 May 2010 to 171.66.16.28. Redistribution subject to ASME license or copyright; see http://www.asme.org/terms/Terms_Use.cfm

In view of the relation (122), Eq. (125) can be transformed to

$$[\mathbf{v} \times \mathbf{w}]\left[\ln \hat{\mathbf{V}}^{(1)}(\alpha_*^C)\right]_3 \mathbf{n}(\alpha_*^C) = 0. \quad (126)$$

The equation obtained coincides exactly with Eq. (53) for the critical angle α_*^L of the Levy problem. Consequently, in the case in question, $\alpha_*^C = \alpha_*^L$.

11 The Levy Problem at the Critical Wedge Angle

At the critical angle two types of particular solutions to Levy's problem occur depending on whether the case (a) or (b) is considered.

$$\begin{pmatrix} \mathbf{u}(r, \phi) \\ \boldsymbol{\phi}(r, \phi) \end{pmatrix} = r\hat{\mathbf{V}}^{(1)}(\phi)\begin{pmatrix} \mathbf{a} \\ k\mathbf{n}(0) \end{pmatrix} + r\left(\hat{\mathbf{I}} \ln \eta + \ln \hat{\mathbf{V}}^{(1)}(\phi)\right)\hat{\mathbf{V}}^{(1)}(\phi)\begin{pmatrix} \mathbf{c} \\ \mathbf{0} \end{pmatrix}, \quad (127)$$

where, however, unlike Eq. (40), the unknown vector $\mathbf{c}$ can have nonvanishing components along both eigenvectors $\boldsymbol{\eta}^{(1)}$ and $\boldsymbol{\eta}^{(2)}$,

$$\mathbf{c} = \omega_0 \boldsymbol{\eta}^{(1)} + \lambda \boldsymbol{\eta}^{(2)} \quad (128)$$

In turn, the vector $\mathbf{a}$ can be considered as being one component,

$$\mathbf{a} = a_{\|}\mathbf{e}, \quad (129)$$

and directed along the vector $\mathbf{e} = \boldsymbol{\eta}^{(1)} \times \boldsymbol{\eta}^{(2)}$. Then, assuming that the matrix $\hat{\mathbf{V}}_3^{(1)}(\alpha)$ has two (but not three) independent eigenvectors, the component $a_{\|}$ together with the unknowns ω_0 and λ is uniquely obtainable from

$$a_{\|}\hat{\mathbf{V}}_3^{(1)}(\alpha)\mathbf{e} + \omega_0\left\{\left[\ln \hat{\mathbf{V}}^{(1)}(\alpha)\right]\hat{\mathbf{V}}^{(1)}(\alpha)\right\}_3\boldsymbol{\eta}^{(1)} + \lambda\left\{\left[\ln \hat{\mathbf{V}}^{(1)}(\alpha)\right]\hat{\mathbf{V}}^{(1)}(\alpha)\right\}_3\boldsymbol{\eta}^{(2)} = -k\left\{\mathbf{n}(\alpha) + \hat{\mathbf{V}}_4^{(1)}(\alpha)\mathbf{n}(0)\right\}. \quad (130)$$

In the particular case of three independent eigenvectors, the vector $\mathbf{a}$ does not enter the problem and hence remains arbitrary, whereas $\mathbf{c}$ is given by

$$\mathbf{c} = -k\left\{\left[\ln \hat{\mathbf{V}}^{(1)}(\alpha)\right]\hat{\mathbf{V}}^{(1)}(\alpha)\right\}_3^{-1}\left\{\mathbf{n}(\alpha) + \hat{\mathbf{V}}_4^{(1)}(\alpha)\mathbf{n}(0)\right\}. \quad (131)$$

At last, we discuss the more difficult case (a), which for elastically homogeneous anisotropic wedges, was recently analyzed by Hwu and Ting (1990). We seek a solution of the form

$$\begin{pmatrix} \mathbf{u}(r, \phi) \\ \boldsymbol{\phi}(r, \phi) \end{pmatrix} = r\hat{\mathbf{V}}^{(1)}(\phi)\begin{pmatrix} \mathbf{a} \\ \mathbf{b} \end{pmatrix} + 2r\hat{\mathbf{V}}^{(1)}(\phi)\left(\hat{\mathbf{I}} \ln \eta + \hat{\mathbf{P}}^{(1)}(\phi)\right) \times \begin{pmatrix} \mathbf{c} \\ \mathbf{d} \end{pmatrix} + r\hat{\mathbf{V}}^{(1)}(\phi)\left(\hat{\mathbf{I}} \ln^2 \eta + 2\hat{\mathbf{P}}^{(1)}(\phi) \ln \eta + \left\{\hat{\mathbf{P}}^{(1)}(\phi)\right\}^2 + \int_0^{\phi}\left[\left\{\hat{\mathbf{V}}^{(1)}(\theta)\right\}^{-1}\hat{\mathbf{N}}(\theta)\hat{\mathbf{V}}^{(1)}(\theta), \hat{\mathbf{P}}^{(1)}(\theta)\right]d\theta\right)\begin{pmatrix} \mathbf{g} \\ \mathbf{h} \end{pmatrix} \quad (132)$$

where three six-dimensional unknown vectors ($\mathbf{a}$, $\mathbf{b}$), ($\mathbf{c}$, $\mathbf{d}$), and ($\mathbf{g}$, $\mathbf{h}$) are to be found from the boundary conditions at the wedge sides which are given in Eq. (41). The condition at the side $\phi = 0$ demands

$$\mathbf{d} = \mathbf{0}, \quad \mathbf{h} = \mathbf{0}, \quad \mathbf{b} = k\mathbf{n}(0). \quad (133)$$

Likewise, the condition at the side $\phi = \alpha$ demands that

$$\hat{\mathbf{V}}_3^{(1)}(\alpha)\mathbf{g} = \mathbf{0},$$

$$\hat{\mathbf{V}}_3^{(1)}(\alpha)\mathbf{c} + \left\{\left[\ln \hat{\mathbf{V}}^{(1)}(\alpha)\right]\hat{\mathbf{V}}^{(1)}(\alpha)\right\}_3\mathbf{g} = \mathbf{0},$$

$$\hat{\mathbf{V}}_3^{(1)}(\alpha)\mathbf{a} + 2\left\{\left[\ln \hat{\mathbf{V}}^{(1)}(\alpha)\right]\hat{\mathbf{V}}^{(1)}(\alpha)\right\}_3\mathbf{c} + \left\{\hat{\mathbf{V}}^{(1)}(\alpha)\left(\left\{\hat{\mathbf{P}}^{(1)}(\alpha)\right\}^2 + \int_0^{\alpha}\left[\left\{\hat{\mathbf{V}}^{(1)}(\theta)\right\}^{-1}\hat{\mathbf{N}}(\theta)\hat{\mathbf{V}}^{(1)}(\theta), \hat{\mathbf{P}}^{(1)}(\theta)\right]d\theta\right)\right\}_3\mathbf{g} = -k\left\{\mathbf{n}(\alpha) + \hat{\mathbf{V}}_4^{(1)}(\alpha)\mathbf{n}(0)\right\}. \quad (134)$$

Since the matrix $\hat{\mathbf{V}}_3^{(1)}(\alpha)$ is supposed to have one independent eigenvector $\boldsymbol{\eta}^{(1)} = \mathbf{n}(0)$, the only possible solution for $\mathbf{g}$ is

$$\mathbf{g} = \omega_0\mathbf{n}(0), \quad (135)$$

where ω_0 is unknown scalar factor. Under the conditions of the case (a) the system for unknowns $\mathbf{c}$ (two components c_1 and c_3) and ω_0,

$$\hat{\mathbf{V}}_3^{(1)}(\alpha)\mathbf{c} + \omega_0\left[\ln \hat{\mathbf{V}}^{(1)}(\alpha)\right]_3\mathbf{n}(\alpha) = \mathbf{0}, \quad (136)$$

has at $\alpha = \alpha_*^L$ a nonzero solution defined to within a scalar factor γ, which together with a_1 and a_3 is uniquely derivable from the third of Eqs. (134).

The particular solutions obtained for both cases (a) and (b) are not self-similar and depend on the parameter R which makes dimensionless the logarithm argument. Because the value of R is not specified here, it is of interest to examine the influence of the choice of R on the solutions (127) and (132). There is no problem in the case (b) where any variation of R results in adding a homogeneous eigensolution. The case (a) is not so trivial, because any change in R in the solution (132) results in adding to it some expression which is not homogeneous but behaves like $r \ln \eta$ and hence is not present among the homogeneous eigensolutions (98). This discrepancy can be overcome by taking into account that at $\alpha = \alpha_*^L$ the solution of the form

$$\begin{pmatrix} \mathbf{u}(r,\boldsymbol{\phi}) \\ \boldsymbol{\phi}(r,\phi) \end{pmatrix} = r\hat{\mathbf{V}}^{(1)}(\phi)\begin{pmatrix} \mathbf{c} \\ \mathbf{0} \end{pmatrix} + \omega_0 r\left(\hat{\mathbf{I}} \ln \eta + \ln \hat{\mathbf{V}}^{(1)}(\phi)\right)\begin{pmatrix} \mathbf{n}(\phi) \\ 0 \end{pmatrix}, \quad (137)$$

where constants $\mathbf{c}$ and ω_0 satisfy Eq. (136), leaves the wedge sides free of tractions and, hence, is an eigensolution of the free-surface wedge. Therefore, any change in R in the solution (132) results in adding both the homogeneous eigensolution varying like r and the eigensolution (137) which behaves like $r \ln \eta$.

12 The Carothers Problem at the Critical Wedge Angle

Let us now examine the behavior of the roots of the eigenvalue equation (101) near the critical wedge angle α_*^C of the Carothers problem. We first notice that according to Eq. (58) the matrix $\hat{\mathbf{V}}_3^{(-1)}(\alpha)$ has relative to the rotated basis ($\mathbf{m}(\alpha)$, $\mathbf{n}(\alpha)$, $\mathbf{t}$) a vanishing second row. Hence, its determinant vanishes and $s(\alpha) = -1$ is a root of Eq. (101) for any wedge angle and rotational inhomogeneity. Thus, there always exists at least one independent eigenvector $\mathbf{a}^{(-1)}$. Let us further assume that it is the only eigenvector. Then it is given by Eq. (61),

$$\mathbf{a}^{(-1)} = \boldsymbol{\xi}^{(1)} = \beta_1\mathbf{m}(\alpha) + \mathbf{n}(\alpha) + \beta_3\mathbf{t} \quad (138)$$

Downloaded 04 May 2010 to 171.66.16.28. Redistribution subject to ASME license or copyright; see http://www.asme.org/terms/Terms_Use.cfm

with uniquely derivable components β_1 and β_3. Let us now derive the criterion for $s = -1$ to be a multiple root. Expanding close to $s = -1$, Eq. (101) into a power series of the index deviation $\delta s = s + 1$, up to the first power of δs, one obtains

$$\det\left\{\hat{\mathbf{V}}_3^{(-1+\delta s)}(\alpha)\right\} = = \delta s\left\{\mathbf{n}(\alpha)\left[\ln\hat{\mathbf{V}}^{(-1)}(\alpha)\right]_3\hat{\mathbf{V}}_1^{(-1)}\right.$$
$$\left.\times(\alpha)\boldsymbol{\xi}^{(1)}\begin{Vmatrix}\left\{\hat{\mathbf{V}}_3^{(-1)}(\alpha)\right\}_{11} & \left\{\hat{\mathbf{V}}_3^{(-1)}(\alpha)\right\}_{13}\\ \left\{\hat{\mathbf{V}}_3^{(-1)}(\alpha)\right\}_{31} & \left\{\hat{\mathbf{V}}_3^{(-1)}(\alpha)\right\}_{33}\end{Vmatrix} + \ldots\right\} = 0. \tag{139}$$

So if $\boldsymbol{\xi}^{(1)}$ is the only eigenvector, $s = -1$ is generally a single root of Eq. (101) and becomes a double root when

$$\mathbf{n}(\alpha)\left[\ln\hat{\mathbf{V}}^{(-1)}(\alpha)\right]_3\hat{\mathbf{V}}_1^{(-1)}(\alpha)\boldsymbol{\xi}^{(1)} = 0, \tag{140}$$

that is at the critical angle $\alpha = \alpha_*^C$ of the Carothers problem. This confirms the results of numerical calculations by Leguillon (1988) for the elastically homogeneous isotropic wedge.

Following Eq. (38) we seek a solution of the Carothers problem at the critical angle as

$$\begin{pmatrix}\mathbf{u}(r,\phi)\\ \boldsymbol{\phi}(r,\phi)\end{pmatrix} = r^{-1}\hat{\mathbf{V}}^{(-1)}(\phi)\begin{pmatrix}\mathbf{a}\\ \mathbf{b}\end{pmatrix}$$
$$+ r^{-1}\left(\hat{\mathbf{I}}\ln\eta + \ln\hat{\mathbf{V}}^{(-1)}(\phi)\right)\hat{\mathbf{V}}^{(-1)}(\phi)\begin{pmatrix}\mathbf{c}\\ \mathbf{d}\end{pmatrix}. \tag{141}$$

The condition of the traction-free side $\phi = 0$ demands that

$$\mathbf{b} = \mathbf{0}, \quad \mathbf{d} = \mathbf{0}. \tag{142}$$

Likewise, the condition of the free side $\phi = \alpha$ yields

$$\hat{\mathbf{V}}_3^{(-1)}(\alpha)\mathbf{c} = \mathbf{0}, \tag{143}$$

whereas

$$\mathbf{c} = \tau\boldsymbol{\xi}^{(1)}, \tag{144}$$

with an unknown scalar factor τ, and

$$\hat{\mathbf{V}}_3^{(-1)}(\alpha)\mathbf{a} + \tau\left[\ln\hat{\mathbf{V}}^{(-1)}(\alpha)\right]_3\hat{\mathbf{V}}_1^{(-1)}(\alpha)\boldsymbol{\xi}^{(1)} = \mathbf{0}. \tag{145}$$

Since $\mathbf{n}(\alpha)\hat{\mathbf{V}}_3^{(-1)}(\alpha) = \mathbf{0}$, the system (145) has a nonzero solution only when the condition (140) is fulfilled, that is at the critical angle of the Carothers problem. The unknowns in the system (145) are τ and two components $a^{(1)}$ and $a^{(2)}$ of the vector $\mathbf{a}$ along the vectors $\mathbf{e}^{(1)}$ and $\mathbf{e}^{(2)}$ (the component along $\boldsymbol{\xi}^{(1)}$ drops out of the system and remains arbitrary), which together with the vector $\boldsymbol{\xi}^{(1)}$ form an orthogonal basis. The solution for τ and two components $a^{(1)}$ and $a^{(2)}$ is defined up to a scalar factor γ, which in turn is obtainable from the moment balance condition.

One should notice that a change in the parameter R in the solution (141) results in adding a homogeneous eigensolution as required.

13 Final Discussion and Conclusion

According to Section 10, the wedge angle α_*^C which is critical for Carothers' problem, is also critical for Levy's one, although the contrary is not necessarily true. The proof was based only on the relation (A8) between the ordered exponentials of opposite indices, which in turn follows solely from the property (A2) of the matrix $\hat{\mathbf{N}}(\phi)$ or, if that is the same, from the symmetry of the elastic constants tensor. Consequently, the coincidence of the critical angles α_*^C and α_*^L is a general property linearly elastic rotationally inhomogeneous media. It is not due to such a factor as material homogeneity.

We defined the critical angles as the wedge angle, at which there exist no self-similar solutions independent on the geometrical parameter R. We also proved that in the Levy problem the nonvanishing of the det $\{\hat{\mathbf{L}}(\alpha)\}$, Eq. (50), ensures the existence of such type solutions. However, the self-similarities can exist also if Eq. (52) is fulfilled, because depending on the right-hand side the system, (49) can have solutions. As an illustration we consider an elastically homogeneous anisotropic wedge of the wedge angle $\alpha = \pi$, or 2π. In this case the matrix $\hat{\mathbf{V}}_3^{(1)}(\alpha)$ has three independent eigenvectors. Hence, a particular solution to Levy's problem is given by Eqs. (127) and (131). In view of

$$\hat{\mathbf{V}}^{(1)}(\pi) = -\hat{\mathbf{I}}, \quad \hat{\mathbf{V}}^{(1)}(2\pi) = \hat{\mathbf{I}}, \tag{146}$$

Eq. (131) reduces to

$$\mathbf{c} = \begin{cases}-(2k/\pi)\hat{\mathbf{B}}^{-1}\mathbf{n}(0)\\ -(k/\pi)\hat{\mathbf{B}}^{-1}\mathbf{n}(0)\end{cases} \text{for}\begin{cases}\alpha = \pi,\\ \alpha = 2\pi,\end{cases} \tag{147}$$

where the matrix $\hat{\mathbf{B}}$ is defined as

$$\left[\ln\hat{\mathbf{V}}^{(1)}(2\pi)\right]_3 = 2\left[\ln\hat{\mathbf{V}}^{(1)}(\pi)\right]_3 = 2\pi\hat{\mathbf{B}} \tag{148}$$

and coincides with the well-known prelogarithmic factor in the elastic energy of a straight dislocation (Steeds, 1973). In the case of general anisotropy all three components c_1, c_2, and c_3 of the vector $\mathbf{c}$ are nonzero and hence the stress derivable from the stress function (127) behaves as $\ln\eta$. However, if there is an appropriate axis of elastic symmetry the components c_1 and c_3 can vanish. For example, according to Steeds (1973),

$$B_{21} = B_{23} = 0 \text{ when}\begin{cases}\text{or} & x_2 \text{ is along a 2, 4, or sixfold axis}\\ & x_3 \text{ is along a 3, 4, or sixfold axis}\end{cases},$$

(twofold axis is equivalent to a mirror plane normal to it) and the vector $\mathbf{c}$ has only one component c_2. In this case stresses derivable from Eq. (127) are self-similar and independent on r. Therefore, the wedge angles $\alpha = \pi, 2\pi$ are not critical for these elastic symmetries in the above accepted sense. It is interesting to note that this is just the case when the vector $\mathbf{g}$ in Eq. (88) vanishes. For isotropic wedges the solutions for $\alpha = \pi$ and 2π have been previously discussed by Dempsey (1981) and Ting (1984, 1985a).

14 Acknowledgment

One of the authors (A. Yu. Belov) is greatly indebted to the SOROS FOUNDATION for a travel grant.

References

Barenblatt, G. I., 1979, *Similarity, Self-similarity and Intermediate Asymptotics*, Consultants Bureau, New York.

Carothers, S. D., 1912, "Plane Strain in a Wedge," *Proceedings of the Royal Society of Edinburgh*, Vol. 23, pp. 292–306.

Dempsey, J. P., 1981, "The Wedge Subjected to Tractions: a Paradox Resolved," *Journal of Elasticity*, Vol. 11, pp. 1–10.

Dundurs, J., and Markenscoff, X., 1989, "The Sternberg-Koiter Conclusion and Other Anomalies of the Concentrated Couple," ASME JOURNAL OF APPLIED MECHANICS, Vol. 56, pp. 240–245.

Hwu, Chyanbin, and Ting, T. C. T., 1990, "Solutions for the Anisotropic Elastic Wedge at Critical Wedge Angles," *Journal of Elasticity*, Vol. 24, pp. 1–20.

Kirchner, H. O. K., 1989, "Elastically Anisotropic Angularly Inhomogeneous Media. II. A New Formalism," *Philosophical Magazine B*, Vol. 60, pp. 423–432.

Kirchner, H. O. K., and Lothe, J., 1986, "On the Redundancy of the N Matrix of Anisotropic Elasticity," *Philosophical Magazine A*, Vol. 53, pp. L7–L10.

Leguillon, D., 1988, "Sur le Moment Punctuel Applique a un Secteur: le Paradox de Sternberg-Koiter," *C. R. Acad. Sci. Paris*, Vol. 307, pp. 1471–1746.

Downloaded 04 May 2010 to 171.66.16.28. Redistribution subject to ASME license or copyright; see http://www.asme.org/terms/Terms_Use.cfm

Levy, M., 1898, *Compt. Rend.*, Vol. 126, p. 1235.
Steeds, J. W., 1973, *Anisotropic Elasticity Theory of Dislocations*, Clarendon Press, Oxford, U.K.
Sternberg, E., and Koiter, W. T., 1958, "The Wedge under a Concentrated Couple: A Paradox in the Two-Dimensional Theory of Elasticity," ASME JOURNAL OF APPLIED MECHANICS, Vol. 25, pp. 575–581.
Stroh, A. N., 1958, "Dislocations and Cracks in Anisotropic Elasticity," *Philosophical Magazine*, Vol. 7, pp. 625–646.
Stroh, A. N., 1962, "Steady State Problems in Anisotropic Elasticity," *Journal of Mathematics and Physics (Cambridge)*, Vol. 41, pp. 77–103.
Timoshenko, S. P., and Goodier, J. N.. 1970, *Theory of Elasticity*, 3rd ed., McGraw-Hill, New York.
Ting, T. C. T., 1984, "The Wedge Subjected to Tractions: a Paradox Reexamined," *Journal of Elasticity*, Vol. 14, pp. 235–247.
Ting, T. C. T., 1985a, "A Paradox on the Elastic Wedge Subjected to a Concentrated Couple and on the Jeffrey-Hamel Viscous Flow Problem," *Zeitschrift fuer Angewandte Mathematik und Mechanik*, Vol. 65, pp. 188–190.
Ting, T. C. T., 1985b, "Elastic Wedge Subjected to Anti-Plane Shear Tractions—A Paradox Explained," *The Quarterly Journal of Mechanics and Applied Mathematics*, Vol. 38, pp. 245–255.
Ting, T. C. T., 1988a, "The Anisotropic Wedge under a Concentrated Couple," *Quarterly Journal of Mechanics and Applied Mathematics*, Vol. 20, pp. 564–578.
Ting, T. C. T., 1988b, "The Critical Angle of the Anisotropic Elastic Wedge Subject to Uniform Tractions," *Journal of Elasticity*, Vol. 20, pp. 113–130.

APPENDIX

In linear elasticity theory the tensor of elastic constants $C_{ijkl}(\phi)$ is generally assumed to have the properties:

(a) due to the symmetry of the stress and strain tensors

$$C_{ijkl}(\phi) = C_{jikl}(\phi) = C_{ijlk}(\phi),$$

(b) due to the existence of the elastic potential $W(\epsilon_{kl})$,

$$C_{ijkl}(\phi) = C_{klij}(\phi).$$

The properties a, b make the elastic constants tensor fully symmetric, owing to which the matrices (17) behave as

$$(ab) = (ba)^t. \tag{A1}$$

In turn, owing (A1), the matrix $\hat{\mathbf{T}}\hat{\mathbf{N}}(\phi)$ is Hermitian,

$$\left(\hat{\mathbf{T}}\hat{\mathbf{N}}(\phi)\right)^t = \hat{\mathbf{T}}\hat{\mathbf{N}}(\phi), \quad \hat{\mathbf{N}}(\phi) = \hat{\mathbf{T}}\hat{\mathbf{N}}(\phi)^t\hat{\mathbf{T}}, \tag{A2}$$

where the matrix $\hat{\mathbf{T}}$ is given in Eq. (41). Using the definition of the ordered exponential of the index s

$$\hat{\mathbf{V}}^{(s)}(\phi) = \exp\left(s\hat{\mathbf{N}}(\theta_{k-1})\delta\theta\right) \times \exp\left(s\hat{\mathbf{N}}(\theta_{k-2})\delta\theta\right)\ldots\exp\left(s\hat{\mathbf{N}}(0)\delta\theta\right), \tag{A3}$$

and its transpose

$$\left[\hat{\mathbf{V}}^{(s)}(\phi)\right]^t = \exp\left(s\hat{\mathbf{N}}^t(0)\delta\theta\right)\ldots \times \exp\left(\hat{\mathbf{N}}^t(\theta_{k-2})\delta\theta\right)\exp\left(s\hat{\mathbf{N}}^t(\theta_{k-1})\delta\theta\right), \tag{A4}$$

and next, taking into account the property (A2), one finds that

$$\hat{\mathbf{T}}\left[\hat{\mathbf{V}}^{(s)}(\phi)\right]^t\hat{\mathbf{T}} = \exp\left(s\hat{\mathbf{T}}\hat{\mathbf{N}}^t(0)\hat{\mathbf{T}}\delta\theta\right)\ldots \times\exp\left(s\hat{\mathbf{T}}\hat{\mathbf{N}}^t(\theta_{k-1})\hat{\mathbf{T}}\delta\theta\right) = = \exp\left(s\hat{\mathbf{N}}(0)\delta\theta\right)\ldots\exp\left(s\hat{\mathbf{N}}(\theta_{k-1})\delta\theta\right). \tag{A5}$$

The ordered exponential of the opposite index has the form

$$\hat{\mathbf{V}}^{(-s)}(\phi) = \exp\left(-s\hat{\mathbf{N}}(\theta_{k-1})\delta\theta\right)\exp\left(-s\hat{\mathbf{N}}(\theta_{k-2})\delta\theta\right)\ldots \times\exp\left(-s\hat{\mathbf{N}}(0)\delta\theta\right) \tag{A6}$$

so that its inverse

$$\left[\hat{\mathbf{V}}^{(-s)}(\phi)\right]^{-1} = \exp\left(s\hat{\mathbf{N}}(0)\delta\theta\right)\ldots \times\exp\left(s\hat{\mathbf{N}}(\theta_{k-2})\delta\theta\right)\exp\left(s\hat{\mathbf{N}}(\theta_{k-1})\delta\theta\right) \tag{A7}$$

coincides with the matrix (A5). Therefore, the relation in question between the ordered exponentials of the opposite indices is given by

$$\hat{\mathbf{T}}\left[\hat{\mathbf{V}}^{(s)}(\phi)\right]^t\hat{\mathbf{T}} = \left[\hat{\mathbf{V}}^{(-s)}(\phi)\right]^{-1}. \tag{A8}$$

Downloaded 04 May 2010 to 171.66.16.28. Redistribution subject to ASME license or copyright; see http://www.asme.org/terms/Terms_Use.cfm

Elastothermodynamic Damping of Fiber-Reinforced Metal-Matrix Composites[1]

K. B. Milligan
Graduate Research Assistant.

V. K. Kinra
General Dynamics Professor,
Fellow ASME.

Center for Mechanics and Composites and
Department of Aerospace Engineering,
Texas A & M University,
College Station, TX 77843-3141

Recently, taking the second law of thermodynamics as a starting point, a theoretical framework for an exact *calculation of the elastothermodynamic damping in metal-matrix composites has been presented by the authors (Kinra and Milligan, 1994; Milligan and Kinra, 1993). Using this work as a foundation, we solve two canonical boundary value problems concerning elastothermodynamic damping in continuous-fiber-reinforced metal-matrix composites: (1) a fiber in an infinite matrix, and (2) using the general methodology given by Bishop and Kinra (1993), a fiber in a finite matrix. In both cases the solutions were obtained for the following loading conditions: (1) uniform radial stress and (2) uniform axial strain.*

Introduction

It is well known that when a material point is subjected to a stress in a reversible adiabatic (i.e., isentropic) process, there is a corresponding change in the temperature at that point; this phenomenon is known as the thermoelastic effect and can easily be predicted using the first and second laws of thermodynamics (Bejan, 1988). For an isotropic material, the thermoelastic effect is given by

$$\left(\frac{\partial T}{\partial \sigma_{kk}}\right)_S = -\frac{\alpha}{\rho c} T \tag{1}$$

where T is the absolute temperature, σ_{kk} is the hydrostatic component of stress, α is the linear coefficient of thermal expansion, ρ is the mass density, c is the specific heat per unit mass, and the subscript S denotes an isentropic process. We note in passing that for isotropic materials, the application of a shear stress does not produce a change in temperature, hence the presence of σ_{kk} in Eq. (1). As a result, inhomogeneities in either the stress field or the material properties or both will result in inhomogeneities in the temperature field and, consequently, in heat conduction from regions of elevated temperature to regions of lowered temperature. As a consequence of the second law of thermodynamics, entropy is produced which manifests itself as the conversion of useful mechanical energy into heat. This process is the origin of elastothermodynamic damping.[2]

Elastothermodynamic damping (ETD) was first studied by Zener (1938a, 1938b, 1948) who considered, among other things, the transverse vibrations of a *homogeneous*, isotropic, Euler-Bernoulli beam. More recently, Alblas (1961, 1981), Chadwick (1962), and Biot (1956) have extended Zener's one-dimensional analysis to three dimensions. Alblas and Chadwick obtained solutions to the coupled elastothermodynamic equations in the form of series expansions in terms of orthonormal eigenfunctions. The ETD of homogeneous plates, shells, and Timoshenko beams has been addressed by Tasi (1963), Shieh (1971, 1975, 1979), Tasi and Herrmann (1964), and Lee (1985). Unfortunately, all of these analyses are confined to materials which are *isotropic* and *homogeneous* and cannot be extended to include composite materials which are inherently *heterogeneous* and, in general, also *anisotropic*. Recently, taking the second law of thermodynamics as a starting point, a theory which may be used for an *exact* calculation of the elastothermodynamic damping in metal-matrix composites (MMCs) has been presented by the authors (Kinra and Milligan, 1994). The theory is exact, quite general, and equally applicable to elastic solids which are isotropic or anisotropic, homogeneous or heterogeneous.

[1]Contributed by the Advanced Energy Systems Division of THE AMERICAN SOCIETY OF MECHANICAL ENGINEERS for presentation at the ASME Winter Annual Meeting, New Orleans, LA, Nov. 28–Dec. 3, 1993.

Contributed by the Applied Mechanics Division of the THE AMERICAN SOCIETY OF MECHANICAL ENGINEERS for publication in the ASME JOURNAL OF APPLIED MECHANICS.

Discussion on this paper should be addressed to the Technical Editor, Professor Lewis T. Wheeler, Department of Mechanical Engineering, University of Houston, Houston, TX 77204-4792, and will be accepted until four months after final publication of the paper itself in the ASME JOURNAL OF APPLIED MECHANICS.

Manuscript received by the ASME Applied Mechanics Division, June 2, 1993; final revision, Apr. 20, 1994. Associate Technical Editor: J. T. Jenkins.

[2]We submit that *elastothermodynamic* is a far more appropriate qualifier for the word damping than *thermoelastic*. Historically (e.g., Boley and Weiner, 1960), the word *thermoelastic* has been used to connote a situation where the cause is an externally applied temperature field (*thermo*), and the effect is an elastic stress field (*elastic*); hence *thermoelastic*. In the present context of damping, there is no externally applied temperature field. Instead, the cause is an externally applied traction field, which produces a stress field (*elasto*), and the effect is a temperature field (*thermo*). Moreover, the dissipation of mechanical energy occurs if and only if the stress field is time dependent (*dynamic*); hence *elastothermodynamic*.

Copyright © 1995 by ASME

Downloaded 04 May 2010 to 171.66.16.28. Redistribution subject to ASME license or copyright; see http://www.asme.org/terms/Terms_Use.cfm

Table 1 Elastothermodynamic properties of selected materials

Material	ρ (10^3 kg/m^3)	E (GPa)	k (J/s-m-K)	c (J/kg-K)	α (10^{-6} /K)	ν	Z (10^{-12} m^2/N)
Al	2.70	70	222	900	23.6	0.333	9.71
Fe	7.87	197	75.4	460	11.8	0.333	3.26
Mg	1.74	44	154	1030	27.1	0.333	15.1
SiC	3.26	460	90.0	1330	4.3	0.333	0.99
TiC	4.50	350	30.3	840	7.0	0.333	1.85

Our motivation for this work is to analyze the damping in continuous fiber-reinforced metal-matrix composites. The total damping of an MMC is due to a large number of relaxation mechanisms: for example, point defects (vacancies and/or interstitials), line defects (dislocations), surface defects (grain boundary sliding), phase transformation, elastothermodynamic relaxation, magnetoelastic relaxation, etc.; see the excellent monograph by Nowick and Berry (1972) and the frontispiece of the classic text by Zener (1948) for more details. Most of the damping research to date has been empirical or semi-empirical in nature. So far as we know, mechanics-based analytical methods for *predicting* the damping due to any of these mechanisms have not been reported. In the absence of such analytical models, it becomes difficult to divide the total damping (measured experimentally) into its various constituents and to design material with high damping. This defines the objective of the present work. In the following we present an analytical treatment of elastothermodynamic damping in a continuous fiber-reinforced MMC. An exact calculation of the ETD in an actual MMC (in which the fibers are distributed randomly; see Fig. 2 of Wren and Kinra (1992)) is clearly beyond the scope of this work; however, as a first step in that direction we calculate the ETD for two canonical boundary value problems possessing an axial symmetry: (1) a fiber in an infinite matrix, and (2) using the general methodology given by Bishop and Kinra (1993), a fiber in a finite matrix. In both cases the solutions were obtained for the following loading conditions: (1) uniform radial stress and (2) uniform axial strain. We have shown that by a proper choice of constituent materials, fiber size and frequency, one can *design* MMCs such that the contribution of the elastothermodynamic damping is a significant fraction of the total observed damping.

General Theory

The complete set of differential equations governing the phenomenon of elastothermodynamic damping has been presented by Kinra and Milligan (1994). Here we give only those equations which are germane to the problem under consideration. We assume that both the fiber and the matrix are made up of isotropic materials.

Conservation of linear momentum:

$$\sigma_{ji,j} = \rho \frac{\partial^2 u_i}{\partial t^2}. \tag{2}$$

Two-way coupled heat-conduction equation:

$$\frac{1}{r}\frac{\partial}{\partial r}\left(r\frac{\partial T}{\partial r}\right) = \frac{\rho c}{k}\frac{\partial T}{\partial t} + \frac{\alpha}{k}T\frac{\partial \sigma_{kk}}{\partial t}. \tag{3}$$

From Table 1 it may be seen that for typical metals subjected to a stress which is well below yield (say 100 MPa), the variations in temperature are extremely small, $\Delta T/T = O(10^{-3})$. Therefore, in the coupling term, T may be replaced by the equilibrium temperature, T_o. Moreover, it is reasonable to assume that such small variations in temperature do not affect the stress field; we then obtain the one-way coupled heat-conduction equation:

$$\frac{1}{r}\frac{\partial}{\partial r}\left(r\frac{\partial T}{\partial r}\right) = \frac{\partial c}{k}\frac{\partial T}{\partial t} + \frac{\alpha}{k}T_o\frac{\partial \sigma_{kk}}{\partial t}. \tag{4}$$

Second law of thermodynamics as it applies to a solid:

$$\dot{s}_p = \frac{\partial s_p}{\partial t} = \frac{k}{\rho T_o^2}\left(\frac{\partial T}{\partial r}\right)^2. \tag{5}$$

Gouy-Stodola theorem (Bejan, 1982; Gouy, 1889; Stodola, 1910) which establishes the connection between entropy production and the dissipation of mechanical energy:

$$\dot{W} = \rho T_o \dot{s}_p. \tag{6}$$

Mechanical energy dissipated during one cycle:

$$\Delta W = \oint \dot{W} dt. \tag{7}$$

Constitutive equation for an isotropic elastic solid (isothermal Hooke's law):

$$\sigma_{ij} = \frac{E}{1+\nu}\left(\epsilon_{ij} + \frac{\nu}{1-2\nu}\epsilon_{kk}\delta_{ij}\right). \tag{8}$$

Elastic energy density:

$$W = \frac{1}{2}\sigma_{ij}\epsilon_{ij}. \tag{9}$$

Local specific damping capacity:

$$\psi = \frac{\Delta W}{W}. \tag{10}$$

Volume-averaged specific damping capacity:

$$\Psi \equiv \frac{\int_V \Delta W dV}{\int_V W dV} = \frac{\int_V \psi W dV}{\int_V W dV}. \tag{11}$$

where T_o is the equilibrium temperature, k is the thermal conductivity, σ_{ij} and ϵ_{ij} are the stress and strain tensors, respectively, u_i is the displacement vector, s_p is the entropy produced per unit mass, $\dot{W}$ is the time rate of dissipation of mechanical energy per unit volume, E is the modulus of elasticity, ν is Poisson's ratio, W is the maximum elastic energy density, ψ is the local specific damping capacity (SDC), Ψ is the volume-averaged SDC, and δ_{ij} is the Kronecker delta.

In the following, we solve two canonical boundary value problems in a cylindrical coordinate system (r, θ, z) where the z-axis occupies the axis of the fiber; all of the field variables depend only on r.

A Fiber in an Infinite Matrix

Uniform Radial Stress. As a first step toward calculating the ETD in fiber-reinforced composites, we consider a fiber of radius a embedded in an infinite matrix of a different material subjected to a uniform far-field radial stress $\sigma_{rr} = \sigma_o e^{i\omega t}$ under a plane strain condition. We will denote the properties of the fiber and the matrix with the subscripts $()_1$ and $()_2$, respectively. It is convenient to introduce a complex temperature

$$T^*(r,t) = T_o^* + V^*(r)e^{i\omega t} \tag{12}$$

where $T_o^* = T_o(1+i)$, $V^*(r)$ is the spatial dependence of the fluctuating part of the temperature, and the superscript $()^*$ is used to denote a complex quantity. The boundary conditions for the thermal problem are an adiabatic boundary at the axis of symmetry ($r = 0$), continuity of temperature and heat flux at the fiber-matrix interface ($r = a$), and that

Downloaded 04 May 2010 to 171.66.16.28. Redistribution subject to ASME license or copyright; see http://www.asme.org/terms/Terms_Use.cfm

the far-field temperature is governed by the thermoelastic effect, Eq. (1)

$$\lim_{r\to\infty} T_2^*(r,t) = T_o^* - \frac{\alpha_2}{\rho_2 c_2} T_o \sigma_{kk_2} e^{i\omega t}. \tag{13}$$

As we shall see, the particular grouping of material properties, $\alpha/\rho c$, captures the essential physics of elastothermodynamic damping. In honor of Zener we would like to call it the Zener coefficient: $Z = \alpha/\rho c$.

Substitution of Eq. (12) into Eq. (4) yields an ordinary differential equation for $V^*(r)$ whose solution is

$$V^* = 2\sigma_o T_o \begin{cases} (1+\nu_2)\left(Z_1\dfrac{1}{R} - Z_2\right)A^* \\ \quad \cdot\left[\mathrm{Ber}(\Omega^{1/2}\xi) + i\mathrm{Bei}(\Omega^{1/2}\xi)\right] \\ \quad -Z_1\dfrac{(1+\nu_2)}{R} \qquad 0 \le \xi < 1 \\ (1+\nu_2)\left(Z_1\dfrac{1}{R} - Z_2\right)B^* \\ \quad \cdot\left[\mathrm{Ker}\left(\dfrac{k_1K_2}{k_2K_1}\Omega^{1/2}\xi\right)\right. \\ \quad \left. +i\mathrm{Kei}\left(\dfrac{k_1K_2}{k_2K_1}\Omega^{1/2}\xi\right)\right] \\ \quad -Z_2(1+\nu_2) \qquad \xi > 1 \end{cases} \tag{14}$$

where we have introduced the following normalized variables: a spatial coordinate $\xi = r/a$, a frequency $\Omega = \omega\rho_1 c_1 a^2/k_1$, and $E_r = E_1/E_2$. Moreover, $K = (\rho ck)^{1/2}$ is the coefficient of heat penetration (Grigull and Sander, 1984), and

$$R = \frac{(1+\nu_1)(1-2\nu_1) + E_r(1+\nu_2)}{2E_r(1+\nu_1)(1-\nu_2)} \tag{15}$$

$$A^* = \frac{K_2\left[\mathrm{Ker}'\left(\dfrac{k_1K_2}{k_2K_1}\Omega^{1/2}\right) + i\mathrm{Kei}'\left(\dfrac{k_1K_2}{k_2K_1}\Omega^{1/2}\right)\right]}{C^*} \tag{16}$$

$$B^* = \frac{K_1\left[\mathrm{Ber}'(\Omega^{1/2}) + i\mathrm{Bei}'(\Omega^{1/2})\right]}{C^*} \tag{17}$$

$$\begin{aligned} C^* = &\left\{K_2\left[\mathrm{Ber}(\Omega^{1/2}) + i\mathrm{Bei}(\Omega^{1/2})\right]\right. \\ &\left.\times\left[\mathrm{Ker}'\left(\frac{k_1K_2}{k_2K_1}\Omega^{1/2}\right) + i\mathrm{Kei}'\left(\frac{k_1K_2}{k_2K_1}\Omega^{1/2}\right)\right]\right\} \\ &-\left\{K_1\left[\mathrm{Ber}'(\Omega^{1/2}) + i\mathrm{Bei}'(\Omega^{1/2})\right]\right. \\ &\left.\times\left[\mathrm{Ker}\left(\frac{k_1K_2}{k_2K_1}\Omega^{1/2}\right) + i\mathrm{Kei}\left(\frac{k_1K_2}{k_2K_1}\Omega^{1/2}\right)\right]\right\}. \end{aligned} \tag{18}$$

Here, $\mathrm{Ber}(x)$ and $\mathrm{Bei}(x)$ are the Thomson functions of the first kind of order zero, and $\mathrm{Ker}(x)$ and $\mathrm{Kei}(x)$ are the Thomson functions of the second kind of order zero. The parameter R originates from the unequal hydrostatic stress, σ_{kk}, in the fiber and the matrix. The temperature field is substituted into Eq. (5) to obtain the rate of entropy production, $\dot{s}_p$. Using the Gouy-Stodola theorem (Eq. (6)) and Eq. (7), the dissipation of mechanical energy during one cycle can be calculated for each region. The elasticity solution corresponding to the given loading condition is used to calculate the elastic energy density throughout the domain. The local SDC is then obtained from Eq. (10):

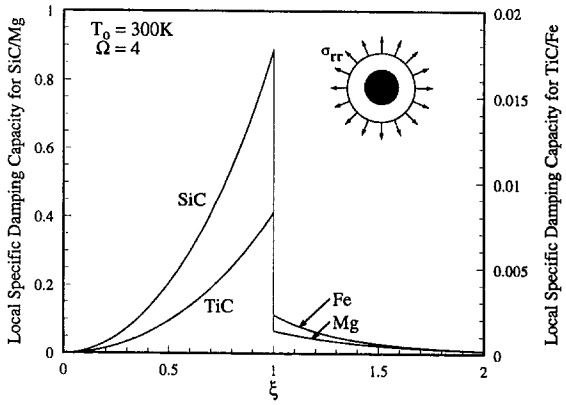

Fig. 1 A fiber in an infinite matrix subjected to a uniform radial stress: the local specific damping capacity across the interface as a function of normalized radial position

$$\psi_1 = 4\pi E_1 \rho_1 c_1 \frac{(1+\nu_1)}{(1-2\nu_1)}(Z_1 - Z_2R)^2 T_o |A^*|^2 \cdot\left[\mathrm{Ber}'^2(\Omega^{1/2}\xi) + \mathrm{Bei}'^2(\Omega^{1/2}\xi)\right] \quad 0 \le \xi < 1 \tag{19}$$

$$\psi_2 = 4\pi E_2 \rho_2 c_2 F\left(Z_1\frac{1}{R} - Z_2\right)^2 T_o |B^*|^2 \cdot\left[\mathrm{Ker}'^2\left(\frac{k_1K_2}{k_2K_1}\Omega^{1/2}\xi\right) + \mathrm{Kei}'^2\left(\frac{k_1K_2}{k_2K_2}\Omega^{1/2}\xi\right)\right] \quad \xi > 1 \tag{20}$$

where

$$F = \frac{(1+\nu_2)}{(1-2\nu_2) + \dfrac{1}{\xi^4}\left[\dfrac{(1+\nu_1)(1-2\nu_1) - E_r(1+\nu_2)(1-2\nu_2)}{(1+\nu_1)(1-2\nu_1) + E_r(1+\nu_2)}\right]^2}. \tag{21}$$

Since the matrix is unbounded, it is not possible to define the volume-averaged damping over the entire domain; therefore, we average Ψ over the volume of the fiber to obtain

$$\Psi_1 = 8\pi E_1 \rho_1 c_1 \frac{(1+\nu_1)}{(1-2\nu_1)}(Z_1 - Z_2R)^2 T_o |A^*|^2 \cdot\frac{1}{\Omega^{1/2}}\left[\mathrm{Ber}(\Omega^{1/2})\mathrm{Ber}'(\Omega^{1/2}) + \mathrm{Bei}(\Omega^{1/2})\mathrm{Bei}'(\Omega^{1/2})\right]. \tag{22}$$

In Fig. 1 we have plotted the local SDC, ψ, as a function of ξ for two material combinations, namely, SiC/Mg and TiC/Fe (note the difference in scales for the two plots). $\Omega = 4$ was chosen because at this frequency ψ is close to its maximum value; see Fig. 2. As expected from previous work on interface damping (Kinra and Milligan, 1994), ψ is maximum at the interface and decreases exponentially away from

Downloaded 04 May 2010 to 171.66.16.28. Redistribution subject to ASME license or copyright; see http://www.asme.org/terms/Terms_Use.cfm

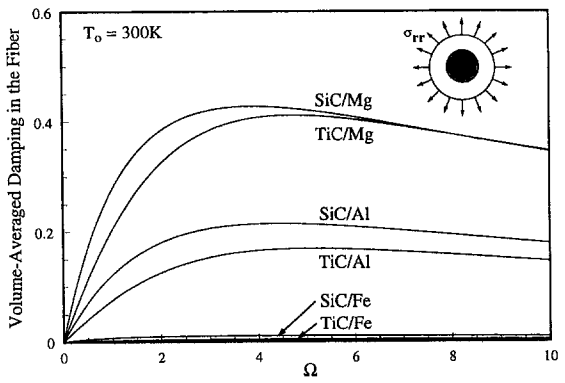

Fig. 2 A fiber in an infinite matrix subjected to a uniform radial stress: the volume-averaged specific damping capacity in the fiber as a function of normalized frequency

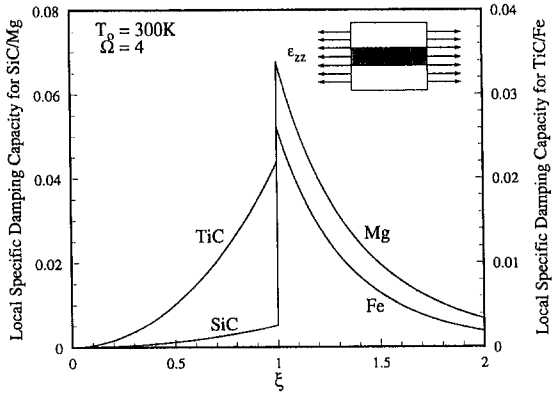

Fig. 3 A fiber in an infinite matrix subjected to a uniform uniaxial strain: the local specific damping capacity across the interface as a function of normalized radial position

the interface. This localization of damping is due to the relatively large temperature gradients near the interface. In Fig. 2 we have plotted Ψ_1, the damping averaged over the volume of the fiber, as a function of normalized frequency, Ω, for two ceramic fiber materials (SiC and TiC) and three metal matrix materials (Al, Fe, and Mg). The elastothermodynamic properties of these materials are given in Table 1. As expected, as $\Omega \to 0$, heat has sufficient time to conduct from regions of elevated temperature to regions of lowered temperature; consequently, essentially isothermal conditions are obtained, and the damping approaches zero. On the other extreme, as $\Omega \to \infty$, heat has no time to conduct; therefore, essentially adiabatic conditions are obtained, and, once again, the damping approaches zero. In between, the damping curve is characterized by a single peak which is reminiscent of a Debye peak (Nowick and Berry, 1972).

Uniform Uniaxial Strain. We now consider the case of a fiber of radius a embedded in an infinite matrix of a different material subjected to a uniform uniaxial strain parallel to the fiber axis: $\epsilon_{zz_1} = \epsilon_{zz_2} = \epsilon_o e^{i\omega t}$. In a manner similar to the previous loading case, we obtain the local SDC.

$$\psi_1 = 4\pi E_1 \rho_1 c_1 \frac{(1+\nu_1)}{(1-2\nu_1)\left[1+4\nu_1 R+2(1-2\nu_1)R^2\right]} \cdot\left[Z_1(1+R)-Z_2\frac{(1-2\nu_1)}{E_r}R\right]^2 T_o|A^*|^2 \cdot\left[\mathrm{Ber}'^2\left(\Omega^{1/2}\xi\right)+\mathrm{Bei}'^2\left(\Omega^{1/2}\xi\right)\right] \quad 0 \le \xi < 1 \quad (23)$$

$$\psi_2 = 8\pi E_2 \rho_2 c_2 D \cdot\left[Z_1(1+R)-Z_2\frac{(1-2\nu_1)}{E_r}R\right]^2 T_o|B^*|^2 \cdot\left[\mathrm{Ker}'^2\left(\frac{k_1K_2}{k_2K_1}\Omega^{1/2}\xi\right)+\mathrm{Kei}'^2\left(\frac{k_1K_2}{k_2K_1}\Omega^{1/2}\xi\right)\right] \quad \xi > 1 \quad (24)$$

where

$$R = \frac{E_r(1+\nu_2)+(1+\nu_1)(1-2\nu_1)}{2\left[\nu_1 E_r(1+\nu_2)-\nu_2(1+\nu_1)(1-2\nu_1)\right]} \quad (25)$$

and

$$D = \frac{E_r^2\left[\nu_1 E_r(1+\nu_2)-\nu_2(1+\nu_1)(1-2\nu_1)\right]^2}{D_1} \quad (26)$$

with

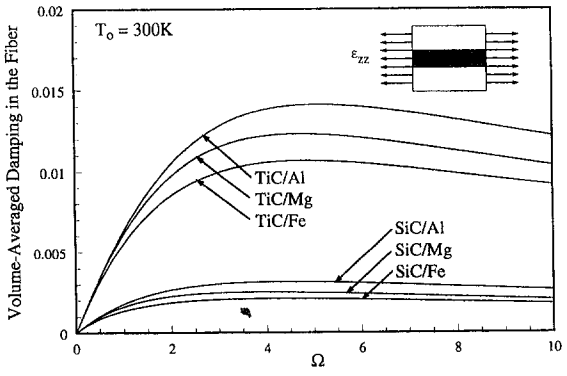

Fig. 4 A fiber in an infinite matrix subjected to a uniform uniaxial strain: the volume-average specific damping capacity in the fiber as a function of normalized frequency

$$D_1 = (1-2\nu_1)^2\left[E_r(1+\nu_2)+(1+\nu_1)(1-2\nu_1)\right]^2 \cdot\left\{1+\frac{2(1+\nu_2)}{\xi^4}\left[\frac{E_r(\nu_1-\nu_2)}{E_r(1+\nu_2)+(1+\nu_1)(1-2\nu_1)}\right]^2\right\}. \quad (27)$$

The SDC average over the volume of the fiber, Ψ_1, is given by

$$\Psi_1 = 8\pi E_1 \rho_1 c_1 \frac{(1+\nu_1)}{(1-2\nu_1)\left[1+4\nu_1 R+2(1-2\nu_1)R^2\right]} \cdot\left[Z_1(1+R)-Z_2\frac{(1-2\nu_1)}{E_r}R\right]^2 T_o|A^*|^2 \cdot\frac{1}{\Omega^{1/2}}\left[\mathrm{Ber}(\Omega^{1/2})\mathrm{Ber}'(\Omega^{1/2})+\mathrm{Bei}(\Omega^{1/2})\mathrm{Bei}'(\Omega^{1/2})\right]. \quad (28)$$

ψ and Ψ_1 are plotted in Figs. 3 and 4 respectively, for the same material combinations as in the previous loading case. It is notable that, in general, the damping in the fiber due to axial strain is orders of magnitude lower than the damping due to radial stress. This phenomenon is attributable to the high modulus of the fiber material which results in a high elastic energy density, W, in the fiber in the former case.

A Fiber in a Finite Matrix

As we endeavor to develop a theory applicable to real fiber-reinforced composites, it becomes necessary to take into consideration the effects of volume fraction, V_f, on the ETD; for this reason we now consider a fiber in a finite

Downloaded 04 May 2010 to 171.66.16.28. Redistribution subject to ASME license or copyright; see http://www.asme.org/terms/Terms_Use.cfm

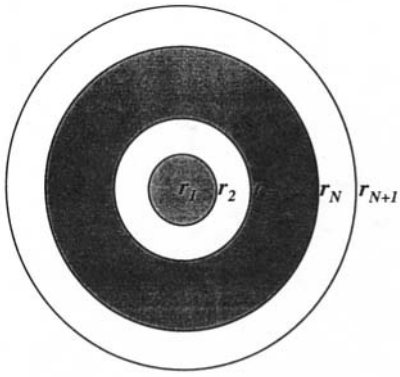

Fig. 5 A finite *N*-layered cylinder with the *z*-axis perpendicular to the plane of the figure

matrix. Using the general methodology given by Bishop and Kinra (1993) for calculating the ETD in an N-layered medium possessing rectangular, cylindrical, or spherical symmetry, we now calculate the damping of a fiber in a bounded matrix. We begin by outlining the equations for a finite N-layered cylinder (see Fig. 5).

The inhomogeneous term in the one-way coupled heat-conduction equation (Eq. (4)) is cast as a heat generation term

$$\frac{1}{r}\frac{\partial}{\partial r}\left(r\frac{\partial T_i}{\partial r}\right) = \frac{\rho_i c_i}{k_i}\frac{\partial T_i}{\partial t} - \frac{1}{k_i}g_i(r,t) \quad \begin{matrix} t>0 \\ r_i < r < r_{i+1} \\ i = 1,2,\ldots,N \end{matrix} \tag{29}$$

where

$$g_i(r,t) = -\alpha_i T_o \frac{\partial \sigma_{kk}}{\partial t}. \tag{30}$$

In the foregoing equations the index i refers to the layer of interest. The initial condition is $T_i(r,t) = T_o$ at $t = 0$ in $r_1 < r < r_{N+1}$. For the case of a simply connected domain, $r_1 = 0$; however, this methodology is equally applicable to a multiply connected domain such as a hollow fiber in a finite matrix in which case $r_1 \neq 0$. The boundary and interface conditions are

$$\frac{\partial T_1}{\partial r} = 0 \qquad r = r_1 \tag{31}$$

$$T_i = T_{i+1} \qquad \begin{matrix} r = r_{i+1} \\ i = 1,2,\ldots,N-1 \end{matrix} \tag{32}$$

$$k_i\frac{\partial T_i}{\partial r} = k_{i+1}\frac{\partial T_{i+1}}{\partial r} \qquad \begin{matrix} r = r_{i+1} \\ i = 1,2,\ldots,N-1 \end{matrix} \tag{33}$$

$$\frac{\partial T_N}{\partial r} = 0 \qquad r = r_{N+1}. \tag{34}$$

Following Özişik (1980), the solution in terms of the Green's function is given by

$$T_i(r,t) - T_o = \sum_{j=1}^{N}\int_{\tau=0}^{t}\int_{r_j}^{r_{j+1}} \xi G_{ij}(r,t|\xi,\tau)\frac{1}{\rho_j c_j}g_j(\xi,\tau)d\xi\, d\tau \tag{35}$$

in $r_i < r < r_{i+1}$, $i = 1,2,\ldots,N$, where the Green's function for the composite medium is

$$G_{ij}(r,t|\xi,\tau) = \sum_{n=0}^{\infty} e^{-\beta_n^2(t-\tau)}\frac{1}{N_n}(\rho_j c_j)\phi_{in}(r)\phi_{jn}(\xi). \tag{36}$$

The norm N_n is given by

$$N_n = \sum_{j=1}^{N}(\rho_j c_j)\int_{r_j}^{r_{j+1}}\xi\phi_{jn}^2(\xi)d\xi \tag{37}$$

where $\phi_{in}(r)$ and β_n are, respectively, the eigenfunctions and eigenvalues of the following eigenvalue problem:

$$\frac{1}{r}\frac{d}{dr}\left(r\frac{d\phi_{in}}{dr}\right) + \frac{\rho_i c_i}{k_i}\beta_n^2\phi_{in} = 0 \quad \begin{matrix} r_i < r < r_{i+1} \\ i = 1,2,\ldots,N \end{matrix} \tag{38}$$

where $\phi_{in} \equiv \phi_{in}(\beta_n, r)$. The subscript n implies that there is a denumerably infinite number of discrete eigenvalues, $\beta_1 < \beta_2 < \ldots < \beta_n < \ldots$ and the corresponding eigenfunctions, $\phi_{in}(\beta_n, r)$. The boundary conditions for Eq. (38) are the same as in Eqs. (31) through (34) but with T_i replaced by ϕ_{in}. The eigenfunctions satisfy the following orthogonality relation:

$$\sum_{j=1}^{N}(\rho_j c_j)\int_{r_j}^{r_{j+1}}\xi\phi_{jm}(\xi)\phi_{jn}(\xi)d\xi = \begin{cases} 0 & m \neq n \\ N_n & m = n \end{cases} \tag{39}$$

where the norm N_n was defined in Eq. (37), and ϕ_{jm}, ϕ_{jn} represent two different eigenfunctions.

We now restrict σ_{kk} to be time-harmonic and write $\sigma_{kk}(r,t) = \sigma_{kk}(r)e^{i\omega t}$, Eq. (30) becomes

$$g_i^*(r,t) = -\alpha_i T_o \sigma_{kk}(r) i\omega e^{i\omega t}. \tag{40}$$

Substituting Eqs. (36) and (40) into Eq. (35) gives the temperature distribution in the ith layer, $T_i^*(r,t)$,

$$T_i^*(r,t) - T_o^* = -T_o\sum_{n=0}^{\infty}\frac{i\omega}{\beta_n^2 + i\omega}\frac{L_n}{N_n}\phi_{in}(r)\left[e^{i\omega t} - e^{-\beta_n^2 t}\right] \tag{41}$$

where

$$L_n = \sum_{j=1}^{N}\alpha_j\int_{r_j}^{r_{j+1}}\xi\sigma_{kk}(\xi)\phi_{jn}(\xi)d\xi. \tag{42}$$

The effects of the initial condition, $T_i(r, t = 0) = T_o$, die out when t becomes large leaving only the desired time-harmonic variations in the temperature. Through a comparison of Eqs. (12) and (41), it is clear that the fluctuating part of the temperature, V^*, is given by

$$V_i^*(r) = -T_o\sum_{n=0}^{\infty}\frac{i\omega}{\beta_n^2 + i\omega}\frac{L_n}{N_n}\phi_{in}(r). \tag{43}$$

Substituting Eq. (43) into Eq. (5) allows the calculation of the energy dissipated per cycle per unit volume in the ith layer, ΔW_i,

$$\Delta W_i = \pi T_o k_i \sum_{m=0}^{\infty}\sum_{n=0}^{\infty} \times\left[\frac{\omega(\omega^2 + \beta_m^2\beta_n^2)}{(\omega^2 + \beta_m^4)(\omega^2 + \beta_n^4)}\frac{L_m}{N_m}\frac{L_n}{N_n}\frac{d\phi_{im}}{dr}\frac{d\phi_{in}}{dr}\right]. \tag{44}$$

The elastic energy density in the ith layer, W_i, can be expressed as

Downloaded 04 May 2010 to 171.66.16.28. Redistribution subject to ASME license or copyright; see http://www.asme.org/terms/Terms_Use.cfm

$$W_i = \frac{1}{2E_i}\left[(1+\nu_i)\sigma_{jl}(r)\sigma_{jl}(r) - \nu_i\sigma_{kk}^2(r)\right] \quad (45)$$

where j, k, and l are the tensorial indices. Substituting Eqs. (44) and (45) into Eq. (10) gives the local SDC in the ith layer, $\psi_i(r)$,

$$\psi_i(r) = \pi T_o k_i \times \frac{\sum_{m=0}^{\infty}\sum_{n=0}^{\infty} \frac{\omega(\omega^2+\beta_m^2\beta_n^2)}{(\omega^2+\beta_m^4)(\omega^2+\beta_n^4)} \frac{L_m}{N_m}\frac{L_n}{N_n}\frac{d\phi_{im}}{dx}\frac{d\phi_{in}}{dx}}{\frac{1}{2E_i}\left[(1+\nu_i)\sigma_{jl}(r)\sigma_{jl}(r) - \nu_i\sigma_{kk}^2(r)\right]}. \quad (46)$$

We now introduce Ψ averaged over the entire volume of the N-layered cylinder. From Eqs. (11), (45), and (46) we obtain

$$\Psi = \pi T_o \frac{\sum_{m=0}^{\infty}\sum_{n=0}^{\infty} \frac{\omega(\omega^2+\beta_m^2\beta_n^2)}{(\omega^2+\beta_m^4)(\omega^2+\beta_n^4)} \frac{L_m}{N_m}\frac{L_n}{N_n}\sum_{i=1}^{N} k_i \int_{r_i}^{r_{i+1}} \xi \frac{d\phi_{im}}{d\xi}\frac{d\phi_{in}}{d\xi}d\xi}{\sum_{i=1}^{N}\int_{r_i}^{r_{i+1}} \frac{1}{2E_i}\xi\left[(1+\nu_i)\sigma_{jl}(\xi)\sigma_{jl}(\xi) - \nu_i\sigma_{kk}^2(\xi)\right]d\xi}. \quad (47)$$

In the following, we consider the case of a fiber in a finite matrix (i.e., $N = 2$) subjected to (1) a uniform radial stress and (2) a uniform uniaxial strain.

Uniform Radial Stress. Consider a fiber of radius a embedded in a finite matrix of radius b subjected to a uniform radial stress $\sigma_{rr} = \sigma_o e^{i\omega t}$, again we consider only the plane strain condition.

The boundary conditions for the thermal problem are an adiabatic boundary at the axis of symmetry ($r = 0$), continuity of temperature and heat flux at the interface ($r = a$), and an adiabatic boundary at the outer surface ($r = b$). The eigenfunctions for the fiber $()_1$ and the matrix $()_2$ are, respectively,

$$\phi_{1n}(\xi) = J_0(\gamma_n\xi) \qquad 0 \le \xi < 1 \quad (48)$$

$$\phi_{2n}(\xi) = A_n J_0(\eta_n\zeta\xi) + B_n Y_0(\eta_n\zeta\xi) \qquad 1 < \xi \le \frac{b}{a} \quad (49)$$

where J_z and Y_z are, respectively, the Bessel functions of the first and second kind of order z, and A_n and B_n are found from the boundary conditions

$$A_n = \frac{J_0(\gamma_n)Y_1(\eta_n)}{J_0(\eta_n\zeta)Y_1(\eta_n) - J_1(\eta_n)Y_0(\eta_n\zeta)} \quad (50)$$

$$B_n = -\frac{J_0(\gamma_n)J_1(\eta_n)}{J_0(\eta_n\zeta)Y_1(\eta_n) - J_1(\eta_n)Y_0(\eta_n\zeta)} \quad (51)$$

with $\xi = r/a$, $\zeta = a/b$, $\gamma_n = \beta_n(\rho_1 c_1/k_1)^{1/2}a$, $\eta_n = \beta_n(\rho_2 c_2/k_2)^{1/2}b$, and β_n as the eigenvalues of the problem. The eigenvalues are the solutions of the following transcendental equations:

$$\begin{vmatrix} J_0(\gamma_n) & -J_0(\nu_n\zeta) & -Y_0(\eta_n\zeta) \\ \gamma_n\frac{K_1}{K_2}J_1(\gamma_n) & -\gamma_n J_1(\eta_n\zeta) & -\gamma_n Y_1(\eta_n\zeta) \\ 0 & \gamma_n J_1(\eta_n) & \gamma_n Y_1(\eta_n) \end{vmatrix} = 0. \quad (52)$$

Since the determinant is odd in β_n, the solution for the thermal problem can be obtained by considering only the positive values of β_n.

From Eq. (43) the fluctuating temperature is given by

$$V^* = \begin{cases} -T_o\sum_{n=0}^{\infty}\frac{i\omega}{\beta_n^2+i\omega}\frac{L_n}{N_n}\phi_1(\xi) & 0 \le \xi < 1 \\ -T_o\sum_{n=0}^{\infty}\frac{i\omega}{\beta_n^2+i\omega}\frac{L_n}{N_n}\phi_2(\xi) & 1 < \xi \le \frac{b}{a} \end{cases} \quad (53)$$

where L_n and N_n are given by Eqs. (42) and (37), respectively. To ensure the validity of our algebra, Eq. (53) was checked as follows: when b/a was allowed to become very large ($b/a = 10^3$ or $\zeta = 10^{-3}$), the numerical results given by Eq. (53) were found to coincide with those given by Eq. (14).

From Eq. (47) the damping averaged over the volume of the fiber and the matrix is given by

$$\Psi = \frac{\Upsilon_1 + \Upsilon_2}{\Upsilon_3 + \Upsilon_4} \quad (54)$$

where

$$\Upsilon_1 = \psi_{o1}\sum_{m=0}^{\infty}\sum_{n=0}^{\infty}\begin{cases} \frac{\Omega\gamma_m\gamma_n(\Omega^2+\gamma_m^2\gamma_n^2)}{(\Omega^2+\gamma_m^4)(\Omega^2+\gamma_n^4)}\frac{Q_m}{R_m}\frac{Q_n}{R_n}\frac{\zeta^2}{\gamma_n^2-\gamma_m^2}\Gamma_{1_{m,n}} & m \ne n \\ \frac{1}{2}\frac{\Omega\gamma_n^2}{\Omega^2+\gamma_n^4}\frac{Q_n^2}{R_n^2}\zeta^2\Gamma_{2_n} & m = n \end{cases} \quad (55)$$

$$\Upsilon_2 = \psi_{o1}\frac{\rho_2 c_2}{\rho_1 c_1}\sum_{m=0}^{\infty}\sum_{n=0}^{\infty}\begin{cases} \frac{\Omega\gamma_m\gamma_n(\Omega^2+\gamma_m^2\gamma_n^2)}{(\Omega^2+\gamma_m^4)(\Omega^2+\gamma_n^4)}\frac{Q_m}{R_m}\frac{Q_n}{R_n}\frac{1}{\eta_n^2-\eta_m^2}\Gamma_{3_{m,n}} & m \ne n \\ \frac{1}{2}\frac{\Omega\gamma_n^2}{\Omega^2+\gamma_n^4}\frac{Q_n^2}{R_n^2}\Gamma_{4_n} & m = n \end{cases} \quad (56)$$

$$\Upsilon_3 = \zeta^2(1+\nu_1)(1-2\nu_1)P_1^2 \quad (57)$$

$$\Upsilon_4 = (1-\zeta^2)E_r(1+\nu_2)(1-2\nu_2)P_2^2 - \zeta^2(\zeta^2-1)E_r(1+\nu_2)P_3^2 \quad (58)$$

with

Downloaded 04 May 2010 to 171.66.16.28. Redistribution subject to ASME license or copyright; see http://www.asme.org/terms/Terms_Use.cfm

$$\Gamma_{1_{m,n}} = \gamma_m J_0(\gamma_m)J_1(\gamma_n) - \gamma_n J_0(\gamma_n)J_1(\gamma_m) \quad (59)$$

$$\Gamma_{2n} = J_1^2(\gamma_n) - J_0(\gamma_n)J_2(\gamma_n) \quad (60)$$

$$\begin{aligned}\Gamma_{3_{m,n}} = {} & A_m A_n\left[\{\eta_m J_0(\eta_m)J_1(\eta_n) - \eta_n J_0(\eta_n)J_1(\eta_m)\}\right. \\ & \left. -\zeta\{\eta_m J_0(\eta_m\zeta)J_1(\eta_n\zeta) - \eta_n J_0(\eta_n\zeta)J_1(\eta_m\zeta)\}\right] \\ & +A_n B_m\left[\{\eta_m Y_0(\eta_m)J_1(\eta_n) - \eta_n J_0(\eta_n)Y_1(\eta_m)\}\right. \\ & \left. -\zeta\{\eta_m Y_0(\eta_m\zeta)J_1(\eta_n\zeta) - \eta_n J_0(\eta_n\zeta)Y_1(\eta_m\zeta)\}\right] \\ & +A_m B_n\left[\{\eta_m J_0(\eta_m)Y_1(\eta_n) - \eta_n Y_0(\eta_n)J_1(\eta_m)\}\right. \\ & \left. -\zeta\{\eta_m J_0(\eta_m\zeta)Y_1(\eta_n\zeta) - \eta_n Y_0(\eta_n\zeta)J_1(\eta_m\zeta)\}\right] \\ & +B_m B_n\left[\{\eta_m Y_0(\eta_m)Y_1(\eta_m) - \eta_n Y_0(\eta_n)Y_1(\eta_m)\}\right. \\ & \left. -\zeta\{\eta_m Y_0(\eta_m\zeta)Y_1(\eta_n\zeta) - \eta_n Y_0(\eta_n\zeta)Y_1(\eta_m\zeta)\}\right] \quad (61)\end{aligned}$$

$$\begin{aligned}\Gamma_{4_n} = {} & A_n^2\left[\{J_1^2(\eta_n) - J_0(\eta_n)J_2(\eta_n)\}\right. \\ & \left. -\zeta^2\{J_1^2(\eta_n\zeta) - J_0(\eta_n\zeta)J_2(\eta_n\zeta)\}\right] \\ & +A_n B_n\left[\{2J_1(\eta_n)Y_1(\eta_n) - J_0(\eta_n)Y_2(\eta_n) - J_2(\eta_n)Y_0(\eta_n)\}\right. \\ & \left. -\zeta^2\{2J_1(\eta_n\zeta)Y_1(\eta_n\zeta) - J_0(\eta_n\zeta)Y_2(\eta_n\zeta)\right. \\ & \left. -J_2(\eta_n\zeta)Y_0(\eta_n\zeta)\}\right] + B_n^2\left[\{Y_1^2(\eta_n) - Y_0(\eta_n)Y_2(\eta_n)\}\right. \\ & \left. -\zeta^2\{Y_1^2(\eta_n\zeta) - Y_0(\eta_n\zeta)Y_2(\eta_n\zeta)\}\right] \quad (62)\end{aligned}$$

$$\begin{aligned}Q_n = {} & 2(1+\nu_1)P_1\zeta^2\frac{1}{\gamma_n}J_1(\gamma_n) + 2\frac{\alpha_2}{\alpha_1}(1+\nu_2)P_2\frac{1}{\eta_n} \\ & \times\left[A_n\{J_1(\eta_n) - \zeta J_1(\eta_n\zeta)\} + B_n\{Y_1(\eta_n) - \zeta Y_1(\eta_n\zeta)\}\right] \quad (63)\end{aligned}$$

$$\begin{aligned}R_n = {} & \frac{1}{2}\left\{\zeta^2\left[J_0^2(\gamma_n) + J_1^2(\gamma_n)\right] + \frac{\rho_2 c_2}{\rho_1 c_1}\right. \\ & \times\left[A_n^2\left\{\left[J_0^2(\eta_n) + J_1^2(\eta_n)\right] - \zeta^2\left[J_0^2(\eta_n\zeta) + J_1^2(\eta_n\zeta)\right]\right\}\right. \\ & +2A_n B_n\left\{\left[J_0(\eta_n)Y_0(\eta_n) + J_1(\eta_n)Y_1(\eta_n)\right]\right. \\ & \left.\left. -\zeta^2\left[J_0(\eta_n\zeta)Y_0(\eta_n\zeta) + J_1(\eta_n\zeta)Y_1(\eta_n\zeta)\right]\right\} \\ & \left.\left. +B_n^2\left\{\left[Y_0^2(\eta_n) + Y_1^2(\eta_n)\right] - \zeta^2\left[Y_0^2(\eta_n\zeta) + Y_1^2(\eta_n\zeta)\right]\right\}\right]\right\} \quad (64)\end{aligned}$$

and

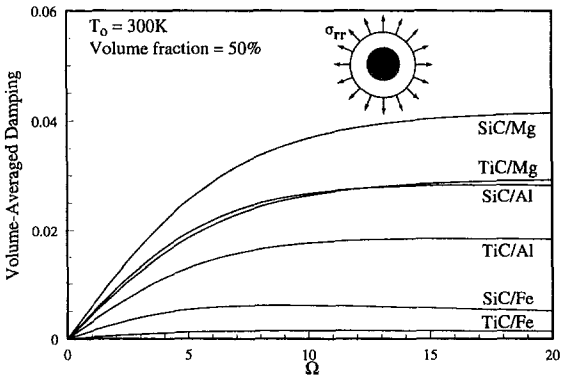

Fig. 6 A fiber in a finite matrix subjected to a uniform radial stress: the volume-averaged specific damping capacity in the fiber as a function of normalized frequency

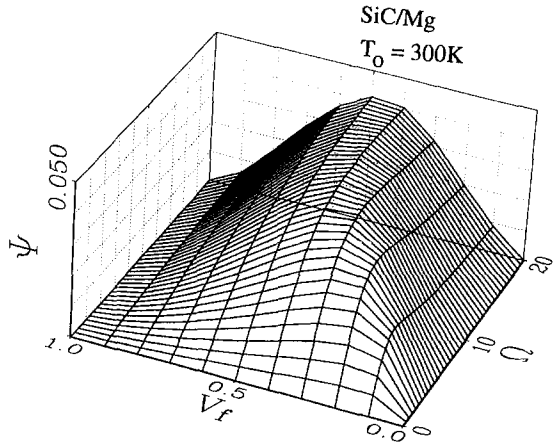

Fig. 7 The effect of volume fraction and normalized frequency on the volume-averaged specific damping capacity for a SIC fiber in an Mg matrix due to a uniform radial stress

where $\psi_{o1} = 2\pi E_1\alpha_1^2 T_o/\rho_1 c_1$ is the modulus of elastothermodynamic damping of the fiber, $E_r = E_1/E_2$, and Ω is normalized with respect to the fiber properties, $\Omega = \omega\rho_1 c_1 a^2/k_1$.

In Fig. 6 we have plotted Ψ for two fiber materials and three matrix materials with a volume fraction $V_f = 50\%$ ($V_f = \zeta^2$, $\zeta \approx 0.707$). The shape of the damping curve is consistent with the expected results, i.e., isothermal conditions as $\Omega \to 0$ resulting in zero damping and adiabatic conditions as $\Omega \to \infty$ also resulting in zero damping. In Fig. 7 we study the effect of volume fraction ($V_f = \zeta^2$) on ETD for a SiC/Mg metal-matrix composite. As expected, as $V_f \to 0$ (all matrix) and as $V_f \to 1$ (all fiber), $\Psi \to 0$. In between these two extremes, Ψ is characterized by a single peak near $V_f = 0.5$.

Uniform Uniaxial Strain. We now consider the case of a fiber of radius a embedded in a finite matrix of radius b

$$P_1 = \frac{2E_r(1-\nu_2)(1+\nu_2)}{(1+\nu_1)(1-2\nu_1)(1-\zeta^2) + E_r(1+\nu_2)\left[1+(1-2\nu_2)\zeta^2\right]} \quad (65)$$

$$P_2 = \frac{E_r(1+\nu_2) + (1+\nu_1)(1-2\nu_1)}{(1+\nu_1)(1-2\nu_1)(1-\zeta^2) + E_r(1+\nu_2)\left[1+(1-2\nu_2)\zeta^2\right]} \quad (66)$$

$$P_3 = \frac{E_r(1+\nu_2)(1-2\nu_2) - (1+\nu_1)(1-2\nu_1)}{(1+\nu_1)(1-2\nu_1)(1-\zeta^2) + E_r(1+\nu_2)\left[1+(1-2\nu_2)\zeta^2\right]} \quad (67)$$

Downloaded 04 May 2010 to 171.66.16.28. Redistribution subject to ASME license or copyright; see http://www.asme.org/terms/Terms_Use.cfm

subjected to a uniform uniaxial strain parallel to the fiber axis $\epsilon_{zz_1} = \epsilon_{zz_2} = \epsilon_o e^{i\omega t}$. The only difference between this problem and the preceding problem is in the elasticity solution (i.e., σ_{kk}). For the present case of axial strain, only the quantities Υ_3, Υ_4, and Q_n take on new values, the remaining quantities are the same:

$$\Upsilon_3 = \zeta^2\left[(1+\nu_1)(1-2\nu_1)P_1^2 + 2\nu_1 P_1 + \frac{(1-\nu_1)}{2(1+\nu_1)(1-2\nu_1)}\right] \quad (68)$$

$$\Upsilon_4 = (1-\zeta^2)\left[\frac{(1+\nu_2)(1-2\nu_2)}{E_r}P_2^2 + 2\frac{\nu_2}{E_r}P_2 + \frac{(1-\nu_2)}{2E_r(1+\nu_2)(1-2\nu_2)}\right] + \zeta^2(1-\zeta^2)E_r(1+\nu_2)P_3^2 \quad (69)$$

$$Q_n = \left[2(1+\nu_1)P_1 + \frac{1}{(1-2\nu_1)}\right]\zeta^2\frac{1}{\gamma_n}J_1(\gamma_n) + \frac{\alpha_2}{\alpha_1}\frac{1}{E_r}\left[2(1+\nu_2)P_2 + \frac{1}{(1-2\nu_2)}\right] \cdot \frac{1}{\eta_n}\left[A_n\{J_1(\eta_n) - \zeta J_1(\eta_n\zeta)\} + B_n\{Y_1(\eta_n) - \zeta Y_1(\eta_n\zeta)\}\right] \quad (70)$$

where

$$P_1 = -\frac{(1+\nu_1)(1-2\nu_1)(1-\zeta^2) + \nu_1 E_r(1+\nu_2)\left[1+(1-2\nu_2)\zeta^2\right]}{P_{d1}} \quad (71)$$

$$P_2 = -\frac{\nu_2(1+\nu_1)(1-2\nu_1)(1-\zeta^2) + E_r(1+\nu_2)\left[\nu_2 + \nu_1(1-2\nu_2)\zeta^2\right]}{P_{d1}} \quad (72)$$

$$P_3 = \frac{-(\nu_1-\nu_2)}{P_{d2}} \quad (73)$$

where

$$P_{d1} = (1+\nu_1)(1-2\nu_1)\{(1+\nu_1)(1-2\nu_1)(1-\zeta^2) + E_r(1+\nu_2)\left[1+(1-2\nu_2)\zeta^2\right]\} \quad (74)$$

$$P_{d2} = (1+\nu_1)(1-2\nu_1)(1-\zeta^2) + E_r(1+\nu_2)\left[1+(1-2\nu_2)\zeta^2\right]. \quad (75)$$

The SDC for this case is plotted in Fig. 8. The shapes of the damping curve are consistent with expected results; however, the damping itself is negligibly small. Due to the very high stiffness of the fibers, this loading condition results in a very large stored energy in the fibers, which increases the denominator in Eq. (10), hence low Ψ.

The numerical results obtained in this paper are qualitatively consistent with previously published experimental results. For example, Wren and Kinra (1992) measured damping in a $[\pm\theta]_s$ P55 graphite/6061 aluminum MMC for $\theta = 0$ deg, 15 deg, 30 deg, 45 deg, 60 deg, 75 deg, and 90 deg

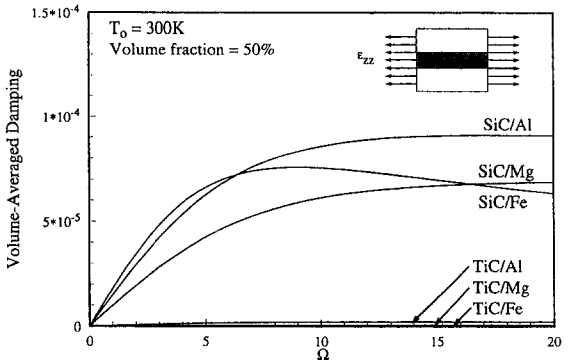

Fig. 8 A fiber in a finite matrix subjected to a uniform uniaxial strain: the volume-averaged specific damping capacity in the fiber as a function of normalized frequency

subjected to a uniaxial stress loading. For loading parallel to the fiber axis ($\theta = 0$ deg), the damping was found to be vanishingly small, $\Psi = O(10^{-3})$; for loading perpendicular to the fiber axis ($\theta = 90$ deg), the damping was found to be *relatively* large, $\Psi \approx 2 \cdot 10^{-2}$. Qualitatively similar results were obtained when these specimens were subjected to flexural vibrations; see Kinra et al. (1991).

Measurements of damping in continuous-fiber-reinforced metal-matrix composites have been reported by several researchers (Timmerman, 1982; Misra and LaGreca, 1984; Timmerman and Doherty, 1984; Steckel, 1985; Steckel and Nelson, 1985; Kinra et al., 1991; Kinra and Wren, 1992; Wren and Kinra, 1992). These MMCs were made up of various different matrix materials (aluminum, magnesium, titanium) and graphite fibers (Pitch-55 or Pitch-100). When the loading was perpendicular to the fiber direction, the total damping was of the order of a few percent. We have shown that by a proper choice of constituent materials, fiber size and frequency, one can *design* MMCs such that the contribution of the elastothermodynamic damping is a significant fraction of the total damping. Consider, for example, a 150-μm diameter SiC fiber in a magnesium matrix (Fig. 6). For $\Omega \approx 20$, Ψ is about four percent. Now $\Omega = 20$ translates to a frequency of 10 KHz which happens to be a frequency of interest to the U.S. Navy (quiet submarines) as well as in designing quiet rotating machines.

Conclusion

In an earlier work (Kinra and Milligan, 1994), we presented a theory which takes the second law of thermodynamics as its starting point and which could be used to calculate the elastothermodynamic damping (ETD) in heterogeneous media. In this paper we have used this theory to solve two canonical problems concerning the ETD in continuous-fiber-reinforced metal-matrix composites. First, an isolated fiber in an infinite matrix was considered. Second, we have

Downloaded 04 May 2010 to 171.66.16.28. Redistribution subject to ASME license or copyright; see http://www.asme.org/terms/Terms_Use.cfm

presented a general methodology for calculating the ETD for an N-layered, bounded, concentric cylinder. Numerical results are presented for $N = 2$, i.e., a fiber in a bounded matrix. In both cases solutions were obtained for the following loading conditions: (1) a uniform radial stress and (2) a uniform uniaxial strain parallel to the fiber.

The largest contribution to the damping comes from the interface region. The frequency dependence of damping is characterized by a single peak (reminiscent of the Debye peak). Consistent with the previously published experimental results, the damping for the case of fiber-normal loading is an order of magnitude higher than that for fiber-parallel loading. Finally, through a proper choice of constituent materials, fiber size and frequency, our analysis can be used to design metal-matrix composites in which the elastothermodynamic damping is a significant fraction of the total damping.

Acknowledgments

This research is supported by the Office of Naval Research through Grant Number N00014-90-J-1130 to Texas A & M University, College Station, TX. The continued and keen interest taken by the program manager, Dr. L. Kabacoff, in the evolution of this work is gratefully acknowledged.

References

Alblas, J. B., 1961, "On the General Theory of Thermo-Elastic Friction," *Apl. Sci. Res.*, Section A, Vol. 10, pp. 349–362.

Alblas, J. B., 1981, "A Note on the Theory of Thermoelastic Damping," *Journal of Thermal Sciences*, Vol. 4, pp. 333–355.

Bejan, A., 1982, *Entropy Generation Through Heat and Fluid Flow*, John Wiley and Sons, New York, p. 21.

Bejan, A., 1988, *Advanced Engineering Thermodynamics*, John Wiley and Sons, New York.

Biot, M., 1956, "Thermoelasticity and Irreversible Thermodynamics," *Journal of Applied Physics*, Vol. 27, No. 3, pp. 240–253.

Bishop, J. E., and Kinra, V. K., 1993, "Elastothermodynamic Damping in Metal-Matrix Composites: One-Dimensional Heat Conduction," *Thermodynamics and the Design, Analysis, and Improvement of Energy Systems*, ASME AES Vol. 30, pp. 127–137.

Boley, B. A., and Weiner, J. H., 1960, *Theory of Thermal Stresses*, John Wiley & Sons, New York.

Chadwick, P., 1962, "Thermal Damping of a Vibrating Elastic Body," *Mathematika*, Vol. 9, pp. 38–48.

Gouy, M., 1889, "Sur L'energie Utilisable," *Journal of Physics*, Vol. 8, p. 501.

Grigull, U., and Sander, H., 1984, *Heat Conduction*, Springer-Verlag, New York, p. 18.

Kinra, V. K., Wren, G. G., Rawal, S. P., and Misra, M. S., 1991, "On the Influence of Ply-Angle on Damping and Modulus of Elasticity of a Metal-Matrix Composite," *Metallurgical Transactions*, Vol. 22A, pp. 641–651.

Kinra, V. K., and Wren, G. G., 1992, "Axial Damping in Metal-Matrix Composites. I: A New Technique for Measuring Phase Difference to 10^{-4} Radians," *Experimental Mechanics*, Vol. 32, No. 2, pp. 163–171.

Kinra, V. K., and Milligan, K. B., 1994, "A Second-Law Analysis of Thermoelastic Damping," ASME JOURNAL OF APPLIED MECHANICS, Vol. 61, No. 1, pp. 71–76.

Lee, U., 1985, "Thermoelastic and Electromagnetic Damping Analysis," *AIAA Journal*, Vol. 23, No. 11, pp.1783–1790.

Milligan, K. B., and Kinra, V. K., 1993, "On the Thermoelastic Damping of a One-Dimensional Inclusion in a Uniaxial Bar," *Mechanics Research Communications*, Vol. 20, No. 2, pp. 137–142.

Misra, M. S., and LaGreca, P. D., 1984, "Damping Behavior of Metal Matrix Composites," *Proceedings of the Vibration Damping Workshop*, AFWAL-TR-84-3064-U-1.

Nowick, A. S., and Berry, B. S., 1972, *Anelastic Relaxation in Crystalline Solids*, Academic Press, New York, New York.

Özişik, M., 1980, *Heat Conduction*, John Wiley & Sons, New York, New York.

Shieh, R., 1971, "Thermoelastic Damping and Its Effect on Flutter of Stressed Panels Situated in a Supersonic Airflow," NASA TND-6448, NASA Langley Research Center, Hampton, VA.

Shieh, R. C., 1975, "Thermoelastic Vibration and Damping for Circular Timoshenko Beams," ASME JOURNAL OF APPLIED MECHANICS, Vol. 42, pp. 405–410.

Shieh, R. C., 1979, "Eigensolutions for Coupled Vibrations of Timoshenko Beams," ASME JOURNAL OF APPLIED MECHANICS, Vol. 46, pp. 169–174.

Steckel, G. L., 1985, "Material Damping Behavior of Gr/Mg Composites," Aerospace Corporation ONR Report Number TOR-0084-A-5726-01(-1), The Aerospace Corporation, El Segundo, CA.

Steckel, G. L., and Nelson, B. A., 1985, "Mechanical Damping Behavior of Graphite-Magnesium," Aerospace Corporation ONR Report Number TOR-0086(6726-01)-1, The Aerospace Corporation, El Segundo, CA.

Stodola, A., 1910, *Steam and Gas Turbines*, McGraw-Hill, New York.

Tasi, J., 1963, "Thermoelastic Dissipation in Vibrating Plates," ASME JOURNAL OF APPLIED MECHANICS, Vol. 30, pp. 562–567.

Timmerman, N. S., 1982, "Damping Characteristics of Metal Matrix Composites," Army Materials and Mechanics Research Center Report, AMMRC-TR-82-19.

Timmerman, N. S., and Doherty, J., 1984, "Loss Factors in Metal Matrix Composites," Army Materials and Mechanics Research Center Report, AMMRC-TR-84-22.

Wren, G. G., and Kinra, V. K., 1992, "Axial Damping in Metal-matrix Composites II: A Theoretical Model and Its Experimental Verification," *Experimental Mechanics*, Vol. 32, pp. 172–178.

Zener, C., 1938a, "Internal Friction in Solids I. Theory of Internal Friction in Reeds," *Physical Review*, Vol. 52, pp. 230–235.

Zener, C., 1938b, "Internal Friction in Solids II. General Theory of Thermoelastic Internal Friction," *Physical Review*, Vol. 53, pp. 90–99.

Zener, C., 1948, *Elasticity and Anelasticity of Metals*, University of Chicago Press, Chicago.

Downloaded 04 May 2010 to 171.66.16.28. Redistribution subject to ASME license or copyright; see http://www.asme.org/terms/Terms_Use.cfm

Damage Deactivation

N. R. Hansen
Senior Member of Technical Staff,
Sandia National Laboratories,
Albuquerque, NM 87115
Mem. ASME

H. L. Schreyer
Professor,
Department of Mechanical Engineering,
University of New Mexico,
Albuquerque, NM 87131
Fellow ASME

A phenomenological algorithm, motivated by the "mode I" microcrack opening and closing mechanism, is developed for the deactivation and reactivation of the damage effects as modeled by certain continuum damage mechanics theories. One-dimensional formulations with and without coupled plasticity are used to elucidate concepts associated with damage deactivation and to suggest multidimensional deactivation formulations applicable to continuum damage theories that employ a second-order tensor as the damage measure. Strain-based projection operators are used to deactivate the damage effects in the damage tensor. Motivated by observations from one-dimensional coupled formulations, both the total and elastic strains must be compressive for the damage to be rendered inactive. By introducing smooth functions to represent the transition from the active to the inactive state, discontinuities in the response are avoided. To illustrate the aspects associated with deactivation, a consistent set of examples using a strain-controlled one-cycle uniaxial stress loading is given for each formulation.

1 Introduction

Materials subjected to ever increasing loads will eventually become damaged. Historically the term "damage" has been associated with a variety of material processes, such as fatigue and plasticity, but recently damage has become synonymous with the field of continuum damage mechanics. With an appropriate set of internal (macroscopic) variables, continuum damage mechanics characterizes microdefects (microcracks and/or microvoids), represents the influence of microdefects on the macroscopic material behavior, and models the evolution of these defects.

The development of continuum damage mechanics models is based on either a micromechanical or a phenomenological approach. The micromechanical technique employs basic mechanics principals on the microscopic scale, such as well-posed boundary value problems and fracture mechanics, to describe the macro behavior. Although fewer assumptions are required and the elegance of the solutions make the micromechanical models interesting, the complexity of the rigorous theories make the current micromechanical representations impractical for large scale numerical implementation. In contrast, the phenomenological theories allocate a set of variables motivated by experimental observations and then employ the principles of irreversible thermodynamics to describe the material response. What the phenomenological models lack in mechanical rigor, they overcome in the simplicity of implementation. As stated by Krajcinovic (1989), "... a much more feasible strategy would, perhaps, involve micromechanically based phenomenological models."

Theories of plasticity, which approximate the dislocation or "slip" of the material on the microscale, are also used to describe inelastic material behavior. Although the material structure is altered and some have described this as a form of damage, in this presentation plasticity is considered to be different from damage. In a general material both damage and dislocation (plasticity) phenomena can occur simultaneously. The existence of both phenomena has motivated several research efforts to couple these theories to form a more general description (Ortiz, 1985; Lemaitre, 1985a; Simo and Ju, 1987; Yazdani and Schreyer, 1990; Ju, 1989; Bammann and Aifantis, 1989; Berthaud et al., 1990).

In order to understand the damaging process, researchers often employ concepts developed in fracture mechanics. The condition characterized by a single crack embedded in a material with a tensile load perpendicular to the length of the crack is called "mode I" crack opening. If the loading is reversed the crack will close and in a one-dimensional case the material behaves as uncracked. When this idea is applied to the microcracks in continuum damage mechanics, the phenomenon is "damage deactivation." The damage still exists but the loading condition can render it inactive. This is different from the concept of damage "healing" where the amount of damage decreases, such as the situation which occurs in salt (Brodsky, 1990). For healing, any new damage evolves from the healed state (reduced damage), yet for damage deactivation, new damage progresses from the previously damaged state. The phenomenon of damage deactivation is not purely a theoretical concept since it is observed experimentally (Ortiz, 1985; Holcomb, 1984; and Berthaud, et al., 1990). Figure 1 is a reproduction of the experimental results published by Berthaud et al. (1990) for plain concrete.

Contributed by the Applied Mechanics Division of THE AMERICAN SOCIETY OF MECHANICAL ENGINEERS for publication in the ASME JOURNAL OF APPLIED MECHANICS.

Discussion on this paper should be addressed to the Technical Editor, Professor Lewis T. Wheeler, Department of Mechanical Engineering, University of Houston, Houston, TX 77204-4792, and will be accepted until four months after final publication of the paper itself in the ASME JOURNAL OF APPLIED MECHANICS.

Manuscript received by the ASME Applied Mechanics Division, Oct. 7, 1993; final revision, May 10, 1994. Associate Technical Editor: R. M. McMeeking.

Copyright © 1995 by ASME

Downloaded 04 May 2010 to 171.66.16.28. Redistribution subject to ASME license or copyright; see http://www.asme.org/terms/Terms_Use.cfm

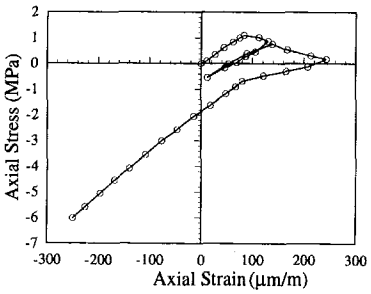

Fig. 1 Stress-strain response of concrete, illustrating damage deactivation (published by Berthaud, Laborderie, and Ramtani (1990))

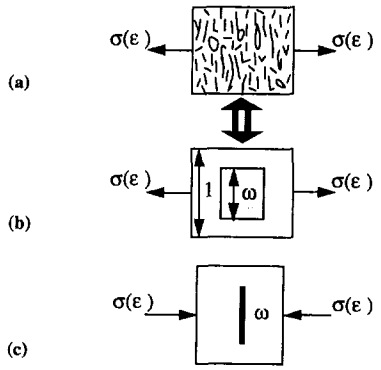

Fig. 2 Schematic of a one-dimensional damaged material: (*a*) distributed microflaws, (*b*) equivalent damage representation, and (*c*) deactivated damage

Notice that after the loading becomes compressive (−) the modulus is restored to the undamaged value.

Many attempts have been made to model the crack closing phenomenon (Holcomb, 1984; Costin, 1983; Ortiz, 1985; Lemaitre, 1987; Ju, 1989; Chaboche, 1992; Berthaud et al., 1990). The very nature of mode I microcrack opening and closing will convert even a simple damage theory into an anisotropic formulation. Because of this evolution of anisotropy, attention must be given to ensure that the damage deactivation algorithm is compatible with the damage theory. To date, no one (including this work) has even attempted the task of damage deactivation including all three fracture modes.

Motivated by mode I microcrack opening and closing phenomena, a phenomenological approach is used to develop an algorithm for the deactivation and reactivation of damage as it affects the constitutive relations. The theory, developed using direct tensor notation, is applicable to continuum damage mechanics theories employing a second-order damage tensor as introduced by Cordebois and Sidoroff (1979). In each section the theory relating to damage deactivation is presented first, followed by a simple example illustrating the theory. For consistency in comparing the results from the various formulations, one cycle of uniaxial stress with strain control is used as the loading function for all examples.

In Section 2, the case of one-dimensional damaged elasticity is presented. This simple case clearly illustrates the concept of mode I microcrack opening and closing. With the insight provided by Lemaitre (1985b) for tensile uniaxial loading, a damage evolution relation is proposed. In Section 3, damage deactivation is applied to one-dimensional elastoplasticity coupled with damage mechanics. By examining the various combinations of the strain components, it is shown that the algorithm used for damaged elasticity is inappropriate for the coupled formulation. A new algorithm which corrects the deficiencies is then presented. The response to the example loading is shown for an elastic-perfectly plastic theory. However, a discontinuity of the stress-strain response is encountered. This is remedied by the introduction of a smoothing function to replace the Heaviside function.

Then in Section 4, the concepts related to damage deactivation are generalized to multidimensions for a class of continuum damage theories which employ a second-order tensor as the damage measure. The mode I opening and closing phenomenon is approximated using strain-based projection operators. A smooth function is employed to avoid discontinuities in the response. For illustrative purposes, the damage function is constructed to mimic the one-dimensional version of the damage evolution. Finally in Section 5, damage deactivation for the case of multidimensional elastoplasticity coupled with damage is considered. The previous sections established the foundation such that this generalization is performed with a minimal amount of additional developments. The example, using a von Mises elastic-perfectly plastic theory, closely parallels the one-dimensional results.

2 One-Dimensional Damaged Elasticity

Continuum damage mechanics has become well established as a technique for modeling a class of inelastic behavior for engineering materials. The underlying premise of continuum damage mechanics is that the material undergoes a change in internal structure due to microcracking and the material properties are subsequently degraded due to the loss of integrity. Several theories exist on how the damaging process evolves, the associated reduction in properties, and the resulting constitutive relationship. However, if the loading path reverses, the effects of damage may become inactive. With a further evolution along the original loading path, the effects of damage may become reactivated. A rigorous method for reflecting these changes is necessary to obtain physically realistic approximate solutions in two and three dimensions. The purpose of this paper is to provide a damage deactivation and reactivation procedure that will be applicable to a class of damage theories. The development of the various damage theories will not be presented in detail but the reader seeking a rather comprehensive presentation is referred to Krajcinovic (1989). Several basic theories are presented for illustrative purposes. The case of one-dimensional damaged elasticity introduces the concepts of continuum damage mechanics and damage deactivation in the most concise manner and is presented in this section. The subsequent sections build upon these basic concepts applicable to coupled and multidimensional formulations. The format for each section is to first present the theory and then illustrate the concepts with a simple example.

2.1 Theory. Let the stress and the strain be denoted by σ and ϵ, respectively. In the absence of damage the stress is linearly related to the strain by a proportionality constant called the elastic stiffness or Young's modulus and denoted by E^0. Consider a one-dimensional elastic material specimen which develops damage (microcracks and microvoids). This specimen under tensile loading is shown schematically in Fig. 2(*a*). A damage parameter, denoted by ω, representing the reduction in load carrying ability of the specimen, or the reduction in the material cross-sectional area, is introduced. An illustration of this damage representation is given in Fig. 2(*b*). The effective stress, representing the stress in the remaining undamaged material, is given as

$$\hat{\sigma} \equiv \frac{\sigma}{1-\omega}. \tag{1}$$

As the value of the damage increases with $0 \leq \omega < 1$ the effective stress increases relative to the stress. With the assumption that the stiffness degrades proportionally to the damage, the damaged material stiffness is

$$E \equiv (1-\omega)E^0. \tag{2}$$

Downloaded 04 May 2010 to 171.66.16.28. Redistribution subject to ASME license or copyright; see http://www.asme.org/terms/Terms_Use.cfm

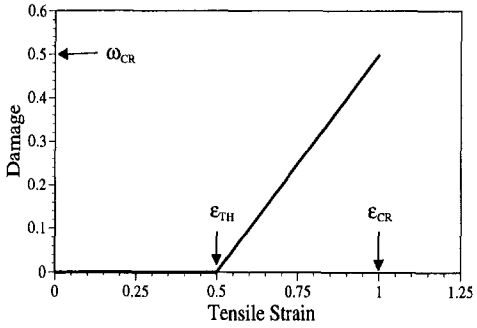

Fig. 3 Proposed damage evolution relationship

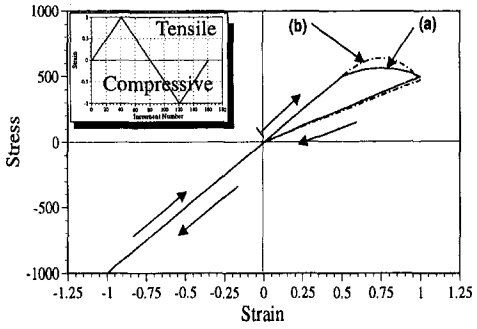

Fig. 4 Stress response to cyclic strain load; (a) One-dimensional elasto-damage formulation and (b) multidimensional elastodamage formulation

Now consider the condition where the load is reversed to a compressive state. Although the damage still exists, the loading condition now renders the damage inactive and the material behaves as if it were undamaged, as shown schematically in Fig. 2(*c*). If the loading is again reversed the damage will progress from the existing damage state, not from a zero damage state and, hence, the material has not *healed*. One method for representing the active state of damage is to let

$$\omega^{\text{act}} = h(\epsilon)\omega \tag{3}$$

where $h(\ )$ is the Heaviside function which equals unity for positive arguments and zero otherwise. Thus the active damage is nonzero when the strain is positive. The active stiffness is given by

$$E^{\text{act}} = E^0 - h(\epsilon)(E^0 - E) = (1 - \omega^{\text{act}})E^0 \tag{4}$$

The stress, including damage deactivation, is now

$$\sigma = E^{\text{act}}\epsilon \tag{5}$$

and the effective stress is

$$\hat{\sigma} = \frac{\sigma}{1 - \omega^{\text{act}}}. \tag{6}$$

2.2 Example. To illustrate the damage deactivation algorithm a simple damage evolution law will be proposed. Motivated by the work of Lemaitre (1985b), the damage is assumed to evolve in a linear fashion for tensile strains above a threshold strain, ϵ_{TH}, up to a critical damage value of ω_{CR} at a strain of ϵ_{CR}. For illustrative purposes the values of $\epsilon_{TH} = 0.5$, $\omega_{CR} = 0.5$, and $\epsilon_{CR} = 1.0$, are selected as shown in Fig. 3. This type of a relationship is based upon monotonically increasing loading. For a general loading, the damage at the nth load increment is defined as the maximum value from all load increments, that is

$$\omega_n \equiv \max(\omega_i)|_{i=1}^{i=n} \tag{7}$$

where ω_i is determined from the strain and Fig. 3. This guarantees that ω is monotonically increasing and hence, no healing is allowed.

One complete strain-controlled load cycle spanning a strain of ± 1.0 is used as the loading path. This input, shown in the upper corner of Fig. 4, will be used also in all subsequent examples. The only material parameter required is the undamaged Young's modulus. A value of $E^0 = 1000$ has been selected to illustrate the behavior of the model. Shown in Fig. 4(*a*) is the stress response resulting from the cyclic strain loading, the damage evolution of Fig. 3, and the use of Eqs. (4) and (5). For strains below 0.5 (the damage threshold, ϵ_{TH}) the modulus remains unchanged. As the strain increases further, the modulus progressively degrades (the damaged unloading modulus is indicated by the slope of the dashed line). At a strain value of $+1.0$, the damaged modulus is one-half the initial value, since the damage has attained a value of 0.5. Upon load reversal the stress response follows this slope until zero strain is reached. When the strain passes through zero the damage is deactivated and the undamaged modulus is restored. For the remaining portion of the load cycle, where the strain reaches a value of -1.0 and returns back to 0.0, the material responds as if undamaged. However, if the strain goes above 0.0, the previous damage value (0.5) is reactivated automatically by the use of the Heaviside function. If the strain were taken above 1.0 then additional damaging would be expected.

3 One-Dimensional Elastoplasticity Coupled With Damage

Damaged elasticity theories, as presented in the previous section, may be most applicable to brittle materials where the inelastic strains are small or nonexistent. If a material exhibits moderate to large inelastic strains then a constitutive theory that couples the damaged elasticity with a mechanism for introducing inelastic strains, such as plasticity, may be more appropriate. Both this and Section 5 are presented in the framework of elastoplasticity coupled with continuum damage mechanics. As will be illustrated, the presence of an inelastic strain complicates the conditions for crack closing (damage deactivation).

3.1 Theory. Small deformation theories assume that the total strain can be decomposed into elastic and plastic components as

$$\epsilon = \epsilon^e + \epsilon^p \tag{8}$$

where ϵ^e and ϵ^p are the elastic and plastic strains, respectively. The undamaged, the damaged and the active damage constitutive relations are, respectively,

$$\sigma = E^0\epsilon^e \quad \sigma = E\epsilon^e \quad \sigma = E^{\text{act}}\epsilon^e. \tag{9}$$

The damaged stiffness, E, was given in Eq. (2), but the determination of the active stiffness, E^{act}, for the coupled formulation is complicated by the introduction of the plastic strain. To illustrate whether the damage is active or inactive consider the specimen damaged to a state ω as shown in Fig. 2(*b*), and further consider the case where the plastic strain is tensile (positive). For this exercise, assume that no further plastic or damage processes are occurring, that is the damage and the plastic strain are constant. Next superimpose a compressive (negative) elastic strain on the specimen, as is illustrated in Fig. 5. If the magnitude of the elastic strain is greater than the magnitude of the plastic strain, then the compressive elastic strain overcomes the tensile plastic strain, the opposite surfaces of the "void" come in contact, the compressive stress can be transmitted across the surfaces, and the material behaves as undamaged, hence, the damage becomes *inactive*. Conversely, if the magnitude of the elastic strain is less than the magnitude of the plastic strain, then

Downloaded 04 May 2010 to 171.66.16.28. Redistribution subject to ASME license or copyright; see http://www.asme.org/terms/Terms_Use.cfm

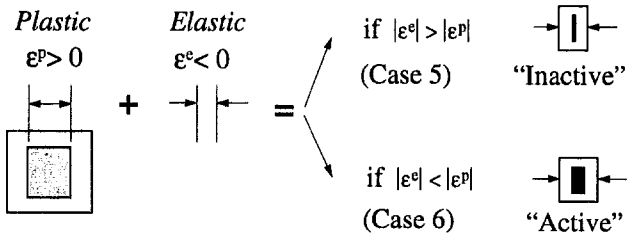

Fig. 5 Conditions for damage deactivation

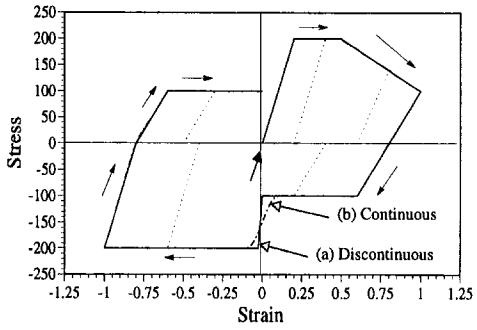

Fig. 6 Stress response to cyclic strain load using one-dimensional coupled formulation; (*a*) without smoothing function, (*b*) with smoothing function

there is not enough elastic strain to overcome the plastic strain and the void remains open or the damage remains *active*. There are a total of eight combinations of elastic and plastic strain variables and by a similar thought process for other conditions, it can be shown that the conditions for damage deactivation are as summarized in Table 1. The two cases discussed correspond, respectively, to Cases 5 and 6. If it were not for Case 4, then the previous formulation based on the total strain would be sufficient, but tensile elastic strains (tensile stresses) are not transmitted across microcrack or microvoid surfaces, the damage remains active, as listed.

For coupled formulations the relations for the active damage and active stiffness must be modified according to the table. Both the total and the elastic strains must be compressive for the damage to be rendered inactive, thus the active damage can be represented by

$$\omega^{\text{act}} = \omega\{1 - [1 - h(\epsilon^e)][1 - h(\epsilon)]\} \tag{10}$$

and the active stiffness is given by

$$E^{\text{act}} = E^0 - (E - E^0)\{1 - [1 - h(\epsilon^e)][(1 - h(\epsilon))]\} = (1 - \omega^{\text{act}})E^0. \tag{11}$$

Table 1 can likewise be generated by the deactivation conditions of compressive total strain under compressive stress loading. Since the elastic strain and the stress are proportional for the one-dimensional formulation, the results are equivalent to the previous presentation. Additional justification for the strain-based approach is presented during the multidimensional formulation.

3.2 Example. The example of the previous section is used again but now with the additional element of plasticity. Consider an elastic-perfectly plastic model with a yield stress of 200. In a coupled elastoplastic damage formulation, the damage evolves as discussed in Section 2.2 and shown in Fig. 3 and the active damage is determined from Eq. (10). The effective stress, defined in Eq. (3), is used in the plasticity model, along with Eqs. (8) and (9), to determine the plastic strain. To illustrate the damage deactivation algorithm, examine the stress-strain response shown in Fig. 6 as curve (a)

Table 1 Active damage conditions for combinations of strain for the elastoplasticity coupled with damage formulation

Case	ε^e	ε^p	Magnitude	ε	Damage
1	+	+	$\|\varepsilon^e\| > \|\varepsilon^p\|$	+	Active
2	+	+	$\|\varepsilon^e\| < \|\varepsilon^p\|$	+	Active
3	+	-	$\|\varepsilon^e\| > \|\varepsilon^p\|$	+	Active
4	+	-	$\|\varepsilon^e\| < \|\varepsilon^p\|$	-	Active
5	-	+	$\|\varepsilon^e\| > \|\varepsilon^p\|$	-	Inactive
6	-	+	$\|\varepsilon^e\| < \|\varepsilon^p\|$	+	Active
7	-	-	$\|\varepsilon^e\| > \|\varepsilon^p\|$	-	Inactive
8	-	-	$\|\varepsilon^e\| < \|\varepsilon^p\|$	-	Inactive

based on a prescribed cyclic strain loading. The dotted lines represent the unloading response and illustrates the degradation in the stiffness modulus. The effective stress follows a perfectly plastic response. Note the discontinuity in the stress-strain response at the point were the damage deactivation occurs. In the case of damaged elasticity the switching of the modulus from a damaged to an undamaged state occurs as the strain is passing through zero and, hence, the response remains continuous. In the coupled elastoplasticity damage formulation the deactivation of damage does not, in general, occur at the zero elastic strain state and a discontinuity occurs. This unrealistic response is remedied in the following section.

3.3 Discontinuity Correction. One method for overcoming the discontinuity discussed above is to replace the Heaviside function with a continuously differentiable or smooth function that varies from 0 to 1 over a transition domain. The use of a continuous function can be interpreted as a physical manifestation of the observation that all of the microcracks do not close instantaneously but, instead, the microcracks close gradually over a finite domain in strain. From a micromechanical viewpoint this representation implies that the asperities on the microcrack surfaces cause the deactivation to not occur instantaneously. For example, a simple continuous function, $q(x)$, defined over the domain $[x_l, x_h]$, is defined as

$$q(x) \equiv \begin{cases} 0.0 & \text{for } (x \le x_l) \\ 0.5\left(1 - \cos\left[\dfrac{\pi(x - x_l)}{x_h - x_l}\right]\right) & \text{for } (x_l < x < x_h) \\ 1.0 & \text{for } (x_h \le x). \end{cases} \tag{12}$$

The material parameters x_l and x_h should be determined experimentally, but a logical choice would be to set $x_l = -x_h$. Graphically, this function is shown in Fig. 7 with the transition occurring over the domain $[-0.1, 0.1]$. The replacement of the Heaviside function in the active damage and active stiffness relations results in

$$\omega^{\text{act}} = \omega\{1 - [1 - q(\epsilon^e)][(1 - q(\epsilon))]\}$$
$$E^{\text{act}} = E^0 - (E - E^0)\{1 - [1 - q(\epsilon^e)][(1 - q(\epsilon))]\} = (1 - \omega^{\text{act}})E^0. \tag{13}$$

With the use of the smoothing function, the stress-strain response is shown as curve (b) in Fig. 6. Notice that the

Downloaded 04 May 2010 to 171.66.16.28. Redistribution subject to ASME license or copyright; see http://www.asme.org/terms/Terms_Use.cfm

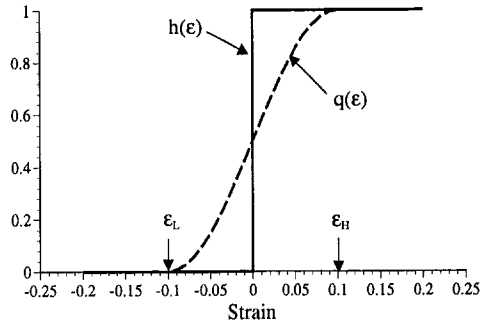

Fig. 7 Postulated smoothing function

discontinuity has been eliminated and the remaining part of the response is unaffected.

Although the use of the Heaviside function for the damaged elasticity formulation does not introduce a discontinuous stress-strain response, the first derivative of the stress with respect to the strain is discontinuous at zero strain. The use of the smoothing function will render the derivative continuous at zero strains. For numerical algorithms, the smoothed constitutive relations may increase the rate of numerical convergence but for all practical purposes, the results from the use of the Heaviside and smoothing functions are nearly indistinguishable for the case of damaged elasticity. In subsequent sections, the use of the smoothing function is preferred for other reasons also, and is recommended for all deactivation algorithms.

4 Multidimensional Damaged Elasticity

The results of the preceding sections on one-dimensional damage deactivation are now generalized for a multidimensional constitutive relation, specifically damaged elasticity in this section. Whereas in one dimension the concepts are clearly illustrated and the variables are simple scalars, in a multidimensional setting the concepts become more abstract. It is intended that by presenting the one-dimensional cases first, the generalization to the more meaningful and more useful multidimensional cases will be easily followed.

4.1 Theory. In a multidimensional framework, the variables that are scalars in a one-dimensional setting are tensors and consistent formulations are more difficult to understand as well as implement. For the undamaged material, Hooke's law or the material constitutive relationship is represented by

$$\boldsymbol{\sigma} = \mathbf{E}^0 : \boldsymbol{\epsilon} \tag{14}$$

where $\boldsymbol{\sigma}$ is the stress tensor (second order), $\boldsymbol{\epsilon}$ is the total strain tensor (second order), $\mathbf{E}^0$ is the undamaged stiffness tensor (fourth order), and ":" is the contraction operator on two indices. The material to be modeled determines the form of the stiffness tensor, the most common being an isotropic material, although this work is not limited to isotropic materials. Theories of continuum damage mechanics describe the progressive degradation in the stiffness tensor in which the damaged elasticity constitutive relationship can be written as

$$\boldsymbol{\sigma} = \mathbf{E} : \boldsymbol{\epsilon} \tag{15}$$

where $\mathbf{E}$ is the damaged secant stiffness tensor (fourth order) that is determined by the specific damage representation theory employed. If the additional element of damage deactivation is included as some type of generalization of the results presented in the previous sections, then the resulting constitutive relation including damage deactivation is

$$\boldsymbol{\sigma} = \mathbf{E}^{\text{act}} : \boldsymbol{\epsilon} \tag{16}$$

where $\mathbf{E}^{\text{act}}$ is the active damaged stiffness tensor (fourth order). The determination of the active stiffness tensor is the primary objective of this work.

4.1.1 Other Deactivation Approaches. The concept of damage deactivation is not novel; many have attempted to formulate an algorithm for multidimensional applications with mixed success. Damage deactivation is also referred to as the active/passive condition and the unilateral condition. Chaboche (1992) has produced a rather thorough review on concepts of damage deactivation including an evaluation of four different multidimensional algorithms. He considered five properties for evaluation of the models. These criteria are complete anisotropy of the damage representation, damage growth in tension and compression, the active secant stiffness tensor must be symmetric according to the Onsager Principle, damage loading surfaces must be continuous (and preferably convex), and the stress (strain) response must be continuous.

The authors of this work agree that anisotropy, symmetry, and continuity are essential ingredients of a reputable deactivation algorithm, but, although the growth of damage in tension/compression and the continuity of the damage loading may be desirable, these features may not necessarily be associated with damage deactivation formulations.

The deficiencies noted by Chaboche (1992) are summarized here. The theory using two scalar variables (Ladeveze and Lemaitre, 1984) is not anisotropic and does not possess a convex loading surface. A theory employing two second-order damage tensors (Ramtani, 1990) does not maintain the symmetry of the stiffness tensor. Not mentioned by Chaboche (1992), but of noteworthy interest is that Ramtani's theory does not fully recover the undamaged stiffness behavior, because the volumetric damage always remains active. A theory (Ju, 1989) that uses the evolved damaged stiffness as the damage measure was shown not to be anisotropic for all loading paths and the deactivation algorithm can result in a discontinuous response. Finally, a vector based theory (Krajcinovic and Fonseka, 1981) was also shown to violate the continuity requirement. The conclusion was there did not exist a deactivation algorithm which satisfied *all* the stated criteria.

4.1.2 Damage Representation Theory. Many theories exist for representing the behavior of damaged materials, from the simple scalar isotropic representations to the complex micromechanical formulations. There are advantages and disadvantages to each theory. A common theory which is a compromise between utility and detail is the one first introduced by Cordebois and Sidoroff (1979). They postulate that a symmetric damage tensor of second-order, $\boldsymbol{D}$, can be used to represent the degradation of the material integrity. The postulated form of the effective stress tensor is

$$\hat{\boldsymbol{\sigma}} \equiv \mathbf{M}(\boldsymbol{D}) : \boldsymbol{\sigma} \tag{17}$$

with

$$\mathbf{M}(\boldsymbol{D}) \equiv (\boldsymbol{i} - \boldsymbol{D})^{-1/2} \wedge (\boldsymbol{i} - \boldsymbol{D})^{-1/2} \tag{18}$$

where $\boldsymbol{i}$ is the second-order identity tensor and the cross composition of two second-order tensors, denoted by the symbol "$\wedge$," is defined by $\boldsymbol{A} \wedge \boldsymbol{B} \equiv A_{ik}B_{jl}(\boldsymbol{e}_i \otimes \boldsymbol{e}_j \otimes \boldsymbol{e}_k \otimes \mathbf{e}_l)$ for an orthonormal basis $\boldsymbol{e}_i$. It has been shown (Murakami, 1988; Hansen, 1992) that this effective-stress relation and damage measure represents an area projection of material damage, and not all of the mechanisms at the microscale can be replicated with such a model. The hypothesis of strain energy equivalence as postulated by Cordebois and Sidoroff (1979) and employed by Chow and Wang (1987) is used to derive the damaged stiffness relation. This hypothesis states that *the strain energy of the damaged material is the same in form as the undamaged material except the stress is replaced by*

Downloaded 04 May 2010 to 171.66.16.28. Redistribution subject to ASME license or copyright; see http://www.asme.org/terms/Terms_Use.cfm

the effective stress. The fourth-order damaged stiffness tensor is given by

$$\mathbf{E}(\boldsymbol{D}) = \mathbf{M}^{-1}(\boldsymbol{D}):\mathbf{E}^0:\mathbf{M}^{-1}(\boldsymbol{D}) \tag{19}$$

For the condition of plane strain, the components of the stress tensor are as follows:

$$\sigma_{11} = (1 - D_1)^2 E^0_{1111}\epsilon_{11} + (1 - D_1)(1 - D_2)E^0_{1122}\epsilon_{22}$$

$$\sigma_{22} = (1 - D_1)(1 - D_2)E^0_{2211}\epsilon_{11} + (1 - D_2)^2 E^0_{2222}\epsilon_{22}$$

$$\sigma_{12} = (1 - D_1)(1 - D_2)E^0_{1212}\epsilon_{12} \tag{20}$$

where D_1 and D_2 are the principle values of the damage tensor. The above stress components are with respect to the principle damage basis. Since the initial stiffness tensor is symmetric, $E^0_{ijkl} = E^0_{klij}$, then regardless of the values of the damage tensor the damaged stiffness tensor is also symmetric.

The components of the effective stress tensor with respect to the principle damage basis are

$$\hat{\sigma}_{11} = (1 - D_1)E^0_{1111}\epsilon_{11} + (1 - D_2)E^0_{1122}\epsilon_{22}$$

$$\hat{\sigma}_{22} = (1 - D_1)E^0_{2211}\epsilon_{11} + (1 - D_2)E^0_{2222}\epsilon_{22}$$

$$\hat{\sigma}_{12} = \sqrt{(1 - D_1)(1 - D_2)}\,E^0_{1212}\epsilon_{12}. \tag{21}$$

The effective stress tensor is symmetric for all values of damage. Also note that the effective stress components exist only in directions of actual or Cauchy stresses. Not all damage representation theories possess this attribute which may be required to replicate certain behavior.

4.1.3 Projection Operators Based on the Heaviside Function. As loading paths change, the damage can become inactive as the microcracks and microvoids are closed. Various methods have been employed to determine which components of the damage tensor or the stiffness tensor to deactivate. These have included stress and strain-based projection operators. Since projection operators are used in the presented formulation, this concept will be reviewed. Ju (1989) introduced a mode I microcrack opening and closing algorithm based on a strain-based projection operator. The concept of projection operators as a method of damage deactivation was first introduced by Ortiz (1985), but he defined an operator which fails to become the fourth-order identity tensor when the load is tensile in all directions. Ju's proposed projection operator is constructed in a series of steps as presented below. First consider the spectral decomposition of the total strain tensor:

$$\boldsymbol{\epsilon} = \sum_{i=1}^{3} \epsilon_i(\boldsymbol{p}_i \otimes \boldsymbol{p}_i) \tag{22}$$

where ϵ_i is the ith principal strain, the unit vector $\boldsymbol{p}_i$ is the corresponding ith principal strain direction (or eigenvalue and eigenvector of $\boldsymbol{\epsilon}$), and the symbol $\otimes$ denotes the tensor product. Next let the positive (tensile) spectral tensor be defined as

$$\mathbf{Q}^{h+} \equiv \sum_{i=1}^{3} h(\epsilon_i)(\boldsymbol{p}_i \otimes \boldsymbol{p}_i). \tag{23}$$

The fourth-order positive spectral projection operator is then defined as

$$\mathbf{P}^{h+} \equiv \boldsymbol{Q}^{h+} \wedge \boldsymbol{Q}^{h+} \tag{24}$$

It follows immediately that if $\boldsymbol{Q}^{h+} = \boldsymbol{i}$, then $\mathbf{P}^{h+} = \mathbf{I}$ where $\boldsymbol{i}$ and $\mathbf{I}$ are the second and fourth-order identity tensors, respectively. This form is equivalent to that proposed by Ju (1989, Eq. (38)), although Ju's appears to be different at first glance. The regular spectral projection tensor, $\boldsymbol{Q}$, defined by Ju (1989, Eq. (37)) is really the second-order identity tensor and can be eliminated from the construction of $\mathbf{P}^{h+}$. The positive projection of the strain tensor is then given by

$$\boldsymbol{\epsilon}^+ = \mathbf{P}^{h+}:\boldsymbol{\epsilon}. \tag{25}$$

By inspection, if all eigenvalues of $\boldsymbol{\epsilon}$ are negative (compressive) then $\mathbf{P}^{h+}$ will be the null tensor and, conversely, if all eigenvalues are positive (tensile) then $\mathbf{P}^{h+}$ corresponds to the fourth-order identity tensor. The tensile nature of this projection is analogous to the mode I crack-opening phenomenon in the field of fracture mechanics, in which the direction of crack propagation is normal to the crack surface in contrast to a shearing-type loading.

4.1.4 Active Damage and Active Stiffness. The portion of the damage tensor, $\boldsymbol{D}$, which remains active under arbitrary loading, is determined by the tensile strain projection of the damage tensor. Recall that this damage measure represents a reduction in cohesive material area that is produced by microcracks and microvoids. Operating on the damage tensor with the tensile-strain-based projector renders inactive any damage which is under compressive mode I loading. This was illustrated in Fig. 2(*c*) for the one-dimensional formulation. Thus the active damage tensor, $\boldsymbol{D}^{\text{act}}$, is defined according to the following:

$$\boldsymbol{D}^{\text{act}} \equiv \mathbf{P}^{h+}:\boldsymbol{D}. \tag{26}$$

The damaged stiffness including damage deactivation or the active stiffness is given by substitution of the active damage into the damage stiffness relation, Eq. (19).

$$\mathbf{E}^{\text{act}} \equiv \mathbf{E}(\boldsymbol{D}^{\text{act}}) = \mathbf{M}^{-1}(\boldsymbol{D}^{\text{act}}):\mathbf{E}^0:\mathbf{M}^{-1}(\boldsymbol{D}^{\text{act}}) \tag{27}$$

This stiffness tensor is symmetric. A similar relation for the effective stress tensor including damage deactivation is obtained by substituting the active damage into the effective stress relation, Eq. (17).

The behavior of this deactivation algorithm is best illustrated by examining the response of the stress components to various load paths. Without loss of generality, consider the case of where the strain tensor and the damage tensor have the same principle basis. We also restrict this illustration to two dimensions (or plane strain). In the first quadrant in strain space ($\epsilon_1 > 0$ and $\epsilon_2 > 0$), the spectral projection operator, Eq. (24), is the identity tensor, therefore, $\boldsymbol{D}^{\text{act}} = \boldsymbol{D}$. The resulting stress components are given by

$$\sigma_1 = (1 - D_1)^2 E^0_{11}\epsilon_1 + (1 - D_1)(1 - D_2)E^0_{12}\epsilon_2$$

$$\sigma_2 = (1 - D_1)(1 - D_2)E^0_{21}\epsilon_1 + (1 - D_2)^2 E^0_{22}\epsilon_2. \tag{28}$$

Conversely, in the third quadrant in strain space ($\epsilon_1 < 0$ and $\epsilon_2 < 0$), the spectral projection operator is the null tensor. Therefore, $\boldsymbol{D}^{\text{act}} = \mathbf{0}$, and the stress components are

$$\sigma_1 = E^0_{11}\epsilon_1 + E^0_{12}\epsilon_2$$

$$\sigma_2 = E^0_{21}\epsilon_1 + E^0_{22}\epsilon_2. \tag{29}$$

During the transition in and out of the other quadrants, undesirable behavior is encountered. Suppose the load path transitions from the first to the second quadrant at a constant value of $\epsilon_2 > 0$. This implies that the D_2 component of damage remains active, but because the component ϵ_1 is changing from positive to negative the corresponding component of the damage, D_1, is likewise switching from active to inactive. In the second quadrant the stress components are

$$\sigma_1 = E^0_{11}\epsilon_1 + (1 - D_2)E^0_{12}\epsilon_2$$

$$\sigma_1 = (1 - D_2)E^0_{21}\epsilon_1 + (1 - D_2)^2 E^0_{22}\epsilon_2. \tag{30}$$

A discontinuity in the σ_1 stress component is observed by examining Eqs. (28) and (30), in particular the second term

Downloaded 04 May 2010 to 171.66.16.28. Redistribution subject to ASME license or copyright; see http://www.asme.org/terms/Terms_Use.cfm

on the right side of the equations. This discontinuity is an artifact of using the Heaviside function for damage deactivation and the Poisson effect. A remedy to this problem is proposed in the following section.

4.1.5 Projection Operator Based on Smooth Functions. To remedy the stress discontinuity in the multidimensional deactivation algorithm, the positive spectral tensor, Eq. (23), and the fourth-order positive spectral projection operator, Eq. (24), must be redefined using a smooth or continuous function instead of the Heaviside function

$$\boldsymbol{Q}^{q+} \equiv \sum_{i=1}^{3} q(\epsilon_i)(\boldsymbol{p}_i \otimes \boldsymbol{p}_i)$$

$$\mathbf{P}^{q+} \equiv \boldsymbol{Q}^{q+} \wedge \mathbf{Q}^{q+}. \tag{31}$$

The exact form of the smooth function, q, will depend on the observed behavior of the material of interest, but for this presentation the function introduced in Eq. (12) will be employed. The positive projection of the strain

$$\boldsymbol{\epsilon}^{+} = \mathbf{P}^{q+} : \boldsymbol{\epsilon} \tag{32}$$

is only valid if the eigenvalues of $\boldsymbol{\epsilon}$ are exterior to the transition domain $[x_l, x_h]$. With this smoothed version of the positive projection operator, the active damage tensor becomes

$$\boldsymbol{D}^{\text{act}} = \mathbf{P}^{q+} : \boldsymbol{D}. \tag{33}$$

The components of the stress presented in the previous discussion are still applicable, the only difference is the damage is not abruptly deactivated but instead gradually transitions from active to inactive, to avoid any discontinuities. Now as the strain path moves from the first to the second quadrant, the D_1 damage smoothly transitions from active to inactive and the stress response is continuous according to Eqs. (28) and (30). In summary, since this damage representation theory is anisotropic, the active stiffness tensor is symmetric, and stress response is continuous using the smooth operator proposed in this section, the criteria established by Chaboche (1992), and listed in Section 4.1.1, have been satisfied.

4.2 Example. The preceding developments focused on representing the effects that damage has on the constitutive behavior irrespective of the damage evolution. There are many models that have been developed which employ the second-order measure for damage representation but with different formulations for the damage evolution. A simple damage evolution model is presented in this section to illustrate the behavior of damage deactivation in a multidimensional setting.

4.2.1 Damage Evolution. Based on the observations in brittle materials where damage evolves in the direction of loading for uniaxial tensile stress but evolves perpendicular to the loading for uniaxial compressive stress, the damage tensor is postulated to evolve in the direction of the tensile strain increment, i.e.,

$$\dot{\boldsymbol{D}} \equiv \dot{\lambda}_D \Delta \boldsymbol{\epsilon}^{+} \tag{34}$$

where $\dot{\lambda}_D$ is the damage consistency parameter and $\Delta\boldsymbol{\epsilon}^{+}$ is the positive projection of the strain increment, given by

$$\Delta \boldsymbol{\epsilon}^{+} \equiv \mathbf{W}^{h+} : \Delta \boldsymbol{\epsilon} \tag{35}$$

where the fourth-order positive tensile strain increment operator, $\mathbf{W}^{h+}$, is defined for the strain increment, $\Delta\boldsymbol{\epsilon}$, in the same manner as $\mathbf{P}^{h+}$ was defined for total strains (see Eq. (24)). For rate-independent materials, the strain increment is defined in terms of a loading parameter. A damage function is introduced which is similar to the yield function employed in plasticity theories. This damage function is constructed to mimic the form of the damage evolution introduced in the one-dimensional formulation and is postulated to be

$$\Phi_A \equiv g^2(\hat{\epsilon}) - \hat{\Omega} \tag{36}$$

where

$$g(\hat{\epsilon}) \equiv \left\langle \omega_{CR} \frac{(\hat{\epsilon} - \epsilon_{TH})}{(\epsilon_{CR} - \epsilon_{TH})} \right\rangle. \tag{37}$$

The parameters, ϵ_{TH}, ϵ_{CR}, and ω_{CR}, are defined in Section 2.2, and $\langle\ \rangle$ is the Macauley bracket. The scalars $\hat{\epsilon}$ and $\hat{\Omega}$ are measures of the total strain and damage tensors, respectively, in the direction of positive total strains and positive strain increments, given by

$$\hat{\epsilon} \equiv \sqrt{(\mathbf{W}^{h+} : \mathbf{P}^{h+} : \boldsymbol{\epsilon}) : (\mathbf{W}^{h+} : \mathbf{P}^{h+} : \boldsymbol{\epsilon})}$$

$$\hat{\Omega} \equiv \sqrt{(\mathbf{W}^{h+} : \mathbf{P}^{h+} : \boldsymbol{D}) : (\mathbf{W}^{h+} : \mathbf{P}^{h+} : \boldsymbol{D})}. \tag{38}$$

As the damage evolves beyond the threshold value (ϵ_{TH}), the stiffness tends to degrade as $(1 - D_i)^2$ for the multidimensional formulation, whereas the stiffness degrades as $(1 - \omega)$ in the one-dimensional formulation. Because of this difference, both the evolution of the damage and the degradation of the stiffness cannot both be replicated exactly. As a compromise the first term in the damage function, Eq. (36), is squared, so that at the critical state ($\epsilon_{CR} = 1.0$ and $\omega_{CR} = 0.5$) of the damage and the stiffness are approximately the same for both the one-dimensional and multidimensional formulations. Finally, the damage consistency parameter is determined by the loading/unloading conditions

$$\dot{\lambda}_D \geq 0 \quad \Phi_I \leq 0 \quad \dot{\lambda}_D \Phi_I = 0. \tag{39}$$

These conditions are standard for unilateral constraint problems such as the yield function employed in plasticity. If $\Phi_I < 0$, the state is internal to the damage surface and by the third condition no further damaging is occurring ($\dot{\lambda}_D = 0$). Conversely, if $\dot{\lambda}_D > 0$ the third condition implies that $\Phi_1 = 0$ and, by the "damage consistency condition", $\hat{\Omega} = g^2(\hat{\epsilon})$.

4.2.2 Results. The damage evolution parameters presented in Fig. 3 and the transition parameters employed in Fig. 7, are used in these simulations. An initial isotropic material with an elastic modulus of 1000 and Poisson's ratio of 0.3 is used for this example. When the damage deactivation algorithm is employed with this anisotropic damage model, the resulting stress-strain response along the loading axis is shown as curve (*b*) in Fig. 4. These results replicate the trends exhibited in the one-dimensional simulations (curve (*a*) in Fig. 4) except for the quadratic rate of damage evolution instead of the linear rate exhibited previously.

5 Multidimensional Elastoplasticity Coupled With Damage

The generalization to multidimensional elastoplasticity coupled with damage is presented in this section. This follows easily based on the one-dimensional formulation for elastoplasticity coupled with damage and the multidimensional damaged elasticity formulations, presented in Sections 3 and 4, respectively. It is apparent that the use of a damage deactivation formulation based only on the total strains, presented in Section 4, will not replicate the conditions given in Table 1, and additional work is required.

5.1 Theory. For infinitesimal deformations, the total strain tensor is decomposed as follows:

$$\boldsymbol{\epsilon} = \boldsymbol{\epsilon}^{e} + \boldsymbol{\epsilon}^{p} \tag{40}$$

Downloaded 04 May 2010 to 171.66.16.28. Redistribution subject to ASME license or copyright; see http://www.asme.org/terms/Terms_Use.cfm

where $\boldsymbol{\epsilon}^e$ is the elastic strain tensor and $\boldsymbol{\epsilon}^p$ is the plastic strain tensor. The coupled elastoplasticity constitutive relationship including damage deactivation is

$$\boldsymbol{\sigma} = \mathbf{E}^{\text{act}} : \boldsymbol{\epsilon}^e. \tag{41}$$

Based on observations from the one-dimensional case of elastoplasticity coupled with damage, the deactivation algorithm for the multidimensional formulation must include a dependency on both compressive total and elastic strains, in addition to the incorporation of a smoothing function for transition to and from the active damage state. Compressive elastic strain as a deactivation criterion is further justified by considering the multidimensional load path of uniaxial compressive stress. It is observed in many materials that lateral damage evolves under this loading. The lateral stress components are zero while the lateral elastic strain components are tensile. If a stress-based criterion was employed, then the deactivation would not be properly represented. A projection operator employing a smooth function based on the total strain tensor was introduced in equation (31). This projection operator is used in addition to a positive projection operator associated with the elastic strain tensor. First consider the spectral decomposition of $\boldsymbol{\epsilon}^e$

$$\boldsymbol{\epsilon}^e = \sum_{i=1}^{3} \epsilon_i^e (\boldsymbol{r}_i \otimes \boldsymbol{r}_i) \tag{42}$$

where ϵ_i^e is the ith eigenvalue and the unit vector, $\boldsymbol{r}_i$, is the corresponding ith eigenvector of $\boldsymbol{\epsilon}^e$. In general, the eigenvectors of $\boldsymbol{\epsilon}$ and $\boldsymbol{\epsilon}^e$ are not equal. The positive (tensile) spectral tensor corresponding to the elastic strain is defined as

$$S^{q+} \equiv \sum_{i=1}^{3} q(\epsilon_i^e)(\boldsymbol{r}_i \otimes \boldsymbol{r}_i). \tag{43}$$

The positive spectral projection operator for the elastic strain (fourth-order tensor) is defined as

$$\mathbf{R}^{q+} \equiv S^{q+} \wedge S^{q+}. \tag{44}$$

Again, the relation for the positive projection of $\boldsymbol{\epsilon}^e$

$$(\boldsymbol{\epsilon}^e)^+ = \mathbf{R}^{q+} : \boldsymbol{\epsilon}^e \tag{45}$$

is only valid if the eigenvalues of $\boldsymbol{\epsilon}^e$ are exterior to the transition domain $[x_l, x_h]$. With the use of the smooth projection operator based on total strains, an elastoplastic "mode I" positive projection operator is defined as follows:

$$\mathbf{T}^{q+} \equiv \mathbf{I} - (\mathbf{I} - \mathbf{P}^{q+}) : (\mathbf{I} - \mathbf{R}^{q+}). \tag{46}$$

The active damage tensor is given by

$$\boldsymbol{D}^{\text{act}} \equiv \mathbf{T}^{q+} : \boldsymbol{D} \tag{47}$$

and the active stiffness tensor is determined according to Eq. (19). In the absence of plastic behavior, $\boldsymbol{\epsilon}^T = \boldsymbol{\epsilon}^e$ resulting in $\mathbf{R}^{q+} = \mathbf{P}^{q+}$ based on Eqs. (31) and (44). By substituting this result into Eq. (46), it can be shown that $\mathbf{T}^{q+}$ degenerate to $\mathbf{P}^{q+}$ in the absence of plastic behavior.

5.2 Uniaxial Stress Example. A multidimensional generalization to the coupled formulation examined in Section 3.2 is illustrated here. A common procedure for coupling elastoplasticity and damage is to substitute the effective stresses in a traditional yield function. Consider von Mises perfect plasticity with associated flow, which implies a yield function of the form

$$\varphi(\hat{\boldsymbol{\sigma}}) = \bar{S} - \sigma_y \tag{48}$$

where σ_y is the yield stress that equals 200 as in Section 3.2, and

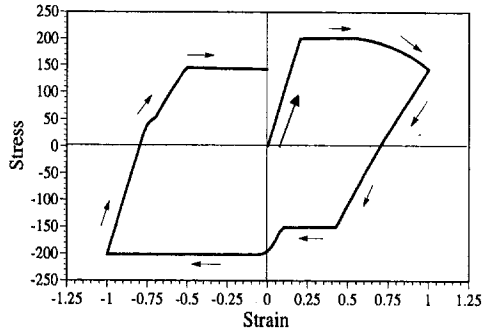

Fig. 8 Stress response to cyclic strain load using multidimensional coupled formulation with smoothing function

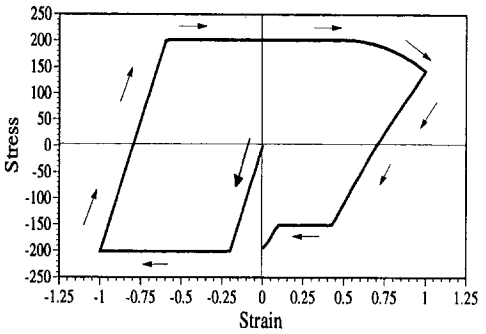

Fig. 9 Stress response to reversed cyclic strain load using multidimensional coupled formulation with smoothing function

$$\bar{S} = \left(\frac{3}{2}\hat{\boldsymbol{\sigma}}^d : \hat{\boldsymbol{\sigma}}^d\right)^{1/2}$$

$$\hat{\boldsymbol{\sigma}}^d = \hat{\boldsymbol{\sigma}} - \frac{1}{3}(\hat{\boldsymbol{\sigma}} : \boldsymbol{i})\boldsymbol{i}. \tag{49}$$

An associative flow rule is assumed, resulting in

$$\boldsymbol{\epsilon}^p = \dot{\lambda}\mathbf{M}(\boldsymbol{D}) : \hat{\boldsymbol{\sigma}}^d \tag{50}$$

where λ is a plasticity consistency parameter that follows the Kuhn-Tucker restrictions analogous to those given in Eq. (39).

With the use of this plasticity model and the multidimensional damage theory of Section 4 including damage deactivation, the axial stress (σ_{11}) versus the total axial strain (ϵ_{11}) is shown in Fig. 8. Prior to the initiation of damage ($\epsilon_{11} = 0.5$), the material behaves as elastic-perfectly plastic. After this point the stiffness tensor begins to degrade. Since the lateral strains are compressive, only the axial components of the damaged stiffness are active. When the path crosses the zero stress axis, the lateral elastic strains become tensile but no damage exists in the lateral directions. As the path approaches the zero strain axis, deactivation of the effect of damage begins in the axial direction. After the path crosses the axis of zero strain, the axial stiffness is restored to the undamaged condition. The axial stiffness returns to the damaged value after the axial elastic strain changes to a tensile state. The damage is not completely reactivated until the stress is greater than zero because of the transition domain employed by the smoothing function.

An additional load case is also illustrative. The prescribed load cycle is reversed so that the cycle progresses through the compressive phase first. With this input, the axial stress-strain response is shown in Fig. 9. During the first 5/8 of the input cycle the material remains undamaged and behaves as an elastic-perfectly plastic cycle. In the final 3/8 of the cycle the damage evolves and degrades the stiffness. It is not until the very last portion of the cycle that the damage deactivation algorithm begins to affect the response.

Downloaded 04 May 2010 to 171.66.16.28. Redistribution subject to ASME license or copyright; see http://www.asme.org/terms/Terms_Use.cfm

6 Conclusions

In modeling the response of materials using continuum damage mechanics, the effects of damage can be inactive under certain states of stress and strain. A method for deactivating and subsequently reactivating the evolved effects of damage has been presented for a class of continuum damage theories. The approach was demonstrated with one-dimensional cases of damaged elasticity and elastoplasticity coupled with damage. Yet, for the case of elastoplasticity coupled with damage, a damage deactivation algorithm dependent only on the total strain was shown to be inappropriate. Motivated by the one-dimensional case, a more suitable algorithm based on both total strain and elastic strain was introduced. In addition, it is shown that for the coupled formulation the use of the Heaviside function results in a discontinuous stress-strain response. This discontinuity is remedied by replacing the Heaviside function with a continuous function defined over a transition domain. Subsequently these results were generalized for multidimensional constitutive relations for both damaged elasticity and coupled formulations. Strain-based projection operators are utilized to invoke the appropriate damage components in the directions of tensile principal strains. The damage deactivation formulation presented here is an algorithm which satisfies the conditions of anisotropy, symmetry of the stiffness tensor, and continuity of the response. The algorithm has been illustrated by providing the stress response for a strain controlled cycle.

Acknowledgments

This work was supported by the U.S. Department of Energy under Contract DE-AC04-76DP00789. This paper is based in part on the first author's Ph.D. dissertation.

References

Bammann, D. J., and Aifantis, E. C., 1989, "A Damage Model for Ductile Metals," *Nuclear Engineering and Design*, Vol. 116, pp. 355–362.

Berthaud, Y., Laborderie, C., and Ramtani, S., 1990, "Damage Modeling and Crack Closure Effect," *Damage Mechanics in Engineering Materials*, ASME Winter Annual Meeting, by J. W. Ju, D. Krajcinovic, and H. L. Schreyer, eds., pp. 263–276.

Brodsky, N. S., 1990, "Crack Closure and Healing Studies in WIPP Salt Using Compression Wave Velocity and Attenuation Measurements: Test Methods and Results," Sandia National Laboratories Technical Report, SAND90-7076.

Chaboche, J.-L., 1992, "Damage Induced Anisotropy: On the Difficulties Associated with the Active/Passive Unilateral Condition," *International Journal of Damage Mechanics*, Vol. 1, pp. 148–171.

Chow, C. L., and Wang, J., 1987, "An Anisotropic Theory of Continuum Damage Mechanics for Ductile Fracture," *Engineering Fracture Mechanics*, Vol. 27, No. 5, pp. 547–558.

Cordebois, J. L., and Sidoroff, F., 1979, "Anisotropie Elastique Induite par Endommagement," Colloque Euromech 115, Grenoble, Editions du CNRS, No. 295, 1982.

Costin, L. S., 1983, "A Microcrack Damage Model for Brittle Rock," Sandia National Laboratories Technical Report, SAND83-1590.

Hansen, N. R., 1992, "Theories of Elastoplasticity Coupled With Continuum Damage Mechanics," Ph.D. Dissertation, University of New Mexico, Albuquerque, NM.

Holcomb, D. J., 1984, "Discrete Memory in Rock: A Review," *Journal of Rheology*, Vol. 28, No. 6, pp. 725–757.

Ju, J. W., 1989, "On Energy-Based Coupled Elastoplastic Damage Theories: Constitutive Modeling and Computational Aspects," *International Journal of Solids and Structures*, Vol. 25, pp. 803–833.

Krajcinovic, D., 1989, "Damage Mechanics," *Mechanics of Materials*, Vol. 8, pp. 117–197.

Krajcinovic, D., and Fonseka, G. U., 1981, "The Continuous Damage Theory of Brittle Materials, Parts I and II," ASME JOURNAL OF APPLIED MECHANICS, Vol. 48, pp. 809–824.

Ladeveze, P., and Lemaitre, J., 1984, "Damage Effective Stress in Quasi-Unilateral Material Conditions," *IUTAM Congress*, Lyngby, Denmark.

Lemaitre, J., 1985a, "Coupled Elasto-Plasticity and Damage Constitutive Equations," *Computer Methods in Applied Mechanics and Engineering*, Vol. 51, pp. 31–49.

Lemaitre, J., 1985b, "A Continuous Damage Mechanics Model for Ductile Fracture," ASME *Journal of Engineering Materials and Technology*, Vol. 107, pp. 83–89.

Lemaitre, J., 1987, "Formulation and Identification of Damage Kinetic Constitutive Equations," *Continuum Damage Mechanics: Theory and Application*, D. Krajcinovic and J. Lemaitre, eds., Springer-Verlag, New York, pp. 37–89.

Murakami, S., 1988, "Mechanical Modeling of Material Damage," ASME JOURNAL OF APPLIED MECHANICS, Vol. 55, pp. 280–286.

Ortiz, M., 1985, "A Constitutive Theory for the Inelastic Behavior of Concrete," *Mechanics of Materials*, Vol. 4, pp. 67–93.

Ramtani, S., 1990, "Contribution a la Modelisation du Comportement Multiaxial du Beton Endommage Avec Description ue Caractere Unilateral," These, Univ. Paris VI.

Simo, J. C., and Ju, J. W., 1987, "Stress and Strain Based Continuum Damage Models, Parts I and II," *International Journal of Solids and Structures*, Vol. 23, pp. 821–869.

Yazdani, S., and Schreyer, H. L., 1990, "Combined Plasticity and Damage Mechanics Model for Plain Concrete," *ASCE Journal of Engineering Mechanics*, Vol. 116, No. 7, pp. 1435–1450.

Downloaded 04 May 2010 to 171.66.16.28. Redistribution subject to ASME license or copyright; see http://www.asme.org/terms/Terms_Use.cfm

Bending of Superelastic Wires, Part I: Experimental Aspects

B. T. Berg[1]
Army High Performance Computing Research Center, University of Minnesota, Minneapolis, MN 55455

A pure-bending apparatus is used to measure the constitutive relationship between applied pure bending moments and the resulting curvatures of a few superelastic alloy wires. The sample nickel-titanium alloy (NiTi) wires change phase when ample bending moments are imposed. Like the material's uniaxial tension stress-strain relationship, the measured moment-curvature relationship shows plateaus of constant moment and hysteresis. The bent shape is circular, except in the mixed phase region where it is composed of a phase mixture of circles. An example of the applications of the measured moment-curvature relations is presented in Part II of this paper where the three-point bending problem is considered.

1 Introduction

Various compositions of nickel-titanium (NiTi) alloys undergo stress-induced austenite-martensite phase transitions at room temperature, e.g., (Jackson, Wagner, and Wasilewski, 1972). The uniaxial tensile behavior of these materials is well known. However, in applications such as orthodontic arch wires, interventional guidewires, and in simple heat engines (Berg, 1994), the bending properties are used, not the tensile properties. Though estimates may be made to predict the bending moment-curvature relationship from the uniaxial stress-strain relationship (Atanackovič and Achenbach, 1989), this involves many assumptions. Presented here are the simple methods and some characteristic results of pure-bending experiments which measure the bending behavior of superelastic NiTi wire.

In particular, Section 2 describes a new pure-bending apparatus. The design uses a dead-loaded body, the moment applicator, to apply a pure and dead moment to the free end of a cantilever beam. The device is unstable with respect to out-of-plane rotations unless the moment applicator is constrained to move in the plane normal to the applied moment. The choice of using a load-controlled device to investigate the phase transition behavior of superelastic materials was made because of the high curvature capability of the device, the simplicity of the device, and because the measurement of the dead load response is of inherent interest in itself. As noted by Bell in a discussion of load-controlled and deformation-controlled experiments (Bell 1984, pp. 125), "...the differences among the data are far from trivial, and represent fundamental changes in the response of the material."

Section 3 presents the measurement process and the measured moment-curvature relationships for various NiTi wires. A bending-moment-induced phase transition was seen during the pure-bending experiments. This behavior is similar to the discontinuous phase change behavior in bending discussed by Fosdick and James (1981). The moment-curvature relationship appears to be effected by prior bending or stretching.

In Part II of this paper, the measured moment-curvature relationship is applied to a three-point bending problem and a comparison is made between experiment and theory.

2 Pure Bending Apparatus and Moment Applicator Stability

2.1 Experimental Device. Many studies on bending by pure moments use four-point bending devices to examine radii of curvatures on the order of 40 to 100 times the beam height. Here the radius of curvature may be less than five times the wire diameter. In particular, when the material under investigation undergoes a moment-induced phase transition, a small change in moment may cause the radius of curvature to change from 25 to 6 times the wire diameter. To achieve this large range in curvatures, my advisor and I devised a moment applicator which translates and rotates through the course of the experiment.

The apparatus used to impose a pure-bending moment on a wire specimen is shown in Figs. 1 and 2. The basic technique is to provide equal and opposite forces which pull on two strings which unwrap from opposite sides of the 25-mm diameter of the moment applicator. The moment applicator, free to translate and rotate in the plane-of-bending, imposes a bending moment on the free end of a cantilevered wire specimen. The 76-mm base of the moment applicator prevents its rotation out of the bending plane. Glass beads on the support plane under the base provide a low-friction surface for the motion of the moment applicator. The strings

[1] Current address: Flexmedics, 12400 Whitewater Drive, Suite 2040, Minnetonka, MN 55343.

Contributed by the Applied Mechanics Division of THE AMERICAN SOCIETY OF MECHANICAL ENGINEERS for publication in the ASME JOURNAL OF APPLIED MECHANICS.

Discussion on this paper should be addressed to the Technical Editor, Professor Lewis T. Wheeler, Department of Mechanical Engineering, University of Houston, Houston, TX 77204-4792, and will be accepted until four months after final publication of the paper itself in the ASME JOURNAL OF APPLIED MECHANICS.

Manuscript received by the ASME Applied Mechanics Division, Jan. 19, 1993; final revision, Mar. 8, 1994. Associate Technical Editor: R. Abeyaratne.

Copyright © 1995 by ASME

Downloaded 04 May 2010 to 171.66.16.28. Redistribution subject to ASME license or copyright; see http://www.asme.org/terms/Terms_Use.cfm

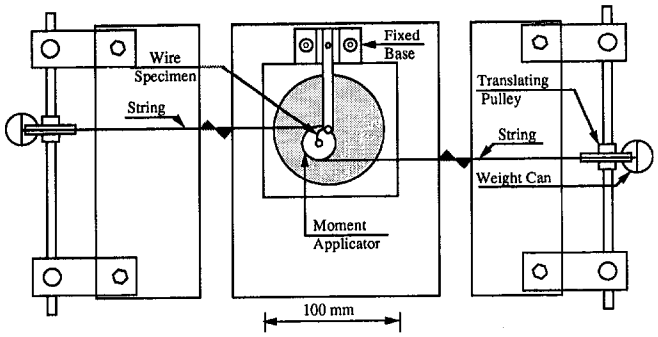

Fig. 1 Top view of the experimental bending apparatus

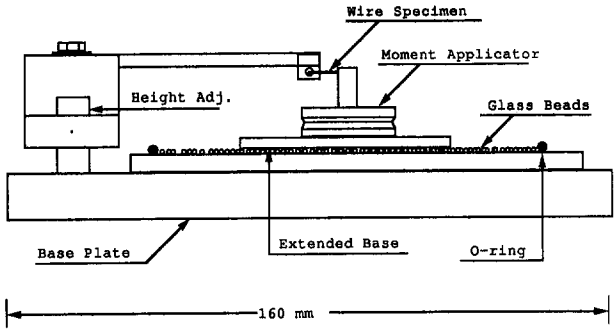

Fig. 2 Side view of the experimental bending apparatus

from the moment applicator are laid over pulleys and are tied to weight cannisters. The pulleys are mounted on linear motion bearings to allow adjustment to keep the strings parallel as the moment applicator translates. Each translating pulley is a 38-mm O.D. aluminum pulley wheel mounted on a 15.9 mm (5/8 in.) I.D. PTFE slug separator bearing mounted on a 6.35 mm (1/4 in.) I.D. linear bearing. Each weight cannister holds the 6.35 mm (1/4 in.) or 9.52 mm (3/8 in.) ball bearings that are added as weights. The apparatus is a soft device in the sense that the loads are determined and the deflections are free.

2.2 Dead Load Stability. The experimental fact that the moment applicator likes to flip over if the base is not large enough was predicted prior to the construction of the apparatus. The dead forces which produce the dead moment add energy that makes the apparatus unstable. Since the method of analysis is applicable to many dead-load situations and provides the mathematical criteria for improving our current design, I will briefly describe the assumptions, state the problem, and state a theorem which governs the stability.

For this analysis of stability of a rigid body with dead forces, it is assumed that: (1) each force is applied at a fixed point of the body; (2) the direction and magnitude of each force is constant; (3) the motion of the rigid body is not constrained, that is, the admissible displacements of the body can be represented by all translations and all rotations.

For a rigid body acted on by n dead forces, define the loading tensor T

$$T \equiv \sum_{i=1}^{n} s_i \otimes F_i, \tag{1}$$

where $s_i \in \Re^3$, with units of length, is the vector from an origin to the point where the force $F_i \in \Re^3$, with units of force, acts.

By energetic considerations, the body is absolutely stable if the strict inequality

$$\mathrm{tr}(T) > \mathrm{tr}(RT), \forall R \in \mathcal{O}^+, \ \Re \neq \infty, \tag{2}$$

is satisfied, where $\mathrm{tr}(\cdot)$ is the trace operator, and $\mathcal{O}^+$ is the set of all proper rotations in $\Re^3$.

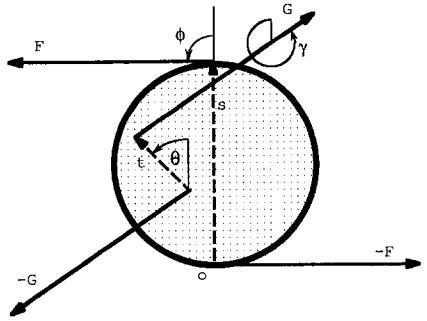

Fig. 3 Geometry of the bending applicator

Theorem 1 (Absolute Stability). Let T be any 3 by 3 matrix. The necessary and sufficient conditions that $\mathrm{tr}(T) > \mathrm{tr}(RT)$, $R \in \mathcal{O}^+$, $\Re \neq \infty$, *are that T is symmetric and that the eigenvalues* $(\{\tau_1, \tau_2, \tau_3\} | \tau_1 \leq \tau_2 \leq \tau_3)$ *of T satisfy* $\tau_1 + \tau_2 > 0$, $\tau_3 \geq \tau_2 > 0$.

For a proof of the theorem see Berg (1994). In the next section, the theorem will be applied to analyze the stability of dead loaded bending devices.

2.3 Stability of Pure Bending Devices. The loading of many pure-bending devices can be idealized as two pairs of forces producing equilibrating couples (four-point loading). Assuming this and after a bit of cancellation, the loading tensor $T = s \otimes F + t \otimes G$, where F and G are one of each pair of equilibrating forces, and s and t are the vectors which connect each force with their equilibrating opposite, respectively, $-F$ and $-G$ (see Fig. 3). The coordinates (in an orthonormal basis) of s, F, t, and G may be expressed.

$$s = \{\sigma, 0, 0\}, \quad F = \{\Phi \cos(\phi), \Phi \sin(\phi), 0\},$$
$$t = \{\tau \cos(\theta), \tau \sin(\theta), 0\},$$
$$G = \{\Gamma \cos(\gamma), \Gamma \sin(\gamma), 0\}. \tag{3}$$

Without loss of generality, assume the scalars σ, τ, Φ, and Γ are greater than zero. Additionally, restrict the angle ϕ such that $\pi > \phi > 0$. This restriction of ϕ is without loss of generality, except for $\phi = 0$, since the direction of increasing angle is arbitrary. Restrict the other angles to their principal values: $\theta \in [0, 2\pi)$, and $\gamma \in [0, 2\pi)$.

Applying Theorem 1 yields the stability requirements

$$\sin(\theta - \gamma) > 0, \tag{4}$$

$$\sin(\theta)\sin(\gamma) > 0, \tag{5}$$

$$\sin(\theta)\sin(\gamma - \phi) > 0, \tag{6}$$

$$\frac{\sin(\theta - \gamma)\cos(\phi)}{\sin(\phi)} + \cos(\theta)\cos(\gamma) > 0, \tag{7}$$

under the restrictions σ, τ, Φ, $\Gamma > 0$ and $\pi > \phi > 0$.

Similar to the problem of a body subject to only two forces, Eqs. (4) and (5) require the projection of the forces G and $-G$ in the direction perpendicular to the s-axis and in the plane of the forces to be tensile; a compressive projection would be unstable. The gray regions and the white regions shown in Fig. 4 satisfy these conditions.

Relations (6) and (7) are dependent on the angle ϕ between s and F. If ϕ approaches zero, the relations (6) and (7) are equivalent to (4) and (5). As a rule, the closer ϕ is to zero—the closer the forces F and $-F$ are to a tensile load—the greater the area on the (θ, γ) plane of stable configurations.

For our experimental loading device, as in shown in Fig. 3, the angle ϕ between s and F is equal to $\pi/2$. With this, the four conditions, Eqs. (2.4) through (7), yield the white regions of stability in the (θ, γ) plane shown in Fig. 4. It is conjec-

Downloaded 04 May 2010 to 171.66.16.28. Redistribution subject to ASME license or copyright; see http://www.asme.org/terms/Terms_Use.cfm

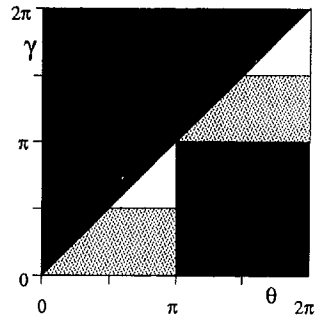

Fig. 4 The (θ, γ) plane corresponding to the stability requirements. The white regions are stable for $\phi = \pi/2$.

tured that for the reaction forces the angle $\theta = \gamma + \pi/2$. The angle γ would typically increase from 0 to approximately $3\pi/2$ radians as the bending moments are increased during the loading half of each experiment. The result is that this loading is unstable for all loads.

In practice, however, with careful adjustment of the fixed end to assure that the wire is in a plane parallel to the plane of the applied forces, the bending motion was fairly stable at small loads even with only a 25-mm diameter base. To increase the stability, the moment applicator base was increased to 75 mm. This kept the experiment in the plane for all subsequent experiments. This constraint does not restrict the interpretation of the moment-curvature relationship *provided* the unconstrained deformation of the specimen with applied pure moments is in the same plane as the moments and without torsion. If the design could be modified to meet the constraints of Theorem 1, then this restriction could be removed.

3 Pure-Bending Experiments

3.1 Experimental Conditions. The wire samples used in the bending experiments are sections of NiTi dental arch wire supplied by Flexmedics Corporation, Minneapolis, Minnesota. The NiTi wire is nominally 55 Ni 45 Ti (weight percent). All the cross-sections are circular except for the last which is rectangular. Diameter measurements are ± 0.0025 mm (0.0001 in.). Where mentioned, the transition temperatures were measured by the changes in electrical resistivity as a function of temperature. These experiments (Mar. 1994) show that the wires undergo $M \leftrightarrow R \leftrightarrow A$ phase transitions (monoclinic, rhombohedral, and cubic phases, respectively). The wires tested are

0.401 mm, fairly straight section of *U*-shaped dental arch wire, as received and after 1 hr at 400°C;

0.457 mm, fairly straight sections of *U*-shaped dental arch wire;

0.518 mm, straight wire, sample #41236, $R \rightarrow M_s = -70°C$, $M \rightarrow R_s = -13°C$, $R \rightarrow A_s = 0°C$;

0.632 mm, straight wire, sample BS040389, $R \rightarrow M_s = -60°C$, $M \rightarrow R_s = -32°C$, $R \rightarrow A_s = -8°C$;

0.907 mm, straight wire, sample BS041989, $R \rightarrow M_s = -60°C$, $M \rightarrow R_s = -21°C$, $R \rightarrow A_s = -10°C$;

0.650 by 0.554 mm, straight wire, sample #S2125 Lot 20971, $R \rightarrow M_s = -65°C$, $M \rightarrow R_s = -16°C$, $R \rightarrow A_s = 1°C$.

The various experiments will be denoted by the date they were performed or started. This notation is useful due to possible changes in material properties as a result of the effects of prior history and of material aging.

Before the bending of the arch wires and the 0.518 mm wire, the samples were bent to a state just beyond the phase transition and held overnight in this state. The next day the wires were unloaded and the bending run was begun. This "training" was done to provide an estimate of the transition moment and in the hope of increasing repeatability. A review of the results shows this training has an effect on the bending behavior.

During the test, the wire is bent slowly—the curvature is measured after a specific period elapses after changing the applied moment. The periods range from 12 min to 12 h. Most commonly the periods are one hour. These slow rates were chosen to assure equilibrium conditions. Weights are applied sequentially up to a peak value, then ordinarily decreased back down to zero. Before adding or removing a portion of the load increment, the strings are fixed. After adding (removing) the weights, the strings are released by simultaneously removing the fixturing. This method of loading overshoots the equilibrium moment level before settling to equilibrium; it is not a quasi-static loading increment though the added loads are kept small. If only part of the load increment has been added, the process is repeated. When the specified waiting period has elapsed, a sequence of wire edge positions are located by eye through a 50x optical microscope and the position of the attached *x-y* micrometer stage is then recorded. The view of the microscope is from above, as in Fig. 1.

3.2 Calculation of Curvature. From any three positions on the sample's edge or center, a curvature can be determined. Calling the three positions (0, 0), (u, v), and (x, y), the radius of curvature is

$$r = \sqrt{\frac{(u^2 + v^2)(x^2 + y^2)\left((u - x)^2 + (v - y)^2\right)}{4(uy - vx)^2}}. \quad (8)$$

Due to the uncertainty in locating the wire edge positions—at best ± 0.002 mm, accounting for both the stage resolution and observer skills—this calculation reliably determines the curvatures only when the circular arc defined by the three points is subtended at the center of curvature by a sufficient angle. To elucidate, call δr the root mean square uncertainty in the radius. Assuming equal uncertainties $\delta L \equiv \delta x = \delta y = \delta u = \delta v$,

$$\delta r = \delta L \sqrt{\left(\frac{\partial r}{\partial x}\right)^2 + \left(\frac{\partial r}{\partial y}\right)^2 + \left(\frac{\partial r}{\partial u}\right)^2 + \left(\frac{\partial r}{\partial v}\right)^2},$$

where δL is the uncertainty in distance. Assume the symmetric points (0, 0), (x, $-y$), (x, $+y$) were measured on the wire edge. Then

$$\delta r = \frac{r\delta L\sqrt{2}}{x} = \frac{\delta L\sqrt{2}}{1 - \cos(\theta/2)},$$

where θ is the angle subtended by the arc at the center such that $x = r(1 - \cos(\theta/2))$. The probable accuracy of the measurement thus depends on the subtended angle, and is probably poor when the angle is small. For small angles of bending or equivalently small curvatures of short specimens, the determination of the radius from three points is too sensitive to small errors in position to be of much use.

A more successful approach to the measurement of curvature is to measure more than three points and apply Gauss's method of least-square differences. Call the measured data the set of n points, $\{(x_i, y_i), i = 1, 2, \ldots n\}$. Assuming the data are measurements of a circle, a good estimate of the radius r and the center (a, b), is given by the minimizing S, the square of deviations from r^2,

$$S = \sum_{i=1}^{n} \left((x_i - a)^2 + (y_i - b)^2 - r^2\right)^2,$$

Downloaded 04 May 2010 to 171.66.16.28. Redistribution subject to ASME license or copyright; see http://www.asme.org/terms/Terms_Use.cfm

over all choices of $\{r, a, b\}$. This minimization yields (a, b) as the solution to the linear equations

$$\begin{vmatrix} n\Sigma x^2 - (\Sigma x)^2 & n\Sigma xy - \Sigma x\Sigma y \\ n\Sigma xy - \Sigma x\Sigma y & n\Sigma y^2 - (\Sigma y)^2 \end{vmatrix} \begin{vmatrix} 2a \\ 2b \end{vmatrix}$$

$$= \begin{vmatrix} n\Sigma x^3 - \Sigma x^2\Sigma x + n\Sigma xy^2 - \Sigma x\Sigma y^2 \\ n\Sigma y^3 - \Sigma y^2\Sigma y + n\Sigma yx^2 - \Sigma y\Sigma x^2 \end{vmatrix} \quad (9)$$

and

$$r = \sqrt{a^2 + b^2 + (\Sigma x^2 + \Sigma y^2 - 2a\Sigma x - 2b\Sigma y)/n}\,. \quad (10)$$

Once the best fit radius of the measured points is determined, the curvature of the beam is calculated. The edge, on the side of the bent beam's arc which contains the center of curvature, will be called the inside edge. Depending on which edges are measured, the estimated curvature is

$$\kappa = \begin{cases} 1/(r_{in} + R) & \text{inside edge measured,} \\ 1/(r_{out} - R) & \text{outside edge measured,} \\ 2/(r_{in} + r_{out}) & \text{both edges measured,} \end{cases} \quad (11)$$

where R is the beam radius or the half width of the beam's cross-section, and r_{in} and r_{out} are calculated from Eqs. (9) and (10) using points on the inner or outer edges.

Better resolution of small curvatures can be achieved by using a longer piece of wire, but at the cost of a lower maximum curvature. The maximum curvature is limited by the moment applicator rotating and translating into the fixed end; i.e., the largest curvature is $2\pi/L$ where is L is the length of the wire.

3.3 Elasticity Scaling. To compare wires of different diameters, the plots have the deformation measure, $R\kappa$, as the abscissa and the stress measure, MR/I, as the ordinate. The curvature is κ, the applied moment is M, the wire radius is R, and the second moment of inertia is I. Call $R\kappa$ the *curvature-strain* and the MR/I the *moment-stress*. Like the stress versus measures for uniaxial tensile tests, these bending measures are valid for nonlinear materials as well as linear materials.

These scalings are results of the scaling law of elasticity: if $y_1 : \Omega \subset \Re^3 \to \Re^3$ is an allowable deformation of an elastic body Ω, then $y_2(x) = \lambda y_1(x/\lambda) \forall x \in \lambda\Omega$ is an allowable deformation of the scaled body $\lambda\Omega$. For application to bending, the curvature-strain measure follows by applying the scaling law to the bending deformations that map lines parallel to the longitudinal axis into circular arcs. This deformation is found for all our initially straight homogeneous prismatic specimens, outside of the phase transformation region. Since in the phase transformation region the deformation is approximated by the best fit circular arc, this measure is also used inside this region. The moment-stress measure follows by using the scaling law to relate the deformation gradients in the two bodies, and then integrating the Piola-Kirchoff stress across each of the two bodies' cross-sections. For details see Berg (1994).

3.4 Experimental Results. In Fig. 5, scaled moment-curvature relationships are presented for the three straight wires with circular cross-sections. Sequentially increasing the applied moments produce the points on the upper curves; decreasing moments produce the points on the lower curves. The three wires had similar heat treatments and show similar moment-curvature relationships. The initial slopes of the 0.632 and 0.907 mm wires' moment-curvature relationships are similar, 69,500 ± 1000 N/mm^2. Their loading transition moment-stresses are also similar, 850 ± 50 N/mm^2. The initial slope of the 0.518 mm wire's moment-curvature relationship (point 2 through 5) is somewhat lower, 60,000 N/mm^2. The post-transition curvature strain is lower for the 0.518 mm wire than the 0.632 and 0.907 mm wires, 0.065 versus 0.079. The unloading transition moment-stress of the 0.907 mm wire is lower than the 0.632 mm wire, 230 versus 370 N/mm^2. As in tensile experiments, the greater the peak curvature-strain, the lower the unloading transition moment-stress.

A second set of experiments were done on the 0.632 mm wire. Prior to the June 1990 bending experiment, the 0.632 mm wire was stretched four times at a strain rate of 2 10^{-4}/sec to 8.6 percent strain (Fig. 6). Three days after this training, the pure-bending experiment was performed on the wire yielding the results displayed in Fig. 7. The resulting moment-curvature relationship is significantly different than the May and June 1989 experiments on the same wire. The initial slope decreased: as calculated from the first four points of each curve, the slopes are 69,100 N/mm^2 in the first experiment, 68,900 in the second and 49,200 in the last. The post-transition curvature-strain also decreased, 0.085 in the first, 0.081 in the second, and 0.063 in the last. The loading transition moment-stress during loading also decreased, from near 900 N/mm^2 in the first two experiments to 700 N/mm^2

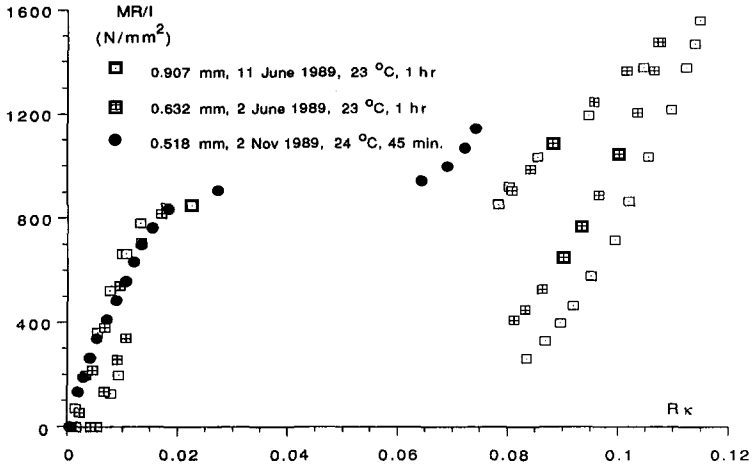

Fig. 5 Moment versus curvature for virgin 0.907, 0.632, and prior bent 0.518 mm NiTi wires

Downloaded 04 May 2010 to 171.66.16.28. Redistribution subject to ASME license or copyright; see http://www.asme.org/terms/Terms_Use.cfm

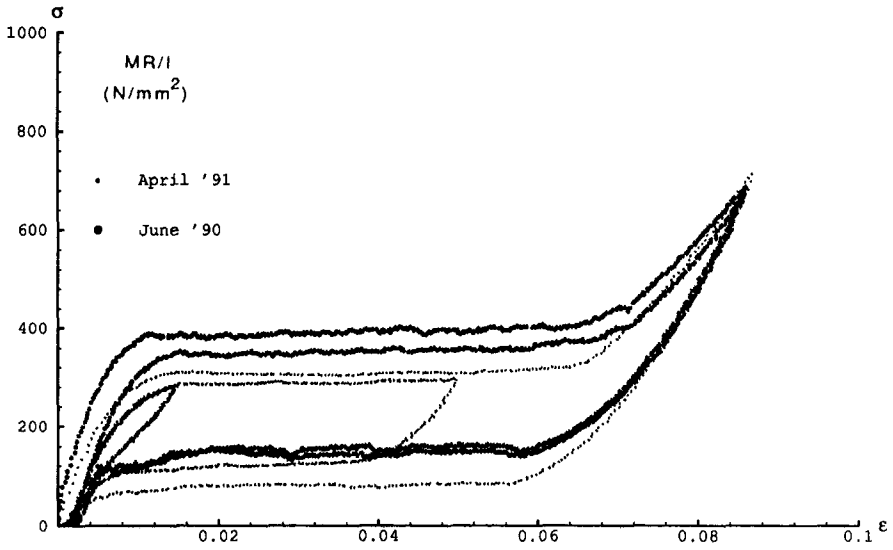

Fig. 6 Stress versus strain relation for the 0.632 mm NiTi wire

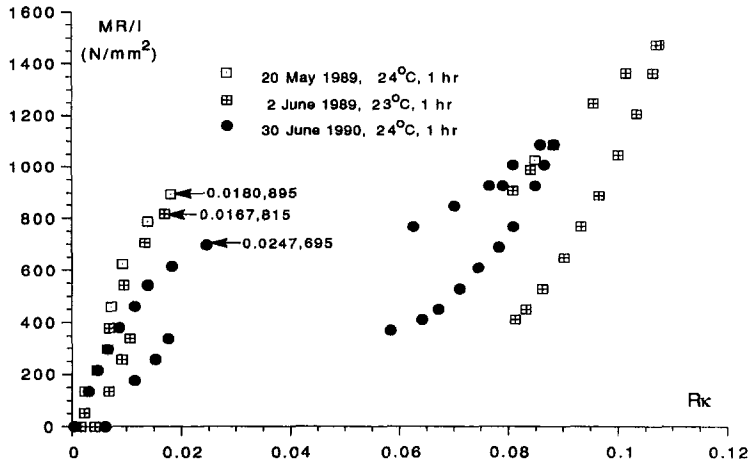

Fig. 7 Moment versus curvature for virgin and prior stretched 0.632 mm diameter NiTi wire

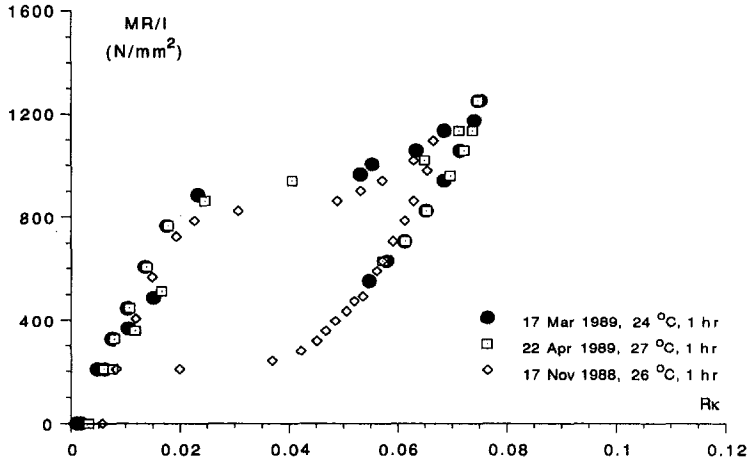

Fig. 8 Moment versus curvature for 0.401 mm diameter NiTi wire

in the last. The reverse transformation moment-stress is fairly constant.

In Fig. 8 the moment-curvature relationship is shown for the 0.401 mm wires. Since the samples are from portions of *U*-shaped dental arch wires, many samples have initial curvature. The 17 Nov. 1988 experiment was on a wire that was heat treated at 450°C for one hour followed by air cooling. The initial slope of all these 0.401 mm wires is significantly lower than for the straight wires, 47,000 ± 4,000 N/mm^2. The post-transition curvature-strain is the smallest of all the specimens.

Prior to the bending of the 0.650 by 0.554 mm wires, the

Downloaded 04 May 2010 to 171.66.16.28. Redistribution subject to ASME license or copyright; see http://www.asme.org/terms/Terms_Use.cfm

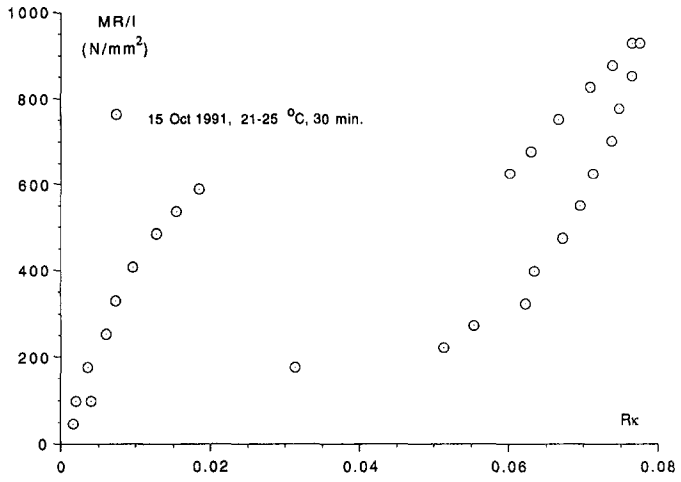

Fig. 9 Moment versus curvature for the exercised 0.650 by 0.554 mm NiTi wire

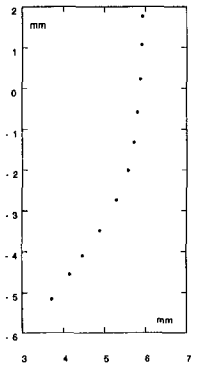

x	y	r
3.719	-5.155	
4.153	-4.547	
4.473	-4.094	132.05
4.880	-3.486	25.61
5.294	-2.740	9.52
5.567	-2.005	5.43
5.719	-1.320	5.42
5.803	-0.577	6.85
5.865	0.233	21.56
5.909	1.071	34.50
5.926	1.767	27.38

Fig. 10 Points on the 0.650 by 0.554 mm wire in the phase transition region, $MR/I = 175$, $Rk = 0.0313$

wires were stretched in uniaxial tension. Following these tensile tests, the wire was bent on the pure bending apparatus. Shown in Fig. 9 are the results of the pure-bending experiment on the rectangular cross-section wire. The curves are qualitatively similar to the results from the circular cross-section wires. There is, however, a notable data point in the middle of the return phase transition.

In Fig. 10, this unusual data point is looked at in detail. By using the three-point calculation of a circle, a local estimate of the radius can be made. As tabulated, there is a much smaller radius in the center of the wire than near the ends. On calculating the curvature-strain from the measured three-point radii, the center's $R\kappa$ is approximately 0.049 and the two ends $R\kappa$ are approximately 0.011. These two values agree with the high curvature and low curvature phases, respectively, as shown in Fig. 9. Hence, in the phase transition region the shape may be thought of as a phase mixture of circles.

3.5 Errors, Reliability, and Interpretation of Results. Since the calculation of curvature is based on the premise that the data always describes a circular arc, having a measure of how well the circular arcs fit the data is desirable. For an error estimate I use the average of the absolute deviations of the pointwise differences between the least-square radius and the distance from measured points to the least square center,

$$\epsilon = \left(\sum_{i=1}^{n} \left| r - \sqrt{(a - x_i)^2 + (b - y_i)^2} \right| \right) / n. \quad (12)$$

This error estimate has been applied to the 0.518 mm NiTi bending experiment. In this experiment I used a 50 × microscope and positioning table which has 0.001 mm resolution. The average of the errors for the entire experiment, averaging ϵ (12) across all the measures, is 0.0023 mm. The largest error occurred just after the phase transition and is 0.007 mm. Relative to the range of radii of curvature, 100 mm to 2.5 mm, these are small distances and thus illustrate how well circles fit the data in this experiment.

However, a single circular arc does not always describe the bent wire very well. During the phase transition process, as the wire bends from one arc to another, the wire is clearly not bent into a circular arc. During the process, the curvature is usually different in different regions on the wire. I have selected three photos, Fig. 11, which show the bent shape of the wire before, during, and after the loading phase transition. Note that the wire's curve in the second case is obviously noncircular; it appears to be composed of perhaps two different curvatures. Another example of the effects of the phase transition on the shape of the bent wire was presented previously.

Since I have shown that the bent wire shape is well described by circular arcs, except near or during the phase transitions, I will now characterize the self-consistency of the curvature measurement. If points on both the inner and outer edges of a specimen are measured, an uncertainty in curvature based on the difference between various least square radii can be easily calculated. Using Eq. (11), the inner versus outer fractional error is defined:

$$\frac{\kappa_{\text{out}} - \kappa_{\text{in}}}{k_{\text{ave}}} = \left(\frac{1}{r_o - R} - \frac{1}{r_i + R} \right) \Big/ \left(\frac{2}{r_o + r_i} \right).$$

Analysis of the 0.518-mm experiment shows that the fractional error was as large as six percent for $R\kappa_{\text{ave}}$ less than 0.01, and less than 0.5 percent for $R\kappa_{\text{ave}}$ greater than 0.06. The uncertainty in curvature is thus estimated to be five percent before the transition, and 0.5 percent after the transition.

The major known uncertainty in the moment is a result of rotational friction in the translating pulley. This not only varies the applied moment on the moment shaft, but adds a moment which varies with position (a bent cantilever problem). Rotational friction was measured by stringing directly between both pulleys and applying equal weights to each side. Additional weights are then added to one side until its pulley breaks free. From this the uncertainty in the measured moments is estimated to be three percent.

Downloaded 04 May 2010 to 171.66.16.28. Redistribution subject to ASME license or copyright; see http://www.asme.org/terms/Terms_Use.cfm

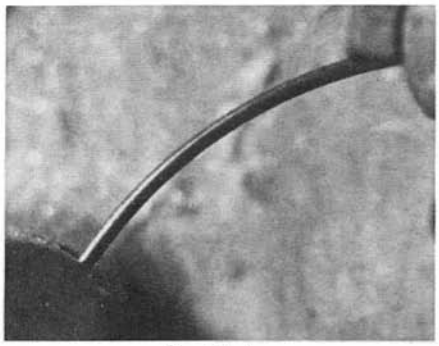

Fig. 11(a)

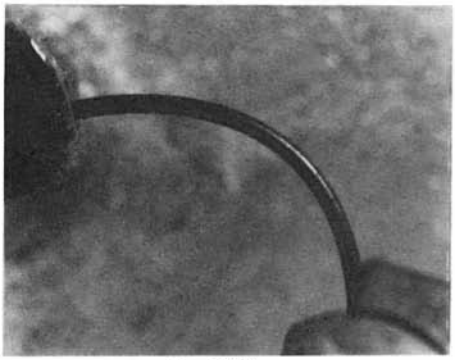

Fig. 11(b)

Fig. 11(c)

Fig. 11 Photographs of a 0.406 mm NiTi wire before, during, and after a bending-induced phase transition due to applied pure-bending moments

Observed negligible uncertainties are the glass ball's frictional force on the moment shaft's motion; the uncertainty in length of the effective moment arm formed by the loaded strings; and how close to parallel the loading strings are.

In spite of the reliability of both the curvature measurement and the moment measurement, the moment-curvature data shows what appears to be significant scatter at a few points, particularly at small curvature. It is believed the scatter is primarily a combination of the uncertainty in curvature at small curvature and the non-quasi-static loading procedure.

As a final note, on review of the data, there appears to be a lowering of the post-transition strain-curvature as a result of prior transformation. This effect is seen by comparison of the 0.401, 0.457, 0.518 mm wire experiments where the wire was bent and held in the transformed state prior to testing pure bending versus the 0.632 and 0.907 mm wire experiments with virgin wire. The effect is also seen to be a result of tensile testing prior to pure bending (the 0.632 and the 0.650 by 0.554 mm wire tests). Prior transformation also appears to lower the transition stress and lower the initial slope of the moment-curvature relationship. Since aging of the material may also play a role in these changes, these effects of prior-transformation will need further experimental investigation.

Acknowledgments

I wish to acknowledge the support of my advisor, Richard James, and the University of Minnesota Army High Performance Computing Research Center fellowship through the Army Research Office, contract number DAALO3-89-C0038.

References

Atanackovič, T., and Achenbach, M., 1989, "Moment-Curvature Relationships for a Pseudoelastic Beam," *Continuum Mechanics and Thermodynamics*, Vol. 1, pp. 73–80.

Bell, J. F., 1984, *The Experimental Foundations of Solid Mechanics* (Mechanics of Solids), Springer-Verlag, Berlin.

Berg, B. T., 1994, *Thermomechanics of Shape Memory Alloy Rods*, Ph.D. thesis, University of Minnesota, Minneapolis, MN.

Fosdick, R. L., and James, R. D., 1981, "The Elastica and the Problem of Pure Bending for a Nonconvex Stored Energy Function," *J. of Elasticity*, Vol. 11, pp. 165–186.

Jackson, C. M., Wagner, H. J., and Wasilewski, R. J., 1972, "55-Nitinol —The Alloy with a Memory, Its Physical Metallurgy, Properties, and Applications," *Technical Report*, National Aeronautics and Space Administration.

Downloaded 04 May 2010 to 171.66.16.28. Redistribution subject to ASME license or copyright; see http://www.asme.org/terms/Terms_Use.cfm

Bending of Superelastic Wires, Part II: Application to Three-Point Bending

B. T. Berg[1]
Army High Performance Computing Research Center, University of Minnesota, Minneapolis, MN 55455

The constitutive relationship between applied pure bending moment and the resulting curvature of a few superelastic alloy wires is applied to the three-point bending problem. Three-point bending experiments on hard and soft loading machines are described. The relationship between the applied deflection and the resulting force in three-point bending is calculated from a nonlinear Euler-Bernoulli rod theory. A numerical procedure used to solve the three-point bending problem for both loading and unloading is briefly described and numerical results are compared with experiment.

1 Introduction

In Part I of this paper, the experimental basis for a bending-induced phase transition in superelastic nickel-titanium alloy (NiTi) alloys was established. In this part the moment-curvature relationship is applied to the three-point bending problem.

Section 2 presents two three-point bending experiments. The three-point bending test is commonly used to characterize material properties of wires, in particular orthodontic arch wires. Substantial differences between the experiments for the same wire before and after training by tensile extension are shown. At a sufficient moment, the local curvature on the bent wire shows a near jump in value consistent with the moment-curvature relationship.

Section 3 presents a mathematical model for the bending behavior of the wires and uses this model to predict the behavior of a wire in three-point bending. For history-independent constitutive relations, energy minimization determines the force required for a prescribed deflection (James 1981). A separate numerical technique is developed, however, to allow the use of history-dependent constitutive relations. This is advantageous when the moment-curvature constitutive relationship has hysteresis as is found with the NiTi samples. The predicted load-deflection relationship is compared with the three-point experiments. They are in relatively good agreement with measured values when similar time scales of bending are used and the wire has been trained by cyclic tensile loading prior to testing.

2 Three-Point Bending Experiments

Two different machines were used to apply three-point bending loads to the NiTi wires. One machine, located at Flexmedics Corporation (Minneapolis, MN), is a hard device that controls the deflection. The machine does this by moving a pair of polytetrafluoroethylene (PTFE) v-blocks in which the wire is placed up against a centered v-tipped rod. The rod is attached to a low deflection load cell that provides the force reading. The upward motion of the base plate that supports the v-blocks is measured with a linear variable displacement transducer (LVDT). The outputs of the LVDT and the load cell are plotted on an x-y plotter. The apparatus is designed for quick testing on commercial products—less than 14 minutes per cycle, typically 2.5 minutes.

To do much slower experiments to assure equilibrium conditions and to measure the shape of the deformed wire, the apparatus illustrated in Fig. 1 was built. The v-block is also made of PTFE to provide low friction edge support. The load is applied by a loop of multifilament string wrapped around the wire. The string is dropped over a pulley where an attached cannister holds the 9.5 mm (3/8 in.) ball bearings which are used as load increments. The string diameter, approximately 0.46 mm at zero load, splays out to 1.1 mm near the peak load. The wire is bent in the horizontal plane so that the bent wire shape can be measured with a microscope attached to an x-y table. In the vertical plane that are v-grooves milled into the PTFE to locate the wire. The height of the PTFE block is approximately 10 mm where the figure is shaded and 6 mm where unshaded. This difference in height creates gaps for the bent wire and the hold-down bolts. The gap is 12.7 mm (0.5 in.). This simple machine is inherently a soft device that imposes a dead load on the wire.

In the load-controlled experiments, the deflection of the

[1] Current address: Flexmedics, 12400 Whitewater Drive, Suite 2040, Minnetonka, MN 55343.

Contributed by the Applied Mechanics Division of THE AMERICAN SOCIETY OF MECHANICAL ENGINEERS for publication in the ASME JOURNAL OF APPLIED MECHANICS.

Discussion on this paper should be addressed to the Technical Editor, Professor Lewis T. Wheeler, Department of Mechanical Engineering, University of Houston, Houston, TX 77204-4792, and will be accepted until four months after final publication of the paper itself in the ASME JOURNAL OF APPLIED MECHANICS.

Manuscript received by the ASME Applied Mechanics Division, Jan. 19, 1993; final revision, Mar. 8, 1994. Associate Technical Editor: R. Abeyaratne.

Copyright © 1995 by ASME

Downloaded 04 May 2010 to 171.66.16.28. Redistribution subject to ASME license or copyright; see http://www.asme.org/terms/Terms_Use.cfm

wire at the center of the gap is measured relative to the locations where each end of the wire is supported by the block. For various reasons, the location and orientation of the x-y axis is not easy to determine precisely. Though the bent shapes at different loads were measured accurately, there are offset errors in the zero reference that had to be corrected.

The results of three-point bending tests on the 0.632 NiTi diameter specimen are shown in Fig. 2. The run time of the displacement controlled experiment was 13 min, the room temperature was 25°C, and the gap was 12.7 mm. The load-deflection data shown in Fig. 2 is representative of the tests on various NiTi samples. An unusual feature of these tests was the drop in the resisting force when the displacement passes some critical value. This drop, during both loading and unloading, was seen in all the displacement controlled tests. Though the dip in the loading portion of the curve may be thought of as due to the onset of transformation, it is hard to reconcile this with the dip in the lower curve where the reverse transformation is almost complete. If the onset of a phase transformation corresponded to a softening of the material, then the dip on the reverse transformation should occur at the beginning of the reverse transformation, not the end.

The load-controlled experiment, also shown in Fig. 2, was done using the device shown in Fig. 1. Prior to this test, the 0.632 mm wire was stretched in tension four times and a portion of the wire was tested in three-point bending, Fig. 4. During this second experiment there was a 30-min wait between most of the measured points. Between two pairs of data points there were overnight waits. The room temperature was 23°C and the gap was 12.7 mm. Where there were significant offset errors, a smoothing of the data was applied. At most, the adjustment was 0.184 mm.

In comparing the two experiments on the same wire, note the large difference in initial slopes. Using linear bending theory, the initial slope of the displacement controlled experiment corresponds to a tensile modulus of approximately 33 kN/mm^2. For the load-controlled experiment, the initial slope corresponds to a tensile modulus between 45 and 50 kN/mm^2. The forces at which the two load-deflection curves flatten out are very similar, 6.2 versus 6.0 N. The return load-deflection curve transition force is also similar, roughly 3.6 versus 3.3 N. The similarity in the return transition force is surprising considering the large difference in the peak deflections.

By measuring the location of the wire's edge, local average curvatures, κ, can be calculated. Assume we have the location of a point on the wire's edge, and the locations of its immediate neighbors on the right and the left. Call the three

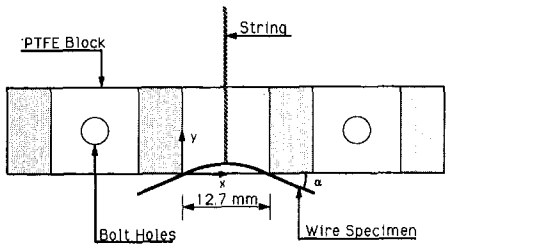

Fig. 1 Top view of three-point bending apparatus

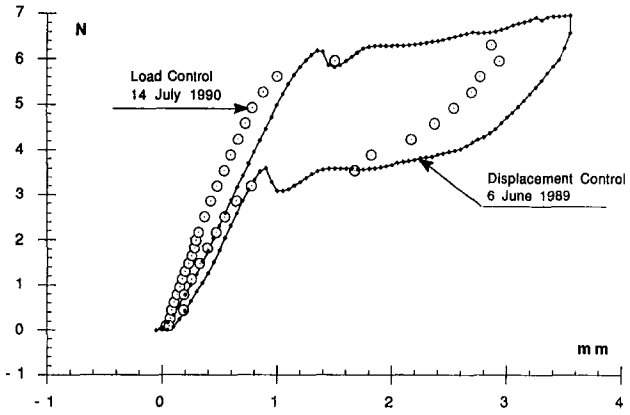

Fig. 2 Three-point bending experiments

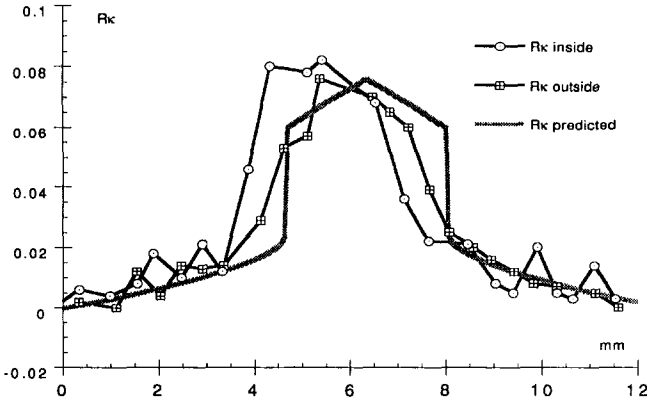

Fig. 3 Curvature-strain versus arclength in three-point bending

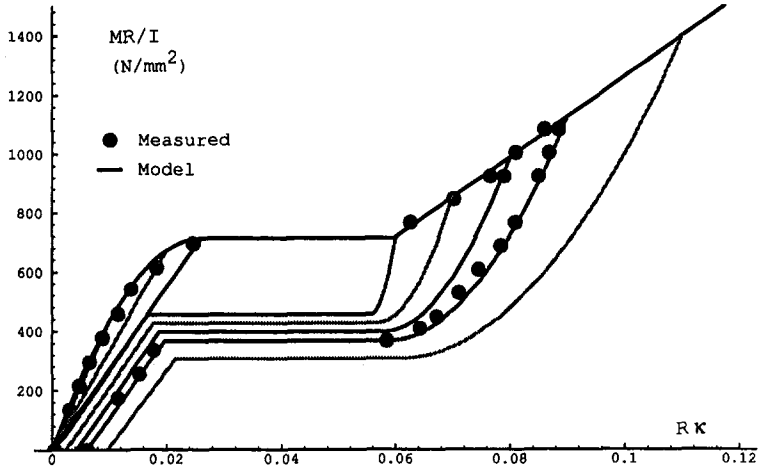

Fig. 4 Moment-curvature relationship for the 0.632 mm wire, June 1990 pure-bending experiment

Downloaded 04 May 2010 to 171.66.16.28. Redistribution subject to ASME license or copyright; see http://www.asme.org/terms/Terms_Use.cfm

positions (0, 0), (u, v), and (x, y). Because three points in a plane define a circle, the local curvature is

$$\kappa = \sqrt{\frac{4(uy - vx)^2}{(u^2 + v^2)(x^2 + y^2)\left((u - x)^2 + (v - y)^2\right)}}. \quad (1)$$

In Fig. 3, the results of this calculation are shown for the peak deflection in the load-controlled experiment shown in Fig. 2. The inside of the arc is defined as the side containing the radius of curvature; R is the wire radius, 0.316 mm. The large curvatures near the center are consistent with the large curvatures following a phase transition. Additionally, the way the local average curvatures quickly change from low values to high values is indicative of a bending-induced phase transition. Also shown on the figure is the predicted curvature from the calculations discussed in the following section.

3 Predicting Three-Point Bending Behavior

In this section, the relationship between the applied deflection and the resulting force in three-point bending is calculated from a model based on a nonlinear Euler-Bernoulli rod theory. First, the moment-curvature data described in Part 1 of this paper is used to determine the moment-curvature relationship. Next, the geometry and equilibrium conditions of the three-point bending problem are described. Finally, a numerical procedure used to solve the three-point bending problem is briefly described and the numerical solutions are compared with experimental results.

3.1 Moment-Curvature Relationship. From the experimental data presented in Part I of this paper, the applied moment is not a single-valued function of the nominal curvature, nor is the curvature a single-valued function of the moment. To obtain a moment-curvature relationship from the experiments, we first consider the situation in which the applied moment increases monotonically from zero. In this case, the experimental data indicates that the moment is a function of curvature. Hence, we assume the existence of a function $M = M_l(\kappa)$, where the subscript l indicates loading. For the 0.632 mm wire, the moment-curvature relationship during loading is

$$M_l(\kappa) = \begin{cases} IE^-(1 - q\kappa R)\kappa & \kappa R \in (0, \kappa^-) \\ M_t & \kappa R \in [\kappa^-, \kappa^+) \\ M_t + IE^+(\kappa - \kappa^+) & \kappa R \in [\kappa^+, \kappa_m) \end{cases} \quad (2)$$

where IE^- and IE^+ are the products of the second moment of inertia and stress moduli, q is a constant which determines the rate at which the slope decreases, R is the wire radius, κ is the curvature, M_t is the transition moment, κ^- is the lower transition curvature, and κ^+ is the upper transition curvature. The curvature as a function of the applied moment is the inverse function which is well defined except at the transition moment where the phase transition occurs. At that moment, which occurs only on a set of measure zero in the problem under consideration, the curvature is chosen to be κ^+. Denote this inverse function during loading by

$$\kappa_l(M) \equiv M_l^{-1}(M), \quad (3)$$

where M_l^{-1} is the inverse function of (2).

When the moments at any point are monotonically decreasing, the experimental data shows that the moment is a function of the curvature and the peak curvature reached during the bending cycle. That is, $M_u = M_u(\kappa(s), \kappa_p(s))$, where the subscript u denotes unloading, $\kappa(s)$ is the current curvature at arclength s, and $\kappa_p(s)$ is the peak curvature reached at s during loading. A good curve-fit to the data is given by

$$M_u(\kappa, \kappa_p) = \begin{cases} M_p\kappa/\kappa_p & 0 \le \kappa_p \le \kappa^-, \quad 0 \le \kappa \le \kappa_p \\ M_j + (M_p - M_j)(\kappa - \kappa_u^+)^2/(\kappa_p - \kappa_u^+)^2 & \kappa^+ \le \kappa_p < \kappa_m, \quad \kappa_u^+ < \kappa \le \kappa_p \\ M_j & \kappa^+ \le \kappa_p < \kappa_m, \quad \kappa_u^- \le \kappa \le \kappa_u^+ \\ M_j(\kappa - \kappa_{pl})/(\kappa_u^- - \kappa_{pl}) & \kappa^+ \le \kappa_p < \kappa_m, \quad 0 \le \kappa < \kappa_u^- \end{cases} \quad (4)$$

where for shorthand $M_p = M_l(\kappa_p)$ (2); $M_j = M_j(\kappa_p)$ is the unloading transformation moment (j for jump); $\kappa_u^+ = \kappa_u^+(\kappa_p)$ is the curvature at which the unloading transformation begins; $\kappa_u^-(\kappa_p)$ is the curvature at which the unloading transformation ends; and $\kappa_{pl}(\kappa_p)$ is the residual plastic curvature at zero moment. M_u, piecewise, brings together a number of simple ideas:

1 If κ_p is less than the lower jump value of curvature on loading κ^-, then $M_u(\kappa, \kappa_p)$ as a function of κ is the linear function from the peak curvature and peak moment, $(\kappa_p, M_l(\kappa_p))$, back to the origin.

2 If κ_p is greater than the upper jump value on loading, κ^+, and the curvature is greater than the curvature at which the unloading transformation begins, $\kappa_u^+(\kappa_p)$, then $M_u(\kappa, \kappa_p)$ as a function of κ, is the quadratic function defined by the conditions that

(a) the return moment equals the peak moment when the curvature is the peak curvature,

$$M_u(\kappa_p, \kappa_p) = M_l(\kappa_p);$$

(b) the moment at the curvature at which the unloading transformation begins is the moment at which the unloading transformation occurs,

$$M_u(\kappa_u^+(\kappa_p), \kappa_p) = M_j(\kappa_p);$$

(c) and the slope of the moment at the curvature at which the unloading transformation begins is zero,

$$0 = \left.\frac{\partial M_u(\kappa, \kappa_p)}{\partial \kappa}\right|_{\kappa = \kappa_u^+(\kappa_p)}.$$

3 If κ_p is greater than the upper jump value on loading, κ^+, and κ is in the transition region $[\kappa_u^-(\kappa_p), \kappa_u^+(\kappa_p)]$, then $M_u(\kappa, \kappa_p)$ as a function of curvature is the constant equal to the unloading transformation moment $M_j(\kappa_p)$.

4 If κ_p is greater than the upper jump value during loading κ_+, and the curvature is less than the curvature at which the unloading transformation ends $\kappa_u^-(\kappa_p)$, then $M_u(\kappa, \kappa_p)$ as function of κ is the line from $(\kappa_u^-(\kappa_p), M_j(\kappa_p))$ to $(\kappa_{pl}, 0)$.

An inverse function for the unloading curvature as a function of the moment and the peak curvature is well defined for all moments except at the transformation moments, $M_j(\kappa_p)$. If the peak curvature at a point is κ_p and the

Downloaded 04 May 2010 to 171.66.16.28. Redistribution subject to ASME license or copyright; see http://www.asme.org/terms/Terms_Use.cfm

Table 1 The specific constants and functions in $M_l(\kappa)$ and $M_u(\kappa, \kappa_p)$ for the 0.632 NiTi mm wire

$E^- = 54365 : \text{N/mm}^2$,
$E^+ = 13672.6 : \text{N/mm}^2$,
$I = \pi R^4/4$,
$q = 19.05$,
$M_t = I/R(713.451 : \text{N/mm}^2)$,
$\kappa^- = 0.0262467/R$,
$\kappa^+ = 0.0597583/R$,
$M_j(\kappa) = (I/R)(370 + 100(\kappa R - .0894)(.056 - .0894)^{-1} : \text{N/mm}^2)$,
$\kappa_u^+(\kappa) = (0.0586 - .0033(\kappa R - .0894)/(.056 - .0894)/R$,
$\kappa_u^-(\kappa) = (0.0497671 + 0.0988024\kappa R))/R$,
$\kappa_{pl}(\kappa) = (-0.0101334 + 0.17926\kappa R)/R$

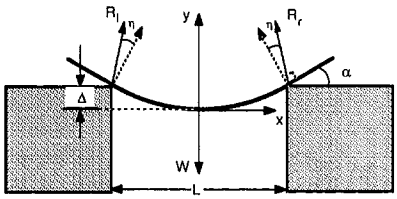

Fig. 5 Geometry of three-point bending problem

moment is $M_j(\kappa_p)$, then the curvature could be any element of the interval $[\kappa_u^-(\kappa_p), \kappa_u^+(\kappa_p)]$. It is assumed that the curvature is $\kappa_u^+(\kappa_p)$. Denote this inverse function during unloading by

$$\kappa_u(M, \kappa_p) \equiv M_u^{-1}(M, \kappa_p), \tag{5}$$

where M_u^{-1} is the inverse function of (4).

Using the data in Table 1, the loading moment-curvature relationship and a few members of the family of unloading moment-curvature relationships are presented in Fig. 4. The precision of the numbers in Table 1 is for continuity of the piecewise functions.

3.2 Geometry and Equilibrium. To describe the three-point bending problem, I will refer to Fig. 5. The variable s shall denote the inextensible arclength of the wire center from the origin to any location on the wire. The function $\theta(s)$ shall denote the tangential angle of the curve relative to the x-axis. The curvature is $\theta'(s)$. The functions $x(s)$ and $y(s)$ are, respectively, the horizontal position and the vertical position. Let a be the length of the arc from the origin $(x = 0,\ y = 0)$ to the support $(x = L/2,\ y = \Delta)$. Δ is the deflection of the center. Let α be the angle at the support, $\alpha \equiv \theta(a)$.

It is assumed that the curve is symmetric about $x = 0$. From the symmetry, $\theta(0) = 0$ and $\theta(s) \in [0, \pi/2)$. Using this symmetry, the domain of interest is restricted to $s \geq 0$. Though the length of wire from the origin to the support increases as the deflection increases, s is bounded by $[0, L/2 + \Delta)$. $\theta(s)$ is an absolutely continuous function with $|\theta'(s)| \leq \kappa_m$ almost everywhere, where κ_m is some maximum value of curvature. Discontinuities in $\theta'(s)$ occur at phase transformations.

Referring again to Fig. 5, the force W acts at the origin and the reaction forces R_r and R_l act at the supports. The force W may be either a dead load or, in the case to be analyzed, the force due to an applied deflection. In the latter case, W is an unknown to be determined as a function of the applied center deflection Δ. To include the effect of friction at the supports, let $\tan(\eta) = \mu$, where μ is the coefficient of friction. The directions of R_l and R_r differ from the normals to the curve by the angle η. Note that the sliding frictional forces change from tensile on loading to compressive on unloading. Hence, when the loading turns into unloading, the coefficient of friction goes from μ to $-\mu$. This explains at least part of the drop in force as the unloading begins (see Fig. 2).

With these definitions, the net force at equilibrium on the positive wire face at any location $s > 0$ is a constant

$$R(s) = W(-\tan(\alpha - \eta)\mathbf{i} + \mathbf{j})/2,$$

where the $\mathbf{i}$ and $\mathbf{j}$ are the unit vectors along the x and y-axes. The moment at any location $s > 0$ is

$$M(s) = W(L/2 - x(s) + \tan(\alpha - \eta)(\Delta - y(s)))/2.$$

Call $K(M, \kappa_p)$ (3) for loading or (5) for unloading. The equilibrium equations can be expressed: for all $s \in (0, a)$,

$$\theta'(s) = K\big(W(L/2 - x(s) + \tan(\alpha - \eta)(\Delta - y(s)))/2, \kappa_p(s)\big), \tag{6}$$

$$x'(s) = \cos(\theta(s)), \tag{7}$$

$$y'(s) = \sin(\theta(s)), \tag{8}$$

with boundary conditions,

$$\theta(0) = 0, x(0) = 0, y(0) = 0, \tag{9}$$

and the length a, applied load W, and end angle α such that

$$\theta'(a) = 0, x(a) = L/2, y(a) = \Delta. \tag{10}$$

It is noted that when the deflection has reached a maximum value, since each point on the wire has its own peak curvature on which the unloading moment-curvature depends, the peak curvature at each point on the wire must be recorded and each point has its own unloading moment-curvature relationship.

If the rod's isothermal free energy was a function of only the curvature, then the three-point bending problem could be solved by a minimization of the free energy (James, 1981). By this method, an invariant of the energy is determined:

$$0 = \theta'(s)\frac{d\Gamma(\kappa)}{d\kappa}\bigg|_{\theta'(s)} - \Gamma(\theta'(s)) - \frac{W\sin(\alpha - \theta(s))}{2\cos(\alpha)}, \tag{11}$$

where $\Gamma(\kappa)$ is the integral of the moment as a function of curvature (2) from 0 to κ. For friction-free loading from zero deflection to some maximum deflection, this first invariant applies, and is used a check on the following numerical method. When there is hysteresis of the type seen in the moment-curvature experiments, then the invariant does not apply. The hysteresis applies during unloading, hence a second method was developed to solve the three-point problem.

3.3 Numerical Solution. To solve the boundary value problem, (6)–(10), for each Δ from 0 to some Δ_{max} and then back to 0, a geometrical technique was developed (Berg, 1991). The technique projects the curve $\{(x(s), y(s))|s \in [0, L/2 + \Delta), x(s) \in [0, L/2]\}$ onto the length $L/2$ and then discretizes this projection into $N + 1$ elements of length $L/(2N)$. Since $\theta(s)$ is monotonic increasing, the curve $\{x, y\}$ can be parameterized in terms of θ. From a point on the curve, Eq. (6), determines the curvature which is used in a geometric predictor-corrector technique to advance the curve $[\{\hat{x}(\theta), \hat{y}(\theta)\}, \theta|\theta \in [0, \alpha]]$. By this technique, the arclength a does not need to be determined, but an iterative technique is still needed to determine the proper values of W and α. The Newton-Raphson method for root finding combined with Brent's method for minimization serve as the iterative technique (Press, Flannery, Teukolsky, and Vetterling, 1986).

To evaluate the efficacy of the numerical technique for the loading problem with no friction, the first integral (11) is evaluated at each point on the curve. The first integrals generated by the geometrical technique are constant, though

Downloaded 04 May 2010 to 171.66.16.28. Redistribution subject to ASME license or copyright; see http://www.asme.org/terms/Terms_Use.cfm

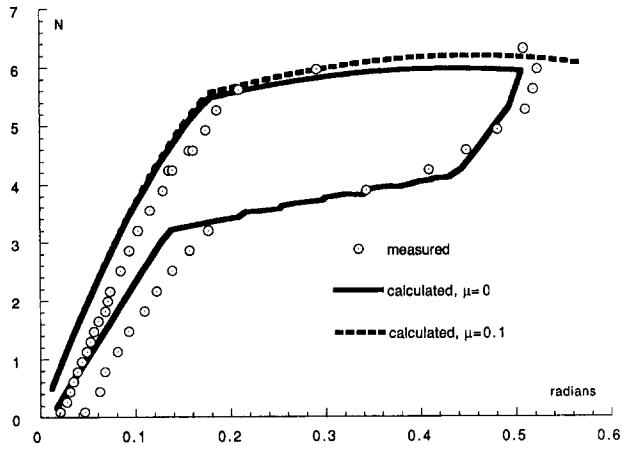

Fig. 6 Three-point bending load versus end angle

not identically zero, in each of the regions before and after the jump. As a measure of this error, the maximum and minimum of the first integral on the 100 grid points are recorded. For the calculated deflections when the friction is zero and there is a jump in curvature, the mean value of the first-integral-maximums for all deflections is 0.173 ± 0.004. The mean value of the corresponding minimums for all deflections is 0.0002 ± 0.0001. When the number of grid points is increased to 200 or 400, the maximum of the first integral drops to an average of 0.088 or 0.045, respectively. This implies that the mean values of the first-integral-maximum converge at a rate linear in the number of grid points. From pointwise data, it is noted that the first integral is approximately the maximum for all points prior to the jump and approximately the minimum for all points after the jump. If there is no jump in curvature, the maximum of first integral is approximately 0.0013 (at $N = 100$). It is concluded that the routine generates integral curves for the loading problem.

For both the loading and unloading, the calculated values are compared with the measurements in Fig. 6. To avoid difficulties with the location and orientation of the x-y axis in determining the deflection, yet provide a measurable test of the theory, I follow a suggestion attributed to Kirchhoff and Pscheidl (Kohlrausch, 1894). They suggest measuring the angle of inclination at each end since the theory predicts a one-one relation between the load and the tangents. From the pointwise data, an average tangent can be determined for each pair of neighboring data points. For the angle of inclination at the end, α, the arithmetic mean of the largest tangent angle for $x > 6$ mm and the absolute value of the largest negative tangent angle for $x < -6$ mm is used. Aside from an offset in the measured angles, the predicted and measured load end-angle relations are similar. Additionally, the comparison between measured local average curvatures and the predicted curvatures, Fig. 3, supports the efficacy of the numerical method and the applicability of the theory.

Acknowledgments

I wish to acknowledge the support of my advisor, Richard James, the use of facilities and the supply of samples by Jim Stice of Flexmedics, and the support of the University of Minnesota Army High Performance Computing Research Center fellowship through the Army Research Office, contract number DAALO3-89-C-0038.

References

Berg, B. T., 1991, "Bending of Superelastic Wires," *Technical Report 91-63*, University of Minnesota, Army High Performance Computing Research Center, Minneapolis, MN.

James, R. D., 1981, "The Equilibrium and Post-Buckling Behavior of an Elastic Curve Governed by a Non-convex Energy," *J. of Elasticity*, Vol. 11, pp. 239–269.

Kohlrausch, F., 1894, *An Introduction to Physical Measurements*, 3rd ed., J. A. Churchill.

Press, W. H., Flannery, B. P., Teukolsky, S. A., and Vetterling, W., 1986, *Numerical Recipes*, Cambridge University Press.

Downloaded 04 May 2010 to 171.66.16.28. Redistribution subject to ASME license or copyright; see http://www.asme.org/terms/Terms_Use.cfm

On the Ordinary, Generalized, and Pseudo-Variational Equations of Motion in Nonlinear Elasticity, Piezoelectricity, and Classical Plate Theories[1]

Yi-Yuan Yu
Professor Emeritus,
Department of Mechanical Engineering,
New Jersey Institute of Technology,
Newark, NJ 07102
Life Fellow, ASME.

Ordinary, generalized, and pseudo-variational equations of motion in three-dimensional theories of nonlinear elasticity and piezoelectricity are presented systematically. These are applied to the derivations of plate equations of the classical type. In contrast to the derivations of plate equations that include thickness and higher-order effects, it is shown that the volume and surface integrals in a three-dimensional ordinary variational equation of motion must now be used jointly in a coupled manner. Details are demonstrated by first treating a classical linear plate. Equations of the classical type for large deflections of laminated composite and piezoelectric plates are then derived, with the famous von Kármán equations of an isotropic homogeneous plate deducible as a special case. Interrelationship among various plate equations is emphasized.

1 Introduction

In our early studies, linear and nonlinear plate and shell equations were derived from an ordinary variational equation of motion in linear elasticity as originally conceived by Kirchhoff (Love 1927), and also from the generalized version of the variational equation in nonlinear elasticity given in our early paper (Yu 1964). Recently we have renewed our efforts on layered and sandwich beams and plates (Yu 1989, 1992a). To derive equations for large deflections, we have proposed the use of a new pseudo-variational equation of motion in nonlinear elasticity. Specifically, we were able to derive equations for large deflections of a variety of beams (Yu 1992b), the von Kármán equations for plates and the Marguerre equations for shallow shells (Yu 1991), thereby justifying the use of the new pseudo-variational equation.

In this paper we first summarize systematically the ordinary, generalized, and pseudo-variational equations of motion in nonlinear elasticity, and then extend our generalized Hamilton's principle and the associated variational equation of motion (Yu, 1964) to further include the piezoelectric effect. Another important aspect of our new effort to be presented in this paper is to deal with derivations of classical plate equations. In contrast to plate equations that include thickness effects, the classical equations are aimed at low-frequency applications. A difference also exists between the direct derivations of these two types of plate equations from the variational equations of motion. In the derivation of plate and shell equations that include thickness and other higher effects (Yu, 1965a, 1965b), the volume and surface integrals in a three-dimensional ordinary variational equation may be integrated independently in a straightforward manner. In contrast, in the derivation of classical type of equations, these volume and surface integrals must be used jointly in a coupled manner, making the derivation much more involved, as will be seen presently. To demonstrate the details of derivation we shall start by treating the simple case of a linear homogeneous elastic, classical plate. This is then followed by derivations of equations of the classical type for large deflections of laminated composite and piezoelectric plates, with the famous von Kármán equations of an isotropic homogeneous plate deducible as a special case. Special attention is paid to the interrelationship among various plate equations.

[1] This work was presented at the symposium on "Non-Classical Problems of the Theory and Behavior of Structures Exposed to Complex Environmental Conditions" in the First Joint Mechanics Meeting of ASME-ASCE-SES in Charlottesville, VA, June 6–9, 1993. A slightly different version of the manuscript appeared in the bound volume AMD-Vol. 164, edited by L. Librescu, ASME, 1993. Some of the results had been presented at the 13th International Congress of Theoretical and Applied Mechanics, Haifa, Israel.

Contributed by the Applied Mechanics Division of THE AMERICAN SOCIETY OF MECHANICAL ENGINEERS for publication in the ASME JOURNAL OF APPLIED MECHANICS.

Discussion on this paper should be addressed to the Technical Editor, Professor Lewis T. Wheeler, Department of Mechanical Engineering, University of Houston, Houston, TX 77204-4792, and will be accepted until four months after final publication of the paper itself in the ASME JOURNAL OF APPLIED MECHANICS.

Manuscript received by the ASME Applied Mechanics Division, Aug. 12, 1993; final revision, Apr. 6, 1994. Associate Technical Editor: W. K. Liu.

Copyright © 1995 by ASME

Downloaded 04 May 2010 to 171.66.16.28. Redistribution subject to ASME license or copyright; see http://www.asme.org/terms/Terms_Use.cfm

The laminated composite and piezoelectric plates are chosen, as a combined use of these has begun to gain importance in recent works on smart and intelligent materials and structures.

2 Variational Equations of Motion in Three-Dimensional Nonlinear Elasticity and Piezoelectricity

We begin by recapitulating our early and recent results on variational equations of motion in three-dimensional nonlinear elasticity.

Ordinary and Pseudo-Variational Equations of Motion in Nonlinear Elasticity. Several cases in nonlinear elasticity were discussed in our early study (Yu, 1964). Although the main purpose of that study was to present a generalized variational equation of motion, it also dealt with ordinary variational equations as special cases. For simplicity the latter are singled out at this point.

In the classical case, Green's nonlinear strain tensor is

$$\epsilon_{ij} = \frac{1}{2}\left(\delta_{ki}u_{k,j} + \delta_{kj}u_{k,i} + u_{k,i}u_{k,j}\right) = \frac{1}{2}\left[\delta_{ki}(e_{kj} + \omega_{kj}) + \delta_{kj}(e_{ki} + \omega_{ki}) + (e_{ki} + \omega_{ki})(e_{kj} + \omega_{kj})\right] \quad (i, j, k = 1, 2, 3) \quad (1)$$

and the ordinary variational equation of motion takes the form

$$\int_{t_0}^{t_1} dt \int_V \left\{\left[\sigma_{ij}\left(\delta_{lj} + e_{lj} + \omega_{lj}\right)\right]_{,i} + f_l - \rho\ddot{u}_l\right\}\delta u_l \, dV - \int_{t_0}^{t_1} dt \int_{S_p} \left\{\sigma_{ij}\left(\delta_{lj} + e_{lj} + \omega_{lj}\right)\nu_i - p_i^*\right\}\delta u_l \, dS = 0 \quad (2)$$

where δ_{ij} is the Kronecker delta, u_i the displacement vector, e_{ij} the linear strain tensor, ω_{ij} the rotation, σ_{ij} the Kirchhoff-Trefftz stress tensor, f_i the body force, ρ the density, p_i the surface traction, an asterisk denotes the prescribed value of a quantity, V the volume, S_p the part of the boundary surface on which traction is prescribed, and t_0 and t_1 are the instants at the ends of a time interval. Equations (1) and (2) correspond to each other exactly in a variational sense. This means that Eq. (2) can be derived exactly by substituting Eq. (1) into Hamilton's principle and carrying out the variations of the displacements.

The simplified nonlinear case of small strains and large rotations is an important simplification of the above classical case in which the rotations are much larger than the linear strains, although both are much smaller than unity. In a manner as suggested for this case by Novozhilov (1948), Eqs. (1) and (2) would reduce to, respectively,

$$\epsilon_{ij} = e_{ij} + \frac{1}{2}\omega_{ki}\omega_{kj} = \frac{1}{2}\left(\delta_{ki}e_{kj} + \delta_{kj}e_{ki} + \omega_{ki}\omega_{kj}\right) \quad (i, j, k = 1, 2, 3) \quad (3)$$

$$\int_{t_0}^{t_1} dt \int_V \left\{\left[\sigma_{ij}\left(\delta_{lj} + \omega_{lj}\right)\right]_{,i} + f_l - \rho\ddot{u}_l\right\}\delta u_l \, dV - \int_{t_0}^{t_1} dt \int_{S_p} \left\{\sigma_{ij}\left(\delta_{lj} + \omega_{lj}\right)\nu_i - p_i^*\right\}\delta u_l \, dS = 0. \quad (4)$$

Unfortunately, Eqs. (3) and (4) no longer correspond to each other variationally. Indeed, it can be shown that a form of ϵ_{ij} corresponding to Eq. (4) does not exist (Yu, 1964). In spite of such shortcomings, we have made effective use of Eq. (4) both in this specific ordinary form (Yu, 1962) and in the generalized form (Yu, 1992c). Indeed, we have proposed to accept it as a pseudo-variational equation of motion (Yu, 1991).

In the recent work (Yu, 1991) we have also proposed to adopt a new simplified nonlinear case, further deduced from Eq. (4). To apply this to plates we choose u_i in the thickness direction and propose to keep only the nonlinear terms associated with δu_z but to linearize terms associated with δu_x and δu_y. Equation (4) then reduces to, now written in the x, y, z components,

$$\begin{aligned}\int_{t_0}^{t_1} dt \int_V \Big\{&\left[\partial\sigma_{xx}/\partial x + \partial\sigma_{yx}/\partial y + \partial\sigma_{zx}/\partial z + f_x - \rho\ddot{u}_x\right]\delta u_x \\ &+ \left[\partial\sigma_{xy}/\partial x + \partial\sigma_{yy}/\partial y + \partial\sigma_{zy}/\partial z + f_y - \rho\ddot{u}_y\right]\delta u_y \\ &+ \left[\partial(\sigma_{xz} - \sigma_{xx}\omega_{zx} + \sigma_{xy}\omega_{yz})/\partial x \right. \\ &+ \partial(\sigma_{yz} - \sigma_{yx}\omega_{zx} + \sigma_{yy}\omega_{yz})/\partial y \\ &\left. + \partial(\sigma_{zz} - \sigma_{zx}\omega_{zx} + \sigma_{zy}\omega_{yz})/\partial z + f_z - \rho\ddot{u}_z\right]\delta u_z\Big\} dV \\ - \int_{t_0}^{t_1} dt \int_{S_p} \Big\{&\left[\sigma_{xx}n_x + \sigma_{yz}n_y + \sigma_{zx}n_z - p_x^*\right]\delta u_x \\ &+ \left[\sigma_{xy}n_x + \sigma_{yy}n_y + \sigma_{zy}n_z - p_y^*\right]\delta u_y \\ &+ \left[(\sigma_{xz} - \sigma_{xx}\omega_{zx} + \sigma_{xy}\omega_{yz})\,n_x \right. \\ &\left. + (\sigma_{yz} - \sigma_{yx}\omega_{zx} + \sigma_{yy}\omega_{yz})\,n_y \right. \\ &\left. + (\sigma_{zz} - \sigma_{zx}\omega_{zx} + \sigma_{zy}\omega_{yz})\,n_z - p_z^*\right]\delta u_z\Big\} dS = 0 \end{aligned} \quad (5)$$

As a corresponding ϵ_{ij} again does not exist, Eq. (5) is also a pseudo-variational equation of motion. Of the three rotations, ω_{xy} no longer appears and only ω_{yz} and ω_{zx} remain in Eq. (5). The former is the rotation about the z-axis that is normal to the plane of the plate, and the latter are rotations about the x and y-axes that are in the plane of the plate. In the new simplified case we have thus assumed that ω_{xy} is much smaller than ω_{yz} and ω_{zx} and can be neglected.

Finally, with nonlinear terms neglected, Eqs. (2), (4), and (5) all reduce to the following linear variational equation of motion:

$$\begin{aligned}\int_{t_0}^{t_1} dt \int_V \Big\{&\left[\partial\sigma_{xx}/\partial x + \partial\sigma_{yx}/\partial y + \partial\sigma_{zx}/\partial z \right. \\ &\left. + f_x - \rho\ddot{u}_x\right]\delta u_x + [\ldots]\,\delta u_y + [\ldots]\,\delta u_x\Big\} dV \\ - \int_{t_0}^{t_1} dt \int_{S_p} \Big\{&\left[\sigma_{xx}n_x + \sigma_{yx}n_y + \sigma_{zx}n_z - p_x^*\right]\delta u_x \\ &+ [\ldots]\,\delta u_y + [\ldots]\,\delta u_z\Big\} dS = 0 \end{aligned} \quad (6)$$

which will be employed to demonstrate the derivation of equations of a linear homogeneous elastic plate.

By setting equal to zero the coefficients of the variations of displacements in the volume and surface integrals separately in an ordinary variational equation of motion, the three-dimensional stress equations of motion and traction boundary conditions may be written in the usual manner in all cases.

Generalized Variational Equations of Motion in Nonlinear Elasticity. Variational principles of different kinds have been proposed by Reissner (1947), Hu (1954, 1955), and Washizu (1955, 1968), among others. By considering variations of not only displacements but also strains and stresses, as adopted by Hu and Washizu, a generalized Hamilton's principle in nonlinear elasticity was introduced by Yu (1964). Also presented by him was the associated generalized variational equation of motion, from which the complete system of three-dimensional stress equations of motion, traction and

Downloaded 04 May 2010 to 171.66.16.28. Redistribution subject to ASME license or copyright; see http://www.asme.org/terms/Terms_Use.cfm

displacement boundary conditions, strain-displacement relations, and stress-strain relations may be written readily. Generalized pseudo-variational equations of motion can similarly be formulated. When variations are restricted to those of the displacements, the generalized variational equation of motion reduces to the ordinary variational Eq. (2) as a special case.

The ordinary variational equation of motion in linear elasticity was extended to include the piezoelectric effect by Mindlin (1984). The generalized Hamilton's principle and variational equation of motion in nonlinear elasticity are extended in this paper to also include the piezoelectric effect. To save space, the results in nonlinear elasticity will not be repeated here but will be considered as those of a special case of coupled nonlinear elasticity and piezoelectricity. The latter will be considered next.

Generalized Variational Equations of Motion in Coupled Nonlinear Elasticity and Piezoelectricity. The generalized Hamilton's principle in coupled nonlinear elasticity and piezoelectricity has the form

$$\delta \int_{t_0}^{t_1} L\, dt = \delta \int_{t_0}^{t_1} (T - U + W)\, dt = 0 \tag{7}$$

where $L = T - U + W$ is now a generalized Lagrangian function and

$$T = \int_V \frac{1}{2} \rho \dot{u}_i \dot{u}_i \, dV$$

$$U = \int_V \left[\sigma_{ij}(\varepsilon_{ij} - \epsilon_{ij}) + H \right] dV \quad (i, j = 1, 2, 3)$$

$$W = \int_V f_i u_i \, dV + \int_{S_p} p_i^* u_i \, dS + \int_{S_u} p_i (u_i - u_i^*)\, dS + \int_{S_\sigma} \sigma^* \phi \, dS + \int_{S_\phi} \sigma (\phi - \phi^*)\, dS. \tag{8}$$

In addition to the notations introduced earlier, ε_{ij} are expressions of the nonlinear strain ϵ_{jj}, as functions of the derivatives of the displacement, such as given in Eqs. (1) and (3), H is the electric enthalpy density, σ the surface charge, ϕ the electric potential, and, similar to S_p, the symbols S_u, S_σ and S_ϕ denote those parts of the boundary surface on which u, σ, and ϕ are prescribed, respectively. The expression for T is the same as in the early work (Yu, 1964). In the expression for U, the strain energy density E in the early work has been replaced by the electric enthalpy density H, these being related to each other by

$$H = E - E_i D_i$$

where E as a function of ϵ_{ij} is assumed to exist, and E_i and D_i are the electric field and electric displacement, respectively. Finally, the expression for W in Eqs. (8) contains two more integrals than before, which are involved with σ and ϕ.

In addition to the variations of displacements, strains and stresses, variations of the electric field, surface charge, and electric potential are further taken independently. By substituting T, U, and W from Eqs. (8) into (7) and carrying out these variations, a generalized variational equation of motion in coupled nonlinear elasticity and piezoelectricity is obtained. The result is written in the form of separate components according to the various types of variations, as follows:

$$\int_{t_0}^{t_1} dt \int_V \left[\frac{1}{2} \left\{ \sigma_{ij} \left(\partial \varepsilon_{ij} / \partial e_{mn} + \partial \varepsilon_{ij} / \partial \omega_{mn} \right) \right\}_{,n} \delta_{lm} + \frac{1}{2} \left\{ \sigma_{ij} \left(\partial \varepsilon_{ij} / \partial e_{mn} - \partial \varepsilon_{ij} / \partial \omega_{mn} \right) \right\}_{,m} \delta_{ln} + f_l - \rho \ddot{u}_l \right] \delta u_l \, dV - \int_{t_0}^{t_1} dt \int_{S_p} \left[\frac{1}{2} \sigma_{ij} \left(\partial \varepsilon_{ij} / \partial e_{mn} + \partial \varepsilon_{ij} / \partial \omega_{mn} \right) \nu_n \delta_{lm} + \frac{1}{2} \sigma_{ij} \left(\partial \varepsilon_{ij} / \partial e_{mn} - \partial \varepsilon_{ij} / \partial \omega_{mn} \right) \nu_m \delta_{ln} - p_l^* \right] \delta u_l \, dS = 0 \tag{9a}$$

$$\int_{t_0}^{t_1} dt \int_{S_u} (u_i - u_i^*)\, \delta p_i \, dS = 0 \tag{9b}$$

$$\int_{t_0}^{t_1} dt \int_V (\epsilon_{ij} - \varepsilon_{ij})\, \delta \sigma_{ij} \, dV = 0 \tag{9c}$$

$$\int_{t_0}^{t_1} dt \int_V \left(\sigma_{ij} - \partial H / \partial \epsilon_{ij} \right) \delta \epsilon_{ij} \, dV = 0 \tag{9d}$$

$$\int_{t_0}^{t_1} dt \int_V (D_i + \partial H / \partial E_i)\, \delta E_i \, dV = 0 \tag{9e}$$

$$\int_{t_0}^{t_1} dt \int_V D_{i'i} \, \delta \phi \, dV - \int_{t_0}^{t_1} dt \int_{S_\sigma} (n_i D_i - \sigma^*) \delta \phi \, dS = 0 \tag{9f}$$

$$\int_{t_0}^{t_1} dt \int_{S_\phi} (\phi - \phi^*)\, \delta \sigma \, dS = 0. \tag{9g}$$

When the piezoelectric effect is suppressed, Eqs. (7) through (9) reduce to the early result in nonlinear elasticity (Yu, 1964) as a special case. In fact, Eqs. (9a – c) have the same form regardless of whether the piezoelectric effect is included or not. The first of these, Eq. (9a), is reducible to the ordinary variational Eqs. (2), (4), (5), and (6) as special cases.

Constitutive Relations in Piezoelectricity. Equation (9d) yields an extension of the stress-strain relations in elasticity and, together with Eq. (9e), provides the following constitutive relations in piezoelectricity:

$$\sigma_{ij} = \partial H / \partial \epsilon_{ij}, \quad D_i = -\partial H / \partial E_i \tag{10}$$

which are responsible for the coupling between elasticity and piezoelectricity. In nonlinear elasticity, the electric enthalpy density H reduces to the strain energy density E, and the first of Eqs. (10) becomes the usual relation that connects the Kirchoff stress tensor with the Green strain tensor. An account of this and other associated relations may be found, for instance, in the standard text by Fung (1965). In general, H is of such a form that the relations given by Eqs. (10) can be either linear or nonlinear. While this can be further elaborated, we only remark that, by extending the two simplified cases from nonlinear elasticity to piezoelectricity, and by restricting ourselves to these cases, H can be shown to have the following simplest possible form:

$$H = \frac{1}{2} c_{ijkl} \epsilon_{ij} \epsilon_{kl} - e_{ijk} E_i \epsilon_{jk} - \frac{1}{2} e_{ij} E_i E_j \tag{11}$$

which is adopted here and in which c_{ijkl}, e_{ijk}, and e_{ij} are components of the elastic stiffness, piezoelectric strain constant, and dielectric permittivity, respectively. Substitution of H from Eq. (11) into Eqs. (10) then yields the constitutive relations in the following linear form:

$$\sigma_{ij} = c_{ijkl} \epsilon_{kl} - e_{kij} E_k, \quad D_i = e_{ijk} \epsilon_{jk} + e_{ij} E_j \tag{12}$$

Downloaded 04 May 2010 to 171.66.16.28. Redistribution subject to ASME license or copyright; see http://www.asme.org/terms/Terms_Use.cfm

with $E_i = -\phi_{,i}$ as usual. These now reflect the essential feature that we are proposing for coupled nonlinear elasticity and piezoelectricity, which is to adopt nonlinear strains in place of the linear strains that are commonly used in linear piezoelectricity.

Equations of Electrostatics. Finally, Eqs. (9*f*, *g*) yield the following three-dimensional equations of electrostatics: the field equation

$$D_{i,i} = 0 \quad \text{in} \quad V \tag{13}$$

and the boundary conditions

$$n_i D_i = \sigma^* \quad \text{on } S_\sigma, \quad \phi = \phi^* \quad \text{on } S_\phi. \tag{14}$$

These are the same as in linear piezoelectricity.

3 Flexural Equations of a Linear Homogeneous Plate

To demonstrate the details of deriving two-dimensional classical plate equations from three-dimensional elasticity, we consider first the simple case of flexure of a linear homogeneous plate. The plate is assumed to have a middle plane in the *xy*-plane, with a plan area A and boundary contour C, and a uniform thickness $2h$ in the z direction.

Only the use of the ordinary variational equation of motion will be described here. We start by assuming the three-dimensional displacements in the form

$$u_x = -z\,\partial w/\partial x, \quad u_y = -z\,\partial w/\partial y, \quad u_z = w \tag{15}$$

where the deflection w is the only plate displacement under consideration. Substituting these into the linear variational Eq. (6) and carrying out integration with respect to z over the plate thickness, we find

$$\begin{aligned}
\int_{t_0}^{t_1} dt \iint_A \{ & \left[\partial M_x/\partial x + \partial M_{yx}/\partial y - Q_x + h(\sigma_{xx}^+ + \sigma_{xx}^-) \right. \\
& \left. + f_x^{(1)} + \rho(2h^3/3)\,(\partial \ddot{w}/\partial x) \right] [-\partial(\delta w)/\partial x] \\
& + \left[\partial M_{xy}/\partial x + \partial M_y/\partial y - Q_y + h(\sigma_{xy}^+ + \sigma_{xy}^-) \right. \\
& \left. + f_y^{(1)} - \rho(2h^3/3)\,(\partial \ddot{w}/\partial y) \right] [-\partial(\delta w)/\partial y] \\
& + \left[\partial Q_x/\partial x + \partial Q_y/\partial y + (\sigma_{zx}^+ - \sigma_{zx}^-) \right. \\
& \left. + f_x^{(0)} - 2\rho h \ddot{w} \right] \delta w \} \, dx dy \\
& - \int_{t_0}^{t_1} dt \iint_A \{ [\sigma_{zx}^+ - p_x^+][-h\partial(\delta w)/\partial x] \\
& + [-\sigma_{xx}^- - p_x^-][h\partial(\delta w)/\partial x] + [\sigma_{xy}^+ - p_y^+][-h\partial(\delta w)/\partial y] \\
& + [-\sigma_{xy}^- - p_y^-][h\partial(\delta w)/\partial y] \\
& + [\sigma_{zx}^+ - p_y^+]\,\delta w + [-\sigma_{zx}^- - p_z^-]\,\delta w \} \, dx dy \\
& - \int_{t_0}^{t_1} dt \oint_C \{ [M_x n_x + M_{xy} n_y - p_x^{(1)}][-\partial(\delta w)/\partial x)] \\
& + [M_{yx} n_x + M_y n_y - p_y^{(1)}][-\partial(\delta w)/\partial y)] \\
& + [Q_x n_x + Q_y n_y - p_z^{(0)}]\,\delta w \} \, ds = 0
\end{aligned} \tag{16}$$

where n_x, n_y are the direction cosines of an outward normal to the cylindrical boundary surface of the plate,

$$(M_x, M_y, M_{xy}, Q_x, Q_y) = \int_{-h}^{h} (\sigma_{xx} z, \sigma_{yy} z, \sigma_{xy} z, \sigma_{zx}, \sigma_{zy})\, dz \tag{17}$$

are the plate stresses or the ordinary bending and twisting moments and transverse shear forces, and

$$(f_x^{(1)}, f_y^{(1)}, f_z^{(0)}) = \int_{-h}^{h} (f_x z, f_y z, f_z)\, dz$$

$$(p_x^{(1)}, p_y^{(1)}, p_z^{(0)}) = \int_{-h}^{h} (p_x z, p_y z, p_z)\, dz$$

define the plate body forces and plate edge tractions, respectively. In this paper the superscripts in parentheses, (0) and (1), are used to denote plate quantities of the zeroth and first order, respectively. In a similar manner, the moments in Eq. (17) may be written in the alternative form

$$M_x = \sigma_{xx}^{(1)}, \; M_y = \sigma_{yy}^{(1)}, \; M_{xy} = \sigma_{xy}^{(1)}.$$

The first integral in Eq. (16) is obtained by applying the volume integral in Eq. (6) to the volume of the plate. The next two integrals are obtained by applying the surface integral in Eq. (6) to the plane boundaries at $z = \pm h$ and to the cylindrical boundary, respectively, under the assumption that only surface transactions, but not displacements, may be prescribed at $z = \pm h$. The two double integrals in Eq. (16) are next combined so that the internal stresses $\sigma_{xx}^{\pm}$, ... at $z = \pm h$ are eliminated. Thus, we find

$$\begin{aligned}
\int_{t_0}^{t_1} dt \iint_A \{ & \left[\partial M_x/\partial x + \partial M_{yx}/\partial y - Q_x + P_x^{(1)} \right. \\
& \left. + f_x^{(1)} + \rho(2h^3/3)\,(\partial \ddot{w}/\partial x) \right] [-\partial(\delta w)/\partial x] \\
& + \left[\partial M_{xy}/\partial x + \partial M_y/\partial y - Q_y + P_y^{(1)} \right. \\
& \left. + f_y^{(1)} + \rho(2h^3/3)\,(\partial \ddot{w}/\partial y) \right] [-\partial(\delta w)/\partial y] \\
& + \left[\partial Q_x/\partial x + \partial Q_y/\partial y + P_z^{(0)} + f_z^{(0)} - 2\rho h \ddot{w} \right] \delta w \} \, dx dy \\
& - \int_{t_0}^{t_1} dt \oint_C \{ \ldots \}\, ds = 0
\end{aligned} \tag{18}$$

where

$$P_x^{(1)} = h[(p_x)_h - (p_x)_{-h}],$$

$$P_y^{(1)} = \ldots, \quad P_z^{(0)} = (p_z)_h + (p_z)_{-h}$$

define the plate surface tractions and the superscripts are used in the same way as before. Terms in Eq. (18) are then rearranged so that it is rewritten in the form

$$\begin{aligned}
\int_{t_0}^{t_1} dt \iint_A \{ & \left[\left[\partial^2 M_x/\partial x^2 + 2\partial^2 M_{xy}/\partial x \partial y + \partial^2 M_y/\partial y^2 \right. \right. \\
& \left. + \partial P_x^{(1)}/\partial x + \partial P_y^{(1)}/\partial y + P_z^{(0)} + \partial f_x^{(1)}/\partial x + \partial f_y^{(1)}/\partial y \right. \\
& \left. + f_z^{(0)} - 2\rho h \ddot{w} + \rho(2h^3/3)\,\nabla^2 \ddot{w} \right] \delta w \\
& \underline{- (\partial/\partial x) \{ \left[\partial M_x/\partial x + \partial M_{yx}/\partial y - Q_x + P_x^{(1)} + f_x^{(1)} \right.} \\
& \underline{\left. u + \rho(2h^3/3)\,(\partial \ddot{w}/\partial x) \right] \delta w \}} \\
& \underline{- (\partial/\partial y) \{ \left[\partial M_{xy}/\partial x + \partial M_y/\partial y - Q_y + P_y^{(1)} + f_y^{(1)} \right.} \\
& \underline{\left. + \rho(2h^3/3)\,(\partial \ddot{w}/\partial y) \right] \delta w \}]]} \, dx\, dy \\
& - \int_{t_0}^{t_1} dt \oint_C \{ \ldots \}\, ds = 0.
\end{aligned}$$

The underlined terms in the double integral are further transformed into a contour integral by Gauss' theorem; thus,

Downloaded 04 May 2010 to 171.66.16.28. Redistribution subject to ASME license or copyright; see http://www.asme.org/terms/Terms_Use.cfm

$$\int_{t_0}^{t_1} dt \iint_A \left[\partial^2 M_x/\partial x^2 + 2\partial^2 M_{xy}/\partial x \partial y + \partial^2 M_y/\partial y^2 + \ldots\right] \delta w \, dx \, dy$$
$$- \int_{t_0}^{t_1} dt \oint_C \left\{\left[\partial M_x/\partial x + \partial M_{yx}/\partial y - Q_x + P_x^{(1)} + f_x^{(1)} + \rho(2h^3/3)(\partial \ddot{w}/\partial x)\right] n_x + \left[\partial M_{xy}/\partial x + \partial M_y/\partial y - Q_y + P_y^{(1)} + f_y^{(1)} + \rho(2h^3/3)(\partial \ddot{w}/\partial y)\right] n_y\right\} \delta w \, ds$$
$$- \int_{t_0}^{t_1} dt \oint_C \{\ldots\} \, ds = 0.$$

It is now interesting to see that, by combining the two contour integrals, the Q_x and Q_y terms are eliminated. By finally transforming the combined contour integral from the x, y to the n, s coordinates in the normal and tangential directions, there results

$$\int_{t_0}^{t_1} dt \iint_A \left[\partial^2 M_x/\partial x^2 + 2\partial^2 M_{xy}/\partial x \partial y + \partial^2 M_y/\partial y^2 + \partial P_x^{(1)}/\partial x + \partial P_y^{(1)}/\partial y + P_z^{(0)} + \partial f_x^{(1)}/\partial x + \partial f_y^{(1)}/\partial y + f_z^{(0)} - 2\rho h \ddot{w} + \rho(2h^3/3) \nabla^2 \ddot{w}\right] \delta w \, dx dy$$
$$- \int_{t_0}^{t_1} dt \oint_{C_p} \left\{\left[\partial M_n/\partial n + 2\partial M_{ns}/\partial s + P_n^{(1)} + f_n^{(1)} - p_n^{(0)} - \partial p_s^{(1)}/\partial s + \rho(2h^3/3)(\partial \ddot{w}/\partial n)\right] \delta w - \left[M_n - p_n^{(1)}\right] \delta(\partial w/\partial n)\right\} ds = 0. \quad (19)$$

Equation (19) is the two-dimensional variational equation of motion of the plate, from which the stress equation of motion and traction boundary conditions may be written in the usual manner. The part of the contour C on which tractions are prescribed has been designated by C_p. Since variations of displacements vanish on the part of C on which displacements are prescribed, C reduces to C_p automatically, and the two become indistinguishable in Eq. (19).

The plate stress-displacement relations have the usual form

$$M_x = D(k_x + \nu k_y) = -(\partial^2 w/\partial x^2 + \nu \partial^2 w/\partial y^2)$$
$$M_y = \ldots$$
$$M_{xy} = D(1-\nu)k_{xy} = -D(1-\nu)\partial^2 w/\partial x \partial y$$

where $D = [E/(1-\nu^2)]2h^3/3$. Substitution of these in the stress equation of motion transforms the latter into a displacement equation of motion. Although the transverse shear forces have disappeared altogether from the final variational equation, they may still be written from the double integral in Eq. (18):

$$Q_x = \partial M_x/\partial x + \partial M_{yx}/\partial y + P_x^{(1)} + f_x^{(1)} + \rho(2h^3/3)(\partial \ddot{w}/\partial x)$$
$$Q_y = \ldots .$$

We note that surface tractions in all three directions of x, y, z have been accommodated in the stress equation of motion. We also note that the effect of rotatory inertia is automatically included, although the effect of transverse shear deformation is not. More importantly, we have just demonstrated that, in deriving plate equations of the classical type, the volume and surface integrals in the variational Eq. (6) must be used *jointly* in a coupled manner.

4 Equations for Large Deflections of a Laminated Composite Plate

We consider next a laminated composite plate, or simply a laminate. Similar to the homogeneous plate, it has a middle plane in the xy-plane, with a plan area A and boundary contour C, and a uniform total thickness $2h$ in the z direction. However, the laminate consists of an arbitrary number of plies, each with a uniform thickness. The fiber reinforcement in each ply is undirectional, but the laminate as a whole can be multi-directional. We let the total number of plies in the laminate be designated by n, with the kth ply extending from $z = h_{k-1}$ to $z = h_k$.

The displacements in the laminate are assumed in the form

$$u_x = u - z\,\partial w/\partial x, \quad u_y = v - z\,\partial w/\partial y, \quad u_z = w \quad (20)$$

which now reflect the coupling between extension and flexure due to large deflections. Of the three rotations, ω_{xy} has already been neglected, and the other two are taken in the form

$$\omega_{zz} = -\partial w/\partial x, \quad \omega_{yz} = \partial w/\partial y. \quad (21)$$

The procedure of derivation for the nonlinear laminate is similar to the one just covered in detail for the linear plate, except that the pseudo-variational Eq. (5) is now used instead of the linear variational Eq. (6). With displacements and rotations substituted from Eqs. (20) and (21), it is necessary to carry out integration with respect to z over the entire thickness of the laminate, that is, to cover the thicknesses of all plies. Without going over the details again, the result is

$$\int_{t_0}^{t_1} dt \iint_A \left\{\left[\partial N_x/\partial x + \partial N_{yx}/\partial y + P_x^{(0)} + f_x^{(0)} - \rho^{(0)}\ddot{u} + \rho^{(1)}\partial \ddot{w}/\partial x\right] \delta u + \left[\partial N_{xy}/\partial x + \partial N_y/\partial y + P_y^{(0)} + f_y^{(0)} - \rho^{(0)}\ddot{v} + \rho^{(1)}\partial \ddot{w}/\partial y\right] \delta v + \left[\partial^2 M_x/\partial x^2 + 2\partial^2 M_{xy}/\partial x \partial y + \partial^2 M_y/\partial y^2 + (\partial/\partial x)(N_x \partial w/\partial x + N_{xy}\partial w/\partial y) + (\partial/\partial y)(N_{xy}\partial w/\partial x + N_y \partial w/\partial y) + \partial P_x^{(1)}/\partial x + \partial P_y^{(1)}/\partial y + P_z^{(0)} + \partial f_x^{(1)}/\partial x + \partial f_y^{(1)}/\partial y + f_z^{(0)} - \rho^{(0)}\ddot{w} - \rho^{(1)}(\partial \ddot{u}/\partial x - \partial \ddot{v}/\partial y) + \rho^{(2)} \nabla^2 \ddot{w}\right] \delta w\right\} dx dy$$
$$- \int_{t_0}^{t_1} dt \oint_{C_p} \left\{\left[N_n - p_n^{(0)}\right] \delta u_n + \left[N_{ns} - p_s^{(0)}\right] \delta u_s - \left[M_n - p_n^{(1)}\right] \delta(\partial w/\partial n) + \left[\partial M_n/\partial n + 2\partial M_{ns}/\partial s + N_n \partial w/\partial n + N_{ns}\partial w/\partial s + P_n^{(1)} + f_n^{(1)} - p_z^{(0)} - \partial P_s^{(1)}/\partial s - \rho^{(1)}\ddot{u}_n + \rho^{(2)}(\partial \ddot{w}/\partial n)\right] \delta w\right\} ds = 0 \quad (22)$$

where the notations are similar to those used before:

$$\left[N_x, N_y, N_{xy}, M_x, M_y, M_{xy}\right] = \sum_{k=1}^{n} \int_{h_{k-1}}^{h_k} \left[\sigma_{xx(k)}, \sigma_{yy(k)}, \sigma_{xy(k)}, \sigma_{xx(k)}z, \sigma_{yy(k)}z, \sigma_{xy(k)}z\right] dz$$
$$P_x^{(0)} = p_x^+ + p_x^-, \; P_y^{(0)} = \ldots, \; P_x^{(0)} = \ldots$$

Downloaded 04 May 2010 to 171.66.16.28. Redistribution subject to ASME license or copyright; see http://www.asme.org/terms/Terms_Use.cfm

$$P_x^{(1)} = h(p_x^+ - p_x^-),\ P_y^{(1)} = \ldots,\ P_n^{(1)} = \ldots,\ P_s^{(1)} = \ldots$$

$$\left[f_x^{(0)}, f_x^{(1)}, f_y^{(0)}, f_y^{(1)}, f_z^{(0)}\right] = \sum_{k=1}^{n} \int_{h_{k-1}}^{h_k} \left[f_{x(k)}, f_{x(k)}z, f_{y(k)}, f_{y(k)}z, f_{z(k)}\right] dz$$

$$\left[\rho^{(0)}, \rho^{(1)}, \rho^{(2)}\right] = \sum_{k=1}^{n} \int_{h_{j-1}}^{h_k} \rho_{(k)}[1, z, z^2]dz$$

$$\left[p_x^{(0)}, p_x^{(1)}\right] = \sum_{k=1}^{n} \int_{h_{k-1}}^{h_k} p_x[1, z]\, dz, \ldots.$$

Equation (22) is the variational equation of motion for large deflections of a laminated composite plate. As in the case of a linear plate, the transverse shear forces Q_x and Q_y have again disappeared from the final result. Similarly, for either a linear or nonlinear laminate, p_x^+, p_x^-, ... represent tractions at the top and bottom boundary planes of the composite plate. Tractions at the interfaces between adjacent plies have cancelled out since they are action and reaction to each other. Finally, it is important to note that the coupling inertia $\rho^{(1)}$ may not vanish for a laminate that is generally anisotropic. This provides dynamic coupling between extension and flexure.

We recall that, in the absence of the piezoelectric effect in nonlinear elasticity, the electric enthalpy density H reduces to the strain energy density E in the first of Eqs. (10). This then shows that the components of the Kirchhoff stress tensor are associated with those of the Green nonlinear strain tensor in the same manner as linear stresses and strains are related to each other in linear elasticity. Similar to the usual linear relations we therefore have

$$\begin{bmatrix} N_x \\ N_y \\ N_{xy} \\ M_x \\ M_y \\ M_{xy} \end{bmatrix} = \begin{bmatrix} A_{11} & A_{12} & A_{16} & B_{11} & B_{12} & B_{16} \\ A_{12} & A_{22} & A_{26} & B_{12} & B_{22} & B_{26} \\ A_{16} & A_{26} & A_{66} & B_{16} & B_{26} & B_{66} \\ B_{11} & B_{12} & B_{16} & D_{11} & D_{12} & D_{16} \\ B_{12} & B_{22} & B_{26} & D_{12} & D_{22} & D_{26} \\ B_{16} & B_{26} & B_{66} & D_{16} & D_{26} & D_{66} \end{bmatrix} \begin{bmatrix} \epsilon_{xx}^{(0)} \\ \epsilon_{yy}^{(0)} \\ 2\epsilon_{xy}^{(0)} \\ \epsilon_{xx}^{(1)} \\ \epsilon_{yy}^{(1)} \\ 2\epsilon_{xy}^{(1)} \end{bmatrix} \tag{23}$$

where the plate stresses are now associated with the Kirchhoff stresses. The extensional, coupling, and flexural stiffnesses are the same as in the linear case:

$$\left[A_{ij}, B_{ij}, D_{ij}\right] = \sum_{k=1}^{n} Q_{ij(k)} \left[(h_k - h_{k-1}), \left(h_k^2 - h_{k-1}^2\right)/2, \left(h_k^3 - h_{k-1}^3\right)/3\right]$$

where $Q_{ij(k)}$ are the off-axis stiffnesses of the kth ply.

In the simplified case of small strains and large rotations the nonlinear strains are

$$\epsilon_{xx} = \partial u/\partial x - z\,\partial^2 w/\partial x^2 + \frac{1}{2}(\partial w/\partial x)^2$$

$$\epsilon_{yy} = \partial v/\partial y - z\,\partial^2 w/\partial y^2 + \frac{1}{2}(\partial w/\partial y)^2$$

$$\epsilon_{xy} = \frac{1}{2}(\partial u/\partial y + \partial v/\partial x) - z\,\partial^2 w/\partial x \partial y + \frac{1}{2}(\partial w/\partial x)(\partial w/\partial y) \tag{24}$$

from which the plate nonlinear strains are

$$\epsilon_{xx}^{(0)} = \partial u/\partial x + \frac{1}{2}(\partial w/\partial x)^2$$

$$\epsilon_{yy}^{(0)} = \ldots$$

$$\epsilon_{xy}^{(0)} = \frac{1}{2}(\partial u/\partial y + \partial v/\partial x) + \frac{1}{2}(\partial w/\partial x)(\partial w/\partial y)$$

$$\epsilon_{xx}^{(1)} = -\partial^2 w/\partial x^2$$

$$\epsilon_{yy}^{(1)} = \ldots$$

$$\epsilon_{xy}^{(1)} = -\partial^2 w/\partial x \partial y. \tag{25}$$

Substitution of Eqs. (25) into (23) yields the plate stress-displacement relations, by means of which the stress equations of motion may be transformed readily into the displacement equations of motion for the laminate.

5 Equations for Large Deflections of a Single-Layered Plate

It is interesting to note that the variational Eq. (22) for a multiple-layered laminate can be applied to a single-layered plate by simply letting

$$\rho^{(0)} = 2\rho h, \quad \rho^{(1)} = 0, \quad \rho^{(2)} = \tfrac{2}{3}\rho h^3.$$

To save space the result deduced will be assigned a new equation number according to the following scheme:

$$\text{Eq. (22) with } \rho^{(0)} = 2\rho h,\ \rho^{(1)} = 0,\ \rho^{(2)} = \tfrac{2}{3}\rho h^3. \tag{26}$$

The stress equations of motion written from Eq. (26) correspond to von Kármán's equations for large deflections of a homogeneous plate. However, the usual form of the original equations in the static case is more restricted. For instance, it includes only the lateral load in the z direction but not tractions in the x and y directions.

6 Equations for Large Deflections of a Piezoelectric Plate

The treatment for large deflections of a single-layered elastic plate may be extended readily to include the piezoelectric effect, by assuming the same displacements and rotations as given in Eqs. (20) and (21). In fact, the first three components of the generalized variational equation, Eqs. (9a, b, c), have the same form regardless of whether the piezoelectric effect is included or not, and Eqs. (24) and (25) as well as (26) remain valid even for a piezoelectric plate. To complete the treatment for the piezoelectric plate, we continue to make use of the other component equations in Eqs. (9). Integration with respect to time is now ignored.

Plate Strain-Displacement Relations. For a piezoelectric plate, these relations are the same as those for an elastic plate, and are given directly by Eqs. (24) and (25). However, the use of the component Eq. (9c) to derive the same results further reveals some interesting and important characteristics of a classical plate. Without dealing with the details, it can be shown readily from Eq. (9c) that, although the transverse shear plate strains $\epsilon_{zx}^{(0)}$ and $\epsilon_{zy}^{(0)}$ vanish, the transverse shear forces Q_x and Q_y need not. This has been mentioned earlier. On the other hand, the transverse normal plate strains $\epsilon_{zz}^{(0)}$ and $\epsilon_{zz}^{(1)}$ are allowed to develop freely, although the transverse normal plate stresses $\sigma_{zz}^{(0)}$ and $\sigma_{zz}^{(1)}$ do not appear in the stress equations of motion and may thus be taken equal to zero.

Constitutive Relations in a Piezoelectric Plate. The constitutive relations in linear piezoelectricity have been addressed by Mindlin (1984), Tiersten (1969) and Lee et al.

Downloaded 04 May 2010 to 171.66.16.28. Redistribution subject to ASME license or copyright; see http://www.asme.org/terms/Terms_Use.cfm

(1987). These have been extended in this paper to cover nonlinear strains according to Eqs. (10), (11), and (12). Equations (10) have also appeared in the form of the two component Eqs. (9*d*, *e*), which are used here.

We start with Eq. (9*d*), now written in the form

$$\iint_A \int_{-h}^{h} \left(\sigma_{ij} - c_{ijkl}\,\epsilon_{kl} + e_{kij}E_k\right)\,\delta\epsilon_{ij}\,dx\,dy\,dz = 0. \quad (27)$$

By incorporating the approximations

$$\begin{aligned} \epsilon_{kl} &= \epsilon_{kl}^{(0)} + z\epsilon_{kl}^{(1)} \quad (k,l = x,y,z) \\ E_k &= E_k^{(0)} + z\,E_k^{(1)} \quad (k = x,y,z) \end{aligned} \quad (28)$$

and integrating with respect to z, Eq. (27) yields

$$\iint_A \left\{\left[\sigma_{ij}^{(0)} - 2h\left(c_{ijkl}\epsilon_{kl}^{(0)} - e_{kij}E_k^{(0)}\right)\right]\,\delta\epsilon_{ij}^{(0)} + \left[\sigma_{ij}^{(1)} - \tfrac{2}{3}h^3\left(c_{ijkl}\epsilon_{kl}^{(1)} - e_{kij}E_k^{(1)}\right)\right]\,\delta\epsilon_{ij}^{(1)}\right\} dx\,dy = 0. \quad (29)$$

The integrand in Eq. (29) consists of six pairs of relations corresponding to the six pairs of variations of the plate strains. Since the transverse shear plate strains $\epsilon_{zy}^{(0)}$, $\epsilon_{zx}^{(0)}$, $\epsilon_{zy}^{(1)}$, $\epsilon_{zx}^{(1)}$ are zero in the classical plate theory, the two corresponding pairs of relations drop out. A third pair that is also associated with the thickness direction has the form

$$\left[\sigma_{zz}^{(0)} - 2h\left(c_{zzkl}\,\epsilon_{kl}^{(0)} - e_{kzz}E_k^{(0)}\right)\right]\,\delta\epsilon_{zz}^{(0)} + \left[\sigma_{zz}^{(1)} - \tfrac{2}{3}h^3\left(c_{xzkl}\epsilon_{kl}^{(1)} - e_{kzz}E_k^{(1)}\right)\right]\,\delta\epsilon_{zz}^{(1)}$$

in which the transverse plate normal stresses $\sigma_{zz}^{(0)}$ and $\sigma_{zz}^{(1)}$ may be put equal to zero because they do not appear in the stress equations, as mentioned earlier. By equating the coefficients of the variations $\delta\epsilon_{zz}^{(0)}$ and $\delta\epsilon_{zz}^{(1)}$ equal to zero, the plate strains $\epsilon_{zz}^{(0)}$ and $\epsilon_{zz}^{(1)}$ themselves may then be solved in terms of the other plate strains and plate electric fields. In fact, when the results are substituted into the remaining three pairs of relations, $\epsilon_{zz}^{(0)}$ and $\epsilon_{zz}^{(1)}$ become eliminated. Equation (29) then reduces to the final form

$$\iint_A \left\{\left[\left(\sigma_{ij}^{(0)} - 2h\left(c_{ijkl}^{*}\,\epsilon_{kl}^{(0)} - e_{kij}^{*}E_k^{(0)}\right)\right]\,\delta\epsilon_{ij}^{(0)} + \left[\left(\sigma_{ij}^{(1)} - \tfrac{2}{3}h^3\left(c_{ijkl}^{*}\,\epsilon_{kl}^{(1)} - e_{kij}^{*}\,E_k^{(1)}\right)\right]\,\delta\epsilon_{ij}^{(1)}\right\} dx\,dy = 0 \quad (30)$$

where

$$\begin{aligned} c_{ijkl}^{*} &= c_{ijkl} - c_{zzkl}\left(c_{ijzz}/c_{zzzz}\right) \\ e_{kij}^{*} &= e_{kij} - e_{kzz}\,\left(c_{ijzz}/c_{zzzz}\right). \end{aligned}$$

Equation (30) is one of the components of the generalized variational equation of motion of the piezoelectric plate, which now yields only three pairs of plate stress-strain relations, with subscripts i and j equal to x or y but no longer z. These are for the plate stresses $\sigma_{xx}^{(0)}$, $\sigma_{xx}^{(1)}$, $\sigma_{yy}^{(0)}$, $\sigma_{yy}^{(1)}$, $\sigma_{xy}^{(0)}$, $\sigma_{xy}^{(1)}$ or, equivalently, N_x, M_x, N_y, M_y, N_{xy}, M_{xy}.

We next consider the other component Eq. (9*e*) similarly, which is written as

$$\iint_A \int_{-h}^{h} \left(D_i - e_{ijk}\epsilon_{jk} - e_{ij}E_j\right)\,\delta E_i\,dx\,dy\,dz = 0. \quad (31)$$

Upon substitution of Eqs. (28) and integration with respect to z, this becomes

$$\iint_A \left\{\left[D_i^{(0)} - 2h\left(e_{ijk}\epsilon_{jk}^{(0)} + e_{ij}E_j^{(0)}\right)\right]\,\delta E_j^{(0)} + \left[D_i^{(1)} - \tfrac{2}{3}h^3\left(e_{ijk}\epsilon_{jk}^{(1)} + e_{ij}E_j^{(1)}\right)\right]\,\delta E_j^{(1)}\right] dx\,dy = 0$$

where

$$\left(D_i^{(0)}, D_i^{(1)}\right) = \int_{-h}^{h} \left(D_i, D_i z\right)\,dz$$

are the plate electric displacements. As in the situation with plate stresses, the results for the electric displacements are similarly modified by replacing e_{ijk} by e_{ijk}^{*} so that the above equation further becomes

$$\iint_A \left\{\left[D_i^{(0)} - 2h\left(e_{ijk}^{*}\epsilon_{jk}^{(0)} + e_{ij}E_j^{(0)}\right)\right]\,\delta E_j^{(0)} + \left[D_i^{(1)} - \tfrac{2}{3}h^3\left(e_{ijk}^{*}\epsilon_{jk}^{(1)} + e_{ij}E_j^{(1)}\right)\right]\,\delta E_j^{(1)}\right] dx\,dy = 0$$

which is another component of the generalized variational equation of the piezoelectric plate and from which the relations for the plate electric displacements may be written immediately.

The plate electric enthalpy density is now

$$H^{(0)} = \int_{-h}^{h} H\,dz = h\left(c_{ijkl}^{*}\epsilon_{ij}^{(0)}\epsilon_{kl}^{(0)} - 2e_{kij}^{*}E_k^{(0)}\epsilon_{ij}^{(0)} - e_{ij}E_i^{(0)}E_j^{(0)}\right) + \tfrac{1}{3}h^3\left(c_{ijkl}^{*}\epsilon_{ij}^{(1)}\epsilon_{kl}^{(1)} - 2e_{kij}^{*}E_k^{(1)}\epsilon_{ij}^{(1)} - e_{ij}E_i^{(1)}E_j^{(1)}\right)$$

from which

$$\begin{aligned} \sigma_{ij}^{(0)} &= \partial H^{(0)}/\partial\epsilon_{ij}^{(0)}, \quad \sigma_{ij}^{(1)} = \partial H^{(0)}/\partial\epsilon_{ij}^{(1)} \\ D_i^{(0)} &= -\partial H^{(0)}/\partial E_i^{(0)}, \quad D_i^{(1)} = -\partial H^{(0)}/\partial E_i^{(1)} \end{aligned}$$

Electrostatics in a Piezoelectric Plate. By introducing the approximation

$$\phi = \phi^{(0)} + z\,\phi^{(1)}, \quad (32)$$

we find from the component Eq. (9*f*)

$$\iint_A \left\{\left[\partial D_x^{(0)}/\partial x + \partial D_y^{(0)}/\partial y + \Sigma^{(0)}\right]\,\delta\phi^{(0)} + \left[\partial D_x^{(1)}/\partial x + \partial D_y^{(1)}/\partial y - D_z^{(0)} + \Sigma^{(1)}\right]\,\delta\phi^{(1)}\right\} dx\,dy - \int_{C_\sigma} \left\{\left[\left(D_n^{(0)} - \sigma^{(0)}\right]\,\delta\phi^{(0)} + \left[\left(D_n^{(1)} - \sigma^{(1)}\right]\,\delta\phi^{(1)}\right\} ds = 0, \quad (33)$$

where C_σ denotes that part of the boundary curve C on which the edge charges are prescribed,

$$\left(\sigma^{(0)}, \sigma^{(1)}\right) = \int_{-h}^{h} \left(\sigma, \sigma z\right)\,dz$$

are the plate edge charges, and

$$\Sigma^{(0)} = (\sigma)_h + (\sigma)_{-h}, \quad \Sigma^{(1)} = h\left[(\sigma)_h - (\sigma)_{-h}\right]$$

the plate face charges. Equation (33) represents still another component of the generalized variational equation for the piezoelectric plate, from which the field equations of electrostatics and edge conditions for prescribed electric charge may be written immediately.

An alternative set of edge conditions for prescribed electric potential may be derived from the remaining component Eq. (9*g*). By making use of Eq. (32), this becomes

$$\int_{C_\phi} \left\{\left[\left(\phi^{(0)} - \phi^{(0)^*}\right]\,\delta\sigma^{(0)} + \left[\left(\phi^{(1)} - \phi^{(1)^*}\right]\,\delta\sigma^{(1)}\right\} ds = 0 \quad (34)$$

which represents one more component equation and from which two-dimensional edge potential conditions may be written similarly.

Downloaded 04 May 2010 to 171.66.16.28. Redistribution subject to ASME license or copyright; see http://www.asme.org/terms/Terms_Use.cfm

7 Concluding Remarks

As is well known, linear classical theory of elastic plates was discussed in detail in the standard reference by Timoshenko (1940), in which the von Kármán equations for large deflections of elastic plates were also treated. Since then linear and nonlinear classical plate equations have been discussed in many books, some of which were cited in our recent work (Yu, 1991). In spite of such wide coverage, the method of deriving classical plate equations from variational equations of motion in three-dimensional elasticity as shown in this paper is new, although some of the results may be derived by other means.

An interesting connection between equations of homogeneous plates and those of laminated composite plates has been pointed out in this paper. Discussions of early equations and associated vibration analyses of sandwich and laminated composite plates and shells, as well as the connection between the two layered types, may be found in our review published recently both in English (Yu, 1989) and in Russian (Yu, 1992a). Additional linear and nonlinear studies of laminated composite plates (Yu, 1992d, 1993) have since been made.

Standard references on three-dimensional piezoelectricity include the books by Cady (1946), Mason (1950), Jaffe, Cook, and Jaffe (1971), and other more recent ones, in which derivations of two-dimensional equations of piezoelectric plates are usually not well covered. In the aforementioned works by Mindlin (1984), Tiersten (1969), and Lee et al. (1987), two-dimensional equations of linear piezoelectric plates were indeed derived. Since their efforts were concentrated on high-frequency vibrations, thickness effects were always included, and the resulting plate equations were not of the classical type. The generalized Hamilton's principle and associated variational equation of motion in coupled three-dimensional nonlinear elasticity and piezoelectricity presented here are also new, and so are the two-dimensional classical equations for large deflections of piezoelectric plates derived therefrom.

Addendum

After this paper had been accepted for publication, another closely related paper (Yu, 1995a) was presented at the Fourth Pan-American Congress of Applied Mechanics in Argentina and published in the congress proceedings. Still a third one, a comprehensive survey paper (Yu, 1995b), will soon be published in the *Journal of Intelligent Material Systems and Structures*. A detailed treatment of vibrations of elastic plates may be found in a forthcoming book (Yu, 1995c), also to be published later this year.

References

Cady, W. G., 1946, *Piezoelectricity*, McGraw-Hill, New York.

Fung, Y. C., 1965, *Foundations of Solid Mechanics*, Prentice-Hall, Englewood Cliffs, NJ.

Hu, H. C., 1954, "On Some Variational Principles in the Theory of Elasticity and the Theory of Plasticity," *Acta Physica Sinica*, Vol. 10, p. 259; also 1955, *Scientia Sinica*, Vol. 4, p. 33.

Jaffe, B., Cook, W. R., and Jaffe, H., 1971, *Piezoelectric Ceramics*, Academic Press, New York.

Lee, P. C. Y., Syngellakis, S., and Hou, J. P., 1987, "A Two-Dimensional Theory for High-Frequency Vibrations of Piezoelectric Crystal Plates With or Without Electrodes," *Journal of Applied Physics*, Vol. 61, pp. 1249–1262.

Love, A. E. H., 1927, *A Treatise on the Mathematical Theory of Elasticity*, 4th ed., Cambridge University Press, Cambridge, UK, p. 166.

Mason, W. P., 1950, *Piezoelectric Crystals and Their Application to Ultrasonics*, D. Van Nostrand Company.

Mindlin, R. D., 1984, "Frequencies of Piezoelectrically Forced Vibrations of Electroded, Doubly Rotated, Quartz Plates," *International Journal of Solids and Structures*, Vol. 20, pp. 141–157.

Novozhilov, V. V., 1948, *Foundations of the Nonlinear Theory of Elasticity* (English translation, 1953, Graylock Press).

Reissner, E., 1947, "On Bending of Elastic Plates," *Quarterly of Applied Mathematics*, Vol. 5, pp. 55–68.

Tiersten, H. F., 1969, *Linear Piezoelectric Plate Vibrations*, Plenum Press.

Timoshenko, S., 1940, *Theory of Plates and Shells*, 1st ed., McGraw-Hill, New York.

Washizu, K., 1955, "On the Variational Principles of Elasticity and Plasticity," M. I. T. Aeroelastic Structures Research Laboratory Report 25.18.

Washizu, K., 1982, *Variational Methods in Elasticity and Plasticity*, 3rd ed., Pergamon Press.

Yu, Y. Y., 1962, "Nonlinear Flexural Vibrations of Sandwich Plates," *Journal of Acoustical Society of America*, Vol. 34, pp. 1176–1183.

Yu, Y. Y., 1964, "Generalized Hamilton's Principle and Variational Equation of Motion in Nonlinear Elasticity Theory, with Application to Plate Theory," *Journal of Acoustical Society of America*, Vol. 36, pp. 111–120.

Yu, Y. Y., 1965a, "On Linear Equations of Anisotropic Elastic Plates," *Quarterly of Applied Mathematics*, Vol. 22, pp. 357–360.

Yu, Y. Y., 1965b, "On Linear Equations of Isotropic Elastic Plates and Shells," *Journal of the Franklin Institute*, Vol. 280, pp. 395–416.

Yu, Y. Y., 1989, "Dynamics and Vibration of Layered Plates and Shells —A Perspective from Sandwiches to Laminated Composites," in bound volume of papers presented at the 30th AIAA/ASME/ASCE/AHS/ASC Structures, Structural Dynamics and Materials Conference, AIAA, pp. 2236–2245; also in *Proceedings of U.S. Papers*, First USSR-US Symposium on Mechanics of Composite Materials, ASME, pp. 231–240.

Yu, Y. Y., 1991, "On Equations for Large Deflections of Elastic Plates and Shallow Shells," *Mechanics Research Communications*, Vol. 18, pp. 373–384.

Yu, Y. Y., 1992a, "Dynamics and Vibration of Layered Plates and Shells—A Perspective from Sandwiches to Laminated Composites," *Mechanics of Composite Materials, Vol. 2, Construction of Composites, Proceedings of the First Soviet-American Symposium*, pp. 99–108, Riga, Latvia. (This is a Russian translation of the earlier review by Yu (1989).)

Yu, Y. Y., 1992b, "Equations for Large Deflections of Homogeneous and Layered Beams with Application to Chaos and Acoustic Radiation," *Composites Engineering*, Vol. 2, pp. 117–136.

Yu, Y. Y., 1992c, "Generalized Variational Equations of Motion in Nonlinear Anisotropic Elasticity and Plate Theories," *Collection of Papers, a Volume Dedicated to the 80th Birthday of Academician V. V. Novozhilov*, edited by Academician N. S. Solomenko, pp. 63–74, Shipbuilding Publishing House, St. Petersburg, Russia.

Yu, Y. Y., 1992d, "Extensional and Flexural Vibrations of Laminated Composite Plates," *Proceedings of the 7th Technical Conference on Composite Materials*, American Society for Composites, Technomic Publishing Co, pp. 962–971.

Yu, Y. Y., 1993, "Nonlinear Large-Deflection Vibrations of Laminated Composite Plates," *Proceedings of the 8th Technical Conference on Composite Materials*, American Society for Composites, Technomic Publishing Co, pp. 1099–1108.

Yu, Y. Y., 1995a, "On Small Strains and Large Rotations in Nonlinear Elasticity and Piezoelectricity," *Proceedings of the Fourth Pan-American Congress of Applied Mechanics*, Vol. I, pp. 477–482.

Yu, Y. Y., 1995b, "Recent Advances in Linear and Nonlinear Dynamic Modeling of Elastic and Piezoelectric Plates," *Journal of Intelligent Materials Systems and Structures* to be published.

Yu, Y. Y., 1995c, *Vibrations of Elastic Plates: Linear and Nonlinear Dynamical Modeling of Sandwiches, Laminated Composites, and Piezoelectric Layers*, Springer-Verlag, New York, to be published.

Downloaded 04 May 2010 to 171.66.16.28. Redistribution subject to ASME license or copyright; see http://www.asme.org/terms/Terms_Use.cfm

Loc Vu-Quoc
Associate Professor,
Mem. ASME.

H. Deng
Graduate Research Assistant.

Department of Aerospace Engineering,
Mechanics and Engineering Science,
University of Florida,
P.O. Box 116250,
Gainesville, FL 32611-6250

Galerkin Projection for Geometrically Exact Sandwich Beams Allowing for Ply Drop-off[1]

A Galerkin projection of the equations of equilibrium for a recent theory of geometrically exact sandwich beams that allow finite rotations and shear deformation in each layer is presented. The continuity of the displacement across the layers is exactly satisfied. The resulting finite element formulation can accommodate large deformation. The number of layers is variable, with layer lengths and thicknesses not required to be the same, thus allowing the modeling of sandwich structures with ply drop-off. Numerical examples are presented which underline the salient features of the formulation. Saint-Venant principle is demonstrated for very short sandwich beams.

1 Introduction

Sandwich structures have been playing an increasingly important role in many areas of engineering. We describe here a follow-up work to that presented in Vu-Quoc and Ebcioğlu (1995) where we derive the equations of motion for geometrically exact sandwich beams and one-dimensional plates. Focusing on the static case in the present work, we develop a Galerkin projection of the resulting nonlinear governing equations of equilibrium.[2]

In the proposed theory, each layer in the beam can have different thickness and length. As such one can use the present formulation to model an important class of multilayer structures having ply drop-off. No restriction is imposed on the magnitude of the displacement field, whose continuity across the layer interfaces is exactly enforced. The layer cross-section in the deformed beam is assumed to remain straight, but not orthogonal to the layer centroidal line, thus shear deformation in each layer is accounted for. Also no restriction is imposed on the rotation of a layer cross-section. It follows that the overall cross-section in the deformed beam is continuous piecewise linear, and can be best thought of as a chain of rigid links, connected by hinges. The overall deformation of a multilayer beam can be described by the deformation of a reference layer. The unknown kinematic quantities are therefore the two displacement components of the deformed centroidal line of a reference layer, and the finite rotations of the layers. The present theory can be used to analyze large deformation in sandwich beams.

The starting point for the development of the Galerkin projection of the governing equations is the nonlinear weak form based on the stress power of sandwich beams, from which expressions of fully nonlinear strain measures are obtained (see Vu-Quoc and Ebcioğlu, 1995). A linearization of this nonlinear weak form is performed for use in the solution for the kinematic quantities using Newton's method. The result of this linearization is a symmetric tangent stiffness operator, which is composed of a geometric part and a material part. Linear and quadratic finite element functions are chosen to form a basis for the Galerkin projection of the linearized equilibrium equations into a finite-dimensional subspace of trial solutions. The tangent stiffness matrix is symmetric, and is evaluated using uniformly reduced integration in all layers to avoid shear locking.[3] There are several ways to assign the boundary conditions in the present theory, e.g., while a clamped boundary condition can be represented by only one way in a single-layer beam (one rotation), it can be represented by six different ways in a sandwich beam (three different rotations). And the same can be said for the assignment of applied moments.

[1]Dedicated to the memory of Professor Juan Carlos Simo whose early demise is a great loss for the applied and computational mechanics community.

[2]Many background references were cited in Vu-Quoc and Ebcioğlu (1994), and will not be repeated in the present follow-up paper, except for particularly relevant ones. We refer to review papers such as Reddy (1989), Noor and Burton (1989), Noor (1990), Reddy and Robbins (1994), and the references therein for various aspects on formulations for multilayer structures. The accuracy of layerwise theory, as compared to single-layer theory with a shear correction factor, has been amply demonstrated in Reddy (1989), where a comparison of transverse shear stress with three-dimensional elasticity solution is provided; see also Reddy (1993). For a theory without shear deformation, see Dong, Pister and Taylor (1962); for theories with shear deformation, see, e.g., Di Sciuva (1987), Pai, Nayfeh, Oh, and Mook (1993), etc.

Contributed by the Applied Mechanics Division of THE AMERICAN SOCIETY OF MECHANICAL ENGINEERS for presentation at the Joint Applied Mechanics and Materials Summer Meeting of the ASME, Los Angeles, CA, June 28–30, 1995.

Discussion on this paper should be addressed to the Technical Editor, Professor Lewis T. Wheeler, Department of Mechanical Engineering, University of Houston, Houston, TX 77204-4792, and will be accepted until four months after final publication of the paper itself in the ASME JOURNAL OF APPLIED MECHANICS.

Manuscript received by the ASME Applied Mechanics Division, Aug. 8, 1994; final revision, Nov. 15, 1994. Associate Technical Editor: J. N. Reddy.

Paper No. 95-APM-7.

[3]See Arnold (1981) for the analysis of reduced integration in the linear single-layer case.

Copyright © 1995 by ASME

Downloaded 04 May 2010 to 171.66.16.28. Redistribution subject to ASME license or copyright; see http://www.asme.org/terms/Terms_Use.cfm

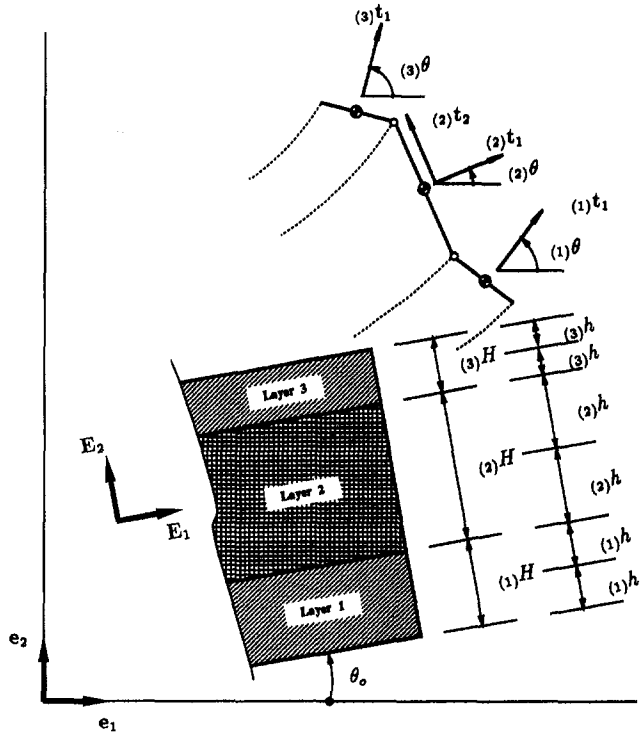

Fig. 1 Sandwich beam / one-dimensional plate: Section profile. Layer thickness. Basis vectors: $_{(1)}\mathbf{t}_2$ and $_{(3)}\mathbf{t}_2$ are now drawn.

Several numerical examples are presented to illustrate the salient features of the present formulation. In particular, the important case of multilayer beams with ply drop-off, under large deformation, is presented. Unlike single-layer beams, the sandwich beam in the present formulation can be used to illustrate clearly the Saint-Venant principle.

2 Equilibrium Equations

2.1 Strong Form. The profile of a sandwich beam and its deformed cross-section is depicted in Fig. 1 where the layers are numbered (1), (2), (3) from bottom to top. As already mentioned, the present theory is valid for layers with unequal length, as occurred in beams with ply drop-off. In our finite element formulation, we allow the number of layers within an element to be variable, while keeping the length of all layers in the same element equal. Since our focus is the development of the expressions for the element matrices, we will henceforth consider the case where all layers have equal length L, without loss of generality. Beams with ply drop-off are modeled by assembling elements with different numbers of layers. Thus let $\mathcal{L} :=]0, L[$ be the domain of the space variable S, on which the equilibrium equations are defined. The thickness of layer (l)—for $l = 1, 2, 3$—is denoted by $_{(l)}H := 2_{(l)}h$.

The deformation map $_{(2)}\mathbf{\Phi}_0$: $\mathcal{L} \to \mathbb{R}^2$ of the centroidal line of the core layer (2), chosen to be the reference layer, is given by[4]

$$_{(2)}\mathbf{\Phi}_0(S) = S\mathbf{E}_1 + \mathbf{u}(S), \quad \mathbf{E}_1 = \cos\theta_0\mathbf{e}_1 + \sin\theta_0\mathbf{e}_2,$$
$$\mathbf{u}(S) = u^\alpha(S)\mathbf{e}_\alpha, \tag{2.1}$$

where $S \in \mathcal{L}$ is the material coordinate, $\mathbf{E}_1$ is the material basis vector along the undeformed beam, $\{\mathbf{e}_1, \mathbf{e}_2\}$ the spatial basis vectors, and $\mathbf{u} = u^\alpha\mathbf{e}_\alpha$ the displacement vector of the material point $S\mathbf{E}_1$ (see also Vu-Quoc and Li, 1993). With $\{_{(l)}\mathbf{t}_1, _{(l)}\mathbf{t}_2\}$ designating the basis vectors attached to a cross-section of layer (l) as shown in Fig. 1, then the deformation maps of centroidal line for layers (1) and (3) can be expressed in terms of $_{(2)}\mathbf{\Phi}_0$ as follows:

$$_{(1)}\mathbf{\Phi}_0 = _{(2)}\mathbf{\Phi}_0 - _{(1)}h_{(1)}\mathbf{t}_2 - _{(2)}h_{(2)}\mathbf{t}_2,$$
$$_{(3)}\mathbf{\Phi}_0 = _{(2)}\mathbf{\Phi}_0 + _{(2)}h_{(2)}\mathbf{t}_2 + _{(3)}h_{(3)}\mathbf{t}_2, \tag{2.2}$$

so that the displacement is continuous at the layer interfaces. The spatial strain measure $_{(l)}\gamma = _{(l)}\gamma^\alpha\mathbf{e}_\alpha$ in layer (l) is given by

$$_{(l)}\gamma := \frac{\partial_{(l)}\mathbf{\Phi}_0}{\partial S} - _{(l)}\mathbf{t}_1 \tag{2.3}$$

The resultant contact force $_{(l)}\mathbf{n} = _{(l)}n^\alpha\mathbf{e}_\alpha$ is related to the spatial strain $_{(l)}\gamma$ by

$$_{(l)}\mathbf{n} = _{(l)}\mathbf{\Lambda} \cdot _{(l)}\mathfrak{C} \cdot _{(l)}\mathbf{\Lambda}^T \cdot _{(l)}\gamma, \tag{2.4}$$

where $_{(l)}\mathbf{\Lambda} = _{(l)}\Lambda^\alpha_\beta\mathbf{e}_\alpha \otimes \mathbf{e}^\beta$ is the rotation tensor defined as follows:

$$_{(l)}\mathbf{t}_\alpha = _{(l)}\mathbf{\Lambda} \cdot \mathbf{E}_\alpha, \quad \left[_{(l)}\Lambda^\alpha_\beta\right] := \begin{bmatrix} \cos_{(l)}\theta & -\sin_{(l)}\theta \\ \sin_{(l)}\theta & \cos_{(l)}\theta \end{bmatrix}, \tag{2.5}$$

with $_{(l)}\theta$ being the rotation angle of layer (l) cross-section, and $_{(l)}\mathfrak{C} = _{(l)}\mathfrak{C}^\alpha_\beta\mathbf{e}_\alpha \otimes \mathbf{e}^\beta$ the tensor of elastic moduli whose matrix of components is

$$\left[_{(l)}\mathfrak{C}^i_j\right] := \begin{bmatrix} _{(l)}EA & 0 \\ 0 & _{(l)}GA_s \end{bmatrix}, \tag{2.6}$$

where $_{(l)}EA$ and $_{(l)}GA_s$ are the axial and shear stiffness coefficients of layer (l). The resultant contact couple $_{(l)}m$ of layer (l) and the curvature $_{(l)}\theta_{,S}$ are related through

$$_{(l)}m = _{(l)}EI\,_{(l)}\theta_{,S}. \tag{2.7}$$

Thus, for a sandwich beam, the five unknown kinematic quantities are gathered in Φ: $\mathcal{L} \to \mathbb{R}^5$ such that

$$\Phi(S) := \left\{u^1, u^2, _{(1)}\theta, _{(2)}\theta, _{(3)}\theta\right\}^T|_{(S)}. \tag{2.8}$$

The contact force $_{(l)}\mathbf{n}$ is related to the kinematic quantities in a nonlinear fashion via (2.1)–(2.4). Further, let

$$\hat{\mathbf{n}} := \sum_{l=1}^{3} {}_{(l)}\mathbf{n} \tag{2.9}$$

denote the total resultant contact force for all layers, and $\bar{\hat{\mathbf{n}}}$: $\mathcal{L} \to \mathbb{R}^2$ the total assigned resultant force distributed along the centroidal line of the reference layer. For layer (l), the assigned couple is denoted by $_{(l)}\bar{\mathfrak{M}}$: $\mathcal{L} \to \mathbb{R}$. The relationship between $_{(l)}\bar{\mathfrak{M}}$ and the resultant contact couple $_{(l)}m$ will be seen in the expressions for the boundary conditions (2.11) below.

We recall below the equation of equilibrium of geometrically exact sandwich beams, derived in Vu-Quoc and Ebcioğlu (1995)

$$\begin{aligned}
&\hat{\mathbf{n}}_{,S} + \bar{\hat{\mathbf{n}}} = 0,\\
&_{(1)}m_{,S} + \left[_{(2)}\mathbf{\Phi}_{0,S} \times _{(1)}\mathbf{n}\right] \cdot \mathbf{e}_3 + _{(1)}h\left(_{(1)}\mathbf{n} \cdot _{(1)}\mathbf{t}_1\right)_{,S}\\
&\qquad + _{(2)}h\,_{(2)}\theta_{,S}\left(_{(1)}\mathbf{n} \cdot _{(2)}\mathbf{t}_2\right) + _{(1)}\bar{\mathfrak{M}} = 0,\\
&_{(2)}m_{,S} + \left[_{(2)}\mathbf{\Phi}_{0,S} \times _{(2)}\mathbf{n}\right] \cdot \mathbf{e}_3 {}_{(2)}h\left(_{(1)}\mathbf{n}_{,S} - _{(3)}\mathbf{n}_{,S}\right)\\
&\qquad \cdot _{(2)}\mathbf{t}_1 + _{(2)}\bar{\mathfrak{M}} = 0,\\
&_{(3)}m_{,S} + \left[_{(2)}\mathbf{\Phi}_{0,S} \times _{(3)}\mathbf{n}\right] \cdot \mathbf{e}_3 - _{(3)}h\left(_{(3)}\mathbf{n} \cdot _{(3)}\mathbf{t}_1\right)_{,S}\\
&\qquad - _{(2)}h\,_{(2)}\theta_{,S}\left(_{(3)}\mathbf{n} \cdot _{(2)}\mathbf{t}_2\right) + _{(3)}\bar{\mathfrak{M}} = 0.
\end{aligned} \tag{2.10}$$

[4]Summation convention on repeated indices is implied, with Greek letters taking values in {1, 2}.

Downloaded 04 May 2010 to 171.66.16.28. Redistribution subject to ASME license or copyright; see http://www.asme.org/terms/Terms_Use.cfm

Let $\{\bar{\mathbf{u}},\ {}_{(1)}\bar{\theta},\ {}_{(2)}\bar{\theta},\ {}_{(3)}\bar{\theta}\}$ represent the assigned displacement and the assigned rotations, respectively. The boundary conditions at $S = 0$ and $S = L$ are then stated as follows:

$$\boxed{\begin{aligned}&\text{Either } \mathbf{u} = \bar{\mathbf{u}} \text{ or } && \hat{\mathbf{n}} = \bar{\hat{\mathbf{n}}},\\ &\quad " \ {}_{(1)}\theta = {}_{(1)}\bar{\theta} \ " && {}_{(1)}m + {}_{(1)}h\left({}_{(1)}\mathbf{n} \cdot {}_{(1)}\mathbf{t}_1\right) = {}_{(1)}\bar{\bar{\mathfrak{M}}},\\ &\quad " \ {}_{(2)}\theta = {}_{(2)}\bar{\theta} \ " && {}_{(2)}m + {}_{(2)}h\left({}_{(1)}\mathbf{n} - {}_{(3)}\mathbf{n}\right) \cdot {}_{(2)}\mathbf{t}_1 = {}_{(2)}\bar{\bar{\mathfrak{M}}},\\ &\quad " \ {}_{(3)}\theta = {}_{(3)}\bar{\theta} \ " && {}_{(3)}m - {}_{(3)}h\left({}_{(3)}\mathbf{n} \cdot {}_{(3)}\mathbf{t}_1\right) = {}_{(3)}\bar{\bar{\mathfrak{M}}},\end{aligned}} \tag{2.11}$$

where $\bar{\bar{\hat{\mathbf{n}}}}$ is the concentrated forces, and ${}_{(l)}\bar{\bar{\mathfrak{M}}}$ the concentrated couples, at the boundaries.

2.2 Stress Power. The above equations of equilibrium and boundary conditions (2.10)–(2.11) can be shown to derive from the balance of the mechanical powers (see Vu-Quoc and Ebcioğlu (1995))

$$\boxed{\mathcal{P}_c = \mathcal{P}_a,} \tag{2.12}$$

for all admissible velocities[5] $\dot{u}^1$, $\dot{u}^2$, ${}_{(1)}\dot{\theta}$, ${}_{(2)}\dot{\theta}$, ${}_{(3)}\dot{\theta}$, where $\mathcal{P}_c$ is the power of contact forces/couples

$$\boxed{\begin{aligned}&\mathcal{P}_c := \sum_{l=1}^{3} {}_{(l)}\mathcal{P}_c,\\ &\text{and } {}_{(l)}\mathcal{P}_c := \int_{\mathcal{L}} \left[{}_{(l)}\mathbf{n} \cdot {}_{(l)}^{[l]}\gamma + {}_{(l)}m \, {}_{(l)}\dot{\theta}_{,S} \right] dS,\end{aligned}} \tag{2.13}$$

and $\mathcal{P}_a$ is the power of assigned forces/couples

$$\boxed{\begin{aligned}\mathcal{P}_a := \int_{\mathcal{L}} &\left\{ \bar{\hat{\mathbf{n}}} \cdot \dot{\mathbf{u}} + \sum_{l=1}^{3} {}_{(l)}\bar{\bar{\mathfrak{M}}} \, {}_{(l)}\dot{\theta} \right\} dS\\ &+ \left[\bar{\bar{\hat{\mathbf{n}}}} \cdot \dot{\mathbf{u}} + \sum_{l=1}^{3} {}_{(l)}\bar{\bar{\mathfrak{M}}} \, {}_{(l)}\dot{\theta} \right]_{S=0}^{S=L}.\end{aligned}} \tag{2.14}$$

In (2.13)–(2.14), the overhead dot "$\cdot$" designates time differentiation, whereas the overhead symbol "$^{[l]}$" designates the time differentiation of a vector quantity, say, $\mathbf{v}$, expressed in the cross-section basis $\{{}_{(l)}\mathbf{t}_1, {}_{(l)}\mathbf{t}_2\}$ of layer (l) while keeping *this* basis *fixed*; we have

$${}_{(l)}^{[l]}\mathbf{t}_\alpha \equiv 0, \quad \text{and} \quad \mathbf{v} = v^\alpha \, {}_{(l)}\mathbf{t}_\alpha \Rightarrow {}^{[l]}\mathbf{v} := \dot{v}^\alpha \, {}_{(l)}\mathbf{t}_\alpha. \tag{2.15}$$

3 Galerkin Projection

We now develop the operator expressions for the weak form of the equilibrium equations based on the balance of power in Section 2.2. These expressions will be linearized and subsequently used in a Galerkin projection for the solution process.

3.1 Weak Form. Let $\mathbf{w}$: $\mathcal{L} \to \mathbb{R}^5$ be the weighting functions corresponding to the five kinematic quantities in (2.8)

$$\mathbf{w} := \left\{ v^1, v^2, {}_{(1)}\varphi, {}_{(2)}\varphi, {}_{(3)}\varphi \right\}^T, \tag{3.1}$$

instead of velocities in (2.13). Gathered in ${}_{(l)}\mathbf{f}_c$: $\mathcal{L} \times \mathbb{R}_+ \to \mathbb{R}^3$ such that

$${}_{(l)}\mathbf{f}_c := \left\{ {}_{(l)}n^1, {}_{(l)}n^2, {}_{(l)}m \right\}^T \tag{3.2}$$

are the contact forces/couple for layer (l). Since the core layer (2) is the reference layer based on which the deformation of all layers is referred to, we focus our attention on this layer first. Based on the expression for ${}_{(l)}\mathcal{P}_c$ in $(2.13)_2$, the weak form for the contact forces/couple in layer (2) can be written as

$${}_{(2)}G_c(\Phi, \mathbf{w}) := \int_{\mathcal{L}} \left[{}_{(2)}\mathbf{n} \cdot {}_{(2)}^{[2]}\gamma + {}_{(2)}m \, {}_{(2)}\varphi_{,S} \right] dS, \tag{3.3}$$

where, in terms of the weighting functions (3.1),

$$\begin{aligned}{}_{(2)}^{[2]}\gamma = &\left[v^1_{,S} + \left(\sin\theta_0 + u^2_{,S} \right) {}_{(2)}\varphi \right] \mathbf{e}_1\\ &+ \left[v^2_{,S} - \left(\cos\theta_0 + u^1_{,S} \right) {}_{(2)}\varphi \right] \mathbf{e}_2,\end{aligned} \tag{3.4}$$

is the expression for the variation of the strain ${}_{(2)}\gamma$ by virtue of (2.15), (2.3), (2.1), and (2.5) (see Vu-Quoc and Ebcioğlu (1994)).[6] Using (3.2) and (3.4), the integrand in (3.3) can be rearranged in matrix form as follows:

$$\boxed{{}_{(2)}G_c(\Phi, \mathbf{w}) = \int_{\mathcal{L}} \left[{}_{(2)}\Xi(\Phi)\mathbf{w} \right] \cdot {}_{(2)}\mathbf{f}_c(\Phi) dS,} \tag{3.5}$$

where

$${}_{(2)}\Xi(\Phi) := \begin{bmatrix} \frac{d}{dS} & 0 & 0 & {}_{(2)}\Xi_1 & 0 \\ 0 & \frac{d}{dS} & 0 & {}_{(2)}\Xi_2 & 0 \\ 0 & 0 & 0 & \frac{d}{dS} & 0 \end{bmatrix}_{3\times 5}, \tag{3.6}$$

and

$${}_{(2)}\Xi_1 := + \left[\sin\theta_0 + u^2_{,S} \right], \tag{3.7}$$

$${}_{(2)}\Xi_2 := - \left[\cos\theta_0 + u^1_{,S} \right]. \tag{3.8}$$

The stress power ${}_{(1)}\mathcal{P}_c$ for layer (1) as given in $(2.13)_2$ can be rewritten as a weak form

$${}_{(1)}G_c(\Phi, \mathbf{w}) := \int_{\mathcal{L}} \left[{}_{(1)}\mathbf{n} \cdot {}_{(1)}^{[1]}\gamma + {}_{(1)}m \, {}_{(1)}\varphi_{,S} \right] dS, \tag{3.9}$$

where, in terms of the weighting functions (3.1),

$$\begin{aligned}{}_{(1)}^{[1]}\gamma = &\left[v^1_{,S} + \left(\sin\theta_0 + u^2_{,S} \right) {}_{(1)}\varphi \right] \mathbf{e}_1\\ &+ \left[v^2_{,S} - \left(\cos\theta_0 + u^1_{,S} \right) {}_{(1)}\varphi \right] \mathbf{e}_2 + {}_{(1)}h \, {}_{(1)}\varphi_{,S} \, {}_{(1)}\mathbf{t}_1\\ &+ {}_{(2)}h \, {}_{(2)}\varphi_{,S} \, {}_{(2)}\mathbf{t}_1 + {}_{(2)}h \, {}_{(2)}\theta_{,S} \left[{}_{(2)}\varphi - {}_{(1)}\varphi \right] {}_{(2)}\mathbf{t}_2,\end{aligned} \tag{3.10}$$

is the expression for the variation of the strain ${}_{(1)}\gamma$ by virtue of (2.15), (2.3), $(2.2)_1$, and (2.5). Rearranging (3.9) in matrix form with the aid of (3.2) and (3.10), we obtain

$$\boxed{{}_{(1)}G_c(\Phi, \mathbf{w}) = \int_{\mathcal{L}} \left[{}_{(1)}\Xi(\Phi)\mathbf{w} \right] \cdot {}_{(1)}\mathbf{f}_c(\Phi) dS,} \tag{3.11}$$

where

$${}_{(1)}\Xi(\Phi) := \begin{bmatrix} \frac{d}{dS} & 0 & {}_{(1)}\Xi_1 & {}_{(1)}\Xi_3 & 0 \\ 0 & \frac{d}{dS} & {}_{(1)}\Xi_2 & {}_{(1)}\Xi_4 & 0 \\ 0 & 0 & \frac{d}{dS} & 0 & 0 \end{bmatrix}_{3\times 5}, \tag{3.12}$$

[5] Consider the dynamics case, where all kinematic quantities are time dependent.

[6] Recall that $\{u^1, u^2\}$ are the components of $\mathbf{u}$ along the basis vectors $\{\mathbf{e}_1, \mathbf{e}_2\}$. In fact, (3.4) is more general than the corresponding expression (3.8) in Vu-Quoc and Ebcioğlu (1995), where $\theta_0 = 0$; we are following here the formulation in Vu-Quoc and Li (1995).

Downloaded 04 May 2010 to 171.66.16.28. Redistribution subject to ASME license or copyright; see http://www.asme.org/terms/Terms_Use.cfm

in which the elements ${}_{(1)}\Xi_i$, for $i = 1, \ldots, 4$, have the following expressions:

$${}_{(1)}\Xi_1 := \underbrace{+\left[\sin\theta_0 + u^2_{,S}\right]}$$
$$+ {}_{(1)}h\cos{}_{(1)}\theta\frac{d}{dS} + {}_{(2)}h\,{}_{(2)}\theta_{,S}\sin{}_{(2)}\theta, \quad (3.13)$$

$${}_{(1)}\Xi_2 := \underbrace{-\left[\cos\theta_0 + u^1_{,S}\right]}$$
$$+ {}_{(1)}h\sin{}_{(1)}\theta\frac{d}{dS} - {}_{(2)}h\,{}_{(2)}\theta_{,S}\cos{}_{(2)}\theta, \quad (3.14)$$

$${}_{(1)}\Xi_3 := {}_{(2)}h\cos{}_{(2)}\theta\frac{d}{dS} - {}_{(2)}h\,{}_{(2)}\theta_{,S}\sin{}_{(2)}\theta, \quad (3.15)$$

$${}_{(1)}\Xi_4 := {}_{(2)}h\sin{}_{(2)}\theta\frac{d}{dS} + {}_{(2)}h\,{}_{(2)}\theta_{,S}\cos{}_{(2)}\theta. \quad (3.16)$$

Similarly, we have for layer (3) the weak form

$${}_{(3)}G_c(\Phi,\mathbf{w}) := \int_{\mathfrak{L}}\left[{}_{(3)}\mathbf{n}\cdot{}_{(3)}\overset{[3]}{\gamma} + {}_{(3)}m\,{}_{(3)}\varphi\right]dS \quad (3.17)$$

in which the variation of the strain ${}_{(3)}\varphi$ is given by

$${}_{(3)}\overset{[3]}{\gamma} = \left[v^1 + \left(\sin\theta_0 + u^2_{,S}\right){}_{(3)}\varphi\right]\mathbf{e}_1$$
$$+\left[v^2 - \left(\cos\theta_0 + u^1_{,S}\right){}_{(3)}\varphi\right] - {}_{(3)}h\,{}_{(3)}\varphi_{,S}\,{}_{(3)}\mathbf{t}_1 - {}_{(2)}h\,{}_{(2)}\varphi_{,S}\,{}_{(2)}\mathbf{t}_1$$
$$- {}_{(2)}h\,{}_{(2)}\theta_{,S}[{}_{(2)}\varphi - {}_{(3)}\varphi]\,{}_{(2)}\mathbf{t}_2. \quad (3.18)$$

Expression (3.18) is the counterpart of (3.10) for layer (3). In matrix form

$$\boxed{{}_{(3)}G_c(GF,\mathbf{w}) = \int_{\mathfrak{L}}\left[{}_{(3)}\Xi(\Phi)\mathbf{w}\right]\cdot{}_{(3)}\mathbf{f}_c(\Phi)dS} \quad (3.19)$$

where

$${}_{(3)}\Xi(\Phi) := \begin{bmatrix} \frac{d}{dS} & 0 & 0 & {}_{(3)}\Xi_3 & {}_{(3)}\Xi_1 \\ 0 & \frac{d}{dS} & 0 & {}_{(3)}\Xi_4 & {}_{(3)}\Xi_2 \\ 0 & 0 & 0 & 0 & \frac{d}{dS} \end{bmatrix}_{3\times 5} \quad (3.20)$$

in which the elements ${}_{(3)}\Xi_i$, for $i = 1, \ldots, 4$, have the following expressions:

$${}_{(3)}\Xi_1 := \underbrace{+\left[\sin\theta_0 + u^2_{,S}\right]}$$
$$- {}_{(2)}h\,{}_{(2)}\theta_{,S}\sin{}_{(2)}\theta - {}_{(3)}h\cos{}_{(3)}\theta\frac{d}{dS}, \quad (3.21)$$

$${}_{(3)}\Xi_2 := \underbrace{-\left[\cos\theta_0 + u^1_{,S}\right]}$$
$$+ {}_{(2)}h\,{}_{(2)}\theta_{,S}\cos{}_{(2)}\theta - {}_{(3)}h\sin{}_{(3)}\theta\frac{d}{dS}, \quad (3.22)$$

$${}_{(3)}\Xi_3 := {}_{(2)}h\,{}_{(2)}\theta_{,S}\sin{}_{(2)}\theta - {}_{(2)}h\cos{}_{(2)}\theta\frac{d}{dS}, \quad (3.23)$$

$${}_{(3)}\Xi_4 := -{}_{(2)}h\,{}_{(2)}\theta_{,S}\cos{}_{(2)}\theta - {}_{(2)}h\sin{}_{(2)}\theta\frac{d}{dS}. \quad (3.24)$$

It can be seen from (3.7), (3.13), and (3.21) that there is a common part between the matrix elements ${}_{(l)}\Xi_1$, for $l = 1, 2, 3$, as indicated by the underbraces; similarly for ${}_{(l)}\Xi_2$ in (3.8), (3.14), and (3.22). Notice that the matrix elements ${}_{(l)}\Xi_1$ and ${}_{(l)}\Xi_2$ are in the same column corresponding to the rotation ${}_{(l)}\theta$, and above the differential operator d/dS. The total weak form of contact forces/couples for a geometrically exact sandwich beam is then given by

$$\boxed{G_c(\Phi,\mathbf{w}) = \sum_{l=1}^{3}{}_{(l)}G_c(\Phi,\mathbf{w}).} \quad (3.25)$$

Gathered in $\bar{\mathfrak{F}}$: $\mathfrak{L}\to\mathbb{R}^4$ are the assigned forces/couples

$$\bar{\mathfrak{F}} := \left\{\bar{n}^1,\ \bar{n}^2,\ {}_{(1)}\bar{\mathfrak{M}},\ {}_{(2)}\bar{\mathfrak{M}},\ {}_{(3)}\bar{\mathfrak{M}}\right\}^T. \quad (3.26)$$

The weak form for assigned forces/couples is as follows:

$$\boxed{G_a(\mathbf{w}) = \int_{\mathfrak{L}}\bar{\mathfrak{F}}\cdot\mathbf{w}dS + \left[\bar{\mathfrak{F}}\cdot\mathbf{w}\right]_{S=0}^{S=L}} \quad (3.27)$$

Let $\mathfrak{V}$ designate the set of admissible weighting functions (see Hughes, 1987). The weak form of the geometrically exact multilayer beam problem is to

$$\boxed{\begin{array}{l}\text{find } \Phi \text{ such that} \\ \qquad G_c(\Phi,\mathbf{w}) = G_a(\mathbf{w}), \quad \forall\mathbf{w}\in\mathfrak{V}.\end{array}} \quad (3.28)$$

3.2 Linearization of Weak Form. Define the residual

$$G(\Phi,\mathbf{w}) := G_c(\Phi,\mathbf{w}) - G_a(\mathbf{w}), \quad (3.29)$$

and consider the incremental formula for the solution

$$\Phi_\epsilon^{(i+1)} := \Phi^{(i)} + \epsilon\Delta\Phi^{(i+1)}, \quad (3.30)$$

where $\Phi^{(i+1)}$ and $\Phi^{(i)}$ are the values of Φ at iterations $(i+1)$ and (i), respectively, of the solution process by Newton's method, and $\Delta\Phi^{(i+1)}$ the incremental value. The linearization of the weak form $G(\Phi,w)$ at $\Phi = \Phi^{(i)}$ can be written as

$$L\left[G(\Phi^{(i)},\mathbf{w})\right] = G(\Phi^{(i)},\mathbf{w}) + DG(\Phi^{(i)},\mathbf{w})\cdot\Delta\Phi^{(i+1)}, \quad (3.31)$$

where the tangent stiffness operator $DG(\Phi^{(i)},\mathbf{w})$ is computed as the directional derivative (with respect to Φ) of G_c by virtue of (3.29)

$$DG(\Phi^{(i)},\mathbf{w})\cdot\Delta\Phi^{(i+1)} = DG_c(\Phi^{(i)},\mathbf{w})$$
$$\cdot\Delta\Phi^{(i+1)} = \frac{d}{d\epsilon}G_c\left(\Phi_\epsilon^{(i+1)},\mathbf{w}\right)|_{\epsilon=0}. \quad (3.32)$$

Then, using (3.25), we can write the tangent stiffness operator as the sum of the contribution from each layer

$$\boxed{DG(\Phi^{(i)},\mathbf{w}) = \sum_{l=1}^{3}D_{(l)}G_c(\Phi^{(i)},\mathbf{w}),} \quad (3.33)$$

keeping in mind the decomposition

$$\boxed{D_{(l)}G_c = \left[D^g + D^m\right]_{(l)}G_c,} \quad (3.34)$$

where D^g is the differential operator that gives rise to the tangent geometric stiffness, and D^m the tangent material stiffness.

In the present section, it is more convenient to use matrix of components of tensors. Define the material properties matrix

$${}_{(l)}\mathfrak{C} := \begin{bmatrix} {}_{(l)}EA & 0 & 0 \\ 0 & {}_{(l)}GA_s & 0 \\ 0 & 0 & {}_{(l)}EI \end{bmatrix}_{3\times 3}, \quad (3.35)$$

Downloaded 04 May 2010 to 171.66.16.28. Redistribution subject to ASME license or copyright; see http://www.asme.org/terms/Terms_Use.cfm

and the rotation matrix

$$ {}_{(l)}\mathbf{\Lambda} := \begin{bmatrix} \cos{}_{(l)}\theta & -\sin{}_{(l)}\theta & 0 \\ \sin{}_{(l)}\theta & \cos{}_{(l)}\theta & 0 \\ 0 & 0 & 1 \end{bmatrix}_{3\times 3}. \tag{3.36} $$

Also let the material contact forces/couple ${}_{(l)}\mathbf{F}_c$ be defined as follows:

$$ {}_{(l)}\mathbf{F}_c := {}_{(l)}\mathbf{\Lambda}^T\, {}_{(l)}\mathbf{f}_c, \quad \text{or} \quad {}_{(l)}\mathbf{f}_c = {}_{(l)}\mathbf{\Lambda}\, {}_{(l)}\mathbf{F}_c, \tag{3.37} $$

where the spatial contact forces/couple ${}_{(l)}\mathbf{f}_c$ was defined in (3.2). Expression $(3.37)_2$ is to be used in the expressions for ${}_{(l)}G_c$ in (3.5), (3.11), (3.19). For each layer, the tangent geometric stiffness is obtained from the linearization of the operators ${}_{(l)}\mathbf{\Xi}$ and ${}_{(l)}\mathbf{\Lambda}$ at $\Phi^{(i)}$, while keeping the material contact forces/couple ${}_{(l)}\mathbf{F}_c$ fixed. On the other hand, the tangent material stiffness is obtained from the linearization of ${}_{(l)}\mathbf{F}_c$ at $\Phi^{(i)}$

$$ D\,{}_{(l)}\mathbf{F}_c(\Phi^{(i)})\cdot\Delta\Phi^{(i+1)} = {}_{(l)}\mathfrak{C}\,{}_{(l)}\mathbf{\Lambda}^{(i)^T}\,{}_{(l)}\mathbf{\Xi}(\Phi^{(i)})\cdot\Delta\Phi^{(i+1)}. \tag{3.38} $$

The contribution of layer (2) to the total tangent geometric stiffness is then

$$ \boxed{ \begin{aligned} &D^g\,{}_{(2)}G_c(\Phi^{(i)},\mathbf{w})\cdot\Delta\Phi^{(i+1)} \\ &\quad = \int_{\mathfrak{L}} \left[{}_{(2)}\Upsilon\mathbf{w}\right]\cdot\left[{}_{(2)}\mathbf{B}(\Phi^{(i)})\,{}_{(2)}\Upsilon\Delta\Phi^{(i+1)}\right] dS, \end{aligned} } \tag{3.39} $$

where

$$ {}_{(2)}\Upsilon := \begin{bmatrix} d/dS & 0 & 0 & 0 & 0 \\ 0 & d/dS & 0 & 0 & 0 \\ 0 & 0 & 0 & 0 & 0 \\ 0 & 0 & 0 & 1 & 0 \\ 0 & 0 & 0 & 0 & 0 \end{bmatrix}_{5\times 5}, \tag{3.40} $$

$$ {}_{(2)}\mathbf{B}(\Phi) := \begin{bmatrix} 0 & 0 & 0 & -{}_{(2)}n^2 & 0 \\ 0 & 0 & 0 & {}_{(2)}n^1 & 0 \\ 0 & 0 & 0 & 0 & 0 \\ -{}_{(2)}n^2 & {}_{(2)}n^1 & 0 & -{}_{(2)}\mathbf{n}\cdot{}_{(2)}\mathbf{\Phi}_{,S} & 0 \\ 0 & 0 & 0 & 0 & 0 \end{bmatrix}_{5\times 5}, \tag{3.41} $$

with

$$ {}_{(2)}\mathbf{n}\cdot{}_{(2)}\mathbf{\Phi}_{,S} = {}_{(2)}n^1\left(\cos\theta_0 + u^1_{,S}\right) + {}_{(2)}n^2\left(\sin\theta_0 + u^2_{,S}\right), \tag{3.42} $$

by virtue of (2.4) and (2.1).

The contribution of layers (1) and (3) to the total tangent geometric stiffness can be collectively expressed by

$$ \boxed{ \begin{aligned} &D^g\,{}_{(1)}G_c(\Phi^{(i)},\mathbf{w})\cdot\Delta\Phi^{(i+1)} \\ &\quad = \int_{\mathfrak{L}} \Big\{ \left[{}_{(l)}\Upsilon_1\mathbf{w}\right]\cdot{}_{(l)}\mathbf{B}_1(\Phi^{(i)})\,{}_{(l)}\Upsilon_1 \\ &\qquad + \left[{}_{(l)}\Upsilon_2\mathbf{w}\right]\cdot{}_{(l)}\mathbf{B}_2(\Phi^{(i)})\,{}_{(l)}\Upsilon_2 \Big\}\cdot\Delta\Phi^{(i+1)} dS, \end{aligned} } \tag{3.43} $$

for $l = 1, 3$. For layer (1), we obtain the following expressions:

$$ {}_{(1)}\Upsilon_1 := \begin{bmatrix} d/dS & 0 & 0 & 0 & 0 \\ 0 & d/dS & 0 & 0 & 0 \\ 0 & 0 & 1 & 0 & 0 \\ 0 & 0 & 0 & 0 & 0 \\ 0 & 0 & 0 & 0 & 0 \end{bmatrix}_{5\times 5}, \tag{3.44} $$

$$ {}_{(1)}\mathbf{B}_1(\Phi) := \begin{bmatrix} 0 & 0 & -{}_{(1)}n^2 & 0 & 0 \\ 0 & 0 & {}_{(1)}n^1 & 0 & 0 \\ -{}_{(1)}n^2 & {}_{(1)}n^1 & -{}_{(1)}\mathbf{n}\cdot{}_{(2)}\mathbf{\Phi}_{,S} & 0 & 0 \\ 0 & 0 & 0 & 0 & 0 \\ 0 & 0 & 0 & 0 & 0 \end{bmatrix}_{5\times 5}, \tag{3.45} $$

with ${}_{(1)}\mathbf{n}\cdot{}_{(2)}\mathbf{\Phi}_{,S}$ having an expansion similar to (3.42), and

$$ {}_{(1)}\Upsilon_2 := \begin{bmatrix} 0 & 0 & 0 & 0 & 0 \\ 0 & 0 & -1 & 1 & 0 \\ 0 & 0 & 1 & -1 & 0 \\ 0 & 0 & 0 & d/dS & 0 \\ 0 & 0 & 0 & 0 & 0 \end{bmatrix}_{5\times 5}, \tag{3.46} $$

$$ {}_{(1)}\mathbf{B}_2(\Phi) := \begin{bmatrix} 0 & 0 & 0 & 0 & 0 \\ 0 & 0 & 0 & {}_{(2)}h\cos{}_{(2)}\theta\,{}_{(1)}n^2 & 0 \\ 0 & 0 & {}_{(1)}\beta_2 & {}_{(2)}h\sin{}_{(2)}\theta\,{}_{(1)}n^1 & 0 \\ 0 & {}_{(2)}h\cos{}_{(2)}\theta\,{}_{(1)}n^2 & {}_{(2)}h\sin{}_{(2)}\theta\,{}_{(1)}n^1 & 0 & 0 \\ 0 & 0 & 0 & 0 & 0 \end{bmatrix}_{5\times 5}, \tag{3.47} $$

with

$$ \begin{aligned} {}_{(1)}\beta_2 &:= -{}_{(2)}h\,{}_{(2)}\theta_{,S}\,{}_{(1)}\mathbf{n}\cdot{}_{(2)}\mathbf{t}_1 \\ &= -{}_{(2)}h\,{}_{(2)}\theta_{,S}\left[{}_{(1)}n^1\cos{}_{(2)}\theta + {}_{(1)}n^2\sin{}_{(2)}\theta\right]. \end{aligned} \tag{3.48} $$

For layer (3) we obtain

$$ {}_{(3)}\Upsilon_1 := \begin{bmatrix} d/dS & 0 & 0 & 0 & 0 \\ 0 & d/dS & 0 & 0 & 0 \\ 0 & 0 & 0 & 0 & 0 \\ 0 & 0 & 0 & 0 & 0 \\ 0 & 0 & 0 & 0 & 1 \end{bmatrix}_{5\times 5}, \tag{3.49} $$

$$ {}_{(3)}\mathbf{B}_1(\Phi) := \begin{bmatrix} 0 & 0 & 0 & 0 & -{}_{(3)}n^2 \\ 0 & 0 & 0 & 0 & {}_{(3)}n^1 \\ 0 & 0 & 0 & 0 & 0 \\ 0 & 0 & 0 & 0 & 0 \\ -{}_{(3)}n^2 & {}_{(3)}n^1 & 0 & 0 & -{}_{(3)}\mathbf{n}\cdot{}_{(2)}\mathbf{\Phi}_{,S} \end{bmatrix}_{5\times 5}, \tag{3.50} $$

Downloaded 04 May 2010 to 171.66.16.28. Redistribution subject to ASME license or copyright; see http://www.asme.org/terms/Terms_Use.cfm

with ${}_{(3)}\mathbf{n} \cdot {}_{(2)}\mathbf{\Phi}_{,S}$ having an expansion similar to (3.42), and

$$ {}_{(3)}\Upsilon_2 := \begin{bmatrix} 0 & 0 & 0 & 0 & 0 \\ 0 & 0 & 0 & 0 & 0 \\ 0 & 0 & 0 & -1 & 1 \\ 0 & 0 & 0 & d/dS & 0 \\ 0 & 0 & 0 & 1 & -1 \end{bmatrix}_{5\times 5}, \tag{3.51} $$

$$ {}_{(3)}\mathbf{B}_2(\Phi) := \begin{bmatrix} 0 & 0 & 0 & 0 & 0 \\ 0 & 0 & 0 & 0 & 0 \\ 0 & 0 & 0 & {}_{(2)}h \cos {}_{(2)}\theta\, {}_{(3)}n^2 & 0 \\ 0 & 0 & {}_{(2)}h \cos {}_{(2)}\theta\, {}_{(3)}n^2 & 0 & {}_{(2)}h \sin {}_{(2)}\theta\, {}_{(3)}n^1 \\ 0 & 0 & 0 & {}_{(2)}h \sin {}_{(2)}\theta\, {}_{(3)}n^1 & {}_{(3)}\beta_2 \end{bmatrix}_{5\times 5}, \tag{3.52} $$

with

$$ {}_{(3)}\beta_2 := {}_{(2)}h\, {}_{(2)}\theta_{,S}\, {}_{(3)}\mathbf{n} \cdot {}_{(2)}\mathbf{t}_1 = {}_{(2)}h\, {}_{(2)}\theta_{,S}\left[{}_{(3)}n^1 \cos {}_{(2)}\theta + {}_{(3)}n^2 \sin {}_{(2)}\theta \right]. \tag{3.53} $$

Recall from (3.39) and (3.43) that the matrices ${}_{(2)}\mathbf{B}$, ${}_{(1)}\mathbf{B}_\alpha$, and ${}_{(3)}\mathbf{B}_\alpha$ (for $\alpha = 1, 2$) are to be evaluated at $\Phi = \Phi^{(i)}$, and so are the quantities in (3.41), (3.42), and in (3.45), (3.47), (3.48), and in (3.50), (3.52), (3.53).

The total tangent *material* stiffness has the following contribution from layer (l):

$$ D^m {}_{(l)}G_c(\Phi^{(i)}, \mathbf{w}) \cdot \Delta\Phi^{(i+1)} = \int_{\mathfrak{L}} \left[{}_{(l)}\Xi(\Phi^{(i)})\mathbf{w} \right] \cdot {}_{(l)}\mathbf{\Lambda}^{(i)}\, {}_{(l)}\mathfrak{C}\, {}_{(l)}\mathbf{\Lambda}^{(i)^T}\, {}_{(l)}\Xi(\Phi^{(i)})\Delta\Phi^{(i)} dS, \tag{3.54} $$

where the expressions for ${}_{(l)}\Xi(\Phi^{(i)})$ are given in (3.6), (3.12), and (3.20).

Finally, the total tangent stiffness operator is obtained by combining (3.33), (3.34), (3.39), (3.43), and (3.54). It is noted that the total tangent stiffness operator is symmetric since each of its constituents is. The increment $\Delta\Phi^{(i+1)}$ is solved for by setting the linearized weak form (3.31) to zero, and thus

$$ \Delta\Phi^{(i+1)} = -\left[DG(\Phi^{(i)}, \mathbf{w}) \right]^{-1} \cdot G(\Phi^{(i)}, \mathbf{w}), \quad \forall \mathbf{w} \in \mathcal{V}. \tag{3.55} $$

3.3 Projection: Galerkin Finite Element. A Galerkin projection of the equilibrium Eqs. (2.10) can be readily carried out by choosing a finite-dimensional subspace $\mathcal{V}^h$ to the space of trial solutions and weighting functions $\mathcal{V}$, assuming for simplicity in the exposition homogeneous essential boundary conditions (see Hughes, 1987). Or equivalently, let $\{N_i\colon \mathfrak{L} \to \mathbb{R}$, for $i = 1, \ldots, n\}$ be a set of basis functions for $\mathcal{V}^h$, then the approximated solution $\Phi^h \in \mathcal{V}^h$ and the approximated weighting function $\mathbf{w}^h \in \mathcal{V}^h$ can be written as follows:[7]

$$ \Delta\Phi(S) \approx \Delta\Phi^h(S) = \sum_{J=1}^{n} \mathbf{d}_J N_J(S) \in \mathbb{R}^{5\times 1}, $$

$$ \mathbf{w}(S) \approx \mathbf{w}^h(S) = \sum_{I=1}^{n} \mathbf{c}_I N_I(S) \in \mathbb{R}^{5\times 1}, \tag{3.56} $$

with $\mathbf{d}_j$, $\mathbf{c}_I \in \mathbb{R}^{5\times 1}$. The matrix equation resulting from the restriction of (3.55) from $\mathcal{V}$ to $\mathcal{V}^h \subset \mathcal{V}$ takes the form[8]

$$ \mathbf{d} = -\mathbf{K}^{-1}\mathbf{r} \in \mathbb{R}^{5n\times 1}, \tag{3.57} $$

where $\mathbf{d} := \{\mathbf{d}_J\} \in \mathbb{R}^{5n\times 1}$ is the matrix of incremental (generalized) displacement, $\mathbf{K} \in \mathbb{R}^{5n\times 5n}$ the tangent stiffness matrix, and $\mathbf{r} \in \mathbb{R}^{5n\times 1}$ the residual matrix. The tangent stiffness matrix is obtained by

$$ \mathbf{K} = \sum_{l=1}^{3} \left[{}_{(l)}\mathbf{K}^g + {}_{(l)}\mathbf{K}^m \right] \in \mathbb{R}^{5n\times 5n}, \tag{3.58} $$

where ${}_{(l)}\mathbf{K}^g = [{}_{(l)}\mathbf{K}^g_{IJ}]$ and ${}_{(l)}\mathbf{K}^m = [{}_{(l)}\mathbf{K}^m_{IJ}]$ are, respectively, the tangent geometric stiffness matrix and the tangent material stiffness matrix of layer (l). Let $\mathfrak{J}_n$ be a unit matrix, i.e.,

$$ \mathfrak{J}_n := \mathrm{Diag}[1, \ldots, 1] \in \mathbb{R}^{n\times n}. \tag{3.59} $$

From (3.39) and (3.43), we obtain, respectively, the tangent geometric stiffness matrices of layer (2)

$$ {}_{(2)}\mathbf{K}^g_{IJ} = \int_{\mathfrak{L}} \left\{ {}_{(2)}\Upsilon[N_I\, \mathfrak{J}_5] \right\}^T \left\{ {}_{(2)}\mathbf{B}(\Phi)\, {}_{(2)}\Upsilon[N_J\, \mathfrak{J}_5] \right\} dS \in \mathbb{R}^{5\times 5}, \tag{3.60} $$

and of layers $l = 1, 3$

$$ {}_{(l)}\mathbf{K}^g_{IJ} = \int_{\mathfrak{L}} \Big(\left\{ {}_{(l)}\Upsilon_1[N_I\, \mathfrak{J}_5] \right\}^T {}_{(l)}\mathbf{B}_1(\Phi)\, {}_{(l)}\Upsilon_1 + \left\{ {}_{(l)}\Upsilon_2[N_I\, \mathfrak{J}_5] \right\}^T {}_{(l)}\mathbf{B}_2(\Phi)\, {}_{(l)}\Upsilon_2 \Big) [N_J\, \mathfrak{J}_5] dS \in \mathbb{R}^{5\times 5}. \tag{3.61} $$

The tangent material stiffness matrix is obtained from (3.54) to yield

$$ {}_{(l)}\mathbf{K}^m_{IJ} = \int_{\mathfrak{L}} \left\{ {}_{(l)}\Xi(\Phi)[N_I\, \mathfrak{J}_5] \right\}^T \times {}_{(l)}\mathbf{\Lambda}\, {}_{(l)}\mathfrak{C}\, {}_{(l)}\mathbf{\Lambda}^T\, {}_{(l)}\Xi(\Phi)[N_J\, \mathfrak{J}_5] dS \in \mathbb{R}^{5\times 5}. \tag{3.62} $$

Finally, the residual matrix $\mathbf{r} = \{\mathbf{r}_I\} \in \mathbb{R}^{5n\times 1}$ in (3.57) is obtained from (3.29) to yield

$$ \mathbf{r}_I = \sum_{l=1}^{3} {}_{(l)}\mathbf{F}_I - \bar{\mathbf{F}}_I \in \mathbb{R}^{5\times 1}, \tag{3.63} $$

where the internal (generalized) force ${}_{(l)}\mathbf{F}_I$ of layer (l) is computed from (3.5), (3.11), or (3.19) so that

[7] The dimension 5 in (3.56) comes from the definitions of Φ in (2.8) and of $\mathbf{w}$ in (3.1) for sandwich beams. It is recalled, however, that since the number of layers in a finite element can vary between 1 and 3, the number of degrees-of-freedom per node varies between 3 and 5.

[8] We omit the superscripts $(i + 1)$ and (i) to keep the exposition clear. Thus, in the context of Newton's method, the argument Φ in the formulae in Section 3.3 should be read as $\Phi^{(i)}$.

Downloaded 04 May 2010 to 171.66.16.28. Redistribution subject to ASME license or copyright; see http://www.asme.org/terms/Terms_Use.cfm

$$\boxed{{}_{(l)}\mathbf{F}_I = \int_{\mathcal{L}} \left\{ {}_{(l)}\Xi(\Phi)[N_I\, \mathfrak{J}_5] \right\}^T {}_{(l)}\mathbf{f}_c(\Phi) dS \in \mathbb{R}^{5\times 1},} \quad (3.64)$$

and the assigned (generalized) force $\mathbf{F}_I$ is computed from (3.27) so that

$$\boxed{\bar{\mathbf{F}}_I = \int_{\mathcal{L}} N_I \bar{\mathfrak{F}} dS + \left[N_I \bar{\mathfrak{F}} \right]_{S=0}^{S=L} \in \mathbb{R}^{5\times 1}.} \quad (3.65)$$

4 Numerical Examples

The finite element formulation for geometrical exact sandwich beams presented in Section 3.3 has been implemented in the Finite Element Analysis Program (FEAP), developed by R. L. Taylor (see Zienkiewicz and Taylor, 1989), and run on a DEC 5000 with the Ultrix 4.2 operating system. The finite element basis functions used in the examples in this section are linear or quadratic. To avoid shear locking, uniformly reduced integration is used to evaluate the tangent stiffness matrix and the residual matrix.

4.1 Sandwich Beam With Identical Layers. Consider a cantilever sandwich beam with three identical layers, subjected to assigned end moments ${}_{(l)}M$, for $l = 1, 2, 3$. Let ${}_{(l)}EA = EA$, ${}_{(l)}GA_s = GA_s$, ${}_{(l)}EI = EI$, for $l = 1, 2, 3$. The cantilever boundary conditions at $S = 0$ are

$$u^1(0) = u^2(0) = {}_{(1)}\theta(0) = {}_{(2)}\theta(0) = {}_{(3)}\theta(0) = 0. \quad (4.1)$$

4.1.1 Normal Moment Distribution. A sandwich beam will behave as a single-layer beam when the rotations in the three layers are constrained to be the same so that the overall beam cross-section remains *plane* in the deformed configuration, i.e.,

$${}_{(1)}\theta = {}_{(2)}\theta = {}_{(3)}\theta = \theta. \quad (4.2)$$

It can be shown that, for sandwich beams with three identical layers and without shear deformation, (4.2) is satisfied if the moments ${}_{(l)}M$ are applied according to the ratio (see Deng and Vu-Quoc (1994) for the detailed derivation)

$$\boxed{{}_{(1)}M : {}_{(2)}M : {}_{(3)}M = 7 : 13 : 7.} \quad (4.3)$$

We refer to (4.3) as the *normal* moment distribution, which will be used in the roll-up of cantilever sandwich beams below. It can be verified that

$${}_{(1)}M + {}_{(2)}M + {}_{(3)}M = E\frac{(6h)^3}{12}\theta = EI_{\text{total}}\theta, \quad (4.4)$$

i.e., the sandwich beam with the normal moment distribution (4.3) has the same bending stiffness as the single-layer beam.

4.1.2 Roll-up Maneuver with Normal Moment Distribution. We now apply the *normal* moment distribution (4.3) to a cantilever sandwich beam having length $L = 1$ and half-thickness $h = 0.01732 \approx 0.01\sqrt{3}$. The material properties are as follows:

$${}_{(l)}EA = 2{,}000{,}000, \quad {}_{(l)}GA_s = 2{,}000{,}000, \quad {}_{(l)}EI = 200, \quad \text{for} \quad l = 1, 2, 3, \quad (4.5)$$

thus making the total bending stiffness equivalent to a single-layer beam to be

$$EI_{\text{total}} = 27EI = 5{,}400. \quad (4.6)$$

The beam is discretized using five linear sandwich elements. The deformed shape of a cantilever (single-layer) beam, when subjected to an assigned tip moment

$$M = EI_{\text{total}}\frac{2\pi}{L}, \quad (4.7)$$

is a full circle with radius $R = L/(2\pi)$. Thus using the ratio (4.3), the distribution of the total moment M over three layers of the sandwich beam is

$${}_{(1)}M = {}_{(3)}M = \frac{7}{27}M = 8796.46,$$
$${}_{(2)}M = \frac{13}{27}M = 16336.3. \quad (4.8)$$

It takes two iterations to converge to the final deformed shape (i.e., the full circle), with the convergence results shown in the table below.

Iteration Number	Euclidean Norm of Residual
0	0.2053363E + 05
1	0.4412925E + 08
2	0.3051970E − 02

The tip displacements of the sandwich beam are

u^1	u^2	${}_{(1)}\theta$	${}_{(2)}\theta$	${}_{(3)}\theta$
− 0.999999	− 2.15292E − 09	6.28319	6.28319	6.28319

Note that the beam tip moved back to coincide with the cantilever end, with a horizontal displacement of 1 and a vertical displacement zero,[9] and the cross-section rotates by $6.28319 \approx 2\pi$ rad. The finite element deformed shape is a pentagon[10] with the nodes lying on the circle of the exact deformed shape. Despite the presence of three layers in the sandwich beam and the more complex system of equations, the results and the rate of convergence are the same as that of the single-layer beam as reported by Simo and Vu-Quoc (1986).

4.1.3 Roll-up Maneuvers: Saint-Venant Principle. We now solve a series of roll-up maneuver problems with different distributions of moments, the results of which will provide an illustration of Saint-Venant principle. The material properties and half-layer thickness selected are now

$$EA = 2{,}000{,}000, \quad GA_s = 700{,}000, \quad EI = 200,$$
$$h = 0.01732051 = 0.01\sqrt{3}. \quad (4.9)$$

4.1.3.1 Long beam. First, a long sandwich beam with $L = 10$ is considered. Appropriate moments will be assigned at the beam tip so that the sandwich beam is rolled up into a full circle. The total thickness of the beam $6h \approx 0.104$ is *small* compared to the radius of the circle of the deformed shape $R = L/(2\pi) = 1.592$. In this case, the distribution of the total assigned tip moment among the layers has negligible effects on the deformed shape; in other words, Saint-Venant principle cannot be illustrated with this choice of geometry. To obtain a smoother figure of the circular deformed shape, we use a uniform discretization with 40 linear sandwich elements. Three calculations are performed with three different moment distributions having the same resultant M computed using (4.7): (*i*) normal distribution, (*ii*) concentrated moment on core layer ${}_{(2)}M = M$, (*iii*) concentrated moment on top layer ${}_{(3)}M = M$. The displacements and layer rotations at the beam tip are[11]

[9] There are round-off errors.

[10] To conserve space, the finite element pentagonal deformed shape is not reproduced here (see Deng and Vu-Quoc (1994)). With refined meshes, the deformed shape is a circle similar to case (*i*) of Fig. 2.

[11] Where "l = normal" means normal distribution of moments in the sense of (4.8).

Downloaded 04 May 2010 to 171.66.16.28. Redistribution subject to ASME license or copyright; see http://www.asme.org/terms/Terms_Use.cfm

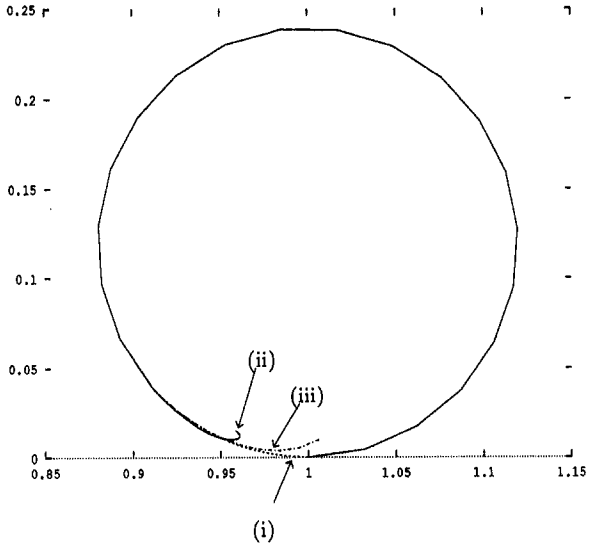

Fig. 2 Sandwich beam with identical layers. Roll-up maneuver. Beam length $L = 0.75$, total thickness $6h = 0.104$. Saint-Venant principle. Moment distributions at beam tip: (i) normal, (ii) $_{(2)}M = M$, (iii) $_{(3)}M = M$.

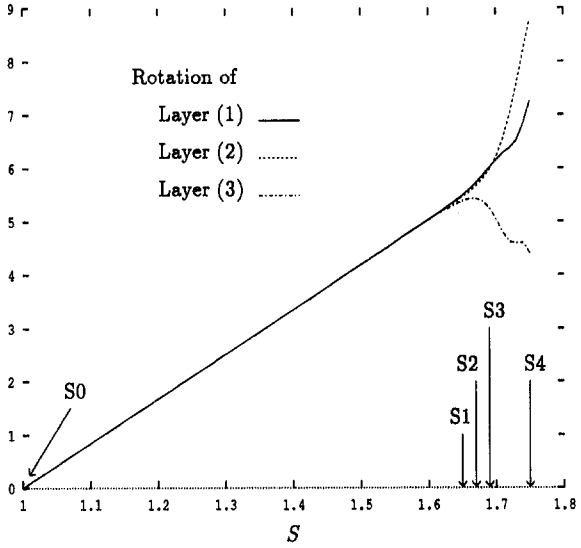

Fig. 3 Shorter sandwich beam with identical layers. Roll-up maneuver. Beam length $L = 0.75$, total thickness $6h = 0.104$. Concentrated moment assigned to core layer $_{(2)}M = M$. Bifurcation of layer rotations. Clamped end at $S = 1$, free end at $S = 1.75$.

$_{(l)}M = M$ $l =$	Displacements and Rotations				
	u^1	u^2	$_{(1)}\theta$	$_{(2)}\theta$	$_{(3)}\theta$
normal	−9.99999	−2.38251E − 10	6.28319	6.28319	6.28319
2	−9.99998	5.31921E − 04	6.18130	6.39316	6.18127
3	−9.99882	5.36146E − 04	6.27634	6.18246	6.47592

It should be noted that the convergence rate is influenced by the magnitude of the shear stiffness (see Deng and Vu-Quoc (1994) for more details).

4.1.3.2 Short beam. Next, to illustrate the effects of non-normal moment distributions and therefore Saint-Venant principle, we consider a beam with *unit* length $L = 0.75$, i.e., the beam is now more than ten times shorter than the one in Section 4.1.3.1, with material properties[12]

$$EA = 2{,}000{,}000, \quad GA_s = 1{,}200{,}000, \quad EI = 200,$$
$$h = 0.01732051 = 0.01\sqrt{3}. \qquad (4.10)$$

The beam will be subjected to an assigned moment that would make a single-layer beam roll up into a full circle of radius $R = L/(2\pi) = 0.1194$ which is of the same order as the total beam thickness of $6h = 0.104$. For such a short beam, remarkable effects due to different non-normal moment distributions will be clearly seen in the deformation near the beam tip. Again, three types of moment distributions as used in Section 4.1.3.1 are studied. The beam domain $S \in [1, 1.75]$ is discretized as follows: For $S \in [1, 1.65]$, a uniform discretization with 20 linear elements is used, and for $S \in [1.65, 1.75]$, a uniform discretization with ten linear elements is used. For all cases of moment distributions, we use ten load steps of equal increments to reach the full moment M; each load step takes about five iterations to converge. The following displacements and layer rotations are obtained.

$_{(l)}M = M$ $l =$	Displacements and Rotations				
	u^1	u^2	$_{(1)}\theta$	$_{(2)}\theta$	$_{(3)}\theta$
normal	−0.750248	1.10700E − 04	6.28319	6.28319	6.28319
2	−0.791437	1.50488E − 02	7.25595	8.76131	4.40996
3	−0.744060	9.93078E − 03	6.12431	5.96892	7.44478

[12]Note that only the value for GA_s is different from the one in (4.9).

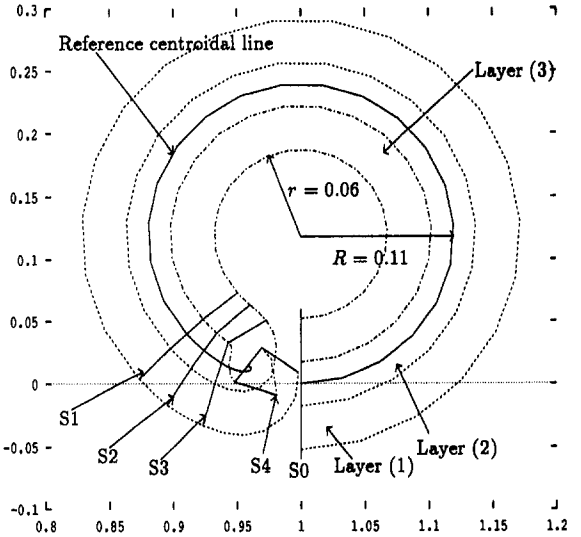

Fig. 4 Sandwich beam with identical layers. Roll-up maneuver. Beam length $L = 0.75$, total thickness $6h = 0.104$. Concentrated moment assigned to core layer $_{(2)}M = M$.

The deformed shapes corresponding to each moment distribution is given in Fig. 2 where the effects of non-normal distribution can be seen near the beam tip. However, such effects diminish rapidly as one moves away from the beam tip, and the three deformed shapes merge into one. This observation is consistent with Saint-Venant principle. The case with concentrated moment assigned at the core layer (2), i.e., $_{(2)}M = M$, yields the most prominent effects at the beam tip. Indeed for this case, the bifurcation in the layer rotations can be seen clearly in Fig. 3. In the interval [1, 1.65], the three layer rotations take on very close values, i.e., the overall cross-section remains close to a plane. From $S = 1.65$ on, i.e., near the beam tip, the three layer rotations begin to diverge sharply from each other. The outer layer rotations are also very different from each other as seen in Fig. 4, where $S0$ corresponds to the cross-section at the clamped end at $S = 1$, $S1$ at $S = 1.65$, $S2$ at $S = 1.67$, $S3$ at $S = 1.69$, and $S4$ at $S = 1.75$ (i.e., the beam tip).

Downloaded 04 May 2010 to 171.66.16.28. Redistribution subject to ASME license or copyright; see http://www.asme.org/terms/Terms_Use.cfm

4.2 Two-Layer Beam With Ply Drop-off. An example of application of the present formulation to the important class of multilayer structures with ply drop-off is now presented. A two-layer beam used in this section is depicted in Fig. 5, where the top layer is shorter than the bottom layer by half, creating a ply drop-off, and thus a sharp discontinuity in the cross-section in the middle of the beam. The present example illustrates the ability to accommodate ply drop-off naturally. The case with small deformation is analyzed in Zinno and Barbero (1994). The following material properties are selected.[13]

$$E = 29{,}000, \quad \nu = 0.294, \quad \chi = \frac{5}{6}, \tag{4.11}$$

for both layers, i.e.,

$${}_{(l)}EA = 14{,}500, \quad {}_{(l)}GA_s = 5{,}602.8, \quad {}_{(l)}EI = 302.1. \tag{4.12}$$

The beam has a length of $L = 5$ and a half-layer thickness $h = 0.25$. The verification of the modeling and the comparison of the results obtained with our theory to those obtained with the Timoshenko beam theory or to the results obtained in Zinno and Barbero (1994) are given in Deng and Vu-Quoc (1994), for both cases (i.e., with or without ply drop-off).

We now consider a roll-up of the two-layer beam with ply drop-off (Fig. 5) by assigning the moment ${}_{(1)}M$ at the tip of layer (1) with increasing magnitude. The loading is divided into ten steps with equal increments $m = 80.983$ for the moment ${}_{(1)}M$, such that the tenth load step we have ${}_{(1)}M = 2\pi {}_{(1)}E\,{}_{(1)}I/(L/2) = 10 \times 80.983$, which is the magnitude of the tip moment to make the thin half of the beam rolled into one full circle.[14] The deformed shape is shown in Fig. 6, where it can be seen that the thin half (i.e., layer (1)) of the two-layer beam is rolled up into a full circle, whereas the thicker half deformed into an arc of a circle. A zoom-in plot of the deformed beam, at the last load step ${}_{(1)}M = 809.83$, and in the neighborhood of the ply drop-off point is given in Fig. 7 where the cross-section at the drop-off point shows clearly a hinge.[15] For a beam with layers of equal length subjected to an assigned moment at its tip, the cross-section at midspan remains (i.e., there is no hinge; see Fig. 4) plane after deformation[16] and thus shear force is negligible at mid-span. On the other hand, in the present example, shear force is introduced due to the ply drop-off. Figure 7 shows a significant shear distortion in the bottom layer, just before the drop-off point.

[13]Young's modulus E, Poisson's ratio ν, shear coefficient χ such that $A_s = \chi A$.

[14]See (4.7) in Section 4.1.2.

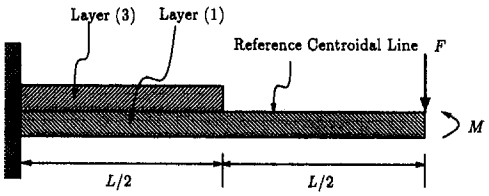

Fig. 5 Two-layer beam with ply drop-off. Long layer (1), inexistent layer (2), short layer (3). Reference centroidal line is the top fiber of layer (1).

5 Closure

We have presented above only selected examples that illustrate the essential features of the present formulation. The reader is referred to Deng and Vu-Quoc (1994) for an extensive collection of numerical examples, and the observed

[15]The cross-section before the drop-off point also develops a hinge (Fig. 7).

[16]Away from the beam tip, since the effect of moment distribution is negligible (Saint-Venant principle), that cross-section remains plane.

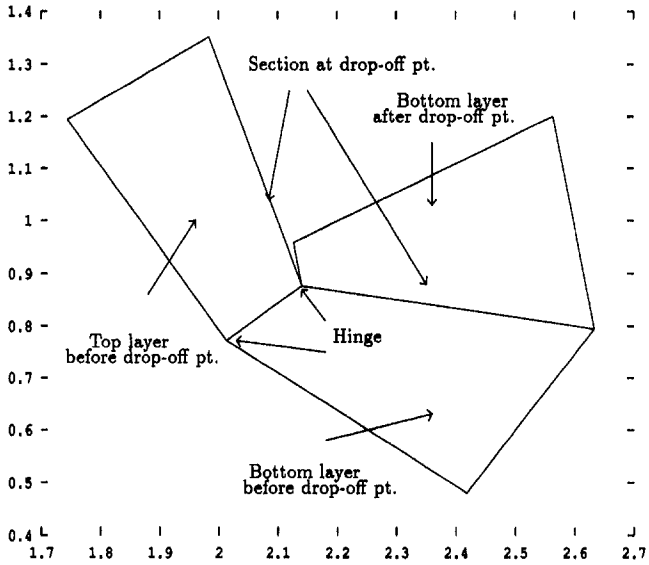

Fig. 7 Two-layer beam with ply drop-off. Roll-up maneuver. Zoom-in figure with one beam element before, and one beam element after the drop-off point. Deformation.

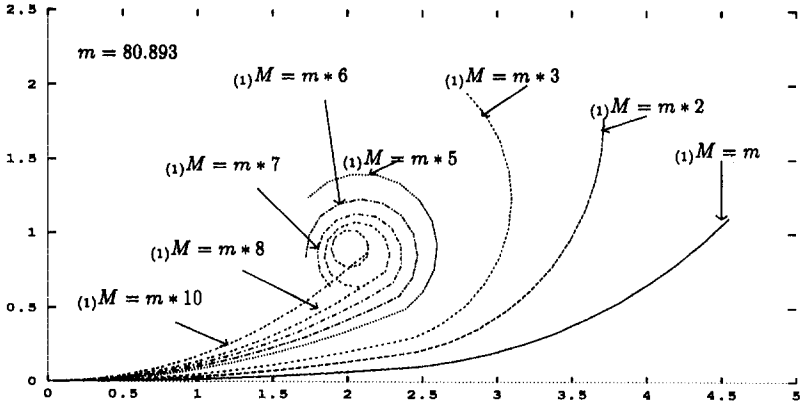

Fig. 6 Two-layer beam with ply drop-off. Roll-up maneuver. Assigned moment at the tip of layer (1). The thinner part of the beam forms a full circle when ${}_{(1)}M = m * 10$.

Downloaded 04 May 2010 to 171.66.16.28. Redistribution subject to ASME license or copyright; see http://www.asme.org/terms/Terms_Use.cfm

numerical behavior.[17] We will report in future publications results concerning the Galerkin projection of the complete equations of motion (the dynamic case), a generalization of the present formulation to the case of multilayer structures with an arbitrary number of layers, and the case with through-the-thickness deformation.

Acknowledgments

The research is supported by a grant from the National Science Foundation, and from the SRAP Program of the Florida Space Grant Consortium. This support is appreciated.

References

Arnold, D. N., 1981, "Discretization by Finite Elements of a Model Parameter Dependent Problem," *Numerische Mathematik*, Vol. 37, pp. 405–421.

Deng, H., and Vu-Quoc, L., 1994, "Galerkin Projection for Geometrically-Exact Multilayer Beams Allowing for Ply Drop-off," Technical Report AeMES-TR-94-03-02, Aerospace Engineering, Mechanics and Engineering Science, University of Florida, Gainesville, FL.

Di Sciuva, M., 1987, "Improved Shear-Deformation Theory for Moderately Thick Multilayered Anisotropic Shells and Plates," ASME JOURNAL OF APPLIED MECHANICS, Vol. 54, pp. 589–596.

Dong, S. B., Pister, K. S., and Taylor, R. L., 1962, "On the Theory of Laminated Anisotropic Shells and Plates," *J. Aero. Sci.*, Vol. 29, No. 8, pp. 969–975.

[17]We obtain an excellent agreement (in the case of small deformation) with the analytical solution based on a formulation of equivalent linear Timoshenko beam due to Heuer (1992).

Heuer, R., 1992, "Static and Dynamic Analysis of Transversely Isotropic, Moderately Thick Sandwich Beams by Analogy," *Acta Mechanica*, Vol. 91, pp. 1–9.

Hughes, T. J. R., 1987, *The Finite Element Method*, Prentice-Hall, Englewood Cliffs, NJ.

Noor, A. K., 1990, "Assessment of Computational Models for Multilayered Anisotropic Plates," *Composite Structures*, Vol. 14, No. 3, pp. 233–265.

Noor, A. K., and Burton, W. S., 1989, "Assessment of Shear Deformation for Multilayered Composite Plates," ASME *Applied Mechanics Review*, Vol. 42, pp. 1–12.

Pai, P. F., Nayfeh, A. H., Oh, K., and Mook, D. T., 1993, "A Refined Nonlinear Model of Composite Plate with Integrated Piezoelectric Actuators and Sensors," *International Journal of Solids and Structures*, Vol. 30, pp. 1603–1630.

Reddy, J., 1989, "On the Generalization of Displacement-Based Laminate Theories," ASME *Applied Mechanics Review*, Vol. 42, pp. S213–222.

Reddy, J. N., 1993, "An Evaluation of Equivalent-Single-Layer and Layerwise Theories of Composite Laminates," *Composite Structures*, Vol. 25, p. 21.

Reddy, J. N., and Robbins, D. H., 1994, "Theories and Computational Models for Composite Laminates," ASME *Applied Mechanics Review*, Vol. 47, p. 147.

Simo, J. C., and Vu-Quoc, L., 1986, "Three-Dimensional Finite-Strain Rod Model. Part II: Computational Aspects," *Computer Methods in Applied Mechanics and Engineering*, Vol. 58, pp. 79–116.

Vu-Quoc, L., and Ebcioğlu, I. K., 1995, "Dynamic Formulation for Geometrically-Exact Sandwich Beams and 1-D Plates," ASME JOURNAL OF APPLIED MECHANICS, in press.

Vu-Quoc, L., and Li, S., 1995, "Dynamics and Sliding Geometrically-Exact Beams: Large Angle Maneuvers and Parametric Resonance," *Computer Methods in Applied Mechanics and Engineering*, Vol. 120, pp. 65–118.

Zienkiewicz, O. C., and Taylor, R. L., 1989, *The Finite Element Method. Volume* 1: *Basic Formulation and Linear Problems*, 4th ed., McGraw-Hill, New York.

Zinno, R., and Barbero, E. J., 1994, "A Three-Dimensional Layer-Wise Constant Shear Element for General Anisotropic Shell-Type Structures," *International Journal for Numerical Methods in Engineering*, Vol. 37, p. 2445.

Downloaded 04 May 2010 to 171.66.16.28. Redistribution subject to ASME license or copyright; see http://www.asme.org/terms/Terms_Use.cfm

Poincare Linear Interpolated Cell Mapping: Method for Global Analysis of Oscillating Systems

J. Levitas

T. Weller

Faculty of Aerospace Engineering,
Technion—Israel Institute of Technology,
32000 Haifa, Israel

A method for global analysis of nonlinear dynamical oscillating systems was developed. The method is based on the idea of introducing a Poincare section into a multidimensional state space of the dynamical system and combine it with an interpolation procedure within the cells which constitute the discretized problem domain of interest. The proposed method was applied to study the global behavior of two nonlinear coupled van der Pol oscillators. Significant saving in calculation time, in comparison with both direct numerical integration and Poincare-like simple cell mapping, is demonstrated.

1 Introduction

Cell mapping is a relatively new advanced computation technique used for global analysis of nonlinear dynamical systems. The method is based on discretization of a state space of a dynamic system (dependent variable) into small regions, cells, and subsequent construction of an integer type mapping of these cells. The technique was first proposed by Hsu (Hsu, 1980; Hsu and Guttalu, 1980) with the introduction of the simple cell mapping method. The simple cell mapping appeared to be a very efficient and easy to implement method. A year later, Hsu (1981) introduced the generalized cell mapping which contrary to the simple cell mapping, where each cell has only one image, accounts for the possibility that a cell may have several different images. The whole mapping is given by a probability matrix and involves a notation of Markov chains. Both, the simple cell mapping and generalized cell mapping, including many applications of these methods, are described in detail by Hsu (1987).

In 1988 Tongue (Tongue and Gu 1988 a,b) presented an interpolated cell mapping. In this method the actual mapped positions of cell vertices are recorded and interior points of the cell are obtained by interpolation. By this procedure the interpolated cell mapping provides the mapping of an entire continuum by mapping of a finite number of cells.

In spite of their efficiency, the main drawback of the mapping techniques is the difficulty associated with the treatment of high-order dimension dynamical systems. To the best of the authors' knowledge, the system of highest order considered by this method involved computations in a R^4 state space. This was solved by the simple cell mapping employing 59^4 cells (Xu, Guttalu, and Hsu, 1985).

Further development of the cell mapping led to the introduction of Poincare-like simple cell mapping (Levitas, Weller, and Singer, 1992). Application of the method reduced the number of dimensions involved in the analysis. This is due to considering only hyperplanes which are Poincare sections in the state space of a multidimensional system. Consequently, this also leads to considerable reduction in memory and computational time in studies of high-order dimensional systems. In principle, the number of introduced Poincare sections is unlimited. Levitas et al. (1992) used the Poincare-like simple cell mapping to restudy the problem of Xu et al. (1985). The calculations involved four three-dimensional hyperplanes, which served as Poincare sections, and discretization of each section into 59^3 cells. Significant savings in computer resources, memory and CPU time, in addition to improvement in the accuracy of the results, in comparison with previous results achieved by the simple cell mapping, were demonstrated. It should be noted that introduction of Poincare section in time for periodic systems was extensively applied by Hsu, Tongue, and their colleagues. However, the spatial Poincare section was previously used only with the Poincare-like simple cell mapping.

In the present paper, attempts were undertaken to further improve and demonstrate the feasibility of applying the mapping techniques for the solution of high-order systems. The idea of reducing the problem dimensions by use of Poincare sections is combined with the interpolated cell mapping method. Since linear interpolation is applied inside the cell, the method is called Poincare linear interpolated cell map-

Contributed by the Applied Mechanics Division of THE AMERICAN SOCIETY OF MECHANICAL ENGINEERS for publication in the ASME JOURNAL OF APPLIED MECHANICS.

Discussion on this paper should be addressed to the Technical Editor, Professor Lewis T. Wheeler, Department of Mechanical Engineering, University of Houston, Houston, TX 77204-4792, and will be accepted until four months after final publication of the paper itself in the ASME JOURNAL OF APPLIED MECHANICS.

Manuscript received by the ASME Applied Mechanics Division, Feb. 19, 1993; final revision, Aug. 31, 1993. Associate Technical Editor: R. L. Huston.

Copyright © 1995 by ASME

Downloaded 04 May 2010 to 171.66.16.28. Redistribution subject to ASME license or copyright; see http://www.asme.org/terms/Terms_Use.cfm

ping. This method and its application is described and discussed in detail in the following sections.

2 Problem Definition

A dynamical system in R^M, described by an autonomous system of nonlinear differential equations of the first order, is studied:

$$\dot{\mathbf{x}} = \mathbf{f}(\mathbf{x}) \tag{1}$$

where $\mathbf{x} = \mathbf{x}(t) \in R^M$ is a state vector, $\mathbf{f}(\cdot): R^M \to R^M$ is a nonlinear function, and $\dot{\mathbf{x}} = d\mathbf{x}/dt$ represents the time derivative of $\mathbf{x}$. The investigation aims at finding, in some region of the state space, all of the steady-state or periodic solutions of the system (1), and at determining the regions of attraction of the asymptotically stable ones. This goal can be achieved by direct numerical integration of Eq. (1), together with a large number of initial conditions, by using either one of the existing cell mapping techniques (simple cell mapping, generalized cell mapping, interpolated cell mapping, Poincare-like simple cell mapping), or by other methods. Each of these approaches has its advantages and drawbacks. Thus, a decision as to which method should be used depends upon the particular problem studied.

In cases where Eq. (1) describes a vibration type problem, it was shown by Levitas, Weller, and Singer (1992) that the use of Poincare-like simple cell mapping is very advantageous. Here the use of Poincare sections, together with an interpolation procedure (Tongue and Gu, 1988a), in mapping techniques will be examined.

3 The Proposed Method

The first step of the procedure is to choose the (M-1)-dimensional Poincare section, $\mathcal{P}$, in the R^M state space. This section reduces the dimension of the space under investigation by keeping one of the coordinates constant. The section $\mathcal{P}$ is chosen in a way which ensures repetitive intersections of the system evolution trajectories with it. Hence, if a system has stable equilibrium points, they must lie on $\mathcal{P}$. When it possesses stable limit cycles, the section should intersect with them. In both cases an appropriate choice of $\mathcal{P}$ might be a section located at a zero value of velocity coordinate. Then, two finite regions, D_G and D_I, are defined in $\mathcal{P}$. As will be explained in the following, the region D_G is used for determination of a grid deformation, due to a single mapping step upon application of Eq. (1) and it is called the "grid deformation domain". The second region, D_I, is the one in which the dynamic behavior of the system is investigated, the "domain of interest". It is reasonable that for the interpolation procedure D_G has to include the D_I ($D_G \supseteq D_I$).

Analysis by the present Poincare linear interpolated cell mapping consists of three different steps: (1) performance of numerical integration to obtain the "one mapping step deformed domain"; (2) interpolation and cell mapping construction; (3) cell mapping unraveling. The third step was extensively discussed previously (Hsu and Guttalu, 1980; Hsu, 1987). Hence, only the first two steps are discussed next.

3.1 One Mapping Step Deformation

The deformation domain is divided into $N_G = \prod_{j=1}^{M-1} N_{jGC}$ grid cells (G-cell), where N_{jGC} is the cell discretization of the D_G domain in the "j"-s space coordinate, and $\prod_{j=1}^{M-1}$ denotes a multiplication of $M-1$ terms. The rectangular N_G G-cells have $N_{GV} = \prod_{j=1}^{M-1} (N_{jGC} + 1)$ vertices, which serve as initial conditions for numerical integration of Eq. (1). The integration is performed by any standard numerical scheme. It begins with an initial condition $\mathbf{x}^0$ and is carried over a very small time step Δt_f to yield $\mathbf{x}^1 = \mathbf{x}(\Delta t_f)$. This first point of the trajectory provides the tendency of the trajectory movement relative to the Poincare section $x_i = \xi_i$ (e.g., in Fig. 1 Poincare section is given by $x_3 = 0$) and is identified by an integer $ID_i = \text{sign}\ (x_i^1 - \xi_i)$. The integration is continued with a new time step Δt_1, usually larger than Δt_f, and the trajectory of the system is furnished by points $\mathbf{x}^k = \mathbf{x}\ (\Delta t_f + (k-1)\Delta t_1)$ $(k = 1, 2, 3, \cdots)$. At every integration step $\mathbf{x}^k\ (t) \to \mathbf{x}^{k+1}\ (t + \Delta t_1)$, the position of $\mathbf{x}^{k+1}$ relative to ξ_i is examined by the sign of $ID_i^*\ (x_i^{k+1} - \xi_i)$. A negative value of this product indicates that the points $\mathbf{x}^k$ and $\mathbf{x}^{k+1}$ lie on opposite sides of ξ_i. Thus, the existence of intersection of the trajectory with $\mathcal{P}$ is determined.

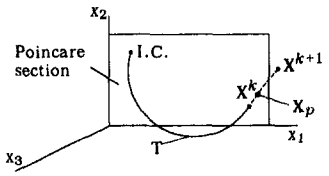

Fig. 1 Two-dimensional Poincare section and determination of the intersection point, $\mathbf{x}_p$. I.C.-initial condition, T-trajectory.

Now, to locate the point of intersection $\mathbf{x}_p$, a "refinement" of the trajectory is performed. This is achieved by returning to the point $\mathbf{x}^k$ and integrating $\mathbf{x}^k(t) \to \mathbf{x}^{k+1}\ (t + \Delta t_2)$ in Eq. (1) over a fine time step Δt_2. Intersection is again searched by checking the sign of $ID_i^*\ (x_i^{k+1} - \xi_i)$. Once it is detected, the point of intersection $\mathbf{x}_p = (x_{1p}, x_{2p}, \cdots, \xi_i, \cdots x_{Mp})$ is obtained by linear interpolation between $\mathbf{x}^k$ and $\mathbf{x}^{k+1}$:

$$\lambda = \frac{\xi_i - x_i^k}{x_i^{k+1} - x_i^k} \tag{2a}$$

$$\mathbf{x}_p = \mathbf{x}^k + \lambda(\mathbf{x}^{k+1} - \mathbf{x}^k) \tag{2b}$$

$$\tau = t_k + \lambda \Delta t_2 \tag{2c}$$

where t_k is a time pertinent to $\mathbf{x}^k$ and τ is the time until intersection occurs (see Fig. 1). The flow chart of the described procedure is shown in Fig. 2.

The above procedure is performed for all N_{GV} initial conditions and the deformed region D_G, consisting of the deformed G-cells, is obtained. This image is called "one mapping step deformed domain" (OMSDD). In the example in Fig. 3, a three-dimensional state space cut by a Poincare section, which coincides with the (x_1, x_2)-plane, is shown. In this figure the deformation domain is divided into 15 G-cells, shown both before and after deformation.

3.2 Interpolation Procedure. The deformation of D_G is obtained by comparing the undeformed and the deformed positions of the vertices of the G-cells. Using this information, any other point, inside the G-cell, can be mapped by linear interpolation inside the cell (Fig. 4) (Tongue and Gu, 1988a). We are interested in the determination of the global behavior of a system in the domain of interest, D_I. Following Hsu (1987), this domain is divided into $N_R = \prod_{j=1}^{M-1} N_{jRC}$ regular cells (R-cells), where N_{jRC} represents discretization of the D_I domain in the "j" coordinate. These R-cells serve the same purposes of cells as in the simple cell mapping: they constitute the actual discretization of the domain of interest; each cell is lumped together in its midpoint; they are employed for construction of a cell mapping of the dynamical system. The whole region outside D_I is represented by one hug cell called "sink." Each R-cell is represented by its middle point which is located at

$$x_j = R_{jL} + (z_j - 0.5)h_{jR}; \quad j = 1, 2, \ldots i-1, i+1, \ldots M$$
$$x_i = \xi_i \tag{3}$$

Downloaded 04 May 2010 to 171.66.16.28. Redistribution subject to ASME license or copyright; see http://www.asme.org/terms/Terms_Use.cfm

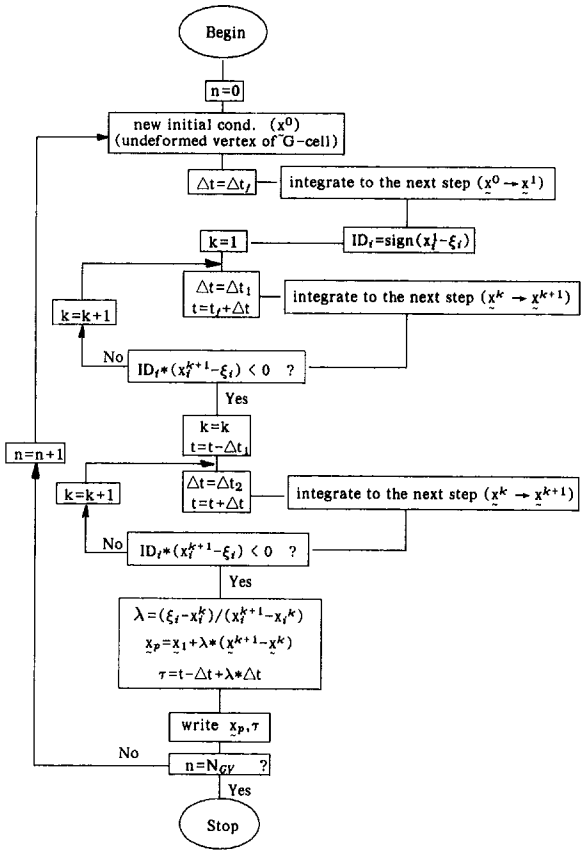

Fig. 2 Flow diagram for determination of intersection point, x_p.

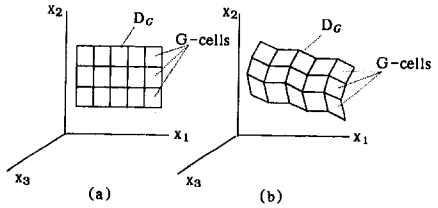

Fig. 3 Grid deformation domain, D_G, in the (x_1, x_2) Poincare section ($N_{1GC} = 5$, $N_{2GC} = 3$); (a) undeformed, (b) deformed

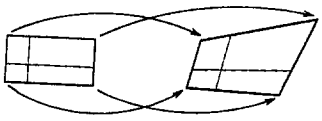

Fig. 4 Linear interpolation inside a two-dimensional G-cell

where z_j, R_{jL}, and h_{jR} are an integer type cell coordinate, a lower bound of D_I in a "j" coordinate, and size of R-cells in a "j" coordinate, respectively. The R-cell is mapped by interpolation into the next step using the information on the deformation of the G-cells. Cell coordinates of the cell to which the interpolated point $\mathbf{x}'$ belongs, are calculated by

$$z_j = \mathrm{Int}\left[\left(x_j' - R_{jL}\right)/h_{jR}\right] + 1$$

$$j = 1, 2, \ldots i-1, i+1, \ldots M. \quad (4)$$

This mapping-interpolation procedure is performed step by step and thus approximates the evolution of the system trajectory. All of the R-cells, through which the point passes, constitute the "cell trajectory" and are recorded.

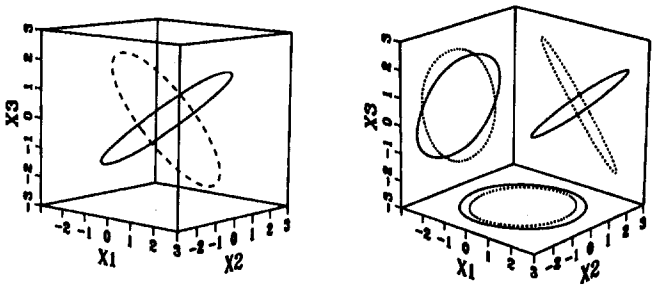

Fig. 5(a) The two stable limit cycles (l.c) of the van der Pol oscillators in a (x_1, x_2, x_3) subspace, and (b) their projections to the coordinate planes. ___ the first l.c., --- the second l.c

It is very inconvenient to present a general $(M-1)$-dimensional interpolation formula. Therefore, an expression for a three-dimensional case is given in subsection 4.2. This formula can be extended to a higher dimension, similar to the way the three-dimensional case was developed from a two-dimensional one (Tongue and Gu, 1989).

The interpolation process is terminated once the point meets an R-cell, which is already located along the cell trajectory. This final R-cell is the one into which the initial R-cell is mapped. By carrying out this procedure, for every R-cell, the cell mapping of the whole D_I is obtained. The domains of attraction of the stable solutions of the dynamical system, described by Eq. (1), are found from this cell mapping by applying the Unravelling Algorithm, developed by Hsu and Guttalu (1980) (see also Hsu, 1987).

4 Example

To demonstrate the above procedure, the global behavior of two van der Pol coupled oscillations, which are described by four ordinary nonlinear differential equations, is presented:

$$\dot{x}_1 = x_2$$

$$\dot{x}_2 = \mu\left(1 - x_1^2\right)x_2 - (1+\nu)x_1 + \nu x_3$$

$$\dot{x}_3 = x_4$$

$$\dot{x}_4 = \mu\left(1 - x_3^2\right)x_4 - (1+\nu+\eta)x_3 + \nu x_1. \quad (5)$$

This system, with the parameters $\mu = 0.1$, $\eta = 0.04$, and $\nu = 0.1$ has two stable limit cycles and an unstable equilibrium point at the origin (Fig. 5). It was previously studied by the simple cell mapping by Xu et al. (1985) (see also Hsu, (1987), and applying the Poincare-like simple cell mapping by Levitas et al. (1992). Hence, this case is a suitable representative example for a comparison between, the assessment of, the present and the previous approaches.

The solution procedure, described in the previous section, is applied for the given example with $M = 4$ next. For clarity and continuity of the presentation and aiming at assisting the reader, some of the steps discussed in Section 3 are repeated in what follows.

The Poincare section is chosen to be the three-dimensional (x_1, x_2, x_3) hyperplane with $\xi_4 = 0$. This means that $\mathcal{P}$ is defined by $x_4 = 0$. The respective domains of grid deformation and of interest are

$$D_G = [-3.5,\ 3.5] \times [-4.0, 4.0] \times [-3.5, 3.5] \quad (6)$$

$$D_I = [-2.5,\ 2.5] \times [-3.0, 3.0] \times [-2.5, 2.5]. \quad (7)$$

Downloaded 04 May 2010 to 171.66.16.28. Redistribution subject to ASME license or copyright; see http://www.asme.org/terms/Terms_Use.cfm

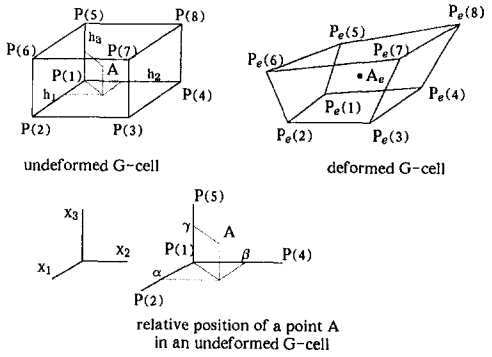

Fig. 6 Initial and deformed shapes of a three-dimensional G-cell

(Note that D_I is a half-open region. This stems from the determination of cell coordinates given in expression (13)).

D_G is chosen to be larger than D_I, to allow the cell trajectory, which at a certain interpolation step can leave the D_I (but still remains in D_G) to return back into it.

4.1 Obtaining of the OMSDD. The one mapping step deformed domain results from numerical integration of Eq. (1) by a fourth-order Runge-Kutta (R-K) procedure. The integration is performed with $\Delta t_f = 0.01$, $\Delta t_1 = 0.1$, $\Delta t_2 = 0.01$ and terminated after first intersection of the system evolution trajectory with the Poincare section $\mathcal{P}$. The occurrence of intersection, as was explained in Section 3, is detected by a change in sign of x_4, as the trajectory passes $\mathcal{P}$. Because the check of sign of x_4 is performed in intervals of Δt_2, the intersection position, $\mathbf{x}_p = (x_{1p}, x_{2p}, x_{3p}, 0)$ is approximated by linear interpolation between the two successive trajectory points $\mathbf{x}^k$ and $\mathbf{x}^{k+1}$, as demonstrated in Fig. 1, and given by the following expression derived from (2):

$$\mathbf{x}_p = \mathbf{x}^k - \frac{x_4^k}{x_4^{k+1} - x_4^k}(\mathbf{x}^{k+1} - \mathbf{x}^k). \tag{8}$$

Execution of the above described procedure for all N_{GV} and recording of all of the terminal $\mathbf{x}_p$ positions yields the one mapping step deformed domain.

4.2 Interpolation and Cell Mapping Construction. The three-dimensional cell, employed in the present analysis, contains eight vertices described by the vectors $\mathbf{P}(1)$, $\mathbf{P}(2)$, . . . , $\mathbf{P}(8)$ which provide initial conditions for the numerical integration. After completion of the integration these points occupy the new end positions, denoted by $\mathbf{P}_e$ (1), $\mathbf{P}_e$ (2), . . . , $\mathbf{P}_e$ (8) (Fig. 6). A point **A**, which lies inside the undeformed cell, has coordinates $(A_1, A_2, A_3, 0)$ and its relative position inside the cell is identified by three numbers α, β, γ:

$$\alpha = (A_1 - P_1(1))/h_{1G}$$
$$\beta = (A_2 - P_2(1))/h_{2G}$$
$$\gamma = (A_3 - P_3(1))/h_{3G} \tag{9}$$

where $P_1(\cdot)$, $P_2(\cdot)$, $P_3(\cdot)$ are the x_1, x_2, x_3 coordinates of the point $\mathbf{P}(\cdot)$, respectively, and h_{jG} $(j = 1, 2, 3)$ are the dimensions of the undeformed G-cell (Fig. 6). The position of this point in the deformed cell is denoted by $\mathbf{A}_e$ and is obtained by interpolation:

$$\mathbf{A}_e = [(1-\alpha)(1-\beta)\mathbf{P}_e(1) + \alpha(1-\beta)\mathbf{P}_e(2) + \alpha\beta\mathbf{P}_e(3) + (1-\alpha)\beta\mathbf{P}_e(4)](1-\gamma) + [(1-\alpha)(1-\beta)\mathbf{P}_e(5) + \alpha(1-\beta)\mathbf{P}_e(6) + \alpha\beta\mathbf{P}_e(7) + (1-\alpha)\beta\mathbf{P}_e(8)]\gamma. \tag{10}$$

This forms a linear interpolation, which takes into account the relative proximity of point **A** (and thus also of $\mathbf{A}_e$) to the cell vertices. In the case of two-dimensional cells it is identical with the expression used by Tongue and Gu (1989).

The starting point of each interpolation is a midpoint of an R-cell:

$$x_j = [R_{jL} + (z_j - 0.5)h_{jR}], \quad (j = 1,2,3)$$
$$x_4 = 0. \tag{11}$$

Assume that this point belongs to a cell "n" given by

$$n = z_1 + N_{1RC}(z_2 - 1) + N_{1RC}N_{2RC}(z_3 - 1) \tag{12}$$

where $1 \le z_j \le N_{jRC}$ $(j = 1, 2, 3)$. The interpolation is carried out, step by step, and the cell coordinates of the new R-cell, to which the interpolated point (x_1', x_2', x_3') belongs, are calculated by

$$z_j = \mathrm{Int}[(x_j' - R_{jL})/h_{jR}] + 1 \quad (j = 1,2,3) \tag{13}$$

and its cell number is given again by (12). (In the present example $R_{1L} = -2.5$, $R_{2L} = -3.0$, and $R_{3L} = -2.5$.) All of the R-cells through which the interpolated point passes belong to the particular cell trajectory which starts from "n." The interpolation is terminated when the point is mapped to the R-cell which is already contained in the cell trajectory, say cell "m." Then, the cell mapping "n"→"m" is determined, and the interpolation procedure begins from the next cell "$n + 1$."

4.3 Results. The determination of the one mapping step deformed domain was executed for different G-cell discretization. The interpolation procedure, corresponding to every case, was carried out for a constant number of the R-cells with the partition $N_{1RC} = N_{2RC} = N_{3RC} = 59$. Thus, the R-cell array contains $59^3 = 205379$ cells. (An identical partition was used by Xu et al. (1985) and Levitas et al. (1992).)

In the present analysis, like in the Poincare-like simple cell mapping, the numerical integration for obtaining the one mapping step deformed domain, is terminated when the trajectory intersection with the Poincare section occurs. Therefore, unlike in the simple cell mapping and interpolated cell mapping, the mapping step time τ, defined in (2c), is different for each initial condition. To estimate τ, the average mapping step time for construction of one mapping step deformed domain, $\tau_{av} = (\sum_{n=1}^{N_{GV}} \tau_n)/N_{GV}$, is calculated.

Furthermore, the number of interpolation steps in each R-cells trajectory is also different. To estimate the average number of interpolation steps in an R-cell trajectory, a value $Is_{av} = (\sum_{n=1}^{N_R} Is_n)/N_r$ is defined. Here , Is_n is the number of interpolation steps in the cell trajectory which starts from the "n" R-cell.

For evaluation of the present results, direct numerical integration of Eq. (5), with 59^3 initial conditions, was carried out by a fourth-order R-K integration scheme. The basic integration step was $\Delta t = 0.1$ and each integration consisted of 3500 steps. This number of steps is found to be adequate to achieve a periodic solution from each initial condition. Only the last 100 steps were recorded and they served for the determination of the limit cycle, to which the initial point attracts. This solution is referred herein as the "exact" one. By comparison of the results yielded by the cell mapping with the "exact" solution, the "stray" R-cells, i.e., the cells whose behavior was mistakenly discovered, are revealed.

All calculations were performed on an IBM RS 6000/560 work station. The direct numerical integration required 56

Downloaded 04 May 2010 to 171.66.16.28. Redistribution subject to ASME license or copyright; see http://www.asme.org/terms/Terms_Use.cfm

Table 1. The results of the PLICM for different G-cell discretizations

G-cell discretization	N_{GV} ($\times 10^3$)	time for OMSDD[1] (sec)	Interpolation time (sec)	Total time (sec)	Number of stray R-cells
$19 \times 19 \times 19$	8	2	104	106	5552
$29 \times 29 \times 29$	27	7	104	111	1556
$39 \times 39 \times 39$	64	15	112	127	986
$49 \times 49 \times 49$	125	30	114	144	556
$59 \times 59 \times 59$	216	52	119	171	232
$69 \times 69 \times 69$	343	82	123	205	284
$79 \times 79 \times 79$	512	122	133	255	856

[1]one mapping step deformed domain

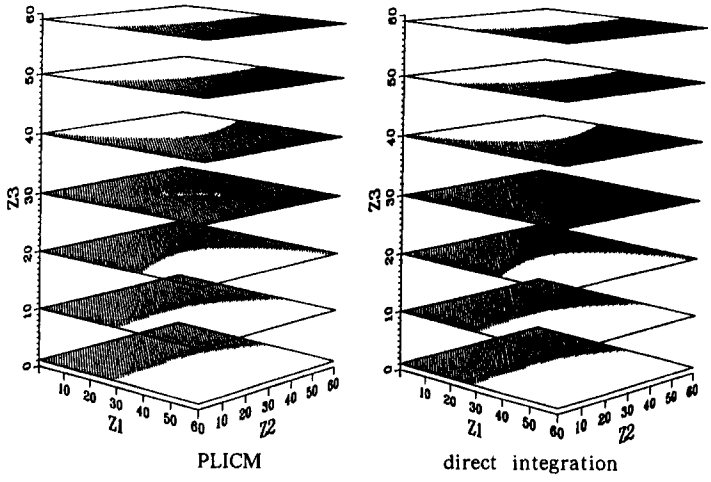

Fig. 7 Domains of attraction yielded by the Poincare linear interpolated cell mapping and by the direct integration. (The first limit cycle attracts the black regions, the second limit cycle attracts the white regions.)

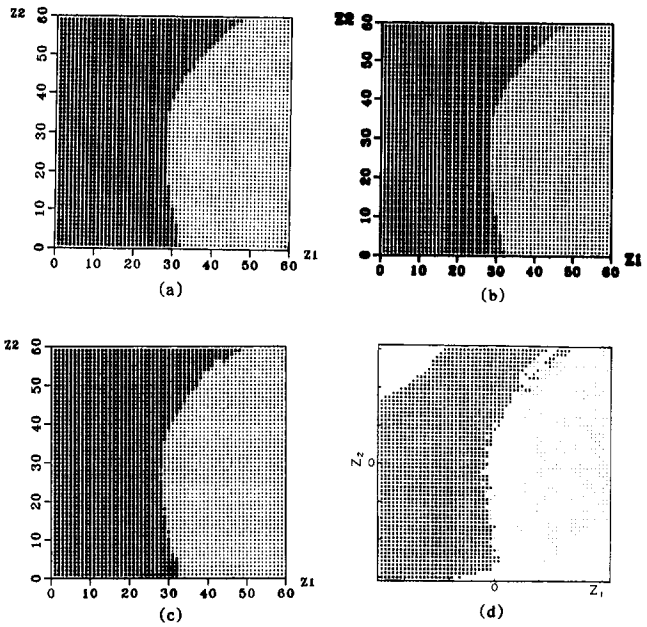

Fig. 8 Comparison of the results obtained by various methods for a section $z_3 = 15$ ($x_3 = 1.2712$). "■"— cells attracted to the first limit cycle, ". "— cells attracted to the second limit cycle. (*a*) direct integration, (*b*) present Poincare linear interpolated cell mapping results, (c) Poincare-like simple cell mapping results (Levitas et al., 1992) and (*d*) simple cell mapping results (Xu et al., 1985)—here " ·"—cells attracted to the first limit cycle.

CPU minutes. The number of stray cells, CPU time consumed to obtain the one mapping step deformed domain and for interpolation for various partitions of D_G are presented in Table 1.

Note that since a value of (No. of "stray" R-cells)/(total number of R-cells) furnishes the relative number of cells with a mistaken behavior, it can serve as an appropriate measure for error estimation. It is seen in Table 1 that for 29^3 G-cells the results obtained by the present method differs from the "exact" ones by only 0.76 percent, whereas they are achieved 30 times faster than by direct numerical integration. Increase in G-cells to 59^3 results in an improved accuracy, 0.11 percent difference, however with a factor of 20 in time saving. The unravelling of the cell mappings in all of the cases required about one second. (Note that the times do not include I/O operations.) For readers who are interested in repeating the calculations some additional results are provided here. For example, for the case of 59^3 G-cells the mapping step times for construction of one mapping step deformed domain were $\tau_{\min} = 0.010$, $\tau_{\max} = 5.950$, $\tau_{av} = 2.936$. The minimum, maximum, and average number of interpolation steps were 1, 141, and 35.182, respectively. Note that one is the minimum possible value of interpolation steps and it appears for the equilibrium cell, i.e., the cell which maps into itself. In the unravelling of the mapping 63 different groups were determined. The minimum, maximum, and average step numbers were 0, 4, and 1.555, respectively. The average values of all other runs were very similar to the above ones. In all runs no cell is attracted by the sink.

In Fig. 7 the three-dimensional structure of the domains of attraction, as they appear in the two-dimensional cell coordinates sections (z_1, z_2), is shown. This structure appears to be antisymmetric about the $z_3 = 30$ ($x_3 = 0$) section. The results are presented for a 59^3 G-cells partition and are compared with those of direct integration. The similarity between the results of the two solution methods is obvious from this figure.

A comparison of the present results with the previous ones (Xu et al., 1985; Levitas et al., 1992) and with direct integration for the section $z_3 = 15$ is presented in Fig. 8. The results of (*a*)–(*c*) are depicted in the cell coordinates which change from 1 to 59. The coordinates of (*d*) change from −29 to 29.)

4.4 Influence of Mapping Step Time. To evaluate the influence of the time mapping step on the results, a calculation of the one mapping step deformed domain which was obtained after two intersections between the system evolution trajectories and $\mathcal{P}$, instead of one, was performed. In application of the Poincare linear interpolated cell mapping the number of prescribed intersections was denoted by $In_{\max}$ (Levitas et al., 1992). This notation is "borrowed" from that study. Consequently, in this case the one mapping step deformed domain is constructed for $In_{\max} = 2$. In these calculations the number of stray R-cells were 10490, 3050, 1858, 1026, 606, 750, and 1100 for 19^3, 29^3, 39^3, 49^3, 59^3, 69^3, and 79^3 G-cells, respectively.

4.5 Comparison With the Poincare-Like Simple Cell Mapping. To compare the present procedure with the Poincare-like simple cell mapping method, the calculations were performed by the Poincare like simple cell mapping, using one Poincare section $x_4 = 0$ and 59^3 cells. These computations, like the Poincare linear interpolated cell mapping were executed by a fourth-order R-K integration algorithm with $\Delta t = 0.1$.

Two cell mappings were constructed, one after ten ($In_{\max} = 10$) and the second after 20 ($In_{\max} = 20$) intersections of the system trajectories with the section $\mathcal{P}$. The number of "stray" cells was 854 in the first case, and 250 in the second one. These numbers are comparable with those obtained by interpolation. The calculations required 397 and 791 CPU

Downloaded 04 May 2010 to 171.66.16.28. Redistribution subject to ASME license or copyright; see http://www.asme.org/terms/Terms_Use.cfm

seconds for $In_{max} = 10$ and $In_{max} = 20$, respectively. Hence, it appears that to achieve accuracy of the same order the Poincare linear interpolated cell mapping is about four times more efficient than the Poincare-like simple cell mapping.

5 Remarks

• It is of significant importance to assess the performance of the proposed Poincare linear interpolate cell mapping and compare it with either the simple cell mapping or interpolated cell mapping methods. A one to one comparison is, however, impossible, because application of both simple cell mapping and interpolated cell mapping involves the "whole" M-dimensional regions of the dynamical system, whereas solution with the Poincare linear interpolated cell mapping or Poincare-like simple cell mapping is associated with reduced $(M - 1)$ dimensional regions. Obviously, the computer resources, needed for use by the simple cell mapping and interpolated cell mapping, are therefore a priori larger than those required by the Poincare-like simple cell mapping and Poincare linear interpolated cell mapping. Nevertheless, some comparison studies between the simple cell mapping and the Poincare-like simple cell mapping for a two coupled van der Pol oscillators problem were undertaken by Levitas et al., (1992) and are presented here: Construction of cell mapping by the Poincare-like simple cell mapping, with $In_{max} = 15$, required 205 CPU minutes with an IBM 3081D machine. The time needed by this computer, for construction of a mapping by the simple cell mapping in accordance with parameters used by Xu et al., (1985), is estimated at seven CPU hours. Comparison of Xu et al., (1985) results with the ones yielded by the Poincare-like simple cell mapping and the "exact" solution, shown in Fig. 8, indicates that the Poincare-like simple cell mapping results agree much better with the "exact" ones that the simple cell mapping results do. It should be noted that in principle it is possible to improve the accuracy of the simple cell mapping by increasing the mapping step time, τ. The average mapping step time in the results obtained by the Poincare-like simple cell mapping was $\tau_{av} = 11.6$. Using this time step with the simple cell mapping, instead of $\tau = 2.2$ employed by the Xu et al., (1985), results of the same accuracy achieved with the Poincare-like simple cell mapping are expected. However, this will require about 37 CPU hours of the previous machine. Unfortunately, no examples with M larger than two were considered by the interpolated cell mapping.

• The main drawback of all cell mapping techniques is the large amount of cells involved in the calculation. This prevents the application of cell mapping to multidimensional dynamical systems. However, both the Poincare-like simple cell mapping and Poincare linear interpolated cell mapping reduce the number of cells in comparison with the simple cell mapping and the interpolated cell mapping. In the example with $M = 2$ of the axially loaded buckled beam (Levitas et al., 1992) 101^2 cells were used by the simple cell mapping and interpolated cell mapping, instead of only 402 cells by the Poincare-like simple cell mapping. For an analysis of the two coupled van der Pol oscillators Xu et al. (1985) used 59^4 cells. The analysis with the Poincare-like simple cell mapping involved application of four Poincare section located at $x_1 = x_2 = x_3 = x_4 = 0$ and $4*59^3$ cells. The present Poincare linear interpolated cell mapping analysis uses one section with 59^3 cells. Note that indeed both the simple cell mapping and interpolated cell mapping provide considerably more information than either the Poincare like-simple cell mapping or Poincare-linear interpolated cell mapping. In the authors' opinion, however, this feature is a weakness of the simple cell mapping and interpolated cell mapping, because they have to manipulate with a large amount of data, most of which usually cannot even be presented. In light of these, the Poincare-type cell techniques are more flexible and more appropriate for analysis of high order dynamic systems.

• A choice of Δt_2 has to insure that the interval $\| \mathbf{x}^{k+1} - \mathbf{x}^k \|$ is small enough for good approximation of the point of intersection $\mathbf{x}_p$, but not too small to cause numerical problems associated with the denominator of Eq. $(2a)$. In the present example for the case of 59^3 G-cells the minimum and the maximum values of $\| \mathbf{x}^{k+1} - \mathbf{x}^k \|$ were 0.001228 and 0.08539, and the minimum and maximum values of $| x_4^{k+1} - x_4^k |$ were $1.868*10^{-6}$ and 0.03694, respectively. Thus, since double precision was used in the calculations there was no "hazard" of encountering numerical problems stemming from the denominator of Eq. $(2a)$.

• The errors contained in the present Poincare linear interpolate cell mapping, in comparison with direct numerical integration, stem from three different sources: interpolation of $\mathbf{x}_p$; approximation of the trajectory by interpolation inside the G-cells; cell mapping of R-cells. Estimation of the relative contribution of these errors is a prime issue for better understanding of the Poincare linear interpolated cell mapping, and its evaluation should be studied.

• It should be noted that some sensitivity of the Poincare linear interpolated cell mapping to discretization into G-cells was detected. For example, for 58^3, 60^3, 78^3, and 80^3 G-cells 698, 718, 150, and 142 stray R-cells, were obtained, respectively.

6 Conclusions

• In the present study a mapping technique, Poincare linear interpolated cell mapping is presented. This method combines the use of spatial Poincare section with the interpolated cell mapping.

• The Poincare linear interpolated cell mapping allows global analysis of multidimensional dynamic systems in a particular subspace of the state space without considering the whole one. This allows a considerable reduction of cells involved in computations.

• The global behavior of two van der Pol nonlinear coupled oscillators is studied by the Poincare linear interpolated cell mapping. The solution is compared with direct numerical integration, which herein is referred to as the "exact" solution.

• The example solved by the Poincare linear interpolated cell mapping yields results, which differ only by 0.76 percent from the "exact" solution, 30 times faster than by direct integration. A solution associated with a smaller 0.11 percent error is found to be 20 times faster than the "exact" one.

• The increase of In_{max} reduces the accuracy of the Poincare linear interpolated cell mapping, contrary to the Poincare-like simple cell mapping.

• In comparison with the Poincare-like simple cell mapping and requiring accuracy of the same order, the Poincare linear interpolated cell mapping appears to be about four times faster.

Acknowledgment

The authors gratefully acknowledge Prof. Emeritus J. Singer for interesting discussions and encouragement during preparation of this article.

References

Hsu, C. S., 1980, "A Theory of Cell-to-Cell Mapping for Dynamical Systems," ASME JOURNAL OF APPLIED MECHANICS, Vol. 47, pp. 931–939.

Downloaded 04 May 2010 to 171.66.16.28. Redistribution subject to ASME license or copyright; see http://www.asme.org/terms/Terms_Use.cfm

Hsu, C. S., 1981, "A Generalized Theory of Cell-to-Cell Mapping for Nonlinear Dynamical Systems," ASME JOURNAL OF APPLIED MECHANICS, Vol. 48, pp. 634–642.

Hsu, C. S., 1987, *Cell-to-Cell Mapping: A Method of Global Analysis for Nonlinear Systems*, Spring-Verlag, New York.

Hsu, C. S., and Guttalu, R. S., 1980, "An Unraveling Algorithm for Global Analysis of Dynamical Systems: An Application of Cell-to-Cell Mappings," ASME JOURNAL OF APPLIED MECHANICS, Vol. 47, pp. 940–948.

Levitas, J., Weller, T., and Singer, J., 1992, "Poincare-Like Simple Cell Mapping for Nonlinear Dynamical Systems," accepted for publication in *Journal of Sound and Vibration*.

Tongue, B. M., and Gu, K., 1988a, "Interpolated Cell Mapping of Dynamical Systems," ASME JOURNAL OF APPLIED MECHANICS, Vol. 55, pp. 461–466.

Tongue, B. M., and Gu, K., 1988b, "A Higher Order Method of Interpolated Cell Mapping," *Journal of Sound and Vibration*, Vol. 125, pp. 169–179.

Tongue, B. M., and Gu, K., 1989, "Adaptive Mesh Strategies for Interpolated Mapping Procedures," *International Journal of Engineering Science*, Vol. 27, pp. 1143–1154.

Xu, J. X., Guttalu, R. S., and Hsu, C. S., 1985, "Domains of Attraction of Multiple Limit Cycles of Coupled van der Pol Equations by Simple Cell Mapping," *International Journal of Nonlinear Mechanics*, Vol. 20, pp. 507–517.

Downloaded 04 May 2010 to 171.66.16.28. Redistribution subject to ASME license or copyright; see http://www.asme.org/terms/Terms_Use.cfm

Noise-Induced Transitions in Weakly Nonlinear Oscillators Near Resonance

R. V. Roy
Department of Mechanical Engineering,
University of Delaware,
Newark, DE 19716
Assoc. Mem. ASME.

We investigate the noise-induced transitions between the oscillatory steady states of a class of weakly nonlinear oscillators excited by resonant harmonic forcing. We begin by deriving a set of averaged equations governing slow variables of the system when the latter is perturbed by both additive white Gaussian noise and by random phase fluctuations of the resonant excitation. We then examine in detail the behavior of the reduced system in the case of cubic stiffness and viscous damping forces. Three regimes are examined: the case of weak damping, the case of near-bifurcation and the more general case when neither of the first two situations apply. In each case we predict the quasi-stationary probability density of the response and the mean time taken by the trajectories to pass from one basin of attraction to the other. These theoretical predictions are based on averaging of a near-Hamiltonian system in the weak damping limit, on center-manifold theory in the near-bifurcation case, or on Wentzell-Kramers-Brillouin (WKB) singular perturbation expansions in the more general case. These predictions are compared with digital simulations which show excellent agreement. We can then determine the probability of a transition for each state and for all parameter values. For this, we compute contour curves of the activation energy of each attractor in the parameter plane to yield a complete picture of the survivability of the system subject to random perturbations.

1 Introduction

The study of the stability of randomly perturbed dynamical systems is of great importance and interest in many fields of engineering and sciences. It has attracted the attention of a great many mathematicians, scientists and engineers: see, e.g., Pontryagin, Andronov, and Witt (1933); Stratonovich (1967); Kozin (1969); Khas'minskii (1980); Freidlin and Wentzell (1984); Horsthemke and Lefever (1984); Roberts (1986). In reliability theory, one is concerned with predicting the probability that the system's response will remain within a safe prescribed region during some given time interval. The problem is commonly referred to as first-passage reliability. When the random perturbations can be modeled as white Gaussian noise processes, reliability analyses can be based on the strong mathematical foundation given by the theory of Markov processes. Probability distribution, and statistics such as mean first-passage time can then be determined as the solution of diffusion-type equations. Unfortunately, these equations are amenable to closed form solutions only in a few cases of limited interest. Most of the exact results known today pertain to linear or one-dimensional nonlinear systems. Far less is available for higher-dimensional nonlinear systems for which approximate analyses must inevitably be developed.

In this paper, we examine the stochastic stability of a class of weakly nonlinear, harmonically forced oscillators, with specific developments and numerical results in the case of linear viscous damping and cubic stiffness. Near resonance, the system may admit more than one possible stable steady-state in the absence of extraneous perturbations. The presence of random disturbances, however small their intensity, may create large, albeit rare excursions of the system, and may cause its response to cross the basin boundary of a given attractor into the basin of another attractor. The problem is to predict the probability of such transitions, or equivalently the mean time taken by the trajectories to reach the basin boundary of the attractor. In Section 2, we first show that near resonance, the analysis can be simplified by an averaging method which reduces the original nonautonomous system to an autonomous one governing slowly varying variables. In Section 3, we apply this technique to a specific nonlinear system (Duffing-type) and first show the possible existence in parameter space of two point attractors of the averaged system. The probabilistic analysis of the system is then performed by weak-noise asymptotics in three different regimes. In Section 3.1, the low-damping regime is first

Contributed by the Applied Mechanics Division of THE AMERICAN SOCIETY OF MECHANICAL ENGINEERS for presentation at the Joint Applied Mechanics and Materials Summer Meeting of the ASME, Los Angeles, CA, June 28–30, 1995.

Discussion on this paper should be addressed to the Technical Editor, Professor Lewis T. Wheeler, Department of Mechanical Engineering, University of Houston, Houston, TX 77204-4792, and will be accepted until four months after final publication of the paper itself in the ASME JOURNAL OF APPLIED MECHANICS.

Manuscript received and accepted by the ASME Applied Mechanics Division, May 18, 1994. Associate Technical Editor: P. D. Spanos.

Paper No. 95-APM-5.

Copyright © 1995 by ASME

Downloaded 04 May 2010 to 171.66.16.28. Redistribution subject to ASME license or copyright; see http://www.asme.org/terms/Terms_Use.cfm

examined; we show that the problem can be further reduced to one variable, namely the Hamiltonian of the undamped system. The details of this approximation can be found in Roy (1994). In Section 3.2, the case of near-bifurcation of the system is treated by the theory of center manifold which again reduces the problem to a single relevant slowly varying variable. Finally, in Section 3.3, the more general case is treated when the dimensionality of the problem cannot be reduced. The resulting probability density function (p.d.f.) and the mean first-passage time must be solved as functions of two independent variables. The corresponding Fokker-Planck-Kolmogorov (FPK) equation and Pontryagin equation are solved asymptotically in the limit of weak disturbances by resorting to a singular perturbative scheme known as the WKB (Wentzell-Kramers-Brillouin) approximation. In Section 3.4, the validity of these results is confirmed by digital simulations.

2 Preliminary: Averaging of Harmonically Forced Oscillators

We first consider the general class of weakly nonlinear oscillators excited by resonant harmonic forces and by random perturbations. Both purely additive random fluctuations and phase fluctuations of the resonant forcing are considered. More specifically, the equation of motion is taken as

$$\ddot{x} + \epsilon f(x, \dot{x}) + \omega^2 x = \epsilon\Gamma\cos(\Omega t + \phi(t)) + \epsilon^{1/2}\xi_1(t) \tag{1}$$

where $\dot{x} = dx/dt$ and $\ddot{x} = d^2x/dt^2$. The parameter $\epsilon \ll 1$ is introduced to characterize the smallness of the nonlinearity f and that of the periodic and random perturbations. The random phase $\phi(t)$ is such that $\dot{\phi} = \epsilon^{1/2}\xi_2(t)$, where $\xi_2(t)$ is a white Gaussian noise considered to be uncorrelated with the random process $\xi_1(t)$ also modeled as a white Gaussian noise. The autocorrelation functions $\langle \xi_1(t)\xi_1(t+\tau)\rangle$ and $\langle \xi_2(t)\xi_2(t+\tau)\rangle$ of the processes ξ_1 and ξ_2 are $D_1\delta(\tau)$ and $D_2\delta(\tau)$, respectively, where δ is the Dirac delta function. From a practical point of view, the feature of primary importance and interest in excited systems is the regime of resonant vibration. Hence, the forcing frequency Ω is assumed to be close to the natural frequency ω of the oscillator; we define $\Omega^2 - \omega^2 = \epsilon\sigma\Omega$, σ being referred to as the detuning frequency. In such a situation, we expect to find in certain ranges of the system's parameters, a nearly harmonic response of frequency Ω, and hence we transform the original system governing $(x, y = \dot{x})$ into a new one governing the van der Pol variables (a, b) according to the relationship

$$\begin{pmatrix} x \\ y/\Omega \end{pmatrix} = \begin{bmatrix} \cos\theta & \sin\theta \\ -\sin\theta & \cos\theta \end{bmatrix}\begin{pmatrix} a \\ b \end{pmatrix}, \tag{2}$$

where $\theta \equiv \theta(t) = \Omega t + \phi(t)$. Differentiation yields the following system of equations:

$$\dot{a} = -\frac{1}{\Omega}(\Omega^2 x + \dot{y})\sin\theta - \epsilon^{1/2} b\xi_2(t), \tag{3}$$

$$\dot{b} = \frac{1}{\Omega}(\Omega^2 x + \dot{y})\cos\theta + \epsilon^{1/2} a\xi_2(t). \tag{4}$$

Then, after substituting $\dot{y} = -\omega^2 x - \epsilon\{f(x, y) - \Gamma\cos\theta\} + \epsilon^{1/2}\xi_1(t)$ and upon using $\Omega^2 - \omega^2 = \epsilon\sigma\Omega$, we find the following system of equations:

$$\dot{a} = -\epsilon\tilde{f}(a, b, \theta)\sin\theta - \frac{\epsilon^{1/2}}{\Omega}\xi_1(t)\sin\theta - \epsilon^{1/2} b\xi_2(t) \tag{5}$$

$$\dot{b} = \epsilon\tilde{f}(a, b, \theta)\cos\theta + \frac{\epsilon^{1/2}}{\Omega}\xi_1(t)\cos\theta + \epsilon^{1/2} a\xi_2(t) \tag{6}$$

$$\dot{\theta} = \Omega + \epsilon^{1/2}\xi_2(t), \tag{7}$$

with $\tilde{f}(a, b, \theta) = \sigma(a\cos\theta + b\sin\theta) - f(x, y)/\Omega + (F/\Omega)\cos\theta$. It becomes apparent that the variables a and b are slowly varying in time and that the fast variations of the angle θ can be averaged out during the time evolution of (a, b) on a time scale of order $1/\epsilon$, as $\epsilon \to 0$. We show in Appendix A that a perturbation analysis of the FPK equation governing the state p.d.f. leads to the following averaged equations:

$$\dot{a} = -\epsilon F(a, b) + \epsilon^{1/2}\xi_1'(t) - \epsilon^{1/2} b\xi_2(t) \tag{8}$$

$$\dot{b} = \epsilon G(a, b) + \epsilon^{1/2}\xi_1''(t) + \epsilon^{1/2} a\xi_2(t), \tag{9}$$

where the functions F and G are given by

$$F(a, b) = \frac{1}{2\pi}\int_0^{2\pi}\tilde{f}(a, b, \theta)\sin\theta d\theta,$$

$$G(a, b) = \frac{1}{2\pi}\int_0^{2\pi}\tilde{f}(a, b, \theta)\cos\theta d\theta, \tag{10}$$

and where the random processes $\xi_1'(t)$, $\xi_1''(t)$, $\xi_2(t)$ are mutually independent with autocorrelations $\langle \xi_1'(t)\xi_1'(t+\tau)\rangle = (D_1/2\Omega^2)\delta(\tau)$, $\langle \xi_1''(t)\xi_1''(t+\tau)\rangle = (D_1/2\Omega^2)\delta(\tau)$, and $\langle \xi_2(t)\xi_2(t+\tau)\rangle = D_2\delta(\tau)$, respectively. Hence, the original three-dimensional system governing (x, y, θ) has been reduced to a two-dimensional one governing the van der Pol variables (a, b). Note that the stochastic differential Eqs. (8) and (9) must be interpreted in the sense of Stratonovich.

In the absence of noise, the fixed points (a_e, b_e) of the averaged Eqs. (8) and (9) can readily be determined. A resonant curve of the system can then be obtained by plotting the variation of the response amplitude $r_e = (a_e^2 + b_e^2)^{1/2}$ versus the excitation frequency Ω. As is well known (Hayashi, 1964; Schmidt and Tondl, 1986), for some values of the system and excitation parameters, the resonant curve of periodically excited nonlinear systems may be characterized by more than one solution. For oscillators governed by Eq. (1), the existence of more than one stable oscillatory state, each with differing frequency, amplitude, and phase characteristics has been widely documented. To each stable solution corresponds a basin of attraction. In the absence of perturbations, once initialized in a given basin, the system will reach the corresponding attractor and will remain there indefinitely: the lifetime of the attractor is infinite. The presence of random perturbations will cause the trajectories of the system to diffuse away from the attractor and will create rare fluctuations, yet sufficiently large for the response to reach the basin boundary of the attractor. Hence, addition of random fluctuations in the system will cause transitions between its stable states, and the lifetime of each state becomes finite. In the next section, we analyze these noise-induced transitions in a Duffing oscillator whose averaged equations admit two point attractors for certain parameter values.

3 Transitions in a Harmonically forced Duffing Oscillator

We examine in this section the effects of purely additive random perturbations in a Duffing oscillator, that is, we let $f(x, y) = 2\eta\omega y + \gamma\omega^2 x^3$, where the parameters η and γ are assumed to be positive, real numbers. We also let $D_2 = 0$, that is, we do not consider the effects of random phase fluctuations of the resonant excitation. Transforming the original variables (x, y) into (a, b), we find from the analysis of the previous section

$$F(a, b) = \eta\omega a + \frac{\sigma}{2}b - \frac{3\gamma\omega^2}{8\Omega}b(a^2 + b^2) \tag{11}$$

Downloaded 04 May 2010 to 171.66.16.28. Redistribution subject to ASME license or copyright; see http://www.asme.org/terms/Terms_Use.cfm

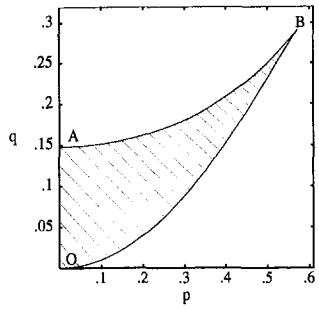

Fig. 1 Domain of bistability (hatched region) in the parameter space, with $p = 2\eta\omega/\sigma$, and $q = (3/4)\gamma\Gamma^2\omega^2/(\sigma\Omega)^3$. For parameters outside this region, the system has a unique stable state. The line *OB* corresponds to the saddle-node bifurcations of S^+. Line *AB* corresponds to the saddle-node bifurcations of S^-.

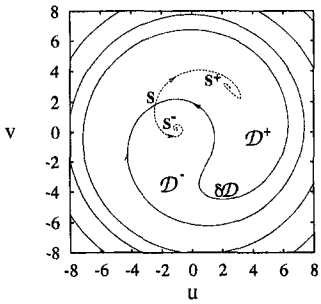

Fig. 2 Phase portrait of (13)–(14) for $p = 0.20$ and $q = 0.08$ showing the four trajectories (stable and unstable manifolds) asymptotic to the saddle point *S*

$$G(a,b) = \frac{\sigma}{2}a - \eta\omega b - \frac{3\gamma\omega^2}{8\Omega}a(a^2+b^2) + \frac{\Gamma}{2\Omega}. \quad (12)$$

The equations governing (a, b) can be nondimensionalized by defining the new variables $u = (\sigma\Omega/\Gamma)a$, and $v = (\sigma\Omega/\Gamma)b$, and after changing t to $2t/(\epsilon\sigma)$:

$$\dot{u} = -pu - v + qv(u^2+v^2) + D^{1/2}\xi_1'(t) \quad (13)$$

$$\dot{v} = u - pv - qu(u^2+v^2) + 1 + D^{1/2}\xi_1''(t) \quad (14)$$

with $p = 2\eta\omega/\sigma$, $q = (3/4)\gamma\Gamma^2\omega^2/(\sigma\Omega)^3$ and $D = D_1\sigma/\Gamma^2$. Note here that the two independent white Gaussian processes ξ_1' and ξ_1'' are of unit intensity. It can readily be shown that the unperturbed ($D = 0$) system admits three fixed points if the parameters (p, q) satisfy the condition

$$\left(\frac{27}{2}q - 1 - 9p^2\right)^2 < (1-3p^2)^3 \quad (15)$$

which corresponds to the hatched region of Fig. 1 in the (p, q)-plane. Two of these fixed points (corresponding to the smallest and largest amplitudes in the van der Pol plane) can be shown to be stable, and they correspond to the two stable coexisting periodic solutions of the original system. The third solution is unstable, and corresponds to a saddle point of the trajectories in the (u, v)-plane. An example of a (u, v)-phase portrait is shown in Fig. 2: S^+ and S^- denote, respectively, the largest amplitude (resonant) and smallest amplitude (nonresonant) point attractors, and S denotes the saddle point. Also shown are the stable and unstable invariant manifolds, that is, the four trajectories asymptotic to the saddle point. Critical to our analysis of noise-induced transitions are the stable invariant manifolds $\partial\mathfrak{D}$ (insets, asymptotic to S as $t \to +\infty$) which separates the two basins of attraction $\mathfrak{D}^+$ and $\mathfrak{D}^-$. $\partial\mathfrak{D}$ is found numerically by integration of the system backwards in time along the direction of the eigenvector associated with the negative eigenvalue of the linearized field at S.

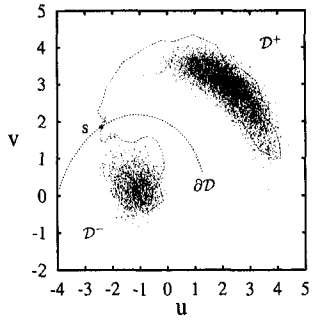

Fig. 3 Scatterplot of trajectories of the Duffing oscillator obtained by Monte Carlo simulation, for the parameters $\epsilon\eta = 0.01$, $\epsilon\gamma = 0.1$, $\omega = 1$, $\Omega = 1.051$, $\epsilon\Gamma = 0.035$, and $D_1 = 0.01$ corresponding to $p = 0.20$, $q = 0.08$, and $D = 0.08$ for the averaged equations. Points (x, y) are sampled every $T = 2\pi/\Omega$ and are mapped into the (u, v)-plane by the van der Pol transformation. The position of S on $\partial\mathfrak{D}$ is shown as well as an escape trajectory from S^- to S^+. Compare with Fig. 2.

We are interested in the analysis of the noise-induced transitions between S^+ and S^- in the limit $D \to 0$ for all values of (p, q) in the domain of bistability of Fig. 1. Three possible regimes need to be distinguished in this analysis, depending on whether the parameters are close to the boundary of this domain or not. For values of (p, q) near the line OA, the damping forces are weak, and an asymptotic analysis may be conducted by considering both p and D as small parameters: the analysis amounts to a stochastic averaging procedure of a near-Hamiltonian system. For values of (p, q) near the line AB, the resonant solution S^+ is in a marginal state of stability, since points on AB correspond to the saddle-node bifurcations of S^+: on AB, the two equilibrium points S^+ and S coalesce and subsequently disappear as one crosses the domain of bistability. Similarly, line OB corresponds to the saddle-node bifurcations of the nonresonant solution S^-. For parameters (p, q) in the vicinity of the bifurcation lines AB and OB it is possible to study the noise-induced transitions of the corresponding states by using the theory of center manifold. The third possible and more general case corresponds to parameter values (p, q) sufficiently far from the boundaries OA, AB, and OB and is dealt with by using a singular perturbative approach in the limit $D \to 0$, treating both p and q as $\mathcal{O}(1)$. In order to study the transitions out of each basin of attraction, we restrict our attention to the prediction of two probabilistic quantities: the response stationary p.d.f. and the mean time taken by the trajectories to reach the boundary $\partial\mathfrak{D}$, starting either in $\mathfrak{D}^+$ or $\mathfrak{D}^-$. Before starting these theoretical developments, we illustrate in Fig. 3 such transitions by numerical simulations of the original (nonaveraged) system (1) whose parameters lead to the values $(p, q) = (0.2, 0.08)$ of the averaged system: the response observed in the van der Pol plane clearly exhibits jumps from one domain to the other, the crossings of the boundary being confined to a small neighborhood of the saddle point.

3.1 Case 1: (p, q) Near Line OA. This case corresponds to weak damping forces, that is $p \to 0$. First note that when p and D vanish, the original and averaged systems are Hamiltonian, the averaged Hamiltonian being

$$H(u,v) = -\frac{1}{2}(u^2+v^2) + \frac{q}{4}(u^2+v^2)^2 - u. \quad (16)$$

The corresponding phase portrait is obtained by plotting H-contours in the (u, v)-plane and is shown in Fig. 4 for $q = 0.015$. It consists of three families of orbits separated by a double homoclinic loop asymptotic to the saddle point S as $t \to \pm\infty$. It is possible to show by a perturbation method that the stationary response p.d.f. $p(u, v)$ of the system is given to leading order by the following expression:

Downloaded 04 May 2010 to 171.66.16.28. Redistribution subject to ASME license or copyright; see http://www.asme.org/terms/Terms_Use.cfm

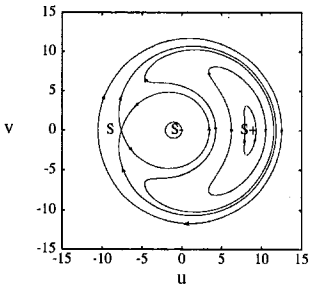

Fig. 4 Phase portrait for $p = 0$ and $q = 0.015$ obtained by plotting the H-contours with $H^+ = -25.07$, $H^- = 0.504$, $H_S = -8.77$. These contours also give the contours of probability density in the low-damping approximation (17).

$$p(u,v) \equiv p(H(u,v)) = \mathfrak{N}\exp\left\{-\frac{1}{D}\Psi(H(u,v))\right\},$$

$$\Psi(H) = 2p\int_{H_S}^{H}\frac{f(h)}{g(h)}dh, \tag{17}$$

where $\mathfrak{N}$ is a constant of normalization, H_S is the value of H corresponding to the double homoclinic loop, and where the functions f and g are given by

$$f(H) = \oint_H \{u\partial_u H + v\partial_v H\}dt,$$

$$g(H) = \oint_H \{(\partial_u H)^2 + (\partial_v H)^2\}dt, \tag{18}$$

the time integration being performed on the H-contours of the unperturbed system ($p = 0$, $D = 0$). For more details on the derivation of these results, see Roy (1994). The mean first-passage times $T^+(u,v)$ and $T^-(u,v)$ to the boundary $\partial\mathfrak{D}$ starting at a point (u,v) of $\mathfrak{D}^+$ and $\mathfrak{D}^-$ respectively can be found in an analogous way. For sufficiently small noise intensity D and for points (u,v) sufficiently far from the boundary, we find that these first-passage times take uniform (i.e., independent of the starting point) expressions given by

$$T(S^+ \to S) = \tau^+\exp\left\{\frac{1}{D}(\Psi(H_S) - \Psi(H^+))\right\}, \tag{19}$$

$$T(S^- \to S) = \tau^-\exp\left\{\frac{1}{D}(\Psi(H_S) - \Psi(H^-))\right\} \tag{20}$$

where H_S, H^+, and H^- are the values taken by H at the points S, S^+, and S^- respectively. For more details on the expressions of the pre-exponential factors τ^+ and τ^-, see Roy (1994).

3.2 Case 2: (p,q) Near Line *AB* or *OB*. For a given value of the parameter p in the interval $[0, 1/\sqrt{3}]$, saddle-node bifurcations occur when the parameter q reaches either of the two critical values q_c given by

$$q_c^+(p) = \frac{2}{27}\left\{1 + 9p^2 - (1 - 3p^2)^{3/2}\right\},$$

$$q_c^-(p) = \frac{2}{27}\left\{1 + 9p^2 + (1 - 3p^2)^{3/2}\right\}. \tag{21}$$

As $q(p) \to q_c^+$ from above, the resonant solution S^+ coalesces with the saddle point S. Similarly, as $q(p) \to q_c^-$ from below, S^- coalesces with S. We let $q = q_c + \epsilon$, where the small parameter ϵ is positive for $q_c = q_c^+$ and negative for $q_c = q_c^-$. The coordinates of the coalescing fixed point are denoted as (u_c, v_c). When the system is near bifurcation, its local behavior can be studied by the center manifold approach. More specifically, the center manifold theorem (Guckenheimer and Holmes, 1983) allows one to systematically eliminate the fast-relaxing variables in terms of the slowly varying ones which define the center manifold of the corresponding fixed point (u_c, v_c). To find the center manifold, we first rotate the coordinate system in the direction of the center and stable spaces by determining the eigenvalues and eigenvectors of the system linearized about (u_c, v_c). We find the eigenvalues $\lambda = 0$ and $\lambda = \lambda_c = -p + 2q_c u_c v_c$ which lead to the transformation

$$\begin{pmatrix} u - u_c \\ v - v_c \end{pmatrix} = \begin{bmatrix} 1 & -\mu_c/\lambda_c \\ 0 & 1 \end{bmatrix}\begin{pmatrix} u_1 \\ v_1 \end{pmatrix} \tag{22}$$

with $\mu_c = -1 + q_c(u_c^2 + 3v_c^2)$. Discarding nonlinear terms of degree higher than two and the noise perturbations, we find the following system of equations:

$$\dot{u}_1 = \epsilon\alpha_{10} + \lambda_c u_1 + \epsilon\alpha_{11}u_1 + \epsilon\alpha_{12}v_1 + au_1^2 + bu_1v_1 + cv_1^2 \tag{23}$$

$$\dot{v}_1 = \epsilon\alpha_{21} + \epsilon\alpha_{12}u_1 + \epsilon\alpha_{22}v_1 + du_1^2 + eu_1v_1 + fv_1^2 \tag{24}$$

where the constants α_{ij}, a, b, c, d, e, and f are functions only of the critical values q_c, u_c, and v_c. As $\epsilon \to 0$ and $(u_1, v_1) \to (0,0)$ we seek an equation of the center manifold in the form

$$u_1 + \epsilon\alpha_{10}/\lambda_c = Av_1^2 + B\epsilon v_1 + C\epsilon^2 \tag{25}$$

where the constants A, B, and C can be determined from Eqs. (23) and (24) by identifying terms of order v_1^2, ϵv_1, and ϵ^2. After a short negligible transient, the dynamics on the center manifold can be approximated to leading order of ϵ and v_1 by

$$\dot{v}_1 = \epsilon\sigma_{20} + \epsilon(\alpha_{22} - e\alpha_{10}/\lambda_c)v_1 + fv_1^2 \tag{26}$$

which is equivalent to, after changing v_1 into $v_1 - \epsilon(\alpha_{22} - e\alpha_{10}/\lambda_c)/2f$

$$\dot{v}_1 = \epsilon\alpha_{20} + fv_1^2. \tag{27}$$

This is the generic form of a saddle-node bifurcation. It is possible to show, following the approach of Knobloch and Wiesenfeld (1983), that the noise perturbations entering into the equation governing u_1 do not affect the equation governing v_1, and hence the stochastic form of the reduced Eq. (27) is given by

$$\dot{v}_1 = (q - q_c)\alpha_{20} + fv_1^2 + D^{1/2}\xi_1''(t) \tag{28}$$

where ϵ has been replaced by $(q - q_c)$. The expressions of α_{20} and f are readily found to be

$$\alpha_{20} = -u_c(u_c^2 + v_c^2),$$

$$f = -\frac{q_c}{\lambda_c^2}(3u_c\mu_c^2 - 2v_c\lambda_c\mu_c + u_c\lambda_c^2). \tag{29}$$

Hence, the dynamical behavior near the saddle-node bifurcation is characterized by the one-dimensional potential $\Psi(v_1) = (q - q_c)\alpha_{20}v_1 + fv_1^3/3$ which possesses a minimum and a maximum corresponding to node N (S^+ or S^-) and to saddle point S, respectively. The quasi-stationary p.d.f. of the response fluctuations within the potential well can readily be found to be

$$p(v_1) = \mathfrak{N}\exp\left\{-\frac{2}{D}\Psi(v_1)\right\} \tag{30}$$

and the mean time taken by the trajectories initially near N to reach the saddle point S is given by the asymptotic exponential law as $D \to 0$:

$$T(N \to S) = 2\pi(\Psi_N''|\Psi_S''|)^{-1/2}\exp\left\{\frac{2}{D}(\Psi_S - \Psi_N)\right\} \tag{31}$$

Downloaded 04 May 2010 to 171.66.16.28. Redistribution subject to ASME license or copyright; see http://www.asme.org/terms/Terms_Use.cfm

where Ψ_S, Ψ_N, Ψ''_S, and Ψ''_N are the values of Ψ and $\Psi'' = d^2\Psi/dv_1^2$ taken at S and N. We find the difference $\Delta\Psi = (\Psi_S - \Psi_N) = (4/3)|(q - q_c)\alpha_{20}|^{3/2}|f|^{-1/2}$. See Gardiner (1983) for details on the solution of one-dimensional FPK and Pontryagin equations. Note that this law is identical in form to the one found in the low-damping regime.

3.3 Case 3: (p, q) Sufficiently Far From Lines *OA*, *AB*, and *OB*. When the parameters (p, q) are sufficiently far from the boundaries of the domain of bistability, the expressions derived for the response p.d.f. and mean first-passage times will not be accurate. The reduction of the system to a lower dimensional one is not possible, and hence, we must attempt to find these quantities as a function of the two independent variables u and v. The approach taken here is based on a singular perturbation scheme known as WKB approximation. This technique is well known in applied mathematics and physics to solve singularly perturbed linear initial value and boundary value problems (see Bender and Orszag, 1978). We are seeking to solve the diffusion (FPK) equation governing the stationary p.d.f. $p(u, v)$ in the limit of $D \to 0$ by assuming the following asymptotic expression:

$$p(u,v) = w(u,v)\exp\left\{-\frac{1}{D}\Psi(u,v) + \mathcal{O}(D)\right\} \quad (32)$$

where both Ψ and w are independent of D, and uniformly valid in the (u, v)-plane. This global approximation is in agreement with the expressions found in the special cases of Sections 3.1 and 3.2. It must be noted that most known closed-form stationary solutions of FPK equations follow this functional form exactly for arbitrary (i.e., not necessarily small) D. The function Ψ is appropriately referred to as the *quasi-potential.* By substituting Eq. (32) into the stationary FPK equation governing p and keeping terms of order D^{-1}, a time-independent Hamilton-Jacobi equation governing Ψ only is obtained:

$$\left[-pu - v + qv(u^2 + v^2)\right]\partial_u\Psi + \left[u - pv - qu(u^2 + v^2) + 1\right]\partial_v\Psi + \frac{1}{2}(\partial_u\psi)^2 + \frac{1}{2}(\partial_v\Psi)^2 = 0. \quad (33)$$

This equation can be interpreted as the Hamilton-Jacobi equation governing the generating function (action) at zero-energy of the two-degree-of-freedom Hamiltonian $\mathcal{H}$ given by

$$\mathcal{H}(u, v, p_u, p_v) = \left(-pu - v + qv(u^2 + v^2)\right)p_u + \left(u - pv - qu(u^2 + v^2) + 1\right)p_v + \frac{1}{2}\left(p_u^2 + p_v^2\right) \quad (34)$$

whose corresponding canonical equations of motion are

$$\dot{u} = \partial_{p_u}\mathcal{H} = \left\{-pu - v + qv(u^2 + v^2)\right\} + p_u \quad (35)$$

$$\dot{v} = \partial_{p_v}\mathcal{H} = \left\{u - pv - qu(u^2 + v^2) + 1\right\} + p_v \quad (36)$$

$$\dot{p}_u = -\partial_u\mathcal{H} = -(-p + 2quv)p_u - \left\{1 - q(3u^2 + v^2)\right\}p_v \quad (37)$$

$$\dot{p}_v = -\partial_v\mathcal{H} = -\left\{-1 + q(u^2 + 3v^2)\right\}p_u - (-p - 2quv)p_v. \quad (38)$$

These equations govern the characteristics of the Hamilton-Jacobi equation and they form the basis of the method of rays (Cohen, 1969; Ludwig, 1975; Graham and Tél, 1984) used to solve diffusion equations. By appropriately choosing initial conditions, a family of rays governed by Eqs. (35)–(38) can be found to cover the (u, v)-plane. Along each ray, the function Ψ is governed by

$$\dot{\Psi} = \frac{1}{2}\left(p_u^2 + p_v^2\right) \quad (39)$$

which shows that Ψ is always monotonically increasing on each ray. The governing equation of the pre-exponential factor w is found by identifying terms of next order D^0 in the FPK equation

$$\left[-pu - v + qv(u^2 + v^2) + \partial_u\Psi\right]\partial_u w + \left[u - pv - qu(u^2 + v^2) + 1 + \partial_v\Psi\right]\partial_v w + \left(-2p + \frac{1}{2}\partial_{uu}\Psi + \frac{1}{2}\partial_{vv}\Psi\right)w = 0 \quad (40)$$

which can be recast along each ray into the equation

$$\dot{w} = -\left(-2p + \frac{1}{2}\partial_{uu}\Psi + \frac{1}{2}\partial_{vv}\Psi\right)w \quad (41)$$

where the second partial derivatives $\partial_{uu}\Psi$ and $\partial_{vv}\Psi$ remain to be found.

Each ray can be initialized by determining the asymptotic form of $p(u, v)$ in a neighborhood of each stable fixed point (u_e, v_e) (S^+ or S^-). The equations of motion (13)–(14) can be linearized about (u_e, v_e) to yield

$$\begin{pmatrix}\dot{u}_1\\ \dot{v}_1\end{pmatrix} = \begin{bmatrix}-p + 2qu_ev_e & -1 + q\left(u_e^2 + 3v_e^2\right)\\ 1 - q\left(3u_e^2 + v_e^2\right) & -p - 2qu_ev_e\end{bmatrix} \times \begin{pmatrix}u_1\\ v_1\end{pmatrix} + \begin{pmatrix}\xi_1'(t)\\ \xi_1''(t)\end{pmatrix} \quad (42)$$

where $u_1 = (u - u_e)$ and $v_1 = (v - v_e)$. It is well known that the response of this system is Gaussian, and hence Ψ and w must be of the form, as $(u, v) \to (u_e, v_e)$

$$\Psi(u,v) = \frac{1}{2}k_{11}(u - u_e)^2 + k_{12}(u - u_e)(v - v_e) + \frac{1}{2}k_{22}(v - v_e)^2 \quad (43)$$

$$w(u, v) = 1. \quad (44)$$

The k_{ij}'s are the elements of a symmetric matrix $\mathbf{K} = \mathbf{S}^{-1}$, $\mathbf{S}$ being the response covariance matrix, solution of the equation

$$\mathbf{BS} + \mathbf{SB}^T = -\mathbf{I}. \quad (45)$$

Here $\mathbf{B}$ is the 2×2 matrix defining the linear system (42) and $\mathbf{I}$ is the identity matrix. Initial conditions for (u, v, p_u, p_v) and (Ψ, w) can then be set according to the Gaussian approximation (43) on a small circle centered at (u_e, v_e) and of radius $\rho \ll 1$:

$$u(0) = u_e + \rho\cos\theta,\ v(0) = v_e + \rho\sin\theta \quad (46)$$

$$p_u(0) = \rho(k_{11}\cos\theta + k_{12}\sin\theta),$$
$$p_v(0) = \rho(k_{12}\cos\theta + k_{22}\sin\theta), \quad (47)$$

$$\Psi(0) = \frac{1}{2}\rho^2\left(k_{11}\cos^2\theta + 2k_{12}\cos\theta\sin\theta + k_{22}\sin^2\theta\right) \quad (48)$$

$$w(0) = 1. \quad (49)$$

Each value of the angle θ specifies a ray $(u(t, \theta), v(t, \theta))$ in the (u, v)-plane obtained by integration of Eqs. (35)–(38) with initial conditions (46)–(49).

To obtain the second partial derivatives of Ψ needed in Eq. (41), the ray equations (35)–(38) must be differentiated

Downloaded 04 May 2010 to 171.66.16.28. Redistribution subject to ASME license or copyright; see http://www.asme.org/terms/Terms_Use.cfm

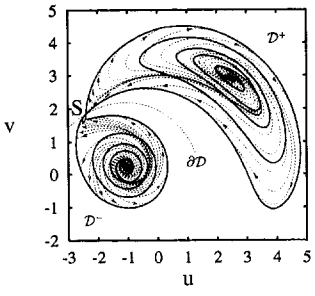

Fig. 5 Contours of quasi-potential Ψ and rays (dashed lines) emanating from S^- and S^+ for $p = 0.20$ and $q = 0.08$. With $\Psi = 0$ at S^-, the five contour levels shown are 0.01, 0.05, 0.1, 0.25, 0.4136 leading to $\mathcal{E}^- = \Psi(S) - \Psi(S^-) = 0.4136$. Similarly, with $\Psi = 0$ at S^+, the five contour levels are 0.01, 0.05, 0.1, 0.2, and 0.5137 leading to $\mathcal{E}^+ = \Psi(S) - \Psi(S^+) = 0.5137$. The rays are initialized on a circle of radius $\rho = 0.01$ centered either at S^- or at S^+. We also find $w_S = 2.42$, $\partial_{ss}\Psi_S = 0.228$, $\lambda_{pS} = 0.364$, $J^+ = 0.04$, and $J^- = 0.158$.

with respect to parameter θ: setting $u_\theta = \partial_\theta u$, $v_\theta = \partial_\theta v$, $q_u = \partial_\theta p_u$, and $q_v = \partial_v p_v$, four additional equations are obtained:

$$\dot{u}_\theta = (-p + 2quv)u_\theta + \{-1 + q(u^2 + 3v^2)\}v_\theta + q_u \quad (50)$$

$$\dot{v}_\theta = \{1 - q(3u^2 + v^2)\}u_\theta + (-p - 2quv)v_\theta + q_v \quad (51)$$

$$\dot{q}_u = -2q(vu_\theta + uv_\theta)p_u - (-p + 2quv)q_u + q(6uu_\theta + 2vv_\theta)p_v - \{1 - q(3u^2 + v^2)\}q_v \quad (52)$$

$$\dot{q}_v = -q(2uu_\theta + 6vv_\theta)p_u - \{-1 + q(u^2 + 3v^2)\}q_u + 2q(vu_\theta + uv_\theta)p_v - (-p - 2quv)q_v \quad (53)$$

with the corresponding initial conditions

$$u_\theta = -\rho \sin\theta, \quad (54)$$

$$v_\theta = \rho \cos\theta, \quad (55)$$

$$q_u = \rho(-k_{11}\sin\theta + k_{12}\cos\theta), \quad (56)$$

$$q_v = \rho(-k_{12}\sin\theta + k_{22}\cos\theta). \quad (57)$$

Then, the functions $\partial_{uu}\Psi$, $\partial_{uv}\Psi$, and $\partial_{uu}\Psi$ are readily determined along each ray from the following relationships:

$$q_u = u_\theta \partial_{uu}\Psi + v_\theta \partial_{uv}\Psi \quad (58)$$

$$q_v = u_\theta \partial_{uv}\Psi + v_\theta \partial_{vv}\Psi \quad (59)$$

$$\dot{p}_u = \dot{u}\partial_{uu}\Psi + \dot{v}\partial_{uv}\Psi. \quad (60)$$

Therefore, the solution of the stationary FPK equation has been reduced to the solution of a system of ten ordinary differential equations yielding the values of $\Psi(u(t,\theta), v(t,\theta))$ and $w(u(t,\theta), v(t,\theta))$ along the rays $(u(t,\theta), v(t,\theta))$ which are specified by varying the parameter θ in the interval $0 \le \theta < 2\pi$. Several contours for the quasi-potential Ψ and a few ray trajectories are shown in Fig. 5 for rays initialized at fixed points S^- and S^+, respectively, for $(p, q) = (0.2, 0.08)$. Note the qualitative agreement with Fig. 3. The quasi-potential is initialized to zero at both S^- and S^+. The last contours shown are the ones which first reach the boundary $\partial\mathcal{D}$. It is seen that these two contours reach $\partial\mathcal{D}$ at the saddle point S which is not surprising since we expect the p.d.f. $p(u, v)$ to have a saddle at S. Hence, it is critical in this procedure to determine the value of θ whose corresponding ray connects the attracting fixed point (S^+ or S^-) to the saddle point S. The method used here is a straightforward shooting procedure. Since Ψ is defined within an additive constant and was arbitrarily set to zero at both S^+ and S^-, these two rays do not yield the same value of Ψ at S. Once these two values have been found, the relative value of Ψ between S^+ and S^- can be adjusted to yield an identical value at S. These rays can be shown to be the most probable paths taken by the system to leave the basin of attractions (Ludwig, 1975), and they yield the values of Ψ, w, $\partial_{uu}\Psi$, $\partial_{uv}\Psi$, and $\partial_{vv}\Psi$ reached at the saddle point.

These quantities play a fundamental role in the determination of the mean first-passage time $T^+(u, v)$ taken by the trajectories to reach the boundary $\partial\mathcal{D}$ for the first time, starting at a point $(u, v) \in \mathcal{D}^+$ (the same analysis holds for $T^-(u, v)$). It is well known that $T^+(u, v)$ satisfies the so-called Pontryagin equation. This equation can be solved asymptotically in the limit $D \to 0$. See Appendix B. Note first that for $D = 0$, $T^+(u, v)$ is infinite since all trajectories starting in $\mathcal{D}^+$ cannot exit this domain. For nonzero but small D, we expect that $T^+(u, v)$ will reach a large constant value for all points (u, v) of $\mathcal{D}^+$, except for the points within a thin layer along the boundary $\partial\mathcal{D}$. Hence, this suggests a boundary layer approximation of the mean first-passage time, that is

$$T^+(u, v) = T(S^+ \to S)\tau^+(u, v) \quad (61)$$

where the boundary layer function τ^+ is assumed to take the value 1 in the inner part of $\mathcal{D}^+$ and the value 0 on $\partial\mathcal{D}$. Hence τ^+ must exhibit a sharp variation across a boundary layer of $\partial\mathcal{D}$ from the value 1 to the value 0. The constant $T(S^+ \to S)$ is assumed to be of order $e^{K/D}$ (K is a positive constant) and is interpreted as mean time taken to go from S^+ to S. This is the basis of the asymptotic analysis of escape rates devised by Matkowsky and Schuss (1977), and by Talkner and Hanggi (1984) (see also Gardiner, 1983). For completeness, we sketch the derivation of the expressions of $T(S^+ \to S)$ and $\tau^+(u, v)$ in Appendix B. We find that $T(S^+ \to S)$ is given in the limit $D \to 0$ by

$$T(S^+ \to S) = \pi\left[2|\partial_{ss}\Psi_S|/\lambda_{pS}J^+\right]^{1/2} w_S^{-1} \exp\{(\Psi_S - \Psi_{S^+})/D\} \quad (62)$$

where $\partial_{ss}\Psi$ is the second derivative of Ψ at S along the tangential direction of $\partial\mathcal{D}$, λ_{pS} is the positive eigenvalue of the linearized system about S, and $J^+ = \det\mathbf{K}^+$:

$$\partial_{ss}\Psi_S = v_u^2\partial_{uu}\Psi_S + 2v_u v_v \partial_{uv}\Psi_S + v_v^2\partial_{vv}\Psi_S \quad (63)$$

$$J^+ = k_{11}^+ k_{22}^+ - k_{12}^{+2} \quad (64)$$

((v_u, v_v) are the components of the unit normal $\boldsymbol{\nu}$ to $\partial\mathcal{D}$ at S). Critical in the derivation of this asymptotic law is the use of the WKB approximation of $p(u, v)$ and the assumption that the first-passages to $\partial\mathcal{D}$ occur in a small neighborhood of S. Again we obtain an Arrhenius-type law of the form $\exp(\mathcal{E}^+/D)$ as in Sections 3.1 and 3.2. This law is similar to the one derived by Kramers (1940) for potential systems. Here the activation energy $\mathcal{E}^+$ is the difference $(\Psi_S - \Psi_{S^+})$ in quasi-potential between S and S^+. It is the minimum difference in quasi-potential between the boundary $\partial\mathcal{D}$ and the attractor S^+. Clearly, it provides a measure of the survivability of the resonant attractor S^+ to white Gaussian noise perturbations. Note that the lifetime of each attractor (also called residence time, or exit-time) is twice the corresponding first-passage time since once on the boundary, trajectories can either return to the attractor or be attracted to the other fixed point with equal probability. We verify in the next section the validity of the results of Sections 3.1, 3.2, and 3.3.

3.4 Numerical Results and Comparison With Monte Carlo Simulation. We first assess the reliability of the asymptotic mean first-passage times $T(S^+ \to S)$ and $T(S^- \to S)$ obtained by the WKB approximation. We choose $p = 0.20$ and $q = 0.08$ for which the values of $\Delta\Psi$, w_S, $\partial_{ss}\Psi_S$, and J have been found in the previous section (see Fig. 5). Note that, for these values of the parameters, the low-damping or

Downloaded 04 May 2010 to 171.66.16.28. Redistribution subject to ASME license or copyright; see http://www.asme.org/terms/Terms_Use.cfm

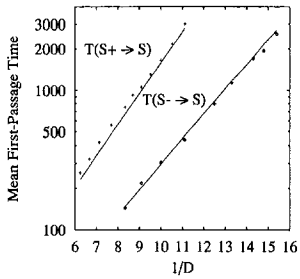

Fig. 6 Mean first-passage times $T(S^+ \rightarrow S)$ and $T(S^- \rightarrow S)$ evaluated by the WKB approximation (62) (continuous lines) for $(p, q) = (0.20, 0.08)$. The Monte Carlo simulation results shown by points represent the average of 1000 realizations.

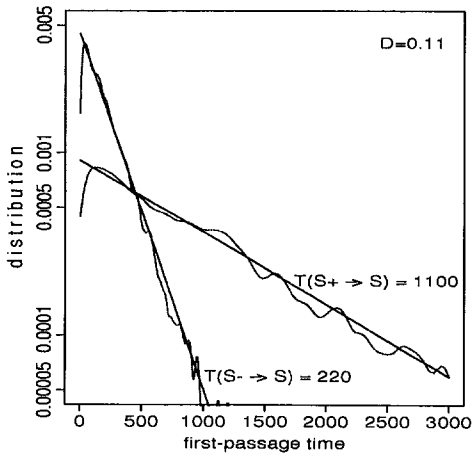

Fig. 7 First-passage time probability densities of the events $S^+ \rightarrow S$ and $S^- \rightarrow S$ for $p = 0.20$, $q = 0.08$, and $D = 0.11$. Comparison with the exponential approximation (straight line) and Monte Carlo simulations (dotted lines with 5000 realizations). Note that the exponential distribution is characterized by a standard deviation equal to the mean. This property was in fact verified in the Monte Carlo simulations.

near-bifurcation approximations of Sections 3.1 and 3.2 cannot be used. We compare these results with Monte Carlo simulation of the same quantities for various values of the noise intensity D. According to Eqs. (62), we expect a linear relationship between $\ln T$ and the inverse of the noise intensity. To measure the times of first passage to the boundary $\partial \mathcal{D}$ by Monte Carlo simulations, we note that this boundary is very well represented in the vicinity of S by the following linear approximation in polar coordinates (r, ϕ):

$$r = r_S + k_S(\phi - \phi_S), \quad k_S = r_S\sqrt{\frac{qr_S^2 - 1}{1 - 3qr_S^2}} \qquad (65)$$

where (r_S, ϕ_S) are the polar coordinates of S in the (u, v)-plane. Since the transitions from one domain to the next occur with overwhelming probability in a small neighborhood of S, we expect to obtain good estimates of the first-passage time by using Eq. (65). But these numerical simulations are very costly, especially for low values of the noise intensity as demonstrated by our exponential asymptotics. Note that the digital simulations are performed on the averaged Eqs. (13)–(14) and not on the original Duffing oscillator. Hence we do not account for the possible deviations of the first-passage times introduced by the averaging procedure of Section 1. We have used 1000 realizations of the first-passage events to compute $T(S^+ \rightarrow S)$ and $T(S^+ \rightarrow S)$. The results are displayed in Fig. 6. They show excellent agreement between the two methods even for relatively large values of the noise intensity D. These results show that we can safely rely on the WKB approximation of the response p.d.f. The practical

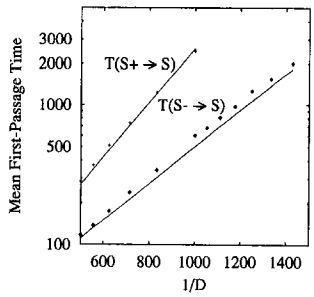

Fig. 8 Mean first-passage times by the near-bifurcation approximation (31) (continuous lines). $T(S^+ \rightarrow S)$ corresponds to $(p, q) = (0.40, 0.156)$ near line OB ($q_c^+ = 0.153$). $T(S^- \rightarrow S)$ corresponds to $(p, q) = (0.40, 0.205)$ near line AB ($q_c^- = 0.208$).

importance of mean first-passage times is demonstrated in Fig. 7 which shows the probability density of the first-passage time derived from Monte Carlo simulations and compared with the exponential distribution $\langle T \rangle^{-1} \exp(-T/\langle T \rangle)$ where the mean time $\langle T \rangle$ is taken to be either $T(S^+ \rightarrow S)$ or $T(S^- \rightarrow S)$. This distribution can be proven to hold under some mild restrictions (Roberts, 1986) and it shows that the statistic $\langle T \rangle$ alone may be used to predict transition probabilities.

When the parameters (p, q) are very close to the lines AB and OB, the determination of the most probable ray of the near-bifurcating state becomes difficult with our shooting method and one must rely on the results of Section 3.2. We consider two cases: $(p, q) = (0.40, 0.205)$ near line AB corresponding to the near-bifurcation of S^-, and $(p, q) = (0.4, 0.156)$ near line OB corresponding to the near-bifurcation of S^+. Again, the results shown in Fig. 8 show good qualitative agreement. Finally, we compare the WKB approximation with the low-damping approximations of Section 3.1 by choosing $(p, q) = (0.01, 0.105)$ near line OA: we find that the activation energies $\mathcal{E}^+$ and $\mathcal{E}^-$ determined by both approximations match very well, but the pre-exponential terms are in disagreement. In fact the WKB method does not give the proper asymptotic limit $T \rightarrow \infty$ as $D \rightarrow 0$ for a constant ratio p/D, correctly predicted by Eqs. (19)–(20) (see Roy, 1994). In the low-damping limit, the saddle point is not the only most probable point of exit across the boundary. The results of Section 3.1 show that all points of the homoclinic loop of the corresponding Hamiltonian system (i.e., $p = 0$) have equal probability density. This explains why the WKB method does not predict proper first-passage times in the limit $p \rightarrow 0$ since assumption was made that the passage of the trajectories to the boundary occur in a small neighborhood of the saddle point. The results derived from Eqs. (19)–(20) are shown in Fig. 9 and compare very well with digital simulations. In the latter, the first-passage events to the boundary have been determined as the first passage events of the Hamiltonian $H(u, v)$ to the level H_S as defined in Section 3.1.

We are now confident that the approximations of Section 3.1, 3.2, and 3.3 are quite reliable, and our goal is to produce a complete picture of the stochastic stability of the system for all values of the parameters (p, q) within the domain of bistability. For this, we produce contour maps of the activation energies $\mathcal{E}^+$ and $\mathcal{E}^-$ in this domain. As long as the parameters are not close to the boundaries OA, AB, and OB, values of $\mathcal{E}^+$ and $\mathcal{E}^-$ are found by the WKB method by determining the most probable ray joining the attracting point to the saddle and computing the difference in quasi-potential on this ray. Otherwise, we rely on the approximations of Sections 3.1 and 3.2. The results are summarized in Fig. 10. First, we note that S^- can have a much higher activation energy than S^+, but overall S^+ is more likely to be found more "stable" (i.e., to better survive random perturba-

Downloaded 04 May 2010 to 171.66.16.28. Redistribution subject to ASME license or copyright; see http://www.asme.org/terms/Terms_Use.cfm

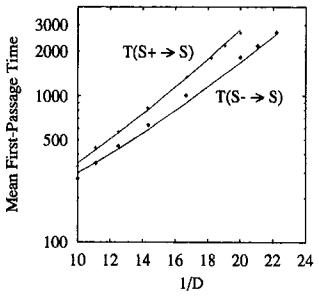

Fig. 9 Mean first-passage times $T(S^+ \to S)$ and $T(S^- \to S)$ evaluated by the low-damping approximation (19)–(20) (continuous lines) for $p = 0.01$ and $q = 0.015$. Here, the Monte Carlo simulation results are found by computing first-passage events of the response to the level $H = H_S = -8.77$.

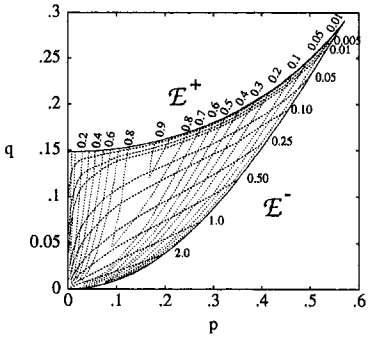

Fig. 10 Level curves of the activation energies $\mathcal{E}^+$ (vertical dotted lines) and $\mathcal{E}^-$ (horizontal dotted lines) in the parameter plane (p, q)

tions of a given intensity) than S^-. We also note that on the bifurcation lines AB or OB, one of the activation energies vanishes as expected, but the other one remains finite.

4 Concluding Remarks

All approximations developed here are asymptotic in the limit of small noise intensity. Monte Carlo simulations, which have been conducted to estimate the range of validity of these methods, have been found to be in good agreement with the theoretical predictions even over a large range of noise intensity. In Sections 3.1 and 3.2, we have found that the approximations lead to potential-like reduced systems and to Arrhenius-type laws for the mean first-passage times. In Section 3.3, the averaged equations cannot be identified to those of a near-potential (or near-Hamiltonian) system. Nevertheless, a similar asymptotic law governing mean first-passage times has been found by forcing the response p.d.f. into a functional form similar to that of potential systems. This forms the basis of the WKB approximation and the boundary layer approximation. Future work will be devoted to the case of random phase fluctuations of the resonant harmonic forcing in the Duffing oscillator, noting that we then have to deal with a system with multiplicative random excitation. We also plan to develop efficient methods to determine the most probable rays by using the fact that these rays are trajectories lying in the stable and unstable manifolds of the fixed points of the resulting Hamiltonian system (Eqs. (35)–(38)). Finally more work is needed to understand the relationship between the WKB approximation of FPK equations and the theory of large deviations developed by Freidlin and Wentzell (1984).

Acknowledgment

The partial support of this work by the grant CMS-94-10201 from the National Science Foundation is gratefully acknowledged.

References

Bender, C. M., and Orszag, S. A., 1978, *Advanced Mathematical Methods for Scientists and Engineers*, McGraw-Hill, New York.

Cohen, J. K., and Lewis, R. M., 1967, "A Ray Method for the Asymptotic Solution of the Diffusion Equation," *J. Inst. Math. Appl.*, Vol. 3, pp. 266–290.

Freidlin, M. I., and Wentzell, A. D., 1984, *Random Perturbations of Dynamical Systems*, Springer-Verlag, New York.

Gardiner, C. W., 1983, *Handbook of Stochastic Methods*, Springer-Verlag, Berlin.

Graham, R., and Tél, T., 1984, "On the Weak-noise Limit of Fokker-Planck Models," *Journal of Statistical Physics*, Vol. 35, Nos. 5–6, pp. 729–748.

Guckenheimer, J., and Holmes, P., 1983, *Nonlinear Oscillations, Dynamical Systems, and Bifurcations of Vector Fields*, Springer-Verlag, New York.

Hayashi, C., 1964, *Nonlinear Oscillations in Physical Systems*, McGraw-Hill, New York.

Horsthemke, W., and Lefever, R., 1984, *Noise-Induced Transitions*, Springer-Verlag, Berlin.

Khas'minskii, R. Z., 1980, *Stochastic Stability of Differential Equations*, Sijthoff & Noordhoff, Alphen aan den Rijn, The Netherlands.

Kozin, F., 1969, "A Survey of Stability of Stochastic Systems," *Automatica*, Vol. 5, pp. 95–112.

Knobloch, E., and Wiesenfeld, K. A., 1983, "Bifurcations in Fluctuating Systems: The Center Manifold Approach," *Journal of Statistical Physics*, Vol. 33, pp. 611–637.

Kramers, H. A., 1940, "Brownian Motion in a Field of Force and the Diffusion Model of Chemical Reactions," *Physica*, Vol. 7, pp. 284–304.

Ludwig, D., 1975, "Persistence of Dynamical Systems under Random Perturbations," *SIAM Review*, Vol. 17, pp. 605–640.

Matkowsky, B. J., and Schuss, Z., 1977, "The Exit Problem for Randomly Perturbed Dynamical Systems," *SIAM J. Appl. Math.*, Vol. 33, pp. 365–382.

Pontryagin, L., Andronov, A., and Witt, A., 1933, "On the Statistical Treatment of Dynamical Systems," (in Russian), *Zh. Eksp. Teor. Fiz.*, Vol. 3, pp. 165–180 (Also translated in *Noise in Nonlinear Dynamical Systems*, 1989), F. Moss and P. V. E. McClintock, eds., Cambridge University Press, Cambridge, U.K.

Roberts, J. B., 1986, "First-Passage Probabilities for Randomly Excited Systems: Diffusion Methods," *Probabilistic Engineering Mechanics*, Vol. 1, pp. 66–81.

Roy, R. V., 1994, "Noise Perturbations of a Nonlinear System with Multiple Steady States," *International Journal of Non-Linear Mechanics*, Vol. 29, pp. 755–773.

Schmidt, G., and Tondl, A., 1986, *Non-linear Vibrations*, Cambridge University Press, Cambridge, U.K.

Stratonovich, R. L., 1967, *Topics of the Theory of Random Noise*, Vol. II, Gordon and Breach, New York.

APPENDIX A

The FPK equation governing the p.d.f. p of the state vector $(a, b, \theta)^T$ solution of Eqs. (5)–(7) is given by

$$(\mathcal{L} - \partial_t)p = 0 \tag{A1}$$

with $\mathcal{L} = -\Omega\partial_\theta + \epsilon\mathcal{L}_1$, the operator $\mathcal{L}_1$ being given by

$$\mathcal{L}_1 = \partial_a(\tilde{f}\sin\theta) - \partial_b(\tilde{f}\cos\theta) + \frac{D_1}{2\Omega^2}\{\sin^2\theta\partial_{aa} + 2\sin\theta\cos\theta\partial_{ab} + \cos^2\theta\partial_{bb}\} + \frac{D_2}{2}\{b^2\partial_{aa} - \partial_a(ab\partial_b) - \partial_b(ab\partial_a) + a^2\partial_{bb}\}. \tag{A2}$$

By letting $t = \tau/\epsilon$, and $p = p_0 + \epsilon p_1 + \ldots$, we find at lowest order of ϵ that p_0 satisfies the equation

$$\partial_\theta p_0 = 0 \tag{A3}$$

and hence $p_0 \equiv p_0(a, b)$ is independent of θ. At the next order of perturbation was find that p_1 satisfies the equation

$$\Omega\partial_\theta p_1 = (\mathcal{L}_1 - \partial_\tau)p_0 \tag{A4}$$

whose solvability condition is

$$\frac{1}{2\pi}\int_0^{2\pi}(\mathcal{L}_1 - \partial_\tau)p_0 d\theta = 0. \tag{A5}$$

Downloaded 04 May 2010 to 171.66.16.28. Redistribution subject to ASME license or copyright; see http://www.asme.org/terms/Terms_Use.cfm

This equation yields the "averaged" FPK equation

$$\partial_\tau p_0 = \partial_a\{F(a,b)p_0\} - \partial_b\{G(a,b)p_0\} + \frac{D_1}{4\Omega^2}(\partial_{aa}p_0 + \partial_{bb}p_0) + \frac{D_2}{2}\{b^2\partial_{aa}p_0 - \partial_a(ab\partial_b p_0) - \partial_b(ab\partial_a p_0) + a^2\partial_{bb}p_0\} \quad \text{(A6)}$$

where F and G are given by Eq. (10). The resulting FPK equation can be identified as that of the process (a, b) governed by the stochastic differential Eqs. (8) and (9).

APPENDIX B

Referring to Fig. B1, the mean first-passage time T to the boundary $\partial\mathcal{D}$ of a domain $\mathcal{D}$ is the solution of the boundary value problem

$$\mathbf{b}(\mathbf{x})\cdot\nabla T + \frac{\epsilon}{2}\nabla^2 T = -1, \quad \mathbf{x}\in\mathcal{D} \quad \text{(B1)}$$

$$T = 0, \quad \mathbf{x}\in\partial\mathcal{D} \quad \text{(B2)}$$

where $\mathbf{x} = (x_1, x_2)$ is the starting point of the trajectory, $\mathbf{b} = (b_1, b_2)$ is the field defining the deterministic flow, $\nabla = (\partial_{x_1}, \partial_{x_2})$. Here, we have assumed two-dimensional isotropic diffusion of size $\epsilon \ll 1$, but this analysis can be generalized to arbitrary diffusion and to higher dimensional problems (see Matkowsky and Schuss, 1977). It is assumed that $\mathcal{D}$ is the basin of attraction of a fixed point $\mathbf{a}$, and the boundary $\partial\mathcal{D}$ is the stable manifold of a saddle point $\mathbf{a}^*$. Note that on $\partial\mathcal{D}$, we have $\mathbf{b}\cdot\boldsymbol{\nu} = 0$, where $\boldsymbol{\nu}$ is the unit outer normal to $\partial\mathcal{D}$. Assuming $T(\mathbf{x}) = T(\mathbf{a}\to\mathbf{a}^*)\tau(\mathbf{x})$ with $T(\mathbf{a}\to\mathbf{a}^*) = \Theta(e^{K/\epsilon})$ $(\epsilon\to 0)$, we find that τ is governed by

$$\mathbf{b}(\mathbf{x})\cdot\nabla\tau + \frac{\epsilon}{2}\nabla^2\tau = 0, \quad \mathbf{x}\in\mathcal{D} \quad \text{(B3)}$$

$$\tau = 0, \quad \mathbf{x}\in\partial\mathcal{D}. \quad \text{(B4)}$$

We expect that $\tau = 1$ at all $\mathbf{x}\in\mathcal{D}$ except in a boundary layer of $\partial\mathcal{D}$. If this function can be found near $\partial\mathcal{D}$, then the constant $T(\mathbf{a}\to\mathbf{a}^*)$ can be determined by multiplying Eq. (B1) by the stationary p.d.f. $p(\mathbf{x})$ solution and by integrating over the domain $\mathcal{D}$:

$$T(\mathbf{a}\to\mathbf{a}^*) = -\frac{2}{\epsilon}\frac{\int_{\mathcal{D}}p(\mathbf{x})d\mathbf{x}}{\int_{\partial\mathcal{D}}p(\mathbf{x})(\nabla\tau\cdot\boldsymbol{\nu})ds}. \quad \text{(B5)}$$

We then replace p by its WKB approximation $w\exp(-\Psi/\epsilon)$ within $\mathcal{D}$ (with $\Psi(\mathbf{a}) = 0$ and $w(\mathbf{a}) = 1$), and evaluate the domain and boundary integrals present in Eq. (B5) asymptotically in the limit $\epsilon\to 0$. Clearly the main contribution of the domain integral comes from the values of p near $\mathbf{a}$, while the main contribution of the boundary integral comes from values of p near the saddle point $\mathbf{a}^*$:

$$\int_{\mathcal{D}}p(\mathbf{x})d\mathbf{x} = \int_{\mathcal{D}}w(\mathbf{x})e^{-\Psi(\mathbf{x})/\epsilon}d\mathbf{x} \sim \int_{\mathcal{D}}e^{-\frac{1}{2}\Psi_{ij}x_ix_j/\epsilon}d\mathbf{x} = 2\pi\epsilon/\sqrt{J(\mathbf{a})} \quad \text{(B6)}$$

where $J(\mathbf{a}) = \det[\Psi_{ij}] = \det[\partial_{x_ix_j}\Psi(\mathbf{a})]$ (the Hessian of Ψ at $\mathbf{a}$), and

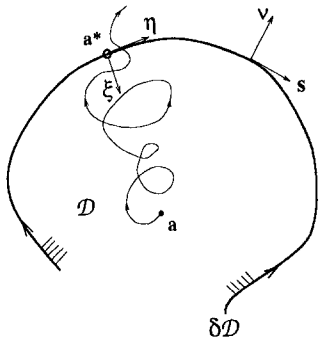

Fig. B1 Noise-induced transition from the basin $\mathcal{D}$ of fixed point a across the boundary $\partial\mathcal{D}$ (the stable manifold of saddle point a*)

$$\int_{\partial\mathcal{D}}p(\mathbf{x})(\nabla\tau\cdot\boldsymbol{\nu})ds \sim \partial_n\tau(\mathbf{a}^*)\left[2\pi\epsilon/|\partial_{ss}\Psi(\mathbf{a}^*)|\right]^{1/2}w(\mathbf{a}^*)\exp(-\Psi(\mathbf{a}^*)/\epsilon) \quad \text{(B7)}$$

where $\partial_n\tau(\mathbf{a}^*)$ is the normal derivative of τ at $\mathbf{a}^*$, and $\partial_{ss}\Psi(\mathbf{a}^*)$ is the second tangential derivative of Ψ at $\mathbf{a}^*$. Hence, the only needed characteristic of the boundary layer function τ is its normal derivative at $\mathbf{a}^*$. We solve Eq. (B3) near $\mathbf{a}^*$ in a coordinate system (ξ, η) centered at $\mathbf{x}^*$, where ξ is the distance measured along $-\boldsymbol{\nu}$ and η is measured along the tangent direction to $\partial\mathcal{D}$ at $\mathbf{a}^*$. After replacing the field $\mathbf{b}(\mathbf{x})$ by its linearization $\mathbf{B}(\mathbf{x}-\mathbf{a}^*)$ about point $\mathbf{a}^*$ and after transforming the coordinate system (x_1, x_2) to (ξ, η), we find

$$\lambda_p\xi\partial_\xi\tau + \left[\lambda_m\eta + (b_{21} - b_{12})\xi\right]\partial_\eta\tau + \frac{\epsilon}{2}\left(\partial_{\xi\xi}\tau + \partial_{\eta\eta}\tau\right) = 0, \quad \text{(B8)}$$

where λ_p and λ_m are the positive and negative eigenvalues of matrix $\mathbf{B} = [\partial_{x_j}b_i(\mathbf{a}^*)]$. Then letting $\xi = \epsilon\bar{\xi}$ and $\tau = \tau_0 + \epsilon\tau_1 + \ldots$, we find that near $\mathbf{a}^*$

$$\lambda_p\bar{\xi}\partial_{\bar{\xi}}\tau_0 + \lambda_m\eta\partial_\eta\tau_0 + \frac{1}{2}\partial_{\bar{\xi}\bar{\xi}}\tau_0 = 0 \quad \text{(B9)}$$

with the boundary conditions $\lim_{\bar{\xi}\to 0}\tau_0 = 0$, and $\lim_{\bar{\xi}\to\infty}\tau_0 = 1$. Seeking a solution of the form

$$\tau_0(\bar{\xi}, \eta) = (2/\pi)^{1/2}\int_0^{\bar{\xi}\gamma(\eta)}e^{-z^2/2}dz \quad \text{(B10)}$$

we find

$$\lambda_m\eta\frac{d\gamma}{d\eta} + \lambda_p\gamma - \frac{1}{2}\gamma^3 = 0. \quad \text{(B11)}$$

This then leads to the value $\gamma(0) = (2\lambda_p)^{1/2}$ at $\mathbf{a}^*$ and to the normal derivative of τ at $\mathbf{a}^*$

$$\partial_n\tau(0,0) = -\partial_\xi\tau_0(0,0) = -(2/\pi\epsilon)^{1/2}\gamma(0) = -(4\lambda_p/\pi\epsilon)^{1/2}. \quad \text{(B12)}$$

Finally, the mean first-passage time from $\mathbf{a}$ to $\partial\mathcal{D}$ is given by the expression

$$T(\mathbf{a}\to\mathbf{a}^*) = \pi\left[2|\partial_{ss}\Psi(\mathbf{a}^*)|/\lambda_p J(\mathbf{a})\right]^{1/2}\frac{e^{\Psi(\mathbf{a}^*)/\epsilon}}{w(\mathbf{a}^*)}. \quad \text{(B13)}$$

Downloaded 04 May 2010 to 171.66.16.28. Redistribution subject to ASME license or copyright; see http://www.asme.org/terms/Terms_Use.cfm

Lagrange's Equations, Hamilton's Equations, and Kane's Equations: Interrelations, Energy Integrals, and a Variational Principle

D. L. Mingori
Mechanical, Aerospace, and Nuclear Engineering Department, 38-137 Engineering IV, University of California, Los Angeles, CA 90024-1597

A new viewpoint is suggested for expressing the governing equations of analytical mechanics. This viewpoint establishes a convenient framework for examining the relationships among Lagrange's equations, Hamilton's equations, and Kane's equations. The conditions which must be satisfied for the existence of an energy integral in the context of Kane's equations are clarified, and a generalized form of Hamilton's Principle is presented. Generalized speeds replace generalized velocities as the velocity variables in the formulation. The development considers holonomic systems in which the generalized forces are derivable from a potential function.

1 Introduction

Analytical mechanics is a very mature subject, having been developed over a period of more than 160 years by such giants of classical mechanics as Euler, Lagrange, and Hamilton. These individuals laid the foundations of analytical mechanics, and the methods they developed are still in constant use. The subject represents one of the triumphs of modern science in terms of its ability to distill the laws of physics into a particularly elegant and compact mathematical form. It continues to draw the interest of scientists and engineers because, in addition to its intellectual appeal, it is an eminently practical subject with important applications in a multitude of engineering situations. For this reason, researchers continue to seek ways to extend its utility.

The work of T. R. Kane during the 1960s and 1970s is an example of recent efforts to achieve an even more useful formulation of analytical mechanics (Kane and Levinson, 1985). Working from D'Alembert's principle, Kane developed an approach which is gaining popularity with many dynamicists of the present day. Among the key innovations introduced by Kane are the notions of generalized speeds, partial velocities, and partial angular velocities. These ideas reduce the labor involved in formulating equations of motion, and make it possible to simplify the final equations provided a judicious choice is made for the generalized speeds. Generalized speeds compliment the notion of generalized coordinates is a more useful way than the more traditional generalized velocities. The ability to fully realize the benefits of Kane's approach are to some extent, dependent on the analysts inventiveness and judgment in selecting the generalized speeds. A similar statement can, of course, be made with respect to the selection of generalized coordinates within the context of a traditional Lagrangian or Hamilton formulation.

The present paper presents a single formulation of classical mechanics which yields Lagrange's equations, Hamilton's equations, and Kane's equations as special cases. It is assumed in this development that the system is holonomic and that all applied forces are derivable from a potential function $V(q, t)$. The author believes the formulation presented here provides useful insights by unifying the three approaches listed above. Perhaps more importantly, the present formulation serves to clarify the conditions needed for the existence of energy integrals within the context of Kane's equations. In particular it is possible to obtain conditions which are simpler, and in some respects more general than those presented in (Kane and Levinson, 1985).

2 Formulation

Lagrange's formulation can be used to write the governing equations for a holonomic system with conservative applied forces as

$$\frac{d}{dt}(L_{\dot{q}}) - L_q = 0 \tag{1}$$

The subscripts q and $\dot{q}$ indicate partial differentiation. Please see the Appendix for details of this notation. The Lagrangian

Contributed by the Applied Mechanics Division of THE AMERICAN SOCIETY OF MECHANICAL ENGINEERS for publication in the ASME JOURNAL OF APPLIED MECHANICS.

Discussion on this paper should be addressed to the Technical Editor, Professor Lewis T. Wheeler, Department of Mechanical Engineering, University of Houston, Houston, TX 77204-4792, and will be accepted until four months after final publication of the paper itself in the ASME JOURNAL OF APPLIED MECHANICS.

Manuscript received by the ASME Applied Mechanics Division, Mar. 15, 1993; final revision, Oct. 15, 1993. Associate Technical Editor: R. L. Huston.

Copyright © 1995 by ASME

Downloaded 04 May 2010 to 171.66.16.28. Redistribution subject to ASME license or copyright; see http://www.asme.org/terms/Terms_Use.cfm

L is defined in terms of the kinetic energy K and potential energy V.

$$L = L(q, \dot{q}, t) = K(q, \dot{q}, t) - V(q, t) \tag{2}$$

Following Kane, introduce a set of generalized speeds $u = [u_1, \ldots, u_n]^T$ which are related to the generalized velocities by an equation of the form

$$u = g(q, \dot{q}, t) \tag{3}$$

Kane explicitly assumes a form for (3) that is linear in the $\dot{q}$'s, i.e.,

$$u = Y(q, t)\dot{q} + Z(q, t) \tag{4}$$

where Y is invertible. The present development does not require a linearity assumption. We do, however, need to assume that (3) can be solved explicitly for $\dot{q}$ as a function of (q, u, t) yielding an expression in the form

$$\dot{q} = f(q, u, t) \tag{5}$$

In (5), f is a column matrix such that the square matrix of partial derivatives f_u is nonsingular. If (3) has the linear form given in (4), then (5) becomes

$$\dot{q} = W(q, t)u + X(q, t) \tag{6}$$

with

$$W(q, t) = Y^{-1}(q, t); \quad X(q, t) = -Y^{-1}(q, t)Z(q, t) \tag{7}$$

In this case,

$$f_u = W(q, t) \tag{8}$$

The introduction of the function f in Eq. (5) is a key step in the development to follow.

The partial derivatives indicated in (1) are based on the traditional approach of expressing L as a function of q, $\dot{q}$, and t. Using (5), the Lagrangian can also be expressed as a function of q, u, and t. Thus we can write

$$L(q, \dot{q}, t) = L[q, f(q, u, t), t] = \mathfrak{L}(q, u, t). \tag{9}$$

Although $L(q, \dot{q}, t)$ and $\mathfrak{L}(q, u, t)$ are equal to each other, they are not equivalent in all respects. In particular, important differences develop when partial derivatives are taken. Using (9) we obtain the following relationships between the partial derivatives of $\mathfrak{L}$ and those of L:

$$\mathfrak{L}_q = L_q + L_f f_q = L_q + L_{\dot{q}} f_q \tag{10}$$

$$\mathfrak{L}_u = L_f f_u = L_{\dot{q}} f_u \tag{11}$$

$$\mathfrak{L}_t = L_f f_t + L_t = L_{\dot{q}} f_t + L_t. \tag{12}$$

Equations (10)–(11) and the assumption that f_u is nonsingular can be used to express $L_{\dot{q}}$ and L_q as

$$L_{\dot{q}} = \mathfrak{L}_u f_u^{-1} \tag{13}$$

$$L_q = \mathfrak{L}_q - \mathfrak{L}_u f_u^{-1} f_q. \tag{14}$$

Substitution of (13)–(14) into (1) then yields

$$\frac{d}{dt}(\mathfrak{L}_u f_u^{-1}) - \mathfrak{L}_q + \mathfrak{L}_u f_u^{-1} f_q = 0. \tag{15}$$

Equation (15) may be viewed as a modified version of Lagrange's equations in which the modified Lagrangian $\mathfrak{L}$ is expressed as a function of (q, u, t) instead of $(q, \dot{q}, t)$. Two variants of (15) will also be of interest in subsequent discussions. The first variant is obtained by simply post-multiplying (15) by f_u to obtain

$$\frac{d}{dt}(\mathfrak{L}_u f_u^{-1}) f_u - \mathfrak{L}_q f_u + \mathfrak{L}_u f_u^{-1} f_q f_u = 0. \tag{16}$$

The second is obtained by straightforward manipulation of the terms in (16).

$$\frac{d}{dt}(\mathfrak{L}_u) + \mathfrak{L}_u f_u^{-1}\left(f_q - \frac{df_u}{dt} f_u^{-1}\right) f_u - \mathfrak{L}_q f_u = 0 \tag{17}$$

Equations (15)–(17) are equivalent and they each describe the same physical laws which govern the system. In order to have a complete set of equations it is necessary to include Eq. (3) or Eq. (5), either of which describes the kinematical relations between u, q, and $\dot{q}$.

One may ask what has been gained by taking a relatively simple equation like (1) and replacing it by what would appear to be a much more complicated set of equations as given in (15), (16), or (17) plus (3) or (5). There are several answers to this question. The first is that the freedom to make various choices for $f(q, u, t)$ is a powerful tool for unifying several formulations which have been used for many years. Another is that the conditions for the existence of an energy integral can be demonstrated in a straightforward manner. Finally, appropriate choices for $f(q, u, t)$ can in some cases lead to a substantially simplified set of equations. These issues are addressed in the following sections.

3 Special Choices for the Function $f(q, u, t)$

A central ingredient in the previous section is the introduction of the function $f(q, u, t)$ in Eq. (5). The analyst is free to select this function in various ways in order to generate governing equations in a useful form. This section provides some examples illustrating how special choices for f lead to several well-known forms for the governing equations.

3.1 Lagrange's Equations. Lagrange's Equations are obtained by choosing

$$f = u. \tag{18}$$

With this choice,

$$f_q = 0, \quad f_u = I_n \quad (n \times n \text{ identity}). \tag{19}$$

Equations (15) and (5) become

$$\frac{d}{dt}(\mathfrak{L}_u) - \mathfrak{L}_q = 0 \tag{20}$$

$$\dot{q} = u \tag{21}$$

which are clearly the same as Lagrange's equations.

3.2 Hamilton's Equations. Some preliminary steps are required before we can see how to choose f to obtain Hamilton's Equations. First define the Hamiltonian $\mathfrak{H}$ as

$$\mathfrak{H}(q, u, t) \triangleq \mathfrak{L}_u f_u^{-1} f - \mathfrak{L}. \tag{22}$$

Next, require that f be chosen such that

$$\mathfrak{L}_u f_u^{-1} = u^T. \tag{23}$$

Equation (23) is equivalent to setting

$$u^T = L_{\dot{q}}|_{\dot{q}=f}. \tag{24}$$

Thus, the generalized speeds are chosen to be equal to the generalized momenta (see (13)). If $L(q, \dot{q}, t)$ has the usual quadratic form, i.e.,

$$L = \frac{1}{2}\dot{q}^T A(q, t)\dot{q} + B^T(q, t)\dot{q} + C(q, t). \tag{25}$$

Then (24) becomes

$$u^T = f^T A + B^T \tag{26}$$

and this leads to the following choice for f:

$$f = A^{-1}u - A^{-1}B. \tag{27}$$

Downloaded 04 May 2010 to 171.66.16.28. Redistribution subject to ASME license or copyright; see http://www.asme.org/terms/Terms_Use.cfm

Next return to the definition of $\mathcal{H}$ and formulate expressions for $\mathcal{H}_q$ and $\mathcal{H}_u$.

$$\mathcal{H}_q = \left(\mathcal{L}_u f_u^{-1}\right) f_q + f^T \left(f_u^{-T} \mathcal{L}_u^T\right)_q - \mathcal{L}_q$$

$$= -\frac{d}{dt}\left(\mathcal{L}_u f_u^{-1}\right) + f^T \left(f_u^{-T} \mathcal{L}_u^T\right)_q \quad (28)$$

$$\mathcal{H}_u = \left(\mathcal{L}_u f_u^{-1}\right) f_u + f^T \left(f_u^{-T} \mathcal{L}_u^T\right)_u - \mathcal{L}_u = f^T \left(f_u^{-T} \mathcal{L}_u^T\right)_u. \quad (29)$$

If (23) is satisfied, then

$$\left(f_u^{-T} \mathcal{L}_u^T\right)_u = I_n, \quad \left(f_u^{-T} \mathcal{L}_u^T\right)_q = 0, \quad \left(f_u^{-T} \mathcal{L}_u^T\right)_t = 0 \quad (30)$$

and $\mathcal{H}_q$ and $\mathcal{H}_u$ become,

$$\mathcal{H}_q = -\dot{u}^T \quad (31)$$

$$\mathcal{H}_u = f^T = \dot{q}^T. \quad (32)$$

Transposing (31) and (32) leads to Hamilton's equations

$$\dot{u} = -\mathcal{H}_q^T \quad (33)$$

$$\dot{q} = \mathcal{H}_u^T. \quad (34)$$

To summarize, if L has the form given in (25), then Hamilton's equations are obtained by choosing f according to (27). If L should have a more general form, then the f leading to Hamilton's equations would be obtained by solving (24) for f.

3.3 Kane's Equations. To obtain Kane's Equations, use Eqs. (16) or (17) (not (15)) and chose an f which is linear in u as given in Eq. (6), i.e.,

$$f = W(q, t)u + X(q, t) \quad (35)$$

With this choice for f, (17) and (5) become

$$\frac{d}{dt}\mathcal{L}_u + \mathcal{L}_u W^{-1}\left[(Wu + X)_q - \dot{W}W^{-1}\right]W - \mathcal{L}_q W = 0 \quad (36)$$

$$\dot{q} = Wu + X. \quad (37)$$

(An equivalent result could be obtained with Eqs. (16) and (5).) The equations which result from taking the partial and total derivatives indicated in Eq. (36) will be identical to Kane's equations for the class of systems under consideration (holonomic with generalized forces derivable from a potential function). However, this does not necessarily mean that the work required to obtain the final equations using (36) will be the same as that required to obtain these equations using Kane's methods as described in (Kane and Levinson, 1985). Based on experience with a small number of examples, the author believes that the methods of (Kane and Levinson, 1985) are generally easier to use. Nevertheless, it is still of considerable theoretical interest that the equations can be expressed as in Eq. (36). In Section 4, for example, the present formulation will be used to clarify the conditions for the existence of an energy integral.

As a final comment it may be noted that (36) is equivalent to the formulation known as Lagrange's Equations for Quasi Coordinates. The quasi-coordinate formulation is described in (Pars, 1979; Whittaker, 1964; Meirovitch, 1970).

4 Energy Integrals

This section uses the foregoing formulation to develop the requirements for the existence of an energy integral and to give the formula for such an integral. This topic is relevant in connection with the construction of energy integrals for Kane's equations as described in (Kane and Levinson, 1985). We begin by taking the total time derivative of the Hamiltonian defined in Eq. (22).

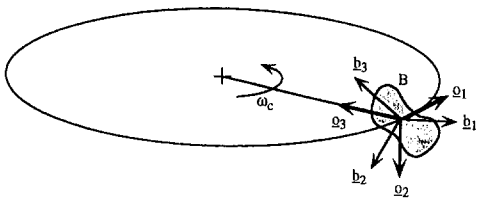

Fig. 1 Orbiting rigid body in and inverse square gravity field

$$\frac{d\mathcal{H}}{dt} = \frac{d}{dt}\left(\mathcal{L}_u f_u^{-1}\right) f + \mathcal{L}_u f_u^{-1}\left(f_u \dot{u} + f_q \dot{q} + f_t\right) - \mathcal{L}_u \dot{u} - \mathcal{L}_q \dot{q} - \mathcal{L}_t \quad (38)$$

Substituting (5) and (15) into (38) leads to

$$\frac{d\mathcal{H}}{dt} = -\mathcal{L}_t + \mathcal{L}_u f_u^{-1} f_t. \quad (39)$$

A necessary and sufficient condition for $\mathcal{H}$ to be a constant is that the right-hand side of (39) be zero. This can be easily checked once $\mathcal{L}$ and f are known. A sufficient condition for the constancy of $\mathcal{H}$ is that $\mathcal{L}$ and f not depend explicitly on time. Note further that substitution of (11) and (12) into (39) yields

$$\frac{d\mathcal{H}}{dt} = -L_{\dot{q}} f_t - L_t + \left(L_{\dot{q}} f_u\right) f_u^{-1} f_t = -L_t. \quad (40)$$

Hence, an alternative statement of the necessary and sufficient condition for $\mathcal{H}$ to be a constant, i.e., an energy integral, is $L_t = 0$. This agrees with the well known condition for the existence of an energy integral in the traditional Lagrangian formulation.

The energy integral test suggested here, namely checking to see if the right hand side of (39) is zero, is considerably more straightforward than the tests given in Chapter 7 of (Kane and Levinson, 1985). One reason for the extra complexity of the development in (Kane and Levinson, 1985) is that their development embraces both nonholonomic and holonomic systems. A second reason, however, is that the form assumed for the Hamilton $\mathcal{H}$ in Eq. (2) of their section 7.2 is too restrictive. It does not allow $\mathcal{H}$ to contain terms which are linear in the generalized speeds. This unnecessary restriction is not imposed on the Hamiltonian $\mathcal{H}$ introduced in the present paper and this increased generality, together with the alternative formulation of the governing equations, simplifies the search for energy integrals. In (Kane and Levinson, 1990), modifications are proposed to the procedures in (Kane and Levinson, 1985) which allow the construction of energy integrals for systems with linear generalized speed terms in the Hamiltonian. This modified procedure addresses the same issue being addressed here, but it does so with a distinctly different approach.

Example. To illustrate the utility of the development in this section, an energy integral will be derived for the rotational motion of a rigid body whose mass center moves in a circular orbit about a fixed mass exerting an inverse square force of attraction. This problem is considered in (Hughes, 1986) and the present development will adopt much of the same notation. The situation is depicted in Fig. 1.

Let

$\mathbf{o} = [\mathbf{o}_1, \mathbf{o}_2, \mathbf{o}_3]^T$ = column of unit vectors parallel to the orbiting axes fixed in the orbiting frame O.

$\mathbf{b} = [\mathbf{b}_1, \mathbf{b}_2, \mathbf{b}_3]^T$ = column of unit vectors parallel to the central principal axes fixed in the body B.

$\boldsymbol{\omega}^{BN}$ = angular velocity of the rigid body B in an inertial frame N.

Downloaded 04 May 2010 to 171.66.16.28. Redistribution subject to ASME license or copyright; see http://www.asme.org/terms/Terms_Use.cfm

$\boldsymbol{\omega}^{BO}$ = angular velocity of B in the orbiting frame O.

$\boldsymbol{\omega}^{ON} = -\omega_c \mathbf{o}_2$ = angular velocity of O in N.

$C = 3 \times 3$ square matrix of direction cosines relating $\mathbf{o}$ to $\mathbf{b}$ according to the equation $\mathbf{b} = C\mathbf{o}$.

The orientation of the body frame B with respect to the orbiting frame O may be described by three Euler angles (θ_1, θ_2, θ_3). These Euler angles will serve as the generalized coordinates for this problem. The Euler angles may be selected in various ways as explained in (Hughes, 1986) but it will not be necessary to make a particular choice here. We will only need to observe that the direction cosine matrix C and the angular velocity $\boldsymbol{\omega}^{BO}$ may be expressed as

$$C = C(\theta) = [c_1(\theta) \vdots c_2(\theta) \vdots c_3(\theta)] \tag{41}$$

and

$$\boldsymbol{\omega}^{BO} = \dot{\theta}^T S^T(\theta_1, \theta_2)\mathbf{b} \tag{42}$$

where

$$\theta \triangleq [\theta_1, \theta_2, \theta_3]; \quad c_i(\theta) = i\text{th column of } c.$$

See Table 2.1 and 2.2 in (Hughes, 1986) for a listing of the formulas for C and the square matrix S for each of 12 distinct choices of the Euler angles.

Using (41) and (42) one can express $\boldsymbol{\omega}^{BN}$ as

$$\begin{aligned}\boldsymbol{\omega}^{BN} &= \boldsymbol{\omega}^{BO} + \boldsymbol{\omega}^{ON} \\ &= \dot{\theta}^T S^T \mathbf{b} - \omega_c \mathbf{o}_2 \\ &= \left[\dot{\theta}^T S^T - \omega_c c_2^T\right]\mathbf{b}\end{aligned} \tag{43}$$

The governing equations for the system of Fig. 1 are given in (Hughes, 1986). Repeated here in matrix notation, they are

$$I\dot{\omega} = -\omega^x I\omega + 3\omega_c^2 c_3^x I c_3 \tag{44}$$

$$\dot{C} = \omega^x C + C\omega_c^x \tag{45}$$

where

$\omega = [\omega_1\ \omega_2\ \omega_3]^T$ = column of inertial angular velocity measure numbers for the body axes, i.e., $\boldsymbol{\omega}_{BN} = \omega^T \mathbf{b}$.

$$I = \begin{bmatrix} I_1 & 0 & 0 \\ 0 & I_2 & 0 \\ 0 & 0 & I_3 \end{bmatrix} = \text{inertia matrix for central principal axes}$$

$$\omega^x \triangleq \begin{bmatrix} 0 & -\omega_3 & \omega_2 \\ \omega_3 & 0 & -\omega_1 \\ -\omega_2 & \omega_1 & 0 \end{bmatrix},$$

$$\omega_c^x \triangleq \begin{bmatrix} 0 & 0 & -\omega_c \\ 0 & 0 & 0 \\ \omega_c & 0 & 0 \end{bmatrix}$$

Hughes (1986) also gives an expression for the energy integral for this system:

$$H = \frac{1}{2}\omega^T I\omega + \omega_c \omega^T I c_2 + \frac{3}{2}\omega_c^2 c_3^T I c_3. \tag{46}$$

The constancy of H can be verified by differentiating H and showing that $\dot{H} \equiv 0$ using (41), (44), (45) and additional kinematical identities from page 10 of (Hughes, 1986). This procedure is straightforward, although somewhat lengthy. We will now see how this integral can be obtained using the method of the present paper.

Using (42) and the definition of ω one can write

$$\omega = S\dot{\theta} - \omega_c c_2. \tag{47}$$

This equation will be used to define the generalized speeds as

$$u \triangleq \omega = S\dot{\theta} - \omega_c c_2 = Y\dot{\theta} + Z. \tag{48}$$

Thus,

$$\dot{\theta} = Y^{-1}u - Y^{-1}Z = S^{-1}u + \omega_c S^{-1}c_2 = f(u, \theta). \tag{49}$$

The kinetic and potential energy expressions for this system can be written as

$$K = \frac{1}{2}u^T I u \qquad V = \frac{3}{2}\omega_c^2 c_3^T I c_3. \tag{50}$$

The Lagrangian then becomes

$$\mathfrak{L} = K - V = \frac{1}{2}u^T I u - \frac{3}{2}\omega_c^2 c_3^T I c_3. \tag{51}$$

Formulate $\mathfrak{H}$ using (22), (49), (51).

$$\begin{aligned}\mathfrak{H} &= \mathfrak{L}_u f_u^{-1} f - \mathfrak{L} \\ &= u^T I Y(Y^{-1}u - Y^{-1}Z) - \frac{1}{2}u^T I u + \frac{3}{2}\omega_c^2 c_3^T I c_3 \\ &= \frac{1}{2}u^T I u - u^T I Z + \frac{3}{2}\omega_c^2 c_3^T I c_3 \\ &= \frac{1}{2}u^T I u + \omega_c u^T I c_2 + \frac{3}{2}\omega_c^2 c_3^T I c_3\end{aligned} \tag{52}$$

By inspection, note that neither $\mathfrak{L}$ nor f contain time explicitly, hence $\mathfrak{L}_t = 0$ and $f_t = 0$. It therefore follows from (39) that $\mathfrak{H}$ is a constant of the motion. The expression in the last line of (52) is identical to the energy integral found by Hughes (see Eq. (46)).

It is worth noting that the energy integral given above contains a term which is linear in the generalized speed matrix u. Thus this integral would not be found by the procedure in (Kane and Levinson, 1985) where it is assumed that linear terms in u are absent from the energy integral. The development of the present paper provides a systematic procedure for finding integrals in the more general case.

5 A Variational Formulation

In 1834, W. R. Hamilton published his famous paper setting forth the principle now known as *Hamilton's Principle* (Hamilton, 1834). This variational principle forms one of the cornerstones of analytical mechanics. As noted in the introduction, Kane's formulation is based on D'Alembert's principle rather than a variational principle similar to Hamilton's principle. The objective of the section is to establish some links between Hamilton's principle and Kane's equations using concepts from optimal control theory. The result is a generalized form of Hamilton's principle. We begin by reviewing a classical problem from the calculus of variations.

5.1 A Result From the Calculus of Variations. Consider a functional $J[q, u]$ defined as

$$J[q, u] = \int_{t_0}^{t_1} \mathfrak{L}(q, u, t)dt \tag{53}$$

where $q(t)$ and $u(t) \in \Re^n$. Suppose q and u are required to satisfy differential constraints in the form

$$\dot{q} = f(q, u, t) \tag{54}$$

Downloaded 04 May 2010 to 171.66.16.28. Redistribution subject to ASME license or copyright; see http://www.asme.org/terms/Terms_Use.cfm

where $f(q, u, t) \in \Re^n$. Suppose further that the initial and terminal conditions on q are specified, i.e.,

$$q(t_0) = q_0; \quad q(t_1) = q_1 \tag{55}$$

We wish to find functions $q = \dot{q}(t)$ and $u = u^*(t)$ such that all of the constraints listed above are satisfied, and the first variation of J is zero. The solution of this problem is discussed in a number of excellent references e.g., (Gelfand and Fomin, 1963; Bryson and Ho, 1975; Althans and Falb, 1966). The usual procedure for dealing with the constraint equations is to add them to the cost functional using a column vector of Lagrange multipliers. This leads to

$$J(q, u) = \int_{t_0}^{t_1} \{ \mathfrak{L}(q, u, t) + \lambda^T(t)[f(q, u, t) - \dot{q}] \} dt \tag{56}$$

The application of standard procedures from the calculus of variations yields the following necessary conditions for the first variation of J to be zero (Athans and Falb, 1966; Bryson and Ho, 1975):

$$\dot{\lambda}^T + \mathfrak{L}_q + \lambda^T f_q = 0 \tag{57}$$

$$\mathfrak{L}_u + \lambda^T f_u = 0 \tag{58}$$

$$\dot{q} = f(q, u, t) \tag{59}$$

$$q(t_0) = q_0; \quad q(t_1) = q_1 \tag{60}$$

Equations (57)–(60) form the basis for the next two sections.

5.2 Interpretations in the Context of Control and Dynamics. As discussed at length in (Bryson and Ho, 1975; Athans and Falb, 1966), Eqs. (53)–(60) have an important interpretation in the field of automatic control. Although it may be something of a digression, this interpretation is briefly outlined here because it may provide useful insights for those readers familiar with optimal control theory. Ultimately our goal is to formulate a generalized version of Hamilton's Principle.

For the control problem, one regards q as the $n \times 1$ state vector for the system to be controlled, and u as the $m \times 1$ control input vector. Normally $m < n$. Equation (54) then becomes the state equation which describes the effect of the control input on the behavior of the system. J is the performance index which is a function of the state q and control u. The optimal control problem is one of finding a control u which minimizes J where J is defined in such a way that $J \geq 0$. A number of textbooks describe the procedure for solving for the optimal control u using Eqs. (57)–(60) (Athans and Falb, 1966; Bryson and Ho, 1975). These procedures will not be described here. Instead, the development is intended to show that with alternative interpretations, Eqs. (53)–(60) are also very relevant to the subject of analytical mechanics.

It was noted that in the control problem, the equation $\dot{q} = f(q, u, t)$ is thought of as the state equation describing the response of the system to the control input u. In the context of analytical mechanics, this equation will have a very different interpretation. Here $\dot{q} = f(q, u, t)$ will be a purely kinematic expression relating the n generalized velocities $\dot{q}$ to the n generalized speeds u and the n generalized coordinates q. As in Sections 2–4 we assume that it is always possible to solve the equation $\dot{q} = f$ explicitly for the n elements of u as functions of q, $\dot{q}$, and t. Thus

$$\dot{q} = f(q, u, t) \Leftrightarrow u = g(q, \dot{q}, t) \tag{61}$$

In fact, the usual procedure will be to define u using the equation on the right side of (61) and then invert this equation to obtain the equation on the left side of (61). As in previous sections of this paper, we assume that f_u is nonsingular.

For the control problem, $\mathfrak{L}$ is a function of control u and state q whose integral we desire to maximize or minimize. In the context of analytical mechanics, the integrand $\mathfrak{L}$ in Eq. (54) is the Lagrangian expressed as a function of q, u, and t. For the mechanics problem, q, u, and λ all have the same dimension n. Furthermore, the assumption that the square matrix f_u is non singular makes it possible to solve Eq. (58) for λ.

$$\lambda^T = -\mathfrak{L}_u f_u^{-1} \tag{62}$$

In general, this is not possible for the control problem since the dimension of u is usually much smaller than the dimension of q. Substituting (62) into (57) yields

$$\frac{d}{dt}(\mathfrak{L}_u f_u^{-1}) - \mathfrak{L}_q + \mathfrak{L}_u f_u^{-1} f_q = 0 \tag{63}$$

which is identical to (15). This means that the generalized Lagrange Eq. (15) can be obtained from the solution of a variational calculus problem just as the standard Lagrangian equation can be obtained from Hamilton's Principle. The next section contains the statement of a generalized form of Hamilton's Principle based on these observations. This statement permits the use of generalized speeds as velocity variables instead of the more standard generalized velocities.

5.3 Generalized Hamilton's Principle. Consider a holonomic mechanical system whose configuration is defined by generalized coordinates q. Introduce a set of n generalized speeds u satisfying the equation

$$u = g(q, \dot{q}, t) \Leftrightarrow \dot{q} = f(q, u, t) \tag{64}$$

Assume the square matrix f_u is nonsingular.

Suppose all working applied forces are derived from a potential function $V(q, t)$ and let $\mathfrak{L}(q, u, t)$ be the Lagrangian for the system expressed as a function of q, u, and t. Then the motion of the system between fixed times t_0 and t_1 is such that the first variation of the integral:

$$\int_{t_0}^{t_1} \mathfrak{L}(q, u, t) dt \tag{65}$$

is zero. In evaluating the first variation, it is required that

1 q, $\dot{q}$, and u satisfy the constraint Eq. (64).

2 $q(t_0) = q_0$, and $q(t_1) = q_1$; i.e., the initial and final configurations are specified.

Note that in the special case where $f(q, u, t) = u$, this principle reduces to the standard form of Hamilton's Principle.

6 Summary

The present paper presents a novel formulation of the equations and principles of analytical mechanics. This formulation makes use of the concept of generalized speeds as suggested by Kane. The new viewpoint establishes a convenient framework for examining the relationships among several formulations including Lagrange's equations, Hamilton's equations, and Kane's equations. It also clarifies and simplifies the conditions which need to be satisfied for the existence of an energy integral within the context of Kane's equations. In addition, a generalized form of Hamilton's Principle is presented. This principle uses generalized speeds as velocity variables in place of the standard generalized velocities.

Downloaded 04 May 2010 to 171.66.16.28. Redistribution subject to ASME license or copyright; see http://www.asme.org/terms/Terms_Use.cfm

Acknowledgment

The author would like to thank Profs. T. R. Kane and R. W. Longman for their useful suggestions during the preparation of this manuscript.

References

Athans, M., and Falb, P. L., 1966, *Optimal Control*, McGraw-Hill, New York.

Bryson, A. E., and Ho, Y. C., 1975, *Applied Optimal Control*, Halstead Press, New York.

Gelfand, I. M., and Fomin, S. V., 1963, *Calculus of Variations*, Prentice-Hall, Englewood Cliffs, NJ.

Hamilton, W. R., 1834, "On a General Method in Dynamics," *Philosophical Transactions*, pp. 247–308.

Hughes, P. C., 1986, *Spacecraft Attitude Dynamics*, John Wiley and Sons, New York.

Kane, T. R., and Levinson, D. A., 1985, *Dynamics Theory and Applications*, McGraw-Hill, New York.

Kane, T. R., and Levinson, D. A., 1990, "Testing Numerical Integrations of Equations of Motions," ASME JOURNAL OF APPLIED MECHANICS, Vol. 57, pp. 248–249.

Meirovitch, L., 1970, *Methods of Analytical Dynamics*, McGraw-Hill, New York, pp. 157–160.

Pars, 1979, *A Treatise on Analytical Dynamics*, Ox Bow Press, Woodbridge, CT.

Whittaker, E. T., 1964, *A Treatise on the Analytical Dynamics of Particles and Rigid Bodies*, Cambridge University Press, London.

APPENDIX

Notation/Definitions

$q = [q_1, q_2, \ldots, q_n]^T = n \times 1$ column vector of generalized coordinates

$u = [u_1, \ldots, u_n]^T = n \times 1$ column vector of generalized speeds

$K = K(q, \dot{q}, t)$ = kinetic energy expressed as a function of q, $\dot{q}$, and t

$\mathcal{K} = \mathcal{K}(q, u, t) = K[q, f(q, u, t), t]$ = kinetic energy expressed as a function of q, u, and t

$V = V(q, t)$ = potential energy

$L = K - V$ = Lagrangian expressed as a function of q, $\dot{q}$, and t

$\mathfrak{L} = \mathcal{K} - V$ = Lagrangian expressed as a function of q, u, and t

$f = f(q, u, t) = n \times 1$ column vector, see Eq. (5)

$\mathcal{H} = \mathcal{H}(q, u, t) \triangleq \mathbf{L}_u f_u^{-1} f - \mathfrak{L}$ = Hamiltonian

Differentiation Conventions. If S = scalar and $x = n \times 1$ vector then

$$S_x = \left[\frac{\partial S}{\partial x_1} \; \frac{\partial S}{\partial x_2} \ldots \frac{\partial S}{\partial x_n} \right] = 1 \times n \text{ row vector}$$

If $V = n \times 1$ vector and $x = n \times 1$ vector then

$$V_x = \begin{bmatrix} V_{1x} \\ V_{2x} \\ V_{nx} \end{bmatrix} = \left[V_{x_1} V_{x_2} \ldots V_{x_n} \right] = n \times n \text{ square matrix.}$$

The i, j element of V_x is $\dfrac{\partial V_i}{\partial x_j}$.

Downloaded 04 May 2010 to 171.66.16.28. Redistribution subject to ASME license or copyright; see http://www.asme.org/terms/Terms_Use.cfm

W.-S. Lee
Assistant Professor,
Department of Applied Chemistry,
Chung-Cheng Institute of Technology,
Ta-Hsi, Tao Yuan 33509, Taiwan

C.-W. Park[1]
Associate Professor,

Department of Chemical Engineering,
University of Florida,
Gainesville, FL 32611

Stability of a Bicomponent Fiber Spinning Flow

Draw resonance instability in a bicomponent fiber spinning flow is investigated using a model in which a Newtonian and an upper-convected Maxwell fluid are the core and skin layers, respectively. This model is to consider a situation where the two fluids have very different extensional rheology. The results indicate a significant influence of the viscoelastic skin layer on the overall flow mechanics even when its relative flow rate is small. It is also predicted that under certain conditions the stability of the bicomponent fiber can be maintained to a higher draw ratio than obtainable with either fluids individually.

1 Introduction

When polymer melts are subjected to a fast drawing process such as fiber spinning, extrusion coating, or film casting, a "draw resonance" instability is often encountered which is characterized by a sustained oscillation in the fiber radius (or film thickness). This instability occurs when the draw ratio, which is the ratio of the final to initial velocities (or the take-up to extrusion velocities), is greater than a certain critical value.

Due to its practical importance draw resonance has been studied extensively during the past several decades (Denn, 1980; Mewis and Petrie, 1987). A theory of draw resonance was first given by Kase and Matsuo (1967) and by Pearson and Matovich (1969). These analyses were for an isothermal spinning of a Newtonian fluid in the absence of inertia, gravity, and surface tension effects, and predicted a critical draw ratio of 20.21. Subsequently, the theory was extended to include the influence of inertia, gravity, and surface tension predicting that inertia and gravity have a stabilizing effect whereas surface tension has the opposite effect (Chang et al., 1981; Schultz and Davis, 1984).

A similar analysis was also applied to non-Newtonian fluids to account for the shear thinning and viscoelastic behaviors of polymeric fluids (Denn et al., 1975; Fisher and Denn, 1976). It is generally agreed that the shear thinning behavior destabilizes the fiber whereas the viscoelasticity stabilizes. Despite many simplifying assumptions, theoretical predictions have shown a reasonable agreement with many experimental observations (Donnelly and Weinberger, 1975; Chang and Denn, 1979; Demay and Agassant, 1985).

All these investigations are for a "single-phase" flow, and little attention has been given to a "multiphase" flow. A multiphase flow refers to a flow situation of a coextrusion process in which more than one polymer is processed at the same time, forming composite materials such as multilayer films or cladded fibers (e.g., optical fibers). Since the characteristics of draw resonance depend on the fluid rheology, an interesting flow situation arises in a coextrusion process when the rheological properties of the constituent materials are quite different from one another.

An example may be the coextrusion of a linear low-density polyethylene and a low-density polyethylene. The former is known to be very prone to draw resonance whereas the latter is not. The spinability of a low-density polyethylene is typically limited by the fracture of the fiber as the stress in the fiber may exceed the cohesive strength of the material (Ziabicki, 1976). The difference in their stability behaviors result from the fundamental differences in their rheological properties (Chang and Lodge, 1972; Minoshima and White, 1986). If these two materials are coextruded, the overall flow mechanics may be determined by the competing influence of the two materials.

In this work we analyze the characteristics of a concentric bicomponent flow in which a Newtonian and an upper-convected Maxwell (UCM) fluid are the core and skin layers, respectively. The UCM model, which has a single relaxation time and a constant viscosity, provides a first approximation to elastic phenomena as it shows significant extension hardening behavior. Thus, this bicomponent flow corresponds to a situation in which one fluid is readily extensible whereas the other can be highly resistant to extension due to viscoelasticity. We assume that the flow is isothermal and the effects of inertia, gravity, and surface tension are negligible. The major emphasis is thereby given to investigating the competing influence of viscous and viscoelastic forces on the overall flow mechanics.

[1] To whom all correspondence should be addressed.

Contributed by the Applied Mechanics Division of THE AMERICAN SOCIETY OF MECHANICAL ENGINEERS for publication in the ASME JOURNAL OF APPLIED MECHANICS.

Discussion on this paper should be addressed to the Technical Editor, Professor Lewis T. Wheeler, Department of Mechanical Engineering, University of Houston, Houston, TX 77204-4792, and will be accepted until four months after final publication of the paper itself in the ASME JOURNAL OF APPLIED MECHANICS.

Manuscript received by the ASME Applied Mechanics Division, Aug. 16, 1993; final revision, Mar. 21, 1994. Associate Technical Editor: T. R. Akylas.

Copyright © 1995 by ASME

Downloaded 04 May 2010 to 171.66.16.28. Redistribution subject to ASME license or copyright; see http://www.asme.org/terms/Terms_Use.cfm

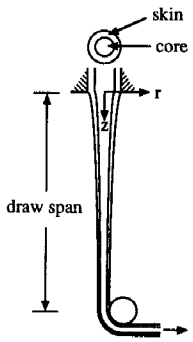

Fig. 1 A schematic of a bicomponent coextrusion fiber spinning (Core: a Newtonian fluid, Skin: an Upper-Convected Maxwell fluid)

2 Time-Dependent Governing Equations

An important aspect of a fiber spinning flow is that the rate of change of the fiber radius along the draw span is very small (Fig. 1). Consequently, one-dimensional approximation is applicable in which the flow field is assumed to be independent of the radial coordinate. This approximation is not valid in the immediate vicinity of the die exit (or the orifice) where the extrudate swell occurs. The extrudate swell, however, is confined to a very short region within about two radii from the die exit. Thus, the exclusion of the extrudate swell region may not be a serious limitation of the present analysis unless the disturbance wavelength is comparable to the fiber radius. The one-dimensional representation of the fiber spinning flow has been the common approach of most investigations to date, and its validity has been proven by numerical analyses (Fisher et al., 1980; Keunings et al., 1983).

A systematic derivation of the one-dimensional equations was given by Schultz and Davis (1982) for a steady Newtonian flow by means of an asymptotic expansion in a small parameter ϵ which is the ratio of the radial to axial characteristic length scales. The analysis was extended later to a viscoelastic fluid by Schultz (1987) and a similar approach has been applied recently to the bicomponent flow by Park (1990).

As given schematically in Fig. 1, we consider an isothermal concentric flow in which the core and skin layers are a Newtonian and a UCM fluid, respectively. In the absence of inertia, gravity, and surface tension effects, the bicomponent flow can be represented by the following one-dimensional equations:

$$\frac{\partial A}{\partial t} + \frac{\partial}{\partial z}(Aw) = 0 \tag{1}$$

$$\frac{\partial}{\partial z}\left[fA\left\{(\tau_{zz} - \tau_{rr}) - \frac{1}{2}(\tau_{\theta\theta} - \tau_{rr})\right\} + 3(1-f)GMA\frac{\partial w}{\partial z}\right] = 0 \tag{2}$$

$$\tau_{zz} + \mathrm{De}\left(\frac{\partial \tau_{zz}}{\partial t} + w\frac{\partial \tau_{zz}}{\partial z} - 2\tau_{zz}\frac{\partial w}{\partial z}\right) = 2G\frac{\partial w}{\partial z} \tag{3}$$

$$\tau_{ij} + \mathrm{De}\left(\frac{\partial \tau_{ij}}{\partial t} + w\frac{\partial \tau_{ij}}{\partial z} + \tau_{ij}\frac{\partial w}{\partial z}\right) = -G\frac{\partial w}{\partial z}\ (ij = rr \text{ or } \theta\theta). \tag{4}$$

The first two equations are the continuity and axial momentum balance, and the rest are the normal components of the constitutive equation for the skin layer. Here A is the total cross-sectional area of the fiber; w is the axial velocity; τ_{zz}, τ_{rr}, and $\tau_{\theta\theta}$ are the axial, radial, and circumferential normal stresses in the skin layer, respectively. Readers may refer to Park (1990) for a rigorous derivation of the one-dimensional Eqs. (1)–(4).

The cross-sectional area A and axial velocity w have been scaled by their values at the die exit A_o and w_o, respectively. The axial distance z and time t have been scaled by the draw span L and the process characteristic time L/w_o. The extra normal stress τ has been scaled on F/A_o, where F is the draw force applied at the take-up $z = 1$. The dimensionless groups that appear in the governing equations are defined as

$$\mathrm{De} = \frac{\lambda w_o}{L}, \quad M = \frac{\mu_c}{\mu_s}, \quad G = \frac{\mu_s A_o w_o}{FL}, \quad f = \frac{Q_s}{Q_T}. \tag{5a,b,c,d}$$

Here λ is the time constant of the upper-convected Maxwell fluid; μ_c and μ_s are the shear viscosities of the core and skin layers; Q_s and Q_T are the skin layer flow rate and the total flow rate, respectively. Deborah number De represents the ratio of the material to process characteristic times. G is the dimensionless reciprocal draw force and f the flow rate fraction of the skin layer which is assumed to be independent of the axial coordinate z.

Summation of all terms in the square bracket of Eq. (2) represents the axial force in the fiber. Thus, the axial momentum equation implies that the total axial force in the fiber is constant along the flow direction. The two terms in the curly bracket of the equation correspond to the counterbalancing axial force by the viscoelastic skin layer whereas the last term is that by the Newtonian core. The difference between the circumferential and radial normal stresses in Eq. (2) (i.e., $\tau_{\theta\theta} - \tau_{rr}$) accounts for the influence of hoop stress resulting from the concentric core-skin structure of the bicomponent flow. Although $\tau_{\theta\theta}$ and τ_{rr} are described by the same differential Eq. (4), they are not necessarily the same since they may have a different boundary condition at $z = 0$.

If the skin layer flow rate fraction f is set to 0, Eq. (2) is reduced to the one for a Newtonian single-phase flow. If $f = 1$, on the other hand, the equation for the spinning of an upper-convected Maxwell fluid is recovered. If De = 0 (i.e., if both core and skin layers are Newtonian fluids but with different viscosities), Eq. (2) is again reduced to the one for a single-phase Newtonian flow regardless of f and M. It suggests that the flow mechanics of the coextrusion spinning of two Newtonian fluids is not affected by the viscosity differences of the core and skin layers.

3 Boundary Conditions

Since the cross-sectional area and axial velocity have been scaled by their values at the die exit, the dimensionless A and w are unity at $z = 0$. At the take-up (i.e., at $z = 1$), either the axial velocity or the axial force may be specified as constant. It is known by Schultz and Davis (1984) that unlike the constant velocity condition, the constant axial force at $z = 1$ results in unconditional stability for a single-phase flow. We expect that this will also be the case for a bicomponent flow. Thus, the constant velocity condition may be more interesting to consider. Furthermore, in a typical industrial operation the velocity at the take-up is held constant. Therefore, only the constant velocity condition is considered in the present analysis:

$$w(0,t) = 1, \quad w(1,t) = Dr, \quad A(0,t) = 1. \tag{6a,b,c}$$

Here Dr is a constant called "draw ratio" which is the ratio of the take-up velocity to the extrusion velocity (i.e., $w(1, t)/w(0, t)$). A prescribed value of Dr is obtained by adjusting the draw force, $1/G$.

An underlying assumption in specifying these velocity con-

Downloaded 04 May 2010 to 171.66.16.28. Redistribution subject to ASME license or copyright; see http://www.asme.org/terms/Terms_Use.cfm

ditions is that no slip occurs at the interface between the two fluids; that is, the axial velocity is uniform over the entire cross-section of the fiber. It should be noted, however, that the axial stress is not necessarily continuous across the fluid-fluid interface although it is uniform within each layer. As mentioned previously, the two terms in the curly bracket of Eq. (2) represent the axial tension born by the viscoelastic skin layer whereas the last term is that in the Newtonian core. Unless the draw ratio or the Deborah number is very small, the axial tension in the viscoelastic skin layer is much greater than that in the Newtonian core due to the significant influence of viscoelasticity; that is, most of the axial force applied to the bicomponent fiber is counterbalanced by the skin layer.

In addition to the above boundary conditions, the stress state of the viscoelastic skin layer at $z = 0$ needs to be specified. The initial stress condition accounts for the strain history of the viscoelastic fluid to that point, and we assume that

$$\tau_{zz} = t_o, \quad \tau_{rr} = t_o - 1,$$

$$\tau_{\theta\theta} = \tau_{rr} \quad \text{at } z = 0. \qquad (7a,b,c)$$

Here t_o is a constant which will be specified later. Although this choice is rather arbitrary, the results indicate that the flow mechanics is insensitive to the initial stress condition. Thus, this arbitrary assignment of the initial stress may not seriously diminish the generality of the present analysis. It has been well established that single-phase fiber spinning flows are also insensitive to initial stress condition (Denn et al., 1975; Gupta et al., 1986).

For a single-phase flow of a UCM fluid (i.e., $f = 1$), specification of τ_{rr} at $z = 0$ is not necessary since its value is determined automatically as $\tau_{zz} - 1$ by the axial force balance once τ_{zz} at $z = 0$ is given. Furthermore, the boundedness of isotropic pressure in the fiber requires that $\tau_{\theta\theta} = \tau_{rr}$ (Park, 1990). In case of a bicomponent flow, however, the initial value of all three normal stresses should be specified. Although τ_{rr} and $\tau_{\theta\theta}$ may be specified independently of τ_{zz}, we have chosen $\tau_{rr} = t_o - 1$ and $\tau_{\theta\theta} = \tau_{rr}$. These τ_{rr} and $\tau_{\theta\theta}$ correspond to the initial stress state of the single-phase flow of a UCM fluid (i.e., $f = 1$) with $\tau_{zz} = t_o$ at $z = 0$. Thus, the present assignment is equivalent to assuming that the skin-layer material experiences the same strain history before it reaches the die exit ($z = 0$) regardless of its flow rate fraction f.

4 Steady-State Solution

The steady solution to system (1)–(7c) is the base state of the bicomponent flow for a stability analysis, and must be determined numerically. Since the solution procedure is straightforward, we omit the details and provide only the results which were obtained using a fourth-order Runge-Kutta method. As pointed out previously, the major interest is in investigating the competing influence of the viscous force of the core and the viscoelastic force of the skin layer. Thus, the shear viscosity ratio M was fixed as unity for all calculations while the flow rate fraction f and Deborah number De of the skin layer were varied.

In Fig. 2, the axial velocity profiles are given for various values of f when De = 0.024. It is known that the velocity profile of a Newtonian fluid is exponential whereas that of a UCM fluid is near linear when the viscoelasticity effect is significant (Denn et al., 1975). Figure 2 indicates that the bicomponent flow follows a similar trend in which the velocity profile changes from an exponential to a linear shape with increasing f. For these results the initial axial stress t_o was specified as 10.

We have repeated the calculation using various values of

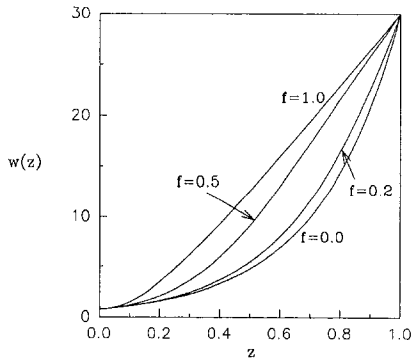

Fig. 2 Axial velocity profiles (Dr = 30, De = 0.024, M = 1.0, t_o = 10)

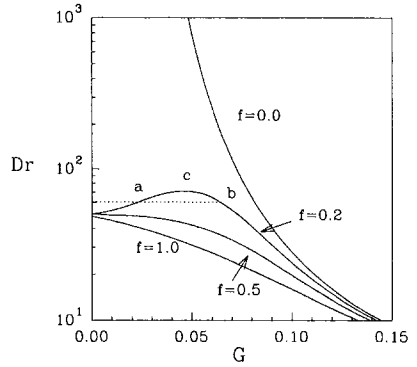

Fig. 3 Draw ratio as a function of reciprocal axial force (De = 0.024, t_o = 10)

t_o ranging from 1 to 100. While the initial value of the axial stress t_o is shown to affect the stress profile up to about ten percent of the draw span from the die exit, its influence on the velocity profile is negligible even in the region near the origin. We have also varied the initial values of the radial and circumferential stresses, and the results indicate that their influence on the velocity profile is also negligible. Furthermore, it is shown that the initial difference between τ_{rr} and $\tau_{\theta\theta}$ decreases rapidly to zero within a few percent of the draw span indicating negligible effect of hoop stress. These results suggest that the initial stress condition has only an insignificant effect on the overall flow mechanics and an arbitrary assignment of it does not seriously affect the results of the analysis. This result is consistent with the findings of Schultz (1987) for a single-phase viscoelastic fluid that the differences between τ_{rr} and $\tau_{\theta\theta}$ due to boundary conditions are restricted to the boundary region near the die exit.

In Fig. 3, the draw ratio Dr is given as a function of the reciprocal draw force G. If $f = 0.0$ (i.e., a Newtonian single-phase flow), Dr increases exponentially with decreasing G since a Newtonian fluid can be stretched indefinitely as the draw force is increased. A UCM fluid, on the other hand, cannot be stretched indefinitely since the draw force becomes unbounded when the draw ratio reaches a certain finite value. The maximum obtainable draw ratio decreases with increasing De, and its value is about 40 when De = 0.024 according to the asymptotic theory (Park, 1990).

In a single-phase flow, the draw ratio increases monotonically with the draw force whether the fluid is a Newtonian or an upper-convected Maxwell fluid (i.e., $f = 0.0$ or 1.0). The relationship between Dr and G for a bicomponent flow, however, is not necessarily monotonic as indicated in Fig. 3. When De = 0.024, the curve for $f = 0.5$ follows the monotonic trend of a single-phase UCM fluid approaching $Dr = 41$ as $G \to 0$. When $f = 0.2$, however, Dr reaches a maximum value of about 62 before the infinite-stress asymptote of 42 is

Downloaded 04 May 2010 to 171.66.16.28. Redistribution subject to ASME license or copyright; see http://www.asme.org/terms/Terms_Use.cfm

approached. Thus, when Dr is between 42 and 62, there exist two steady-state solutions for $f = 0.2$ (e.g., points a and b in Fig. 3).

The existence of the maximum draw ratio at a finite G for a small f may be due to the competing influence of the viscous and viscoelastic forces of the core and skin-layer. When the draw ratio is small, the viscous force dominates the flow mechanics whereas the viscoelastic force does when the draw ratio is large. Thus, a transition may occur from a viscous force dominant mode to a viscoelastic force dominant mode as the draw force (or draw ratio) is increased gradually. For a relatively large value of f (e.g., $f = 0.5$), the transition may occur at a draw ratio smaller than the infinite-stress asymptote. Consequently, Dr increases monotonically with decreasing G. If f is small (e.g., $f = 0.2$), on the other hand, the viscous force is dominant up to a draw ratio much larger than the asymptotic value. As the draw force is further increased, the viscoelastic force finally becomes dominant acting against further stretching of the fluid resulting in a maximum Dr at a finite value of G (point c in Fig. 3).

Without a formal stability analysis we may speculate that the low-G branch solution (i.e., the portion of the $f = 0.2$ curve where $G < 0.05$ including point a) is unstable since it is apparently nonphysical for the draw ratio to decrease with increasing draw force (i.e., decreasing G). On the other hand, considering the fact that a Newtonian single-phase flow is unstable when $Dr > 20.21$ whereas a UCM fluid can be always stable if De is large enough (Fisher and Denn, 1976), the high-G branch solution may or may not be stable depending on the value of De. If the entire high-G branch happens to be stable under a certain condition, it may have an interesting implication in that the highest draw ratio for a stable bicomponent flow can be larger than those obtainable individually with each fluids. In Section 6, the stability of the steady solutions is investigated through a linear stability analysis.

5 Coextrusion Versus Spinning of a Bicomponent Mixture

It has been described previously that the hoop stress has a negligible influence on the overall mechanics of the bicomponent flow. In the absence of hoop stress effect (i.e., $\tau_{rr} = \tau_{\theta\theta}$ for all z), the axial momentum Eq. (2) is reduced to

$$\frac{\partial}{\partial z}\left[fA(\tau_{zz} - \tau_{rr}) + 3(1-f)GMA\frac{\partial w}{\partial z}\right] = 0. \quad (8)$$

It is interesting to note that this equation is equivalent to the one for a single-phase spinning of an upper-convected Jeffreys fluid (or Oldroyd fluid B) which may represent a UCM fluid solution in a viscous Newtonian solvent. Using the same scalings as in Eqs. (1)–(5), the dimensionless axial momentum balance for the steady spinning of an upper-convected Jeffreys fluid is given as (Gupta et al., 1986; Phan-Thien, 1987; Bechtel et al., 1992):

$$\frac{d}{dz}\left[A(\tau_{zz}^p - \tau_{rr}^p) + 3GMA\frac{dw}{dz}\right] = 0 \quad (9)$$

Here the superscript p indicates the stress contribution from "polymer." The dimensionless groups G and M in the above equations are the same as those in (2) with μ_c and μ_s replaced by μ^s and μ^p, respectively indicating the shear viscosities of "solvent" and "polymer" instead of "core" and "skin". If the polymer and solvent shear viscosities are rescaled as $f\mu^p$ and $(1-f)\mu^s$, respectively, Eq. (9) becomes exactly the same as (8). This striking similarity implies that the spinning characteristics of a bicomponent fiber may be very similar to those of an intimate mixture of the two components.

In the absence of the hoop stress term, the same result is obtained whether the UCM fluid is the core or the skin layer. Furthermore, the applicability of Eq. (8) is not limited to a two-layer (i.e., core skin) flow. As long as the fiber consists of the two materials (i.e., a Newtonian and a UCM fluid), (8) should be applicable to multilayer fibers with the two materials alternating. If the fiber contains an infinite number of layers, it may be equivalent to an intimate mixture of the two materials. Therefore, the resemblance between Eq. (8) and (9) may not be surprising. Such resemblance between the coextrusion spinning and the spinning of polymer blends may also occur in other fast drawing processes such as extrusion coating or film casting. It is interesting to point out that the drawing characteristics of polymer blends are in fact observed to be similar to those of coextrusion in those industrial operations.

Multiple steady solutions similar to those in Fig. 3 have been also noted for a single-component spinning of an upper-convected Jeffreys fluid (Mackay and Petrie, 1992). To our knowledge, however, a stability analysis for such a flow is not available yet. Thus, the linear stability analysis presented in the following section should be also relevant to the single-component spinning of an upper-convected Jeffreys fluid.

6 Linear Stability Analysis

The stability of a steady solution to infinitesimal disturbances is determined by followng the standard procedure of the perturbation analysis in which solutions of the following form are sought:

$$A(t,z) = A^{ss}(z)\{1 + \alpha(z)e^{\lambda t}\} \quad (10)$$

$$w(t,z) = w^{ss}(z)\{1 + \beta(z)e^{\lambda t}\} \quad (11)$$

$$\tau_{zz}(t,z) = \tau_{zz}^{ss}(z)\{1 + \gamma(z)e^{\lambda t}\} \quad (12)$$

$$T(t,z) = T^{ss}(z)\{1 + \delta(z)e^{\lambda t}\} \quad (13)$$

Here the superscript ss denotes the steady-state (or base state). The new variable T, which is defined as $\tau_{zz} - \tau_{rr}$, is introduced since it is more convenient to work with than τ_{rr} (Fisher and Denn, 1976). The perturbation functions α, β, γ, and δ are assumed to be very small, and the real part of λ, which is the eigenvalue of a normal mode, determines the stability of the steady solution.

By substituting (10)–(13) into the system partial differential Eqs. (1)–(4) and linearizing the perturbation, the following homogeneous ordinary differential equations are derived:

$$w^{ss}(\alpha' + \beta') = -\lambda\alpha \quad (14)$$

$$\begin{aligned}3(1-f)GM\Big[&(w^{ss})^2\beta'' + w^{ss}(w^{ss})'\beta' \\ &+\{w^{ss}(w^{ss})'' - \{(w^{ss})'\}^2\}\beta\Big] = \big[f\{T^{ss}(w^{ss})' \\ &-(T^{ss})'w^{ss}\} - 3(1-f)GM\{w^{ss}(w^{ss})'' - \{(w^{ss})'\}^2\}\big]\alpha \\ &-\{fT^{ss}w^{ss} + 3(1-f)GMw^{ss}(w^{ss})'\}\alpha' \\ &+f\{T^{ss}(w^{ss})' - (T^{ss})'w^{ss}\}\delta - (fT^{ss}w^{ss})\delta' \quad (15)\end{aligned}$$

$$\begin{aligned}\big[&\mathrm{De}\{(\tau_{zz}^{ss})'w^{ss} - 2\tau_{zz}^{ss}(w^{ss})'\} \\ &-2G(w^{ss})'\big]\beta - 2w^{ss}(\mathrm{De}\,\tau_{zz}^{ss} + G)\beta' \\ &+\big[\tau_{zz}^{ss} + \mathrm{De}\{(\tau_{zz}^{ss})'w^{ss} - 2\tau_{zz}^{ss}(w^{ss})'\} \\ &+\lambda(\mathrm{De}\,\tau_{zz}^{ss})\big]\gamma + (\mathrm{De}\,w^{ss}\tau_{zz}^{ss})\gamma' = 0 \quad (16)\end{aligned}$$

$$\begin{aligned}\big[&\mathrm{De}\{T^{ss}(w^{ss})' + (T^{ss})'w^{ss}\} \\ &-3(w^{ss})'(\mathrm{De}\,\tau_{zz}^{ss} + G)\big]\beta + w^{ss}\{\mathrm{De}(T^{ss} - 3\tau_{zz}^{ss}) - 3G\} \\ &\times\beta' - \{3\,\mathrm{De}\,\tau_{zz}^{ss}(w^{ss})'\}\gamma + \big[T^{ss} + \mathrm{De}\{T^{ss}(w^{ss})' \\ &+(T^{ss})'w^{ss}\} + \lambda(\mathrm{De}\,T^{ss})\big]\delta + \mathrm{De}\,T^{ss}w^{ss}\delta' = 0. \quad (17)\end{aligned}$$

Downloaded 04 May 2010 to 171.66.16.28. Redistribution subject to ASME license or copyright; see http://www.asme.org/terms/Terms_Use.cfm

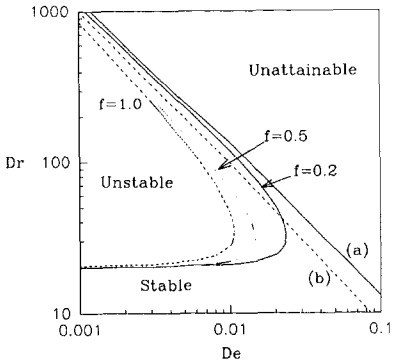

Fig. 4 The dependence of the critical draw ratio on De (Curve a: the maximum *Dr* for *f* = 0.2, curve b: the infinite-stress asymptotic *Dr* for *f* = 1.0)

Here the prime denotes the differentiation with respect to the axial coordinate z. The boundary conditions for the eigensystem follow from (6*a*)–(7*c*):

$$\alpha(0) = \beta(0) = \gamma(0) = \delta(0) = \beta(1) = 0. \quad (18a,b,c,d,e)$$

Equations (14)–(18*e*) constitute an eigenvalue problem for which nontrivial solutions exist only for certain values of λ. If all eigenvalues have negative real parts, the perturbations defined by (10)–(13) decay to zero and consequently, the steady-state solution is stable to infinitesimal disturbances.

Several mathematical approaches may be taken to solve the eigenvalue problem. In the present work, the eigenvalues are determined by reducing the system to an algebraic eigenvalue problem by replacing the spatial derivatives with finite differences (Gelder, 1971; Geyling and Homsy, 1980; Chang et al., 1981). Richardson extrapolation is then used to obtain the limiting value of λ as the number of discretisation points tends to infinity. Through a sequence of such calculations, the critical draw ratio at which the real part of the first (or largest) eigenvalue becomes zero is determined as a function of Deborah number for various f, and the results are shown in Fig. 4.

Figure 4 indicates that the stability characteristics of the bicomponent flow is similar to that of a UCM fluid in which two stable regions (one at a low value of *Dr* and the other at a higher value of *Dr*) exist below a certain critical De. Although the upper stable region may be an artifact of the UCM model which may not be realized in actual spinning flows, the rapid increase in the critical draw ratio near a certain critical De may represent a realistic behavior of viscoelastic fluids at least qualitatively. When $f = 1.0$, the critical De is 0.011 above which the draw resonance is not encountered. With decreasing f from 1.0 to 0.2, the critical De increases from 0.011 to 0.024. Since a Newtonian fluid is unstable when $Dr > 20.21$, this result indicates that the draw resonance of a Newtonian fluid can be suppressed to a higher draw ratio by a coextrusion with a viscoelastic fluid. The stabilizing effect, however, may be realized only when the viscoelastic fluid has a sufficiently large Deborah number beyond the critical value.

While the stabilizing effect of viscoelasticity may be predictable without a detailed analysis, the present result further indicates that the stability of the bicomponent fiber can be sustained to a much higher draw ratio than obtainable with either fluids individually. In Fig. 4 the maximum attainable draw ratios for $f = 0.2$ and $f = 1.0$ are also shown as the curve (a) and (b), respectively. The maximum *Dr* curve for $f = 1.0$ corresponds to the infinite-stress asymptote whereas that for $f = 0.2$ is the locus of the maximum points of *Dr* versus G curve (i.e., point c in Fig. 3). When $f = 0.5$, the maximum attainable *Dr* almost coincides with that for $f = 1.0$.

According to the linear stability analysis, the low-G branch solution for $f = 0.2$ described in Fig. 3 is always unstable as expected. The entire high-G branch solution, on the other hand, is stable if De is larger than a certain critical value (which is 0.024 for $f = 0.2$). Thus, the maximum point c in Fig. 4 is accessible in this case; that is, it is possible to obtain a much higher draw ratio with the coextrusion than obtainable with either the UCM or Newtonian fluids if De is larger than the critical value. For example, if a skin layer material is chosen so that De is about 0.024, a stable spinning is possible up to $Dr = 62$ when $f = 0.2$. This draw ratio is much larger than the value which is obtainable with either the core material ($Dr_{max} = 20.21$) or the skin material ($Dr_{max} = 40$) for the same value of De. A similar behavior of an Oldroyd fluid B has been observed previously by Gupta et al. (1986) and Waters and Petrie (1978).

The unbounded stress at a finite value of *Dr* is the typical characteristics of the Maxwellian-type models which may not be realistic quantitatively. However, it is conceivable that the fiber should break above a certain finite stress level (or below a finite value of G in Fig. 3) which may correspond to the cohesive strength of the material. The critical stress beyond which the fiber fracture occurs may appear in Fig. 4 as a monotonically decreasing curve similar to the curve (b), and it must be located below (b). Furthermore, a recent work by Mackay and Petrie (1992) has indicated that the spinning of a FENE-P model shows multiple steady solutions which are similar to those in Fig. 3. A FENE-P (Finitely Extensible Nonlinear Elastic) model, which is known to be useful in predicting the kinematics of extensional flows, allows draw ratios that are much larger than the limiting values of the Maxwellian-type models. Thus, the existence of the maximum *Dr* (point c in Fig. 3) is not simply an unrealistic consequence of the UCM model, and it may be possible for the present prediction to be observed experimentally.

7 Conclusions

The viscoelastic skin layer is found to play a significant role in determining the overall mechanics of the bicomponent flow even when its relative flow rate is small. Thus, the onset of draw resonance of a Newtonian fluid can be delayed to a higher value of draw ratio by the coextrusion. While this stabilizing effect of viscoelasticity is predictable based on previous investigations, an interesting behavior has been also found in that the stability of the bicomponent flow can be maintained to a higher draw ratio than obtainable with either components individually. This prediction may have important practical implications if proven experimentally.

It has been also found that similarities exist in the governing equations for the bicomponent coextrusion fiber spinning and the spinning of a blend of the two components. It implies that the spinning characteristics of a coextruded fiber may be very similar to those of a blend of the two components. The present analysis is for a fiber spinning flow. Nevertheless, the results should be relevant to other fast drawing processes such as extrusion coating or film casting considering the similarities between the mathematical descriptions for these flows.

Acknowledgment

This work was supported by the National Science Foundation (DDM-9101729) and the Electric Power Research Institute (RP8007-16).

Downloaded 04 May 2010 to 171.66.16.28. Redistribution subject to ASME license or copyright; see http://www.asme.org/terms/Terms_Use.cfm

References

Bechtel, S. E., Cao, J. Z., and Forest, M. G., 1992, "Practical Application of a High Order Perturbation Theory for Slender Viscoelastic Jets and Fibers," *Journal of Non-Newtonian Fluid Mechanics*, Vol. 41, pp. 201–273.

Chang, H., and Lodge, A. S., 1972, "Comparison of Rubberlike-Liquid Theory with Stress-Growth Data for Elongation of a Low-Density Branched Polyethylene Melt," *Rheologica Acta*, Vol. 11, pp. 127–129.

Chang, J. C., and Denn, M. M., 1979, "An Experimental Study of Isothermal Spinning of a Newtonian and a Viscoelastic Liquid," *Journal of Non-Newtonian Fluid Mechanics*, Vol. 5, pp. 369–385.

Chang, J. C., Denn, M. M., and Geyling, F. T., 1981, "Effects of Inertia, Surface Tension and Gravity on the Stability of Isothermal Drawing of Newtonian Fluids," *Industrial and Engineering Chemistry Fundamentals*, Vol. 20, pp. 147–149.

Denn, M. M., 1980, "Continuous Drawing of Liquids to form Fibers," *Annual Review of Fluid Mechanics*, Vol. 12, pp. 365–387.

Denn, M. M., Petrie, C. J. S., and Avenas, P., 1975, "Mechanics of Steady Spinning of a Viscoelastic Liquid," *AIChE Journal*, Vol. 21, pp. 791–799.

Donnelly, G. J., and Weinberger, C. B., 1975, "Stability of Isothermal Fiber Spinning of a Newtonian Fluid," *Industrial and Engineering Chemistry Fundamentals*, Vol. 14, pp. 334–337.

Demay, Y., and Agassant, J. F., 1985, "Experimental Study of the Draw Resonance in Fiber Spinning," *Journal of Non-Newtonian Fluid Mechanics*, Vol. 18, pp. 187–198.

Fisher, R. J., and Denn, M. M., 1976, "A Theory of Isothermal Melt Spinning and Draw Resonance," *AIChE Journal*, Vol. 22, pp. 236–246.

Fisher, R. J., Denn, M. M., and Tanner, R. I., 1980, "Initial Profile Development in Melt Spinning," *Industrial and Engineering Chemistry Fundamentals*, Vol. 19, pp. 195–197.

Gelder, D., 1971, "The Stability of Fiber Drawing Processes," *Industrial and Engineering Chemistry Fundamentals*, Vol. 10, pp. 534–535.

Geyling, F. T., and Homsy, G. M., 1980, "Extensional Instabilities of the Glass Fiber Drawing Process," *Glass Technology*, Vol. 21, pp. 95–102.

Gupta, R. K., Puszynski, J., and Sridhar, T., 1986, "Steady Spinning of the Oldroyd Fluid B," *Journal of Non-Newtonian Fluid Mechanics*, Vol. 21, pp. 99–113.

Kase, S., and Matsuo, T., 1967, "Study on Melt Spinning: II. Steady State and Transient Solutions of Fundamental Equations Compared with Experimental Results," *Journal of Applied Polymer Science*, Vol. 11, pp. 251–287.

Keunings, R., Crochet, M. J., and Denn, M. M., 1983, "Profile Development in Continuous Drawing of Viscoelastic Liquids," *Industrial and Engineering Chemistry Fundamentals*, Vol. 22, pp. 347–355.

Mackay, M. E., and Petrie, C. J. S., 1992, "An Unusual Prediction Utilizing FENE-P Rheological Models in the Fiber Spinning Problem," *Journal of Non-Newtonian Fluid Mechanics*, Vol. 41, pp. 365–372.

Mewis, J., and Petrie, C. J. S., 1987, "Hydrodynamics of Spinning Polymers," *Encyclopedia of Fluid Mechanics*, Vol. 6, N. P. Cheremisinoff, ed., Gulf Publishing, Houston, pp. 111–139.

Minoshima, W., and White, J. L., 1986, "A Comparative Experimental Study of the Isothermal Shear and Uniaxial Elongational Rheological Properties of Low Density, High Density and Linear Low Density Polyethylenes," *Journal of Non-Newtonian Fluid Mechanics*, Vol. 19, pp. 215–274.

Park, C.-W., 1990, "Extensional Flow of a Two-Phase Fiber," *AIChE Journal*, Vol. 30, pp. 197–206.

Pearson, J. R. A., and Matovich, M. A., 1969, "Spinning a Molten Threadline Stability," *Industrial and Engineering Chemistry Fundamentals*, Vol. 8, pp. 605–609.

Phan-Thien, N., 1987, "On the Asymptotic Behavior of an Oldroyd Fluid B in Steady Spinning Flow," *Journal of Non-Newtonian Fluid Mechanics*, Vol. 25, pp. 129–136.

Schultz, W. W., 1987, "Slender Viscoelastic Fiber Flow," *Journal of Rheology*, Vol. 31, pp. 733–750.

Schultz, W. W., and Davis, S. H., 1982, "One-Dimensional Liquid Fibers," *Journal of Rheology*, Vol. 26, pp. 331–345.

Schultz, W. W., and Davis, S. H., 1984, "Effects of Boundary Conditions on the Stability of Slender Viscous Fibers," ASME JOURNAL OF APPLIED MECHANICS, Vol. 52, pp. 1–5.

Waters, N. D., and Petrie, C. J. S., 1978, "The Existence of Solutions for a Stretching Jet," *Journal of Non-Newtonian Fluid Mechanics*, Vol. 4, pp. 161–166.

Ziabicki, A., 1976, *Fundamentals of Fibre Formation*, John Wiley and Sons, New York, pp. 181–185.

Downloaded 04 May 2010 to 171.66.16.28. Redistribution subject to ASME license or copyright; see http://www.asme.org/terms/Terms_Use.cfm

M. A. Awal
Graduate Research Assistant.

T. Kundu[1]
Professor,
Mem. ASME.

Department of Civil Engineering
and Engineering Mechanics,
University of Arizona,
Tucson, AZ 85721

$V(z)$ Curve Synthesis Using Two Ultrasonic Transducers

Traditionally V(z) *curves are generated by acoustic microscopes. However, because of the high costs of the commercially available acoustic microscopes, their use is rather limited. In this paper it is shown how* V(z) *curves, which contain quantitative information about the material under inspection, can be generated using two ultrasonic transducers instead of an acoustic microscope. A theoretical analysis is given to synthesize* V(z) *curves of orthotropic plates by this technique. A basic mechanics problem of the reflection of plane waves by an orthotropic plate immersed in a fluid is solved for this purpose. Theoretically synthesized* V(z) *values are compared with experimental results.*

Introduction

In last two decades acoustic microscopes have been used for different purposes, for subsurface imaging as well as for quantitative measurements. Material scientists used this apparatus for measuring velocity and attenuation of surface waves in a material in an attempt to obtain the elastic properties of the material (Kushibiki et al., 1982a, 1983) and to measure material anisotropy (Kushibiki et al., 1982b, 1983). Using this instrument, scientists also measured the coating thickness and coating properties in a coated solid (Weglein, 1980; Weglein and Mal, 1991); detected internal defects and cracks in different types of materials (Yamanaka et al., 1982; Weaver et al., 1985; Ishikawa et al., 1989; Ahn and Achenbach, 1991; Gomez et al., 1991); detected delaminations in electronic circuit boards and integrated circuit (IC) chips (Miller, 1985; Semmens and Kessler, 1989; Ranasinghe et al., 1990); obtained residual stress patterns (Liang et al., 1983); and measured rate of surface hardening (Yamanaka et al., 1985) and surface roughness (Gopalan et al., 1989). Biologists used this instrument to determine elastic properties of living and dead cells (Hildebrand et al., 1984; Litniewski and Bereiter-Hahn, 1990; Kundu et al., 1991, 1992) and acoustic properties of arteries (Lockwood et al., 1990), and investigators in dielectric materials research used it to detect the inhomogeneity in piezoelectric wafers (Chubachi, 1989).

Although the concept of ultrasonic quantitative measurements was developed long back (Dunn and Fry, 1959) the modern day application of acoustic microscopes in quantitative measurements started after the work of Lemon and Quate (1972) with point focus beams for isotropic materials and that of Kushibiki and Chubachi (1985) with line focus beams for anisotropic materials. The quantitative measurements are done by constructing and analyzing the $V(z)$ curve, also known as the acoustic material signature or AMS of the specimen (Kundu et al., 1985; Chubachi, 1989). This curve is synthesized by varying the distance (z) between the focal point of the lens and the specimen surface and plotting the variation of the voltage (V), generated by the acoustic microscope.

In this paper the $V(z)$ curve is synthesized by two ultrasonic transducers in a pitch-catch arrangement instead of an acoustic microscope. Experimental results are compared with theoretical predictions. It is shown here that the details of the $V(z)$ curve thus generated depend on the material properties of the specimen as one should expect.

Atalar and Koymen (1986, 1987) generated $V(z)$ curves of step reflectors using ultrasonic transducers instead of conventional acoustic microscope lens in a different arrangement. They used axicons to focus waves parallel to the liquid-solid interface. In their arrangement z was measured in the direction parallel to the liquid-solid interface.

Experimental Setup

Schematic diagram of the transmitter-receiver arrangement is shown in Fig. 1. As shown in this figure two ultrasonic transducers are used, one as a transmitter and the second one as a receiver, in the pitch-catch arrangement. Each transducer has a cylindrical concave front face with a radius of curvature (R_c) of 5 cm and width 1 cm. These transducers can generate cylindrically focussed acoustic beam pulses of frequency varying from 0.25 to 2.5 MHz. Cylindrical shapes are needed to measure direction dependent material properties in anisotropic solids (Kushibiki and Chubachi, 1985). The transmitter transmits acoustic signal in the form of a single pulse or a group of pulses into the water. This

[1]To whom all correspondence should be addressed.

Contributed by the Applied Mechanics Division of the THE AMERICAN SOCIETY OF MECHANICAL ENGINEERS for publication in the ASME JOURNAL OF APPLIED MECHANICS.

Discussion on this paper should be addressed to the Technical Editor, Professor Lewis T. Wheeler, Department of Mechanical Engineering, University of Houston, Houston, TX 77204-4792, and will be accepted until four months after final publication of the paper itself in the ASME JOURNAL OF APPLIED MECHANICS.

Manuscript received by the ASME Applied Mechanics Division, Sept. 7, 1993; final revision, Mar. 24, 1994. Associate Technical Editor: I. M. Daniel.

Copyright © 1995 by ASME

Downloaded 04 May 2010 to 171.66.16.28. Redistribution subject to ASME license or copyright; see http://www.asme.org/terms/Terms_Use.cfm

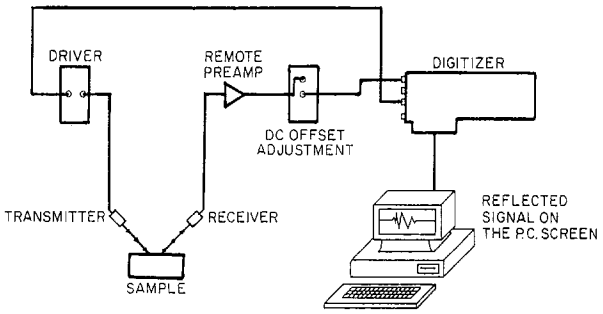

Fig. 1 Experimental set-up to generate $V(z)$ curve using two ultrasonic transducers

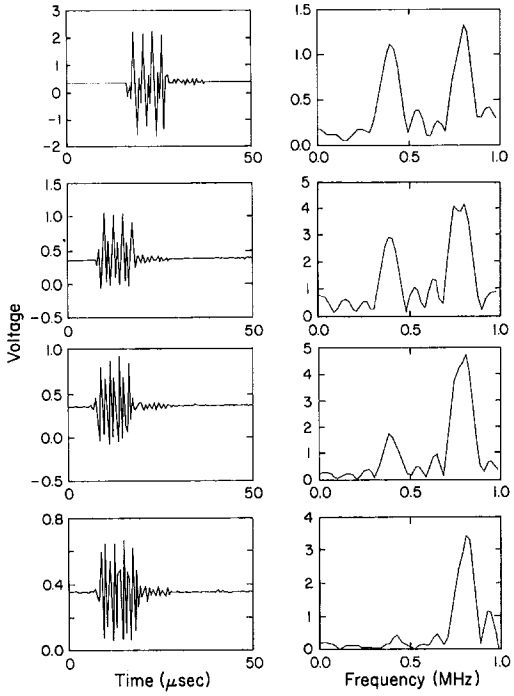

Fig. 2 Time histories (left column) and spectra (right column) of reflected signals for the aluminum plate reflector. Four rows are for $z = 0.1$, 0.4, 0.6, and 0.9 in. z is minimum at the top row and maximum at the bottom row.

signal propagates through water and then strikes the specimen. The reflected signal is received by the receiver. If the receiver is positioned such that the specularly reflected beam can reach the receiver, then whenever a leaky wave is generated, the strength of the received signal goes down. However, when the reflecting surface is positioned slightly off focus then the receiver is placed away from the specularly reflected beam and reflected signals become strong when leaky waves are generated. Atalar, Koymen, and Degertekin (1990, 1992) used this principle in their design of the Lamb wave lens.

$V(z)$ Curve Synthesis. $V(z)$ curve or AMS of a specimen can be obtained using this set up by vertically moving the transducers, thus by changing z (distance between the focal line of the transducers and the reflecting surface of the specimen) and generating different reflected signals for different values of z. Then Fourier spectra of these signals are taken. Spectral values over a wide frequency range (0 to 1 MHz) are thus obtained as shown in Fig. 2 for an aluminum plate reflector of thickness 6.35 mm. Time histories and frequency spectra are shown in the left and right columns, respectively. Both transmitters and receivers are set at a 30-deg angle with respect to the vertical axis. The angle will

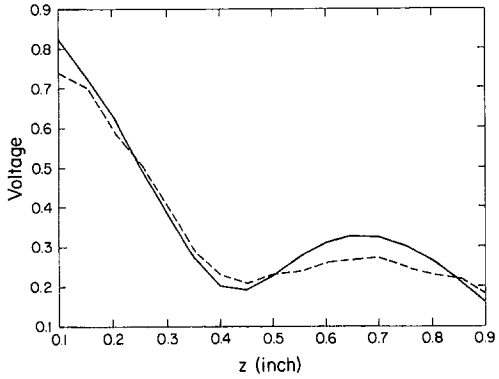

Fig. 3 Theoretical (solid line) and experimental (dotted line) $V(z)$ curves of 6.35-mm thick aluminum plate at 0.8 MHz

be denoted by the term "transducer angle" from now on. Experimental data are obtained for 17 different values of z, starting from $z = 0.1$ in. (2.54 mm) to 0.9 in. (22.86 mm) at an interval of 0.05 in. (1.27 mm). However, in Fig. 2 only four spectra and time histories are shown corresponding to $z =$ 0.1, 0.4, 0.6, and 0.9 in. The reflected signals are multiplied by an amplifying factor by the preamplifier before plotting. Hence, their numerical values do not have any significance. Their relative strength variations, and not their absolute magnitudes, are of interest to us. One can notice that in Fig. 2 two relatively strong peaks are present near 0.4 and 0.8 MHz frequencies. It indicates that surface acoustic wave (SAW) have been generated at these two frequencies for a 30-deg transducer angle. $V(z)$ curves are constructed at these frequency values because at other frequencies the signal may be significantly affected by the noise.

After frequency spectra for different z are obtained, then the spectral values at a specific frequency, say 0.8 MHz, can be plotted against z and thus the $V(z)$ curve is synthesized. Experimentally obtained $V(z)$ curve in this manner at 0.8 MHz is shown by dotted lines in Fig. 3 for the aluminum plate. While plotting the $V(z)$ curve all experimental values have been multiplied by a constant scaling factor to nullify the effect of the preamplifier and to make the signal values numerically closer to the theoretical predictions. The scaling factor is obtained by taking ratios of the theoretical V and the experimental V at three different (maximum, minimum, and central) values of z and then taking the average value.

A similar analysis is carried out after replacing the aluminum plate by a unidirectional graphite-epoxy composite plate of 2-mm thickness. The plate is positioned such that the transmitter, receiver and the fiber direction are all in the same plane. This orientation of the plate will be identified as the 0-deg orientation. For the transducer angle equal to 30 deg the reflected signals, and hence the $V(z)$ curves are found to decay very fast with z. This is probably due to the fact that at 30 deg surface acoustic waves (SAW) are not generated in the composite plate unlike the aluminum plate. Transducer angle is then gradually changed and at 40 deg some interesting variations of the reflected signals with z are obtained possibly due to SAW generation. Figure 4 shows time history and spectral plots at $z = 0.1$, 0.25, 0.4, and 0.6 in. Two peaks near 0.3 and 0.55 MHz indicate SAW generation at these two frequencies. Since the peak near 0.55 MHz shows an interesting behavior of growth and decay $V(z)$ curve at 0.55 MHz is constructed and shown in Fig. 5.

The composite specimen is then rotated by 90-deg so that the straight line connecting the transmitter and the receiver is now perpendicular to the fiber direction. Quick decay of the reflected signals with z for 40-deg transducer angle is observed, indicating the absence of SAW. The transducer angle is then gradually changed and at 50 deg the decay rate

Downloaded 04 May 2010 to 171.66.16.28. Redistribution subject to ASME license or copyright; see http://www.asme.org/terms/Terms_Use.cfm

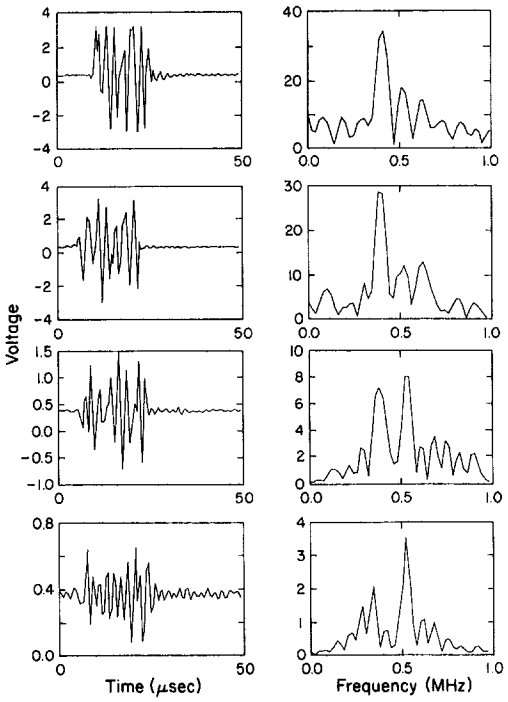

Fig. 4 Same as Fig. 2 but the specimen here is a 2-mm thick graphite-epoxy composite plate in 0-deg orientation and $z = 0.1$, 0.25, 0.4, and 0.6 in.

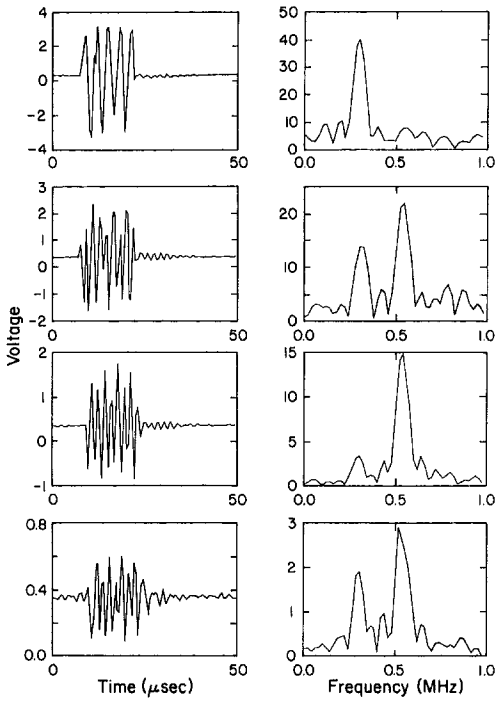

Fig. 6 Same as Fig. 2 but the specimen here is a 2-mm thick graphite-epoxy composite plate in 90-deg orientation and $z = 0.1$, 0.25, 0.4, and 0.6 in.

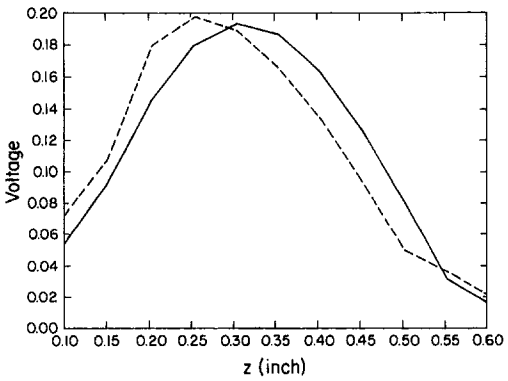

Fig. 5 Theoretical (solid line) and experimental (dotted line) $V(z)$ curves of 2-mm thick graphite-epoxy composite plate in 0-deg orientation of 0.55 MHz

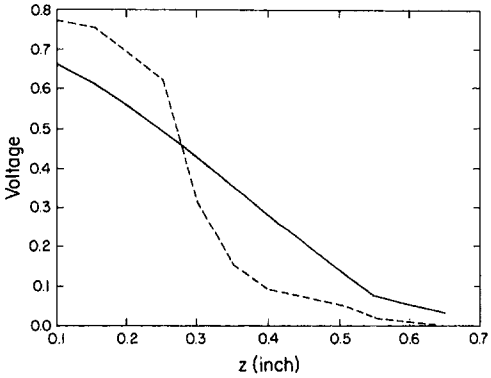

Fig. 7 Theoretical (solid line) and experimental (dotted line) $V(z)$ curves of 2 mm-thick graphite-epoxy composite plate in 90-deg orientation at 0.4 MHz

is found to be comparatively less, as shown in Fig. 6 for $z = 0.1$, 0.25, 0.4, and 0.6 in. The strongest peak is observed at 0.4 MHz and $V(z)$ curve is constructed for this frequency as shown by the dotted line in Fig. 7. Unlike Figs. 3 and 5 in Fig. 7, the $V(z)$ curve monotonically decays. This difference in the $V(z)$ curve trend may be explained in the following manner. For the transducer-receiver arrangements of Figs. 3 and 5 interference between some specular and nonspecular rays occurs (Kundu and Maxfield, 1993) giving rise to constructive and destructive interference, but for Fig. 7, since the transducer angle is large (50 deg), no such interference occurs.

To synthesize these experimental results analytically, a rigorous theoretical analysis must be carried out for orthotropic plate specimens. This analysis is shown in the following section.

Analytical Formulation

In this section mathematical steps for synthesizing AMS of an orthotropic plate specimen are given. Geometry of the problem of our interest is shown in Fig. 8. The line-focus cylindrical transducer (T) generates a converging acoustic beam and part of it, after being specularly or nonspecularly reflected by the specimen surface, strikes the receiver. The reflector specimen is a plate of thickness h. Radius of curva-

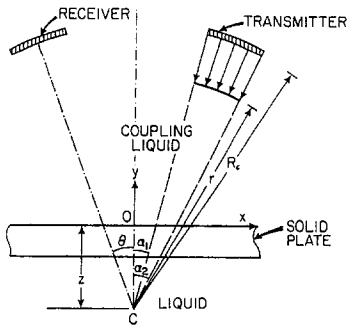

Fig. 8 Problem geometry for the theoretical analysis

Downloaded 04 May 2010 to 171.66.16.28. Redistribution subject to ASME license or copyright; see http://www.asme.org/terms/Terms_Use.cfm

ture of the transducers is R_c. The incident angle of the striking beam varies from a minimum value of α_1 to a maximum value of α_2. To synthesize the AMS, the wave potential of the incident field is first computed. Then by Fourier inversion techniques the reflected field is evaluated. Similar technique was followed by Bertoni and Tamir (1973) to synthesize the reflected field generated by a nonconverging bounded acoustic beam striking a solid isotropic half-space immersed in water. For a converging incident beam, as generated here, the direct Fourier transform of the incident field is very difficult. Hence, the stationary phase method (Jeffreys and Jeffreys, 1950) is adopted to compute the Fourier transform of the incident field in an approximate manner.

Incident Field. The acoustic wave field produced by the line-focus transducer has a cylindrical wave front. From energy consideration one can arrive at the potential expression of this propagating wave at a distance r from the focal point (Fig. 8).

$$\varphi_i = P(x)\sqrt{\frac{R_c}{r}}\exp\left[ik_f(R_c - r)\right] \tag{1}$$

In the above expression the amplitude of the wave generated by the transducer is assumed to be 1. $k_f = \omega/\alpha_f$, ω is the circular frequency of the generated acoustic signal and α_f is the acoustic wave velocity in the coupling fluid. $P(x)$ is the pupil function of the lens, which in the most general case takes into account the nonuniform excitation of the transducer and any aberration and edge diffraction effects. In the simplest case for an ideal situation,

$$\begin{aligned} P(x) &= 1 \quad \text{if } z\tan\alpha_1 \le x \le z\tan\alpha_2 \\ &= 0 \quad \text{if } x < z\tan\alpha_1,\ x > z\tan\alpha_2. \end{aligned} \tag{2}$$

Since r varies along the reflecting surface, the incident wave potential is a function of the horizontal coordinate, x, on the reflecting surface as given below,

$$\varphi_i(x,0) = \frac{P(x)\sqrt{R_c}}{\sqrt[4]{x^2+z^2}}\exp\left[ik_f\left(R_c - \sqrt{x^2+z^2}\right)\right]. \tag{3}$$

Reflected Field. To obtain the reflected field, first the Fourier inversion of Eq. (3) is carried out with respect to x to obtain

$$\varphi_i(k,0) = \sqrt{R_c}\,e^{ik_f R_c}A(k) \tag{4}$$

where

$$A(k) = \int_0^\infty \frac{P(x)\exp\left[ikx - ik_f\sqrt{x^2+z^2}\right]}{\sqrt[4]{x^2+z^2}}dx. \tag{5}$$

Values of $A(k)$ can be obtained approximately by stationary phase method. Kundu (1988) computed similar integrals for converging acoustic beams using stationary phase method. Similar steps are followed here and details are omitted, final results being

$$A(k) = \sqrt{2\pi k_f}\exp\left[-i\left(\eta z + \frac{\pi}{4}\right)\right] \tag{6}$$

where

$$\begin{aligned} \eta &= \sqrt{k_f^2 - k^2} \quad \text{for } |k| \le k_f \\ \eta &= i\sqrt{k^2 - k_f^2} \quad \text{for } |k| \ge k_f \end{aligned} \tag{7}$$

and $P(x_o)$ is equal to 1 for $z.\tan\alpha_1 < x < z.\tan\alpha_2$ or $(k_f.\tan\alpha_1)^2/(1+\tan^2\alpha_1) < k^2 < (k_f\tan\alpha_2)^2/(1+\tan^2\alpha_2)$. $P(x_o)$ is zero beyond these limits and $x_o = kz/\eta$.

The reflected field at any point (x, y) can be obtained by simply multiplying $\phi_i(k,0)$ by the plane wave reflection coefficient $R(k)$ of the reflector and a propagating term of the form $e^{-ikx+i\eta y}$ and then inverting it.

$$\varphi_r(x,y) = \frac{1}{2\pi}\int_{-\infty}^{\infty} R(k)\varphi_i(k,0)e^{i(-kx+\eta y)}dk \tag{8}$$

Computation of $R(k)$. The plane wave potential in the fluid is given by

$$\varphi_f = \left[e^{-i\eta y} + R(k)e^{-i\eta y}\right]e^{-ikx} \tag{9}$$

in the fluid half-space above the plate and

$$\varphi_f = T(k)e^{-ikx - i\eta(y-H)} \tag{10}$$

in the fluid half-space below the plate. Reflection and transmission coefficients are denoted by $R(k)$ and $T(k)$, respectively, and the plate thickness is h. k in the parenthesis means that R and T are functions of the wave number k.

When the vertical plane containing the incident beam coincides with a symmetry direction (0 deg or 90 deg) then the wave field in an orthotropic plate can be expressed in terms of displacements following the steps given in Karim and Kundu (1991) and Awal (1994)

$$u = \left[A_1e^{-ip_1y} + A_2e^{-ip_2y} + A_3e^{-ip_3y} + A_4e^{-ip_4y}\right]e^{-ikx} \tag{11}$$

$$v = \left[A_1S_1e^{-ip_1y} + A_2S_2e^{-ip_2y} + A_3S_3e^{-ip_3y} + A_4S_4e^{-ip_4y}\right]e^{-ikx} \tag{12}$$

where u and v are the displacements along the x and y directions, respectively. p_j $(j = 1, 2, 3, 4)$ are the four roots of the following fourth-order algebraic equation of p.

$$\begin{aligned} C_{22}C_{66}p^4 + p^2\left[k^2\left(C_{11}C_{22} - C_{12}^2 - 2C_{12}C_{66}\right)\right. \\ \left. - \rho\omega^2(C_{22} + C_{66})\right] \\ + \rho^2\omega^4 - k^2\rho\omega^2(C_{11} + C_{66}) + k^4C_{11}C_{66} = 0 \end{aligned} \tag{13}$$

and

$$S_j = \frac{\rho\omega^2 - k^2C_{11} - C_{66}p_j^2}{kp_j(C_{12} + C_{66})} \tag{14}$$

where C_{ij}, $(i, j = 1, 2 \text{ or } 6)$ relate the stress and strain of an orthotropic material in the following manner:

$$\sigma_i = C_{ij}\epsilon_j \tag{15}$$

where σ_1 and σ_2 represent normal stresses in the x and y directions and σ_6 is the shear stress in the xy-plane. Similarly, normal and shear strains are also denoted by the same subscripts, 1, 2, and 6. Repeated index j of Eq. (15) indicates summation over 1, 2, and 6. For orthotropic materials, C_{16}, C_{26}, C_{61}, and C_{62} are equal to zero.

Stresses at any point in the fluid and solid can be calculated from the potentials and displacements defined by Eqs. (9) to (12) and (15). Then the vanishing shear stress and continuity of normal stress and displacement components at the top and bottom fluid-solid interfaces give six equations which are (Awal, 1994),

Downloaded 04 May 2010 to 171.66.16.28. Redistribution subject to ASME license or copyright; see http://www.asme.org/terms/Terms_Use.cfm

$$A_1(p_1 + kS_1) + A_2(p_2 + kS_2) + A_3(p_3 + kS_3) + A_4(p_4 + kS_4) = 0$$

$$A_1 i(C_{21}k + S_1 p_1 C_{22}) + A_2 i(C_{21}k + S_2 p_2 C_{22}) + A_3 i(C_{21}k + S_3 p_3 C_{22}) + A_4 i(C_{21}k + S_4 p_4 C_{22}) = \lambda k_f^2 (1 + R(k))$$

$$A_1 S_1 + A_2 S_2 + A_3 S_3 + A_4 S_4 = i\eta(-1 + R(k)) \quad (16)$$

for the top interface, and

$$A_1(p_1 + kS_1)Q_1 + A_2(p_2 + kS_2)Q_2 + A_3(p_3 + kS_3)Q_3 + A_4(p_4 + kS_4)Q_4 = 0$$

$$A_1 i(C_{21}k + S_1 p_1 C_{22})Q_1 + A_2 i(C_{21}k + S_2 p_2 C_{22})Q_2 + A_3 i(C_{21}k + S_3 p_3 C_{22})Q_3 + A_4 i(C_{21}k + S_4 p_4 C_{22})Q_4 = \lambda k_f^2 T(k) q$$

$$A_1 S_1 Q_1 + A_2 S_2 Q_2 + A_3 S_3 Q_3 + A_4 S_4 Q_4 = i\eta T(k) q \quad (17)$$

for the bottom interface. In these equations $Q_j = \exp(ip_j h)$, $q = \exp(i\eta h)$, p_j ($j = 1, 2, 3, 4$) is the jth root of Eq. (13) and S_j is obtained from Eq. (14).

The six equations given above are then solved for the six unknowns, $R(k)$ (the reflection coefficient), $T(k)$ (the transmission coefficient), A_1, A_2, A_3, and A_4 (the unknown coefficients of Eqs. (11) and (12)). This is how the plane wave reflection coefficient $R(k)$ of an orthotropic plate is obtained.

After computation of $A(k)$ and $R(k)$ the reflected field $\phi_r(x, y)$ can be obtained from Eq. (8), which can be rewritten in the following form:

$$\varphi_r(x, y) = \sqrt{R}\,.\exp\left(\frac{ik_f R}{2\pi}\right) \times \int_{\frac{k_f \tan\alpha_1}{\sqrt{1+\tan^2\alpha_1}}}^{\frac{k_f \tan\alpha_2}{\sqrt{1+\tan^2\alpha_2}}} R(k)A(k)e^{i(\eta y - kx)}dk. \quad (18)$$

The numerical integration of the above equation is carried out by a variable interval adaptive integration scheme developed by Kundu and Mal (1985).

AMS thus computed for the 6.35-mm thick Al plate and 2-mm thick graphite-epoxy composite plate along and across the fiber directions are shown by solid lines in Figs. 3, 5, and 7, respectively. For the analytical $V(z)$ synthesis the material properties of the graphite-epoxy composite plate are taken as $C_{11} = 160.7$ GPa, $C_{12} = 6.44$ GPa, $C_{22} = 13.9$ GPa, $C_{66} = 7.08$ GPa, density = 1580 kg/m^3 (after Karim et al., 1988). Good agreements between theoretical and experimental AMS curves are noted in Figs. 3 and 5. In Fig. 7, although the trend is similar, the rate of decay of the $V(z)$ curve with z is not same for experimental and theoretical values. This is probably due to different simplifications adopted in the theoretical modeling and also due to the difference between the true values of the material properties and the values taken in these calculations.

Concluding Remarks

In this paper it is shown how one can detect the generation of surface acoustic waves at different frequencies for a specific transducer-receiver arrangement by taking Fourier transform of reflected signals. From these reflected signal spectra $V(z)$ curves at different frequencies can be constructed. Thus $V(z)$ curves of isotropic and orthotropic plates have been experimentally synthesized using two ultrasonic transducers in pitch-catch arrangements. Experimental results have been compared with theoretical predictions and a reasonably good agreement between the two have been obtained. A fundamental mechanics problem of the plane wave reflection by an orthotropic plate has been solved. This solution is used to analytically synthesize the $V(z)$ curve for the experimental setup considered here. By this technique $V(z)$ curve at a number of frequency values can be obtained simply by recording and analyzing the reflected signals. For this experiment the incident signal can be made of a few number of pulses in time domain; constant frequency continuous pulse excitation is not necessary.

The main difference between this approach and currently available methods is that in this method one does not need an acoustic microscope lens to generate $V(z)$ curves. Earlier works on two transducer in pitch-catch arrangements only looked at reflection coefficients or SAW generation modes but never $V(z)$ curves were synthesized. $V(z)$ curves synthesized in this paper have shown significant variations with the change of material properties of the reflecting specimen. Hence these $V(z)$ curves are very sensitive to elastic constants of the material. This observation is encouraging because then, in principle, by inverting these $V(z)$ curves, say by a simplex algorithm (Kundu, 1992), one should be able to obtain the elastic constants of the specimen.

Acknowledgment

Financial support from the National Science Foundation under contract number DMC-8807661 and from the Air Force Office of Scientific Research under contract number F49620-90-C-09076 to carry out this research is gratefully acknowledged.

References

Ahn, V. S., and Achenbach, J. D., 1991, "Response of Line Focus Acoustic Microscope to Specimen Containing a Subsurface Crack," *Ultrasonics*, Vol. 29, No. 6, pp. 482–489.

Atalar, A., and Koymen, H., 1986, "$V(z)$ of the Surface Acoustic Wave Focusing System," *IEEE Ultrasonic Symposium Proceedings*, IEEE, New York, Cat. No. 86CH2375-4, pp. 727–730.

Atalar, A., and Koymen, H., 1987, "Use of a Conical Axicon as a Surface Acoustic Wave Focusing Device," *IEEE Transactions on Ultrasonics, Ferroelectrics, and Frequency Control*, IEEE, New York, Vol. UFFC-34, No. 1, pp. 53–63.

Atalar, A., Koymen, H., and Degertekin, L., 1990, "Characterization of Layered Materials by the Lamb Wave Lens," *IEEE Ultrasonics Symposium Proceedings*, IEEE, New York, IEEE Cat. No. 90CH2938-9, pp. 359–362.

Atalar, A., Koymen, H., and Degertekin, L., 1992, "A Lamb Wave Lens for Acoustic Microscopy," *IEEE Transactions on Ultrasonics, Ferroelectrics, and Frequency Control*, IEEE, New York, Vol. 39, No. 6, pp. 661–667.

Awal, M. A., 1995, "Low Frequency Acoustic Microscopy for Material Characterization," Ph.D. Dissertation, Department of Civil Engineering and Engineering Mechanics, University of Arizona.

Bertoni, H. L., and Tamir, T., 1973, "Unified Theory of Rayleigh-Angle Phenomena for Acoustic Beams at Liquid-Solid Interface," *Applied Physics*, Vol. 2, pp. 157–172.

Chubachi, N., 1989, "Ultrasonic Microscope and Its Application to Dielectric Materials Research," *Ferroelectrics*, Vol. 91, pp. 143–153.

Dunn, F., and Fry, W. J., 1959, "Ultrasonic Absorption Microscope," *Journal of the Acoustical Society of America*, Vol. 31, pp. 632–633.

Gomez, M. J., Rodriguez, R., Durand, J., Ferdj-Allah, H., Hadjoub, Z., Attal, J., and Doghmane, A., 1991, "Characterization and Identification of Berlinite Crystals by Acoustic Microscopy," *Journal of Materials Research*, Vol. 6, No. 11, pp. 2484–2489.

Gopalan, K., Roberts, R. A., Markovich, J. G., Vaitekunas, J. J., 1989, "High-Speed Digital Peak Detector and Averager for Acoustic Microscopy," *IEEE Instrumentation and Measurement Technology Conf.*, IEEE, New York, Cat. #89CH2707-8, pp. 54–56.

Hildebrand, J. A., and Rugar, D., 1984, "Measurement of Cellular Elastic Properties by Acoustic Microscopy," *Journal of Microscopy*, Vol. 134, pp. 245–260.

Ishikawa, I., Kanda, H., Katakura, K., and Senba, T., 1989, "Measurement of a Damaged Layer Thickness with Reflection Acoustic Microscope," *IEEE Transactions on Ultrasonics Ferroelectrics and Frequency Control*, Vol. 36, No. 6, pp. 587–592.

Downloaded 04 May 2010 to 171.66.16.28. Redistribution subject to ASME license or copyright; see http://www.asme.org/terms/Terms_Use.cfm

Jeffreys, H., and Jeffreys, B. S., 1950, *Methods of Mathematical Physics*, 2nd ed., Cambridge University Press, Cambridge, U.K., p. 505.

Karim, M. R., and Kundu, T., 1991, "Dynamic Response of an Orthotropic Half-Space with a Subsurface Crack: In-Plane Case," ASME JOURNAL OF APPLIED MECHANICS, Vol. 58, pp. 988–995.

Karim, M. R., Mal, A. K., and Bar-Cohen, Y., 1988, "Inversion of Leaky Lamb Wave Data by Simplex Algorithm," *Journal of the Acoustical Society of America*, Vol. 88, pp. 482–491.

Kundu, T., 1988, "A Theoretical Analysis of Acoustic Microscopy with Converging Acoustic Beams," *Applied Physics B: Photophyiscs and Laser Chemistry*, Vol. 46, pp. 325–331.

Kundu, T., 1992, "Inversion of Acoustic Material Signature of Layered Solids," *Journal of the Acoustical Society of America*, Vol. 91, No. 2, pp. 591–600.

Kundu, T., Bereiter-Hahn, J., and Hillmann, K., 1991, "Measuring Elastic Properties of Cells by Evaluation of Scanning Acoustic Microscopy $V(z)$ Values Using Simplex Algorithm," *Biophysical Journal*, Vol. 59, pp. 1194–1207.

Kundu, T., Bereiter-Hahn, J., and Hillmann, K., 1992, "Calculating Acoustical Properties of Cells: Influence of Surface Topography and Liquid Layer Between Cell and Substrate," *Journal of the Acoustical Society of America*, Vol. 91, No. 5, pp. 3008–3017.

Kundu, T., and Mal, A. K., 1985, "Elastic Waves in a Multilayered Solid due to a Dislocation Source," *Wave Motion*, Vol. 7, pp. 459–471.

Kundu, T., Mal, A. K., and Weglein, R. D., 1985, "Calculation of the Acoustic Material Signature of a Layered Solid," *Journal of the Acoustical Society of America*, Vol. 77, No. 2, pp. 353–361.

Kundu, T., and Maxfield, B., 1993, "A New Technique for Measuring Rayleigh and Lamb Wave Speeds," *Journal of the Acoustical Society of America*, Vol. 93, No. 6, pp. 3066–3073.

Kushibiki, J., and Chubachi, N., 1985, "Material Characterization by Line-Focus-Beam Acoustic Microscope," *IEEE Transactions on Sonics & Ultrasonics*, Vol. SU-32, pp. 189–212.

Kushibiki, J., Ohkubo, A., and Chubachi, N., 1982a, "Effect of Leaky SAW Parameters on $V(z)$ Curves Obtained by Acoustic Microscopy," *Electron Letters*, Vol. 18, p. 668.

Kushibiki, J., Ohkubo, A., and Chubachi, N., 1982b, "Material Characterization by Acoustic Line-Focus Beam," *Acoustical Imaging*, Vol. 12, pp. 101–111.

Kushibiki, J., Matsumoto, Y., and Chubachi, N., 1983, "Material Characterization by Acoustic Microscope with Line-Focus Beam," *Acoustical Imaging*, Vol. 13, pp. 193–202.

Lemons, R. A., and Quate, C. F., 1973, "A Scanning Acoustic Microscope," *Proceedings of the IEEE Symposium*, pp. 18–20.

Liang, K., Khuri-Yakub, B. T., Bennett, S. D., and Kino, G. S., 1983, "Phase Measurements in Acoustic Microscopy," *Proc. Ultrasonics Symposium*, Vol. 2, Atlanta, GA, p. 591.

Litniewski, J., and Bereiter-Hahn, J., 1990, "Measurements of Cells in Culture by Scanning Acoustic Microscopy," *Journal of Microscopy*, Vol. 158, pp. 95–105.

Lockwood, G. R., Ryan, L. K., Hunt, J. W. and Foster, F. S., 1990, "High Frequency Ultrasound Vascular Tissue Characterization," *Ultrasonics Symposium Proceedings*, Cat.# 90CH2938-9, IEEE Piscataway, NJ, pp. 1409–1412.

Miller, A. J., 1985, "Scannning Acoustic Microscopy in Electronics Research," *IEEE Trans. Son. Ultrason.*, Vol. SU-32, pp. 320–324.

Ranasinghe, D. W., Whyte, I. G., Wakefield, B., and Mingay, P., 1990, "Design Verification and Quality Control of Integrated Circuits in an Industrial Environment," *Microelectronic Engineering*, Vol. 12, pp. 15–26.

Semmens, J. E., and Kessler, L. W., 1989, "Nondestructive Evaluation of Debonding within Plastic Integrated Circuit Packages Using Different Methods of Acoustic Microscopy," *IEEE/CHMT European International Electronic Manufacturing Technology Symposium*, Cat.# 89CH2720-1, IEEE Piscataway, NJ, p. 322.

Weaver, J. M. R., Somekh, M. B., Briggs, G. A. D., Peck, S. D., and Illett, C., 1985, "Application of the Scanning Acoustic Microscope to the Study of Materials Science," *IEEE Transactions on Sonics and Ultrasonics*, Vol. SU-32, pp. 302–312.

Weglein, R. D., 1980, "Acoustic Microscopy Applied to SAW Dispersion and Film Thickness Measurement," *IEEE Transactions on Sonics and Ultrasonics*, Vol. SU-27, pp. 82–86.

Weglein, R. D., and Mal, A. K., 1991, "Elastic Characterization of Diamond Films by Acoustic Microscopy," *Surface and Coatings Technology*, Vol. 47, pp. 677–686.

Yamanaka, K., Enomoto, Y., and Tsuya, Y., 1982, "Application of Scanning Acoustic Microscope to the Study of Fracture and Wear," *Acoustic Imaging*, Vol. 12, pp. 79–87.

Yamanaka, K., Enomoto, Y., and Tsuya, Y., 1985, "Acoustic Microscopy of Ceramic Surfaces," *IEEE Transactions on Sonics and Ultrasonics*, Vol. SU-32, pp. 313–319.

Downloaded 04 May 2010 to 171.66.16.28. Redistribution subject to ASME license or copyright; see http://www.asme.org/terms/Terms_Use.cfm

Fractal Dimensions in Elastic-Plastic Beam Dynamics

P. S. Symonds
Fellow ASME.

J.-Y. Lee[1]
Mem. ASME.

Division of Engineering,
Brown University,
Providence, RI 02912

Calculations of two types of fractal dimension are reported, regarding the elastic-plastic response of a two-degree-of-freedom beam model to short pulse loading. The first is Mandelbrot's (1982) self-similarity dimension, expressing independence of scale of a figure showing the final displacement as function of the force in the pulse loading; these calculations were made with light damping. These results are equivalent to a microscopic examination in which the magnification is increased by factors of 10^2; 10^4; and 10^6. It is found that the proportion and distribution of negative final displacements remain nearly constant, independent of magnification. This illustrates the essentially unlimited sensitivity to the load parameter, and implies that the final displacement in this range of parameters is unpredictable. *The second fractal number is the* correlation dimension *of Grassberger and Procaccia (1983), derived from plots of Poincare intersection points of solution trajectories computed for the undamped model. This fractional number for strongly chaotic cases underlies the random and discontinuous selection by the solution trajectory of the potential well leading to the final rest state, in the case of the lightly damped model.*

1 Introduction

The present paper extends previous work of Lee et al. (1992). Our point of view is that of people interested in permanent (plastic) deformations of structures due to impact or other short pulse loading. In the previous paper it was shown that the problem of an ordinary beam exhibiting the simplest elastic-plastic behavior, and subjected to a force pulse producing moderate plastic strains, may, as result of seemingly minor changes in the support conditions, exhibit chaotic vibrations. It then becomes essentially *unsolvable* as far as the final deflected state is concerned. In certain ranges of the parameters, all predicted final displacements are meaningless. The present paper aims to provide further insight on this surprising result.

Details of the model (see Fig. 1) and the governing equations are given in Lee and Symonds (1992) and Lee et al. (1992). Briefly, it is an extension of the single-degree-of-freedom Shanley model previously used (Symonds and Yu, 1985; Genna and Symonds, 1988), but with deformable cells placed at the quarterpoints as well as the midpoint of the span. The ends are attached to fixed pins. The cells are modeled as sandwich beam sections, whose flanges exhibit elastic-perfectly plastic behavior in tension and compression. Rigid bars connect the cells, so that with symmetric deflections and neglect of axial inertia forces, a two-degree-of-freedom configuration is defined by the quarterpoint and midpoint displacements w_1 and w_2, respectively. The two second-order equations of motion are coupled cubic equations in (w_1, w_2), whose coefficients contain the four plastic stains. The latter are functions of time in an initial period, governed by plastic yield and flow equations. The structure under this loading *shakes down*, so that the plastic strains eventually become constant. The equations of the subsequent motion then are coupled autonomous Duffing equations. The plastic strains in the coefficients essentially define the geometry of a shallow arch. They play a critical role in the response behavior. Here the load parameter is taken as the force during the pulse, whose duration is fixed at 0.5×10^{-3} s.

In physical terms, because of the end fixity the plastic

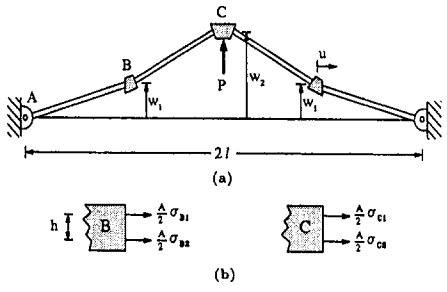

Fig. 1 Two-degree-of-freedom beam model. (*a*) symmetric deflected configuration; (*b*) deformable cells at quarterpoints B and midpoint C, treated as sandwich beam sections.

[1]Present address: Department of Mechanical Engineering, Korea Military Academy, Seoul, Korea.

Contributed by the Applied Mechanics Division of THE AMERICAN SOCIETY OF MECHANICAL ENGINEERS for publication in the ASME JOURNAL OF APPLIED MECHANICS.

Discussion on this paper should be addressed to the Technical Editor, Professor Lewis T. Wheeler, Department of Mechanical Engineering, University of Houston, Houston, TX 77204-4792, and will be accepted until four months after final publication of the paper itself in the ASME JOURNAL OF APPLIED MECHANICS.

Manuscript received by the ASME Applied Mechanics Division, June 15, 1993. Associate Technical Editor: D. J. Inman.

Copyright © 1995 by ASME

Downloaded 04 May 2010 to 171.66.16.28. Redistribution subject to ASME license or copyright; see http://www.asme.org/terms/Terms_Use.cfm

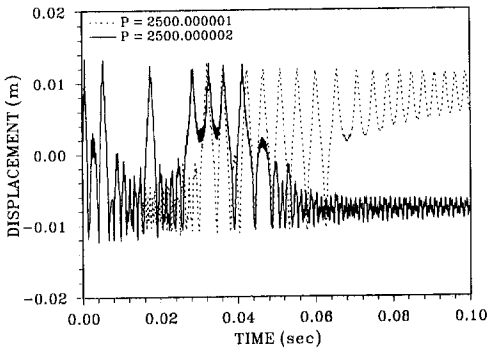

Fig. 2 Examples of time histories of midpoint displacement: two cases whose final values are plotted in Fig. 4(*d*) as functions of the pulse force

strains transform the structure from a beam to a shallow arch. The primary requirement for chaotic effects to appear is that the supports prevent axial motions, with consequent geometrical nonlinearity. But additional conditions must be satisfied: namely, that extensional plastic strains are induced in a certain range of small magnitudes, the pulse must be sufficiently short and the damping sufficiently weak; in this class of (autonomous) problems, the calculation must employ a multi-degree-of-freedom model.

To illustrate explicitly the behaviors concerned, in Fig. 2 are shown time histories of the midpoint displacement for two pulse forces, furnished by a numerical technique valid for nonlinear geometrical and material behaviors. For a pulse force 2500.000001 N the final displacement is predicted to be about 9.9 mm. If the pulse force is changed to 2500.000002 N, a final deflection of about -7.5 mm, is predicted. (These are two of the 101 calculations in the interval from 2500.0000 to 2500.0001 shown in Fig. 4(*d*).) There is no way of telling which is the "correct value." 9.9 mm or -7.5 mm. (Note that the load 2500 N is not a bifurcation or other special value.) The extreme sensitivity implies unpredictability of the final displacement. In what follows, all forces are in newtons. For brevity we may omit the symbol N.

2 Fractal Structure of the Final Displacement

The final displacement for a damping ratio $\zeta = 0.01$ is plotted in Fig. 3 as a function of the pulse force P, taken from Lee et al. (1992). For pulse force P between about 1600 and 3400 the diagram shows a rapid alternation between positive and negative values ("positive" meaning in the direction of the applied impulse). Figure 4(*a*) shows the interval $2500 \le P \le 2700$, with load step $dP = 2$. With the enlarged scale, it can be seen that the subintervals or "segments" of negative and positive displacement have widths and spacing that vary in a seemingly random fashion; the positive segments are somewhat wider than the negative ones. Further calculations show that this diagram is illusory. What is seen as a "negative segment" at this scale actually consists of an infinite number of positive and negative segments of vanishingly small size. In other words, it covers an irregular "Cantor dust" (Mandelbrot, 1982).

Figures 4(*a*)–4(*d*) show final deflections for pulse forces P in four intervals $\Delta P = 200$, 1, 0.01, 0.0001, respectively. In each of these P is chosen according to the formula

$$P = 2500 + i\Delta P/100; \quad i = 0, 1, 2, \ldots 100. \qquad (1)$$

Thus the minimum segment (load increment dP) varies from 2 to 10^{-6}, as the interval ΔP is reduced from 200 to 10^{-4}. The negative final displacements appear in essentially similar patterns in the four cases of Figs. 2(*a*)–2(*d*). To express this

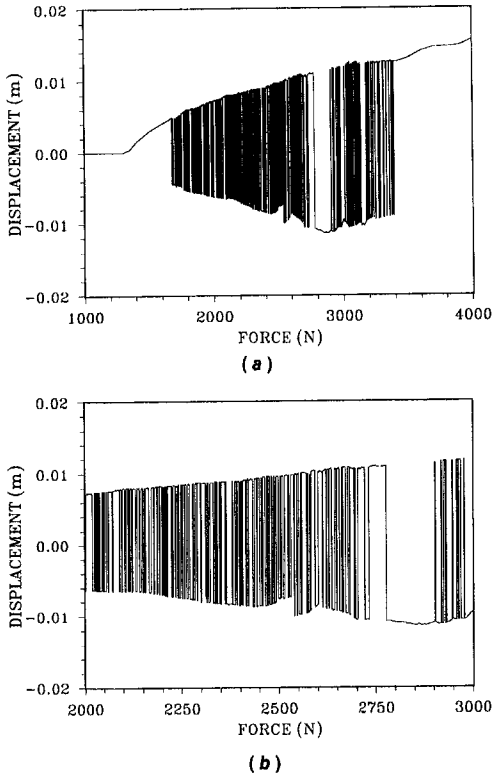

Fig. 3 Final midpoint displacements plotted as function of pulse force P with fixed pulse duration 0.5×10^{-3} sec and damping ratio $\zeta = 0.01$, computed at force increments $dP = 2.0$ newtons. (*a*) shows displacements over full range from wholly elastic to arch behavior; (*b*) shows portion of diagram in (*a*) to expanded scale.

quantitatively we use the formula for a "similarity dimension" D suggested by Mandelbrot (1982):

$$Ns^D = 1; \quad D = -(\log N)/(\log s) \qquad (2a, 2b)$$

where N is the number of negative segments and s is the average size of the segments, computed by adding the lengths of all the negative segments in the interval and dividing by N. To make the calculation for each interval, we adjust the scales so that the interval is unity in each case. The results are shown in Table 1.

Considering that the scale changes by a factor greater than 10^6, the agreement among the four values of D is remarkable, reflecting fractal self-similar structure of boundaries between attracting basins. Figure 2(*b*) shows two of the displacement-time histories whose end states are plotted in Fig. 4(*d*). The meaning of "unpredictability" of the final state is well demonstrated.

For comparison, we note the similar calculation for the Cantor set obtained by removing the middle third of a line segment of unit length, and of all the subsequently obtained segments. After n operations, the initial unit segment has become $N = 2^n$ segments, each of length $s = 1/3^n$. Applying Eq. (2*b*), we obtain $D = (n \log 2)/(n \log 3) = 0.6309 \ldots$ Again, when the autonomous damped *single*-degree-of-freedom model is considered, it is found that $s = 1/N$ and $D = 1$; no chaotic vibrations or fractal geometry are exhibited in this case (Borino et al., 1989).

3 Correlation Fractal Dimension

The behavior of an undamped model ($\zeta = 0$) is now considered, subjected to pulses of fixed duration 0.5×10^{-3} sec and force magnitudes P over a wide range. In Lee et al. (1992) and Lee and Symonds (1992) we illustrated several

Downloaded 04 May 2010 to 171.66.16.28. Redistribution subject to ASME license or copyright; see http://www.asme.org/terms/Terms_Use.cfm

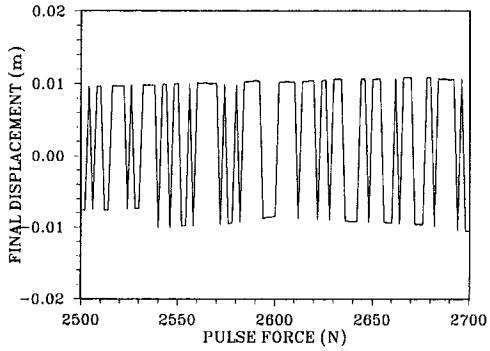

Fig. 4(*a*) Interval $\Delta P = 200$, increment $dP = 2.0$

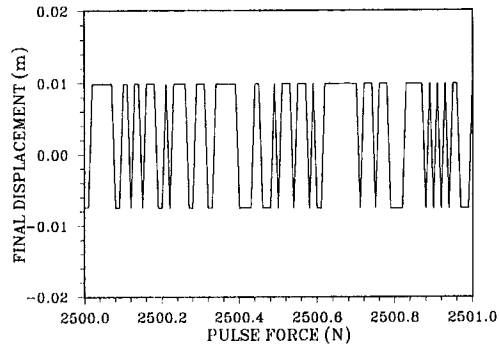

Fig. 4(*b*) Interval $\Delta P = 1.0$, increment $dP = 10^{-2}$

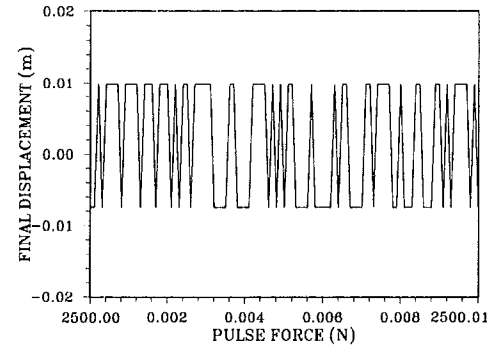

Fig. 4(c) Interval $\Delta P = 10^{-2}$, increment $dP = 10^{-4}$

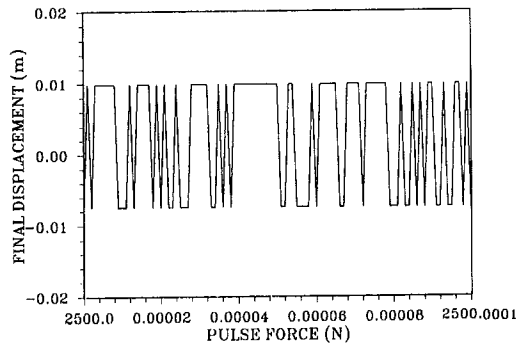

Fig. 4(*d*) Interval $\Delta P = 10^{-4}$, increment $dP = 10^{-6}$

Fig. 4 Final displacements computed as described for Fig. 3, for four force intervals ΔP and corresponding force increments $dP = \Delta P/100$, starting from $P = 2500$ newtons.

Table 1 Data for calculation of self-similarity dimension D

Figure No.	Interval ΔP	N	s	D
4(*a*)	200.0000	24	0.0163	0.77
4(*b*)	1.0000	22	0.0173	0.76
4(*c*)	0.0100	24	0.0192	0.80
4(*d*)	0.0001	23	0.0170	0.77

ways of depicting and characterizing the response, in particular contrasting elastic (nonlinear) behavior with the chaotic behavior that may occur when plastic strains are present. In this class of problem, where external excitation is limited to a short pulse, much help is obtained from *energy diagrams* of the type introduced by Borino et al. (1989). After the plastic strains have reached their final values, the elastic strain energy (potential energy) can be plotted as a fixed surface over the plane of the displacements (w_1, w_2). There is then a certain level of available *total energy* (current potential plus kinetic energy), which remains constant, in the absence of damping or other dissipative mechanism. The intersection curve of the fixed plane representing this total energy with the fixed strain energy surface defines the region of the (w_1, w_2) coordinate plane in which the solution must lie, for a given problem.

Properties of particular solutions are advantageously brought out by Poincaré diagrams. These show the response state at times defined by the intersection of the solution trajectory with particular planes in the four-dimensional phase space (w_1, w_2, $\dot{w}_1$, $\dot{w}_2$). Here we choose intersections of the velocity plane $\dot{w}_1 = 0$ and plot points in the plane (w_1, w_2) of the displacements. In a particular problem of pulse loading, when the responses is quasi-periodic, points corresponding to successive intersections lie on a smooth curve. When the response is strongly chaotic they form a "cloud" of points scattered over the allowed region of the displacement plane (see Fig. 14 of Lee et al., 1992). In "weakly chaotic" responses, as predicted by KAM theory (see, e.g., Tabor, 1989), we have found (at a given energy level) mixtures of regular curves, fixed points, and clouds of scattered points in highly complex but characteristic patterns (Carini et al., 1993). Here we consider only some typical strongly chaotic examples. With a sufficiently long run, it seems probable that in these cases a vanishingly small region surrounding every allowed point would be visited. Their discontinuous nature is indicated by a fractal dimension between 1 and 2.

The *correlation dimension* D_c is defined (Grassberger and Procaccia, 1983) as

$$C(r) = \lim_{r \to 0} A r^{Dc} \tag{3a}$$

$$D_c = \lim_{r \to 0} \Delta[\log C(r)]/\Delta(\log r) \tag{3b}$$

where A is a constant of proportionality and $C(r)$ is the correlation function, equivalent to the probability that the separation between pairs of points in a cloud consisting of n points will be less than the distance r, in the limit as n approaches infinity. If there are n Poincare points in a given case, with known coordinates, the $n(n-1)$ distances between each point and every other point are first tabulated. Choosing a sequence of suitably small distances r, the number of pairs whose separation is less than r is readily calculated for each r. D_c is given approximately by the slope of the line obtained by plotting log $C(r)$ against log r. Figure 5(*a*) shows these plots for three cases in which the response is quasi-periodic, namely $P = 1000$, 1700, 4200. Then the Poincaré points fall on regular curves, and the slope furnishes D_c close to unity ($D_c = 0.98$). In contrast, Fig. 5(*b*) shows the plots for three strongly chaotic cases, $P = 2500$, 2800, and 3000. The slopes of the linear portion furnish $D_c = 1.41$, 1.44, and 1.35, respectively, by Eq. (3*b*). The

Downloaded 04 May 2010 to 171.66.16.28. Redistribution subject to ASME license or copyright; see http://www.asme.org/terms/Terms_Use.cfm

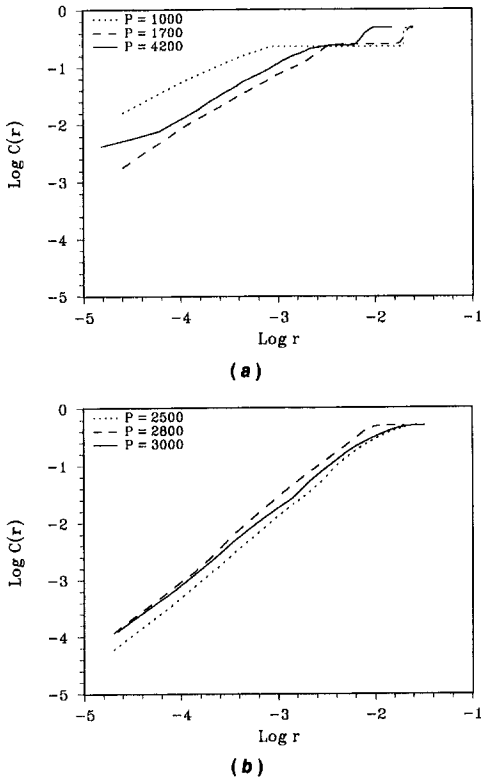

Fig. 5 Plots of log $C(r)$ versus log r for calculation of correlation fractal dimension from Poincare section portraits (as in Lee et al., 1992, Fig. 14) of undamped response. (*a*) shows plots for three pulse forces at which the response is quasi-periodic: $D_c \cong 1.0$; (*b*) shows plots for three strongly chaotic cases: $D_c \cong 1.4$.

expected results $D_c \cong 1$ and $D_c > 1$ are obtained. We should add that our n was about 1000 for the quasi-periodic cases and about 2000 for the chaotic cases; larger values would be desirable.

4 Conclusions

The occurrence of negative final displacements of a lightly damped pulse-loaded beam model has been re-examined by computing the final value over load intervals ranging from 200 to 10^{-4} newtons, starting at 2500 newtons, and taking 100 load steps in each interval. The patterns of positive and negative values exhibit a basic similarity independent of the size of the load steps. A *similarity dimension* $D = 0.78$ approximately fits all four cases. This illustrates the extreme sensitivity of the response to the pulse force, and adds insight on why the final displacement *cannot be predicted by any numerical process*, at these (strongly chaotic) load levels. The *correlation dimension* for strongly chaotic undamped responses is relevant also to the chaotic response phase of lightly damped responses, prior to transition, where the trajectory in phase space chooses either the negative or the positive potential well in a discontinuous and apparently random manner.

Acknowledgment

Support from the National Science Foundation under Grant MSS-9024607 (Dr. Ken P. Chong, Program Officer) is gratefully acknowledged.

References

Borino, G., Perego, U., and Symonds, P. S., 1989, "An Energy Approach to Anomalous Damped Elastic-Plastic Response to Short Pulse Loading," ASME JOURNAL OF APPLIED MECHANICS, Vol. 56, pp. 430–438.

Carini, A., Castiglioni, L., and Symonds, P. S., 1993, "Regular and Chaotic Responses of a Fixed-Ended Beam Model with Assigned Plastic Strains: (1) Illustrative Examples for a Hamiltonian System," in preparation.

Genna, Francesco, and Symonds, P. S., 1988, "Dynamic Plastic Instabilities in Response to Short Pulse Excitation—Effects of Slenderness Ratio and Damping," *Proceedings of the Royal Society of London*, Vol. A417, pp. 31–44.

Grassberger, P., and Procaccia, I., 1983, "Characterization of Strange Attractors," *Physical Review Letters*, Vol. 50, No. 5, pp. 346–349.

Lee, J.-Y., and Symonds, P. S., 1992, "Extended Energy Approach to Chaotic Elastic-Plastic Response to Impulsive Loading," *International Journal of the Mechanical Sciences*, Vol. 34, No. 2, pp. 139–157.

Lee, J.-Y., Symonds, P. S., and Borino, G., 1992, "Chaotic Responses of a Two-Degree-of-Freedom Elastic-Plastic Beam Model to Short Pulse Loading," ASME JOURNAL OF APPLIED MECHANICS, Vol. 59, pp. 711–721.

Mandelbrot, B. B., 1982, *The Fractal Geometry of Nature*, W. H. Freeman, San Francisco, CA.

Symonds, P. S., and Yu, T. X., 1985, "Counterintuitive Behavior in a Problem of Elastic-Plastic Beam Dynamics," ASME JOURNAL OF APPLIED MECHANICS, Vol. 52, pp. 517–522.

Tabor, M., 1989, *Chaos and Integrability in Nonlinear Dynamics*, John Wiley and Sons, New York.

Downloaded 04 May 2010 to 171.66.16.28. Redistribution subject to ASME license or copyright; see http://www.asme.org/terms/Terms_Use.cfm

A. M. Hasofer

M. Grigoriu

School of Civil and Environmental Engineering, Cornell University, Hollister Hall, Ithaca, NY 14853-3501

A New Perspective on the Moment Closure Method

Introduction

Moments and other probabilistic characteristics of a response process X_t satisfying a nonlinear stochastic differential equation can be obtained exactly in only a few special cases. As a result, closure and other approximate methods are generally used to estimate statistics of X_t in nonlinear random vibration problems. The closure method retains from the infinite hierarchy of equations of moments of X_t the first n equations. These equations cannot be solved because they generally involve moments of order one to $N > n$. The number n of moment equations is arbitrary and referred to as the closure level. The traditional closure algorithms are based on postulated relationships between moments of order larger and smaller than the closure level that are present in the first n moment equations. These additional closure conditions provide sufficient information for solving the truncated hierarchy of moment equations. Central moment, Gaussian, cumulant, and other techniques were proposed to close the moment equations (Adomian, 1983; Bolotin, 1984; Ibrahim, 1984; Richardson, 1964). Numerical results show that most closure techniques are usually satisfactory.

This paper shows by an example that the success of the closure method has nothing to do with the particular way in which the moment equations are closed. The paper also develops asymptotic expressions for the moments of the response process in the example as the number of moment equations considered in the analysis increases indefinitely. Results show that the method of moments is incorrect asymptotically.

The Example

Let X_t be a scalar diffusion process satisfying the Itô differential equation

$$dX_t = -\left(X_t + \alpha X_t^3\right)dt + \sqrt{\beta}\,dB_t \tag{1}$$

in which $\alpha \geq 0$, $\beta \geq 0$, and dB_t are independent identically distributed Gaussian variables with mean zero and variance dt. The stationary probability density function $f(x;\ \alpha)$ of X_t satisfies the Fokker-Planck equation

$$-\frac{d}{dx}\left[-(x + \alpha x^3)f - \frac{\beta}{2}\frac{df}{dx}\right] = 0 \tag{2}$$

and is

$$f(x;\alpha) = c\exp\left[-\frac{2}{\beta}\left(\frac{x^2}{2} + \alpha\frac{x^4}{4}\right)\right] \tag{3}$$

in which c is a constant equal to

$$c^{-1} = \frac{1}{\sqrt{2\alpha}}e^{-\frac{1}{4\alpha\beta}}K_{1/4}\left(\frac{1}{4\alpha\beta}\right) \tag{4}$$

where $K_\nu(z)$ denotes the modified Bessel function of the second kind.

The probability density function $f(x;\ \alpha)$ approaches $f(x) = f(x;\ 0)$ as $\alpha \to 0$ because

$$\lim_{\alpha\to 0} f(x;\alpha) = \lim_{\alpha\to 0} c \lim_{\alpha\to 0} \exp\left[-\frac{2}{\beta}\left(\frac{x^2}{2} + \alpha\frac{x^4}{4}\right)\right]$$

$$= \exp\left(-\frac{x^2}{\beta}\right)\lim_{\alpha\to 0} c, \tag{5}$$

$$K_\nu(z) \sim \sqrt{\frac{\pi}{2z}}\,e^{-z}\left(1 + \frac{4\nu^2 - 1}{8z} + \ldots\right) \tag{6}$$

as $|z| \to \infty$ (1), and

Contributed by the Applied Mechanics Division of THE AMERICAN SOCIETY OF MECHANICAL ENGINEERS for publication in the JOURNAL OF APPLIED MECHANICS.

Discussion on this paper should be addressed to the Technical Editor, Professor Lewis T. Wheeler, Department of Mechanical Engineering, University of Houston, Houston, TX 77204-4792, and will be accepted until four months after final publication of the paper itself in the JOURNAL OF APPLIED MECHANICS.

Manuscript received by the ASME Applied Mechanics Division, Dec. 18, 1991; final revision, Mar. 15, 1993. Associate Technical Editor: P. D. Spanos.

Copyright © 1995 by ASME

Downloaded 04 May 2010 to 171.66.16.28. Redistribution subject to ASME license or copyright; see http://www.asme.org/terms/Terms_Use.cfm

$$\lim_{\alpha\to 0} c^{-1} = \lim_{\alpha\to 0} \frac{1}{\sqrt{2\alpha}} e^{\frac{1}{4\alpha\beta}} \times \left[\sqrt{\frac{\pi}{2\frac{1}{4\alpha\beta}}}\, e^{-\frac{1}{4\alpha\beta}} \left(1 + \frac{4\left(\frac{1}{4}\right)^2 - 1}{8\frac{1}{4\alpha\beta}} + \ldots \right) \right] = \sqrt{\pi\beta}\,. \tag{7}$$

Therefore, the stationary moments

$$\mu_r(\alpha) = \int_{-\infty}^{\infty} x^r f(x;\alpha)dx \tag{8}$$

of X_t for $\alpha > 0$ approach the moments

$$\mu_r = \int_{-\infty}^{\infty} x^r f(x)dx \tag{9}$$

of X_t for $\alpha = 0$ as $\alpha \to 0$.

Solution of Moment Equations

The stationary moments $\mu_m(\alpha) = EX_t^m$ of X_t in Eq. 1 satisfy the infinite hierarchy of difference equations (Arnold, 1973; Bolotin, 1984; Ibrahim, 1984)

$$\alpha\mu_{m+4}(\alpha) + \mu_{m+2}(\alpha) - \frac{\beta(m+1)}{2}\mu_m(\alpha) = 0, m = 0,2,4,\ldots \tag{10}$$

Only even order moments are involved in these equations because $f(x;\alpha)$ is symmetric about the origin as it can be seen from the equation of motion of X_t. The initial conditions are

$$\mu_0(\alpha) = 1$$
$$\mu_2(\alpha) = EX_t^2. \tag{11}$$

An alternative form of Eqs. (10) and (11) is

$$\alpha u_{q+2} + u_{q+1} - \frac{\beta(2q+1)}{2}u_q = 0, q = 0,1,2,\ldots \tag{12}$$

with the notations $m = 2q$ and $u_q = \mu_{2q}$. The initial conditions are $u_0 = \mu_0(\alpha) = 1$ and $u_1 = \mu_2(\alpha) = EX_t^2$.

The moments μ_m of X_t for $\alpha = 0$ satisfy the difference equations

$$\mu_{m+2} - \frac{\beta(m+1)}{2}\mu_m = 0, m = 0,2,4,\ldots \tag{13}$$

with the initial condition given by the first equality in Eq. (11). The equation can also be given in the form

$$v_{q+1} - \frac{\beta(2q+1)}{2}v_q = 0, q = 0,1,2,\ldots \tag{14}$$

with the notations $m = 2q$ and $v_q = \mu_{2q}$. The initial condition of this equation is $v_0 = \mu_0 = 1$.

The moments of X_t can be obtained recursively from Eq. (14) when $\alpha = 0$ because this equation only depends on the value $v_0 = 1$, an expected result because Eq. (1) is linear in this case. On the other hand, it is not possible to find the moments of X_t when $\alpha > 0$ because EX_t^2 in Eq. (11) is not known. A closure technique can be used for solution. For example, consider the equalities in Eq. (12) for $q = 0,1,\ldots n$. There are $(n+1)$ equations and $n+2$ unknowns, the moments $u_1, u_2, \ldots, u_{n+1}, u_{n+2}$. A closure method is needed for solution. According to the hypothesis of quasi-normality (Bolotin, 1984, p. 248), it can be postulated that the relationship between the moments u_{n+2} and u_{n+1} of order $2(n+2)$ and $2(n+1)$ of X_t coincides with the relationship between moments of similar order for Gaussian variables, i.e.,

$$u_{n+2} = \frac{\beta(2n+3)}{2}u_{n+1}. \tag{15}$$

The condition in Eq. (15) can be used to find the moments $u_1, u_2, \ldots, u_{n+1}$ approximately at closure level n.

Table 1 gives exact and approximate moments of X_t in Eq. 1 with $\beta = 2$ for several values of α and closure level n. The exact moments have been obtained by numerical integration using the stationary density in Eqs. (3) and (4). The numerical values in the table are rounded to the first two decimals. More accurate values of EX_t^2 are also given in the table. Results show that the approximate moments obtained by the closure method in Eq. (15) are satisfactory for all cases considered in the table. Moreover, the use of many other closure technique yield satisfactory results. For example, the approximate moments of X_t for $\beta = 2$ in Tables 2 and 3 correspond to the closure condition.

$$u_{n+2} = \gamma\alpha^{-1}u_{n+1} \tag{16}$$

The approximate moments based on this closure condition are accurate for a wide range of positive and negative values of γ provided that the closure level is sufficiently large.

Results in Tables 1 and 3 suggest that the closure method for the diffusion process in Eq. (1) is a hoax in the sense that its success has nothing to do with the way in which the moment equations are closed. This observation is formalized by the theorem of the next section.

Table 1 Exact and approximate moments of X_t

Order	Exact	Closure level, n			
		4	10	50	70
		$\alpha = 0.1$			
2	0.82	0.82	0.82	0.82	0.82
4	1.82	1.83	1.82	1.82	1.82
6	6.28	6.16	6.28	6.28	6.28
8	28.39	30.16	24.42	28.39	28.39
10	155.91	129.26	155.51	155.91	155.91
		$\alpha = 0.01$			
2	0.97	0.97	0.97	0.97	0.97
4	2.79	2.79	2.79	2.79	2.79
6	13.08	13.08	13.08	13.08	13.08
8	84.59	84.70	84.64	84.64	84.64
10	692.03	686.76	693.34	693.34	693.34
		$\alpha = 0.001$			
2	1.00	1.00	1.00	1.00	1.00
4	2.98	2.98	2.98	2.98	2.98
6	14.77	14.78	14.78	14.78	14.78
8	102.28	102.54	102.54	102.54	102.54
10	905.84	912.82	912.94	912.94	912.94
		$\alpha = 0.0001$			
2	1.00	1.00	1.00	1.00	1.00
4	3.00	3.00	3.00	3.00	3.00
6	14.97	14.98	14.98	14.98	14.98
8	104.44	104.75	104.75	104.75	104.75
10	933.25	941.73	941.73	942.24	943.26

Note: $EX_t^2 = 0.8175625$; 0.9721424; 0.9970115; and 0.9996862 for $\alpha = 0.1$; 0.01; 0.001; and 0.0001.

On the Closure Method

It will be shown in this section that the success of the closure method applied to the process X_t in Eq. (1) is the

Downloaded 04 May 2010 to 171.66.16.28. Redistribution subject to ASME license or copyright; see http://www.asme.org/terms/Terms_Use.cfm

Table 2 Exact and approximate moments of X_t ($\gamma = 1$)

Order	Exact	Closure level, n			
		4	10	50	70
		$\alpha = 0.1$			
2	0.82	0.82	0.82	0.82	0.82
4	1.82	1.83	1.82	1.82	1.82
6	6.28	6.18	6.28	6.28	6.28
8	28.39	29.83	28.39	28.39	28.39
10	155.91	134.23	155.95	155.91	155.91
		$\alpha = 0.01$			
2	0.97	0.97	0.97	0.97	0.97
4	2.79	2.79	2.79	2.79	2.79
6	13.08	13.08	13.08	13.08	13.08
8	84.59	87.45	84.64	84.64	84.64
10	692.03	393.52	693.34	693.34	693.34
		$\alpha = 0.001$			
2	1.00	1.00	1.00	1.00	1.00
4	2.98	2.98	2.98	2.98	2.98
6	14.77	14.78	14.78	14.78	14.78
8	102.28	102.99	102.54	102.54	102.54
10	905.84	463.44	912.94	912.94	912.94
		$\alpha = 0.0001$			
2	1.00	1.00	1.00	1.00	1.00
4	3.00	3.00	3.00	3.00	3.00
6	14.97	14.98	14.98	14.98	14.98
8	104.44	104.80	104.75	104.75	104.75
10	933.25	441.63	941.90	942.24	942.92

Table 3 Exact and approximate moments of X_t ($\alpha = 0.1$)

Order	Exact	Closure level, n			
		4	10	50	70
		$\gamma = 10{,}000$			
2	0.82	0.82	0.82	0.82	0.82
4	1.82	1.88	1.82	1.82	1.82
6	6.28	5.54	6.28	6.28	6.28
8	28.39	38.74	28.48	28.39	28.39
10	155.91	0.03	154.49	155.91	155.91
		$\gamma = 0.001$			
2	0.82	0.82	0.82	0.82	0.82
4	1.82	1.80	1.82	1.82	1.82
6	6.28	6.58	6.29	6.28	6.28
8	28.39	24.26	28.34	28.39	28.39
10	155.91	218.11	156.66	155.91	155.91
		$\gamma = -0.001$			
2	0.82	0.82	0.82	0.82	0.82
4	1.82	1.80	1.82	1.82	1.82
6	6.28	6.58	6.29	6.28	6.28
8	28.39	24.24	28.34	28.39	28.39
10	155.91	218.38	156.66	155.91	155.91
		$\alpha = 10{,}000$			
2	0.82	0.82	0.82	0.82	0.82
4	1.82	1.88	1.82	1.82	1.82
6	6.28	5.53	6.28	6.28	6.28
8	28.39	38.75	28.48	28.39	28.39
10	155.91	−0.03	154.49	155.91	155.91

result of a very unusual property of the moment equation. This property can be stated as follows. There is a unique value of the initial condition u_1 such that all u_n are non-negative. For any other value of u_1 the sequence u_n will eventually take negative values. From Eq. (12),

$$u_q = a_q + b_q u_1, q = 1, 2, 3, \ldots \tag{17}$$

in which the sequences $\{a_q\}$ and $\{b_q\}$ satisfy the difference equations

$$\alpha a_{q+2} + a_{q+1} - (2q+1)a_q = 0$$
$$\alpha b_{q+2} + b_{q+1} - (2q+1)b_q = 0$$
$$(q = 0, 1, 2, \ldots) \tag{18}$$

for $\beta = 2$ and initial conditions $a_0 = 1$; $a_1 = 0$; $b_0 = 0$; $b_1 = 1$. Consider the change of variables $a_q = (-\alpha)^{-q} p_q$ and $b_q = -(-\alpha)^{-q} r_q$. Then, p_q and r_q satisfy the difference equations

$$p_{q+2} = p_{q+1} + \alpha(2q+1)p_q$$
$$r_{q+2} = r_{q+1} + \alpha(2q+1)r_q$$
$$(q = 0, 1, 2, \ldots) \tag{19}$$

with $p_0 = 1$, $p_1 = 0$, $r_0 = 0$, $r_1 = \alpha$. The sequences $\{p_q\}$ and $\{r_q\}$ are non-negative and nondecreasing.

Lemma. Let u_1 be the exact value of the stationary second moment of X_t in Eq. (1). Then,

$$\text{(i)} \frac{p_{2n'+1}}{r_{2n'+1}} \le u_1 \le \frac{p_{2n}}{r_{2n}} \text{ for every } n \text{ and } n';$$
$$\text{(ii)} \left\{\frac{p_{2n}}{r_{2n}}\right\} \text{ and } \left\{\frac{p_{2n+1}}{r_{2n+1}}\right\} \text{ are} \tag{20}$$

decreasing and increasing sequences, respectively; and

$$\text{(iii)} \lim_{n\to\infty} \frac{p_n}{r_n} = u_1.$$

Proof. (i) The sequence of moments u_q in Eq. (17) is non-negative. Therefore, $u_1 \le p_{2n}/r_{2n}$ because $u_{2n} \ge 0$, $b_{2n} = -(-\alpha)^{-2n} r_{2n} \le 0$, and $a_{2n} = (-\alpha)^{-2n} p_{2n}$. Similarly, $u_1 \ge p_{2n+1}/r_{2n+1}$ because $u_{2n+1} \ge 0$, $b_{2n+1} = -(-\alpha)^{-(2n+1)} r_{2n+1} \ge 0$ and $a_{2n+1} = (-\alpha)^{-(2n+1)} p_{2n+1}$.

(ii) Consider the inequality $a/b \le c/d$ in which a, b, c, and d are positive numbers. It can be shown by direct calculations that

$$\frac{a}{b} \le \frac{a + \zeta c}{b + \zeta d} \le \frac{c}{d}$$

for any $\zeta \ge 0$. Therefore, from Eqs. (19) and (20),

$$\frac{p_{2n+2}}{r_{2n+2}} = \frac{p_{2n+1} + \alpha(4n+1)p_{2n}}{r_{2n+1} + \alpha(4n+1)r_{2n}} \le \frac{p_{2n}}{r_{2n}},$$

such that the sequence $\{p_{2n}/r_{2n}\}$ decreases with n. Similar considerations can be used to show that $\{p_{2n+1}/r_{2n+1}\}$ is an increasing sequence.

(iii) It can be shown by direct calculations and using Eq. (19) that the difference between the following upper and lower bounds on u_1 is

$$\frac{p_{2n+2}}{r_{2n+2}} - \frac{p_{2n+3}}{r_{2n+3}} = \frac{p_{2n+2}}{r_{2n+2}} - \frac{p_{2n+2} + \alpha(4n+3)p_{2n+1}}{r_{2n+2} + \alpha(4n+3)r_{2n+1}}$$
$$= \left(\frac{p_{2n+2}}{r_{2n+2}} - \frac{p_{2n+1}}{r_{2n+1}}\right)\rho_n \tag{21}$$

in which

$$\rho_n^{-1} = 1 + \frac{1}{\alpha(4n+3)}\frac{r_{2n+2}}{r_{2n+1}} \ge 1 + \frac{1}{\alpha(4n+3)}. \tag{22}$$

Similar calculations give

$$\frac{p_{2n+2}}{r_{2n+2}} - \frac{p_{2n+1}}{r_{2n+1}} = \left(\frac{p_{2n}}{r_{2n}} - \frac{p_{2n+1}}{r_{2n+1}}\right)\lambda_n \tag{23}$$

Downloaded 04 May 2010 to 171.66.16.28. Redistribution subject to ASME license or copyright; see http://www.asme.org/terms/Terms_Use.cfm

in which

$$\lambda_n^{-1} = 1 + \frac{1}{\alpha(4n+1)} \frac{r_{2n+1}}{r_{2n}} \geq 1 + \frac{1}{\alpha(4n+1)}. \quad (24)$$

Define a sequence $\{\xi_n\}$ by

$$\xi_n^{-1} = \frac{p_{2n}}{r_{2n}} - \frac{p_{2n+1}}{r_{2n+1}}, n = 1, 2, \ldots. \quad (25)$$

This sequence is non-negative by (i) and, from Eqs. (21) to (25), we have

$$\xi_{n+1}^{-1} = \frac{p_{2n+2}}{r_{2n+2}} - \frac{p_{2n+3}}{r_{2n+3}} = \rho_n \lambda_n \xi_n^{-1} \quad (26)$$

such that

$$\xi_n = \xi_1 \left(\prod_{i=1}^{n} \rho_i^{-1} \right) \left(\prod_{i=1}^{n} \lambda_i^{-1} \right) \quad (27)$$

in which $\xi_1 = 1 + 1/(3\alpha)$. Both products in Eq. (27) tend to infinity as $n \to \infty$ so that $\lim_{n\to\infty} \xi_n = \infty$ or, equivalently, $\lim_{n\to\infty} p_{2n}/r_{2n} = \lim_{n\to\infty} p_{2n+1}/r_{2n+1}$. From Eq. (20), the ratio p_n/r_n converges to u_1 as $n \to \infty$.

A theorem stating that the infinite product $\prod_{n=1}^{\infty} (1 + x_n)$, $x_n \geq 0$ is convergent/divergent when the infinite sum $\sum_{n=1}^{\infty} x_n$ is convergent/divergent can be used to prove that $\prod_{n=1}^{\infty} \rho_n^{-1}$ and $\prod_{n=1}^{\infty} \lambda_n^{-1}$ are unbounded (7). Indeed, let $x_n = \frac{1}{\alpha(4n+3)}$ such that $\rho_n^{-1} = 1 + x_n \frac{r_{2n+2}}{r_{2n+1}} \geq 1 + x_n$. According to the Raabe test (7), the sum $\sum_{n=1}^{\infty} x_n$ is divergent because $n\left(\frac{x_n}{x_{n+1}} - 1\right) = \frac{n}{n + \frac{3}{4\alpha}} \leq 1$ for all values of n.

Therefore, $\prod_{n=1}^{\infty} (1 + x_n) = \infty$ and $\prod_{n=1}^{\infty} \rho_n^{-1} = \infty$ because $\rho_n^{-1} \geq 1 + x_n$.

Table 4 gives the ratios p_n/r_n, p_n/p_{n-1}, and r_n/r_{n-1} for several values of n and α. Comparisons with Tables 1–3 show that p_n/r_n approach the exact moment $u_1 = EX_t^2$ as n increases, a result predicted by the lemma. Moreover, the ratios p_n/p_{n-1} and r_n/r_{n-1} are practically equal for sufficiently large values of n.

Theorem. Let $\{k_n\}$ be any sequence of non-negative numbers. Set

$$u_{n+1} = k_n u_n \quad (28)$$

for an arbitrary n and solve Eq. (12) for $q = 0, 1, \ldots, n-1$ subject to $u_0 = 1$ and the closure condition in Eq. (28). Let $u_1(n)$ be the resulting (approximate) value of the second moment $u_1 = \mu_2 = EX_t^2$ of process X_t. Then

$$\lim_{n\to\infty} u_1(n) = u_1. \quad (29)$$

Moreover,

$$| u_1(n) - u_1 | \leq \epsilon_n \quad (30)$$

in which the sequence $\{\epsilon_n\}$ is independent of $\{k_n\}$ and $\epsilon_n \to 0$ as $n \to \infty$.

Table 4 Ratios for p_n and r_n

n	p_n/r_n	p_n/p_{n-1}	r_n/r_{n-1}
	$\alpha = 0.1$		
3	0.7692	1.0000	1.3000
10	0.8177	1.9209	1.9202
20	0.8176	2.5066	2.5066
30	0.8176	2.9557	2.9557
40	0.8176	3.3342	3.342
	$\alpha = 0.01$		
3	0.9709	1.0000	1.0300
10	0.9721	1.1499	1.1499
20	0.9721	1.2898	1.2898
30	0.9721	1.4080	1.4080
40	0.9721	1.5125	1.5125
	$\alpha = 0.001$		
3	0.9970	1.0000	1.0030
10	0.9970	1.0168	1.0168
20	0.9970	1.0358	1.0358
30	0.9970	1.0542	1.0542
40	0.9970	1.0719	1.0719
	$\alpha = 0.0001$		
3	0.9997	1.0000	1.0003
10	0.9997	1.0017	1.0017
20	0.9997	1.0037	1.0037
30	0.9997	1.0057	1.0057
40	0.9997	1.0076	1.0076

Proof. The approximate value of $u_1(n)$ is

$$u_1(n) = -\frac{a_{n+1} - k_n a_n}{b_{n+1} - k_n b_n} = \frac{p_{n+1} + \alpha k_n p_n}{r_{n+1} + \alpha k_n r_n} \quad (31)$$

From the definition of $u_1(n)$ in Eq. (31), the inequalities in Eq. (20) and properties of fractions used to prove (ii) in the lemma, the approximate value of u_1 can be bounded by $p_{2n+1}/r_{n+1} \leq u_1(2n) \leq p_{2n}/r_{2n}$ and $p_{2n+2}/r_{2n+2} \leq u_1(2n+1) \leq p_{2n+1}/r_{2n+1}$. These inequalities and the bounds on u_1 in the lemma give the result in Eq. 30 where $\epsilon_{2n} = \epsilon_{2n+1} = p_{2n}/r_{2n} - p_{2n+1}/r_{2n+1} \geq p_{2n+1}/r_{2n+1} - p_{2n+1}/r_{2n+1}$. According to the lemma, $\epsilon_{2n} = \epsilon_{2n+1} = \xi_n^{-1}$ converges to zero as $n \to \infty$.

Corollary 1. If $\{k_n\}$ in the theorem is allowed to be negative $u_1(n)$ may not converge to u_1 as $n \to \infty$.

Proof. Let k_n be defined by

$$\frac{p_{n+1} + \alpha k_n p_n}{r_{n+1} + \alpha k_n r_n} = u_1^* \quad (32)$$

where $u_1^* \neq u_1$ is a constant. In this case, the approximate value $u_1(n)$ of u_1 coincides with u_1^* for all values of n. Therefore, $\lim_{n\to\infty} u_1(n) = u_1^* \neq u_1$.

For example, the approximate values of EX_t^{2q} are 1, 0, 30, -300, and 5100 for $q = 1, 2, 3, 4$, and 5 when $\alpha = 0.1$, and $\{k_n\}$ satisfies Eq. (32) with $u_1^* = 1.0$. The closure method is unsatisfactory for this sequence $\{k_n\}$.

Corollary 2. Suppose that the sequence $\{k_n\}$ in the theorem is bounded but otherwise arbitrary. Then $u_1(n)$ converges to u_1 as $n \to \infty$.

Proof. From Eq. (31) an alternative form of $u_1(n)$ is

$$u_1(n) = \frac{p_n}{r_n} \cdot \frac{p_{n+1}/p_n + \alpha k_n}{r_{n+1}/r_n + \alpha k_n}$$

Downloaded 04 May 2010 to 171.66.16.28. Redistribution subject to ASME license or copyright; see http://www.asme.org/terms/Terms_Use.cfm

such that

$$\lim_{n\to\infty} u_1(n) = \lim_{n\to\infty} \frac{p_n}{r_n} \lim_{n\to\infty} \frac{p_{n+1}/p_n + \alpha k_n}{r_{n+1}/r_n + \alpha k_n}.$$

The first limit is equal to u_1 by the lemma. The second limit is equal to unity because

$$\lim_{n\to\infty} \left(\frac{p_{n+1}}{p_n}\right) \Big/ \left(\frac{r_{n+1}}{r_n}\right) = \lim_{n\to\infty} \frac{p_{n+1}}{r_{n+1}} \lim_{n\to\infty} \frac{r_n}{p_n} = u_1 \frac{1}{u_1} = 1,$$

by the lemma, $\{\alpha k_n\}$ is bounded by hypothesis, and the sequences $\{p_{n+1}/p_n\}$ and $\{r_{n+1}/r_n\}$ become unbounded as $n \to \infty$. Therefore, $(p_{n+1}/p_n + \alpha k_n)/(r_{n+1}/r_n + \alpha\ k_n) \cong (p_{n+1}/p_n)/(r_{n+1}/r_n)$ for sufficiently large values of n. The fact that the sequences p_{n+1}/p_n and r_{n+1}/p_n diverge as $n \to \infty$ follows from the asymptotic analysis in the next section.

The practical implication of this corollary is that $u_1(n)$ approximates satisfactorily u_1 irrespective of the particular bounded sequence $\{k_n\}$ provided that the closure level n is sufficiently large. Results in Table 3 are consistent with this statement.

Corollary 3. It follows from the lemma that, for some n, $a_n + b_n u_1^*$ will become negative if $u_1^* \neq u_1 = EX_t^2$. Otherwise, u_1^* would satisfy part (i) of the lemma for every n, and would therefore not differ from u_1.

Asymptotic Behavior of Moments of X_t

Consider the diffusion process in Eq. (1) with $\beta = 2$. This section develops asymptotic expressions for the moments of X_t as order q approaches infinity.

Case 1($\alpha = 0$). The successive application of Eq. (14) gives

$$v_q = \mu_{2q} = (2q-1)(2q-3)\ldots\ (1) = \frac{(2q)!}{q!\,2^q}, \quad (33)$$

an expected result because X_t is a Gaussian process. An asymptotic expression of v_q and μ_{2q} can be obtained from the Stirling formula (Abramowitz and Stegan, 1970)

$$v_q = \mu_{2q} \sim e^{-q} 2^{q+\frac{1}{2}} q^{q+\frac{1}{2}}, \quad \text{as } q \to \infty \quad (34)$$

for large values of q.

The controlling factor of this asymptotic solution is

$$CF_{(\alpha=0)} = q^q, \quad \text{as } q \to \infty \quad (35)$$

because this factor is the most rapidly changing component in Eq. 34 as $q \to \infty$ (Bendar and Orszag, 1978, pg. 80). The moments $\mu_{2q} = v_q$ of X_t for $\alpha = 0$ grow at the rate q^q as $q \to \infty$.

Case 2($\alpha > 0$). Consider the change of variables $u_q = \alpha^{-q} v_q$ in Eq. (12). The new variables v_q satisfy the difference equations

$$v_{q+2} + v_{q+1} - (2q+1)\alpha v_q = 0, \quad q = 0, 1, 2, \ldots \quad (36)$$

or

$$D^2 v_q + 3Dv_q - ((2q+1)\alpha - 2)v_q = 0, \quad q = 0, 1, 2, \ldots \quad (37)$$

where $Dv_q = v_{q+1} - v_q$. The term $(2q+1)\ \alpha - 2$ can be approximated by $2\alpha q$ for large values of q. The differential equation analog to Eq. (37) is (Bendar and Orszag, 1978, pg. 207)

$$\frac{d^2 v(\xi)}{d\xi^2} + 3\frac{dv(\xi)}{d\xi} - 2\alpha\xi v(\xi) = 0. \quad (38)$$

The asymptotic solution and the controlling factor of v_q as $q \to \infty$ can be obtained from Eq. (38) for $\xi \to \infty$ or, equivalently, from

$$\frac{d^2 v(z)}{dz^2} + p_1(z)\frac{dv(z)}{dz} + p_0(z)v(z) = 0 \quad (39)$$

as $z \to z_0 = 0$, in which $\xi = 1/z$, $p_1(z) = 2/z - 3/z^2$, and $p_0(z) = -2\alpha/z^s$. Point z_0 is neither an ordinary nor a regular singular point because the functions $p_s(z)$ and $(z - z_0)^{2-s} p_s(z)$, $s = 0, 1$, are not analytic in a neighborhood of z_0. Therefore, $z_0 = 0$ is an irregular singular point (Bendar and Orszag, 1978, p. 63). The relationship between Eqs. (36) and (39) indicates that infinity is an irregular singular point for Eq. (36).

The controlling factor of the solution v_q of Eq. 36 as $q \to \infty$ near the irregular singular point at infinity can be obtained by following a method by Bendar and Orszag (1978, p. 216). Consider the change of variables in Eq. (36).

$$v_q = e^{Sq} \quad (40)$$

that give

$$v_q e^{D^2 S_q + 2DS_q} + v_q e^{DS_q} - (2q+1)\alpha v_q = 0 \quad (41)$$

because $v_{q+1} = e^{S_{q+1}} = e^{DS_q} e^{S_q} = v_q e^{DS_q}$ and $v_{q+2} = v_{q+1} e^{DS_{q+1}} = v_q e^{DS_q} e^{DS_{q+1}} = v_q e^{D^2 S_q} e^{2DS_q}$. This equation simplifies to

$$v_q e^{2DS_q} + v_q e^{DS_q} - 2\alpha q v_q = 0 \quad (42)$$

as $q \to \infty$ provided that $D^2 S_q \ll 2DS_q$. In this case, e^{DS_q} is the positive solution of the quadratic equation $y^2 + y - 2\alpha q = 0$, such that

$$e^{DS_q} \sim \sqrt{2\alpha q}, \quad \text{as } q \to \infty \quad (43)$$

and

$$DS_q \sim \log\sqrt{2\alpha q}, \quad \text{as } q \to \infty. \quad (44)$$

The solution of this equation is $S_q - S_1 = \sum_{s=1}^{q-1} \log\sqrt{2\alpha s}$ and can be approximated by the integral (Bendar and Orszag, 1978, p. 216)

$$S_q \sim \int^q \log\sqrt{2\alpha s}\, ds \sim q\log\sqrt{2\alpha} + \frac{1}{2} q\log q, \quad \text{as } q \to \infty. \quad (45)$$

The controlling factor of the solution v_q of Eq. (36) is

$$CF_{(\alpha>0)} = q^{q/2}, \quad \text{as } q \to \infty \quad (46)$$

as it can be seen from Eqs. (40) and (45).

From Eqs. (35) and (46) there is a discontinuity in the asymptotic behavior of the stationary moments of X_t in Eq. (12) of large order. The controlling factors of the moments of X_t are q^q and $q^{q/2}$ for $\alpha = 0$ and $\alpha > 0$, as $q \to \infty$. Their determination is not based on any approximation for solving the infinite hierarchy of moment equations, such as closure techniques. The moments of X_t increase at a much slower rate for $\alpha > 0$ than for $\alpha = 0$. This shows that the method of moments is asymptotically incorrect.

There is no discontinuity in the moments of X_t when the

Downloaded 04 May 2010 to 171.66.16.28. Redistribution subject to ASME license or copyright; see http://www.asme.org/terms/Terms_Use.cfm

analysis is based on the probability density function $f(x; \alpha)$ of X_t. This density approaches the Gaussian probability corresponding to $\alpha = 0$ as shown in Eqs. (2)–(7). Therefore, the moments $\mu_r(\alpha)$ of X_t in Eq. 8 for $\alpha > 0$ approach the corresponding moments of X_t in Eq. 9 for $\alpha = 0$ as $\alpha \to 0$.

Conclusions

A simple nonlinear stochastic differential equation was used to demonstrate that the success of the closure method is not the result of a particular closure technique. The success is the result of the unusual behavior of the moment equations. Moreover, it was shown that the closure method is incorrect asymptotically as the number of moment equations considered in the analysis increases indefinitely.

References

Abramowitz, M., and Stegan, J. A., 1970, *Handbook of Mathematical Functions*, Dover Publications, New York.

Adomian, G., 1983, *Stochastic Systems*, Academic Press, New York.

Arnold, L., 1973, *Stochastic Differential Equations: Theory and Applications*, John Wiley and Sons, New York.

Bendar, C. M., and Orszag, S. A., 1978, *Advanced Mathematical Methods for Scientists and Engineers*, McGraw-Hill, New York.

Bolotin, V. V., 1984, *Random Vibration of Elastic Systems*, Martinus Nijhoff Publishers, Boston, MA.

Ibrahim, R. A., 1984, *Parametric Random Vibration*, Research Studies Press, New York.

Rectorys, K., ed., 1969, *Survey of Applicable Mathematics*, M.I.T. Press, Cambridge, MA.

Richardson, J. M., 1964, "The Application of Truncated Hierarchy Techniques in the Solution of a Stochastic Linear Differential Equation," *Proceedings Symposium on Applied Mathematics*, Vol. 16, R. Bellman, ed., AMS, New York, pp. 290–302.

Downloaded 04 May 2010 to 171.66.16.28. Redistribution subject to ASME license or copyright; see http://www.asme.org/terms/Terms_Use.cfm

Journal of Applied Mechanics

Brief Notes

A Brief Note is a short paper that presents a specific solution of technical interest in mechanics but which does not necessarily contain new general methods or results. A Brief Note should not exceed 1500 words *or equivalent* (a typical one-column figure or table is equivalent to 250 words; a one line equation to 30 words). Brief Notes will be subject to the usual review procedures prior to publication. After approval such Notes will be published as soon as possible. The Notes should be submitted to the Technical Editor of the JOURNAL OF APPLIED MECHANICS. Discussions on the Brief Notes should be addressed to the Editorial Department, ASME, United Engineering Center, 345 East 47th Street, New York, N. Y. 10017, or to the Technical Editor of the JOURNAL OF APPLIED MECHANICS. Discussions on Brief Notes appearing in this issue will be accepted until two months after publication. Readers who need more time to prepare a Discussion should request an extension of the deadline from the Editorial Department.

Fourier Series Solution for the Dugdale Crack in a Cylindrical Shell

Yee-Chung Fu[1,3] and C. R. Steele[2,3]

A Fourier series method has been used by Kwok (1994) to calculate the energy release rate for a cylindrical shell with a circumferential through crack. In this note the same method is applied to calculate the Dugdale plastic model.

A cylindrical shell with a circumferential through crack under remote tension and bending is shown in Fig. 1. The standard procedure is followed in order to find out the stress intensity and the energy release rate. The cylindrical shell and force condition are symmetric with respect to the midplane so that displacement in the axial direction is zero on the midplane except on the crack face.

The technique of expansion and contraction matrices will be used. The Fourier series of displacement field at the midplane is written as

$$u^{\Gamma}(\theta) = \begin{cases} \sum_{n=1}^{N} U_n^{\Gamma} \sin\dfrac{(2n-1)\pi}{\theta_1}\left(\theta + \dfrac{\theta_1}{2}\right), & -\dfrac{\theta_1}{2} \le \theta \le \dfrac{\theta_1}{2} \\ 0, \quad \text{elsewhere} \end{cases} \tag{1}$$

$$u^{\Omega}(\theta) = \sum_{m=0}^{M} U_m^{\Omega} \cos m\theta, \quad -\pi \le \theta \le \pi \tag{2}$$

Where N, M are the numbers of harmonics which are used to describe the displacement field in the crack and global domain; $u^{\Gamma}(\theta)$ and $u^{\Omega}(\theta)$ approach the real displacement field as N and M increase. $M \approx N^*2a/2\pi r$ which provides the same resolution for the two different expansion series. The crack and the global domains are defined as $\Gamma(-\theta_1/2 \le \theta \le \theta_1/2)$ and $\Omega(-\pi \le \theta \le \pi)$. Equating the two Fourier series of (1) and (2) in the Ω domain and setting $n = 1,2,\ldots,N$, and $m = 0,1,2,\ldots,M$, yields the following equation:

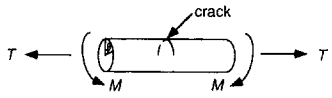

Fig. 1 A cylindrical shell under remote bending and tension

$$U_m^{\Omega} = \sum_{n=1}^{N} E_{mn} U_n^{\Gamma} \tag{3}$$

where

$$E_{mn} = \frac{1}{\pi}\int_{-\frac{\theta_1}{2}}^{\frac{\theta_1}{2}} \cos m\theta \sin\frac{(2n-1)\pi}{\theta_1}\left(\theta + \frac{\theta_1}{2}\right)d\theta, \quad (m \ne 0)$$

E_{mn} is called the "expansion matrix"; it transfers the Fourier coefficients from the crack domain (U_n^{Γ}) to the global domain (U_m^{Ω}). Similarly, the traction on the crack face can be treated as

$$f^{\Gamma}(\theta) = \sum_{n=1}^{N} F_n^{\Gamma} \sin\frac{(2n-1)\pi}{\theta_1}\left(\theta + \frac{\theta_1}{2}\right), \quad -\frac{\theta_1}{2} \le \theta \le \frac{\theta_1}{2} \tag{4}$$

$$f^{\Omega}(\theta) = \sum_{m=0}^{M} F_m^{\Omega} \cos m\theta, \quad -\pi \le \theta \le \pi. \tag{5}$$

Equating (4) and (5) in the crack domain $\left(-\dfrac{\theta_1}{2} \le \theta \le \dfrac{\theta_1}{2}\right)$ yields the following equation:

$$F_n^{\Gamma} = \sum_{m=1}^{M} C_{nm} F_m^{\Omega}, \tag{6}$$

where

$$C_{nm} = \frac{2}{\theta_1}\int_{-\theta_1/2}^{\theta_1/2} \sin\frac{(2n-1)\pi}{\theta_1}\left(\theta + \frac{\theta_1}{2}\right)\cos m\theta d\theta, \quad (m \ne 0).$$

C_{nm} is called the "contraction matrix," it transfers the Fourier coefficients from the global domain (F_m^{Ω}) to the crack domain (F_n^{Γ}).

[1]Graduate Student.
[2]Professor, Fellow ASME.
[3]Division of Applied Mechanics, Durand Building, Stanford University, Stanford, CA 94305.

Contributed by the Applied Mechanics Division of THE AMERICAN SOCIETY OF MECHANICAL ENGINEERS for publication in the ASME JOURNAL OF APPLIED MECHANICS. Manuscript received and accepted by the ASME Applied Mechanics Division, May 9, 1994. Associate Technical Editor: C. F. Shih.

Copyright © 1995 by ASME

Downloaded 04 May 2010 to 171.66.16.28. Redistribution subject to ASME license or copyright; see http://www.asme.org/terms/Terms_Use.cfm

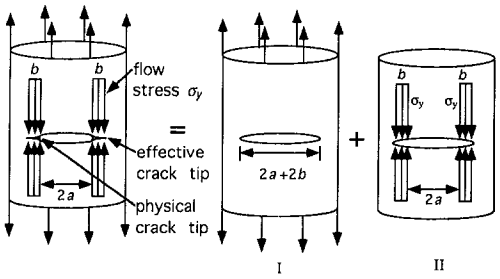

Fig. 2 Force decomposition for the Dugdale crack model

In the global domain, the Fourier coefficients of traction and displacement are related by a stiffness matrix $\mathbf{K}^{\Omega}$:

$$\mathbf{F}^{\Omega}_{m\times 1} = \mathbf{K}^{\Omega}_{m\times m}\mathbf{u}^{\Omega}_{m\times 1} \tag{7}$$

Combining Eqs. (3), (6), and (7) yields the following equation:

$$\begin{aligned}\mathbf{f}^{\Gamma}_{n\times 1} &= \mathbf{C}_{n\times m}\mathbf{K}^{\Omega}_{m\times m}\mathbf{E}_{m\times n}\mathbf{u}^{\Gamma}_{n\times 1}\\ &= \mathbf{K}^{\Gamma}_{n\times n}\mathbf{u}^{\Gamma}_{n\times 1}\\ \mathbf{K}^{\Gamma}_{n\times n} &= \mathbf{C}_{n\times m}\mathbf{K}^{\Omega}_{m\times m}\mathbf{E}_{m\times n}\end{aligned} \tag{8}$$

in which $\mathbf{K}^{\Gamma}_{n\times n}$ is the stiffness matrix in the crack domain. It relates displacement to traction in the crack domain. If an arbitrary displacement field in the crack domain is given, the traction in the crack domain can be found, and vice versa. The energy release rate can also be found with this relationship (Kwok, 1994).

Figure 2 shows the Dugdale crack model. In front of a physical crack tip the normal stress along the crack line is equal to the flow stress σ_y to a certain extension length b, and is less than the flow stress beyond that distance. The unknown extension length b denotes the length of the plastic zone is called the "Dugdale zone." It is convenient to consider an effective crack which is longer than the physical crack $(2a)$ as shown in Fig. 2. The effective crack length $(2a + 2b)$ is the physical crack length plus the Dugdale zone on both sides. The normal stress in the Dugdale zone, the yield stress, tends to close the crack. The length of b is chosen such that the stress singularity disappears at the effective crack tip (Broek, 1986). The next step is to determine the length of the Dugdale zone and the crack-tip opening displacement (CTOD).

Figure 2 also shows the decomposition of the traction on the effective crack face and on the boundary. The two decomposed traction are employed to compute the displacement fields separately; the two displacement fields will be summed together later. The physical crack length $2a$ and the normal stress $\sigma(\theta)$ on the boundary is known, where $\sigma(\theta) = \sigma_{\max}\cos\theta$ and $\sigma_{\max} = M/\pi r^2 t$ for a remote bending moment M, r is the radius of the cylindrical shell, and t is the thickness; with (7), the energy release rate or the stress intensity of the first part in Fig. 2 is obtained.

The subsequent task is to adjust the length b of the second part and change the traction direction in order to have a same stress intensity as the first part to make the total stress intensity zero. The slope of displacement at the crack tip is either infinity or zero. If the stress intensity is zero then the crack tip is closed and the slope of displacement is zero at the crack tip. Since only a finite number of terms in the Fourier series is used the slope cannot go to infinity. However, the two slopes do have to be the same in order to cancel each other for closed crack tips of an effective crack. Differentiating (1) yields the following equation:

$$\sum_{n=1}^{N} U^{\Gamma}_{nI}\left(\frac{2n-1}{\theta_1}\right) = \sum_{n=1}^{N} U^{\Gamma}_{nII}\left(\frac{2n-1}{\theta_1}\right). \tag{9}$$

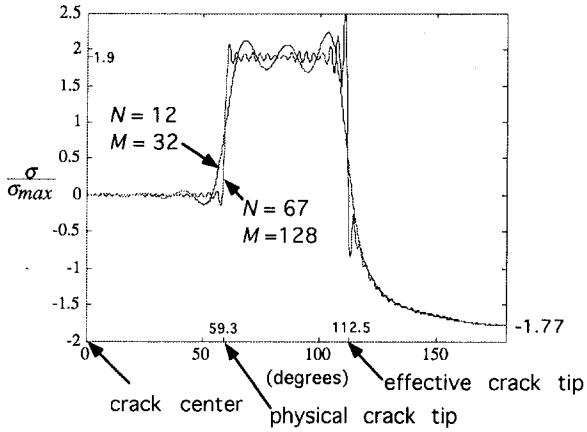

Fig. 3 Stress distribution on the midplane of a cylindrical shell from the crack center to half of the circumference

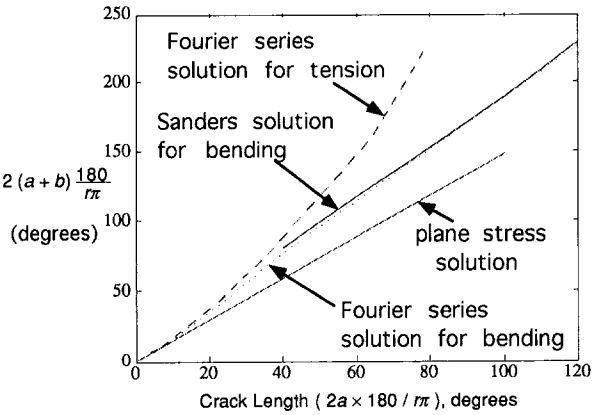

Fig. 4 The effective crack length versus physical crack length for bending and tension loading

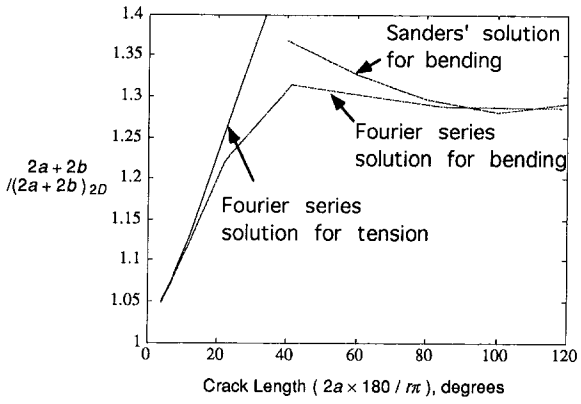

Fig. 5 The ratio of the effective crack length for cylinder to the plane stress solution versus physical crack length ($2a$)

The left-hand side of (9), from the Part I in Fig. 2, is known; the right-hand side is a function of b which is to be determined. Two examples are shown in the following section.

For an example, the data is set as: radius/thickness = 40, radius = 25.4 mm, Young's modulus = 0.2×10^{12} Pa, Poisson's ratio = 0.3, $\sigma_y/\sigma_{\max} = 1.9$, $\sigma(\theta) = \sigma_{\max}\cos\theta$ and the number of the harmonics at crack domain, N, is set to 12.

If the physical crack length is small the stress field around the crack approaches the plane stress analytical solution. Figure 3 shows the stress field along the midplane from the crack center to half of the circumference. The physical crack length is 118.6 deg and the effective crack length 225 deg in Fig. 3. At $\theta = 180$ deg the stress is $-1.77\sigma_{\max}$ which does

Downloaded 04 May 2010 to 171.66.16.28. Redistribution subject to ASME license or copyright; see http://www.asme.org/terms/Terms_Use.cfm

not exceed the compressive flow stress. It also shows that the Fourier series converges rapidly, for twelve harmonics in the crack domain the stress has already converged to $-1.77\sigma_{max}$ at $\theta = 180$. In Fig. 4, the physical crack length is chosen as the variable. The effective crack length for remote bending and remote tension of the cylinder is shown. As the crack length increases the curve for bending is very close to the result of Sanders (1987). Figure 5 shows the same information but for the ratio of effective crack length to that for the plane stress solution. When the crack length, $2a$, approaches zero the ratio approaches unity which provides a verification of the Fourier series solution. Sanders' solution is derived from the semi-membrane theory which is appropriate for a thin cylindrical shell with a large size crack.

Thus the Fourier series method appears to be a general and efficient technique for the Dugdale crack calculation in a cylindrical shell. It is suitable for thin and thick shells with a small or large crack. The setup time and computation for one configuration requires about one minute on a Sparc 10 workstation.

References

Broek, D., 1986, *Elementary Engineering Fracture Mechanics*, 4th rev. ed., Martinus Nijhoff, Dordrecht, The Netherlands.

Kwok, F. M. W., 1994, "Fourier Series Method for Cracks in Polygonal Plates and Shells of Revolution," Ph.D. Thesis, Stanford University, Stanford, CA.

Sanders, J. L., Jr., 1987, "Dugdale Model for Circumferential Through-Cracks in Pipes Loaded by Bending," *International Journal of Fracture*, Vol. 34, pp. 71–81.

On the Partly Bonded Thermoelastic Circular Inhomogeneity

M. A. Kattis[1,2] and S. A. Meguid[1,2]

The thermoelastic problem of an infinite elastic plane containing a partly bonded circular inhomogeneity of different thermomechanical properties is considered. Based upon the solution of a perfectly bonded inhomogeneity established in the current work, the complex stress intensity factor of the interfacial crack problem is obtained for full heat-conductive conditions of an "open" crack and for a linear temperature change at infinity.

Introduction

Theoretical studies on thermoelastic crack problems based on the more realistic condition of "radiation" across the crack have shown that the degree of the heat conductivity at crack surfaces affects the magnitude of the stress intensity factors and depends drastically upon the crack size (Barber, 1976; Kuo, 1990a,b; Thangjitham and Choi, 1993). The crack size effect implies that, for a given set of thermal conductivity and heat conductance coefficient, an extremely small crack can be treated as an insulated crack, and a very long crack can be treated as a fully heat conductive crack (Kuo, 1990a).

Considered in this note is the thermoelastic interface crack problem of a circular inhomogeneity contained in an infinite plane matrix for fully heat conductive conditions at the crack surfaces. The matrix and inhomogeneity consist of isotropic and homogeneous materials of different thermomechanical properties, and the thermal condition at infinity is a linear temperature change. Based on the solution of the corresponding thermoelastic problem of a perfectly bonded inhomogeneity established in this work, explicit forms of the complex stress intensity factor of the interface crack are obtained in terms of the two-phase Dundurs parameters. To ensure no contact between the crack surfaces, except that due to the logarithmic oscillation, the assumption of an "open" crack is adopted (Kuo, 1990b).

Perfectly Bonded Inhomogeneity

Consider that the circular region $|z| \le R$ of a complex z-plane is occupied by a material of different thermomechanical properties than that of the surrounding region that corresponds to an infinite elastic matrix. Assume that the two phases are isotropic and homogeneous media and the matrix is subjected to a temperature change $T_\infty + q_\infty y/k_{t1}$ of the reference temperature at infinity, where T_∞ and q_∞ denote a uniform temperature change and a uniform heat flow along the y-axis, respectively, and k_{t1} is the coefficient of thermal conductivity of the matrix. According to Muskhelishvili (1953), the resultant force $\mathfrak{F}$ on an arc, and the displacement D can be written in terms of two complex potentials W and $\mathfrak{W}$ and a temperature function F such that

$$2i\mathfrak{F} = {}'W(z) + z\overline{W(z)} + {}'\overline{\mathfrak{W}(z)}, \tag{1}$$

$$4\mu D = \kappa\,{}'W(z) - z\overline{W(z)} - {}'\overline{\mathfrak{W}(z)} + 2\beta_t' F(z), \tag{2}$$

where $\kappa = 3 - 4\nu$ and $\beta_t = 4\mu a_t(1 + \nu)$ for plane strain, $\kappa = (3 - \nu)/(1 + \nu)$ and $\beta_t = 4\mu a_t$ for plane stress, with μ and ν being the shear modulus and Poisson's ratio, respectively, and a_t is the coefficient of linear thermal expansion. Left prime functions denote indefinite integration with respect to the appropriate variable. For the heat conduction problem, the total heat flow $\mathfrak{Q}$ on an arc and the temperature T can be expressed in terms of the complex potential F by

$$-\frac{i}{k_t}\mathfrak{Q} = F(z) - \overline{F(z)}, \tag{3}$$

$$T = F(z) + \overline{F(z)}, \tag{4}$$

where k_t is the thermal conductivity. Assuming a perfect thermal contact and a perfect bonding between the two phases, the following conditions should be satisfied along the interface

$$\mathfrak{Q}_1 = \mathfrak{Q}_2, \quad T_1 = T_2, \tag{5}$$

$$\mathfrak{F}_1 = \mathfrak{F}_2, \quad D_1 = D_2, \tag{6}$$

where the subscripts 1 and 2 are used to denote quantities associated with the matrix and inclusion, respectively.

Using the two-phase potential method developed by the authors (Kattis and Meguid, 1994), the complex potentials of the two phases satisfying the above interfacial conditions for plane stress conditions are found as

$$W_1(z) = \frac{4\mu_1 a_{1t} K q_\infty i R^2}{k_{t1}(1 + \kappa_1)}\frac{1}{z} \tag{7}$$

$$\mathfrak{W}_1(z) = \frac{4\mu_1(a_{t2} - a_{t1})(1 + \Lambda)T_\infty}{(1 + \kappa_1)(1 - \Omega)}\frac{1}{z^2}$$

---

[1]Engineering Mechanics and Design Laboratory, Department of Mechanical Engineering, University of Toronto, Toronto, Ontario M5S 1A4, Canada.

[2]Mem. ASME.

Contributed by the Applied Mechanics Division of THE AMERICAN SOCIETY OF MECHANICAL ENGINEERS for publication in the ASME JOURNAL OF APPLIED MECHANICS. Manuscript received by the ASME JOURNAL OF APPLIED MECHANICS, May 6, 1993; final revision, Aug. 12, 1994. Associate Technical Editor: D. M. Parks.

Downloaded 04 May 2010 to 171.66.16.28. Redistribution subject to ASME license or copyright; see http://www.asme.org/terms/Terms_Use.cfm

not exceed the compressive flow stress. It also shows that the Fourier series converges rapidly, for twelve harmonics in the crack domain the stress has already converged to $-1.77\sigma_{max}$ at $\theta = 180$. In Fig. 4, the physical crack length is chosen as the variable. The effective crack length for remote bending and remote tension of the cylinder is shown. As the crack length increases the curve for bending is very close to the result of Sanders (1987). Figure 5 shows the same information but for the ratio of effective crack length to that for the plane stress solution. When the crack length, $2a$, approaches zero the ratio approaches unity which provides a verification of the Fourier series solution. Sanders' solution is derived from the semi-membrane theory which is appropriate for a thin cylindrical shell with a large size crack.

Thus the Fourier series method appears to be a general and efficient technique for the Dugdale crack calculation in a cylindrical shell. It is suitable for thin and thick shells with a small or large crack. The setup time and computation for one configuration requires about one minute on a Sparc 10 workstation.

References

Broek, D., 1986, *Elementary Engineering Fracture Mechanics*, 4th rev. ed., Martinus Nijhoff, Dordrecht, The Netherlands.

Kwok, F. M. W., 1994, "Fourier Series Method for Cracks in Polygonal Plates and Shells of Revolution," Ph.D. Thesis, Stanford University, Stanford, CA.

Sanders, J. L., Jr., 1987, "Dugdale Model for Circumferential Through-Cracks in Pipes Loaded by Bending," *International Journal of Fracture*, Vol. 34, pp. 71–81.

On the Partly Bonded Thermoelastic Circular Inhomogeneity

M. A. Kattis[1,2] and S. A. Meguid[1,2]

The thermoelastic problem of an infinite elastic plane containing a partly bonded circular inhomogeneity of different thermomechanical properties is considered. Based upon the solution of a perfectly bonded inhomogeneity established in the current work, the complex stress intensity factor of the interfacial crack problem is obtained for full heat-conductive conditions of an "open" crack and for a linear temperature change at infinity.

Introduction

Theoretical studies on thermoelastic crack problems based on the more realistic condition of "radiation" across the crack have shown that the degree of the heat conductivity at crack surfaces affects the magnitude of the stress intensity factors and depends drastically upon the crack size (Barber, 1976; Kuo, 1990a,b; Thangjitham and Choi, 1993). The crack size effect implies that, for a given set of thermal conductivity and heat conductance coefficient, an extremely small crack can be treated as an insulated crack, and a very long crack can be treated as a fully heat conductive crack (Kuo, 1990a).

[1]Engineering Mechanics and Design Laboratory, Department of Mechanical Engineering, University of Toronto, Toronto, Ontario M5S 1A4, Canada.

[2]Mem. ASME.

Contributed by the Applied Mechanics Division of THE AMERICAN SOCIETY OF MECHANICAL ENGINEERS for publication in the ASME JOURNAL OF APPLIED MECHANICS. Manuscript received by the ASME JOURNAL OF APPLIED MECHANICS, May 6, 1993; final revision, Aug. 12, 1994. Associate Technical Editor: D. M. Parks.

Considered in this note is the thermoelastic interface crack problem of a circular inhomogeneity contained in an infinite plane matrix for fully heat conductive conditions at the crack surfaces. The matrix and inhomogeneity consist of isotropic and homogeneous materials of different thermomechanical properties, and the thermal condition at infinity is a linear temperature change. Based on the solution of the corresponding thermoelastic problem of a perfectly bonded inhomogeneity established in this work, explicit forms of the complex stress intensity factor of the interface crack are obtained in terms of the two-phase Dundurs parameters. To ensure no contact between the crack surfaces, except that due to the logarithmic oscillation, the assumption of an "open" crack is adopted (Kuo, 1990b).

Perfectly Bonded Inhomogeneity

Consider that the circular region $|z| \le R$ of a complex z-plane is occupied by a material of different thermomechanical properties than that of the surrounding region that corresponds to an infinite elastic matrix. Assume that the two phases are isotropic and homogeneous media and the matrix is subjected to a temperature change $T_\infty + q_\infty y/k_{t1}$ of the reference temperature at infinity, where T_∞ and q_∞ denote a uniform temperature change and a uniform heat flow along the y-axis, respectively, and k_{t1} is the coefficient of thermal conductivity of the matrix. According to Muskhelishvili (1953), the resultant force $\mathfrak{F}$ on an arc, and the displacement D can be written in terms of two complex potentials W and $\mathfrak{W}$ and a temperature function F such that

$$2i\mathfrak{F} = {}'W(z) + z\overline{W(z)} + {}'\overline{\mathfrak{W}(z)}, \tag{1}$$

$$4\mu D = \kappa\,{}'W(z) - z\overline{W(z)} - {}'\overline{\mathfrak{W}(z)} + 2\beta_t' F(z), \tag{2}$$

where $\kappa = 3 - 4\nu$ and $\beta_t = 4\mu a_t(1 + \nu)$ for plane strain, $\kappa = (3 - \nu)/(1 + \nu)$ and $\beta_t = 4\mu a_t$ for plane stress, with μ and ν being the shear modulus and Poisson's ratio, respectively, and a_t is the coefficient of linear thermal expansion. Left prime functions denote indefinite integration with respect to the appropriate variable. For the heat conduction problem, the total heat flow $\mathfrak{Q}$ on an arc and the temperature T can be expressed in terms of the complex potential F by

$$-\frac{i}{k_t}\mathfrak{Q} = F(z) - \overline{F(z)}, \tag{3}$$

$$T = F(z) + \overline{F(z)}, \tag{4}$$

where k_t is the thermal conductivity. Assuming a perfect thermal contact and a perfect bonding between the two phases, the following conditions should be satisfied along the interface

$$\mathfrak{Q}_1 = \mathfrak{Q}_2, \quad T_1 = T_2, \tag{5}$$

$$\mathfrak{F}_1 = \mathfrak{F}_2, \quad D_1 = D_2, \tag{6}$$

where the subscripts 1 and 2 are used to denote quantities associated with the matrix and inclusion, respectively.

Using the two-phase potential method developed by the authors (Kattis and Meguid, 1994), the complex potentials of the two phases satisfying the above interfacial conditions for plane stress conditions are found as

$$W_1(z) = \frac{4\mu_1 a_{1t} K q_\infty i R^2}{k_{t1}(1 + \kappa_1)}\frac{1}{z} \tag{7}$$

$$\mathfrak{W}_1(z) = \frac{4\mu_1(a_{t2} - a_{t1})(1 + \Lambda)T_\infty}{(1 + \kappa_1)(1 - \Omega)}\frac{1}{z^2}$$

Copyright © 1995 by ASME

Downloaded 04 May 2010 to 171.66.16.28. Redistribution subject to ASME license or copyright; see http://www.asme.org/terms/Terms_Use.cfm

$$-\frac{4\mu_1 a_{1t} q_\infty i R^2}{k_{t1}(1+\kappa_1)}\left[2\left(\frac{1+\Lambda}{2}\delta - K\right)\frac{R^2}{z_3} + K\frac{1}{z}\right] \quad (8)$$

$$F_1(z) = \frac{q_\infty i}{2k_{1t}}\left(z - K\frac{R^2}{z}\right) + \frac{T_\infty}{2} \quad (9)$$

for the matrix, and

$$W_2(z) = -\frac{4\mu_1(a_{t2}-a_{t1})(1+\Lambda)T_\infty}{(1+\kappa_1)(1-\Omega)} - \frac{4\mu_1\delta q_\infty i(1+\Lambda)}{k_{1t}(1+\kappa_1)}z, \quad (10)$$

$$\mathfrak{W}_2(z) = 0, \quad F_2(z) = \frac{q_\infty i}{(1+k)k_{t1}}z + \frac{T_\infty}{2} \quad (11)$$

for the inhomogeneity, where

$$\delta = \frac{2a}{1+k} - 1, \quad K = \frac{1-k}{1+k}, \quad \Lambda = \frac{\alpha+\beta}{1-\beta}$$

$$\text{and} \quad \Omega = -\frac{\alpha-\beta}{1-\beta}$$

with α and β denoting the Dundurs two-phase parameters (Dundurs, 1970) given by

$$\alpha = \frac{\Gamma(1+\kappa_1)-(1+\kappa_2)}{\Gamma(1+\kappa_1)+1+\kappa_2}, \quad \beta = \frac{\Gamma(\kappa_1-1)-(\kappa_2-1)}{\Gamma(1+\kappa_1)+1+\kappa_2}$$

and $k = k_{t2}/k_{t1}$, $a = a_{t2}/a_{t1}$, $\Gamma = \mu_2/\mu_1$. By virtue of (1), (10), and (11), the interface traction can be calculated for the more general case where the heat flow q_∞ is inclined at an angle γ with respect to the positive x-axis. It is found that

$$\sigma_\rho + i\sigma_{\rho\theta} = p_t + p_q z \quad (12)$$

with

$$p_t = \frac{4\mu_1(a_{t1}-a_{t2})(1+\Lambda)T_\infty}{(1+\kappa_1)(1-\Omega)},$$

$$p_q = \frac{2\mu_1 a_{t1}\delta q_\infty e^{-i\gamma}(1+\Lambda)}{k_{t1}(1+\kappa_1)}$$

where σ_ρ and $\sigma_{\rho\theta}$ are the stress components with respect to the polar coordinates ρ and θ ($z = \rho e^{i\theta}$). When $T_\infty = 0$, the interface traction has a constant magnitude and for a given direction of the heat flow, the interface is separated in two symmetrical semicircular arcs of tensional and compressional normal interface stresses σ_ρ. When $\delta > 0$, the compressional arc corresponds to the side in which the heat flows into the inclusion.

Partly Bonded Inhomogeneity

Consider now the case in which a temperature change $T_\infty - \mathrm{Re}(q_\infty e^{-i\gamma}z)/k_{t1}$ is applied to the matrix and an interface crack is located along the arc $|\theta| \le \phi$ (Fig. 1). If the interface thermal continuity is assumed to be maintained, the additional state owing to the crack presence can be determined by considering the corresponding isothermal problem of equal and opposite tractions $-p_t - p_q z$ at each crack face. Assuming conditions of an "open" interface crack (Kuo, 1990), the fracture parameters at the crack tip can be derived from the W-potential of the isothermal crack problem. Introducing a tangential Cartesian coordinate system (X, Y) at the crack tip $e^{-i\phi}$ as in Fig. 1, the complex stress intensity factor in terms of the W-potential of the matrix can be written in the form (Rice, 1988; Malyshev and Salganik, 1965):

$$\bar{K} = \frac{1}{2}\sqrt{\frac{\pi}{2}}(1-\beta)L^{-\epsilon i}\lim_{t\to 0}[t^\tau W_1] \quad (13)$$

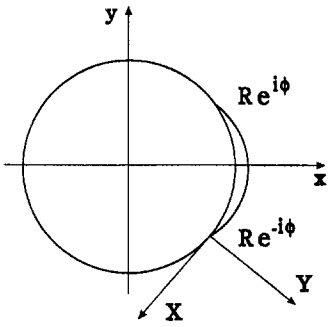

Fig. 1 Partly bonded circular elastic inhomogeneity in an elastic plane matrix

with

$$\tau = \frac{1}{2} + i\epsilon, \quad \epsilon = \frac{1}{2\pi}\ln\frac{1+\beta}{1-\beta}$$

where $t = e^{i\pi/2+i\phi}(z - \mathrm{Re}^{i\phi})$ represents a point of the matrix at the neighborhood of the crack tip with respect to the local system. The parameter L is a characteristic crack length and is introduced so that the stress intensity factor has dimensions *stress*(*length*)$^{1/2}$. The W-potential of the current isothermal problem is derived by extending England's solution for the case of a linear traction (England, 1966); the following form is obtained:

$$\frac{1-\beta}{2}W_1(z) = -p_t\mathfrak{A} - p_q\left[z + \frac{L^2\mathfrak{B}}{2R} - G_\infty(z)X(z)\right] + \left(p_t\mathfrak{A} - p_q\frac{L^2\mathfrak{B}}{2R}\right)(z - Rd)X(z) \quad (14)$$

where

$$X(z) = (z - \mathrm{Re}^{i\phi})^{-\bar{\tau}}(z - \mathrm{Re}^{-i\phi})^{-\tau},$$

$$G_\infty(z) = z^2 - Rdz + R^2(d^2 - D)$$

with

$$L = 2R\sin\phi$$

$$\mathfrak{A} = \frac{1 + 2\alpha_1 - \beta_1}{1 + 2\alpha_1 - \beta_1 de^{-2\epsilon\phi}},$$

$$\mathfrak{B} = \frac{\beta_1|\tau|^2\left[\alpha_1 - \beta_1 de^{-2\epsilon\phi} - (1+\alpha_1)e^{2\epsilon i}\right]e^{-2\epsilon\phi}}{(1 + 2\alpha_1 - \beta_1 de^{-2\epsilon\phi})(1 + \beta_1 de^{-2\epsilon\phi})},$$

$$\alpha_1 = \frac{1+\alpha}{1-\alpha}, \quad \beta_1 = \frac{1+\beta}{1-\beta},$$

$$d = \cos\phi + 2\epsilon\sin\phi,$$

$$D = \frac{1}{4}\left[1 + 4\epsilon^2 + (3 - 4\epsilon^2)\cos^2 2\phi + 8\epsilon\sin 2\phi\right].$$

$X(z)$ is the Plemelj function defined on the crack arc and that branch is taken into account for which $zX(z) \to 1$ as $z \to \infty$. The complex stress intensity factor is obtained from (13) and (14) in the following form:

$$\bar{K} = \mathfrak{C}\bar{\tau}\sqrt{\frac{L\pi}{2}}\,e^{i\phi/2 - \epsilon\phi} \quad (15)$$

where

$$\mathfrak{C} = p_t\mathfrak{A} + p_q\frac{L^2\mathfrak{B}}{2R} - ip_q\left(\bar{\tau} + \frac{i}{\tan\phi}\right)\frac{L}{2}.$$

Downloaded 04 May 2010 to 171.66.16.28. Redistribution subject to ASME license or copyright; see http://www.asme.org/terms/Terms_Use.cfm

For a rigid inclusion with an insulated boundary ($\mu_2 \to \infty$ and $a_{t2} = k_{t2} = 0$) and for a uniform temperature change ($q_\infty = 0$), Eq. (15) gives

$$\bar{K} = \frac{\mu_1 a_{t1} q_\infty}{k_{t1}} \bar{\tau} \left(\bar{\tau} + \frac{i}{\tan \phi} \right) L \sqrt{\frac{\pi L}{2}} \times \exp\left(-\epsilon\phi + i \frac{\phi + \pi - 2\gamma}{2} \right), \quad (16)$$

$$\bar{K} = \frac{4\mu_1(1 + \Lambda)(a_{t1} - a_{t2})T_\infty}{(1 + k_1)(1 - \Omega)} \bar{\tau} \sqrt{\frac{\pi L}{2}} \exp\left(-\epsilon\phi + i \frac{\phi}{2} \right). \quad (17)$$

Equations (16) and (17) are in agreement with those of the literature (Kattis and Duka, 1990; Muller and Schmauder, 1992).

References

Barber, J. R., 1980, "Steady-State Thermal Stresses Caused by an Imperfectly Conducting Penny-shaped Crack in an Elastic Solid," *Journal of Thermal Stresses*, Vol. 3, pp. 77–83.

Dundurs, J., 1970, "Some Properties of Elastic Stresses in a Composite," *Proceedings of the 6th Annual Meeting of the Society of Engineering Science*, Vol. 5, pp. 203–216.

England, A. H., 1966, "An Arc Crack Around a Circular Elastic Inclusion," ASME JOURNAL OF APPLIED MECHANICS, Vol. 33, pp. 637–640.

Malyshev, B., and Salganik, R. L., 1965, "The Strength of Adhesive Joints Using the Theory of Cracks," *International Journal of Fracture Mechanics*, Vol. 1, pp. 114–128.

Kattis, M. A., and Duka, E. D., 1990, "Thermal Stresses in an Elastic Plane Matrix Containing a Circular Inclusion with an Interface Crack," *Ceramics Today—Tomorrow's Ceramics*, Elsevier Science Publishers B.V., pp. F37–F45.

Kattis, M. A., and Meguid, S. A., 1994, "Two-Phase Potentials for the Treatment of an Elastic Inclusion in Plane Thermoelasticity," ASME JOURNAL OF APPLIED MECHANICS, in press.

Kou, A., 1990a, "Effects of Crack Surface Heat Conduction on Stresses Intensity Factors," ASME JOURNAL OF APPLIED MECHANICS, Vol. pp. 354–358.

Kou, A., 1990b, "Interface Crack Between Two Dissimilar Half Spaces Subjected to a Uniform Heat Flow at Infinity-Open Crack," ASME JOURNAL OF APPLIED MECHANICS, Vol. 57, pp. 359–364.

Muller, W. H., and Schmauder, S., 1992, "On the Behavior of r- and θ-Cracks in Composite Materials Under Thermal and Mechanical Loading," *International Journal of Solids and Structures*, Vol. 29, pp. 1907–1918.

Muskhelishvili, N. I., 1953, *Some Basic Problems of the Mathematical Theory of Elasticity*, P. Noordhoff Co., Groningen, Holland.

Rice, J. R., 1988, "Elastic Fracture Mechanics Concepts for Interfacial Cracks," ASME JOURNAL OF APPLIED MECHANICS, Vol. 55, pp. 299–316.

Dislocation Inside an Isotropic Elliptical Inclusion Surrounded by an Anisotropic Medium

M. H. Santare[1]

Background

Dislocation-inclusion interaction solutions not only help in the understanding of hardening mechanisms, they also can be used as Green's functions for crack-inclusion interaction solutions. The isotropic problem was first solved by Dundurs and Mura (1964) for the circular inclusion where the dislocation is in the matrix. Dundurs and Sendeckyj (1965) solved the similar problem where the dislocation is inside the inclusion. Elliptical inclusions were considered by Stagni and Lizzio (1983) for the dislocation in the matrix and Warren (1983) for the dislocation in the inclusion. Recently, Qaissaunee and Santare (1994) solved the problem for confocal ellipses where the dislocation is in either the inner or outer region. These elliptical studies each solved the problem in terms of infinite series using the complex displacement potentials (see Muskhelishvili, 1953).

Several researchers have revisited the problem for the cases where the inclusion, matrix or both are anisotropic. Using the methodology proposed by Stroh in (1958), Wu (1992) solved for the elastic interaction between a dislocation in an anisotropic medium containing an elliptical hole or rigid inclusion. In the following year, Hwu and Yen (1993), solved the more general problem of an anisotropic inclusion embedded in an anisotropic matrix under general loading. They also followed the formalism of Stroh (1958) and show as a special case the solution for an elliptical inclusion with an edge dislocation in the matrix. In the same year, Wang and Tarn (1993) solve the point force and dislocation problems in the vicinity of an elliptical hole or rigid inclusion. They employ the more classical complex potential approach and include an interesting discussion on the validity of mapping for this type of problem. The present study, uses complex displacement potentials to solve for the elastic field due to a dislocation inside an isotropic, elliptical inclusion surrounded by an anisotropic matrix for cases where the out-of-plane axis is oriented such that the in-plane and out-of-plane problems in the matrix are uncoupled.

Solution

In plane problems of anisotropic elasticity, it is convenient to use the complex variables z, z_1 and z_2, as suggested by Milne-Thompson (1960) such that

$$z = x + iy, \quad (1)$$

$$z_i = x + \lambda_i y. \quad (2)$$

where λ_1 and λ_2 are complex constants which depend upon the material properties. Specifically, they are the roots of the following characteristic equation,

$$s_{11}\lambda^4 - 2s_{16}\lambda^3 + (2s_{12} + s_{66})\lambda^2 - 2s_{26}\lambda + s_{22} = 0, \quad (3)$$

where s_{ij} are the planar anisotropic compliances written in contracted matrix form.

We can write the planar displacements and tractions in an anisotropic medium in terms of two complex potentials $\psi_1(z_1)$ and $\psi_2(z_2)$ as follows:

$$2(u + iv) = p_1\psi_1(z_1) + p_2\psi_2(z_2) + \bar{q}_1\bar{\psi}_1(\bar{z}_1) + \bar{q}_2\bar{\psi}_2(\bar{z}_2), \quad (4)$$

$$X + iY = -i\left[\delta_1\psi_1(z_1) + \delta_2\psi_2(z_2) + \bar{\gamma}_1\bar{\psi}_1(\bar{z}_1) + \bar{\gamma}_2\bar{\psi}_2(\bar{z}_2) \right]. \quad (5)$$

In these expressions

$$p_i = s_{12} - s_{16}\lambda_i + s_{11}\lambda_i^2 + i\left(s_{22} - s_{26}\lambda_i + s_{12}\lambda_i^2\right)/\lambda_i, \quad (6)$$

$$\bar{q}_i = s_{12} - s_{16}\bar{\lambda}_i + s_{11}\bar{\lambda}_i^2 + i\left(s_{22} - s_{26}\bar{\lambda}_i + s_{12}\bar{\lambda}_i^2\right)/\bar{\lambda}_i \quad (7)$$

and

$$\gamma_i = \frac{1}{2}(1 - i\lambda_i), \quad (8)$$

[1]Department of Mechanical Engineering, University of Delaware, Newark, DE 19716-3140. Assoc. Mem. ASME.

Contributed by the Applied Mechanics Division of THE AMERICAN SOCIETY OF MECHANICAL ENGINEERS for publication in the ASME JOURNAL OF APPLIED MECHANICS. Manuscript received by the ASME Applied Mechanics Division, July 8, 1994; final revision, Aug. 29, 1994. Associate Technical Editor: D. M. Barnett.

Downloaded 04 May 2010 to 171.66.16.28. Redistribution subject to ASME license or copyright; see http://www.asme.org/terms/Terms_Use.cfm

For a rigid inclusion with an insulated boundary ($\mu_2 \to \infty$ and $a_{t2} = k_{t2} = 0$) and for a uniform temperature change ($q_\infty = 0$), Eq. (15) gives

$$\bar{K} = \frac{\mu_1 a_{t1} q_\infty}{k_{t1}} \bar{\tau}\left(\bar{\tau} + \frac{i}{\tan\phi}\right) L\sqrt{\frac{\pi L}{2}} \times \exp\left(-\epsilon\phi + i\frac{\phi + \pi - 2\gamma}{2}\right), \quad (16)$$

$$\bar{K} = \frac{4\mu_1(1+\Lambda)(a_{t1} - a_{t2})T_\infty}{(1+k_1)(1-\Omega)} \bar{\tau}\sqrt{\frac{\pi L}{2}} \exp\left(-\epsilon\phi + i\frac{\phi}{2}\right). \quad (17)$$

Equations (16) and (17) are in agreement with those of the literature (Kattis and Duka, 1990; Muller and Schmauder, 1992).

References

Barber, J. R., 1980, "Steady-State Thermal Stresses Caused by an Imperfectly Conducting Penny-shaped Crack in an Elastic Solid," *Journal of Thermal Stresses*, Vol. 3, pp. 77–83.

Dundurs, J., 1970, "Some Properties of Elastic Stresses in a Composite," *Proceedings of the 6th Annual Meeting of the Society of Engineering Science*, Vol. 5, pp. 203–216.

England, A. H., 1966, "An Arc Crack Around a Circular Elastic Inclusion," ASME JOURNAL OF APPLIED MECHANICS, Vol. 33, pp. 637–640.

Malyshev, B., and Salganik, R. L., 1965, "The Strength of Adhesive Joints Using the Theory of Cracks," *International Journal of Fracture Mechanics*, Vol. 1, pp. 114–128.

Kattis, M. A., and Duka, E. D., 1990, "Thermal Stresses in an Elastic Plane Matrix Containing a Circular Inclusion with an Interface Crack," *Ceramics Today—Tomorrow's Ceramics*, Elsevier Science Publishers B.V., pp. F37–F45.

Kattis, M. A., and Meguid, S. A., 1994, "Two-Phase Potentials for the Treatment of an Elastic Inclusion in Plane Thermoelasticity," ASME JOURNAL OF APPLIED MECHANICS, in press.

Kou, A., 1990a, "Effects of Crack Surface Heat Conduction on Stresses Intensity Factors," ASME JOURNAL OF APPLIED MECHANICS, Vol. pp. 354–358.

Kou, A., 1990b, "Interface Crack Between Two Dissimilar Half Spaces Subjected to a Uniform Heat Flow at Infinity-Open Crack," ASME JOURNAL OF APPLIED MECHANICS, Vol. 57, pp. 359–364.

Muller, W. H., and Schmauder, S., 1992, "On the Behavior of r- and θ-Cracks in Composite Materials Under Thermal and Mechanical Loading," *International Journal of Solids and Structures*, Vol. 29, pp. 1907–1918.

Muskhelishvili, N. I., 1953, *Some Basic Problems of the Mathematical Theory of Elasticity*, P. Noordhoff Co., Groningen, Holland.

Rice, J. R., 1988, "Elastic Fracture Mechanics Concepts for Interfacial Cracks," ASME JOURNAL OF APPLIED MECHANICS, Vol. 55, pp. 299–316.

Dislocation Inside an Isotropic Elliptical Inclusion Surrounded by an Anisotropic Medium

M. H. Santare[1]

Background

Dislocation-inclusion interaction solutions not only help in the understanding of hardening mechanisms, they also can be used as Green's functions for crack-inclusion interaction solutions. The isotropic problem was first solved by Dundurs and Mura (1964) for the circular inclusion where the dislocation is in the matrix. Dundurs and Sendeckyj (1965) solved the similar problem where the dislocation is inside the inclusion. Elliptical inclusions were considered by Stagni and Lizzio (1983) for the dislocation in the matrix and Warren (1983) for the dislocation in the inclusion. Recently, Qaissaunee and Santare (1994) solved the problem for confocal ellipses where the dislocation is in either the inner or outer region. These elliptical studies each solved the problem in terms of infinite series using the complex displacement potentials (see Muskhelishvili, 1953).

Several researchers have revisited the problem for the cases where the inclusion, matrix or both are anisotropic. Using the methodology proposed by Stroh in (1958), Wu (1992) solved for the elastic interaction between a dislocation in an anisotropic medium containing an elliptical hole or rigid inclusion. In the following year, Hwu and Yen (1993), solved the more general problem of an anisotropic inclusion embedded in an anisotropic matrix under general loading. They also followed the formalism of Stroh (1958) and show as a special case the solution for an elliptical inclusion with an edge dislocation in the matrix. In the same year, Wang and Tarn (1993) solve the point force and dislocation problems in the vicinity of an elliptical hole or rigid inclusion. They employ the more classical complex potential approach and include an interesting discussion on the validity of mapping for this type of problem. The present study, uses complex displacement potentials to solve for the elastic field due to a dislocation inside an isotropic, elliptical inclusion surrounded by an anisotropic matrix for cases where the out-of-plane axis is oriented such that the in-plane and out-of-plane problems in the matrix are uncoupled.

Solution

In plane problems of anisotropic elasticity, it is convenient to use the complex variables z, z_1 and z_2, as suggested by Milne-Thompson (1960) such that

$$z = x + iy, \quad (1)$$

$$z_i = x + \lambda_i y. \quad (2)$$

where λ_1 and λ_2 are complex constants which depend upon the material properties. Specifically, they are the roots of the following characteristic equation,

$$s_{11}\lambda^4 - 2s_{16}\lambda^3 + (2s_{12} + s_{66})\lambda^2 - 2s_{26}\lambda + s_{22} = 0, \quad (3)$$

where s_{ij} are the planar anisotropic compliances written in contracted matrix form.

We can write the planar displacements and tractions in an anisotropic medium in terms of two complex potentials $\psi_1(z_1)$ and $\psi_2(z_2)$ as follows:

$$2(u + iv) = p_1\psi_1(z_1) + p_2\psi_2(z_2) + \bar{q}_1\bar{\psi}_1(\bar{z}_1) + \bar{q}_2\bar{\psi}_2(\bar{z}_2), \quad (4)$$

$$X + iY = -i\left[\delta_1\psi_1(z_1) + \delta_2\psi_2(z_2) + \bar{\gamma}_1\bar{\psi}_1(\bar{z}_1) + \bar{\gamma}_2\bar{\psi}_2(\bar{z}_2)\right]. \quad (5)$$

In these expressions

$$p_i = s_{12} - s_{16}\lambda_i + s_{11}\lambda_i^2 + i\left(s_{22} - s_{26}\lambda_i + s_{12}\lambda_i^2\right)/\lambda_i, \quad (6)$$

$$\bar{q}_i = s_{12} - s_{16}\bar{\lambda}_i + s_{11}\bar{\lambda}_i^2 + i\left(s_{22} - s_{26}\bar{\lambda}_i + s_{12}\bar{\lambda}_i^2\right)/\bar{\lambda}_i \quad (7)$$

and

$$\gamma_i = \frac{1}{2}(1 - i\lambda_i), \quad (8)$$

[1]Department of Mechanical Engineering, University of Delaware, Newark, DE 19716-3140. Assoc. Mem. ASME.

Contributed by the Applied Mechanics Division of THE AMERICAN SOCIETY OF MECHANICAL ENGINEERS for publication in the ASME JOURNAL OF APPLIED MECHANICS. Manuscript received by the ASME Applied Mechanics Division, July 8, 1994; final revision, Aug. 29, 1994. Associate Technical Editor: D. M. Barnett.

Copyright © 1995 by ASME

Downloaded 04 May 2010 to 171.66.16.28. Redistribution subject to ASME license or copyright; see http://www.asme.org/terms/Terms_Use.cfm

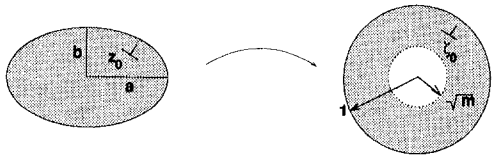

Fig. 1 Problem geometry in the physical z-plane and mapped ζ-plane

$$\delta_i = \frac{1}{2}(1 + i\lambda_i). \tag{9}$$

We can simplify the problem by mapping the elastic region in the physical z-plane onto a region of simpler geometry in the ζ-plane as shown in Fig. 1, by the function

$$z = \omega(\zeta) = R\left(\zeta + \frac{m}{\zeta}\right). \tag{10}$$

In this expression, $R = (a + b)/2$, $m = (a - b)/(a + b)$ where a and b are the semimajor and semiminor elliptical axes. This function maps the region outside the elliptical contour onto the region outside the unit circle $|\zeta| = 1$ and the region inside the elliptical contour onto the annulus with inside radius $|\zeta| = \sqrt{m}$ and outside radius $|\zeta| = 1$. The dislocation is located at the point z_0 in the physical plane which maps to the point ζ_0 in the mapped plane.

Applying this mapping, the variables z_1 and z_2 undergo induced mappings, as discussed in Milne-Thomson (1960),

$$z_i = \omega(\zeta_i) = \omega_i(\zeta). \tag{11}$$

Therefore, the unknown potentials can be written as

$$\psi_1 = A\ln\zeta + \sum_{k=-\infty}^{\infty} a_k \zeta^k, \tag{12}$$

$$\psi_2 = B\ln\zeta + \sum_{k=-\infty}^{\infty} b_k \zeta^k \tag{13}$$

where the terms A, B, a_k, a_{-k}, b_k, and b_{-k} are yet to be determined.

For an isotropic medium the displacements and tractions can be written in terms of two other complex potentials ϕ and η,

$$2\mu(u + iv) = \kappa\phi(z) - \overline{\eta}(z), \tag{14}$$

$$X + iY = -i[\phi(z) + \overline{\eta}(z)], \tag{15}$$

where μ is the shear modulus of the material and κ is the Kossolov constant which is related to the Poisson's ratio through the equation $\kappa = 3 - 4\nu$ in plane strain and $\kappa = (3 - \nu)/(1 + \nu)$ in plane stress. For the problem where a dislocation of magnitude $b_x + ib_y$ is located inside an isotropic elliptical inclusion, the complex potentials can be written in terms of the mapping variable ζ, as follows:

$$\phi = R\alpha\ln\zeta + \sum_{k=1}^{\infty} C_k \zeta^{-k} + \sum_{k=-\infty}^{\infty} c_k \zeta^k, \tag{16}$$

$$\eta = R\overline{\alpha}\ln\zeta + \sum_{k=1}^{\infty} D_k \zeta^{-k} + \sum_{k=-\infty}^{\infty} d_k \zeta^k. \tag{17}$$

In the potentials above α, C_k and D_k are known and represent the elastic field due to the dislocation alone (see Qaissaunee and Santare, 1994).

$$\alpha = \mu\frac{b_y - ib_x}{\pi R(\kappa + 1)} \tag{18}$$

$$C_k = R\alpha\frac{1}{k}\left[\zeta_0^{-k} + \left(\frac{m}{\zeta_0}\right)^{-k}\right] \tag{19}$$

$$D_k = R\left[\alpha\frac{m\zeta_0^2 - \left(\bar{\zeta}_0 + m/\bar{\zeta}_0\right)\zeta_0 + 1}{\zeta_0^2 - m} + \overline{\alpha}\frac{1}{k}\right]\zeta_0^{-k}$$
$$-R\left[\alpha\frac{\zeta_0^2/m - \left(\bar{\zeta}_0 + m/\bar{\zeta}_0\right)\zeta_0 + m^2}{\zeta_0^2 - m} - \overline{\alpha}\frac{1}{k}\right]\left[\frac{m}{\zeta^0}\right]^{-k} \tag{20}$$

In order to determine the unknowns (A, B, a_k, b_k, c_k, d_k, a_{-k}, b_{-k}, c_{-k}, and d_{-k}), in Eqs. (12), (13), (16), and (17), we match the displacements and the tractions between the isotropic inclusion, Eqs. (14)–(15), and the anisotropic medium outside the inclusion, Eqs. (4)–(5), along the interface at $\zeta = \sigma = e^{i\theta}$;

$$\kappa\phi(\sigma) - \overline{\eta}(\sigma) = \mu\big[p_1\psi_1(\sigma) + p_2\psi_2(\sigma) + \bar{q}_1\bar{\psi}_1(\bar{\sigma}) + \bar{q}_2\bar{\psi}_2(\bar{\sigma})\big], \tag{21}$$

$$\phi(\sigma) + \overline{\eta}(\sigma) = \delta_1\psi_1(\sigma) + \delta_2\psi_2(\sigma) + \overline{\gamma}_1\bar{\psi}_1(\bar{\sigma}) + \overline{\gamma}_2\bar{\psi}_2(\bar{\sigma}). \tag{22}$$

Since the stresses at infinity vanish, $a_k = b_k = 0$ from Eqs. (12) and (13). The tractions and displacements inside the inclusion will be continuous across the real axis which implies

$$c_{-k} = m^k c_k, \tag{23}$$

$$d_{-k} = m^k d_k + (1 - m^2)km^{k-1}c_k. \tag{24}$$

Making the appropriate substitutions into Eqs. (21) and (22) gives two equations in the unknown constants. First, we equate the multivalued terms in these relations which gives us

$$\delta_1 A + \delta_2 B - \overline{\gamma}_1\overline{A} - \overline{\gamma}_2\overline{B} = 0, \tag{25}$$

$$p_1 A + p_2 B - \bar{q}_1\overline{A} - \bar{q}_2\overline{B} = \frac{(\kappa + 1)}{\mu}R\alpha. \tag{26}$$

Next we consider the remaining, single valued, terms for both k positive and k negative. The following set of equations results:

$$\overline{\gamma}_1\bar{a}_{-k} + \overline{\gamma}_2\bar{b}_{-k} - c_k - m^k\bar{d}_k - (1 - m^2)km^{k-1}\bar{c}_k = \overline{D}_k, \tag{27}$$

$$\delta_1 a_{-k} + \delta_2 b_{-k} - m^k c_k - \bar{d}_k = C_k, \tag{28}$$

$$\mu\bar{q}_1\bar{a}_{-k} + \mu\bar{q}_2\bar{b}_{-k} - \kappa c_k + m^k\bar{d}_k + (1 - m^2)km^{k-1}\bar{c}_k = \overline{D}_k, \tag{29}$$

$$\mu p_1 a_{-k} + \mu p_2 b_{-k} - \kappa m^k c_k + \bar{d}_k = \kappa C_k. \tag{30}$$

Equations (25)–(30) can be solved for the unknowns A, B, a_{-k}, b_{-k}, c_k, and d_k.

Acknowledgment

I would like to thank the University of Surrey, Guildford, Surrey, U.K., for partial support of this research.

References

Dundurs, J., and Mura, T., 1964, "Interaction Between an Edge Dislocation and a Circular Inclusion," *Journal of the Mechanics and Physics of Solids*, Vol. 12, pp. 177–189.

Dundurs, J., and Sendeckyj, G. P., 1965, "Edge Dislocation Inside a Circular Inclusion," *Journal of the Mechanics and Physics of Solids*, Vol. 13, pp. 141–147.

Hwu, C., and Yen, W. J., 1993, "On the Anisotropic Elastic Inclusions in Plane Elastostatics," ASME JOURNAL OF APPLIED MECHANICS, Vol. 60, pp. 626–632.

Milne-Thomson, L. M., 1960, *Plane Elastic Systems*, Springer-Verlag, Berlin.

Downloaded 04 May 2010 to 171.66.16.28. Redistribution subject to ASME license or copyright; see http://www.asme.org/terms/Terms_Use.cfm

Muskhelishvili, N. I., 1953, *Some Basic Problems of the Mathematical Theory of Elasticity*, 3 ed., P. Noordhoff Ltd., Groningen, Holland.

Qaissaunee, M. T., and Santare, M. H., 1995, "Edge Dislocation Interacting with an Elliptical Inclusion Surrounded by an Interfacial Zone," *Quarterly Journal of Mechanics and Applied Mathematics*, to appear.

Stagni, L., and Lizzio, R., 1983, "Shape Effects in the Interaction Between an Edge Dislocation and an Elliptical Inhomogeneity," *Applied Physics A*, Vol. 30, pp. 217–221.

Stroh, A. N., 1958, "Dislocations and Cracks in Anisotropic Elasticity," *Philosophical Magazine*, Vol. 7, pp. 625–646.

Wang, Y.-M., and Tarn, J.-Q., 1993, "Green's Functions for Generalized Plane Problems of Anisotropic Bodies with a Hole or a Rigid Inclusion," ASME JOURNAL OF APPLIED MECHANICS, Vol. 60, pp. 583–588.

Warren, W. E., 1983, "The Egde Dislocation Inside an Elliptical Inclusion," *Mechanics of Materials*, Vol. 2, pp. 319–330.

Wu, K.-C., 1992, "Interaction of a Dislocation with an Elliptic Hole or Rigid Inclusion in an Anisotropic Material," *Journal of Applied Physics*, Vol. 72, No. 6, pp. 2156–2163.

On the Directional Stability of a Propagating Crack

C. Q. Ru[1] and R. C. Batra[2]

Directional stability and the related dynamic crack curving have received considerable attention, e.g., see Yoffe (1951), Cotterell (1966), Cotterell and Rice (1980), Ramulu and Kobayashi (1983), Freund (1990), Gao (1993), and Marder and Gross (1994). The common assumption made by many authors is that the crack grows in the direction of the maximum hoop stress at the crack tip. Cotterell (1966) further stated that the crack is stable if the deviated crack tip will return to the original path. Here we supplement these two by postulating that for a directionally stable crack path, the absolute value of the angle of deviation of the crack should never increase. The critical speed for crack curving predicted by this criterion is found to agree well with the test data.

We consider a crack that has deviated by an infinitesimal angle, θ_0, from the original horizontal direction of propagation, as shown in Fig. 1. We assume that further extension of the deviated crack will be along a direction inclined clockwise at an angle θ^* to its current path. Cotterell (1966) and Cotterell and Rice (1980) have derived the following relationships for a quasi-static crack:

$$-\theta^* = \beta\theta_0 \text{ with } \beta = 1 - \frac{8T}{K_I}\sqrt{\frac{dL}{2\pi}}$$

$$\text{and } \frac{K_{II}}{K_1} = \left(\frac{1}{2} - \frac{4T}{K_I}\sqrt{\frac{dL}{2\pi}}\right)\theta_0 \quad (1)$$

where dL is the length of the deviated crack path, T the remote transverse loading, and K_I and K_{II}, respectively, are the Mode-I and Mode-II stress intensity factors at the deviated crack tip. It is readily seen that, if the T-term in Eq. (1) is neglected, then $\beta = 1$ and the crack-path is neutrally stable. This is why the sign of the T-term determines the directional stability of quasi-static crack paths even when the absolute value of this term is significantly less than unity. However, such is not the case for a propagating crack. Experiments (Ramulu and Kobayashi (1983) and Ravi-Chandar and Knauss (1984)) have shown that the Cotterell criterion is not valid for a propagating crack path. It is well known, see, e.g., Williams and Ewing (1972) and Kitagawa et al. (1975), that the large angle of deviation will lead to crack curving. Therefore, we assume that the directional stability should be associated essentially with the decay of the deviation angle. Thus, in addition to Cotterell's stability condition $(-\theta^*/\theta_0) > 1$ we postulate that $(-\theta^*/\theta_0) < 2$ for the stability of the propagating crack. That is, the absolute value of the angle of deviation will never grow for a directionally stable crack-path and, therefore, the absolute value of the new deviation angle must be less than the initial deviation angle $|\theta_0|$. This certainly holds for a quasi-static crack.

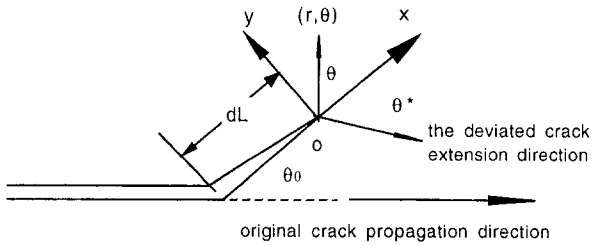

Fig. 1 Deviated semi-infinite propagating crack tip

Following Freund (1990), Ramulu et al. (1982) and Xu and Keer (1992), and using the notations of Ramulu et al. (1982) in the coordinate frame attached to the crack-tip as shown in Fig. 1, the hoop stress $\sigma_{\theta\theta}$ at the crack tip for infinitesimal deviations of the crack path can be expressed as

$$\sigma_{\theta\theta} = \frac{K_I B_I}{\sqrt{2\pi r}}\left\{\frac{C}{2}\theta^2 + \frac{4S_1S_2}{\gamma} - \gamma\right\} - \frac{K_{II}B_{II}\theta}{2S_2\sqrt{2\pi r}}B + T\theta^2;$$

$$\gamma = \left(1 + S_2^2\right). \quad (2)$$

Here B_I, B_{II}, S_1, and S_2 are functions of the crack-tip speed c, the dilatational wave speed c_1, shear wave speed c_2 and the Rayleigh wave speed c_R, $B = \gamma(S_2^2 - S_1S_2) + 8S_1S_2 - 2\gamma^2$ and $C = 4 - (14 + 3S_2^2)S_1S_2/\gamma + 4S_1S_2 + \gamma(3S_1^2 - 2)/4$. The crack is assumed to extend in the direction for which the hoop stress $\sigma_{\theta\theta}$ attains its maximum value. Thus we determine angle θ^* by $\sigma_{\theta\theta,\theta} = 0$ with $\sigma_{\theta\theta,\theta\theta} < 0$, and $1 < (-\theta^*/\theta_0) < 2$. The result is

$$1 < \frac{-\theta^*}{\theta_0} = -\frac{(m/\theta_0)B_{II}B}{2S_2\left[B_IC + 2\sqrt{2\pi r_c}T/K_I\right]} < 2 \quad (3)$$

where r_c is a certain critical distance (Williams and Ewing (1972) and Ramulu and Kobayashi (1983)) and $m = K_{II}/K_I$.

For the sake of simplicity, we consider the case for which the effect of T-related term is less important and therefore set $r_c = 0$. Thus, according to Cotterell (1966) for the quasi-static case, and Ma and Burgers (1987) for the dynamic case, we have $m = 1/2\theta_0 + O(\theta_0\sqrt{dL})$ for the quasi-static case, and $\alpha = m/\theta_0 > 1/2$ for the dynamic case.

The numerical analysis shows that critical values for conditions $(-\theta^*/\theta_0) > 1$, $\sigma_{\theta\theta,\theta\theta} < 0$, and $C(c) = 0$, coincide with each other and are significantly higher than the experimental value of $c \approx 0.5c_R$. For example, for $\nu = 0.25$ and 1/3, the critical values are $(c/c_2) = 0.63$ and 0.67, respectively. However, it is found that the critical value given by $(-\theta^*/\theta_0) < 2$

[1]Department of Mechanical Engineering, University of Alberta, Edmonton, AB T6G 2G8, Canada.

[2]Department of Engineering Science and Mechanics, Virginia Polytechnic Institute and State University, Blacksburg, VA 24061-0219. Fellow ASME.

Contributed by the Applied Mechanics Division of THE AMERICAN SOCIETY OF MECHANICAL ENGINEERS for publication in the ASME JOURNAL OF APPLIED MECHANICS. Manuscript received by the ASME Applied Mechanics Division, May 31, 1994; final revision, Sept. 27, 1994. Associate Technical Editor: J. W. Rudnicki.

Downloaded 04 May 2010 to 171.66.16.28. Redistribution subject to ASME license or copyright; see http://www.asme.org/terms/Terms_Use.cfm

Muskhelishvili, N. I., 1953, *Some Basic Problems of the Mathematical Theory of Elasticity*, 3 ed., P. Noordhoff Ltd., Groningen, Holland.

Qaissaunee, M. T., and Santare, M. H., 1995, "Edge Dislocation Interacting with an Elliptical Inclusion Surrounded by an Interfacial Zone," *Quarterly Journal of Mechanics and Applied Mathematics*, to appear.

Stagni, L., and Lizzio, R., 1983, "Shape Effects in the Interaction Between an Edge Dislocation and an Elliptical Inhomogeneity," *Applied Physics A*, Vol. 30, pp. 217–221.

Stroh, A. N., 1958, "Dislocations and Cracks in Anisotropic Elasticity," *Philosophical Magazine*, Vol. 7, pp. 625–646.

Wang, Y.-M., and Tarn, J.-Q., 1993, "Green's Functions for Generalized Plane Problems of Anisotropic Bodies with a Hole or a Rigid Inclusion," ASME JOURNAL OF APPLIED MECHANICS, Vol. 60, pp. 583–588.

Warren, W. E., 1983, "The Egde Dislocation Inside an Elliptical Inclusion," *Mechanics of Materials*, Vol. 2, pp. 319–330.

Wu, K.-C., 1992, "Interaction of a Dislocation with an Elliptic Hole or Rigid Inclusion in an Anisotropic Material," *Journal of Applied Physics*, Vol. 72, No. 6, pp. 2156–2163.

On the Directional Stability of a Propagating Crack

C. Q. Ru[1] and R. C. Batra[2]

Directional stability and the related dynamic crack curving have received considerable attention, e.g., see Yoffe (1951), Cotterell (1966), Cotterell and Rice (1980), Ramulu and Kobayashi (1983), Freund (1990), Gao (1993), and Marder and Gross (1994). The common assumption made by many authors is that the crack grows in the direction of the maximum hoop stress at the crack tip. Cotterell (1966) further stated that the crack is stable if the deviated crack tip will return to the original path. Here we supplement these two by postulating that for a directionally stable crack path, the absolute value of the angle of deviation of the crack should never increase. The critical speed for crack curving predicted by this criterion is found to agree well with the test data.

We consider a crack that has deviated by an infinitesimal angle, θ_0, from the original horizontal direction of propagation, as shown in Fig. 1. We assume that further extension of the deviated crack will be along a direction inclined clockwise at an angle θ^* to its current path. Cotterell (1966) and Cotterell and Rice (1980) have derived the following relationships for a quasi-static crack:

$$-\theta^* = \beta\theta_0 \text{ with } \beta = 1 - \frac{8T}{K_I}\sqrt{\frac{dL}{2\pi}}$$

$$\text{and } \frac{K_{II}}{K_1} = \left(\frac{1}{2} - \frac{4T}{K_I}\sqrt{\frac{dL}{2\pi}}\right)\theta_0 \quad (1)$$

where dL is the length of the deviated crack path, T the remote transverse loading, and K_I and K_{II}, respectively, are the Mode-I and Mode-II stress intensity factors at the deviated crack tip. It is readily seen that, if the T-term in Eq. (1) is neglected, then $\beta = 1$ and the crack-path is neutrally stable. This is why the sign of the T-term determines the directional stability of quasi-static crack paths even when the absolute value of this term is significantly less than unity. However, such is not the case for a propagating crack. Experiments (Ramulu and Kobayashi (1983) and Ravi-Chandar and Knauss (1984)) have shown that the Cotterell criterion is not valid for a propagating crack path. It is well known, see, e.g., Williams and Ewing (1972) and Kitagawa et al. (1975), that the large angle of deviation will lead to crack curving. Therefore, we assume that the directional stability should be associated essentially with the decay of the deviation angle. Thus, in addition to Cotterell's stability condition $(-\theta^*/\theta_0) > 1$ we postulate that $(-\theta^*/\theta_0) < 2$ for the stability of the propagating crack. That is, the absolute value of the angle of deviation will never grow for a directionally stable crack-path and, therefore, the absolute value of the new deviation angle must be less than the initial deviation angle $|\theta_0|$. This certainly holds for a quasi-static crack.

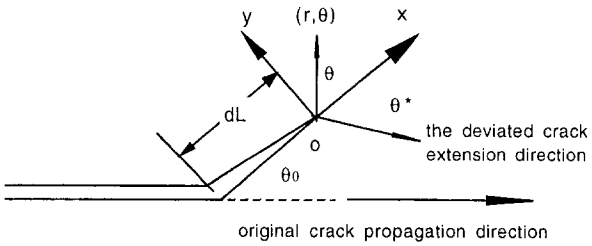

Fig. 1 Deviated semi-infinite propagating crack tip

Following Freund (1990), Ramulu et al. (1982) and Xu and Keer (1992), and using the notations of Ramulu et al. (1982) in the coordinate frame attached to the crack-tip as shown in Fig. 1, the hoop stress $\sigma_{\theta\theta}$ at the crack tip for infinitesimal deviations of the crack path can be expressed as

$$\sigma_{\theta\theta} = \frac{K_I B_I}{\sqrt{2\pi r}}\left\{\frac{C}{2}\theta^2 + \frac{4S_1S_2}{\gamma} - \gamma\right\} - \frac{K_{II}B_{II}\theta}{2S_2\sqrt{2\pi r}}B + T\theta^2;$$

$$\gamma = \left(1 + S_2^2\right). \quad (2)$$

Here B_I, B_{II}, S_1, and S_2 are functions of the crack-tip speed c, the dilatational wave speed c_1, shear wave speed c_2 and the Rayleigh wave speed c_R, $B = \gamma(S_2^2 - S_1S_2) + 8S_1S_2 - 2\gamma^2$ and $C = 4 - (14 + 3S_2^2)S_1S_2/\gamma + 4S_1S_2 + \gamma(3S_1^2 - 2)/4$. The crack is assumed to extend in the direction for which the hoop stress $\sigma_{\theta\theta}$ attains its maximum value. Thus we determine angle θ^* by $\sigma_{\theta\theta,\theta} = 0$ with $\sigma_{\theta\theta,\theta\theta} < 0$, and $1 < (-\theta^*/\theta_0) < 2$. The result is

$$1 < \frac{-\theta^*}{\theta_0} = -\frac{(m/\theta_0)B_{II}B}{2S_2\left[B_IC + 2\sqrt{2\pi r_c}T/K_I\right]} < 2 \quad (3)$$

where r_c is a certain critical distance (Williams and Ewing (1972) and Ramulu and Kobayashi (1983)) and $m = K_{II}/K_I$.

For the sake of simplicity, we consider the case for which the effect of T-related term is less important and therefore set $r_c = 0$. Thus, according to Cotterell (1966) for the quasi-static case, and Ma and Burgers (1987) for the dynamic case, we have $m = 1/2\theta_0 + O(\theta_0\sqrt{dL})$ for the quasi-static case, and $\alpha = m/\theta_0 > 1/2$ for the dynamic case.

The numerical analysis shows that critical values for conditions $(-\theta^*/\theta_0) > 1$, $\sigma_{\theta\theta,\theta\theta} < 0$, and $C(c) = 0$, coincide with each other and are significantly higher than the experimental value of $c \approx 0.5c_R$. For example, for $\nu = 0.25$ and 1/3, the critical values are $(c/c_2) = 0.63$ and 0.67, respectively. However, it is found that the critical value given by $(-\theta^*/\theta_0) < 2$

[1]Department of Mechanical Engineering, University of Alberta, Edmonton, AB T6G 2G8, Canada.

[2]Department of Engineering Science and Mechanics, Virginia Polytechnic Institute and State University, Blacksburg, VA 24061-0219. Fellow ASME.

Contributed by the Applied Mechanics Division of THE AMERICAN SOCIETY OF MECHANICAL ENGINEERS for publication in the ASME JOURNAL OF APPLIED MECHANICS. Manuscript received by the ASME Applied Mechanics Division, May 31, 1994; final revision, Sept. 27, 1994. Associate Technical Editor: J. W. Rudnicki.

Copyright © 1995 by ASME

Downloaded 04 May 2010 to 171.66.16.28. Redistribution subject to ASME license or copyright; see http://www.asme.org/terms/Terms_Use.cfm

Table 1 Value of α for $\theta_0 = 0.196$, $\nu = 0.25$ and the examination of the stability condition (3)

c/c_R	0.1	0.3	0.5	0.7
α	0.66	0.82	0.91	1.09
$(-\theta^*/\theta_0) < 2$	valid	valid	violated	violated

Table 2 Dependence of the critical speed c^* on Poisson's ratio ν

Poisson's ratio ν	0	0.10	0.15	0.20	0.25	0.30	1/3	0.35	0.40	0.50
Critical speed c^*/c_R	0.45	0.47	0.48	0.49	0.51	0.53	0.54	0.55	0.57	0.58
c^*/c_2		0.39	0.42	0.43	0.45	0.47	0.49	0.50	0.51	0.53	0.56

is significantly lower than that given by $(-\theta^*/\theta_0) > 1$. In other words, the stability condition $(-\theta^*/\theta_0) < 2$ is first violated as the propagation speed c increases.

To examine it, we must know the value of α. We consider the stress-wave loading. Cotterell and Rice (1980) have shown that the linearized analysis gives a reasonable estimate for $|\theta_0| < 15$ deg, therefore we use values of K_I and K_{II} for dynamic kinking under stress-wave loading with the deviation angle $\theta_0 \approx 0.196 \approx 11.24$ deg and $\nu = 0.25$ given by Burgers (1983) and Ma and Burgers (1987). The corresponding values of α and the result of applying condition $(-\theta^*/\theta_0) < 2$ are listed in Table 1. Therefore, the critical speed c^* satisfies $0.3c_R < c^* < 0.5c_R$ for $\nu = 0.25$ which agrees well with the experimental data for Homalite-100 given in Table 1 of Ravi-Chandar and Knauss (1984). A narrower range of bounds for c^* could not be obtained because of a lack of test data.

We now consider the time-independent constant loading on the crack surface. Results given in Burgers (1983) show that the relations between the static and dynamic SIFs for Mode-I and Mode-II given by Freund (1990) may be used to arrive at the approximate results for these cases within five percent error when $|\theta_0| < \pi/4$. Thus we follow Freund (1990) and arrive at $\alpha = \sqrt{((1 - c/c_1)/(1 - c/c_2))}/2 > 1/2$ and evaluate the dependence of the critical speed on Poisson's ratio ν; the results are given in Table 2. These agree well with the experimental data for Glass and Plexiglass listed in Table 1 of Ravi-Chandar and Knauss (1984). The increase in the critical speed with the increase in Poisson's ratio is in qualitative agreement with the results of Xu and Keer (1992); however, the value of the critical speed given here is significantly lower than that given by them for the same value of Poisson's ratio. In conclusion, we have proposed a criterion for determining the directional stability of a propagating crack. Neglecting the effects of T-stress, the critical speed predicted by the proposed stability condition (3) is found to be in good agreement with the experimental value of $0.5c_R$.

Acknowledgment

This work was supported by the U.S. Office of Naval Research through a grant to the University of Missouri-Rolla with Dr. Y. Rajapakse as program officer and the Virginia Polytechnic Institute as a subcontractor.

References

Burgers, P., 1983, "Dynamic Kinking of Crack in Plane Strain," *International Journal of Solids and Structures*, Vol. 19, pp. 735–752.

Cotterell, B., 1966, "Notes on the Paths and Stability of Crack," *International Journal of Fracture Mechanics*, Vol. 2, pp. 526–533.

Cotterell, B., and Rice, J. R., 1960, "Slightly Curved or Kinked Cracks," *International Journal of Fracture*, Vol. 16, pp. 155–169.

Freund, L. B., 1990, *Dynamic Fracture Mechanics*, Cambridge University Press, Cambridge, U.K.

Gao, H., 1993, "Surface Roughening and Branching Instability in Dynamic Fracture," *Journal of the Mechanics and Physics of Solids*, Vol. 41, pp. 457–486.

Kitagawa, H., Yuuki, R., and Ohira, T., 1975, "Crack-morphological Aspects in Fracture Mechanics," *Engineering Fracture Mechanics*, Vol. 7, pp. 515–529.

Ma, C. C., and Burgers, P., 1987, "Dynamic Mode-I and Mode-II Crack Kinking Including Delay Time Effects," *International Journal of Solids and Structures*, Vol. 23, pp. 897–918.

Marder, M., and Gross, S., 1994, "Origin of Crack-Tip Instability," to appear.

Ramulu, M., Kobayashi, A. S., and Kang, B. S. J., 1982, "Dynamic Crack Curving and Branching in Line-Pipe," ASME *Journal of Pressure Vessel and Technology*, Vol. 104, pp. 317–322.

Ramulu, M., and Kobayashi, A. S., 1983, "Dynamic Crack Curving: A Photoelastic Evaluation," *Experimental Mechanics*, Vol. 23, pp. 1–9.

Ravi-Chandar, K., and Knauss, W. G., 1984, "An Experimental Investigation into Dynamic Fracture: III. On Steady-state Crack Propagation and Crack Branching," *International Journal of Fracture*, Vol. 26, pp. 141–154; 189–200.

Xu,Y., and Keer, L. M., 1992, "Non-planar Deviation of an Initially Straight Moving Crack," Vol. 41, pp. 577–586.

Williams, J. G., and Ewing, P. D., 1972, "Fracture under Complex Stress: The Angled Crack Problems," *International Journal of Fracture Mechanics*, Vol. 2, pp. 441–446.

Yoffe, E. H., 1951, "The Moving Griffith Crack," *Philosophical Magazine*, Vol. 42, pp. 739–750.

Instability of Tangential Discontinuities in Elastic Solids

A. A. Koulakov[1]

Introduction

Exploration of the stability of the interface between two elastic media of an arbitrary shape with respect to short wavelength disturbances far away from the boundaries can be approximately reduced to the consideration of the dynamics of perturbations of the interface between two elastic half-spaces. An isotropic elastic half-space has a negative effective Young's constant with respect to a load, moving with super-Rayleigh, subsonic speed (Cole and Huth, 1958). The situation when two elastic half-spaces are in contact and move with relative velocity bigger than the sum of Rayleigh velocities of the media can in principle produce instability. The present paper is dedicated to this instability.

The problem is considered in the approximation of flat deformations. To avoid generation of cavities these half-spaces are pressed toward each other by a uniform external pressure that is deliberately bigger than any perturbation. Thus, negative normal pressure is allowed for the perturbation. The problem is somewhat analogous to the instability of a tangential discontinuity in a homogeneous compressible medium (see, e.g., Landau and Lifshitz, 1987).

Analysis

We suppose that two elastic media occupy $z > 0$ and $z < 0$ regions of space with all the displacements being in the x-z plane. In equilibrium the upper medium 1 is moving with uniform velocity V in the x direction. The lower medium 2 is at rest. We shall consider the stability of the equilibrium state with respect to the single-wavelength perturbation of

[1]School of Physics and Astronomy, University of Minnesota, 116 Church Street, SE, Minneapolis, MN 55455.

Contributed by the Applied Mechanics Division of THE AMERICAN SOCIETY OF MECHANICAL ENGINEERS for publication in the ASME JOURNAL OF APPLIED MECHANICS. Manuscript received by the ASME Applied Mechanics Division, Aug. 1, 1994; final revision, Oct. 6, 1994. Associate Technical Editor: D. M. Barnett.

Downloaded 04 May 2010 to 171.66.16.28. Redistribution subject to ASME license or copyright; see http://www.asme.org/terms/Terms_Use.cfm

Table 1 Value of α for $\theta_0 = 0.196$, $\nu = 0.25$ and the examination of the stability condition (3)

c/c_R	0.1	0.3	0.5	0.7
α	0.66	0.82	0.91	1.09
$(-\theta^*/\theta_0) < 2$	valid	valid	violated	violated

Table 2 Dependence of the critical speed c^* on Poisson's ratio ν

Poisson's ratio ν	0	0.10	0.15	0.20	0.25	0.30	1/3	0.35	0.40	0.50
Critical speed c^*/c_R	0.45	0.47	0.48	0.49	0.51	0.53	0.54	0.55	0.57	0.58
c^*/c_2		0.39	0.42	0.43	0.45	0.47	0.49	0.50	0.51	0.53	0.56

is significantly lower than that given by $(-\theta^*/\theta_0) > 1$. In other words, the stability condition $(-\theta^*/\theta_0) < 2$ is first violated as the propagation speed c increases.

To examine it, we must know the value of α. We consider the stress-wave loading. Cotterell and Rice (1980) have shown that the linearized analysis gives a reasonable estimate for $|\theta_0| < 15$ deg, therefore we use values of K_I and K_{II} for dynamic kinking under stress-wave loading with the deviation angle $\theta_0 \approx 0.196 \approx 11.24$ deg and $\nu = 0.25$ given by Burgers (1983) and Ma and Burgers (1987). The corresponding values of α and the result of applying condition $(-\theta^*/\theta_0) < 2$ are listed in Table 1. Therefore, the critical speed c^* satisfies $0.3c_R < c^* < 0.5c_R$ for $\nu = 0.25$ which agrees well with the experimental data for Homalite-100 given in Table 1 of Ravi-Chandar and Knauss (1984). A narrower range of bounds for c^* could not be obtained because of a lack of test data.

We now consider the time-independent constant loading on the crack surface. Results given in Burgers (1983) show that the relations between the static and dynamic SIFs for Mode-I and Mode-II given by Freund (1990) may be used to arrive at the approximate results for these cases within five percent error when $|\theta_0| < \pi/4$. Thus we follow Freund (1990) and arrive at $\alpha = \sqrt{((1 - c/c_1)/(1 - c/c_2))}/2 > 1/2$ and evaluate the dependence of the critical speed on Poisson's ratio ν; the results are given in Table 2. These agree well with the experimental data for Glass and Plexiglass listed in Table 1 of Ravi-Chandar and Knauss (1984). The increase in the critical speed with the increase in Poisson's ratio is in qualitative agreement with the results of Xu and Keer (1992); however, the value of the critical speed given here is significantly lower than that given by them for the same value of Poisson's ratio. In conclusion, we have proposed a criterion for determining the directional stability of a propagating crack. Neglecting the effects of T-stress, the critical speed predicted by the proposed stability condition (3) is found to be in good agreement with the experimental value of $0.5c_R$.

Acknowledgment

This work was supported by the U.S. Office of Naval Research through a grant to the University of Missouri-Rolla with Dr. Y. Rajapakse as program officer and the Virginia Polytechnic Institute as a subcontractor.

References

Burgers, P., 1983, "Dynamic Kinking of Crack in Plane Strain," *International Journal of Solids and Structures*, Vol. 19, pp. 735–752.

Cotterell, B., 1966, "Notes on the Paths and Stability of Crack," *International Journal of Fracture Mechanics*, Vol. 2, pp. 526–533.

Cotterell, B., and Rice, J. R., 1960, "Slightly Curved or Kinked Cracks," *International Journal of Fracture*, Vol. 16, pp. 155–169.

Freund, L. B., 1990, *Dynamic Fracture Mechanics*, Cambridge University Press, Cambridge, U.K.

Gao, H., 1993, "Surface Roughening and Branching Instability in Dynamic Fracture," *Journal of the Mechanics and Physics of Solids*, Vol. 41, pp. 457–486.

Kitagawa, H., Yuuki, R., and Ohira, T., 1975, "Crack-morphological Aspects in Fracture Mechanics," *Engineering Fracture Mechanics*, Vol. 7, pp. 515–529.

Ma, C. C., and Burgers, P., 1987, "Dynamic Mode-I and Mode-II Crack Kinking Including Delay Time Effects," *International Journal of Solids and Structures*, Vol. 23, pp. 897–918.

Marder, M., and Gross, S., 1994, "Origin of Crack-Tip Instability," to appear.

Ramulu, M., Kobayashi, A. S., and Kang, B. S. J., 1982, "Dynamic Crack Curving and Branching in Line-Pipe," ASME *Journal of Pressure Vessel and Technology*, Vol. 104, pp. 317–322.

Ramulu, M., and Kobayashi, A. S., 1983, "Dynamic Crack Curving: A Photoelastic Evaluation," *Experimental Mechanics*, Vol. 23, pp. 1–9.

Ravi-Chandar, K., and Knauss, W. G., 1984, "An Experimental Investigation into Dynamic Fracture: III. On Steady-state Crack Propagation and Crack Branching," *International Journal of Fracture*, Vol. 26, pp. 141–154; 189–200.

Xu,Y., and Keer, L. M., 1992, "Non-planar Deviation of an Initially Straight Moving Crack," Vol. 41, pp. 577–586.

Williams, J. G., and Ewing, P. D., 1972, "Fracture under Complex Stress: The Angled Crack Problems," *International Journal of Fracture Mechanics*, Vol. 2, pp. 441–446.

Yoffe, E. H., 1951, "The Moving Griffith Crack," *Philosophical Magazine*, Vol. 42, pp. 739–750.

Instability of Tangential Discontinuities in Elastic Solids

A. A. Koulakov[1]

Introduction

Exploration of the stability of the interface between two elastic media of an arbitrary shape with respect to short wavelength disturbances far away from the boundaries can be approximately reduced to the consideration of the dynamics of perturbations of the interface between two elastic half-spaces. An isotropic elastic half-space has a negative effective Young's constant with respect to a load, moving with super-Rayleigh, subsonic speed (Cole and Huth, 1958). The situation when two elastic half-spaces are in contact and move with relative velocity bigger than the sum of Rayleigh velocities of the media can in principle produce instability. The present paper is dedicated to this instability.

The problem is considered in the approximation of flat deformations. To avoid generation of cavities these half-spaces are pressed toward each other by a uniform external pressure that is deliberately bigger than any perturbation. Thus, negative normal pressure is allowed for the perturbation. The problem is somewhat analogous to the instability of a tangential discontinuity in a homogeneous compressible medium (see, e.g., Landau and Lifshitz, 1987).

Analysis

We suppose that two elastic media occupy $z > 0$ and $z < 0$ regions of space with all the displacements being in the x-z plane. In equilibrium the upper medium 1 is moving with uniform velocity V in the x direction. The lower medium 2 is at rest. We shall consider the stability of the equilibrium state with respect to the single-wavelength perturbation of

[1]School of Physics and Astronomy, University of Minnesota, 116 Church Street, SE, Minneapolis, MN 55455.

Contributed by the Applied Mechanics Division of THE AMERICAN SOCIETY OF MECHANICAL ENGINEERS for publication in the ASME JOURNAL OF APPLIED MECHANICS. Manuscript received by the ASME Applied Mechanics Division, Aug. 1, 1994; final revision, Oct. 6, 1994. Associate Technical Editor: D. M. Barnett.

Copyright © 1995 by ASME

Downloaded 04 May 2010 to 171.66.16.28. Redistribution subject to ASME license or copyright; see http://www.asme.org/terms/Terms_Use.cfm

the frictionless interface between them. All the displacements and stresses in the perturbation are supposed to be proportional to $\exp(ikx - i\omega t)$.

One of the ways to treat the problem is to introduce the response function of an elastic half-space. For the lower half-space we define it as follows:

$$p_{n2} = -\Delta_2(\xi) \cdot u_z, \tag{1}$$

where p_{n2} is the normal pressure on the surface, u_z is the normal displacement, $\Delta_2(\xi)$ is the response function, and $\xi = \omega/k$ is the velocity of the perturbation moving along the surface. The minus sign makes the response function positive at $\xi = 0$, so that a depression ($u_z < 0$) which is not moving creates positive deviation from the background pressure: $p_{n2} > 0$. The form of Δ is well-known (Murty, 1975; Barnett et al., 1988):

$$\Delta = \frac{\rho C_t^2 F(\xi)}{\gamma_l(1 - \gamma_t^2)} \cdot k, \tag{2}$$

where

$$F(\xi) = 4\gamma_l\gamma_t - \left(1 + \gamma_t^2\right)^2$$

is the left-hand side of the dispersion relation for Rayleigh waves,

$$\gamma_{l,t}(\xi) = \sqrt{1 - \xi^2/C_{l,t}^2}.$$

The response function is real for $-C_t \le \xi \le C_t$ and is positive for $-C_R \le \xi \le C_R$. At $\xi = \pm C_R$ it changes sign in accordance with the mentioned inversion of the effective Young's constant. The second derivative of the function is negative in the region $-C_t \le \xi \le C_t$. For the moving upper half-space the same equation as (1) is valid, but the velocity field is shifted by V:

$$p_{n1} = \Delta_1(\xi - V) \cdot u_z. \tag{3}$$

The condition of continuity of the normal pressure gives the dispersion relation for the perturbation:

$$\Delta(\xi) \equiv \Delta_1(\xi - V) + \Delta_2(\xi) = 0. \tag{4}$$

Equation (4) agrees with that obtained by Murty (1975) and by Barnett et al. (1988) in the limit $V = 0$.

Consider the case of two identical media. In this case the dispersion function Δ has a point of symmetry $\xi = V/2$. Assuming that the relative velocity is smaller than the sum of velocities of transverse waves, since the second derivatives of both of the response functions are negative, we can say that the function has a maximum at this point. When $V/2 < C_R$, the function value at $\xi = V/2$ is positive and (4) has two real roots. If $V/2 > C_R$, the graph of the dispersion function cannot intersect the real axis and two conjugated roots appear in the complex plane, one of them giving the instability. So, for two identical media the critical velocity is equal to the sum of the Rayleigh velocities of two half-spaces. The properties of Δ exactly at the critical point deserve some attention:

$$\Delta\left(\tilde{\xi}, \tilde{V}\right) = 0, \quad \frac{\partial\Delta}{\partial\xi}\left(\tilde{\xi}, \tilde{V}\right) = 0, \tag{5}$$

where $\tilde{\xi}$, $\tilde{V}$ are the critical parameters.

The situation with two slightly different media is topologically the same. Only the critical parameters are different. To calculate them one should apply (5) to the function (4). If $\tilde{V} = C_{R1} + C_{R2} + \delta\tilde{V}$, $\tilde{\xi} = C_{R2} + \delta\tilde{\xi}$, perturbation theory with $\delta\tilde{\xi} \ll \tilde{\xi}$, $\delta\tilde{V} \ll \tilde{V}$, gives as a solution of the system (5)

$$\delta\tilde{V} \approx \frac{1}{2}\frac{\left(\Delta_2'(C_{R2}) - \Delta_1'(C_{R1})\right)^2}{\Delta_2'(C_{R2}) \cdot \Delta_1''(C_{R1}) + \Delta_1'(C_{R1}) \cdot \Delta_2''(C_{R2})},$$

$$\delta\tilde{\xi} \approx \Delta'(C_{R1})\frac{\Delta_2'(C_{R2}) - \Delta_1'(C_{R1})}{\Delta_2'(C_{R2}) \cdot \Delta_1''(C_{R1}) + \Delta_1'(C_{R1}) \cdot \Delta_2''(C_{R2})}. \tag{6}$$

One can find the increment of the instability near the critical point by applying perturbation analysis to (4). If $V = \tilde{V} + \delta V$, $\xi = \tilde{\xi} + \delta\xi$, $\delta\xi \ll \tilde{\xi}$, $\delta V \ll \tilde{V}$, using properties of $\tilde{\xi}$ and $\tilde{V}$ (5), one can obtain

$$\delta_\xi \approx \frac{\Delta_1''\left(\tilde{\xi} - \tilde{V}\right)}{\Delta''\left(\tilde{\xi}, \tilde{V}\right)}\delta V \pm \sqrt{\frac{2|\Delta_2'(\tilde{\xi})|}{\Delta''\left(\tilde{\xi}, \tilde{V}\right)}\delta V}. \tag{7}$$

Since $\Delta''(\tilde{\xi}, \tilde{V}) < 0$, the expression under the root becomes negative when $\delta V > 0$, yielding two complex solutions, one of which is unstable.

Discussion

The instability discussed above includes the mentioned instability of tangential discontinuities in a homogeneous compressible medium as a limiting case. If the media are identical, by using the symmetry properties of the dispersion function, one can easily find that the instability takes place in some strip of relative velocities $2C_R < V < 2C_{R2}$, with $C_R < C_t$ and $C_{R2} > C_l$. In the limit $C_t \to 0$, $C_l \to C$ solid state becomes homogeneous compressible. In this limit $C_R \to 0$, and $C_{R2} \to C\sqrt{2}$. The strip degenerates into $0 < V < C\sqrt{8}$, which coincides with the result given by Landau and Lifshitz (1987).

Formulas (6) are valid only if the difference in elastic constants and densities of the two half-spaces is not very big. Notice that correction to the critical velocity is of the second order in the differences between the material properties and is always positive. It is not very large, however. The correction to the critical velocity of perturbation is linear with respect to the differences between the material properties.

The formula for the increment of instability shows that the analysis based on the effective stationary Young's constant, which becomes negative, does not make any sense for nonsteady modes. Suppose for simplicity that we have identical media. The solution of time-dependent equations (Goldshtein, 1965) shows that the equilibrium between the half-space and the moving load is established in time $\tau_{EQ} \propto \lambda/(V - 2C_R)$. The time of the development of the instability can be estimated as $\tau_{INST} \propto \lambda/\sqrt{C_t(V - 2C_R)}$, in accordance with (7). It is seen that close to the critical point $\tau_{EQ} \gg \tau_{INST}$, so that the stationary solution does not have time to appear. That is why the picture of stresses and deformations is qualitatively different below and above the critical velocity. For stationary modes the perturbation of normal pressure is in phase with displacement of the surface. For nonstable modes they are shifted with respect to each other by $\pm\lambda/4$. The variation of normal pressure has maxima at the points of inflection of the displacement. The growth of the instability brings about the formation of cavities at these points.

Acknowledgments

The author would like to thank Dr. Yu. A. Dreizin and Dr. A. Glinov from Branch of the Institute of Atomic Energy in Moscow for useful discussions. The author is also grateful to T. Boinske from the University of Minnesota for help in preparing the manuscript.

Downloaded 04 May 2010 to 171.66.16.28. Redistribution subject to ASME license or copyright; see http://www.asme.org/terms/Terms_Use.cfm

References

Barnett, D. M., Gavazza, S. D., and Lothe, J., 1988, "Slip Waves Along the Interface between Two Anisotropic Elastic Half-spaces in Sliding Contact," *Proceedings of the Royal Society of London*, Vol. A415, pp. 389–419.

Cole, J., and Huth, J., 1958, "Stresses Produced in a Half Plane by Moving Loads," ASME JOURNAL OF APPLIED MECHANICS, Vol. 25, pp. 433–436.

Goldshtein, R. V., 1965, "Rayleigh Waves and Resonant Phenomena in Elastic Solids," *Journal of Applied Mathematics and Mechanics*, Vol. 29, pp. 608–619.

Landau, L. D., and Lifshitz, E. M., 1987, *Fluid Mechanics*, Pergamon Press, New York, pp. 322–323.

Murty, G. S., 1975, "Wave Propagation at an Unbounded Interface between Two Half-Spaces," *Journal of the Acoustical Society of America*, Vol. 58, pp. 1094–1095.

A Treatment of Internally Constrained Materials

J. Casey[1]

1 Introduction

Internal constraints, such as incompressibility or inextensibility, are of considerable importance in continuum mechanics, and various ways of treating them have been described in the literature (Adkins, 1961; Rivlin, 1956, 1960; Green and Adkins, 1960; Ericksen and Rivlin, 1954; Truesdell and Noll, 1965; Green, Naghdi, and Trapp, 1970; Gurtin and Podio-Guidugli, 1973; Green and Naghdi, 1977; Wang, 1979; Beatty, 1987; Beatty and Hayes, 1992; Cohen and Wang, 1987; Podio-Guidugli and Vianello, 1989; Antman and Marlow, 1991; Carlson and Tortorelli, 1994a,b). In the approach suggested by Truesdell and Noll (1965), which is widely adopted, the stress tensor in a constrained material is assumed to be expressible as the sum of two parts: (1) a part which is prescribed by a constitutive equation; and (2) a part which is associated with the constraint and is indeterminate and workless.[2] While the latter approach offers some advantages, it is not clear from a physical viewpoint why such an additive decomposition should exist, and particularly why the part of the stress which is associated with the constraint response is workless.[3] The purpose of the present Note is to present an alternative approach to the subject, in which the form of the stress tensor in the constrained material is motivated by considerations concerning the class of unconstrained materials from which the constrained material may be regarded as being derived, and the assumption of worklessness of the constraint response is not made. Attention is confined to finitely deforming elastic materials, but the procedure described here can be extended to other materials as well.

We wish to discuss theoretically materials which are obtained in practice by physically constraining elastic materials internally in some way—for example, by introducing a system of thin, inextensible, flexible cables lying along the X_1-direction in the undeformed configuration of the body. In the latter case, subsequent deformations of the body are restricted by the inextensibility condition $E_{11} = 0$ on strain and, moreover, the body can sustain any component of traction applied along the X_1-direction (at least in some finite range). While we may regard such a material as being derived from an elastic material, it should be kept in mind that the constrained material is not itself an elastic material in the strict sense of that term. For, if it were, a unique value of axial traction would be associated with any given strain, and, in particular, with zero strain.

2 Preliminaries

For any deformable continuum $\mathcal{B}$, let $\mathbf{F}$ be the deformation gradient and $\mathbf{E} = \frac{1}{2}(\mathbf{F}^T\mathbf{F} - \mathbf{I})$ the Lagrangian finite strain tensor. Also, recall the relations

$$\rho_0 = \rho J, \quad J\mathbf{T} = \mathbf{F}\mathbf{S}\mathbf{F}^T, \tag{1}$$

where $J = \det \mathbf{F} > 0$, ρ_0 is the density of the body in a fixed reference configuration and ρ is its density at time t, $\mathbf{T}$ is the Cauchy stress tensor, and $\mathbf{S}$ is the symmetric Piola-Kirchhoff stress tensor. An inner product between any two (second-order) tensors $\mathbf{A}$ and $\mathbf{B}$ is given by $\mathbf{A} \cdot \mathbf{B} = \mathrm{tr}(\mathbf{A}^T\mathbf{B})$.

If the body consists of unconstrained material, it can undergo an arbitrary motion, and for any given particle $X \in \mathcal{B}$, the strain at X can take on any value in the region $\mathcal{E}$ of six-dimensional strain space defined by $\det(2\mathbf{E} + \mathbf{I}) > 0$. If the material of $\mathcal{B}$ is internally constrained, $\mathbf{E}$ is confined to lie on a (smooth) five-dimensional hypersurface $\mathcal{S}$ in $\mathcal{E}$, defined by a constraint equation of the form[4]

$$\phi(\mathbf{E}) = 0. \tag{2}$$

$\mathcal{S}$ is referred to as the *constraint manifold*. A normal to $\mathcal{S}$ is given by the gradient $\partial\phi/\partial\mathbf{E}$.[5] For any motion of the body of internally constrained material, it is necessary that

$$\frac{\partial\phi}{\partial\mathbf{E}} \cdot \dot{\mathbf{E}} = 0, \tag{3}$$

where the superposed dot signifies material time differentiation.

3 Green-Elastic Materials Subject to an Internal Constraint

Suppose that the body $\mathcal{B}$ consists of Green-elastic (or hyperelastic) material. Then, for each particle $X \in \mathcal{B}$, there exist constitutive functions $\bar{\mathbf{S}}(\mathbf{E})$ and $\bar{\epsilon}(\mathbf{E})$, which for each strain $\mathbf{E} \in \mathcal{S}$ deliver a unique value of stress $\mathbf{S}$ and a unique strain energy ϵ per unit mass,[6] and which satisfy the relation

$$\bar{\mathbf{S}}(\mathbf{E}) \cdot \dot{\mathbf{E}} = \rho_0 \frac{\partial\bar{\epsilon}}{\partial\mathbf{E}}(\mathbf{E}) \cdot \dot{\mathbf{E}}. \tag{4}$$

[1]Department of Mechanical Engineering, University of California at Berkeley, Berkeley, CA 94720-1740. Mem. ASME.

Contributed by the Applied Mechanics Division of THE AMERICAN SOCIETY OF MECHANICAL ENGINEERS for publication in the ASME JOURNAL OF APPLIED MECHANICS. Manuscript received by the Applied Mechanics Division, Sept. 19, 1994; final revision, Dec. 2, 1994. Associate Technical Editor: R. Abeyaratne.

[2]See Sect. 30 of their monograph.

[3]Even in analytical mechanics, which is the source of many of our ideas about constrained systems, not all constraint responses are workless under virtual displacements; although worklessness of this type is commonly assumed in the derivation of Lagrange's equations, it is not necessary to do so (see Casey, 1994).

[4]More primitively, the constraint function can be assumed to depend on $\mathbf{F}$; the usual invariance requirements under superposed rigid motions of the continuum then imply that the function must be expressible in the form (2).

[5]This notation will be understood to mean $\frac{1}{2}\{\frac{\partial\phi}{\partial\mathbf{E}} + (\frac{\partial\phi}{\partial\mathbf{E}})^T\}$.

[6]The dependence of the response functions on X (corresponding to inhomogeneity of the material), and on the choice of reference configuration, will not be indicated explicitly in our notation.

Downloaded 04 May 2010 to 171.66.16.28. Redistribution subject to ASME license or copyright; see http://www.asme.org/terms/Terms_Use.cfm

References

Barnett, D. M., Gavazza, S. D., and Lothe, J., 1988, "Slip Waves Along the Interface between Two Anisotropic Elastic Half-spaces in Sliding Contact," *Proceedings of the Royal Society of London*, Vol. A415, pp. 389–419.

Cole, J., and Huth, J., 1958, "Stresses Produced in a Half Plane by Moving Loads," ASME JOURNAL OF APPLIED MECHANICS, Vol. 25, pp. 433–436.

Goldshtein, R. V., 1965, "Rayleigh Waves and Resonant Phenomena in Elastic Solids," *Journal of Applied Mathematics and Mechanics*, Vol. 29, pp. 608–619.

Landau, L. D., and Lifshitz, E. M., 1987, *Fluid Mechanics*, Pergamon Press, New York, pp. 322–323.

Murty, G. S., 1975, "Wave Propagation at an Unbounded Interface between Two Half-Spaces," *Journal of the Acoustical Society of America*, Vol. 58, pp. 1094–1095.

A Treatment of Internally Constrained Materials

J. Casey[1]

1 Introduction

Internal constraints, such as incompressibility or inextensibility, are of considerable importance in continuum mechanics, and various ways of treating them have been described in the literature (Adkins, 1961; Rivlin, 1956, 1960; Green and Adkins, 1960; Ericksen and Rivlin, 1954; Truesdell and Noll, 1965; Green, Naghdi, and Trapp, 1970; Gurtin and Podio-Guidugli, 1973; Green and Naghdi, 1977; Wang, 1979; Beatty, 1987; Beatty and Hayes, 1992; Cohen and Wang, 1987; Podio-Guidugli and Vianello, 1989; Antman and Marlow, 1991; Carlson and Tortorelli, 1994a,b). In the approach suggested by Truesdell and Noll (1965), which is widely adopted, the stress tensor in a constrained material is assumed to be expressible as the sum of two parts: (1) a part which is prescribed by a constitutive equation; and (2) a part which is associated with the constraint and is indeterminate and workless.[2] While the latter approach offers some advantages, it is not clear from a physical viewpoint why such an additive decomposition should exist, and particularly why the part of the stress which is associated with the constraint response is workless.[3] The purpose of the present Note is to present an alternative approach to the subject, in which the form of the stress tensor in the constrained material is motivated by considerations concerning the class of unconstrained materials from which the constrained material may be regarded as being derived, and the assumption of worklessness of the constraint response is not made. Attention is confined to finitely deforming elastic materials, but the procedure described here can be extended to other materials as well.

We wish to discuss theoretically materials which are obtained in practice by physically constraining elastic materials internally in some way—for example, by introducing a system of thin, inextensible, flexible cables lying along the X_1-direction in the undeformed configuration of the body. In the latter case, subsequent deformations of the body are restricted by the inextensibility condition $E_{11} = 0$ on strain and, moreover, the body can sustain any component of traction applied along the X_1-direction (at least in some finite range). While we may regard such a material as being derived from an elastic material, it should be kept in mind that the constrained material is not itself an elastic material in the strict sense of that term. For, if it were, a unique value of axial traction would be associated with any given strain, and, in particular, with zero strain.

2 Preliminaries

For any deformable continuum $\mathcal{B}$, let $\mathbf{F}$ be the deformation gradient and $\mathbf{E} = \frac{1}{2}(\mathbf{F}^T\mathbf{F} - \mathbf{I})$ the Lagrangian finite strain tensor. Also, recall the relations

$$\rho_0 = \rho J, \quad J\mathbf{T} = \mathbf{F}\mathbf{S}\mathbf{F}^T, \tag{1}$$

where $J = \det \mathbf{F} > 0$, ρ_0 is the density of the body in a fixed reference configuration and ρ is its density at time t, $\mathbf{T}$ is the Cauchy stress tensor, and $\mathbf{S}$ is the symmetric Piola-Kirchhoff stress tensor. An inner product between any two (second-order) tensors $\mathbf{A}$ and $\mathbf{B}$ is given by $\mathbf{A} \cdot \mathbf{B} = \mathrm{tr}(\mathbf{A}^T\mathbf{B})$.

If the body consists of unconstrained material, it can undergo an arbitrary motion, and for any given particle $X \in \mathcal{B}$, the strain at X can take on any value in the region $\mathcal{E}$ of six-dimensional strain space defined by $\det(2\mathbf{E} + \mathbf{I}) > 0$. If the material of $\mathcal{B}$ is internally constrained, $\mathbf{E}$ is confined to lie on a (smooth) five-dimensional hypersurface $\mathcal{S}$ in $\mathcal{E}$, defined by a constraint equation of the form[4]

$$\phi(\mathbf{E}) = 0. \tag{2}$$

$\mathcal{S}$ is referred to as the *constraint manifold*. A normal to $\mathcal{S}$ is given by the gradient $\partial\phi/\partial\mathbf{E}$.[5] For any motion of the body of internally constrained material, it is necessary that

$$\frac{\partial\phi}{\partial\mathbf{E}} \cdot \dot{\mathbf{E}} = 0, \tag{3}$$

where the superposed dot signifies material time differentiation.

3 Green-Elastic Materials Subject to an Internal Constraint

Suppose that the body $\mathcal{B}$ consists of Green-elastic (or hyperelastic) material. Then, for each particle $X \in \mathcal{B}$, there exist constitutive functions $\bar{\mathbf{S}}(\mathbf{E})$ and $\bar{\epsilon}(\mathbf{E})$, which for each strain $\mathbf{E} \in \mathcal{S}$ deliver a unique value of stress $\mathbf{S}$ and a unique strain energy ϵ per unit mass,[6] and which satisfy the relation

$$\bar{\mathbf{S}}(\mathbf{E}) \cdot \dot{\mathbf{E}} = \rho_0 \frac{\partial\bar{\epsilon}}{\partial\mathbf{E}}(\mathbf{E}) \cdot \dot{\mathbf{E}}. \tag{4}$$

[1]Department of Mechanical Engineering, University of California at Berkeley, Berkeley, CA 94720-1740. Mem. ASME.

Contributed by the Applied Mechanics Division of THE AMERICAN SOCIETY OF MECHANICAL ENGINEERS for publication in the ASME JOURNAL OF APPLIED MECHANICS. Manuscript received by the Applied Mechanics Division, Sept. 19, 1994; final revision, Dec. 2, 1994. Associate Technical Editor: R. Abeyaratne.

[2]See Sect. 30 of their monograph.

[3]Even in analytical mechanics, which is the source of many of our ideas about constrained systems, not all constraint responses are workless under virtual displacements; although worklessness of this type is commonly assumed in the derivation of Lagrange's equations, it is not necessary to do so (see Casey, 1994).

[4]More primitively, the constraint function can be assumed to depend on $\mathbf{F}$; the usual invariance requirements under superposed rigid motions of the continuum then imply that the function must be expressible in the form (2).

[5]This notation will be understood to mean $\frac{1}{2}\{\frac{\partial\phi}{\partial\mathbf{E}} + (\frac{\partial\phi}{\partial\mathbf{E}})^T\}$.

[6]The dependence of the response functions on X (corresponding to inhomogeneity of the material), and on the choice of reference configuration, will not be indicated explicitly in our notation.

Copyright © 1995 by ASME

Downloaded 04 May 2010 to 171.66.16.28. Redistribution subject to ASME license or copyright; see http://www.asme.org/terms/Terms_Use.cfm

Since at each point $\mathbf{E} \in \mathcal{E}$, the latter relation holds for all strain trajectories through $\mathbf{E}$, and hence for all $\dot{\mathbf{E}}$,[7] it follows that

$$\bar{\mathbf{S}}(\mathbf{E}) = \rho_0 \frac{\partial \bar{\epsilon}}{\partial \mathbf{E}}(\mathbf{E}). \tag{5}$$

We now introduce an internally constrained material which, in a sense that will be made clear shortly, can be derived from some set of Green-elastic materials. For each particle of the constrained material, the strain energy density is specified by a function ϵ' which is defined only on the constraint manifold $\mathcal{S} \subset \mathcal{E}$:

$$\epsilon = \epsilon'(\mathbf{E}), \quad \mathbf{E} \in \mathcal{S}. \tag{6}$$

The stress in the constrained material is $\mathbf{S}$; it is assumed that $\mathbf{S}$ is uninfluenced by strain rate. A more important assumption on $\mathbf{S}$ is motivated by the following considerations.

In the vicinity of the hypersurface $\mathcal{S}$, we may express each tensor $\mathbf{E}$ as the sum of a piece $\mathbf{E}'$ that corresponds to a unique point of $\mathcal{S}$ and the remainder, which is orthogonal to $\mathcal{S}$. Thus, $\mathbf{E}'$ is obtained from $\mathbf{E}$ by perpendicular projection. We now extend the function ϵ' into the space immediately surrounding $\mathcal{S}$ by setting $\epsilon'(\mathbf{E}) = \epsilon'(\mathbf{E}')$ in this region. Further, we define a family of scalar functions

$$\rho_0 \bar{\epsilon}(\mathbf{E}) = \rho_0 \epsilon'(\mathbf{E}) + f(\mathbf{E}) \tag{7}$$

in the vicinity of $\mathcal{S}$, where f is any sufficiently smooth function that vanishes on $\mathcal{S}$ ($f(\mathbf{E}) = 0$, $\mathbf{E} \in \mathcal{S}$). Finally, we extend the family of functions $\bar{\epsilon}$ in any smooth manner whatsoever to all of the open set $\mathcal{E}$. We have now constructed a family of functions which we can regard as strain energy functions of Green-elastic materials. It follows from (5) and (7) that

$$\bar{\mathbf{S}}(\mathbf{E}) = \rho_0 \frac{\partial \epsilon'}{\partial \mathbf{E}}(\mathbf{E}) + \frac{\partial f}{\partial \mathbf{E}}(\mathbf{E}). \tag{8}$$

Each of the strain energy functions in (7) coincides on $\mathcal{S}$ with the strain energy function of the internally constrained material, i.e.,

$$\bar{\epsilon}(\mathbf{E}) = \epsilon'(\mathbf{E}), \quad \mathbf{E} \in \mathcal{S}. \tag{9}$$

The family of Green-elastic materials constructed in the above manner is said to *match* the constrained material on $\mathcal{S}$.[8]

Taking a material derivative of both sides of (7), and appealing to (5), one sees that

$$\bar{\mathbf{S}} \cdot \dot{\mathbf{E}} = \rho_0 \frac{\partial \epsilon'}{\partial \mathbf{E}} \cdot \dot{\mathbf{E}} + \frac{\partial f}{\partial \mathbf{E}} \cdot \dot{\mathbf{E}}. \tag{10}$$

Since f is constant on $\mathcal{S}$, the term $\dfrac{\partial f}{\partial \mathbf{E}} \cdot \dot{\mathbf{E}}$ vanishes on $\mathcal{S}$, and hence, for any motion satisfying the constraint (2), one has

$$\bar{\mathbf{S}} \cdot \dot{\mathbf{E}} = \rho_0 \frac{\partial \epsilon'}{\partial \mathbf{E}} \cdot \dot{\mathbf{E}}. \tag{11}$$

Thus, all of the Green-elastic materials that match the internally constrained material on $\mathcal{S}$ have the same stress power for any motion that satisfies the constraint. *We now make the assumption that the stress* $\mathcal{S}$ *in the constrained material has the very same stress power.* Thus, we assume that

$$\mathbf{S} \cdot \dot{\mathbf{E}} = \bar{\mathbf{S}} \cdot \dot{\mathbf{E}} \tag{12}$$

for any matching Green-elastic material. At each point on $\mathcal{S}$, Eq. (12) holds for all tangent vectors satisfying (3). Introducing a Lagrange multiplier λ, we therefore have

$$\left\{ \mathbf{S} - \bar{\mathbf{S}} - \lambda \frac{\partial \phi}{\partial \mathbf{E}} \right\} \cdot \dot{\mathbf{E}} = 0 \tag{13}$$

for *all* $\dot{\mathbf{E}}$. And, since the terms in braces do not depend on the rate of strain, it follows that

$$\mathbf{S} = \bar{\mathbf{S}} + \lambda \frac{\partial \phi}{\partial \mathbf{E}}, \quad \mathbf{E} \in \mathcal{S}. \tag{14}$$

In other words, the stress $\mathbf{S}$ in the constrained material is the sum of the stress $\bar{\mathbf{S}}$ in *any* matching Green-elastic material plus an arbitrary piece which is orthogonal to the constraint manifold. It is now clear that the stress power of the latter piece is actually zero.

Some further important observations may be made:

(a) It is obvious that if we are given *any* Green-elastic material, with strain energy density $\bar{\epsilon}$, a corresponding constrained material can be gotten by evaluating the strain energy of the given material on the constraint manifold; the stress in the constrained material is then given by (14), with $\bar{\mathbf{S}}$ now standing for the stress in the given Green-elastic material evaluated on $\mathcal{S}$. In general, $\bar{\mathbf{S}}$ will have a nonzero component orthogonal to $\mathcal{S}$.

As an example, consider a neo-Hookean material subject to the constraint of incompressibility. For a neo-Hookean material,

$$\rho_0 \bar{\epsilon} = \mu \operatorname{tr} \mathbf{E}, \tag{15}$$

where $\mu > 0$ is a material constant. In view of (5),

$$\bar{\mathbf{S}}(\mathbf{E}) = \mu \mathbf{I}. \tag{16}$$

The incompressibility constraint, namely $J = 1$, can be expressed in the form

$$\phi(\mathbf{E}) = \det(2\mathbf{E} + \mathbf{I}) - 1 = 0. \tag{17}$$

Now,

$$\frac{\partial \phi}{\partial \mathbf{E}} = 2\mathbf{C}^{-1}, \quad \mathbf{E} \in \mathcal{S} \tag{18}$$

and hence, recalling (14), the stress in the constrained neo-Hookean material is of the form

$$\mathbf{S} = \mu \mathbf{I} + \lambda \mathbf{C}^{-1}, \tag{19}$$

where the factor of 2 has been absorbed in the Lagrange multiplier. Note that no limiting process is involved in obtaining a constrained material in this manner.[9]

(b) Recalling the construction of the function $\epsilon'(\mathbf{E})$ in the vicinity of the constraint manifold, it is evident that the level surfaces $\epsilon'(\mathbf{E}) =$ constant are orthogonal to $\mathcal{S}$, and hence that the gradient of ϵ', evaluated on $\mathcal{S}$, lies in the tangent space to $\mathcal{S}$. If we now resolve the stress tensor $\mathbf{S}$ into a

[7] Our constitutive equations, depending as they do only on the value of $\mathbf{E}$ at the particle X, can be discussed with reference to a homogeneous piece of material undergoing a *homogeneous* motion. The strain compatibility relations are then automatically satisfied, and any $\mathbf{E}$ and any $\dot{\mathbf{E}}$ can be chosen in (4). Antman and Marlow (1991) discuss constraints in a global context, in which case compatibility issues become pertinent.

[8] A hint to the above construction is contained in the passages on pp. 12–13 of Adkins (1961), pp. 175–176 of Rivlin (1960), and pp. 32–35 of Green and Adkins (1960). Some geometrical restrictions should be placed on $\mathcal{S}$, but it is not likely that these limit consideration of the types of constraint functions that arise physically.

[9] Thus, the present method stands in contrast to a common method of obtaining an incompressible material from a homogeneous isotropic linearly elastic material by letting the bulk modulus tend to infinity. Here, we would simply take the stress corresponding to an isochoric motion for any given pair of elastic moduli and add on an arbitrary hydrostatic stress. The procedure of Truesdell and Noll (1965) also avoids limiting processes.

Downloaded 04 May 2010 to 171.66.16.28. Redistribution subject to ASME license or copyright; see http://www.asme.org/terms/Terms_Use.cfm

component $\mathbf{S}_{\|}$ tangential to $\mathcal{S}$ and a component $\mathbf{S}_{\perp}$ normal to $\mathcal{S}$, it follows with the aid of (11) and (14) that[10]

$$\mathbf{S}_{\|} = \rho_0 \frac{\partial \epsilon'}{\partial \mathbf{E}}, \quad \mathbf{E} \in \mathcal{S}. \tag{20}$$

We may regard the constrained material as a *constraint-manifold-Green-elastic* material: to each $\mathbf{E} \in \mathcal{S}$, the function ϵ' assigns a unique $\mathbf{S}_{\|}$ tangential to $\mathcal{S}$.

(c) If there is a second constraint of the type (2), the dimension of the manifold $\mathcal{S}$ is reduced to four, and two Lagrange multipliers will appear in the expression corresponding to (14); up to six (independent) constraints can be treated by this procedure, at which stage the material becomes rigidly constrained and $\mathbf{S}$ is completely indeterminate.

4 Cauchy-Elastic and Other Materials Subject to an Internal Constraint

For Cauchy-elastic materials, a constitutive function $\bar{\mathbf{S}}$ exists, but there may be no strain energy function. For such materials, the construction in Section 3, which is based directly on the strain energy function, must be modified. A clue to how constraints in such materials can be dealt with is suggested by Remark (b) in Section 3, where it was observed that the component $\mathbf{S}_{\|}$ of stress in a constrained Green-elastic material is uniquely defined (by (20)) at each point of the constraint manifold. Thus, we will suppose that for a Cauchy-elastic material subject to the internal constraint (2), the surface component of the stress $\mathbf{S}$ is given by a constitutive function $\mathbf{S}'$:

$$\mathbf{S}_{\|} = \mathbf{S}'(\mathbf{E}), \quad \mathbf{E} \in \mathcal{S}. \tag{21}$$

Again, we take $\mathbf{S}$ to be independent of strain-rate. Further, we assume that for any Cauchy-elastic material whose surface component of stress matches $\mathbf{S}'$ on $\mathcal{S}$, the stress power of the Cauchy-elastic material during any motion that satisfies the constraint is equal to the stress power of the constrained Cauchy-elastic material. For any matching Cauchy-elastic material, we then have

$$\bar{\mathbf{S}} \cdot \dot{\mathbf{E}} = \mathbf{S} \cdot \dot{\mathbf{E}} = \mathbf{S}' \cdot \dot{\mathbf{E}} \tag{22}$$

for all $\dot{\mathbf{E}}$ satisfying (3). Consequently, the stress in the constrained material is of the form

$$\begin{aligned} \mathbf{S} &= \bar{\mathbf{S}} + \lambda \frac{\partial \phi}{\partial \mathbf{E}} \\ &= \mathbf{S}' + \bar{\lambda} \frac{\partial \phi}{\partial \mathbf{E}}, \quad \mathbf{E} \in \mathcal{S} \end{aligned} \tag{23}$$

where $\bar{\lambda}$ and λ are Lagrange multipliers.

Again, we can start out with any Cauchy-elastic constitutive function $\bar{\mathbf{S}}$, specialize it to $\mathcal{S}$, add on an arbitrary part orthogonal to $\mathcal{S}$, and thereby obtain the corresponding internally constrained material.

References

Adkins, J. E., 1961, "Large Elastic Deformations," *Progress in Solid Mechanics*, Vol. II, I. N. Sneddon and R. Hill, eds., North-Holland, Amsterdam, pp. 1–60.

Antman, S. S., and Marlow, R. S., 1991, "Material Constraints, Lagrange Multipliers, and Compatibility. Applications to Rod and Shell Theories," *Archive for Rational Mechanics and Analysis*, Vol. 116, pp. 257–299.

Beatty, M. F., 1987, "Topics in Finite Elasticity: Hyperelasticity of Rubber, Elastomers, and Biological Tissues—With Examples," ASME *Applied Mechanics Reviews*, Vol. 40, pp. 1699–1734.

Beatty, M. F., and Hayes, M. A., 1992, "Deformations of an Elastic, Internally Constrained Material. Part I: Homogeneous Deformations," *Journal of Elasticity*, Vol. 29, pp. 1–84.

Carlson, D. E., and Tortorelli, D. A., 1994, "On Hyperelasticity with Internal Constraints," *Recent Advances in Engineering Science: Proceedings of the 31st Annual Technical Meeting of the Society of Engineering Science*, Oct. 10–12, Texas A & M University, D. H. Allen and D. C. Lagoudas, eds.; abstract is missing; completed paper to appear in *Journal of Elasticity*.

Carlson, D. E., and Tortorelli, D. A., 1994b, "On the Theory of Thermoelasticity in the Presence of Internal Constraints," *Abstracts of Contributed Papers: Twelfth U.S. National Congress of Applied Mechanics*, June 27–July 1, University of Washington, Seattle, p. 125.

Casey, J., 1994, "Geometrical Derivation of Lagrange's Equations for a System of Particles," *American Journal of Physics*, Vol. 62, p. 836–847.

Cohen, H., and Wang, C.-C., 1987, "On the Response and Symmetry of Elastic Materials with Internal Constraints," *Archive for Rational Mechanics and Analysis*, Vol. 99, pp. 1–36.

Ericksen, J. L., and Rivlin, R. S., 1954, "Large Elastic Deformations of Homogeneous Anisotropic Materials," *Journal of Rational Mechanics and Analysis*, Vol. 3, pp. 281–301.

Green, A. E., and Adkins, J. E., 1960, *Large Elastic Deformations and Non-Linear Continuum Mechanics*, Clarendon Press, Oxford, U.K.

Green, A. E., and Naghdi, P. M., 1977, "A Note on Thermodynamics of Constrained Materials," ASME JOURNAL OF APPLIED MECHANICS, Vol. 44, p. 787.

Green, A. E., Naghdi, P. M., and Trapp, J. A., 1970, "Thermodynamics of a Continuum with Internal Constraints," *International Journal of Engineering Science*, Vol. 8, pp. 891–908.

Gurtin, M. E., and Podio-Guidugli, P., 1973, "The Thermodynamics of Constrained Materials," *Archive for Rational Mechanics and Analysis*, Vol. 51, pp. 192–208.

Podio-Guidugli, P., and Vianello, M., 1989, "Constraint Manifolds for Isotropic Solids," *Archive for Rational Mechanics and Analysis*, Vol. 105, pp. 105–121.

Rivlin, R. S., 1956, "Large Elastic Deformations," *Rheology: Theory and Applications*, Vol. 1, F. R. Eirich, ed., Academic Press, New York, pp. 351–385.

Rivlin, R. S., 1960, "Some Topics in Finite Elasticity," *Structural Mechanics: Proceedings of the 1st Symposium on Naval Structural Mechanics*, Aug. 11–14, Stanford University, J. N. Goodier, and N. J. Hoff, eds., Pergamon Press, New York, pp. 169–198.

Truesdell, C., and Noll, W., 1965, "The Non-Linear Field Theories of Mechanics," *Handbuch der Physik*, S. Flügge, ed., Vol. III/3, Springer-Verlag, New York, pp. 1–602.

Wang, C.-C., 1979, *Mathematical Principles of Mechanics and Electromagnetism—Part A: Analytical and Continuum Mechanics*, Plenum Press, New York.

[10] It is worth pointing out also that when (8) is evaluated on $\mathcal{S}$, the two terms on the right-hand side become orthogonal to one another: the first one lies in the tangent space to $\mathcal{S}$ and the second one is orthogonal to $\mathcal{S}$.

Divergence Instability of a Spinning Disk With Axial Spindle Displacement in Contact With Evenly Spaced Stationary Springs

Jen-San Chen[1,3] and Cheng-Chou Wong[2,3]

The titled problem is studied numerically by finite element calculation and analytically by three-mode eigenfunction expansion. It is found that divergence instability of the coupled system is

[1] Associate Professor.

[2] Graduate Student.

[3] Department of Mechanical Engineering, National Taiwan University, Taipei, Taiwan 107, R.O.C.

Contributed by the Applied Mechanics Division of THE AMERICAN SOCIETY OF MECHANICAL ENGINEERS for publication in the ASME JOURNAL OF APPLIED MECHANICS. Manuscript received by the ASME Applied Mechanics Division, Sept. 26, 1994; final revision, Nov. 14, 1994. Associate Technical Editor: F. Y. M. Wan.

Downloaded 04 May 2010 to 171.66.16.28. Redistribution subject to ASME license or copyright; see http://www.asme.org/terms/Terms_Use.cfm

component $\mathbf{S}_{\|}$ tangential to $\mathcal{S}$ and a component $\mathbf{S}_{\perp}$ normal to $\mathcal{S}$, it follows with the aid of (11) and (14) that[10]

$$\mathbf{S}_{\|} = \rho_0 \frac{\partial \epsilon'}{\partial \mathbf{E}}, \quad \mathbf{E} \in \mathcal{S}. \tag{20}$$

We may regard the constrained material as a *constraint-manifold-Green-elastic* material: to each $\mathbf{E} \in \mathcal{S}$, the function ϵ' assigns a unique $\mathbf{S}_{\|}$ tangential to $\mathcal{S}$.

(c) If there is a second constraint of the type (2), the dimension of the manifold $\mathcal{S}$ is reduced to four, and two Lagrange multipliers will appear in the expression corresponding to (14); up to six (independent) constraints can be treated by this procedure, at which stage the material becomes rigidly constrained and $\mathbf{S}$ is completely indeterminate.

4 Cauchy-Elastic and Other Materials Subject to an Internal Constraint

For Cauchy-elastic materials, a constitutive function $\bar{\mathbf{S}}$ exists, but there may be no strain energy function. For such materials, the construction in Section 3, which is based directly on the strain energy function, must be modified. A clue to how constraints in such materials can be dealt with is suggested by Remark (b) in Section 3, where it was observed that the component $\mathbf{S}_{\|}$ of stress in a constrained Green-elastic material is uniquely defined (by (20)) at each point of the constraint manifold. Thus, we will suppose that for a Cauchy-elastic material subject to the internal constraint (2), the surface component of the stress $\mathbf{S}$ is given by a constitutive function $\mathbf{S}'$:

$$\mathbf{S}_{\|} = \mathbf{S}'(\mathbf{E}), \quad \mathbf{E} \in \mathcal{S}. \tag{21}$$

Again, we take $\mathbf{S}$ to be independent of strain-rate. Further, we assume that for any Cauchy-elastic material whose surface component of stress matches $\mathbf{S}'$ on $\mathcal{S}$, the stress power of the Cauchy-elastic material during any motion that satisfies the constraint is equal to the stress power of the constrained Cauchy-elastic material. For any matching Cauchy-elastic material, we then have

$$\bar{\mathbf{S}} \cdot \dot{\mathbf{E}} = \mathbf{S} \cdot \dot{\mathbf{E}} = \mathbf{S}' \cdot \dot{\mathbf{E}} \tag{22}$$

for all $\dot{\mathbf{E}}$ satisfying (3). Consequently, the stress in the constrained material is of the form

$$\begin{aligned} \mathbf{S} &= \bar{\mathbf{S}} + \lambda \frac{\partial \phi}{\partial \mathbf{E}} \\ &= \mathbf{S}' + \bar{\lambda} \frac{\partial \phi}{\partial \mathbf{E}}, \quad \mathbf{E} \in \mathcal{S} \end{aligned} \tag{23}$$

where $\bar{\lambda}$ and λ are Lagrange multipliers.

Again, we can start out with any Cauchy-elastic constitutive function $\bar{\mathbf{S}}$, specialize it to $\mathcal{S}$, add on an arbitrary part orthogonal to $\mathcal{S}$, and thereby obtain the corresponding internally constrained material.

References

Adkins, J. E., 1961, "Large Elastic Deformations," *Progress in Solid Mechanics*, Vol. II, I. N. Sneddon and R. Hill, eds., North-Holland, Amsterdam, pp. 1–60.

Antman, S. S., and Marlow, R. S., 1991, "Material Constraints, Lagrange Multipliers, and Compatibility. Applications to Rod and Shell Theories," *Archive for Rational Mechanics and Analysis*, Vol. 116, pp. 257–299.

Beatty, M. F., 1987, "Topics in Finite Elasticity: Hyperelasticity of Rubber, Elastomers, and Biological Tissues—With Examples," ASME *Applied Mechanics Reviews*, Vol. 40, pp. 1699–1734.

Beatty, M. F., and Hayes, M. A., 1992, "Deformations of an Elastic, Internally Constrained Material. Part I: Homogeneous Deformations," *Journal of Elasticity*, Vol. 29, pp. 1–84.

Carlson, D. E., and Tortorelli, D. A., 1994, "On Hyperelasticity with Internal Constraints," *Recent Advances in Engineering Science: Proceedings of the 31st Annual Technical Meeting of the Society of Engineering Science*, Oct. 10–12, Texas A & M University, D. H. Allen and D. C. Lagoudas, eds.; abstract is missing; completed paper to appear in *Journal of Elasticity*.

Carlson, D. E., and Tortorelli, D. A., 1994b, "On the Theory of Thermoelasticity in the Presence of Internal Constraints," *Abstracts of Contributed Papers: Twelfth U.S. National Congress of Applied Mechanics*, June 27–July 1, University of Washington, Seattle, p. 125.

Casey, J., 1994, "Geometrical Derivation of Lagrange's Equations for a System of Particles," *American Journal of Physics*, Vol. 62, p. 836–847.

Cohen, H., and Wang, C.-C., 1987, "On the Response and Symmetry of Elastic Materials with Internal Constraints," *Archive for Rational Mechanics and Analysis*, Vol. 99, pp. 1–36.

Ericksen, J. L., and Rivlin, R. S., 1954, "Large Elastic Deformations of Homogeneous Anisotropic Materials," *Journal of Rational Mechanics and Analysis*, Vol. 3, pp. 281–301.

Green, A. E., and Adkins, J. E., 1960, *Large Elastic Deformations and Non-Linear Continuum Mechanics*, Clarendon Press, Oxford, U.K.

Green, A. E., and Naghdi, P. M., 1977, "A Note on Thermodynamics of Constrained Materials," ASME JOURNAL OF APPLIED MECHANICS, Vol. 44, p. 787.

Green, A. E., Naghdi, P. M., and Trapp, J. A., 1970, "Thermodynamics of a Continuum with Internal Constraints," *International Journal of Engineering Science*, Vol. 8, pp. 891–908.

Gurtin, M. E., and Podio-Guidugli, P., 1973, "The Thermodynamics of Constrained Materials," *Archive for Rational Mechanics and Analysis*, Vol. 51, pp. 192–208.

Podio-Guidugli, P., and Vianello, M., 1989, "Constraint Manifolds for Isotropic Solids," *Archive for Rational Mechanics and Analysis*, Vol. 105, pp. 105–121.

Rivlin, R. S., 1956, "Large Elastic Deformations," *Rheology: Theory and Applications*, Vol. 1, F. R. Eirich, ed., Academic Press, New York, pp. 351–385.

Rivlin, R. S., 1960, "Some Topics in Finite Elasticity," *Structural Mechanics: Proceedings of the 1st Symposium on Naval Structural Mechanics*, Aug. 11–14, Stanford University, J. N. Goodier, and N. J. Hoff, eds., Pergamon Press, New York, pp. 169–198.

Truesdell, C., and Noll, W., 1965, "The Non-Linear Field Theories of Mechanics," *Handbuch der Physik*, S. Flügge, ed., Vol. III/3, Springer-Verlag, New York, pp. 1–602.

Wang, C.-C., 1979, *Mathematical Principles of Mechanics and Electromagnetism—Part A: Analytical and Continuum Mechanics*, Plenum Press, New York.

[10] It is worth pointing out also that when (8) is evaluated on $\mathcal{S}$, the two terms on the right-hand side become orthogonal to one another: the first one lies in the tangent space to $\mathcal{S}$ and the second one is orthogonal to $\mathcal{S}$.

Divergence Instability of a Spinning Disk With Axial Spindle Displacement in Contact With Evenly Spaced Stationary Springs

Jen-San Chen[1,3] and Cheng-Chou Wong[2,3]

The titled problem is studied numerically by finite element calculation and analytically by three-mode eigenfunction expansion. It is found that divergence instability of the coupled system is

[1] Associate Professor.

[2] Graduate Student.

[3] Department of Mechanical Engineering, National Taiwan University, Taipei, Taiwan 107, R.O.C.

Contributed by the Applied Mechanics Division of THE AMERICAN SOCIETY OF MECHANICAL ENGINEERS for publication in the ASME JOURNAL OF APPLIED MECHANICS. Manuscript received by the ASME Applied Mechanics Division, Sept. 26, 1994; final revision, Nov. 14, 1994. Associate Technical Editor: F. Y. M. Wan.

Copyright © 1995 by ASME

Downloaded 04 May 2010 to 171.66.16.28. Redistribution subject to ASME license or copyright; see http://www.asme.org/terms/Terms_Use.cfm

induced only when two times the number of nodal diameters 2n *is equal to a multiple of the number of stationary springs* N, *but* n *itself is not a multiple of* N.

Introduction

It has been known in the wood cutting industry that allowing the central clamping collar of the circular saw to slide freely along the axis of rotation can improve the stability of the cutting process. Mote's paper (1977), in which the collar was modeled as a line mass without stiffness, appears to be the first publication trying to explain the effects of the rigid-body translation on the stability of the floating circular saw. Mote's model failed to explain the observed improvement in stability that occurs by allowing the collar to slide freely, so Price (1987) extended Mote's model by considering the disk and collar system as an elastic plate with two concentric regions of different thickness. As the thickness ratio of the collar and plate becomes very large, Price's calculations show that the divergence instability induced by load system stiffness can be eliminated. These papers are mainly concerned with the dynamics of a spinning disk with axial spindle displacement in contact with a *single* stationary load system. In the wood cutting industry, however, the saw blade is usually restrained from lateral vibration by the presence of more than one guide pad. This Note presents the calculation results and analytical verification on the divergence instability of a spinning disk with axial spindle displacement in contact with multiple stationary springs.

Equations of Motion

The motion of a spinning flexible disk with axial translation can be described in two coordinates frames. The local frame *o-xyz* is attached to the rigid, massless collar and translates in the Z-direction relative to the inertial frame *O-XYZ*. Both the Z- and the z-axes are coincident with the rotation axis of the floating circular disk. The disk is clamped by the collar on the inner radius $r = a$ and free on the outer radius $r = b$. The position of the collar is measured by Z from the origin O. The elastic transverse displacement w of the disk is measured with respect to the local *o-xyz* frame. The disk rotates about the *oz*-axis with constant rotation speed Ω and is in contact with N evenly spaced point springs. By D'Alembert's principle, the equation of motion of the disk in terms of w and with respect to the nonrotating local coordinate system (r, θ) can be written as

$$\rho h\left(w_{,tt} + 2\Omega w_{,t\theta} + \Omega^2 w_{,\theta\theta}\right) + D\nabla^4 w - \frac{h}{r}(\sigma_r r w_{,r})_{,r} - \frac{h\sigma_\theta}{r^2} w_{,\theta\theta} + \rho h\ddot{Z} = -\sum_{j=1}^{N} \frac{k_z}{r}\delta(r-\xi)\delta(\theta-\theta_j)(w+Z). \quad (1)$$

The parameters ρ, h, and D are the mass density, thickness, and flexural rigidity of the disk, respectively. $\delta(\cdot)$ is the Dirac delta function. The point springs are evenly located on a circle with radius $r = \xi$, where $a \le \xi \le b$. The membrane stresses σ_r and σ_θ are due to the centrifugal effect.

By considering the force balance in the Z-direction between the total inertial force on the disk and the forces exerted by the stationary springs k_z, one can obtain an additional equation of motion

$$m\ddot{Z} + \int_0^{2\pi}\int_a^b \rho h w_{,tt} r dr d\theta + \sum_{j=1}^{N} k_z\left[w(\xi,\theta_j) + Z\right] = 0 \quad (2)$$

where m is the mass of the circular plate.

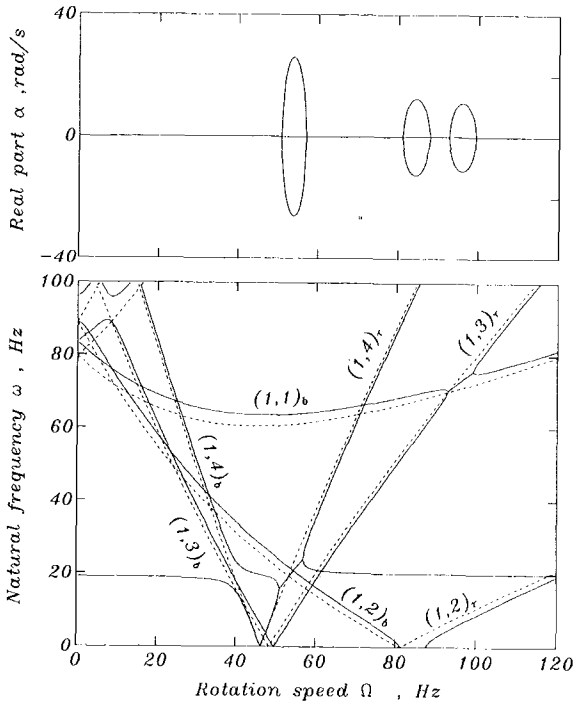

Fig. 1 Eigenvalues of the spinning disk in contact with four stationary springs k_z = 3000 N / m

Numerical Results

The eigenvalues of the coupled system are obtained by a finite element computation which is similar to the one presented in Ono et al. (1991). The material properties of the disk used in the calculations are $\rho = 7.84 \times 10^3 \text{kg/m}^3$, $D = 19.36$ Nm, $h = 1.02$ mm, $a = 101.6$ mm, $b = 203.2$ mm. Figure 1 shows the cases when the spinning disk is in contact with four evenly spaced stationary springs k_z at the radial position $\xi = 0.9b$. The ordinates are the natural frequency ω and the real part α of the eigenvalue ($\lambda = \alpha + i\omega$). The solid lines represent the cases for stiffness $k_z = 3000$ N/m. The dashed lines correspond to the case of a freely spinning disk with rigid-body translation (i.e., $k_z = 0$). Attention is focused on the divergence instability when a backward wave meets its complex conjugate near the critical speed. Figure 1 shows that divergence instability is induced when $(1, 2)_b$ meets its complex conjugate, but no divergence instability is induced when $(1, 3)_b$ and $(1, 4)_b$ meet their complex conjugates. Mode label $(m, n)_b$ represents a backward wave with m nodal circles and n nodal diameters. Subscripts "f" and "r" in the mode label in Fig. 1 represent a forward and a reflected wave, respectively. From these observations and additional calculations not shown here it is found that divergence instability is induced when $2n$ is equal to a multiple of N and n itself is not a multiple of N.

In order to study the behavior of divergence instability as k_z changes, we consider the case when Ω is fixed at 85 Hz, just higher than the critical speed $\Omega_c = 81$ Hz of mode (1, 2). The solid lines in Figs. 2(a), (b), and (c) show the eigenvalue λ as a function of k_z when $N = 2$, 3, and 4, respectively. In Fig. 2(a), the two eigenvalues are purely imaginary except when $k_z^- < k_z < k_z^+$. When $k_z^- < k_z < k_{z_f}^+$, the eigenvalues are complex numbers. In Fig. 2(b) the two eigenvalues are always purely imaginary, with one increasing monotonically with k_z and the other decreasing as k_z increases until $k_z = k_z^*$. As $k_z > k_z^*$ this eigenvalue increases from zero as k_z increases. This represents the phenomenon that critical speed increases in the $\lambda - \Omega$ diagram when k_z increases. In Fig. 2(c) one of

Downloaded 04 May 2010 to 171.66.16.28. Redistribution subject to ASME license or copyright; see http://www.asme.org/terms/Terms_Use.cfm

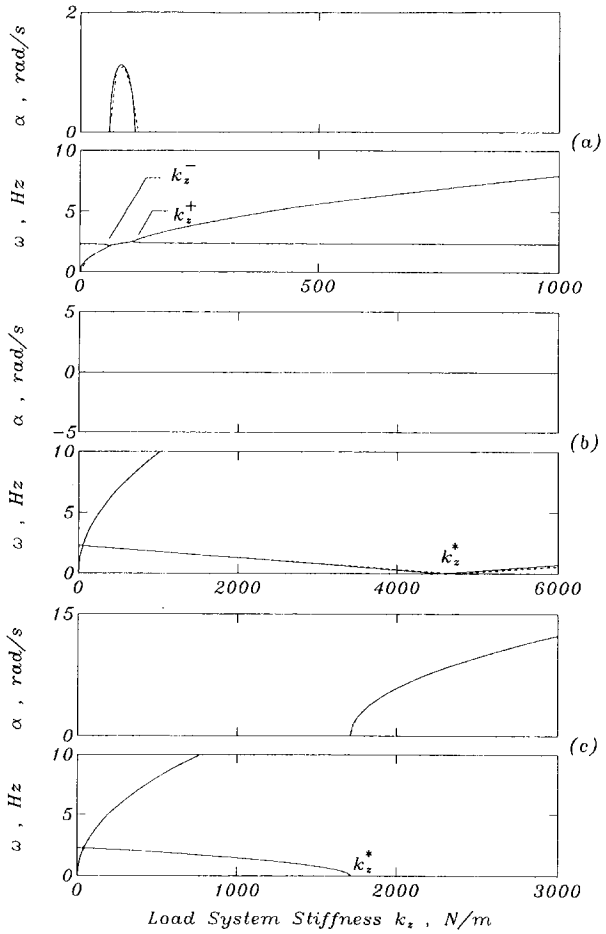

Fig. 2 Relation between eigenvalues and stiffness k_z when the disk is spinning at Ω = 85 Hz and in contact with (a) two, (b) three, and (c) four springs, respectively

the eigenvalues is always purely imaginary and the other becomes a real number when $k_z > k_z^*$. This means that the divergence instability is induced when $k_z > k_z^*$.

Eigenfunction Expansion Method

Equations (1) and (2) can be rewritten in the matrix operator form

$$\mathbf{M}\mathbf{u}_{,tt} + \mathbf{G}\mathbf{u}_{,t} + (\mathbf{K} + \hat{\mathbf{K}})\mathbf{u} = \mathbf{0}, \tag{3}$$

where the vector $\mathbf{u}$ is defined as $\mathbf{u} \equiv \begin{Bmatrix} w \\ Z \end{Bmatrix}$. The matrix operators **M**, **G**, and **K** are associated with the freely spinning disk, while $\hat{\mathbf{K}}$ is associated with the stationary point springs. The inner product between two eigenvectors $\mathbf{u}_1$ and $\mathbf{u}_2$ is defined as

$$\langle \mathbf{u}_1, \mathbf{u}_2 \rangle = \int_0^{2\pi} \int_a^b \bar{w}_1 w_2 r dr d\theta + \bar{Z}_1 Z_2. \tag{4}$$

the overbar means complex conjugate. The orthogonality relations among eigenfunctions of a freely spinning disk with respect to operators **M**, **G**, and **K** in Eq. (3) have been established in Wong (1994).

In order to study the eigenvalue changes near the critical speed, we express the eigenfunction of Eq. (3) in terms of the eigenfunctions of three neighboring modes of the freely spinning disk

$$\mathbf{u} = c_1 \mathbf{u}_{mn} + c_2 \bar{\mathbf{u}}_{mn} + c_3 \mathbf{u}_{00} \tag{5}$$

where $\mathbf{u}_{mn} = \begin{Bmatrix} w_{mn} \\ 0 \end{Bmatrix}$ and $\mathbf{u}_{00} = \begin{Bmatrix} 0 \\ 1 \end{Bmatrix}$. $w_{mn} = R_{mn}(r)e^{in\theta}$ is the eigenfunction of the mode (m, n) with $n \neq 0$, whose natural frequency is ω_{mn}. $R_{mn}(r)$ is a real-valued function of r. Substituting Eq. (5) into (3) and taking the inner product between each of the three eigenfunctions and both sides of Eq. (3) with use of the orthogonality properties described in Wong (1994), we obtain a system of three homogeneous linear algebraic equations with unknowns c_1, c_2, and c_3. For the existence of nontrivial solutions the determinant of the coefficient matrix should vanish. Consequently, the eigenvalue λ can be obtained by solving the following equation:

$$\alpha_0\lambda^6 + (\beta_0 + \beta_1\epsilon)\lambda^4 + (\gamma_0 + \gamma_1\epsilon + \gamma_2\epsilon^2)\lambda^2 + (\eta_1\epsilon + \eta_2\epsilon^2 + \eta_3\epsilon^3) = 0 \tag{6}$$

where

$$\alpha_0 = 4AR_{mn}^{*2}, \quad \beta_0 = 4A(S_{mn}^2 + R_{mn}^{*2}\omega_{mn}^2),$$

$$\beta_1 = 4R_{mn}^* N[R_{mn}^* + AR_{mn}^2(\xi)],$$

$$\gamma_0 = 4A\omega_{mn}^2 S_{mn}^2,$$

$$\gamma_1 = 4N[S_{mn}^2 + R_{mn}^{*2}\omega_{mn}^2 + R_{mn}^2(\xi)A\omega_{mn}S_{mn}],$$

$$\gamma_2 = R_{mn}^2(\xi)[4R_{mn}^*(N^2 - \kappa_1) + R_{mn}^2(\xi)A(N^2 - \kappa_2)],$$

$$\eta_1 = 4N\omega_{mn}^2 S_{mn}^2,$$

$$\eta_2 = 4R_{mn}^2(\xi)\omega_{mn}S_{mn}(N^2 - \kappa_1),$$

$$\eta_3 = R_{mn}^4(\xi)[N^3 - (2\kappa_1 + \kappa_2)N + \kappa_3]$$

and

$$\epsilon = k_z/\rho h, \quad A = \pi(b^2 - a^2), \quad R_{mn}^* = \pi\int_a^b R_{mn}^2(r)rdr,$$

$$S_{mn} = \pi R_{mn}^*(2n\Omega + \omega_{mn}), \quad \kappa_1 = \sum_{j=1}^{N}\sum_{k=1}^{N} e^{2in\pi(j-k)/N},$$

$$\kappa_2 = \sum_{j=1}^{N}\sum_{k=1}^{N} e^{4in\pi(j-k)/N},$$

$$\kappa_3 = \sum_{j=1}^{N}\sum_{k=1}^{N}\sum_{l=1}^{N} 2\cos\left[\frac{2n\pi(2l - j - k)}{N}\right].$$

The roots of Eq. (6) are solved and plotted as dashed lines in Fig. 2. It can be seen that the three-mode expansion is an excellent approximation to the finite element solution.

Case I. Neither n nor $2n$ is a multiple of N. In this case $\kappa_1 = \kappa_2 = \kappa_3 = 0$. The eigenvalues can be solved as

$$\lambda_0^2 = -\frac{\epsilon N}{A} \quad \text{and} \quad \lambda_\pm^2 = -(G + H) \pm 2\sqrt{GH}$$

where G and H are two positive real numbers

$$G = n^2\Omega^2, \quad H = (n\Omega + \omega_{mn})^2 + \frac{\epsilon NR_{mn}^2(\xi)}{2R_{mn}^*}.$$

It is clear that all the eigenvalues remain purely imaginary as the stiffness parameter ϵ changes. λ_0 corresponds to the mode with frequency proportional to $\sqrt{k_z}$ in Fig. 2(*b*). λ_+ corresponds to the mode with frequency decreasing to zero as k_z increases. λ_+ changes sign when $\epsilon = \epsilon^* = -\frac{2S_{mn}\omega_{mn}}{NR_{mn}^2(\xi)}$, which corresponds to k_z^* in Fig. 2(*b*). λ_- is an extra root and corresponds to mode $(m, n)_f$, whose natural frequency is beyond the range of Fig. 2. Therefore no diver-

Downloaded 04 May 2010 to 171.66.16.28. Redistribution subject to ASME license or copyright; see http://www.asme.org/terms/Terms_Use.cfm

gence instability will be induced by the stationary springs in this case.

Case II. $2n$ is a multiple of N, but n itself is not a multiple of N. In this case $\kappa_1 = \kappa_3 = 0$, and $\kappa_2 = N^2$. The eigenvalues can be solved as

$$\lambda_0^2 = -\frac{\epsilon N}{A} \quad \text{and}$$

$$\lambda_\pm^2 = -(G+H) \pm 2\sqrt{GH + \frac{\epsilon^2 N R_{mm}^2(\xi)}{16 R_{mn}^{*2}}}.$$

It is obvious that λ_0^2 and λ_-^2 are always negative and correspond to stable modes. On the other hand the sign of λ_+^2 depends on ϵ. It can be shown that λ_+^2 becomes positive when $\epsilon > \epsilon^* = -\dfrac{S_{mn}\omega_{mn}}{N R_{mn}^2(\xi)}$. The eigenfunction corresponding to positive λ_+^2 is an unstable mode with zero natural frequency. In other words, divergence instability is induced in this case. It is noted that ϵ^* corresponds to k_z^* in Fig. 2(*c*).

Case III. n is a multiple of N. In this case $\kappa_1 = \kappa_2 = N^2$ and $\kappa_3 = 2N^3$. It is difficult to derive the explicit expression for λ^2 in this case. However, we can show that the roots for λ^2 are one negative real number and two complex conjugate numbers when $\epsilon_-^* < \epsilon < \epsilon_+^*$, where

$$\epsilon_\pm^* = \frac{A\omega_{mn}^2\left[2P - Q \pm \sqrt{Q(-8P+Q)}\right]}{2N(P+Q)}$$

$$P = R_{mn}^*(n\Omega + 4\omega_{mn}), \quad Q = A\omega_{mn}R_{mn}^2(\xi)$$

The real λ^2 corresponds to the stable mode $(m, n)_f$. The eigenfunctions corresponding to complex conjugate λ^2 are two modes with the same nonzero natural frequency, one with positive and the other with negative real parts. Therefore merged-type instability occurs in this case. It is noted that $\epsilon_\pm^*$ correspond to $k_z^\pm$ in Fig. 2(*a*).

References

Mote, C. D., Jr., 1977, "Moving Load Stability of a Circular Plate on a Floating Central Collar," *Journal of the Acoustical Society of America*, Vol. 61, pp. 439–447.

Ono, K., Chen, J.-S., and Bogy, D. B., 1991, "Stability Analysis for the Head-Disk Interface in a Flexible Disk Drive," ASME JOURNAL OF APPLIED MECHANICS, Vol. 58, pp. 1005–1014.

Price, K. B., 1987, "Analysis of the Dynamics of Guided Rotating Free Center Plates," Ph.D. dissertation, University of California, Berkeley, CA.

Wong, C.-C., 1994, "Vibration and Stability of a Spinning Disk in Contact With Evenly Spaced Stationary Load Systems," Master Thesis, Department of Mechanical Engineering, National Taiwan University, Taipei, Taiwan.

Radial Stresses in Composite Thick-Walled Shafts

Naki Tutuncu[1]

Introduction

Increasing use of thick-walled composite tubes as machine elements necessitates the investigation of through-the-thickness stresses. These stresses might be due to externally applied loads such as pressure, torque or axial force, or due to thermal loads. A possible case which includes all of the above is presented by Tutuncu and Winckler (1993) with the assumptions that the cylindrical tube is long, i.e., no end effects are considered, and stresses and strains are independent of the circumferential coordinate. Based on the same assumptions, the present paper will address the problem of determining radial stresses in composite rotating shafts resulting solely from centrifugal forces which constitute the body force in radial direction.

In conventional applications of cylindrical tubes as hollow shafts, the radial stresses may rightfully be neglected for they are of much less magnitude as compared with axial and hoop stresses. In laminated structures, however, these stresses may be of great concern because the transverse strength of a typical laminate is much less than its axial strength. Assuming the strength in radial direction is approximately equal to the transverse strength, a relatively small radial stress might cause delamination in the structure.

A displacement based linear elasticity approach will be presented. The tubes in question may be multilayered allowing the possibility of each layer being made of a different orthotropic material placed at an arbitrary angle to the tube axis. For a complete discussion of stresses in thick-walled tubes with the absence of body forces the reader is referred to the papers by Pagano and Halpin (1968), Hyer, Cooper, and Cohen (1986), Hyer and Rousseau (1987), and Tutuncu and Winckler (1993).

Differential Equation and Boundary Conditions. Consider a helical wound composite cylinder which is rotating at an angular velocity ω. As a result of the assumptions made, the problem is reduced to a planar elasticity problem where the radial, circumferential, and axial displacements are given, respectively, as follows:

$$u_r = u(r), \quad u_\theta = v(z,r), \quad u_z = w(z,r). \tag{1}$$

The strain-displacement relations reduce to

$$\epsilon_r = \frac{du}{dr}, \quad \epsilon_\theta = \frac{u}{r}, \quad \epsilon_z = \frac{\partial w}{\partial z}, \quad \gamma_{r\theta} = \frac{\partial v}{\partial r} - \frac{v}{r},$$

$$\gamma_{\theta z} = \frac{\partial v}{\partial z}, \quad \gamma_{zr} = \frac{\partial w}{\partial r}. \tag{2}$$

The equilibrium equation in radial direction is

$$\frac{d\sigma_r}{dr} + \frac{\sigma_r - \sigma_\theta}{r} + \omega^2 \rho r = 0 \tag{3}$$

where $\omega^2\rho r$ is the body force per unit volume and ρ is the density of the material.

On the account of the fact that all stresses are considered to be functions of r only and the boundary conditions $\tau_{rz} = \tau_{r\theta} = 0$ at $r = R_i$, the shearing stresses τ_{rz} and $\tau_{r\theta}$ vanish, and the remaining two equilibrium equations, with the absence of body forces in axial and circumferential directions, are identically satisfied. The constitutive relation is then written as

$$\begin{Bmatrix} \sigma_r \\ \sigma_\theta \\ \sigma_z \\ \tau_{\theta z} \end{Bmatrix} = \begin{bmatrix} C_{11} & C_{12} & C_{13} & C_{14} \\ C_{12} & C_{22} & C_{23} & C_{24} \\ C_{13} & C_{23} & C_{33} & C_{34} \\ C_{14} & C_{24} & C_{34} & C_{44} \end{bmatrix} \begin{Bmatrix} \epsilon_r \\ \epsilon_\theta \\ \epsilon_z \\ \gamma_{\theta z} \end{Bmatrix}. \tag{4}$$

Note that in cross-ply laminates, the extension-shear coupling terms C_{14}, C_{24}, C_{34} would not appear. Following the steps outlined by Tutuncu and Winckler (1993), the circumferential and axial displacements are found as follows:

[1]Assistant Professor, Department of Mechanical Engineering, Çukurova University, 01330 Adana, Turkey.

Contributed by the Applied Mechanics Division of THE AMERICAN SOCIETY OF MECHANICAL ENGINEERS for publication in the ASME JOURNAL OF APPLIED MECHANICS. Manuscript received by the ASME Applied Mechanics Division, July 7, 1994; final revision, Dec. 29, 1994. Associate Technical Editor: G. J. Dvorak.

Downloaded 04 May 2010 to 171.66.16.28. Redistribution subject to ASME license or copyright; see http://www.asme.org/terms/Terms_Use.cfm

gence instability will be induced by the stationary springs in this case.

Case II. $2n$ is a multiple of N, but n itself is not a multiple of N. In this case $\kappa_1 = \kappa_3 = 0$, and $\kappa_2 = N^2$. The eigenvalues can be solved as

$$\lambda_0^2 = -\frac{\epsilon N}{A} \quad \text{and}$$

$$\lambda_\pm^2 = -(G+H) \pm 2\sqrt{GH + \frac{\epsilon^2 N R_{mm}^2(\xi)}{16 R_{mn}^{*2}}}.$$

It is obvious that λ_0^2 and λ_-^2 are always negative and correspond to stable modes. On the other hand the sign of λ_+^2 depends on ϵ. It can be shown that λ_+^2 becomes positive when $\epsilon > \epsilon^* = -\dfrac{S_{mn}\omega_{mn}}{N R_{mn}^2(\xi)}$. The eigenfunction corresponding to positive λ_+^2 is an unstable mode with zero natural frequency. In other words, divergence instability is induced in this case. It is noted that ϵ^* corresponds to k_z^* in Fig. 2(*c*).

Case III. n is a multiple of N. In this case $\kappa_1 = \kappa_2 = N^2$ and $\kappa_3 = 2N^3$. It is difficult to derive the explicit expression for λ^2 in this case. However, we can show that the roots for λ^2 are one negative real number and two complex conjugate numbers when $\epsilon_-^* < \epsilon < \epsilon_+^*$, where

$$\epsilon_\pm^* = \frac{A\omega_{mn}^2\left[2P - Q \pm \sqrt{Q(-8P+Q)}\right]}{2N(P+Q)}$$

$$P = R_{mn}^*(n\Omega + 4\omega_{mn}), \quad Q = A\omega_{mn}R_{mn}^2(\xi)$$

The real λ^2 corresponds to the stable mode $(m, n)_f$. The eigenfunctions corresponding to complex conjugate λ^2 are two modes with the same nonzero natural frequency, one with positive and the other with negative real parts. Therefore merged-type instability occurs in this case. It is noted that $\epsilon_\pm^*$ correspond to $k_z^\pm$ in Fig. 2(*a*).

References

Mote, C. D., Jr., 1977, "Moving Load Stability of a Circular Plate on a Floating Central Collar," *Journal of the Acoustical Society of America*, Vol. 61, pp. 439–447.

Ono, K., Chen, J.-S., and Bogy, D. B., 1991, "Stability Analysis for the Head-Disk Interface in a Flexible Disk Drive," ASME JOURNAL OF APPLIED MECHANICS, Vol. 58, pp. 1005–1014.

Price, K. B., 1987, "Analysis of the Dynamics of Guided Rotating Free Center Plates," Ph.D. dissertation, University of California, Berkeley, CA.

Wong, C.-C., 1994, "Vibration and Stability of a Spinning Disk in Contact With Evenly Spaced Stationary Load Systems," Master Thesis, Department of Mechanical Engineering, National Taiwan University, Taipei, Taiwan.

Radial Stresses in Composite Thick-Walled Shafts

Naki Tutuncu[1]

Introduction

Increasing use of thick-walled composite tubes as machine elements necessitates the investigation of through-the-thickness stresses. These stresses might be due to externally applied loads such as pressure, torque or axial force, or due to thermal loads. A possible case which includes all of the above is presented by Tutuncu and Winckler (1993) with the assumptions that the cylindrical tube is long, i.e., no end effects are considered, and stresses and strains are independent of the circumferential coordinate. Based on the same assumptions, the present paper will address the problem of determining radial stresses in composite rotating shafts resulting solely from centrifugal forces which constitute the body force in radial direction.

In conventional applications of cylindrical tubes as hollow shafts, the radial stresses may rightfully be neglected for they are of much less magnitude as compared with axial and hoop stresses. In laminated structures, however, these stresses may be of great concern because the transverse strength of a typical laminate is much less than its axial strength. Assuming the strength in radial direction is approximately equal to the transverse strength, a relatively small radial stress might cause delamination in the structure.

A displacement based linear elasticity approach will be presented. The tubes in question may be multilayered allowing the possibility of each layer being made of a different orthotropic material placed at an arbitrary angle to the tube axis. For a complete discussion of stresses in thick-walled tubes with the absence of body forces the reader is referred to the papers by Pagano and Halpin (1968), Hyer, Cooper, and Cohen (1986), Hyer and Rousseau (1987), and Tutuncu and Winckler (1993).

Differential Equation and Boundary Conditions. Consider a helical wound composite cylinder which is rotating at an angular velocity ω. As a result of the assumptions made, the problem is reduced to a planar elasticity problem where the radial, circumferential, and axial displacements are given, respectively, as follows:

$$u_r = u(r), \quad u_\theta = v(z,r), \quad u_z = w(z,r). \tag{1}$$

The strain-displacement relations reduce to

$$\epsilon_r = \frac{du}{dr}, \quad \epsilon_\theta = \frac{u}{r}, \quad \epsilon_z = \frac{\partial w}{\partial z}, \quad \gamma_{r\theta} = \frac{\partial v}{\partial r} - \frac{v}{r},$$

$$\gamma_{\theta z} = \frac{\partial v}{\partial z}, \quad \gamma_{zr} = \frac{\partial w}{\partial r}. \tag{2}$$

The equilibrium equation in radial direction is

$$\frac{d\sigma_r}{dr} + \frac{\sigma_r - \sigma_\theta}{r} + \omega^2 \rho r = 0 \tag{3}$$

where $\omega^2\rho r$ is the body force per unit volume and ρ is the density of the material.

On the account of the fact that all stresses are considered to be functions of r only and the boundary conditions $\tau_{rz} = \tau_{r\theta} = 0$ at $r = R_i$, the shearing stresses τ_{rz} and $\tau_{r\theta}$ vanish, and the remaining two equilibrium equations, with the absence of body forces in axial and circumferential directions, are identically satisfied. The constitutive relation is then written as

$$\begin{Bmatrix} \sigma_r \\ \sigma_\theta \\ \sigma_z \\ \tau_{\theta z} \end{Bmatrix} = \begin{bmatrix} C_{11} & C_{12} & C_{13} & C_{14} \\ C_{12} & C_{22} & C_{23} & C_{24} \\ C_{13} & C_{23} & C_{33} & C_{34} \\ C_{14} & C_{24} & C_{34} & C_{44} \end{bmatrix} \begin{Bmatrix} \epsilon_r \\ \epsilon_\theta \\ \epsilon_z \\ \gamma_{\theta z} \end{Bmatrix}. \tag{4}$$

Note that in cross-ply laminates, the extension-shear coupling terms C_{14}, C_{24}, C_{34} would not appear. Following the steps outlined by Tutuncu and Winckler (1993), the circumferential and axial displacements are found as follows:

[1]Assistant Professor, Department of Mechanical Engineering, Çukurova University, 01330 Adana, Turkey.

Contributed by the Applied Mechanics Division of THE AMERICAN SOCIETY OF MECHANICAL ENGINEERS for publication in the ASME JOURNAL OF APPLIED MECHANICS. Manuscript received by the ASME Applied Mechanics Division, July 7, 1994; final revision, Dec. 29, 1994. Associate Technical Editor: G. J. Dvorak.

Copyright © 1995 by ASME

Downloaded 04 May 2010 to 171.66.16.28. Redistribution subject to ASME license or copyright; see http://www.asme.org/terms/Terms_Use.cfm

$$v(r,z) = rzC \tag{5}$$

$$w(z) = zD. \tag{6}$$

The radial displacement u is found by solving the following differential equation:

$$r^2u'' + ru' - \lambda^2 u = \frac{C_{23} - C_{13}}{C_{11}}Dr + \frac{C_{24} - 2C_{14}}{C_{11}}Cr^2 - \frac{\rho\omega^2}{C_{11}}r^3 \tag{7}$$

where $\lambda^2 = C_{22}/C_{11}$. The complete solution of (7) for a typical ply is written as

$$u = A_1 r^{\lambda} + A_2 r^{-\lambda} + \frac{C_{13} - C_{23}}{C_{11}(\lambda^2 - 1)}Dr + \frac{2C_{14} - C_{24}}{C_{11}(\lambda^2 - 4)}Cr^2 + \frac{\rho\omega^2}{C_{11}(\lambda^2 - 9)}r^3 \tag{8}$$

where A_1, A_2, C, and D are to be determined from the boundary conditions. In the event that $\phi = 90$ deg (fibers are aligned in the direction of the tube axis) $\lambda^2 = 1$, $C_{13} = C_{23}$, $C_{14} = C_{24} = 0$, and Eq. (7) is resolved to yield

$$u = A_1 r + \frac{A_2}{r} - \frac{\rho\omega^2}{8C_{11}}r^3. \tag{9}$$

Also, for the cases when $\lambda^2 = 4$ and 9, the radial displacement takes the following form:

$$u = A_1 r^2 + A_2 r^{-2} + \frac{C_{13} - C_{23}}{3C_{11}}Dr + \frac{(2C_{14} - C_{24})(1 - 4\,\mathrm{Log}\,r)}{16C_{11}}Cr^2 + \frac{\rho\omega^2}{5C_{11}}r^3, (\lambda^2 = 4) \tag{10}$$

$$u = A_1 r^3 + A_2 r^{-3} + \frac{C_{13} - C_{23}}{8C_{11}}Dr + \frac{2C_{14} - C_{24}}{5C_{11}}Cr^2 + \frac{(1 - 6\,\mathrm{Log}\,r)\rho\omega^2}{36C_{11}}r^3, (\lambda^2 = 9) \tag{11}$$

For an n-layer cylinder, there is a different set of A_1 and A_2 for each layer. In general, then, a total of $2n + 2$ constants are to be determined. The necessary boundary conditions are (a) no radial stress on the inner and outer surfaces, (b) radial stresses and displacements are continuous at layer interfaces, and (c) no externally applied torque and axial load. Once the displacements are determined, the strains and, using the constitutive relation, the stresses are easily found.

Results

A two-layer angle-ply thick-walled cylinder made from T300/5208 rotating at a unit angular velocity is considered for numerical results. Due to the nature of the solution, stresses at higher velocities simply differ by the factor ω^2. The inner and outer radii, respectively, are $R_i = 0.10$ m., $R_0 = 0.12$ m. Elastic properties of the material are $E_z = 181$ GPa, $E_\theta = E_r = 10.3$ GPa, $\nu = 0.28$, $E_s = 7.17$ GPa and its specific gravity is 1.57.

Figure 1 shows that the magnitude of radial stress through the thickness for $(\pm\phi)$ lay-up does not depend strongly on ϕ. This fact can be used to advantage in designing a composite shaft. The designer does not have to worry about the particular lay-up to minimize the radial stress build-up. For example, a lay-up of (± 45), which provides maximum torsional stiffness, can be chosen without much reservation. The same conclusion cannot be drawn when cross-ply laminates are rotated with respect to the tube axis as Fig. 2 shows; the magnitude of the radial stress is higher, and as the laminate is rotated, considerable change in magnitude is observed.

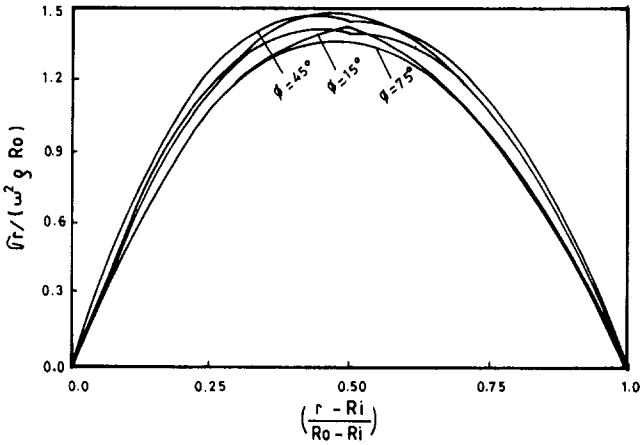

Fig. 1 Radial stress distribution in $(\pm\phi)_T$ shaft

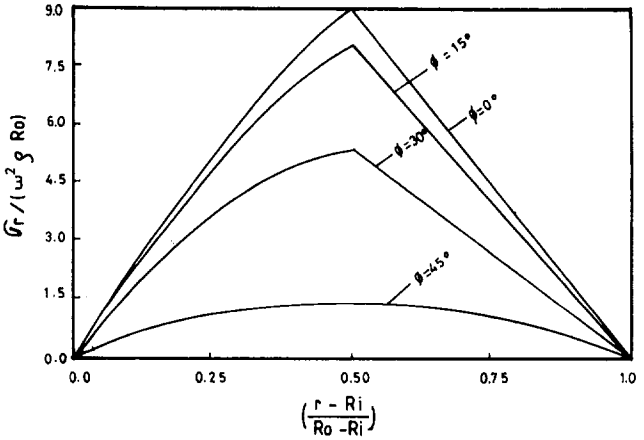

Fig. 2 Radial stress distribution in $(\phi, \phi + \pi/2)_T$ shaft

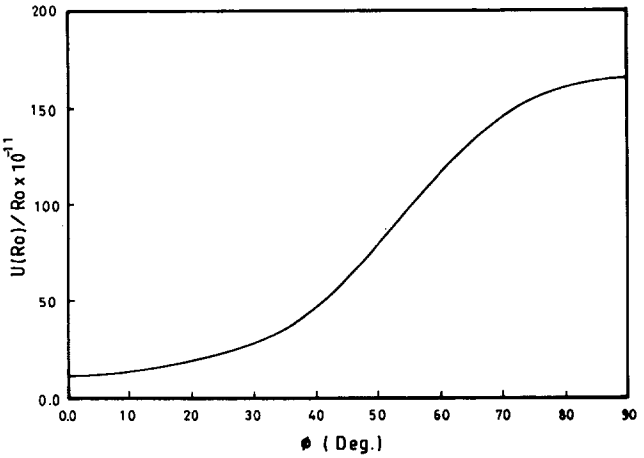

Fig. 3 Radial displacement at $r = R_0$ in $(\pm\phi)_T$ shaft

The deformations of the $(\pm\phi)$ shaft as the lay-up changes are shown in Figs. 3–5. Nondimensionalized radial displacement at $r = R_0$ is shown in Fig. 3. By Eq. (5), CR_0 gives the twist rate on the outer surface of the shaft. For $\phi = 0$ deg and 90 deg there is no extension-shear coupling, and, therefore, no twist due to radial stress. Due to the balanced nature of the lay-up it is also possible to design for zero twist for ϕ

Downloaded 04 May 2010 to 171.66.16.28. Redistribution subject to ASME license or copyright; see http://www.asme.org/terms/Terms_Use.cfm

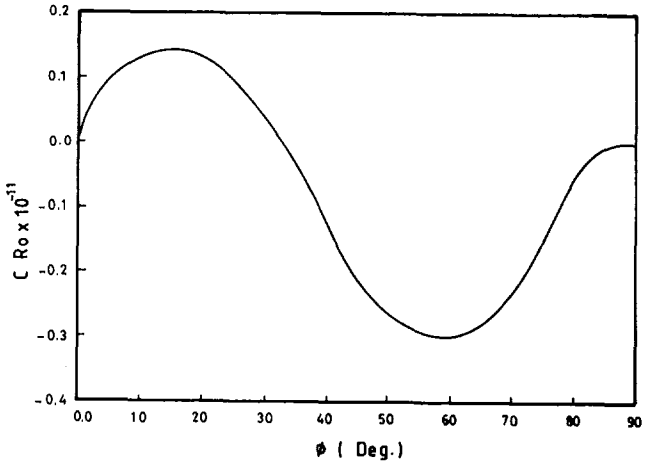

Fig. 4 Induced twist rate in $(\pm\phi)_T$ shaft

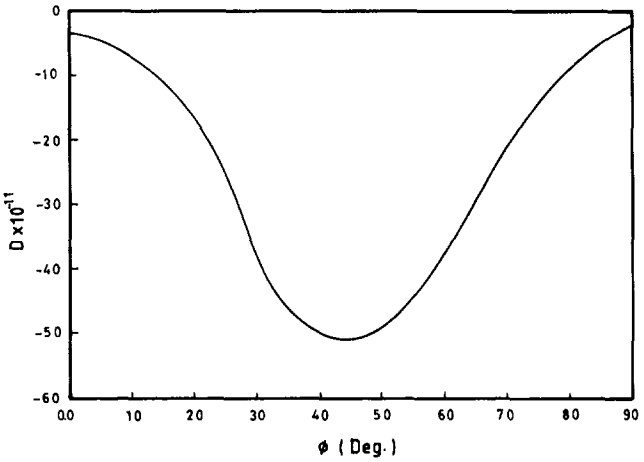

Fig. 5 Sensitivity of induced axial contraction to lay-up in $(\pm\phi)_T$ shaft

different from 0 deg or 90 deg. Due to the three-dimensional state of stress, unlike the prediction of the classical laminated plate theory, zero twist does not occur at $\phi = 45$ deg as it can be seen in Fig. 4. Finally, a graph of D versus ϕ, which shows the sensitivity of induced axial contraction to lay-up, is given in Fig. 5.

References

Hyer, M. W., Cooper, D. E., and Cohen, D., 1986, "Stresses and Deformations in Cross-Ply Composite Tubes Subjected to a Uniform Temperature Change," *J. Thermal Stresses*, Vol. 9, pp. 97–117.

Hyer, M. W., and Rousseau, C. Q., 1987, "Thermally-Induced Stresses and Deformations in Angle-Ply Composite Tubes," *J. Composite Materials*, Vol. 21, No. 5, pp. 454–480.

Pagano, N. J., and Halpin, J. C., 1968, "Tension Buckling of Anisotropic Cylinders," *J. Composite Materials*, Vol. 2, No. 2, pp. 154–167.

Tutuncu, N., and Winckler, S. J., 1993, "Stresses and Deformations in Thick-Walled Cylinders Subjected to Combined Loading and a Temperature Gradient," *J. Reinforced Plastics and Composites*, Vol. 12, No. 2, pp. 198–209.

Downloaded 04 May 2010 to 171.66.16.28. Redistribution subject to ASME license or copyright; see http://www.asme.org/terms/Terms_Use.cfm

Journal of Applied Mechanics

Discussion

Two-Dimensional Grained Composites of Extreme Rigidity[1]

Y. Grabovsky.[2]

1 Introduction and Some Notation

The recent article of Vigdergauz (1994) shows that periodically placed inclusions of the proper size and shape can generate an elastically extremal composite in the setting of two-dimensional plate theory. The derivation of the microstructure is correct and quite interesting. But the paper goes on, in Section 4, to "evaluate" the effective Hooke's law associated with this composite.

I wish to point out in this note that Section 4 of Vigdergauz' paper contains an irremediable error. Therefore the problem of evaluating this composite's Hooke's law remains at present open.

Throughout this note I will use the notations of S. Vigdergauz. I will refer to specific equations in Vigdergauz (1994) by prefixing them with the letter V. The equation numbers without prefixes refer to the formulas in this note.

2 Periodicity

From the double periodicity (henceforth referred to as periodicity) of the tensor M, using formulas (V1) and the existence of a *single-valued* potential ϕ_2 it follows that ϕ_2 is quasi-periodic, while $\bar{z}\phi_2'' + \psi_2'$ is periodic. Therefore, for periods w_k, $k = 1, 2$ ($w_1 = 1$, $w_2 = i$) we have

$$\overline{w_k}\phi_2''(z) + \psi_2'(z + w_k) = \psi_2'(z).$$

Integrating we obtain

$$\psi_2(z + w_k) - \psi_2(z) = \rho_k - \overline{w_k}\phi_2'(z), \tag{1}$$

where ρ_k, $k = 1, 2$ are some complex constants of integration. From (1) we obtain

$$\psi_2(z - 1) - \psi_2(z) = \rho_1 - \phi_2'(z),$$
$$\psi_2(z - i) - \psi_2(z) = \rho_2 - i\phi_2'(z). \tag{2}$$

Obviously, formulas (2) are inconsistent with formulas (V3). From now on we will "replace" the incorrect formulas (V3) with formulas (2).

3 Properties of $\Omega_0(z)$

The function $\Omega_0(z)$ is defined as the potential ψ_2 for "equal-strength load" associated to principal average moments P_0 and Q_0. This function is quasi-periodic. Therefore Ω_0 can be written as a sum of a periodic function and a linear function:

$$\Omega_0(z) = F_0(z) + q_1 z + q_2 \bar{z}, \tag{3}$$

where q_1 and q_2 are some complex constants and $F_0(z)$ is periodic (but not analytic!). Integrating the formula (V11) over the boundary of the inclusion and using the relation (3) we obtain

$$2ic_1 d_0 = \oint_{\Gamma_0} \Omega_0(t)dt = \oint_{K_{00}} \Omega_0(t)dt = 2iq_2.$$

So

$$\Omega_0(z) = F_0(z) + q_1(z) + c_1 d_0 \bar{z},$$

or

$$\Omega_0(z + w_k) = \Omega_0(z) + q_1 w_k + c_1 d_0 \overline{w_k}. \tag{4}$$

4 Formulas (V18) Lead to Contradiction

Let us assume the ansatz (V18). By (V18) and (4) we obtain

$$\psi_2(z + w_k) - \psi_2(z) = C_k - d_0^{-1}\big((B_0 + q_1)w_k + c_1 d_0 \overline{w_k}\big)\phi_2'(z), \tag{5}$$

where C_k are some complex constants (their exact values are unimportant). Comparing (5) with (1) we get

$$d_0^{-1}\big((B_0 + q_1)w_k + c_1 d_0 \overline{w_k}\big) = \overline{w_k},$$

whence letting $w_1 = 1$ and $w_2 = i$ we obtain

$$B_0 + q_1 = c_2 d_0,$$
$$B_0 + q_1 = -c_2 d_0. \tag{6}$$

Since $d_0 \neq 0$ the formulas (6) cannot possibly be true. Thus the ansatz (V18) leads to a contradiction. The same calculation shows that the assumption of a constant field in the inclusion for bending moments other than "equal-strength" moments always leads to a contradiction.

Author's Closure[3]

I fully agree with the comments made by Dr. Y. Grabovsky. The representation of the function $\psi_2(z)$ for an arbitrary loading given in Eq. (18) (Section (4) is inconsistent with its translation properties.

However, the basic idea of writing the potentials $\varphi_j(z)$, $\psi_j(z)$, $j = 1, 2$ in terms of the characteristic function $\Omega_0(z)$ seems correct to me. I believe that the error can be corrected by additional mathematical manipulations. I am presently pursuing this problem.

[1] By S. Vigdergauz and published in the June 1994 issue of the ASME JOURNAL OF APPLIED MECHANICS, Vol. 61, pp. 390–394.

[2] Deparment of Mathematics, Carnegie-Mellon University, Pittsburgh, PA 15213.

[3] S. Vigdergauz, R & D Division, Israel Electric Corporation, Ltd., P.O. Box 10, Haifa 31000, Israel.

Copyright © 1995 by ASME

Downloaded 04 May 2010 to 171.66.16.28. Redistribution subject to ASME license or copyright; see http://www.asme.org/terms/Terms_Use.cfm

Buckling of Composite Conical Shells[4]

M. Baruch[5]. In his calculations Liyong Tong assumed that the stiffness coefficients of a composite conical shell are constants. That is, the coefficients A_{11}, A_{22}, A_{12}, A_{66}, B_{11}, B_{22}, D_{11}, D_{22}, D_{12}, and D_{66} are independent of the coordinates of the conical shell.

In a recent paper Baruch, Arbocz, and Zhang (1994) showed that due to the geometry of the conical surface, in connection with the filament winding process necessary to build the laminated conical shell, constant stiffness coefficients can never be achieved. The stiffness coefficients of a laminated conical shell vary always and are defined functions of the coordinates of the shell. It is also shown that by proper filament winding process these functions, although still strong, can be made to be functions of the longitudinal coordinate only.

Hence the calculations performed by Liyong Tong are for some imaginary composite conical shell which cannot be practically realized.

Reference

Baruch, M., Arbocz, J., and Zhang, G. Q., 1994, "Laminated Conical Shells—Considerations for the Variations of the Stiffness Coefficients," *Proceedings of the 35th AIAA/ASME/ASCE/AHS/ASC S.S.D.M. Conference*, Hilton Head, SC, pp. 2505–2516 (also Report LR-671, Apr. 1992, TU Delft, The Netherlands).

Author's Closure[6]

When a laminated conical shell is fabricated using the filament winding process, the stiffness coefficients are functions of the coordinates of the shell. This is because the thickness and fiber orientation of each ply vary with the coordinates. It is difficult, if not impossible, to include these factors in the analytical solution. A special case for filament wound conical shells was investigated by Tong et al. (1991) who assumed that the stiffness coefficients are functions of the longitudinal coordinate only. In addition to the filament winding process, hand lay-up is another possible manufacturing process for laminated conical shells. In this process, each ply laid up on the mandrel consists of a number of splices. Evidently, for each ply the thickness is constant while the ply angle varies. Hence, assuming that the stiffness coefficients be constants is an approximation of the real laminated conical shells made using both processes. The assumption may be more appropriate for the laminated conical shells fabricated using the hand lay-up process than these using the filament winding process.

Reference

Tong, L., Tabarrok, B., Xiong, Y., and Wang, T. K., 1991, "Buckling Analysis of Axially Compressed Composite Conical Shells With Varying Stiffness," *Proceedings of the First Canadian International Composite Conference and Exhibition*, Montreal, Canada, Sept. 4–6, pp. 536–544.

[4]By Liyong Tong and published in the Sept. 1994 issue of the ASME JOURNAL OF APPLIED MECHANICS, Vol. 61, pp. 718–719.

[5]Professor Emeritus, Faculty of Aerospace Engineering, Technion—Israel Institute of Technology, Haifa 32000, Israel.

[6]Liyong Tong, Senior Research Engineer, Cooperative Research Center for Aerobspace Structures, 361 Milperra Road, Bankstown, NSW 2200, Australia.

Swerve During Three-Dimensional Impact of Rough Rigid Bodies[7]

G. P. Mac Sithigh[8]. Professor Stronge's paper is a welcome addition to the all-too-sparse literature on its subject. Indeed, the only other modern paper which treats a three-dimensional impact as an evolving process would appear to be Keller's (1986). I, myself, consider the problem in a forthcoming paper (1994). In light of my results, some points in Prof. Stronge's paper seem to me to warrant clarification.

Let $\mathbf{i}_1$, $\mathbf{i}_2$ be an orthonormal basis for the tangent plane at the impact site, let τ be the cumulative normal impulse, and let $\mathbf{v}_t := v_t[\cos\theta\mathbf{i}_1 + \sin\theta\mathbf{i}_2]$ be the relative slip velocity. Let μ be the coefficient of friction at the impact site. Define μ_*, and θ_*, such that the (rescaled) friction force required to maintain a state of stick is $\mathbf{f} := -\mu_*[\cos\theta_*\mathbf{i}_1 + \sin\theta_*\mathbf{i}_2]$. Then Keller's equations of evolution for $\mathbf{v}_t$ may be written as

$$\frac{dv_t}{d\tau} = g(\mu, \theta), \tag{1}$$

$$v_t\frac{d\theta}{d\tau} = h(\mu, \theta), \tag{2}$$

for certain functions $g(\cdot)$ and $h(\cdot)$.

Clearly, μ_* and θ_* must satisfy $g(\mu_*, \theta_*) = h(\mu_*, \theta_*) = 0$. Moreover, swerve-free motions can occur only for directions θ such that $h(\mu, \theta) = 0$. I show that, depending on the values of certain parameters, $h(\mu, \cdot)$ has either two or four zeros. In the two-root case, these two values of θ will not in general differ by π, and neither of them will coincide with θ_*. However, in problems whose impact-geometry is sufficiently symmetrical, θ_* and $\theta_* + \pi$ will be roots of $h(\mu, \cdot)$ for all values of μ. In this symmetrical situation there will, in general, be a range of μ-values for which the four-root case obtains.

In this discussion of the possibility that slip resumes after momentarily ceasing, Professor Stronge seems to assume that if this happens, the new direction of slip must be (in the present notation) θ_*. In fact, the correct condition for this to occur is that $h(\mu, \cdot)$ should have a zero, θ_1, say, with $g(\mu, \theta_1) > 0$. Provided $\mu < \mu_*$, it turns out that there exists exactly one such θ_1, and it is the new slip direction. In the symmetrical case, $\theta_1 = \theta_*$. Thus, Professor Stronge's assertion is true for sufficiently symmetrical impact geometries, but is not true in the generality claimed.

Professor Stronge does not discuss the four-root case.

Finally, an analysis of this type tacitly assumes that normal relative velocity is a monotone function of τ. There exists a critical value of μ, in excess of which this ceases to be so. This critical value depends only on the inertial properties of the colliding bodies, and on the geometry of impact. For a particular example, I find typical values for it to be in the range 1.6–3.0. While these are very high, such values of μ are to be found in the tribological literature. Thus, a model failure of this sort is a real, if remote, possibility.

References

Keller, J. B., 1986, "Impact with Friction," ASME JOURNAL OF APPLIED MECHANICS, Vol. 53, pp. 1–4.

Mac Sithigh, G. P., 1994, "Three-Dimensional Rigid-Body Impact with Friction," submitted for publication.

[7]By W. J. Stronge and published in the Sept. 1994 issue of the ASME JOURNAL OF APPLIED MECHANICS, Vol. 61, pp. 605–611.

[8]Associate Professor, Department of Mechanical and Aerospace Engineering, and Engineering Mechanics, University of Missouri-Rolla, Rolla, MO 65401. Mem. ASME.

Copyright © 1995 by ASME

Downloaded 04 May 2010 to 171.66.16.28. Redistribution subject to ASME license or copyright; see http://www.asme.org/terms/Terms_Use.cfm

Author's Closure[9]

For three-dimensional impacts where the initial speed of sliding is small enough that slip vanishes before separation, when slip vanishes the points of contact subsequently either stick or sliding resumes in a new direction, θ_*. As Professor Mac Sithigh correctly points out, in general, θ_* is not directly opposite to the direction $\bar{\phi} - \pi$ of the tangential constraint force for stick. In a second phase of slip, the direction θ_* depends on the inertia properties and the coefficient of friction μ. For an asymmetrical impact configuration with a limiting coefficient of friction for stick $f\,(=\mu_*)$, it is only in the limit as $\mu \to f$ that $\theta_* \to \bar{\phi}$.

Professor Mac Sithigh mentions that for some impact configurations, this analysis yields the correct sign for normal acceleration only if the coefficient of friction is less than a limiting or critical value. In my 1990 paper (*Proc. Roy. Soc. London*, Vol. A431, p. 169) I used the term "jamb" to describe impacts where the coefficient of friction was larger than the critical value. For these impacts, an initial change in velocity is not a continuous function of the normal impulse τ. The phenomenon of jamb is associated with Painleve's paradox as explained by Lötstedt (1981); it is likely to be important for surface damage due to abrasive wear during impact.

Reference

Lötstedt, P., 1981, *Angew. Math. Mech.*, Vol. 61, pp. 605–616.

On the Geometry of Nonholonomic Dynamics[10]

J. G. Papastavridis[11]. We would like to point out the following:

1 This is a clearly and carefully written paper; but, unfortunately, it does not contain anything new either mechanically or mathematically; see for e.g., Kondo (1955–1968), Ferrarese (1963), Gugino (1936), Dobronravov (1970, 1976), Hamel (1949), Prange (1935), Synge (1936), Schouten (1954), Vagner (1941), and Vranceanu (1936). Even its example (ball rolling on spinning turntable) can be found in Dobronravov (1976, pp. 201–209) in greater detail.

2 Further, its statement (p. 689) that Lagrange's equations are nothing but a *mathematical* rearrangement of Newton's laws (projections of the latter on certain "tangent directions" in configuration space) and its related implication that, therefore "virtual concepts" are pointless and/or irrelevant, are fundamentally flawed. To go from Newton to Lagrange, Hamel et al., one needs physical, or constitutive, postulates for the constraint reactions, in addition to the well-known differential-geometric transformation of the inertia terms. Schematically: Lagrange = Newton/Euler + Constitutive Postulate. As in continuum mechanics, one cannot do elasticity (fluid mechanics) without Hooke's (Navier-Stokes') "law;" because without them the problem is, in general, indeterminate, i.e., has more unknowns than equations. Here is why: the equations of motion of a typical system particle P: $m_p\mathbf{a}_p = \mathbf{F}_p + \mathbf{R}_p$ (where $m_p/\mathbf{a}_p/\mathbf{F}_p/\mathbf{R}_p$ = mass/acceleration/impressed force (usually known)/constraint reaction (unknown), on P; $p = 1, \ldots, N \equiv \#$ particles) contain $6N$ scalar unknowns: $3N$ for the $\mathbf{a}_p$, and $3N$ for the $\mathbf{R}_p$. To find them we have $3N$ scalar equations of motion (above); h equations of geometrical constraints: $f_H(t, \mathbf{r}_p) = 0$ $(H = 1, \ldots, h)$, and m velocity constraints: $\phi_D(t, \mathbf{r}_p, \dot{\mathbf{r}}_p) = 0$ $(D = 1, \ldots, m)$; i.e., so far we have: $6N - (3N + h + m) = (3N - h) - m \equiv n - m \equiv f$ more unknowns. The missing f equations are generated by a *physical* postulate about the $\mathbf{R}_p$'s; e.g., the D'Alembert-Lagrange principle of "ideal constraints," for passive (contact, rolling) reactions; the transformations of the projected inertia terms are important but secondary to Lagrangean mechanics. And this leads inescapably to virtual displacements/work, etc.—the symbol $\delta(\ldots)$ is not the issue. For example, how does the author propose to handle systems under general nonlinear constraints $\phi_D(t, q, \dot{q}) = 0$ $(D = 1, \ldots, m)$ and/or servo/control constraints, without additional physical postulates involving virtual displacements/work?

3 Unfortunately, Cheteav seems unaware of *all* nonholonomic mechanics authors: except Poincaré whose (less than a (total) 2-page paper) deals only with a very special case of nonholonomic "coordinates," and says nothing about such constraints. In addition, Hamel (1949—whose approach is fundamentally different and far superior to Poincaré's) explains clearly that by taking $q_{n+1} = \pi_{n+1} \equiv t$(—ime), his equations extend easily the general *rheonomic*, case; see also Prange (1935).

4 The terminology "generalized speeds" for the $\dot{\pi}^k$ is inconsistent. The $\dot{q}^k$ and $\dot{\pi}^k$ are, respectively, the contravarient holonomic and nonholonomic components of the same (system) velocity vector (see, e.g., Schouten (1954)).

5 Finally, the statement (p. 693) that nonholonomically constrained motions "will ... take place on a lower dimensional point set (of dimension $n_u < n$)" is incorrect. The global motion still takes place in an n-dimensional space; but it is restricted locally.

References

Dobronravov, V. V., 1970, *Fundamentals of Nonholonomic System Dynamics*, Vischaya Shkola, Moscow, pp. 147–184.

Dobronravov, V. V., 1976, *Foundations of Analytical Mechanics*, Vischaya Shkola, Moscow, pp. 201–209.

Ferrarese, G., 1963, "Sulle equazioni di moto di un sistema sogetto a un vincolo anolonmo mobile," *Rendiconti di Matematica, Inst. Nazional di alta Matematica*, Vol. 22, pp. 351–370.

Gugino, E., 1936, "Deduzione unitaria delle equazioni dinamische del Maggi e dell'Appell," *Rend Atti R. Accad. Naz. Roma*, 6th Series, Vol. 23, pp. 406–421.

Hamel, G., 1949, *Theoretische Mechanik*, Springer, Berlin, p. 474.

Kondo, K., editor, *RAAG Memoirs of the Unifying Study of the Basic Problems in Engineering Sciences by Means of Geometry*, 4 Volumes, Gakujutsu Bunken Fukyu-Kai, Tokyo, 1955–1968.

Prange, G., 1935, "Die allgemeinen Integrationsmethoden der analytischen Mechanik," *Encyklopädie der Math. Wissenschaften*, V. 4, Pt. 2, Art's. 12, 13, pp. 505–804, Teubner, Leipzig.

Schouten, J. A., 1954, *Tensor Analysis for Physicists*, 2nd ed., Oxford Univ. Press, Oxford, UK, pp. 194–197 (reprinted by Dover).

Synge, J. L., 1936, "Tensorial Methods in Dynamics, *University of Toronto Press, Toronto*.

Vagner, V., 1941, "Geometrical Interpretation of the Motion of a Nonholonomic Dynamical System," *Trudi Seminara po Vektornomu i Tensornomu analizi*, V. 5.

Vranceanu, G., 1936, *Les espaces nonholonomes*, Gauthier-Villars, Paris.

Author's Closure[12]

1 I do not claim that there is anything mechanically new. What is mathematically new can be discussed. Some novelty is in the notation which makes it clear that the main difference between Lagrange's method for coordinate and for noncoordinate velocity components lies in the noncommutation of certain operators.

2 What Papastavridis says here is essentially that you cannot solve the equations of motion, if you do not have expressions for, or "know," the forces. But in this respect Lagrange's equations do not differ from Newton's. Neither $\dot{\mathbf{P}} = \mathbf{F}$ nor $(d/dt)(\partial T/\partial \dot{q}^a) - (\partial T/\partial q^a) = Q_a$, where $\mathbf{F} \cdot \boldsymbol{\tau}_a \equiv Q_a$, can be solved unless one knows $\mathbf{F}$ or Q_a, respectively.

[9]W. J. Stronge, Department of Engineering, University of Cambridge, Cambridge CB2 1PZ, U.K.

[10]By H. Essén and published in the Sept. 1994 issue of the ASME JOURNAL OF APPLIED MECHANICS, Vol. 61, pp. 689–694.

[11]Associate Professor of Mechanics, School of Mechanical Engineering, Georgia Institute of Technology, Atlanta, GA 30332-0405.

[12]H. Essén, Department of Mechanics, Royal Institute of Technology, S-100 44 Stockholm, Sweden.

Downloaded 04 May 2010 to 171.66.16.28. Redistribution subject to ASME license or copyright; see http://www.asme.org/terms/Terms_Use.cfm

True, there is the constitutive relation (or assumption, or idealization) of "ideal" constraints which make the expressions for Q_a easy to get in terms of certain contributions (the "applied" forces) to the vector **F**. But, should the constraints be non-ideal, so that there is sliding (kinetic) friction; $F = \mu N$, where N is the normal force, and μ the coefficient of kinetic friction, then the Lagrange equations, $(d/dt)(\partial T/\partial \dot{q}^a) - (\partial T/\partial q^a) = Q_a$, are still valid and can, for example, help us calculate the sliding friction contribution to Q_a if we know the motion.

In this sense I still think it is wrong to say that there is a "Principle" that must be invoked to get Lagrange's equations. A constitutive relation is not a "principle" but a mathematical model of forces which sometimes holds, sometimes not. A thorough recent study of derivations of Lagrange's equations by Casey (1994) takes the same point of view as the present author as regards these matters.

3 No comment.

4 No comment.

5 My choice of wording may have been unfortunate here. Papastavridis' statement is correct.

Reference

Casey, J., 1994, "Geometrical Derivation of Lagrange's Equations for a System of Particles," *American Journal of Physics*, Vol. 62, pp. 836–847.

Analytical Solution of Hill's Equation[13]

R. T. Shield[14]. The author attempts to solve a nonlinear second-order p.d.e. for a function $u(x, y)$ by introducing a function $\phi(x, y)$. Equations (3) introduce ϕ by defining the derivatives ϕ_x, ϕ_y in terms of the unknown function u. However, in order for ϕ to exist, u must satisfy a compatibility equation obtained from (3) by setting $\partial\phi_x/\partial y$ equal to $\partial\phi_y/\partial x$, giving an additional nonlinear second-order p.d.e. for u which will not hold in general. Thus the method of solution is invalid.

Author's Closure[15]

One of the most difficult things in engineering discipline is to give an analytical solution to nonlinear differential equations encountered in science. However, on the other hand, the simplest thing is to criticize pre-established methods or solutions. I think Professor Shield prefers the second one. After the equation of motion is obtained, the establishment of a solution method becomes a pure mathematical problem. From the mathematical point of view, such transformations as those given by Eqs. (3) in the paper can well be introduced on the condition that they satisfy the equation of equilibrium and the boundary conditions. If there had been a compatibility equation as Professor Shield claimed but not showed, that would surely be Eq. (5), which is a different form of the equation of equilibrium. As can be followed from the references, the comparison of results of the present method with the numerical ones also show that the predictions of the theory are in excellent agreement with those given by numerical methods, without leaving any suspicion on the method. A second paper which is in the pipeline considers nonregular boundaries and also proves that the method gives excellent results and such claims cannot be regarded.

[13] By Y. Pala and published in the Dec. 1994 issue of the ASME JOURNAL OF APPLIED MECHANICS, Vol. 61, pp. 1000–1001.

[14] 1314 Fork Point Road, Oriental, NC 28571.

[15] Y. Pala, University of Uludag, Engineering Faculty, Gorukle, Bursa, Turkey.

Copyright © 1995 by ASME

Downloaded 04 May 2010 to 171.66.16.28. Redistribution subject to ASME license or copyright; see http://www.asme.org/terms/Terms_Use.cfm